OWL CONCEPT DESIGN REPORT

Phase A Design Review

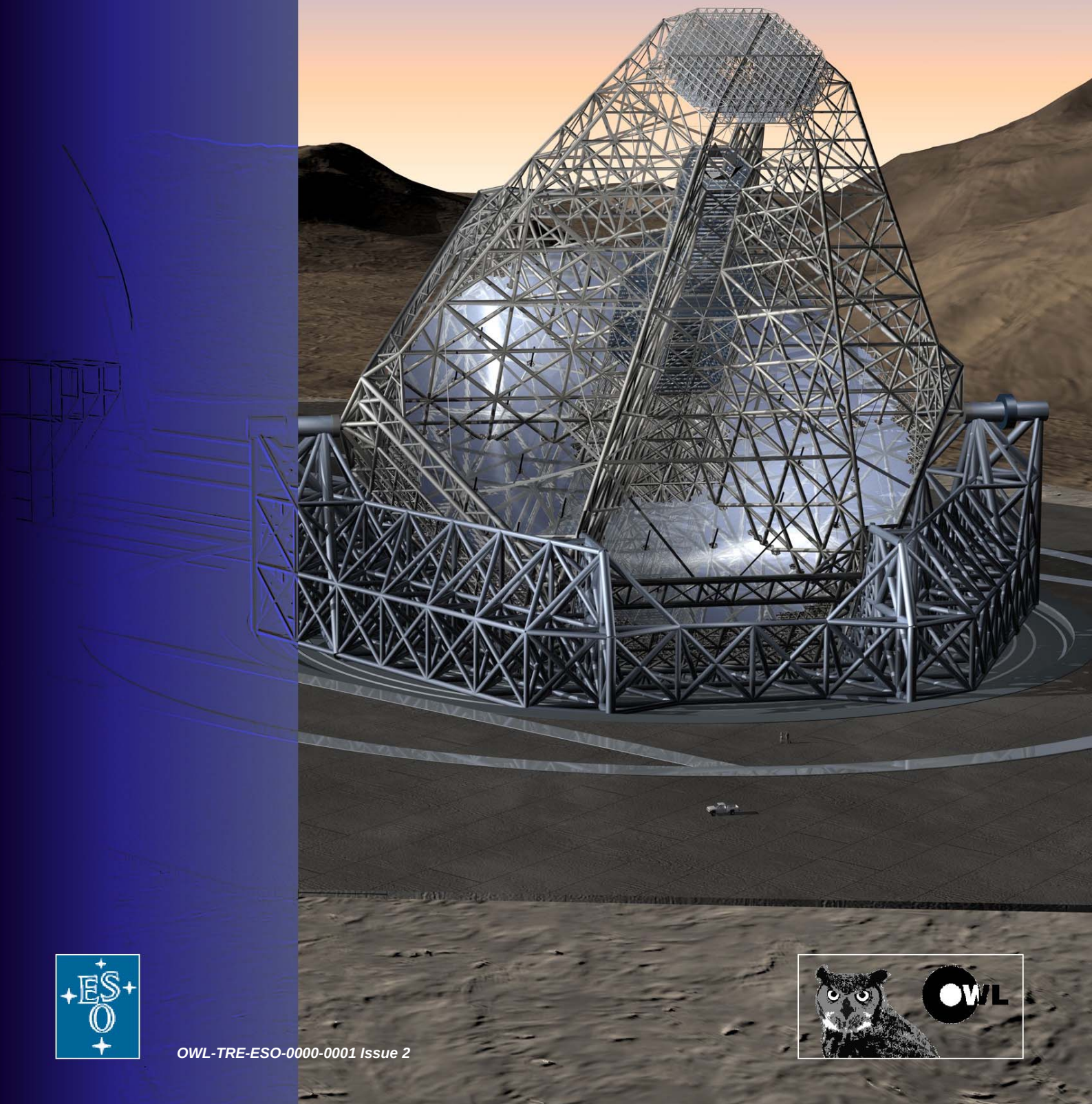

OWL-TRE-ESO-0000-0001 Issue 2

Executive Summary

This book documents the work done at ESO in the past several years towards a conceptual design of an extremely large telescope. It was named OWL for the eponymous bird's keen night vision and for being OverWhelmingly Large.

At the outset, the goals of the design work were to seek answers to two key questions:

1. Is there an underlying physical reason for the fact that optical telescopes have been increasing in size by a factor of only two, approximately every 50 years since they were invented?
2. Is there a way to contain the cost law of telescopes, traditionally proportional to the diameter to the 2.6^{th} power?

The underlying motivations for the first question were both scientific and technical:

- The increase in sensitivity of optical-infrared telescopes in the last 50 years has been due mostly to the improvements of detectors (they represent 80% of the total enhancement) rather than increases in diameter. Since detectors have achieved near-perfect efficiency, maintaining the present trend in scientific productivity requires a leap in aperture size – to 100-m by 2020.
- Strong science cases, like the imaging and characterization of Earth-like planets around other stars or the spectroscopy of the faint galaxies and other objects (e.g. gamma ray bursters and supernovae) at the edge of the Universe – to be discovered by future space missions like JWST or by OWL itself, require diameters of 100-m or more.
- The theoretically unlimited scalability of telescopes introduced by Keck with segmentation made thinking of a quantum jump in mirror diameter at least a reasonable possibility, and moved the principal challenges of a conceptual study towards other telescope subsystems (e.g. mechanics, kinematics). The existence of astronomical equipment (radio telescopes) of sizes up to 100 meters was an inspiring precedent, even taking into account their more relaxed requirements due to the much longer wavelengths.
- With the coming to maturity of wavefront control techniques, in particular adaptive optics, high angular resolution is no longer the domain of space astronomy. Future projects and missions would advantageously capitalize on healthy and cost-effective complementarities with extremely large ground-based telescopes performing at the diffraction limit. Instruments working at the diffraction limit do not necessarily increase in size with telescope diameter – depending on the field of view required.

The fundamental objective of the OWL study became trying to find an answer to the question "is a 100m filled aperture telescope feasible for about one billion Euro?". One billion is the limit that was thought "reasonable" for a large endeavor like this one since it represents an increase of a factor ≤ 2 with respect to projects already accomplished (VLT) or in development (ALMA), and would be comparable to, if not smaller than, an average, shorter lived space-borne astronomical experiment.

It should be noted however, that the financing of such a project was not explored during this design phase. Perhaps naively, it was felt that if the case were strong enough, new sources of income could be sought during the following phases of the design. Nevertheless, we are aware of the realities of the world and to the extent possible, the solutions explored were chosen for their (downsize) scalability. In fact, different designs for smaller apertures have also been analyzed and are presented in the report. If the conceptual design work were to be judged satisfactory, the following phase would concentrate on addressing the impact of financial issues and include, if appropriate, substantial re-design activities.

This report is not a complete picture of how one would build a 100-m telescope, but rather a set of approaches to, and investigations of, the challenges that we would face in building such an enormous telescope in a manageable timescale and at the lowest possible cost.

The challenge facing ESO engineers and their collaborators in academia and industry, has been to develop our 100-m concept to the point of delivering a believable budget. Clearly smaller, but still enormous, telescopes are feasible. What has been learnt from the specific developments described here is that a telescope as large as 100, or even 120-m, can be constructed using the technology available to us today. This report aims to convince the reader that such a project can potentially be done within the human and technical resources available to our community. There is still scope and need, however, for an overall harmonization of the telescope with its instrumentation in order to optimize its scientific performance.

This report is a description of research and development. The reader will find chapters that are much more advanced than others. In some cases, this is a result of our prioritization of areas we felt were more prone to potential “showstoppers”. In other cases, the developments just led us to delve deeper. Other areas are less well developed. We are fully aware of this and we actively and openly invite readers to assist us to develop these areas further.

This report has been structured as if it were a Phase A study. A requirements section is followed by detailed examination of the issues generated by the requirements and a discussion of the solutions. However, in some areas, this study process has not been closely followed nor completed and this is evident in the associated text.

While a lot of work has gone on the science case for Extremely Large Telescopes (ELTs), and a brief summary is given in the report, this is not the report’s main focus. For the purposes of this report, we assume that a 100-m telescope is a scientific goal. What then would such a telescope look like? Telescopes have been around for a long time and there has been an evolution of their design towards a set of successful (engineers can build them, astronomers can use them) Ritchey-Chrétien Cassegrain telescopes (e.g. the VLT) and a few Gregorian ones (e.g. Magellan). The mounts have changed from equatorial to alt-az, making the Nasmyth focus available as a perfect platform for heavier instruments, without the light loss of a coudé train. Most importantly, the concept of active optics control, pioneered by ESO for the NTT, has made the present 8-10 m size scale feasible. Larger telescopes with spherical primaries such as HET and SALT have also been built, but the former is just now overcoming the limitations imposed by the construction and the latter has just had first light. Moreover, although they collect light and track objects, the strict limitation of a fixed altitude axis makes them very special cases of what the average astronomer would regard as a telescope. Other ideas floated for this class of telescope include making the two mirrors move on different structures i.e., pointing the primary and then moving the secondary to point towards the primary with another system. We also looked into these approaches at a very early stage of our OWL concept discussions, but none came to fruition.

One natural approach to ELTs is to continue the evolution along the Ritchey-Chrétien path. This is exactly what both the TMT and GMT projects are doing, to create larger (still challenging!) versions of respectively Keck and MMT. However, somewhere near 30-m diameter, the underlying concept in most telescope designs ceases to be realistic in terms of timescale and cost. Retaining the NTT/VLT active optics and the Keck segmented mirrors approaches, the OWL concept borrows from the serialized production common in industry to make a 100-m feasible. In particular, choosing a spherical primary brings colossal advantages in timescale, risk and cost because it is amenable to mass production. In fact, serialized production is applied across the board to the mechanical structure, the supports and the actuators, to provide not only huge time and cost advantages but also excellent technical performance and manageable operation (maintenance) solutions. These gains will percolate to

the labor-intensive erection stage of the facility. Not only would these approaches provide much needed time and cost gains, they will additionally enable the possibility of an early start of scientific use of the telescope via a partially filled aperture at night while proceeding with the completion of the primary mirror.

What is the price to pay? Why has this not been done in the past?

There is a rather large price to pay by requiring the addition of a very large 4-mirror corrector, including two 8-m class mirrors, to the light path in order to cancel the spherical aberration and to provide a wide – by 100-m standards – diffraction limited field of view. This however has to be put into perspective. A 100-m telescope is bound to operate most of the time with Adaptive Optics correction, mostly utilizing Multi-Conjugate Adaptive Optics (MCAO). Until mass-produced AO actuator unitary cost (including control and integration costs) drop to a very small fraction of their present value, the ideal approach to ELT AO of paving the primary with hundred of thousands of actuators is not viable. This implies a corrector consisting of at least two manageable size mirrors placed at strategic locations, conjugated to the main atmospheric turbulence layers. The proposed OWL corrector will follow this approach and it should be noted that the total number of reflections prior to the detector of CONICA on the VLT is actually (slightly) larger than those projected for the ONIRICA MCAO camera on OWL.

The OWL design brings the wavefront sensing and the correcting optics into the telescope train and uses them as an integral part of the facility. This is a natural extrapolation of the active telescope pioneered by ESO. At the NTT, deforming the primary was nice to have (it corrected the polishing errors more than anything else) but the true novelty was that, for the first time, a telescope could keep itself actively collimated. A third of an arcsecond images could be obtained by visiting astronomers to a common user facility. The VLT, the next logical step in the evolution, not only keeps itself aligned but also optimizes the shape of the primary to correct for gravity deformations and removes the shakes that affect any structure exposed to the elements. Hundreds of hours of 0.3 arcsecond imaging and spectroscopy are provided to VLT users. OWL, by design, keeps itself aligned, fixes gravity deformations, removes the shakes and corrects for the atmosphere, in addition to relaxing fabrication tolerances. The design proposed is an evolutionary one in both control and optics.

ESO realizes that it has no direct experience with segmentation although the proposed OWL design has two segmented mirrors. The reader will find frequent reference in this report to the experience of others. Of course, we have gained a huge amount of confidence regarding issues such as phasing from the experience of our Californian colleagues who built and operate the segmented Keck telescopes and must be regarded as the experts in segmentation. The Californian design for an ELT has a much smaller diameter primary mirror than our 100-m concept, but – due to their smaller unit size – not a significantly different number of segments. The phasing problem clearly scales as the number of interfaces that each segment will have. That depends on their shape rather than number. The complexity of the control does however depend linearly on the number of segments. We therefore will argue that even though we do not yet have direct, hands-on experience with segmented mirrors, this is a problem we believe has an affordable solution. As the report shows, not only are we working in-house to gain expertise through the Active Phasing Experiment, but also an excellent collaboration with the GTC team is already in place through FP6. In fact, technical time at the GTC, specifically to gain experience with segmentation, is foreseen as part of the in-kind contribution of Spain to join ESO.

A lot of thought, both by ESO and industry, has been put into the challenge of manufacturing, testing and shipping the thousands of segments needed for OWL. The confidence of industry is of course reassuring, although one must not be blinded by the enthusiasm of optical firms to supply thousands of tons of precision glass. In the report you will find that more than one supplier would be keen to bid. Moreover, the manufacturing experience for a serialized production of mirror segments is already in place within Europe. The cost, in time and money, of climbing the learning curve of segmentation has already been paid. We are ideally placed to take advantage of this.

The development of the mechanics within the report is probably the most advanced aspect described. Ingenious solutions to the challenges of constructing, transporting and erecting an enormous telescope have been developed over the years. The evolution presented in the report shows a progressively stiffer and cheaper design. The present concept can be retroactively understood as a ‘fractal’ design. This comes from the search for a solution that would provide

minimal weight (60 times less dense that a VLT Unit telescope) with extremely rigid and a fast thermal exchange, i.e. have minimal volume and maximal area. The optical design evolved to match what could be built mechanically. It is clear that moving structures of the size proposed can be fabricated and erected. They already exist, even in astronomy.

The design presented is a clear step in the evolution of the control of telescopes. When moving weights were used to drive telescopes, feedback was non-existent. The wonders of guiding (whether by eye or automatically) brought higher accuracy requirements on the control of the telescope mounts. Even today, most telescopes will move hundreds of tons of metal and glass to keep the object within a slit. The requirements on the telescopes have become progressively stricter. The VLT, although built to exacting requirements (azimuth tracks to 10 milli-arc seconds rms), has revealed a better way of working. Control of the focal plane is better than control of the mount. On OWL, we will take this philosophy to the natural next stage. We will not try to track thousands of tons to astronomical accuracies. The design, with its multiple mirrors ahead of the focus, allows us to control the focal plane to keep the objects in the 'slits'. The mechanics of OWL are thereby made easier to build and move. The complexity has moved to where the scales are manageable with our current engineering skills. You will see this approach in the adapter-rotator chapters where innovative designs for the multiple guide probes are presented. While the terminology has stuck, these 'guide' probes no longer guide the telescope but rather sense aberrations from tip and tilt, focus, astigmatism, coma etc. They no longer move the telescope but rather the optics. Other control loops feed downwards to the mount. Together with its fractal mechanical design, the OWL control system concept provides us with some optimism for achieving operationally the exacting wavefront tolerance – 10 nm rms – even when a sizable wind (at least 12 m/s) is blowing on the telescope structure. in open-air.

Obviously the adaptive optics challenge we face is enormous. However, we take solace in the fact that even a gradual implementation would allow some solid science to be done early. Exo-planet detection is a special case as it needs none of the multiple lasers and exceedingly complex wavefront sensors and adaptive mirrors associated with full Multi-Conjugate Adaptive Optics systems. Rather, it requires just a baseline single conjugate AO with a bright natural star right in the center. On the other hand, achieving good light concentration in the H-band diffraction peak – not necessarily extreme AO with 85% plus Strehl – calls for a deformable mirror with close to 10^5 actuators and an associated fast Real-Time Computer. This feat is provisionally planned only for the 2^{nd} phase of AO deployment on the OWL facility.

From this point to where we would like ultimately to be, is a complex path. Multiple lasers, ground layer, multi-conjugate, multi-object and other flavors of adaptive optics are all discussed in the report. We have grown most in confidence in the area of AO from the evolution that has taken place before our very eyes – and hands – during the last decade. When the first unit telescope of the VLT was being erected, AO at ESO was ADONIS on the 3.6-m at La Silla. It was complex and far from a common user facility. AO at the VLT does not require specialist operators and is self-optimizing. In as much as down time can reflect robustness, AO at the VLT is just another tool. Lasers and the survivors from the pantheon of AO will evolve to similar levels of robustness. Clearly we do not wish OWL to be their test-bed and, for this reason, deformable mirrors are being constructed for the VLT. Furthermore, a laboratory/on-sky demonstrator of multi-conjugation techniques (MAD) is already partly integrated and has achieved closed-loop "first light" in the laboratory.

The project schedule to first light is defined mainly by the production of the 8-m mirrors of the corrector, with commitments for their procurement delayed until major subsystems such as enclosure and telescope structure have reached final design. The project schedule is also such that the longest possible amount of R&D time is foreseen for AO development. A progressive implementation of capabilities over at least another 15 years of development will be required before the most difficult requirements are met. It is clear however that, if by the time of the preliminary design review, the AO prospects of substantial advances are not convincingly on the right path, a thorough reassessment of the telescope size and capabilities should be made, quite independently of budget or other considerations.

All telescopes need a home. A global search, coordinated amongst all interested parties, is ongoing to find the right one. A home with, or near to infrastructure, not particularly seismic, with good weather and welcoming hosts would be very nice. As you will find in the report, options exist. They are being evaluated before a final recommendation is to be made. Detailed design

will need to take into account the site specifics and therefore a decision will need to be made soon. We all recall the early plans for the VLT enclosures and the big changes that the move to Paranal entailed for the project.

For a telescope such as OWL, the instruments can no longer be regarded as add-ons designed and strapped onto the telescope at the last minute. Selecting and designing an instrumentation set that could fulfill the major science drivers selected for OWL should be seen as a last crucial step, “closing the loop” on the feasibility of the whole project. We have started to investigate this issue only about a year ago because we felt that a consolidated telescope design was necessary to define a set of preliminary interfaces. Quite naturally, initial results, presented in this report, point more to identified problems than to their solutions. What lies ahead in achieving more powerful facilities, is a need for identifying key enabling technologies – e.g. moving from static to active instruments. Clearly we need to make meaningful tradeoffs between the essentially unlimited astronomical appetite for field of view and target multiplexing, and associated technical and cost constraints. Ample time and resources will be allocated in the OWL Phase B to explore innovative solutions, in synergy with the activities of the FP6 ELT Design Study.

In parallel, a thorough iteration of the optical design to take into account requirements identified during the instrument conceptual design studies should also take place and is included in the proposed plan.

The instrument studies already included here consist of a healthy mix between potential ‘work horse’ instruments (e.g. ONIRICA, MOMFIS) and more focused or specialized instruments designed to answer specific questions (e.g. CODEX) or to open an entirely new window in astrophysics (e.g. QuantEye). They confirm that a larger telescope will open up the discovery space leading to exciting new science. While not embracing all the possibilities that can be imagined, they do suggest that designing and building such instruments for a 100m telescope will be a challenging exercise which may require tradeoffs on both the instrument and telescope sides in order to reach the best compromise in terms of overall scientific performance.

After reading the report, we hope that, as discussed earlier in this summary, the reader will be convinced that the question of ‘can we?’ is answerable with a qualified ‘yes’. Qualified by ‘but it will be quite some work’ for ESO, for its community and for the whole astrophysical community at large. The next crucial step ahead for us will be to determine the telescope size that we can afford, in terms of risks, financial and human resources, and timescales for the construction. And to start designing it.

Content

Index of tables **26**

Index of figures **31**

1. Scope **51**

2. Overview **53**

2.1 Objectives ***53***

2.2 Scientific potential of a 100-m class telescope ***54***

2.3 Context ***58***

2.4 The OWL concept ***60***

2.4.1 The history of telescope growth. 60

2.4.2 A giant telescope in an industrial context 61

2.5 Top level requirements ***62***

2.6 Design overview ***64***

2.6.1 Telescope optics 65

2.6.2 Structural design 71

2.6.3 A controlled opto-mechanical system 73

2.6.4 Enclosure, open air operation 78

2.6.5 Instrumentation 80

2.7 Progressive implementation ***83***

2.8 Observatory operation ***85***

2.9 Site considerations ***86***

2.10 Plans for final design and construction ***88***

2.11 Cost estimate 91

2.12 The ELT Design Study 93

2.13 Scalability 95

2.13.1 Science 95

2.13.2 Requirements 96

2.13.3 Concept design 97

2.13.4 Cost and schedule 98

2.14 Risk areas 99

2.14.1 Environmental risks 100

2.14.2 System risks 102

2.14.3 Risk management 107

3. Science case 109

3.1 Introduction 109

3.2 Science with OWL 110

3.2.1 OWL performance 111

3.2.1.1 Confusion about confusion 111

3.2.1.2 Étendue, or the AΩ product 111

3.2.1.3 Signal-to-noise vs diameter D 111

3.2.1.4 The power of a 100m telescope 112

3.2.1.5 The wavelength range 114

3.2.2 The highlight science cases 116

3.2.2.1 Terrestrial Planets In Extra-Solar Systems 116

3.2.2.2 Resolved Stellar Populations in a representative sample of the Universe 118

3.2.2.3 The First Objects And Re-Ionization Structure Of The Universe 118

3.2.2.3.1 The highest Redshift Galaxies 118

3.2.2.3.2 Galaxies at the end of Re-ionization 119

3.2.2.3.3 Probing the universe during the re-ionization epoch 120

3.3 Requirements from the science case 121

4. Top level requirements 127

4.1 Introduction 127

4.2 Overall requirements 127

4.2.1 The OWL telescope 127

4.2.2 The Conceptual Design (Phase A) 128

4.2.3 Evolution of the Top Level requirements 128

4.2.4 Operational lifetime 128

4.2.5 Location of OWL 128

4.2.6 Optical design 128

4.2.7 Maintenance 129
4.2.8 Instrumentation 129
4.2.9 Coating optimization 129
4.2.10 Astronomical site monitor 129
4.2.11 Safety 129
4.3 Performance requirements 129
4.3.1 Telescope transmission 130
4.3.2 Emissivity 130
4.3.3 Sky coverage 130
4.3.4 Image quality 130
4.3.4.1 Telescope 130
4.3.4.2 Adaptive Optics 130
4.3.4.2.1 Telescope AO 131
4.3.4.2.2 Single Conjugate AO 131
4.3.4.2.3 Multi Conjugate AO 131
4.3.4.2.4 Ground Layer AO 132
4.3.4.2.5 Multi-Object AO 132
4.3.4.2.6 Extreme AO 132
4.3.4.2.7 AO at optical wavelengths 133
4.3.4.2.8 Laser Guide Stars 133
4.3.5 Atmospheric dispersion compensation 133
4.3.6 Atmospheric refraction 133

5. System Engineering 135

5.1 Level 1 requirements 135

5.2 Design constraints and guidelines 137

5.3 Complex Systems, methods and modelling 138
5.3.1 Complex System 138
5.3.2 Methods 139
5.3.2.1 Science and Engineering. 139
5.3.2.1.1 System Design 140
5.3.2.1.1.1 Top Level Requirements 140
5.3.2.1.1.2 System Requirements Management 140
5.3.2.1.1.3 Functional Analysis 141
5.3.2.1.1.4 Logical Architecture Definition 142
5.3.2.1.2 Physical Design & Manufacturing 143
5.3.2.1.2.1 Physical Design 144
5.3.2.1.2.2 Manufacturing 144
5.3.2.1.3 System Integration 144
5.3.2.2 Tools 145
5.3.3 Modelling 145
5.3.3.1.1 Modelling Approach 145

5.3.3.1.2 Architecture Concept 148
5.3.3.2 DOORS Model, System requirements management 151

5.4 Disturbances Characterization 152
5.4.1 Environment 152
5.4.1.1 Wind 152
5.4.1.1.1 Wind characterization from literature 152
5.4.1.1.1.1 Wind Velocity, integral length and turbulence intensity Profiles 152
5.4.1.1.1.2 Power Spectral Density 153
5.4.1.1.2 Computational Fluid Dynamics (CFD) 155
5.4.1.1.3 Full scale measurements 157
5.4.1.1.4 Wind tunnel measurements 158
5.4.1.2 Atmospheric turbulence (AO) 159
5.4.1.3 Temperature, humidity, rain, snow, ice, dust, radiation 161
5.4.1.4 Microseismicity 164
5.4.2 System Induced Disturbances 164
5.4.3 Human induced disturbance 164
5.4.3.1 Camp, hotel, sewage, transport, etc 164
5.4.3.2 Power generation 164
5.4.3.3 Light pollution 165
5.4.4 Survival load case of the opto-mechanical elements 165
5.4.4.1 Earthquake 165
5.4.4.2 Wind 166
5.4.4.3 Temperature 167

5.5 Error budgets 167

5.6 Reliability, Availability, Maintainability, Safety (RAMS) 180
5.6.1 Product Assurance Roles & Responsibilities 180
5.6.2 Safety 180
5.6.2.1 General 180
5.6.2.2 Safety Assurance Program and organization 181
5.6.2.3 Safety assurance activities 181
5.6.3 Reliability and Maintainability 181
5.6.3.1 Failure Tolerance 181
5.6.3.2 Single point failure list 181
5.6.3.3 Reliability and Maintainability Data File 181
5.6.3.3.1 Reliability Engineering 182
5.6.3.3.1.1 Reliability Analyses 182
5.6.3.3.2 Maintainability Engineering 182
5.6.3.3.2.1 Establishment of Maintainability Requirements 182
5.6.3.3.2.2 Maintainability Inputs to Maintenance Plan 183
5.6.3.3.2.3 Maintainability Analyses 183
5.6.3.3.2.4 Maintainability Demonstration 183
5.6.4 Conclusion – OWL Dependability Objective Sheet 184

6. Telescope optics 185

6.1 Requirements and guidelines 185

6.2 Optical design 188

6.2.1 Design trade-off 188
6.2.2 Baseline design 194
6.2.3 Optional corrector 198
6.2.4 Reduced aperture designs 198
6.2.5 Future design iterations 201

6.3 Optical characteristics 202

6.3.1 Nominal optical quality 202
6.3.2 Vignetting 206
6.3.3 Stray light and baffling 207
6.3.4 Emissivity 208
6.3.5 Sensitivity analysis 209
6.3.6 Imaging of turbulent layers 213
6.3.7 Imaging of Laser Guide Stars 216

6.4 Diffraction and high contrast imaging 218

6.4.1 Diffraction 218
6.4.1.1 Structure of PSF in diffraction-limited regime 218
6.4.1.1.1 Pupil modelling elements 218
6.4.1.1.2 Secondary mirror support 220
6.4.1.1.3 “Missing” segments 220
6.4.1.1.4 Ropes 221
6.4.1.1.5 Diffraction by the gaps 221
6.4.1.2 PSF representation: intensity slices 223
6.4.1.3 Effects of phasing errors on the PSF 224
6.4.1.3.1 Diffraction associated to piston and tip-tilt 224
6.4.1.3.2 Intensity slice representation (FoV=1”, λ=650nm) 224

6.5 Optics design and fabrication 226

6.5.1 Segments 226
6.5.1.1 Segment size and distribution 227
6.5.1.2 Segments thermo-mechanical properties 229
6.5.1.3 Segments substrates 230
6.5.1.4 Segments polishing 236
6.5.1.5 Segments supports 240
6.5.2 Corrector optics 241

6.6 Safety 245

7. Non-adaptive wavefront control 247

7.1 Requirements 247

7.2 General control architecture 248
7.2.1 Wind rejection 251
7.2.2 Friction compensation 256
7.2.3 Field stabilization 260

7.3 Pre-alignment 263

7.4 Active optics 265
7.4.1 Introduction 265
7.4.2 Alignment of the segments in M1 and M2 265
7.4.3 Correction of mirror deformations 266
7.4.4 Correction of the rigid-body alignment of the mirrors 268
7.4.5 Relationship between various types of aberrations 269
7.4.6 Operation with adaptive optics 269

7.5 Phasing 270
7.5.1 Phasing strategy 270
7.5.2 Blind phasing 270
7.5.3 Position sensors 271
7.5.4 On-sky calibrations 271
7.5.4.1 Optical Phasing 271
7.5.4.2 On-sky phasing techniques - overview 271
7.5.4.2.1 Modified Shack-Hartmann technique 271
7.5.4.2.2 Modified Mach-Zehnder technique 272
7.5.4.2.3 Phase filtering technique 273
7.5.4.2.4 Diffraction image technique 274
7.5.4.2.5 Pyramid technique 275
7.5.4.2.6 CCD 275
7.5.4.3 Open loop performance 276
7.5.4.3.1 The optical signal 276
7.5.4.3.2 The CCD images 276
7.5.4.3.3 Signal analysis 277
7.5.4.3.4 Results 278
7.5.4.3.5 Increase of the capture range 279
7.5.4.3.6 Calibration 279
7.5.4.4 Identification of the borders 280
7.5.4.5 Closed-loop results 280
7.5.4.6 Phasing OWL 281
7.5.4.6.1 Phasing of one petal 281
7.5.4.6.2 Phasing of the petals 285
7.5.4.6.3 Measurements under aberrations 285
7.5.4.6.4 Disentangling M1&M2 285
7.5.5 Control of segmented mirrors (M1 & M2) 286

7.6 Active Phasing Experiment (APE) 295
7.6.1 Opto-mechanical design 295

7.6.2 Internal Metrology 297
7.6.3 The Phasing WaveFront Sensor Module 297
7.6.4 Schedule and observations 297

8. Adaptive Optics 299

8.1 Introduction 299

8.2 First generation Adaptive Optics 299

8.2.1 Single Conjugate Adaptive Optics 300
8.2.1.1 Performance requirements 301
8.2.1.2 Implementation Concept 303
8.2.1.2.1 M6 Adaptive Mirror unit 303
8.2.1.2.2 Visible wavefront sensor unit 306
8.2.1.2.3 Infrared Pyramid WFS 309
8.2.1.2.4 Real Time Computer (RTC) 312
8.2.1.3 Predicted performance 313
8.2.1.3.1 Visible Shack Hartmann wavefront sensor 313
8.2.1.3.2 Infrared Pyramid Wavefront sensor 314
8.2.1.3.3 Performance at 10 microns and beyond 316
8.2.1.3.4 Effect of the outer scale of turbulence on performance 317
8.2.1.4 Near-Term development plan 318
8.2.1.4.1 Modelling and Simulation 318
8.2.1.4.2 AO Concept and design 319
8.2.1.4.3 AO key elements status and development 321
8.2.1.4.4 Testing a large DM in closed loop 334
8.2.1.4.5 Detectors for wavefront sensors 336
8.2.1.4.6 Real Time Computer 337
8.2.2 Ground Layer Adaptive Optics 342
8.2.2.1 Performance requirements 344
8.2.2.2 Implementation Concept 346
8.2.2.2.1 Corrector and wavefront sensors 346
8.2.2.2.2 Control and Real Time Computer 346
8.2.2.3 Predicted performance 348
8.2.2.3.1 Sky coverage 348
8.2.2.4 Near-Term development plan 352
8.2.2.4.1 Modelling and Simulation 352
8.2.2.4.2 AO concept and design 352
8.2.2.4.3 AO key component status and development 353
8.2.3 Distributed Multi Object Adaptive Optics 354
8.2.3.1 Implementation Concept 356
8.2.3.1.1 Overview 356
8.2.3.1.2 Wavefront sensor 357
8.2.3.1.3 Micro deformable mirror 357
8.2.3.1.4 Control and Real Time computer 358

8.2.3.2 Predicted performance 360
8.2.3.3 Near-Term development plan 361
8.2.3.3.1 Modelling and Simulation 362
8.2.3.3.2 AO Concept and design 362
8.2.3.3.3 AO key component status and development 363

8.3 Second generation Adaptive Optics 363

8.3.1 Multi Conjugate Adaptive Optics 364
8.3.1.1 Performance requirements 365
8.3.1.2 Implementation Concept 366
8.3.1.2.1 Corrective elements 366
8.3.1.2.2 Wavefront sensors 367
8.3.1.2.3 MCAO control 367
8.3.1.2.4 Real Time Computer 367
8.3.1.3 Predicted performance 368
8.3.1.3.1 MCAO sky coverage 368
8.3.1.3.2 Simulation Results 369
8.3.1.4 Mid-Term development plan 373
8.3.1.4.1 Modelling and Simulation 373
8.3.1.4.2 MCAO design 373
8.3.1.4.3 MCAO calibration issues 374
8.3.1.4.4 AO key component status and development 375
8.3.2 Extreme Adaptive Optics and High Contrast Imaging: EPICS project 381
8.3.2.1 EPICS Top level performance requirements 381
8.3.2.2 EPICS Adaptive Optics concept 381
8.3.2.2.1 Common path system: 382
8.3.2.2.2 Individual Channel paths 384
8.3.2.3 Coronagraphy 384
8.3.2.4 Correction of co-phasing errors 386
8.3.2.5 EPICS performance 388
8.3.2.6 Technological requirements for EPICS 389
8.3.2.7 Future development plan 390

8.4 Third generation Adaptive Optics 392

8.4.1 Introduction 392
8.4.2 Toward the 3rd generation AO systems with LGSs 392
8.4.2.1 From Single Conjugate to Laser Tomography AO 392
8.4.2.2 Laser assisted Ground Layer Adaptive Optics 393
8.4.2.3 Laser Assisted Multi-Conjugate Adaptive Optics 394
8.4.2.4 Laser Assisted Multi-Object Adaptive Optics 395
8.4.3 ELTs and LGSs issues 395
8.4.4 Potential solutions to LGS issues 397
8.4.4.1 Spot Elongation 397
8.4.4.2 Spot aberrations 397
8.4.4.3 Fratricide effect 398
8.4.5 New Laser Guide Star concepts 398

8.4.5.1 Pseudo Infinite Guide Stars ... 398
8.4.5.2 Sky Projected Laser Array Shack-Hartmann ... 399
8.4.5.3 Virtual Wavefront Sensor ... 399
8.4.5.4 Variable Wavefront Sensors ... 400
8.4.5.5 Laser Guided AO with on-sky phase shifting Interferometry ... 401
8.4.6 Strategies of the LGS program for OWL ... 404
8.4.6.1 Background ... 404
8.4.6.2 Status and planned tasks ... 404

9. Telescope structure and kinematics ... 407

9.1 Design Principles ... 407

9.2 Design Assumption ... 409

9.3 Design Evolution ... 409

9.3.1 1997 Design ... 411
9.3.2 1998 Design ... 411
9.3.3 1999 Design ... 412
9.3.4 2000 Design ... 414
9.3.5 2002 Design ... 414
9.3.6 2004 Design ... 415
9.3.7 2005 Design (current baseline). ... 416

9.4 Conceptual Design. ... 416

9.4.1 Structural design ... 417
9.4.1.1 Material selection ... 417
9.4.1.2 Structural element selection ... 418
9.4.2 Fractal Design ... 419
9.4.2.1 Base module ... 419
9.4.3 Azimuth Structure. ... 420
9.4.4 Altitude Structure. ... 421
9.4.4.1 Primary mirror obscuration ... 423
9.4.4.2 Structural ropes ... 423
9.4.4.2.1 Material selection ... 424
9.4.4.2.2 Wind on ropes ... 425
9.4.4.3 Focal Stations ... 426
9.4.4.3.1 Alternative focal station. ... 427
9.4.5 Sub-Systems design. ... 428
9.4.5.1 Kinematics ... 428
9.4.5.1.1 Torque requirement. ... 428
9.4.5.1.2 Acceleration. ... 428
9.4.5.1.3 Friction Drive & Bearing. ... 428
9.4.5.1.4 Hydrostatic pads and direct drive. ... 434
9.4.5.1.5 Magnetic Levitation ... 435
9.4.5.2 Corrector. ... 437

9.4.5.3 M3 and M4 Unit 438
9.4.5.4 M5 Unit 438
9.4.5.5 M6 Unit 438
9.4.5.5.1 Interface to the corrector 439
9.4.5.5.2 M6 Unit design volume 439
9.4.6 Segments support system. 440
9.4.6.1 Segment assembly. 441
9.4.6.2 Extractors. 441
9.4.6.3 Position Actuators characteristics. 442
9.4.6.3.1 Axial stiffness 442
9.4.6.3.2 Load cases. 442
9.4.6.3.3 Accuracy. 442
9.4.6.3.4 Stroke 442
9.4.6.3.5 Closed Loop Bandwidth. 443
9.4.6.3.6 Maximum tracking rate 443
9.4.6.3.7 Maximum slewing rate 443
9.4.6.3.8 Heat dissipation. 444
9.4.7 Wind Evaluation Breadboard 444
9.4.7.1 WEB layout. 444
9.4.8 Internal Metrology 446
9.4.9 Thermal control and design provision 446
9.4.9.1 Thermally controlled volumes 446
9.4.9.2 Passive thermal control of the mechanical steel structure. 447
9.4.10 Safety 447
9.4.11 Mass & Moment breakdown. 448

9.5 Structural analysis 448
9.5.1 Analysis tree 450
9.5.2 Static Analysis 451
9.5.2.1 Gravity 452
9.5.2.2 Steady State Wind 453
9.5.3 Thermal analysis 454
9.5.4 Dynamic Analysis 458
9.5.4.1 Modal 458
9.5.4.2 Dynamic Wind Load 463
9.5.4.2.1 Macro scale wind effect on segmented mirrors 464
9.5.4.2.2 Micro scale wind effect on phasing error 467
9.5.4.3 Effect of soil and foundation 469
9.5.5 Safety Analysis 471
9.5.5.1 Wind 471
9.5.5.2 Earthquake 472
9.5.5.3 Buckling 472
9.5.5.4 Fatigue 473
9.5.5.5 Pretension of ropes 474

9.6 Structure design Options 475

9.6.1 Base line High configuration (2005 design) ... 475
9.6.2 Glass Ceramic low configuration ... 475
9.6.3 SiC high and low configurations ... 476
9.6.4 Glass Ceramic 60 m configuration ... 477

10. Adapter-Rotator ... 479

10.1 Requirements ... 479

10.2 Constraints ... 480

10.3 Notional Design ... 481

10.3.1 Pick-up mirrors ... 482

10.4 Adapter-Rotator configuration vs instruments and functions ... 483

11. Enclosure and infrastructures ... 485

11.1 Telescope enclosure ... 485

11.1.1 Baseline design description ... 487
11.1.2 Concrete works ... 495
11.1.3 Structure and mechanisms ... 497
11.1.4 Alternatives ... 501

11.2 Infrastructures ... 506

11.2.1 Mirrors maintenance ... 508
11.2.2 Laboratories ... 509
11.2.3 Control room and personnel offices ... 510
11.2.4 Air conditioning and chilled water plants ... 510
11.2.5 Fluid distribution ... 511
11.2.6 Power station ... 511
11.2.7 Personnel accommodation building ... 512
11.2.8 Site preparation ... 512
11.2.8.1 Camp and first infrastructures ... 513
11.2.8.2 Earth works for telescope platform ... 513
11.2.8.3 Access roads to the Observatory ... 515
11.2.8.4 Miscellaneous ... 516

12. Instrumentation ... 517

12.1 Technical instrumentation ... 517

12.2 Science instrumentation ... 518

12.2.1 Scope of the instrument concept studies ... 518
12.2.2 Instrument Concept Studies ... 519
12.2.3 CODEX: high resolution. ultra-stable VIS-R spectrograph ... 519

12.2.3.1 QuantEYE 523
12.2.3.2 Hyper-telescope NIR camera 526
12.2.3.3 ONIRICA: OWL NIR Imaging Camera 527
12.2.3.4 MOMFIS: Multi Object. Multi Field Near –IR Spectrograph 534
12.2.3.5 EPICS: Exo- Planet Imaging Camera Spectrograph 537
12.2.3.5.1 Science drivers 538
12.2.3.5.2 Targets 538
12.2.3.5.3 Top level requirements 539
12.2.3.5.3.1 Instrument. general 539
12.2.3.5.3.2 Instrument main observing modes and performance requirements 540
12.2.3.5.3.3 Requirements to the site . the telescope and observing time 541
12.2.3.5.4 InstrumentConcept 541
12.2.3.5.5 Adaptive optics 542
12.2.3.5.6 Coronagraphy 543
12.2.3.5.7 Instruments 543
12.2.3.5.7.1 Differential Imager 543
12.2.3.5.7.2 Integral Field Spectrograph 544
12.2.3.5.7.3 Differential Polarimeter 544
12.2.3.5.8 Integration times for a 5 σ detection in case of background limited observation 545
12.2.3.5.9 Need for 100m 548
12.2.3.5.10 Systematic Errors 548
12.2.3.5.11 Technological requirements for EPICS 548
12.2.3.6 T-OWL: Mid-Infrared Imager 549
12.2.3.7 SCOWL : Imager at Submillimeter Camera at OWL 553
12.2.4 Versatile Instruments and Dedicated Experiments or Surveys 557
12.2.5 Telescope Interface and Deployment Considerations 557
12.2.6 Adaptive Optics Requirement Overview 559
12.2.7 Detector Requirement Overview 559

13. Transport and integration 561

13.1 Transport 561
13.1.1 Design provisions 561
13.1.1.1 Mechanics 561
13.1.1.2 Optics 562

13.2 Site integration 562
13.2.1 Design provisions 563
13.2.1.1 Mechanics 563
13.2.1.2 Alignment metrology 563
13.2.1.3 Telescope truss structure integration 564
13.2.1.3.1 Phase 1 564
13.2.1.3.2 Phase 2 565
13.2.1.3.3 Phase 3 565
13.2.1.3.4 Phase 4 566

13.2.1.3.5 Phase 5 567
13.2.1.3.6 Phase 6 567
13.2.1.3.7 Phase 7 568
13.2.1.4 Segment integration 569
13.2.1.4.1 Segment handling tool 570
13.2.1.5 Optics 573
13.2.1.5.1 Initial alignment 573
13.2.2 Safety 574

14. Site Characterisation 575

14.1 Introduction 575
14.1.1 Instrumentation and methods 575
14.1.1.1 Cloudiness 575
14.1.1.2 Precipitable Water Vapor 576
14.1.1.3 Aerosol Extinction 576
14.1.1.4 Seeing 576
14.1.1.5 Turbulence Vertical Profiles 576
14.1.1.6 Turbulence Outer Scale 577
14.1.1.7 Wave front coherence time 577

14.2 Parameters space 577
14.2.1 General astronomy 577
14.2.1.1 Cloudiness 577
14.2.1.2 Precipitable water vapour 578
14.2.1.3 Aerosol Extinction 581
14.2.1.3.1 Saharan dust 581
14.2.1.3.2 Contrails 582
14.2.1.4 Sky background 583
14.2.1.5 Seeing 584
14.2.2 Telescope design & operation 585
14.2.2.1 Wind. temperature and humidity 585
14.2.2.2 Seismicity 585
14.2.2.3 Topology. soil characteristics 586
14.2.2.4 Infrastructures 587
14.2.3 AO observations 588
14.2.3.1 Lower atmosphere turbulence and wind 588
14.2.3.2 Higher atmosphere turbulence and wind 590
14.2.3.3 Full Atmospheric profiles 591
14.2.3.4 Sodium layer 593

14.3 Site selection strategy 593
14.3.1 Identification of potential candidates 593
14.3.2 Characterization of the parameter space 597
14.3.3 Analysis of climate stability 598
14.3.3.1 The experience of ESO Observatory 598

14.3.3.2 FRIOWL 599

14.4 Site preservation and monitoring 602

14.4.1 Local Seeing control 602

14.4.2 Astronomical Site Monitoring Station 603

15. Maintenance and operations 607

15.1 Maintenance 607

15.1.1 Design provisions 607

15.1.1.1 Human access and handling 607

15.1.1.1.1 Human access 607

15.1.1.1.2 Handling Facilities 608

15.1.1.2 Corrector Handling 609

15.1.1.3 M6 Unit Handling 610

15.1.1.4 Primary mirror covers handling 611

15.1.1.4.1 Covers Docking and undocking operations. 612

15.1.1.5 Sliding Enclosure 613

15.1.1.6 Secondary mirror handling 614

15.1.2 Safety 615

15.2 Observatory operations 615

15.3 Science operations 617

16. Management 619

16.1 Introduction 619

16.2 Programme organization 622

16.3 Programme management and control 627

16.4 Programme team 628

16.5 Programme phases 629

16.6 Schedule 630

16.7 Cost of the programme 632

16.7.1 Cost estimate methodology 632

16.7.2 Cost 632

16.7.3 Staffing 633

16.7.3.1 Design phase 633

16.7.3.2 Construction phase 633

16.7.3.3 Operations phase 633

Design parameters – Summary 634

References **641**

Acknowledgements **649**

Contributors **652**

Appendix 1. The ELT Design Study **655**

A-1.1 Work Packages *655*

A-1.2 Wavefront control *660*

A-1.3 Optical fabrication *666*

A-1.4 Mechanics *667*

A-1.5 Enclosure & wind studies *669*

A-1.6 Adaptive Optics *669*

A-1.7 Operations *670*

A-1.8 Instrumentation *670*

A-1.9 Site characterization *671*

A-1.10 Integrated modelling *672*

Appendix 2. ELT Design Study Participants **673**

Appendix 3. System status at construction readiness review **677**

Appendix 4. Phase B Schedule estimate **683**

Appendix 5. Phase C/D schedule estimate **689**

Appendix 6. Cost estimate **703**

Appendix 7. Software tools **707**

Appendix 8. Optical design – criteria and merit function **711**

Appendix 9. Optional corrector **715**

Index of tables

Table 2-1 Summary of top level requirements 63
Table 2-2. Baseline design, optical characteristics. 65
Table 2-3.Segments characteristics. 69
Table 2-4 Instrument Concept Studies 81
Table 2-5. Subsystems status at start of segments integration. 84
Table 2-6. OWL cost estimate, capital investment. 92
Table 2-7 Summary of exo-planet capability as a function of ELT size 95
Table 2-8 Summary of studies of resolved stellar populations as a function of ELT size 96
Table 2-9 Summary of studies of the high-redshift Universe as a function of ELT size 96
Table 2-10. Dependence of main telescope requirements on diameter D 97
Table 2-11. Summary of environmental risks (a few comments still to be incorporated). 101
Table 2-12. System risks 103
Table 2-13. Areas of Risk Impact. 108
Table 3-1. Primary science cases 110
Table 3-2. (From Science Book) Gains in magnitude for the same signal-to-noise and exposure time when observing unresolved sources in the background-limited regime. The gains are shown relative to an 8m telescope delivering 0.5” images. 113
Table 3-3. (from [118]) IR performance of several ELTs compared to that of the JWST space telescope, in terms of the point source sensitivity ratio ELT/JWST. In the near-infrared an ELT outperforms a 6.5m cold (~30K) space telescope such as JWST (bold font shows ratio > 0.5). 114
Table 3-4. Diffraction limit (Res, in milliarcsecond) and corresponding limiting magnitudes for various telescope sizes, under identical conditions and assumptions (i.e. same Strehl ratio of 50%, efficiency 30%, sky background from Paranal, no atmospheric extinction). While the absolute values may change with assumptions, the relative ones should not. 115
Table 3-5. Summary of the capabilities of a sub-mm instrument on OWL compared to those of ALMA. 116
Table 3-6. Science requirements. S stands for Strehl ratio 121
Table 3-7 Requirements from the main science cases (adapted from Hook [120]) 126
Table 4-1. Single conjugate AO requirements. 131
Table 4-2. Multi-conjugate AO requirements 132

Table 4-3. Ground-layer AO requirements. 132

Table 4-4 Multi Object AO requirements 132

Table 4-5. Extreme AO requirements. 132

Table 4-6. AO requirements at optical wavelengths (provisional). 133

Table 4-7. Effect of differential displacement due to atmospheric refraction between meridian and one hour from meridian. RA and DEC are right ascension and declination, Sep is the separation between the stars, Displ is the relative differential displacement in milliarcsec at one hour from meridian, and ΔT is the maximum exposure time in minutes to have a displacement < 10% of the diffraction peak. 134

Table 5-1. Image quality requirements, non-adaptive modes. 136

Table 5-2. Image quality requirements, with first and second generation adaptive optics. 137

Table 5-3. Failure / damage hierarchy and allowable rate of occurence. 137

Table 5-4. Structural subsystem. 149

Table 5-5. Optic model, inputs and outputs. 149

Table 5-6. Control loops. 150

Table 5-7. Integrated Model - Intermediate steps. 150

Table 5-8. Integrated Model validation methods. 151

Table 5-9: Typical expected median values of the atmospheric turbulence parameters based on the experience at existing observatories. 161

Table 5-10: Various environmental conditions on Paranal. 162

Table 5-11: Temperature conditions on Paranal. 164

Table 5-12: Earthquake characteristics for two different sites. 166

Table 5-13: Survival wind speed for telescope and enclosure structure. 167

Table 5-14: Survival temperature conditions for the telescope and enclosure structure. 167

Table 5-15. Image quality budget - main positions. 169

Table 5-16. OWL Image quality budget in SCAO mode. 170

Table 6-1. Optical design: guidelines and objectives. M=Mandatory; C=Critical; D=Desirable. 186

Table 6-2. Ratings for designs No 1 to 4. (*) P=Pass; F=Fail. 193

Table 6-3. Baseline design, optical prescription. 197

Table 6-4. 4-mirror f/15 design, 60-m aperture; optical prescription. 199

Table 6-5. 4-mirror f/15, 60-m aperture design. Nominal optical quality. 199

Table 6-6. Baseline design, optical quality. 202

Table 6-7. Expected emissivity at 2.2 μm, classical Al or Au coatings. 208

Table 6-8. Expected emissivity at 2.2 μm, Gemini enhanced Ag coatings. 208

Table 6-9. Baseline design, sensitivity matrix. 211

Table 6-10. Baseline design, sensitivity matrix, corrector decenters (rigid body). 212

Table 6-11. Segments characteristics. 227

Table 6-12. Compared performance of Zerodur, fused silica and silicon carbide with respect to through-thickness CTE and thermal gradients (1.6-m flat-to-flat, 70 mm thick segments). 230

Table 7-1 Altitude axis: summary of the design results 255

Table 7-2 Azimuth axis: summary of the design results 255

Table 8-1: Spectral Envelope of maximum Tip-tilt signal (mirror tilt) to be corrected by M6AM. On-sky tip-tilt is ~ mirror tilt/20. 302
Table 8-2: SCAO Strehl ratio (%) with the visible wavefront sensor 302
Table 8-3: SCAO Strehl ratio (%) with the infrared wavefront sensor 302
Table 8-4: Requirements for the Calico- Mux development funded by Caltech and ESO 311
Table 8-5: Local Loop Characteristics 327
Table 8-6: Analog performance (Capacitive Sensor) 327
Table 8-7: Characteristics of potential materials for thin shells. 330
Table 8-8: Main characteristics of the OWL large DMs 333
Table 8-9: Essential characteristics of the VLT adaptive secondary mirror. 333
Table 8-10: AO systems commissioned or under development. SPARTA support starts with MAD 338
Table 8-11: GLAO Ensquared Energy (%) in 50mas pixel over 6' FOV 346
Table 8-12: GLAO – Gain in Ensquared Energy in 50mas pixel over 6' FOV, corrected PSF vs. seeing. 346
Table 8-13: GLAO Ensquared Energy variation in 50 mas pixel over FOV (PSF uniformity) 346
Table 8-14. Field references. 360
Table 8-15: MCAO performance (Strehl Ratio, %) over 1' FOV vs. seeing and NGS magnitudes; 366
Table 8-16: MCAO Strehl Ratio variation (in rms Sr) over the 1' FOV; 366
Table 8-17. Four technologies to achieve the XAO requirements 390
Table 8-18: Quantitative evaluation of the known LGS issues versus telescope diameter 397
Table 9-1: Design guidelines 409
Table 9-2: Kevlar available grades. 424
Table 9-3: Main axes friction drive and bearing topology. 433
Table 9-4: Load cases. 433
Table 9-5: Main axes torque requirement. 433
Table 9-6: Friction drive generated torque 434
Table 9-7: Cost breakdown of OWL's drive and bearing systems 434
Table 9-8: Maglev main requirements 435
Table 9-9. Bearings & drives linear generate forces. 436
Table 9-10. Minimum required stiffness. 437
Table 9-11: Telescope mass breakdown 448
Table 9-12: Mass moment of inertia 448
Table 9-13: Mass and inertia budget of the FE model in zenith configuration. 450
Table 9-14: Differential rigid body motions of the optical elements due to gravity. 452
Table 9-15: Worst case rigid body and PTV motions of M1 and M2 segments due to static wind. 453
Table 9-16: Eigenfrequencies and effective masses of zenith configuration. 458
Table 9-17: Eigenfrequencies and effective masses of 30 º configuration. 458
Table 9-18: Eigenfrequencies and effective masses of 60 º configuration. 458

Table 9-19: 1σ maximum piston displacement of M1 and M2 due to von Karman wind load spectra applied to complete mirrors area. 467

Table 9-20: 1σ maximum displacements of M1 and M2 segments (part of the mirror area loaded). 467

Table 9-21: Maximum stresses. safety margins and displacements or survival wind load cases. 471

Table 9-22: High configuration 475

Table 9-23: Low configuration. 476

Table 9-24. Design options. overall properties. 478

Table 10-1. Adapter-rotator requeirements for a set of representative instruments. 483

Table 10-2: Adapter-rotator requirements for a set of representative AO Systems. 484

Table 10-3 Adapter-rotator requirements for Active Optics. 484

Table 11-1. Main sites characteristics. 486

Table 11-2: Concrete and steel quantities 496

Table 11-3: Power consumption estimation 511

Table 11-4: Volume of earth to be removed to prepare the site. 515

Table 12-1. Instrument Concept Studies. 518

Table 12-2. Gain in photon statistics with telescope size 525

Table 12-3 Magnitude limits for point sources at 100m. 60m and 30m 529

Table 12-4 Magnitude limits (S/N=5) for 1 hour integration time for OWL and JWST 530

Table 12-5 Proposed wave-lengths set for the differential imager 543

Table 12-6: Characteristics of Earth-like planets used in the simulation. 546

Table 12-7: Characteristics of Jupiter-like planets used in the simulation. 546

Table 12-8 Main characteristics of SCOWL 555

Table 12-9 AO Requirements from Instruments * : seeing-reduced image quality desirable +: high frequency monitoring of water content of atmosphere desirable 558

Table 12-10 Detector Array Requirement 559

Table 14-1: PWV (mm) statistics for Paranal (January - August 1998) and Chajnantor (January - September 1999) for satellite and ground based site monitor measurements of PWV. .. 579

Table 14-2: Site locations and information 579

Table 14-3: Typical IR Backgrounds at Paranal (mag/arcsec-2). from J. Cuby et al.. The Messenger 101. p.3. September 2000. Note that K. L and M values include telescope background. 584

Table 14-4: Average background at Paranal (mag/arcsec-2). from >4000 FORS1 exposures during Apr.-Sep. 2001. by F. Patat. UBVRI Night Sky Brightness at ESO-Paranal during sunspot maximum. The Messenger 115. March 2004. 584

Table 14-5: 50-years horizontal ground peak acceleration (g units) with 10% probability of exceedence. 585

Table 14-6: Soil characteristics for Paranal area (Site 1) and La Palma (Site II) 587

Table 14-7: NCEP / NCAR Reanalysis datasets used 600

Table 14-8: ECMWF Reanalysis datasets used (ERA-15) 600

Table 14-9:TOMS Aerosol datasets used 601

Table 15-1: Human access. 608

Table 15-2 Sliding enclosure maintenance requirements 613
Table 16-1. Total estimated cost (incl. contingency and overheads) 632
Table 16-2. Estimated human resource requirements, design phase. 633

Table A- 1. ELT Design Study - overview of the Work Packages. 660
Table A- 2. Position sensors main specifications. 660
Table A- 3. Position actuators, essential characteristics. 662
Table A- 4. Function of merit, criteria and relative weights. 712
Table A- 5. Mandatory requirements. 712
Table A- 6. Merit function; guidelines for ratings. 714
Table A- 7. Optional corrector, optical prescription. 717

Index of figures

Figure 2-1. Using primary distance indicators to disentangle cosmological models. The plot shows the apparent magnitude difference relative to an empty universe of several cosmological models as a function of redshift. Regions of application for various methods of distance estimates with OWL are indicated. 56

Figure 2-2 Simulation of observations of Supernovae with OWL.The current data from ground and space observations are shown. These observations will allow to determine the cosmic SN rate, and help disentagle cosmological models (e.g. whether a “quintessence field” or a “phantom energy” exist)..... 57

Figure 2-3 Brief history of the telescope. Stars are refractors, asterisks are speculum reflectors and circles are glass reflectors. Some specific telescopes are named. 60

Figure 2-4 Improvement in sensitivity of telescopes expressed in “equivalent diameter of a perfect telescope” = $\sqrt{(\eta D^2)}$, with η the telescope overall efficiency (the dashed line is an aid to the eye, not a fit). 61

Figure 2-5. Layout of the OWL observatory. 64

Figure 2-6. Layout of the baseline optical design. 66

Figure 2-7. Primary mirror geometry (3048 segments). 70

Figure 2-8. Secondary mirror geometry (216 segments). 71

Figure 2-9. Telescope structure, overall layout. 72

Figure 2-10. Structural steel module 73

Figure 2-11. Friction drive 73

Figure 2-12. First light results with MAD (laboratory conditions). Atmospheric turbulence is emulated with phase screens. Seeing 0.5 arc seconds, coherence time 5 ms, wavelength 2.2 μm. Adaptive loop frequency 210 Hz. 77

Figure 2-13. PSD of turbulent wind speed in open air and inside VLT enclosure (no wind screen). 79

Figure 2-14. Sliding enclosure (courtesy CL-MAP)..... 80

Figure 2-15. Design phase, major milestones. 89

Figure 2-16. Phase C/D major milestones. 90

Figure 2-17. ELT Design Study, Work Breakdown Structure..... 93

Figure 2-18. ELT Design Study, overall schedule..... 94

Figure 2-19. Unit cost vs. quantity (industrial data)..... 99

Figure 3-1. Time needed to achieve the same S/N on diffraction-limited telescopes as a ratio to the time needed on a 100m, i.e. t/t100 (note the background limited, t/t100 ∝ D4, and shot noise limited, t/t100 ∝ D2, regimes)..... 112

Figure 3-2. (From Science Book) The theoretical diffraction limits (λ/D) for 8m, 30m and 100m telescopes are plotted at three wavelength values corresponding approximately to the J, H and K infrared bands (horizontal bars). Also plotted are curves of projected angular size as a function of redshift for objects of various physical sizes (10pc, 50pc, 300pc and 1kpc) for two sets of cosmological parameters: (ΩM,ΩΛ)=(0,0) and (0.3,0.7) for the lower and upper curves respectively. 113

Figure 3-3. Observability of major emission lines with redshift. 114

Figure 3-4 Simulated image of a solar-type system at 10 parsec (32 light-years)..... 117

Figure 3-5 (From Science Book) Synthetic Colour-Magnitude Diagram computed using constant star formation rate from 13 Gyr ago to the present. The age of the stars are coded in different colours. Labels indicate different evolutionary phases: BL - blue loop; HB - Horizontal Branch; RC – Red Clump; RGB – red giant branch; AGB – asymptotic giant branch; MS – main sequence. From [119]. 119

Figure 3-6 Simulation of the formation of the galaxies in the Local Group in a cold dark matter scenario, by Ben Moore, Zurich, astronomy and cosmology research group (www.nbody.net). 120

Figure 5-1 : Project V-diagram. 140

Figure 5-2: Requirements breakdown. 141

Figure 5-3: Schematic example of functional breakdown. 142

Figure 5-4. OWL architecture example. 142

Figure 5-5: Phase A “open loop” design iterations 143

Figure 5-6: Block diagram of the OWL Integrated Model 146

Figure 5-7: Relationship between the height above the ground and the mean velocity 153

Figure 5-8: Model velocity-PSD close to the M1 segments 154

Figure 5-9: Force PSD averaged over three different areas 155

Figure 5-10: Instantaneous pressure field on M1 156

Figure 5-11: Comparison of PSDs obtained by CFD with model PSDs 156

Figure 5-12: JBO Lovell Radio Telescope with pressure sensors 157

Figure 5-13 : Pressure power spectrum on the reflector of the Jodrell Bank Telescope 158

Figure 5-14: Pressure PSD measured in a wind tunnel 159

Figure 5-15. Respective areas of action of active and adaptive optical systems as a function of the spatial and temporal frequency of the perturbations 159

Figure 5-16: VLTI-Vinci Optical path difference power spectrum and Kolmogorov model saturation for aperture distances larger than the outer scale L_0 (credit. E. di Folco, ESO 2004) 160

Figure 5-17: Steel pipe exposed to sun radiation 162

Figure 5-18: Temperature evolution 163

Figure 5-19: Environmental conditions. 163

Figure 5-20: Acceleration response spectrum (Telescope, MLE, 0.34 g, 1.5 % damping)..... 166

Figure 6-1. Implied characteristics. 187

Figure 6-2. Mechanical implementation of different optical designs. 189

Figure 6-3. Baseline optical design (design No 1). 190

Figure 6-4. Ritchey-Chretien design (design No 2)..... 190
Figure 6-5. Four mirror, spherical primary & flat secondary mirrors solution (design No 3). 191
Figure 6-6. Four-mirror, conic M1 & M2 design (design No 4)..... 191
Figure 6-7. Four-mirror solution; f/0.89 spherical primary mirror 192
Figure 6-8. 5-mirror solution, f/1.42 spherical primary mirror..... 192
Figure 6-9. Baseline optical design, major dimensions..... 195
Figure 6-10. Baseline design, optomechanical implementation. 196
Figure 6-11. 4-mirror f/15 design, 60-m aperture..... 198
Figure 6-12. Optical test set-up for the testing of a convex, aspherical 8-m class mirror..... 200
Figure 6-13. 60-m four mirror design with f/0.75 parabolic primary mirror..... 200
Figure 6-14. Coaxial design with f/5 focus. Field of view 6 arc minutes, f/1.3 primary mirror... 201
Figure 6-15. Baseline design; Strehl Ratio vs field of view. 202
Figure 6-16. Baseline design; rms spot size (arc seconds) vs field radius. 203
Figure 6-17. RMS wavefront error (microns) vs field radius. 203
Figure 6-18. Point Spread functions at 0.5 microns. Box size 0.040 arc seconds..... 204
Figure 6-19. Ensquared energy at 0.5 microns. Scale: 100 microns = 0.0342 arc seconds. ... 204
Figure 6-20. Point Spread functions at 2.2 microns. Box size 0.200 arc seconds..... 205
Figure 6-21. Ensquared energy at 2.2 microns. Scale: 500 microns=0.171 arc seconds. 205
Figure 6-22. Distortion..... 206
Figure 6-23. Vignetting by M5 as a function of M5 diameter. 206
Figure 6-24. Possible set of baffles..... 207
Figure 6-25. Pupil mask (emissivity budget). The pupil mask covers all obstructed areas except the inter-segment gaps and tensioning ropes. 209
Figure 6-26. Aberrated layer image. 213
Figure 6-27. Adaptive correction error (wavefront RMS) for 1 km conjugate defocus..... 214
Figure 6-28. Image quality of the pupil conjugation; field of view 1 arc minute diameter. 215
Figure 6-29. Image quality of the pupil conjugation; field of view 3 arc minutes diameter. 215
Figure 6-30. Image quality of the pupil conjugation; field of view 6 arc minutes diameter. 216
Figure 6-31. Spot diagrams, LGS at 90 km on-axis and 3 arc minutes off-axis. 217
Figure 6-32. Wavefront map, LGS at 90 km, 3 arc minutes off-axis..... 217
Figure 6-33. Model of the pupil for studying diffraction effects 218
Figure 6-34 PSF from the pupil presented above. The field of view is 1 arc second diameter, wavelength is 650 nm. Here and further: logarithmic scale. 219
Figure 6-35 Diffraction by the “spider”. PSF box size 0.72” 220
Figure 6-36 Diffraction by “missing” segments. PSF box size 0.72” 221
Figure 6-37 Diffraction by the ropes. PSF box size 0.72” 221
Figure 6-38. Mechanism of the formation of diffraction peaks (gaps): the grid factor (dots) is multiplied by the segment PSF. Left: without gaps; except for the central one all peaks of the grid factor fall into zeros of the segment PSF_s. Right: with gaps; peaks no longer coincide with PSF_S zeros..... 222
Figure 6-39 Diffraction by intersegments gaps of the primary (left) and of the secondary mirrors (right). Box size 0.72 arc secons. 222

Figure 6-40 Intensity slice representation of OWL PSF between 10^{-5} and 10^{-7}. Most diffraction artefacts are apparent. 223

Figure 6-41 Intensity slice representation of OWL PSF with 30nm and 56nm wavefront RMS residual segmentation piston, tip-tilt errors on two segmented mirrors. 226

Figure 6-42. Segment unit product tree. 227

Figure 6-43. Primary and secondary mirror segments distributions. 228

Figure 6-44. Primary mirror geometry, obscurations and intersegments gaps variation. 229

Figure 6-45. Primary mirror segment blank. 231

Figure 6-46. Secondary mirror segment blank. 232

Figure 6-47. Zerodur hexagonal cast. Courtesy Schott. 233

Figure 6-48. CTE homogeneity of Zerodur. Courtesy Schott. 233

Figure 6-49. Thermo-mechanical figure of merit. 234

Figure 6-50. Precursor (left) and 1-m sintered SiC segment (right). Courtesy Boostec. 235

Figure 6-51. Segments optical quality (rms slope) specifications. 237

Figure 6-52. Segments optical quality (rms amplitude) specifications. 238

Figure 6-53. Interferogram of a LAMOST 1-m spherical segment prototype. Courtesy REOSC. 239

Figure 6-54. Segment deflection on axial support. Zerodur, thickness 70 mm. 240

Figure 6-55. M4 aspherization profile. 241

Figure 6-56. M4 slope difference with respect to best fitting sphere. 242

Figure 6-57. High spatial frequency wavefront error, VLT primary mirror. 243

Figure 6-58. M4 optical test set-up. 244

Figure 6-59. M4 nominal interferogram, double pass. 244

Figure 7-1. Wavefront control - overall layout. 248

Figure 7-2 Wavefront Control Architecture for OWL 249

Figure 7-3 Block diagram of the closed-loop system 251

Figure 7-4 Normalized PSD of the wind loads applied to different height: altitude configuration 252

Figure 7-5 Frequency characteristics of altitude models for four different configurations 252

Figure 7-6 Frequency characteristics of azimuth models for two different configurations 253

Figure 7-7 Output sensitivity function as a a measure of both the rejection of perturbation and the robustness for the altitude axis 254

Figure 7-8 Output sensitivity function as a measure of both the rejection of perturbations and the robustness for the azimuth axis 254

Figure 7-9 PSD of tracking error on the main bearing (altitude axis 30 deg) – open-loop (dashed), closed-loop (solid) 255

Figure 7-10 Main bearing (altitude axis) tracking error for 30 deg configuration 255

Figure 7-11 Left) bogie subjected to various forces-- Right) friction as a function of velocity 256

Figure 7-12. Tracking a ramp reference signal in closed-loop. Left: slope 0.1 arcsec/sec stick-slip motion. Right: slope 0.5 arcsec/sec; stick-slip disappears. 257

Figure 7-13 Block-diagram of bogie control system: feedback + feed-forward friction compensation strategy 258

Figure 7-14 Closed loop simulation of seven bogies (with friction compensation), one bogie is passive which exhibits small stick-slip motion, oscillations are induced on other bogies. 258

Figure 7-15 Closed-loop simulation of the altitude axis at 30 deg tracking a ramp reference signal with a slope of 0.1 arcsec/sec: left) no feed-forward friction compensation---right) with feed-forward friction compensation 259

Figure 7-16 Closed-loop simulation of altitude, 30-deg configuration 260

Figure 7-17 Wavefront error (tilt) on the sky- Altitude simulation: zenith configuration, main axis control with different wind loads applied to different levels 260

Figure 7-18 PSD of the wavefront error (tilt) on the sky 261

Figure 7-19 Wavefront error (tilt) after field stabilization correction as a function of the closed-loop bandwidth 261

Figure 7-20 Block diagram of the closed-loop control of M6: field stabilization 262

Figure 7-21 PSD of the corrected tilt wave front error on the sky 262

Figure 7-22 Simulation results: wavefront errors before and after correction, tilt motions of the M6 unit and the input torque applied to the unit. 263

Figure 7-23. Field of View of the Shack-Hartmann sensors on M3 and M4. 268

Figure 7-24. Two types of lenslet and their projection onto the edge of the segments 272

Figure 7-25. Shape of the PSF for piston steps ranging from 0 to λ/2. 272

Figure 7-26. Conceptual setup of a Modified Mach-Zehnder interferometer. 273

Figure 7-27. Mach-Zehnder signal profile for a piston step of $\pi/2$ and for different optical path differences between the two arms. Theoretical predictions are on the left hand side and experimental results on the right hand side 273

Figure 7-28. Phase mask principle 274

Figure 7-29. Signal obtained with a mechanical piston step of 230 nm. 274

Figure 7-30. Signal obtained with the diffraction image technique (courtesy A. Schumacher) 275

Figure 7-31. Signal obtained with the pyramid sensor for a piston step between square segments (courtesy S. Esposito) 275

Figure 7-32. Position and surface piston levels of the hexagonal subapertures on the piston plate used for the laboratory tests (A=0nm, B=18nm, C=50nm, D=325nm). 276

Figure 7-33. Phasing sensor signal from the multisegment phase plate without (left) and with (right) turbulence. 277

Figure 7-34. Sensor signals and fitted curves for one border for the two cases without (upper plot) and with (lower plot) turbulence. Note the change of the character of the signal : from an oscillating behaviour to smooth wings according to the function f. 278

Figure 7-35. ZEUS measurements: amplitude of te signals versus known piston steps without (a) and with a turbulent generator (b). Note the reduction of the amplitude of the fitted sine curve from 0.65 to 0.29. 278

Figure 7-36. Hough transform of the signal (left) and the detected lines (right). 279

Figure 7-37. Piston steps distribution: Initial (a) and after 6th loop (b). The grey scale is in nm. 280

Figure 7-38. Closed loop simulations. Gain 0.5. Initial wave front RMS = 322.5nm, final RMS = 12.7nm. 281

Figure 7-39 Indexation of the segments 282

Figure 7-40. Indexation of the borders between the segments 283

Figure 7-41. The signal from the gaps obtained by a high-pass filtering (a), two spatial Fourier filters (b), and the filtered patterns for the secondary (c) and primary (d) mirrors. 286

Figure 7-42 Scheme of segment system configuration 287
Figure 7-43 PSD of wind load on one segment 288
Figure 7-44 Position error RMS as a function of control bandwidth of each actuator 288
Figure 7-45 Closed-loop position error PSD compared to open loop PSD 289
Figure 7-46 Closed-loop response of system--- closed-loop bandwidth: 10Hz 290
Figure 7-47 Closed-loop simulation ---- with AFC, closed-loop bandwidth 10Hz 290
Figure 7-48 Closed-loop simulation ---- with AFC, closed-loop bandwidth 5Hz 291
Figure 7-49 Reaction force on back structure and wind load on segment 292
Figure 7-50 PSD of wind load and reaction force and back structure 292
Figure 7-51 Seven segment configuration 293
Figure 7-52 Wind load force on seven segments 294
Figure 7-53 Seven segment closed-loop simulation: edge sensor readings and absolute position of the segments. 294
Figure 7-54: 3D view APE on the nasmyth platform 296
Figure 7-55: 3D view of the ASM 296
Figure 7-56: Conceptual design of the IM 297
Figure 8-1: M6 Adaptive Mirror located in the corrector structure of the telescope. 300
Figure 8-2: Single Conjugate Adaptive Optics concept 300
Figure 8-3: Limited corrected FoV due to anisoplanatism in the SCAO concept 302
Figure 8-4: Statistical distribution of the outer scale 303
Figure 8-5: Conjugation altitudes of the M6AM unit 303
Figure 8-6: Geometrical characteristics of the M6 Adaptive Mirror 304
Figure 8-7: Control scheme of the M6AM unit and interface with the active optics. 305
Figure 8-8: Transmission of the wavefront sensor pick-up dichroic 306
Figure 8-9: Defocus of the wavefront sensor versus field position 307
Figure 8-10: Technology concept of the WFS L3CCD detector 307
Figure 8-11: Quantum Efficiency with deep depletion enhancement in the red 308
Figure 8-12: OWL pupil dissector for the Shack Hartmann wavefront sensor 308
Figure 8-13: Shack Hartmann wavefront sensor concept 309
Figure 8-14: Pyramid wavefront sensor concept 311
Figure 8-15: SCAO Shack Hartmann or Pyramid Real-time architecture 312
Figure 8-16: Strehl vs. Magnitude for the SH-WFS (without RON), in K, H, J bands (top to bottom), for the good seeing model (left) and bad seeing model (right). Results are on-axis 313
Figure 8-17: VLT Planet Finder performance for different Readout Noise 313
Figure 8-18: Ensquared Energy versus pixel size (K-H-J; top to bottom), for good seeing (left) and bad seeing models (right). Bright stars are considered. 314
Figure 8-19: Affect of anisoplanatism on the performance of the SCAO system, in K, H and J bands (top to bottom), in good seeing model (left), and bad seeing (right). 314
Figure 8-20: Strehl vs. Magnitude for the IR PYR (without RON on the left, 5e- ron rms on the right), in K, H, J bands (top to bottom), for the good seeing model. Results are on-axis. 315

Figure 8-21: Long Exposure PSF with 10000 ph/subap/integ (bright NGS), for the K band (left) and J-band (right). Both pictures are on-axis. Stretch is logarithmic..... 315

Figure 8-22: EE vs. pixel size, in the K, H and J bands, good seeing, and bright guide star. .. 316

Figure 8-23: Shape for the DM during closed loop. The "spikes" near the telescope central obstruction, created by diffraction effects on the PYR WFS. 316

Figure 8-24: On-axis strehl versus wavelength for a bright reference star 317

Figure 8-25: Point Spread Functions obtained with SCAO. From left to right 2.2, 5 and 10 µm. Good seeing conditions, bright on-axis star. 317

Figure 8-26: P-V DM mechanical stroke requirements versus spatial frequency for a seeing of 1.5” and different outer scales (Courtesy, T. Fusco-ONERA)..... 318

Figure 8-27: Strehl (on-axis) vs. L0, for the SH based SCAO system (good seeing), in K, H and J bands 318

Figure 8-28: Conceptual design for the 1120mm diameter, 1170 actuators VLT deformable secondary mirror..... 322

Figure 8-29: Force/thin shell mirror (VLT design) based on Cold plate, Reference body & thin shell. A Hexapod, attached to the cold plate, provides fine focusing & centering (Courtesy, Microgate/ADS, Italy)..... 322

Figure 8-30: Closer view of the actuator distribution on one half of the DSM (Courtesy Microgate/ADS) 323

Figure 8-31: Light weighting scheme of the VLT design Reference Body; estimated weight (Zerodur) is 27kg while a monolithic design would lead to 130 kg (Courtesy Microgate/ADS, Italy)..... 324

Figure 8-32: Double side polishing device for flat shell. Six shells, maximum diameter of 68mm each can be polished at once (Courtesy SESO, France) 325

Figure 8-33: The successive steps of thin shell slumping (Courtesy INAF) 326

Figure 8-34: Scheme of internal control loop of actuator positions (left hand side). Feed-forward force added to the control schematic on the right hand side..... 327

Figure 8-35: Mode stiffness versus mode number for the VLT DSM..... 328

Figure 8-36: Theoretical Influence Function of a thin shell DM. Left: the IF (scale in mm), right: the associated stress in the glass (square grid of actuator at 29mm spacing, 2mm thick) 329

Figure 8-37. Permanent magnet mounted on the shell..... 330

Figure 8-38. Permanent magnet sizing. 330

Figure 8-39: Shell thickness producing 15 nm rms gravitational sag (30nm rms wavefront error) vs. actuator pitch..... 331

Figure 8-40: Shell gravitational sag (nm) vs. act. pitch for Zerodur, ULE, Borosilicate, Steel & CVCSiC. 331

Figure 8-41: Shell deformation or stroke. Absolute analytical model accuracy: 50%; valid for relative material comparison..... 332

Figure 8-42: Optical diagram of the VLT Deformable Secondary Mirror test setup..... 334

Figure 8-43: Mechanical setup of the VLT deformable secondary mirror Test facility..... 335

Figure 8-44: Possible test setup for the OWL M6. In the case of spherical mirror a corrector is needed for aberration compensation (not shown here) 335

Figure 8-45: Quantum Efficiency curves of the L3 CCD and the PN-sensor..... 336

Figure 8-46: Pn-Sensor readout principle for the 256x256 detector. 337

Figure 8-47: Left: Shack-Hartmann read-out; right: Pyramid read-out 341

Figure 8-48: SPARTA Architecture 342

Figure 8-49: Preliminary statistics of the turbulence profile at Paranal 343

Figure 8-50: Fraction of turbulence located at 200 m as measured by the SLODAR at Paranal 344

Figure 8-51: Ground Layer Adaptive Optics concept 344

Figure 8-52: GLAO real-time hardware architecture 347

Figure 8-53: Frequency of circular 6 arcmin diameter fields as a function of the number of NGS included at the North Galactic Pole for different NGS limiting magnitudes 349

Figure 8-54: Frequency of circular 6 arcmin diameter fields as a function of the number of NGS included on them at at l=0° and b=|50°| for different NGS limiting magnitudes. 349

Figure 8-55: Performance of the VLT MACAO system on UT4 350

Figure 8-56: GLAO Ensquared Energy in 50mas for seeing of 0.53”(left) and 1” (right) at 0.5μm; 6 NGSs 350

Figure 8-57: Gain of EE in 50mas brought by GLAO relative to seeing for seeing of 0.53”(left) and 1” (right) at 0.5μm; 6 NGSs 350

Figure 8-58: EE vs field of view position (K-band); 3NGS in 3’ plus 3 NGSs [3-6’]; faint star 1e-/sub-aperture/s, good seeing model 351

Figure 8-59: Corrected PSF with GLAO using 6 NGSs, 6', good seeing (left) and bad seeing (right), K band, on-axis, 10ph / subap / NGS top curve is GLAO, bottom curve is the uncorrected seeing. 351

Figure 8-60: Effect of the outer scale of turbulence (L_0) on the Strehl obtained with GLAO with 3 NGSs within 3' FOV; good seeing; Top to bottom: K, H, J. 351

Figure 8-61: HAWK-I concept based in CPU-only SPARTA architecture. With the new FPGA architecture the number of computational units will be reduced. 353

Figure 8-62: Concept of Multi-object Adaptive Optics or Distributed Adaptive Optics with wavefront sensors in open loop 354

Figure 8-63: MOAO concept with the wavefront sensor in pseudo closed loop 355

Figure 8-64: GLAO combined with MOAO concept with the wavefront sensor in open loop (right) and in pseudo closed loop (left) 356

Figure 8-65: MOMFIS schematic functional diagram (Courtesy LAM, France) 357

Figure 8-66: MOMFIS general view of the implementation: in the focal plane small pick-off mirrors are positioned with a robot, directing the target beams steering mirrors and the reference star beams to the WFS. The steering mirrors direct in turn the beam to the DM and IFU units (Courtesy LAM, France) 358

Figure 8-67: MOAO control loops 359

Figure 8-68: MOAO Real-Time Computer Concept. The diagram shows an example with only 4 wave-front sensors with local DM and 6 clusters each serving one IFU. The Dm on the right side is the M6AM. 360

Figure 8-69: Gain in Ensquared Energy in a 50 mas pixel for each scientific target, H band, 1” seeing. 361

Figure 8-70. Left: mean distance to the center of the field (arcmin) for the considered constellations. Right: integrated magnitude of all the used NGSs 361

Figure 8-71: Optical setup of SESAME (Courtesy LESIA) 362

Figure 8-72: General MCAO concept (left). Star Oriented MCAO concept (right). Each NGS wavefront is measured with dedicated WFS and the signals are recombined to determine the correction to be applied to each DM conjugated at different altitudes. 364

Figure 8-73: Opto-mechanical concept of ONIRICA (Courtesy INAF) 365

Figure 8-74: Architecture for a SH-based MCAO system with reduced number of reconstructed modes. 368

Figure 8-75: Frequency of circular 6 arcmin diameter fields as a function of the number of NGS included on them at the North Galactic Pole (left) and at an intermediate galactic latitude l=0° b=50° (right) 369

Figure 8-76: Strehl (K-band) as a function of the NGS number distributed on a 6 arcmin FoV optimized in the central 1 arcmin. Solid line: Mv=5, dashed line: Mv=16, dashed-dotted line: Mv=17, dashed-dotted-dotted line: Mv=18. For each magnitude: top line on-axis, bottom line: off-axis. 370

Figure 8-77: Strehl (on-axis) for the good seeing model, MCAO, 3 NGSs, 2' FOV, K, H, J (top to bottom), Mv=16 corresponds to 5 photons/subap/frame..... 370

Figure 8-78: Numerical simulations of MCAO correction (Strehl ratio in K band, H and J bands (top to bottom)) on a 6 NGS asterism (Mv=5 (left plot) and Mv~16 (right plot)), the good seing model (~0.5'' was used). Correction is optimized for a 1' FoV (diameter)..... 370

Figure 8-79: Barycentre speed of a G2-V star due to the differential atmospheric refraction between the WFS effective wavelength and the instrument observing in K band for different target declinations 371

Figure 8-80: Barycentre speed of a B5-V star (top) and a M5-V (bottom) with respect to a G0-V star observed in J Band. The curves stop when the Zenithal distance is larger than 60°. 372

Figure 8-81: Mapping of the FoV for interaction matrix estimation in MCAO 375

Figure 8-82: The MAD bench installed in the ESO optical laboratory during testing..... 376

Figure 8-83: Optical layout of MAD. 377

Figure 8-84: Left: the SH WFS area during integration. Right: the LOWFS during final testing. 378

Figure 8-85: Left: MACAO bimorph DM used for conjugation at 8.5 Km. Right: the multi layer turbulence generator MAPS. 378

Figure 8-86: MAD first light SCAO closed loop 379

Figure 8-87: MAD first light GLAO closed loop. Only one phase screen at 6 Km altitude has been used and the guide stars were located on a circle of 1.5' diameter. The FWHM reduction factor is ~2.5. 379

Figure 8-88: Encircled energy gain in the first light GLAO closed loop. At the FWHM radius of the corrected image the gain is ~2. 380

Figure 8-89: Common path XAO concept for EPICS. 384

Figure 8-90: Individual scientific channel path. 384

Figure 8-91: 5-sigma detection level after differential imaging for 0.1 nm rms differential chromatic error before the coronagraph (circular average). λ = 1600 nm. 385

Figure 8-92: Residuals after dual imaging with a perfect coronagraph (left), and a double stage Lyot coronagraph with prolate apodization (right.) 386

Figure 8-93: AO correction of co-phasing residuals. Left: initial co-phasing errors. Right: best fit with DM2 (0.67 actuator separation). 386

Figure 8-94: Residual left by best fit of DM_2..... 387

Figure 8-95: Cut in wave-front maps of Figure 8-102 and In Figure 8-94. Solid line: initial co-phasing errors (piston and tip-tilt, 20 nm rms). Dashed line: DM_2 fit. Dotted-dashed-line: residual error figure after correction by DM_2 (6 nm rms error residual of high spatial frequencies). 387

Figure 8-96: Effect of co-phasing on coronagraphic image at 1600 nm (Circular average of 2D image). Solid line: PSF without coronagraph. Dashed line: Coronagraphic image with initial

co-phasing residuals of 20 nm rms. Dotted-dashed line: Coronagraphic image of residuals after AO correction (6 nm rms). 388

Figure 8-97: Strehl ratio versus wave-length. 388

Figure 8-98: Theoretical point spread function after a perfect coronagraph. 389

Figure 8-99: Probability to find a NGS/Galaxy versus magnitude over 2' FoV. Top to bottom: Galactic plane, 180-20°, Galactic Pole 393

Figure 8-100: Performance (gain in EE compared to seeing) of a single on-axis LGS. Solid: on-axis, dash: off-axis. Top to bottom: K, H and J bands. The good seeing model was used (0.5''). 394

Figure 8-101: LGS MCAO performance (K-band). Tip - Tilt stars at LGS positions. 395

Figure 8-102: Pseudo Infinite Guide Star conceptual layout. 398

Figure 8-103: Sky-Projected Laser Array Shack-Hartmann conceptual layout. 399

Figure 8-104: Virtual wavefront sensor conceptual layout. 400

Figure 8-105: Variable wavefront sensor conceptual layout. 401

Figure 8-106: Basic principle of measuring atmospheric turbulence with phase shifting interferometry. 402

Figure 8-107 Schematic arrangement of a multiconjugate correction with lasers and LPSI. ... 403

Figure 8-108: Fiber laser 404

Figure 8-109: CW Raman laser 405

Figure 8-110: Hollow Core Photonic Crystal fibre. 405

Figure 9-1: locked rotor mode evolution 410

Figure 9-2: Rotating Mass evolution. 410

Figure 9-3: 1997 design, rocking chair design I. 411

Figure 9-4: 1997 design, rocking chair design II. 411

Figure 9-5: 1998 design. Four petals design. 412

Figure 9-6: 1999 design I. Decoupled M2 unit. 413

Figure 9-7: 1999 design II. Light rocking chair design. 413

Figure 9-8: 1999 design III. Cradle and bearings design. 413

Figure 9-9: 2000 design. Cradle and bearings design evolution. 414

Figure 9-10: 2002 design. Cradle and bearings design evolution. 415

Figure 9-11: 2004 design. Fractal design. 415

Figure 9-12: OWL telescope structure. Side view. 416

Figure 9-13: OWL telescope structure. Side view. 417

Figure 9-14: Structural materials stiffness and strength. 418

Figure 9-15: Typical welded node. 419

Figure 9-16: Base Fractal pattern. 419

Figure 9-17: Base Module. 420

Figure 9-18: Node exploded view 420

Figure 9-19: Azimuth Structure 420

Figure 9-20: Azimuth structure and foundation interface 421

Figure 9-21: Altitude Structure 422

Figure 9-22: Top view..... 422
Figure 9-23: Sets of parallel rope..... 424
Figure 9-24: Rope mechanical interface..... 424
Figure 9-25: Wind vortex shedding. 425
Figure 9-26: Cable damping system. (Courtesy of ULB). 425
Figure 9-27: Active damping concept. (Courtesy of ULB)..... 425
Figure 9-28: Focal station layout. 426
Figure 9-29: Focal station external dimensions. 427
Figure 9-30: Focal station external dimensions. Side view. 427
Figure 9-31: Fibre fed focal station. 427
Figure 9-32: Axial and Radial Bogies. 429
Figure 9-33: Bogie layout 429
Figure 9-34: Axial And Radial Bogies cross section. 429
Figure 9-35: Azimuth bogies location. 430
Figure 9-36: Computer controlled hydraulic cylinders of the master bogies..... 431
Figure 9-37: Communicating vessels measurement..... 432
Figure 9-38: Bogies breadboard test setup..... 433
Figure 9-39. MagLev for trains 436
Figure 9-40. OWL MagLev available design location. 436
Figure 9-41: Corrector 437
Figure 9-42: M6 lay out design and location 438
Figure 9-43: M6 unit overall dimensions. 439
Figure 9-44: Optical bems intersection 439
Figure 9-45: M6 available design volume. 440
Figure 9-46: Segment support system. 441
Figure 9-47: Hexagonal segment assembly..... 441
Figure 9-48: Layout of WEB. 445
Figure 9-49: WEB Functional Layout. 445
Figure 9-50: Air conditioning layout..... 447
Figure 9-51: Inner ventilation. 447
Figure 9-52: FE Model of OWL in zenith configuration. 449
Figure 9-53: Side view of FE Model of OWL 60º from zenith. 450
Figure 9-54. Analysis tree flow chart. 451
Figure 9-55: Vertical uz displacement distribution due to gravity for zenith configuration. Complete structure (left) and mirrors M1 to M6 (right). 453
Figure 9-56: Displacement distribution due to gravity for 60º configuration. Complete structure in global vertical uz direction (left) and mirrors in normal displacements (right). 453
Figure 9-57. Normal displacement distribution of optical elements under static wind at60º..... 454
Figure 9-58: Vertical z-displacement distribution due to uniform temperature change of 10° C. 455

Figure 9-59: Equivalent stress distribution due to temperature change of 10° C. 455
Figure 9-60: Temperature distribution due to sun radiation at 60° altitude angle. 456
Figure 9-61: Vertical (uz) displacement distribution due to sun radiation at 60° altitude angle. 457
Figure 9-62: Equivalent stress distribution due to sun radiation at 60° altitude angle. 457
Figure 9-63: Mode shape of first eigenfrequency in zenith configuration at 1.59 Hz. 459
Figure 9-64: Altitude locked rotor mode shape in zenith configuration at 2.58 Hz. 459
Figure 9-65: Azimuth locked rotor mode shape in zenith configuration at 2.86 Hz. 460
Figure 9-66: Piston mode of altitude and corrector structure at 4 Hz. 460
Figure 9-67: Piston mode of M2 unit structure at 7.3 Hz. 461
Figure 9-68: FE models of M1(left) and M2 cell (right) structures. respectively. 461
Figure 9-69: Piston mode of M1 Cell structure alone at 5.1 Hz. 462
Figure 9-70: Piston mode of M2 cell structure alone at 7.8 Hz. 462
Figure 9-71: Natural frequencies versus mode number. 463
Figure 9-72: Effective masses versus frequency. 463
Figure 9-73: 1σ normal displacement distribution of M1. 465
Figure 9-74: 1σ normal displacement distribution of M2. 465
Figure 9-75: 1σ response PSD of piston displacement of M1 466
Figure 9-76: 1σ response PSD of piston displacement of M2. 466
Figure 9-77: 1σ response PSD of segments piston displacement of M1. 468
Figure 9-78: 1σ response PSD of segments piston displacement of M2. 468
Figure 9-79: FE-model and major dimensions of the OWL with foundation and soil. 470
Figure 9-80: Transfer function from wind load to y-deflection of M1. 471
Figure 9-81: SMITH diagram 474
Figure 9-82: Base line. High configuration 475
Figure 9-83: Low configuration 476
Figure 9-84: OWL scaled down 60 meters 477
Figure 10-1: Adapter Rotator 479
Figure 10-2: Adaptor Rotator location 480
Figure 10-3: Adapter Rotator section 481
Figure 10-4: Adapter Rotator Instrument design volume 482
Figure 10-5: Pickup mirror scan range 482
Figure 11-1: Cargolifter building 487
Figure 11-2: Baseline lay-out (courtesy CI-Map) 489
Figure 11-3. Top view of the enclosure and telescope foundations. 490
Figure 11-4: Principle scheme of natural cooling of the enclosure volume 491
Figure 11-5 Simple thermal model of the enclosure 492
Figure 11-6 Typical temperature evolution of the enclosure assuming site 5 m/s wind speed. 493
Figure 11-7 Enclosure opening cycle (courtesy CI-Map). 494

Figure 11-8: Enclosure foundations overview day park position (above). Night park position (bottom) 495
Figure 11-9: Typical reinforcement 497
Figure 11-10 Typical cladding panel 498
Figure 11-11: Main arch 499
Figure 11-12: Hinge (courtesy cl-MAP) 499
Figure 11-13: Conceptual design of the drive system 500
Figure 11-14: Principle of the air supporting structure (courtesy Airlight) 502
Figure 11-15: Lay out of the alternative design of the OWL enclosure 503
Figure 11-16. Two halves concept (right below teh VLT telescopes platform) 503
Figure 11-17: Radome concept (cupola) for OWL (courtesy cl-MAP) 504
Figure 11-18: Radome concept using air cushion technology (courtesy AirLight) 505
Figure 11-19 Arch-like structure fixing the arches holding the membranes 506
Figure 11-20 Airtensity concept radome enclosure open 506
Figure 11-21: Ventarrones (top right of the figure) 507
Figure 11-22: La Palma 507
Figure 11-23: Horizontal in-line coating plant (courtesy SISTEC-It) 509
Figure 11-24: Ventarrones: Observatory lay out (auxiliary building side above; hotel side below) 514
Figure 11-25 The enclosure installed in La Palma 515
Figure 12-1. The CODEX concept. The simulation represents two observations of the Ly α forest of the same QSO taken at time T_0 (dotted line) and at time T_0+10^7 years (continuous). CODEX/OWL will measure this effect for a separation of the two epochs as short as 10 years by comparing a large sample of high S/N QSO absorption spectra obtained with OWL. 520
Figure 12-2. Expected wavelength shift for different cosmological models: Standard Cold Dark Matter (lower line. no cosmological constant) and Λ Cold Dark Matter (middle line) with cosmological constant = 0.7. The upper line gives the difference of the two. The signature of the non-zero cosmological constant is the change in sign of the wavelength shift. 521
Figure 12-3. Magnitude distribution of known brightest QSO's vs. redshift. From photon statistics and simulations of measurements in the Ly α forest at different redshift one derives the "iso-accuracy" curves plotted in the diagram. The required 1 cm/s/ accuracy is obtained with all the QSO below the 'iso-accuracy' curve in 2000 hours integration (80m telescope. total efficiency 14%. S/N= 13600). In reality the required statistics will be obtained by observing with shorter integrations different QSOs (~40) distributed over the whole sky and at different redshifts. 521
Figure 12-4. Optical Layout of one of the CODEX units. Each spectrograph is contained in a volume of ~3x2x1 meter. The 5 Units will be identical. 522
Figure 12-5. Statistics of photon arrival times in light beams with different entropies. Light may carry more information than that revealed by imaging and spectroscopy: Photons from given directions with given wavelengths give the same astronomical images and spectra. though the light may differ in statistics of photon arrival times. These can be "random". as in maximum-entropy black-body radiation (Bose-Einstein distribution with a certain "bunching" in time). or may be quite different if the radiation deviates from thermodynamic equilibrium. (Loudon: The Quantum Theory of Light. 2000). 524
Figure 12-6 Current optical concept for a QuantEYE detector head: a distributed detector array and a segmented aperture. The collimator-lens system magnifies 1/60 times (collimator

focal length = 600 mm. lens focal length = 10 mm). giving a nominal spot size of 50 μm for a 1arcsec source..... 525

Figure 12-7 The concept of the Hypertelescope 526

Figure 12-8: NIR C-M diagram from therotical isocrones by Girardi wt al. (2002. A&A 391.195) 528

Figure 12-9 The PSF radial intensity distribution as derived from MCAO assessment for the central field of ONIRICA at OWL and used in the simulation of photometry in crowded stellar fields 529

Figure 12-10 The limiting (S/N=5) magnitude $K_{(AB)}$ for point sources as a function of the exposure time 529

Figure 12-11 The limiting (S/N=5) magnitude K(AB) for point sources as a function of the exposure time for OWL and the JWST (assuming same instrument and detector performance)..... 530

Figure 12-12 Optical layout of ONIRICA (central field) 531

Figure 12-13: Concept of the channel splitting in ONIRICA. The FoV splitting is provided by a pyramidal mirror located at the intermediate focal planes. 531

Figure 12-14: Sketch of a single unit of a Smart Fast Camera 532

Figure 12-15: The picture on the left illustrates the SFC concept in which the light of a wide FoV is divided by a lenslet array. 532

Figure 12-16: Opto-mechanical layout of ONIRICA including the two. wide and narrow. channels. The tubular trusses have the function to stiff the cryogenic tubes. 533

Figure 12-17 Two views of the instrument envelope in the instrument bay 533

Figure 12-18 MOMFIS conceptual optical layout (see text). 535

Figure 12-19. Overall MOMFIS implementation in the focal station..... 536

Figure 12-20. Illustration of the MOMFIS operation. Image Correction is performed locally along the line of sight of the target before image slicing and wavelength dispersion. 537

Figure 12-21. Contrast vs. angular separation for different types of planets. (Courtesy O. Lardiere)..... 538

Figure 12-22: Number of stars versus distance from Earth for different spectral types..... 539

Figure 12-23: O_2 A-band at high spectral resolution. 541

Figure 12-24: EPICS will be composed of three spectral channels for the scientific instruments and one for wave-front sensing. 542

Figure 12-25: Differential Imager based on dichoics splitting the beam in 4 wavelengths. 543

Figure 12-26: Block diagram for the EPICS polarimetric mode concept..... 544

Figure 12-27: Optical scheme for the high precision polarimetric mode in EPICS 545

Figure 12-28: Example of halo intensity with perfect coronagraph after adaptive optics correction . Error sources: servo-lag. photon noise (30 % transmission + L3CCD noise excess in WFS). chromatic seeing. aliasing. fitting. static aberration (5 nm rms). 546

Figure 12-29: Minimum exposure time as a function of distance to detect at 5 σ an Earth-like planet in the H20 band (1.25μm. r_0=12.1cm. τ_0=10mn. Simple Differential Imaging. 0.08μm bandwidth. 0.44 atmospheric transmission) 547

Figure 12-30: Minimum exposure time as a function of distance to detect at 50 σ a Jupiter-like planet in the CH4 band (1.60μ. r_0= 12.1cm. τ_0= 10ms. Simple Differential Imaging. 0.055μm bandwidth) 547

Figure 12-31. Rotation curve of the nucleus Seyfert 2 galaxy NGC 7582 (M. Wold. 2005). Circles: VLT-VISIR measurements using the [NeII] line at 12.8μm with a spatial resolution of 0.4" (40pc). Lines: models with different masses of the central blac hole..... 549

Figure 12-32: Optical concept of one of the imaging-low resolution spectroscopy of T-OWL.. 550

Figure 12-33. Sensitivity of T-OWL as compared to other thermal infrared facilities for imaging of stellar-like sources. 551

Figure 12-34. The effect of a “growing” telescope primary on the PSF . Each frame is a 2x2arcsec^2 field with the resulting PSF. The columns from left to right correspond to year after year until completion of the OWL-. The rows are for three filling strategies: the top row is by starting with a 100m x 100m cross. the middle row is a ring-like geometry starting from the outside and the lower row is a ring-like geometry starting from the inside. 553

Figure 12-35: Dust mass detectable (10σ) by SCOWL at 450μm around nearby stars as a function of distance. The upper green line represents the mass of the dusty system ε Eri. and the lower line the dust mass of our own Solar System. 554

Figure 12-36: SCOWL cryostat cross section. 556

Figure 13-1: Structural nodes container 561

Figure 13-2: Pipe elements shipping 562

Figure 13-3: Azimuth tracks alignment metrology. 563

Figure 13-4: Structural elements alignment. 563

Figure 13-5: Azimuth tracks integration 565

Figure 13-6: Azimuth Basement integration. 565

Figure 13-7: Azimuth first floor integration 566

Figure 13-8: Azimuth structure complete integration 566

Figure 13-9: Altitude lower part integration. 567

Figure 13-10: Altitude M1 cell and central tower integration. 567

Figure 13-11: altitude structure complete integration 568

Figure 13-12: Segment Support Structure. 569

Figure 13-13: Segments integration. 570

Figure 13-14: Segment handling tool. notional design 570

Figure 13-15: Segment handling tool. notional design 571

Figure 13-16: Handling of segment on the extractor. 571

Figure 13-17: Clamped and constrained segment. 572

Figure 13-18: Un-clamped and un-constrained segment 572

Figure 13-19: Segment coarse pre-phasing 573

Figure 13-20: Segment fine pre-phasing 573

Figure 14-1: Fraction of time that skies are clear (%) at night for the years 1999 and 2000 over Canaries. NW Africa and Southern Spain (A. Erasmus. ESO Interim Report. Oct. 2004) 578

Figure 14-2: Locations of the sites in Chile. Bolivia and Argentina that were compared using satellite data. Contours show the topography at 500m intervals (see Table 14-2). 580

Figure 14-3: PWV percentile values at each site under clear conditions 580

Figure 14-4: The Carlsberg Meridian Circle (CAMC) database at La Palma 581

Figure 14-5: Diurnal Atmospheric Extinction over Teide Observatory (Tenerife. Canary Islands). Ref: A. Jimenez et al.. Fig.4 581

Figure 14-6: Correlation of satellite UV and ground based V monthly averaged measurements CAMC AE>0.20. NIMBUS7 AE>0.2. Pixel center < 55km from ORM 582

Figure 14-7: World map of jet aircraft contrails in 1992 (top). and predicted for 2050 (bottom). from [72] 583

Figure 14-8: Seeing vs. local wind direction (0=North. 90=East etc.) and velocity at Paranal for best (right) and worst (left) observing conditions (2001-2004. over 778127 samples; J. Navarrete. ESO Observatory) 584

Figure 14-9: Peak ground acceleration (PGA) that a site can expect during the next 50 years with 10 percent probability GSHAP (Global Seismic Hazard Assessment Project) 586

Figure 14-10: Site view 587

Figure 14-11: SLODAR Shack-Hartman pattern using narrow (left) and wide (right) binaries. 589

Figure 14-12: An example SLODAR determination of r0. Left: Measured Zernike coefficient variances. σj (crosses) and the theoretical (Noll) fit (solid line). Right: Calculated value of r0 versus WFS integration number (2ms CCD integrations at 190Hz) 589

Figure 14-13 One-dimensional simulated cross-correlation (solid line) and autocorrelation (broken line) in the direction of the binary separation for a 24x24 sub-aperture. 590

Figure 14-14: MASS principle. scintillation of a single star is measured through 4 concentric annular apertures. 590

Figure 14-15: Relative contribution of the various atmospheric slabs to the integral of the turbulence obtained by combining SLODAR and MASS profiler data after reduction of the overlap area. The common database covers about 116 hours from February to August 2005. 592

Figure 14-16: Complete atmospheric turbulence profile reconstructed from contemporaneous combined SLODAR and MASS measurements. 592

Figure 14-17: Observatorio Roque de los Muchachos (ORM). La Palma. Canary Islands. Spain (http://www.otri.iac.es/sitesting/) 594

Figure 14-18: Morocco Anti-Atlas mountain area has the highest percentage of photometric nights along the North African continental west coast 595

Figure 14-19: Paranal North area proposes several candidate sites along what could become "the photon valley" of the 21st century 596

Figure 14-20: the Macon range. to the East of the huge Arizaro salt flat in NW Argentina allies high altitude (>4500m) and lower seismic activity (http://www.iate.oac.uncor.edu/tolar/) 597

Figure 14-21: 20th century PDO "events" persisted for 20-to-30 years. while typical ENSO events persisted for 6 to 18 months 598

Figure 14-22: Monthly statistics of photometric nights at Paranal and La Silla and their relation to El-Nino Southern Oscillation Index 599

Figure 14-23: Monthly statistics of seeing at Paranal and La Silla and their relation to El-Nino Southern Oscillation Index 599

Figure 14-24: The FRIOWL user interface 602

Figure 14-25: DIMM seeing (1mn average) versus contemporaneous UT1 Cassegrain Active Optics Image Quality (atmospheric dispersion corrected) estimates for January-August 2005 (compilation. J. Navarrete. Paranal). 603

Figure 14-26: UT1-UT2 comparison of contemporaneous Cassegrain Active Optics Image Quality (atmospheric dispersion corrected) estimates for January-August 2005 (compilation. J. Navarrete. Paranal). 604

Figure 14-27: ISAAC. K (lower graph) and H (upper graph) band zenith image quality as measured (dots) and as exprected from DIMM after outer scale correction following [63]; M. Casali. I.R. image quality at the VLT. ESO Internal Report. 02 June 2005. 605

Figure 15-1: Accessibility 609

Figure 15-2: Corrector integration route 609

Figure 15-3: M6 unit integration route. 610
Figure 15-4: M6 unit integration route inside the corrector 610
Figure 15-5: M6 unit integration access 611
Figure 15-6: Primary mirror cover docking operation..... 612
Figure 15-7: Covers on Primary mirror..... 612
Figure 15-8 lifting platform for inspection and maintenance of cladding..... 614
Figure 15-9: OWL horizontal parking configuration. 614
Figure 15-10: Secondary mirror handling facilities..... 615
Figure 16-1. ESO Management structure. 621
Figure 16-2. OWL organizational structure. 626
Figure 16-3. High level schedule..... 631

Figure A- 1. Allocated volume for the Position sensors (Glass ceramic blanks). 661
Figure A- 2. Allocated volume for the Position sensors (Silicon Carbide blanks). 661
Figure A- 3. Position actuators. Implementation and design volume..... 662
Figure A- 4. WEB 0º layout (zenith), side view. 663
Figure A- 5. WEB 60º layout, front view. 663
Figure A- 6. Block-Diagram of APE..... 664
Figure A- 7. APE optical design; the telescope focus is at the bottom of the figure. PWFS: Pyramid WaveFront Sensor; BS: Beam Splitter; ASM: Active Segmented Mirror. 665
Figure A- 8. 1-m silicon carbide BOOSTEC blank prototype. 667
Figure A- 9. Friction drive breadboard 668
Figure A- 10. Optional two-mirror corrector (f/2.1 focus, 4 arc minutes total field of view). 715
Figure A- 11. Optional corrector; Strehl Ratio vs field radius. 716
Figure A- 12. Optional corrector; RMS spot size, RMS wavefront error vs. field radius. 716

Abbreviations & acronyms

ADC	Atmospheric Dispersion Compensator
AO	Adaptive Optics
AGN	Active Galactic Nucleus (Nuclei)
APE	Active Phasing Experiment
CCD	Charge-Coupled Device
CELT	California Extremely Large Telescope
CFD	Computational Fluid Dynamics
CPU	Central Processing Unit
CTE	Coefficient of Thermal Expansion
DIMM	Differential Image Motion Monitor
DM	Deformable Mirror
DM	Deformable Mirror
EEE	Electrical, Electronic, Electro-mechanical Parts
ELT	Extremely Large Telescope
ESO	European Southern Observatory
FMECA	Failure Mode Effect and Criticality Analysis
FoV	Field of View
FP6	EC Framework Programme 6
FPGA	Field-Programmable Gate Array
GLAO	Ground-Layer Adaptive Optics
GTC	Gran Telescopio Canarias
HCI	High Contrast Imaging
HET	Hobby-Eberly Telescope
IFU	Intergral Field Unit
IQ	Image Quality
IR	Infrared
IVV	In Vino Veritas
LGS	Laser Guide Star
LRU	Line Replaceable Unit
M1	Primary Mirror
M2	Secondary Mirror
M3	Tertiary Mirror
M4	Quaternary Mirror
M5	Fifth mirror
M5AM	M5 Adaptive Mirror unit
M6	Sixth Mirror
M6AM	M6 Adaptive Mirror unit
MAD	Multi-Conjugate Adaptive Optics Demonstrator
mas	milli-arc second
MCAO	Multi-Conjugate Adaptive Optics
MEM(s)	Micro-ElectroMechanical device(s)
MLE	Maximum Likely Earthquake
MOAO	Multi Object Adaptive Optics
MOEM(s)	Micro-Opto-ElectroMechanical Device(s)
NGS	Natural Guide Star

NIR	Near Infrared
ORM	Observatorio Roque de los Muchachos (La Palma, Canary Islands).
PID	Proportional-Integral-Derivative (controller)
PIGS	Pseudo-Infinite Guide Stars
ppm	part per million
PSD	Power Spectral Density
PSF	Point Spread Function
R&M	Reliability & Maintainability
RD	Reference Document
RMS	Root Mean Square
RON	Read-Out Noise
RTC	Real-Time Computer
SALT	South African large Telescope
SCAO	Single-Conjugate Adaptive Optics
SH	Shack-Hartmann
SPLASH	Sky-Projected Laser Array Shack-Hartmann
SNe	SuperNovae
SRD	Software Requirement Document
UT	Unit Telescope (VLT)
VLT	Very Large Telescope
WEB	Wind Evaluation Breadboard
WFE	WaveFront Error
WFS	WaveFront Sensor

1. Scope

This document presents the conceptual design study undertaken by ESO to assess the feasibility of building a 100-m class optical and near-infrared extremely large telescope – called OWL. It contains detailed studies of the key subsystems as well as proposed project implementations and engineering solutions. While recognizing that any modern observatory is an integrated system of telescope, instruments, data, operations and communications subsystems, this study chooses to focus on the technical feasibility and associated costs of the major subsystems of a particular design approach that meets a set of science cases appropriate to a 100-m class facility.

The OWL system is still in a highly dynamic design phase, and the completion of the conceptual design of all subsystems does not entail irreversible design decisions. Indeed, the proposed design phases have been scheduled in a manner that allows requirements to be iterated and design options to be pursued well into the overall design process. In particular, the modular opto-mechanical concept makes it possible to consider relatively fast and significant reconfigurations. This flexibility would clearly only exist if the eventual telescope size falls within a range (~60-m to ~120-m) compatible with modular design and extensive parallelization of supply, integration and maintenance lines. Notwithstanding possible changes of major requirements, the ensuing preliminary design phase would start with a re-assessment of the current opto-mechanical design with a view to incorporating feedback from recent instrument studies. For evident reasons, the latter could only be initiated after defining a plausible telescope design to a reasonable level of detail.

Chapter 2 of this document provides a broad overview of the OWL concept, preliminary conclusions and possible plans including summary reports on related activities. In particular, these reports cover the generic development of enabling technologies undertaken by an ESO lead collaboration of 27 partners, including industry, with financial support by the European Commission (Framework Programme 6, ELT Design Study).

Chapter 3 is a brief summary of the science case, addressed in more details elsewhere (RD526) in the general context of Extremely Large Telescopes.

Chapter 4 provides the subsequent top-level scientific and technical requirements. It is well understood that the design, construction and operation of a system the size and complexity of OWL requires more than technical feasibility of its subsystems. Chapter 5 provides an overview of the proposed System Engineering approach, including methods, tools and essential parameters. Chapters 6 to 13 provide a relatively detailed description of the design and underlying analysis. Some areas are addressed in more detail than others, in particular where separate, supporting reports were not available in time for this review. To a more limited extent, the same applies to Chapter 14, devoted to site considerations.

Observatory and science operations are briefly addressed in Chapter 15. Management aspects, including plans, schedule and cost estimates are provided in Chapter 16. Roughly 70% of the estimated capital investment (e.g. segments, telescope structure, enclosure) are supported by industrial studies undertaken by experienced suppliers under ESO contract. The remaining 30% are either internal estimates or, in the case of adaptive optics subsystems, (generous) allocations. At the time of writing of this document, further industrial studies are under way or

planned. It is anticipated that the ensuing preliminary design phase would include extensive interaction with industrial suppliers, with a view not only to consolidating design solutions and exploring alternative ones, but also to strengthening confidence in the eventual schedule and cost. A summary table of the baseline design characteristics is provided towards the end of this document.

Maximum and reliable scientific capability, as well as constant awareness of requirements, of design, production, integration and operation constraints, including engineering, cost and schedule considerations, have played a major role in the development of OWL. They will continue to do so in the ensuing phases. The same applies to risk assessment and management. The number of degrees of freedom and the complexity of the control systems are challenging enough. Wherever possible, the OWL design is tailored to minimize supply and technological risks, even with adaptive optics –the first generation adaptive mirror of OWL relies on the simplest optical form: a flat surface. Control schemes will be tested well before glass needs to be cast; the Multi-conjugate Adaptive Optics Demonstrator (MAD) is already being tested in the laboratory, with promising results. The development of generic technologies and concepts is proceeding with the ELT Design Study, gathering partners across European academia and industry under ESO's lead. Combined active optics and segmented mirror control will be tested on-sky with the Active Phasing Experiment. While OWL does indeed include overwhelming challenges, we believe that they can be managed – and that none of them taken individually may compare to the one originally taken with the VLT, when the fabrication of its most essential element -the primary mirror- was, perhaps, the most daring challenge taken up by the scientific community and by industry in decades of telescope-making.

2. Overview

2.1 Objectives

In view of the scale of the project, it was understood from the start that the conceptual design had to reach a level of technical maturity higher than usual for such a phase. For this reason, issues of feasibility of at least the principal subsystem were given high priority during the study.

The main goals of the Conceptual Design phase were the following:

- To develop a design for a 100m telescope based on scientific requirements
- To explore technical solutions leading to a minimization of cost
- To identify items requiring extensive R&D
- To validate the feasibility of the chosen solutions through analysis, tests and/or dedicated industrial studies
- To include in the design safety, maintenance and operations considerations that would contain the eventual operating costs
- To assess the feasibility of appropriate astronomical instrumentation
- To develop realistic schedule and cost estimates
- To identify the main risks of the chosen approach

This book describes the work done at ESO to achieve these goals.

It is to be reviewed by a panel of international experts, including some of the outstanding members of the telescope-design community whose arguments and criticism will greatly assist in the evolution of ESO's ELT effort.

It is also an occasion to document ESO's conceptual design work and to make it available to the community, to seek their feedback. To this end, the first day of the Review will be an Open Day of presentations with ample discussion time, to which anybody interested can participate. We plan to make this report widely available after the Review, although some parts containing confidential information from Industry will have to be omitted. Topical meetings on specific aspects of the design are also foreseen in 2006 in order to invite community help in shaping the next phase of the design.

The main objectives of the Review are the following:

- Assess the OWL approach, its strengths and weaknesses
- Analyze feasibility issues
- Evaluate cost and schedule estimates

- Identify the principal risks of the project
- Identify areas to be further explored
- Assess whether it is appropriate and desirable to move to the Preliminary Design phase, with the goals to:
    - Reassess the design parameters and solutions
    - Incorporate results from the European Commission sponsored ELT design Study
    - Explore other/better technical solutions
    - Produce a Preliminary Design of a viable/affordable ELT, to undergo PD Review within the next three years.
- Advise ESO about possible future courses of action.

A note on Instrumentation

Although preliminary reports of the instrumental conceptual studies under way by the Community and ESO are presented, these are not meant to be reviewed at the same in-depth level as the telescope design. The reasons are the following:

- These studies have started only recently (consolidation of the optical and mechanical design as well as of the science cases having been a prerequisite for the studies)
- The main aim of these studies is to assess the feasibility of instrumentation able to carry out the critical science goals and to feed back requirements to the telescope design if necessary
- The final design of the telescope (size, optics, mechanics) may change in Phase B and therefore the interfaces and parameters used are only indicative at this stage. A coherent instrumentation plan with the instrument priorities will be prepared during Phase B.

2.2 Scientific potential of a 100-m class telescope

State of the art optical and infrared astronomy over the last decade or so was driven by the current generation of 8 to 10m class telescopes, which produced a large fraction of all new discoveries. The vast improvement in sensitivity and precision allowed by the next step in technological capabilities, from today's telescopes to the new generation of 50-100m telescopes with integrated adaptive optics capability, will be the largest such enhancement in the history of telescopic astronomy. It is likely that the major scientific impact of OWL will be discoveries we cannot predict, so that its scientific legacy will also vastly exceed even that bounty which we can predict today.

Nevertheless, for the planning of such a powerful new facility, science drivers based on today's knowledge have to be considered. The science case for OWL is truly breathtaking. All aspects of astronomy, from studies of our own solar system to the furthest observable objects at the edge of the visible universe, will be dramatically advanced by the enormous improvements attainable in collecting area and angular resolution: major new classes of astronomical objects will become accessible to observation for the first time. Other objects, which we can either only barely detect or whose existence we can only indirectly infer today, will be accessible for detailed studies. Our understanding of the universe near and far will either be challenged or confirmed. A thorough review of the science driver for an ELT has been outlined in the Science Book produced by the OPTICON working group on ELT science. That book contains numerous specific science projects to be carried out with ELTs. It also contains three highlight science goals which have been used as reference for the design goals. These goals are summarized in Chapter 3. Here, we briefly review some of the topics where OWL will provide new insights.

Terrestrial planets in extra-solar systems.

Detection of exo-planets has become routine in only a few years. The field will now move on to identify planetary systems and their characterisation. Are their patterns of planet masses, orbits, structure and other properties with their parent stars? What can be learned about the formation mechanism and their evolution in different planetary systems? How do massive planets influence the formation (or destruction) of smaller planets? How does a binary companion star affect the formation of planets? These questions can be addressed by statistical samples of planetary systems. The larger the sample the better. An OWL-type telescope has access to this parameter space, which is largely excluded for smaller telescopes. The ultimate goal is, of course, the detection of earth-like planets in the habitable zone. The role of Jupiter to 'protect' the inner solar system from comets and hence as a warranty for long periods without major impacts has long been recognised. The existence of a similar guardian planet can be assumed to be needed for life on another planet. The characterisation of exo-planetary systems is the next step towards exo-Earths.

A pre-requisite for life as we know it is water in liquid form. The places in a stellar system where water can exist is the habitable zone around the star, the size of which depends on the luminosity of the star. The search for planets within that narrow annulus around a star requires both extreme light gathering power to detect the faint planet and extreme telescope size to separate the planet from the bright star light. The challenge is to observe an object that is about 10^{10} times fainter than its parent star. Not all stars have planets and few will have planets in the habitable zone, so the largest possible sample of stars has to be surveyed to increase the likelihood of detecting planets on which life could exist. The required telescope for this kind of observations needs to be truly extremely large: the number of stars that can be studied is proportional to the spatial resolution to the cube (or to D^3, with D the telescope diameter). The time for different telescopes to achieve the same signal to noise in the background-dominated regime is proportional to D^4. A 100m telescope can in principle detect an earth-like planet around a solar-type star out to a distance of 100 light years, which means that there are about 500 stars of this type to be surveyed. Key to the achievement of this challenging goal is the light gathering that will allow improving the contrast between planet and star through the detection of in situ spectroscopic features. As a huge bonus, it would then be possible to characterize planetary surfaces and atmospheres. The search for biomarkers in the planet atmosphere has the potential to provide first indications of extraterrestrial life. It is clear that larger planets and planets with larger separation from their star would easily be detected by a 100m telescope and open up the field of planet demographics down to low-mass planets. Such statistics will provide the clues for the detailed understanding of the formation of stars and their planetary systems; for example which stars have planets, what is required to form planets, what is the chemical composition of the parent stars and are there planets around special stars (e.g. white dwarfs, very old halo stars). As an added bonus, targets for future space missions (and viceversa) will also be provided, fully exploiting the synergy between ground and space. The quest for high contrast imaging sets stringent requirements on the development of adaptive optics. Various methods are under investigation, e.g. coronagraphy, nulling interferometry, extreme Adaptive Optics, simultaneous differential imaging (SDI), and have already shown promises of high contrast (e.g. NACO/SDI at the VLT has achieved ~ $5 \cdot 10^4$).

Dark matter and dark energy.

Observations from space and ground imply that dark matter exists on the scale of galaxies and beyond, and that dark energy is pervading the universe. Particle physics has been unable to date to identify the dark matter particles and evidence for their existence as well as clues about their nature are still coming solely from astrophysics. It is interesting in this context that constraints set by astronomy on the mass of the neutrino are as stringent as the best upper limits from experiment. Similarly, through a detailed study of the growth of structure in the universe, it should be possible to derive further constraints on properties of dark matter.

Key constraints on the nature of the dark matter will come from observations of the assembly of galaxies at high redshift. OWL will not only resolve the distant galaxies into their luminous components, but will also be able to obtain spectroscopy for individual components which will then be used to trace the kinematics within the galaxies (and in their extended dark-matter

haloes) and determine the amount of dark matter required to build them. These observations will provide mass measurements of galaxies independently of the brightness of the galaxies. OWL will be able to observe regular HII regions to very high redshifts (z ~ 5), and will be able to map the dark matter content of individual galaxies throughout the observable universe. This will provide astronomers with a detailed evolutionary history of the clumping of dark matter throughout the observable universe.

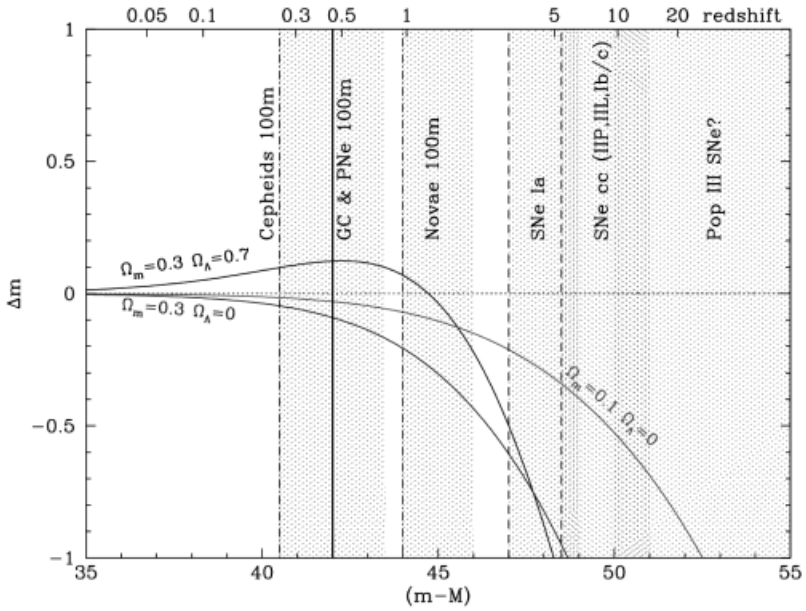

Figure 2-1. Using primary distance indicators to disentangle cosmological models. The plot shows the apparent magnitude difference relative to an empty universe of several cosmological models as a function of redshift. Regions of application for various methods of distance estimates with OWL are indicated.

The nature of dark energy is even more mysterious. Evidence for dark energy comes from observations of supernovae, which serve as standard candles to map the distance of objects as a function of redshift. Such observations shows that SNe at z < 1 appear fainter and therefore more distant than expected in an empty universe without dark energy, while those at z > 1 appear brighter and therefore closer. This is illustrated in Figure 2-1. The interpretation of these observations is that dark energy exerts a negative pressure and hence accelerates the universal expansion. The combination of the SN results with measurement of fluctuations in the cosmic microwave leads to the conclusion that about two thirds of the global energy comes from this dark (or vacuum) component. OWL can test the expansion history of the universe with several different astrophysical objects thus decreasing the dependency on possibly unknown systematic effects. Pulsating Cepheids, globular clusters, planetary nebulae and novae could be observed to distances where the effect of dark energy can be measured (Figure 2-1).

The differences between the cosmic expansion rate in different cosmological models increases strongly as a function of redshift. A 100m ELT will be able to detect supernovae possibly all the way to the time when the universe became transparent to light. By accurately determining the potential variations of the strength of dark energy in early times, one can answer the fundamental question of whether dark energy corresponds to Einstein's cosmological constant or to some "quintessence field" as suggested by modern versions of quantum field theories. The need for these observations is critical. In the words of the Astronomer Royal, Sir Martin Rees, "Cosmologists can now proclaim with confidence (but with some surprise too) that in round numbers, our universe consists of 5% baryons, 25% dark matter, and 70% dark energy. It is indeed embarrassing that 95% of the universe is unaccounted for: even the dark matter is of quite uncertain nature, and the dark energy is a complete mystery"

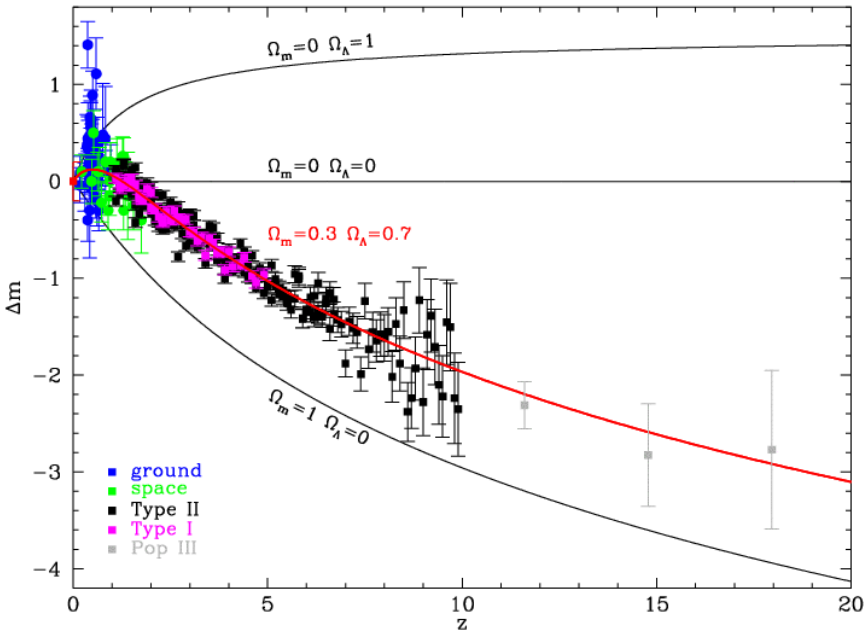

Figure 2-2 Simulation of observations of Supernovae with OWL.The current data from ground and space observations are shown. These observations will allow to determine the cosmic SN rate, and help disentagle cosmological models (e.g. whether a "quintessence field" or a "phantom energy" exist).

High redshift Supernovae

The detection and study of SNe is important for at least two reasons: (1) their use as *calibrated* standard candles provides a direct measurement of the expansion rate of the Universe *H(z)*, and allows to measure its acceleration/deceleration and to determin the exact epoch in which the universe experimented the transition between deceleration and acceleration; and (2) the evolution of the cosmic SN rate provides a direct measurement of the cosmic star formation rate (SFR). Indeed the rate of core-collapse SN explosions is a direct measurement of the death of stars with masses > 8 M⊙ while type Ia SNe provide the history of star formation of moderate mass stars, 3 - 8 M⊙. Simulations of observations carried out with OWL, which fully exploit the potential of diffraction limited observations in a 2×2 arc minute field in the K band, yield about 400 SNe (in about ~1000 hours of observing time), which can studied up to *z*~15. OWL would open also the possibility of detecting the very powerful SNe from the primordial stellar population (or Pop III) that are expected to be produced by pair-creation in zero-metallicity, very massive stars (140-260 M⊙). Figure 2-2 shows the result of the simulation, which includes the expected measurement errors and the cosmic variance in the SN brightness (i.e. the variability in absolute luminosity of individual SNe). Present day data from ground and space observations are also shown.

Direct measurement of the cosmic acceleration/deceleration.

Enormous collecting areas together with extreme instrumental stability also open the very exciting prospect of measuring the early deceleration of the universe in a direct way. The results mentioned above indicate that our universe has undergone a phase of acceleration following one of deceleration. So far most of the results in this area have come from measurements of the geometry of the universe, which do not directly probe the acceleration. A direct measurement of the acceleration itself has always been considered impossible with the present generation of telescopes. However, with a sufficient flux of photons, and with a spectrograph stability of the order of 1 cm s^{-1} over 10 years, changes in the recession velocity of absorption lines in the Lyman-α forest of bright quasars out to z ~ 5 can be detected. This would allow a real physics experiment to be carried out with OWL, whose results would be unequivocal, model-independent and assumptions-free. A stability of a few cm s^{-1} is challenging but has already been achieved with e.g. the HARPS instrument at the ESO 3.6m telescope. Development is needed to maintain this stability over a long period of time.

Resolved stellar populations

One of the important goals of OWL is to measure individual stars in all morphological types of galaxies. First HST and now the current 8-10m telescopes have opened this research field for galaxies in the Local Group and the brightest stars in other nearby galaxies. Spectroscopy with the ground-based telescopes is limited to the most luminous stars in the Local Group. This means that we still need to extrapolate our detailed understanding of stars in even the local Universe from what we know about stars in our Milky Way. OWL will make stars in galaxies out to the Virgo and Fornax clusters accessible. In particular, it would provide for the first time the opportunity to observe stars in elliptical galaxies (Centaurus A, Sculptor Group, Leo I Group and others at distances less than Virgo). The history of stars in dwarf, normal and elliptical galaxies are certainly different and we will not have a complete picture of stellar evolution until we understand the histories of stars in different galaxies.

Need for a proper instrumentation package

Defining and validating solid concepts for a comprehensive instrumentation package that has the potential to address the major science drivers of the proposed facility is an essential part of the feasibility assessment of any ELT project. Conceptual studies for OWL instrumentation started only a year ago, as the development of the project provided a first definition of the essential interfaces between the instruments and the telescope. These 7 studies, typically one-year long, are being conducted in many Institutes across Europe and their status and results are summarized in chapter 12. They cover a very large fraction of the parameter space, from the Visible to the sub-mm range and from imaging to high-resolution spectroscopy. The key science drivers of exo-planets detection and characterization and of follow-up of the very high-z Universe are addressed. This short program is considered as the first step to the more elaborate point design studies very soon pursued in the frame of the ELT Design Study and described in apprendix A-1.8.

It should be noted that instrumental activities relevant to OWL (or any other ELT) instrumentation actually started some years ago, albeit in a more diffuse way. The now 18-month old OPTICON FP6 program supports the development of a number of "1st generation" key components especially in the areas of adaptive optics (wavefront sensors, deformable mirrors, real-time computing), smart optics (cryogenic slicers, moving cryogenic buttons) and dispersers (cryogenic near-IR Phase gratings). Also some of the 2nd generation VLT instruments, currently under development, are actually exploring ELT instrumentation enabling concepts: the KMOS multi-object near-IR spectrometer uses cryogenic arms with slicers; MUSE is based on a large set of 24 strictly identical spectrometers; the recently completed Planet Finder feasibility study has investigated many important approaches to exoplanet searches including advance coronagraphy and differential imaging/spectroscopy.

2.3 Context

The decade 2010-2020 will see the maturity of the current generation of telescopes (VLT, Keck, Gemini, Subaru, LBT, GTC, HET, SALT, Magellan etc) equipped with a second generation of instruments often performing at the diffraction limit through advanced Adaptive Optics (AO) systems. Interferometry will have come out of its infancy to operate in the faint object regime (K~20) and to produce astrometric results in the μas range. ALMA will provide mm and sub-mm astronomers with a facility "equivalent" to optical ones (both in terms of service offered to the community and of resolution and sensitivity). And a new generation of ground based optical/NIR 30 to 100m telescopes now on the drawing board (TMT, GMT, Euro-50, OWL etc) may open a completely new window on the Universe and produce unprecedented results (with resolution ~ mas and sensitivity hundreds or even thousands of times beyond what is available today).

Evolution of existing facilities: Adaptive Optics. AO, now in its "adolescence", will soon outgrow the current limitations (single natural (N) or laser (L) guide star (GS), limited field of

view, small sky coverage) through the development of Multi-Conjugated AO (or other forms of atmospheric tomography). MCAO uses multiple NGS/LGS systems to provide a wider corrected field of view, and is now being developed at several existing observatories: for example, Gemini is building an MCAO system for its instrumentation. ESO is building MAD (McAo Demonstrator) to see first light at the VLT in early 2006 as an enabling experiment for the new VLT instruments and for OWL. An optimal implementation of AO is considered of outmost importance. Thus in Phase B telescope and instrument designs have to be iterated – taking into account the latest results from prototype experiments and advanced atmospheric modeling - to ensure the highest possible scientific return on investment.

Evolution of existing facilities: Second generation instruments. Among the second generation instrumentation considered by ESO (but similar ones are under study at many other observatories) are a multi micro-mirror, distributed classical AO system instrument (FALCON) to study in detail many individual objects in the telescope's FoV at the same time; AO-fed planet finders using nulling interferometry coronagraphs; NIR multiobject wide-field spectro-imagers; image slicer-based multi integral field spectrographs; very wide wavelength coverage “fast” shooters, able to do simultaneous spectroscopy from 0.3 to 3μm. The underlying philosophy is one of sampling the instrumentation parameter space (wavelength, resolution, FoV, image quality, multiplex, synergy with other space or ground facilities, etc) based on clear science requirements.

Evolution of existing facilities: Interferometry. Both Keck-I and VLTI have achieved fringes in 2001. VLTI, both with auxiliary 1.8m telescopes and with the VLT 8m telescopes, is currently in continuous science operations with its instruments MIDI and AMBER. It will soon evolve towards imaging, both with the present generation of instruments (e.g. AMBER, which has already demonstrated 3-telescope measurements of phase closure) and with PRIMA (Phase Referenced IMAging, a dual feed facility providing stabilization of the fringes of a faint object by tracking the fringes of a bright reference star within one arcminute). These instruments will be used to image planetary systems, the inner regions of AGNs, and objects as faint as K~20. It will also provide astrometric measurements down to a few μas, thus enabling the possibility of direct detection of extrasolar planets and their orbits.

ALMA. The Atacama Large Millimeter Array, an example of major project collaboration between Europe and the US, is a variable configuration array of 50 12m antennas working in the 0.3 to 10 mm wavelength range to be put at 5000m in Chajnantor in the Desert of Atacama. ALMA is a 50/50 partnership, with ESO managing the European side and AUI the American side. It will have high angular resolution (to below 0.01" with baseline >10 km) and high sensitivity (area ~ 5,600m^2). ALMA will be able to study galaxy formation in the very early Universe, resolve the far infrared background in its wavelength range, study star formation deep in dark clouds, search for protostars, analyze star and planet formation processes, and study the bodies of our solar system. The project is in its Phase 2 (construction, 2005-2012), and is scheduled to start interim operations with a reduced number of antennas as early as 2009.

Space missions. JWST, XEUS, TPF/Darwin precursor missions and others will explore the heavens from above the atmosphere, exploiting the freedom from turbulence, sky absorption and sky background. In view of the possibilities opened by adaptive optics, the optical/NIR capabilities of a “small” (5 to 10m) telescope in space may not be always competitive with those of 30 to 100m telescopes on the ground. It is not inconceivable that 10 years from now it may make more sense to go to space only for those wavelengths for which the advantage is overwhelming (x-ray, UV, thermal IR etc, which is the case of the projects mentioned above), leaving the optical and NIR to adaptive ground based telescopes that for similar costs could provide much higher angular resolution and sensitivity (but probably not as large field of view). It is not premature to consider such a possibility, even acknowledging how much it depends on very demanding developments in adaptive optics. However, in the long term, the cost of putting matter into orbit may be substantially less than today: in this case, not having to contend with air and gravity may become attractive enough that we consider moving *all* our telescopes to space. This is probably a choice for the generation of telescopes after the next.

2.4 The OWL concept

Over the last few years several design studies are being carried out of the telescopes the astronomers believe they will need in the 2010s. They range between 20 and 100 meter in diameter and, to a more or less critical extent, they all try to break one or both of the traditional laws of the art of telescope making: the *cost law* ($\propto D^{2.6}$) and the *growth law* (the next generation telescope is twice as large as, and ~ 35 years after, the previous one). The rationale for having larger than two increases in diameter comes from the science cases; the one for reducing costs to "reasonable" totals is the goal of achieving the required funding.

2.4.1 The history of telescope growth.

Figure 2-3 shows the history of the telescope diameter, with a few future telescopes (TMT and OWL) added for reference. There are two aspects that are immediately evident: (1) "local" scatter notwithstanding, the trend of diameter increase has remained substantially constant since Galileo (doubling every 50 years or so) and (2) the *quantum jump* between a 10 and a 100m telescope is similar to that between the night-adapted naked eye and the first telescope, which certainly bodes well for the potential for new discoveries. During the 20th century there has been some acceleration, with the doubling happening every ~35 years, (see e.g. the "California progression" with the Hooker [2.5m, 1917], Hale [5m, 1948], and Keck [10m, 1992] telescopes).

One point that perhaps is not immediately evident, though, is that in the last 50 years there has been a larger increase in telescope sensitivity due to improvements in detectors than to increases in diameter (Figure 2-4). Now that detectors are at efficiencies close to 100%, *large improvements can be obtained only through large increases in diameter*. For example, at the times of photographic plates, with efficiency of a few percent, even the 5-meter Hale telescope was only equivalent to a 1-meter "perfect" telescope (i.e. one with 100% efficiency).

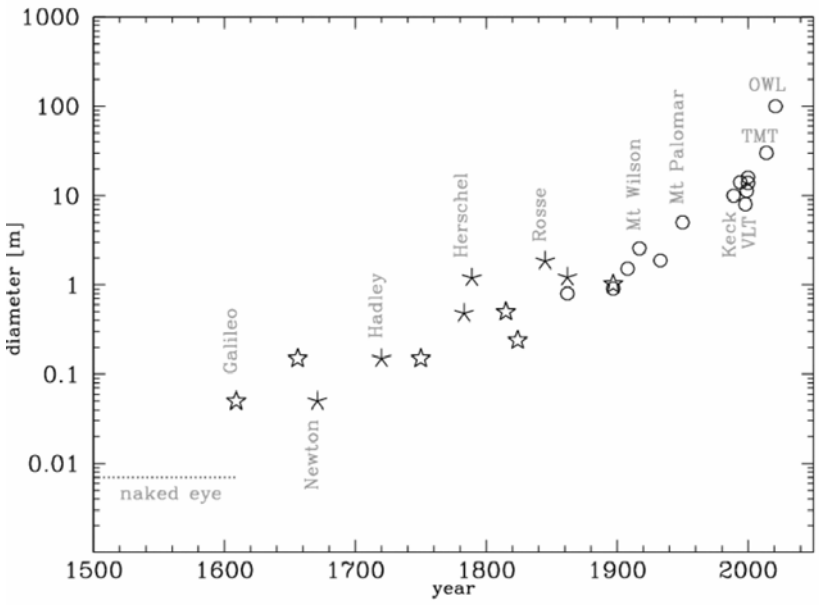

Figure 2-3 Brief history of the telescope. Stars are refractors, asterisks are speculum reflectors and circles are glass reflectors. Some specific telescopes are named.

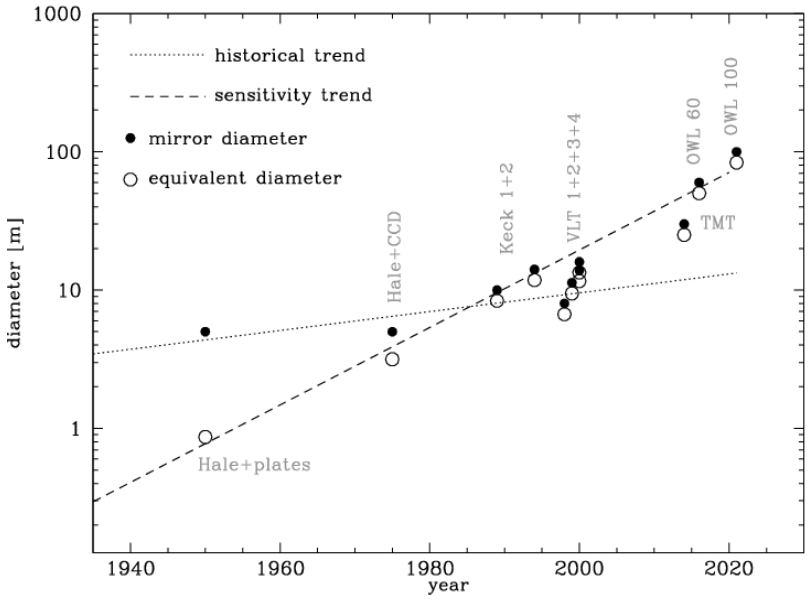

Figure 2-4 Improvement in sensitivity of telescopes expressed in "equivalent diameter of a perfect telescope" = $\sqrt{(\eta D^2)}$, with η the telescope overall efficiency (the dashed line is an aid to the eye, not a fit).

2.4.2 A giant telescope in an industrial context

Traditionally, larger telescopes were most demanding in terms of industrial effort because the burden of providing larger apertures depended on suppliers taking significant technological risks. To a limited extent the VLT moved away from that tradition, its active optics allowing significant relaxation of fabrication tolerances. Still, the casting and polishing of 8-m class primary mirrors, not to mention the design and fabrication of a lightweight, fast steering secondary mirror, represented risky and costly challenges at the time. OWL moves one decisive step further in the direction of supplier-friendly solutions, with a design such that most costly subsystems, in particular mirror segments & supports, telescope structure and drive systems, do rely on proven, low risk technologies. The reward of the implied design compromises is a most favorable cost in relation to size. Indeed, the benefits of low risk processes and serial production cannot be overstated, with modules unit costs at one fifth to one tenth of their single unit prices[1] and with attractive lead-times. According to industrial studies[2], OWL segments (7,000 m²) can be produced in 8-9 years at a cost of about M€ 300 (i.e. 43 k€/m²). These figures[3] should be compared with the VLT's 200 m² in 10 years at a cost of 67 M€ (330 k€/m²). Similarly, the fractal design of the telescope moving part, based on very few simple standard or serially produced components, leads to a low-cost, small lead-time, yet very performant structure.

Indeed, modular design and serial production automatically imply serial integration and favorable supply lead-times. Also, this can be matched by a favourable integration lead-time, thereby largely compensating for the apparent schedule disadvantage of an extremely large telescope with a diameter much beyond 30-m.

This does not mean that there are no challenging technological developments associated with OWL. *Au contraire*, such areas as getting the successive generations of adaptive optics based

[1] according to industrial data.

[2] Five competitive studies for the blanks production and two for their polishing; see RD6, RD7, RD8, RD9, RD10, RD11, RD12.

[3] which include industrial facilitization. One year has been discounted from the actual VLT schedule to account for the fact that REOSC, with ESO's agreement, delayed the last VLT primary by more than one year in order to accommodate the Gemini mirrors in its production plans. The VLT primary mirrors price has been adjusted to 2002, starting with 1989 prices.

field correction and, less daunting but still highly demanding, the instrumentation that could fulfill its ambitious science drivers will require enduring and coordinated effort at both the European and World level throughout the entire life of the facility.

2.5 Top level requirements

The science case can be distilled into a set of requirements that the telescope and instruments have to meet to achieve the goals. Primary among these are the large collecting area and the best possible image quality. The ensuing Top Level Requirements are discussed in detail in Chapter 4 and are summarized here.

The telescope collecting area requirement is 6500m^2 or larger. This is driven by the highlight science cases of earth analogue exo-planets and resolved stellar populations in a representative section of the Universe. The Codex instrument science case (measuring directly the deceleration of the expansion of the Universe) also drives to the largest possible size, as do many other specific science goals (e.g. primordial stellar populations).

The wavelength coverage requirement covers the range from the V band to 25μm, with UV-Blue as a goal. A strong case for mid infrared coverage up to the sub-mm range is made (where OWL would be a wide field complement to ALMA), so extending the coverage to these wavelengths is also a goal.

The focal ratio of the telescope should be such that the focal plane has a “reasonable” (less than 2m) dimension for the required field of view: a lower limit of F/6 is set, to be traded off with the consideration that larger F/ratios would simplify the instrumentation.

The image quality requirement for the telescope optics is to provide diffraction limited performance over the science field of view (see below). The image quality requirement for adaptive optics depends on the AO mode and on wavelength and is specified in RD41. Reference values are 0.65 (goal 0.75) Strehl in the K band for single conjugate AO, 0.40 (goal 0.50) Strehl in the K band for multi conjugate AO, 0.90 (goal 0.94) Strehl in the K band and 0.40 in the V band for extreme AO. The corresponding requirements for the first generation of instruments are 80% of these values.

The emissivity of the telescope needs to be minimized for observations in the thermal infrared. Every effort should be made in Phase B to develop high reflectivity coatings and proper baffling so that the total emissivity of the telescope is kept below 15% (goal 10%).

The field of view science requirement varies from extremely small fields (a few arcseconds) to several arcminutes and may not be always compatible with the image quality requirement. The possibility of having a “large” field with partial or little AO correction is implicit in several science goals, but seeing limited performance in imaging may be physically impossible to achieve (at least in broad bands) as the sky background may saturate the pixels in a much shorter time than the fastest read out time (so that even if possible an observation would have unacceptably long overheads). The science field of view requirement (diameter) is 0.5 (goal 1) arcminutes in the V band, and 2 (goal 3) arcminutes in the K band. The total field of view of the telescope must allow the selection of guide stars for guiding, active optics and adaptive optics. A minimum of 8 arminutes will provide acceptable sky coverage (although laser guide stars may be needed for adaptive optics).

The transmission of the telescope will be maximized, and studies shall be performed in the design phase to identify appropriate coatings. Based on the properties of various existing types of Ag-based coatings, the requirement is set at 98% (goal 99%) per reflecting surface at 1 μm, with less than 1% degradation during operations.

At least 4 (goal 6) focal stations should be provided. At least one of them should be gravity invariant.

The available fraction of sky will depend on site selection. The sky coverage of the telescope shall be to 60 (goal 70) degrees of zenith distance. The zenith avoidance area shall be the smallest compatible with the maximum rotational velocity of the structure, and be no more than 1 (goal 0.5) degree. Ways to correct for the effect of relative differential displacements in "wide" field observations due to atmospheric refraction shall be developed in Phase B (e.g. post-processing, active optical elements, operational strategies etc).

Site selection will be made before the engineering level 1 requirements need to be frozen. The choice of the site shall be the result of a thorough trade off analysis of atmospheric, logistical, seismic and ground properties, and of astronomical considerations (e.g. available fraction of the sky, light pollution). Low cloud coverage, low precipitable water vapour, moderate ground-level wind, adequate turbulence characteristics (turbulence profile, amplitude, and coherence time) will be major selection criteria. The site shall as a goal be suited to observations also in the mid to far (sub-mm) infrared.

The operational lifetime of OWL shall be larger than 30 (goal 40) years.

Parameter	Requirement	Goal	Comments
Telescope area	> 6500 m^2	> 7000 m^2	
Wavelength coverage	0.4 to 25 μm	0.30 to > 850 μm	
Image quality (AO)			
SCAO	0.65 Strehl @ K	0.75 Strehl @ K	By telescope in
MCAO	0.40 Strehl @ K	0.50 Strehl @ K	<seeing> = 0.6"
GLAO	3.5× EE gain	5× EE gain	
ExAO	0.90 Strehl @ K	0.96 Strehl @ K	0.40 Strehl @ V
Emissivity	< 15%	< 8%	Protected Ag in Phase A
Field of view	> 6 arcmin	> 10 arcmin	
Throughput (0.55 – 25 μm)	> 90%	> 92%	Protected Ag in Phase A
Focal stations	> 4	> 6	At least one should be gravity invariant
Sky coverage	1 – 60 degree (ZD)	0.5 – 70	
Operational lifetime	> 30 years	> 40 years	
Technical downtime	< 3%	2%	3 years after start of operations
Operating cost	< 3% per year	2%	Of capital cost. Does not include new instruments
ADC: residual dispersion	0.2 pixel	0.1 pixel	Over any one Johnson band

Table 2-1 Summary of top level requirements

Maintenance concepts leading to simple procedures shall be developed so that the telescope meets the top level requirements during operations, with a technical downtime of 3% (goal 2%). The technical downtime requirement applies when the observatory is in routine operations (i.e. 3 years after start of science)

The operating costs of the OWL observatory shall be kept below 3% of the capital investment[4] (this figure does not include costs for new instrumentation). This will be achieved by design (high reliability and easy to maintain telescope and instruments) and by appropriate operations plans.

[4] This is roughly what costs today to operate Paranal, excluding instrumentation costs.

Atmospheric dispersion correction shall be provided, either by the telescope or, if too complex, by the instruments. Active, closed loop compensation may be necessary at the angular resolution of OWL: this shall be studies in Phase B. The residual dispersion after correction shall be smaller than 0.2 pixel for a given instrument at a given wavelength. Ways should be explored in Phase B to assess feasibility of using atmospheric dispersion as a dispersive element of some instrument (e.g. with partial correction so that it is kept constant over some range of zenith distance).

The top level requirements are summarized in Table 2-1.

2.6 Design overview

The design of the OWL observatory builds on VLT experience and, within the limits imposed by science objectives, pays highest attention to fabrication constraints. More specifically, it gives priority to maximizing aperture and to providing a multi-purpose facility at minimal construction and operation costs, within a competitive time schedule and in compliance with predictable industrial capacity. To the maximum possible extent it relies on proven, modular solutions compatible with serial production schemes, thereby allowing it to break away from traditional cost scaling laws. Such breakthrough, however, seems only possible with a very large telescope size. Modular design and serial production may no longer be highly cost- and schedule-effective below 50- to 60-m as the number of identical parts (e.g. segments, actuators, structural modules, friction drives, etc.) decreases substantially.

Figure 2-5 shows the layout of the telescope structure and of the sliding enclosure on a hypothetical site. Table 2-2 gives the overall optical characteristics of the design.

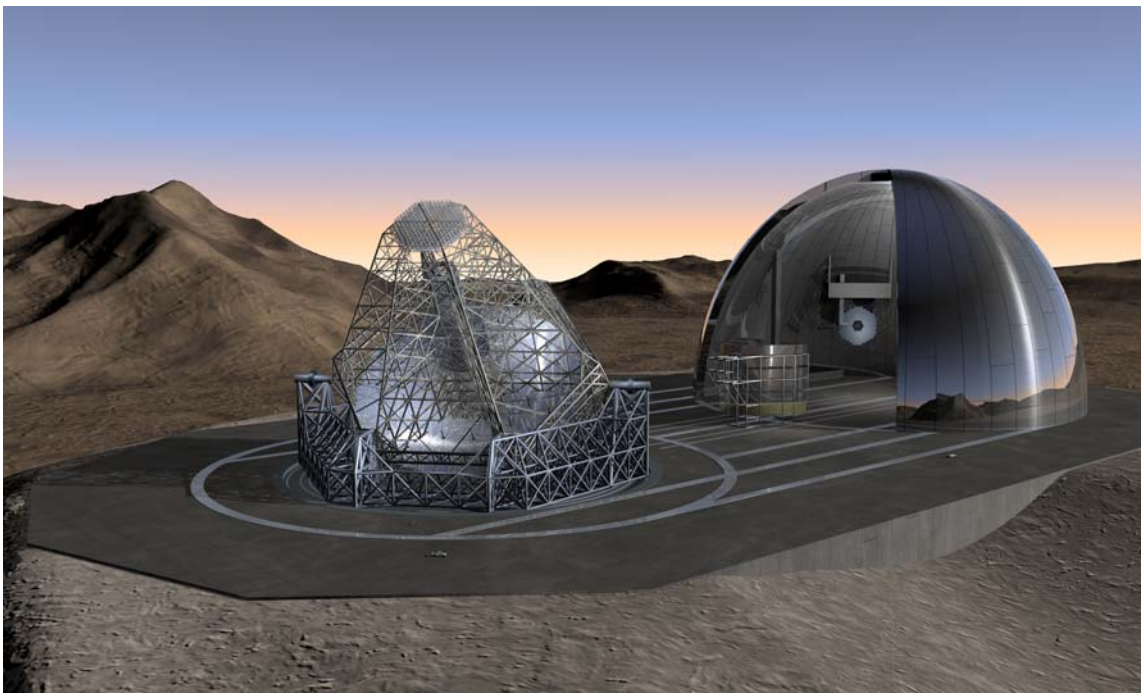

Figure 2-5. Layout of the OWL observatory.

2.6.1 Telescope optics

Quite a number of optical designs have been evaluated. The crucial objective of maximizing aperture while minimizing costs inevitably led to evaluating spherical primary mirror solutions against aspherical ones.

Solutions have been rated at system level against merit functions incorporating feasibility, performance, maintainability, risk and cost (see 6.2.1). In addition, the opto-mechanical design is required to provide suitable surfaces for field stabilization, active and adaptive optics functions. Active optics corrects for large amplitude, low spatial and temporal frequency errors, and adaptive optics for moderate to low amplitude, high spatial and temporal ones. A single subsystem cumulating all active and adaptive functions is deemed too challenging if feasible at all.

Characteristic	
Telescope diameter	100m
Focal ratio	6
Primary mirror focal ratio	1.25
Total field of view (diameter)	10 arc minutes
Unvignetted field of view (diameter)	6 arc minutes
Optical quality at the edge of the curved field	0.056 arc seconds RMS
Diffraction-limited field of view[5] (diameter, curved field)	
Visible (0.5 μm)	2.37 arc mins
IR (2.2 μm)	4.08 arc mins
IR (5.0 μm)	6.00 arc mins
Secondary mirror diameter	25.6m
Central obscuration (linear)	35%

Table 2-2. Baseline design, optical characteristics.

Monolithic relay mirrors were constrained to a diameter not exceeding 8.3-m in order not to require new developments in blank fabrication. VLT experience also showed that beyond ~8.4-m, transport in Europe would become fairly complex as waterways (locks) would no longer fit with the implied container dimensions. This is a fairly severe constraint; attractive 100-m designs requiring 10- to 11-m class monolithic mirrors were ruled out but would have to be re-considered if the telescope diameter were reduced to ~70-m or less, with a corresponding reduction of the diameter of the monolithic mirrors.

Finally, strong emphasis was put on sensitivity to misalignment over large scales, e.g. primary-secondary mirror centring. Flexure of the telescope structure under gravity, thermal, and wind loads will inevitably be large (plausibly maximal) at the location of the secondary mirror[6]. An optical solution which minimizes depointing and wavefront errors associated to unit M1-M2 decentres will therefore be favourable in terms of correction range.

A detailed trade-off involving a representative sample of the solutions explored so far is presented in section 6.2.1. The baseline design eventually selected is a 6-mirror solution (Figure 2-6), with segmented, spherical primary and flat secondary, and a corrector made of 4 elements, including two 8-m class active mirrors and two adaptive mirrors, 2.3-m and 3.2 –m (M6 and M5), conjugated to ground and 8-km, and corresponding to first and second generation adaptive systems, respectively. In the first two years of science operation, and while the aperture is growing from a 50-m equivalent collecting area, it is planned to use a temporary, passive M5 unit and operate in single conjugate or ground layer correction only.

[5] Strehl Ratio ≥ 0.80, curved field.

[6] A lightweight secondary mirror would certainly be helpful, but the telescope structure will still bend under its own weight.

The flat secondary mirror leads to generous centring tolerances for the pair M1-M2 and, thanks to the structural design, lateral decentres are privileged over tilt. According to Finite Element analysis, the secondary mirror tilt is relatively low and could be compensated with the M2 segments position actuators[7], which are identical to those of the primary mirror segments. Tight alignment tolerances inevitably show up inside the corrector, however on a scale comparable to that of the VLT. The corrector itself needs to be centred within typically one mm and a few arc seconds of its ideal position.

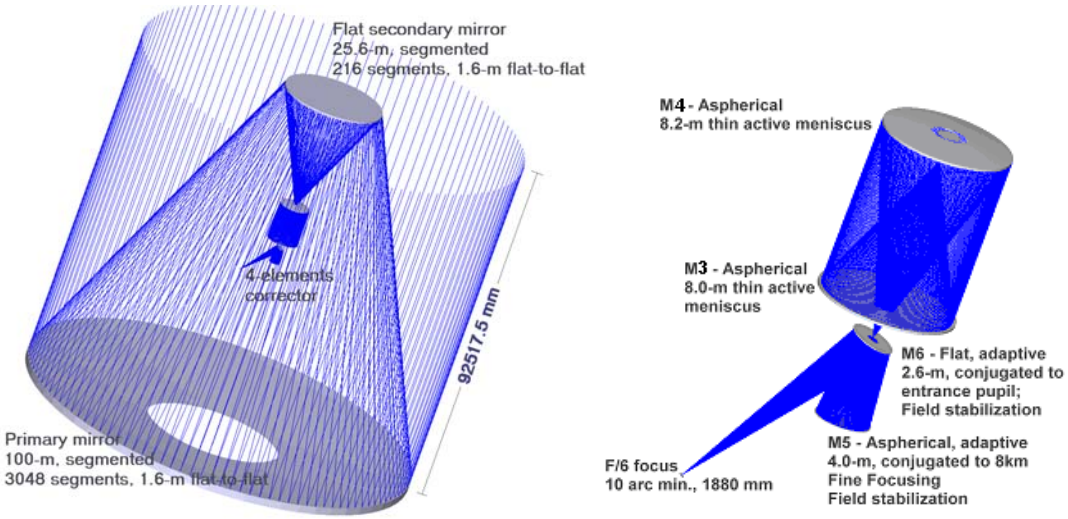

Figure 2-6. Layout of the baseline optical design.

The selection of a spherical primary mirror solution has been the result of extensive analysis, encompassing system and fabrication considerations.

Fabrication - The shape of the primary has an evident and strong impact on fabrication issues.

Aspherical solutions

There are two proven processes for the polishing of aspherical segments.

The first one is stressed-polishing, pioneered with the Keck telescopes. Warping harnesses are mounted onto circular segments, bending moments applied, and the segment polished spherical. The moments are predetermined to ensure that the segment will reach the desired aspherical shape upon their relaxation. The segments are then cut hexagonal, after which fine correction is done with computer-controlled, small tool or ion-beam polishing.

In order to ensure a predictable stress relaxation, stressed polishing requires the back face of the segment to be polished, and implies stringent specifications for residual stresses in the blank. For the same reason, a structured (lightweight) geometry of the segments is excluded, and the process works best with small aspherical departure from best fitting sphere, which privileges small segments (for the CELT, this was one of the reasons for choosing a segment size of 1-m outer diameter [3]).

The second process is the one used by REOSC (SAGEM) to figure the GTC segments. In that case, segments are directly computer-controlled ground and polished aspherical using relatively small tools. Temporary wasters are glued at the edges of the segments to prevent excessive turned-down edges. Again, ion-beam polishing is used in the final stages of figuring, after removal of the wasters. As shown in [4] the results obtained with GTC segments are outstanding, with residual surface errors in the 10 nm RMS range.

The main issue with aspherical segments is not figuring but testing. The test set-up shall be able to guarantee the matching of the segments, i.e. to measure their aspheric shape and

[7] A relatively large actuator stroke (15 mm required, goal 30 mm) is required to compensate for the primary mirror cell deformations..

differential defocus with an accuracy of a few nm. With 36 segments, there are 6 different families of identical segments, and there is one family adjacent to each of the other five. For GTC, one segment of this family was polished first, and kept as a reference for the ensuing production. Segments were mounted next to and phased with the reference one, then tested at centre of curvature through a nulling system [4]. Care must be taken when adjusting the radial position of the segment under test, for a decentre would translate into decentring aberrations. This elegant solution, regrettably, cannot be extended to large apertures. Profilometry could be an alternative to interferometric measurements, albeit with poor time efficiency as very high spatial sampling is required through the entire figuring process to capture high frequency terms, in particular edge misfigure.

Spherical solutions

The polishing and above all testing of identical, spherical segments could follow a much simpler and safer process, with less potential restriction on material and lightweighting. The baseline solution proposed by suppliers (see RD11 and RD12) is to polish segments with full size stiff tools and test them against a unique matrix. In view of the large tool working area, the process is inherently more efficient (in terms of overall removal rate per unit of time) than small tools. In addition large stiff tools are also inherently more favourable than small ones for what concerns high spatial frequency errors. At this stage, glued wasters are still considered to prevent excessive edge misfigure, but there is circumstantial evidence that the edge misfigure would be much easier to control than with small tools, and that wasters might not be necessary. Further tests are planned on the silicon carbide prototypes of the ELT Design Study (see A-1.3). Although a significant proportion of the segments would probably meet specifications at the end of the stiff tool cycles, fine correction with small tool or ion-beam polishing is foreseen as well. The number of polishing machines required to meet the specified delivery rate (about 3,000 segments in 6 years) is relatively low (5-6 grinding machines and 5-6 polishing ones, plus one ion-beam or small-tool machine) – in any case much lower than what would be required for aspherical segments. Polishing of segments by batches on planetary polishers may be an attractive alternative, but the baseline solution appears more cost-effective beyond ~1-m segment size. In addition, parallelization of the production line is safer in relation to the impact of individual machine failure.

Experienced suppliers have expressed concerns about the timely feasibility of a large number of even moderately aspherical segments. The polishing of 42 aspherical segments for the GTC by a world-leading manufacturer will have taken about five years, required extensive development and costly solutions for the control of misfigure up to the edges of the segments[8], and required a facility comparable to that built to figure the VLT primary mirror[9]. The “pipeline” output at the end of this learning process is currently 1 mirror per 2 weeks. It does not appear possible to produce 3,000 such mirrors in a comparable timeframe without extensive R&D, followed by massive infrastructure investment. In contrast, the polishing of LAMOST spherical segments with large and stiff tools produced smooth surfaces up to the edges in a relatively straightforward manner [1]. Another relevant example is the polishing of 1.8-m aluminium mirrors under ESO contract in 1990: 28 hours machine time from ground state to final polish [2].

In brief, aspherical segments, whether polished by stressed polishing with harnesses tuned to individual segments or by computer-controlled small tool figuring, are far from ideally suited for reliable serial production. The same applies, perhaps to an even larger extent, to their optical testing, on top of possible reservations as to curvature matching.

In conclusion, fabrication (cost, risk, performance) considerations unequivocally point towards spherical primary mirror solutions.

System considerations - Fabrication, schedule, cost and risks, however, are far from being the only relevant considerations when selecting the primary mirror shape. A system analysis shows that beyond 20-30m aperture size, there is no practical way to meet optical performance requirements and implement all required wavefront control functions, including adaptive optics,

[8] In comparison to Keck, edge misfigure tolerances are about an order of magnitude tighter in the GTC and future ELTs, OWL included.

[9] The facility actually *is* the VLT primary mirror production one, reconverted for GTC segments.

with less than four surfaces[10] –except by relying on a primary mirror made of adaptive segments with an extreme correction range. Serially produced adaptive segments seem presently out of question within a foreseeable timescale.

Even if adaptive segments could reliably be made within an affordable cost and timescale, such solution would imply that the telescope's most advanced –and perhaps the most evolutive- technology be frozen at the earliest stage of the project[11], and that future upgrades be essentially ruled out. Last but not least, adaptive segments do not resolve any issue which could definitively not be addressed by other means, in a less elegant but certainly more realistic and cost-effective manner.

Opto-mechanical design - The opto-mechanical design allows for 6 focal stations, switching being done by rotating the M6 mirror about the telescope axis. One focal station is reserved for technical instrumentation exclusively; the other 5 may be occupied by one science instrument each.

Two versions of the 6-mirror solution have been explored in detail, with an f/1.42 (see Reference Document RD1) or f/1.25 primary mirror (RD2). The latter is that referred to as baseline in the present document. The optical quality is significantly better than that provided by a Ritchey-Chrétien formula and exceeds the requirements by more than a factor two in terms of diffraction-limited field of view. The central obscuration is fairly large (35% linear i.e. central obscuration diameter = 0.35 x pupil diameter) and essentially imposed by the dimensions of the hole in the tertiary mirror and by the field of view such hole shall allow through.

Although the baseline design may seem less effective than traditional two-mirror ones in terms of transmission and emissivity, it provides all required wavefront control functions up to IR dual-conjugate adaptive optics, which a Ritchey-Chrétien would not.

For small field at 5.0 μm and beyond, the baseline 4-mirror corrector could be replaced by an optional two-mirror one (see section 6.2.3) delivering diffraction-limited image quality (Strehl Ratio ≥ 0.80) over 33, 52 and 74 arc seconds, at λ=2.2, 5.0 and 10.0 μm, respectively. The exit focal ratio is f/2.1 and the total field of view is 4 arc minutes[12], with a geometrical image quality of 0.21 arc seconds RMS at the edge of the field. The optional corrector includes a 6.1-m thin meniscus active mirror and a 4.1-m adaptive one. Both mirrors are strongly aspherical. In view of the large mirrors sizes, high frequency (>1 Hz) field stabilization would have to be provided in the instrument. The estimated downtime required for the exchange of the correctors is 48 hours.

The optical design is not considered final; phase B will start with a critical re-assessment of the entire optical design. In case the baseline 6-mirror solution would eventually be re-confirmed, the following adjustments would be explored:

- Allowing for a larger secondary mirror, and shortening the distance M1-M2 by ~12.83-m (the size of one structural module), or slightly increasing the primary mirror focal ratio;
- Increasing the allowable design volume for the adaptive M6 unit.
- Increasing the focal ratio.
- Decreasing the angle between the exit beams after M6 and the telescope axis.

The short focal ratio (f/6) is an evident area of concern for instrumentation, adapter and on-sky metrology. One should note, however, that the entire control system is driven by focal plane metrology. This implies very high dimensional accuracy and stability at the level of these metrology systems. Increasing the focal plane dimensions would proportionally relax tolerances. Flexures, however, would increase more rapidly with the increase of the focal plane dimensions. A thorough trade-off is planned in the design phase.

[10] See also 6.1.

[11] According to current plans the final design of the primary mirror must be frozen by 2008 at the latest.

[12] 3 arc minutes unvignetted.

Tentative optimization runs indicate that implementing such changes might be possible to some extent. In addition, requirements set by instruments exploratory studies[13] may lead to significant re-designing of the telescope opto-mechanics, within the limits set by top level requirements, engineering constraints and by modular design compatible with serial production. Experience with the opto-mechanical design trade-off shows that the modular design allows for a relatively straightforward re-configuration of the telescope structure i.e. a re-configuration of the optical design does not necessarily imply a complete overhaul of the structural design.

Segments characteristics, segments production

Segment size has been the subject of an early trade-off, the main evaluation parameters being the complexity of the control system (number of degrees of freedom), risks and costs. At the upper limit (8-m) of proven mirror technologies, the estimated total cost[14] of raw blanks is M€ 510 (delivery ex works). Beyond 2.3-m flat-to-flat, standard transport containers are ruled out and beyond ~2.5-m, active supports are inevitably required to prevent excessive material costs. For these reasons the upper limit for the segment size has been set to 2.3-m.

Very small segments (a few tens of centimetres) would be favourable in terms of material costs, polishing, transport, handling and –at least when individually taken- maintenance. The number of degrees of freedom increases however rapidly with decreasing segment size. According to Chanan [6], ~4,000 units is the upper limit for on-sky calibration with current (Keck) techniques.

Characteristic		**Value**
Substrate		Zerodur, ULE or Astro-Sital
Shape / type		Hexagonal / solid
Dimensions	Flat-to-flat Thickness	1.6-m 70-mm
Radius of curvature	Primary mirror Secondary mirror	250-m Flat
Support	Axial Lateral	18 points whiffle-tree 1 central support
Quantity	Primary mirror Secondary mirror	3048 216

Table 2-3.Segments characteristics.

Parametric studies undertaken by the industry (substrates, polishing) with dimensions of 1.3, 1.8 (initial baseline) and 2.3-m flat-to-flat, indicate that the optimal dimension in relation to cost is somewhere between 1.3 and 1.8-m flat-to-flat[15]. As a result, the dimension has been set to 1.6-m flat-to-flat and the thickness reduced from 80 to 70 mm, which should lead to a slight cost reduction. The segments size is also chosen as an integer divider (1:8) of the structural module size, thereby allowing for higher standardization of interfaces. A preliminary optimisation and analysis of a possible 18-points segment axial support system has been performed (see also 6.5.1.5). Quilting under gravity is ~60 nm wavefront RMS. Provided that the geometry of the polishing support is identical to that in the telescope, this error would be polished out and its opposite would only appear when the telescope is pointing away from zenith[16]. At the operational limit z=60^{o}, it would have an amplitude of ~30 nm wavefront RMS (see 6.5.1.5). Alternatively, the surface deflection could be programmed into the polishing robots in the final

[13] At the time of writing of this document, the results of such studies were too preliminary to allow for a thorough re-assessment of the telescope opto-mechanical design.

[14] Based on 2005 prices for an 8-m ULE blank (CORNING communication), with a 60% unit price reduction for large quantity (~140 units) and a 1.3 USD to 1.0 € exchange rate.

[15] See also RD6, RD7, RD8, RD9. RD10. RD11, RD12.

[16] Within the framework of the VLT project, REOSC polished a spherical gauge mirror, 1.7-m diameter, for the validation of the axial support interface and for the calibration of the spherometer in the fine grinding stage of the 8-m mirrors. Interferograms showed that quilting under gravity had been polished out, down to measurement accuracy (less than 10 nm RMS wavefront).

stage of polishing. For the secondary mirror segments, with a projected size of 6.25-m on the entrance pupil, partial compensation by the Adaptive Optics ought to be possible. The current baseline characteristics of the segments are listed in Table 2-3. At the time of writing of this document, the option of moderately (50%) lightweight blanks at marginal cost increase is under evaluation.

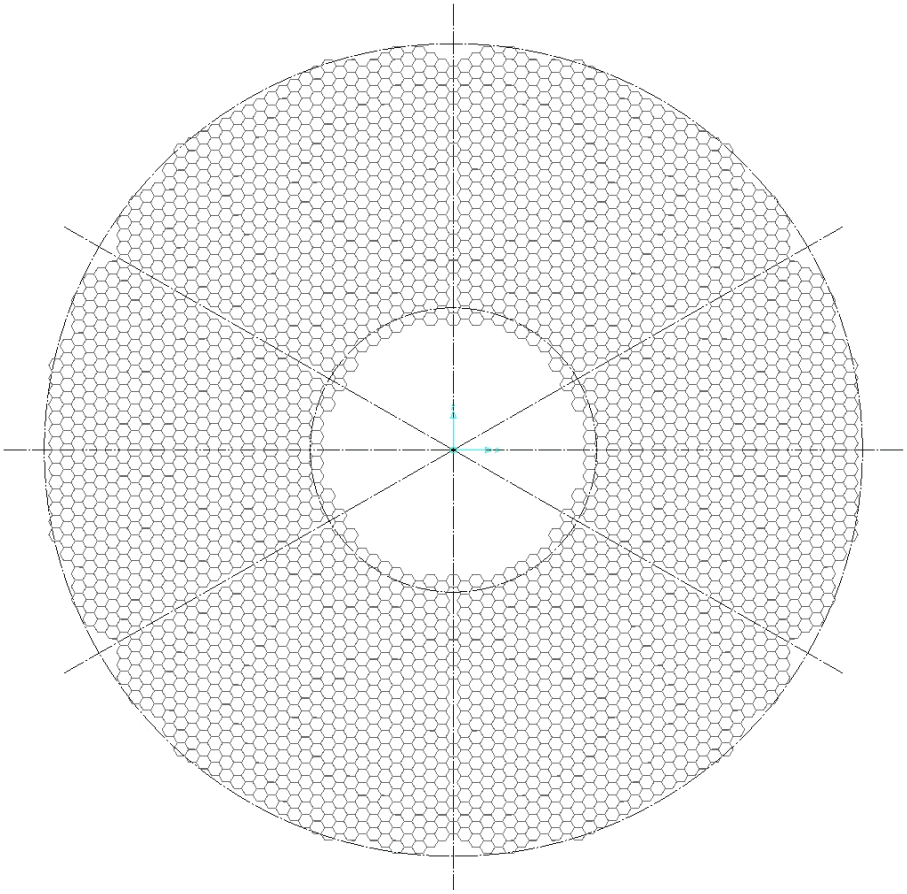

Figure 2-7. Primary mirror geometry (3048 segments).

The primary and secondary mirror geometries are shown in Figure 2-7 and Figure 2-8.

It is worth noting that suppliers reported that they now have adequate facilities for the production of OWL segments (melting tanks and ceramization furnaces).

Silicon Carbide is considered as a serious alternative to conventional low-expansion glass or glass-ceramic. According to industrial studies[17], feasibility per se is not a critical issue and cost, polishing included, would not be very substantially higher than with conventional materials. The reasons for such promising if somewhat surprising conclusion are twofold: serial production, and moderate specifications as to light-weighting[18]. Although cryogenic tests undertaken for space applications have repeatedly shown excellent properties in this respect, possible CTE inhomogeneities and bimetallic effects between the bulk of the substrate and its polishable overcoating might rule the technology out in view of the stringent requirements applying with segmented apertures (see RD3). The issue is investigated within the framework of the ELT Design Study (section 2.12), with the production of up to 8 prototypes, 1-m class. Specifications could be relaxed with active deformable segments but such solution would imply added cost and undesirable control complexity. In the case of M2, minor, low spatial frequency figure

[17] see RD9, RD10, RD11, RD12.

[18] The specified aerial mass being 70 kg/m² or less, i.e. far more generous than for space applications.

changes should be acceptable as the projected size of segments onto the pupil (about 6.4-m) is significantly larger than the sampling of the lowest order adaptive optics corrector.

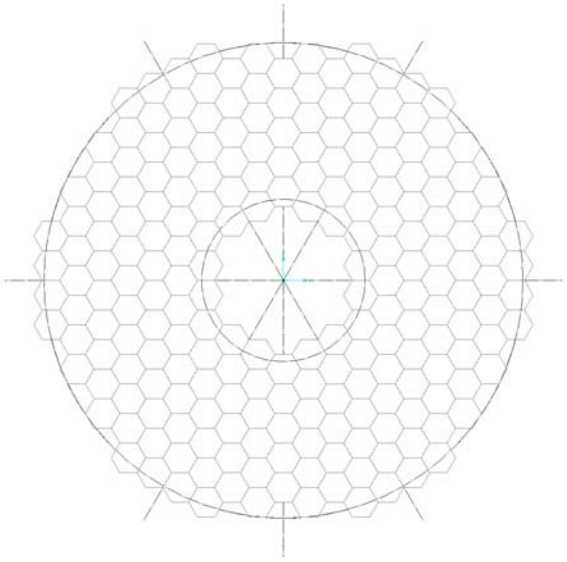

Figure 2-8. Secondary mirror geometry (216 segments).

Owing to their all-identical characteristics, including spherical shape, the polishing of OWL segments implies enormous simplification and substantial performance advantages with respect to aspherical ones. Experienced suppliers expressed serious concerns about figuring aspherical segments to tight specification in a timely manner. In brief, they fail to see a cost-effective solution towards industrial polishing and testing of about 3,000 aspherical segments in a timeframe comparable to what is needed by a world-leading optical manufacturer to polish the 42 GTC ones[19].

It was initially thought that figuring of OWL segments could be done by replication or polishing on planetary machines [5]. Replication has been ruled out as the durability of a master could probably not be guaranteed beyond a few dozen replications. According to suppliers, planetary polishing might be convenient for small segment sizes (1.3-m) but would entail large investments and unpredictable performance for larger ones. The preferred solution is to set a sufficient number of polishing robots for the parallel figuring of segments. Optical testing would be done interferometrically against a convex matrix, an optimal solution in terms of curvature matching of the segments.

Industrial studies referred to herein conclude that OWL segments could be produced within a competitive timeframe and at a cost broadly in-line with ESO's internal assessment – namely 6 years production cycle after a 2-3 years facilitization, and a total cost of the order of 300 M€, polished segments, ex works.

2.6.2 Structural design

The design of the telescope structure has evolved considerably (see section 9.3) since the setting of the first concept [5], with a moving mass decreasing from 45,000 to 13,400 tons and a first locked rotor eigenfrequency increasing from 0.5 to 2.7 Hz.

The telescope structure (Figure 2-9) relies on a modular design, with most parts made of mild steel. Modules (Figure 2-10) will be made of standard pipes and serially produced nodes. Modules will be assembled on-site; all pipes and pre-assembled nodes can be transported in standard containers. Kevlar ropes provide for pre-stressing and torsional stiffness. The overall

[19] Including 6 spares, and taking into account the tighter requirements underlying diffraction-limited performance.

structure has a 6-fold symmetry, thereby allowing for an ideal match with the segments geometry and a clean geometry of the aperture hence of the theoretical diffraction pattern.

The aptly named *fractal design* (see section 9.4.2) not only allows for highest standardization hence low cost, ease of supply, integration and maintenance, it also allows for distributed load transfers from the optical subsystems to substructures and eventually foundations –thereby preventing excessive stress concentration.

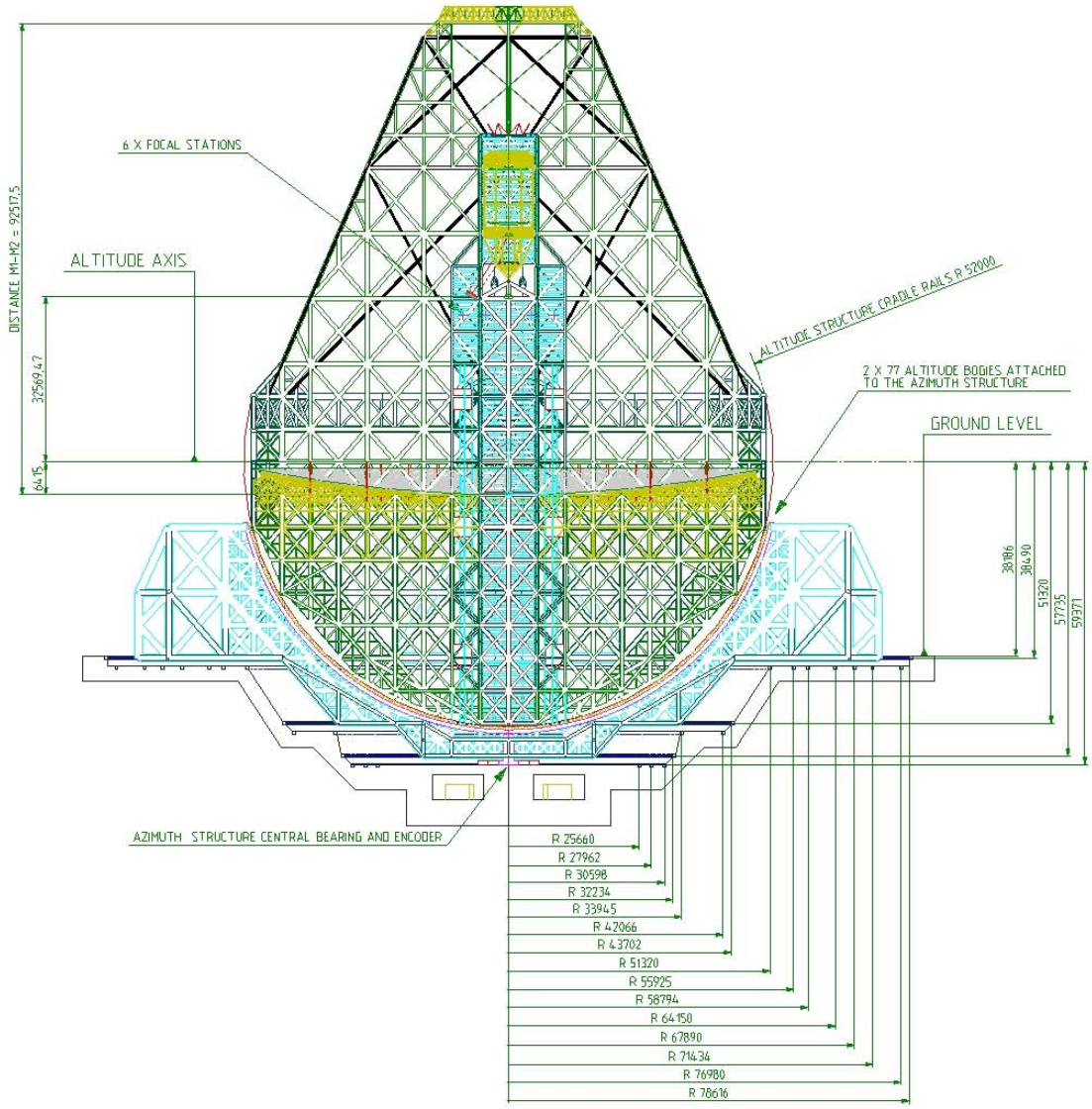

Figure 2-9. Telescope structure, overall layout.

The Alt-Az kinematics of the telescope is provided by way of friction drives (Figure 2-11), with 246 units on 12 azimuth tracks and 154 units on two altitude cradles. Friction wheels are slightly spherical to prevent excessive stresses generated by misalignment (see RD13). Individual drives interface to the structure by means of hydraulic jacks, which can be connected for e.g. seasonal re-adjustment of the load distribution.

The operational range is 0 to 60 degrees zenithal distance, with a blind spot of 0.5 degrees radius about zenith. The maximum slewing speed is 0.1 degree/s, i.e. pointing is realized in a timescale comparable to that of the VLT. The kinematics allows the telescope to point horizontally for maintenance purposes. A series of preliminary analysis (see RD16) show that the telescope should be able to track within 0.3 arc seconds RMS, friction and 10 m/s wind speed taken into account. The residual error shall be compensated by the fast tip-tilt mirror M6.

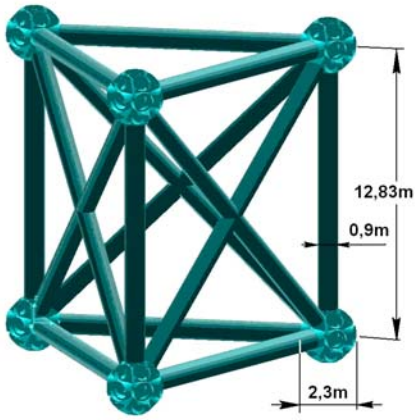

Figure 2-10. Structural steel module

Hydraulic bearings and tracks were ruled out because of the associated tight dimensional tolerances and of the length of the tracks. Magnetic levitation is an attractive alternative in view of the implied relaxation of dimensional tolerances[20], of its potential ability to provide high stiffness by way of the control system, and of safety aspects. This option will be assessed in the framework of the ELT Design Study (section A-1.4).

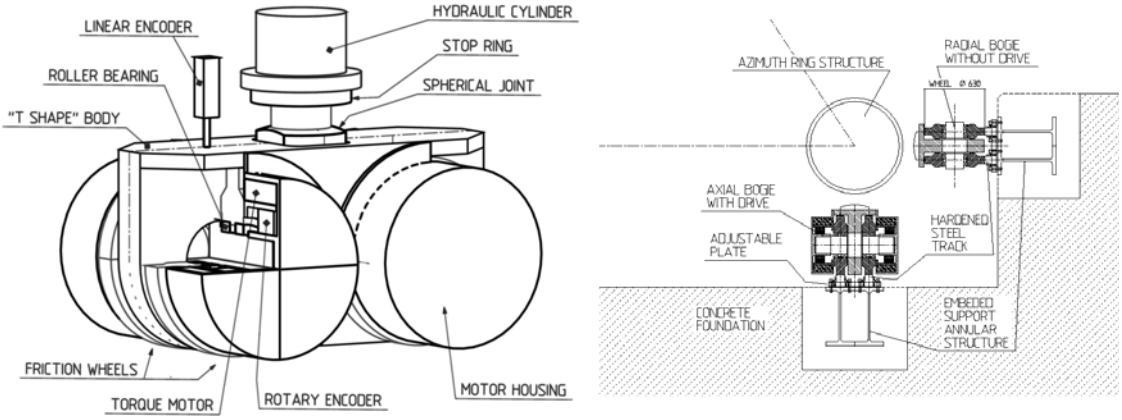

Figure 2-11. Friction drive

2.6.3 A controlled opto-mechanical system

Regardless of its opto-mechanical design, a telescope much larger than VLT or Keck must inevitably integrate extensive control systems, including but not limited to adaptive optics. Indeed adaptive optics deals with relatively limited error amplitudes, and cannot realistically solve all problems at once. A system the size of OWL must accommodate for large deflections and integrate all control systems necessary to bring it into a state where the adaptive control loop can be closed rapidly.

The wavefront control concept will be described in details later in this document; we give a brief summary below. The general strategy is to implement successive control systems, with decreasing correction amplitude and increasing bandwidth. We distinguish 6 control loops

1. **Pre-alignment**, which deals with coarse alignment of the secondary mirror, of the corrector, and of the surfaces within the corrector. The essential objective is to allow the subsequent acquisition of guide stars and to allow the active optics loop to be closed. The errors to be corrected result essentially from gravity load and changing thermal conditions. The required

[20] An order of magnitude more generous than with friction drives.

bandwidth is low (typically less than 0.1 Hz), and the accuracy (typically10 ppm) compatible with simple metrology solutions, e.g. fibre extensometers between M1, M2 and the corrector, and within the corrector. The secondary mirror tilt alignment can be achieved with the segments position actuators[21].

2. **Tracking and field stabilization**, which shall ensure that the target remains at a stable position on the detector. This includes several loops, with increasing bandwidth and accuracy, and decreasing amplitudes:

   - Tracking by the telescope drives –down to an estimated accuracy of 0.3 arc seconds RMS, taking into account 10m/s wind speed and friction in the telescope drives. The metrology signals are provided by the telescope encoders and by the guide probes; the bandwidth is limited by the stiffness of the structure (2.6 Hz locked rotor frequency). The errors corrected by this loop include mostly the effect of low frequency wind buffeting, friction, of gravity and thermal changes.
   - Mid-frequency (up to ~10 Hz) field stabilization with the M6 tip-tilt unit. The corresponding error source is mostly wind buffeting. The expected amplitude requirement is less than ~1 arc seconds RMS on sky or 20 arc seconds of M6 tip-tilt, plausibly less. As this tip-tilt correction is to be provided by fast steering the entire M6 unit, this is considered as a critical requirement. The metrology signal shall be provided by the guide probes.
   - High frequency (up to ~100 Hz) field stabilization using the adaptive M6 thin shell. The corresponding error sources are atmospheric tilt and residuals associated with wind buffeting. Under normal conditions (outer scale ~30-m) atmospheric tilt will most likely be negligible. A 0.1 arc seconds error on-sky corresponds to ~2 arc seconds on the mirror i.e. ±13 μm at the edge of the adaptive mirror. The metrology signal shall be provided by the adaptive optics wavefront sensors.

   At the time of writing of this document, conceptual designs of the M6 are pursued under ESO contracts. We assume that the tip-tilt compensation by M6 will be provided in two stages, the subunit being mounted on a gimball mount or equivalent for low frequencies, high frequencies up to ~100 Hz being compensated by the adaptive support.

   The above assumes that several guide probes (5 to 7) tracking different references will allow disentangling field-independent tilt from the field-dependent atmospheric one[22]. These probes are required for active optics (see below) as well.

3. **Active optics**, which deals with residual alignment and focus errors, surfaces misfigure, and possibly low frequency (<1 Hz) wind buffeting. This includes several loops:

   - Active alignment. The goal is to finish off the pre-alignment[23] and in particular compensate for decentring coma without introducing significant de-pointing or decentring astigmatism (linear with the field of view). Decentres of powered surfaces inside the corrector may be used to cancel out field-independent decentring coma. As 3rd and 5th order terms need to be addressed, two surfaces among M3, M4 and M5 must be actuated. Actuating all three mirrors would allow correcting 3rd order decentring astigmatism as well. This will probably not be required but further analysis will be performed in phase B for confirmation.

     To prevent de-pointing, the surfaces shall be rotated about their centre of curvature. Taking pre-alignment into account, the amplitudes are fairly small.

     As an alternative, constant 3rd and 5th order coma could be corrected by an active deformation of M4 (pupil). Preliminary calculations indicate that this might be possible,

[21] The primary and secondary mirror segments are mounted on identical actuators, and the required range of these actuators is set by the deformations of M1 cell. Flexures in the M2 cell being substantially lower, the unused range can be used to re-position the secondary mirror as a rigid body.

[22] If any; the telescope diameter being much larger than the expected outer scale of turbulence, atmospheric tilt ought to be negligible.

[23] Which is expected to align the corrector and secondary mirror to typically ± 1 mm in x-y-z and 2 to 4 arc seconds in tip-tilt, and the surfaces inside the corrector to typically ± 0.1 mm in x-y-z and ~1 arc seconds in tip-tilt.

but a more thorough analysis will be undertaken in phase B to ascertain that the M4 force budget is sufficient, before taking a final decision.

Active alignment shall also compensate for the residual misalignment between the corrector and the interface with instrumentation, by way of M6 tip-tilt and M5 refocus.

- Active focusing. Coarse focusing up to ~0.1 Hz is provided by M2, using the segments position actuators[24]. Fine focusing is to be provided by M5 up to ~1 Hz down to an accuracy compatible with the M6 adaptive range. Curvature changes of the primary and secondary mirrors must be tracked to prevent scalloping of the wavefront (first derivative discontinuity at inter-segment edges) and the position actuators reaching their range limit. A first option would be to monitor lateral displacements of the segments by way of the position sensors, as in the South African Large Telescope. A second option would be to measure the scalloping of the wavefront by way of an active optics Shack-Hartmann wavefront sensor with 7 or 19 sub-pupils per segment. This second option implies longer integration time for the wavefront sensor and is limited to ~0.05 Hz bandwidth.
- Active deformation of M3 and M4. The goal is to compensate permanent or slowly varying, low spatial frequency terms. The M3 and M4 mirrors have mechanical properties comparable to that of the VLT primary mirrors, and the design of their active support system will be similar. Assuming low (a few microns at most) amplitudes at the highest temporal frequency (~1 HZ), the implied extrapolation from the VLT active support system seems reasonable. Since M4 is conjugated to the entrance pupil but M3 is not, several reference stars are required to disentangle constant terms from field-dependent ones. The conjugation M4-M1 also requires that M1 curvature (not detected by position sensors) be monitored to prevent that either position or force actuators reach their maximum range. Monitoring of segments lateral displacements, as in the SALT, is an option; another one is to measure the scalloping of the wavefront with a properly sampled Shack-Hartmann sensor.

All active optics functions use the same wavefront sensors at the f/6 focus. It is assumed that the adaptive optics subsystem will periodically offload low frequency (≤ 1Hz) terms to active optics, thereby preventing excessive range of the adaptive correctors.

4. **Phasing**. Segments phasing errors must be corrected locally i.e. there is no way to compensate one mirror phasing errors by moving the segments of another one (except if these mirrors are conjugates and have identical segmentation geometries). The general principle is identical to that of the Keck and GTC i.e. phasing will be performed in closed loop on inter-segments position sensors, which will be periodically re-calibrated on-sky. Non-interlocking capacitive sensors developed for the SALT have far better characteristics (accuracy, drift, ease of implementation) than the 20-years old Keck ones, and in all likelihood will meet the not-to-exceed cost requirement of € 1,500 per unit for a production of about 20,000 units. An alternative technology (inductive sensors) will be evaluated in the framework of the ELT Design Study.

   According to Chanan et al [6] the Keck on-sky calibration solution could be extended up to ~4,000 segments. Several alternatives are being evaluated, and will be checked on-sky by way of the Active Phasing Experiment (see appendix A-1.3). As several segments may have to be replaced daily for re-coating, the process must guarantee that upon individual re-integration segments are phased to an accuracy compatible with the capture range of the calibration technique (see 7.5.2).

   A significant drawback of OWL design is multiple segmentation (primary and secondary mirrors). The segmentation patterns are however perfectly determined, and disentangling the primary and secondary mirror phase errors is a matter of proper signal processing of pupil images or adequate conjugation of wavefront sensors images.

5. **Active atmospheric dispersion compensation**. A notional design of a Longitudinal Atmospheric Dispersion Compensator (LADC) has been briefly explored. A combination of Corning glasses A88-66 and B81-41 seems to give satisfactory results over the wave band

[24] Identical to the primary mirror segments actuators i.e. overdimensioned for gravity loads at the level of M2.

400 to 500 nm. The fast f/6 focal ratio is, however, inconvenient as it leads to significant coma and chromatism. Active deformation of M3 and M4 could, to some extent, compensate for non-chromatic terms but this would imply that the ADC covers the entire field of view, including active and adaptive on-sky metrology references, which translates into 2-m class prisms. Atmospheric dispersion compensation will have to be implemented in the instruments that require it, possibly in closed loop on sky. Exploratory work has started in the framework of the ELT Design Study (see A-1.8).

Wavefront sensors shall have their own ADC, but accuracy requirements are more generous.

The effect of anomalous refraction has been assessed and found to be negligible over OWL wave-bands (see RD4).

6. **Adaptive optics.** So far, adaptive optics based correcting systems have filled important new observing niches on 8-10 m class telescopes by providing near-infrared imaging, and very recently imaging spectroscopy, up to their diffraction limit. “Classical” instruments, using seeing-limited images directly delivered by the telescope, remain however their main staples. This is going to change completely with the new ELT generation: even with a 30-m “only” telescope, most observations will require some degree of AO correction; with a 60 to 100-m, virtually all observations will require much enhanced imaging quality, quite often up to the diffraction limit, to fulfil their scientific potential as mentioned briefly in section 0 and presented in detail in Chapter 2.

   Although the technological challenges posed by adaptive optics are arguably the most demanding of the entire system, there is optimism as the development of successive generations of key concepts and components is picking up considerable momentum. Notably at the European level, numerous R&D activities are being conducted in that field in the frame of OPTICON and of the ELT Design Study. Equally lively and largely complementary activities are being pursued on the other side of the Atlantic, mainly through the Center for Adaptive Optics and the NSF Adaptive Optics Development program. OWL plans encompass a gradual implementation of AO capabilities. It should be noted that adaptive units are not required for first light; provisional M5 and M6 units are foreseen in order to allow engineering time before the implementation of adaptive optics.

   First generation Adaptive Optics – OWL first generation adaptive optics (see section 8.2) will allow start of science operations and encompass IR Single-Conjugate Adaptive Optics (SCAO, see section 8.2.1), and Ground-Layer Adaptive Optics (GLAO, see 8.2.2). The deformable mirror will be the flat, elliptical M6 (2440 x 2660 mm²), with an interactuator spacing of ~25 mm and a total of 6670 actuators i.e. 98 actuators across the pupil diameter (see also section 8.2.1.2.1). Mirror M6 nearly coincides with the exit pupil but its tilt angle (16^{o}) will limit its performance in wide-field adaptive optics (see section 6.3.6). At the time of writing of this document, feasibility studies have been contracted to industry for the entire M6 adaptive unit. The baseline wavefront sensor would be a 97 x 97 subapertures Shack-Hartmann; an infrared Pyramid Wavefront sensor is evaluated as an alternative. In the latter case, the required low read-out noise detector exceeds dimensions available today. One can reasonably assume that such (512 x 512) detector would be readily available in time for OWL first generation AO. As for the Real-Time Computer (RTC), the technology is essentially available today –albeit at a presumably high cost and with a non-optimal architecture.

   Distributed Multi Object Adaptive Optics (MOAO, see 8.2.3) may also become part of OWL first generation adaptive optics if the corresponding instrument (MOMFIS, see section 12.2.3.4) is eventually implemented.

   The first generation OWL adaptive optics will rely exclusively on Natural Guide Stars (NGS).

   Second generation Adaptive Optics – The second generation adaptive optics capability of OWL (see 8.3) starts with the replacement of the passive, temporary M5 unit with an adaptive one. This should allow for a limited Multi-Conjugate Adaptive Optics (MCAO) i.e. for a limited but not negligible increase of the corrected field of view. Mirror M5 is conjugated to an altitude of ~7 km. The diameter of this mirror would be 3920 mm for 10 arc minutes unvignetted field of view but this diameter could be reduced to 3630 or 3420 mm if slight vignetting (a few percent area) in the active, respectively adaptive control fields could

be tolerated (see also section 6.3.2) and provided that it would not impair wavefront sensing on Laser Guide Stars (this is still to be addressed).

MCAO is not yet fully proven on-sky. A demonstrator (Multi-conjugate Adaptive optics Demonstrator or MAD) is currently in the last phases of integration and will be installed at a VLT focus for testing on sky. MAD recently achieved first MCAO light in the laboratory (Figure 2-12).

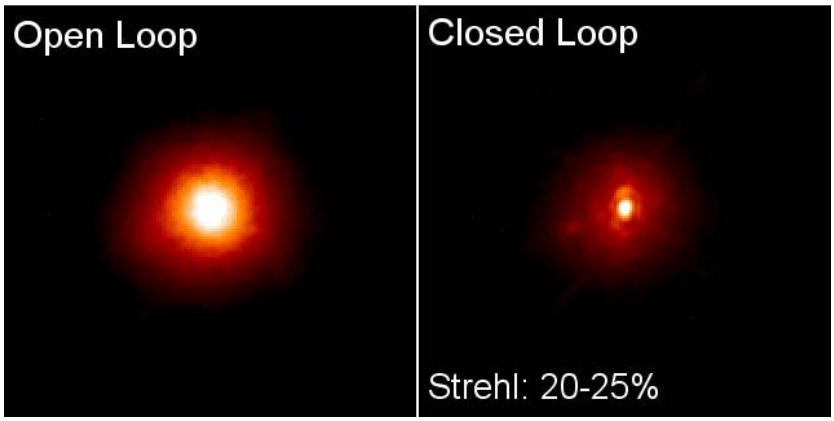

Figure 2-12. First light results with MAD (laboratory conditions). Atmospheric turbulence is emulated with phase screens. Seeing 0.5 arc seconds, coherence time 5 ms, wavelength 2.2 μm. Adaptive loop frequency 210 Hz.

In the current baseline, the MCAO control scheme is star-oriented, by opposition to layer-oriented. As for the GLAO system, on-sky metrology would rely on six wavefront sensors patrolling a field of view of up to 6 arc minutes. This scheme is however preliminary and a thorough trade-off between layer- and star-oriented correction schemes will be conducted in the detailed design phase.

The second generation adaptive optics capability will rely on Natural Guide Stars. The requirements and implementation concept are described in section 8.3.

The second tier of OWL 2nd-generation AO capability covers extreme and high contrast adaptive optics and is currently addressed by EPICS (see 8.3.2), with exoplanets as its primary science target. In brief, EPICS is an instrument incorporating advanced coronagraphic techniques and post-focus high order AO correction on a small field, with a bright guide star. The post-focal deformable mirror could be based on the emerging MOEMS technology – actuator pitch <300μm- or on a significant extension of the piezo-technology with actuator pitch <1mm. The low order correction will be covered by the M6 unit.

The second generation OWL adaptive optics will rely exclusively on Natural Guide Stars and would enter operation about two years after the first generation, while segments integration will still be proceeding, with the telescope having an equivalent diameter of ~80-m.

Third generation Adaptive Optics – The third generation AO systems shift emphasis from correction capability to implementation of Laser Guide Stars (LGS), hence of increased sky coverage. The main issues at stake are essentially related to the facts that LGS are at finite distance –cone effect, image elongation- and that they are generated by beams propagating upwards through the atmosphere, thereby preventing measurement of global tilt. With Extremely Large Telescopes, the distance to the LGS spot is not negligible in relation to the telescope focal length, and their images are not only strongly affected by defocus, but also by predictable but unavoidable aberrations. In brief, the telescope is required to do macro photography and normal imaging *at the same time*. In addition, distance to the LGS changes with zenithal distance. The brute force solution would be to implement active elements in the on-sky metrology, allowing measurement noise on the LGS to be brought down to acceptable levels, while relying on Natural Guide Stars for the compensation of low

order aberrations (see RD1). There might, hopefully, be alternatives (see 8.4), whereby the LGS themselves would be generated or the light beams received from them spatially filtered in a way as to minimize the effect of finite distance. Substantial effort in such directions is being spent in the framework of the ELT Design Study (see A-1.6). It is evidently too early to conclude whether brute (almost certainly complex and expensive) force will prevail. Concepts shall be developed in OWL phase B down to preliminary but not final design level.

According to current plans, the third generation adaptive optics systems will enter operation at the time of completion of the segments integration.

2.6.4 Enclosure, open air operation

Enclosure requirements and concepts have evolved considerably in the last decades, with a dramatic shift of priorities, maximal shielding from external excitations –mostly wind- at the cost of generating significant local turbulence giving way to natural flushing of local turbulence at the cost of higher wind excitation. Such shift is closely related to the evolution of control systems, and in particular to the fact that local, thermal turbulence is less predictable and occurs at higher spatial and spectral frequency. It is thus more difficult to compensate than wind buffeting on the telescope structure and optical components, actually requiring –and taxing the capabilities of- a full blown adaptive optics system.

Wind tunnel tests performed in 1992 and 1994 (see RD523 and RD524) to characterize the wind flow inside the VLT enclosure and behind a wind screen showed a significant reduction of pressure at low frequencies. Above ~0.1 Hz, however, the situation was reversed, with the Power Spectral Density (PSD) inside the enclosure systematically higher than that of open air turbulence (Figure 2-13). This is due to a smaller outer scale and higher intensity of turbulence at high frequencies after interaction between the incoming free flow and the structures of the wind screen.

According to tests (see RD523 and RD524), from which representative turbulence PSD have been derived using a von Karman model, wind screens provide some level of shielding at all frequencies, the actual efficiency depending on screen porosity and wind orientation. Shielding is most effective at all frequency when the porosity (ratio of free to closed areas) of the screen is in the range of 20%.

Wind pressure leads to tracking errors and may generate primary and secondary mirror shape errors. Preliminary simulations under 10 m/s wind speed indicate that the telescope kinematics should be able to track within 0.3 arc seconds RMS, friction in the drives taken into account. The residual error could be compensated by M2 or M6, at the cost of either a field-independent coma term (compensation with M2) or a field-dependent defocus (compensation with M6). It should be noted that with a flat secondary mirror the design is insensitive to lateral M1-M2 decenter.

Compensation of the effect of wind pressure on the primary and secondary mirrors is essentially a matter of bandwidth of the phasing control system, not of amplitude (gravity-induced deflections imply much larger amplitudes anyway). Simulations using a relatively crude (Von Karman) wind model show that with a proper controller, residual phasing errors are virtually negligible (see also 7.5.5). With 10 m/s wind speed and assuming a 60 Hz first eigenfrequency of the segment axial support system, absolute position error is 9 nm RMS with a closed loop bandwidth of 5 Hz, 6 nm RMS with 10 Hz and 4 nm RMS with 20 Hz. These numbers assume 2 nm RMS sensor noise. They correspond to local, high spatial frequency residuals and assume the segments are exposed to free air flow.

Due to the key importance of mastering wind effects, long before any metal is cut, we are nevertheless pursuing aggressively a comprehensive set of studies. Computational Fluid Dynamics (CFD) analysis performed under ESO contract in 2001-2002 led initially to suspiciously optimistic results. Indeed it was found out that frequencies above ~0.5 Hz were not properly sampled, and external experts expressed doubts about the current ability of CFD to produce realistic data at higher frequencies. Simple models are currently used in wind tunnel tests to evaluate CFD in relation to measurements; wind tunnel tests are foreseen in the ELT Design Study (see A-1.5) and in the course of OWL phase B. In addition, pressure

measurements on the Jodrell Bank radio telescope have started and the results are being fed back into the models.

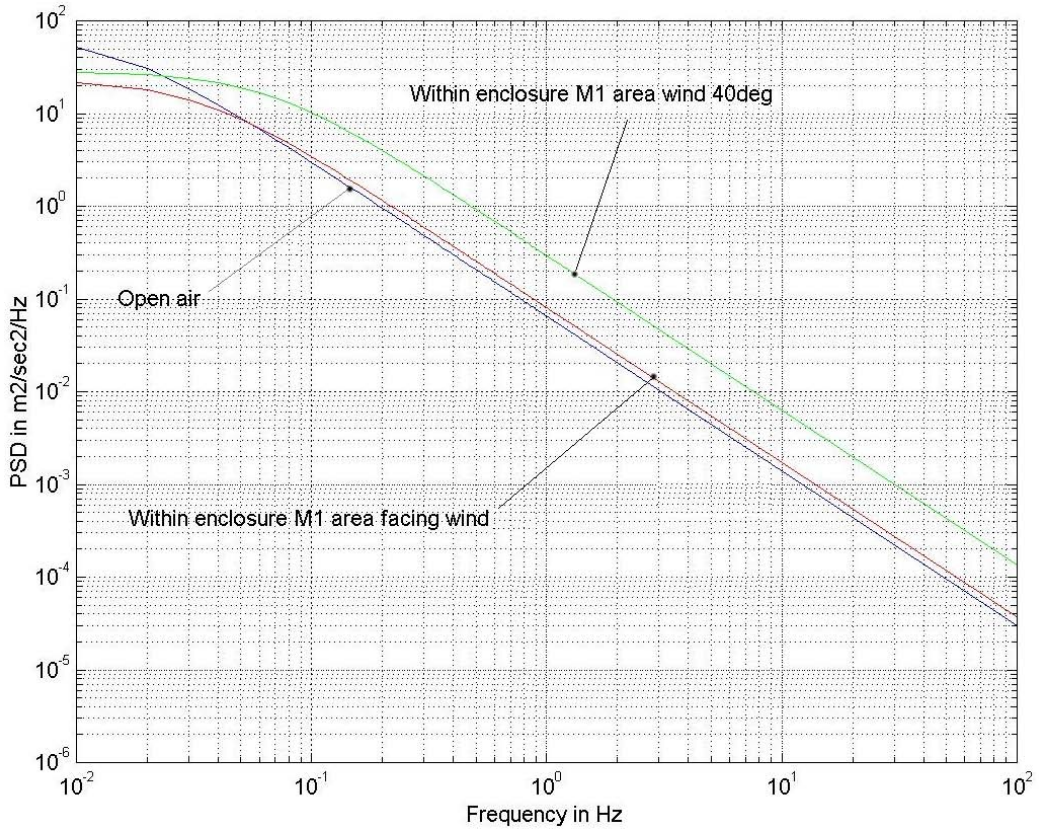

Figure 2-13. PSD of turbulent wind speed in open air and inside VLT enclosure (no wind screen).

Representative data will be obtained in the framework of the ELT Design Study with the Wind Evaluation Breadboard (WEB, see section A-1.2), and fed back into the specifications and design of the telescope, including its control systems.

In view of the above, the current baseline is open-air operation. As a backup, wind screens embedded into the azimuth structure could shield the primary mirror up to ~30 degrees zenithal distance. It should also be noted that low average ground wind speed is a crucial site selection criterion for adaptive optics.

The telescope will be protected against adverse meteorological conditions by a sliding enclosure (Figure 2-14). The enclosure would slide down along the statistically prevailing wind, with a travel distance such that pressure turbulence induced by the enclosure would be mostly averaged out before hitting the telescope in case of unfavorable wind direction. This enclosure will provide passive thermal shielding only; dedicated mirror covers, corrector and instrument housings are foreseen to provide daytime cooling of sensitive subsystems. The mirror covers (6 petals for each primary and secondary mirror) slide out of the telescope for operation. One cover is to be equipped with handling and cleaning units for segments maintenance.

Secondary mirror covers would most plausibly be unnecessary if the segments are made of silicon carbide, whose favorable thermal conductivity would allow the segments to follow ambient temperature.

Alternative enclosure designs have been briefly evaluated but so far different configurations implied considerably higher steel masses hence significantly higher costs, without providing critical advantages. The trade-off may however have to be revisited if the site eventually selected does not provide sufficient space for the travel of a sliding enclosure concept.

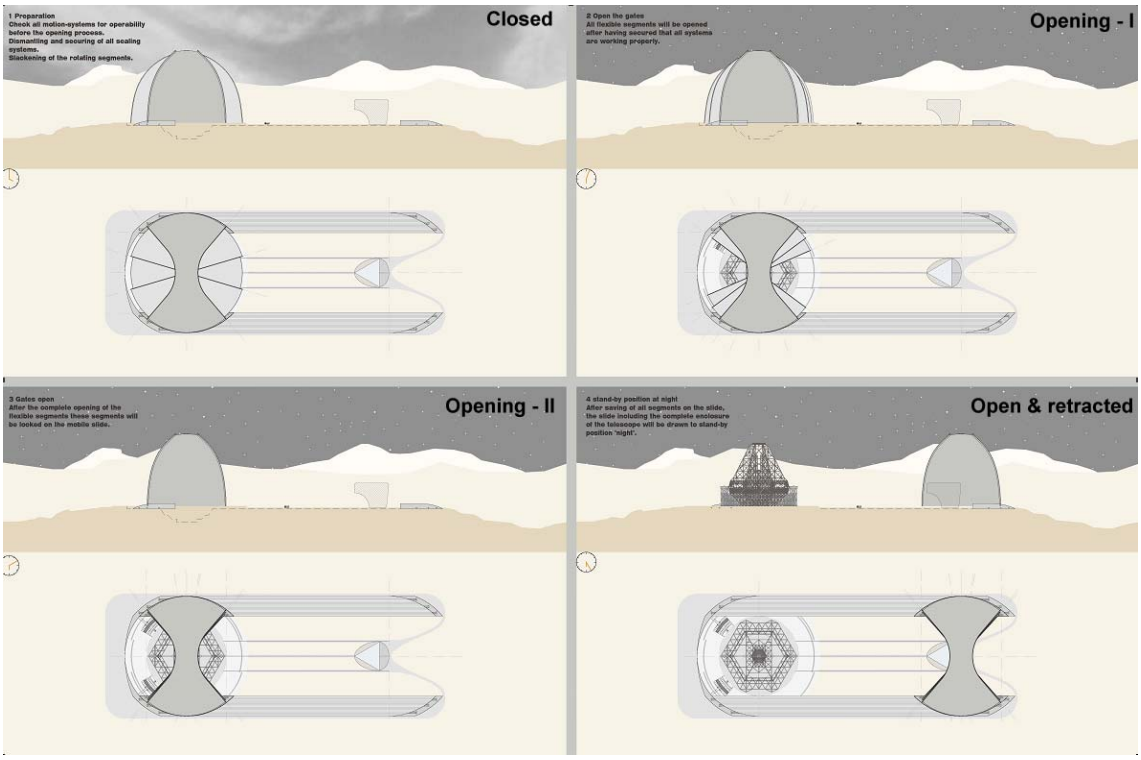

Figure 2-14. Sliding enclosure (courtesy CL-MAP)

2.6.5 Instrumentation

It is generally recognized that it is essential to develop instrument concepts very early in the design of a new telescope. Instruments represent the vital link between the photon-collecting bucket, however sophisticated and powerful, and the scientific goals of the project. As such instrument studies probe effectively the telescope interface and operation scheme and they verify whether the required scientific observations can be obtained with feasible and affordable instruments. This path has been followed by the VLT project where an instrumentation plan was developed almost a decade before first light. For OWL, ESO has launched in 2004 8 instrument concept studies (see Table 2-4) in collaboration with several European institutes.

In the selection of the initial instrument concepts, we have been guided by the science cases identified in the OPTICON study of the science case for a generic 50-100 m ELT and by preliminary studies on the OWL scientific goals. The selected instruments offer various imaging and spectroscopic modes of observing and operate in different wavelength bands from the blue to sub millimetres. They are well representative of the different possible modes of operation of OWL and probe well the telescope ultimate capability. The sample is however by no mean exhaustive of all potentially unique observations to be done with an ELT of the OWL class. High resolution spectroscopy in the near infrared, astrometry at the diffraction limit are examples of two interesting modes not explored in this phase.

Six of the studies were led by P.I. from different European Institutes, two were coordinated by ESO. The instruments study teams were asked to identify the specific science drivers and use them to define the requirements, to develop an instrument concept and to evaluate its performance at OWL. They had to compare them with what it is expected in the next decades from major ground-based and space-born facilities like ALMA and the JWST. They had also to address the dependence on telescope diameter in the range 50-100m and to underline any critical aspects by interfacing with the telescope.

This first survey of possible OWL instruments saw the active involvement of more than 100 astronomers and engineers who through this exercise become familiar with ELT properties and produced a first batch of attractive optomechanical solutions. For many of the astronomers in particular it was a first impact with the “overwhelming” capabilities of a 100m but also with the

differences, and in some cases the limitations, with respect to the 10m class telescopes we are used to work with. All responded in a quite enthusiastic way to the new challenge.

Instrument	Wavelength range	Main Capability	Primary Science Goals	Institutes
CODEX	0.4-0.7 μm	High velocity accuracy, visual spectrograph	To measure the dynamics of the Universe	ESO, INAF-Trieste, Geneve Obs., IoA Cambridge
Quant EYE	0.4-0.8 μm	Photometry at 10^{-3} - 10^{-9} second resolution	Astrophysical phenomena varying at sub-millisecond time scale	Padova Univ. & Lund University
HyTNIC	1.1-1.6 μm	High-contrast diffraction-limited imaging	Imaging of massive planets, bright galactic and extra-gal. sources	LISE- Collège de France
EPICS	0.6- 1.9μm	Camera-Spectrograph at diffraction limit	Imaging and spectroscopy of earth-like planets	ESO + ext. experts
MOMFIS	0.8-2.5 μm	Near IR spectroscopy using many deployable IFUs	Masses of high z galaxies, regions of star formation, GC stars	CRAL, LAM, OPM
ONIRICA	0.8-2.5 μm	NIR Imaging Camera on a field up to 3 x 3 arcmin	Faint stellar and galaxy population	INAF Arcetri & Heidelberg MPIfA
T-OWL	2.5-20 μm	Thermal, Mid Infrared Imager and Spectrograph	Search, study of planets, high redshift Hα galaxies	MPIfA Heidelberg, Leiden Univ., ASTRON, ESO
SCOWL	250-450-850 μm	Imaging at sub-millimetre wavelengths	Surveys of dusty regions, of extragalactic fields for star-forming galaxies	ATC

Table 2-4 Instrument Concept Studies

The eight studies had from 4 to 12 months to be completed. The results are summarized in section 12.2 and the full study reports are reference documents to this volume. Overviews of the interface aspects, of the Adaptive Optics and of the Detectors array requirements are given in section 12.2.5, 12.2.6 and 12.2.7, respectively.

According to the wavelength range where they operate, the instrument highlights can be outlined as follows:

- There are two of the instruments foreseen to operate in the Blue-Visual and Red wavelength bands with natural seeing image quality: CODEX and QuantEYE. They both use the outstanding collecting power of OWL to do unique science. CODEX makes use of the photon plethora to achieve high S/N ratio, high resolution spectroscopy of faint stars and quasars with unmatched (~1 cm/s) velocity accuracy. Main science goal is the direct measurement of the dynamics of the universe, but several other fields of astrophysics will be boosted by CODEX observations. QuantEYE on the contrary explores the temporal dimension of the photon flux. By covering the time resolution 10-3 – 10-9 s, it will permit for the first time to explore the quantum properties of the light from a variety of astrophysical sources.
- There are two "wide" field instruments for NIR wavelengths (0.8 – 2.5 μm): ONIRICA, the imaging camera, and MOMFIS, the multi field-unit spectrograph. Both address many of the "classical" ELT science cases and as such reveal the power but also the peculiarities of observing with OWL. The ONIRICA team has identified diffraction limited imaging over a field of ~ 30" as the primary observing mode. Using a MCAO system one can expect Strehl of 30 % in the diffraction peak of the PSF over the field in periods of good natural seeing.

With this performance the imaging capability of ONIRICA clearly surpasses JWST in limiting magnitudes of stellar sources. Detailed studies of stellar population in Virgo and beyond become possible. The baseline concept of MOMFIS foresees 30 IFU units which can be positioned over a 3' x 3' field of OWL. Its main scientific goal is spectroscopy of high redshift galaxies (z > 4). Their expected half-light sizes are typically ~ 0".1 and this value drives the IFU size to sub arc second and the sampling to 20-30 mas. At a spectral resolution of 4000, MOMFIS would be more powerful than JWST in spectroscopy of faint high redshift candidates identified by multi-color JWST imaging. While working far from the diffraction limit, MOMFIS requires a distributed AO system (MOAO) to deliver a moderate concentration of light at the sampling resolution. A first run of simulations with natural guide stars has shown that this might be possible but with limited sky coverage.

- One of the key science cases for OWL is the search for Earth-like planets close to nearby stars. Starting from the results of the Planet Finder studies for the VLT, EPICS addresses various observational approaches to detect and characterize Earth and Jupiter-like planets: differential imaging, polarimetry, NIR IFU spectroscopy and FTS spectroscopy. The spectral range where these modes should operate span from the Visual to the J band. EPICS will require a third generation AO system (XAO) to achieve the diffraction limit with high Strehl at the wavelengths of operation. A set of simulations carried out during the study suggest that an Earth-like planet could indeed be detected with EPICS at a 100m OWL telescope. The selection of the final instrument configuration, of its primary observing modes and the prediction on its ultimate performance will have however to wait for more extensive modelling in the successive phase of the project.
- T-OWL is an imager-spectrograph to operate in the thermal infrared between 2.5 and 20 μm. In this spectral region the requirement on the AO system are relatively modest. In the bands where the atmosphere is transparent, T-OWL will outperform MIRI at the JWST in the observations of point-like sources. A wide range of targets from dusty planetary systems to black holes in the nuclei of active galaxies will be the primary science goals of T-OWL.
- SCOWL is a large field (~ 2'.5) submillimetre camera to observe in the three submillimetre bands at 350, 450 and 850 μm. It capitalizes on the expertise acquired with SCUBA1 and SCUBA2 instruments and uses it to draw the concept of a powerful survey instrument. SCOWL would supply the ALMA interferometer with a wide range of newly-discovered sources for detailed investigation. It benefits from the diffraction limit given from the OWL size (~1 ") without the need of an AO system. It does require a very high and dry site.
- HyTNIC presents the concept of hypertelescope as a multi-element imaging interferometric array having a densified pupil. It allows direct imaging with high resolution during the segment-filling phase of the M1 preparation with a very simple NIR camera, providing observations of unique scientific value before OWL's completion.

As a conclusive statement of this section, we underline that the instrument concept studies have become available toward the end of the Blue Book preparation. While some advanced feedback from the studies has been already taken into account, the global results of the studies will be fully folded in the telescope design at the beginning of the next phase of the OWL project only.

Finally, with a look at the future steps in this area, we remark that the OWL Instrumentation effort has been coordinated with the work on ELT instruments foreseen within the ELT Design Study (see A-1.8**).** At the kick-off meeting of the ELT instrument "Small Studies" in September 2005, 8 instruments were identified which very much will extend or complement the work carried out for OWL. Many of the OWL Instrument Concept Study teams are involved in this effort and will put to best use their newly acquired expertise there.

2.7 Progressive implementation

A by-product of segmentation is that the telescope can deliver sky images before full completion of the aperture. Such feature has been taken advantage of with the Keck and will be with GTC. With only 36 segments, however, the integration time scale is too short to allow for anything but engineering work until the aperture is filled. With OWL, a segments integration time scale in the range of 5 to 6 years, in-line with the segments production scheme, would leave far more time than required for engineering purposes. Taking into account the fact that the start of segments integration is, according to current plans, contingent to on-site acceptance of major subsystems, including enclosure, telescope structure and kinematics, alignment metrology, corrector and provisional, passive M5 and M6 units, to name a few, and allowing for 19 months of engineering and 5 months of commissioning time, science operation with a partially filled aperture ought to be possible long before completion of the entire project: already several hundreds of segments will be able of delivering useful images. Actually the integration plan for the segments does require the telescope to be fully operable on-sky and will indeed make critical use of this to phase newly installed segments. Even so, a large fraction of the nights will be free for possible science use. The instrument studies have started assessing the possibility of working with a partially filled aperture. More analysis is necessary to determine whether a solution based on specific instrumentation and AO system for a given equivalent size (which would then last for an extended period) may be an alternative.

The progressive implementation scheme is also optimized to allow maximum development time for the adaptive units and to allow on-sky engineering with provisional, passive units before their delivery. In addition, a stepwise, progressive integration and testing of the system –in particular control systems- allows for equally progressive debugging.

The path to first, seeing-limited light is determined by the final design and construction of the telescope enclosure, structure, kinematics, and essential control systems: internal alignment, phasing, active optics, field stabilization. Taking into account the fact that the actual critical path is the supply of the 8-m mirrors of the corrector rather than the supply of the highly standardized enclosure, telescope structure and kinematics, seeing-limited first light ought to be possible within 6 years of ordering the fabrication of the 8-m mirrors[25].

Segments integration will start after integration of a dummy corrector and testing of the telescope kinematics and internal metrology. Preliminary requirements for the segments integration and maintenance are given in RD5. The enabling milestones for the start of integration of the primary mirror segments are outlined in Table 2-5. According to the current design and plans, segments integration and maintenance are only allowed during daytime.

The expected integration rate is two segments per day, the necessary infrastructure is basically that required for segments maintenance. Indeed the maintenance infrastructure has a capacity much larger than required for the sole integration purposes, and implies no particularly advanced technology (see RD5). The maximum required capacity of the maintenance line peaks at an average of 5.1 segments per day, replaced or newly integrated in the sixth year of integration, assuming relatively short-lived, conventional aluminium coatings. The maintenance rate decreases to an average of 4.2 segments per day in normal operation. Rotating spares and using multiple lines to wash and coat individual segments (in contrast to a single line able to handle several segments at once) allows for a robust maintenance scheme, with generally progressive and/or low impact of failure at any given stage of maintenance (see RD5).

Segments integration will follow the four phases described below. Timelines are indicative and correspond to the baseline plan.

[25] The first VLT 8-m blank was delivered within 5 years after ordering (from SCHOTT) and the first finished mirror within 6 years after signature of the polishing contract (with REOSC, now SAGEM). Both contracts implied the construction of dedicated facilities. In the meantime, the SCHOTT facility has been dismantled and the REOSC one converted for the production of GTC segments.

Subsystem	Status	Enabling milestone
Telescope enclosure	Fully functional	On-site Provisional Acceptance
Telescope structure incl. kinematics	Fully functional	On-site Provisional Acceptance
M1 & M2 Mirror covers No 1 incl.		
Covers structures & kinematics	Fully functional	On-site Provisional Acceptance
Handling tool[26]	Fully functional	On-site Provisional Acceptance
Local storage racks	Fully functional	On-site Provisional Acceptance
Rack transporter	Fully functional	On-site Provisional Acceptance
M1 & M2 Mirror covers No 2 incl. in-situ cleaning unit(s)	Fully functional	On-site Provisional Acceptance
M1 & M2 covers No 3 to 6	Fully functional	On-site Provisional Acceptance
Corrector	Dummy corrector integrated and tested	De-integration of dummy corrector
Telescope pre-alignment metrology	Functional up to dummy corrector as rigid body.	Tests up to dummy corrector as rigid body completed.
Coating tanks	Fully functional	On-site Provisional Acceptance
Washing units	Fully functional	On-site Provisional Acceptance
Segments handling carts	Fully functional	On-site Provisional Acceptance
Segments maintenance lab	Fully functional	On-site Provisional Acceptance
Segments units	At least 7 M2 segment units ready for integration, coated, tested.	Successful phasing of a 7-segments module of M2 in the segments maintenance lab.

Table 2-5. Subsystems status at start of segments integration.

Phase 1 Blind integration of the M1 and M2 mirror segments.

The plan is to start integration of segments in blind mode only. Blind mode is meant for in-situ coarse phasing (no on-sky calibration). At this stage of telescope integration, the corrector is not yet available but the system has been tested with the dummy corrector.

Phase 1 starts when all conditions specified in Table 2-5 are met and ends at first light with the acceptance of the corrector, with temporary non-adaptive M5 and M6 units, and including the focal plane metrology systems.

According to current plans phase 1 lasts 6 months, at the end of which first light occurs with an equivalent diameter of 57-m (collecting area).

Phase 2 Daytime blind integration, night-time phasing on sky

Phase 2 starts with seeing-limited first light and ends with first AO light (single conjugate IR AO with M6 unit). In phase 2 the telescope is operating in seeing-limited, engineering mode only.

According to current plans phase 2 lasts 7 months, at the end of which the provisional M6 passive unit is replaced by the final AO one and first AO light occurs. At this stage the equivalent telescope diameter is about ~67-m.

Phase 3 Daytime blind integration, night-time phasing on sky.

During phase 3 engineering night-time related to segments integration and control shall decrease to negligible proportions. Phase 3 coincides with the commissioning of the first stage of adaptive optics and ends with the start of science operations. At this stage the telescope equivalent diameter is ~75-m.

Phase 4 Daytime blind integration, night-time phasing on sky.

[26] Including its on-board phasing metrology.

Phase 4 covers essentially the filling of the full aperture, with completion by mid-2021. During this phase, integration of segments and related control systems shall only exceptionally interfere with science operations.

First light will occur in seeing-limited mode with temporary, non-adaptive M5 and M6 units. Note that the LISE laboratory (OHP) is currently studying a focal instrument concept along the Labeyrie Hyper-Telescope approach to use such a diluted aperture for high resolution / high contrast imaging. IR single-conjugated AO will become possible after replacement of the temporary M6 unit by the final, adaptive one, with science operations starting shortly after. At this point it is expected that engineering night-time will be negligible in relation to science time. The telescope diameter will be about 50-m in terms of collecting area; the angular resolution will depend on the still to be determined filling geometry but could be that of a 100-m if integration of the segments would start from the outer edge of the pupil.

Dual conjugate IR adaptive optics will start less than two years later, with the provisional M5 unit replaced by the adaptive one.

2.8 Observatory operation

The OWL observatory will be operated in ways significantly different from even the largest current optical observatories. While inheriting innovative concepts that have been successfully implemented at the VLT/VLTI, the planned operations of OWL will also heavily rely on the experience gathered by ESO in the operation of ALMA. The possibility of building OWL on a new site, as was done with the VLT, would offer the advantage of planning the entire observatory infrastructure and operations around the facility.

As the paradigm at modern observatories already shows, the OWL observatory must be designed as a facility that includes not only the telescope, instrumentation, and on-site infrastructure and staff, but also all the remote locations where development and segments of operations take place, such as instrument building, software development including scientific data processing tools, data archiving and distribution, and support to the users community, among others.

The extended partial completion phase that OWL will undergo offers opportunities for the early scientific exploitation of an already unique facility, also enabling its progressive technical and scientific validation. There is a clear parallel with ALMA, which will take advantage of such extended transition stage to set up all aspects of operations including personnel training and systems validation. Furthermore, the continuous maintenance needs of such a complex facility will benefit from the experience acquired in that stage in which demanding technical and scientific activities will coexist.

The ultimate scientific legacy of OWL will reside in the quality of its data products. Such quality relies on the capabilities of the telescope and its instrumentation, but also on the careful implementation of operational procedures for their full characterization and calibration, quality control, and instrument health checking. Such procedures are in turn essential for the population of an archive containing science-ready products that facilitate their reusability, mainly by means of their publication in the Virtual Observatory that is expected to constitute a fundamental tool for observational research in astrophysics by the time that OWL becomes operational. The full-scale implementation of an end-to-end system at the VLT and VLTI has provided ESO with a very important capital of know-how and lessons learned from which ALMA will also greatly benefit, and that will be an essential part of the design of operations at OWL. The operations planning in the data flow area will have to adapt to the expected data rates. The data volume will not be much different from the upcoming surveys telescopes (e.g. VST, VISTA, LSST) and already routinely applied to particle physics experiments (CERN). Improvements in the technological development, even if slowed from the currently still holding expansion laws for CPU, data storage and data transmission increases, will be sufficient to handle the data rates from a telescope like OWL.

Whether the projects executed at the OWL will follow current time distribution paradigms at general-purpose facilities like the VLT, or be largely focused on experiments requiring the exclusive use of the observatory for an extended period of time in order to achieve far-reaching goals, or a combination of both, will depend on the demands of the scientific community and the general development of observational astrophysics in the next decade. Operation mainly or exclusively by specialized observatory staff is envisaged, and this will be taken into account when deciding on staffing, policies, procedures, and tools. Such specialized interaction will be frequently needed both to exploit the technical capabilities of OWL to the limit, and to maximize the scientific output of the limited time available.

An essential part of the success of a modern observatory is the availability to the research astronomers of tools that allow the full scientific exploitation of the datasets. This will be even more so for OWL, given the foreseeable complexity of its instrumentation and of the process of removal of the instrumental signature given, for instance, the structure of the delivered PSF. Dedicated software to be made available to the end users and able to fully process the data delivered by the instrument up to the science-ready level will be regarded as an integral part of each instrument. Such software will meet the requirements needed to be integrated in the main data reduction environments existing at the time of OWL operations, and will deliver products in compliancy with the Virtual Observatory.

2.9 Site considerations

Site characterization and selection has an overwhelming impact on eventual performance (operational efficiency, quality of science data) and, potentially, cost and schedule. The selection of Paranal as the VLT site may arguably have been the single most relevant decision in relation to VLT performance. Cost and schedule should not be underestimated either, as a significant cost increase may eventually require a reduction of the telescope diameter[27] and as a significantly longer schedule could make the project unattractive.

There is no such thing as the perfect ground based site; as with the telescope design, the eventual site selection is the result of a trade-off between at times conflicting constraints and priorities. The parameter space has grown considerably since the mid-20th century, and is due to grow considerably more for Extremely Large Telescopes. The performance of relatively wide-field adaptive optics, in particular, is contingent to the structure of atmospheric turbulence (see section 14.2.3). Good seeing is no longer good enough; instead of an integrated parameter, a thorough statistical description of the vertical structures and time constants of atmospheric turbulence become equally relevant.

Merit functions encompassing priorities and relevance to performance, cost and schedule must be established, with a view to allowing a difficult –and soon irreversible- decision to be taken in proper knowledge of its consequences. Such merit function will include fixed and reasonably well quantified parameters, such as topology, soil properties, and their predictable impact on the system performance and cost (e.g. the telescope foundations). Other parameters will be of a statistical nature, and will have to be assessed in a probabilistic context. Others will be inherently speculative, such as political stability or local manpower costs. Finally, long-term variation of relevant parameters must be taken into account to the maximum possible extent (see also section 14.3.3). Climate change is an established fact; its long-term prediction and modelling are, as of today, notoriously inaccurate. Ignoring them for such reason would however be irrational and, potentially, disastrous.

The OWL site characterization and the definition of figures of merit should encompass, as a minimum, the following criteria (the ordering of the list is without any prioritization):

1. Cloudiness;

[27] Downtime related to weather conditions, for example, might be traded against statistical performance during “uptime” or against a significant reduction of the telescope diameter excluding certain science cases.

2. Humidity, Precipitable Water Vapor;
3. Atmospheric Extinction;
4. Seeing or turbulence coherence length;
5. Ground temperature, air temperature gradient and microthermal turbulence over the first 100 m;
6. Vertical structure of the atmospheric turbulence, with a resolution not worse than +- 500 m in altitude up to ca. 20km;
7. Isoplanatic angle;
8. Turbulence coherence time;
9. Outer scale of the atmospheric turbulence;
10. Sodium layer mean density and annual variation;
11. Wind speed and direction;
12. Precipitations (snow, rain, ice, fog);
13. Airborne aerosols, including dust chemical composition, particle size distribution and abrasive characteristics;
14. Site topology;
15. Soil properties, including typical stiffness,
16. Seismicity;
17. Survival loads (earthquakes, wind, precipitations);
18. Present and future potential light pollution; contrails;
19. Access to pre-existing infrastructures (roads, harbor, etc.); development costs;
20. To the foreseeable extent, long-term exposure to climate change;
21. To the foreseeable extent, potential long-term political stability.
22. Site-dependent operational costs, including, to the foreseeable extent, local manpower costs.

These parameters shall be characterized in a consistent form, and the instrumentation required to acquire them, where appropriate, shall follow standards allowing rigorous comparison of potential candidates (see also section 14.1.1). A detailed merit function will be set in the design phase, with weights reflecting priorities and, where sufficient data are available, individual sites ratings.

Gathering and compiling data form only part of the search for and characterization of an OWL site. Understanding sites properties on micro- (a few km) and macro- (a few 100 km or more) scales is essential to predicting performance-relevant characteristics and their probable evolution with time. Software tools have been elaborated in the framework of the OWL concept study, with a view to providing easy access to available meteorological databases over past decades (see section 14.3.3.2). Models can be established, cross-checked by comparing their prediction to measured performance at well documented sites (e.g. Paranal, La Palma), and then applied to the search for (or to predict performance) of other, less well documented candidates. Doing so should allow to bypass years if not decades of measurements, and to reach an informed decision in a faster and more efficient way.

Site search and characterization are evidently not exclusive ESO activities. The matter is the subject of a world-wide cooperation. Part of this effort is addressed within the framework of the ELT Design Study (see section A-1.9), whereby two well known sites (Paranal area and La Palma) will be characterized in relation to properties relevant to Extremely Large Telescopes. This is *not* meant for those two sites having already made it to the shortlist, but as an equivalent to point designs i.e. taking an a priori and fictive decision, then proceeding with design and analysis in order to understand its full consequences.

ESO's own experience in site characterization is extensive and dates back to the earliest days of the VLT programme. Considerable expertise has been accumulated since then (see 14.3.1) and shared with ELT proponents worldwide.

2.10 Plans for final design and construction

The schedule for design and construction of OWL is essentially determined by five factors:

1. the dates at which necessary financial commitments (including all resources required to execute the scope of work) can be made, and the dates at which such resources become available;
2. the telescope size, the implied industrial capacity to supply long-lead items, and the dimensioning of integration lines;
3. the ability of the supply, integration and maintenance plans and implied infrastructures to allow early operation and cope with a progressive implementation of scientific capabilities, without significant overheads on science time.
4. the progress of technology in the area of advanced wavefront control, in particular adaptive optics;
5. the duration of the preliminary and detailed design phase.

The first factor is arguably the most determinant; its impact can be alleviated to some extent if significant but not major commitments[28] can be made to secure, at an early stage, the procurement of long-lead items (essentially the 8-m mirrors), the final design of the enclosure and telescope structure, and the first generation adaptive mirror technology.

The second factor is strongly influenced by the design directions underlying the OWL concept, in particular the reliance on serial production and integration schemes and on proven and reliably predictable technologies. This not only allows for favourable cost scaling laws, but also allows for fast and flexible supply, production and integration cycles. As such, the penalty implied by large size can be offset by supply and integration times much faster than those associated to custom designs of subsystem, assemblies, and parts.

The same comment applies to the third factor, which influences the dimensioning of the integration and maintenance infrastructures. As impressive as those may eventually be, they are essentially a matter of adequate planning, optimized process flow, and investment.

The fourth factor corresponds to the main technological risk area and calls for continued investment in development and design, most particularly in the area of large and/or densified[29] adaptive mirrors.

The fifth factor only weakly depends of the telescope size and, as such, does not imply a significant schedule disadvantage compared to other Extremely Large Telescope projects. In this respect, it should be noted that OWL benefits from sustained design and analysis activities since 1997, including industrial studies. The implied competitive advantage should not be underestimated.

Detailed plans have been developed for the design and for the construction and integration phases (see chapter 16). These plans allow for maximum development time for critical technologies (such as adaptive optics and laser guide stars) and timely feedback from the ELT Design Study. Figure 2-15 shows the major milestones. After consolidation of the management and product assurance plans and procedures, the first two years would concentrate on conceptual design iterations, analysis, error budgeting, finalizing subsystems requirements, site

[28] In practice, less than 10% of the total estimated cost.

[29] Actuator density.

search and characterization. The optical design would be frozen towards the end of the second year, after two feedback iterations -most notably to take into account the outcome of instrument studies. Also included in the first two years is the subcontracting of a process flow study, with a view to streamlining the construction and operation processes, to defining the optimal maintenance structures, and to incorporating the study results in the system design where appropriate. Although the ELT Design study already includes prototypes SiC segments, additional and complementary effort is foreseen in order to finalize the decision on segments substrates within the third year of design.

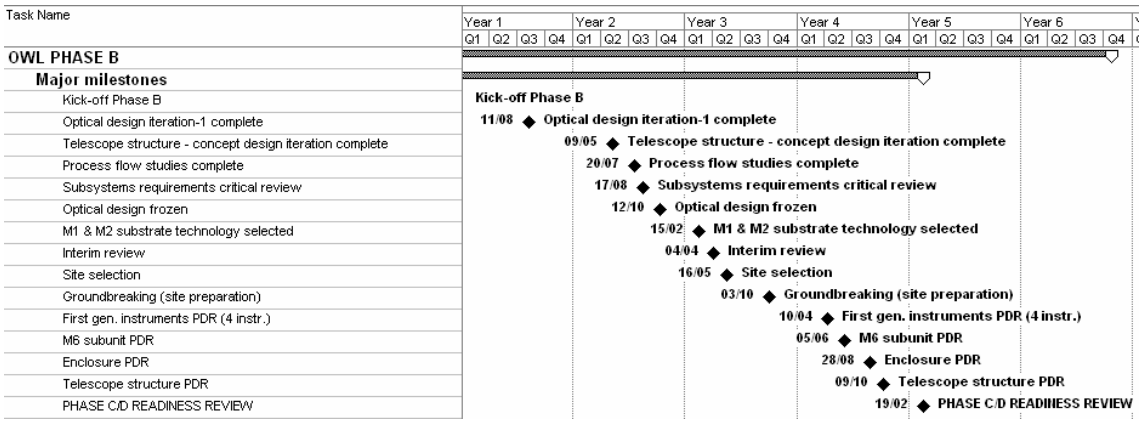

Figure 2-15. Design phase, major milestones.

By the end of the second year, results of the Active Phasing Experiment (APE, in ELT Design Study) will lead to the detailed definition of the control systems.

Site selection is planned mid-way through the design phase and is required to finalize requirements on the infrastructures, enclosure and foundations. The second half of the design phase would concentrate mainly on

- Preliminary and final design of the enclosure;
- Preliminary and final design of the telescope structure (including mirror covers and wind shields, if any),
- Preliminary design and prototyping of the first generation adaptive subunit (M6),
- Preliminary designs of at least two first generation instruments,
- Detailed definition, specifications, price inquiries for all major units / subunits, including all integration, verification, maintenance and operation infrastructures and equipment;
- Site preparation (access roads, storage areas, temporary infrastructures, first stage power supply);
- Finalization of Assembly, Integration and Verification (AIV) plans.

Ideally, each of the first 3 items above would be covered, for risk mitigation, by two competitive contracts until Preliminary Design (and, for M6, prototypes) before granting contracts for final designs.

The design phase also includes

- Iterations of the Top Level Requirements, in close cooperation with the scientific community, and subsequent iterations of Level 1 requirements and of error budgets;
- Substantial R&D effort in adaptive optics technologies, including laser guide stars, deformable mirrors, metrology systems; in wavefront control (including tests on GTC), and high contrast imaging;
- Extensive analysis, modelling and tests, including wind tunnel testing;
- Prototype segments (1:1 scale), including axial and lateral support systems.

The baseline plan for the design phase does not include any financial commitment ahead of phase C/D capital investments, except for initial site preparation and the first stage of the power plant.

Phase C/D would start after the readiness review planned at the beginning of the 5th year (2010, assuming a start of the design phase early 2006). The status of all subsystems, units, and subunits at the readiness review is detailed in chapter 16. At this stage, time-critical subsystems will be in the final design phase. Figure 2-16 shows the schedule of the major milestones.

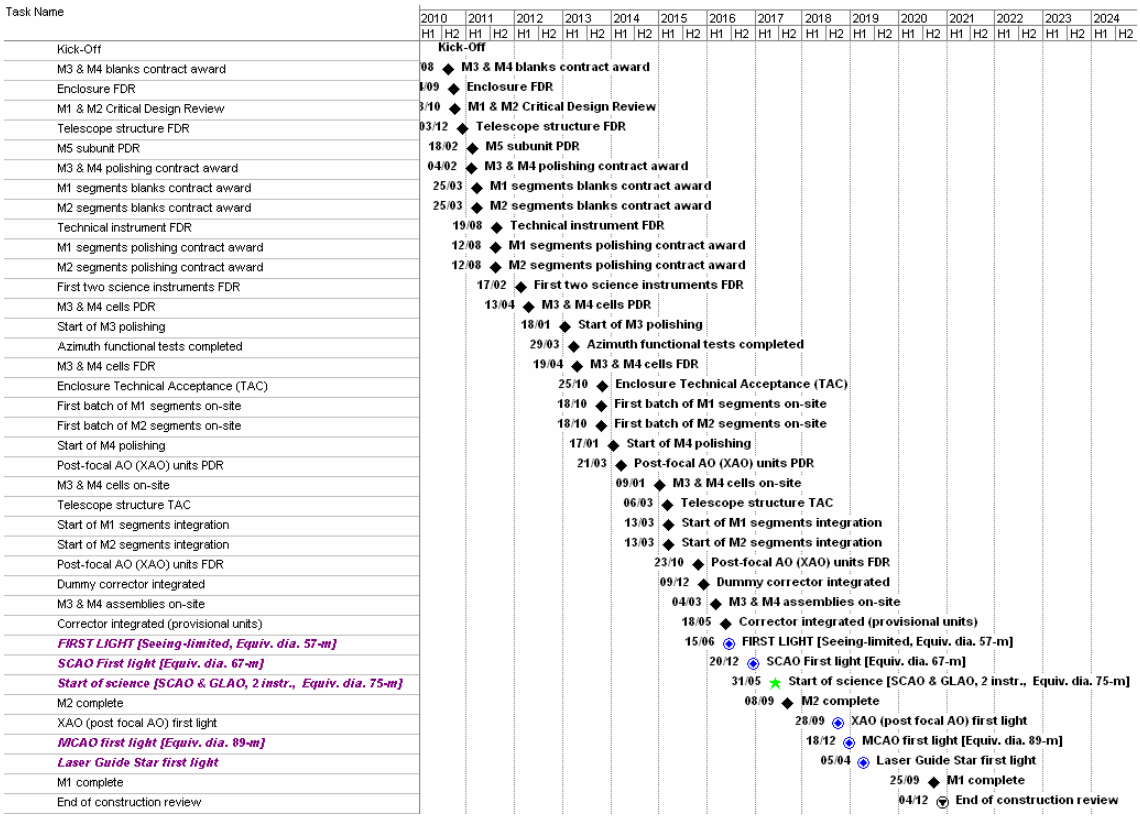

Figure 2-16. Phase C/D major milestones.

The telescope structure and kinematics would be integrated in parallel to the enclosure i.e. the structure and kinematics shall be designed to survive open air environmental conditions. Segments integration would start after completion of the telescope structure and kinematics (see RD5 for a complete definition of enabling milestones and of required equipment), and be interrupted for each major handling (e.g. of the corrector).

As a general rule, no glass goes into parent units or subsystems prior to dummy testing as a minimum, and no subsystem or unit goes to the telescope prior to extensive off-line testing. The same applies with integration and maintenance lines.

First light would occur by mid-2016 with provisional, non-adaptive M5 and M6 units. At that stage the telescope would have an equivalent diameter of 57-m. The total time for integration of the segments is identical to the production cycle (6 years). The equivalent diameter after first light depends on the capacity of the integration lines. Because such lines rely on essentially the same equipment as maintenance, and assuming that any segment would need maintenance more than once every 6 years, integration rate is accelerated in the first 1.5 year (however not to full capacity).

The 6 months following first light are devoted to extensive engineering tests and observing runs in seeing-limited mode. Thereafter the corrector is removed, the 8-m mirrors coated, the adaptive M6 unit integrated and the corrector re-integrated into the telescope for first light in SCAO mode. At that point the telescope would have a collecting area equivalent to that of a 67-

m one. After another 6 months and with an equivalent diameter of 75-m, the telescope would enter into science operation. The aperture would be completed by 2020.

In the baseline plan, segments deliveries occur about 1.5 years ahead of the required date; no attempt has been made yet to optimize the schedule and smooth the cash flow profile. The production of the 8-m mirrors is on the critical path to first light. The schedule to first light could most probably be accelerated by up to a year if the 8-m blanks were ordered one year before completion of the design phase.

The segments production and integration is on the critical path to full completion. Potential segments suppliers claim that facilitization of their production units would take less time than anticipated (2 years) but this has not been taken into account.

2.11 Cost estimate

The OWL cost estimate is collated from the results of industrial studies (most notably, segments production, telescope structure and kinematics, enclosure), internal estimates based on past experience (e.g. the 8-m mirrors), and allocations (e.g. adaptive mirrors).

Several estimates have been produced, depending on major technology choices –e.g. segments substrates, enclosure concept, etc. A detailed presentation is provided in chapter 16. The baseline or *best estimate* is based on conventional substrates for the segment blanks and assumes an enclosure cost close to the upper limit indicated by industrial studies. The total estimated cost for capital investment 1.255 B€ (Table 2-6), including 35.5 M€ in the design phase. These figures do not include ESO manpower, estimated at about 85 Full-Time Equivalents (FTEs) for phase B and 300 FTEs for phase C/D. The FTEs allocation assumes extensive subcontracting of most design and construction activities to expert suppliers, and no major in-house new software development.

The allocation for instruments is 50 M€ (excluding ESO manpower), assuming at least two first generation instruments. A significant allocation is made for maintenance infrastructures and facilities, under the assumption that such maintenance would be performed on-site. A study is planned in the design phase to ascertain whether this should be the case, or whether part of the maintenance could be relocated or even outsourced.

The estimate for control systems should be understood as reflecting the budget for central control only; subsystems own control systems are included in the corresponding subsystems estimates.

It should be noted that according to industrial studies, major cost saving could be realized

- if the segments were made of Astro-Sital or if low-cost silicon carbide solution(s) could be demonstrated;
- if the enclosure could rely on low-cost *tensiarity* principles proposed by AirLight (RD40).

In the most optimistic case the potential cost savings are in excess of 300 M€. As these options developed after drafting ESO's current long-range plan, no supporting R&D costs are currently budgeted in the design phase of the baseline plan. Risk mitigating measures, such as subcontracting competitive preliminary designs for the enclosure, for the telescope structure and kinematics, and for the first generation adaptive subunit are not included either,

A rough order of magnitude (ROM) estimate of the underlying R&D activities which would have to be undertaken in the design phase to properly evaluate these cost-effective alternatives amounts to 15 M€ (i.e. the capital investment in phase B would increase to 50.5 M€).

As indicated in section 2.10, ordering the 8-m blanks ahead of the construction phase would allow accelerating the schedule to first light by about one year. Depending on supplier, this may translate into a commitment of up to 35 M€ to be transferred from the construction into the

design phase. Such commitment would have to be made within the third year of the design phase to secure the accelerated schedule.

Item	Phase	
Project Management		**143.6**
Contingency	C/D	110.8
Process flow & costing studies	B	0.5
Overheads (transports & insurance)	C/D	32.3
Project Engineering		**12.4**
Wind tunnel testing	B	0.8
R&D, major breadboards and experiments	B	11.6
Site infrastructure		**87.4**
Enclosure		**169.6**
Design	B	7.0
Enclosure foundations	C/D	28.8
Kinematics	C/D	16.9
Enclosure structures	C/D	115.0
Enclosure Maintenance Units	C/D	1.9
Telescope structure & kinematics		**186.6**
Design	B	7.7
Azimuth structures	C/D	77.1
Altitude structures	C/D	60.4
Wind screens	C/D	2.8
Mirror covers	C/D	17.1
Telescope foundations	C/D	19.0
Telescope diagnostic systems.	C/D	1.9
Telescope structure & kinematics maintenance units	C/D	0.9
Optomechanical subsystems		**552.1**
Actuators, position sensors - designs & prototypes	B, C/D	4.1
Segments development & prototyping	B	2.8
Primary mirror unit	C/D	329.5
Secondary mirror unit	C/D	23.3
Corrector unit	C/D	132.0
Focal stations	C/D	24.6
Telescope pre-alignment unit	C/D	0.4
Optomechanical subsystems maintenance facilities	C/D	35.5
Instrumentation		**72.0**
Technical instrumentation	C/D	8.0
Science instrumentation	C/D	50.0
Post-focal AO units	C/D	10.0
Instruments maintenance facility	C/D	4.0
Laser Guide Stars Subsystem		**10.7**
Laser units	C/D	5.0
Beam Propagation units	C/D	3.0
Control & Metrology units	C/D	2.0
LGS maintenance facility	C/D	0.7
Central Control Systems		**19.5**
Site characterization		**0.8**
TOTAL		***1254.6***

Table 2-6. OWL cost estimate, capital investment.

2.12 The ELT Design Study

In March 2004 a proposal for a technology development towards ELTs was submitted to the European Commission for funding within framework Programme 6. The proposal has been approved and the project is running since January 1st, 2005.

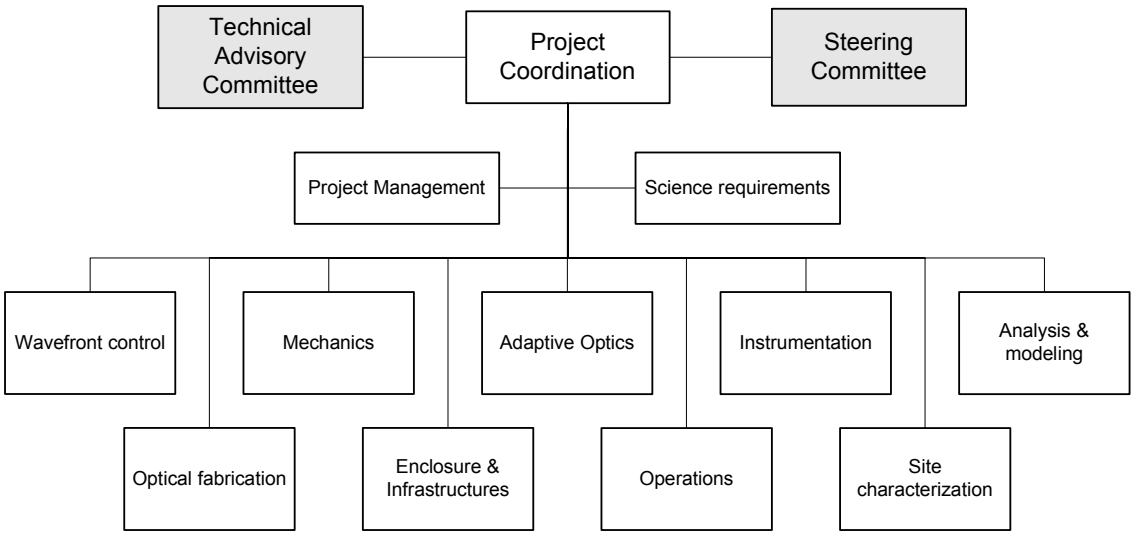

Figure 2-17. ELT Design Study, Work Breakdown Structure.

The project covers the development of enabling technologies and concepts required for the construction of a European extremely large optical and infrared telescope, with a diameter in the 50- to 100-m range. To this end, it builds on existing European design studies, on leading industrial and academic expertise in the relevant fields, and gathers resources across the European academic and industrial communities for a preparatory effort on crucial components, subsystems and concepts. To the possible extent, and contrarily to what its name would imply, the ELT Design Study is design-independent. Indeed, it focuses on technical issues relevant to any system design. The ELT Design Study is complementary to OWL design; both are conceived as parallel activities, the synergies and respective schedules allowing timely and cost-effective feedback between the two. It follows that, from OWL point of view, the ELT Design Study covers most of the concept and technology developments that would have to be undertaken in parallel with the detailed system design. As a result, the ELT Design Study does not imply a diversion of resources to another ELT project, but allows for the sharing of common efforts, to the benefit of the scientific community.

The project gathers 30 partners under ESO's lead (see Appendix 2 for a list of the participants). The total estimated cost is M€ 31.6, including M€ 8.4 in Community support. ESO's total contribution to the project amounts to M€ 11.740, out of which M€ 9.379 is covered by ESO internal funding. Figure 2-17 shows the Work Breakdown Structure and Figure 2-18 the estimated schedule.

An overview of the Work Packages is provided in Appendix 1. A complete definition of the scope of work is given in reference document RD509.

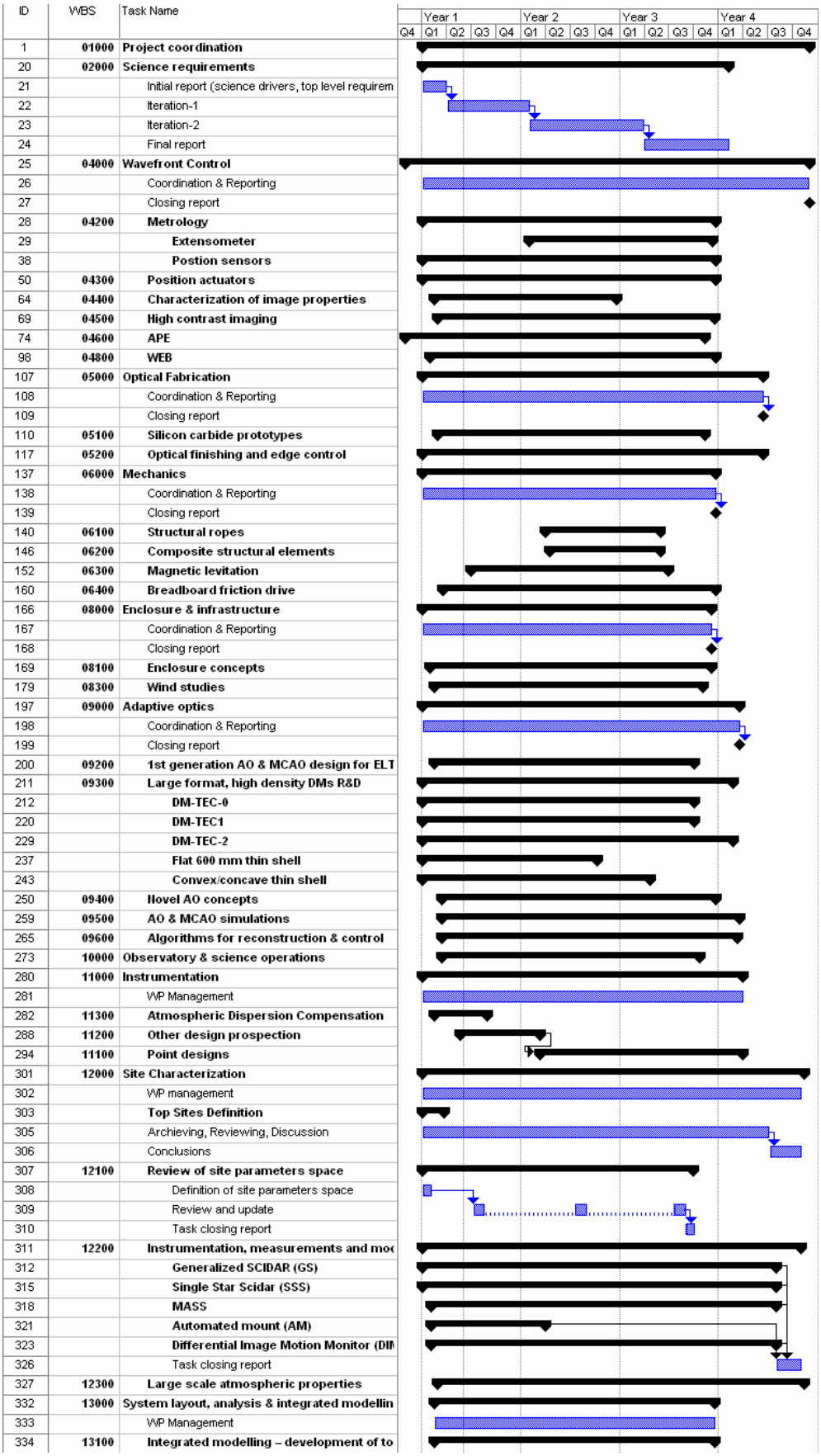

Figure 2-18. ELT Design Study, overall schedule.

2.13 Scalability

The design of OWL is based to the largest possible extent on serialized production of identical parts. It is therefore to be expected that the results of the studies and the analysis of options presented in this report have an intrinsic scalability to different telescope sizes. What the range of scalability is, how the optical design may evolve as a function of size or how the scientific goals are affected by a smaller or larger diameter than the one considered here need a dedicated study, which will be carried out at the beginning of Phase B.

Here we provide some preliminary considerations and figures.

2.13.1 Science

Annex A of the Science Book looks at the comparative scientific performance of different ELT sizes for the highlight science cases. The results are summarized in Table 2-7 to Table 2-9, showing that the full achievement of the science goals can be met only with a 100-m OWL (although admittedly this is a somewhat circular argument, since the science case was developed for telescope sizes of 50 to 100m to start with).

How a science case scales with size depends not only on the collecting area and the resolution but also on a number of aspects related to the telescope design and to the required technology developments, and how these scale with the diameter. Parameters like field of view (both its size and its coverage: contiguous, sparse etc), limiting magnitude, required angular resolution at a given wavelength, number and type of targets, spectral resolution, sensitivity to polarization, etc, all play a role in determining how a science case scales with diameter. Moreover, some cases may have a "scaling law" that affects only the completeness of their samples, while others may be enabled only above a certain size (an example is the exo-earth science case).

Content of information is also a relevant issue when comparing the scientific capabilities of telescopes of different sizes. For telescopes at the diffraction limit, a given number of pixels cover an angular field proportional to D^{-2}. Assuming that the number of pixels is independent of diameter (in principle it is limited by how many we can afford and by the size of the optics that we can build in the camera containing them), the question of how much information there is in the field of view, or what fraction of pixels contain data on astronomical objects rather than the background, depends very much on the science case and should be carefully analyzed in a study of "science scalability" (does the number of objects increase with increasing sensitivity, does seeing them in better detail offset the fact that there may be fewer of them, etc). This may also lead to different ways of sampling the telescope field of view (as in the multi-IFU vs slit mask approach to multi-object spectroscopy: is there scope for relocatable multi imagers?).

An in-depth analysis of these issues will be carried out at the beginning of Phase B.

20m	- Direct detection of Jovian-mass planets in wide orbits around nearby solar-like stars - Radial velocity search on fainter stars (increasing available volume by a factor of 200)
30m	- Imaging of young (<10Myr) Jovian planets around stars in star-forming regions up to 75pc away - Detection and classification of mature Jovian planets around stars within 10-20pc - Possible detection of one Earth-like planet within ~5pc
100m	- Survey of 1,000 solar-like stars and direct detection of a number of earth-like planets within 30pc - Time-resolved photometry of Earth-like planets (albedo & weather) - Spectroscopy of earth-like planets and search for "Biomarkers" - Study of entire exo-planetary systems

Table 2-7 Summary of exo-planet capability as a function of ELT size

20m	- Resolution of the oldest stellar populations in Magellanic Clouds and Local Group dwarf spheroidals (Sculptor, Fornax, Carina) and the Sagittarius dwarf - Resolution of the brightest giant stars in galaxies in the Virgo cluster - Observations of halo giants in Local Group galaxies (high-resolution spectroscopy)
30m	- Age/metallicity measurements of resolved populations in M31/M32 at ~750kpc (imaging) - Determination of star formation and chemical enrichment histories of galaxies out to Cen A (nearest active galaxy)
100m	- Age/metallicity measurements of resolved populations, reaching the Virgo and Fornax clusters at 16-20Mpc - Detailed study of galaxy formation in a representative sample of the Universe

Table 2-8 Summary of studies of resolved stellar populations as a function of ELT size

20m	- Ly-alpha emission-line spectroscopy from 6<z<10 - Possible detection of z~10 objects (depending on their nature)
30m	- Possible detection of z~10 objects (depending on their nature) - Spectroscopy of "earliest galaxies" found by JWST - IGM studies to z~10 using brightest GRBs as background sources
100m	- Detection of z>10 objects - Spectroscopy of "galaxies" to z~20 (depending on their nature). Such objects may even be resolved with a 100m - IGM studies at z>10 (GRBs, QSOs, PopIII SNe as background)

Table 2-9 Summary of studies of the high-redshift Universe as a function of ELT size

2.13.2 Requirements

Requirements for a telescope depend on the science case, so a proper assessment of how they vary with telescope diameter can be made only after the study mentioned above has been completed. There are however some general scaling considerations: some requirements may remain the same whatever the size of the telescope (e.g. the emissivity) or may vary with the area (e.g. the number of degrees of freedom of AO mirrors). Some may have subtler diameter dependence (e.g. they may disappear if they were set by a science case no longer achievable with a different size). Special cases are the focal ratio, which is set by the viability of different optical designs for different sizes, and the wavelength coverage under adaptive optics correction, where achieving short wavelength AO may be limited to smaller telescopes.

Table 2-10 summarizes our current understanding of the dependence of the requirements on the telescope size.

Requirement	**Dependence on D**	**Comments**
Collecting area	D^2	
Wavelength coverage	D^0	Set by science requirements. Achieving shorter wavelength AO may depend on D
Focal ratio	D^0	But different D's may allow different designs with different F/ratios
Image quality (opt design)	D^0	e.g. "Diffraction limit over 5 arcmin"
Diffraction limit	D^{-1}	
Emissivity	D^0	Depends on reflectivity and baffling

Requirement	Dependence on D	Comments
Field of View	D^0	Depends on science case.
Transmission	D^0	Equals $\{\Pi_i\eta_i - \ldots\}$ $i=1,N_{mirrors}$
Focal stations	D^0	Larger telescopes may have more room for instruments
Sky coverage	D^0	
Zenith avoidance	D^1	Depends on maximum rotation speed of the structure
Image quality (AO)	D^0	Req depends only on science
Diffraction limit	D^{-1}	
Number of actuators	D^2	
Operational lifetime	D^0	
Technical downtime	D^0	Maintenance may take longer (but not be necessarily more complex) for larger D's
Operating costs	$D^{1.5}$ (?)	Depends mostly on cost law but with a fixed component
ADC residual dispersion	D^{-1}	Constant in terms of pixels

Table 2-10. Dependence of main telescope requirements on diameter D

2.13.3 Concept design

Operational considerations and data management requirements set aside, we can consider an extremely large telescope as a controlled opto-mechanical system. Consequently, the upper size limit is governed by the feasibility and complexity of the optics, of the control systems, structure and kinematics. Feasibility of instrumentation is of course also a limiting factor.

The use of Alt-Az mounts enables very effective ways to improve load transfers and simplify structural design, while at the same time allowing for much smaller (hence much less expensive) enclosures. Closed-loop autoguiding allowed for a relaxation of exacting tolerances on the telescope kinematics. However, casting and polishing large, homogeneous mirrors, and maintaining their shape and alignment in operation imposes strict limits on scalability. Keck, NTT and VLT each addressed these limitations, with spectacular results. Optical segmentation would allow scaling up to the limit of possible industrial production. Active wavefront control would allow optomechanical structures to be controlled up to the limit of affordable control complexity. Such limits are of a very different nature than former ones, and aperture sizes significantly larger than that of OWL should be possible. Control systems rely on fast-evolving metrology and IT technologies, and industrial studies for the production of OWL segments indicate that 3,000 segments would be well within the limit. It should also be noted that the most difficult control system is in adaptive optics, with a number of degrees of freedom comparable or larger than that of the telescope itself combined with a much higher bandwidth.

On the basis of OWL studies and analyses we conclude that beyond ~130-m, adequate structural performance and safety could no longer be guaranteed without extensive use of advanced, composite structural materials with consequent sharp increases in cost.

The difficulty to make monolithic mirrors beyond proven sizes (~8-m) also sets an intermediate range beyond which multiple segmentation becomes inevitable. A 100-m design with a powered, monolithic 8-m class secondary mirror would theoretically be feasible but all such designs explored so far had significant drawbacks in terms of sensitivity to:

- decentres
- vignetting
- availability of suitably located and sized surfaces for adaptive optics
- in the case of a spherical primary mirror, the delivered image quality.

Further design options would have to be explored before proposing any definite conclusion; our judgement is that multiple segmentation becomes a necessary compromise beyond ~70-80 m.

The lower size limit for an Extremely Large Telescope is not a matter of technical feasibility per se, but of overall design and cost (see section 2.13.4). The OWL optical design is quite similar to that of HET and SALT. Extrapolating upwards from more classical solutions, one should note that scaled-up versions of existing designs (basically a larger Keck with VLT flavour in control systems) must also overcome significant, specific technical hurdles. Large secondary mirrors point towards Gregorian solutions, with correspondingly longer structures or a shorter primary mirror focal ratio, limited field of view and high sensitivity to decentres. All current 30 to 50-m class designs allow for a limited number of reflections, at the cost of large, aspheric adaptive secondary mirrors comparable to that proposed for OWL second generation adaptive optics.

In general, we expect that overall design choices made for OWL would hold within a downscaling to ~60-m, with comparable functionality, similar hierarchical distribution of functions, perhaps with a significantly different optical design and, at the lower limit, single segmentation. The situation is far less clear in the 20-50 m range. It is worth recalling that all studies made for 30- to 50-m telescopes opted for more conventional design solutions. It is plausible that below 60-m, the compromises underlying the OWL design would have to be re-balanced, leading to a leaner, but far less cost-effective, design.

2.13.4 Cost and schedule

The schedule and cost-effectiveness of the OWL design are mainly due to

- design tradeoffs (e.g. open air operation, spherical primary mirror, large lightweight structural design, low-cost kinematics),
- low fabrication and supply risks,
- and above all, reliance on standard parts or serial production.

Design tradeoffs - HET and SALT are spectacular examples of how far design compromises may impact costs. Arguably the largest optical telescopes, they have been built at a cost lower than the 3-4-m class telescopes commissioned in the 1970s and 1980s. HET and SALT designs also incorporated low supply risks (spherical, 1-m class segments) and low cost enclosures. They may have benefited from serialized production of segments and structural elements, but to a far more limited extent than OWL. On the other hand, with its alt-az kinematics, OWL does not go as far as HET and SALT in design compromises, which henceforth would play a more limited role in terms of cost reduction.

Open air operation and relaxed requirements on the enclosure (no air conditioning), however, leads to very significant cost savings. Enclosures for 3- to 4-m class telescopes of the second half of the 20th century represented more than 50% of the total project investment. With NTT and VLT this figure has been brought down to 20-30% and the trend is due to hold.

Lightweight structural design - Although the cost per unit mass of structural, passive mechanics is very low, the OWL design, with a volumic mass about 60 times lower than that of the VLT, allows for notable cost savings. A downscaled version of the current structural design to 60-m leads to a factor two reduction in moving mass (see section 9.6.4) hence, in first approximation, to the same factor two on the telescope structure. This is probably optimistic as the mass ratio between high cost functional (drives, actuators) and low-cost structural (passive) mechanics increases with decreasing telescope size.

OWL friction drives come at a cost comparable to that of the VLT's hydraulic pads and tracks. We do not expect that dimensional tolerances for hydraulic pads and tracks could be met with apertures significantly larger than that of the VLT. No detailed assessment of the cost of friction drives for a 60-m class telescope has been made; we expect, however, such cost to be roughly proportional to moving mass i.e. a factor 2 lower.

Standardization - With the current OWL design, approximately 82% of the total mass (excluding foundations, enclosure and infrastructure) of the telescope is made of standard steel

elements, and approximately 17 % of serially produced[30] parts (structural nodes, drives, segments, actuators, etc). Only 1% of the total mass corresponds to custom-made units (8-m mirror units, adaptive units, etc). Figure 2-19, taken from a leading optical manufacturer, shows the relation between unit cost and total quantity. The model applies to conceptually simple items, which can however be the result of a complex process (optical parts being a typical example). Parts or units themselves made of standard components would follow a less favourable law.

Still, capital investment in production facilities is a significant fraction (~30-50%) of supply costs, at least for the segments (see e.g. RD6 to RD12). It is in the area of structural mechanics, not optics, that cost benefits induced by standardization are maximal.

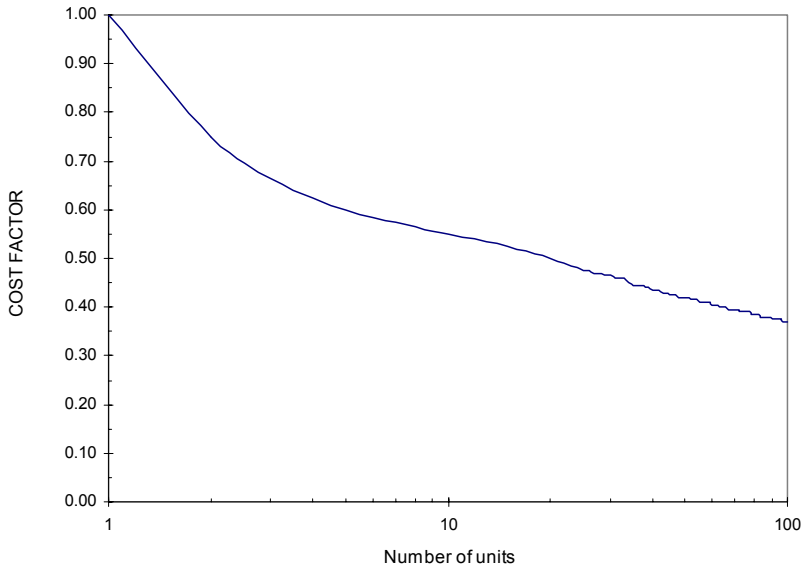

Figure 2-19. Unit cost vs. quantity (industrial data).

As for schedule, scaling the aperture would affect the construction but not the design phase, which is only weakly design dependent (provided, of course, that the design phase capitalizes on the effort already put into the conceptual design phase).

With the current OWL design the schedule to first light is essentially set by the production of the 8-m mirrors and of the first generation adaptive unit. Downscaling to ~60-m is likely to lead to a redesign of the optics but active mirrors in the 4- to 8-m and adaptive ones in the 2-3 m range would still be required. As a result, downscaling would not lead to a very significant reduction of schedule. We anticipate that a 60-m telescope designed and built on the principles underlying OWL would see first light about one year earlier than the current design.

2.14 Risk areas

Any project has associated risks, and one as complex as OWL will need appropriate risk management. A Risk Review is planned early after the start of Phase B.

This section describes the risks identified in the course of the conceptual design, and indicates plausible mitigating actions. We separate the risks areas in two main categories: environmental risks, e.g. natural phenomena that may affect the safety of the observatory or atmospheric

[30] At least a few hundred units.

effects on science performance, and system risks, e.g. critical technological developments or manufacturing difficulties.

We describe the processes and the underlying philosophy of risk management that ESO has in place for its projects, as applicable to the OWL design and development.

100

2.14.1 Environmental risks

OWL has to be able to cope with a variety of environmental conditions, from atmospheric effects on the structure or on the optical quality that affect observations, to extreme natural phenomena like earthquakes or storms that may jeopardize its integrity.

The conceptual design presented here addresses most of these risks by setting level one requirements that account for them and by exploring design solutions that allow mitigating or minimizing them.

Table 2-11 summarizes some of the most important environmental risks, and possible mitigating solutions and/or areas where further development is needed. It should be noted that not all the possible solutions have been studied (dedicated studies are planned in Phase B). Of those already considered, not all have been analyzed with the same level of detail as some can only be addressed properly after the design iteration at the beginning of Phase B and/or once a site has been selected. However, awareness of the risks and their possible consequences will be a driving input in the site selection.

Problem	**Effect**	**Possible solution(s) (non mutually exclusive)**
Wind buffeting	Tracking errors, phasing errors	• High mechanical stiffness • Control loops optimized for perturbation rejection • Lightweight segments • Accelerometer feed forward/feedback • Embedded wind screen / mesh • Lower the altitude axis of 12.8 m. To be crosschecked with thermal turbulence compatibility. • Prevailing direction wind screen • Site selection criterion (low ground wind speed required for adaptive optics as well)
Differential refraction	Position of stars in “large” field of view varies differentially as zenithal distance changes (up to > 2 mas/hour at 1 arc minute distance)	• Observe at $\pm$ 1 hour from meridian • Post processing (requires background limited short exposures ~ 0.1 PSF/rate and extremely low RON in optical) • Smaller field of view at wavelengths shorter than I-band (< 2 arc minute) • Variable curvature cylindrical optics
Atmospheric turbulence	Seeing, scintillation	Adaptive optics. Requires: • Good site (long $\tau 0$ i.e. low ground and jet stream wind speeds) • High order correction (> 10,000 dof) • Very fast computers • Gradual approach (IR SCAO first) • R&D on large deformable mirrors
Atmospheric dispersion	Source light dispersed by atmosphere	• Atmospheric dispersion compensator • Needs to correct to ~ 0.2 pix • More than one glass (?) • Active dispersion correction • At instrument/sensor level

Problem	Effect	Possible solution(s) (non mutually exclusive)
		• Partial correction to use atmosphere as dispersive element in an instrument (?)
Earthquake	Potentially devastating	• Structural stiffness, damping, higher steel grade. • Composite materials for highly seismic site. • Telescope low mass • Smooth transmission of loads. • Foundation tailored to ground geo-mechanical characteristics. • Site selection criteria (low level of earthquake, stiff local soil conditions) • Self deploying safety devices (e.g. mirror clamps, airbags etc) • Kinetic energy absorbers • Energy absorption on the x-y plane due to azimuth wheel and track friction. • Energy absorption on the z direction using the bogies hydraulic whiffle tree needle valve. • Hierarchical acceptable damage strategy (human safety paramount)
Exceptional precipitations, snow, ice, storms, fire	Potentially devastating	• Design requirements, safety margins • Redundant, self-powered “closing” mechanisms • Early warning (off-site real time monitors) • Shelters (human safety), evacuation procedures • Fire fighting facilities / equipment • Lightening strikes protection facilities and embedded in the concept (Faraday cage) • Site selection
Pollution, contrails, dust, light contamination	Decrease of performance, downtime, possible reliability issues (dust contamination of electromechanical assemblies)	• Slight overpressure in enclosure (dust) • Increase preventive maintenance (dust) • Dust deposition rejecting concept of the telescope structure. • Telescope tracks protection and cleaning system. • Local dust and thermal protection of critical subsystems and components (Optics, electronics, etc.) • Site selection • Several opportunities for baffling (stray light)

Table 2-11. Summary of environmental risks (a few comments still to be incorporated).

2.14.2 System risks

The main system risks are listed in Table 2-12. The risk management methodology is outlined in section 2.14.3. In the following we address each of them very briefly.

	Area	Risk	
1.	**System size & complexity**		
1.1.	Design, AIV	Traceability, project processes, number of interfaces	Performance Cost Schedule
1.2.	Maintenance	Permanent and intensive maintenance	Cost Performance
2.	**Adaptive optics**		
2.1.	Adaptive mirror unit		
2.1.1.	Number of degrees of freedom	Complexity, reliability	Performance Cost Schedule
2.1.2.	Mirror shell	Production, interface glass/actuator	Performance Cost Schedule
2.1.3.	Safety	Handling, mirror integrity	Performance
2.1.4.	Field stabilization	Failure to meet accuracy / dynamic range requirements	Performance
2.1.5.	Vibrations	Failure to meet image quality requirements	Performance
2.2.	Real-Time computer	Number of degrees of freedom	Performance
2.3.	Detector, wavefront sensor	Readout noise, frequency, size	Performance
2.4.	MCAO	Not yet proven on-sky	Performance
2.5.	XAO	Requires new corrector technology (MOEMs)	Performance, Cost
3.	**Laser Guide Stars**		
3.1.	Laser	Laser technology, reliability	Performance Cost
3.2.	Wavefront sensing	Aberrated reference, enormous defocus	Performance
4.	**Phasing**		
4.1.	Calibrations	2 mirrors to phase (on-sky calibration)	Performance Cost
4.2.	On-sky metrology	Accuracy, capture range	Performance
4.3.	Reliability	Number of actuators, sensors	Performance
5.	**Wind (open air)**		
5.1.	Tracking	Image quality, downtime	Performance
5.2.	Mirrors deflections	Image quality, downtime	Performance
6.	**Integrated wavefront control**		
6.1.	Complexity	Nesting / overlap / cross-talk; reliability	Performance
7.	**Optical fabrication**		
7.1.	Segments	Production	Cost, schedule
7.2.	Segments	Edge misfigure (turned-down edges)	Performance

	Area	Risk	
	7.3. Aspheric mirrors	M4 figuring and testing.	Cost Schedule Performance Cost
8.	**Telescope structure & kinematics**		
	8.1. Construction	Production, integration	Schedule
	8.2. Kinematics	Friction	Performance
	8.3. Open air integration	Must withstand environmental conditions during integration	Cost Schedule
9.	**Enclosure, infrastructure**	Enclosure size, wind load	Cost

Table 2-12. System risks

1. System size and complexity

1.1. Design, AIV

The overall system complexity and the implied number of interfaces call for strong System Engineering, configuration and interfaces management. Although the number of degrees of freedom is substantially larger with OWL than with VLTI, the overall number of possible configurations is somewhat lower and the overall number of independent functions comparable.

1.2. Integration, maintenance

Integration and maintenance processes need some form of “Industrialization”. Process flow studies by expert consultant are foreseen in the design phase. De-localisation, off-line maintenance and outsourcing will be studied in the design phase.

High standardization and the availability of spares as a maintenance buffer (e.g. segments assemblies) are favourable factors.

System robustness / partial or progressive loss of performance associated to maintenance failure is a design criterion. Multiple maintenance lines allowing parallel processing of individual assemblies vs. single line processing several assemblies in a single run will be evaluated in the design phase.

2. Adaptive Optics

2.1. Adaptive mirror units

Concept design studies and analysis are currently being contracted out (2 competitive studies) to industry. A complete re-assessment of risks shall be undertaken in the design phase.

2.1.1. Number of degrees of freedom

Reliability will depend on actuator technology and may have significant cost impact. The performance impact of single actuator failure should be marginal -in particular with force actuators (LBT technology). Prototyping and extensive testing is foreseen in the design phase. Adaptive mirror units shall make maximum possible use of Line-Replaceable Units (electronics, actuators) and allow rapid replacement in case of failure. Extensive diagnostics shall be incorporated in the design of the units.

2.1.2. Mirror shell

According to suppliers, the production of a thin (~1mm) two metre-class shell suitable for M6 does not seem to be a major challenge. The flat shape of the mirror is an essential factor and may allow cost-effective production. Samples of low-cost LCD screen and Borofloat® sheets have been tested for optical quality and the results are very encouraging. Such sheets are available up to 2.3-m

width at a cost of about € 1,000.- a piece. Several thicknesses, starting with 0.7-mm are available in standard production. According to the first test results (20 × 20 cm² samples), only minor post-polishing would be required –if any.

The same does not apply to the M5 unit (3.4 to 3.9-m, depending on allowable vignetting on the wavefront sensors). Longer development time is allocated to this unit.

Interface to actuators and lateral support systems are areas of concern. Prototyping and extensive qualification of the interfaces is foreseen in the design phase.

Temporary, non-adaptive M5 and M6 subunits are included in the plan to allow for engineering runs prior to the integration of the first adaptive subunit (M6). Single conjugate, ground layer and extreme AO do not depend on the availability of the adaptive M5.

2.1.3. Safety

Handling equipment and procedures shall be defined in the design phase. It should be noted that handling of thousands of large glass shells is routine operation in the glass industry.

2.1.4. Field stabilization

The large pupil compression factor on M6 (~1:40) implies large (1:20) angular magnification between on-sky and mirror angles (i.e. 1 arc second on-sky corresponds to ~20 arc seconds mirror tilt). This most probably will require a two-stage tip-tilt compensation, the fine stage being provided by the adaptive shell itself.

2.1.5. Vibrations

Active vibration damping will be evaluated in the design phase. Maximum reaction forces at interfaces are included in the specifications for the conceptual design studies.

2.2. Real-time computer

The number of degrees of freedom and the bandwidth of the control system imply demanding requirements. According to our analysis, however, the requirements for OWL first generation adaptive optics could be met with already existing technology (see section 8.2.1.2.4).

2.3. Detectors, wavefront sensors

Extensive detector development is foreseen in the design phase. According to our analysis, the requirements for OWL first generation adaptive optics could be met with already existing technology (see section 8.2.1.2).

2.4. MCAO

MCAO is not yet fully proven on-sky. Recently the Multi-conjugate Adaptive optics Demonstrator (MAD) had MCAO first light in laboratory. On-sky results are expected by 2006.

2.5. XAO

Extreme Adaptive Optics most probably implies an entirely different mirror technology, MOEMs being the most likely one. The availability of first stage, large amplitude correction with M6 is a positive factor as it relaxes amplitude requirements on the high order corrector. Provisions have been made for substantial R&D well into the construction phase.

3. Laser guide stars

In the current plans, Laser Guide Stars AO is foreseen as third generation adaptive optics so as to allow for maximum development time. This is not an irreversible decision and the

implementation would be accelerated if allowed by the progress of concepts and related technologies.

3.1. Laser technology, reliability

With the VLT Laser Guide Star Facility ESO and its partners are gaining experience in the laser technologies. With a number of new generation of Sodium LGS systems entering into operation worldwide, we expect significant development in this area (see also section 8.4.6).

3.2. Wavefront sensing

Spot elongation, defocus and aberrated LGS conjugation may lead to prohibitively complex implementation and limited performance. Complex and active relay optics may be required (see RD1). There are, however, hopeful developments towards entirely different ways to do wavefront sensing on Laser Guide Stars (see section 8.4.4).

4. Phasing

4.1. Double segmentation

The need to calibrate both primary and secondary mirrors metrologies (position sensors) independently is an added complexity. Current efforts in filtering techniques and pattern recognition to disentangle the primary and secondary mirrors phasing errors are giving encouraging results.

It should be noted that one focal station (No 6) is reserved for a permanently mounted technical instrument, with ample design space for on-sky metrology systems.

As a backup, M2 position sensors specifications could be tightened (higher stability) to allow in-situ recalibration with an independent metrology[31] at a manageable time interval. A major cost increase of the position sensors for the secondary mirror would not have a strong impact on the overall project costs[32].

4.2. On-sky metrology (calibrations)

According to Chanan [6], the Keck on-sky calibration technique can be implemented up to ~4,000 segments. Alternatives are under development, all successfully tested in the laboratory, and a pyramid wavefront sensor has recently been tested on-sky (on WHT with segmented AO mirror).

The Active Phasing Experiment (APE) will allow a rigorous comparison of performance of at least three techniques. Further experiments are foreseen on GTC.

4.3. Reliability

With about twice as many sensors as strictly required, the system is over-determined. The performance impact of phasing failures (a few segments) has been analyzed and found to be negligible (see RD21). Local vs. global control and error propagation shall be evaluated in the design phase.

5. Wind (open air)

Substantial effort is being invested in simulations, wind tunnel testing, and measurements on Jodrell Bank radio telescope. This effort will be pursued in the design phase and in the ELT Design Study, in particular with the Wind Evaluation Breadboard (see appendix A-1.2).

5.1. Tracking

[31] One option would be to fit dual wavelength interferometers (such as that used in APE, see appendix A-1.2) in the M2 covers to allow daytime calibration. Assuming that position sensors would meet drift specifications over 20 days, 12 segments (2 per interferometer) would have to be re-calibrated every day. The estimated cost of this additional equipment is about M€ 3.6, including translation mechanisms inside the M2 covers.

[32] A factor 10 increase compared to the sensors of the primary mirror would lead to a total cost overshoot of about 12 M€.

According to first analysis (see section 7.2.1) wind rejection would not be a major issue. The relatively stiff structure and the insensitivity of the optical design to lateral decentres are favourable factors.

5.2. Mirror deflections

According to first analysis (see section 7.5.5), high spatial and temporal frequency intersegment motion under wind excitation can be controlled to negligible amplitudes.

Preliminary simulations show that residual phasing errors can be significantly reduced by adaptive optics (see section 8.3.2.4).

There is, in addition, room for improvement in the design: local stiffness (segments supports), feed forward on the basis of accelerometers signal. Silicon Carbide would be an advantage (bandwidth of the control system).

Wind screens embedded into the azimuth structure would protect M1 until z~30 degrees. Studies of this option have been cautiously included in the plans.

Finally, it should be noted that sites with low ground wind speed will be favoured for adaptive optics as well.

6. Integrated wavefront control

Integrating all wavefront control loops into transparent and reliable operation is perhaps the most serious challenge for any Extremely Large Telescope. Extensive integrated modelling is foreseen in the design phase. Defining, evaluating and optimizing control schemes in representative conditions is one of the major objectives of the Active Phasing Experiment (see appendix A-1.2).

7. Optical fabrication

7.1. Segments production

The cost and schedule risk for the segments production is critical but probability of occurrence is deemed moderate to low by expert manufacturers (see RD6 to RD12). The spherical shape of the segments is a major advantage.

Cost estimates by different optical manufacturers (polishing) are in very good agreement. Cost estimates for the substrates are rather disparate, owing to the very different underlying technologies (silicon carbide or conventional glass-ceramic).

According to current plans there is a 14 month buffer time between the delivery of the first segments and the start of their integration into the telescope. This buffer could be extended at the cost of a smaller equivalent diameter at first light.

7.2. Edge misfigure

Edge misfigure might lead to significant loss of performance, in particular for high contrast imaging.

Controlling edge misfigure to tight specifications (spatial extension, amplitude) could be a major difficulty, with significant cost and/or schedule impacts. The technique used for GTC segments was to mount wasters on the segments edges. This allowed the segments to be polished to tight specifications up to their edges.

According to suppliers the spherical shape of OWL segments is a favourable factor in that it allows using mostly large, stiff polishing tools. Tests will be made in the framework of the ELT Design Study to polish silicon carbide with minimal edge misfigure and without wasters.

Coronagraphic techniques (see RD22) may alleviate the problem and allow for tolerance relaxation.

7.3. Aspheric mirrors

Figuring and above all testing of the most aspheric mirror (M4) is a major challenge. Owing to the angular magnification (~6) between sky angle and mirror slope the specifications for surface slope errors can be significantly relaxed compared to the VLT

[9]. In addition, a substantial fraction (40%) of the VLT primary mirror active force range was used for the conversion between Nasmyth and Cassegrain. This allocation could be transferred to the correction of residual figuring errors.

It should be noted that the equivalent mirror in the SALT corrector has a similar slope deviation[33] from best fitting sphere. We are not aware that this led to particular difficulties.

The highest risk is with M4 test set-up. A setup has been identified but implementation is extremely challenging (see section 6.5.2). This set-up relies on large (~1.6-m for the largest) spherical, glassy Zerodur lenses. Using computer-generated holograms combined with lenses should alleviate the difficulty to some extent.

In order to account for lengthy test procedures in the final stages of polishing, the time allocation for the polishing of M4 is about 2.4 times longer than the time it took to figure the last VLT primary mirror.

8. Telescope structure & kinematics

8.1. Construction

The telescope structure & kinematics being on the sub-critical path, delays would likely affect the schedule to first light.

The modular design and very high standardization are favourable in allowing parallel supply lines.

According to plans final design would start at the earliest possible date following site selection.

8.2. Kinematics

OWL kinematics cannot realistically rely on classical hydraulic pads / tracks solutions, with their exacting dimensional tolerances. According to our analysis (see section 9.4.5.1.3) friction can be compensated to acceptable levels. Measurements and tests will be performed in the framework of the ELT Design Study (breadboard friction drive, see appendix A-1.4). Magnetic levitation is also to be studied in the same context.

8.3. Open air integration

According to current plans the telescope structure and kinematics (without corrector) would be exposed to natural environment during erection. This may have cost and schedule impacts, depending on the site meteorological conditions. A complete evaluation is foreseen in the design phase.

9. Enclosure

Wind drag is a potential issue. With relatively conventional solutions (sliding enclosure) this leads to a total cost higher than initially anticipated.

The total cost estimate presented in this document takes this issue into account.

Alternative enclosure concepts and technologies (see RD40) may allow major cost reduction.

The enclosure is close to sub critical path; according to plans final design would start at the earliest possible date following site selection.

2.14.3 Risk management

The purpose of this section is to outline the methodology ESO intends to use to guarantee sound planning as part of the execution of the OWL project, in order to anticipate potential obstacles to timely and cost-effective performance, and that processes are in place to mitigate and/or minimise the risks. The OWL project plan is detailed in the Integrated Master Schedule.

[33] which, as far as polishing difficulty is concerned, is more indicative than aspheric departure.

The first element of this process will be to conduct a Risk Review soon after starting Phase B. This Review will focus on risk identification and on improving the following:

- Concise Risk Descriptions. Descriptions must contain Cause and Effect definitions. Named Risk Owners must clearly define the Probability of occurrence and the Impact if the risk should materialise against the prescribed 3 impact areas of Quality, Cost and Schedule.

- Risk Mitigations Actions. Individual Risk Mitigations must be targeted at specific risk impacts (for example, to add more resources to an activity is aimed at reducing schedule impact. The aim of the mitigations must be clear and must be prepared by the risk owner.
- Risk Contingency Plans. These define alternatives only to be taken if a risk occurs or a mitigation plan has failed to have the intended effect.

Following this review the OWL project office will carry out quarterly programme reviews with all the parties involved to share and discuss the top risks. A 'snapshot' of the current risk status will always be available in the Project Risk Register.

Risk Management is Project Management *in action* and generally fosters effective communication between the key areas of the project. To establish and effectively implement mitigation or contingency plans, each action must be: specific, measurable, achievable, realistic and time bound.

The risk impact will be determined using the criteria listed in Table 2-13.

Cost	Quality	Schedule	Impact / Value SEVERITY
Cost increase to OWL Project > XX MEuro	Failure to deliver a major product to an acceptable standard	Delay of > 6 months of a Top Event from the IMS	CRITICAL
Cost increase to OWL Project between CC and XX MEuro	Failure to meet key criteria against OWL specification and no work around currently identified	Delay of 2 – 6 months of a Top Event or 4 – 6 months of a major event from the IMS	HIGH
Cost increase to OWL Project between BB and CC MEuro	Failure to meet key criteria against OWL specification but work around identified	Delay of 0 – 2 months of a Top Event or 2 – 4 months of a major event from the IMS	MEDIUM
Cost increase to OWL Project between AA and BB MEuro	Failure to a criteria against OWL specification that does not significantly affect overall performance	Delay of 0 – 2 months of a major event from the IMS	LOW

Table 2-13. Areas of Risk Impact.

Probability of occurrence of the Risk will be categorised into 1 of 4 criteria:

- Very High. Risk will materialise almost certainly.
- High. Risk would not materialise under optimistic assumptions only.
- Medium. Risk may or may not materialise under normal circumstances. No clear evidence found to support either possibility.
- Low. Risk would materialise under pessimistic assumptions only.

A combination of the Risk Severity and Risk Probability provides a ranking of risks that the Management Team can then address with appropriate attention.

3. Science case

3.1 Introduction

When the development of the OWL concept started in 1997, its size was set to the rather overwhelming 100-m diameter in order to be able to reach three main science goals: the spectroscopy of faint (though not the faintest) galaxies to be discovered by the then 8-m diameter NGST; the observation of solar type stars in the Virgo cluster of galaxies; and the detection of earth-like planets around other stars. These science cases were supported by qualitative and quantitative arguments and by simulations [117], and provided a first set of requirements on which the concept design work could be based. Although sufficient as a starting point, these preliminary science cases were however developed in a crude, even naïve, way. In particular, they accounted only approximately for instrumental effects.

In March 2000 the OPTICON network was formed under the aegis of the European Commission Framework Program FP5, and is now continuing into FP6. One of its core activities is to produce a science case for a European ELT of diameter from 50 to 100m. The OWL efforts in this direction merged in a natural way in the new activity (in fact, ESO was leading the science case working group during FP5). Since then and with large participation of the astronomical community (more than 100 astronomers are involved) a series of science cases have been developed to an ever-increasing level of detail and depth. These results have just been published by OPTICON (see RD526), which represents the basic reference for this chapter. For simplicity we will refer to it as the "*Science Book*". It is part of the documentation sent to reviewers.

In this chapter, after a brief overview of the capabilities of OWL, we summarize the results of the science book and derive from them a set of scientific requirements for the telescope and instruments that in turn will form the basis of the top-level requirements for OWL. It should however be stressed that the science case and the conceptual design have been developed in parallel so that not only some cross talk has taken place but also the process of setting the design requirements has not followed the straightforward path described here.

Readers interested in a more in depth discussion of the science case are referred to the *Science Book*. Science cases that are the drivers for the instrument conceptual studies are described in chapter 12. They expand and complement the science cases developed in the *Science Book*.

3.2 Science with OWL

The science case for Extremely Large Telescopes (ELTs) covers a vast range of topics from our own solar system to the furthest observable objects at the edge of the visible Universe. Table 4.1 gives an overview of the main science cases presented in the *Science Book*. They include the quest for terrestrial planets (including possibly the detection of exo-biospheres) in extra-solar systems; the study of stellar populations in a large sample of the Universe (including in elliptical galaxies, missing today – sometimes referred to as the "Virgo or bust!" science case); the still mysterious relation between matter, dark matter and dark energy (with their link to particle physics); the star formation history of the Universe and the evolution of the Cosmos from big bang to today; the first objects and the epoch of re-ionization (including primordial stars and their role); the *direct* measurement of the expansion rate of the Universe (with no assumptions, no extrapolations, no models).

Are there terrestrial planets orbiting other stars?	Direct detection of earth-like planets in nearby extra-solar systems and a first search for bio-markers (e.g. water and oxygen) may become feasible.
How typical is our Solar System? What are the planetary environments around other stars?	Direct detection of proto-planetary disks will become possible around many nearby very young stars. In mature planetary systems, detailed spectroscopic analysis of Jupiter-like planets, determining their composition and atmospheres, will be feasible. Study of the planets and small bodies in our Solar System will complement space missions.
When did galaxies form their stars?	When and where did the stars now in galaxies form? Precision studies of individual stars determine ages and the distribution of the chemical elements, keys to understanding galaxy assembly and evolution. Extension of such analyses to a representative section of the Universe is the next challenge in understanding the visible Universe.
How many super-massive black holes exist?	Do all galaxies host central monsters? When and how did super-massive black holes form and evolve in the nuclei of galaxies? Extreme resolution and sensitivity is needed to extend these studies to normal and low-mass galaxies in order to address these key puzzles.
When and where did the stars and the chemical elements form?	Can we meet the grand challenge to trace star formation back to the very first star ever formed? By finding and analyzing distant galaxies, gas clouds, and supernovae, the history of star formation and of the creation of the chemical elements can be fully quantified.
What were the first objects?	Were stars the first objects to form? Were these first stars the source of the ultraviolet photons which re-ionized the Universe some 200 million years after the Big Bang, and made it transparent? These objects may be visible through their supernovae/hypernovae or their surrounding ionization zones.
How many types of matter exist? What is dark matter? Where is it?	Most matter does not emit any electromagnetic radiation and can be identifed only through its gravitational pull on surrounding visible objects. By mapping the detailed growth and kinematics of galaxies out to high redshifts, we can observe dark-matter structures in the process of formation.
What is dark energy? Does it evolve? How many types are there?	Direct mapping of space-time topology, using the most distant possible tracers, is the key to defining the dominant form of energy in the Universe. This is arguably the biggest single question facing not only astrophysics but also fundamental physics as a whole.
Extending the age of discovery	In the last decades astronomy has revolutionized our knowledge of the Universe and established it as the ultimate physics laboratory. The next big steps are likely to be discoveries of unimagined new physical processes.

Table 3-1. Primary science cases

Three cases have been identified in the *Science Book* as highlight science cases both because they have generated high levels of enthusiasm and discussion, and since they are seen as some of the most exciting prospects for ELTs since they push the limits of what can be achieved (and will provide some of the more challenging technical specifications for the telescope). These are i) terrestrial exoplanets, ii) resolved stellar populations in a representative section of the Universe, and iii) first lights and the re-ionization history of the Universe. These set the collecting power requirement at a minimum of 60m for iii)[34], and to 100m for i) and ii). The *Science Book* analyzes to what extent different telescope sizes affect specific science cases. More discussion on tradeoffs between scientific capabilities and telescope size can be found in 2.13.1.

3.2.1 OWL performance

Before summarizing the highlight science cases that determine the requirements of the telescope and instruments there are some general aspects of the scientific performance of OWL that deserve some comments.

3.2.1.1 Confusion about confusion

There is some concern that ELTs may hit the confusion limit, thereby voiding their very *raison d'être.* Much of this concern comes from past observations at poor angular resolution (e.g. X-ray data or deep optical images taken with 2" seeing in the '80s). Recent results with much better spatial resolution lead to resolving the "confusion" into individual objects (e.g. the X-ray background, now mostly if not completely resolved, or the HDF images showing 20 times more empty space than astronomical objects). Ultimately, some confusion level may be reached (e.g. using imagers not working at the full diffraction limit) but the 3-dimensional nature of astronomical objects (position and velocity) virtually ensures it will not be a limiting factor with OWL. In fact, a lack of confusion may offer information on the covering factor of galaxies, and seems tantalizingly connected to Olbers' paradox.

3.2.1.2 Étendue, or the AΩ product

The AΩ product is often used to compare the capabilities of telescopes of different sizes. This is very dangerous, as it may lead to surprising (and wrong) conclusions. For example, nobody would claim from $A\Omega_{\text{human eye}} \approx A\Omega_{\text{FORS@VLT}} \approx A\Omega_{30\text{"@OWL}}$ that these three "telescopes" are interchangeable in performance. Instead, it would be perfectly correct to deduce from $A\Omega_{\text{LSST}} \approx 120\ A\Omega_{\text{VIMOS@VLT}}$ that the 8-m LSST will offer a much better wide field capability than the VLT. The point is that when comparing telescopes of different sizes one cannot leave sensitivity out, and therefore AΩ-based comparisons make sense only for telescopes of similar size. A much better estimator of relative performance is the time needed to achieve a given scientific goal.

3.2.1.3 Signal-to-noise vs diameter D

A too common misapprehension regards the dependence on D of signal *S* and signal-to-noise

$$S/N = S / \sqrt{(S + Bgd \times n_{pix}\,\Omega_{pix} + n_{pix} \times RN^2)} \qquad \textit{Eq. 3-1,}$$

where *Bgd* is the background flux per unit surface, Ω_{pix} is the pixel angular area, n_{pix} the number of pixels involved, and RN the readout noise. Too often one finds an $S \propto D^4$ assumption when the telescope works at the diffraction limit which is (alas!) not true: while the *peak* of the PSF indeed scales as D^4, its *integral* within a typical λ/D pixel increases as D^2 only. This means that the S/N is proportional to D^2 in the background-limited regime ($S \propto D^2$, $Bgd \propto D^2$, $\Omega_{pix} \propto D^{-2}$, $S/N \propto D^2/\sqrt{\text{const}}$), and to D in the shot noise regime ($S/N \propto D^2/\sqrt{D^2}$).

The time to achieve the same S/N for telescopes of different size is proportional to $(S/N)^2$ and is a better estimator of the relative performance of different telescope diameters (see Figure 3-1; this of course makes sense only when comparing a given science case). The relative merits of

[34] possibly also i) if terrestrial exoplanets are very common

different telescopes are therefore a function not only of diameter but also of particular science cases.

For example, in the exo-earths science case (see below), which is in the background-limited regime for any realistic scenario (unless AO delivers almost exactly 100% Strehl, the 10^{10} contrast between star and planet makes any residual from the AO correction much brighter than the planet), a 30m telescope would need ~ 120 times longer exposures than a 100m to observe star/planet systems that both can resolve.

3.2.1.4 The power of a 100m telescope

Current Adaptive Optics systems on 8-m class telescopes have recently demonstrated performance close to the theoretical diffraction limit. Figure 3-2 shows the diffraction limits for 8m, 30m and 100m telescopes compared to the typical sizes of astronomical objects. While 8m telescopes can resolve large regions within galaxies (between 300 and 1000pc in size) at redshifts around unity, Extremely Large telescopes can, given appropriate adaptive optics capability, resolve structures of a few tens of parsecs in size, the approximate size of a major star-forming region, at similar redshifts.

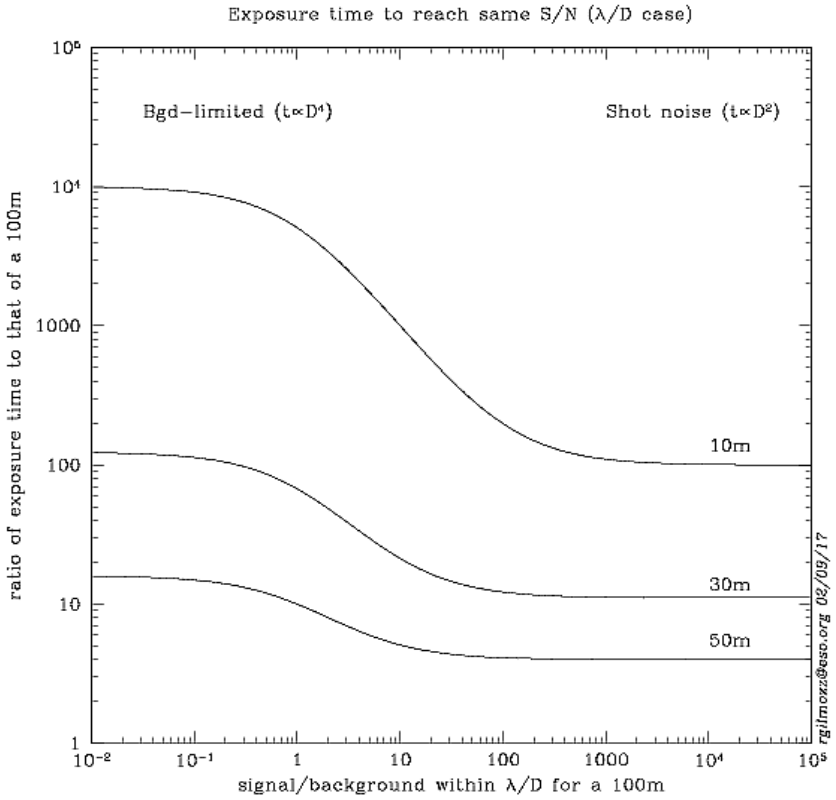

Figure 3-1. Time needed to achieve the same S/N on diffraction-limited telescopes as a ratio to the time needed on a 100m, i.e. t/t100 (note the background limited, t/t100 ∝ D4, and shot noise limited, t/t100 ∝ D2, regimes).

A smaller diffraction limit combined with increased light-collecting aperture translates into great gains in sensitivity as telescope diameter is increased, particularly for unresolved point sources. For example a 100m telescope with perfect diffraction-limited images would reach about 8 magnitudes fainter for point sources than an 8m telescope that delivers 0.5 arcsec images, for the same signal-to-noise and exposure time (in the near IR). In this simple scaling argument, we have assumed perfect diffraction-limited images (Strehl = 1). Even with a moderate Adaptive Optics (AO) correction that results in the majority of the light falling inside a 0.1 arcsec aperture, a 100m telescope would give a gain of 4.5 magnitudes for point sources compared to an 8m telescope producing 0.5 arcsec images, a factor of 60 in intensity (Table 3-2).

8m	30m	100m	Comments
0.0	1.4	2.7	Seeing limited
1.0	2.4	3.7	e.g. Ground-layer AO
1.7	3.2	4.5	
0.6	3.5	6.1	e.g. Multi-conjugate AO
2.4	5.2	7.8	Theoretical limit

Table 3-2. (From Science Book) Gains in magnitude for the same signal-to-noise and exposure time when observing unresolved sources in the background-limited regime. The gains are shown relative to an 8m telescope delivering 0.5" images.

Table 3-3 shows the comparison between ELTs of various sizes and JWST, showing that in the near infrared ground based astronomy is very competitive, and highlighting the potential for synergy between space and ground (very similar to today's complementarity between HST and the 8-10m class telescopes). In the case of extended objects the comparison is more difficult to quantify as it depends on the science case and on several parameters like the field of view and frequency on sky of the objects of interest (e.g. for z ~ 7 galaxies OWL would have a sensitivity advantage of a factor ~ 40 which would be partly offset by JWST's larger field of view of 10 x 10 arcmin; a large multiplex would strengthen OWL's advantage).

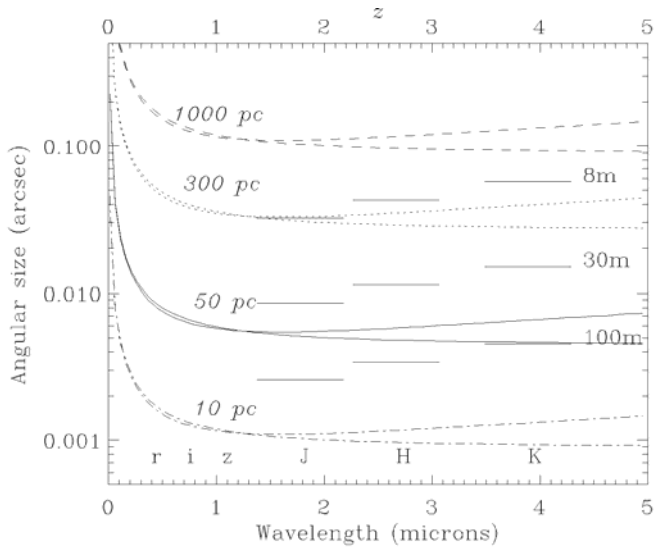

Figure 3-2. (From Science Book) The theoretical diffraction limits (λ/D) for 8m, 30m and 100m telescopes are plotted at three wavelength values corresponding approximately to the J, H and K infrared bands (horizontal bars). Also plotted are curves of projected angular size as a function of redshift for objects of various physical sizes (10pc, 50pc, 300pc and 1kpc) for two sets of cosmological parameters: (ΩM,ΩΛ)=(0,0) and (0.3,0.7) for the lower and upper curves respectively.

Table 3-4 provides the resolution and 3-σ limiting magnitude in the optical near infrared for various telescope sizes, in the simplified assumption that the performance is the same at all wavelengths for all telescopes. Although clearly highly improbable in certain combination of size and wavelength (it is unlikely that we could achieve high Strehl ratios in the U band with a 100m OWL, for example), the table is useful as a reference as it demonstrates the relative performance of various telescope sizes.

The science cases have made use of an exposure time calculator developed by ESO[35].

[35] http://www.eso.org/observing/etc/bin/gen/form?VIEW.APPLIC.HTM=ins-elt.htm

λ (μm)	Imaging (R=5)				Spectroscopy (R=10,000)			
	20m	30m	50m	100m	20m	30m	50m	100m
1.25	2.1	3.6	10.2	34.8	5.8	9.1	15.8	30.6
1.6	1.2	2.3	6.2	22.7	5.8	9.1	15.8	30.4
2.2	0.92	2.1	4.0	6.1	4.5	7.4	13.2	25.8
3.5	**0.036**	**0.080**	**0.221**	0.86	0.50	1.1	2.9	10.9
4.9	**0.005**	**0.020**	**0.054**	**0.20**	**0.042**	**0.095**	**0.27**	1.00
12	**0.012**	**0.030**	**0.079**	**0.30**	**0.088**	**0.200**	0.54	2.15
20	**0.004**	**0.031**	**0.088**	**0.33**	**0.045**	**0.107**	**0.30**	1.15
25	**0.004**	**0.031**	**0.088**	**0.33**	**0.039**	**0.088**	**0.24**	0.92

Table 3-3. (from [118]) IR performance of several ELTs compared to that of the JWST space telescope, in terms of the point source sensitivity ratio ELT/JWST. In the near-infrared an ELT outperforms a 6.5m cold (~30K) space telescope such as JWST (bold font shows ratio > 0.5).

3.2.1.5 The wavelength range

A large fraction of the ELT science cases lies in the near infrared domain. For the cosmology case, this is obviously a consequence of the expansion of the Universe (Figure 3-2): with increasing light gathering and spatial resolution with diameter, a 30-m telescope may actually tackle best the cosmology cases in the [Z-J] region, a 50-m in [J-H] and a 100-m in [H-K_s]. For the exo-earths science case, the H-band offers a more favorable luminosity contrast between the parent star and the putative planet than shorter wavelengths; also the challenge to attain a high Strehl ratio, while already tough in H, is certainly much more accessible than in the optical domain. A strong push towards visible wavelengths (*I* and *R* bands), with at minimum moderate adaptive optics correction, comes however from exo-earths spectroscopy and from the Virgo stellar population science driver. A special case is that of the Codex experiment to measure directly the cosmic expansion rate as a function of redshift that works only in the visible and would benefit from (some level of) AO correction but would still be feasible in the seeing limited regime.

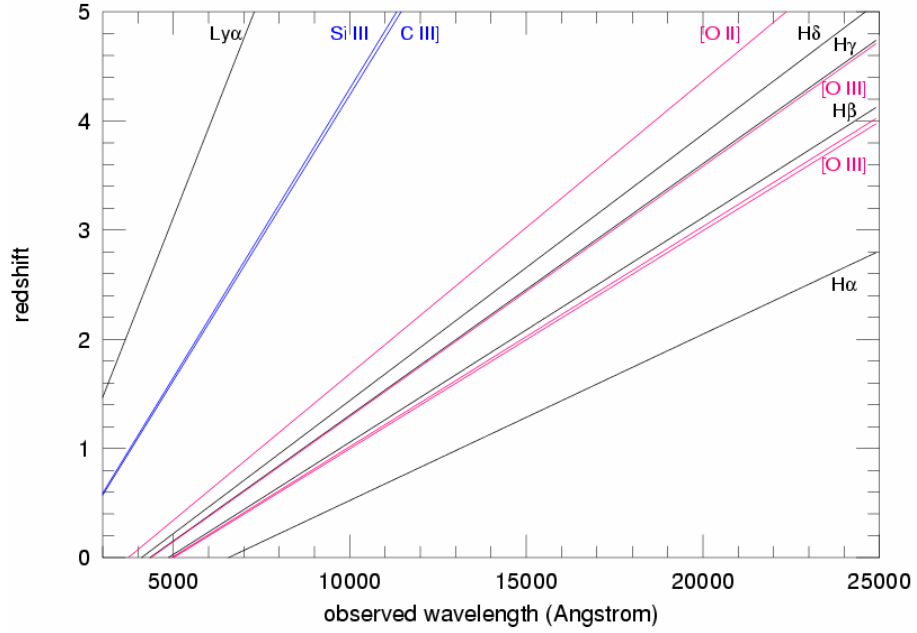

Figure 3-3. Observability of major emission lines with redshift.

Tel	U		B		V		R		I		J		H		K	
[m]	Res	mag	Res	mag	Res	mag	Res	mag	Res	mag	Res	mag	Res	mag	Res	mag
10	9.1	32.3	11.1	33.1	13.8	32.1	17.6	31.7	22.1	30.6	31.8	28.3	41.8	26.6	54.9	25.3
20	4.5	33.8	5.5	34.6	6.9	33.6	8.8	33.2	11.1	32.1	15.9	29.8	20.9	28.1	27.4	26.8
30	3.0	34.7	3.7	35.5	4.6	34.4	5.9	34.0	7.4	33.0	10.6	30.7	13.9	29.0	18.3	27.7
40	2.3	35.3	2.8	36.1	3.5	35.1	4.4	34.7	5.5	33.6	8.0	31.3	10.4	29.6	13.7	28.3
50	1.8	35.8	2.2	36.6	2.8	35.6	3.5	35.2	4.4	34.1	6.4	31.8	8.4	30.1	11.0	28.8
60	1.5	36.2	1.8	37.0	2.3	35.9	2.9	35.6	3.7	34.5	5.3	32.2	7.0	30.5	9.1	29.2
70	1.3	36.5	1.6	37.4	2.0	36.3	2.5	35.9	3.2	34.8	4.5	32.5	6.0	30.8	7.8	29.6
80	1.1	36.8	1.4	37.7	1.7	36.6	2.2	36.2	2.8	35.1	4.0	32.8	5.2	31.1	6.9	29.9
90	1.0	37.1	1.2	37.9	1.5	36.8	2.0	36.4	2.5	35.4	3.5	33.1	4.6	31.4	6.1	30.1
100	0.9	37.3	1.1	38.1	1.4	37.1	1.8	36.7	2.2	35.6	3.2	33.3	4.2	31.6	5.5	30.3

Table 3-4. Diffraction limit (Res, in milliarcsecond) and corresponding limiting magnitudes for various telescope sizes, under identical conditions and assumptions (i.e. same Strehl ratio of 50%, efficiency 30%, sky background from Paranal, no atmospheric extinction). While the absolute values may change with assumptions, the relative ones should not.

Compelling cases have been made for the thermal infrared (see e.g. the science case of the T-OWL instrument in chapter 12), as well as for the sub-mm range where an OWL-like telescope would offer a powerful wide-field searching capability for the ALMA Observatory (Table 3-5).

	SCOWL (100m)		ALMA	
	850μm	450μm	850μm	450μm
Flux sensitivity (mJy/√sec)	0.3	0.6	1.9	11
Dust mass sensitivity (cf SCUBA-2)	70	170	11	9
Resolution (arcsec)	2.1	1.1	0.02	0.01
Confusion limit (mJy)	0.01	0.005	4e-4	2e-4
Mapping speed (time per square degree to 0.01mJy)	2 days	10 days	7yr	900yr

Table 3-5. Summary of the capabilities of a sub-mm instrument on OWL compared to those of ALMA.

3.2.2 The highlight science cases

The HST, Spitzer and other astronomical satellites, complemented and expanded by the present generation of 8- to 10-m ground based telescopes now in operation, have generated a new view of our universe. The universe is now thought to be dominated by dark matter and vacuum energy, with stars forming as early as 200 Myrs after the Big Bang at a redshift between 10 and 20. Jets, outflows and disks around stars have been shown to be a common by-product of starformation. A large fraction of all stars in today's universe is surrounded by planets, more than 100 or them have been detected.

Astronomy faces many challenges in the investigations of the coming decade: the luminosity contrast between parent star and planets (factor of billions) has so far prevented direct imaging of a planet in all but a single special case. Stellar populations can be studied in detail only in the nearby universe, devoid of the massive and important elliptical galaxies. Alternative theories of galaxy formation cannot be disentangled, as we cannot yet see the far away faint building blocks. Cosmological distances are measured using secondary indicators such as supernovae Ia. The sources of the re-ionization of the universe are too faint to be detected. The existence of super-massive black holes inside high redshift Quasi-Stellar Objects (Quasars) is a challenge to our ideas of how black holes form, and indirectly to our understanding of stellar evolution.

JWST will replace HST within the next decade. However, as it is the case in the current HST/VLT era, powerful ground-based telescopes are necessary for detailed studies of interesting objects. Only an ELT such as OWL will provide the capabilities to achieve the necessary breakthroughs. Of all the science cases listed in the "science book", three are the strongest drivers for the technical requirements of OWL. These "highlight science cases" are summarized below.

3.2.2.1 Terrestrial Planets In Extra-Solar Systems

The recent discovery that a large fraction of all solar-type stars host massive planets has opened a new domain for research. With current large telescopes, it is in principle possible to directly image massive planets in orbit around relatively faint stars. However, the more interesting less massive planets around solar-type stars, which are similar to Earth and might harbour life, are out of the reach of current telescopes. One of the most exciting prospects for OWL is the possibility of not only *directly detecting* (by imaging) earth-like planets orbiting other stars, but also *studying* large numbers of them in detail (via spectroscopy) and even find indicators of life on them.

The habitable zone around a star is the region where water on earth-like planets can exist in its three phase states. Water is a pre-requisite for life as we know it. The detection of terrestrial planets in this zone relies on them being illuminated by their parent star. The reflected light makes such planets bright enough so that OWL could easily detect them if they were well separated from any bright star (see Figure 3-4 for a simulation). The challenge of detecting Earth-like exo-planets is the fact that their projected distances from the parent stars are extremely small, and that the star is about 10 billion times brighter than the planet.

Not all stars have planets and few will have planets in the habitable zone. Therefore, a large number of possible candidate stars has to be surveyed to find a habitable planet, and the closest one is likely to be at a relatively large distance. The number of stars that can be studied is proportional to the spatial resolution to the cube (i.e. to D^3, where D is the telescope diameter). The time to achieve the same signal to noise in the background-dominated regime is proportional to D^4. A 100m telescope can in principle detect an earth-like planet around a solar-type star out to a distance of 100 light years, which means that there are about 500 stars of this type to be observed. By contrast, there are only about 100 candidate stars for a 50m telescope and less than 15 stars for a 30m telescope. Unless the population of earth-like planet is unexpectedly large, it is therefore unlikely that a 30m telescope will be able to detect such a planet. However, a 100m telescope such as OWL will have a much better chance achieving this challenging goal. A key to success is the light gathering that will allow improving the contrast between planet and star through the detection of in situ spectroscopic features.

Once exo-planets have been imaged, spectroscopy can be used to determine properties of their surfaces and atmospheres. The state of the surface (liquid or solid) and the existence of "bio-markers" such as water, oxygen, carbon dioxide and methane atmosphere has the potential to provide first indications of extraterrestrial life. An extremely large telescope is needed to collect sufficient light from a faint planet to be able to analyze it spectroscopically. This science is unique to OWL and cannot be carried out with a 30m telescope (see Figure 3-4).

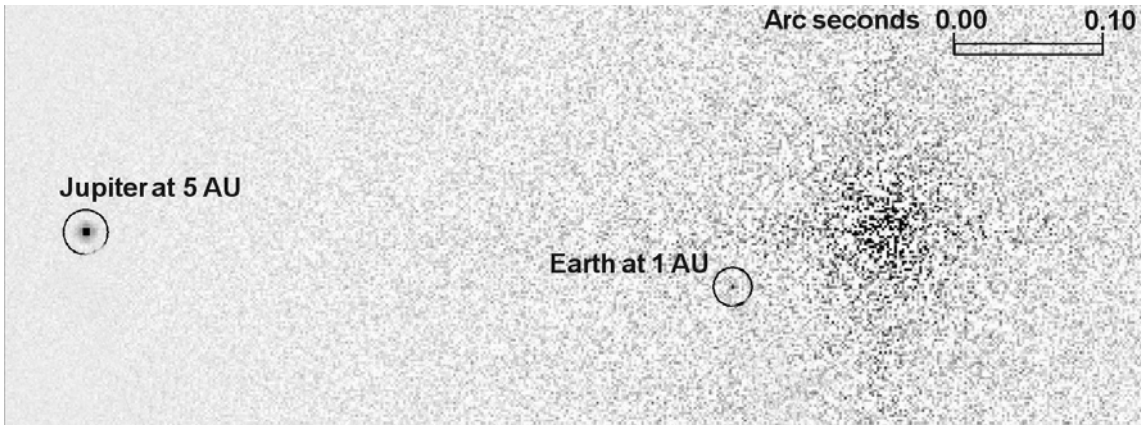

Figure 3-4 Simulated image of a solar-type system at 10 parsec (32 light-years)

While searching for terrestrial planets, OWL will also detect the larger giant gas planets (equivalents of Saturn and Jupiter) in the exo-systems. From this we can determine how common are systems with multiple planets of varying sizes (like our own solar system). We can also characterize systems in different environments, such as around metal-poor stars, white dwarfs, massive stars and brown dwarfs. Such statistics will provide the clues for the detailed understanding of the formation of stars and their planetary systems, for example which stars have planets, what is required to form planets, what is the chemical composition of the parent stars and are there planets around special stars (e.g. white dwarfs, very old halo stars or very young T Tauri stars). Only by doing this can we determine to what extent our own solar system and Earth itself is unique, and assess the probability that other planetary systems could support life.

3.2.2.2 Resolved Stellar Populations in a representative sample of the Universe

How did all the galaxies that we observe around us today come to be formed? This remains one of the most intriguing questions in modern astronomy. It is now generally believed that galaxies form out of dark matter halos at large redshifts. As the initially small density perturbations grow, baryons fall into the dark matter potential wells. Eventually, stars start to form and their light makes the baryonic component of galaxies visible. At high redshifts, global galaxy properties can be investigated to test this picture. However, individual stars at the redshifts at which galaxies from are out of reach even for a 100m telescope. Such stars can only be resolved in galaxies within the local universe. The lifetime of low mass stars is comparable to the age of the universe or even longer. Therefore, some of the stars which formed very early in the universe are still there today and are therefore observable in local galaxies. By picking out stellar populations of different ages, the star formation history of galaxies can be reconstructed. This is illustrated in Figure 3-5.

Mergers between galaxies are thought to play an important part in the build-up of the galaxies we see today. If so, we would expect to see evidence of these past mergers. Indeed, recent studies of individual stars in our own Milky Way galaxy have revealed populations of stars with distinct ages and composition. These distinct populations are thought to be remnants of previous mergers, and give clues as to when the main mergers in the Milky Way's history happened. Up until now such studies have been limited to our own Galaxy and its nearest neighbors. However it is unknown whether these are special cases and whether the merger history is similar for all galaxy types. In particular, our own galaxy is a spiral galaxy, and no examples of large elliptical galaxies are within reach of current telescopes for this type of study.

To study a representative section of the Universe requires reaching at least the nearest large galaxy clusters which contain large elliptical galaxies. This means observing galaxies in the Virgo or Fornax clusters at distances of 16 or 20 Mega-parsecs respectively. The challenge here is twofold. Firstly, individual stars at these distances appear very faint (about V=35 magnitudes). Secondly the stars must be individually resolved from each other in order to determine their ages and chemical composition. As in the case of detecting faint planets, both these challenges are addressed in parallel with an extremely large telescope - the sheer collecting area allows the colours (hence ages and chemical composition) of very faint stars to be measured (by imaging), and the diameter of the telescope allows the image of each star to be sufficiently sharp that they can be separated even in crowded regions (provided the telescope is equipped with an adaptive optics system that allows it to observe close to the diffraction limit). Again, initial feasibility studies look very promising - simulations show that a 100m class telescope could observe individual stars within galaxies in the Virgo cluster, and determine their ages (even for the oldest, hence faintest stars) and composition with sufficient accuracy that a picture of the galaxies' history could be derived.

3.2.2.3 The First Objects And Re-Ionization Structure Of The Universe

3.2.2.3.1 The highest Redshift Galaxies

Over the past decade, a broad consensus on the main ingredients and the evolution of the universe emerged. In this so-called concordance model, the universe’s main ingredients are dark energy and dark matter which contribute about 96% of the density, while observable normal matter represents only about 4% of the density. About 380000 years after the Big Bang, these baryons cooled enough for hydrogen to become neutral. It took at least another 200 Myrs before the first generation of stars formed. Within the first billion years, massive black holes also formed and started to power bright quasars. The first stars and quasars both produced UV photons, which gradually re-ionized the intergalactic matter. A simulation of the galaxy formation process is shown in Figure 3-6. Key evidence for this picture comes from observations of the Cosmic Microwave Background (CMB) with the WMAP satellite and other instruments. Current large telescopes can detect galaxies up to a redshift of about 7. At such redshifts, the age of the universe was only 800 Myrs. Spectroscopy of quasars at similar redshifts revealed that they are already evolved objects and contain metals, which must have been produced in a previous generation of stars at even earlier times. A major goal of OWL will be to detect and investigate

the very first generation of galaxies which contains these stars. These galaxies at redshift 10 or above will be extremely faint and quite rare, but their angular size is expected to be large enough to be easily resolved by OWL. Detailed predictions for this population of galaxies are naturally quite uncertain, and it might be necessary to use foreground galaxy clusters as gravitational lenses in order to be able to detect them. JWST will be able to produce candidate lists for the first generation of galaxies, but only an ELT will be able to confirm them spectroscopically. Spectroscopy will also allow to determine the spectral properties of the earliest stars, possibly allowing identification of galaxies with a substantial population III component.

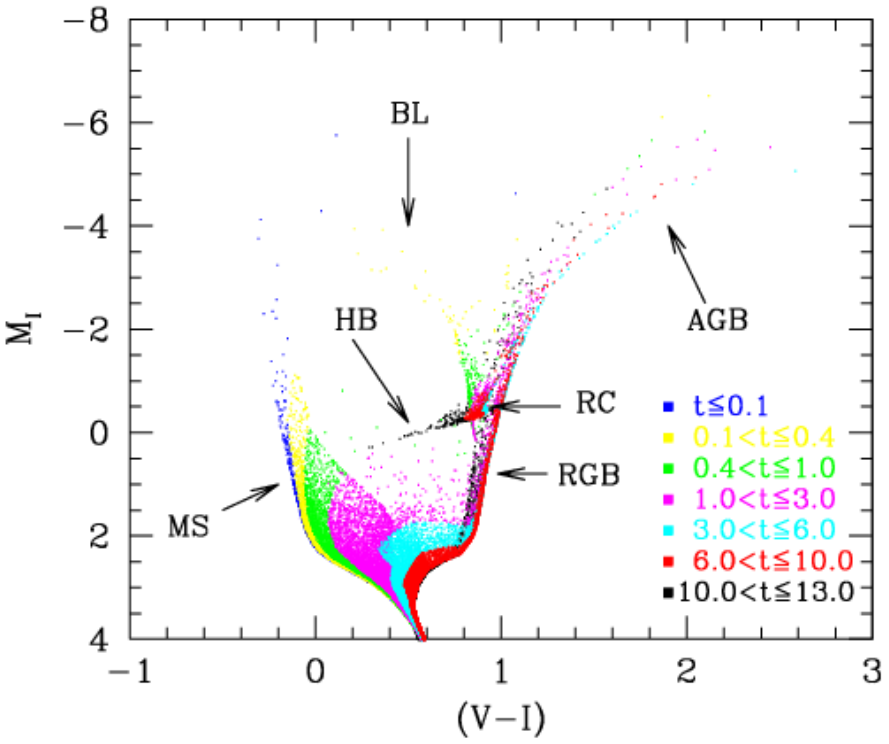

Figure 3-5 (From Science Book) Synthetic Colour-Magnitude Diagram computed using constant star formation rate from 13 Gyr ago to the present. The age of the stars are coded in different colours. Labels indicate different evolutionary phases: BL - blue loop; HB - Horizontal Branch; RC – Red Clump; RGB – red giant branch; AGB – asymptotic giant branch; MS – main sequence. From [119].

3.2.2.3.2 Galaxies at the end of Re-ionization

One of the most important questions about the evolution of the universe is: what are the sources responsible for the re-ionization of the intergalactic matter (IGM)? Stars in the first galaxies, Active Galactic Nuclei (AGNs) and the first quasars compete for the re-ionization of the IGM. Although galaxies are less luminous than quasars, they are far more numerous and might therefore be the main source of photons which re-ionize the IGM. To answer this question, galaxies and quasars in the redshift range from about 5 to redshifts only slightly lower than those of the very first galaxies have to be investigated in detail.

Candidate star-forming galaxies out to redshift about 6.5 have already been discovered and spectroscopically confirmed. These galaxies are high-redshift analogues of Lyman Break Galaxies at redshift of 3. They have typical sizes of about 0.1 to 0.2 arcsec. The objects detected thus far typically have AB magnitudes of i=25.5 and z'=25.5 at a surface density of 500 and 160 per square degree, per unit redshift at z=5.5 and z=6.0 respectively. Identical objects at z=9 and 16 would have magnitudes of J_{AB}=27 and K_{AB}=28 respectively, and apparent sizes between 0.1 and 0.4 arcsec. Such very high-redshift objects would be detectable with JWST by broadband photometric Lyman-Break techniques. However, only a 100m ELT can provide key diagnostics of both the inter-stellar medium and stellar populations in these galaxies by intermediate resolution spectroscopy in the near IR (up to redshifts 15-17).

3.2.2.3.3 Probing the universe during the re-ionization epoch

Spectroscopy of quasars at a redshift of about 6 shows that at that epoch, a significant fraction of the IGM is still neutral. On the other hand, analysis of CMB polarization measurements suggests the presence of ionized IGM at a redshift of about 17. What happened between those two epochs is completely unknown. Several scenarios for the reionization history of the universe have been proposed. One such scenario consists of two distinct re-ionization epochs, one due to the first generation of massive stars and a later one due to the first quasars and galaxies. Another scenario assumes a slower, highly inhomogeneous re-ionization period. Absorption features imprinted by the IGM on spectra of objects within the re-ionization epoch will allow distinguishing between these scenarios. The first "fairly bright" objects which are bright enough to carry out OWL spectroscopy will thus not only be markers of the beginning of the re-ionization epoch, but also be crucial for probing the inhomogeneous structure and metal enrichment of the IGM from metal absorption lines in their spectra due to intervening ionized structures of the IGM.

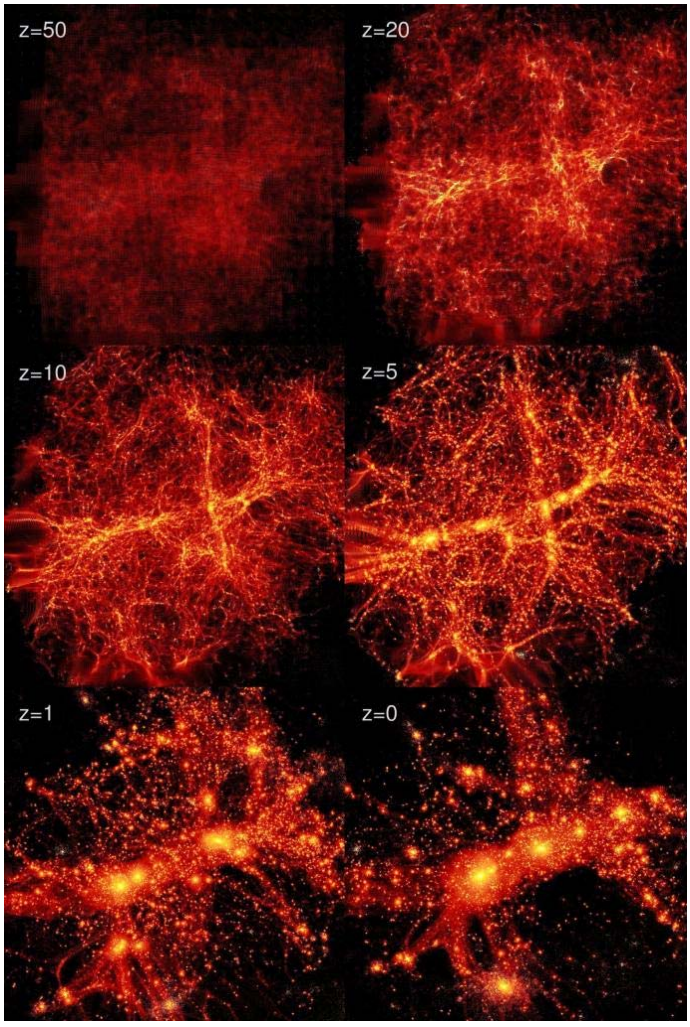

Figure 3-6 Simulation of the formation of the galaxies in the Local Group in a cold dark matter scenario, by Ben Moore, Zurich, astronomy and cosmology research group (www.nbody.net).

Short-lived gamma-ray bursts (GRBs) are an obvious population that can be detected up to z~15-20 and therefore serve as "background" sources. Explosions of population III stars (which are fainter than GRBs) can be used to probe the IGM at z~<12, although this population is rapidly disappearing with time for regions with metal enrichment higher than 1/10000 of the solar value. Although the epoch of quasar formation is a fully open question, the SLOAN quasars at redshifts around 6 which are powered by supermassive black holes suggests that a population of intermediate mass black holes might exist during the epoch of re-ionization. This population could power quasars of intermediate luminosity, which could be used to probe the

IGM up to at least redshifts of about 10. All these objects are rare. GRBs and the supernovae resulting from the explosions of population III stars will be discovered in dedicated missions/ telescopes. JWST should provide lists of quasars at the highest redshift. Probing the physics of the IGM at redshifts from 10 to 20 requires intermediate/high resolution spectroscopy in the near IR, which can only be carried out with telescopes of the 60-100m class due to the predicted low fluxes of these first "background" objects.

3.3 Requirements from the science case

The requirements derived from the science case are summarized in Table 3-7. They cover a wide section of the parameter space, and it may not be possible to meet all of them with a single technical solution.

The requirements can be distilled into a small number of broad categories, as indicated in Table 3-6, from which the top-level requirements of both OWL and its instruments have been developed. While the aim is to preserve as much as possible of the critical science, some of these requirements appear mutually incompatible, and some tradeoffs are necessary. One prime example is field of view: fully optimizing the telescope system adaptive optics capability (as required by most science cases) makes it very difficult technically to get a diffraction-limited field of view larger than a few arcminutes. Even with such relatively small fields, requirements on detectors become rapidly prohibitive: Nyquist diffraction-limited sampling (2 pixels per Airy disk) of a one arcmin field near infrared image already requires ~ 1 G pixels; in the optical, one would need to deploy ~ 7 G pixels (although it is unclear at the moment whether it is possible to correct such a “wide” field at optical wavelengths: the requirement from the science cases developed so far is around 10 arcsec). Cost is certainly an issue: for such a size to be affordable, IR chips cost per pixel should drop from the present ~ 10 cent to below 1 cent, for which according to the manufacturers there seem to be concrete possibilities (see section 12.2.7). Also, with such huge arrays, we are already looking at developing and deploying multi-ton cryogenic vessels for the near-IR and even more at optical wavelengths. In addition, the amount of information to process is huge, and methods to sample the focal plane in a targeted way (e.g. relocatable multi integral field units and multi imagers) look attractive, although they of course would not work for survey work. Handling Petabytes of data will be a challenge of its own.

Specification	Requirement	Minimum	Goal
Telescope size	Maximize > 60m	≥ 60m	100m
Wavelength coverage	0.5 – 25 μm	0.7 – 10 μm	0.3 – 850 μm
Field of view	Maximize	> 0.5 arcmin > 1 arcmin	Opt: 2 arcmin IR: 6 arcmin
Image quality	Diffraction limit	S >0.8 (K, SCAO) S >0.4 (V, ExAO) S >0.3 (K, MCAO, 2′×2′)	Highest contrast over FoV & spectral range
Spectral resolution	100 – 10^5	100 – 10^5	10 – 10^6
Throughput	Maximize	m_K > 29.5 in 1 hour	m_K > 30.5 in 1 hour
Emissivity	Minimize	< 10%	< 6%
Site	AO friendly mid and far IR	<seeing> ≤ 0.6″ τ_0 > 3 ms low PVW, > 2500m	<seeing> ≤ 0.5″ τ_0 > 5 ms low PVW, > 4000m

Table 3-6. Science requirements. S stands for Strehl ratio

Table 3-6 shows that the requirements from the science case drive towards the largest possible telescope size, with diffraction limited performance over a wide wavelength range and with a substantial field of view. Although two columns of requirements are given (minimum and goal) these should be understood as independently valid for each specification (for example the OWL top level requirement for size is according to the goal while the field of view is based on the minimum). The top-level requirements are the result of a trade-off between trying to represent as large as possible a fraction of the science cases and providing the capabilities required by the critical science highlights. Feedback from what is considered feasible (e.g. in the area of adaptive optics correction) is also folded into the tradeoffs.

	FOV	Spatial Resolution (arcsec)	Spectral (R)	Wavelength (microns)	Dynamic Range	Target density
Planets and Stars						
Exoplanets						
HIGHLIGHT CASE: Terrestrial planets in habitable zones	~1"x1"	diff. lim. S=0.7-0.9	500-1000	0.6-1.4	10^{10} at 0.03"	~1000 in sky
Giant planets	~1"x1"	0.001-0.002	10-100	0.5-2.5	10^{7}-10^{8}	Few x 1000 in sky
Mature Gas-giant planets	few arcsec	diff. lim. high S		1.0-10.0	10^{7}-10^{8}	Few x100 in sky
Earth-like moons						
- Reflex velocity			few x10,000			
- Astrometric wobble	very small	diff. lim.		~1.0		
- Spectral detection			>10	1.0 - 5		
- Transits & eclipses				1.0 - 5		
Rings around extra-solar planets	single sources	0.01	100-1000	0.5 - 4	10^{7}-10^{9}	
Planets around young stars in the solar neighborhood	few arcsec	0.002	10-100	0.6 -10	10^{8}	Few x100 in sky
Free-floating planetary-mass objects	1-few arcsec	0.01	10-100	1.0 - 10		100s to 1000s in sky
Our Solar system	up to ~1'x1'	diff. lim.	TBD	Opt - therm-IR		
Stars & circumstellar disks						
Probing birthplaces	up to ~1'x1'	0.002-0.01	up to 100,000	1.0 - 5		Up to 300/sq "
"	"	0.02-0.04	"	10 to 20		"
Structure in inner disks	few arcsec	diff. lim.		2, 10 and 17	10^{5} at 0.1"	
Embedded young stellar objects	few arcsec	diff. lim.	~100,000	5.0 - 20		
Jets and outflows		diff. lim.	~100 (NB imaging)	0.5 - 2		
Debris around other stars	3'x3'	diff. lim. (~1", no AO)	350-850		10^{2} within 0.5"	All stars within 100pc

	FOV	Spatial Resolution (arcsec)	Spectral (R)	Wavelength (microns)	Dynamic Range	Target density
The lives of massive stars						
Early Phases		as high as possible		NIR & MIR		
Mature phase outflows		diff. lim.		NIR & MIR		
Normal and Peculiar stars	~1"x1"	diff. lim. S~0.9	up to 100,000	0.6 (Ha)		
Asteroseismology	30'	no AO needed	80,000		> few x 10^5	500 per field
Chemical composition : chronometry	30"x30"		30,000-150,000	0.3 - 0.7		
The Death of Stars						
Mass fn of black holes and neutron stars			~1000	NIR		
Isolated neutron stars	single sources		~100	Op		
Black holes in globular clusters	5"	~0.001	~5 and 20,000	Opt and NIR		Crowded fields
Microlenses			~100	1 - 2.5		
Stars and Galaxies						
The Interstellar medium						
Temperature and density probes			10,000 to 10^6	7 to 25		
Fine structure in the ISM						
High redshift	single sources			NIR		
Dust properties via polarimetry						
Heavily extinguished regions						

	FOV	Spatial Resolution (arcsec)	Spectral (R)	Wavelength (microns)	Dynamic Range	Target density
HIGHLIGHT CASE : Resolved Stellar Populations						
- Imaging	5"x5" or larger	diff. lim. (S TBD)	~5	V to K	TBD	Very crowded fields.
- Spectroscopy	few arcmin	0.002-0.02	3-8,000 & 20-40,000	V to K		in specific galaxies
Resolved stars in stellar clusters	~2"x2"	0.003	~25	0.4 - 0.6	TBD	Very crowded fields.
Spectral observations of star clusters		few mas	30,000			
The stellar IMF				1.0 - 10		
Extragalactic massive stars beyond the LG	~1'x1'	0.02-0.1	1000 - 10,000	V+R (+IJHK)		few tens / field
Stellar kinematic archaeology	few arcsec	diff. lim.	10,000 -100,000	V to K		many nearby galaxies
The intracluster stellar population	few tens of ″	diff. lim. (S TBD)	~5	NIR (J & K)		few tens / sq"
The cosmic SFR from supernovae	2'x2'	diff. lim. (S=0.5)	~ 5 and ~2,000	NIR (JHK)		4-8 per field per year
Young, massive star clusters	~2'x2'	0.03 - 0.04	> 40,000	>0.8		many nearby galaxies
Black Holes - monsters in Galactic Nuclei	5"x5"	few mas	few x 1000	Opt & NIR		

	FOV	Spatial Resolution (arcsec)	Spectral (R)	Wavelength (microns)	Dynamic Range	Target density
# Galaxies and Cosmology						
Cosmological Parameters						
Dark Energy						
Type Ia SNe as distance indicators	2'x2'	diff. lim. (S=0.5)	~5 and ~2,000	NIR (JHK)		4-8 / field / year
GRBs as distance indicators	5'x5'		8,000 to 10,000	0.8 - 2.4		single targets
Expansion History						
From primary distance indicators						
CODEX: Cosmic Differential Expansion	single sources	0.2	>100,000 (400,000)	0.4 - 0.7		

	FOV	Spatial Resolution (arcsec)	Spectral (R)	Wavelength (microns)	Dynamic Range	Target density
HIGHLIGHT CASE: First Light - The First Galaxies and the Ionisation State of the Early Universe						
Galaxies and AGN at the end of reionisation	> 5' x 5'	0.01 - 0.02 50% EED	5,000-10,000			0.2 - 5 / sq'
- most distant sources	> 5' x 5'	0.1 - 0.2 50% EED	few x 100	1.0 - 2.4		"?
Probing the reionisation history	single sources	diff. lim.	1000 - 10,000	JHK		
Early chemical evolution of the IGM	single sources	Any (if imaged sliced)	10,000	0.4 - 0.9		
Evolution of galaxies						
Physics of high redshift galaxies - Req	2' diam.	0.05	5,000	0.5 - 2.5		0.1 to 10 /sq'
" - Goal	10' diam.	0.01 - 0.02	10,000	0.3 - 2.5		"
Assembly of galaxy haloes - Req	2' diam.	0.1	5,000	1 - 2.5		0.1 to 10 /sq'
" - Goal	10' diam.	0.05	10,000	0.7 - 2.5		"
The SFR over the history of Universe a)	3' x 3'	0.1	~5	0.5 - 2.2		few tens /sq'
b)	10' x 10'	0.05	~5	0.3 - 2.2 + FIR		few per unit z / sq'
Fundamental Constants	single sources	< 0.01	300,000	Opt		

Table 3-7 Requirements from the main science cases (adapted from Hook [120])

4. Top level requirements

4.1 Introduction

The top level requirements are derived from the science case and are a set of overall specifications for the design of the telescope, including its instrumentation, so that it can fulfil the science objectives. The science case is itself still evolving, and the top level requirements will be adapted to reflect new input until such a time when the level 1 (engineering) requirements needs to be frozen (in the preliminary design phase).

The knowledge of what can be considered technologically realistic also enters into the process of setting the requirements, and some tradeoffs between different needs are sometimes necessary.

The top level requirements are the basis from which are derived the level 1 requirements that define, at system and subsystem level, how to achieve the desired performance.

The top level requirements do not specify the details of the engineering solutions (these are spelled out in the level 1 requirements), although in some areas where it may be helpful to drive technological development (e.g. in adaptive optics), or where there are known limitations (physical, e.g. atmospheric properties, or technological) more elaborate requirements may be necessary. For example, a requirement for telescope tracking would not appear to be within the scope of the top level requirements as it is implicit in the requirements for image quality, but the effects of atmospheric refraction (that will limit the range of zenithal distances at which “wide” field observations can be carried out) need to be reflected in the top level requirements (to avoid the risk of setting stringent level 1 requirements for capabilities of the telescope that cannot be used).

4.2 Overall requirements

4.2.1 The OWL telescope

OWL will be a 100m-class, adaptive optics telescope working in the optical, infrared and, as a goal, in the sub-mm wavelength ranges. It will have a collecting area of ~ 7,000 m^2, deliver diffraction-limited performance and be equipped with a suite of instruments able to achieve the main science goals of the project.

As the fabrication and integration of primary mirror segments may take several years, ways to use the telescope for science before the primary is completely filled shall be explored.

4.2.2 The Conceptual Design (Phase A)

The conceptual design of OWL will have the goal to assess the feasibility of a 100m telescope. To this end, it will be based on technical and technological solutions that are, to the maximum extent possible, proven and reliable. In particular, R&D should be limited to areas where present day technology would not suffice (e.g. in adaptive optics) or to validate options to specific solutions (e.g. alternatives to glass for the mirrors).

Options for designs of different aperture should be analyzed. A 100-m *baseline* design should be developed in detail, and its properties used as interface to subsystem studies.

Phase A should provide an indicative analysis of cost, schedule and performance variations in relation to telescope size and design.

It is to be understood that if the project goes to the next phase (preliminary design), the requirements and baseline design will be thoroughly re-assessed.

4.2.3 Evolution of the Top Level requirements

The present requirements apply to Phase A (Conceptual Design) and B (Preliminary and Detailed Design Phases). It is understood, however, that the conceptual design may occasionally fail to demonstrate compliance, under the proviso that plausible remedies to be undertaken in Phase B are clearly identified and planned for.

As the science case develops, requirements may be added or changed to reflect the new input. To the maximum possible extent, project phases should be planned in a way allowing requirements to be frozen at the latest reasonably possible stage. At the end of the detailed design, when comprehensive plans for assembly, integration and testing, and for operations are developed, the top level requirements may be extended to include requirements pertaining to these future stages of the project.

Should the size of the telescope need to be modified, the top level requirements will be modified as well according to the appropriate prescriptions (e.g. scaling the requirements according to their functional dependence on diameter D: none, $\propto D$, $\propto D^2$ etc).

4.2.4 Operational lifetime

The operational lifetime of OWL is expected to exceed 30 years and the design should be developed accordingly. During this time, OWL, its instruments, its adaptive optics, its data systems (collectively referred to as the OWL system) are expected to undergo significant upgrades and enhancements in response to the advances of technology and the evolution of the science case.

4.2.5 Location of OWL

The search of a site for OWL will continue until the moment the site properties need to be incorporated in the final design. The choice of the site will be the result of a thorough trade off analysis of atmospheric, logistical, seismic and ground properties, and of astronomical considerations (e.g. available fraction of the sky). Low cloud coverage, low precipitable water vapour, moderate ground-level wind, adequate turbulence characteristics (turbulence profile, amplitude, and coherence time) will be major selection criteria. The site should ideally be suited to observations also in the mid to far (sub-mm) infrared.

4.2.6 Optical design

The optical design of OWL will provide diffraction-limited performance in a 2 arcmin (diameter) field of view in the K band (goal 3 arcmin), and in a 0.5 arcmin field of view in the V band (goal 1 arcmin). The total field of view, i.e. scientific plus technical, will be 8 arcmin or more. The final

focal ratio will provide a focal plane such that the optical beam is transmitted to the instruments without auxiliary optics. The design will have the means to transfer the focus to at least 4 focal stations where instruments can be mounted.

4.2.7 Maintenance

Once operational, the OWL facility will be maintained in such a way that allows the top level requirements to be preserved during operations, with a technical downtime of less than 3% (goal 2%). The OWL design will include maintenance concepts from the conceptual design phase in order to simplify technical activities and to reduce the operational costs of the facility.

4.2.8 Instrumentation

OWL will have a number of fixed, semi-permanently mounted instruments. These will be modified, upgraded or replaced at well announced times after an approved program to do so has been executed and documented. Some instruments will be general-use observatory facilities; others might be specialized experiments with a well-defined finite life program. A number of concept designs will be developed during the design phase of the telescope, with a choice of those to enter Preliminary and Final design to be taken about two years into the telescope Phase B.

4.2.9 Coating optimization

The coating of OWL shall cover the wavelength range from 0.5 to 25μm, with blue-UV and sub-mm microwave reflectivity as a goal. Every effort to achieve the highest possible reflectivity shall be made. During the conceptual design phase, protected Ag coating as developed recently by the Gemini Observatory will be assumed. Studies about the feasibility of extending its blue-UV reflectivity will be performed during Phase B.

4.2.10 Astronomical site monitor

An astronomical site monitor will be part of the OWL observatory and will provide means to characterize the atmospheric conditions above the observatory as well as monitor meteorological conditions. It will be defined and designed in Phase B. Options to have multiple monitors at various distances from the site in order to predict/foresee changes in atmospheric conditions shall be explored.

4.2.11 Safety

Safety during construction and operations will be a driver of the design. Concepts will be developed during Phases A and B so that guaranteeing the safety (human resources and hardware) can be achieved in a simple, verifiable and logical way.

4.3 Performance requirements

This section defines the minimum acceptable performance capabilities of the OWL facility as required by the science case.

4.3.1 Telescope transmission

The telescope shall have freshly coated reflectivity (per surface) of 98% (goal 99%) from 1 to 25 μm, 95% (goal 98%) from 0.5 to 1 μm, and > 90% (TBC) to 1mm. Blue-UV sensitive coatings shall be a goal. Coating reflectivity shall not degrade by more than 1% during operations.

4.3.2 Emissivity

The telescope shall be designed so that its total emissivity at wavelengths above 2μm will not exceed $(1-\eta)^n$ with $\eta(\lambda)$ the reflectivity per mirror and n the number of mirrors[36], and in any case be less than 15% (telescope only, goal 8%). Baffling will be included in the design to avoid direct view of the sky or of any part of the structure.

4.3.3 Sky coverage

The fraction of the sky accessible to OWL will depend on the site selection. This parameter shall be included in the site selection trade-off.

The telescope shall operate at zenith distances from 1 to 60 degrees (goal 0.5 to 70 degrees). Ways to counter the zenith distance limitations imposed by atmospheric refraction to observations in "wide" field (0.5 arcmin in V, 2 arcmin in K, see 4.3.6) shall be explored in Phase B. These will include as a minimum post-processing, active optical elements and appropriate operational strategies.

4.3.4 Image quality

Image quality is as much a driver as collecting power for almost all the science objectives of OWL. If highly improved energy concentration down to the diffraction limit cannot be achieved, much of the *raison d'être* of OWL would disappear. Therefore this section goes into a somewhat more detailed discussion.

4.3.4.1 Telescope

The image quality delivered by the telescope design will be such that the corresponding correction carried out by adaptive optics to reach the diffraction limit performance will be kept at a minimum.

4.3.4.2 Adaptive Optics

Adaptive Optics is probably the most demanding technological development to achieve the science goals of OWL. In a very concrete sense we consider it as a *go/no-go* milestone for the project. To allow maximum development time, AO will be developed in successive stages, with a progressive increase of capabilities.

Science "first light" (whether or not with a partially filled primary) will provide at least single conjugate AO correction in the near infrared.

The requirements for Adaptive Optics are set according to the following:

- The first generation of AO correction is required to achieve at least 80% of the stated requirements. It is not required that the first generation include the most demanding techniques (e.g. extreme AO).
- The requirements are intended for observations within 30 degrees of zenith. Larger zenith distance degradation (due both to the atmospheric behaviour and to the allowed zenith-dependent performance of the telescope) is acceptable.

[36] If the reflectivity is different for different mirrors this becomes $\prod(1-\eta_i)$, i=1,n

- For the purpose of simulations before the final site characteristics are defined, all atmospheric parameters and statistics shall be those of Paranal.
- When a requirement is given at only one wavelength or band, it is understood that the instrumental realization will provide correction at adjacent bands.
- For ground layer AO, the requirements are set as ensquared energy (EE) rather than Strehl
- An attempt at taking into account seeing and reference star magnitude is made for some modes. If at instrument design level it is found that the relationship between these has a different behaviour, the most stringent requirement shall be the driver.
- Sky coverage will be driven by the individual science cases. However, for the purpose of this chapter, the following should be assumed for the first generation of instruments:
    - Exoplanets: all available stars (V<10) within the zenith limitation
    - Cosmology: sky coverage provided by NGS (~20% at K at galactic poles, MCAO)
    - In the long term, the sky coverage for cosmology should reach 80% at K at GPs.
- Field of view values are intended as diameter of a circular field of view unless expressed otherwise (e.g. 2 x 2 arcsec² is a square field of view)

4.3.4.2.1 Telescope AO

The telescope will include in its optics adaptive mirrors that will provide “system” AO correction. They either provide the full correction in certain modes (e.g. IR SCAO, IR GLAO, dual conjugate IR AO), or represent a first stage of a complex AO system, with other stages probably integrated in an instrument.

The requirements for SCAO, MCAO and GLAO are to be understood as requirements for the system-delivered AO correction.

4.3.4.2.2 Single Conjugate AO

SCAO will be used in a variety of conditions. Its range of application will be 1 to 5 µm. The field of view will be > 30”. Requirements are given at J and K band, with usual extrapolation to other wavelengths assumed. Values are the on axis correction.

Star mag	Seeing	Strehl (J)	Strehl (K)
13.5	0.4	0.45	0.75
	0.6	0.35	0.65
	0.8	0.25	0.55
	1.2	0.10	0.40
15.5	0.4	0.15	0.45
	0.6	0.10	0.35
	0.8	0.05	0.25

Table 4-1. Single conjugate AO requirements.

4.3.4.2.3 Multi Conjugate AO

MCAO will operate between 1 and 2.5 µm, over a field of view of at least 2×2 arc minutes², in a variety of observing conditions. The star magnitude is to be intended as the integrated magnitude of the multiple reference stars. A ±10% departure from the mean of the PSF across the field of view will be acceptable.

Star mag	Seeing (arc secs)	Strehl		
		J	H	K
13.5	0.4	0.20	0.35	0.45
	0.6	0.15	0.30	0.40
	0.8	0.10	0.25	0.35

Table 4-2. Multi-conjugate AO requirements.

4.3.4.2.4 Ground Layer AO

GLAO is intended to provide reduced-seeing images, formally with a Strehl Ratio of a few percent. The performance values are expressed in Ensquared Energy (EE), and represent the improvement with respect to seeing within a 50 mas pixel. GLAO will operate between 1 and 2.5 µm, over a field of view of at least 3 arc minutes. A ±5% variation from the mean of the PSF across the field of view will be acceptable.

Star mag	Seeing (arc secs)	EE gain		
		J	H	K
13.5	0.6	2.5	3.0	3.5
	1.2	2.0	2.5	3.0

Table 4-3. Ground-layer AO requirements.

4.3.4.2.5 Multi-Object AO

Multi-Object AO (also called Distributed AO) aims to provide a higher level of energy concentration in an even larger field of view by performing pseudo closed-loop SCAO corrections on a number (~ 10-20) of selected objects in the field. Minimum specifications are given in the Table below, with a goal 4 times higher.

Star mag	Seeing (arc secs)	EE gain		
		J	H	K
13.5	0.6	40	60	80
	1.2	10	15	20

Table 4-4 Multi Object AO requirements

4.3.4.2.6 Extreme AO

It is understood that this is the most demanding technique, driven by the exoplanets science case. It is envisaged that the best (10%) seeing conditions will be available for such science case.

Star mag	Seeing (arc secs)	Strehl Ratio			
		V	J	H	K
< 10	< 0.6	0.40	0.87	0.92	0.96

Table 4-5. Extreme AO requirements.

4.3.4.2.7 AO at optical wavelengths

It shall be the ultimate goal of OWL to provide diffraction-limited images at optical wavelengths. It is conceivable that the first step in this direction will be the adaptation of Extreme AO technology developed for the IR to SCAO for the Optical domain.

The star magnitude is intended as the magnitude of a single reference star or the integrated magnitude of multiple reference stars, whether natural or artificial.

Star mag	Seeing (arc secs)	Strehl Ratio		
		V	R	I
< 10	0.4	0.4	0.5	0.6
	0.6	0.3	0.4	0.5
	0.8	0.2	0.3	0.4

Table 4-6. AO requirements at optical wavelengths (provisional).

4.3.4.2.8 Laser Guide Stars

Single and multiple laser guide star systems will be necessary to either/both extend the sky coverage and/or to provide sufficient flux to perform the wavefront analysis. Detailed feasibility of LGS systems will be studied in Phase B, as will ways to counter the limitations imposed by the out-of-focus nature of LGS images at ~ 90 km altitude (e.g. pulsed lasers, readout gating, extra optics etc).

4.3.5 Atmospheric dispersion compensation

Atmospheric dispersion will be corrected, either at telescope level or, if too difficult, at instrument level. Ways should be explored in Phase B to assess feasibility of using atmospheric dispersion as a dispersive element of some instrument (e.g. with partial correction so that it is kept constant over some range of zenith distance).

The compensation shall be such that the residual dispersion will be less than 0.2 pixels of the relevant instrument at the relevant wavelength. The transmission of the compensator should exceed 97%.

At the spatial resolution scale of OWL, active closed loop compensations may be necessary.

4.3.6 Atmospheric refraction

In diffraction-limited observations and for fields of view larger than several arc seconds, the differential position displacement at different locations due to refraction may prevent long exposures. Unless the readout noise of detectors is extremely low (so that short exposure can be co-added after geometrical alignment), or techniques to reformat the focal plane can be developed (e.g. with active cylindrical optical elements), this may represent a problem for a 100m telescope.

The effect in the K band at the edges of a 2-arcmin field between meridian and one hour after (or before) is summarized in Table 4-7 for various values of the declination. The effect is computed for two stars separated by 1 arcmin in right ascension (RA) or declination (DEC) for the K band (i.e. for a total field of view of 2 arcmin as the center of the FoV can be kept fixed by the control system), and for stars separated by 30 and 15 arcsec in the V band (FoV of 1 and 0.5 arcmin respectively). The observatory parameters are those of Paranal.

If one assumes that the maximum acceptable differential displacement per single exposure is 10% of the diffraction limit, the maximum exposure time is indicated for the V and K bands. The time limit is set by the smaller of the two exposure times in RA and DEC. This effect is only very mildly wavelength dependent, so extrapolation at other bands is straightforward.

A diffraction-limited field of view of 2 arcmin in the V band is not at present a science requirement (and given that the exposure times computed for K have to be divided by ~ 4 to apply to the V band it may prove a very challenging goal, matched only by the challenge of paving such a field with 0.7 mas pixels). For the V band the effect is computed both for 1 and 0.5 arcmin FoV. The latter is the present science requirement. The required readout noise so that the short exposures can be background-limited (to allow geometrical correction before co-addition) should be $RON^2 < 0.2 \times$ background/pixel, and is well within the capabilities of present day detector technology in the IR. For the V band, where the background is ~ 1 photon per minute per half-PSF pixel, post-processing alone may not be the solution to the problem (especially is the field is ≥ 1 arcmin and at substantial zenith distance). The other options mentioned above may be the only recourse.

	Effect in 2' FoV, K band				Effect in 1' FoV, V band				Effect in 0.5' FoV, V band			
	Sep in RA		Sep in DEC		Sep in RA		Sep in DEC		Sep in RA		Sep in DEC	
Decl	Displ [mas]	ΔT [min]	Displ [mas]	ΔT [min]	Displ [mas]	ΔT [min]	Displ [mas]	ΔT [min]	Displ [mas]	ΔT [min]	Displ [mas]	ΔT [min]
35	-2.88	12	-2.15	15	-1.46	6	-1.09	8	-0.73	11	-0.55	15
25	-1.75	19	-0.92	36	-0.89	9	-0.47	18	-0.44	19	-0.24	35
15	-1.24	27	-0.48	> 60	-0.63	13	-0.24	34	-0.31	26	-0.12	> 60
5	-0.97	34	-0.27	> 60	-0.50	17	-0.14	> 60	-0.25	34	-0.07	> 60
-5	-0.83	40	-0.16	> 60	-0.42	20	-0.08	> 60	-0.21	39	-0.04	> 60
-15	-0.76	44	-0.08	> 60	-0.38	22	-0.04	> 60	-0.19	43	-0.02	> 60
-25	-0.73	45	-0.02	> 60	-0.37	22	-0.01	> 60	-0.19	45	-0.01	> 60
-35	-0.75	44	0.04	> 60	-0.38	22	0.02	> 60	-0.19	44	0.01	> 60
-45	-0.81	41	0.11	> 60	-0.41	20	0.06	> 60	-0.21	40	0.03	> 60
-55	-0.95	35	0.23	> 60	-0.48	17	0.12	> 60	-0.24	34	0.06	> 60
-65	-1.20	28	0.45	> 60	-0.61	14	0.23	37	-0.30	27	0.11	> 60
-75	-1.68	20	0.91	36	-0.85	10	0.46	18	-0.43	19	0.23	36
-85	-2.76	12	2.18	15	-1.39	6	1.11	7	-0.70	12	0.56	15

Table 4-7. Effect of differential displacement due to atmospheric refraction between meridian and one hour from meridian. RA and DEC are right ascension and declination, Sep is the separation between the stars, Displ is the relative differential displacement in milliarcsec at one hour from meridian, and ΔT is the maximum exposure time in minutes to have a displacement < 10% of the diffraction peak.

It is clear that higher latitude sites would suffer less from this effect, but a choice of site at moderately low latitude guarantees access to a larger fraction of the sky, so higher latitudes may not be the solution.

This effect should be considered in instrumentation using similar or larger fields of view, e.g. multi-object spectrographs using mini IFUs, as these may need to be repositioned in the FoV to maintain the objects properly centered.

5. System Engineering

5.1 Level 1 requirements

Level 1 Requirements constitute the highest level engineering requirements and are second only to Top Level Requirements, from which they are derived in part. They provide the link between the eventual user's objectives and the project and engineering frameworks, including essential characteristics.

Level 1 Requirements also include indirect ones, as well as guidelines and targets. Those may reflect constraints and objectives not directly related to scientific objectives but to technical, programmatic, or even legal considerations (e.g. compliance with legal safety standards).

At this stage, characteristics covered by OWL Level 1 Requirements are generally given two values (or two set of values), one corresponding to the biding requirement, one for the desirable (non-binding) goal.

Level 1 Requirements are documented in RD41. Items addressed in this document include:

1. Definitions and conventions, e.g. common terminology, coordinate systems;
2. Environmental conditions – the same as for the VLT until final site selection;
3. Requirements
    - 3.1. Design guidelines
    - 3.2. Optical characteristics
    - 3.3. Optical quality
    - 3.4. Atmospheric dispersion compensation
    - 3.5. Wavefront control, including accuracy requirements
    - 3.6. Structure & Kinematics
    - 3.7. Interface to instruments
    - 3.8. Local seeing, thermal control
    - 3.9. Cleanliness
    - 3.10. Enclosure characteristics
    - 3.11. Operations, including reliability, operational lifetime, science operations, maintenance
    - 3.12. Site infrastructure, including site services, offices, lodging, etc.
    - 3.13. Performance evaluation and monitoring
4. Site characterization, monitoring and preservation
5. Safety

Level 1 Requirements are essentially functional ones. However, because they must make some broad assumptions as to the technologies and concepts that may eventually be required to fulfil Top Level Requirements, they are not fully design-independent –even though every attempt should be made at removing such dependency.

Table 5-1 gives the image quality requirements in seeing-limited mode, after successive closing of individual non-adaptive control loops. These requirements are very preliminary and essentially set the maximum allowable amplitude of quasi-static, low to mid-spatial frequency terms and the maximum residual errors which will have to be compensated by adaptive optics. It should be noted a given slope requirement translates into more generous amplitude than with a smaller telescope –0.1 arc seconds of astigmatism, for instance, corresponds to a wavefront coefficient 12.5 times larger with OWL than with VLT.

In addition, non-adaptive wavefront control systems shall have such characteristics that residual telescope errors (including turbulence induced by local heat sources), which will have to be compensated by Adaptive Optics, do not exceed 20% (goal 10%) of the available adaptive correction range.

Mode	**On-axis image quality**		**Image quality off-axis (1.5 arc min)**	
	Requirement	Goal	Requirement	Goal
Open loop	1.5 arc seconds RMS	1 arc second RMS	N/A	N/A
After internal alignment	1 arc seconds RMS	0.5 arc seconds RMS	1.5 arc seconds RMS	0.5 arc seconds RMS
Idem + active centring & focusing	0.5 arc seconds RMS	0.2 arc seconds RMS	0.7 arc seconds RMS	0.3 arc seconds RMS
Idem + phasing + active deformation of flexible mirrors + field stabilization[37]	0.10 arc seconds RMS	0.08 arc seconds RMS	0.12 arc seconds RMS	0.10 arc seconds RMS

Table 5-1. Image quality requirements, non-adaptive modes.

With a view to allowing sub-mm observations without on-sky metrology, image quality on-axis shall be 1.0 arc seconds RMS (goal 0.5 arc seconds RMS) or better over a 30 minutes exposure, with the following loops running:

a. Internal alignment (running on internal metrology systems);

b. Phasing (running on position sensors);

c. Active centring (running on look-up tables);

d. Active focusing (running on look-up tables);

e. Active surfaces deformation (running on look-up tables).

Table 5-2 gives the image quality requirements after adaptive correction (first generation single conjugate, second generation dual-conjugate). In dual-conjugate mode, the maximum variation of the Strehl Ratio over the field of view shall be less than or equal to ±10%.

These requirements are in-line with the top level ones. In the event of conflict between Table 5-1 or Table 5-2 and the level 1 requirements specified in RD41, the content of RD41 shall be taken as superseding.

At the time of writing of this document, image quality requirements in Ground-Layer Adaptive Optics and Extreme Adaptive Optics modes are still under review.

Level 1 requirements also includes the hierarchy and allowable rate of occurrence of damages or major failures. The term out of operations is not meant to include preventive / regular maintenance but includes corrective maintenance if such corrective maintenance implies loss of science time.

[37] Non-adaptive field stabilization.

Star magnitude	Seeing (arc seconds)	Wavefront RMS on-axis (μm)	Field of view (arc minutes, diameter)
Single-conjugate adaptive optics			
13.5	0.4	0.180	N/A
	0.6	0.200	N/A
	0.8	0.230	N/A
	1.2	0.300	N/A
15.5	0.4	0.274	N/A
	0.6	0.302	N/A
	0.8	0.344	N/A
Multi-conjugate adaptive optics			
13.5 (integrated over all guide stars)	0.4	0.252	3
	0.6	0.234	3
	0.8	0.302	3

Table 5-2. Image quality requirements, with first and second generation adaptive optics.

Category	Type	Definition	Max. allowable probability or rate of occurence
I	Catastrophic	*Complete loss of system or threat to personnel safety.* OR *Repair cost exceeds 10% of capital investment.*	0
II	Catastrophic	*System is out of operation for 2 months or more,* OR *Repair cost exceeds 5% of capital investment,* whichever comes first.	0.01% over 30 years
III	Critical	*System is out of operations for up to 2 months* OR *Repair cost exceeds 1% of capital investment,* whichever comes first.	0.05% over 30 years
IV	Major	System is out of operation for up to 1 calendar week.	Once every 10 years
V	Significant	System is not able to allow science time for up to 1 calendar week.	Once every 5 years
VI	Minor	System is not able to allow science time for 24 hours.	3 times per year

Table 5-3. Failure / damage hierarchy and allowable rate of occurence.

5.2 Design constraints and guidelines

Overall design constraints and guidelines are also covered in the applicable Level 1 Requirements (RD41). They are reproduced here below:

1. Reliance on proven[38] technology, materials and processes is a high priority requirement, from design to operations.
2. Reliance on serially produced parts or standard parts and assemblies is a high priority requirement.
3. Deviation from the above requirements shall only be considered

[38] At fully tested prototype level as a minimum.

a. where strictly required,

b. or where significant gains in performance, cost or schedule can reasonably be expected.

4. In such case (3.b hereabove), backup solutions shall be identified and developed at least to preliminary design level.

5. The system design and its implementation shall allow maximum possible development time for unproven technology, materials or processes –without, however, delaying the start of science operations.

6. The system design and its implementation shall allow a start of science operations as soon as possible after (technical, seeing-limited) first light, with negligible engineering overheads, reduced pupil area, and single conjugate IR Adaptive Optics with Natural Guide Stars.

7. To the possible extent, design solutions allowing progressive loss of performance in case of failure shall have preference over solutions implying significant loss of performance in case of failure.

8. From system to component level, and from the earliest phases of design inception, high priority shall be given to operation and maintenance considerations –with a view to

   - Minimizing system integration and operational resources (in particular, non-standard hardware as well as specialized human resources);
   - Facilitating maintenance and minimizing operational complexity;
   - Guaranteeing, to the maximum possible extent, system integrity and safety of human resources.

   To this end, preliminary designs, from system to component level, shall include operation and maintenance plans, including preliminary definition of related hardware and resource usage.

5.3 Complex Systems, methods and modelling

This section provides a brief overview of OWL System Engineering aspects. It starts with a broad comparison of OWL with other Complex Systems. System Engineering methods are discussed qualitatively. The flow of activities across disciplines is discussed, with emphasis on traceability and compliance verification. Requirements shall be traceable from their inception and verified at the appropriate project level, within a determined timeframe and along clear processes and pre-defined procedures. Project Documents and Project Configuration Control Procedures shall be outlined along such principles. The last part of this section deals with the quantitative aspects of System Engineering, including modelling tools.

In the following the OWL Observatory is defined as *system*, while the telescope, enclosure, instruments, Data Management, etc. are referred to as *sub-systems* (see also RD37).

5.3.1 Complex System

A consistent system engineering approach is recognized as being of paramount importance to the design of OWL. Complexity is a characteristic common to most large-scale engineering projects. Complex systems are mainly characterized by their large number of assemblies, parts, components, but also by the resources (including human resources) their design, construction, and operation require, and by the large number of interfaces and interdependencies between them [77], [78]. Breaking down into smaller and more manageable subsystems, possibly organized in hierarchical structures, implies intense, multi-directional information flow and requires efficient coordination mechanisms.

The engineering of OWL as a complex system will be conceived to achieve the following objectives:

- Ensure appropriate oversight and understanding of the system, its scientific and engineering characteristics, including underlying risks and susceptibility to failures.
- Develop tools and organizational methods to quantify, track, and visualize, system designs and to support trade-off analysis and decision-making processes.

Key element of a system approach are modelling and computer simulations. Models provide a means of understanding complex phenomena and of evaluating the overall response of the system to specified disturbances (e.g. a change of environmental condition or of a specific design characteristics). By using mathematical models along with advanced analysis tools and simulation environments, the system design and performance can be evaluated before construction begins.

OWL as a controlled opto-mechanical system will integrate the knowledge base and mathematical tools used in at least three engineering disciplines: structural mechanics, optics, and control systems. The rapidly growing computing power does not necessarily imply that an integrated model complete down to all possible details is the one-fits-all modeling tool. In practice, high accuracy and fidelity are often traded against simplicity, which often takes superseding priority. It is indeed natural to seek techniques (e.g. use of reduced models) that reduce model complexity and computational effort to a level commensurate to the level of detail required to asses an evolving design.

5.3.2 Methods

5.3.2.1 Science and Engineering.

A V-diagram (Figure 5-1) shows symbolically how Science and Engineering interface. OWL characterization is divided in 2 main structures:

- Science, the top part under the responsibility of scientists with the support of engineers.
- Engineering, the lower part under the responsibility of engineers with the support of scientists.

Both structures are involved, to variable extent, during all project phases.

System Design. The left part of the diagram corresponds to phases A and B –conceptual and preliminary / final design, respectively. Experience shows that during these phases about 80% of the project cost and technical solutions are committed. Phase A and B take typically take 20% of the project schedule. Changes of requirements and design iterations are possible until final design, but costs associated to changes tend to increase with time.

System Integration. The right part of the diagram corresponds to phases C and D. It is the counter part of the System Design. Each level of the System Design shall have a corresponding verification activity during system integration. Changes of requirements during the system integration normally generate high costs and substantial delays.

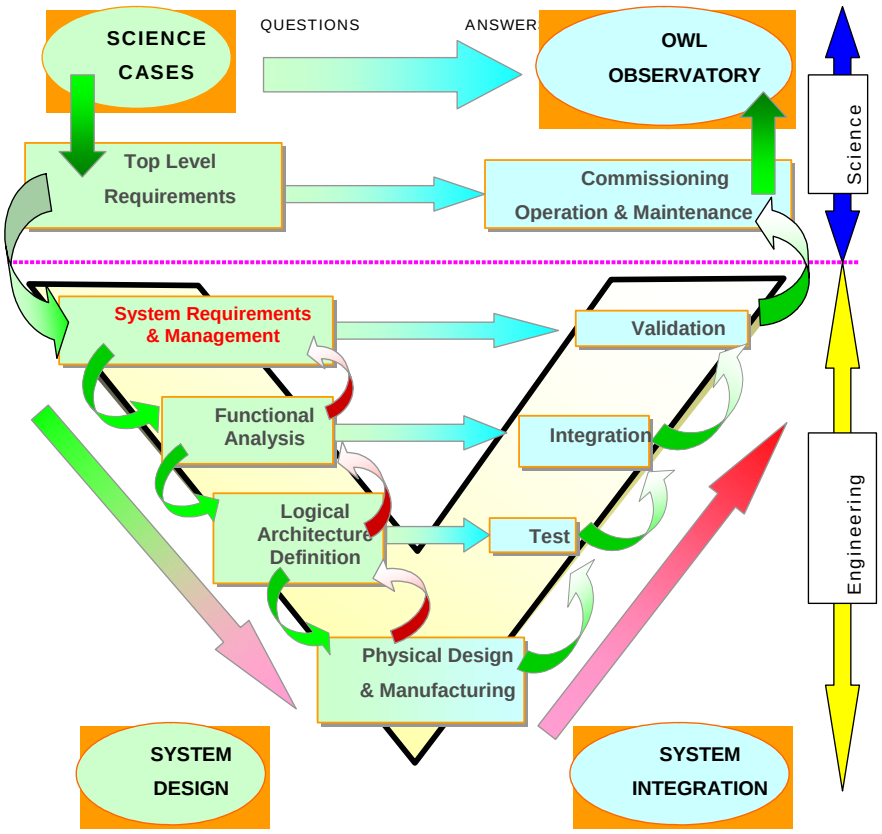

Figure 5-1 : Project V-diagram.

5.3.2.1.1 System Design

5.3.2.1.1.1 Top Level Requirements

The first tasks of the System Engineering are to interpret Top Level Requirements in terms of technical and programmatic characteristics of the the project, and derive level 1 requirements. Level 1 requirements are briefly addressed in section 5.1 and provided in RD41.

5.3.2.1.1.2 System Requirements Management

The role of the System Requirements Management is to provide a unified system engineering environment for

- Controlling requirements definitions and evolution;
- Controlling compliance with requirements;
- The setting and application of validation and certification processes;
- Ensuring optimal use of in-house experience and knowledge;
- Assessing the impact of changes on project performance and schedule;

The System Requirement Management is an iterative process which increases the understanding of requirements and generates a requirement breakdown structure (Figure 5-2).

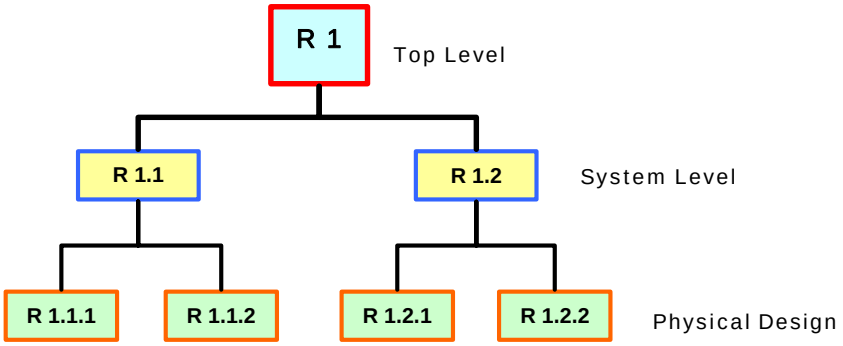

Figure 5-2: Requirements breakdown.

It is an iterative process which encompasses:

- Interpreting Top Level Requirements, translating into system definitions;
- Capture candidate technical and non-technical requirements;
- Breaking down requirements, deriving individual, non-ambiguous specifications ;
- Analysis
  - Categorizing and prioritizing requirements;
  - Establishing database attributes;
  - Establishing allocations and traceability;
  - Reconciling with, capturing decision rationale;
- Formalization
  - Formalizing traceability;
  - Allocating requirements;
  - Configuration Management;
  - Defining Interfaces requirements;
- Changes and impacts management
  - Defining requirements test & validation plan;
  - Providing Compliance and Traceability Matrices;
  - Verifying Traceability;
  - Resolving Discrepancies and facilitating agreement;
  - Establishing requirements baseline;
- Tracking and auditing evolution;
- Defining verification method(s);
- Creating and maintening baseline and definitions.

5.3.2.1.1.3 Functional Analysis

The Functional Analysis defines:

- The functional decomposition of the system;
- The functional Flow;
- The functional Data Flow.

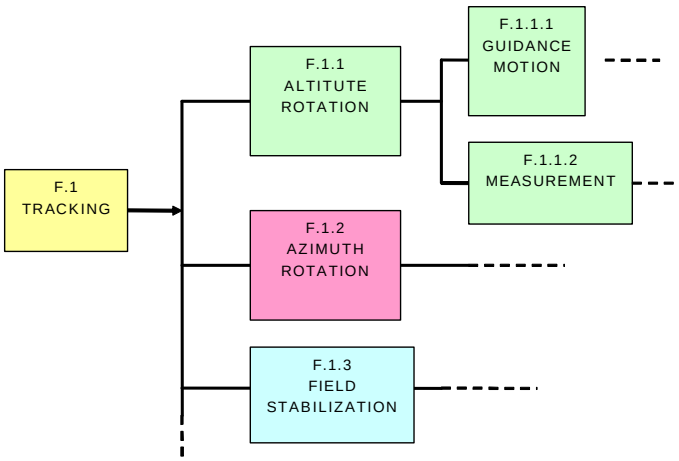

Figure 5-3: Schematic example of functional breakdown.

It is an iterative process which encompasses:

- Defining functional needs and functions requirements;
- Defining Functions, breaking down into sub-functions including their associated requirements;
- Defining detailed operational scenarios;
- Defining functional interfaces;
- Allocating requirements to functions;
- Defining acceptance criteria;
- Establishing and maintaining the functional baseline.

5.3.2.1.1.4 Logical Architecture Definition

The objectives of the Definition of the Logical Architecture are:

- To capture the pre-existing System Architecture knowledge base;
- To provide guidelines and support trade-off studies;
- To optimize Cross-Products System Re-use and Standardization;
- To share a unique system architecture across the project.

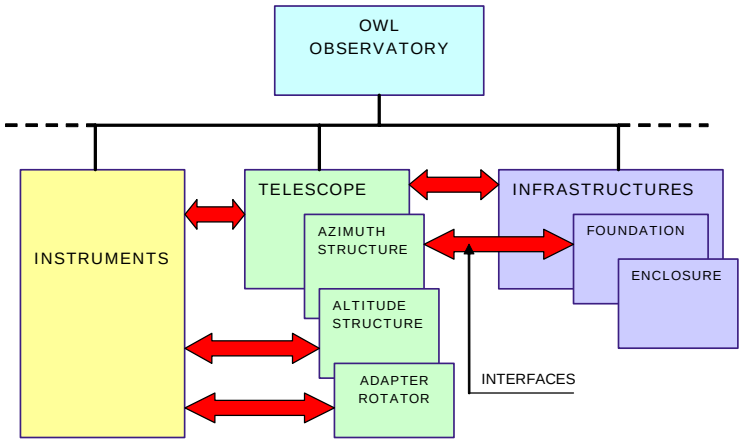

Figure 5-4. OWL architecture example.

It is an iterative process which encompasses:

- Defining the system architecture;
- Allocating functions to system architecture;
- Allocating requirements to system architecture;
- Defining/refining system interfaces (internal and external);
- Defining alternative product and processes solutions;
- Establishing a product architecture baseline

5.3.2.1.2 Physical Design & Manufacturing

Physical Design and Manufacturing is the connecting link between the system design and integration. Activities performed during Phase A of the physical design, manufacturing of prototypes, and experiments belong to the System Design, while other activities such as issuing of low level specifications, detailed development and drawings, belong to the system integration.

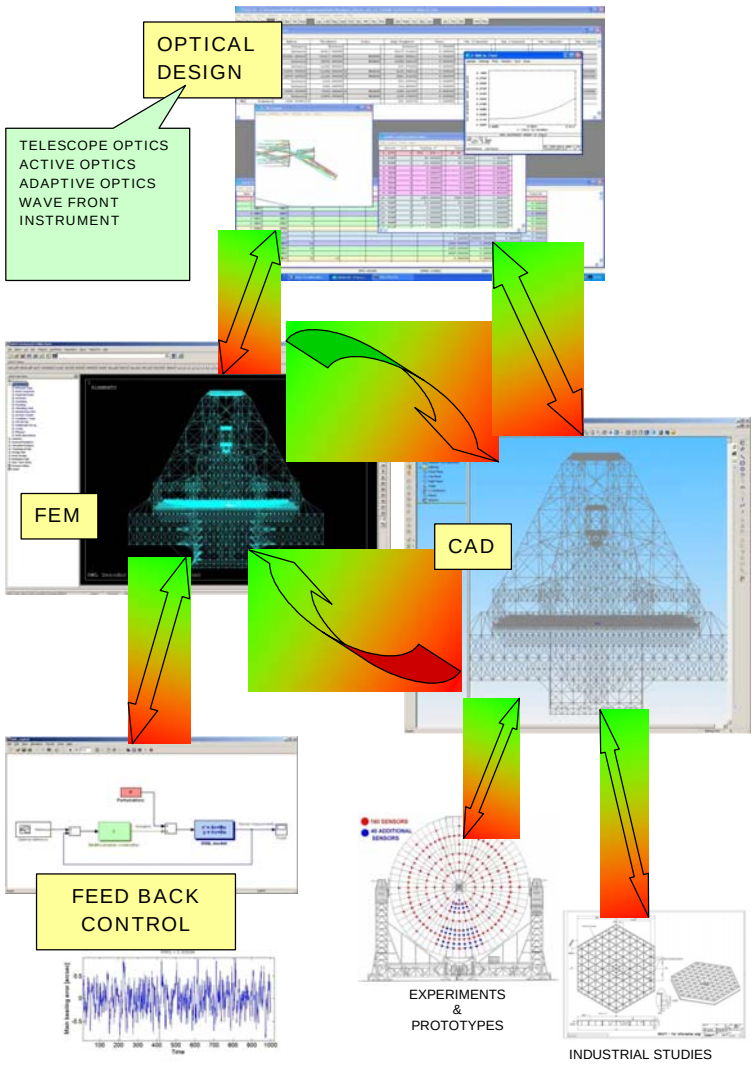

Figure 5-5: Phase A "open loop" design iterations

5.3.2.1.2.1 Physical Design

Phase A - The Physical Design performed during Phase A can be considered an *Open Loop* Design, which involves 3 major disciplines (Figure 5-5).

During this phase the Physical Design provides feed-back to:

- The system architecture;
- The functional architecture;
- The Level 1 Requirements;
- The Error Budget tree and definitions;
- The cost and schedule evaluations;

It also provides a realistic set of disturbances (see section 5.4) and hardware to be implemented into the integrated modelling (see section 5.3.3).

Phase B - The Physical Design to be performed during Phase B shall elaborate, to a higher level of details, on the work performed during Phase A. Optimal use of pre-existing knowledge base is essential. Extensive external studies and prototype activities will be integrated into the Physical Design. In-House detailed development of the Physical Design should be restricted to the fields or disciplines where ESO has mature expertise or where doing so has clear schedule or costs advantages. Interoperability of the results provided by external activities with the ESO tools (see section 5.3.3) used in the Integrated Modelling shall be taken into account.

5.3.2.1.2.2 Manufacturing

Manufacturing of parts and sub-systems shall follow established procedures, and in particular be covered by appropriate documentation (as a minimum, Statement of Work and Technical Specification).

Two types of manufacturing activities are distinguished:

- Manufacturing of prototypes, demonstrators, experiments etc. At the time of writing of this document, this type of activity has already started e.g. within the framework of the ELT Design Study (see 2.12);
- Manufacturing of parts and sub-systems. This type of manufacturing will normally start with Phase C; except where necessary for schedule reasons and where the state of the design allows for advanced manufacturing of such time-critical parts and sub-systems.

  Depending on factors such as technological risk, schedule, cost, and internal knowledge, this type of manufacturing may be based on:

  - Functional specification.
  - Conceptual designs.
  - Detailed design.

Interoperability of data packages, supplied by external contractors, with the ESO Tools (see section 5.3.2.2) used in the Integrated Modelling shall be taken into account.

5.3.2.1.3 System Integration

The System Integration is the result of two processes: the technical integration process per se, and its management at project and system level.

Technical processes include:

- Technical risk management;
- Changes Management;
  - History of the Engineering Changes;
  - Current version;

- Engineering Changes to be implemented in the near future;
- Change requests, Waivers.

Management processes include

- Risk Management (schedule, cost);
- Human resources management;
- Workflow;
- Work Breakdown Structure.
  - Operation Breakdown Structure;
  - Maintenance Breakdown Structure;
  - Cost Breakdown Structure.

To each level of the System Integration corresponds a counterpart of the System Design. These 2 parts are linked by a verification plan which includes Verification Procedures tailored to the Part, Sub-system or System to be verified.

5.3.2.2 Tools

Interoperability of results generated at ESO or supplied by external activities, is mandatory. Efficiency during the System Design, Integration and Operation largely depends on a streamlined exchange of coherent data between disciplines and entities. Appendix 7 lists the major software tools currently used at ESO.

5.3.3 Modelling

Engineering of complex, large scale systems like OWL requires powerful and sophisticated tools within specific technical disciplines such as mechanics, optics and control engineering. In order to reliably simulate interactions, cross-coupling effects, system responses, and to evaluate global performance, integrated modelling is required. Integrated modelling is a numerical simulation technique for dynamic system analysis combining various engineering disciplines. It is considered to be an important tool to evaluate the global performance and error budgets of OWL. Crucial design decisions may be based on the results of integrated modelling simulations. However, the integrated model is not intended to replace the specialized tools and models specific to each individual discipline, e.g. finite element modelling for mechanics, ray tracing for optical design and optimization, dedicated tools for control engineering, etc. Instead, it tries to fill gaps between these specialized models. Consequently, only components and subsystems relevant to global performance should be represented within the integrated model.

It must be noted that integrated model results can be made reliable only if the complexity of the system is gradually increased and if the individual subsystems are extensively tested, and, where possible, validated independently. The subsystems models are individual toolboxes and require clear input and output definitions and clear interfaces with other subsystems.

A modular concept allows easily exchanging subsystems and increasing the level of complexity step wise. Modelling for OWL builds on the experience garnered by ESO with VLT and VLT-I end-to-end modelling.

5.3.3.1.1 Modelling Approach

The main objectives of an OWL integrated model are:

- To quantify the effect of external disturbances, including but not limited to wind load on the telescope structures and mirror segments and assess global performance (image quality).
- To demonstrate the stability and efficiency of parallel local control loops affected by sensor noise, model uncertainties, actuator dynamics and limited stroke within the global dynamic control system.

- To assess the performance of the hierarchical control loops, and especially of the optical reconstructor, which has to manage wavefront corrections and offloads across different control loops.
- To determine the optimal characteristics (bandwidth, stroke) of the individual control loops, including active hardware and metrology systems.
- To support the definition and evaluation of possible operational scenarios.

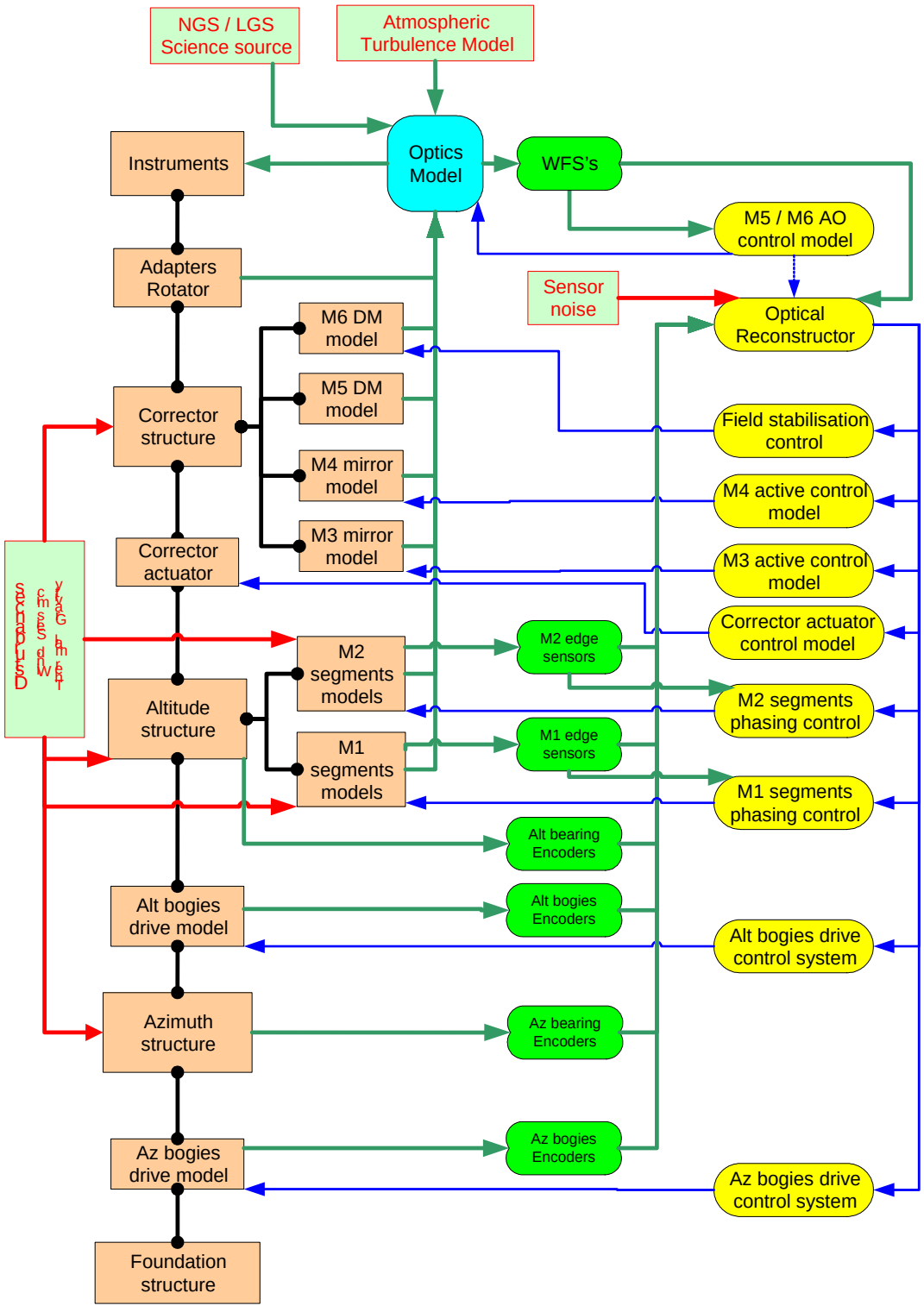

Figure 5-6: Block diagram of the OWL Integrated Model

The simulation model is realized as a state-space model, which is generated in Matlab environment. Depending on the model size and complexity, the simulation will be performed within Matlab or the model will be exported to a suitable modelling environment, which could rely on using a high-end computer or on parallelization using a PC-cluster if required.

Figure 5-6 shows a preliminary block diagram of the OWL integrated model. The diagram layout is driven by the logical architecture of the main structural components. The telescope structure including all relevant masses and elastic components will be modelled in ANSYS FEM. The complete finite element model includes sub-models for the foundation, azimuth structure, altitude structure with the segmented mirrors M1 and M2 mounted, and the corrector structure which supports the mirrors M3, M4, M5 and M6, the adapter rotators and the instruments. The complete structural model is built in a modular way in ANSYS, based on sub-models according to clearly defined interfaces and the desired configuration, e.g. pointing, locked or controlled altitude/azimuth axis, etc. Using static and modal results from the FE-model, the dynamic model of the structure for the integrated model is generated as a reduced modal state space model by using the generation and condensation modules of the SMI toolbox[39]. Input may include, in particular:

a) External forces e.g. wind loads, seismic loads;

b) Force actuators, e.g. bogie drives: a pair of forces acting on two nodes in opposite direction, which are not directly coupled by any stiffness, i.e. the structural model contains a rigid body mode in this specific degree of freedom;

c) Displacement actuators, e.g. segment actuators, M6 tip/tilt actuators: a pair of forces acting on two nodes in opposite direction, which are directly coupled by the actuator stiffness. As such forces cause local deformation, which are in general not very well represented by the first structural modes (of a global model), a static compensation will be used (reflecting the loss of flexibility due to the modal reduction) resulting in a feed-through component in the state space model.

The outputs are expressed as linear combinations of nodal degrees of freedom and their velocities (for friction modelling), e.g. sensor signals, best-fit rigid body motions of mirrors and segments, encoder signals, etc.

The linear optical models are generated in BeamWarrior[40], which can handle both global and local coordinate systems. Hence the coupling between telescope structure and the telescope optics is done in global coordinates to avoid errors caused by transformations of coordinates. The optical model incorporates all relevant optical elements (segmented mirrors M1 and M2, active mirrors M3, M4 and tip/tilt mirror M6) as well as obscurations, and propagates the light from an unresolved point source (science source, Natural Guide Stars or Laser Guide Stars) to the image plane or the pupil. The propagation takes into account the actuation, respectively perturbation, of all optical components, i.e. rigid body motion of segments and all mirrors M3 to M6, and deformation of active mirrors (M3 and M4).

In addition to this, the integrated model includes the possibility to model the effect of active optics, using simplified models for the wavefront sensors and the active mirrors. At the time being, the simulation ends at the focal plane, but possibilities are foreseen to allow adding an instrument model at a later stage.

The adaptive optics is not introduced into the initial Integrated Model, but simplified models and assumption are used to simulate e.g. off-loading of the adaptive mirrors. However, the time history of the wavefront errors can be given to a detailed AO simulation, which currently does not give any direct feedback into the Integrated Model. The bandwidth difference between the Adaptive Optics (AO) and the other telescope control loops, and their impact of AO onto simulation time are the main reason for splitting both simulations. The matter will be reviewed in the design phase, and if necessary, a full coupling implemented.

---

[39] The Structural Modeling Interface (SMI) toolbox developed by ESO and the Technical University of Munich is a Matlab based software which can efficiently reduce large FE models and create state space models used in Matlab.

[40] BeamWarrior is an optical software program which has been developed by ESO and Astrium GmbH in ANSI C language. It is based on geometrical- and wave-optical models and will be extended to simulate segmented mirrors.

The Integrated Model represents the major control loops which impact global performance. These are the main axis control loops, the segment phasing control loops, the field stabilisation, the active optics and the off-loading for the adaptive optics mirrors.

A major component of an integrated model is certainly the disturbance models, where the following ones are the most important for OWL:

- Wind load models describing typical wind disturbance scenarios using either standard spectra, full scale measurements, wind tunnel data, or results from Computational Fluid Dynamics analysis. Both the spatial correlation and the temporal spectrum should be representative for the modelled site (see section 5.4.1.1).
- Quasi-static loads (gravity and thermal deformations) and micro-seismic effects are expected to be less critical for the dynamic simulation of the telescope performance. However, if relevant, these loads can be added at a later stage.
- Suitable atmospheric turbulence models like Kolmogorov turbulence or phase screens, depending on the modelling of the WFS and the design of the optical reconstructor (see section 5.4.1.1)
- Friction models for friction drives.
- Sensors read-out noise, drift and background noise.
- Other errors such as actuators non-linearity, hysteresis, modelling errors.

In order to assemble the components and eventually the complete model, scripts are provided using the relevant configuration information stored in a configuration data file. Scripts and functions for post-processing are provided to generate:

- Optical characteristics such as Point Spread Functions, wavefront visualizations at different locations in the optical train, wavefront fit coefficients, etc.
- Error budget contributions;
- Power Spectral Density of various outputs.

Components, tools and scripts developed within the framework of the ELT Design Study (see A-1.10 and RD525) and which can be easily adapted to the OWL Integrated Model will be incorporated accordingly.

5.3.3.1.2 Architecture Concept

This section addresses the concept of OWL Integrated Model architecture. For all major disciplines the subsystems modules and their interfaces are described in more detail.

The structural subsystem includes the modules listed in Table 5-4. The optics model provides the relation between the inputs and outputs as described in Table 5-5. The control loops represented in the OWL integrated model are listed in Table 5-6.

The full Integrated Model is not built at once, but gradually assembled from otherwise verified and validated components. Intermediate models and simulations (Table 5-7) are used to generate an eventual reliable integrated model (see also Figure 5-6). At the time of writing this document steps no. 1 a) to 3 a) of Table 5-7 are completed.

To ensure credibility and fidelity of the Integrated Model, validation of the global model and of its individual components, subsystems, scripts and tools is mandatory. Typical validation methods are briefly indicated in the Table 5-8.

Mechanical substructure	Input load	Structural Interface	Local control system	Position monitoring	Output
Foundation	Seismic load	Az bogies	Az Bogies control	Encoder	
		Az bearing			
Azimuth structure	Wind load	Az bogies	Az Bogies control	Linear encoders	Bogie normal forces, positions and velocities
	Bogie driving forces	Alt bogies	Alt Bogies control	Linear encoders	
		Alt bearings		Encoders	
		Az bearing		Encoder	
					Central bearing rotation
Altitude structure	Wind load	Alt bogies	Alt Bogies control	Linear encoders	Main bearing rotation
	Bogie driving forces	Corrector support	Corrector actuator control	Encoders	Bogie normal forces, positions and velocities
	M1 actuators	M1 segments	M1 phasing control	M1 edge sensors	M1 edge sensors
	M2 actuators	M2 segments	M2 phasing control	M2 edge sensors	M2 edge sensors
Corrector	Corrector actuator	Corrector support	Corrector actuator control	Encoders	Corrector position
	M3 actuators	M3 support	M3 active control		M3 position
	M4 actuators	M4 support	M4 active control		M4 position
		M5 support			
	M6 tip/tilt actuators	M6 support	M6 tip/tilt control		M6 position
		Instruments			
Instruments		Corrector			Image plane position

Table 5-4. Structural subsystem.

Subsystem	Input	Interface	Output
M1 & M2 segments	Position	M1 and M2 structure	
M3 and M4	Position and surface deformation	M3 and M4 structure	
M5 and M6	Position	M5 and M6 structure	
	Surface deformation	M5 and M6 AO control model	
Instrument entrance	Position	Instrument structure	WFE

Table 5-5. Optic model, inputs and outputs.

Control group	Control loop	Control system / dynamics involved	Sensor	Actuator	Controller
Main axes control	Azimuth axis	Telescope structure	Azimuth encoder	Azimuth bogies	Feedback controller + feed forward friction compensation
	Altitude axis		Altitude encoder	Altitude bogies	
Segment phasing	M1 phasing	M1 segments / Telescope structure	Edge sensors + WFS	Segment actuators	Local feedback + optical reconstructor command
	M2 phasing	M2 segments / Telescope structure			
Field stabilization		M6 unit / Telescope structure or decoupled	WFS	M6 tip/tilt actuators	Feedback + optical reconstructor command
Active optics	M3/M4 active optics	M3/M4 active support model	WFS	M3/M4 active supports	Optical reconstructor command
Optical reconstructor		All control loops above	WFS + edge sensors + AO command	-	

Table 5-6. Control loops.

Step	Major simulation	Substep	
1	Main axes control (tracking) for frontal wind load lateral wind load with pointing to zenith, 30, 45, 60 deg, respectively.	a) b) c)	Altitude axis control Azimuth axis control Altitude + azimuth axis control
2	Field stabilization with M6	a) b)	Fixed backside structure OWL structure
3	Segment phasing with wind load on segments	a) b) c) d) e)	Single segment control (including noise) Small area of segments on a simplified backside structure using segment position information Small area of segments on a simplified backside structure using (fast) edge sensors (including sensor noise models and drift) and (slow) segment position information (WFS)\ M2 segment control on the OWL structure M1 segment control on the OWL structure
4	Main axes control and segment phasing	a) b) c)	Only step 1 + step 3 Simplified Optical reconstructor WFS-based reconstructor
5	Full model	a) b) c)	Without AO off-loading With AO off-loading Increase gradually the level of detail for different components

Table 5-7. Integrated Model - Intermediate steps.

Component	Validation method
Mechanical structure	FE Analyses, hand-calculations, tests
Foundation stiffness	Soil measurements, FE analyses
Bogies friction	Tests
Wind loading	Wind tunnel, full scale measurements, CFD analysis
Seismic loading	Measurements on Paranal
Edge sensors noise	Tests of capacitive sensors
Segments control	APE
Idem + active optics + field stabilization	APE
BeamWarrior	Analyses, comparison with Zemax
ANSYS	Standard FE program
SMI toolbox	FE Analyses

Table 5-8. Integrated Model validation methods.

5.3.3.2 DOORS Model, System requirements management

A software tool will be used to manage the requirements and links between them. The current tool is the *Dynamic Object Oriented Requirements System* (DOORS)

OWL observatory requirements are provisionally broken down into 3 hierarchical levels:

1. Top Level Requirements generated by the Science Cases..
2. System Requirements (Level 1 requirements. Level 2 requirements. etc.)
3. Design Specifications. (Low level specifications, Drawings, Etc.)

Each level shall conform to Regulations, Standards, Acceptance tests.

The high complexity of the project requires a consistent system requirement management, which shall take the following issues into account:

- Limits of individuals to assimilate the whole system down to all its parts.
- Evolution of scientific requirements, technologies, and site characteristics, increasing the number of system or sub-systems options.
- Duration of the project which may reach 20 years. Turn over of personnel is inevitable
- Development of the budget.
- Development of the schedule.

System requirement management is necessary to effectively manage and control the evolving design and integration of OWL observatory. The benefit of the system requirement management are:

- Traceability from scientific requirements to implementation.
- Impact assessment of proposed changes.
- Controlled access to current project information.
- Migration of information between personnel.
- Change control.
- Human resources management.

5.4 Disturbances Characterization

This section provides a overview of OWL System Engineering aspects related to the disturbances which will influence the performance and the integrity of OWL during its complete lifetime. The environment, the system and the human induced disturbances effect the telescope performances, while the survival load cases effect its integrity.

5.4.1 Environment

The disturbances discussed in this section effects the operation of the Telescope and are generated by the natural environment in which the telescope is integrated. The main environmental disturbances are: Wind, Atmosperic Turbulence, Temperature and Microseismicity.

5.4.1.1 Wind

OWL will be affected by wind disturbances in several ways:

- Pointing and tracking by the large scale wind torques on the whole structure.
- Deformations of the structure generating misalignments of the optical components by large scale wind pressures. Here the optical components are regarded as undeformable rigid bodies.
- Deformations of the large segmented mirrors by large scale pressure variations over the area of the whole mirror causing deformations of the supporting cell structure.
- Differential rigid body movements of neighbouring segments caused by pressure variations with scales of the order of a segment.
- Deformations of individual segments due to small scale pressure variations.

For a design of the actuators and the control algorithms which correct the effects of theses disturbances one needs information about the static and dynamic characteristics of the wind loads. For telescopes the relevant range of the turbulence characteristics and scales is extremely wide, including very large scales in undisturbed wind flow (open air) and relatively small scales generated by the interaction of the wind with the structural parts of the telescope or of structures which are in front of the telescope.

The basis for such information will be well established models applicable to the geometry of a telescope in an open air environment (sections 5.4.1.1.1.1 and 5.4.1.1.1.2). In addition, there are three other sources of information. First, computer simulations which can give information about time averaged pressure fields as well as dynamic properties, but are not capable to reach the interesting regime of small scale and high frequency fluctuations (section 6.4.1.1.2), second, wind tunnel tests which have to cope with the large reduction factors of up to 100 imposed by the proposed size of 100 m for the telescope and a size of a model of the order of 1 m in the wind tunnel (section 5.4.1.1.4), and third, full scale measurement at existing large radio telescopes like the 76 meter telescope at Jodrell Bank (section 5.4.1.1.3).

5.4.1.1.1 Wind characterization from literature

5.4.1.1.1.1 Wind Velocity, integral length and turbulence intensity Profiles

In an undisturbed boundary layer the characteristics of velocity and pressure variations can be described by standard models like the von Karman spectrum and the Taylor hypothesis. At any given height *z* above the ground only three parameters are required in the context of these models: first, the time–averaged or mean wind speed $\overline{U}(z)$, second, the turbulence intensity *I,* and third, an integral lenghts *L* describing roughly the size of the largest eddies. For telescopes

like OWL which reach heights of about 100m above the ground level values for these parameters have to given for different heights.

The mean wind velocity can be modelled by a power law. This is shown together with an alternative logarithmic model in Figure 5-7 a surface roughness similar to that at Paranal, a height of the boundary layer of of 270 m, and a velocity of 10 m/s at a height of 10 m.

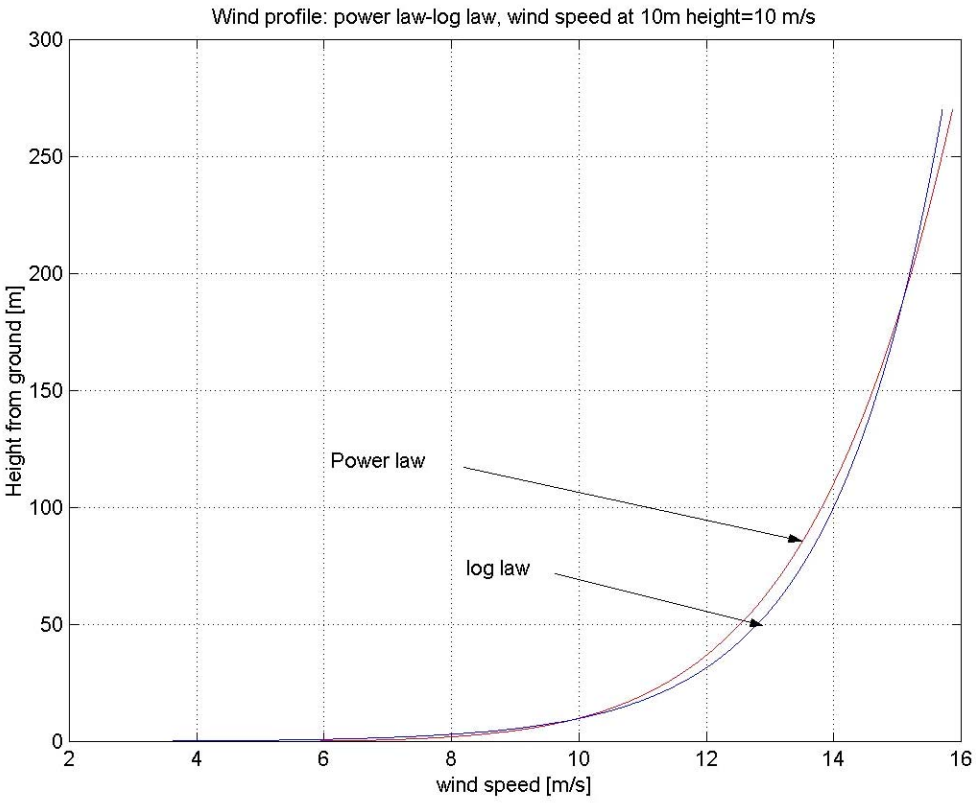

Figure 5-7: Relationship between the height above the ground and the mean velocity

The values for the three parameters $\overline{U}(z)$, *I* and *L* used in this study for heights from 16 to 130 meters are approximately 11m/s to 14 m/s for the mean wind speed, 0.16 to 0.12 for the turbulence intensity, and 80 m to 100 m for the integral length.

5.4.1.1.1.2 Power Spectral Density

Wind action is a stochastic phenomenon which is conveniently described by the Power Spectral Densities (PSD) of the wind speed and the aerodynamic pressure on the surfaces and by correlation functions for these parameters.The pressure field will strongly depend on the orientation of the telescope with respect to the wind direction, the zenith distance of the pointing, and the location on the mirror. One may have the following wind load cases :

- When the telescope is pointing into the wind the characteristics of the incoming wind are not significantly modified on the telescope surface.The power spectra and correlations of the pressure fields should therefore be similar to the ones in the boundary layer.
- When the telescope is pointing away from the wind or towards the zenith there will be recirculation zones at the edges of the mirror with different power spectra and correlation functions.
- Parts of the mirror will be obstructed by the structure supporting the secondary mirror. In some telescopes this structure is a truss sructure and the turbulence behind it may have the characteristics of grid turbulence with an integral length *L* of the order of the grid size.

At the VLT ESO had good experience with using the von Karman spectrum representing the wind-energy content over a large frequency range. The spectrum depends only on the previously introduced parameters $\overline{U}$ *L* and *I*:

$$S_U(f) = (I\overline{U})^2 (4L/\overline{U})(1+70.78(fL/\overline{U})^2)^{-5/6}$$

Two parameters derived from this expression are the zero frequency energy f_0 and the corner frequency f_c. The latter marks the beginning of the the inertial range in which the energy content decreases with a power of –5/3 of the frequency:

$$f_0 = 4LI^2U$$

$$f_c = \overline{U}/(L \cdot 70.78^{1/2}).$$

Adapting the values for the parameters f_0 and f_c the von Karman model can, in a first approximation, also be applied to other types of conditions like for example to the grid turbulence expected downwind from the suppert structures. To properly simulate these situations one has to retrieve information on the integral length and on the turbulence intensity of such flows. This will be done in the framework of the ELT study, WP 8300, and also in the future development of OWL.

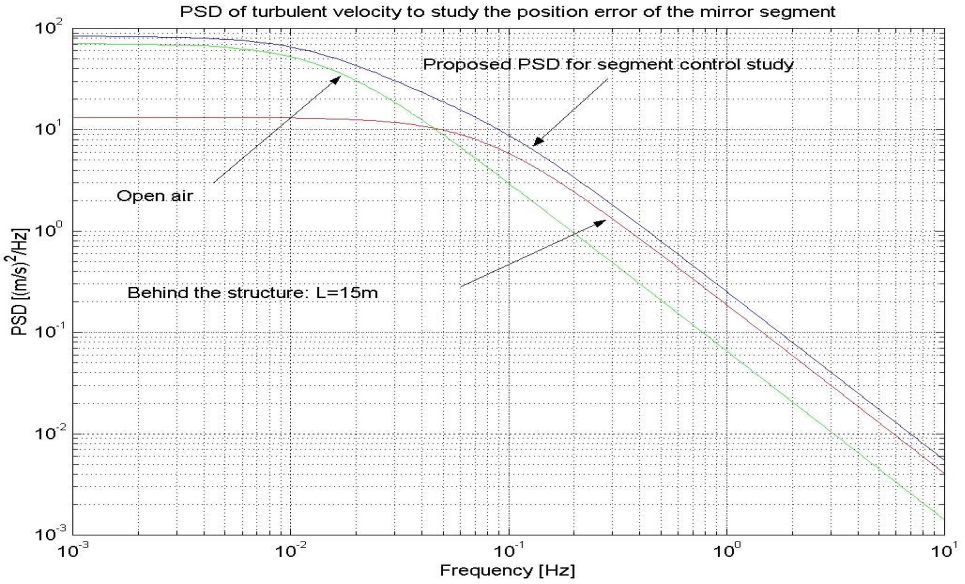

Figure 5-8: Model velocity-PSD close to the M1 segments

For the time being it has been decided to approximate the PSD on the complete structure, on the primary and the secondary mirror by making assumptions about the integral length and turbulence intensity of the flows and assuming that the different flows affecting the loads on the different parts are statistically independent from each other, and that therefore the corresponding PSDs can be added up. These assumptions are certainly not fully justified. However, we believe that they result in somewhat conservative PSDs, overestimating the effects of the wind on the telescope.

Three different PSD have been generated for the study of the control systems of the axes, the primary and the secondary mirror. For the control of the axes five PSD have been generated for five different heights, as well as an average PSD for simplified control analyses.

The PSD of the turbulent velocities at the level of M1 is shown in Figure 5-8 by the curve labeled ‘open air’. For any wind direction most of the segments of M1 and M2 will be behind the

support structure for the secondary mirror and the corrector, that is they will be affected by grid turbulence. The integral length is set to L = 15 m which is roughly the size of the gaps in the grid, and the other parameters to $\overline{U}$ = 10m/s and I = 0.15. The corresponding PSD for M1 is shown in Figure 5-8 by the red curve.

The PSDs of the forces are derived from the PSDs of the velocities:

$$S_F(f) = 4(\overline{F}/\overline{U})^2 S_U(f)\chi_a(f),$$

where F is the static force calculated as $F = 0.5 \cdot c_D \overline{U}^2 A\rho$, c_D is the drag coefficient of the area *A*, and ρ the air density. For the aerodynamic attenuation function χ_a, which models the statistical averaging of the small eddies on large surfaces, the following semi-empirical formula has been used for the design of the VLT and in this study:

$$\chi_a = (1 + 2f\sqrt{A}/\overline{U})^{-1}$$

.

Examples for averaged PSDs for a unit force with A=5, 10, and 8000 m^2, the latter applicable for the control of the main axes, are shown in Figure 5-9

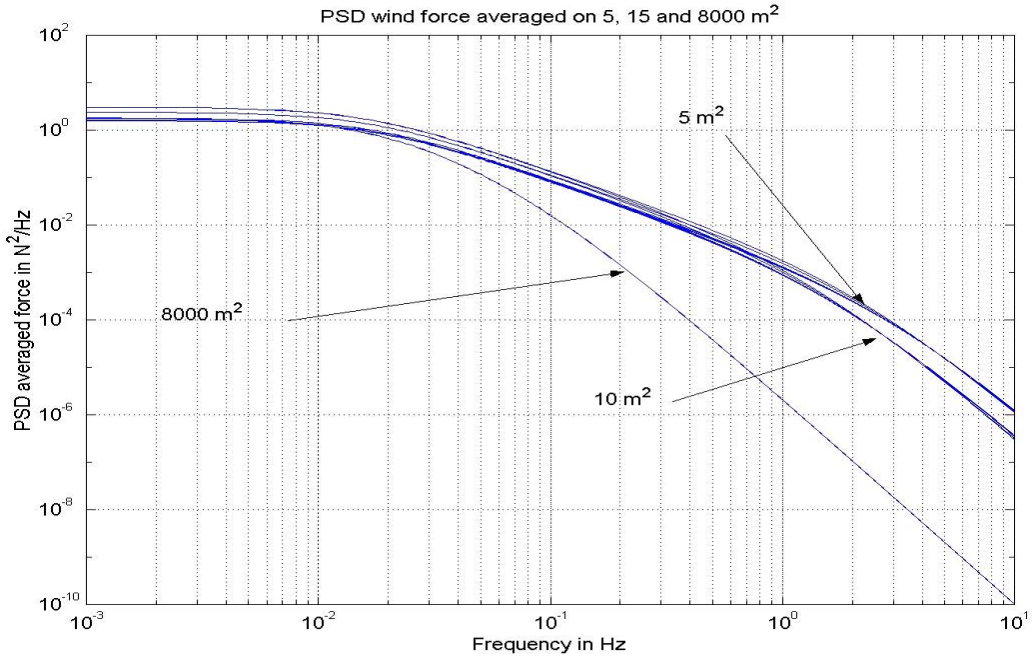

Figure 5-9: Force PSD averaged over three different areas

5.4.1.1.2 Computational Fluid Dynamics (CFD)

Computational fluid dynamics programs can be used to calculate characteristics of flows in arbitrary geometries. One type, the so-called direct numerical simulations (DNS), is capable of delivering both average flow properties as well as dynamic properties as time series and power spectral densities. However, the information is only reliable up to a certain frequency which is determined by the size of the volume elements and the average wind speeds.

During 2001 and 2002 ESO placed an industrial study to calculate PSDs for the actual OWL geometry using the PowerFLOW® code. The largest volume elements had edge sizes 4 m and the smallest ones of 0.4 m. With a wind speed of 10 m/s this limits the frequencies up to which reliable information can be extractred to about 5 Hz. Figure 5-10 shows an instantaneous

pressure field on the primary mirror and the lower parts of the structure for the wind coming from the left. Apparently, the average wind speed is strongly reduced behind the M2 support structure.

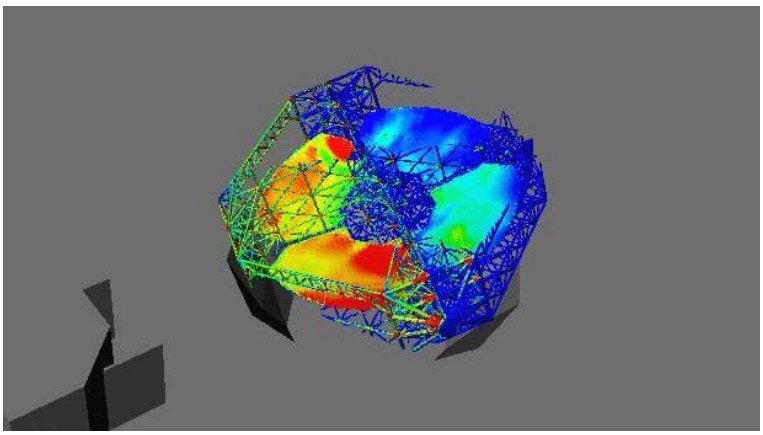

Figure 5-10: Instantaneous pressure field on M1

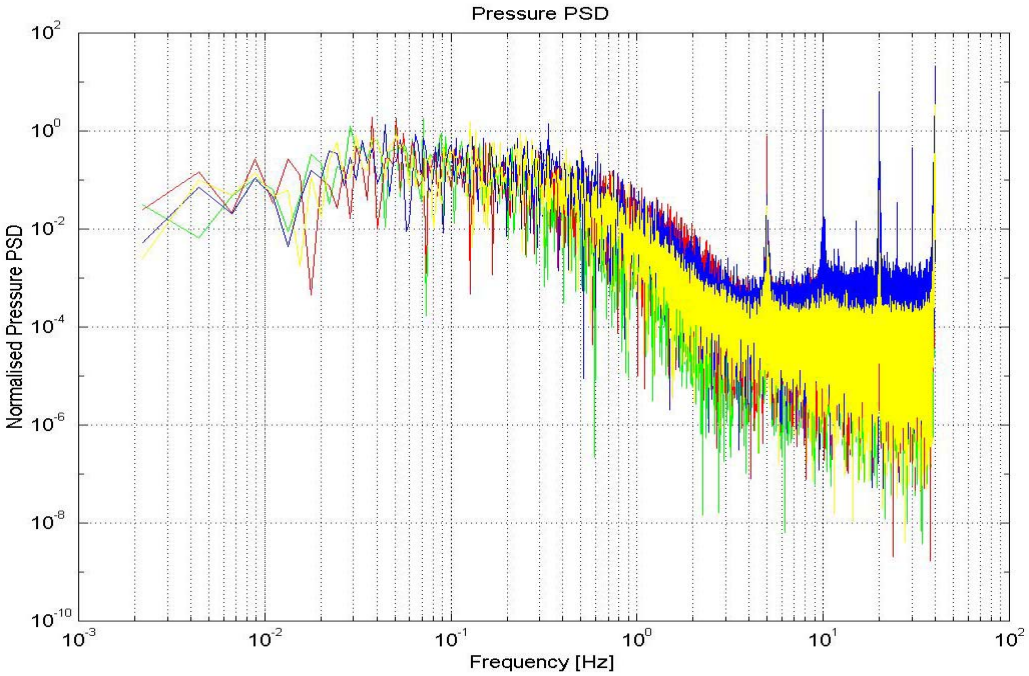

Figure 5-11: Comparison of PSDs obtained by CFD with model PSDs

Figure 5-11 shows the pressure PSD on one location on M1. The maximum frequencies for which the PSD is above the noise level is, as expected of the order of 4 Hz. The corner frequency is a approximately 0.3Hz which is much higher than expected in a free boundary layer. The reason fro this is that the turbulence in the computer simulation is primarily generated by the building in front of the telescope and by structures around M1.

CFD calculations can not give information over the whole range of frequencies which are of interest for the telescope design. However, for large scales it seems to be possible to calculate the corner frequency, if one assumes that for higher frequencies the PSD follows the -7/3 law for the pressures. Small scale PSDs have to calculated with smaller, more detailed models. In the ELT study, Work Package 8300, CFD codes will be used simulate the complete system

including the site, the enclosure and the telescope, and to compare the results with measurements in a wind tunnel.

5.4.1.1.3 Full scale measurements

Pressure fluctuations are measured on the surface of the 76 m radio telescope at Jodrell Bank. The expected load cases, depending on the orientation of the telescope with respect to the wind, have been listed in section 5.4.1.1.1.2.

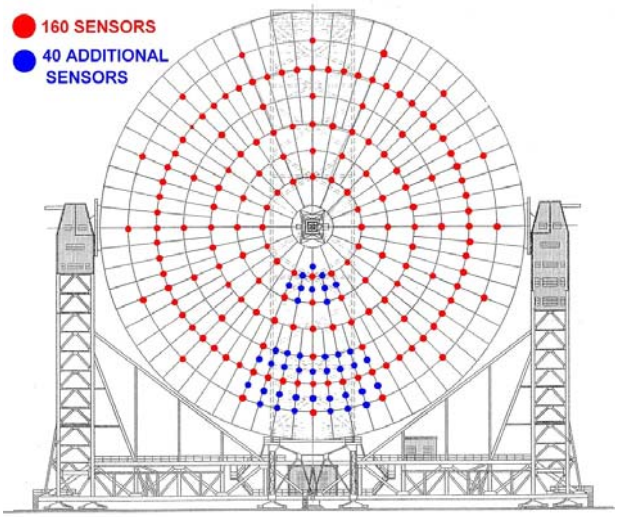

Figure 5-12: JBO Lovell Radio Telescope with pressure sensors

To measure the overall pressure distribution 160 pressure sensors are distributed over the mirror as shown in Figure 5-12.They are located in the gaps between the panels of the reflector. In addition, 40 sensors will be distributed over the smaller areas, to measure pressure variations over a smaller scale. The 76 m radio telescope at Jodrell Bank is an ideal candidate for such measurements.

- It is located on a plain which guarantees that for most of the time the incoming wind in the turbulent boundary layer has reasonably well known characteristics. To measure the wind speed and its orientation and to check the power spectrum an ultrasonic anemometer will be installed on a mast at a height of 20 m. above the ground at a location where the wind flow is not affected by the telescope or other buildings.
- The front surface is not, at least when the telescope is pointing into the wind, obstructed by parts of the telescope structure or other infrastructure in front of it.

ESO is very grateful to the staff at Jodrell Bank for the permission to perform these measurements at their telescope and for generous assistance during the setup of the measuring devices. The sensors have been designed and installed by the firm PSP Technologien im Bauwesen in Aachen.

At a height of approximately 50 m above the ground and a wind speed of 10 m/s the corner frequency of von Karman power spectrum is expected to be at approximately 0.02 Hz. Figure 5-13 shows the power spectrum of the pressure fluctuations measured on the reflector at a distance of 20 m from its center and an angle of 35 degrees counting counterclockwise from the top. The elevation was 58 degrees, the azimuth angle 1 degree, the wind speed 10 m/sec, the wind direction 330 degrees, the sampling 8 kHz, and the total measuring time 73 minutes. The limitation to frequencies of approximately 30 Hz is due to the dynamic range of the measuring chain. The corner frequency is close to the expected corner frequency and the slope in the inertial regime is very close to the expected slope of -7/3, shown in the figure by the red line. The measurements therefore show that at least for the measured configuration the assumptions underlying the von Karman spectrum are satisfied.

Measurements for other configurations and wind conditions will be done in the near future. PSDs at all locations, correlation functions between the pressures at all locations, and correlation functions based on filtered time series, where the high-bandpass filter describes the capability to correct aberrations up to given frequencies, will be calculated.

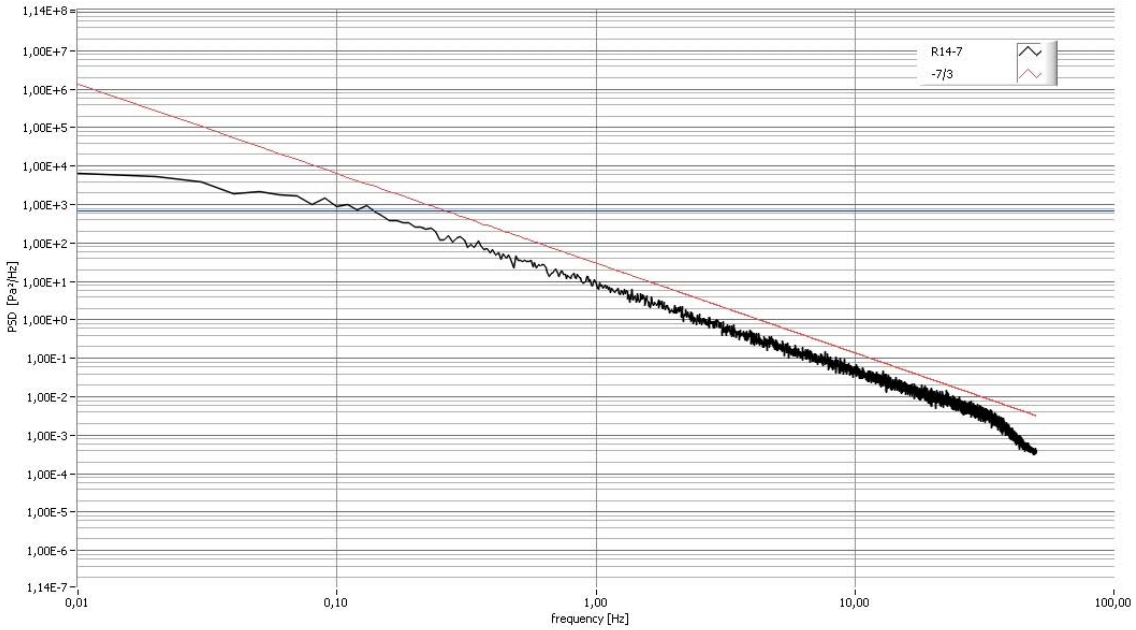

Figure 5-13 : Pressure power spectrum on the reflector of the Jodrell Bank Telescope

5.4.1.1.4 Wind tunnel measurements

The wind speed used in the wind tunnel measurements will approximately be the same as the ones in the full scale measurements. The integral length will be of the order of 1 m and therefore about 100 times smaller than in the full scale measurements. Therefore also the Reynolds number will be 100 times smaller. To keep at least the other important dimensionless parameter, the Strouhal number, at the same value as the one characterising the full scale measurements, the highest detectable frequencies should be 100 times higher than the highest detectable frequencies in the full scale measurements, that is they should be of the order of 1000 Hz. Wind tunnel measurements have been done by two institutes under ESO contract to check up to which frequencies wall pressures can be measured by standard pressure sensors. At both institutes a circular plate with a diameter of 500 mm was placed in a boundary layer wind tunnel with widths of approximately 2.5 m and heights of approximately 2 meters. The plates were inclined by 18 degrees with respect to the horizontal position towards the wind and the center was at 500 mm above the ground. The most important measured parameter was the power spectral density. For frequencies up to 100 Hz the results of the two measurements were in good agreement decreasing in the inertial regime above 10 Hz with a slope of -7/3 as expected from Kolmogorov theory. But, in the equally important interval between 100 Hz and 1000 Hz, the power spectral density was flat or even had a local maximum in one of the measurements whereas it continued to decline with the -7/3 slope in the other measurement. In both measurements the signals were above the noise level over the whole frequency interval. An additional problem was caused by acoustic waves which are created by the wind generator in the tunnel. Fortunately they seem to have well defined peaks and can therefore be eliminated numerically during the processing of the data. Figure 5-14 shows the PSD of pressure fluctuations measured in the wind tunnel at the center of the plate. The curve is an average of 732 measurements of 300 s duration, with a sampling rate of 10 kHz, and a wind speed 20 m/s. The red line shows the -7/3 slope expected from Kolmogorov turbulence in the inertial regime.

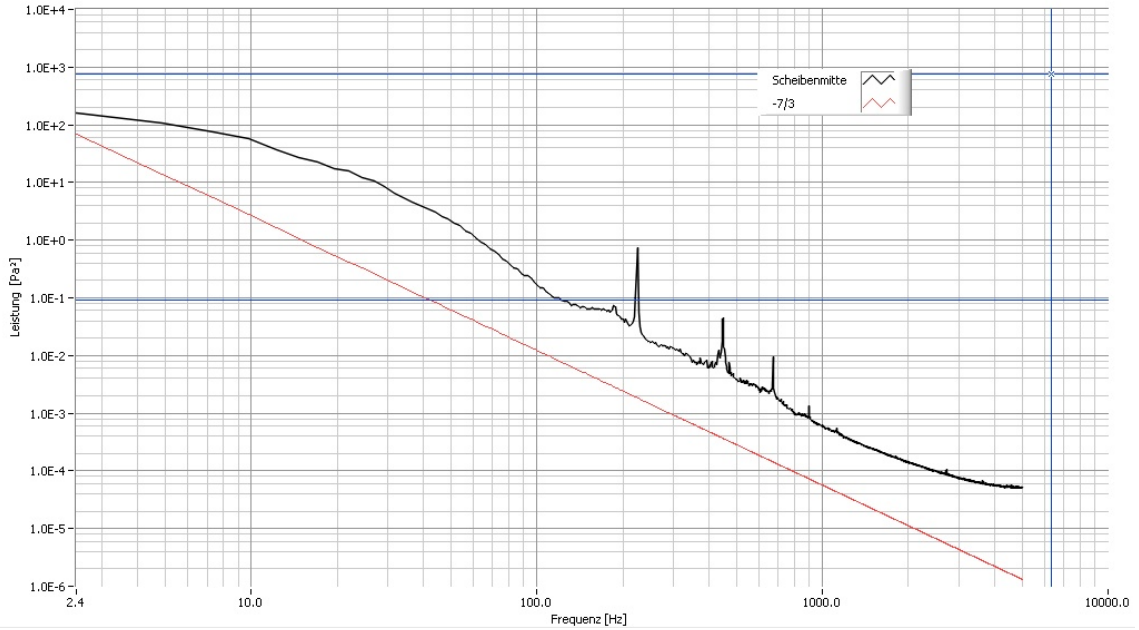

Figure 5-14: Pressure PSD measured in a wind tunnel

The conclusions are that pressure fluctuations can reliably be measured in wind tunnel experiments up to frequencies of approximately 1500 Hz. However, the discrepancies between the two measurements in the frequency interval between 100 Hz and 1000 Hz have to be explained before continuing with wind tunnel measurements using a 1:70 model of the Jodrell Bank Radio Telescope.

5.4.1.2 Atmospheric turbulence (AO)

While wind load is handled by several active systems as detailed in section 5.4.1.1, correcting the effects of atmospheric turbulence is the task of adaptive optics. The overlap area between the two techniques can be described in terms of spatial and temporal frequency range as shown on Figure 5-15. In the case of the atmospheric turbulence, the perturbations on the incoming wavefront are described in terms of amplitude and phase fluctuations.

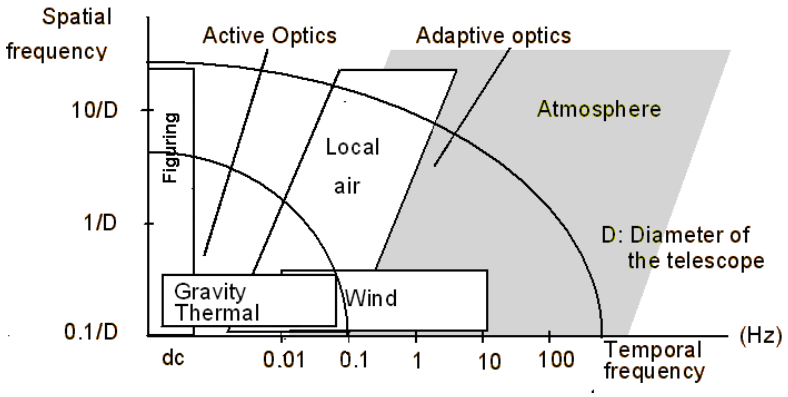

Figure 5-15. Respective areas of action of active and adaptive optical systems as a function of the spatial and temporal frequency of the perturbations

The amplitude fluctuations are the result of flux inhomogeneities in the pupil plane due to interference patterns of waves refracted within the various turbulence layers. This so-called 'flying shadow' pupil plane pattern translates into to the scintillation of the stellar flux in the focal plane. The scintillation cannot be corrected by adaptive optics techniques and is even considered as a noise source in the wave front sensing process. The scintillation increases with

smaller apertures and is highly chromatic. It is generally characterized by an index defined as the long term normalized variance of the flux of a stellar source integrated over the pupil.

Within the inertial range, the wave front phase fluctuations are of Kolmogorov type (i.e.: the power density spectrum of the index of refraction fluctuations decays as the 11/3rd power of the spatial frequency) for any developed isotropic turbulence as encountered in the free atmosphere. Thanks to this, it is sufficient to know the distribution along the path of the index of refraction structure coefficient of the atmosphere Cn^2 ($m^{-1/3}$) to fully characterize the wave front phase perturbations at any wavelength. The inertial range is limited on the one end by the outer scale of the turbulence L_0 (m, typically 10^1 to 10^2, no site dependency proven) and, on the other end, by the inner scale l_0 (m, typically 10^{-3}, site independent) where the energy is turned into heat dissipation because of viscosity forces. For telescopes of diameter (or interferometers of baseline) larger than the outer scale L_0, the effects of the turbulence are less severe than predicted by the Kolmogorov distribution because of a saturation of the power spectrum as shown in the example of Figure 5-16. The characterization of the wavefront for scales comparable to OWL diameter is one of the tasks assigned to the ELT Design Study site monitoring work package (see appendix A-1.9)..

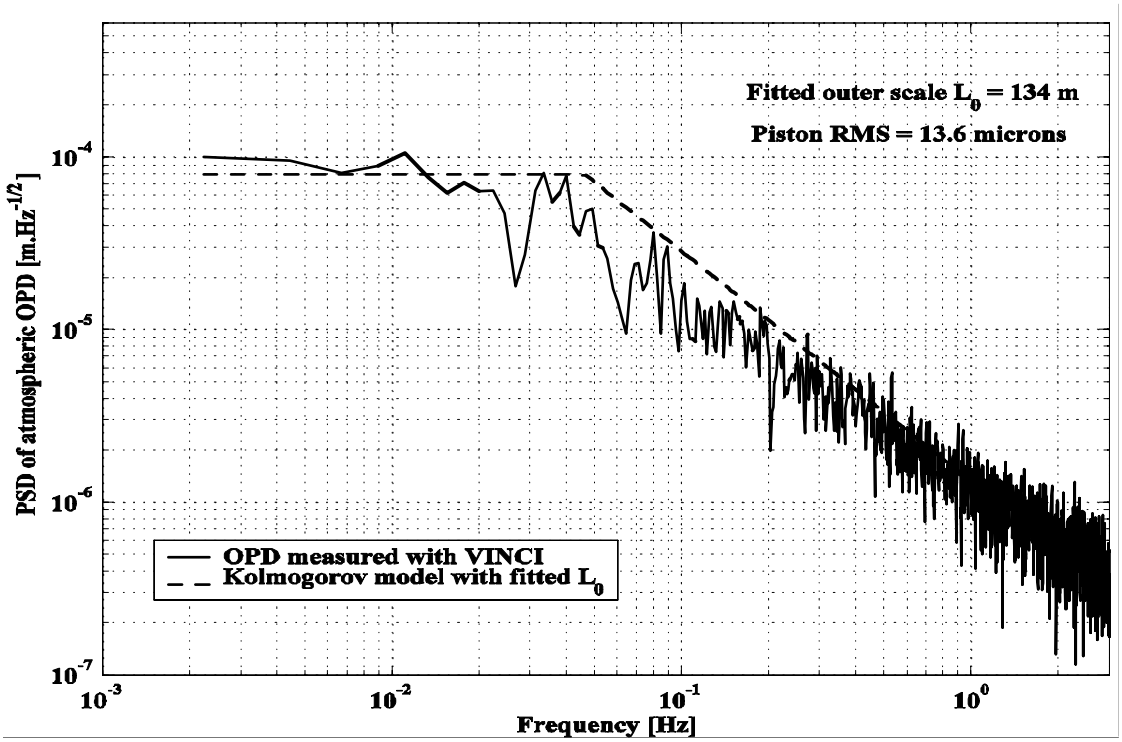

Figure 5-16: VLTI-Vinci Optical path difference power spectrum and Kolmogorov model saturation for aperture distances larger than the outer scale L_0 (credit. E. di Folco, ESO 2004)

For classical adaptive optics techniques which sense and correct the wave front at the entrance pupil of the telescope, it is enough to characterize the wave front by the atmospheric perturbations integrated over the whole light path. In the tri-dimensional space, the relevant parameters are the overall radius of coherence r_0 (m), its coherence time τ_0 (s) and its angular coherence θ_0 (arcsec). While r_0 and τ_0 constrain the design in terms of number of actuators and velocity of the control loop, θ_0 determines both the size of the corrected field and the availability of natural guide stars for wave front sensing measured as sky coverage (%). θ_0 can be generalized to the case of MCAO to explain the larger corrected field of view [123].The limitation in sky coverage can (at least on 8-10m class telescopes) be alleviated by the adjunction of artificial laser guide stars. The wavefront coherence radius r_0 can also be translated into seeing, defined as the focal image angular size (FWHM, full width at half maximum, arcsec) before AO correction. The efficiency of the AO correction is measured in terms of Strehl, which is the ratio of the achieved maximum image intensity to its theoretical value at the diffraction limit. For GLAO systems (see 8.2.2), another metric, the ensquared energy within a given pixel size is

used. In the evaluation of the performance of the proposed AO systems (see section 8), two models for the atmospheric conditions are taken, corresponding to good atmospheric turbulence conditions (about 20-30% best conditions) and bad turbulence conditions (~70% worst conditions). These models have different r_0, θ_0, τ_0 to allow to see the impact on the performance of the AO.

For designing more elaborated, or partial adaptive optics systems based on techniques such as MCAO (see 8.3.1) and GLAO (see 8.2.2), it is necessary to know the vertical distribution of the atmospheric C_n^2 (h). The instruments and methods developed for this purpose are described in section 14.2.3.

For reference, waiting for the final site selection, median values of the various atmospheric parameters expected at a suitable candidate are given in Table 5-9

Atmospheric Turbulence Parameters	Range of median
Seeing (arcsec at zenith and 5000A)	0.6-0.8
r_0 (m at zenith and 5000A)	0.13-0.17
tau_0 (s at zenith and 5000A)	0.003-0.010
$theta_0$ (arcsec at zenith and 5000A)	2-4

Table 5-9: Typical expected median values of the atmospheric turbulence parameters based on the experience at existing observatories.

The effect of L_0 on the AO is to reduce the required stroke for the deformable mirror(s), since low spatial frequencies (which would carry large amplitudes) are reduced. Also, for a telescope the size of OWL, the seeing limited PSF changes significantly due to L_0, and a very small diffraction peak (containing only a very small fraction of the energy) can appear [122]. In the AO simulations, the Paranal median value of 25m for L_0 was taken [121]. The effects of L_0 on the AO performance is studied in RD26.

5.4.1.3 Temperature, humidity, rain, snow, ice, dust, radiation

As the observatory site has not been selected yet, the environmental conditions at Paranal are assumed. Apart from the temperature variation, which is defined in more detail in the next chapter, Table 5-10 summarizes the relative humidity, rain fall, snow and ice height, dust as well as the air pressure and air density conditions on Paranal.

Temperature variation - The objective of the Paranal temperature measurements described in RD34 is to provide experimental information to calibrate the thermal models (see section 9.5.3) which are used during the following project phases:

- System Design.
- System Integration.
- Commissioning.
- Operation.

In the Paranal experiment the temporal surface temperatures of a typical part of steel pipe, as used in the OWL framework structure (1m diameter, 10 mm wall thickness, 2 m long) has been measured. The steel pipe was placed on the telescope platform of the Paranal observatory, and the evolution of its temperature over several days measured at various points and under different conditions. Also environmental parameters, such as wind speed and direction, relative humidity and ambient temperature were measured simultaneously, to be able to correlate them with the pipe temperatures

The pipe was placed on a 1,6 m high steel structure, see Figure 5-17. Measurements were done in different configurations:

- Exposed to sun radiation, with inner air volume stagnating.
- Exposed to sun radiation, with inner air flow.
- Protected to sun radiation, with inner air volume stagnating

The measurement results also aimed at evaluating the time the passive system needs to reach thermal equilibrium between ambient and pipe surface temperature. Figure 5-18 shows a typical temperature evolution over several days at the ambient conditions shown in Figure 5-19. As expected the inside and outside surface temperatures are very close to each other. Moreover, soon after the sunset the steel structure temperature goes below ambient temperature.

Environmental condition	**Paranal**
Relative humidity operational range Max. relative humidity (with condensation)	5 % to 90 % 90 %
Max. rain precipitation in 1 hour Max. rain precipitation in 24 hours Rainfall in 1 year Wind speed for blowing rain	100 mm N/A 100 mm 18 m/s
Max. operational snow height (enclosure only) Max. survival snow height (enclosure only)	65 mm 65 mm
Max. operational ice height (enclosure only) Max. survival ice height (enclosure only)	50 mm 50 mm
Dust contamination	TBD
Sun radiation (enclosure only)	1120 W/m^2
Air pressure Air density	750 mb +/- 50 mb 0.96 kg/m^3

Table 5-10: Various environmental conditions on Paranal.

Figure 5-17: Steel pipe exposed to sun radiation

The steel pipe has been painted in matte-black on the outside surface. OWL will cope radiation effects (heating during the day and cooling during the night) by a proper selection of surface treatments and paints. The telescope structure will be treated with low emissivity coating/paint The design of the observatory platform will ensure low solar absorption during the day (white concrete or white traffic paint).

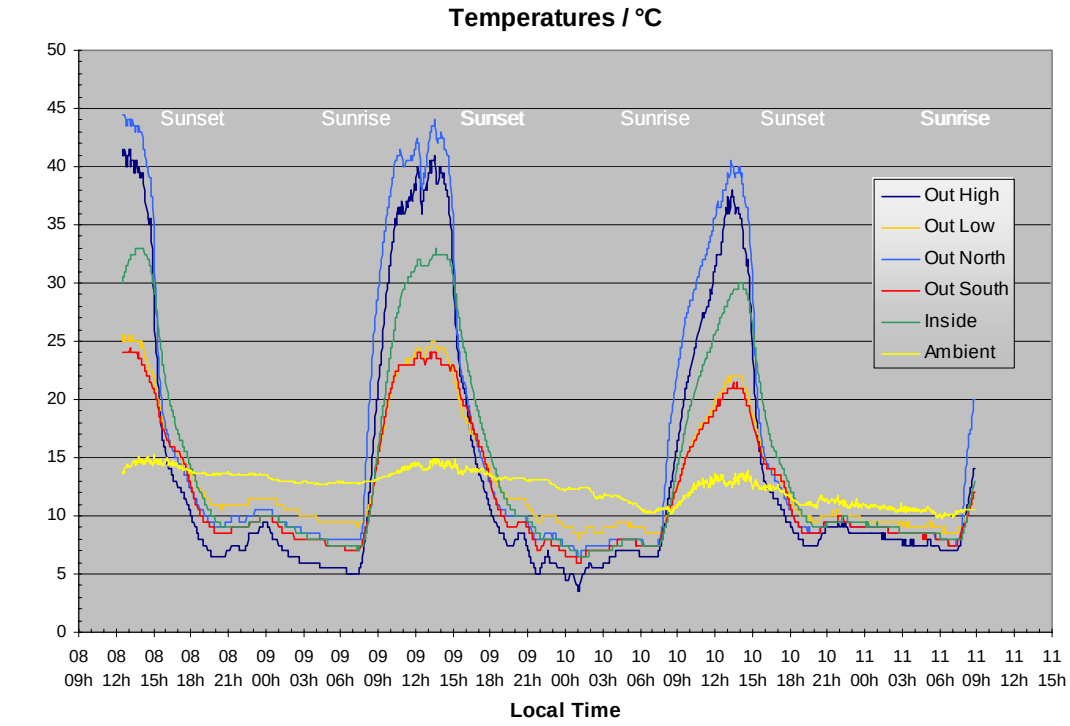

Figure 5-18: Temperature evolution

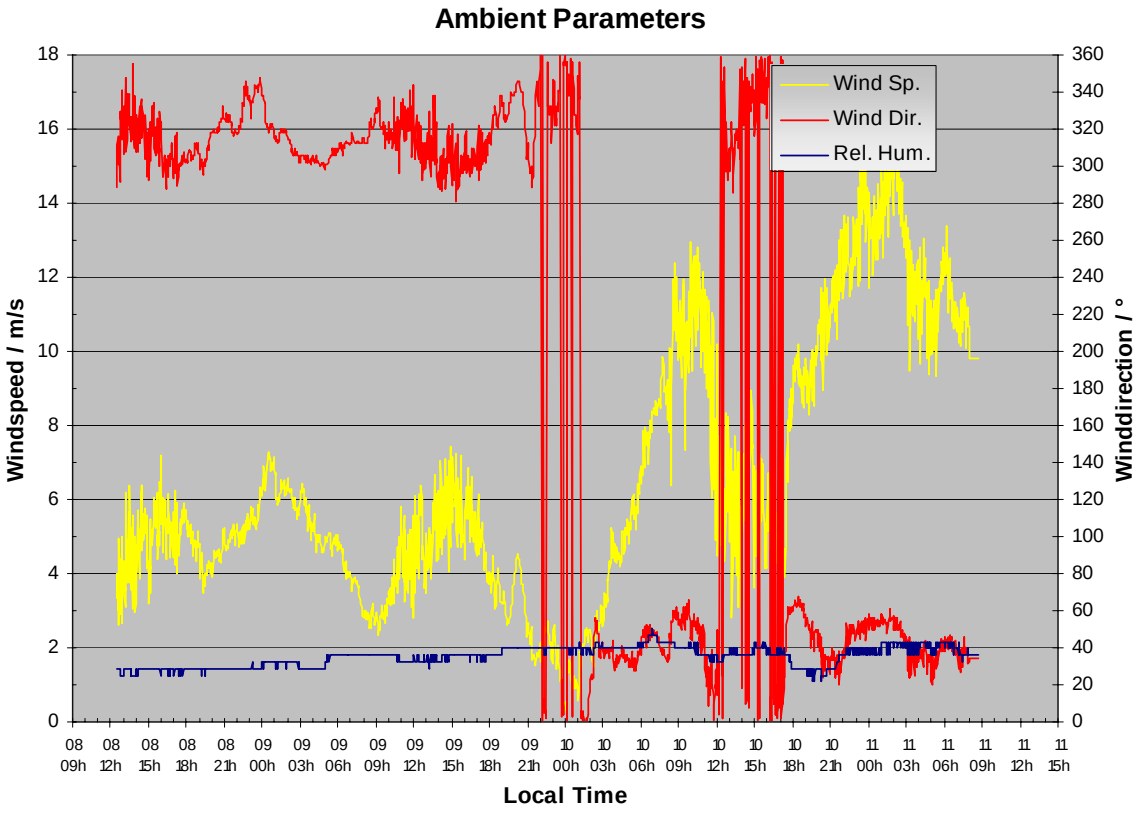

Figure 5-19: Environmental conditions.

The temperature definitions (see Table 5-11) to be applied for the thermal analyses are based on the Paranal conditions and the thermal pipe experiment.

Environmental condition	Paranal
Temperature operational	0 to +15 °C
Typical temperature gradient at night time	0.7 °C/h
Average air temperature difference between day and night	4 °C

Table 5-11: Temperature conditions on Paranal.

5.4.1.4 Microseismicity

The microseismic noise is a complex disturbance which is transmitted to the telescope via the foundation and may affect the operation of the telescope. The main sources of this phenomena can be natural, human and system induced. Detailed analyses on microseismicity will be performed progressively according to the available data, which will be acquired in the next phases.

5.4.2 System Induced Disturbances

Once the system is put into operation, it will inevitably generate self-disturbances in the various sub-systems. Typical sources of these disturbances are electro-mechanical devices installed on the telescope itself or in its vicinity. Detailed analyses will be performed progressively according to the available data, which will be acquired in the next phases.

5.4.3 Human induced disturbance

An observatory is a manned base. The activities of several individuals and the services provided for thems will introduce disturbances to the environment and to the operation of the telescope. The positive experience gained at the Paranal Observatory will be fully used for defining measures to minimize the impact on the performance of the telescope.

5.4.3.1 Camp, hotel, sewage, transport, etc

The hotel will host personnel working during day time as well as astronomers on duty at night This will cause activities going on almost around the clock.that need to be coordinated or restricted to avoidserious impacts on the observations. To minimise interactions between the support installations like the hotel, the offices, and the workshops on the one hand and the telescope on the other hand, the two areas will be located at different heights and as far apart as economically reasonable.

Starting at sunset, the transport of persons and goods will be restricted inside the observatory area and forbidden on the telescope platform. The disturbances to the environment introduced by sewage and sanitary installations will be avoided by using closed loop treatment plants as on Paranal.

To avoid vibrations spreading to the telescope area any equipment generating vibrations will be mounted on independent foundations and on damping devices to reduce spourious noise to specified levels.

5.4.3.2 Power generation

Power generation, depending on which system will be selected, is a source of acoustic, thermal and vibrational disturbances.

OWL will probably require at total power supply of 14 MW, which can be supplied by four power generators designed to produce 4.5 MW each at an altitude of 300 m. As for Paranal, the installation will be far from the telescope area in an acoustically insulated enclosure. The

transformers close to the area of the technical buildings will be mounted on mechanically damped foundations.

5.4.3.3 Light pollution

At sunset all the buildings will be obscured using blinders. Any vehicle traffic will use parking lights only. For this reason the roads will be equipped with weak side lights radiating at road level only.

5.4.4 Survival load case of the opto-mechanical elements

The characterization of the survival load case depends on the environmental conditions of the observatory site. As the site has not yet been selected, two typical observing sites with different environmental and geotechnical characteristics are used as a basis for the characterization of the disturbances and the definition of the load cases:

Site 1: Ventarrones 2837 m, Northern Chile

Site 2: Observatory Roque de Los Muchachos, La Palma in the Canary Islands

This selection does not imply a pre-selection of these sites.To guarantee the safety of the system and the subsystems under survival loads detailed stress analyses have to be performed in more advanced design phases of the project. The stress analysis shall combine the individual design loads and conditions according to standard norms, whereby for specific subsystems or components different load combinations may apply.

The result of the load combinations shall be evaluated for the maximum stress criteria, e.g. yield strength for metallic material, rupture strength for brittle material (glass, glass ceramics) and CFRP strength criteria for CFRP material. More details about the criteria for mechanical acceptability can be found in RD49.

5.4.4.1 Earthquake

Apart from relatively small earthquakes which might occur several times during the lifetime of the observatory the following two types of earthquake categories characterized by their probability of occurrence have been defined:

- Operating Basis Earthquake (OBE): Earthquake of moderate size but with high probability of occurrence
- Maximum Likely Earthquake (MLE): Earthquake of large magnitude, but with lower probability of occurrence

The characteristic earthquake parameters are defined in Table 5-12. Based on these parameters the acceleration response spectra are determined according to the currently applicable European Standard (Eurocode 8, “Design of structures for earthquake resistance”, Part 1, BS EN 1998-1:2004). Different damping ratios are assumed for the telescope structure and the enclosure. Due to its larger deformations the enclosure structure can dissipate more energy than the telescope which justifies the higher damping ratio of 2 %. The damping ratio for the telescope structure under MLE and 0.34 g is assumed to be 1.5 %.

The earthquake and geotechnical characteristics of site 1 are assumed to comply with those specified on Paranal. The corresponding disturbances have the worst horizontal and vertical response spectra for the telescope structure, shown in Figure 5-20. The maximum spectral accelerations in this case are 1.14 g in vertical and 1.06 g in horizontal direction, respectively. According to the spectra the frequency bands for the peak accelerations are between 2 and 6.3 Hz for the horizontal and between 6.3 and 20 Hz for the vertical component. In order to take into account the magnification effects of the structure’s resonance frequencies, the final verification of the earthquake compliance shall be done with the Response Spectrum analysis technique as defined in Eurocode 8.

In addition it has to be taken into account that the earthquake may occur at any configuration of the telescope and the enclosure.

Subsystems like instruments, mirror units, electronic boxes, handling devices, etc. must also be verified against earthquake events occurring at the observatory. In many cases this verification can be carried out independently from the telescope structure. The appropriate requirements and method are described in RD49.

Characteristics	OBE		MLE	
	Site 1	Site 2	Site 1	Site 2
Peak ground horizontal acceleration	0.24 g	0.04 g	0.34 g	0.04 g
Probability of exceedance	50 %	50 %	10 %	10 %
Repetition period	25 years	25 years	100 years	100 years
Duration	65 s	65 s	200 s	200 s
Ground type[41]	A	A	A	A
Damping ratio[42] (Telescope structure)	1.0 %	1.0 %	1.5 %	1.0 %
Damping ratio (Enclosure structure)	2.0 %	2.0 %	2.0 %	2.0 %

Table 5-12: Earthquake characteristics for two different sites.

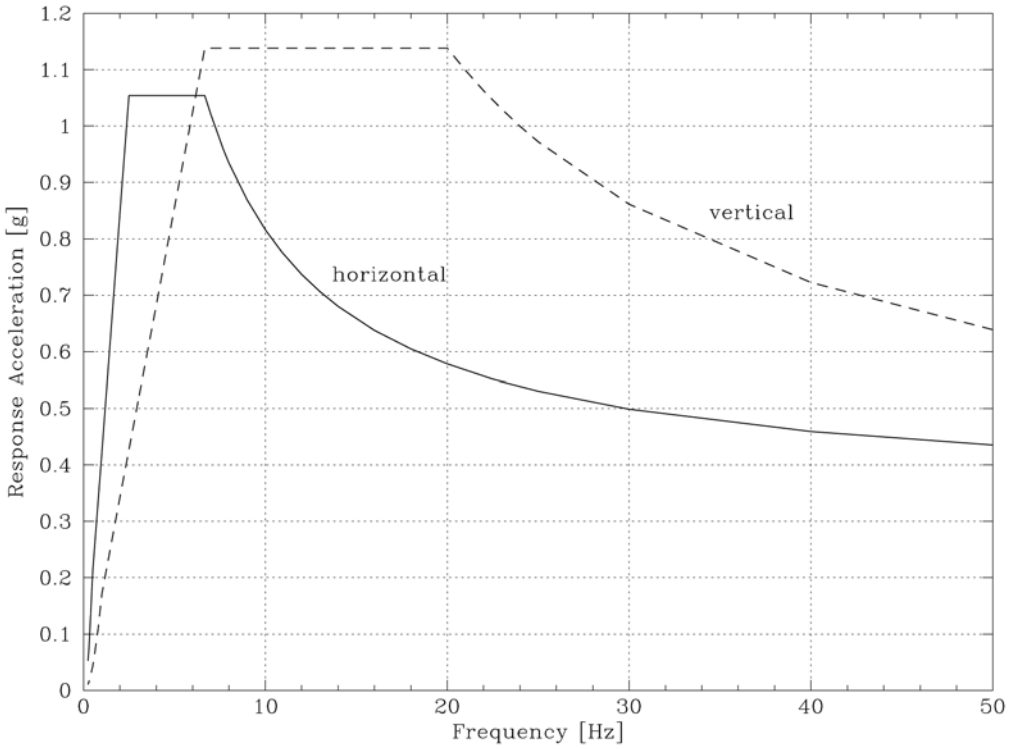

Figure 5-20: Acceleration response spectrum (Telescope, MLE, 0.34 g, 1.5 % damping).

5.4.4.2 Wind

Subsystems like the telescope and the enclosure structure shall withstand the survival maximum wind speeds. The enclosure shall protect the telescope and return to nominal performance once the wind speed has returned to its operational level. As listed in Table 5-13 different survival wind speeds are specified for the telescope and the enclosure for both sites. These survival wind speeds have been estimated from measurements performed on these

[41] Ground type A is defined as rock or other rock-like geological formation.

[42] Damping ratio is the percentage of critical damping.

sites. The values in the table are 1.5 times the highest wind speeds ever recorded since the beginning of the site testing.

Subsystem	Survival wind speed in [m/s]	
	Site 1	Site 2
Telescope	27	27
Enclosure	51	67

Table 5-13: Survival wind speed for telescope and enclosure structure.

It is assumed, that at wind speed above 27 m/s the enclosure is fully closed and protects the telescope. The force distribution caused by survival wind loads may be derived from applicable standard norms or from adequate CFD analyses. For the verification of the safety under survival loads hese forces may be applied as quasi-static loads.

5.4.4.3 Temperature

The performance of the telescope and the subsystems has to be verified under extreme temperature conditions which may occur during the installation of the telescope and of the enclosure as well as during the operation. The latter may occur as an accidental scenario, e.g. the enclosure cannot be closed during the day. Table 5-14 summarizes the survival temperature conditions for site 1 and 2 for both the telescope and the enclosure structure.

Subsystem	Air Temperature survival	
	Site 1	Site 2
Air temperature [°C]	-10 to +30	-10 to +35
Sun radiation [W/m^2]	1120	1200

Table 5-14: Survival temperature conditions for the telescope and enclosure structure.

5.5 Error budgets

OWL error budgets shall include, as a minimum, image quality, pointing, emissivity and reliability budgets. The emissivity budget is provided in section 6.3.4 and will not be recalled here. At the time of writing of this document, the pointing budget has not been addressed yet; there is however no à priori concern about meeting the requirement of 1 (goal 0.5) arc second RMS (see RD41). Establishing a sound and realistic reliability budget requires more studies then available yet, in particular in the area of adaptive mirrors. Those are either ongoing or planned for in the design phase. Preliminary analysis have however been performed with a view to understanding the system susceptibility to individual failures, e.g. phasing failures (see RD21) or failures in the segments maintenance line (RD5).

In view of the different possible modes of operation (seeing-limited, single or multi-conjugate adaptive optics, extreme adaptive optics, etc.), several distinct optical quality budgets must be drawn, including:

1. Optical quality in “blind” mode i.e. without on-sky metrology. The underlying scientific rationale is daytime, sub-mm observations. In blind mode, wavefront control loops are

closed on internal metrology (phasing, pre-alignment) or iterated on the basis of look-up tables. The optical quality budget in blind mode applies on-axis only.

2. Optical quality in seeing-limited mode. This mode assumes that all non-adaptive wavefront control loops are closed (on local metrology or on-sky, as applicable). The optical quality in seeing-limited mode not only sets the performance requirements for such science applications that do not require adaptive correction, but also the maximum allowable telescope residual errors that will have to be compensated by adaptive optics in more demanding modes. The optical quality budget in seeing-limited mode applies to the total science field of view (3 arc minutes). Active optics wavefront sensing in the entire 10 arc minutes field of view must however be taken into account when assessing image quality within the science field of view.

3. Optical quality in Single Conjugate Adaptive Optics (SCAO) mode. This mode assumes that all non-adaptive wavefront control loops are closed (on local metrology or on-sky, as applicable) first, followed by the single conjugate adaptive optics loop, with M6 as the correcting element. The M6 adaptive shell is assumed to compensate not only for atmospheric turbulence but also for

   3.1. quasi-static residual errors with a spatial frequency of up to ~0.5 m^{-1} in the entrance pupil i.e. 50 cycles per pupil diameter[43];

   3.2. fast, small amplitude (less than ~0.5 arc seconds RMS) tracking errors.

   The optical quality budget in SCAO mode applies on-axis only. Active optics wavefront sensing in the entire 10 arc minutes field of view must however be taken into account when assessing image quality on-axis.

4. Optical quality in Ground Layer Adaptive Optics (GLAO) mode. The active elements and assumptions are the same as in SCAO mode, with the following exceptions:

   4.1. overall quality requirements are relaxed as this mode aims at seeing reduction, not diffraction limited resolution;

   4.2. the GLAO mode budget applies to a 6 arc minutes field of view (diameter) and includes PSF stability.

5. Optical quality in Multi-Object Adaptive Optics (MOAO) mode. At the time of writing of this document the underlying requirements still need to be clarified. It is expected that the MOAO error budget will closely resemble the GLAO one, with tighter allocations for diffraction-limited resolution but extended correction capability for very high spatial frequency errors.

6. Optical quality in Multi-Conjugate Adaptive Optics (MCAO) mode. This mode assumes adaptive compensation with M6 and M5 adaptive shells. The MCAO mode budget applies to a 3 arc minutes field of view (diameter) and includes PSF stability. As for SCAO, quasi-static errors up to 50 cycles per pupil diameter are to be compensated by the AO units. The MCAO mode includes PSF stability requirements.

7. Optical quality in Extreme Adaptive Optics (XAO) mode. This mode assumes first-order adptive correction by M6 shell, and post-focal, very high spatial frequency AO correction. The XAO budget applies to the on-axis image quality only. Active optics wavefront sensing in the entire 10 arc minutes field of view must however be taken into account when assessing image quality within the science field of view. The XAO budget closely resembles the SCAO one, however with extended correction capability for minor quasi-DC residuals up to 250 cycles per pupil diameter[44].

The structure of the error budget is identical for all modes and given in Table 5-15. The budget is broken down according to major subsystems and functions. A subsystem allocation (e.g. M1 error budget) does not include errors associated to related control systems (e.g. phasing), which

[43] Or one actuator every ~1-m. For comparison, the VLT active primary mirrors are theoretically able to provide correction up to ~5 cycles per pupil diameter and have an optical quality of ~30 nm RMS wavefront (best 17 nm) after active correction.

[44] Or one actuator every ~20 cm in the entrance pupil.

are treated separately in the error allocation of this specific control system. In other terms, the M1 error budget assumes a perfect phasing; phasing residuals are to be found in the allocation to phasing, and include environmental factors e.g. wind. The error budget before closing said control system sets the maximum amplitude that will be passed on to it. Contingency is managed at system level.

No	Position
1.	As-designed
2.	M1
3.	M2
4.	M3
5.	M4
6.	M5
7.	M6
8.	Corrector (rigid body)
9.	Environment
10.	Tracking
11.	Non-AO wavefront control
11.1.	Pre-alignment
11.2.	Phasing
11.3.	Active focusing
11.4.	Active centring
11.5.	Active surfaces deformations
11.6.	Field stabilisation
12.	Ground layer AO
13.	Single conjugate AO
14.	Dual conjugate AO
15.	Multi-Object AO
16.	Extreme AO (XAO)

Table 5-15. Image quality budget - main positions.

A preliminary image quality budget in SCAO mode is given in Table 5-16. It is potentially the most demanding as the adaptive optics correction capability in this mode provides limited compensation –if any- for relatively high spatial frequencies such as the print-through of M1 segments support, the residual M4 polishing errors. This budget is the result of a first top-down iteration. Error budgets in the other modes are currently under elaboration.

Table 5-16. OWL Image quality budget in SCAO mode.

OWL ERROR BUDGET v. 0.1 **System error budget after closing non-adaptive and single-conjugate adaptive loops**			**Active loops**	
CRITERION RMS wavefront amplitude **UNITS** nm **OFF-AXIS** 1.5 arc minutes	**On-axis**	**Off-axis**	X	Pre-alignment
			X	Phasing
			X	Active focusing
			X	Active centring
			X	Active surfaces deformation
			X	Field stabilisation
				Ground layer AO (M6)
			X	Single conjugate AO (M6)
REQUIREMENT	**180**	**N/A**		Dual conjugate AO (M5+M6)
TOTAL BUDGET	**175**	**N/A**		Multi-Object AO (M6 + post-focal AO)
Contingency	**43**	**N/A**		Extreme AO (XAO)
As-designed	0	N/A		
M1	68	N/A		
M2	52	N/A		
M3	43	N/A		
M4	77	N/A		
M5	54	N/A		
M6	50	N/A		
Corrector (rigid body)	9	N/A		
Environment	25	N/A		
Tracking	14	N/A		
Non-AO wavefront control	42	N/A		
Pre-alignment	0	N/A		
Phasing	42	N/A		
Active focusing	0	N/A		
Active centring	0	N/A		
Active surfaces deformations	0	N/A		
Field stabilisation	0	N/A		
Ground layer AO	0	N/A		
Single conjugate AO	87	N/A		
Dual conjugate AO	0	N/A		
Multi-Object AO	0	N/A		
Extreme AO (XAO)	0	N/A		

As-designed	**0**				**0**			
M1	**68**				**0**			
Rigid body		10				0		
Overall curvature			5				0	
Segments average curvature				0			N/A	*Amplitude & frequency low enough for full AO correction*
Integration				0			N/A	*Amplitude & frequency low enough for full AO correction*
Gravity				0			N/A	*Amplitude & frequency low enough for full AO correction*
Thermal				0			N/A	*Amplitude & frequency low enough for full AO correction*
Wind				5			N/A	*Uncorrected residual only (>~ 100Hz)*
Lateral decentres			5				0	
Integration				0			N/A	*Amplitude & frequency low enough for full AO correction*
Gravity				0			N/A	*Amplitude & frequency low enough for full AO correction*
Thermal				0			N/A	*Amplitude & frequency low enough for full AO correction*
Wind				5			N/A	*Uncorrected residual only (>~ 100Hz)*
Tip-tilt			5				0	
Integration				0			N/A	*Amplitude & frequency low enough for full AO correction*
Gravity				0			N/A	*Amplitude & frequency low enough for full AO correction*
Thermal				0			N/A	*Amplitude & frequency low enough for full AO correction*
Wind				5			N/A	*Uncorrected residual only (>~ 100Hz)*
Piston			5				0	
Integration				0			N/A	*Amplitude & frequency low enough for full AO correction*
Gravity				0			N/A	*Amplitude & frequency low enough for full AO correction*
Thermal				0			N/A	*Amplitude & frequency low enough for full AO correction*
Wind				5			N/A	*Uncorrected residual only (>~ 100Hz)*
Segments		62				0		
Substrates			35				0	
In-segment CTE inhomogeneities				35			N/A	*Mostly effect of through-thickness CTE gradient*
Inter-segments CTE inhomogeneities				5			N/A	
Polishing			32				0	
All terms except edge misfigure				30			N/A	*Over full pupil; individual segments may exceed*
Edge misfigure				12			N/A	*Assumes edge misfigure <1 fringe over 10 mm*

OWL Image quality budget in SCAO mode (continued)

Axial supports		31				0				
Print-through			25				N/A			*Gravity; assumed to be mostly polished out.*
Thermal			10				N/A			
Integration			15				N/A			
Bonding stresses				5				N/A		
I/F dimensional errors				10				N/A		
I/F force & moments errors				10				N/A		
Lateral supports		26				0				
Print-through			20				N/A			
Thermal			10				N/A			
Integration			12				0			
Bonding stresses				5				N/A		
I/F dimensional errors				8				N/A		
I/F force & moments errors				8				N/A		
Mirror seeing	25				N/A					
M2	**52**				**0**					
Rigid body	13				0					
Overall curvature		5				0				
Segments average curvature			0				N/A			*Amplitude & frequency low enough for full AO correction*
Integration			0				N/A			*Amplitude & frequency low enough for full AO correction*
Gravity			0				N/A			*Amplitude & frequency low enough for full AO correction*
Thermal			0				N/A			*Amplitude & frequency low enough for full AO correction*
Wind			5				N/A			*Uncorrected residual only (>~ 100Hz)*
Lateral decentres		5				0				
Integration			0				N/A			*Amplitude & frequency low enough for full AO correction*
Gravity			0				N/A			*Amplitude & frequency low enough for full AO correction*
Thermal			0				N/A			*Amplitude & frequency low enough for full AO correction*
Wind			5				N/A			*Uncorrected residual only (>~ 100Hz)*
Tip-tilt		5				0				
Integration			0				N/A			*Amplitude & frequency low enough for full AO correction*
Gravity			0				N/A			*Amplitude & frequency low enough for full AO correction*
Thermal			0				N/A			*Amplitude & frequency low enough for full AO correction*
Wind			5				N/A			*Uncorrected residual only (>~ 100Hz)*
Piston		10				0				
Integration			0				N/A			*Amplitude & frequency low enough for full AO correction*
Gravity			0				N/A			*Amplitude & frequency low enough for full AO correction*
Thermal			0				N/A			*Amplitude & frequency low enough for full AO correction*
Wind			10				N/A			*Uncorrected residual only (>~ 100Hz)*

OWL Image quality budget in SCAO mode (continued)

Segments		43				0				*Effect twice larger than with M1*
Substrates			16				0			
In-segment CTE inhomogeneities				15				N/A		*Most corrected by M6 (~6-7 actuators / M2 segment diameter)*
Inter-segments CTE inhomogeneities				5				N/A		*Idem*
Polishing			32				0			
All terms except edge misfigure				30				N/A		*Over full pupil; individual segments may exceed*
Edge misfigure				12				N/A		*Assumes edge misfigure <1 fringe over 10 mm*
Axial supports			21				0			
Print-through				15				N/A		*Assumed to be mostly polished out; corrected by M6*
Thermal				5				N/A		*Partially corrected by M6*
Integration				14				0		
Bonding stresses					8				N/A	*Partially corrected by M6*
I/F dimensional errors					8				N/A	*Partially corrected by M6*
I/F force & moments errors					8				N/A	*Partially corrected by M6*
Lateral supports			11				0			
Print-through				8				N/A		*Partially corrected by M6*
Thermal				8				N/A		*Partially corrected by M6*
Integration				12				0		
Bonding stresses					5				N/A	*Partially corrected by M6*
I/F dimensional errors					8				N/A	*Partially corrected by M6*
I/F force & moments errors					8				N/A	*Partially corrected by M6*
Mirror seeing		25				N/A				
M3	**43**					**0**				
Rigid body		9				0				*Within corrector considered as rigid body*
Lateral decentres			5				0			
Integration				0				N/A		*Amplitude & frequency low enough for full AO correction*
Gravity				0				N/A		*Amplitude & frequency low enough for full AO correction*
Thermal				0				N/A		*Amplitude & frequency low enough for full AO correction*
Wind				5				N/A		*Uncorrected residual only (>~ 100Hz)*
Tip-tilt			5				0			
Integration				0				N/A		*Amplitude & frequency low enough for full AO correction*
Gravity				0				N/A		*Amplitude & frequency low enough for full AO correction*
Thermal				0				N/A		*Amplitude & frequency low enough for full AO correction*
Wind				5				N/A		*Uncorrected residual only (>~ 100Hz)*
Piston			5				0			
Integration				0				N/A		*Amplitude & frequency low enough for full AO correction*
Gravity				0				N/A		*Amplitude & frequency low enough for full AO correction*
Thermal				0				N/A		*Amplitude & frequency low enough for full AO correction*
Wind				5				N/A		*Uncorrected residual only (>~ 100Hz)*

OWL Image quality budget in SCAO mode (continued)

Mirror misfigure	37					0				
Substrate - CTE inhomogeneity		10					N/A			*Mostly compensated by active optics*
Polishing		30					0			*Assumes polishing support = operational support*
Matching			5					N/A		*Mostly corrected by active optics and M6*
Other terms			30					N/A		*Comparable to VLT M1 (not best)*
Axial supports		14					0			
Print-through			10					N/A		*Mostly polished out*
Thermal			5					N/A		
Integration			9					0		
Bonding stresses				5					N/A	*Mostly compensated by AO*
I/F dimensional errors				5					N/A	*Mostly compensated by AO*
I/F force & moments errors				5					N/A	*Mostly compensated by AO*
Lateral supports		11					0			
Print-through			10					N/A		*Mostly compensated by AO*
Thermal			5					N/A		*Mostly compensated by AO*
Integration			14					0		
Bonding stresses				8					N/A	*Mostly compensated by AO*
I/F dimensional errors				8					N/A	*Mostly compensated by AO*
I/F force & moments errors				8					N/A	*Mostly compensated by AO*
Mirror seeing	20				N/A					*Some AO compensation expected*
M4	**77**				**0**					
Rigid body	9					0				*Within corrector considered as rigid body*
Lateral decentres		5					0			
Integration			0					N/A		*Amplitude & frequency low enough for full AO correction*
Gravity			0					N/A		*Amplitude & frequency low enough for full AO correction*
Thermal			0					N/A		*Amplitude & frequency low enough for full AO correction*
Wind			5					N/A		*Uncorrected residual only (>~ 100Hz)*
Tip-tilt		5					0			
Integration			0					N/A		*Amplitude & frequency low enough for full AO correction*
Gravity			0					N/A		*Amplitude & frequency low enough for full AO correction*
Thermal			0					N/A		*Amplitude & frequency low enough for full AO correction*
Wind			5					N/A		*Uncorrected residual only (>~ 100Hz)*
Piston		5					0			
Integration			0					N/A		*Amplitude & frequency low enough for full AO correction*
Gravity			0					N/A		*Amplitude & frequency low enough for full AO correction*
Thermal			0					N/A		*Amplitude & frequency low enough for full AO correction*
Wind			5					N/A		*Uncorrected residual only (>~ 100Hz)*

OWL Image quality budget in SCAO mode (continued)

Mirror misfigure	74				0				
Substrate - CTE inhomogeneity		10				N/A			*Mostly compensated by active optics*
Polishing		71					0		*Assumes polishing support = operational support*
Matching			10					N/A	*Mostly corrected by active optics and M6*
Other terms			70					N/A	*Comparable to VLT M1 (not best)*
Axial supports		14					0		
Print-through			10					N/A	*Mostly polished out*
Thermal			5					N/A	
Integration			9					0	
Bonding stresses				5				N/A	*Mostly compensated by AO*
I/F dimensional errors				5				N/A	*Mostly compensated by AO*
I/F force & moments errors				5				N/A	*Mostly compensated by AO*
Lateral supports		11					0		
Print-through			10					N/A	*Mostly compensated by AO*
Thermal			5					N/A	*Mostly compensated by AO*
Integration			12					0	
Bonding stresses				5				N/A	*Mostly compensated by AO*
I/F dimensional errors				5				N/A	*Mostly compensated by AO*
I/F force & moments errors				10				N/A	*Mostly compensated by AO*
Mirror seeing	20				N/A				*Some AO compensation expected*
M5	**54**				**0**				
Rigid body	9				0				*Within corrector considered as rigid body*
Lateral decentres		5					0		
Integration			0					N/A	*Amplitude & frequency low enough for full AO correction*
Gravity			0					N/A	*Amplitude & frequency low enough for full AO correction*
Thermal			0					N/A	*Amplitude & frequency low enough for full AO correction*
Wind			5					N/A	*Uncorrected residual only (>~ 100Hz)*
Tip-tilt		5					0		
Integration			0					N/A	*Amplitude & frequency low enough for full AO correction*
Gravity			0					N/A	*Amplitude & frequency low enough for full AO correction*
Thermal			0					N/A	*Amplitude & frequency low enough for full AO correction*
Wind			5					N/A	*Uncorrected residual only (>~ 100Hz)*
Piston		5					0		
Integration			0					N/A	*Amplitude & frequency low enough for full AO correction*
Gravity			0					N/A	*Amplitude & frequency low enough for full AO correction*
Thermal			0					N/A	*Amplitude & frequency low enough for full AO correction*
Wind			5					N/A	*Uncorrected residual only (>~ 100Hz)*

OWL Image quality budget in SCAO mode (continued)

Mirror misfigure	47					0				
Substrate - CTE inhomogeneity		10					N/A			*Mostly compensated by active optics*
Polishing		35					0			*Assumes polishing support = operational support*
Matching			5					N/A		*Mostly corrected by active optics and M6*
Other terms			35					N/A		*Comparable to VLT M1 (not best)*
Axial supports		22					0			
Print-through			10					N/A		*Mostly polished out*
Thermal			10					N/A		
Integration			17					0		
Bonding stresses				10					N/A	*Mostly compensated by AO*
I/F dimensional errors				10					N/A	*Mostly compensated by AO*
I/F force & moments errors				10					N/A	*Mostly compensated by AO*
Lateral supports		18					0			
Print-through			15					N/A		*Mostly compensated by AO*
Thermal			10					N/A		*Mostly compensated by AO*
Integration			17					0		
Bonding stresses				10					N/A	*Mostly compensated by AO*
I/F dimensional errors				10					N/A	*Mostly compensated by AO*
I/F force & moments errors				10					N/A	*Mostly compensated by AO*
Mirror seeing	25				N/A					*Some AO compensation expected*
M6	**50**				**0**					
Rigid body	7					0				*Within corrector considered as rigid body*
Lateral decentres		0					0			
Integration			0					N/A		*Flat mirror*
Gravity			0					N/A		*Flat mirror*
Thermal			0					N/A		*Flat mirror*
Wind			0					N/A		*Flat mirror*
Tip-tilt		5					0			
Integration			0					N/A		*Amplitude & frequency low enough for full AO correction*
Gravity			0					N/A		*Amplitude & frequency low enough for full AO correction*
Thermal			0					N/A		*Amplitude & frequency low enough for full AO correction*
Wind			5					N/A		*Uncorrected residual only (>~ 100Hz)*
Piston		5					0			
Integration			0					N/A		*Amplitude & frequency low enough for full AO correction*
Gravity			0					N/A		*Amplitude & frequency low enough for full AO correction*
Thermal			0					N/A		*Amplitude & frequency low enough for full AO correction*
Wind			5					N/A		*Uncorrected residual only (>~ 100Hz)*

OWL Image quality budget in SCAO mode (continued)

Mirror misfigure	43					0			
Substrate - CTE inhomogeneity		5				N/A			*Mostly compensated by active optics*
Polishing		25					0		*Assumes polishing support = operational support*
Matching			0				N/A		*Mostly corrected by active optics and M6*
Other terms			25				N/A		*Comparable to VLT M1 (not best)*
Axial supports		29					0		
Print-through			20				N/A		*Mostly polished out*
Thermal			10				N/A		
Integration			19					0	
Bonding stresses				15				N/A	*Mostly compensated by AO*
I/F dimensional errors				5				N/A	*Mostly compensated by AO*
I/F force & moments errors				10				N/A	*Mostly compensated by AO*
Lateral supports		18					0		
Print-through			15				N/A		*Mostly compensated by AO*
Thermal			10				N/A		*Mostly compensated by AO*
Integration			15					0	
Bonding stresses				10				N/A	*Mostly compensated by AO*
I/F dimensional errors				5				N/A	*Mostly compensated by AO*
I/F force & moments errors				10				N/A	*Mostly compensated by AO*
Mirror seeing	25				N/A				*Some AO compensation expected*
Corrector (rigid body)	**9**				**0**				
Lateral decentres	5					0			
Integration		0				N/A			*Amplitude & frequency low enough for full AO correction*
Gravity		0				N/A			*Amplitude & frequency low enough for full AO correction*
Thermal		0				N/A			*Amplitude & frequency low enough for full AO correction*
Wind		5				N/A			*Uncorrected residual only (>~ 100Hz)*
Tip-tilt	5					0			
Integration		0				N/A			*Amplitude & frequency low enough for full AO correction*
Gravity		0				N/A			*Amplitude & frequency low enough for full AO correction*
Thermal		0				N/A			*Amplitude & frequency low enough for full AO correction*
Wind		5				N/A			*Uncorrected residual only (>~ 100Hz)*
Piston	5					0			
Integration		0				N/A			*Amplitude & frequency low enough for full AO correction*
Gravity		0				N/A			*Amplitude & frequency low enough for full AO correction*
Thermal		0				N/A			*Amplitude & frequency low enough for full AO correction*
Wind		5				N/A			*Uncorrected residual only (>~ 100Hz)*

OWL Image quality budget in SCAO mode (continued)

Environment	**25**			**0**		
Local heat sources		20		N/A		
Telescope seeing		15		N/A		*Telescope structure*
Tracking	**14**			**0**		
Friction		10		N/A		*Mostly compensated by field stabilisation (incl. fast thin shell)*
Wind		10		N/A		*Mostly compensated by field stabilisation (incl. fast thin shell)*
Metrology (encoders)		0		N/A		*Amplitude & frequency low enough for full AO correction*
Non-AO wavefront control	**42**			**0**		
Pre-alignment		**0**			**0**	
Metrology			0		N/A	*Amplitude & frequency low enough for full AO correction*
Actuation			0		N/A	*Amplitude & frequency low enough for full AO correction*
Phasing		**42**			**0**	
Metrology (incl. signal processing)			20		N/A	*Excluding on-sky metrology (calibration)*
Calibration			10		N/A	*Assumes bright star (v < 8)*
M1 segments actuation			25		N/A	*Incl. wind and after AO correction*
M2 segments actuation			25		N/A	*Incl. wind and after AO correction*
Active focusing		**0**			**0**	
Metrology (incl. signal processing)			0		N/A	*Amplitude & frequency low enough for full AO correction*
Actuation			0		N/A	*Amplitude & frequency low enough for full AO correction*
Active centring		**0**			**0**	
Metrology (incl. signal processing)			0		N/A	*Amplitude & frequency low enough for full AO correction*
Actuation			0		N/A	*Amplitude & frequency low enough for full AO correction*
Active surfaces deformations		**0**			**0**	
Metrology (incl. signal processing)			0		N/A	*Amplitude & frequency low enough for full AO correction*
Fitting			0		N/A	*Amplitude & frequency low enough for full AO correction*
M3 force actuation			0		N/A	*Amplitude & frequency low enough for full AO correction*
M4 force actuation			0		N/A	*Amplitude & frequency low enough for full AO correction*
Field stabilisation		**0**			**0**	
Metrology			0		N/A	*Amplitude & frequency low enough for full AO correction*
Actuation			0		N/A	*Amplitude & frequency low enough for full AO correction*

OWL Image quality budget in SCAO mode (continued)

Ground layer AO	**0**		**0**		
Metrology (incl. signal processing)	N/A		N/A		
Non-common path	N/A		N/A		
M6 actuation	N/A		N/A		
Single conjugate AO	**87**		**0**		
Metrology (incl. signal processing)	85		N/A		
Non-common path	10		N/A		
M6 actuation	15		N/A		
Dual conjugate AO	**0**		**0**		
Metrology (incl. signal processing)	N/A		N/A		
Non-common path	N/A		N/A		
M5 actuation	N/A		N/A		
M6 actuation	N/A		N/A		
Multi-Object AO	**0**		**0**		
Metrology (incl. signal processing)	N/A		N/A		
Non-common path	N/A		N/A		
M6 actuation	N/A		N/A		
Post-focal actuation	N/A		N/A		
Extreme AO (XAO)	**0**		**0**		
Metrology (incl. signal processing)	N/A		N/A		
Non-common path	N/A		N/A		
M6 actuation	N/A		N/A		
Post-focal actuation	N/A		N/A		

OWL Image quality budget in SCAO mode (continued)

5.6 Reliability, Availability, Maintainability, Safety (RAMS)

5.6.1 Product Assurance Roles & Responsibilities

Product Assurance Tasks that ESO will take and undergo in detail in the next design phases are:

- System Safety
- Reliability Engineering
- Quality Assurance
- Review and Inspection
- Procurement Product Assurance
- Material and Process Control
- Manufacturing and process control
- NonConformance Control & Reporting:
  - Problem Reporting
  - Material Review Board
  - Failure Analysis and Corrective Action report
- EEE Parts Engineering and Electronic Packaging
- Software Quality Assurance
- Configuration Control

All the above mentioned tasks will be undertaken considering applicable and reference document such as

Failure Rates (example the ESA, PSS-01-302)

FMECA Requirements (ESA doc, PSS-01-303)

Reliability prediction of Electronic prediction (MIL-HDBK-217)

5.6.2 Safety

5.6.2.1 General

The design team will establish and implement a safety program compliant with the safety requirements. This program will be described in a dedicated section of the Product Assurance Plan of next design phase.

Compliance with the requirements below shall not relieve ESO from complying other countries national safety regulations or those where the telescope, or any related ground support equipment, is planned to be used.

5.6.2.2 Safety Assurance Program and organization

ESO will nominate a person with adequate background and experience as responsible project team member for system safety engineering tasks. Availability and access to the necessary data to adequately perform the safety tasks will be assured.

5.6.2.3 Safety assurance activities

During next detailed design phase it will be evaluated the design and operation of the telescope, identify hazards, and control measures, verify their implementation and certify that the telescope is safe and complies with the applicable safety requirements. ESO will ensure that the safety verifications are reflected in the overall OWL verification plan.

5.6.3 Reliability and Maintainability

Reliability is the probability that a system will provide its functions within specified performance limits for a specified period of time in specified conditions.

Maintainability is a characteristic of design and integration, which is expressed as the probability that a system will be retained in or restored to a specific condition within a given period of time.

Reliability and Maintainability Assurance is aimed to ensure that design reliability and maintainability will not be compromised by competing requirements such as cost and time, and to verify and provide evidence of compliance with requirements.

Maintainability requirements for software are not covered in this chapter.

Consequence Severity Categories

For the purpose of identifying failures criticality in reliability analyses, classification of Table 5-3 (section 5.1) shall be used.

By default the unclassified failures (i.e. not resulting in any of the above) are considered as negligible.

5.6.3.1 Failure Tolerance

All failure modes of criticality Category 1 shall be eliminated from the design, minimised or controlled in accordance with the applicable safety failure tolerance requirements. In addition, no single failure or operator error shall have major consequences (Category 2).

5.6.3.2 Single point failure list

Items of criticality Category 1 failures which are not maintainable, and all items with Category 2 failures will be listed in a Single Point Failure (SPF) list. The SPF list will be subjected to detailed study and formal approval. The request for approval shall be submitted with a rationale for retention explaining technical reasons and potential special provisions during development (e.g. testing), production and operation, to minimise the failure probability.

5.6.3.3 Reliability and Maintainability Data File

ESO will maintain a project reliability and maintainability data file as part of his overall product assurance documentation system. The file will contain, as a minimum, the following:

- R&M Analyses, lists, reports and input data.
- R&M recommendation status log.
- Supporting analyses and documentation.

5.6.3.3.1 Reliability Engineering

Reliability engineering will focus on the prevention, detection and correction of reliability design deficiencies. Reliability engineering will be an integral part of the item design process, including design changes. The means by which reliability engineering contributes to the design, and the level of authority and constraints on this engineering discipline, will be identified in the reliability program plan.

5.6.3.3.1.1 Reliability Analyses

FMECA

ESO will prepare Failure Modes Effects and Criticality Analyses according to specific procedures such as the PSS-01-303 or MIL-STD-1629A.

FMECA will be initially performed, in the early detailed project phase, at the level of system functions and/or functional paths. As the design advances, the FMECA will be refined and completed down to unit level, with the exception of safety critical circuits and circuit interfacing external elements for which FMECA will be performed down to component level.

The objectives of the FMECA shall include:

- Identification of the effects of assumed failures, including identification of hazards in support of safety analyses and to determination of the need for redundancies, inhibits or fail-safe features.
- Demonstration of compliance with applicable safety and reliability failure tolerance requirements.
- Identification of available or needed monitoring devices for the symptoms of a failure which can be observed via monitoring or telemetry.
- Identification of inputs for maintenance activities.

The following failure modes will be considered in the FMECA:

- Out of sequence operation.
- Failure to operate at prescribed time.
- Failure to cease operation at prescribed time.
- Failure during operation.
- Degradation or out of tolerance operation.
- For failure of EEE parts:
    - Short circuit,
    - Open circuit,
    - Incorrect function.
- Incorrect commands or sequence of commands.
- Incorrect software functions.

FMECA shall include consideration of hardware/software interaction to ensure that software is designed to react in an acceptable way to hardware failure (e.g. sensors). Results shall be inputs for the Software Requirements Document (SRD).

5.6.3.3.2 Maintainability Engineering

5.6.3.3.2.1 Establishment of Maintainability Requirements

Maintainability requirements that will be applied to the system, or item being developed shall be established on the basis of the system maintenance concept.

The system maintenance concept will be proposed during the next design phase.

5.6.3.3.2.2 Maintainability Inputs to Maintenance Plan

The maintainability function will provide inputs to develop a maintenance plan prepared to support the maintenance concept approved.

These inputs shall include estimates of preventive and corrective maintenance requirements (including task times and frequencies) and the proportion of failures that will be localised by automatic, semi-automatic and manual means.

5.6.3.3.2.3 Maintainability Analyses

Maintainability Prediction

Maintainability prediction shall be performed and employed as a design tool to assess and compare design alternatives with respect to specified maintainability quantitative requirements. Maintainability predictions shall be used as a basis for estimating human resource requirements.

Maintainability predictions shall be performed considering:

- The time required to diagnose (i.e. detect and isolate) item failures, the time required to remove and replace the defective item.
- The time required to return the system/subsystem to its original configuration and to perform the necessary checks.
- The item failure rates.

Maintainability Support to other Engineering Analyses

The maintainability function shall participate in the trade-off studies and support the following engineering analyses as a minimum:

a) Line Replaceable Units (LRU) optimisation, by considering safety criticality, reliability, costs, fault diagnostics capability, and unit replacement times.

b) Identification of hazards induced by maintenance activities.

c) Diagnostic alternatives to effectively detect and isolate failures at LRU level and accurately verify system restoration.

d) Use of condition monitoring methods to optimise the preventive maintenance interventions.

e) Determination of maximum number of maintenance actions that each LRU can be subjected to without degradation in performance and/or reliability.

f) Minimisation and standardisation of maintenance tools.

5.6.3.3.2.4 Maintainability Demonstration

Maintainability demonstration shall be performed to verify that the identified preventive and corrective maintenance activities can be successfully performed. In particular to verify the:

- ability to detect, diagnose, isolate and remove faulty LRU's.
- safety of maintenance actions;
- accessibility;
- repairs, when replacement is not foreseen;
- performance of inspections and tests after replacement/repair.

5.6.4 Conclusion – OWL Dependability Objective Sheet

Refinement of the following Product Assurance requirements will be part of the detailed design phase:

SAFETY

- No event relevant to the OWL telescope jeopardizing the personnel (Catastrophic event) must be expected during the OWL lifetime
- No event relevant to the OWL Telescope causing the total loss of the OWL facility (Critical event) must be expected during the OWL lifetime

AVAILABILITY

- The maximum expected probability of any event relevant to OWL causing the failure to start an observation (Major 2 event) must be [for example 15^{-2} (1.5%)]; a value of Mean Time to Repair of 8h shall be expected.
- No event relevant to the OWL telescope causing the telescope unavailability for more than 1 week. (Major 1 event) must be expected during the OWL lifetime.

RELIABILITY

- The maximum expected frequency of any event causing a forced observation interruption (Significant 2 event) must be (for example 3.0^{-4} /h), referred to the actual operating time.

6. Telescope optics

6.1 Requirements and guidelines

The design shall be optimized along the objectives outlined in Table 6-1. These objectives are derived from science and level 1 requirements and from indirect, engineering requirements (see table). They apply to a 100-m aperture design. Implied characteristics are derived in Figure 6-1. With a conventional two-mirror design, the need for field stabilization and embedded active and adaptive optics, together with the maximum size of the adaptive corrector, would imply a four-metre class secondary mirror performing all active and adaptive functions, on top of of field stabilization. A compact telescope structure (length ~ diameter) leads to a ~f/1 primary mirror, and an acceptable linear field dimension (~2-m) implies a relatively fast telescope focal ratio (~f/6-f/7). A Ritchey-Chretien design with such characteristics has a ~20-25 arc seconds diffraction-limited field of view (λ=0.5 μm). It follows that a conventional two-mirror solution cannot meet requirements, in addition to implying unrealistic constraints on the secondary mirror technology[45]. An all-aspherical, three mirror solution would not, either. In order to provide a real image of the pupil (ground layer), the secondary mirror would have to be concave; with a M1-M2 separation of ~100-m and a maximum secondary mirror diameter of 8.3-m, this implies a f/0.93 aspherical primary mirror. In order to produce a ~4m diameter exit pupil (adaptive mirror), the secondary mirror would have to be concave, f/0.45. In addition, the adaptive mirror (M3) would obstruct all rays travelling from the primary towards the secondary mirror. Allowing for a linear obscuration ratio of ~50% by M3 would require a f/0.25 secondary mirror. We conclude that the minimum number of surfaces is 4. As a result, a spherical primary mirror solution may become an attractive option, in line with the crucial objective of maximizing aperture while minimizing costs.

Aspherical primary mirror solutions imply severe limitations on the fabrication and maintenance processes. Those may be acceptable with a few dozen segments, but may become prohibitive with a few thousands. Aspherical segments could be polished in a way mimicking spherical polishing, whereby segments are mounted onto a warping harness tuned to provide the desired shape upon relaxation. This implies tight requirements on residual stresses in the substrate, and is most probably incompatible with lightweight, structured blanks. It also favours smaller segments, with a correspondingly smaller deviation from best fitting sphere –although in the case of OWL, the individual segments focal ratio would be large hence their allowable diameter large enough for such disadvantage to be inconsequential. In addition, the machine time required to finish the segments after edge-cutting is anything but predictable –at least until a representative sample has been produced. Even though ion-beam polishing, magnetic rheology polishing and small computer-controlled tools techniques have proven and excellent converging characteristics, none of these techniques can reasonably compete with full-size rigid tool

[45] We refer to the amplitude of the adaptive shell deformations but not necessarily tip-tilt correction. Field stabilization and adaptive compensation may be combined in a two-stage unit, with large amplitude, low temporal frequencies taken care of by a tip-tilt mount allowing rigid body motion of the corrector and adaptive support.

polishing. The latter not only allows for a much favorable wear law –in proportion to tool area- but also for intrinsically smoother surfaces.

More importantly perhaps, in the aspherical case optical testing requires that the setup be tailored to families of segments, with evident matching risks and time overheads. Spherical solutions, on the contrary, offer the opportunity to measure all segments against a unique reference, according to a straightforward procedure.

Objective / guideline	Reasons	
Field aberrations over the science field (3 arc minutes diameter) shall be axisymmetrical or negligible.	Compensation of asymmetrical field aberrations in the science instrument is generally impossible.	M
Optical quality shall be maximized over a field of view at least twice larger than that directly implied by top level requirements.	Avoid field aberration offsets in wide-field Adaptive Optics control (ground layer AO, MCAO).	M
The total number of surfaces shall be minimized.	Minimal emissivity and maximal throughput.	C
Obscurations shall be minimized	Throughput, image contrast at intermediate angular frequencies	C
Total length shall be optimized for minimal structure and enclosure dimensions.	Cost (including enclosure), structural performance.	C
Sensitivity to misalignments shall be minimized.	Relaxed tolerances, low sensitivity to wind-induced misalignments.	C
The total linear field of view (diameter) shall be in the range of ~2-m	Allow for (presumably) sufficient design space while limiting flexures e.g. in sensors arms.	D
The field of view (diameter) available for adaptive optics wavefront sensing shall be 6 arc minutes.	Large field AO sensing (MCAO, GLAO)	M
The field of view (diameter) available for non-adaptive wavefront sensing shall be maximized.	Sky coverage not limited by non-adaptive wavefront control.	C
The design shall provide suitable surfaces for active optics, including deformable mirror(s), active centring, focusing, and field stabilization	Compensation of inevitable, large amplitude and low frequency errors.	M
Field stabilization shall be done in a pupil image	Avoid pupil motion	M
The design shall provide a suitably located surface for single-conjugate IR SCAO and GLAO. Additional surface(s) for MCAO would be an advantage.	IR single-conjugate AO and GLAO provided by the telescope.	M D
The adaptive mirror(s) shall preferably have dimensions not smaller than 2-m and not larger than 4-m. Adaptive mirrors shall preferably be monolithic.	Moderate extrapolation from current adaptive secondary mirror technology (~1-m diameter with ~27 mm interactuator spacing).	C
An intermediate focus suitable for AO calibration (interaction matrices) would be an advantage.	Avoid the need for on-sky calibration (overheads on science, possibly less accurate than in-situ calibration with an artificial reference).	D
Monolithic mirrors shall be less than 8.3m in diameter (useful area).	Larger monolithic mirrors would require lengthy technology development.	M
Segments shape and material shall preferably - be compatible with serial production and maintenance; - be compatible with processes minimizing high spatial frequency misfigure; - allow moderate to high lightweighting ratio.	 Construction and operation costs; Optical quality; Structural performance and control bandwidth	 C C D

Table 6-1. Optical design: guidelines and objectives. M=Mandatory; C=Critical; D=Desirable.

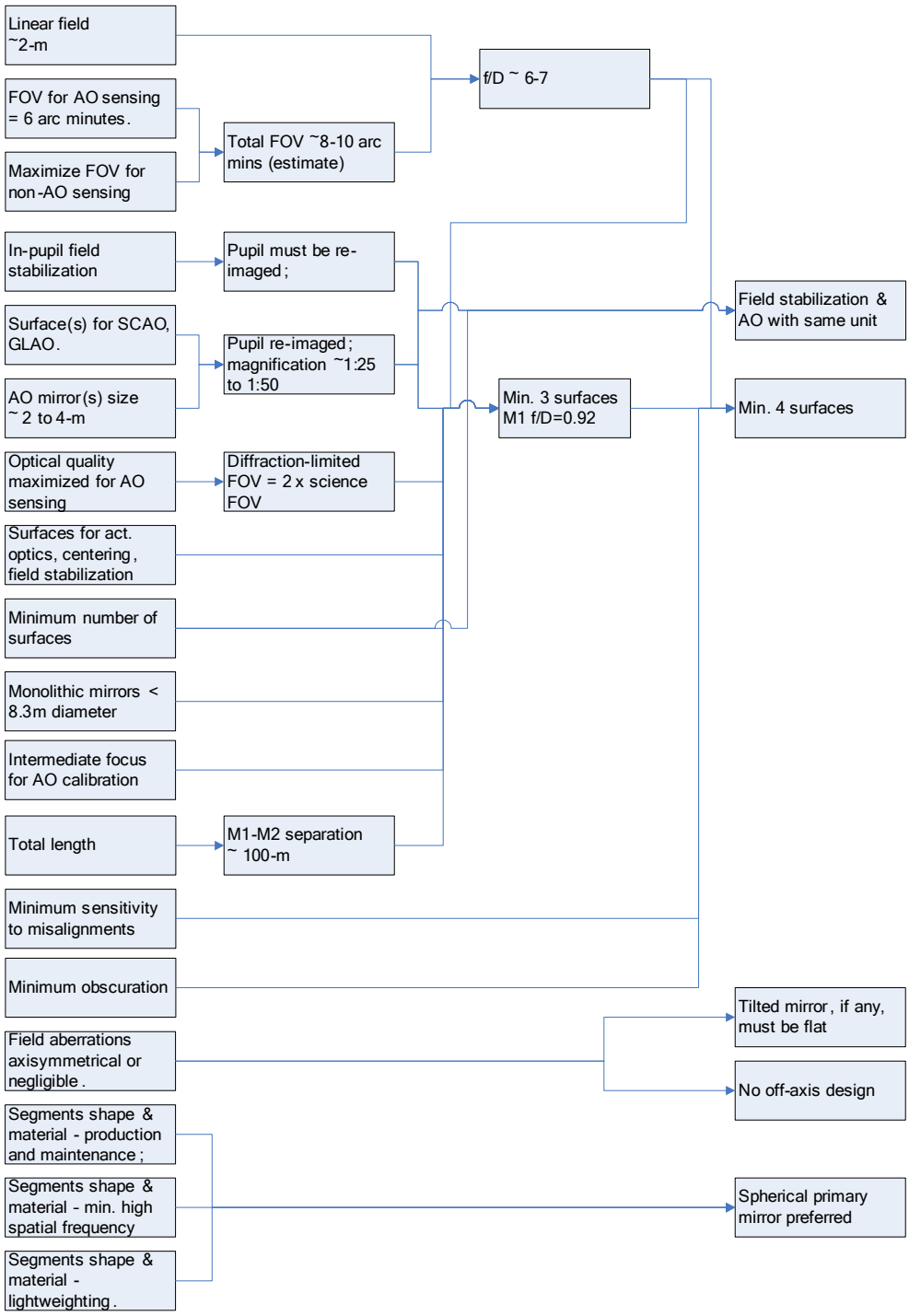

Figure 6-1. Implied characteristics.

Spherical primary mirror solutions have crucial advantages in terms of cost, risk, and performance:

- Ideally suited for serial production and maintenance of all-identical segments; low industrial risks;
- Optical testing against a unique reference matrix possible; very low risk of inter-segments matching errors;
- Smaller number of spares than with aspherical solutions;

- Fast polishing process, full-sized rigid tools possible; no need for warping harness, higher process yield;
- Polishing with large rigid tools may allow segments to be polished hexagonal without wasters or post-polish cutting to shape (hence relaxed specifications for blanks residual stresses);
- Polishing with large rigid tools is intrinsically more favorable in relation to high spatial frequency errors;
- Compatibility with lightweight segments technology46.

With an expected number of segments in the range of 3,000 units, compatibility with serial production is an advantage that can hardly be over-emphasized. Reliable optical testing against a unique matrix is also of primordial importance. In the aspherical case optical testing requires that the setup be tailored to families of segments, with evident matching risks and time overheads.

In brief, feasibility per se is not enough; even without consideration for cost, a production rate of about 1 segment per day necessarily requires predictable and largely automated processes. A spherical primary mirror is not a mandatory requirement but plausibly a critical one.

On the negative side, primary mirror solutions require a complex corrector for spherical and field aberrations. In practice, a strongly aspherical mirror will have to be conjugated to the primary mirror. Size and feasibility of this aspheric mirror will play against a short primary mirror focal ratio and imply either a structure longer than desirable or a very large (segmented) secondary mirror.

The requirements and guidelines outlined above imply that the optical design must be set up in a more complex, methodical approach than that applicable to traditional designs. In particular, optical solutions are subject to a lengthy iteration process to provide –if possible- suitable conjugates for adaptive, single-conjugate or multi-conjugate adaptive optics.

6.2 Optical design

6.2.1 Design trade-off

Several optical design solutions have been explored [9], starting with a four-mirror solution [10]. Two- and three-mirror solutions are ruled out as shown in section 6.1. Because of its modular design, the telescope structure could rapidly be re-configured for a quick evaluation of structural characteristics (see Figure 6-2 for examples based on a former family of structural design solutions).

As the minimum number of surfaces implied by the requirements and guidelines is four, there are strong cost, performance and risk incentives to explore spherical primary mirror solutions (see section 6.1). Other solutions have nevertheless been explored –more than can be accounted for in this report. These solutions have been rated against merit functions – essentially a list of relevant criteria. Each criterion is attributed a weight indicative of the criticality of the corresponding characteristic. Weights and ratings are evidently subjective. Results can **only** be used to identify clear trends but not to resolve “close matches”.

Appendix 8 lists the criteria included in the function of merit, together with their relative weights. This function of merit is plausibly incomplete and will require update, most notably to take into account the results of ongoing instruments design studies, of AO simulations, and of developments in the area of wavefront sensing with Laser Guide Stars. The design must comply with the mandatory requirements also listed in Appendix 8.

[46] Although warping harness could theoretically be used with lightweight segments, their design and operation would likely be incompatible with serial production, and predictability of the final shape is likely to be poor.

Ratings associated to feasibility (e.g. to adaptive mirror dimensions) make implicit assumptions as to the current state of technology, probable design solutions or plausible evolution thereof. Ratings will be re-assessed in the preliminary design phase; substantial changes in the optical design could be accommodated within the first year of the design phase, and significant ones within the first two years. Both criteria and the way ratings are attributed have, for obvious reasons, evolved throughout the conceptual design phase.

It appeared quite early in the design phase that the telescope size and the maximum allowable monolithic mirror diameter (8.3-m) impose strong geometrical constraints on the design. Otherwise attractive options were ruled out for this specific reason, as 10- to 12-m class monolithic mirror, if feasible at all, would require technology developments incompatible with a competitive schedule. By way of consequence, this also means that a relaxation of telescope diameter to ~60-70m would allow for a larger number of options, some of which substantially more attractive than the current baseline (see also RD6 and section 6.2.4).

The maximum dimension of monolithic surfaces is inspired from past experience, including but not limited to the VLT. In particular, the technology development underlying even a modest extrapolation from existing blanks dimensions always required more time and effort than anticipated. According to current schedule estimates, 8-m class mirrors for OWL are already on the critical path and their schedule can probably not be compressed by much. Larger dimensions (~10-m) would plausibly imply an additional 3 to 4 years to first light, on top of significant investments in suitable production infrastructures.

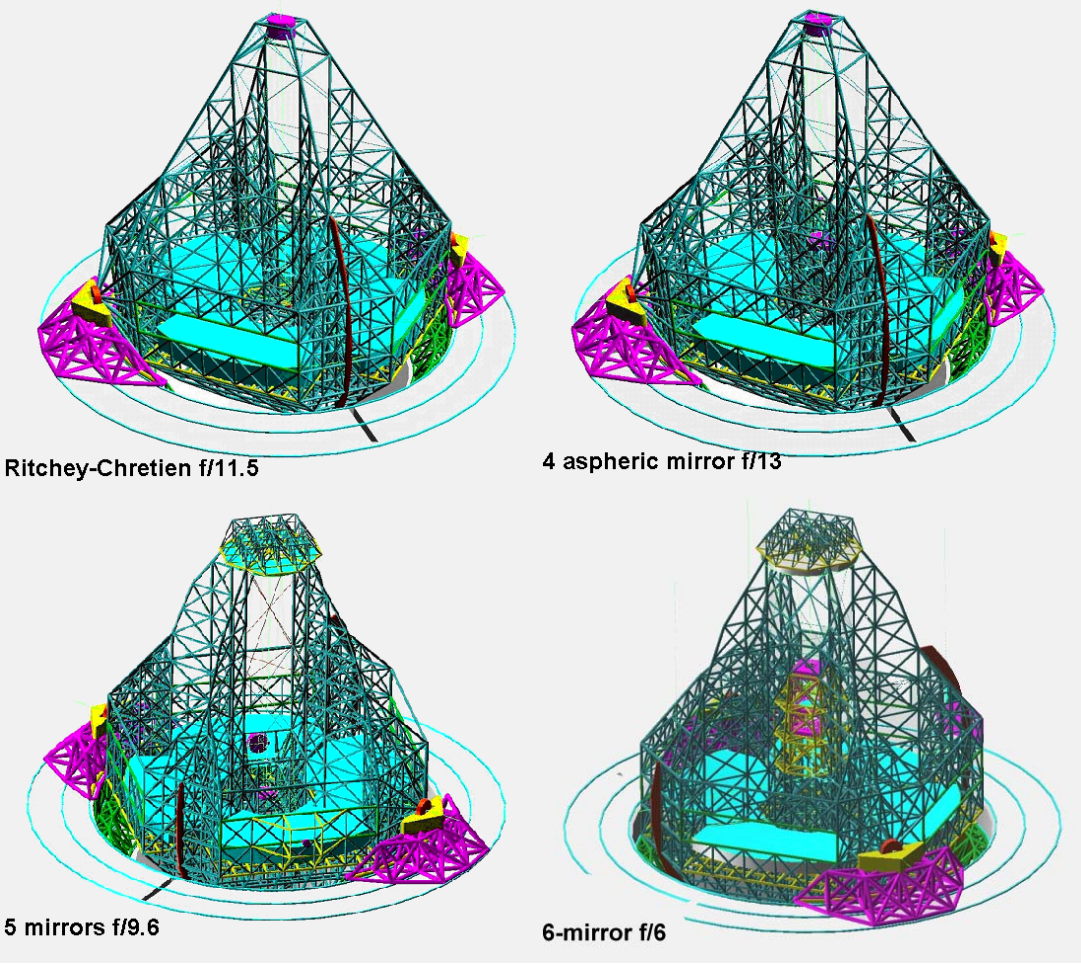

Figure 6-2. Mechanical implementation of different optical designs.

Figure 6-3 to Figure 6-6 show a few of the designs which have been evaluated. Although it does not comply with mandatory requirements, a Ritchey-Chrétien is included for reference. Design No 3 corresponds to the optional corrector (see section 6.2.3). The ratings for these four

designs are given in Table 6-2. Even when allowing for partly subjective weight and ratings allocations, the current baseline stands as best compromise.

These designs are only a sample of all those which have been briefly explored. Figure 6-7 shows an interesting solution, with an extremely fast (f/0.89) primary mirror and a failry well corrected 10 arc minutes field of view, with a wavefront error in the range of 1.5 μm RMS at the edge of the field. The exit focal ratio can be set in the f/8 to f/15 range. This design was rejected because of the enormous obscuration (47% linear), and the prohibitive size of the monolithic mirrors M2 and M3 (9.4 and 10.5-m). A folded version, with flat secondary mirror and relaxed focal ratio of the primary, might alleviate these problems but the instrumentation would be inconveniently located between the flat secondary and the corrector.

Figure 6-8 shows a five-mirror solution, with f/1.42 spherical primary and a convex, spherical secondary mirror. Field aberrations within 10 arc minutes field diameter are stronger (by a factor ~5) than with the baseline and with the design of Figure 6-7. This can probably be improved by further optimization. The Nasmyth-type focus is a major advantage for instrumentation. All monolithic mirrors are less than 8.3-m diameter. This design was rejected because none of the surfaces have adequate dimension and/or location for adaptive optics and field stabilization.

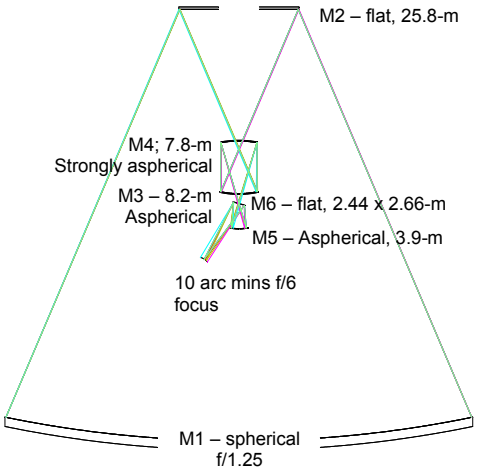

Figure 6-3. Baseline optical design (design No 1).

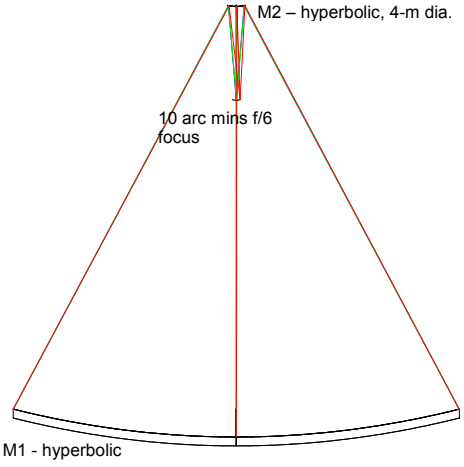

Figure 6-4. Ritchey-Chretien design (design No 2).

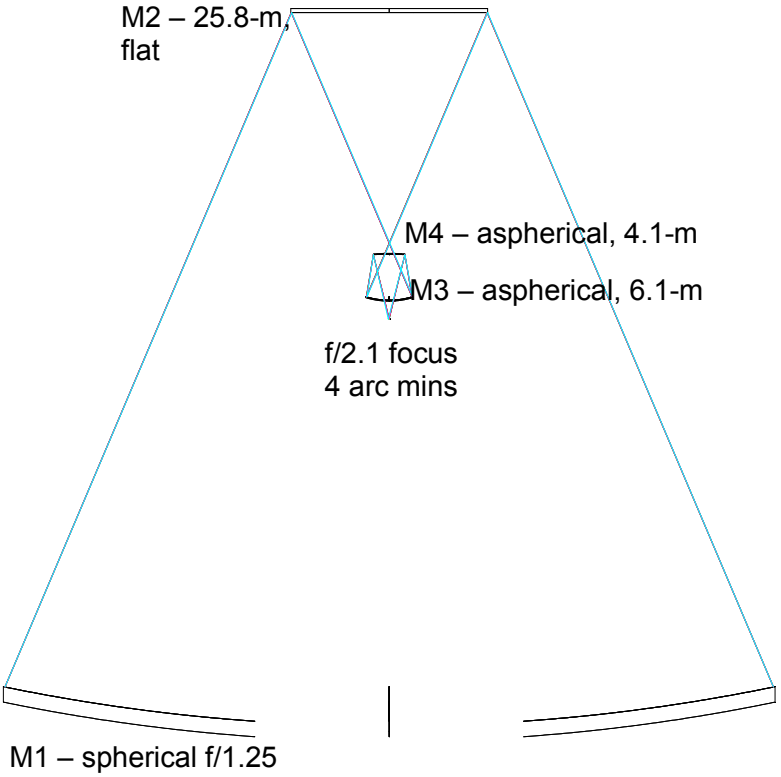

Figure 6-5. Four mirror, spherical primary & flat secondary mirrors solution (design No 3).

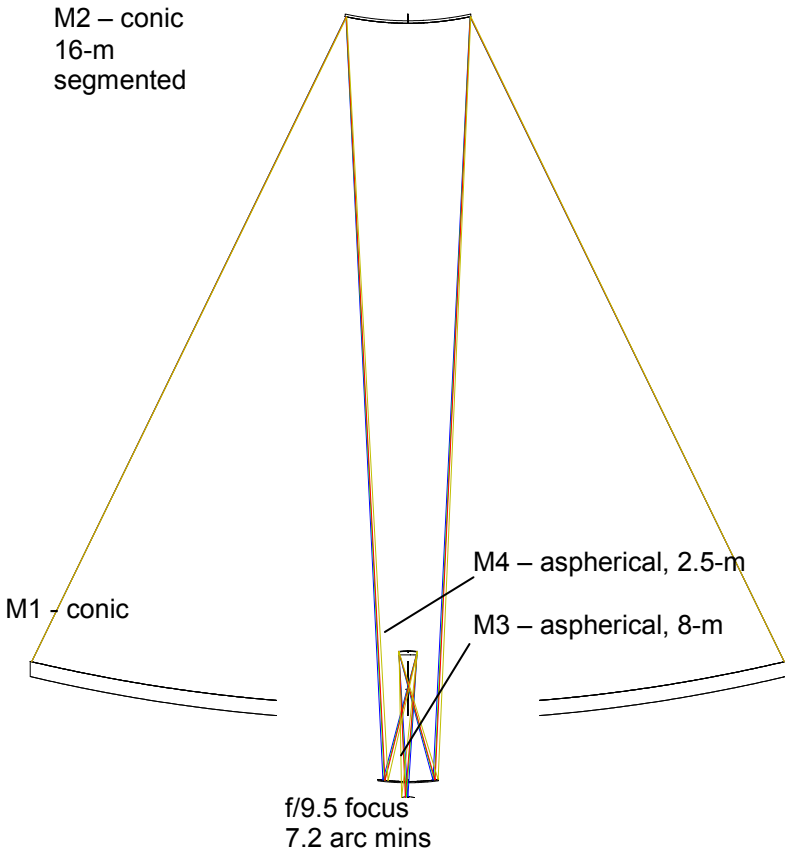

Figure 6-6. Four-mirror, conic M1 & M2 design (design No 4).

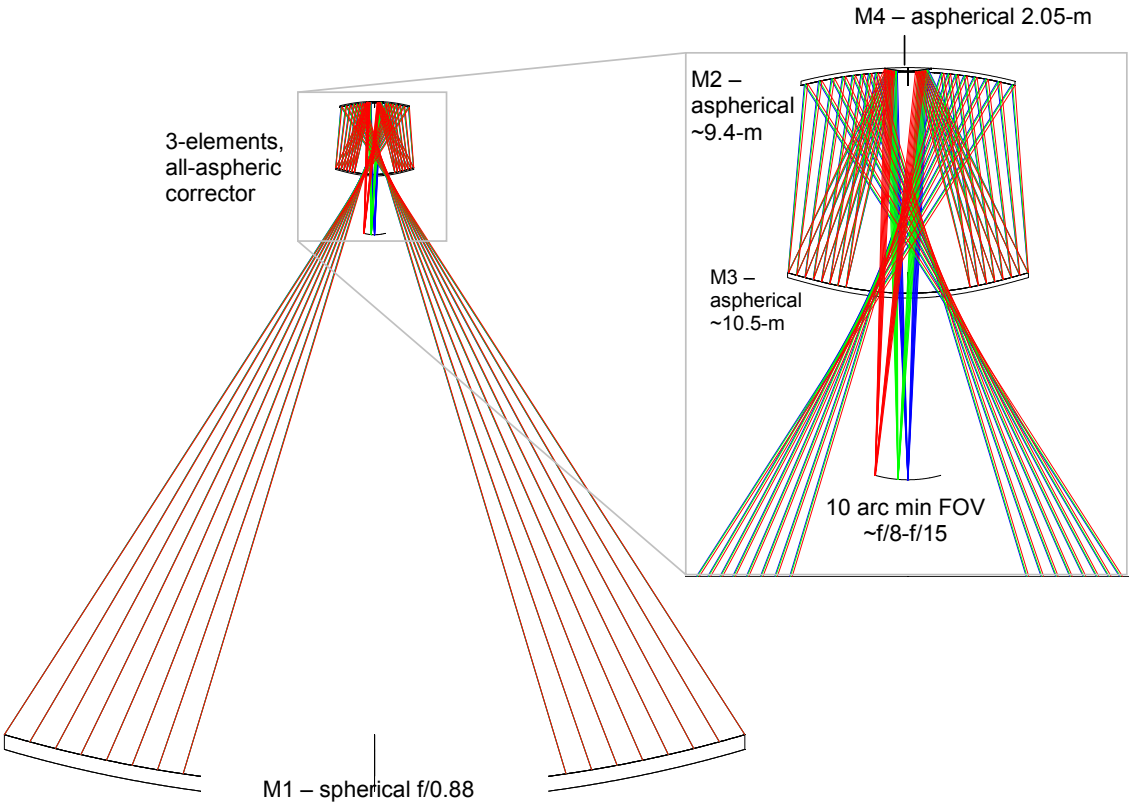

Figure 6-7. Four-mirror solution; f/0.89 spherical primary mirror .

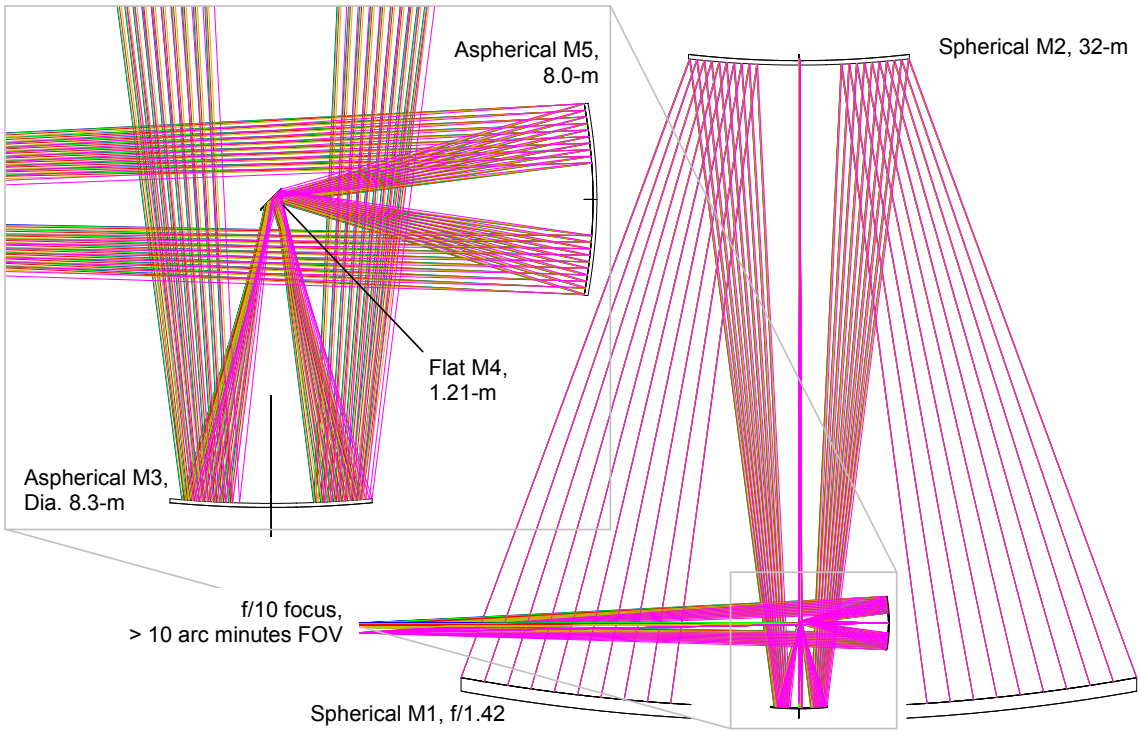

Figure 6-8. 5-mirror solution, f/1.42 spherical primary mirror.

	Design No	1	2	3	4
Mandatory requirements (*)		P / F	P / F	P / F	P / F
1	Field aberrations over the science field (3 arc minutes diameter) shall be axisymmetrical or negligible.	P	P	P	P
2	Diffraction-limited (Strehl Ratio ≥ 0.80, λ=0.5μm) over at least 1 arc minute FOV.	P	**F**	**F**	P
3	The field of view (diameter) available for adaptive optics wavefront sensing shall be 6 arc minutes.	P	P	**F**	P
4	The design shall provide suitable surfaces for active optics, including deformable mirror(s), active centring, focusing, and field stabilization	P	P	P	P
5	Monolithic mirrors shall be less than 8.3m in diameter	P	P	P	P
6	Field stabilization shall be done in a pupil image	P	P	**F**	P
7	The design shall provide a suitably located surface for single-conjugate IR SCAO and GLAO.	P	P	P	P
Requirement / characteristic	**Weight**	**Rating**	**Rating**	**Rating**	**Rating**
1	Diffraction-limited FOV	5	3	0	0	5
2	Total field of view (0.1 arc seconds RMS image quality or unacceptable vignetting)	5	4	0	0	2
3	Optical quality at edge of field of view	3	4	0	0	5
4	Field curvature	3	0	3	2	2
5	Focal ratio	3	5	5	0	0
6	Maximum monolithic mirror diameter	5	1	5	3	4
7	Emissivity (number of surfaces)	5	3	7	5	5
8	Sensitivity to M1-M2 decenters	5	4	1	4	3
9	Sensitivity to M1-M2 axial despace	5	3	3	3	3
10	Sensitivity to decenters of M3, M4, …	3	3	5	3	3
11	Sensitivity to axial despace of M3, M4,	3	2	5	2	2
12	Central obscuration	3	2	5	2	2
13	Vignetting in the science field	5	5	5	5	5
14	Vignetting outside the science field	2	5	5	5	5
15	M1-M2 separation	5	4	4	4	4
16	Structure aspect ratio	4	3	4	3	3
17	Built-in IR adaptive optics (SCAO & GLAO)	5	3	5	5	5
18	Built-in IR MCAO	5	3	0	0	0
19	Separation of active and adaptive functions	5	3	0	0	0
20	SCAO / GLAO mirror dimensions	5	5	1	0	1
21	MCAO mirrors dimensions	5	2	0	0	0
22	Intermediate focus for AO calibration	2	3	0	0	3
23	Number of segmented mirrors	4	3	5	3	3
24	Feasibility of secondary mirror	5	5	1	5	5
25	Difficulty of fabricating most aspheric mirror(s)	4	1	1	1	3
26	Compatibility with serial production & maintenance of segments	5	5	1	5	1
27	Segments optical testing	4	5	1	5	1
28	Compatibility with lightweight segments	3	5	1	5	0
29	Baffling options	2	4	0	1	1
30	Allowable design volume for active/adaptive units	2	2	5	5	5
31	Allowable design volume for instruments	3	5	3	5	3
32	Access to gravity-stable platform(s)	3	0	0	0	0
33	Rapid switch between permanently mounted instruments possible (without additional relay optics).	2	5	0	0	0
SCORE (Σ Weight x Rating); maximum = 640			**429**	**310**	**322**	**334**

Table 6-2. Ratings for designs No 1 to 4. (*) P=Pass; F=Fail.

6.2.2 Baseline design

The baseline optical design is described in RD2; its overall geometry is shown in Figure 6-9 and the mechanical implementation in Figure 6-10. This baseline is a recent update of the former one (RD1), with a focal ratio of the primary mirror reduced from the former f/1.42 to the current f/1.25. At the time of writing of this document, the update has not yet been propagated to all areas of the system. Most notably, instruments concepts are still based on the former design. Differences are however minor and unlikely to have any significant impact on instrument concepts.

The present section concerns optical design only; considerations related to pupil and segments geometries are addressed in section 6.5.1.1.

The essential features of the baseline optical design are

- A spherical, f/1.25 primary mirror;
- A flat, 25.8-m secondary mirror;
- A four-elements corrector, with two active mirrors (M3 and M4), 8-m class, and two adaptive ones (M5 and M6), with diameters of ~2.5 and 4.0-m, respectively.

Prescription data are given in Table 6-3. The image surface is given as a conic, for minimum rms image size on the wavefront sensors[47]. The M1-M2 separation is such that the diameter of the secondary mirror is twice the size of a structural module.

The diameters are indicative only and will have to be re-calculated, taking into account tolerances on vignetting for wavefront sensing with natural and laser guide stars. These tolerances have not been calculated at the time of writing of this document; it is plausible that the diameters of surfaces M3 and M5 will eventually be reduced.

Fictive surfaces in the design listing (No 1, 4, 7, and 8) correspond to M2 obscuration, M4 hole, M3 hole, and M6 hole, respectively.

The image quality at the edge of the 10 arc minutes, f/6 focus is 0.052 arc seconds rms (see section 6.3.1 for detailed image quality data). The linear field diameter is 1780.7 mm and the image scale on-axis is 2.924 mm / arc second.

Central obscuration is 35% linear. Central obscuration and field of view are related through the dimension of M3 central hole; a larger obscuration would permit a larger field of view, which is limited by vignetting (M3 central hole) rather than by optical quality.

The entrance pupil is the primary mirror and the exit pupil is co-located with M6. The backfocal distance (M6 i.e. exit pupil to focus) is 13994.53 mm.

The strengths of this design are essentially

- Excellent image quality in the field of view;
- Low sensitivity to the (flat) secondary mirror decenters;
- Availability of two surfaces, M6 and M5, for adaptive compensation;
- Availability of two surfaces, M3 and M4, for active optics (low time frequency, high amplitude deformation of flexible mirrors);
- Availability of all wavefront control functions, including field stabilization, with no more than 6 surfaces.
- Compatibility with serially produced segments (spherical primary, flat secondary);
- Baffling opportunities.

Stringent centering tolerances inevitably appear, albeit within the corrector, which is favourably located. A complete sensitivity analysis is provided in section 6.3.5.

[47] Moving the sensors on a spherical rather than conic surface does however not yield to significant errors.

The main weaknesses of the design are:

- Tilted AO mirror, limiting performance with GLAO;
- Fairly short focal ratio;
- Fairly strong field curvature, concave in the direction of propagation of light.
- Large, segmented secondary mirror;
- Limited design space for M6 AO unit;
- No gravity-stable instrument location;
- Extreme aspherization of mirror M4 (12.7 mm deviation from best fitting sphere).

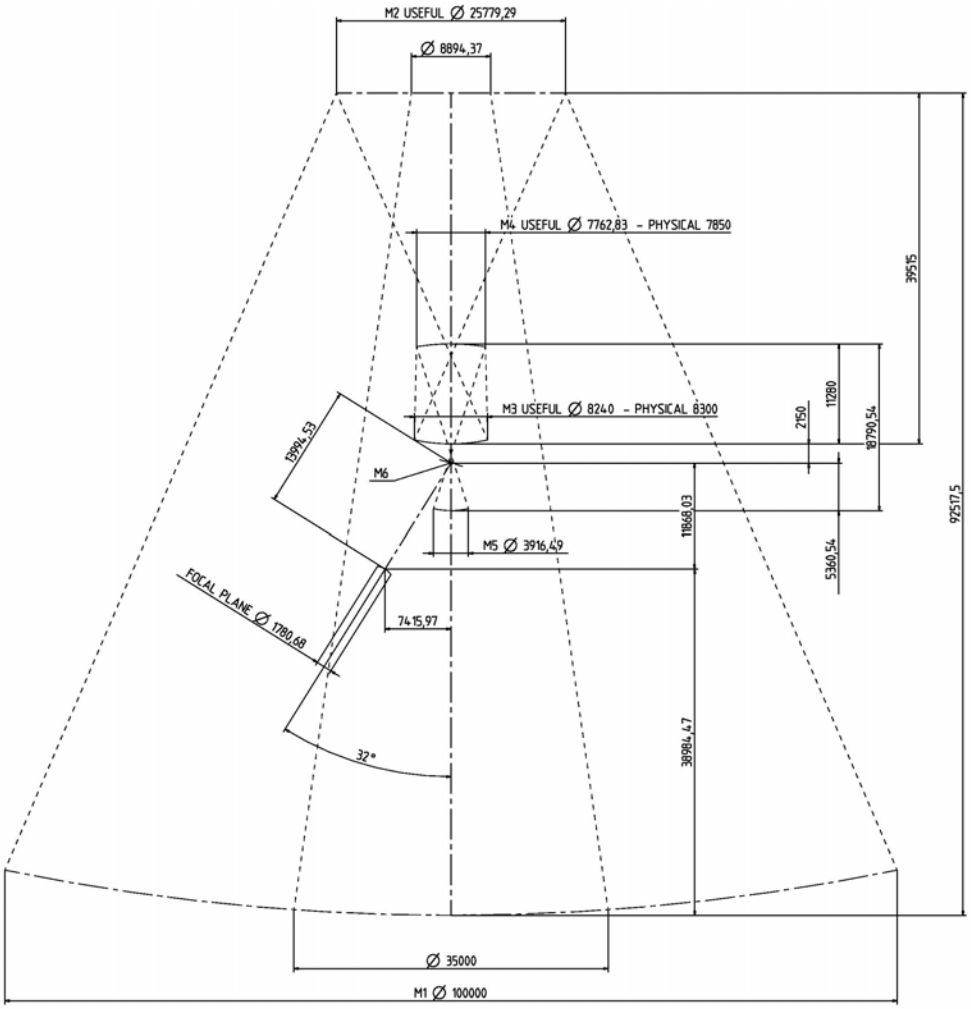

Figure 6-9. Baseline optical design, major dimensions.

Field aberrations include high order terms and are not accurately described with 36 Zernike Polynomials.

Further optimization of the design seems possible to some extent; a slightly longer focal ratio (~f/6.5) would probably be possible if required. The secondary mirror dimension (25.8-m) being smaller than the linear obscuration (35%), it is possible to relax the focal ratio of the primary mirror to f/1.32 without increasing the mirrors spearation, and with subsequent advantages in terms of feasibility of M4, and possibly a reduced tilt and increased design space of M6. The increased secondary mirror diameter (30-m) would, however, no longer be an integer multiple of

the standard size of the structural modules, thus implying a more complex interface to the telescope structure.

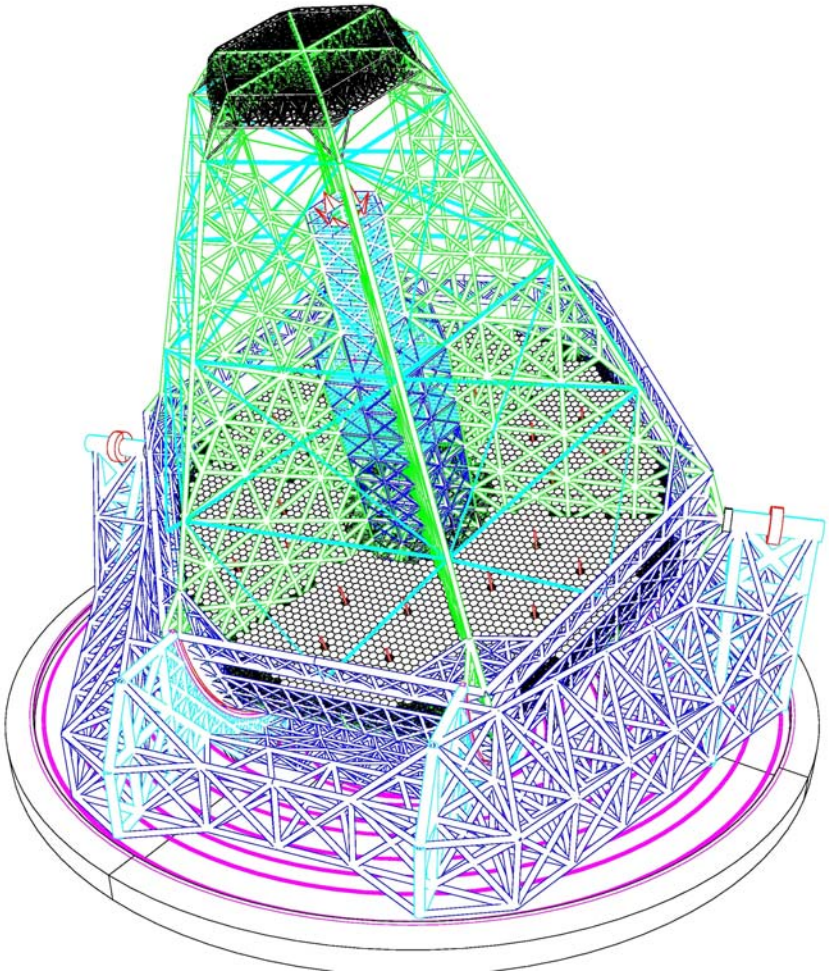

Figure 6-10. Baseline design, optomechanical implementation.

System/Prescription Data

```
File OWL-1250-92518-100m-11.ZMX
Surfaces                :              11
Stop                    :               2
System Aperture         : Entrance Pupil Diameter = 100000
Effective Focal Length  :        602364.9 (in image space)
Entrance Pupil Diameter :          100000
Entrance Pupil Position :         92517.5
Exit Pupil Diameter     :        2316.556
Exit Pupil Position     :       -13968.31
Field Type              : Angle in degrees
Maximum Radial Field    :      0.08333333
Primary Wavelength      :             0.5 µm
Lens Units              :   Millimeters
```

SURFACE DATA SUMMARY:

Surf	Type	Radius	Thickness	Glass	Diameter	Conic
OBJ	STANDARD	Infinity	Infinity		0	0
1	STANDARD	Infinity	92517.5		100254.4	0
STO	STANDARD	-250000	-92517.5	MIRROR	100000	0
3	STANDARD	Infinity	28235	MIRROR	25779.29	0
4	STANDARD	Infinity	11280		1820.15	0
5	EVENASPH	-18690	-11280	MIRROR	8241.896	0
6	EVENASPH	19970	11280	MIRROR	7762.828	0

```
7      STANDARD    Infinity          2150                 1665.273          0
8      STANDARD    Infinity          5360.54               721.3222         0
9      EVENASPH       -8504         -5360.54   MIRROR     3916.487          0
10     STANDARD    Infinity         13994.53   MIRROR     2608.574          0
IMA    STANDARD        2209.788                           1780.683     -1.295298
SURFACE DATA DETAIL:

Surface OBJ     : STANDARD
Surface   1     : STANDARD M2 OBSCURATION
 Aperture       : Circular Aperture
 Minimum Radius :         15000
 Maximum Radius :         51000
Surface STO     : STANDARD M1
 Aperture       : Circular Aperture
 Minimum Radius :         17500
 Maximum Radius :         50200
Surface   3     : STANDARD M2
 Aperture       : Circular Aperture
 Minimum Radius :          4400
 Maximum Radius :         12900
Surface   4     : STANDARD HOLE M4
Surface   5     : EVENASPH M3
 Coeff on r  2  :                0
 Coeff on r  4  :   9.9615208e-014
 Coeff on r  6  :  -7.4588943e-021
 Coeff on r  8  :   5.0822357e-028
 Coeff on r 10  :  -2.6489928e-035
 Coeff on r 12  :   9.3682602e-043
 Coeff on r 14  :  -1.9628184e-050
 Coeff on r 16  :   1.8115665e-058
 Aperture       : Circular Aperture
 Minimum Radius :             0
 Maximum Radius :          4090
Surface   6     : EVENASPH M4
 Coeff on r  2  :                0
 Coeff on r  4  :  -2.0050643e-013
 Coeff on r  6  :  -8.3000578e-022
 Coeff on r  8  :  -4.8126671e-029
 Coeff on r 10  :   1.8076695e-036
 Coeff on r 12  :  -2.7869116e-044
 Coeff on r 14  :                0
 Coeff on r 16  :                0
 Aperture       : Circular Aperture
 Minimum Radius :             0
 Maximum Radius :          3890
Surface   7     : STANDARD HOLE M3
Surface   8     : STANDARD HOLE M6
Surface   9     : EVENASPH M5
 Coeff on r  2  :                0
 Coeff on r  4  :   1.2236767e-013
 Coeff on r  6  :  -1.1194562e-020
 Coeff on r  8  :   8.8474514e-027
 Coeff on r 10  :  -1.2274556e-034
 Coeff on r 12  :  -1.1526053e-039
 Coeff on r 14  :   3.4012362e-046
 Coeff on r 16  :  -3.0833076e-053
 Aperture       : Circular Aperture
 Minimum Radius :           210
 Maximum Radius :          2000
Surface  10     : STANDARD M6
 Tilt/Decenter  : Tilt X = 16
 Aperture       : Elliptical Aperture
 X Half Width   :          1220
 Y Half Width   :          1330
Surface IMA     : STANDARD IMAGE
```

Table 6-3. Baseline design, optical prescription.

6.2.3 Optional corrector

For IR applications beyond 2.2 μm and with limited field requirements, the nominal corrector could be replaced by a simpler 2-mirror design (see Appendix 9). The two mirrors of the corrector would be 6.1 and 4.1-m diameter, respectively. They would receive IR-optimized reflective coatings. The 4.1-m mirror (M4) is conjugated to the pupil and could therefore provide either ground layer or single conjugate adaptive correction. In view of the long wavelength range, actuator interspacing needs not to be pushed beyond current technology. A 1.2-m spacing in the entrance pupil would correspond to ~49 mm interactuator spacing on M4 and a total of 5,054 actuators. According to simulations the expected AO performance would be

r_0~0.19-m	(seeing ~0.5 arc secs at 0.5 μm)	λ = 5 μm	Strehl Ratio ~87%
		λ = 10 μm	Strehl Ratio ~96%
r_0~0.10-m	(seeing ~1.0 arc secs at 0.5 μm)	λ = 5 μm	Strehl Ratio ~71%
		λ = 10 μm	Strehl Ratio ~91%

Under favorable seeing conditions (less than ~0.5 arc seconds in the visible i.e. r_o~1.2-m in K band), performance would still be reasonable in K band. A six-petal segmentation of M4 would be possible –being it an image of the entrance pupil- with maximum gap size of 40 mm.

6.2.4 Reduced aperture designs

Optical solutions have been explored at notional level, in the assumption of a relaxed specification on aperture size (see RD48 for a full report). At 80-m, the 4-mirror design shown in section 6.2.1, Figure 6-7, does no longer require monolithic mirrors larger than 8-m. Several possible configurations between f/15 and f/30 have been briefly evaluated. Although further optimization might be possible, the diffraction-limited field of view is rather limited and the location of the science instrumentation rather inconvenient.

At 60-m the palette of options becomes wider. In addition, a segmented secondary mirror may no longer be required. Figure 6-11 shows a 4-mirror f/15.5 design. It is essentially a beam compressor with spherical 60-m primary and aspherical 8-m convex secondary mirrors, combined with a Gregorian re-imager. Optical design data are given in Table 6-4. The field of view is 10 arc minutes diameter. The linear obscuration is 33% and set by the quaternary mirror. Mirror M4, with a diameter of 2.7-m and located in a pupil, would be suitable for single conjugate adaptive optics. The diffraction-limited field of view is close to 2 arc minutes diameter in the visible and close to 4 arc minutes in K band (see Table 6-5). A potential disadvantage of this design is its relatively strong sensitivity to decentres.

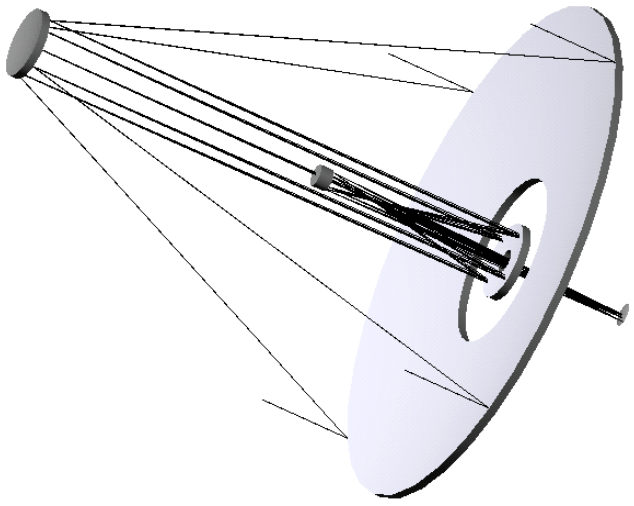

Figure 6-11. 4-mirror f/15 design, 60-m aperture.

Mirror	Diameter (m)	Radius of curvature (m)	Profile	Distance to next surface (mm)
M1	60.0	-145000	Sphere	61500
M2	8.2	-2057	Asphere	61500
M3	8.5	-3571	Asphere	23265
M4	2.6	-697	Asphere / adaptive	38500
Image	2.7	5.360	Sphere	-

Table 6-4. 4-mirror f/15 design, 60-m aperture; optical prescription.

Fabrication of the convex, aspherical secondary mirror is difficult but a possible test set-up has been calculated. The mirror would be tested at centre of curvature in double pass (Figure 6-12). The nulling system is made of a 650-mm aspheric, diamond-turned mirror combined with a 11.4-m spherical mirror. The latter could be undersized if stitching of subapertures could be tolerated, or segmented (e.g. 6 petals).

Field of view (radius)	RMS wavefront error (nm)	Strehl Ratio at 500 nm	Strehl Ratio at 2000 nm
On-axis	9	0.987	0.999
0.5 arc min	11	0.982	0.999
1.0 arc min	44	0.732	0.981
2.0 arc min	190	0.003	0.699
3.0 arc min	446	0.000	0.140
4.0 arc min	810	0.000	0.002
5.0 arc min	1350	0.000	0.000

Table 6-5. 4-mirror f/15, 60-m aperture design. Nominal optical quality.

Mirrors M3 and M4 are concave and could probably be tested through Oeffner compensators.

A modified, folded f/20 version of this design allows the beams to be folded along the elevation axis, thereby providing 2 convenient Nasmyth foci, in addition to the Cassegrain one.

A solution with a parabolic, f/0.75 primary mirror has also been briefly evaluated (Figure 6-13). The design is extremely compact, and therefore very favorable in relation to structural stiffness and enclosure cost. The primary mirror being parabolic, M1-M2 decentres do not introduce coma but astigmatism only (linear with the field of view). However, depointing is still a potential issue. Nominal optical quality is excellent, with a diffraction-limited (Strehl Ratio ≥ 0.80) field of view in excess of 3 arc minutes in the visible and 6 arc minutes in K band.

Off-axis parabolic segments could be tested in double pass against a reference flat. Matching of the segments indidivual curvature is however an issue and no convenient solution have been found so far.

Reduced aperture designs are, at the time of writing of this document, very notional.

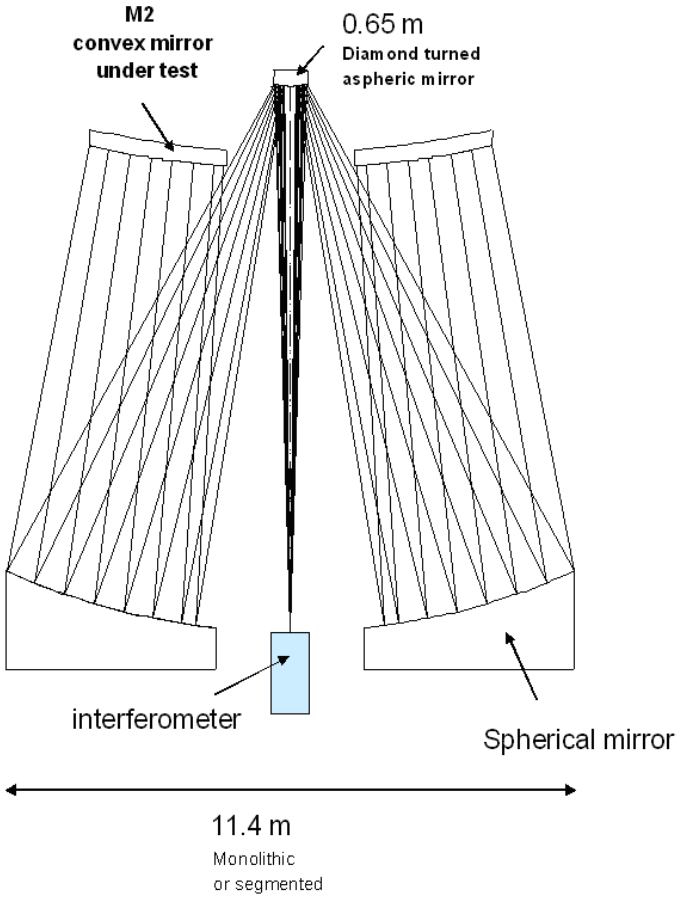

Figure 6-12. Optical test set-up for the testing of a convex, aspherical 8-m class mirror.

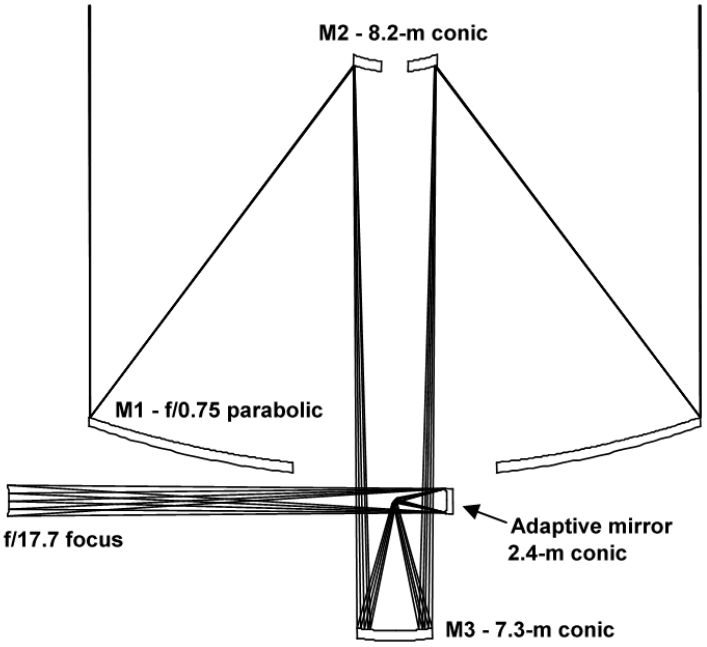

Figure 6-13. 60-m four mirror design with f/0.75 parabolic primary mirror.

6.2.5 Future design iterations

According to plans, the preliminary design phase will start with a re-assessment of the current optical design solution, taking into account, in particular, results from instrument studies and AO simulations.

At the time of writing of this document, exploratory work has already begun with a view to producing a fully co-axial design, thereby removing the undesirable tilt of M6 conjugate and allowing, if requested, to transport a small part of the field, by way of additional relay optics, down to the elevation axis and eventually to Nasmyth-type platforms.

Effort is currently concentrating on a solution whereby the mirror M6 is coaxial, spherical and convex. Optical quality in the field of view is excellent but transferring a 10 arc minutes field of view through a hole in M5 seems impossible unless M5 hole is enlarged to such proportion that the beam footprints on M5 will be vignetted outside a 5-6 arc minutes field of view. This vignetting does not affect science targets, but its implication on the active control loops needs to be assessed. In practice this makes the reconstruction of the desired M4 and M3 active deformation more complex, but the availability of several off-axis guide stars for active optics should allow sufficient overlap between beams footprints to permit accurate fitting of the active optics modes. Indeed the situation is more favorable than in the VLT, where significant vignetting by the tertiary mirror occurs beyond 10 arc minutes off-axis, and where only one wavefront sensor is available. On the negative side, this design requires a reduction of the focal ratio to ~f/4-f/5 in order to avoid increasing obscuration much beyond 35%.

Another design iteration which is under way at the time of writing of this document is a minor update of the baseline, with a f/1.32 instead of f/1.25 primary mirror, and a 30-m flat secondary mirror. It is expected that this update will allow more design space for M6 unit, a slightly longer focal ratio (~f/6.5 instead of f/6), and somewhat smaller field aberrations and aspherization of M4.

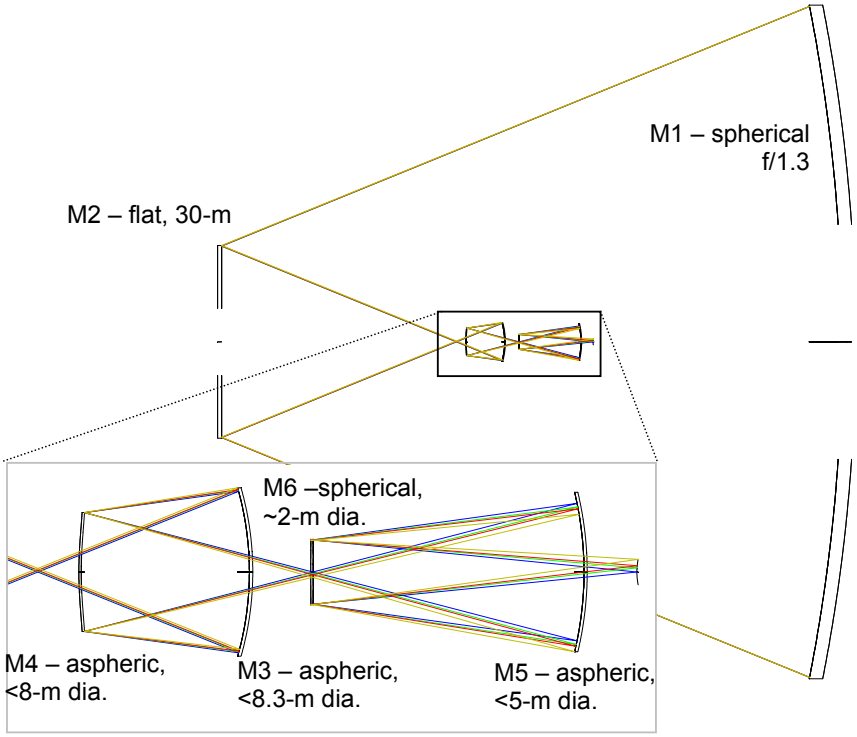

Figure 6-14. Coaxial design with f/5 focus. Field of view 6 arc minutes, f/1.3 primary mirror.

6.3 Optical characteristics

6.3.1 Nominal optical quality

The optical quality (Strehl Ratio) of the baseline 6-mirror design is given in Figure 6-15 (Strehl Ratio, up to 3 arc minutes off-axis), Figure 6-16 (RMS spot size up to 5 arc minutes off-axis), and Figure 6-17 (wavefront RMS, up to 5 arc minutes off-axis). Results are summarized in Table 6-6.

Monochromatic Point Spread Functions at 0.5 and 2.2 microns are shown in Figure 6-18 and Figure 6-20; ensquared energy in Figure 6-19 and Figure 6-21. None of these figures takes segmentation into account; the pupil shape is annular. It should be noted that non-axisymmetrical diffraction artefacts (Figure 6-18 and Figure 6-20) will be blurred by differential field-pupil rotation.

Diffraction-limited field of view (Strehl Ratio ≥ 0.80)		
λ=0.5 μm (on curved field with R=2209.8 mm)	142 arc seconds	(diameter)
λ=2.2 μm (on curved field with R=2215.4 mm)	245 arc seconds	(diameter)
λ=5.0 μm (on curved field with R=2243.1 mm)	360 arc seconds	(diameter)
Image quality at edge of field		
Wavefront RMS	1.476 μm	
RMS spot size	0.052 arc seconds	

Table 6-6. Baseline design, optical quality.

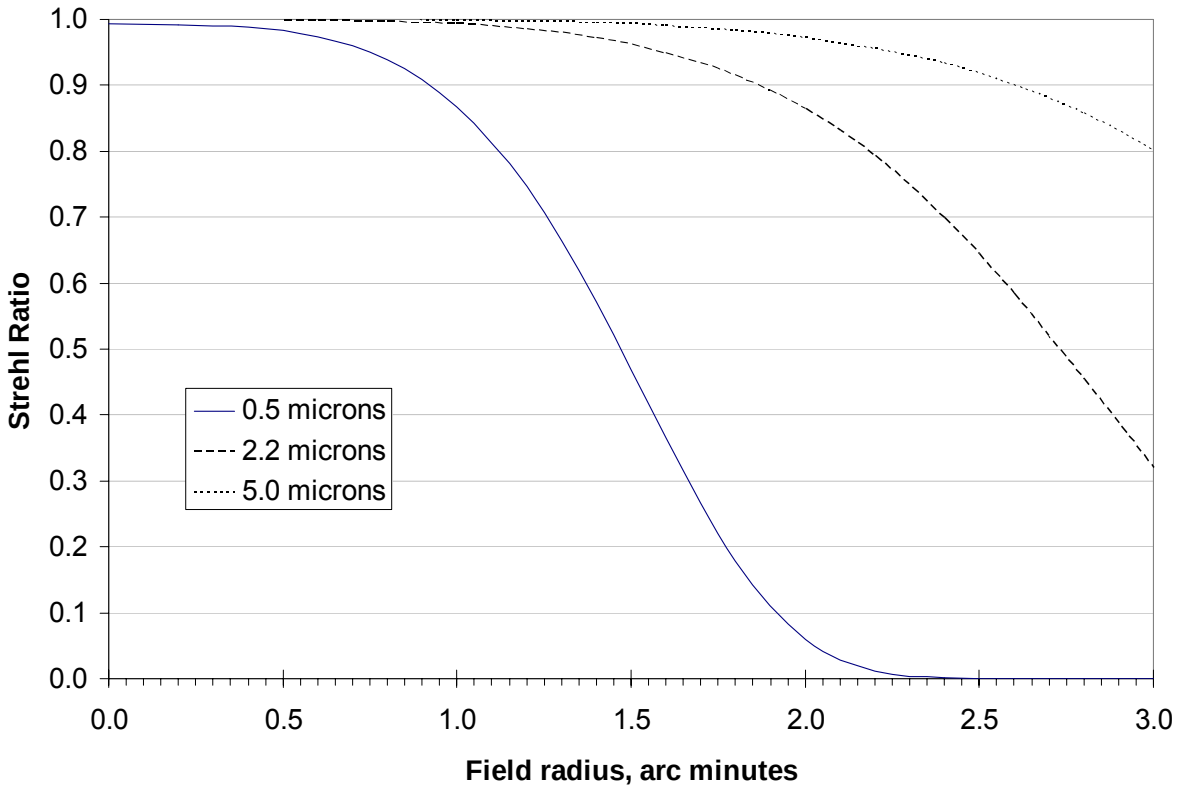

Figure 6-15. Baseline design; Strehl Ratio vs field of view.

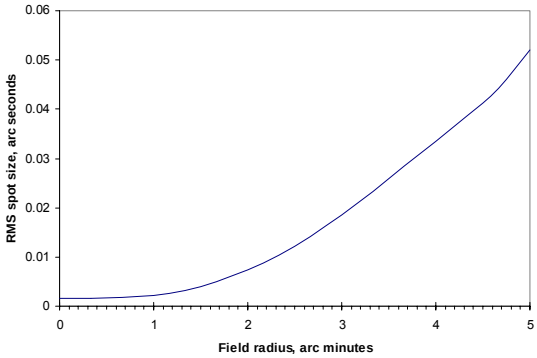

Figure 6-16. Baseline design; rms spot size (arc seconds) vs field radius.

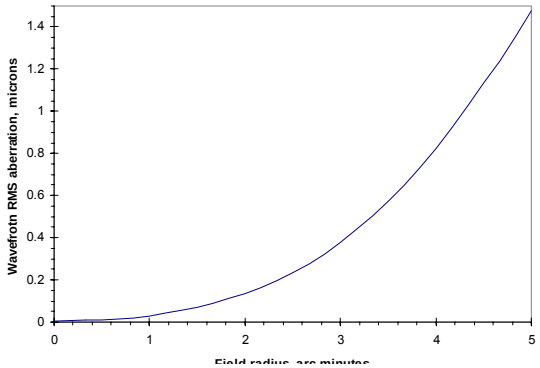

Figure 6-17. RMS wavefront error (microns) vs field radius.

Distortion is fairly small (1.31% at the edge of the field, see Figure 6-22). Distortion is defined here as $(\rho-\rho_p)/\rho_p$, where ρ is the radial coordinate of the impact of the real chief ray onto the image surface, and ρ_p the radial coordinate of the impact of the paraxial chief ray. A calculation based on image centroid may lead to slightly different figures.

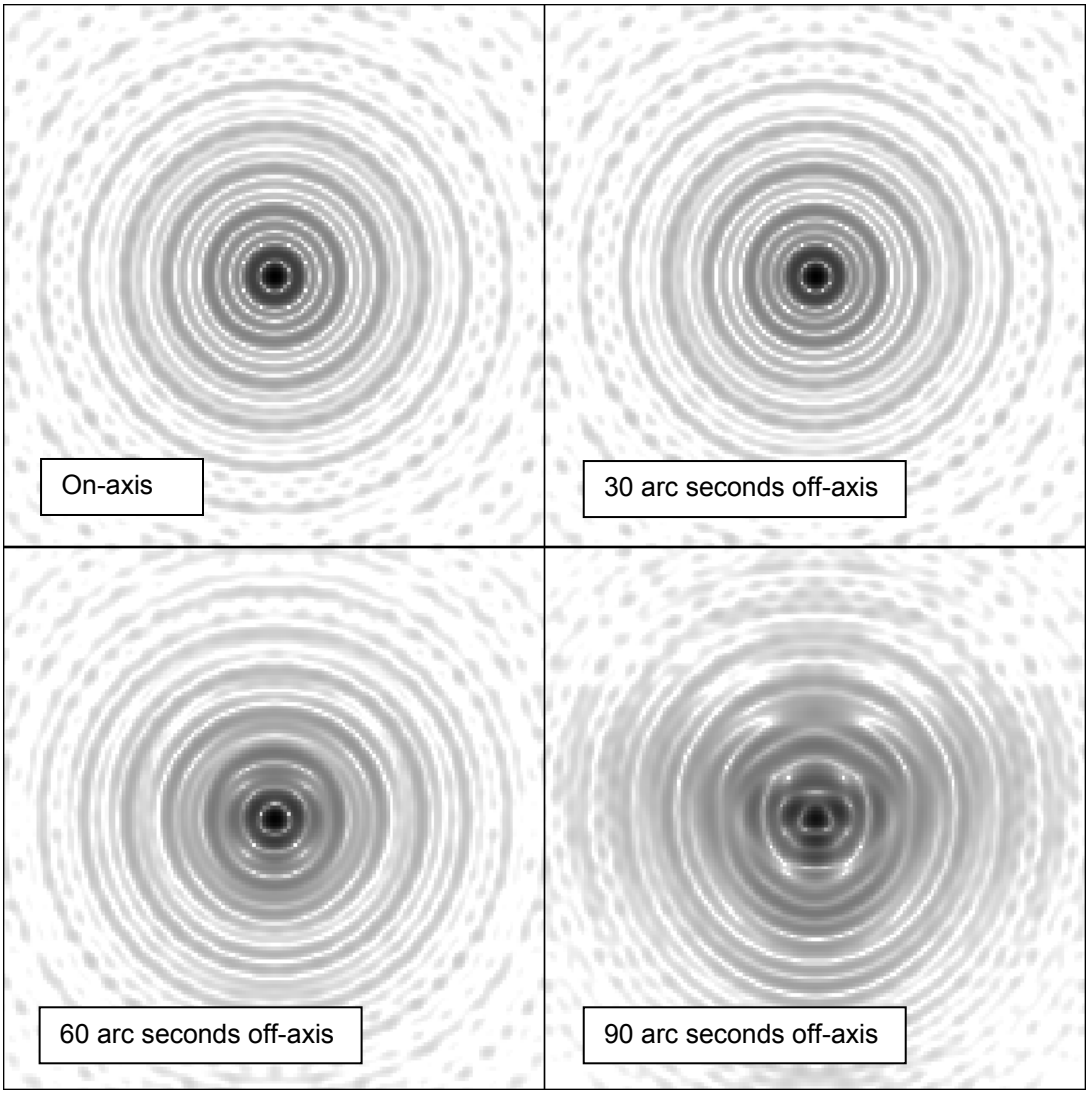

Figure 6-18. Point Spread functions at 0.5 microns. Box size 0.040 arc seconds.

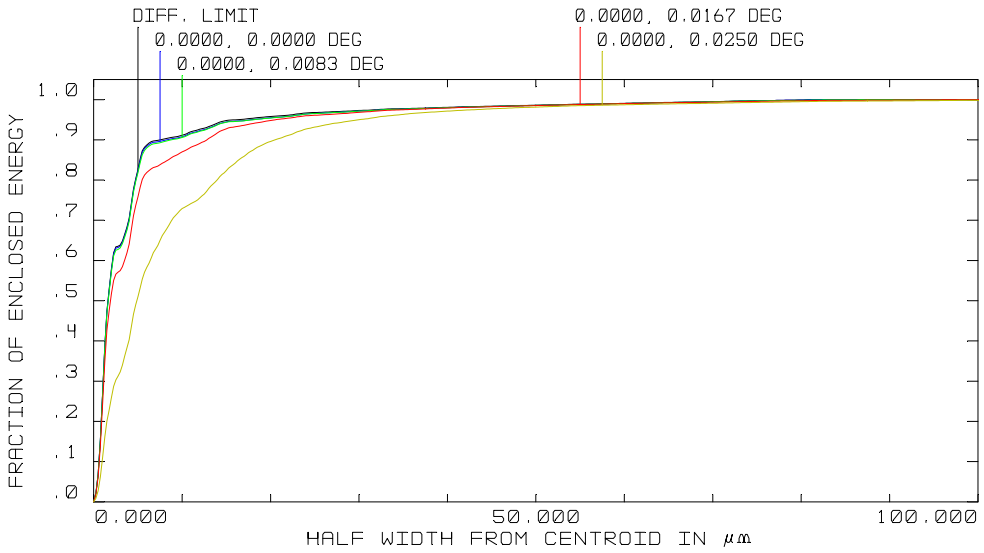

Figure 6-19. Ensquared energy at 0.5 microns. Scale: 100 microns = 0.0342 arc seconds.

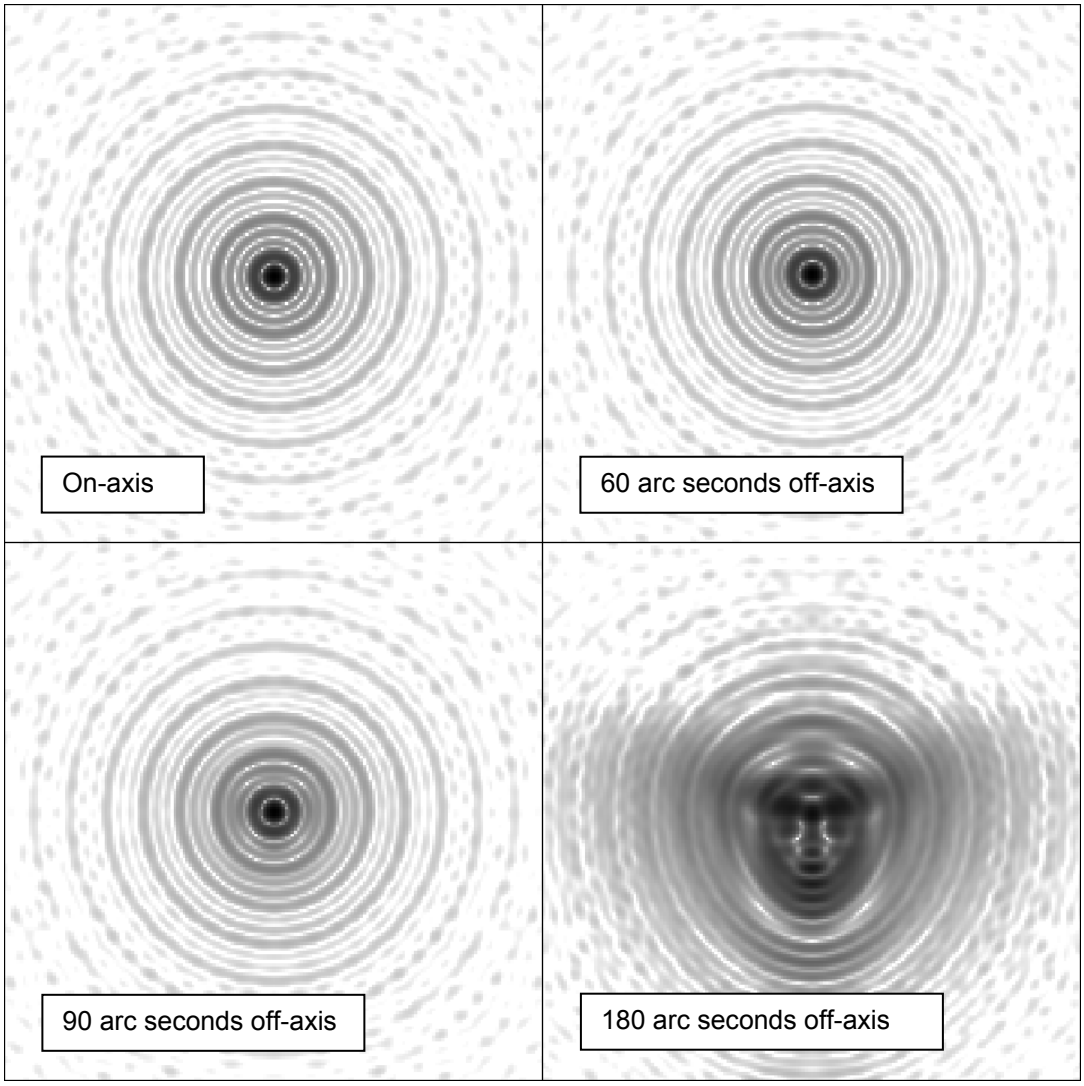

Figure 6-20. Point Spread functions at 2.2 microns. Box size 0.200 arc seconds.

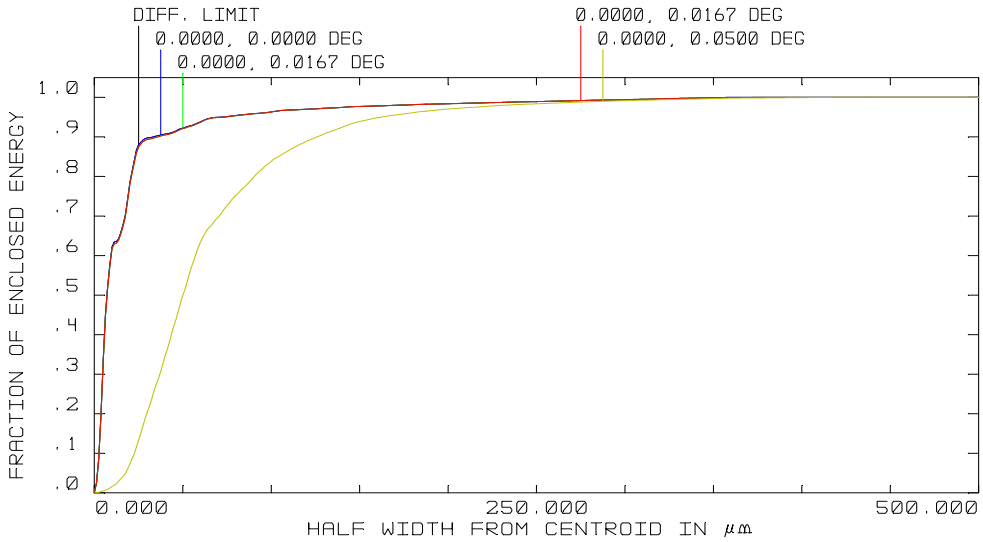

Figure 6-21. Ensquared energy at 2.2 microns. Scale: 500 microns=0.171 arc seconds.

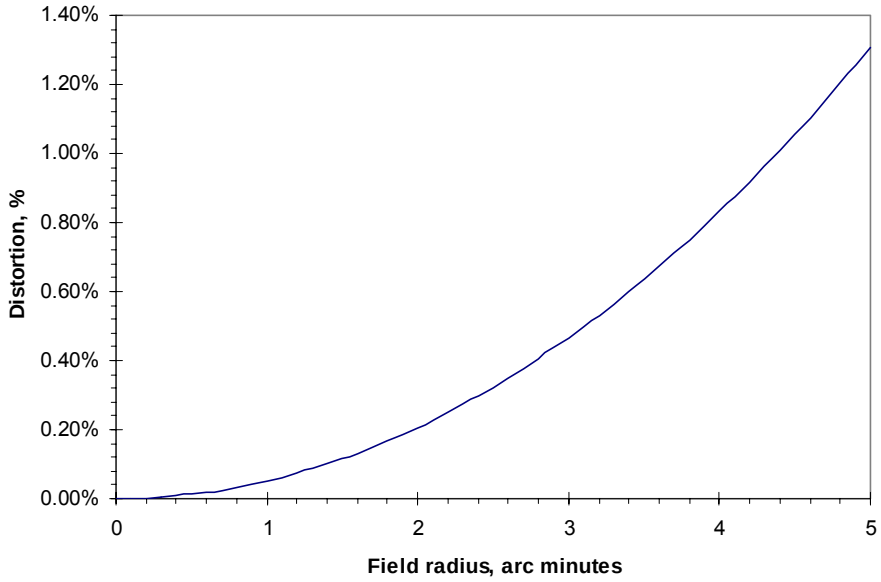

Figure 6-22. Distortion.

6.3.2 Vignetting

With the dimensions given in section 6.2.2, vignetting is completely negligible over the entire 10 arc minutes field of view. It may, however, be profitable to allow slight vignetting outside the 6 arc minutes diameter of the the Adaptive Optics control field of view, or even to allow vignetting to start at 3 arc minutes (outside the science field). The useful diameter of M5 as a function of the unvignetted field is

Unvignetted field	10 arc minutes	M5 diameter	3916.4 mm
Unvignetted field	6 arc minutes	M5 diameter	3629.0 mm
Unvignetted field	3 arc minutes	M5 diameter	3412.6 mm

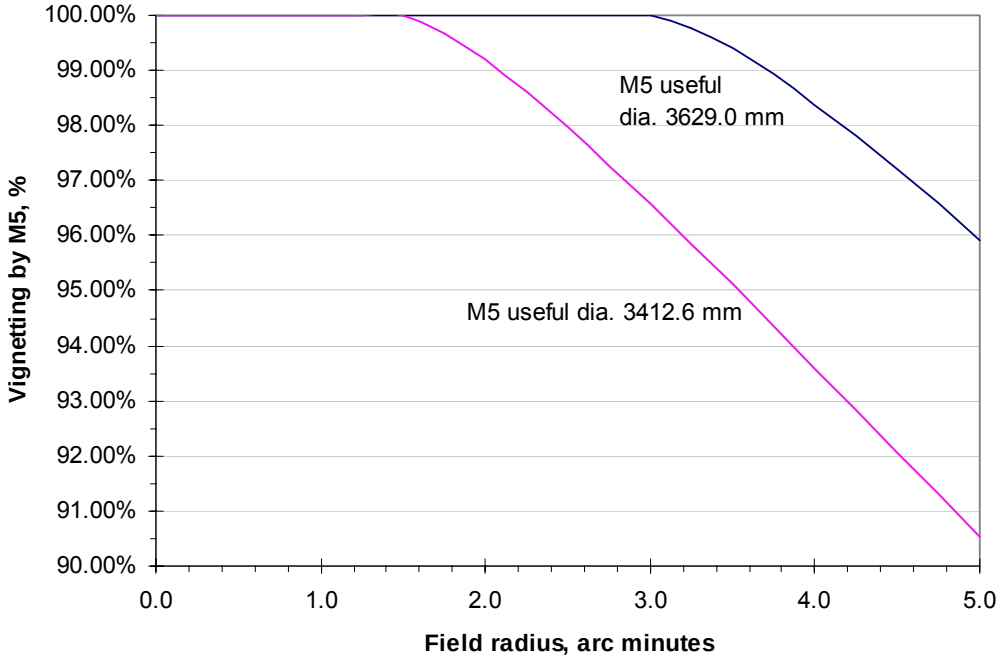

Figure 6-23. Vignetting by M5 as a function of M5 diameter.

Figure 6-23 shows the vignetting by M5, in the field of view for the two possible sizes of M5. The effect on active and possibly adaptive wavefront sensing ought to be small if not entirely negligible. It should be noted that the outer rim of M5, which would not be seen by the adaptive optics wavefront sensors, need to be controlled by the active optics ones. It would be simpler and probably better to allow vignetting of the corresponding light beams (outside the central 6 arc minutes i.e. M5 useful diameter 3629 mm instead of 3916.4 mm). A decision can however not be taken at this point, as the full implications on re-imaging of laser guide stars need to be assessed.

A similar reasoning applies with M3. The useful diameter is 8241.8 mm for an unvignetted field of view of 10 arc minutes; it can be reduced to 7963.8 mm if vignetting is allowed outside the central 3 arc minutes, with a maximum of 1.4% at the edge of the 10 arc minutes full field.

6.3.3 Stray light and baffling

The 4-mirror OWL corrector gives ample opportunity to provide good baffling, avoiding any risk of getting skylight not coming through the right mirror sequence, a must for a telescope operating in open air. The simple set of baffles shown in Figure 6-24 is fully adequate: although the first of the two intermediate images suffer from huge geometrical aberrations, the two field stops (defined by these baffles and the hole in M6) and the two pupil stops (defined by M4 and M6) are sufficient to prevent geometrical stray light coming from the sky (e.g. from the Moon) to be seen by the telescope focal plane. Good performance in terms of stray light is thus expected in the non-thermal spectral domain (Visible & near-IR up to the “blue” part of the H-band). Note however that a very bright source, and in particular the Moon, will also give some diffuse light depending on the cleanliness of the telescope mirrors, especially M1. This may restrict sky coverage during bright Moon periods for some type of observations (short wavelengths, coarse spatial resolution and/or small spectral resolution). A detailed analysis with adequate software tools is foreseen in Phase B.

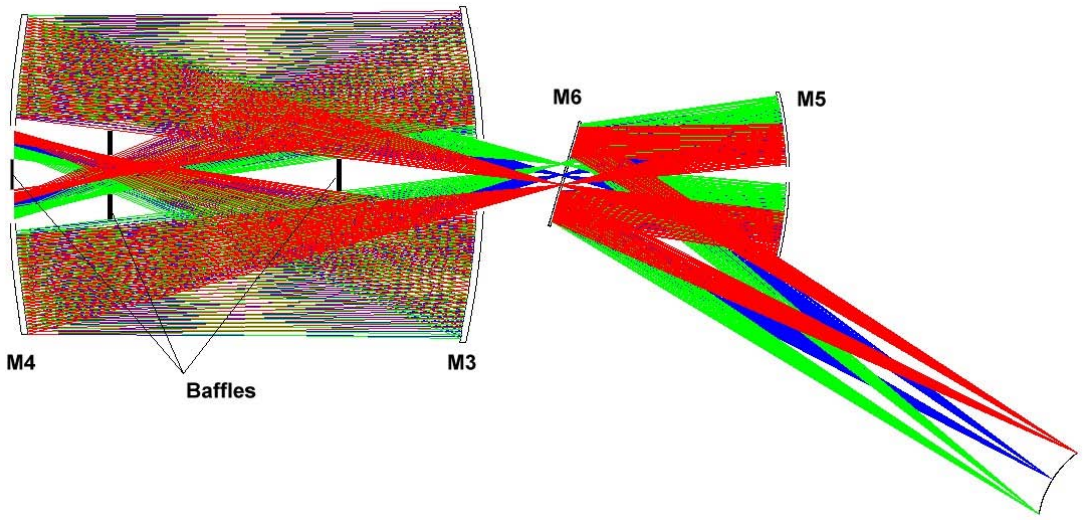

Figure 6-24. Possible set of baffles.

In the thermal IR on the other hand, it is essential that a cold stop be put on an optically good image of the pupil to mask for the strong thermal radiation coming from the corrector inner mechanics. This is a non trivial optical requirement put on each instrument project. It should be relatively easy to meet for multi-imagers and integral field spectrometers working at high spatial resolution since their linear field of view is small. This is more difficult for wide-field imaging, and case by case studies with the proper software tools are needed during Phase B.

6.3.4 Emissivity

The expected emissivity at 2.2 μm is given in Table 6-7. All obscured areas are assumed to have 100% emissivity. The figure without pupil mask (2nd column) is given for background information only. The pupil mask is shown in Figure 6-25. We assume 3% emissivity with classical Al coatings (3rd column), 1% with optional gold coatings, and a longitudinal ADC with 1% emissivity per interface glass-air. The overall emissivity figure is plausibly pessimistic as the facing-down secondary mirror and the fairly well protected corrector surfaces should normally be cleaner than the primary mirror. In addition, a cold plate located behind the primary and secondary mirrors may reduce the emissivity by the gaps.

Source	w/o pupil mask	with pupil mask	Pupil mask + Gold coated M2-M4	Pupil mask + Optional corrector	Pupil mask + Optional corrector + gold-coated M2
M1	3.0%	3.0%	3.0%	3.0%	3.0%
M2	3.0%	3.0%	1.0%	3.0%	1.0%
M3	3.0%	3.0%	1.0%	1.0%	1.0%
M4	3.0%	3.0%	1.0%	1.0%	1.0%
M5	3.0%	3.0%	3.0%		
M6	3.0%	3.0%	3.0%		
M1+ M2 gaps	1.2%	1.2%	1.2%	1.2%	1.2%
Ropes	1.1%	1.1%	1.1%	1.1%	1.1%
Spiders + missing segments	6.1%				
Central obscuration	11.9%				
Subtotal w/o ADC	**38.3%**	**20.3%**	**14.3%**	**10.3%**	**8.3%**
Total	**42.3%**	**24.3%**	**18.3%**	**14.3%**	**12.3%**

Table 6-7. Expected emissivity at 2.2 μm, classical Al or Au coatings.

Source	w/o pupil mask	with pupil mask	Pupil mask + Optional correcor
M1	1.5%	1.5%	1.5%
M2	1.5%	1.5%	1.5%
M3	1.5%	1.5%	1.5%
M4	1.5%	1.5%	1.5%
M5	1.5%	1.5%	
M6	1.5%	1.5%	
M1+M2 gaps	1.2%	1.2%	1.2%
Ropes	1.1%	1.1%	1.1%
Spiders + missing segments	6.1%		
Central obscuration	11.9%		
Subtotal w/o ADC	**29.3%**	**11.3%**	**8.3%**
ADC (1% per surface)	4.0%	4.0%	4.0%
Total	**33.3%**	**15.3%**	**12.3%**

Table 6-8. Expected emissivity at 2.2 μm, Gemini enhanced Ag coatings.

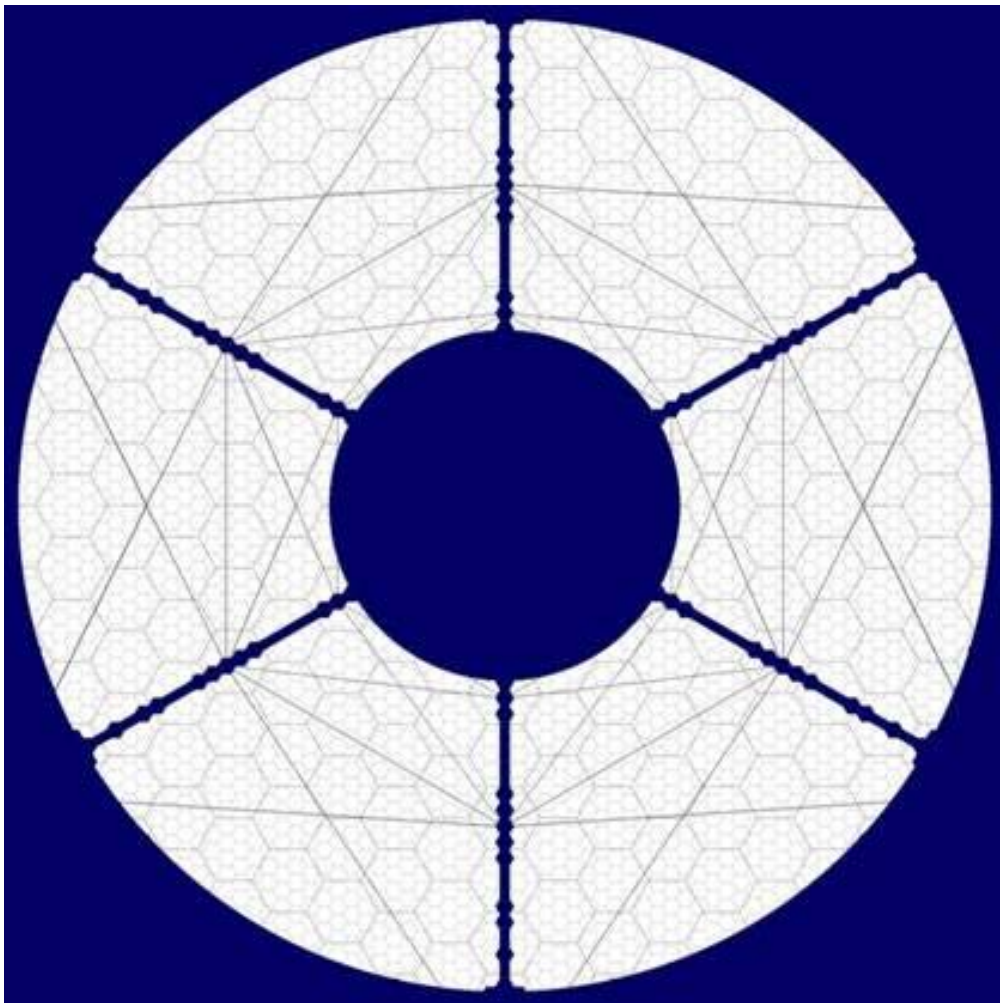

Figure 6-25. Pupil mask (emissivity budget). The pupil mask covers all obstructed areas except the inter-segment gaps and tensioning ropes.

The proposed segments maintenance infrastructure (see RD5) would allow the secondary mirror to be gold-coated within 43 days. In a science operation scenario whereby the telescope would have to be IR optimized over a significant span of time, one could reasonably assume that the mirrors M2 to M4 would receive temporary gold coatings. In the 43 days transition phases a variable reflectivity of the pupil would have to be tolerated. The telescope downtime would be limited to that required for the gold-coatings of M3 and M4 i.e. 5 to 7 calendar days.

Long-term durability data about the Gemini enhanced Ag coatings are not available at the time of writing of this report. Early performance results are however very promising, with a reported emissivity of less than 1.5% per reflective surface. Would such coatings be eventually selected, OWL emissivity would be as given in Table 6-8.

6.3.5 Sensitivity analysis

The sensitivity matrix (depointing and aberration coefficients for unit decenters) is given in Table 6-9. Field-dependent and field-independent terms are listed separately. Field-dependent terms are given at 1.5 arc minutes off-axis i.e. at the edge of the science field. Lateral decenters and tip-tilt introduce 3rd and 5th order coma (constant), and 3rd and 5th order astigmatism (linear in the filed of view). In addition, lateral decenters and tip-tilt may introduce a tilt of the image surface, i.e. a linear defocus.

The effect of corrector decenters (rigid body motion) about M4 vertex is given in Table 6-10. As expected, the effect of lateral decenters is identical to that of primary mirror decenters. The effect of tilt is much smaller.

Because of the short focal ratio of the primary mirror, M1, M2 and corrector piston are critical. Defocus will be best corrected by M2 for relatively large amplitudes and low time frequencies, fine correction being done with M5. M2 segments supports being identical to those of the primary mirror, they have the necessary range to compensate for up to 15 mm of despace. Excessive M5 refocus would require active deformation of M3 and M4 to compensate for the change in the prescription of field aberrations. Although theoretically possible, this is considered as a backup only, in case the required amplitude of M5 motion would exceed acceptable limits.

It should be noted that unit lateral decenters of M3 and M4 tend to compensate each other (coma terms), which is favorable since both mirrors will inherently move in the same direction under wind and gravitational loads.

It is expected that the internal metrology system, with a resolution of ~10 ppm, will allow centering all surfaces to within ~1 mm and ~2-3 arc seconds. Residuals will have to be compensated by active centering, with on-sky metrology.

OWL SENSITITVITY ANALYSIS — **ALL DATA ARE DIFFERENTIAL VALUE(DECENTERED) - VALUE(NOMINAL)**

Analysis file **OWL-1250-92518-100m-11sens.ZMX** — **Coordinates systems**

Units	dx, dy, dz	mm	About surface vertex	dx, dy, dz, da, db in surface ref. system, xy plane tangent to vertex
	da, db	arc seconds	About surface vertex	da = rotation about x; db = rotation about y
	dx_sky, dy_sky	arc secs		dz positive in the direction of ray propagation after surface
	Zernike	Coeff., microns (circular Zernikes)		Zernikes: x, y in-pupil coordinates
	WFE RMS	microns		*FIELD TERMS ARE GIVEN AT 1.5 ARC MINUTE OFF-AXIS ALONG +Y (*)*

Mirror	Decenter		Depointing		WFE RMS		Zernike coefficients												
							Field-independent							Field-dependent					
	Type	Ampl.	dx_sky	dy_sky	On-axis	Off-axis	Focus	Spher 3	Spher 5	Coma 3		Coma 5		Focus	Ast 3		Ast 5		
										x	y	x	y		x	y	x	y	
1	dx	1.000	1.652	0.000	2.831	2.830	0.000	0.000	0.000	2.699	0.000	0.009	0.000	0.000	0.000	-0.018	0.000	-0.001	
1	dy	1.000	0.000	1.652	2.831	2.827	0.000	0.000	0.000	0.000	2.699	0.000	0.009	0.005	0.018	0.000	0.001	0.000	
1	dz	1.000	0.000	0.000	23.095	23.095	40.002	0.001	0.000	0.000	0.000	0.000	0.000	0.000	0.000	0.000	0.000	0.000	
1	da	1.000	0.000	2.002	3.433	3.428	0.000	0.000	0.000	0.000	3.271	0.000	0.011	0.026	0.023	0.000	0.001	0.000	
1	db	1.000	-2.002	0.000	3.433	3.431	0.000	0.000	0.000	-3.271	0.000	-0.011	0.000	0.001	-0.001	0.021	0.000	0.001	
2	dx	1.000	0.000	0.000	0.000	0.000	0.000	0.000	0.000	0.000	0.000	0.000	0.000	0.000	0.000	0.000	0.000	0.000	
2	dy	1.000	0.000	0.000	0.000	0.000	0.000	0.000	0.000	0.000	0.000	0.000	0.000	0.000	0.000	0.000	0.000	0.000	
2	dz	1.000	0.000	0.000	46.192	46.192	80.007	0.003	0.000	0.000	0.000	0.000	0.000	0.000	0.000	0.000	0.000	0.000	
2	da	1.000	0.000	-0.520	4.349	4.348	0.000	0.000	0.000	0.000	-4.122	0.000	-0.013	-0.006	-0.026	0.000	0.000	0.000	
2	db	1.000	0.520	0.000	4.349	4.349	0.000	0.000	0.000	4.122	0.000	0.013	0.000	0.000	-0.001	-0.027	0.000	0.000	
3	dx	1.000	-1.243	0.000	33.029	33.032	-0.013	0.002	0.000	32.088	0.000	0.803	0.000	0.000	-0.012	-0.002	0.002	-0.046	
3	dy	1.000	0.000	-1.243	33.029	33.038	-0.013	0.002	0.000	0.000	32.088	0.000	0.803	0.014	0.014	0.000	0.044	0.000	
3	dz	1.000	0.000	0.000	22.945	22.946	39.740	-0.408	0.265	0.000	0.000	0.000	0.000	0.000	0.000	0.000	0.000	0.000	
3	da	1.000	0.000	-0.113	3.516	3.516	0.000	0.000	0.000	0.000	3.358	0.000	0.033	-0.044	0.012	0.000	-0.001	0.000	
3	db	1.000	0.113	0.000	3.516	3.516	0.000	0.000	0.000	-3.358	0.000	-0.033	0.000	-0.001	0.000	0.011	0.000	-0.001	
4	dx	1.000	-1.625	0.000	38.625	38.628	-0.007	0.002	0.001	-37.455	0.000	-0.866	0.000	0.000	-0.011	0.093	0.002	0.075	
4	dy	1.000	0.000	-1.625	38.625	38.633	-0.007	0.002	0.001	0.000	-37.455	0.000	-0.866	-0.301	-0.083	0.000	-0.077	0.000	
4	dz	1.000	0.000	0.000	11.966	11.970	20.719	-0.660	0.255	0.000	0.000	0.000	0.000	0.001	-0.001	0.000	0.000	0.000	
4	da	1.000	0.000	0.157	0.276	0.277	0.000	0.000	0.000	0.000	0.282	0.000	0.021	0.098	0.017	0.000	0.006	0.000	
4	db	1.000	-0.157	0.000	0.276	0.276	0.000	0.000	0.000	-0.282	0.000	-0.021	0.000	0.000	0.000	0.016	0.000	0.006	
5	dx	1.000	1.559	0.000	2.765	2.766	0.006	0.000	0.000	2.668	0.000	0.054	0.000	0.000	0.001	-0.073	0.000	-0.028	
5	dy	1.000	0.000	1.559	2.765	2.780	0.006	0.000	0.000	0.000	2.668	0.000	0.054	0.489	0.072	0.000	0.028	0.000	
5	dz	1.000	0.000	0.000	13.108	13.109	22.702	-0.249	-0.009	0.000	0.000	0.000	0.000	0.002	-0.002	0.000	0.000	0.000	
5	da	1.000	0.000	0.064	0.053	0.056	0.000	0.000	0.000	0.000	0.049	0.000	-0.001	0.119	-0.010	0.000	0.000	0.000	
5	db	1.000	-0.064	0.000	0.053	0.053	0.000	0.000	0.000	-0.049	0.000	0.001	0.000	0.000	0.000	-0.010	0.000	0.000	
6	dx	1.000	0.000	0.000	0.000	0.000	0.000	0.000	0.000	0.000	0.000	0.000	0.000	0.000	0.000	0.000	0.000	0.000	
6	dy	1.000	0.000	0.000	0.000	0.000	0.000	0.000	0.000	0.000	0.000	0.000	0.000	0.000	0.000	0.000	0.000	0.000	
6	dz	1.000	0.000	0.000	1.988	1.988	3.443	0.002	0.000	0.000	0.000	0.000	0.000	0.001	-0.001	0.000	0.000	0.000	
6	da	1.000	0.000	-0.046	0.000	0.019	0.000	0.000	0.000	0.000	0.000	0.000	0.000	-0.117	0.000	0.000	0.000	0.000	
6	db	1.000	0.046	0.000	0.000	0.000	0.000	0.000	0.000	0.000	0.000	0.000	0.000	0.000	0.000	0.000	0.000	0.000	
TOTAL			***-1.202***	***1.887***	***119.282***	***119.282***	***206.586***	***-1.303***	***0.513***	***-2.839***	***2.839***	***-0.052***	***0.052***	***0.288***	***0.009***	***0.012***	***0.006***	***0.006***	

Table 6-9. Baseline design, sensitivity matrix.

OWL SENSITITVITY ANALYSIS — **ALL DATA ARE DIFFERENTIAL VALUE(DECENTERED) - VALUE(NOMINAL)**

Analysis file **OWL-1250-92518-100m-11sens.ZMX** — **Coordinates systems**

Units

dx, dy, dz	mm	About M4 vertex
da, db	arc seconds	About M4 vertex
dx_sky, dy_sky	arc secs	
Zernike	Coeff., microns (circular Zernikes)	
WFE RMS	microns	

dx, dy, dz, da, db in surface ref. system, xy plane tangent to vertex
da = rotation about x; db = rotation about y
dz positive in the direction of ray propagation after surface
Zernikes: x, y in-pupil coordinates
FIELD TERMS ARE GIVEN AT 1.5 ARC MINUTE OFF-AXIS ALONG +Y (*)

Mirror	Decenter		Depointing		WFE RMS		Zernike coefficients												
							Field-independent							Field-dependent					
	Type	Ampl.	dx_sky	dy_sky	On-axis	Off-axis	Focus	Spher 3	Spher 5	Coma 3		Coma 5		Focus	Ast 3		Ast 5		
										x	y	x	y		x	y	x	y	
Corrector	dx	1.000	-1.652	0.000	2.832	2.830	0.000	0.000	0.000	-2.699	0.000	-0.009	0.000	0.000	0.000	0.018	0.000	0.001	
Corrector	dy	1.000	0.000	-1.652	2.832	2.828	0.000	0.000	0.000	0.000	-2.699	0.000	-0.009	-0.005	-0.018	0.000	-0.001	0.000	
Corrector	dz	1.000	0.000	0.000	23.095	23.095	40.002	0.001	0.000	0.000	0.000	0.000	0.000	0.000	0.000	0.000	0.000	0.000	
Corrector	da	1.000	0.000	0.034	1.787	1.787	0.000	0.000	0.000	0.000	1.691	0.000	0.005	0.000	0.011	0.000	0.000	0.000	
Corrector	db	1.000	-0.034	0.000	1.787	1.787	0.000	0.000	0.000	-1.691	0.000	-0.005	0.000	0.000	0.000	0.011	0.000	0.000	
TOTAL			***-1.686***	***-1.618***	***23.150***	***23.150***	***40.002***	***0.001***	***0.000***	***-4.390***	***-1.007***	***-0.014***	***-0.004***	***-0.004***	***-0.007***	***0.029***	***-0.001***	***0.001***	

Table 6-10. Baseline design, sensitivity matrix, corrector decenters (rigid body).

6.3.6 Imaging of turbulent layers

Aberrations (including defocus) in the conjugation between layers and their presumably conjugated mirrors introduce errors in the adaptive correction. An aberrated image of a given layer implies that rays emanating from different sky sources and intersecting in the physical turbulent layer will impact the conjugate (adaptive mirror) at different locations. For the sake of simplicity, let us consider a single, infinitely thin layer and its aberrated conjugate (Figure 6-26). Assuming that light ray number 1 emanates from the reference source, and assuming a perfect adaptive correction for this ray (e.g. adaptive mirror supported by an infinite number of supports), we can easily calculate the adaptive correction error on rays emanating from the science sources (rays 2 or 3 in Figure 6-26. Let r_0 be the atmospheric coherence length in the turbulent layer, and r'_0 the equivalent dimension as projected onto the adaptive mirror. Lert dh' be the transverse geometrical aberration of the layer image, the reference ray (dh'=0) being that emanating from the reference source, which will see a perfect correction. Assuming constant magnification, r'_0 and dh' are proportional to equivalent quantities r_0 and dh transposed back to the object space. A Kolmogorov model being perfectly adequate over such dimensions, the wavefront mean square phase distortion σ^2 between the reference and the science target will be given by the structure function:

$$\sigma^2 = 6.88\ (dh / r0)^{5/3} \qquad \textit{Eq. 6-1.}$$

In general dh will be field-dependent; if the field of view θ is negligible (Single-Conjugate Adaptive Optics or SCAO), dh=0 and the adaptive correction will not be impaired by aberrations in the layer conjugation. This is no longer the case with Multi-Conjugate Adaptive Optics (MCAO) or Ground-Layer Adaptive Optics (GLAO). Statistically, however, the mean square correction error should decrease with the number of references and converge towards σ^2/N, where N is the number of reference sources, assumed to be uniformly distributed.

It should be noted that Eq. 6-1 gives the mean square aberration of the rays intersecting in A' only; the overall error of the correction at a given field position results from the integral of Eq. 6-1 over the conjugate area.

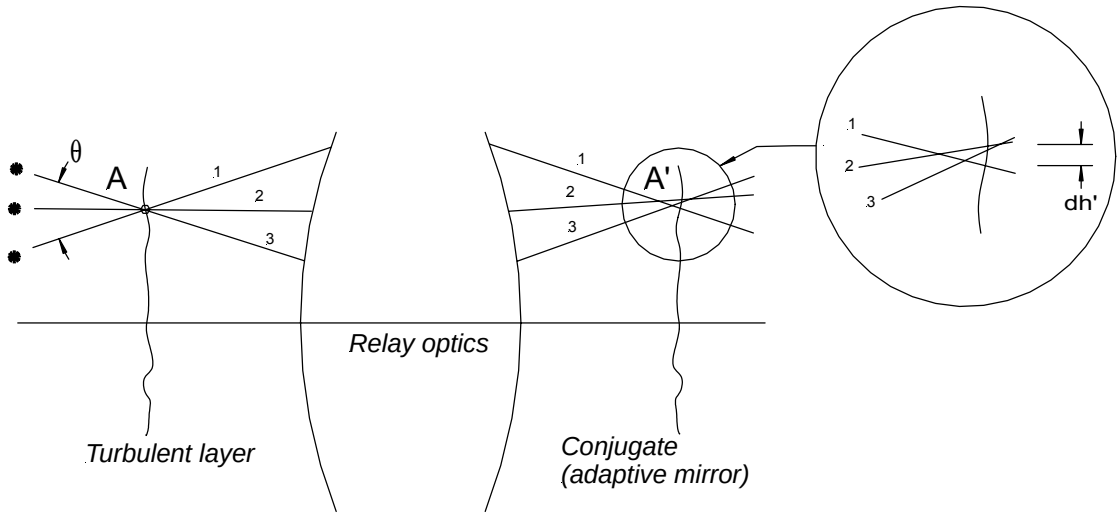

Figure 6-26. Aberrated layer image.

The case of a defocused image of a layer is the simplest to evaluate. Let ε be the despace of the conjugate with respect to the actual layer, in the object space, and θ be the field separation between the science target and the reference. With $dh = \varepsilon\,\theta$, we find that a 1 km despace, a 1 arc minute separation between the reference and science target and an atmospheric coherence length of 1 meter (good seeing, K band) leads to a ~$\lambda/7$ RMS correction error. Figure 6-27

shows the RMS correction error (wavefront, λ units) for a 1 km despace, as a function of r_0 and for three different angular separations between the reference and the science target.

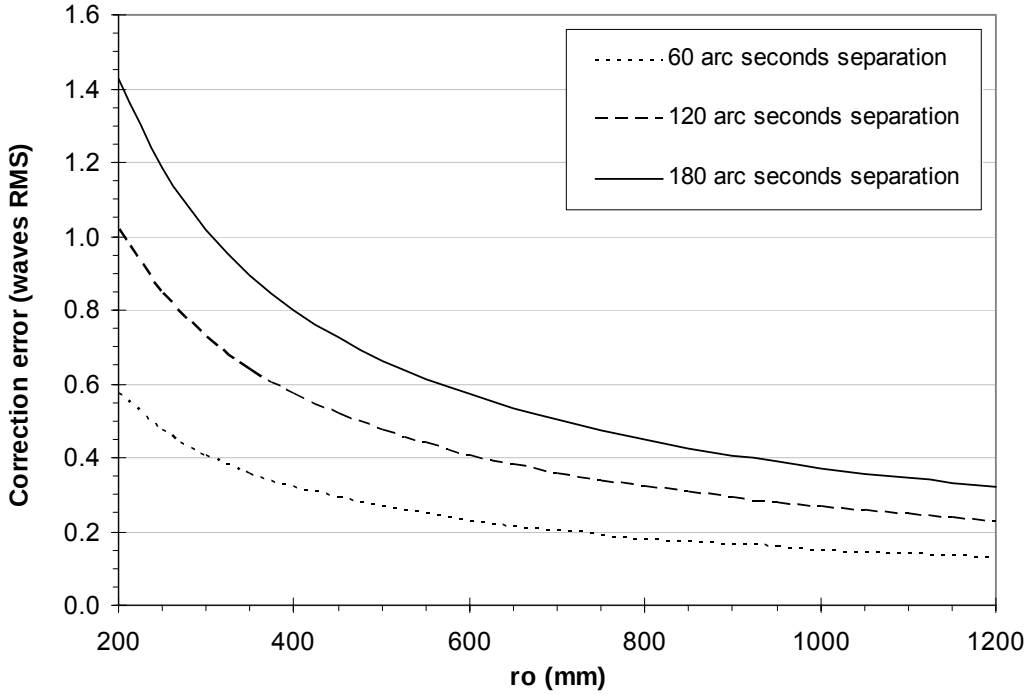

Figure 6-27. Adaptive correction error (wavefront RMS) for 1 km conjugate defocus

We shall now evaluate the impact of OWL aberrations of the pupil re-imaging on M6, including the effect of M6 tilt. Figure 6-28, Figure 6-29, and Figure 6-30 show the spot diagrams of the imaging of the entrance pupil onto M6, along the tilted axis of M6, with 1, 3 and 6 arc minutes field diameter. The effect of the mirror tilt is evident; the assymmety between "lower" and "upper" edges is due to an overall defocus, M6 vertex not being exactly coincident with the vertex of the exit pupil. Spot coordinates refer to the chief ray of the conjugation entrance-exit pupils i.e. the reference ray corresponds to an on-axis science target. The maximum geometrical spot radius is 5.8mm, 18mm, and 38mm, with 30, 90 and 180 arc seconds off-axis reference sources, respectively. Assuming an atmospheric coherence length corresponding to ~25 mm on M6[48], the corresponding dh/r_0 at the upper edge of the mirror of 0.23, 0.72 and 1.50, respectively. The adaptive correction errors are ~λ/8, λ/3 and λ/1.7 wavefront RMS for the corresponding rays. These errors are the maxima over the pupil area; the overall accuracy of the adaptive correction will result from the integrated effect over the entire mirror area –most of which is providing a substantially better conjugation. In addition, large corrected fields require several guide stars and as previously mentioned, the error should statistically decrease as $1/\sqrt{N}$, where N is the number of reference sources.

The current baseline design has not been constrained to having M6 vertex optimally located for ground layer and multi-conjugative adaptive optics. Preliminary checks indicate that a re-optimization ought to be possible without significant changes in the design.

[48] i.e. corresponding to the expected inter-actuator separation.

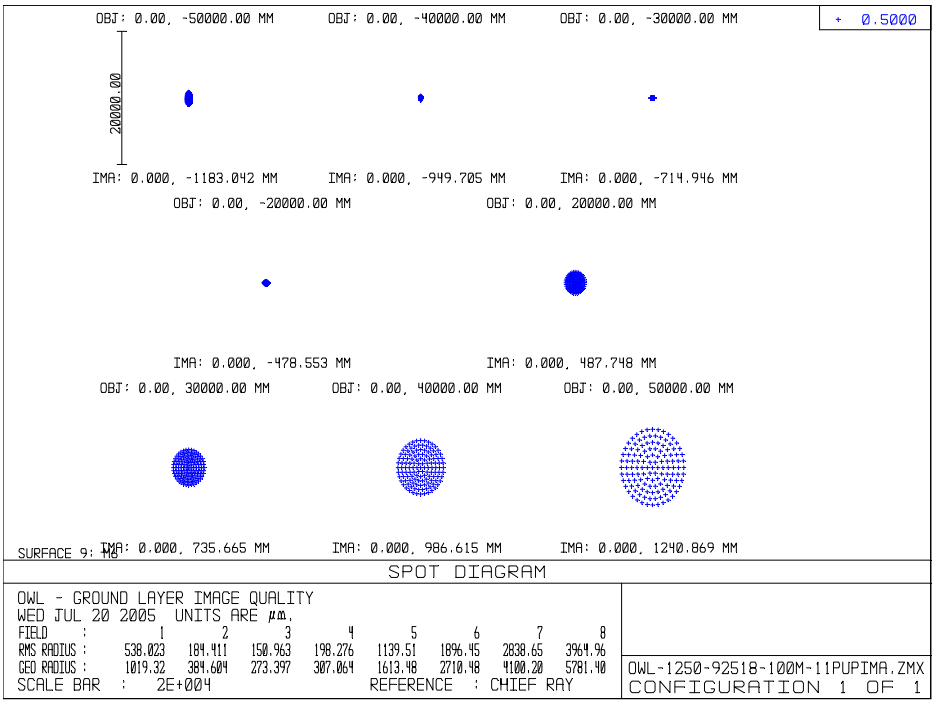

Figure 6-28. Image quality of the pupil conjugation; field of view 1 arc minute diameter.

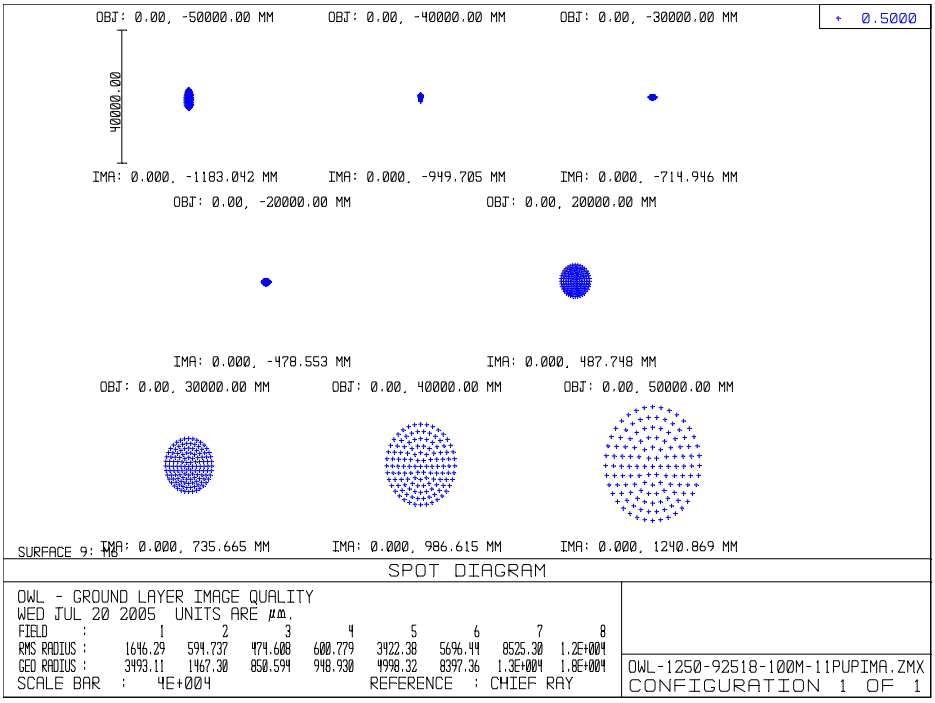

Figure 6-29. Image quality of the pupil conjugation; field of view 3 arc minutes diameter.

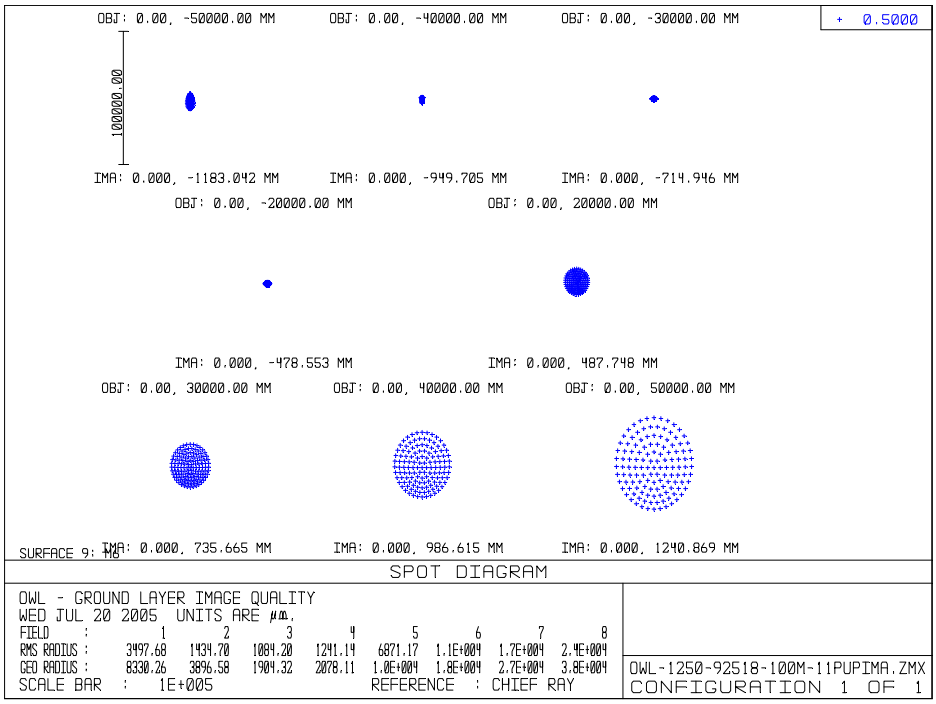

Figure 6-30. Image quality of the pupil conjugation; field of view 6 arc minutes diameter.

6.3.7 Imaging of Laser Guide Stars

Geometrical imaging properties for Laser Guide Stars (LGS) have been checked in full details with a previous iteration of the optical design (see RD1). At the time of writing of this document, only a brief analysis has been done with the baseline design. The main aberration is evidently defocus and, and as shown in RD1 it is proportional to D^2 but does not depend on the optical prescription. Higher order terms do not seem to be strongly design-dependent, and even after refocus, image quality is very poor. Figure 6-31 shows the spot diagram for a point-like LGS at 90 km distance, on-axis and 3 arc minutes off-axis, after refocus (the LGS image is 5879.7 mm behind the nominal focus). Figure 6-32 shows the wavefront 3 arc minutes off-axis. The off-axis image quality is about 1.5 arc seconds RMS.

As shown in RD1, this implies that not only tip-tilt, but also defocus, third and fifth order terms would have to be tracked on Natural Guide Stars (NGS), and that the LGS AO wavefront sensors would have to incorporate active surfaces for the compensation of low order terms in order to reduce the noise of measurement of higher order terms. Sampling on the NGS reference would be comparable to sampling of the tip-tilt on an 8-10 m class telescope. It should be noted that the pupil diameter being much larger then the outer scale of turbulence, low order atmospheric terms should, in principle, remain conveniently small.

Practical implementation of the above concept would certainly imply complex relay optics. Novel approaches towards wavefront sensing on Laser Guide Stars might eventually provide simpler solutions. The matter is being addressed within the framework of the ELT Design Study (see also section 8.4 and following).

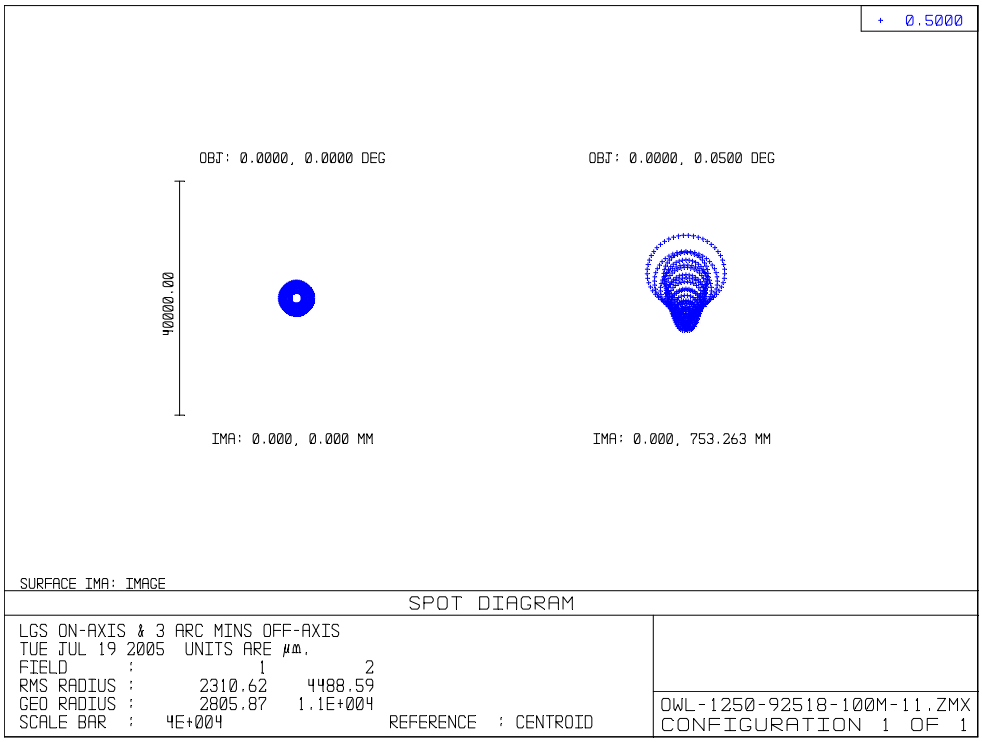

Figure 6-31. Spot diagrams, LGS at 90 km on-axis and 3 arc minutes off-axis.

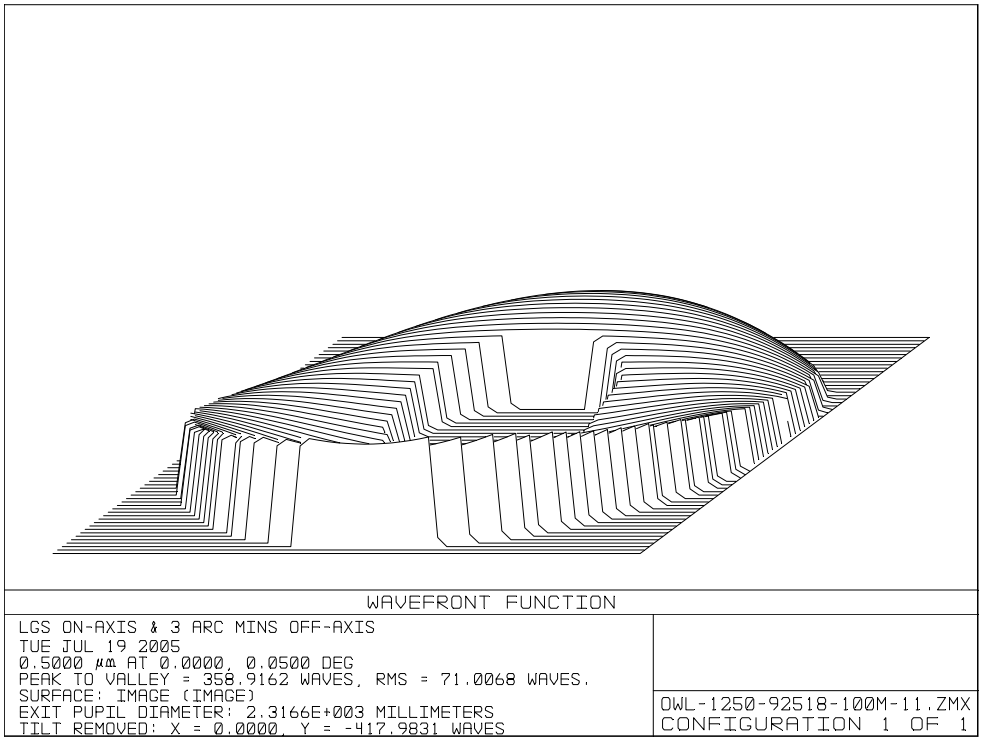

Figure 6-32. Wavefront map, LGS at 90 km, 3 arc minutes off-axis.

6.4 Diffraction and high contrast imaging

This section provides a brief description of diffraction effects associated to OWL segmentation and pupil shape. As a related topic, high contrast imaging and coronagraphy are addressed in RD22.

6.4.1 Diffraction

6.4.1.1 Structure of PSF in diffraction-limited regime

The properties of the PSF produced by the OWL pupil in diffraction limit regime is necessary for an adequate interpretation of astronomical data. The PSF possesses unique features particular to a segmented telescope with a large numbers of segments.

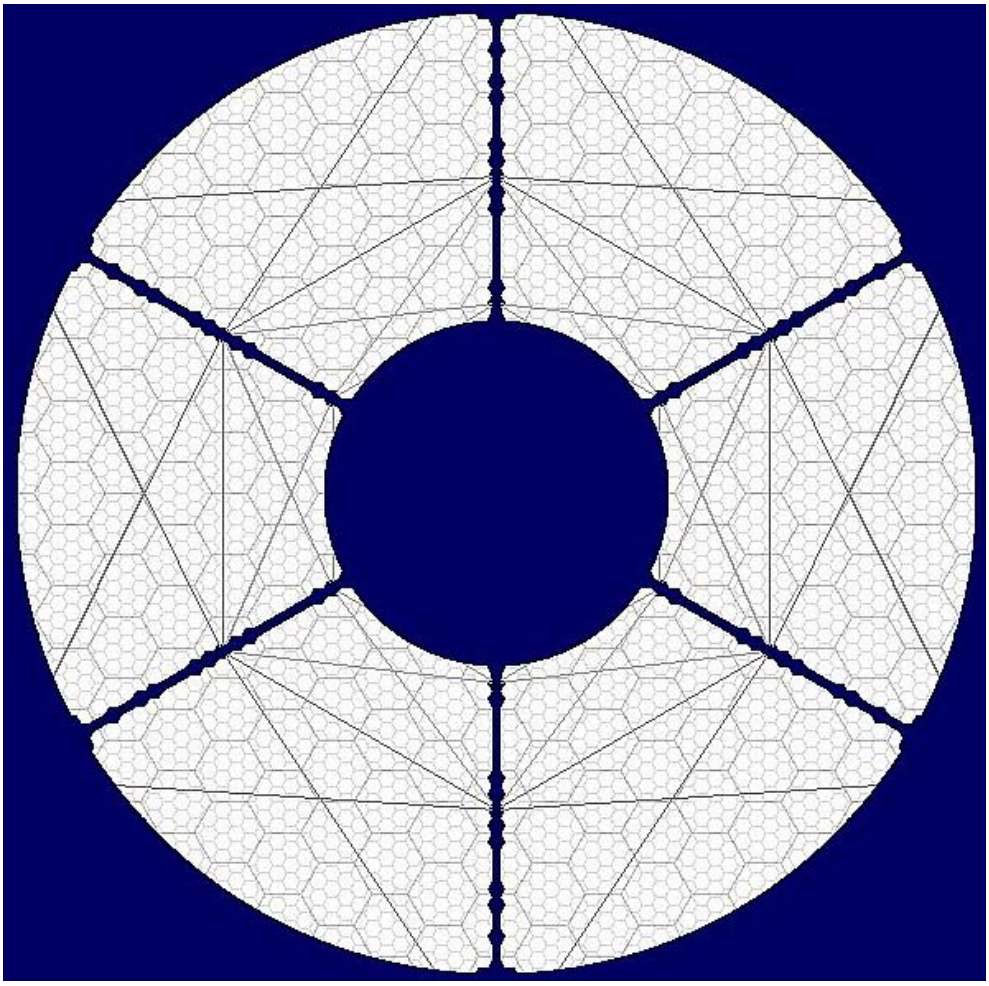

Figure 6-33. Model of the pupil for studying diffraction effects

6.4.1.1.1 Pupil modelling elements

The following pupil elements were included into the model:

1. A Circular mask with an inner diameter 35m and an outer diameter 97m. These dimensions are set to mask the irregular outer contour of the combined primary and secondary mirrors.

2. The obscuration by structural beams (spiders), which have a 1-m width, projected onto the entrance pupil
3. “Missing” segments under the structural beams. These correspond to the location of beams connecting the upper structures to those behind the primary mirror.
4. The ropes, with 50 to 70 mm width, projected onto the entrance pupil.
5. Primary mirror gaps: the segments are all identical, with a flat-to-flat dimension of 1.6m. Paving the primary mirror sphere with all identical segments implies irregular inter-segment gaps. The optimal segments distribution leads to gaps of 4mm to 16mm, with an average of 10mm. Taking into account 2 mm bevels at the segments edges, the averaged gap size used in simulations is 14 mm. To accommodate for gap size smaller than resolution of the numerical grid, the gray pixel method is used.
6. Secondary mirror gaps: the flat secondary mirror has constant gaps of 3.75mm. Taking 2mm bevels into account, the gaps of the secondary mirror are modelled with a width of 7.75mm. The two mirrors are superimposed using geometrical projection. The magnification factor for the secondary mirror is 3.8975.

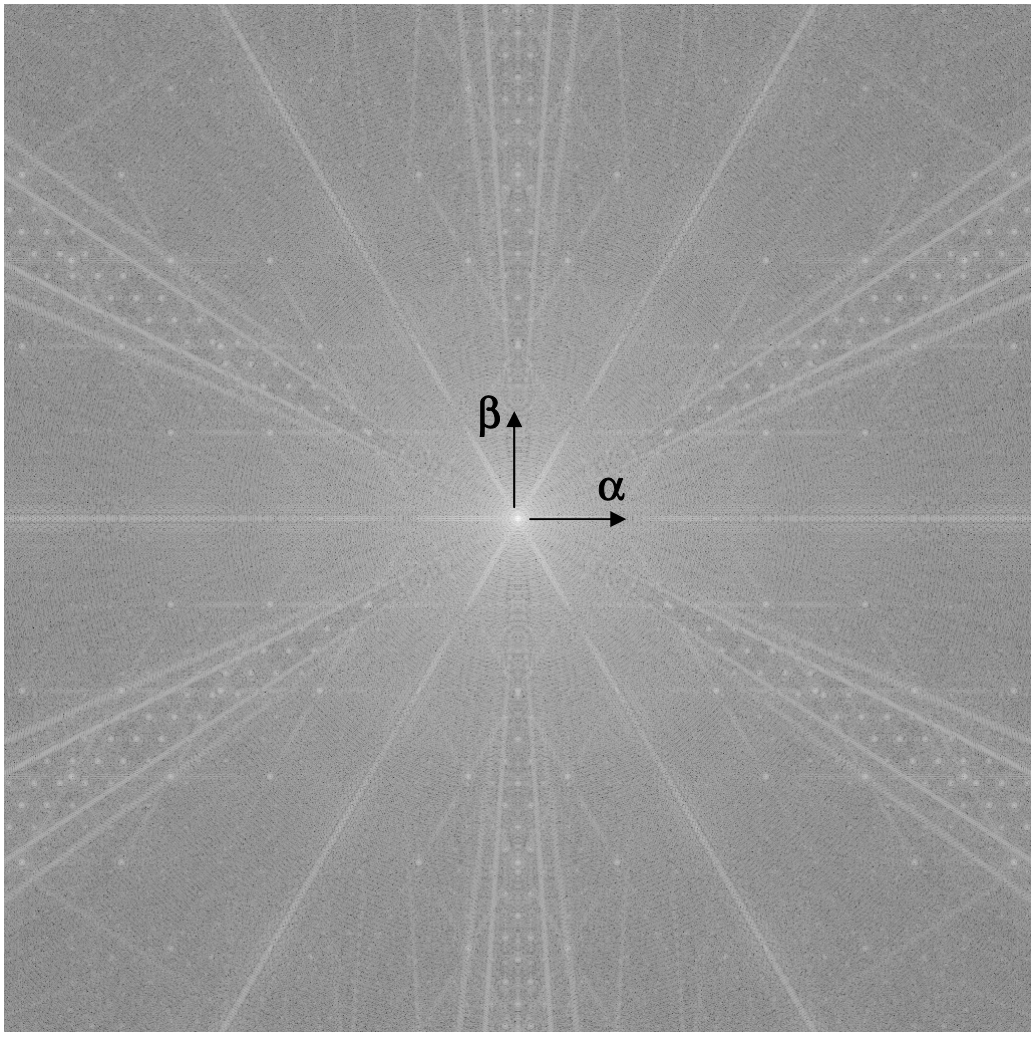

Figure 6-34 PSF from the pupil presented above. The field of view is 1 arc second diameter, wavelength is 650 nm. Here and further: logarithmic scale.

The PSF obtained by Fourier transform of the pupil is shown in Figure 6-34. Individual contributions by the pupil elements can be distinguished. Note that the diffraction pattern reveals the geometry of the aperture. Each of the features possesses a $\pi/3$ symmetry. This symmetry is preserved in the diffraction pattern, which makes the diffraction elements

separable from other effects (e.g. adaptive optics residuals). In order to describe this symmetry it is helpful to introduce the term *direction of diffraction*. There are two major directions of diffraction: α-direction is along the Ox plus 5 obtained by the rotation Ox by $\pi/3$; β – direction is the same for Oy.

In the following we shortly describe each of pupil effects separately.

6.4.1.1.2 Secondary mirror support

The spikes (diffraction lines) repeat the geometry of the spiders, rotated by 90º. The diffraction lines are periodic (Figure 6-35). Their thickness (a_1) and their period (a_2) are defined by the dimensions (b_1, b_2) of the spiders:

$$a_1 = \frac{\lambda}{b_1} = 0.206\frac{0.65\ \mu m}{66\ m} = 0.001 arc\sec$$
$$a_2 = \frac{\lambda}{b_2} = 0.206\frac{0.65\ \mu m}{1\ m} = 0.13 arc\sec$$

Eq. 6-2.

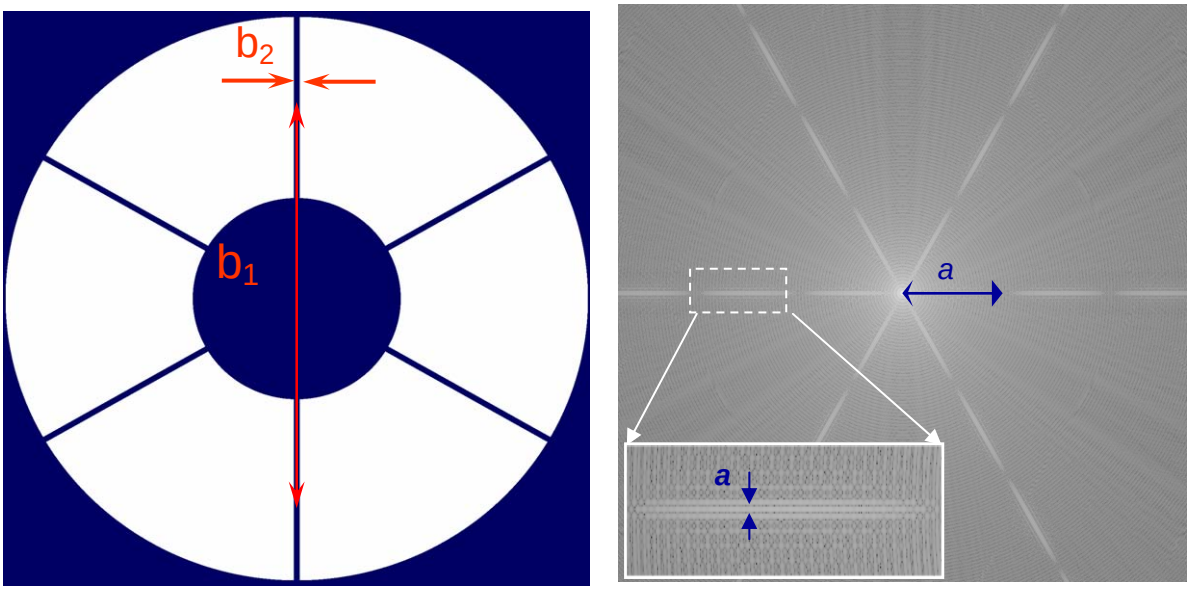

Figure 6-35 Diffraction by the "spider". PSF box size 0.72"

6.4.1.1.3 "Missing" segments

This element produces the diffraction pattern consisting of the short lines connecting the points of the high – order diffraction peaks. The diffraction is the strongest in β-direction (Figure 6-36).

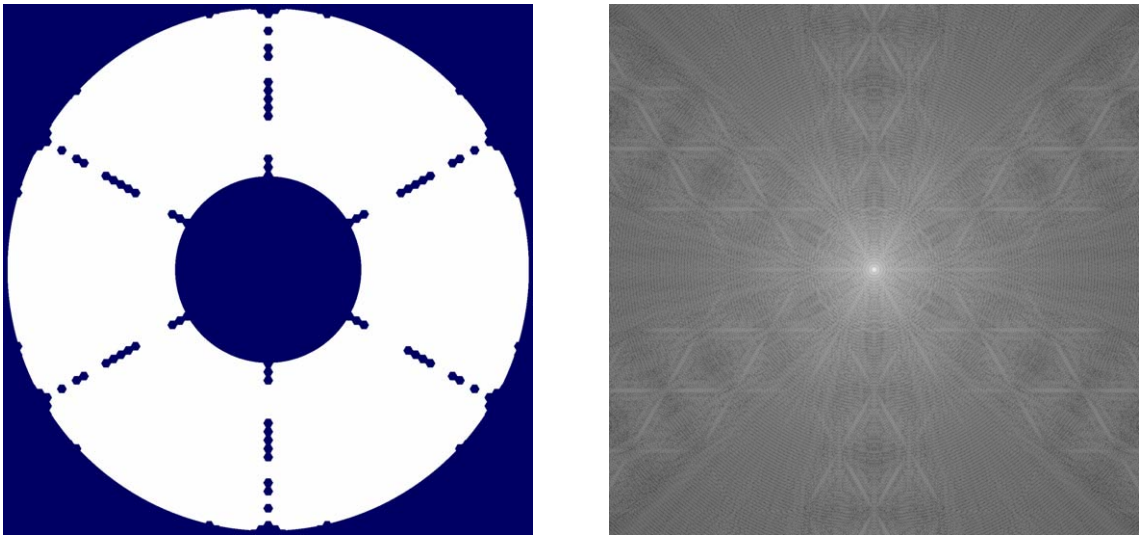

Figure 6-36 Diffraction by "missing" segments. PSF box size 0.72"

6.4.1.1.4 Ropes

The radial rays observed in the PSF are produced by the ropes. This pattern has also $\pi/3$ symmetry and most of the diffraction is within ±6° about β-direction (Figure 6-37).

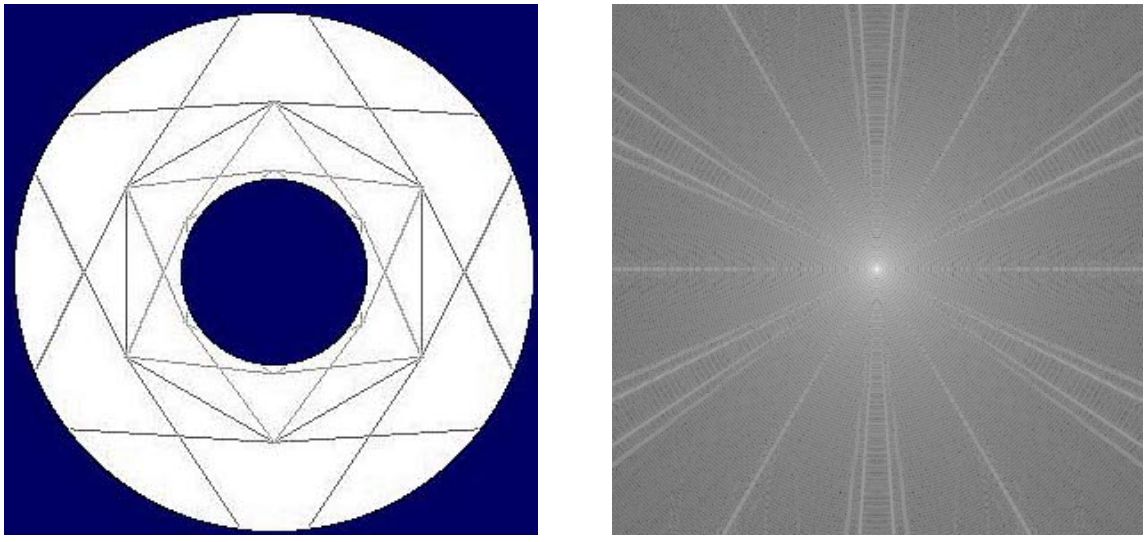

Figure 6-37 Diffraction by the ropes. PSF box size 0.72"

6.4.1.1.5 Diffraction by the gaps

Mechanism of diffraction pattern formation

Inter-segment gaps make the segmented mirror act as a diffraction grating. By analogy with diffraction gratings the residual PSF is the product of two factors: a "grid factor" (GF) which is the Fourier transform of the segmentation grid, usually a periodic function of sharp peaks, and the point spread function P_s of an individual segment [83], [84]. Without gaps the peaks of the

GF fall onto the zeros of the single segment PSF and in the product only central peak is observed (Figure 6-38).

The introduction of gaps enlarges P_s while it leaves the grid function GF unchanged. As a result higher order peaks appear. Relative peak intensity is the value of P_s at the locations of GF peaks.

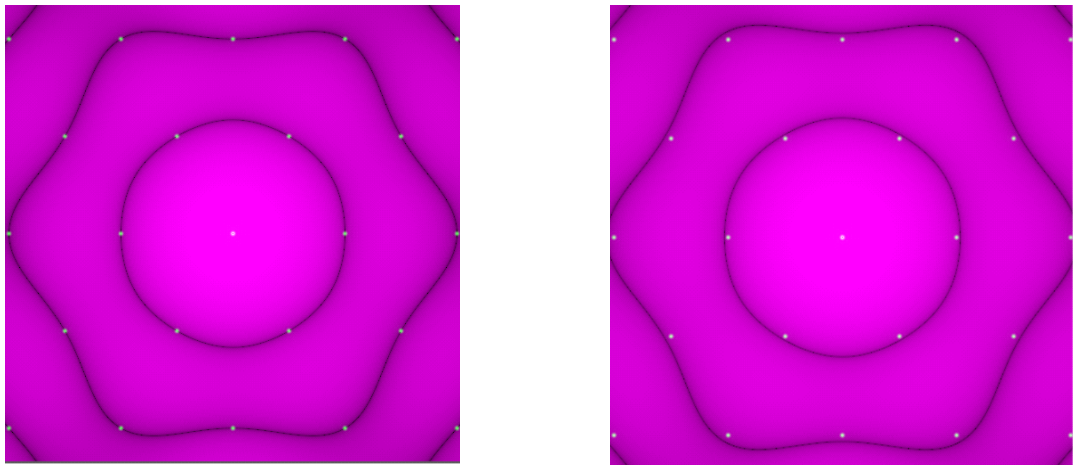

Figure 6-38. Mechanism of the formation of diffraction peaks (gaps): the grid factor (dots) is multiplied by the segment PSF. Left: without gaps; except for the central one all peaks of the grid factor fall into zeros of the segment PSF_s. Right: with gaps; peaks no longer coincide with PSF_S zeros.

The position of the peaks is defined by the segments center to center separation and the wavelength. The intensity of the peaks only by the gap size related to the segment size.

The well understood principle of diffraction peaks formation allows their formal classification. This classification allows to define the intensity of the peak knowing its angular distance from the central point. For example, the 6 brightest peaks closest to the center (in the classification they are referred to as A_1 peaks) are located at a distance equal to $2\lambda/(\sqrt{3}d)$ and have an intensity relative to the central point of $0.68g/d$ (g – gap size, d – segment size). This gives $5.2\cdot10^{-5}$ for the primary mirror of OWL (the result obtained in simulation is $4.5\cdot10^{-5}$).

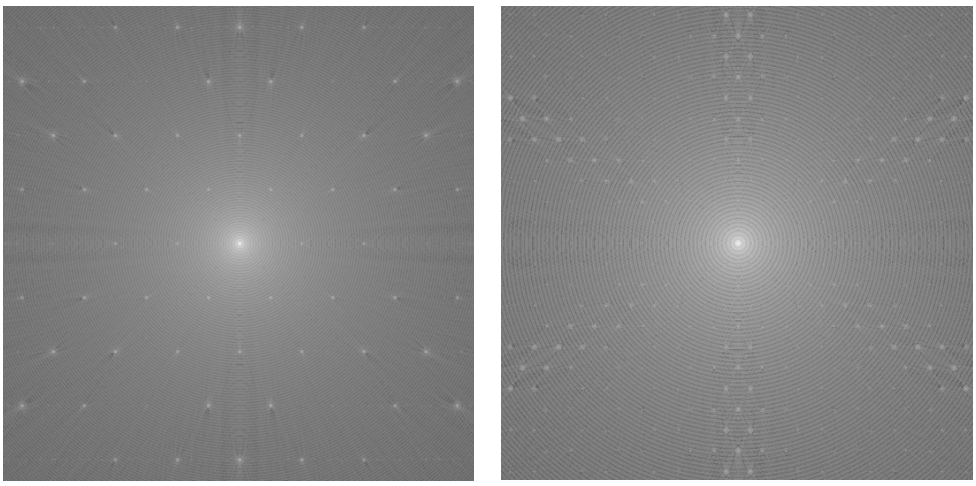

Figure 6-39 Diffraction by intersegments gaps of the primary (left) and of the secondary mirrors (right). Box size 0.72 arc secons.

Gaps on primary and secondary mirrors

Although gaps on the primary mirror vary from 4 to 16mm, all segments contribute equally to the diffraction pattern and diffraction peaks appear as with regular gaps (averaged size). The simulations performed with varying gap size have confirmed this and therefore the analysis was done with the averaged gap size. Gaps on the secondary mirror are all identical.

Because of the scaling factor, segments on the secondary mirror are ~4 times larger, and therefore the peaks are 4 times closer to the central peak, as shown in Figure 6-39.

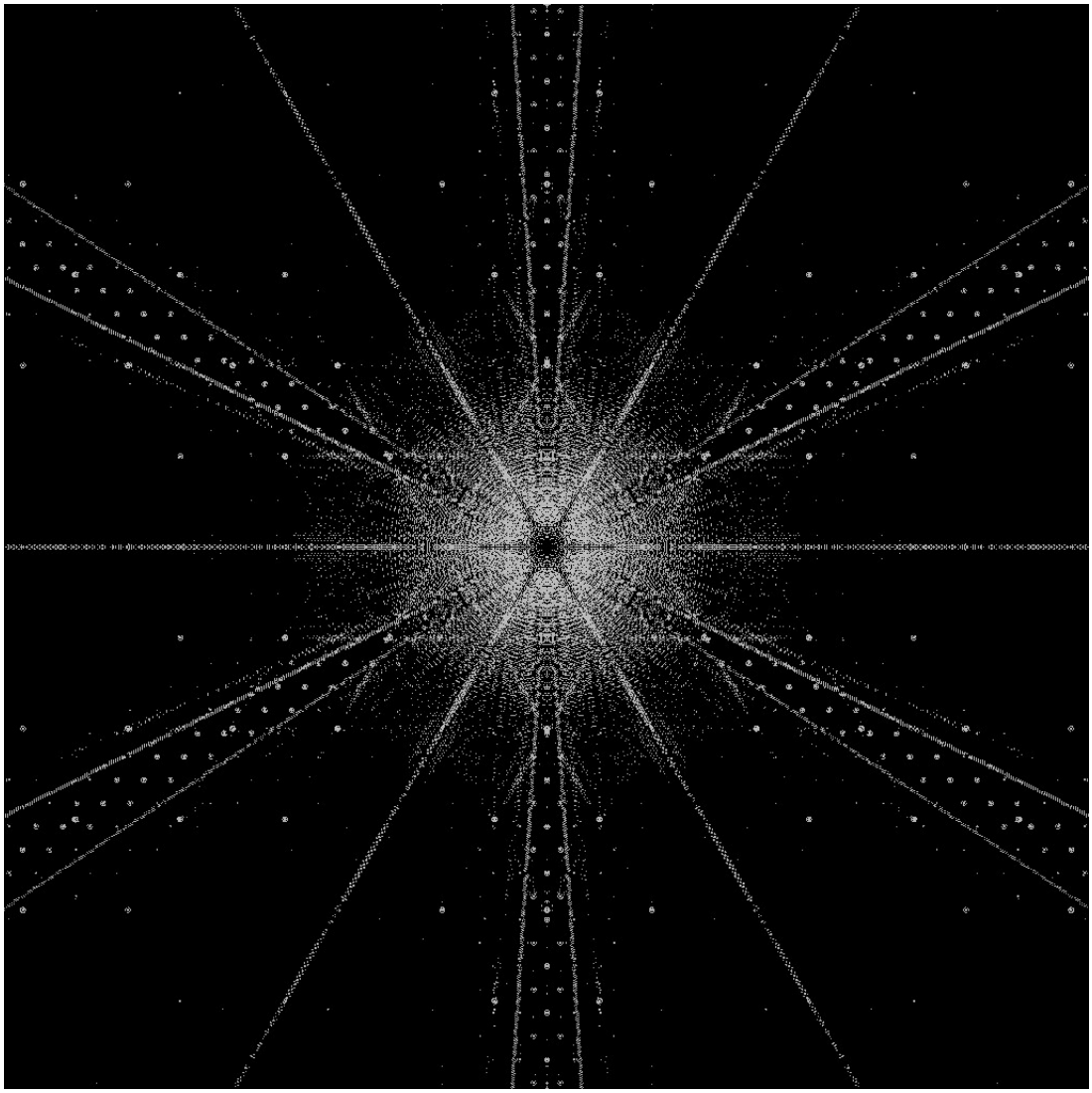

Figure 6-40 Intensity slice representation of OWL PSF between 10^{-5} and 10^{-7}. Most diffraction artefacts are apparent.

6.4.1.2 PSF representation: intensity slices

So far while describing the PSF we concentrated only on its geometrical properties, without regard to relative intensity. One can do the detailed analysis of each diffraction element with intensity measurement at each point, as it was done for instance for gaps [84]. Here, for a more representative description we show the PSF at different intensity intervals. Figure 6-40 shows that most of the effect is in the range 10^{-5} and 10^{-7}.

6.4.1.3 Effects of phasing errors on the PSF

6.4.1.3.1 Diffraction associated to piston and tip-tilt

The effect of the piston and tip-tilt on the PSF has been studied in detail according to the generalized formalism, i.e. through the representation using grid factor (GF) and PSF of the individual piston (P_s). Here we summarize the conclusion of this study.

Piston errors

The random piston errors cause a loss of intensity in the central peak and produce speckles. The speckle distribution corresponds to the distribution of the piston errors. The ensemble averaged speckled field for the given wavefront rms is $PSF_s \cdot [1-\exp(-rms^2)]/N$, where *rms* is the phase error (in radians) and *N* is the number of segments. Therefore, the outline of the speckled field repeats the shape of P_s but with reduced amplitude. The speckles are concentrated in the angular intervals $[0.25\lambda/d \div 1.2\lambda/d]$, $[1.2\lambda/d \div 2.2\lambda/d]$,… . The averaged width of each individual speckle has the size of the Airy disk from the whole mirror. The number of speckle in the first interval is of the order of the number of segments and their averaged intensity falls as N^{-1}.

Tip-tilt errors

A segmented aperture with random tip-tilt errors behaves as a randomly blazed 2D diffraction grating in that the loss of intensity in the central peak is accompanied by the appearance of a regular structure of diffraction peaks and a speckled halo. The position and relative intensity of the peaks is independent of the number of segments, while the averaged speckle intensity falls as N^{-1}. In weakly segmented mirrors (few tens of segments) the regular pattern is lost in speckles, but for highly segmented ones (few hundreds of segments) the regular pattern dominates. The outline of the speckled field is a modified PSF P_s, whose FWHM proportional to the tip-tilt error wavefront *rms*. The position of the diffraction peaks is given by the grid factor, i.e. is defined by segments center to center separation, wavelength and hexagonal geometry. For any value of the wave front *rms* the brightest peaks are the ones closest to the center six peaks (in the classification A_1 peaks) at $2\lambda/(\sqrt{3}d)$, that is 0.097" for d=1.6m and λ=0.65μm. For tip-tilt $rms=\lambda/8$ they have relative intensity $6 \cdot 10^{-3}$. For the small $rms < \lambda/15$ the intensity of A_1 peaks can be estimated as $0.01 \cdot rms^4$ (rms in radians). The position and intensity of all possible peaks can be also found using the classification mentioned above.

6.4.1.3.2 Intensity slice representation (FoV=1", λ=650nm)

Assuming random errors limited by the noise of the control system (actuators, sensors), the residual segmentation piston and tip-tilt would have a statistics close to a Gaussian distribution. The simulated PSF produced by random piston and tip-tilt errors are shown in Figure 6-41. Two representative cases, total rms (including the two segmented mirrors) of 30 nm and 56 nm, are presented. The wavelength is 650nm. The Strehl ratio follows the Marechal approximation:

$$St = \exp\left(-rms^2\right) \qquad \textit{Eq. 6-3.}$$

which gives St=0.92 for 30nm case and St=0.75 for 56nm case.

The residual PSF are shown in Figure 6-41 for the two values of RMS. Again we used the intensity slice representation. The overall speckles distribution follows the shape of the PSF of an individual segment of the primary mirror. A series of intensity slices is shown in Figure 6-41.

Full range *rms* = 30 nm *rms* = 56 nm

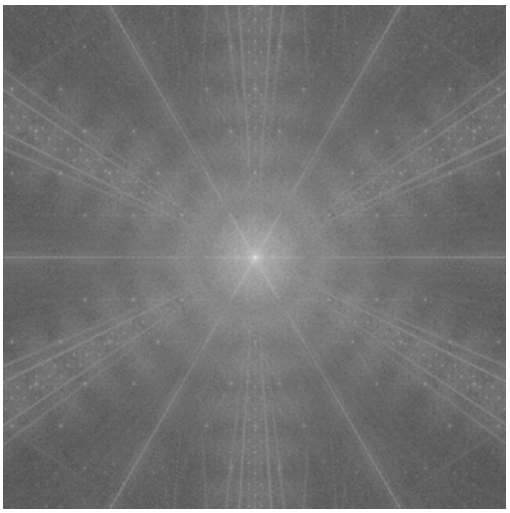

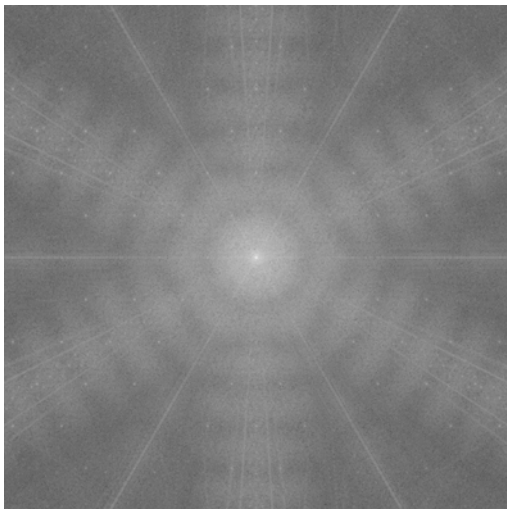

intensity slice 1 to 10^{-4} *rms* = 30 nm *rms* = 56 nm

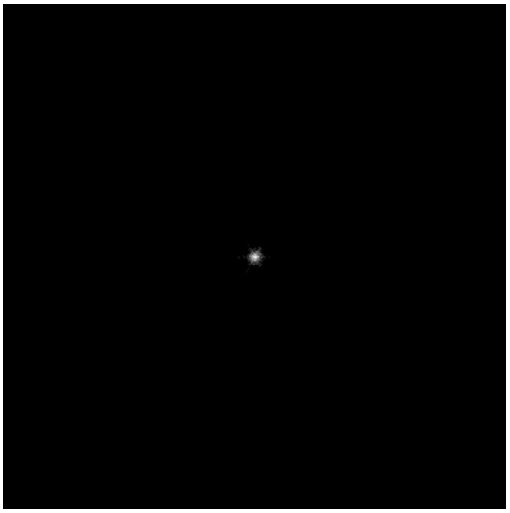

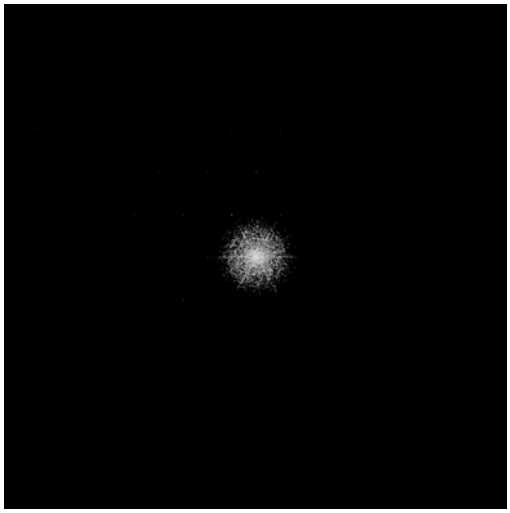

intensity slice 10^{-5} to 10^{-6} *rms* = 30 nm *rms* = 56 nm

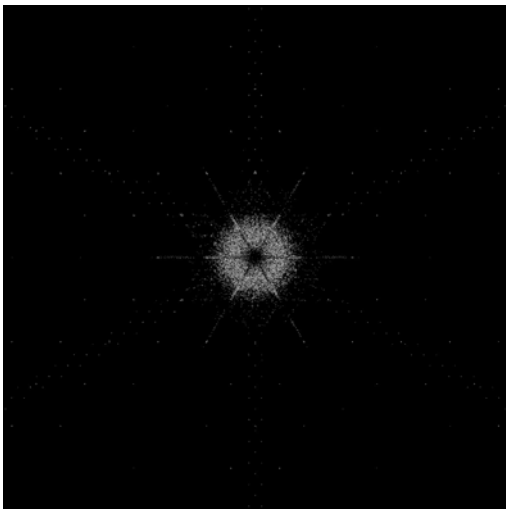

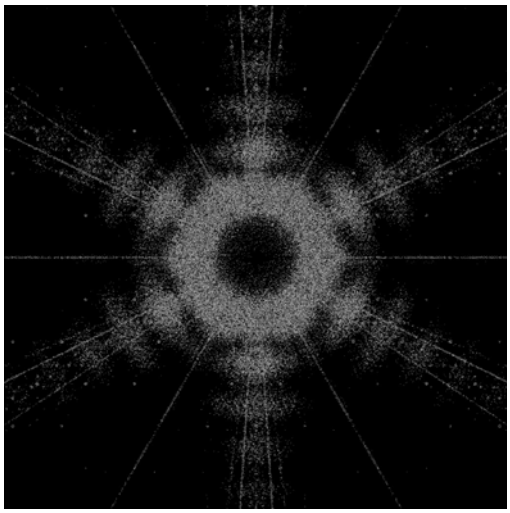

intensity slice 10^{-6} to 10^{-7} *rms* = 30 nm *rms* = 56 nm

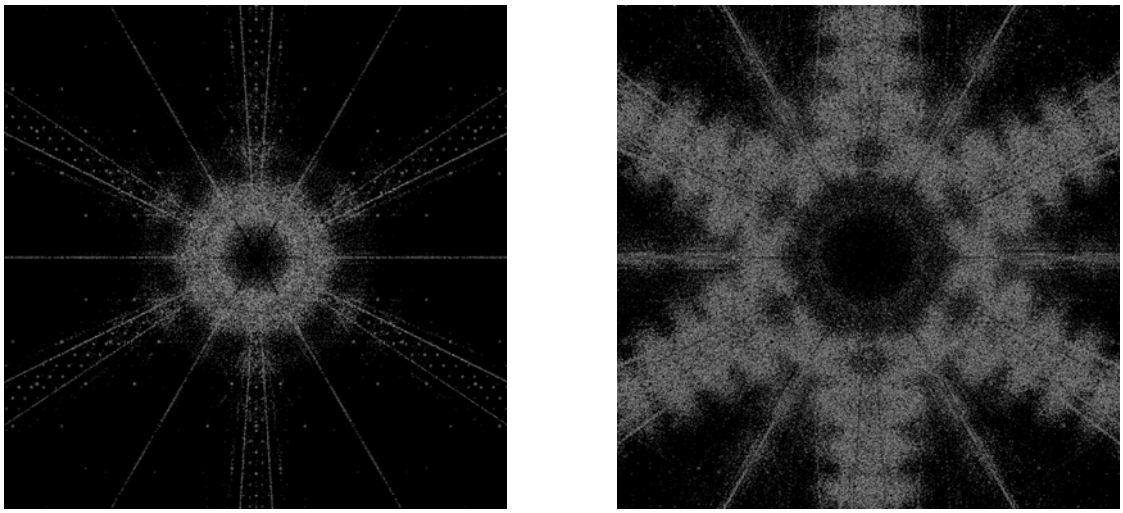

intensity slice 10^{-7} to 10^{-8}

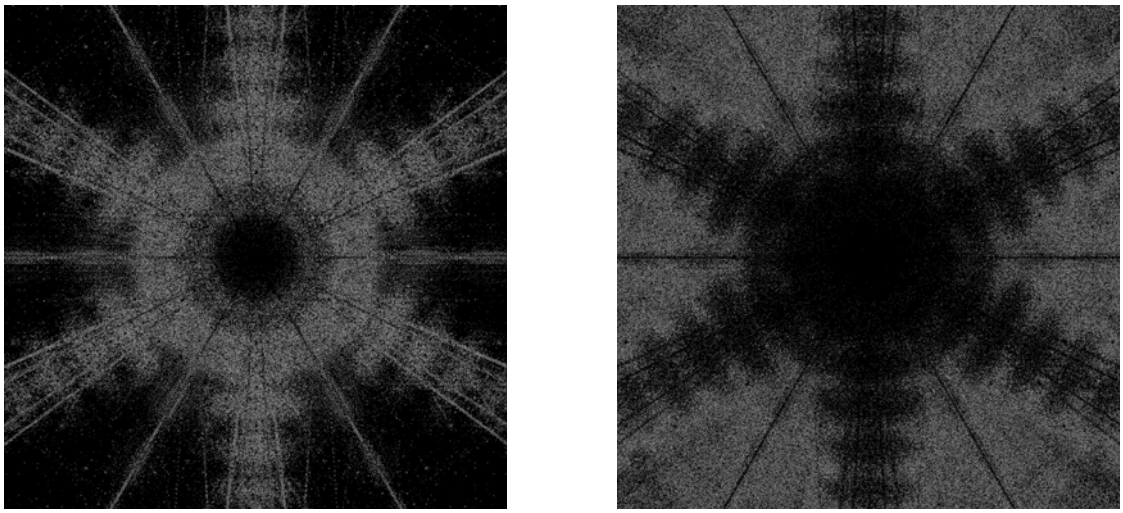

Figure 6-41 Intensity slice representation of OWL PSF with 30nm and 56nm wavefront RMS residual segmentation piston, tip-tilt errors on two segmented mirrors.

6.5 Optics design and fabrication

6.5.1 Segments

The segments product tree (excluding related documentation) is shown in Figure 6-42. The overall characteristics of the segments are given in Table 6-11. In the following sections we concentrate on segments distribution, support system, overall properties and fabrication issues.

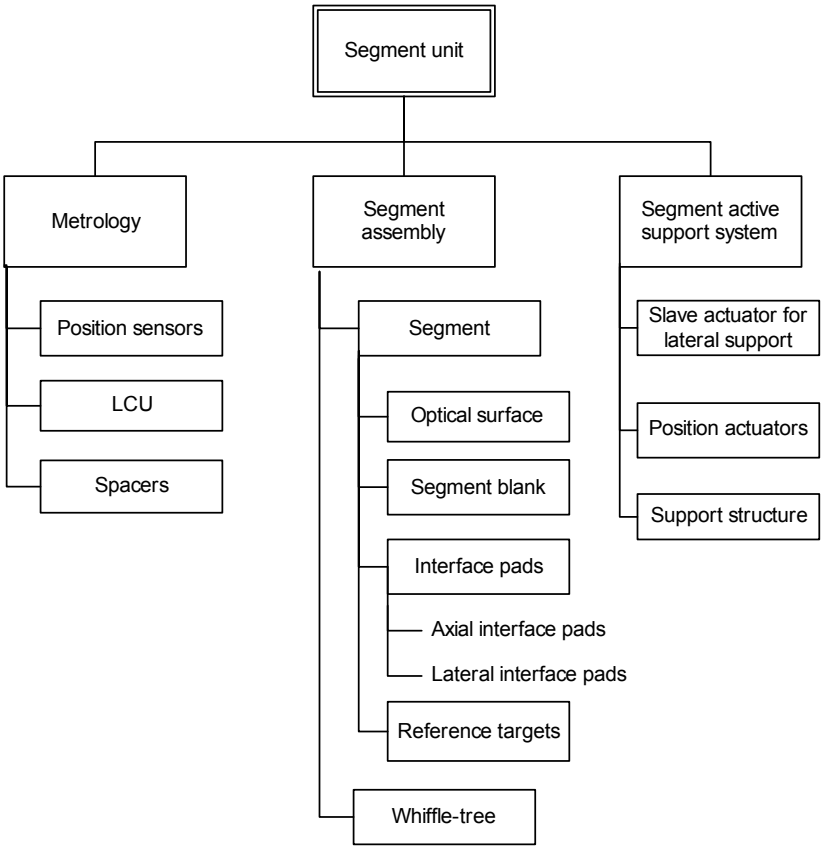

Figure 6-42. Segment unit product tree.

Characteristic		Value
Substrate		Zerodur, ULE or Astro-Sital
Shape / type		Hexagonal / solid
Dimensions	Flat-to-flat Thickness	1.6-m 70-mm
Radius of curvature	Primary mirror Secondary mirror	250-m Flat
Support	Axial Lateral	18 points whiffle-tree 1 central support
Quantity	Primary mirror Secondary mirror	3048 216

Table 6-11. Segments characteristics.

6.5.1.1 Segment size and distribution

The segments being spherical, optical figuring techniques do not imply the size limitations which may otherwise affect aspherical segments (e.g. maximum departure from a spherical surface, which could be generated by a warping harness). Handling and above all transport considerations point towards relatively small segments size, if possible compatible with standard transportation sizes i.e. 2.3-m flat-to-flat (the inner size of a standard 20 or 40 ft transport container). Larger segments would evidently simplify the position control (phasing) control system and reduce diffraction artefacts associated with intersegments gaps, but would imply excessive mirror masses and imply additional control complexity if their shape had to be

controlled actively. Industrial studies also concur[49] with a sharp cost increase beyond ~1.8-m. Small segments, a few tens centimetres, would have significant mass and handling advantages, and allow for higher bandwidth of their position control system. Beyond 4,000-5,000 units i.e. below ~1.2-m in size, however, it is generally felt that the complexity and cost of the position control system would negate the advantages brought by the smaller size.

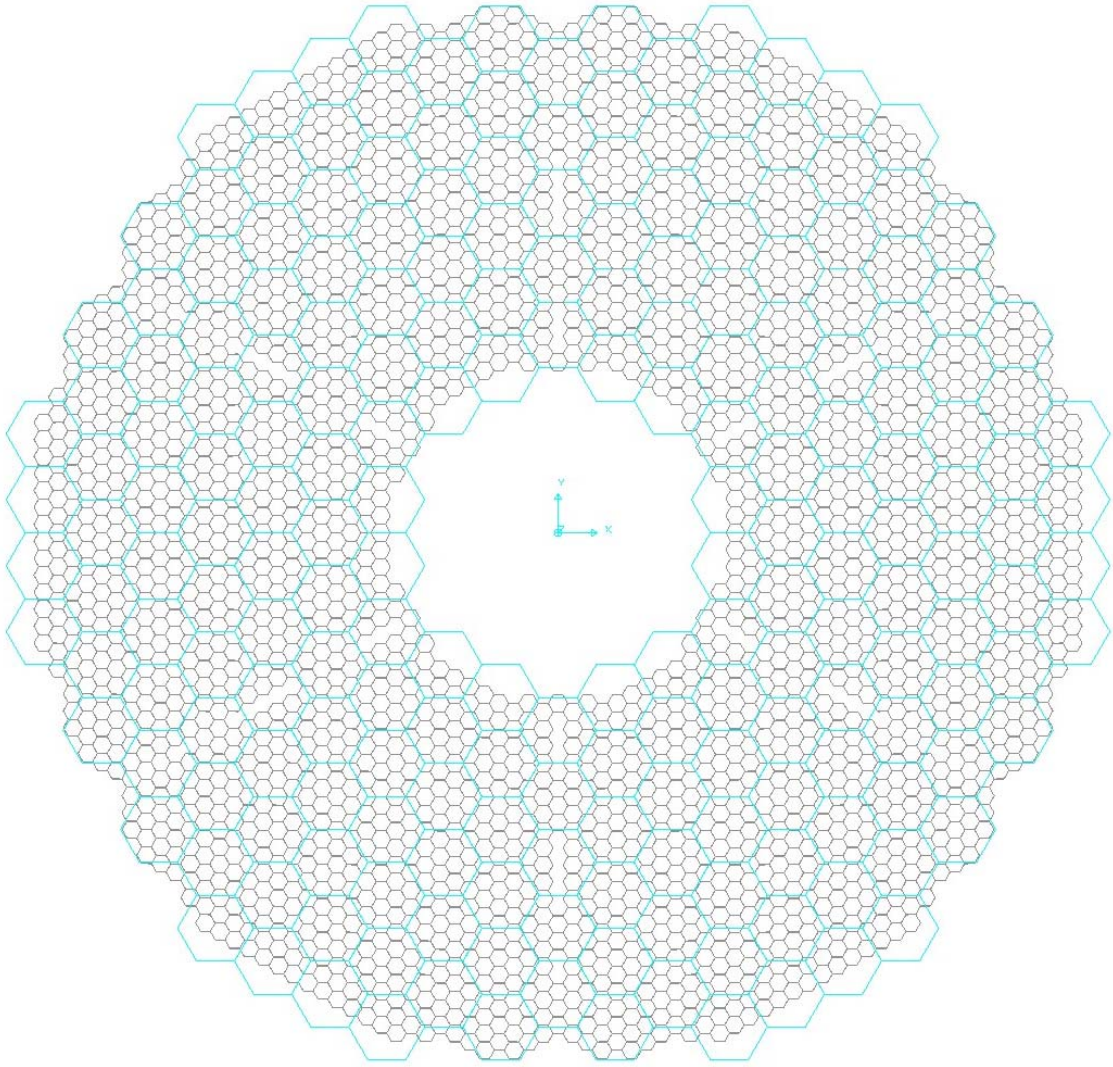

Figure 6-43. Primary and secondary mirror segments distributions.

The baseline segment size is 1.6-m flat-to-flat, with all segments identical. The dimension has been chosen as an integer divider (1:8) of the structural module size, thereby allowing for higher standardization of interfaces, and close to the presumed optimal in terms of production costs. The distribution of the primary and secondary mirror segments projection onto the pupil is shown in Figure 6-43. A refinement of the pupil geometry is likely as few (36) outer primary mirror segments appear to be strongly vignetted by the secondary mirror external contour.

In order to accommodate for the interfaces of the upper structures with the primary mirror cell and for supports of the mirror covers, the pupil is not uniformely paved but has obscurations with a six-fold symmetry (Figure 6-44).

All segments having the same dimensions, intersegments gaps are variable, from 4 to 14 mm (see RD46[50]). The radial intersegment gap is constant (14 mm) and the azimuthal variable (4 to

[49] See RD6, RD7, RD8, RD9, RD10, RD11, RD12.

[50] The values given in RD46 correspond to the former design iteration, with a longer focal ratio of the primary mirror.

13.5 mm). The azimuthal gap decreases with increasing radial coordinate of the segments (see Figure 6-44). A significant drawback of variable gaps is a potential loss of positioning accuracy with capacitive edge sensors[51]. An alternative technology (inductive sensors) is being assessed within the framework of the ELT Design Study (see RD504). The backup solution is to hold the position sensors on dismountable shims in order to guarantee that inter-sensors gaps remain constant. This would imply added sensors design complexity and segments maintenance complexity and, potentially, larger average intersegments gaps in order to accommodate for reasonable design space of the sensors interface with the segments.

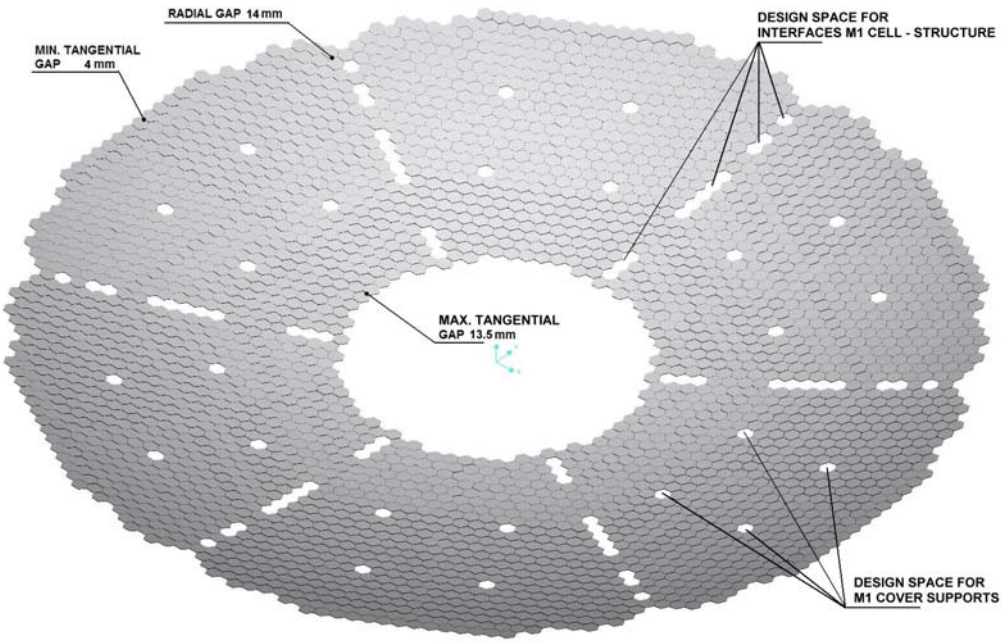

Figure 6-44. Primary mirror geometry, obscurations and intersegments gaps variation.

Primary and secondary mirror segments are identical but for their figure. A solution whereby the secondary mirror segments would have different size or outer cut, with its projected pattern onto the primary mirror coinciding with that of the primary mirror itself or with groups of segments in the prmary mirror, was briefly considered. This would be advantageous as one mirror phasing errors could be compensated by the other one. This is true, however, for a very small field of view only, as the patterns do no longer coincide off-axis. The tolerance would be comparable to the angular size of the secondary mirror gaps as seen from the primary mirror i.e. ~9 arc seconds for a 4 mm M2 intersegment gap. This approach was therefore abandoned.

6.5.1.2 Segments thermo-mechanical properties

A particular difficulty with segmented apertures is the tight tolerance on the repeatability of curvature between segments. While the overall curvature of a segmented mirror is still a matter of (a normally more generous) tolerance on the optical prescription, inter-segment curvature errors must be included in the segment misfigure or wavefront error budget.

Let us assume a tolerance of $\lambda/4$ peak-to-valley maximum allowable wavefront error (Maréchal criterion). A 1.6-m flat-to-flat dimension translates into a segment maximum radius of a=924 mm. The wavefront error W associated to a given error dR on the radius of curvature is given by

[51] According to FOGALE, SALT's supplier for its capacitive sensors, the accuracy specification is 50 nm Peak-to-Valley in piston (100 nm wavefront) and inter-segments gap variation (12 mm) is the single most important contributor to the allocated error budget.

$$W = \frac{dR}{4}\left(\frac{a}{R}\right)^2 \qquad \textit{Eq. 6-4.}$$

With the primary mirror (R = 250000 mm) and λ=0.5 μm, we find dR=9.6 mm i.e. dR/R=0.0038%. This is an extremely stringent tolerance, which not only implies tight optical figuring constraints but also stringent material specifications. The potential concerns, as detailed by Nelson et al for the Keck telescope [12] are:

1. differential change of curvature between segments (primary mirror only, the secondary being assumed flat).
2. differential segment thickness expansion, and thereby a differential displacement of the optical surfaces with respect to position sensors.
3. CTE or thermal gradients within individual segments.

All three effects have been investigated with Zerodur, fused silica and silicon carbide (see RD3[52]) and the first two found negligible. The third one, however, is critical (see Table 6-12). Silicon carbide has a slight advantage because of its excellent thermal conductivity but through-thickness CTE variations are still critical. The bulk of the optical surface deformation is defocus. It should be noted, however, that for lack of precise data, the calculation underlying Table 6-12 is extremely pessimistic since it assumes a linear through-thickness CTE gradient. There is circumstancial evidence that this is not the case; silicon carbide mirrors and structures, for example, have shown remarkable stability (a few micrometers) over wide thermal excursion down to cryogenic temperatures. Whether this is also true for silicon carbide mirrors overcoated with a polishable cladding remains to be proven. This issue is being addressed in the framework of the ELT Design Study, with the fabrication and testing of up to 8 silicon carbide segment prototypes, 1-m class (see RD510).

Error source: CTE and thermal gradient within segments; variation 5 K between operational and fabrication temperature.	Zerodur (class 2)			Fused Silica			Silicon Carbide		
	Wavefront RMS (nm)			Wavefront RMS (nm)			Wavefront RMS (nm)		
	M1	M2	**Total**	M1	M2	**Total**	M1	M2	**Total**
Front-back $\delta\alpha=10^{-8}$ K^{-1}	153	153	**216**	153	153	**216**	153	153	**216**
Heat flow dispersion 3 $W.m^{-2}$	50	50	**70**	17	17	**24**	9	9	**13**
TOTAL (RMS SUMMATION)			**227**			**218**			**217**

Table 6-12. Compared performance of Zerodur, fused silica and silicon carbide with respect to through-thickness CTE and thermal gradients (1.6-m flat-to-flat, 70 mm thick segments).

A possible solution to reduce the effect of CTE inhomogeneities and/or avoid CTE specifications which would exclude otherwise attractive materials is to specify the segments figure at median operation temperature so as to minimize the operational departure from factory conditions. This solution would only require that the segments be tested at operational temperature; figuring could still be executed at normal factory temperature and would only have to be tuned to produce the desired curvature at test temperature. Assuming a matrix test configuration, the technical difficulty and extra cost of cooling the test set-up (matrix and segment) down to ~5 ^{o}C, although not negligible, is still affordable (see RD11 and RD12).

6.5.1.3 Segments substrates

The baseline segment substrate is low-expansion glass or glass-ceramic (Astro-Sital, ULE or Zerodur), with Silicon carbide as an actively pursued alternative. Preliminary blanks specifications are given in RD42 and RD43. The segments dimensions have slightly evolved

[52] The results in RD3 are obtained with 80 mm thick, 1.8-m flat-to-flat segments. Results shown in Table 6-12 have been scaled to the baseline segment dimensions: 70 m thick, 1.6-m flat-to-flat.

since the time of writing of these reference documents, the dimensions provided in Figure 6-45 and Figure 6-46 are superseding.

Parametric studies for the blanks production in low-expansion glass or glass-ceramic have been undertaken by suppliers under ESO contract (see RD6, RD7, RD8). Equivalent studies have been undertaken with silicon carbide (see RD9 and RD10). The specified leadtime from signature of supply contract to the delivery of the last segment was 10 years, with 8 years as a goal. It came out of the studies that the faster schedule could be met, in some instances at an even lower (by ~5%) cost than the longer one. The specified leadtime included a 2 to 3 years provision for facilitization.

These studies covered three possible dimensions: 1.3, 1.8 and 2.3-m flat-to-flat. All studies concurred that the cost vs diameter curve was rather flat, with the lower and upper dimensions slightly (~5-10%) to significantly (~30-40%) more expensive. Yield was conservatively assumed to be constant over the production cycle i.e. no provisions were made for otherwise plausible improvements of yield with time and accumulated experience. Due to facility limitations, ULE is cost-effective with dimensions of up to 1.5-m.

With Zerodur, Astrosital and ULE, production of OWL segments blanks would require duplication of existing infrastructures but no particular process development. Schott and Corning recently reported a substantial increase in capacity, motivated by a surge in the market for large Zerodur and ULE components. In a follow-up of the initial study Schott reported that with a total capacity of 700 tons/year its current facilities are now close to meeting the requirements for the supply of OWL segments. According to Schott this capacity could be increased by up to 20% without requiring major investment. Schott also gained experience with hexagonal casts (Figure 6-47), allowing for 17% savings on raw material. A single cast could be cut into up to 3 segments. Availability of such facitlities at the time of purchase of OWL blanks is evidently not guaranteed, but further extension is possible. Facilitization would take less time than initially anticipated (~1 instead of 2-3 years) and production could ramp up within the second year after signature of the contract.

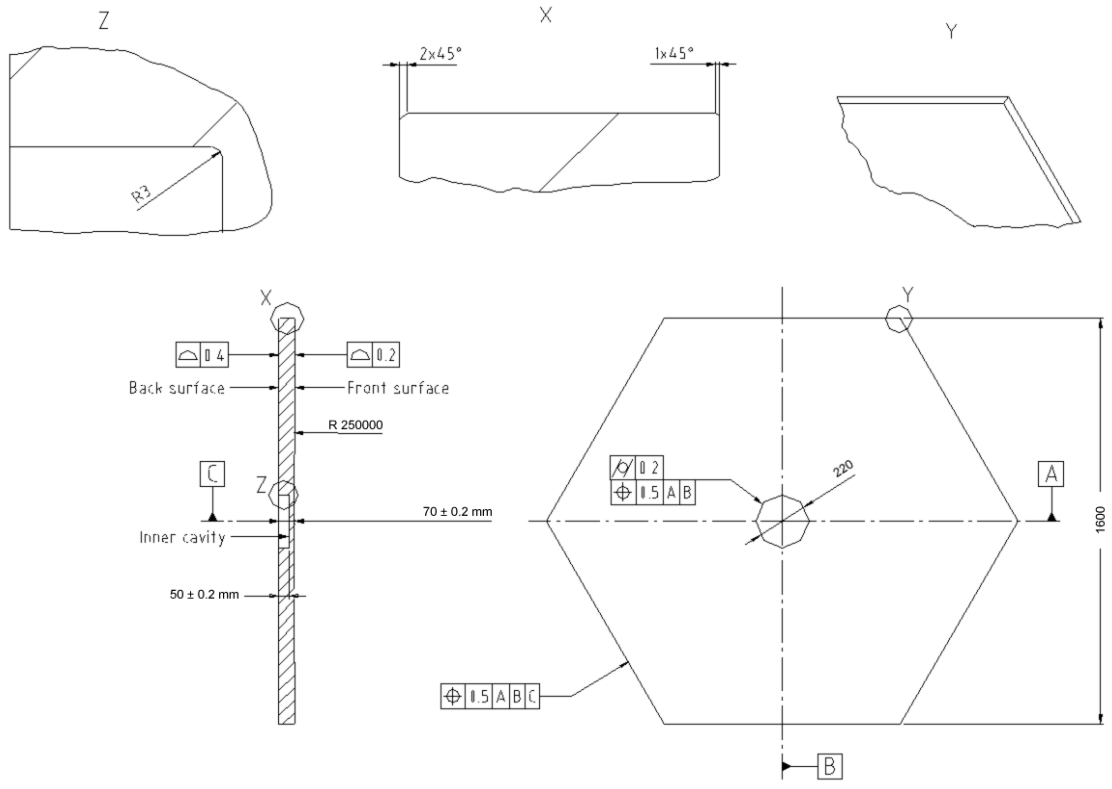

Figure 6-45. Primary mirror segment blank.

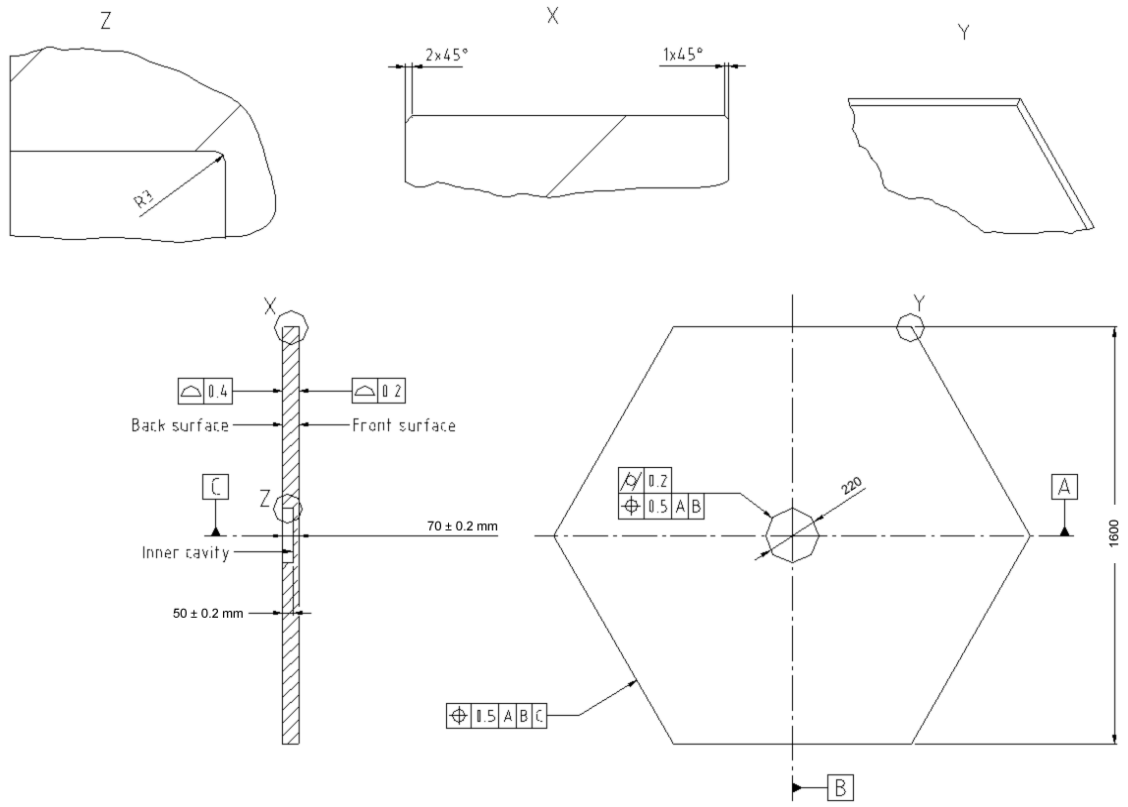

Figure 6-46. Secondary mirror segment blank.

With several hundreds of segments produced, robust statistics reveal the consistent and excellent homogeneity of Zerodur (Figure 6-48). Through-thickness CTE gradients, a possible concern for segmented apertures (see RD3), are below 0.010×10^{-6} K^{-1}, with measured values most frequently below 0.002×10^{-6} K^{-1}.

At the time of writing of this document, the option of segments moderate lightweighting is under investigation. Recent process developments would allow a substantial gain in machining time. The process has been verified on ~1-m Zerodur slabs. Provided the lightweighting geometry remains simple (circular pockets) and the lightweighting ratio does not exceed ~50%, thereby allowing safe rib and front plate thickness, lightweight, 70-mm thick, 1.6-m flat-to-flat segments blanks might be produced within a manageable cost increase.

Low-expansion glass or glass-ceramic is the current baseline for OWL segments, but the development of silicon carbide as an alternative is actively pursued. Figure 6-49 shows the thermo-mechanical figure of merit of several materials. The x-axis corresponds to the ratio of the CTE divided by thermal conductivity (representative of transient surface change under thermal load) and the y-axis corresponds to the inverse of the specific stiffness i.e. the ratio of density divided by Young's modulus (representative of e.g. total mass for a specified deflection under external load). The superior characteristics of silicon carbide are evident.

Figure 6-47. Zerodur hexagonal cast. Courtesy Schott.

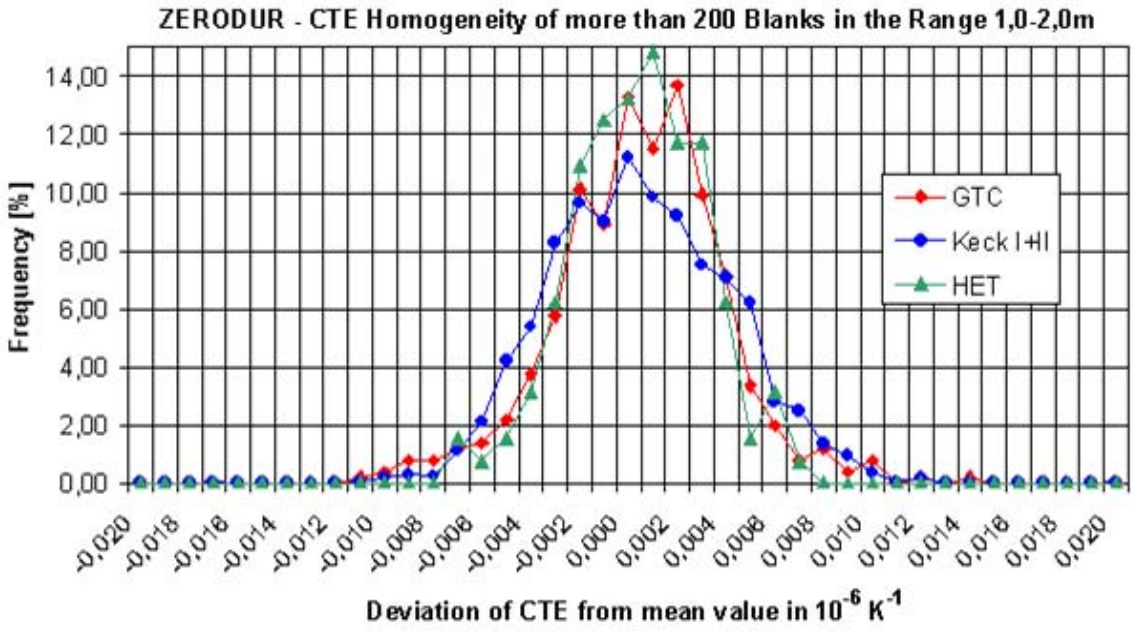

Figure 6-48. CTE homogeneity of Zerodur. Courtesy Schott.

Silicon carbide would allow for a substantially lower (by a factor ~6) segments mass, thereby implying an estimated 30% reduction of the telescope moving mass[53], relaxed segment actuator specifications and, potentially, higher control bandwidth. In view of its excellent thermal conductivity it would simplify thermal control, the primary and/or secondary mirrors being able to

[53] This figure includes a substantial reduction of the telescope structural mass.

passively reach thermal equilibrium with ambient conditions. Secondary mirror covers would no longer be required. Surface hardness is also an advantage in terms of durability.

Silicon carbide mirrors have been produced since the mid-80s, generally for ultra-lightweight, stable space structures and reflective optics. An industrial study commissioned in 1989 under ESO contract for the VLT 1.12-m secondary mirrors, concluded that such mirrors would be feasible and have an aerial mass of about 40 Kg/m². A contract was subsequently placed for the supply of the four electromechanical M2 units, with silicon carbide mirrors. After a machining accident at the silicon carbide supplier premises, however, the contract had to be cancelled as the supplier's mother company decided to close its activities in the area of optical substrates, which it regarded as a fringe market. The reason given for the accident was essentially related to inadequate, worn out machining tools –i.e. nothing that could not have been easily remedied. The VLT secondary mirrors were eventually made in Beryllium, at a significantly higher cost.

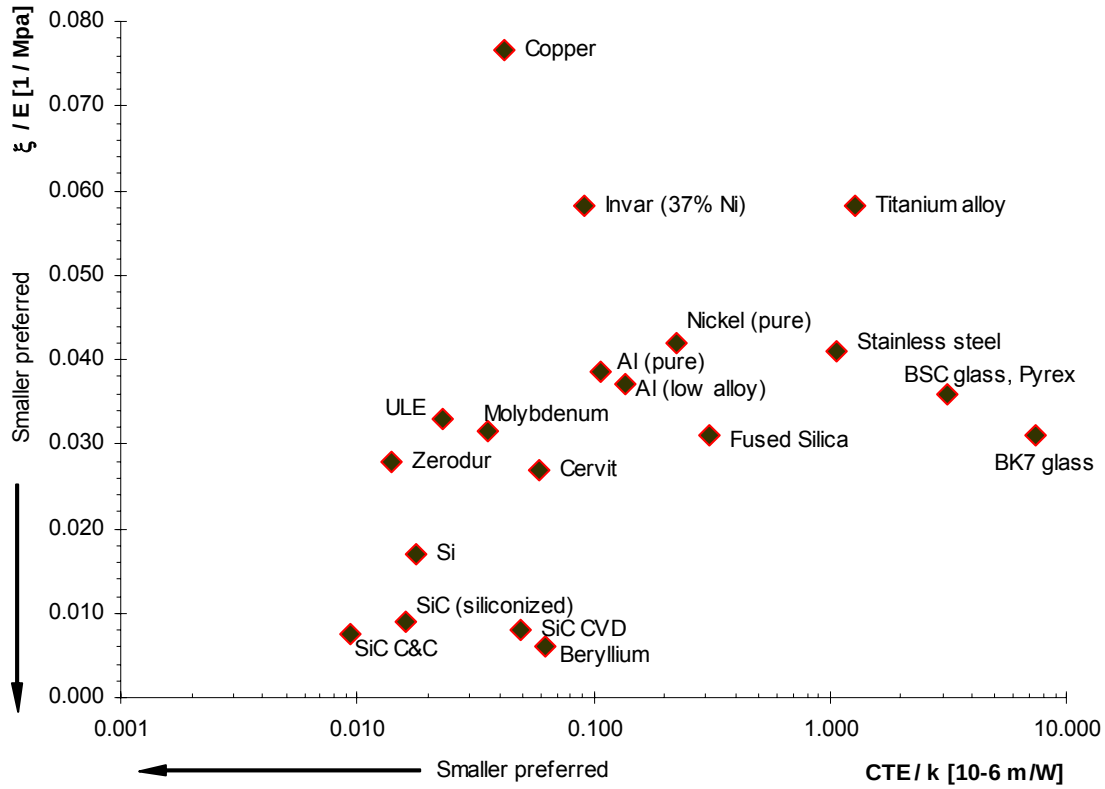

Figure 6-49. Thermo-mechanical figure of merit.

Silicon carbide has been traditionally regarded as a high-end, very expensive technology. The main reason is the extremely low mass target underlying space applications. In addition to requiring numerous and expensive qualification tests and models, this implies lengthy machine cycles as tool speed must be reduced to prevent breakage of exceedingly thin ribs. With low material cost and relatively fast (a dew days at most) cold-to-cold sintering or infiltration processes, there is no intrinsic reason for silicon carbide blanks to be more expensive than conventional materials (figuring and polishing, however, are considerably more costly, see 6.5.1.4). This has been, to some extent, confirmed by studies contracted to European suppliers (see RD9 and RD10) for the production of OWL segments, priority being given to minimal cost over aerial density (goal 70 kg/m² or less). Depending on supplier, process, and on whether blanks would be delivered with polishable overcoating or not, cost estimates range from about half the cost of solid glass-ceramic ones to comparable figures.

Boostec sintered blanks are made from SiC powder, cold-pressed with an organic binder at ~1000 Bar into a precursor ("green body", see Figure 6-50) which is subsequently machined to

near-net shape before de-binding and eventually sintering at ~2100 °C. Shrinking upon sintering is about 15% linear but reproducible[54]. The final blank is polishable but residual porosity (~1%-3%, depending on powder size) is generally incompatible with visible optical applications. Machining operations of the sintered blank must be minimized in view of its hardness[55]. Material ground out of the precursor could be recycled. Blanks up to 1.3-m could be made from a single pressed precursor, size being limited by the availability of suitable cold isostatic pressing facilities. Larger segments would be assembled from smaller precursor parts by brazing, bonding or bolting prior to infiltration –with brazing as the baseline solution. This technique has been successfully applied to the 3.5-m Herschel primary mirror [13]. There is no evidence of discontinuity or weakness at the brazed joints. Boostec reports a CTE homogeneity in the range of 0.005×10^{-9} K^{-1}, measured on different batches over several years.

Four segment blank prototypes (Figure 6-50), 1-m flat-to-flat, have been delivered by Boostec under ESO contract and will be polished and tested within the framework of the ELT Design Study (see A-1.3). Up to four more will be procured from a different supplier (see RD510).

Figure 6-50. Precursor (left) and 1-m sintered SiC segment (right). Courtesy Boostec.

ECM CESIC blanks are made by infiltrating a felt with silicon, at approximately 1800 °C, without significant dimensional change down to ~0.015% of linear dimensions. As with sintered silicon carbide, most machining can (and should) be done on the precursor. Beyond 1-m or 80-mm thickness, blanks must be assembled by bonding several parts before infiltration. There is no evidence of any discontinuity of weakness at the joints. Raw material being the major cost position, the option of assembling the entire back structure from smaller, serially produced plates and joints ("Lego" approach), could be an alternative to machining it out of a solid prescursor. A small (30cm) demonstrator blank has been produced.

Residual carbon content prevents clean optical finish and CESIC blanks also require a polishable overcoating, typically ~200-300 μm thick. One option is to depose a polishable slurry (ECM proprietary process) prior to a second firing run.

Both Boostec and ECM see no major issue in complying with a production cycle of 6 years after up to 2 years facilitization. In both cases a dedicated facility would have to be built, but the required equipment would be a mere duplication of existing ones. It is worth noting that both suppliers are operating furnaces already compatible with OWL segments characteristics. With sintered silicon carbide, the required yield for OWL would be about 50 tons/year, i.e. a significant but not major increase in relation to a 350 tons worldwide production in 2001. Based on the experience gathered with the 3.5-m blank for the Herschel IR telescope [13], it appears that an aerial mass specification lower than the specified maximum of 70 Kg/m² might be achievable without significant overcost.

[54] Typically ~0.4% of linear size.

[55] Hardness of the precursor material is low, thereby permitting fast machining. In this state the blank is however fragile, which is one of the reasons for the high cost of ultra-lightweight, thin ribs structures. Ribs, front plate thickness and lightweighting geometry of OWL segments could be kept within safe values.

A third European supplier (SNECMA) is currently in the process of validating an attractive technology (StarSic), whereby siliconization of the precursor and deposition of a polishable overcoating would be performed in one single furnace run. The process would therefore be potentially cost-effective. Preliminary results of thermal tests on a first 15-cm polishing sample are quite promising, with surface deflections in the range of $\lambda/8$ between room temperature and -10 °C. These deflections are probably related to a less-tan optimal machining of the precursor, which resulted in an irregular overcoating thickness after polishing. SNECMA already operates large facilities and has been a supplier of polishable overcoatings (ICVI) for silicon carbide mirrors.

6.5.1.4 Segments polishing

Preliminary specifications for the figuring and polishing of OWL primary and secondary mirror segments are given in RD44 and RD45 for glass-ceramic and silicon carbide segments, respectively. Optical quality requirements are summarized in Figure 6-51 (wavefront slope) and Figure 6-52 (wavefront amplitude). They include specifications applicable to any single segment and specifications applicable to the entire production. The overall wavefront error specification corresponds to seeing-limited operation; residuals after removal of low order terms take into account a minor correction of residual errors by the adaptive mirror M6, while residuals after removal of low- and mid-frequency terms take into account higher order adaptive optics correction. Preliminary definitions of low- and mid-order terms are given in terms of Zernike polynomials (see RD44 and RD45). Slopes are not directly measured but calculated from phase maps and therefore, strongly affected by the measurement noise on wavefront amplitude. Slopes specifications will eventually be replaced in favour of a finer descriptive of the allowable spectral content of the misfigure.

The definitions (polynomial orders) are different for the primary and secondary mirror segments, to take account of the different segments projected size onto the pupil. In the case of primary mirror segments, low order terms are third order aberrations, mid-frequency ones include seventgh order terms. The corresponding orders for the secondary mirror segments are 7^{th} (low order) and 11^{th} (mid-spatial frequency), respectively. The specifications given in Figure 6-51 and Figure 6-52 include curvature deviation from an average calculated on the basis of the 15 first produced segments.

In order to guarantee best performance in operational conditions and minimize the effect of through-thickness CTE gradients (see RD3), the specifications require that segments be tested at the presumed median operational temperature (5 °C). Figuring and polishing may of course be performed at room temperature.

Optical replication had been briefly considered at an earlier stage. This technology had been successfully developed by CERGA, now part of Observatoire de la Côte d'Azur, with ESO support in the late 1980s. The high forces applied during unmolding, however, imply high stresses in the parts and durability of the master is a potential issue. In addition, surface stresses generated during polimerization of the ~0.2 mm thick epoxy layer may lead to unpredictable warping. This path was, therefore, abandoned.

Two competitive studies have been performed under ESO contract, both for the polishing of either glass-ceramic or silicon carbide segments, and with segments dimensions of 1.3, 1.8 and 2.3-m flat-to-flat. Total price variation between the two lower sizes seems negligible. The larger size would lead to a price increase of ~20%. The specified schedule was 10 years from signature of the contract to the delivery of the last segment, with eight years as a goal. Both suppliers claim they could meet the goal. Facilitization would take 2 to 3 years and is included in the specifed shedule.

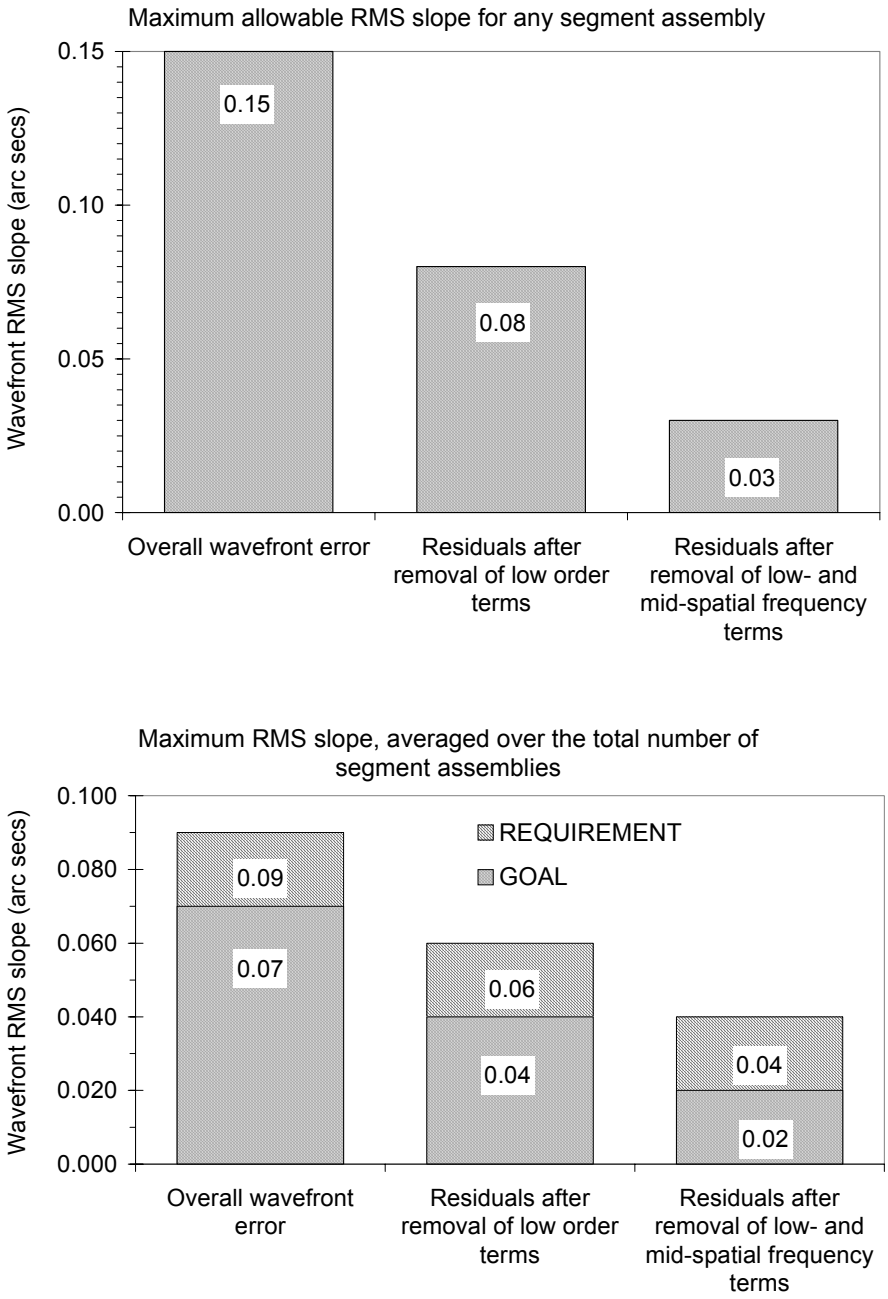

Figure 6-51. Segments optical quality (rms slope) specifications.

The suppliers considered planetary or double-side polishing as well as figuring and polishing on computer-controlled individual machines. Performance, reliability and cost of large planetary polisher is a potential issue with segments beyond ~1-m in size, and both optical manufacturers eventually selected parallel grinding and polishing of individual segments, to be complemented by either ion-beam or small tool computer-controlled polishing. The required production capacity is about 1.6 segments per day with 1.8-m segments, taking into account a 1% loss rate and assuming 6 working days per week, 46 working weeks per year. Processing several segments simultaneously on large machines is rather inconvenient as it would require complex handling and assembling operations, safety issues, and be less robust in terms of impact of failure on the production rate.

With polyurethane-coated large tools, the total number of machines is relatively modest anyway: 2 grinding computer-controlled machines, 5 polsihing ones (1.8-m segments). A dedicated production facility would have to be built. According to suppliers its size would be two to three

times the size of the factory built by REOSC for the prodcution of the VLT primary mirrors. No new, unproven or particularly challenging equipment would have to be developped.

According to specifications the segments would have to be acid-etched (back surface). The segments being passively supported during polishing and in operation, such acid-etching might be unnecessary. Removing this operation would lead to a small but significant reduction of total price.

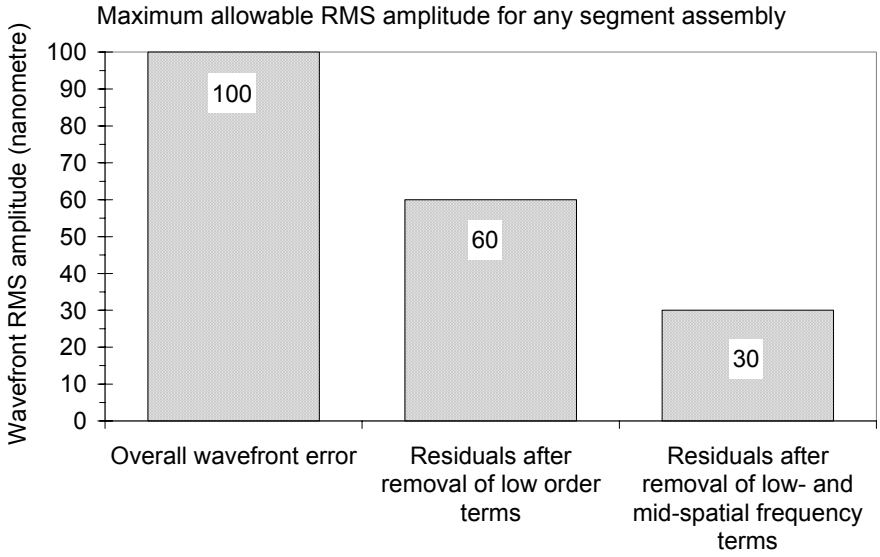

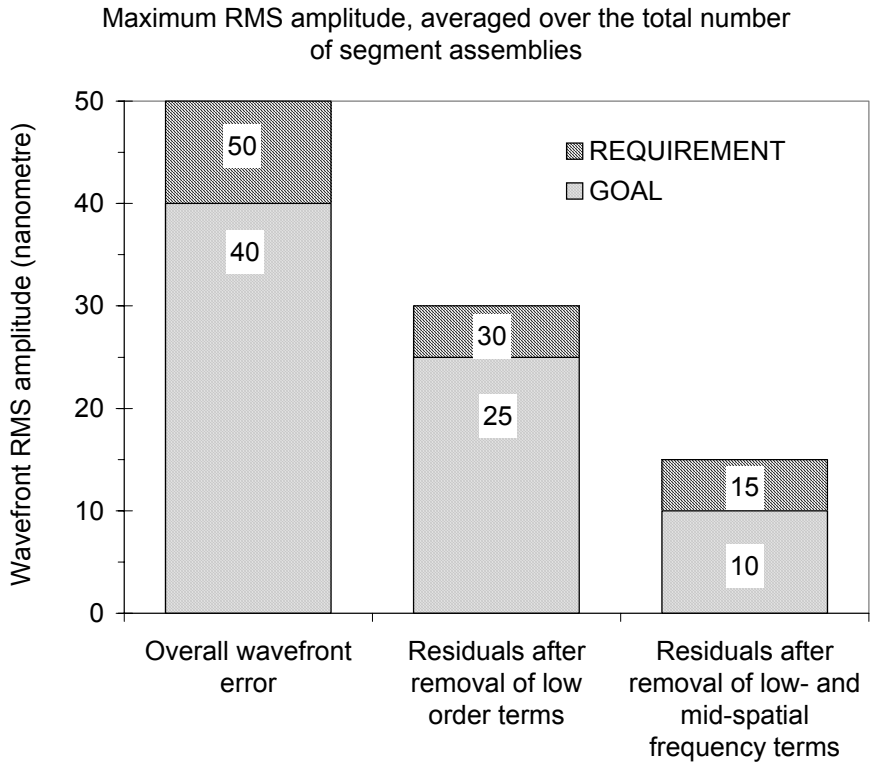

Figure 6-52. Segments optical quality (rms amplitude) specifications.

Wasters (polishing extensions) would be assembled onto the segments edges to reduce edge misfigure, as done with GTC segments. The spherical shape of OWL primary mirror is however favorable in that it allows the use of large, stiff tools, which are inherently better in relation to high spatial frequency errors, including edge misfigure. It is worth noting that a prototype LAMOST segment (spherical) has been polished without wasters, to adequate quality. Removing the need for wasters would lead to a significant reduction in total price. Further tests are necessary and will be performed on 1-m silicon carbide segments, within the framework of the ELT Design Study (see A-1.3).

Segments would be tested interferometrically through a common matrix, segments mounted onto their operational support systems, face up for the primary mirror, face down for the secondary mirror ones. Segments would be tested against a matrix (convex for the primary, flat for the secondary mirror). Two matrices are required, one for testing at room temeperature in the early phases of polishing, one for testing at 5 °C before finishing and for acceptance testing.

With 1.8-m glass-ceramic segments, industrial price estimates coincide within a few percents, and are broadly (within ~10%) in-line with ESO's internal estimate made at an earlier stage.

Polishing of silicon carbide segments is far more expensive. First, SiC segments are not directly polishable and an overcoating is required after fine grinding. Possible options include CVD, ICVI or depostion of a polishable slurry, the latter applicable with ECM infiltrated blanks only. Second, the grinding and polishing of silicon carbide requires very expensive abrasives –boron carbide and diamond- and no convenient solution has been found to recycle the slurries after use. Processing time is longer in view of the higher hardness of the material. Homogeneity of the thickness of the overcoating is also a potential issue for the optical manufacturer. Taking these factors into account, the polishing of silicon carbide segments is a factor 2.1 to 2.6 more expensive that the polishing of glass-ceramic ones. In addition, there is a potential issue of surface stresses and CTE mismatch between the bulk of the substrate and the polishable overcoating, as already mentioned.

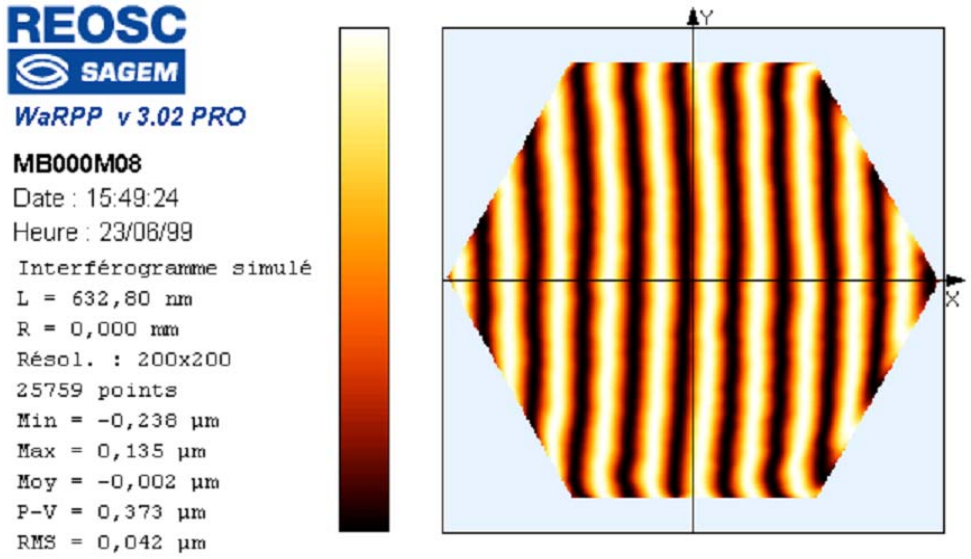

Figure 6-53. Interferogram of a LAMOST 1-m spherical segment prototype. Courtesy REOSC.

The additional cost of coating and polishing SiC segments, however, might be offset by the lower cost of raw blanks, the lower cost (mass) of the telescope structure and of the segments supports, and by the potentially higher bandwidth of the segments position control. Actuator cost and performance in relation to segment mass not having been evaluated at the time of writing of this document, a rigorous cost analysis is not possible yet. Actuator characteristics vs segment mass will be evaluated within the framework of the ELT Design Study (see A-1.2).

Furthermore, cost-effective alternatives to diamond slurries and to CVD or ICVI overcoatings might be available, and will be tested within the framewrok of the ELT Design Study (see A-1.3). Progress in the development by SNECMA of polishable blanks also ought to be closely

followed. According to plans, OWL primary mirror technology should be frozen by early 2008. By that time, and within the framewrok of the ELT Design Study, up to eight prototype segments will have been polished and tested, with different substrates and different possible overcoatings. These prototype segments are flat and will be measured interferometrically against a flat reference, at different temperatures, with a view to detecting CTE inhomogeneities and CTE mismatch between the polishable overcoating and the bulk of the substrate.

6.5.1.5 Segments supports

A preliminary parametric study of the segments axial support has been performed, with a view to deriving an optimal compromise between support geometry, segment thickness, and tolerances of support pads position. This study is documented in RD47. With similar segments dimensions, Keck and GTC opted for a 36-axial supports. Considering the number of OWL segments, it would be highly desirable to reduce the complexity of the support system. There are hopefully a number of factors that may allow doing so.

Figure 6-54 shows the deflection under gravity of a 70 mm thick Zerodur segment (one 60° sector shown), 1.6-m flat-to-flat, on an optimized distribution of 18 axial supports, and as predicted by Finite Element Modelling (FEM). The surface deflection is 31 nm RMS. A series of 50 runs with random axial position errors of up to ±1 mm leads to less than 1 nm i.e. negligible standard deviation.

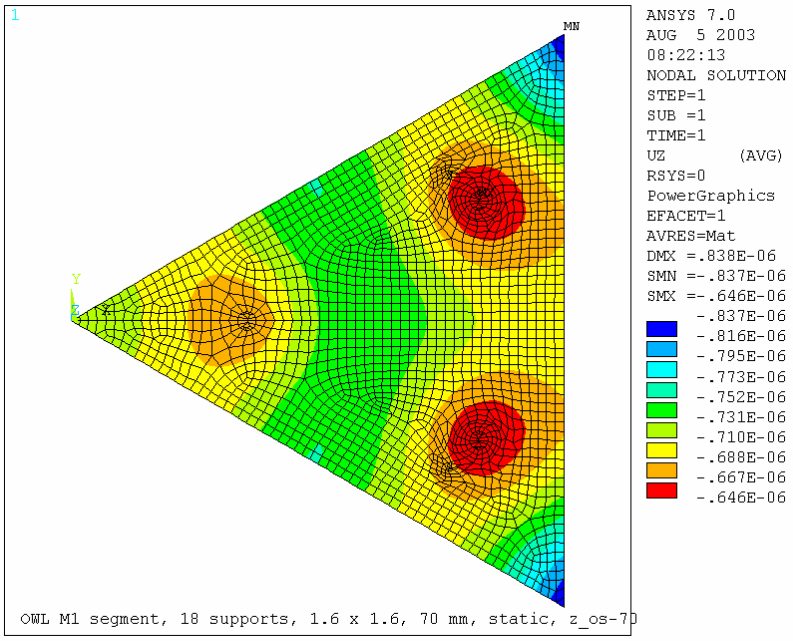

Figure 6-54. Segment deflection on axial support. Zerodur, thickness 70 mm.

A surface deflection of 31 nm RMS (62 nm RMS wavefront) would in principle not be acceptable. If, however, the error could be polished out with segment laying horizontal, it would follow a cosine of zenithal distance (z) law. In operation up to 60° form zenith, it would de facto be reduced by a factor two compared to the model shown herein –i.e. the axial support print-through would vary from 0 at zenith to 16 nm RMS at z=60°. Whether this is possible has actually been proven by REOSC (now SAGEM) in the lat 1980s. Within the framework of the VLT primary mirror polishing contract, REOSC supplied a 1.7-m Zerodur blank and polished it to serve as a reference (gauge) for the calibration of spherometric measurements on the 8-m mirrors. The spherical gauge mirror was polished with large stiff tools on supports mimicking those of the 8-m mirrors. No evidence of the print-through predicted by Finite Element Modelling (about 52 nm wavefront RMS) could be detected, even though the gauge was tested interferometrically. Even though the VLT primary mirrors were polished with flexible tools, no

evidence of any-print-through could be found either (the accuracy of the measurements was better than 10 nm wavefront RMS).

Actually, figuring and polishing of the segments on the same support distribution as in the telescope will *inevitably* converge towards the desired shape with the segment lying horizontal.

This, however, applies only to the primary mirror segments. In the case of the secondary mirror, the error would be doubled. A possible way around would be to test the (flat) secondary mirror segments against a reference, with the segments facing down. In the last runs of polishing (either small tool or ion-beam figuring), the residual misfigure on support could be corrected by the polishing process –provided that doing so does not require more than one or two polishing runs, which seems to be the case. Furthermore, spatial frequencies on the secondary mirror correspond to ~4 times lower frequencies in the pupil. With a separation of ~60 cm between M2 segments supports, residual flexures of the segments would be seen by the adaptive systems as DC errors with a spatial period of ~2.4-m in the pupil and a fairly small amplitude compared to atmospheric turbulence.

No analysis has been done with silicon carbide segments. The higher specific thickness of silicon carbide, together with the moderate requirements on lightweighting, should lead to more favorable results.

All the above remains fairly notional. Further design, analysis and tests will be required once the segments substrate and exact geometry will be finalized. According to plans, phase B includes design and testing of prototype segments and support systems. Analysis shall cover the performance of axial and lateral supports in relation to gravity, thermal change, allowable integration errors, and spurious bending moments. Should results not allow the segments to be supported on 18 axial supports, a 36 supports system is considered as a backup.

6.5.2 Corrector optics

In the following we concentrate on the fabrication of the 8-m class tertiary and quaternary mirrors. The adaptive M5 and M6 mirrors are described in sections 8.3 and 8.2.1.2.1, respectively.

For M3 and M4 the baseline approach is to follow as closely as possible the VLT 8-m mirror design, including fabrication, handling, transport, operation and maintenance concepts.

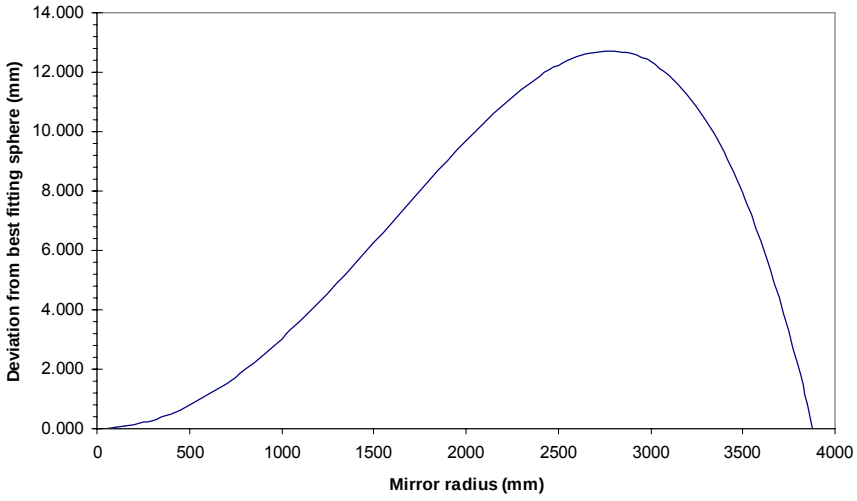

Figure 6-55. M4 aspherization profile.

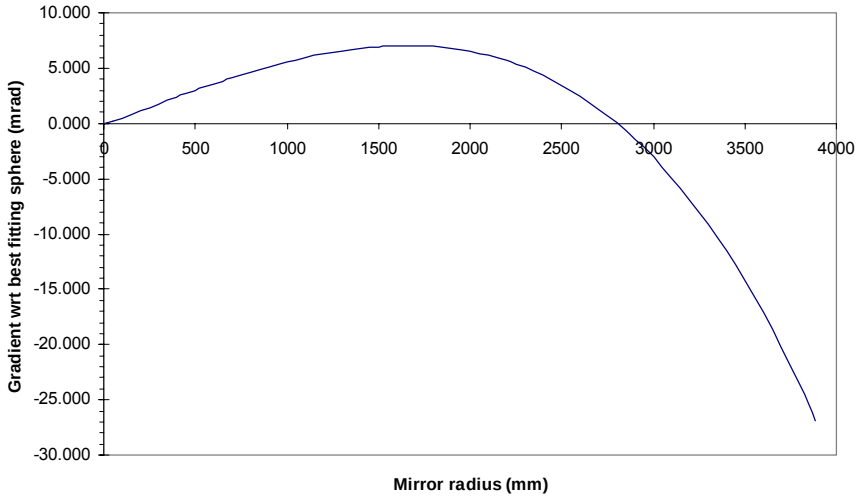

Figure 6-56. M4 slope difference with respect to best fitting sphere.

With radii of curvature 18.690-m and 19.970-m, respectively, M3 and M4 have a larger sag than the VLT primary mirrors. As a result, the last 8-m Zerodur blank still available at SCHOTT would be suitable for M4 with a final thickness of ~135 mm, to be compared to 175 mm for the VLT primary mirrors (the situation is much less favorable for M3). Although not impossible, such thinning would imply a significant densification of support systems for optical fabrication, transport, handling and operation. On the positive side, higher mirror flexibility and higher aerial density of the active support would allow for the correction of higher order modes than in the VLT. There is however no strong incentive to do so at this stage.

Attempts have been made to modify the optical design with a view to increasing at least one of the two 8-m class mirror radius of curvature to a VLT blank-compatible value, without success – unless the primary mirror focal ratio is relaxed[56]. According to SCHOTT, re-building the VLT 8-m production facility for 2 blanks would lead to fairly high costs. This situation would certainly change if the 8-m blanks were to be ordered together with the segment blanks as a global package.

For 8-m ULE blanks, CORNING provided more attractive if only indicative prices on the basis of Gemini specifications, with a radius of curvature changed to 19-m. Here again, there would be a substantial (20%) price reduction in the event of a joint order for the segments and 8-m blanks. According to CORNING, the first blank would be delivered ex works 24 months after placing the order, followed by the second one 16 months later. This schedule seems optimistic but could be secured by an advanced order of raw material.

M3 and M4 are storng aspheres, with 1.96-mm and 12.0 mm.departure from best fitting sphere, respectively. Figure 6-55and Figure 6-56 show the aspherization profile and slope variation with respect to best fitting sphere of M4. The latter is more representative of difficulty to produce a smooth surface, and about 40 times stronger than with a VLT primary mirror. In the following we concentrate on M4, which is by far the most difficult to polish and test.

Low spatial frequency terms are of no concern as the mirror will be actively supported. With the VLT, about 80 N active forces were required to correct for low spatial frequency misfigure. This is less than 10% of the full active range, about half of which is used for the conversion Nasmyth to Cassegrain. As no such conversion is required with OWL, the allowable low frequency terms or the actuator range could be relaxed in comparison to VLT. Figure 6-57 shows the high spatial frequency content of the VLT primary mirrors, in terms of wavefront RMS vs subpupil diameter. The smallest tool used in the very final stages of polishing of the fourth mirror was about 30 cm in diameter. With a slope deviation from best fitting sphere 40 times larger with OWL M4 than

[56] With a f/1.42 primary mirror, the sag of M4 is only 13 mm larger than that of a VLT primary mirror and the remaining SCHOTT blank would be usable, with a final mirror thickness of ~160 mm.

with VLT M1, one would expect a misfigure about 40 times worse, with the same tools and processes as for the VLT.

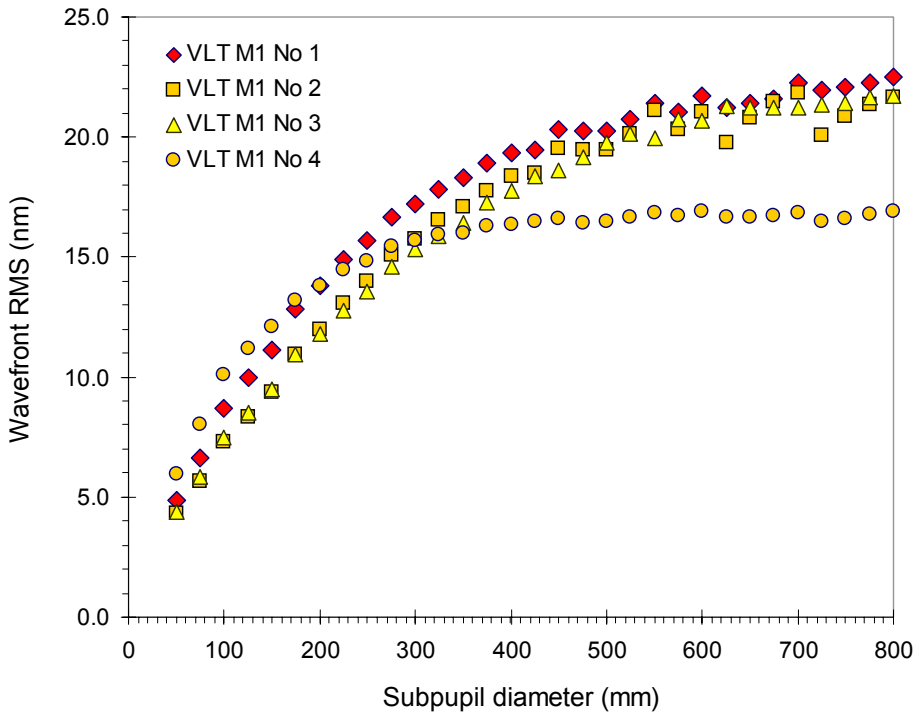

Figure 6-57. High spatial frequency wavefront error, VLT primary mirror.

With a magnification of 12.5 between M4 and the entrance pupil, the cut-off of the first generation adaptive optics would correspond to a period of ~80 mm on M4. From Figure 6-57 and applying the above scaling factor of 40 we infer that residual errors would be in the 200-300 nm wavefront RMS range. This is, hopefully, grossly pessimistic.

The optical quality specification for M4 is still to be finalized. The expected requirements are

- Wavefront RMS better than ~60 nm RMS after active and first generation adaptive correction (~80 mm spatial period on the mirror)
- Wavefront RMS better than ~10 nm RMS after active and high order (~10 mm spatial period) adaptive correction.

There has been very significant progress in optical fabrication since the polishing of the VLT primary mirrors. In addition, these mirrors were polished without making particular effort on minimizing spatial periods below ~0.5-m. Neverthelss, comprehensive studies by experienced optical manufacturers are still required. We expect OWL M4 to require very small tools (~1 cm) in the last stages of polishing, and a correspondingly long processing time.

While M3 could most probably be tested at centre of curvature through an Oeffner nulling system, M4 requires a considerably more complex test set-up. One option would be to test it against M3 and through a all-spherical 3-lenses compensator (Figure 6-58, simulated interferogram in Figure 6-59). This set-up has been conceived only to demonstrate that a theoretical solution not relying on aspheric optics or Computer-Generated Holograms exists – albeit a very inconvenient one in terms of practical implementation. The largest lens is 1.6-m in size and could be made of glassy Zerodur. M3 would have to be mounted upside down above M4. The set-up is extremely sensitive to decentres of the nulling system. This could, however, be alleviated by performing the optical tests at different azimuthal orientation of M4 (as was done with the VLT primary mirror) or by axially rotating the nulling system to disentangle non-axisymmetrical terms. Centring of the null-lens could be done to a few microns by inserting

symmetrical masks in the causticf of aberrations and re-centring the null-lens until obscurations are symmetrical[57].

One should also take into account the fact that M3 and M4 are active i.e. a considerable relaxation of low order terms is possible.

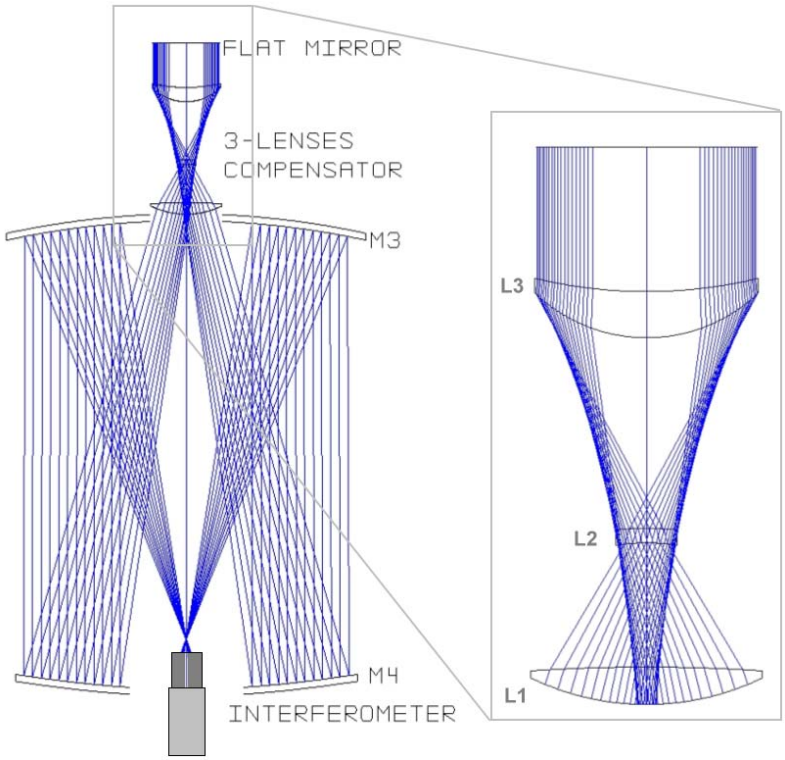

Figure 6-58. M4 optical test set-up.

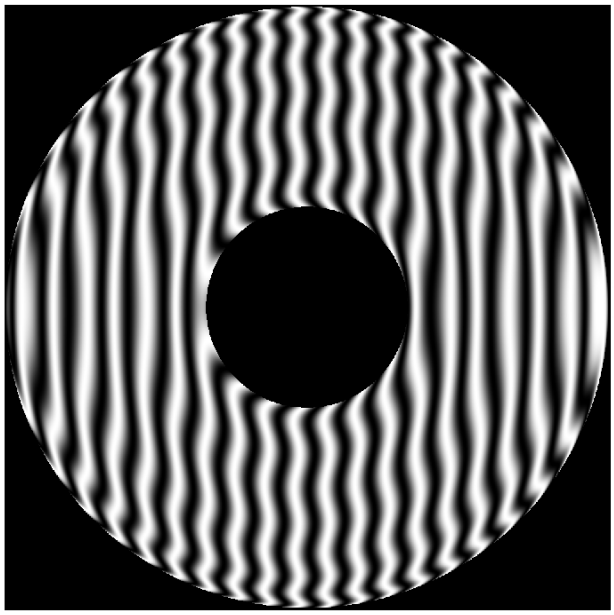

Figure 6-59. M4 nominal interferogram, double pass.

[57] This procedure was applied to the VLT primary mirror and proved not only accurate but also easy –the null-lens was centred to a few hundredth of a mm without particular effort.

6.6 Safety

The probability of failure P of a glass-ceramic part depends on the following parameters:

- Tensile stress σ
- Total area A of the part under stress
- Duration t of the load generating tensile stress
- Surface finish
- Material Weibull modulus □.

More specifically, the tensile stress σ_A over an area A and corresponding to a probability of breakage P is given by

$$\sigma_A = \sigma_0 \left(\frac{A_0}{A} \ln \frac{1}{1-P} \right)^{1/\lambda} \qquad \textit{Eq. 6-5,}$$

where σ_0 is the tensile stress over an area A_0 and corresponding to a $1\text{-}e^{-1}$ i.e. 63 % breakage probability. With Zerodur, D151 surface finish, σ_0=53.7 MPa and λ=14, while with acid-etched D64 it is σ_0=219.8 MPa and λ =6. In that case Eq. 6-5 assumes a 2 seconds load. If the duration t [in seconds] of the load is not 2 seconds, the tensile stress σ_{At} corresponding to the probability P is

$$\sigma_{At} = \sigma_A \left(\frac{t}{2} \right)^{-0.0417} \qquad \textit{Eq. 6-6.}$$

Conservatively assuming D151 on all surfaces, 11 MPa tensile stress over all surfaces of a segment would lead to a breakage probability of 10^{-5} over 2 seconds load time. The corresponding figures for 24 hours and 40 years loads are 6.9 and 4.6 MPa, respectively. These limits apply, however, to a single individual segment and are representative of desirable stress limits upon handling and transport only. Stress limits in operation shall assume that the complete mirror is under load. Assuming a total load area of 14,000 m², the allowable tensile stress limits for a 10^{-5} overall probability of failure are 6.2 MPa for a 2 seconds load, 4.0 MPa for a 24 hours load, and 2.7 Mpa for a 40 years (i.e. permanent) load.

For reference, interfaces and equipments for the VLT primary mirrors have been designed with a 3 MPa tensile stress limit for permanent load and 5 MPa for short-term (24 hours) loads. Only under extreme conditions (temperature ≤ -10 °C, leading to local stresses in bonded joints; earthquake; excessive vibrations and load transfers during transportation to site) could the limits be approached –but not exceeded Under normal operation, tensile stresses in the VLT 8-m mirrors are an order of magnitude below the specified limits.

With silicon carbide the situation is more favorable because of higher strength limits and lower masses. Stress concentration at the discontinuities of lightweight structures should hoever not be underestimated and a complete stress anaylis, taking into account actual segment geometry, will be required. The same comment applies with lightweight Zerodur.

With OWL and in normal operation, highest tensile stresses would in principle occur within the mirrors facing down i.e. the secondary, quaternary and M6 mirrors. Applying to above stress limits calculated for a complete 14,000 m² loaded area is, therefore, conservative. It is worth noting that the aerial density of OWL segments axial supports, with 18 supports and a segment size of 1.6-m, is comparable to that of the VLT primary mirrors, with 450 pads (3 pads per axial support tripod) and a mirror diameter of 8.2-m.

Whereby breakage of a single segment during transport or handling outside the telescope would not be catastrophic –assuming such breakage would not pose a threat to human safety-,

failure in the telescope could evidently lead to catastrophic damage –in particular with M2 segments-, not to mention inacceptable threat to human safety.

A suitable strategy for the preservation of human and system safety during transport, integration, operation and mainentnace still needs to be developed, taking the above into account. Possible measures to improve safety include:

- Acid etching of critical areas (interfaces);
- Safety support systems preventing large blocks to fall through in case of breakage;
- Protective canvas, reinforced mirror covers (M2) and corrector cage (M3 to M6);
- Suitable handling procedures, avoiding human presence under load; minimizing human intervention.

Transport, integration and maintenance aspects are also addressed in sections 13.1.1.2, 13.2.1.4, and 15.1.2.

7. Non-adaptive wavefront control

7.1 Requirements

One of the objectives of OWL is diffraction limited imaging at all wavelengths. This is only possible with a concerted control of all optical elements correcting both the wavefront errors introduced by the optical elements themselves and those introduced by the atmosphere. Traditionally the control mechanisms are classified according to the origins of the wavefront errors, their frequency content, and their ranges of correction.

- **Pre-alignment.**

  At the end of the integration of the telescope (or after major maintenance operations) the optical elements are both misaligned with respect to each other and intrinsically deformed to such an extent that automatic measurements of the wavefront errors would fail. At this stage one needs a coarse alignment to reach the accuracies required for automatic correction procedures[58].

- **Active optics.**

  Active optics is defined as the correction of all errors which are generated by misalignments and deformations of the optical elements at frequencies lower than 0.1 Hz

- **Phasing of segmented mirrors.**

  The phasing of the two segmented mirrors is done at three levels. At the highest level, with optical measurements done at the beginning of the night, it can be regarded as a part of the active optics system. The global shapes of the segmented mirrors are corrected and, as a by-product, reference values for the edge sensors at the segment borders are defined. At the second level the corrections are based entirely on the measurements of the piston steps by the edge sensors at a rate of a few Hertz. While the highest two levels apply coupled corrections of the positions of the segments, the third level corrects the positions of single segments only, relying on measurements of parameters like accellarations of individual segments. This lowest stage may be required for the correction of wind effects at frequencies above 3 Hz.

- **Guiding and field stabilisation.**

  The control of the image position is done in two frequency regimes based on signals from a guiding camera. At low temporal frequencies up to the order of 1 Hz, guiding corrects the image position by controlling the azimuth and altitude positions of the telescope structure. At frequencies up to 10Hz, field stabilisation corrects residual errors in the image position

[58] In practice we expect the pre-alignment loop to run permanently (at very low frequency) in order to ensure that the system is always in a state allowing fast and linear convergence of the subsequent control loops.

with M6, either by rigid body movements of the support of M6 or by an overall tilt introduced into the thin adaptive mirror.

- **Atmospheric dispersion correction**

  Corrections to the level of a few milliarcseconds can most likely only be achieved with a closed-loop system estimating the residual chromatic aberrations due to the atmosphere. This requires a dedicated sensor measuring the positions of images obtained with light at two or more different narrow wavelength bands.

- **Adaptive Optics**

  Adaptive optics, which will be described in a separate chapter, is capable of correcting, at least partially, all types of wavefront errors by appropriate optical elements in the optical train. These can be either part of the telescope optics or of the instruments. Adaptive optics relies on signals obtained with high sampling rates of the order of up to a few hundred Hertz by dedicated wavefront sensors.

The following diagram shows the hierarchy and the dependencies between the various components of the wavefront control system. An arrow from a subsystem A to a subsystem B indicates that A imposes certain requirements on B, or more explicitly, that A can only work if certain accuracies have been reached or parameters been defined by B.

Several control loops, some of them with a critical dynamic behaviour, are combined in the non-adaptive control. A description of the architecture of the complete control system is given in the next section. The sections 7.3 to 7.5 will discuss the components of the non-adaptive control system listed above in more detail.

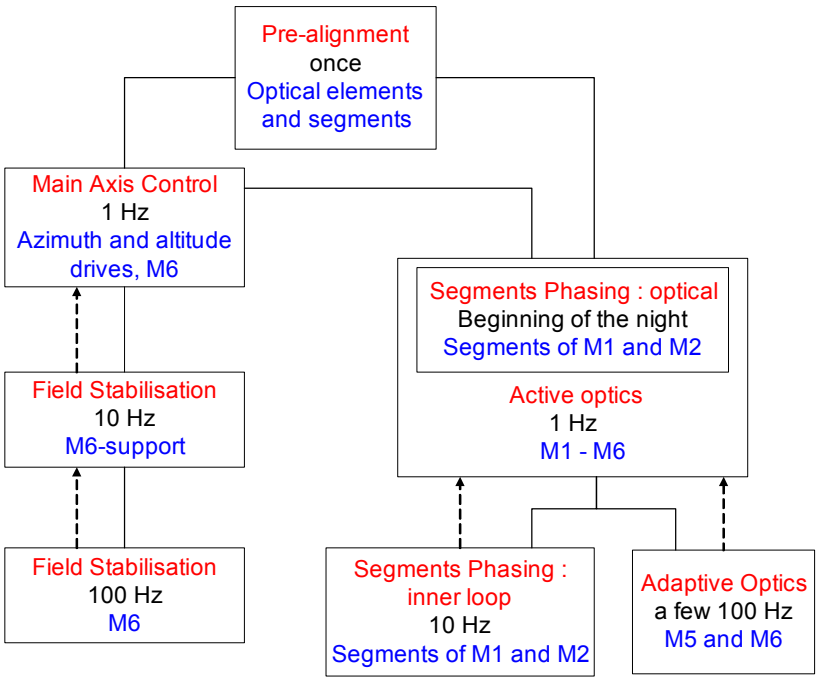

Figure 7-1. Wavefront control - overall layout.

7.2 General control architecture

OWL as an opto-mechanical system is continuously affected by two kinds of perturbations, which are the main sources of wavefront errors:

1. Atmospheric turbulence which generates errors in the incoming wavefront.
2. Perturbations such as wind buffing, gravity deflections, thermal deformation, and friction forces, which generate wavefront errors through deformations of optical assemblies or of the structure of the telescope.

The main objective of the wavefront control system is to compensate the effects of these perturbations, and hence to correct the wavefront errors. In addition, the control system is responsible for the tracking of the telescope. Based on the nature of the perturbations such as their amplitudes and their temporal and spatial frequencies, the tasks of the telescope control system are distributed to different subsystems, with their characteristic sensors and actuators. The main control subsystems of OWL are: main axes control, phasing and segment control of M1 and M2, active optics (AcO) including M3 and M4 active deformation, field stabilization with M6 and adaptive optics (AO) with M5 and M6. The non-adaptive control subsystems shall reduce the wavefront errors to such a level that the adaptive optics control system can correct the remaining wavefront errors (including atmospheric turbulence) with the available range of its actuators.

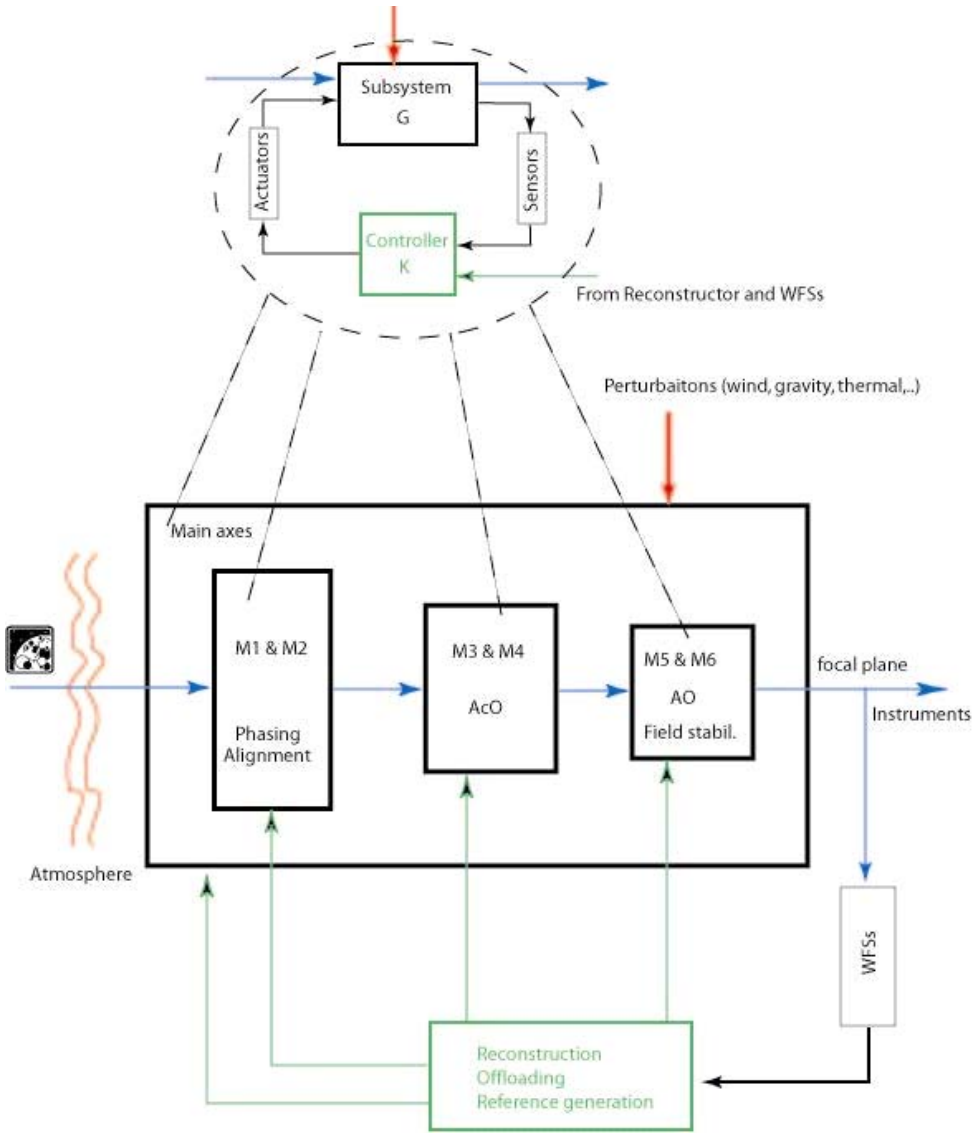

Figure 7-2 Wavefront Control Architecture for OWL

Each telescope control subsystem may be made of several hundreds control loops working simultaneously, possibly interacting with other loops in the same or in different subsystems. This

suggests that the control system is complex and thus a clear structure should be drawn to guarantee the correct and optimum functionality of the systems as a whole, i.e. a general control concept of telescope. For a large-scale and complex system [22], [23] such as OWL, an appropriate concept and architecture would be a hierarchical structure with a decentralized control.

At a lower level of the control hierarchy, each subsystem acts independently (decentralized), that is each control subsystem uses only local sensors and local actuators for closing a control loop. The main role of control at this level is perturbation rejection. Feed-forward control strategies for repeatable and predictable perturbations such as load variations or friction are foreseen. Feedback control laws should be designed for rejecting the dynamical and non-predictable perturbations such as wind buffeting. At a higher level of the hierarchy, a supervisor block receives the data from a wavefront sensor as an input. The main functionalities of this unit are the wavefront reconstruction on the one hand and the generation of optimal references for each control subsystem on the other hand. The determination of the optimal solution is based on the objectives of the control and the operational limits and constraints of the system. Figure 7-2 shows the block-diagram of the wavefront control architecture of OWL.

Since wavefront aberrations can be corrected by the control of the segments of M1 and M2, by deforming M3 and M4, by aligning the optical elements, and by the adaptive optics system, it is important to understand the combined effects of the corrections on the final measured wavefront. The constraints on the control bandwidth and limits on the stroke of the actuators of each subsystem offer guidelines for distributing the corrections to different subsystems. A general strategy is to offload or cascade the slow low order aberrations with large amplitudes from faster control subsystems to slower control subsystems, e.g. from the adaptive optics to the active optics or from the rigid body motion of M6 to the main axis or M2. However, due to the complexity of the problem it is necessary to derive the best solution from an optimization procedure.

The coupling between different control systems (optical and dynamical) should be understood and studied in detail. The separation and decoupling of some subsystems can be deduced from the time-scale separation principle. For instance, the adaptive optics control system with its relative high control bandwidth and small stroke can be decoupled from other subsystems and studied separately. However, in order to correct the effects of the wind on the telescope and to achieve the desired performance it seems that a relative high control bandwidth is required for some subsystems. This implies that there could possibly be an interaction between the actions applied by the control system and the resonance modes of the telescope structure, e.g. between the segment control system and telescope structure coupled through the segment support structure, or tip/tilt control of the M6 unit and corrector. Although these interactions are expected to be small because of the large mass ratios between the subsystems, they should be analyzed in detail and taken into account in the design of the controllers.

The local control loops should be designed based on the dynamical models as well as on the available knowledge about the disturbances acting on the system. Robust controllers should be chosen to guarantee the stability and the performance in the presence of modelling errors and uncertainties. In addition, to be able to increase the control bandwidth without the risk of exciting the resonance modes, active vibration damping and isolation techniques must be applied where needed [20].

In this section, the dynamical performance of the tracking with the main axes and the field stabilization by tip/tilt movements of M6 are investigated. There are two main sources of perturbation on the structure, wind buffeting on the one hand and torques due to rolling friction acting on the wheel/track interface of each friction drive unit on the other hand. The objective of the control system is to minimize the tracking errors with the main axes and the residual wavefront errors with the M6 tip/tilt unit in the presence of perturbations. Control strategies for improving the performance of the system are proposed. The performance of the closed-loop system is verified by simulations.

7.2.1 Wind rejection

The most important disturbance acting on the telescope structure is wind buffeting at different locations in the structure. Due to the large mass and the low resonance frequency of 2.6 Hz of the locked rotor mode only a limited control bandwidth is available. In addition the dynamical behaviour of the telescope and the influence of the wind loads on the main axes vary significantly with the altitude angle of the telescope because of variations of the resonance frequencies of the structural modes with the altitude position of the telescope. In many applications PID (Proportional-Integral-Derivative) controllers achieve a satisfactory performance. They can often be used for processes that are difficult to control provided that no extreme performance is required. However, if the performance has to be pushed to the limits, as it is the case with the stringent specification (1 arcsec RMS) for the tracking error with the main axes, other well-adapted types of controllers should be chosen. Good candidates for such a task are polynomial controllers [11], [15] which have been used in the simulations in this section.

The design of robust controllers for the azimuth and altitude axes is based on the dynamical models of the telescope structure. The details of the design and the results of the simulations for 4 altitude angles (zenith, 30 deg, 45 deg, and 60 deg) and two wind directions (frontal, lateral) are documented in RD17.

The main idea behind the design is to parameterise a controller that reshapes the control sensitivity function, i.e. the closed-loop transfer function from wind load perturbation to the main axis position, in such a way that the error is minimized for the frequencies where the effect of wind is most important. The block diagram of a multivariable closed-loop system describing the underlying control problem is presented in Figure 7-3, where *G* represents the transfer function between the input forces from the bogies[59] and the measured output *y(t)* ('main bearing angular position' for altitude and 'central bearing angular position' for azimuth axis). *K* is the controller transfer function and *H* represents the transfer function from wind load forces to the output measurements.

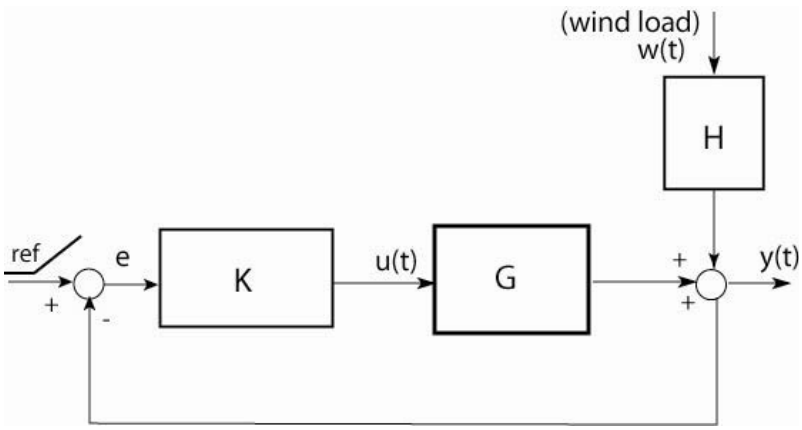

Figure 7-3 Block diagram of the closed-loop system

[59] In this part of the study, bogies are considered as rigid, and the force introduced by a bogie is the sum of the forces (torques) generated by the motors attached to the wheels of the bogie.

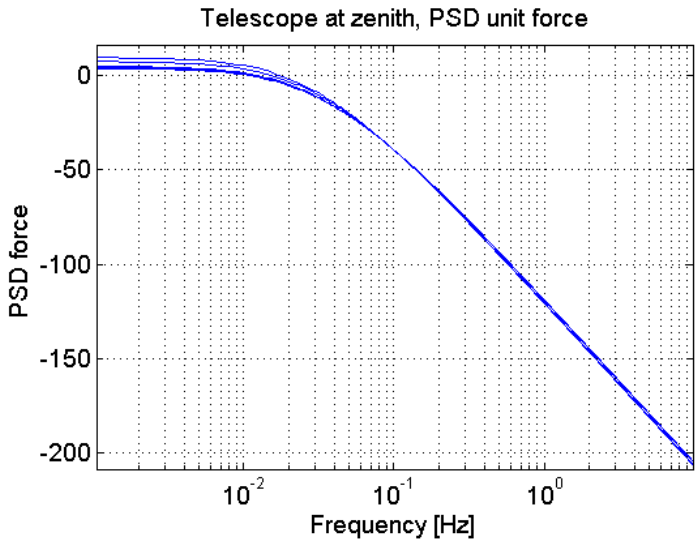

Figure 7-4 Normalized PSD of the wind loads applied to different height: altitude configuration

To proceed, models of the wind loads and a model of the telescope structure are required. Wind buffeting is a stochastic phenomenon and thus the Power Spectral Density (PSD), either of the speed or of the aerodynamics load, is a convenient way to characterize it. The PSDs which are used for this study are given 5.4.1.1.1.2). They are calculated for different heights from ground, i.e. for different wind speeds starting from 10m/s in lower heights and increasing up to 14 m/s at the top of the telescope. Time signals (wind force) with equivalent statistical characteristics can be obtained from these spectra. These perturbations are applied at five different sections of telescope structure (see RD527). Figure 7-4 shows the normalized power spectral densities of the wind forces for the altitude axis with the telescope pointing to the zenith. Here 'normalized' means that PSD is divided by the static wind force acting on specified telescope areas. However, during the simulations the PSD will be multiplied by the actual average force which scales with the wind speed.

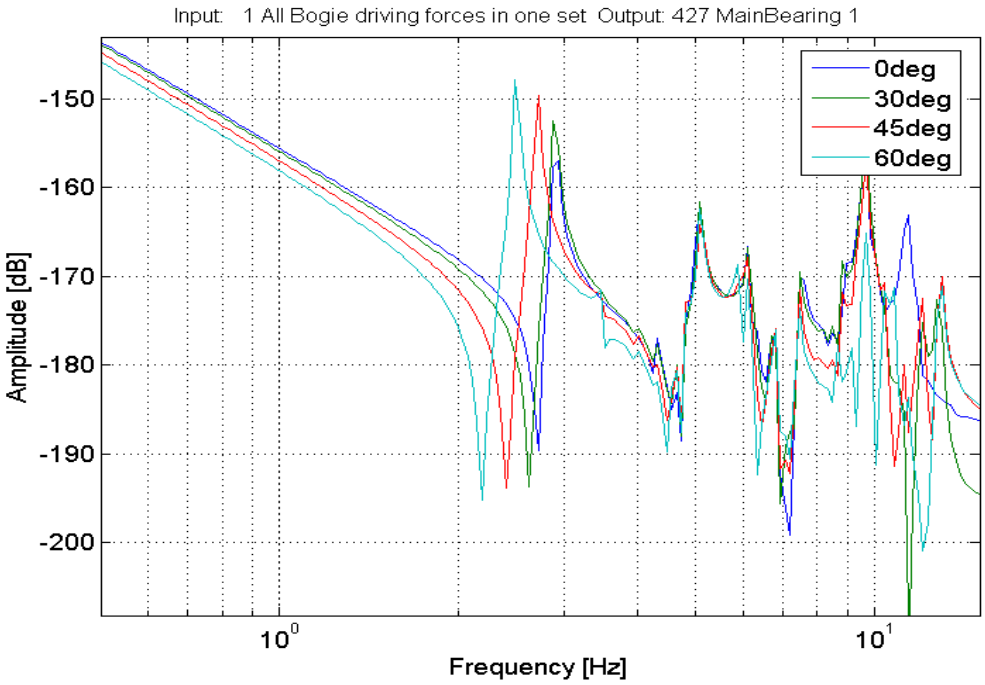

Figure 7-5 Frequency characteristics of altitude models for four different configurations

Based on finite element analyses, state-space models for different configurations have been created. These configurations can be divided in two groups for the control of the azimuth or the altitude axis. There are four altitude configurations corresponding to four different zenith distances: 0 deg (zenith), 30 deg, 45 deg and 60 deg, and two azimuth configurations corresponding to two zenith distances of 30 deg and 60 deg. To be able to use these models for the control design, the order of these models has been reduced. The models are available as continuous state-space objects in Matlab. For more details about configurations, corresponding models, and model reduction the reader is referred to RD527.

The frequency characteristics of the models (*G*) for four altitude configurations and two azimuth configurations are shown in Figure 7-5 and Figure 7-6, respectively.

Figure 7-5 shows that the natural frequencies of the first resonant mode of the altitude models decrease from the zenith to the 60-degree configuration with those of the zenith and the 30-deg configurations being very similar. Figure 7-6 shows that the dynamics of the azimuth models for the 30 degree and the 60 degree configurations are also nearly identical.

Robust controllers are now designed with the objective of tracking errors of less than 0.3 arcsec RMS, taking into account the system and disturbance models. The nominal models used for the design of the controllers for both axes are the reduced order models of the telescope at 30 degrees. Their robustness is verified for the other configurations. The details of the design procedure are given in RD17. The desired closed-loop bandwidths for the altitude and azimuth axes are chosen as 1.8 Hz and 0.6 Hz, respectively. The corresponding control sensitivity functions for both axes are shown in Figure 7-7 and Figure 7-8 respectively. The effect of the rejection of the effects of the wind load can be observed in Figure 7-9 which compares the PSDs of the open- loop responses with the PSDs of the closed-loop responses. The controller reduces the PSD errors significantly for frequencies up to 1Hz.

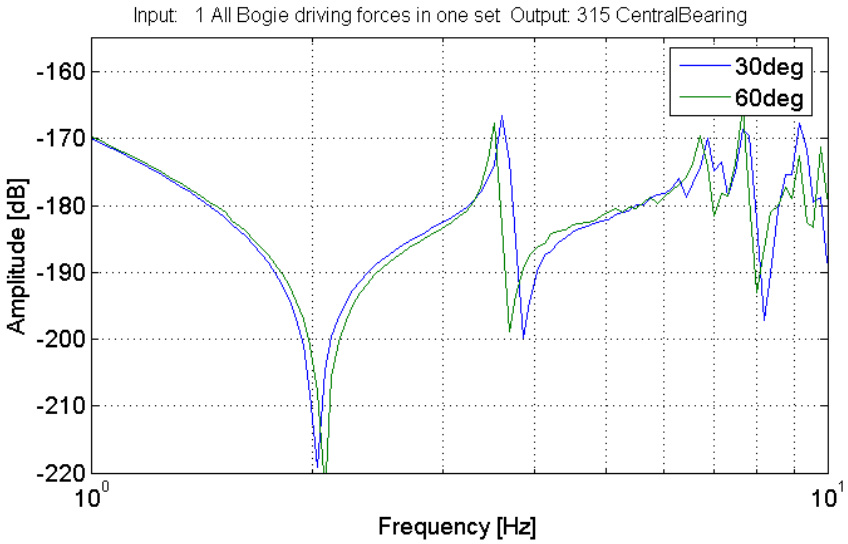

Figure 7-6 Frequency characteristics of azimuth models for two different configurations

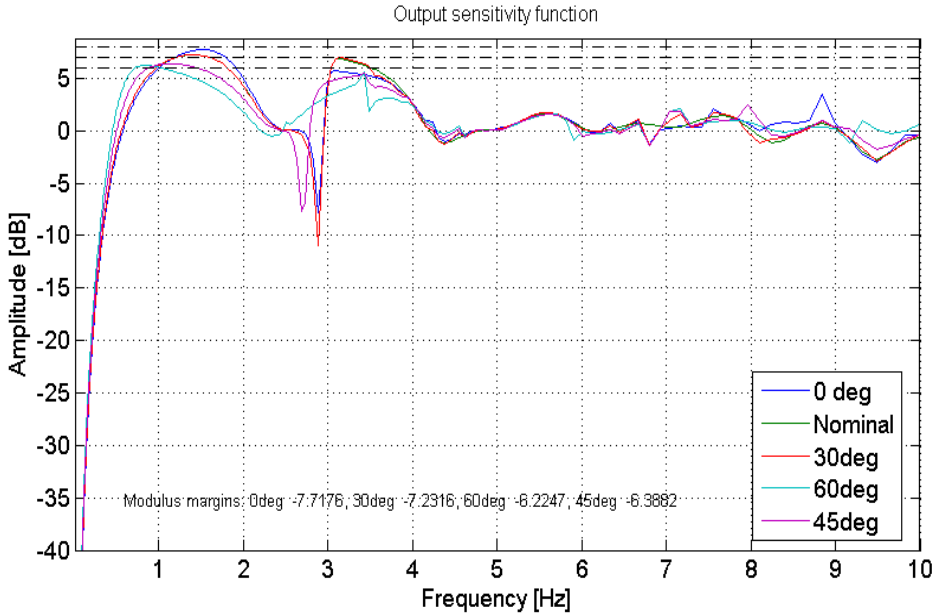

Figure 7-7 Output sensitivity function as a a measure of both the rejection of perturbation and the robustness for the altitude axis

A simulation has been done for the closed-loop system (both axes and different configurations) with a ramp reference signal having a slope of 0.5 arcsec/sec. The tracking error (main bearing of the altitude axis) for the 30-deg configuration is shown in Figure 7-10. The controller is tested for all available telescope configurations. The results are summarized in Table 7-1 and Table 7-2. They show that the requirement of a modulus margin of less than -8dB is always fulfilled with the chosen design.

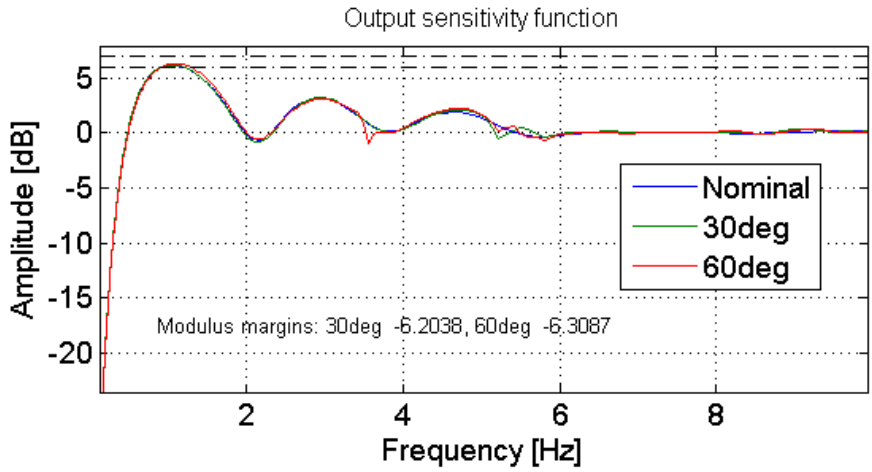

Figure 7-8 Output sensitivity function as a measure of both the rejection of perturbations and the robustness for the azimuth axis

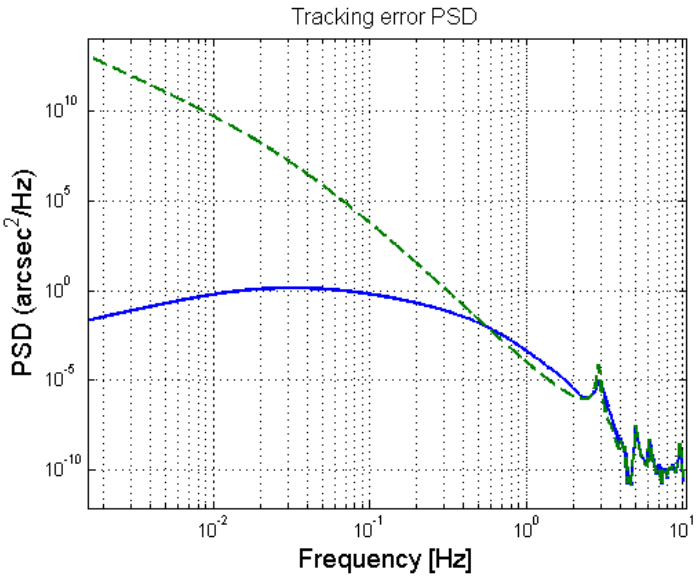

Figure 7-9 PSD of tracking error on the main bearing (altitude axis 30 deg) – open-loop (dashed), closed-loop (solid)

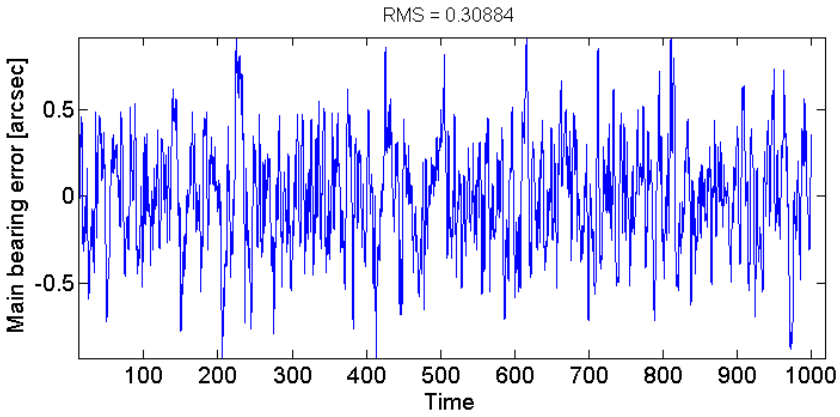

Figure 7-10 Main bearing (altitude axis) tracking error for 30 deg configuration

zenith distances	Modulus margin [dB]	Main Bearing RMS error [arcsec]
0 deg	-7.7	0.19
30 deg	-7.2	0.31
45 deg	-6.3	0.27
60 deg	-6.2	0.32

Table 7-1 Altitude axis: summary of the design results

zenith distances	Modulus margin [dB]	Central Bearing RMS error [arcsec]
30 deg	-6.2	0.044
60 deg	-6.3	0.036

Table 7-2 Azimuth axis: summary of the design results

7.2.2 Friction compensation

Friction drives, also called bogies, are used for the main axes of the telescope. The description of the friction drives and the bearing system is given in section 9.4.5.1.3. The azimuth axis will be equipped with about 250 units distributed on eight tracks and the altitude axis with about 150 units on two elevation cradles. They ensure a homogeneous load distribution on the structure. Each bogie consists of four spherical or cylindrical wheels which are independently driven by brushless ring torque motors. One of the main sources of tracking and positioning errors on the main axes of the telescope is the 'rolling' friction torque acting on the wheel/track interface of each bogie. Close to zero velocity the friction force is a nonlinear function of the velocity and the applied force (see Figure 7-11). In the control of systems with friction the undesirable effects are oscillatory motions around the desired reference trajectory due to stick-slip events. In recent years, extensive research on modelling, identification and compensation of friction have been done. For a comprehensive survey of the approaches and some promising results the reader is referred to [17].

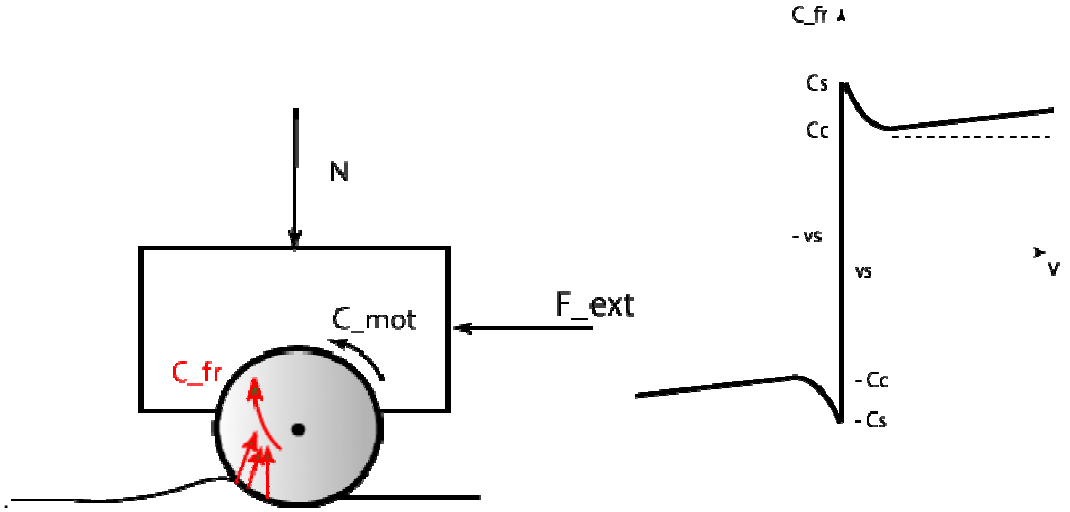

Figure 7-11 Left) bogie subjected to various forces-- Right) friction as a function of velocity

The effect of the non-linearity of the friction on the wheel/track interfaces of the bogies and the control strategies for the compensation of the friction have been studied in RD14, RD15, and RD18. Here, the approach and the main results are summarized.

- In order to distinguish the friction related effects from other oscillatory behaviours related to the telescope structure, first a dynamical model of a bogie was created with the telescope represented by an 'equivalent inertial mass'. Two different friction models, LuGre [19] and Karnopp [18], were used for the friction on the wheel/track interfaces. Both models capture the stick-slip effect. The LuGre model in addition captures the properties related to micro displacements of two surfaces in the pre-sliding regime. Stick-slip effects occur only if the telescope is moving at very low velocities. Figure 7-12 shows the stick-slip oscillation when the telescope is tracking in closed loop with a reference velocity of 0.1 arcsec/sec (main axes). For a higher reference velocity like 0.5 arcsec/sec the stick-slip effects disappear.

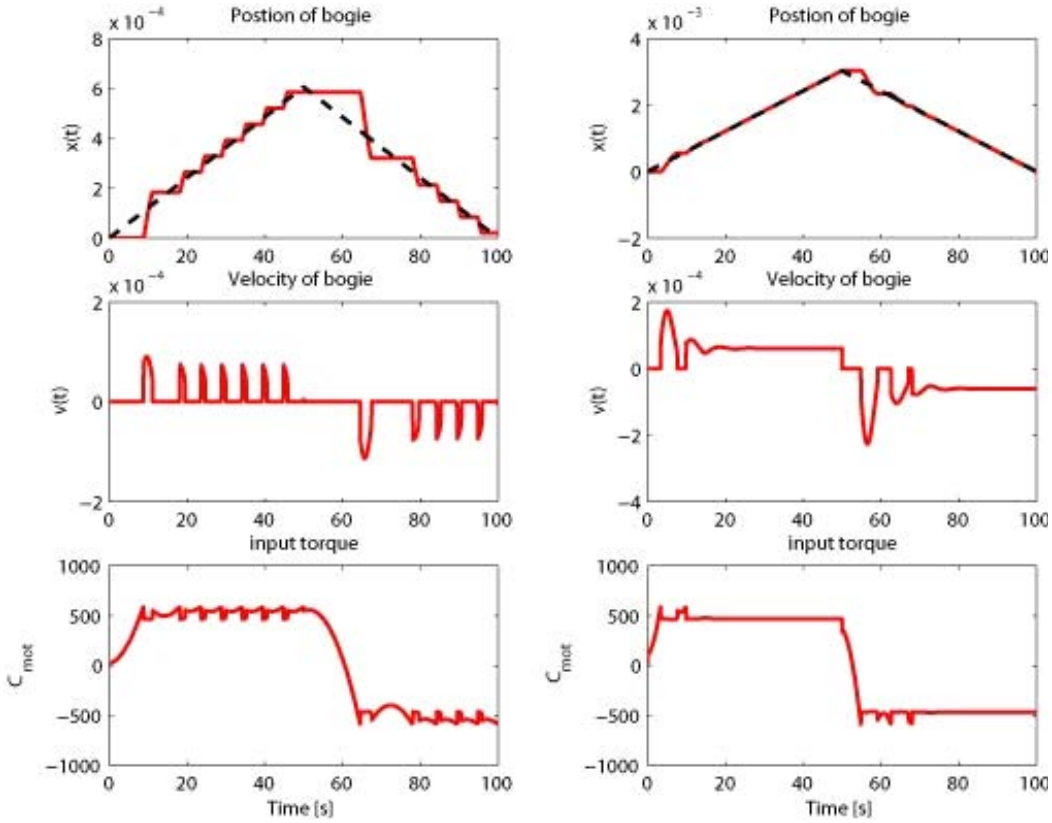

Figure 7-12. Tracking a ramp reference signal in closed-loop. Left: slope 0.1 arcsec/sec stick-slip motion. Right: slope 0.5 arcsec/sec; stick-slip disappears.

There are two main approaches for friction compensation:

- A non-model based approach using mainly stiff, i.e. high gains proportional and derivative terms in the feedback controller. The advantage is that the approach is robust since the feedback controller is used for the rejection of the perturbations. However, since only a limited closed-loop bandwidth for the control of the main axes of telescope is available, the use of high gain parameters in the controller is neither feasible nor advisable.
- A model based compensation method which consists of two steps, first an estimate of the friction, i.e. an identification of friction model parameters, and second, an application of a feed-forward control term based on the estimate of the friction in the first step to cancel the effect of the friction.

- A model-based friction compensation strategy is proposed for an interconnected system of bogies (see RD15). The block diagram of the control strategy is shown in Figure 7-13.

  Some of the bogies may be 'passive', i.e. they will not be equipped with motors. Since passive bogies do not have any control input the effect of friction on those bogies has to be compensated by the 'active' bogies by adapting the feed-forward compensation term. If the interconnections of the bogies are not perfectly rigid as it is in reality the nonlinear effects of the friction on the passive bogies cannot instantaneously be eliminated by a control action (see RD15) Therefore, oscillations can be introduced in the system due to a stick-slip motion on the passive bogies[60], as can be seen in Figure 7-14 showing the results of a closed-loop simulation of seven interconnected bogies where one is considered to be passive. This problem could be solved either by increasing the stiffness of connections, increasing the damping through a selection of appropriate lubricants for the wheel/track contact surface, or ultimately making all bogies in azimuth axis active. This issue will be

[60] Stick-slip with relative small amplitudes compared to the case friction is not compensated.

investigated in detail in the framework of the ELT Design Study: 'Characterization of Friction Drives and Bearings' (see RD514).

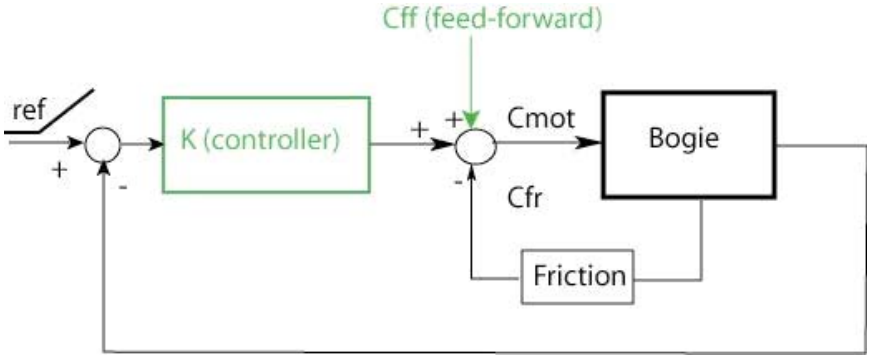

Figure 7-13 Block-diagram of bogie control system: feedback + feed-forward friction compensation strategy

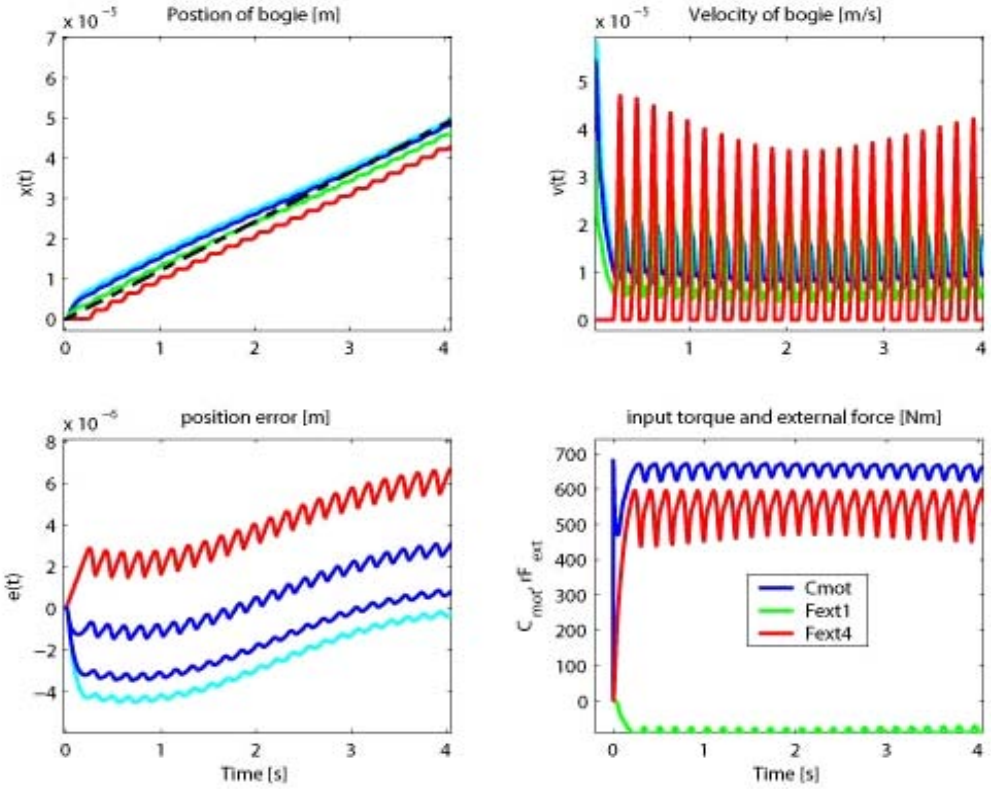

Figure 7-14 Closed loop simulation of seven bogies (with friction compensation), one bogie is passive which exhibits small stick-slip motion, oscillations are induced on other bogies.

- Since the compensation strategy relies on pre-defined friction models, the influence of variations of the model parameters has been investigated. Even if the two key parameters in the friction model are over- or underestimated by as much as 20% the effect of stick-slip events can still be compensated (see RD15). The guidelines for estimating the friction parameters are discussed in RD18.
- As stated earlier, in the initial approach the telescope has been modelled by a rigid body with an equivalent inertia. Such an assumption provided a good insight into the problem and gave some guidelines for the control strategy. To verify the efficiency of the approach a complete dynamical state-space model of the telescope has been generated by finite element (FE) analyses and a procedure applied to reduce the model. Bogies are

represented as pure force generators. The friction models, which include the non-linear effects, have been incorporated into the state-space models for the azimuth and altitude axes at bogie points (see RD16). Figure 7-15 shows the results of a simulation for the closed-loop response of the altitude axis in the absence and the presence of the feed-forward friction compensation. Note that here the feed-forward compensation is considered to be ideal, i.e. based on a perfect knowledge of the friction parameters. The effect of a mismatch of friction parameters is discussed in RD15.

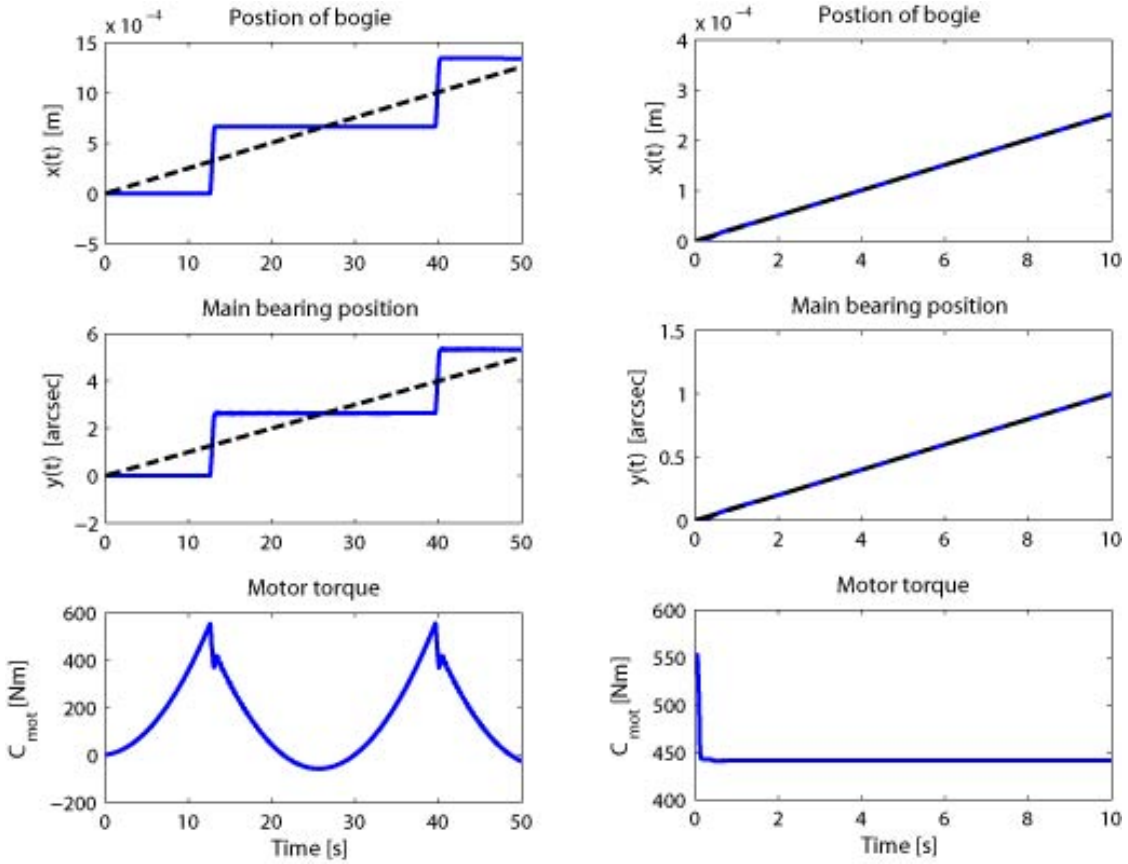

Figure 7-15 Closed-loop simulation of the altitude axis at 30 deg tracking a ramp reference signal with a slope of 0.1 arcsec/sec: left) no feed-forward friction compensation---right) with feed-forward friction compensation

- Finally, in the last stage the closed-loop behaviour of the system has been simulated in the presence of both wind load and friction perturbation. The overall control strategy is to read the main axis encoder position errors and apply the polynomial controller designed for the wind rejection. The controller generates the input torque to the system at each bogie point. The local feed-forward friction compensation is applied to each bogie (see RD17, RD16). Figure 7-16 shows the simulation results for the altitude axis in the 30-deg configuration tracking a ramp reference with a slope of 0.1 [arcsec/sec].

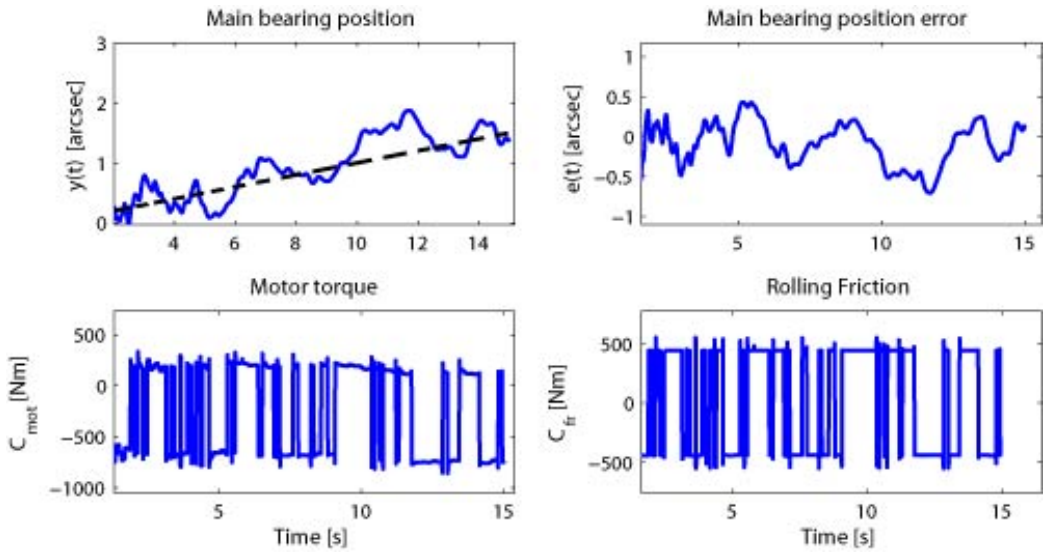

Figure 7-16 Closed-loop simulation of altitude, 30-deg configuration

7.2.3 Field stabilization

One of the main tasks of M6 is field stabilization, i.e. fast tip/tilt correction of residual tracking errors induced by wind buffetting on the structure. This would be achieved in two steps, with a coarse stage for large amplitudes and fine correction with the adaptive shell. In the following we show that a bandwidth of a few Hz for the coarse stage would be sufficient to reduce errors to within the expected range of the thin shell.

As shown in the previous section, the effect of the wind on the main axes can substantially be reduced by an appropriate control of the main axes. An efficient perturbation rejection on the main axes also reduces, due to the coupling of the main axes to the rest of the structure, the effect of wind on the whole structure including support structures of mirrors. However, the residuals are still too large for the correction capabilities of the adaptive thin shell of M6. To reduce the errors to values within the correction range of the thin shell, the bulk of the residual tip/tilt errors should first be corrected by the M6 tip/tilt control unit.

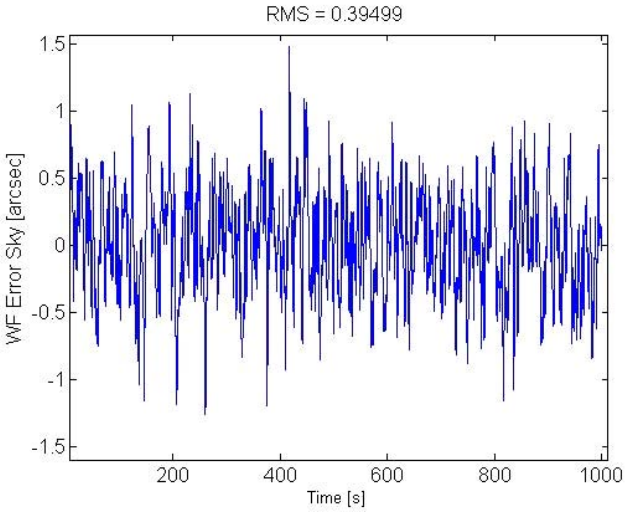

Figure 7-17 Wavefront error (tilt) on the sky- Altitude simulation: zenith configuration, main axis control with different wind loads applied to different levels

Apart from deformations of the individual optical elements, wavefront errors due to wind buffeting are produced by rigid-body movements, that is misalignments, of the optical elements.

To get an estimate of the amplitudes and frequencies of the misalignments of all mirrors in six degrees of freedom the closed-loop response of the complete OWL structure to a wind from the –y direction has been simulated. The effects of the obtained misalignments on the wavefront are computed with the optical sensitivity matrix of OWL (see RD2). Figure 7-17 and Figure 7-18 show the tilt components of the wavefront error in sky coordinates as time series and PSDs for the zenith configuration.

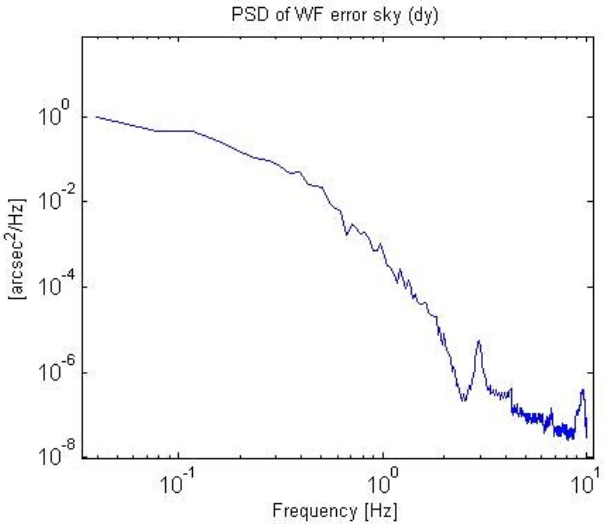

Figure 7-18 PSD of the wavefront error (tilt) on the sky

Field stabilization can be achieved by steering the M6 unit actively. The wavefront error has been calculated as a function of the control bandwidth[61]. The result is shown in Figure 7-19 and indicates that with an ideal control an accuracy of 0.01 arcsec can be achieved with a closed-loop bandwidth of about 1Hz (and prior to adaptive correction).

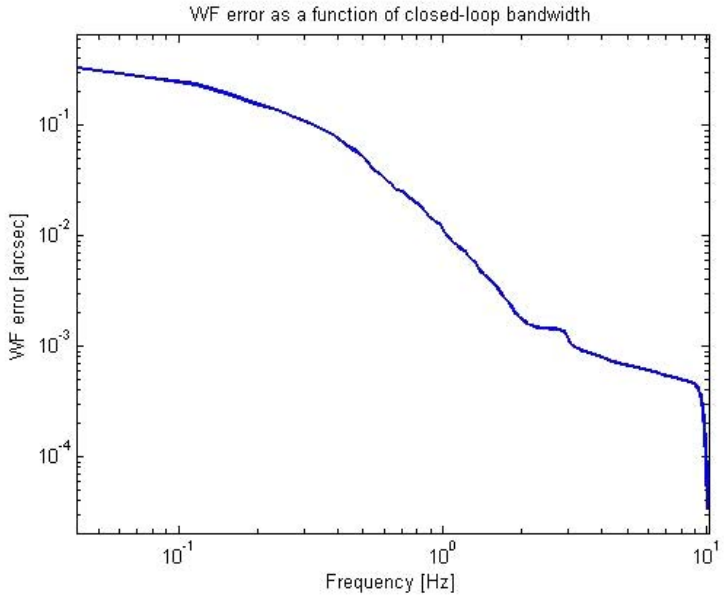

Figure 7-19 Wavefront error (tilt) after field stabilization correction as a function of the closed-loop bandwidth

[61] It is assumed that the closed-loop control rejects the perturbation 'perfectly' up to the closed-loop bandwidth and is not effective elsewhere. Although such perfect control action is not realistic, it gives a first estimate about the lower limit of the required closed-loop bandwidth.

A 2-degree-of-freedom model of M6 has been constructed. The dimensions of the M6 unit are given in Section 9.4.5.5. The mass of the mirror is estimated to be about 500 kg (Zerodur mirror), and the frequency of the first resonance modes for the tip and tilt motions are assumed to be 60 Hz. The ensueing wavefront error, that is the image tilt, can again be obtained with the help of the optical sensitivity matrix. The closed-loop control scheme is shown in Figure 7-20. The objective is to design a controller *K* which minimizes the residual wavefront error, seen as a perturbation in the control loop. *G_M6* represents the transfer function between torque generated by actuators and the tip and tilt motions of the M6 unit.

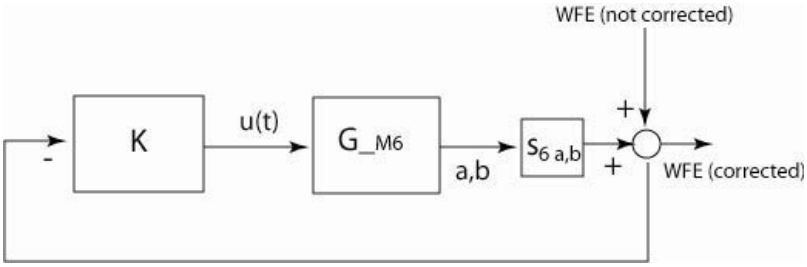

Figure 7-20 Block diagram of the closed-loop control of M6: field stabilization

The design of the controller K depends on the PSD of the uncorrected wavefront error and the dynamical model of the M6 unit. The bandwidth of the control system is provisionally defined as 2 Hz. Figure 7-22 shows the time series obtained in a simulation of the closed-loop response of the M6 unit. The closed-loop control of the tilt motion of M6 improves the performance to the an accuracy of approx. 0.01 arcsec RMS. Figure 7-21 compares the PSD of the tilt wavefront error before and after the field stabilization.

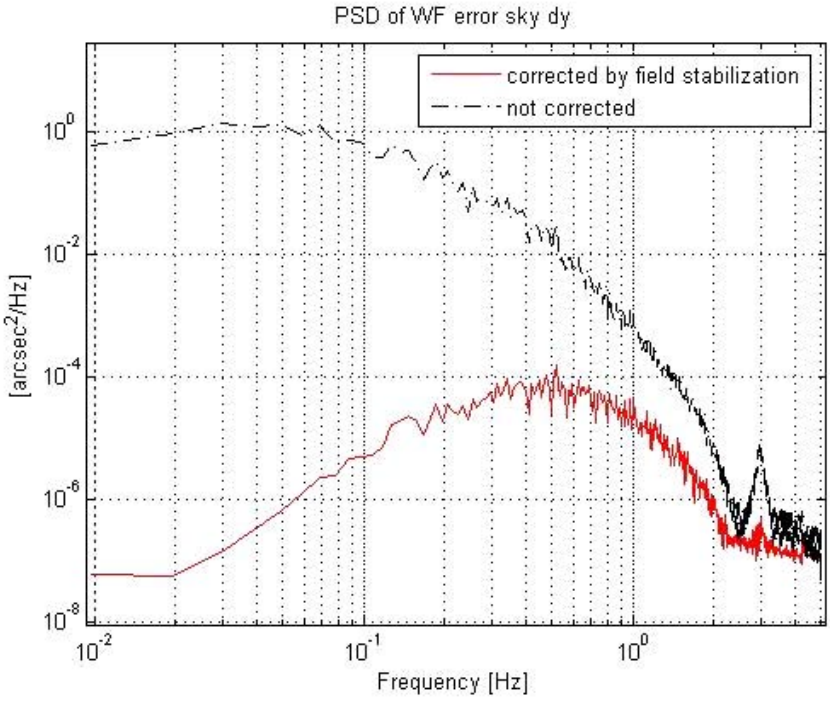

Figure 7-21 PSD of the corrected tilt wave front error on the sky

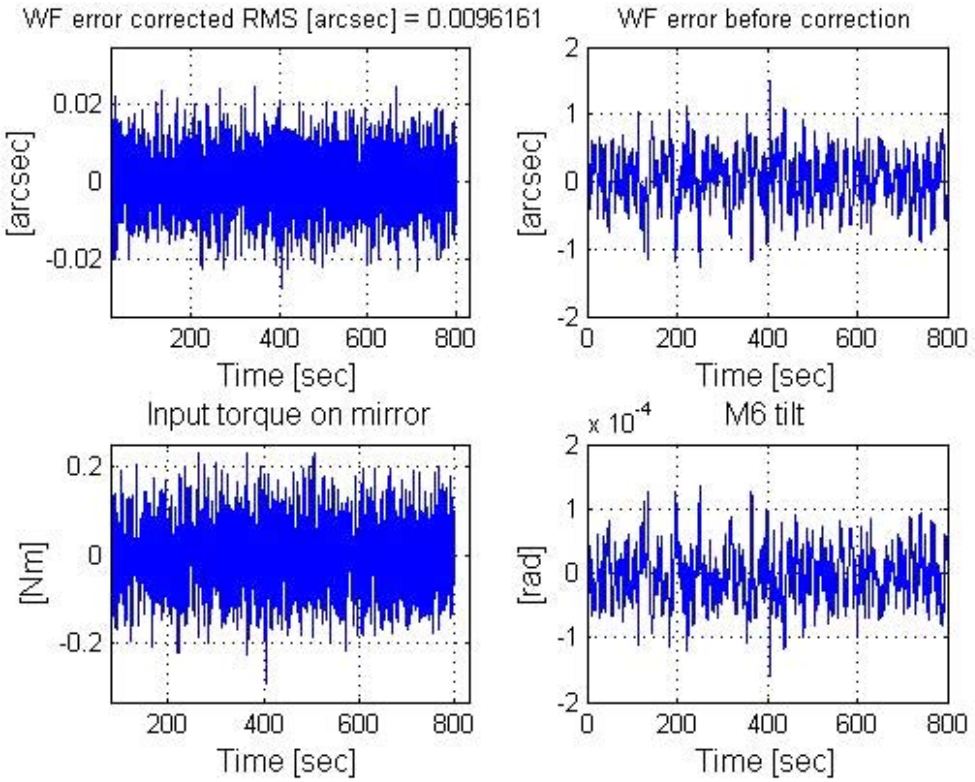

Figure 7-22 Simulation results: wavefront errors before and after correction, tilt motions of the M6 unit and the input torque applied to the unit.

The residual M6 tilt corresponds to actuator strokes of 0.25 mm. The reaction forces to the movements of the actuators could excite the support system of the M6 unit and the structure of the corrector. To avoid undesirable resonances, the M6 unit may be be isolated from the support system by a compensation mass moving in the direction opposite to the mirror as in the M2 unit of the VLT [28]. Currently the conceptual designs of the M6 unit, taking into account the issue of resonances, are going on under ESO contracts.One possible solution for reducing the required stroke on the actuators is to offload the correction in the very low frequency range to the main axes or eventually to M2. Figure 7-19 shows that the wavefront error can be reduced by a factor of three, if tilt corrections are done by the M2 unit at frequencies up to 0.2 Hz. As a consequence, the stroke needed for corrections with M6 would be reduced. As M2 is segmented, the feasibility of such an overall tip/tilt motion of M2 will be addressed and studied in Phase B.

7.3 Pre-alignment

In a perfectly aligned telescope the optical axes of all mirrors are congruent with the mechanical axis of the adapter. Initially, at the end of the installation, the mirrors will be misaligned with respect to the axis of the adapter, the flexible meniscus mirrors will be deformed, and the segments of the segmented mirrors will be misaligned in piston as well as in tip and tilt. At this stage automatic means used by the active optics for the correction of the errors may fail because the errors may exceed the limits the optical analysis methods can cope with. The following pre-alignment procedure will reduce the wavefront errors to levels acceptable for the active optics system.

1. The segmented mirrors can be coarsely aligned with the help of the edge sensors. These must be glued to the rims of the mirrors with an accuracy of approximately 200 micrometers with respect to the front surface of the segment. By moving individual segments and detecting when adjacent sensors go out of range, the differential displacements between the mirrors at the locations of each pair of sensors can be measured. From the data of all pairs of sensors the optimum movements of all segments, which minimize the rms of the differential displacements, can be calculated and applied. At the end of this procedure the rms of the errors due to segment misalignments, excluding the effects of the undetectable segment defocus mode, should be of the order of a few hundred micrometers.
2. With the help of a spherometer, positioned at the corners of the newly installed segments, the piston errors can be reduced to a few nanometers. The correction of the defocus mode will be left to the stage of the automatic corrections.
3. All other mirrors could be aligned with respect to its neighbours starting from M6 based on the input from the fibre extensiometer. This requires an installation of fibre links between specified locations on all pairs of successive mirrors.

Finally, a second round of aligning the segments in tip and tilt in the segmented mirror could be done on-sky by stacking the images from the individual segments. Because of the small ratio of the size of the subapertures corresponding to the segments on M1 to the overall size of M1 such a stacking will also correct the comparatively low spatial order effects of any misalignments of the mirrors or of any elastic deformations of the meniscus mirrors on the wavefront. This is of course only true for the field position of the wavefront sensor unit used for stacking the images. The image quality should, for this field position, only be limited by the wavefront errors of individual segments, by the accuracy of the stacking itself, and by piston phasing errors of the segmented mirrors. However, at other field positions, additional wavefront errors due to still existing mirror misalignments and elastic deformations still exist.

At the end of the pre-alignment, we expect residual errors to be within the following range:

- Misalignments of the mirrors as rigid bodies:
  - Positions of M1 and M2: approximately 1 mm
  - Positions of M3, M4, M5 and M6: approximately 0.5 mm
  - Tilts of M1 and M2: approximately 2-3 arcseconds
  - Tilts of M3, M4, M5 and M6: approximately 1 arcsecond
- Deformations of the meniscus mirrors:
  - M3 and M4: approximately 30 micrometer wavefront r.m.s.
  - M5 passive: at most 2 to 3 micrometer wavefront r.m.s.
  - M6 and the adaptive M5: depends on the design, but is assumed to be small if the positions on the front surfaces of the adaptive mirrors are measured against a reference surface.
- M1 defocus mode : no empirical data available.

From this point on the remaining errors can be deduced from simultaneous measurements with wavefront sensors distributed over the field and be corrected by rigid-body realignments of the mirrors, corrections of the shapes of the meniscus mirrors, and alignments of the individual segments within the segmented mirrors.

7.4 Active optics

7.4.1 Introduction

The purpose of the active optics system is the correction of all types of wavefront aberrations introduced by comparatively slow misalignments and surface deformations of the optical elements in the telescope at low temporal frequencies. The expected focal surface in the adapter is the reference surface, where all measurements of the errors which are introduced by the misalignments and the deformations are made. From these measurements one has to identify the sources of the wavefront aberrations. This is not straightforward since the wavefront errors generated by different mirrors may completely or at least to a large extent compensate each other in the focal surface. The error sources can in some cases only be distinguished from each other by analysing comparatively small field dependent effects. On the whole, the problem is quite complex with two segmented and four flexible mirrors, even if a few of them generate only a restricted set of wavefront errors.

A very formal way of solving this problem would be to write down a vector of all significant error sources and another vector of a sufficient number of possible aberrations at various locations in the field. Assuming that a linear description is sufficient, the connection between the two vectors is established by a so-called influence or sensitivity matrix. A singular value decomposition of this matrix would show which set of well distinguishable measurements would be generated by which set of well distinguishable error sources. The corresponding eigenvalues would show the significance of each pair of measurements and sources. Such an approach would also show groups of sources which could be well separated from each other. In addition those error sources can be found whose effects are effectively indistinguishable in the focal surface. Because of the large number of segments and mirrors this procedure leads to a very large matrix which may be difficult to invert. In addition, it may not give much insight into the effects of the various error sources. Therefore, the following procedure splits the correction into three steps, described in the three following sections: the alignment of the segmented mirrors, the correction of surface deformations of the individual mirrors, and the alignment of the mirrors regarded as rigid bodies.

7.4.2 Alignment of the segments in M1 and M2

Since only a small number of segments will be added to M1 and M2 at a time one can assume that most of the segments of these mirrors are already well aligned. The alignment of the segments, especially the newly installed ones, will be done with the following procedure at the beginning of the night.

1. Based on measurements with one of the Shack-Hartmann sensors all segments can be aligned in tip and tilt. With sufficiently bright guide stars the wavefront errors will be of the order of at most a few nanometers over each subaperture corresponding to one segment. Because of the large number of segments, especially in the primary mirror, the slopes of the smooth low-order aberrations in the wavefront, generated by misalignments or deformations of the other mirrors, are effectively constant over the small subapertures corresponding to individual segments. These slope errors can therefore to a large extent be corrected by appropriate tilts of the segments. For a given low-order aberration the residual aberrations over a given segment subaperture are well defined. This effect is referred to as scalloping. Under the assumption that the deformations of the individual segments are small the slopes of the wavefront are well corrected, at least for the field position of the Shack-Hartmann sensor. The residual major wavefront error is then generated by piston steps at the interfaces of adjacent segments.
2. The piston steps at the interfaces of adjacent segments are measured by optical sensors using multiple wavelengths techniques. The goal of this correction is to reduce the piston steps to less than 100 nm and therefore to avoid the 2π ambiguity in subsequent narrow-band measurements.

3. Narrow-band measurements with bright stars, which can reach accuracies of a few nanometers for the estimate of the piston steps, will be used to align the segmented mirrors. At this point there are two possible ways of proceeding with the alignment.

   - Correction of piston errors only.

     The basis for such a correction will be the average of the piston error along each intersegment edge. The segmented mirrors would then be well aligned in piston, but not in tip and tilt, since the individual segments are still compensating the slope errors introduced by the other mirrors. These low spatial frequency wavefront errors have to be corrected at a later stage by measuring scalloping effects or field aberrations. Because of the propagation of the noise σ_n in the measurements of the piston steps the rms σ_1 of the wavefront error introduced by this correction will be $\sigma_1 \approx 0.5\sigma_n$ [37], [38]. With σ_n expected to be of the order of a few nanometers, the wavefront error due to segment piston errors will therefore be negligible.

   - Correction of piston, tip and tilt errors.

     The basis for such a correction will be two measurements of piston steps along each intersegment edge, giving both the relative average piston error and the relative tilts at the edges of adjacent segments. After this correction the segmented mirrors will be aligned in piston, tip and tilt, but the effects of the slope errors generated by the other mirrors and the rigid-body misalignments would reappear in the final wavefront. To prevent this, the differences in the wavefront slopes before and after the alignment of the segments in the segmented mirrors have to be offloaded to the other mirrors as changes in rigid-body alignments or changes of the shapes of M3 and M4. If the optical sensor is not capable of detecting relative tilts perpendicular to the edge, but only relative piston displacements, an appreciable amount of the segmented mirror defocus mode may exist. Because of the propagation of the noise σ_n in the measurements of the piston steps the rms σ_2 of the wavefront error introduced by this correction will, excluding the error due to the defocus mode, be approximately $\sigma_2 \approx 15\sigma_n$ [37], [38].

     The readings of the edge sensors, which in the current design are also not capable of detecting the defocus mode, will be stored as reference values for the continuous closed-loop alignment corrections of the segmented mirrors via the edge sensors.

The second option of the ones described above will be the baseline.

4. The correction of the M1 and M2 defocus modes can be left either to the stage where all the mirror deformations will be corrected or it can be done by measuring so-called scalloping effects, as described below. The M1 and M2 defocus modes with constant slopes over individual segments has already largely been compensated during step 1 of this procedure by a smooth defocus aberration generated by the changes of the shape of the monolithic mirrors M3 and M4 or by axial deplacements of mirrors. The residual aberration is a defocus aberration that is identical on all the individual segments. A Shack-Hartmann sensor with 19 lenslets in each subaperture corresponding to one segment can measure this differential defocus, and therefore the coefficient of the M1 and M2 defocus modes. Because of the large number of photons available with long integration times of the order of 100 seconds even the differential defocus on a single segment can be measured with an accuracy of a few nanometers. Owing to the large number of segments the error in the overall differential defocus will then be negligible. After the correction of the defocus modes the segments of the primary and secondary mirror will be aligned.

7.4.3 Correction of mirror deformations

Deviations of the shapes of the large meniscus mirrors M3 and M4 from their ideal shapes can be due to optical manufacturing and to incorrect support forces. From the experience with the VLT the initial wavefront aberrations of M3 are expected to be of the order of 20 μm rms for 3rd order astigmatism and 3 μm rms for trefoil. For M5 the corresponding figures are expected to be

of the order of 3 μm and 0.5 μm. Because of the elastic properties of the meniscus mirrors the deformations in the form of elastic modes decrease rapidly with the order of the modes. The highest modes which are, for large changes of the telescope altitude angle, appreciably affected by the support forces with systematic variations of their coefficients of the order of 20 nm are modes like the lowest mode of rotational symmetry six and the third mode of symmetry zero. The lowest 30 elastic modes are therefore sufficient for the description of the errors in the mirror shapes of M3 and M4.

As in the VLT, a sampling of the wavefront with 20 by 20 subapertures over the pupl is sufficient for an accurate estimate of the coefficients of all these modes. The size of the subapertures on M1 is then approximately 5 meters by 5 meters. In the VLT stars of magnitude 13 deliver, with integration times of 30 seconds, a sufficient number of photons to reduce the errors on the coefficients of the wavefront aberrations due to photon noise to less than the errors introduced by the atmosphere [41]. Since the area of a subaperture in OWL is approximately 100 times larger than the area of a corresponding subaperture in the VLT one can either choose shorter integration times of the order of one second or use fainter stars. In principle, this would offer the possibility to apply closed-loop corrections of mirror deformations and alignments at frequencies up to approximately 1 Hz. However, for such short integration times, the effects of the atmosphere, in particular the effects of the limited size of the isoplanatic angles have to be investigated.

The major problem in a telescope with several deformable mirros is to distinguish in the final wavefront the contributions generated by the individual mirrors, since errors introduced by one mirror can be compensated by errors introduced by other mirrors. The wavefront analysers cannot distinguish between aberrations generated by the deformations of mirrors which are conjugated to each other. Therefore, the effects of the deformations of M1, M4 and M6 are indistinguishable. Also M2 falls into this group since it is sufficiently close to the pupil. However, if the mirrors are not conjugated to each other, such compensations are in general only effective for one field angle, leaving additional wavefront aberrations at other field angles. If the deformations are expressed in terms of Zernike polynomials, these field aberrations can be calculated analytically if the center and the radius of the imprints of the beam on the mirror are known for arbitrary field positions [39] [41].

This is shown in Figure 7-23. The footprints of the beam on M3 are different for different field angles. The Shack-Hartmann sensors therefore sample different areas of M3.

Therefore, in principle, one should be able to distinguish between the aberrations generated by M3, M4 and the group M1, M2, M4 and M6.

The measurement of the aberrations over subapertures of the mirrors is similar to the measurement of aberrations introduced by layers in the atmosphere conjugated to these subapertures. Techniques developed for adaptive optics can therefore be applied to the active optics wavefront sensing [42], [43]. First tests in this direction have shown promising results.

The dependence of these additional aberrations on the field position is different from the field dependence of the additional field aberrations generated by rigid body misalignments. They can therefore be distinguished from each other if a sufficient number of sensors is available in the field.

In OWL the ratios of the shifts of the centers of the beam to the radii of M3 and M5 for a field radius of 1 arcminute are approximately 0.01 for M3 and 0.04 for M5.

The field aberration generated by 3rd order astigmatism is only a special type of distortion. For a field angle of 5 arcminutes a deformation of 20 μm on M3 is equivalent to an apparent shift of the sky position of 0.01 arcseconds. The deformations of the different mirrors in form of 3rd order astigmatism can therefore effectively not be distinguished from each other by measurements in the focal surface.

A deformation in form of trefoil generates 3rd order astigmatism with a linear radial dependence and a more complicated angular dependence. For 3 μm of trefoil on M3 the modulus of the additional 3rd order astigmatism is approximately 150 nm at the edge of the field and therefore detectable. However, within the inner field with a radius of 1 arcminute the modulus is only of the order of 30 nm.

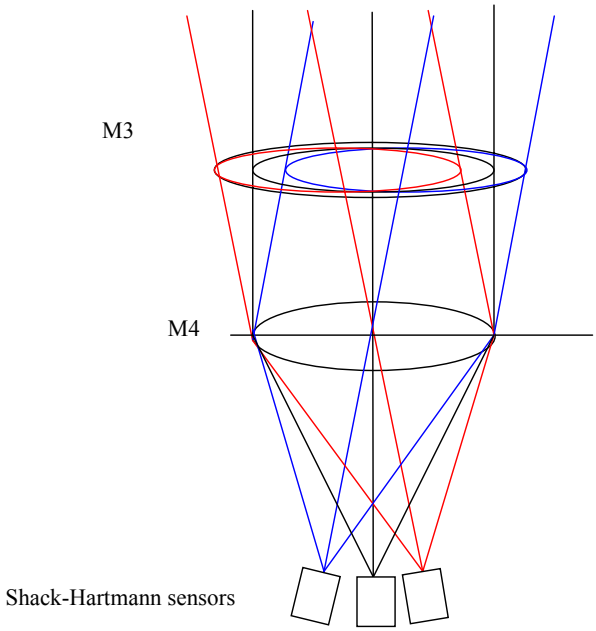

Figure 7-23. Field of View of the Shack-Hartmann sensors on M3 and M4.

The effects of deformations in form of higher order modes is even smaller and it may therefore be sufficient to distinguish only the trefoil deformations coming from M3, M5 and from the group M1, M2, M4 and M6. However, it is no problem to extend this type of analysis to a larger set of modes [40]. Since the radial field dependencies of the aberrations generated by higher modes may not be linear, wavefront sensors are required at at least three different moduli of the field angles. With a total of six sensors at at least three different orientations of the field angles a sufficiently large number of field aberrations can be measured. This has been confirmed by simulations in [40].

7.4.4 Correction of the rigid-body alignment of the mirrors

In general, rigid-body misalignments of the individual mirrors in five degrees of freedom will generate aberrations in addition to the nominal aberration of the centered optical system. These additional aberrations are characterized by their field dependencies. Lateral displacements of the flat mirrors M2 and M6 do not generate aberrations. In total, there are 26 degrees of freedom for the generation of wavefront aberrations with rigid-body movements of the individual mirrors. The number of wavefront sensors required to measure the 26 unknown parameters can be estimated as follows.

1. The expansion of the Hamilton characteristic function up to fifth order contains 26 types of aberrations, where the non-rotationally symmetric aberrations like third order astigmatism with a quadratic field dependence have been counted twice. This set contains 15 different Zernike polynomials. The larger number of terms in the expansion means that the same Zernike polynomial can occur with different field dependencies.
2. Field distortions and field curvatures may be difficult to measure due to a limited accuracy of the positioning of the guide probes. If one neglects these types of aberrations the number of terms in the Hamilton characteristic function is reduced to 18 and the number of Zernike polynomials to 13. The maximum field order in the expansion terms is quadratic.
3. At a given field location only the coefficients of the Zernike polynomials can be measured. To obtain the full information one has to measure also the field dependence of these coefficients. This requires, for a quadratic field dependence, at least three sensors at different radial field positions. For the non-rotationally symmetric coefficients one also needs to know their orientation which requires at least three sensors in azimuth direction.

Therefore, six sensors, all measuring the coefficients of 13 Zernike polynomials, should be sufficient to determine the 18 unknown parameters.

Simulations for a three-mirror telescope are presented in [39]. Six wavefront sensors measuring a total of 78 coefficients will also be sufficient to include the estimate of shape deformations discussed in the previous section.

An additional complication is that field-independent aberrations generated by alignment errors can be corrected by deformations of the pupil mirrors M4 and M6. If this was the case these aberrations would reappear after a correction of the alignment and the corresponding surface deformations of M4 and M6 would have to be removed.

Ideally, all alignment corrections would avoid changes of the pointing of the telescope. For the powered mirrors only rotations around their centers of curvature would then be permitted restricting the correction capabilities. However, such a restriction would only be required if the pointing model was made without the active optics system in operation. Therefore, a final pointing model has to be done for all sky positions with a fully aligned telescope under the control of active optics.

7.4.5 Relationship between various types of aberrations

Three different types of wavefront aberrations due to telescope errors will be present in OWL.

- Pure optical aberrations, which are described by Zernike polynomials. These aberrations are predominantly generated by rigid-body misalignments of the mirrors.
- Elastic deformations of monolithic mirrors which are described by the elastic modes of the monolithic mirrors.
- Modes introduced by the propagation of errors in the measurements of piston steps at intersegment boundaries. In the low order limit these modes can be described by Bessel functions [38].

The active optics system has to take the conversions between these mathematical descriptions into account, for example, when sets of coefficients of field aberrations determined by the optical design and described by Zernike polynomials, have to be subtracted from related sets of coefficients of elastic modes measured at the field positions of the wavefront sensors.

7.4.6 Operation with adaptive optics

Whenever the adaptive optics corrections are applied by M5 or M6, most of the slowly varying errors introduced by the telescope optics will first be corrected by the adaptive optics system. After a while, because of the accumulation of the often large lowest order aberrations, the actuators of M6 will run out of their correction range. M5 and M6 will then have to download some of their corrections of the wavefront errors due to the telescope optics to the other mirrors controlled by the active optics system.

These adaptive optics corrections by M5 and M6 provide, however, only a partial correction of the wavefront errors introduced by the telescope. M6 and M5 will only correct aberrations which are conjugated to the ground layer, which is close to the pupil, and to a layer at approximately 10 km, which is conjugated to M5. Aberrations generated by surface deformations of M3, which is neither conjugated to M5 nor to M6, or by rigid-body misalignments can only partially be corrected by M5 and M6 for arbitrary field positions..

The active optics wavefront sensors could then still measure these accumulating field aberrations. Even between downloads from the adaptive optics system the active optics system could then correct alignment and shape errors of individual mirrors based on the information about the aberrations at several field positions. Upon a download from the adaptive optics system, the active optics system would then only redistribute those aberrations that could not be attributed to a specific mirror, to one or more mirrors depending on the available ranges and range margins of those mirrors.

7.5 Phasing

7.5.1 Phasing strategy

One of the specific tasks associated with segmented telescopes is *phasing*, requiring an active control of the position of each individual segment in three degrees of freedom: translation along the optical axis (piston) and rotation about two axes perpendicular to the optical axis (tip-tilt). Three hardware systems are required for the *active segment control*: *capacitive or inductive edge sensors* which provide real time information about the relative segment displacements, *segment actuators* which compensate for these displacements, and a *phasing camera*. The inner loop with the edge sensors and the actuators is a fast correction for the segment displacements with a bandwidth of approximately 10 Hz, running continuously during the operation of the telescope. The phasing camera traces the slow changes in the wave front shape, providing the new reference values for the edge sensors.

The calibration of the edge sensors is performed once at the beginning of the night. An alternative concept would be to operate the phasing camera also during the operation of the telescope with a frequency of approximately 0.03 Hz and then recalibrate the edges sensors with the measurement of the phasing camera. This option is valid provided that a sufficiently bright reference star for the phasing camera can be found in the field of view.

The unphased telescope would have the resolution of the aperture of one segment and will deliver images full of speckles. To decrease the speckle effects to a level which would not exceed the residual errors after adaptive optics corrections, the remaining tolerable wavefront error, due to the misalignment of the segment, has to be less than 30 nm RMS. The importance of the phasing of segment mirrors in a telescope has been demonstrated in several papers [83], [84], [85].

The analysis in this section is restricted to the correction of the piston, tip and tilt errors of the segments. During the operation of the telescope the phasing corrections are based on signals from edge sensors at intersegment borders. An optical phasing procedure that is done at the beginning of the night with bright stars will supply the reference values for the edge sensors.

Two of the OWL mirrors will be segmented. Section 7.5.4.6.4 presents a technique to disentangle the segmentation errors of M1 and M2.

7.5.2 Blind phasing

Blind phasing is meant for segment alignment without on-sky metrology. Normally, blind phasing would be performed only during integration of the system, prior to first light, or during daytime re-integration of segments after off-line maintenance.

The concept is still very notional. Segments would be re-integrated into the aperture by means of a movable handling tool located inside one of the mirror covers (see also 13.2.1.4). Once the load transfer from the tool to the segment support is completed and interfaces are locked, the handling tool, fitted with position sensors, would be used as a spherometer. Adjacent segments, already in place and phased to the accuracy of the position sensors, would serve as calibrating gauge for the spherometer.

Spherometry measurements are made by optical manufacturers to sub-micron accuracy. The accuracy requirement for OWL handling tool-spherometer will eventually have to be in line with the capture range of on-sky phasing calibrations, which is expected to be at least a few microns (multiple wavelength). Should a higher accuracy be required, the contact measurements could be replaced by interferometric ones, using a dual wave interferometer (same principle as for APE internal metrology, see appendix A-1.2).

7.5.3 Position sensors

In existing segmented mirror telescopes the edge sensors use capacitance measurements. This is a proven technology which reaches accuracies of the order of a few nanometers RMS. However, capacitance measurements are sensitive to environmental conditions as for example high relative humidity. A different technology, which can reach the same accuracies, but is less sensitive to environmental factors, is based on inductance measurements.

The flat electrodes used for the capacitance sensors are replaced by a set of coils. Edge sensors using this technology will be developed within the ELT study in the FP6 programme (see appendix A-1.2 belowA-1.2. The most important specifications are a noise of less than 0.2 nm RMS / sqrt(Hz) within the frequency bandpass from1 Hz to 100 Hz and of less than 5 nm RMS / sqrt(Hz) within the frequency bandpass from 6e-6 Hz to 1 Hz, a measuring range of +/- 5 mm, and an absolute accuracy of 0.1% of the measuring range.

7.5.4 On-sky calibrations

7.5.4.1 Optical Phasing

This section presents various techniques which have been developed and proposed for the optical phasing of the segments, and also results of simulations and laboratory tests if available. One of the techniques for optical phasing is analysed in more detail.

Without optical phasing the misalignments of the segments can be of the order of several micrometers (see also 7.5.2), which is a problem for the narrow-band phasing sensors suffering from a 2π ambiguity. This can be solved with multi-wavelength techniques.

Three new phasing camera concepts are currently studied: the curvature sensor, the pyramid sensor, and the spatial phase filtering sensor. The basic principle for all three techniques is a modification of the wave front reflected by the mirror surface in such a way that the amplitude of the detected wave conveys the information about the phase discontinuities or the derivatives of the wavefront. This amplitude coding is achieved by a defocusing of the beam in the curvature sensor, by a spatial filtering in the image plane in the pyramid, and spatial phase filtering in the last sensor.

7.5.4.2 On-sky phasing techniques - overview

Different concept of phasing camera have been developed worldwide, some of them are based on wavefront sensors used in adaptive optics. All phasing cameras presented below have the capability to measure piston and tip-tilt misalignments. A brief description of these sensors is given together with some results of simulations and laboratory tests. Most of these sensors will be compared with each other within the APE project which is part of the FP6 program.

7.5.4.2.1 Modified Shack-Hartmann technique

This application of the Shack-Hartmann technique has first been proposed first by Chanan [86] and been used for the phasing of the segments in the Keck telescopes. Lenslets or optical devices with a similar functionality focus the light from circular subapertures centered on points on the interface between two neighbouring segments as shown in Figure 7-24 on the left hand side. A slightly modified version could be used for OWL, where the two circular lenslets on each edge are replaced by one cylindrical lenslet covering the full length of one edge, as shown in Figure 7-24 on the right hand side. The information about the phase steps is primarily obtained from changes in the diffraction pattern, as shown in Figure 7-25 for monochromatic light and no disturbance by the atmosphere.. The PSF has one maximum when the two segments are phased and two decentered peaks when for a piston of λ/2.

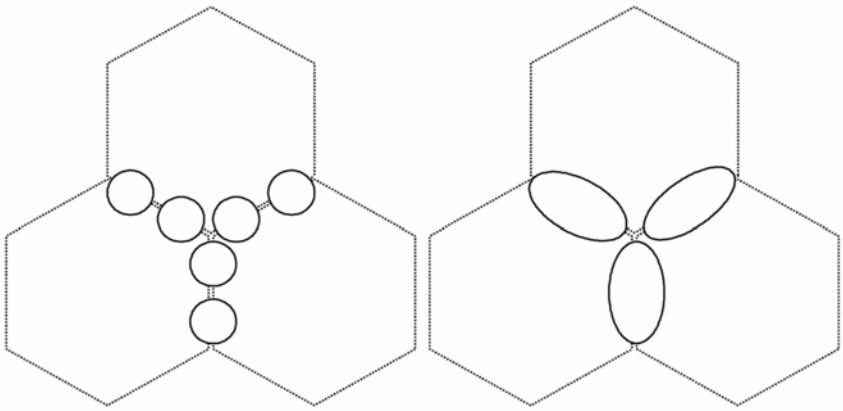

Figure 7-24. Two types of lenslet and their projection onto the edge of the segments

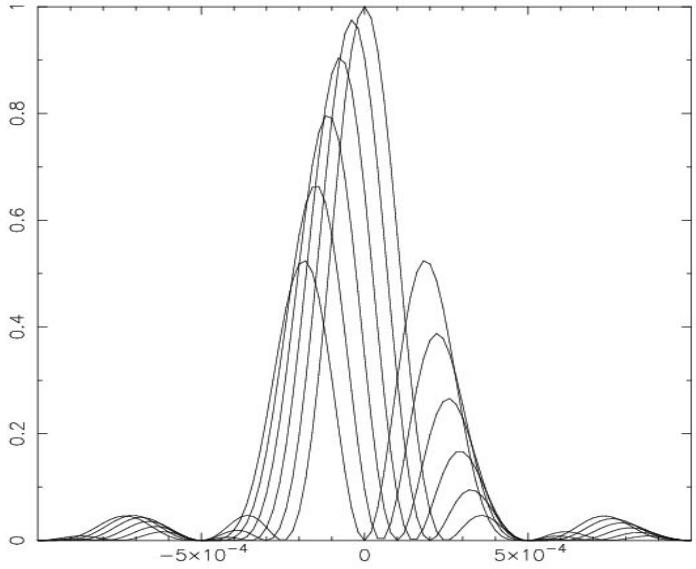

Figure 7-25. Shape of the PSF for piston steps ranging from 0 to λ/2.

7.5.4.2.2 Modified Mach-Zehnder technique

The concept of the Modified Mach Zehnder, shown in Figure 7-26, has been developed at the Laboratoire d'Astrophysique de Marseille (LAM) [87][88].

The general principle of this modified Mach-Zehnder interferometer is to introduce a spatial filter at an intermediate focus in one of the two arms and to use the light from that arm as a reference. After recombining the light of the two arms the signal is concentrated near the borders between the segments with an amplitude which depends on the piston step, the phase difference between the two arms and atmospheric disturbances as shown in Figure 7-27.

The difficulty with this sensor is to set and maintain a specified optical path difference between the two arms, and to align the two arms to avoid shearing effects and defocussing. K. Dohlen from LAM has proposed a concept, called phase filtering technique, which avoids such alignment problems.

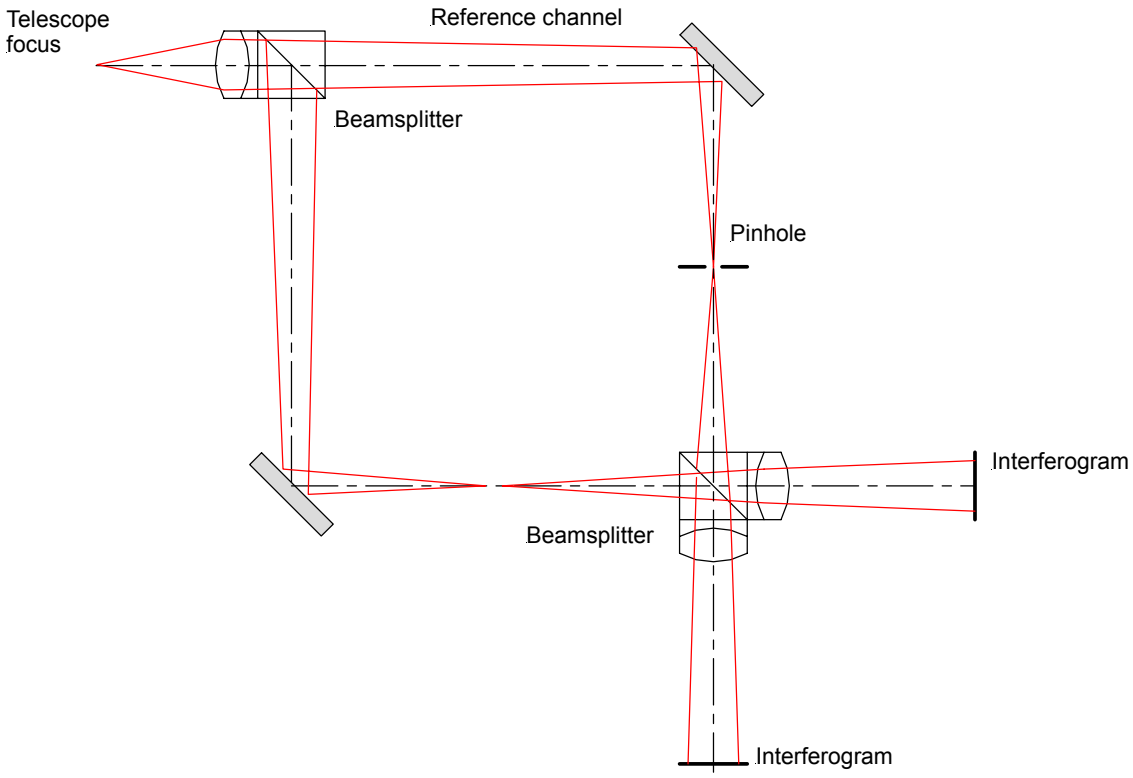

Figure 7-26. Conceptual setup of a Modified Mach-Zehnder interferometer.

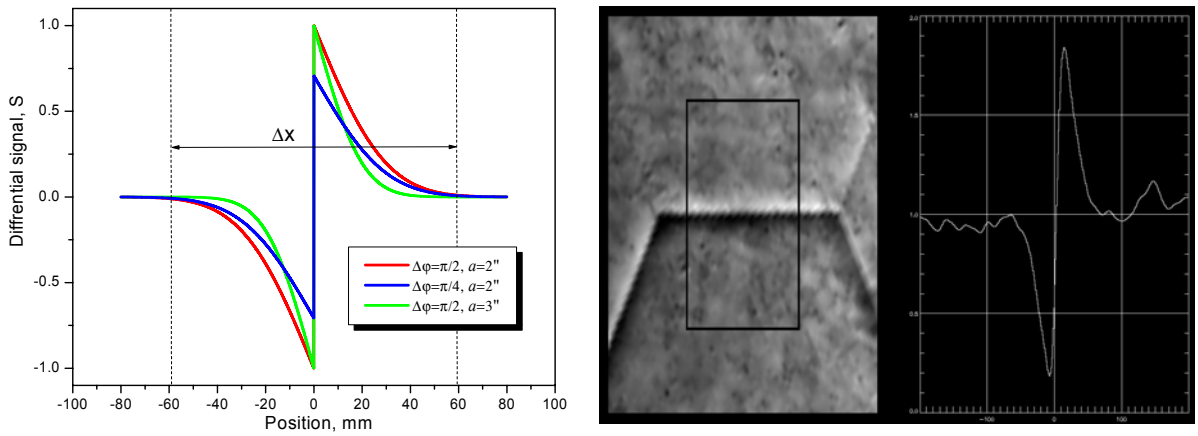

Figure 7-27. Mach-Zehnder signal profile for a piston step of π/2 and for different optical path differences between the two arms. Theoretical predictions are on the left hand side and experimental results on the right hand side.

7.5.4.2.3 Phase filtering technique

The image of the star is filtered by a phase plate which is made of a transmissive mask with a diameter of the size of the full width at half maximum of the seeing disk (around 0.6 arcsec) etched onto a glass plate as shown in Figure 7-28. The purpose is to introduce an optical path difference between the center and the outer regions of the image.

This mask is placed at the focus of the telescope and the segmented mirror is imaged onto a CCD by a lens. A typical OPD for the phase mask is around λ/9, which is 75 nm at a wavelength of 675 nm. Figure 7-29 shows the signal obtained with a mechanical piston step between two segments of 230 nm and an OPD introduced by the mask of λ/9.

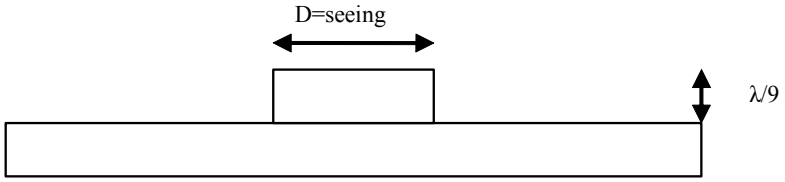

Figure 7-28. Phase mask principle.

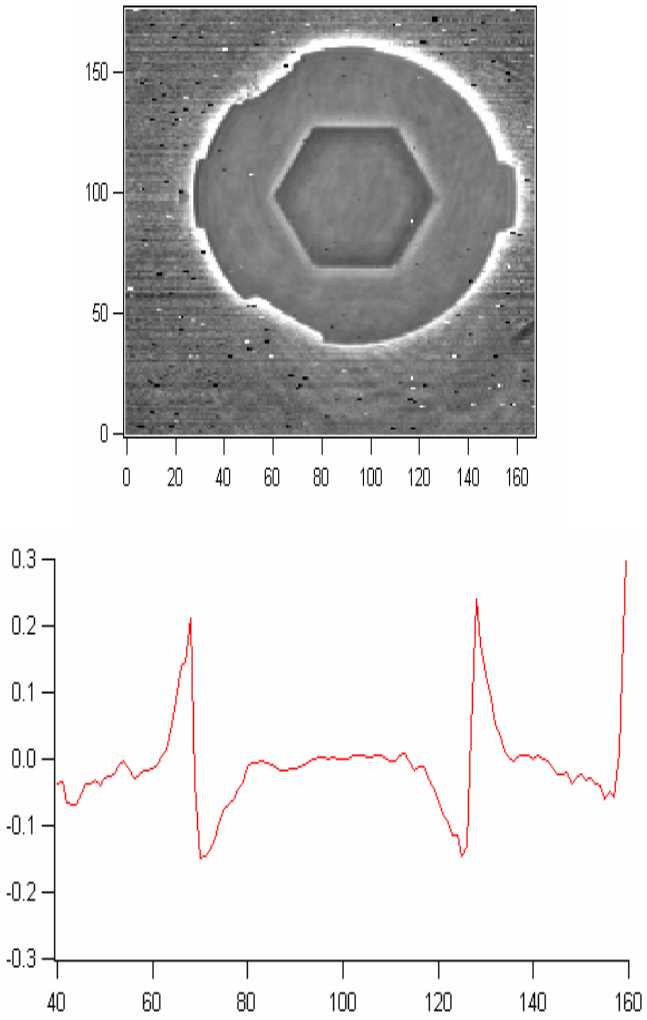

Figure 7-29. Signal obtained with a mechanical piston step of 230 nm.

7.5.4.2.4 Diffraction image technique

The concept has been developed by A. Schumacher R. Gonzales and J. Fuensalida at the Instituto Astrofisica Canarias (IAC) [94], [95] and at Keck [96]. The technique is based on curvature sensing [93], a method well developed and frequently applied in adaptive optics systems. The principle of the diffraction image technique is to take a defocused image of the segmented mirror. An example is shown in Figure 7-30.

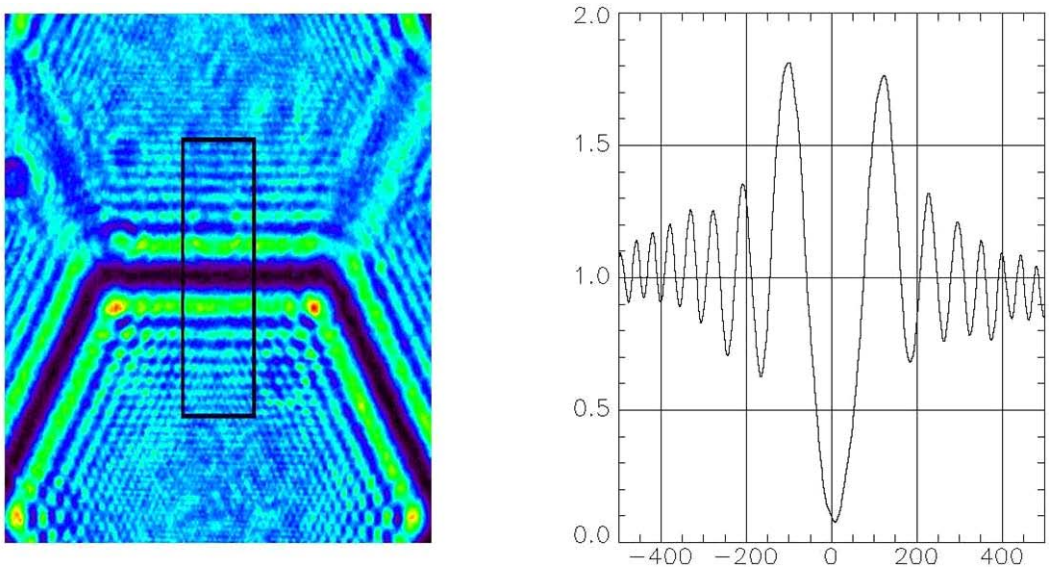

Figure 7-30. Signal obtained with the diffraction image technique (courtesy A. Schumacher)

7.5.4.2.5 Pyramid technique

This technique, first developed at the Osservatorio Astrofisico di Arcetri for wavefront sensing in adaptive optics, has also been proposed for the measurement of piston steps in segmented mirrors [97]. It is a two-dimensional knife edge test, linearised by appropriate movements of a glass pyramid. Figure 7-31 shows the signal created by a piston step between square segments.

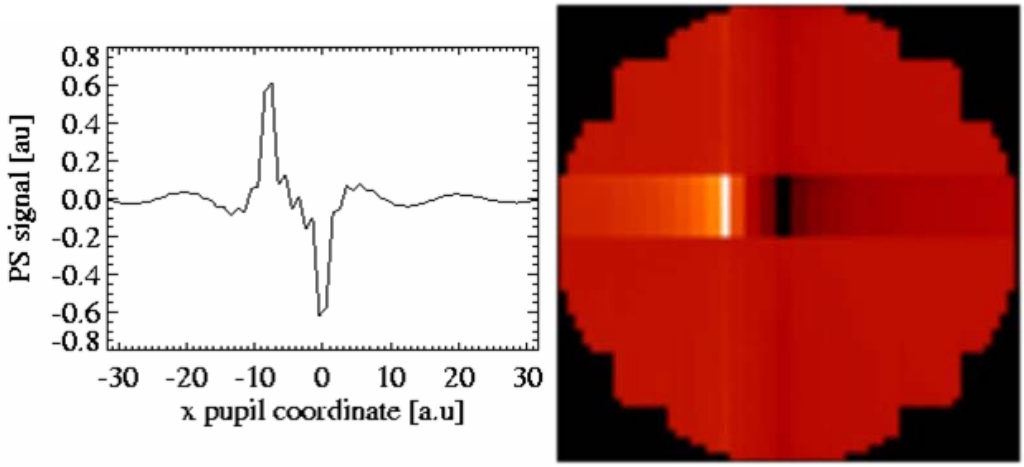

Figure 7-31. Signal obtained with the pyramid sensor for a piston step between square segments (courtesy S. Esposito)

7.5.4.2.6 CCD

On a CCD with 4000*4000 pixels with a total size of 50*50 mm^2 one edge of a segment is sampled by approximately 40 pizels, while the typical signal obtained with one of the sensors is sampled by approximately 10 pixels perpendicular to the edge. Such a sampling is sufficient for an anlysis of the signals. Each pixel corresponds to a surface of 625 mm^2 on M1 and receives 10000 photons for typical integration times of 30 seconds, a bandwidth of 50 nm and reference star of magnitude 10.

7.5.4.3 Open loop performance

To derive the information about the phase error from the signal delivered by a phasing sensor, different techniques can be used. The next section shows an example of a signal retrieval algorithm applied to the signal obtained in the laboratory with one of the sensors described above: the phase filtering technique.

7.5.4.3.1 The optical signal

The information about the phase step between two adjacent segments is recorded in an output signal which is localized at the intersegment border. The analytical expression for the signal, without taking into account the effects of atmospheric disturbances, is given by:

$$S = \; - \; \left(1 - f\left(b|x|\right)\right) \left\{ \underbrace{f\left(b|x|\right)\left(1-\cos(\varphi_0)\right)\left(1-\cos(\Delta\varphi)\right)}_{\substack{term\ 1 \\ symmetric}} - \underbrace{sign(x)\sin(\varphi_0)\sin(\Delta\varphi)}_{\substack{term\ 2 \\ anti-symmetric}} \right\} \qquad \textit{Eq. 7-1,}$$

where *x* is a coordinate perpendicular to the border, with the origin x=0 on the border, $\Delta\varphi$ is a phase difference between two segments, φ_0 is a phase shift on the phase plate, *b* is parameter related to the diameter of the plate and the wavelength by $b = 0.6\pi a/\lambda$, and the function $f(bx)$ is the normalized sine integral. To take into account the smoothing of the signal due to atmospheric disturbances the Gaussian probability function can be used instead of sine integral. Therefore two types functions are used in the analysis for the signals:

$$f(bx) = \frac{2b}{\pi}\int_0^x \frac{\sin(bx')}{bx'}dx' \quad \text{or} \quad f(bx) = \frac{2b}{\sqrt{\pi}}\int_0^x \exp\left(-b^2x'^2\right)dx' \qquad \textit{Eq. 7-2}$$

7.5.4.3.2 The CCD images

The reflective piston plate used for the laboratory test had hexagonal subapertures and different steps as shown in Figure 7-32:

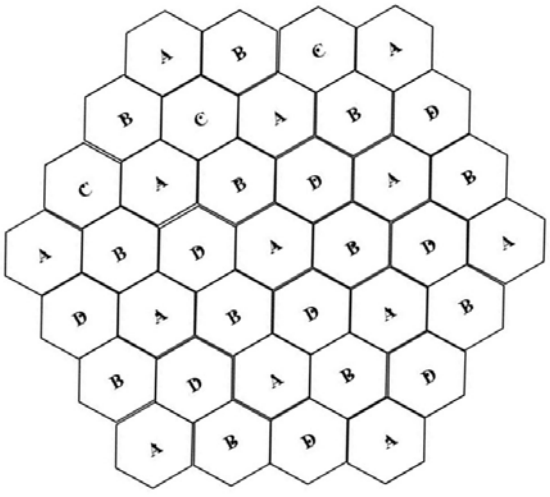

Figure 7-32. Position and surface piston levels of the hexagonal subapertures on the piston plate used for the laboratory tests (A=0nm, B=18nm, C=50nm, D=325nm).

The CCD image in Figure 7-33, shows for the two cases without and with turbulence in the optical path (seeing 0.36") shows a strong difference in the contrast.

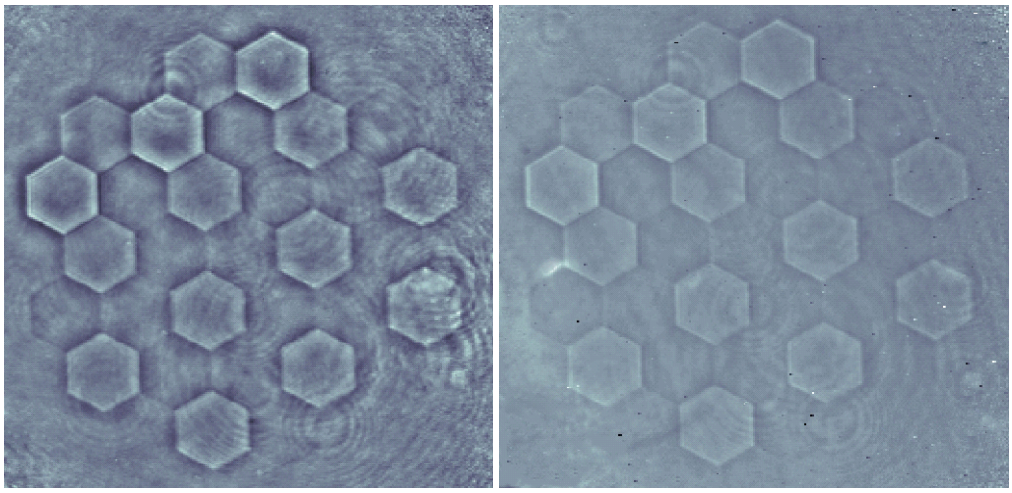

Figure 7-33. Phasing sensor signal from the multisegment phase plate without (left) and with (right) turbulence.

7.5.4.3.3 Signal analysis

To make full use of the knowledge about the analytical shape of the signal a fitting approach has been chosen for the signal analysis. Based on analytical expressions the following function has been fitted to the data:

$$S(x) = a_1 - \left[1 - f\left(a_4|x-a_3|\right)\right]\left[f\left(a_4|x-a_3|\right)\left(1-\cos(\varphi_0)\right)\left(1 \pm \sqrt{1-a_2{}^2}\right) - a_2 \cdot sign(x-a_3)\sin(\varphi_0)\right] \quad \textit{Eq. 7-3,}$$

where the fitted parameters are: a_1 - constant background; a_2 - amplitude which is proportional to sin(Δφ), where Δφ is the phase of the piston step; a_3 - shift of the edge with respect to the border; a_4 – parameter defined by the filter diameter.

The profile of the signal together with the fitted curve are shown for one of the borders in Figure 7-34 for two cases without (upper plot) and with (lower plot) the effects of atmospheric turbulence.

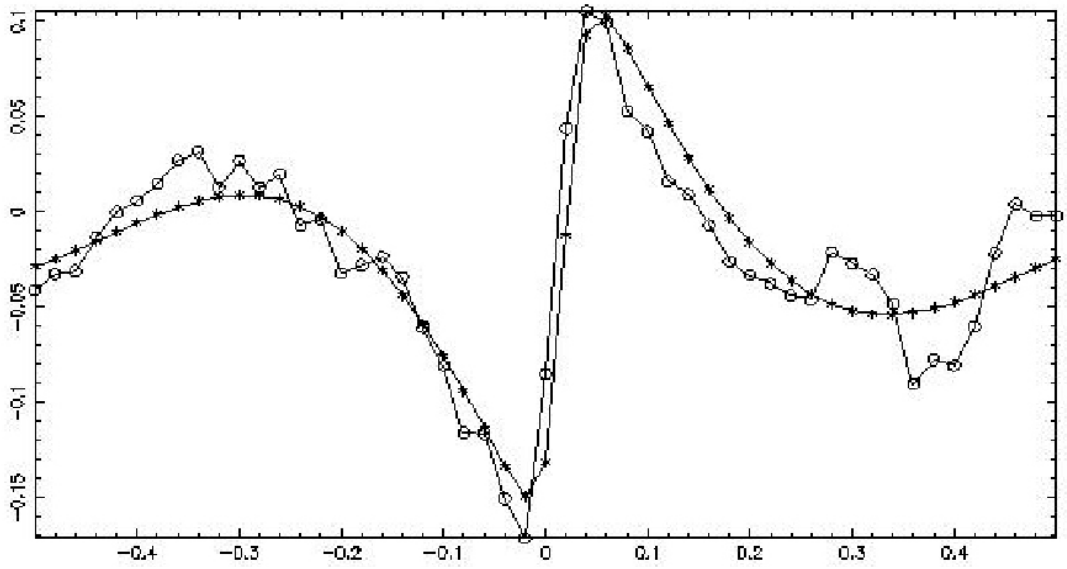

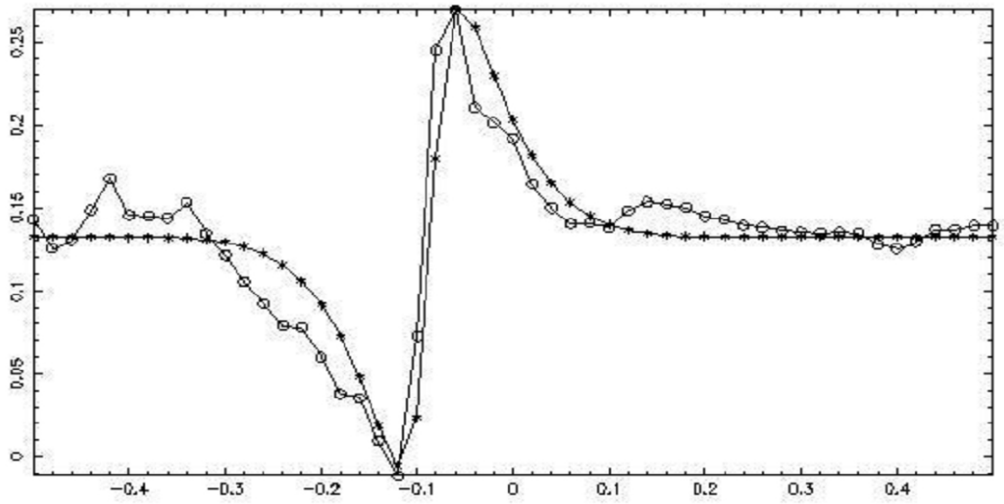

Figure 7-34. Sensor signals and fitted curves for one border for the two cases without (upper plot) and with (lower plot) turbulence. Note the change of the character of the signal : from an oscillating behaviour to smooth wings according to the function f.

7.5.4.3.4 Results

The fitting procedure was applied to the signals from all borders. Figure 7-35 shows for two measurements without and with a turbulence generator plots of the fitted amplitudes a_2 versus the piston steps known from the specifications for the piston plate. The solid lines represent sine curves with an amplitude *C* fitted to the data in the plots. The RMS errors of the measurements can be obtained from the scatter of the measured data around the sine curves. They are 17 nm for the measurements without and 19 nm for the measurements with the turbulence generator. The small difference between the RMS values indicates that the scatter is not strongly dependent on the turbulence but rather defined by other sources of noise. The parameter C depends on the value of the seeing introduced by the turbulence. For the case without turbulence parameter *C* was found to be 0.65 which is in good agreement with the theoretically expected value of 0.7. A seeing of 0.6 arcseconds reduces the parameter C to 0.29. The atmospheric turbulence reduces the amplitude of the sine curve, but does not shift it. The determination of this parameter as a function of atmospheric seeing from calibrations or from theory is essential for the choice of the closed-loop gain.

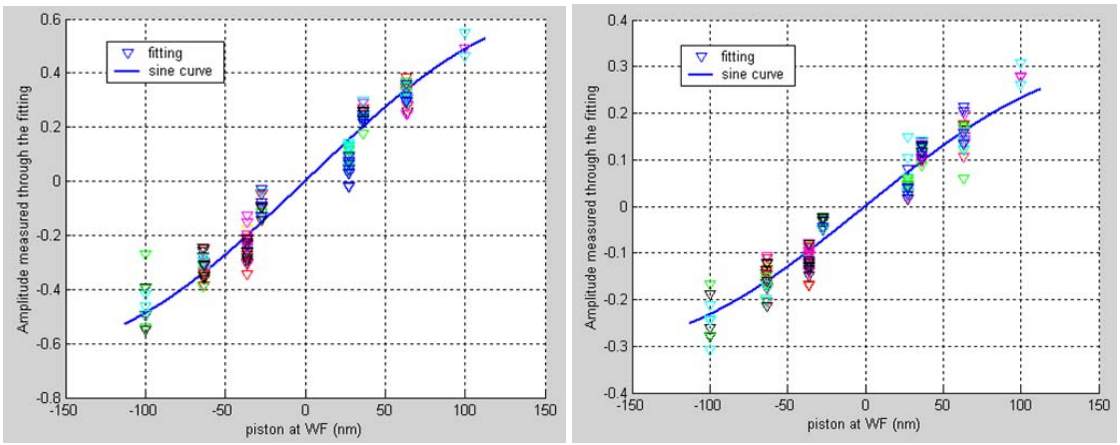

Figure 7-35. ZEUS measurements: amplitude of te signals versus known piston steps without (a) and with a turbulent generator (b). Note the reduction of the amplitude of the fitted sine curve from 0.65 to 0.29.

7.5.4.3.5 Increase of the capture range

Before optical phasing the misalignment of the segments can be several micrometers, whereas the capture range for measurements with quasi-monochromatic light is limited to $\lambda/2$. Methods for unwrapping the phase using multiple wavelengths techniques have been developed for interferometry [98].

The capture range is defined by two factors, namely the wavelengths and the measurement error, with the latter being the major limiting factor. Neverleless, for the small measurement errors of less than 10 nm the capture range is critically sensitive to the set of the chosen wavelengths. Even a small change in a wavelength can considerably affect the results.

7.5.4.3.6 Calibration

The algorithm for the reconstruction of the piston steps requires the knowledge of the parameter *C*. In the previous section *C* was determined by fitting a sine curve to measured data with a priori known abscissa values. In practice, *C* is an unknown parameter which has to be defined by calibrations or theory. To obtain the parameter C from a calibration procedure with well defined piston steps have to be introduced and the response of the sensors measured. Strictly speaking, the response of a sensor is not a symmetrical sine function centered on the origin as assumed above in the analysis of the experimental data, but rather a de-centered function:

$$a_2 = \mathrm{C}\sin(\Delta\varphi + \varphi_1) + \mathrm{B} \qquad \textit{Eq. 7-4,}$$

where φ_1, *B* and the previously introduced parameter *C* depend in a random fashion on many external factors such as the non uniformity of the illumination, the system alignment, gaps, the quality of the segment edges, etc. For example, a difference in the edge profiles of two adjacent segments increases the parameter φ_1. This parameter is important for the final phasing precision: the iterative algorithm will converge to φ_1 instead of zero, unless this parameter is known from the calibration. As the calibration implies initially phased segments, the calibration of 3000 OWL segments on the sky is a time consuming task. The foreseen base-line is the use of pre-calibrations. The static aberrations of the segments, including the aberrations at the edges, are the most severe sources for phasing errors. These factors have to be taken into account at the level of the surface maps of the segments. The influence of the parameter *C* due to, for example, a change of the seeing during the operation can be taken into account by an appropriate tuning of the gain in the closed-loop control.

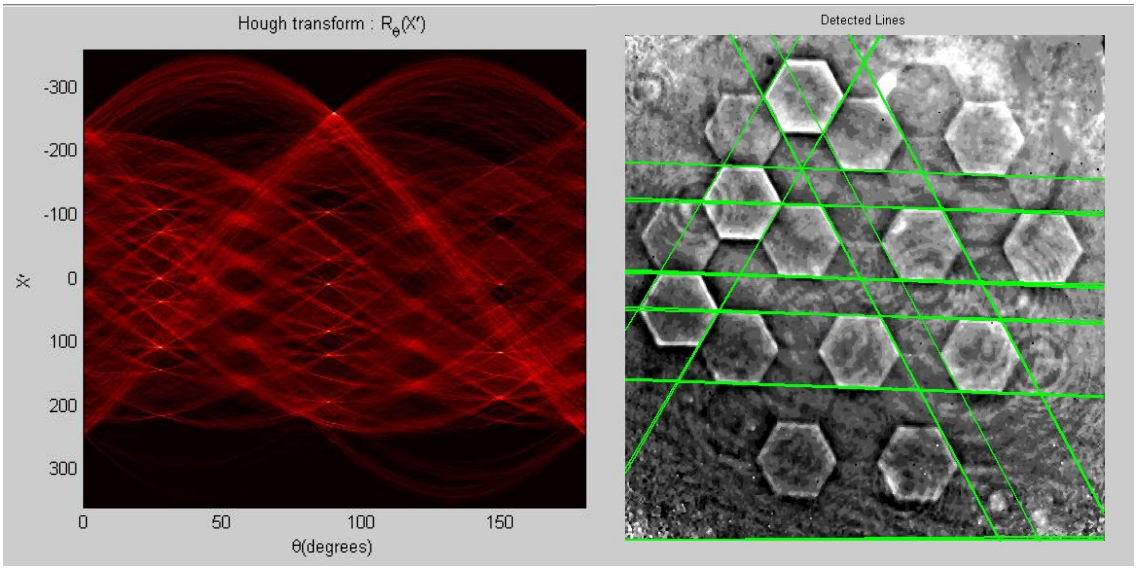

Figure 7-36. Hough transform of the signal (left) and the detected lines (right).

7.5.4.4 Identification of the borders

The algorithms described above require the determination of the location of the intersegment borders on the CCD with a precision better than one pixel. The Hough transform is a suitable algorithm to detect lines, circles, ellipses or other figures which have a known functional description. Before applying it to an image, the contrast in the image should be increased via the Sobel operator, which performs a 2-D spatial gradient measurement on an image and thereby emphasizes regions of high spatial frequency expected at the borders between segments. Figure 7-36 shows the application of the Sobel and Hough transforms to an image obtained with the phase filtering sensor.

7.5.4.5 Closed-loop results

A fitting technique has been implemented for measuring the piston steps between neighbouring segments in a segmented mirror. For the correction of the piston steps one needs the relationship between the piston movements of all of the segments and the resulting piston steps at all intersegment borders. This is given by a system of linar equations $\mathbf{Ax} = \mathbf{b}$, where **A** is a matrix, **x** a vector containing the piston movements, and **b** a vector containing the piston steps. The matrix **A** is a sparse matrix consisting only of of values -1, 0, 1 and can be calculated analytically from the geometry of the mirror. The control matrix **B**, which calculates the piston movements from the measured piston steps is the inverse of **A**, obtained by singular value decomposition (SVD). Since the system equation is over-determined, as there more borders than segments, the method automatically provides a best fit in the least square sense of the piston movements to the piston steps and thereby reduces the error. The only piston error which can not be detected and corrected by this method is a global piston movement of the mirror.

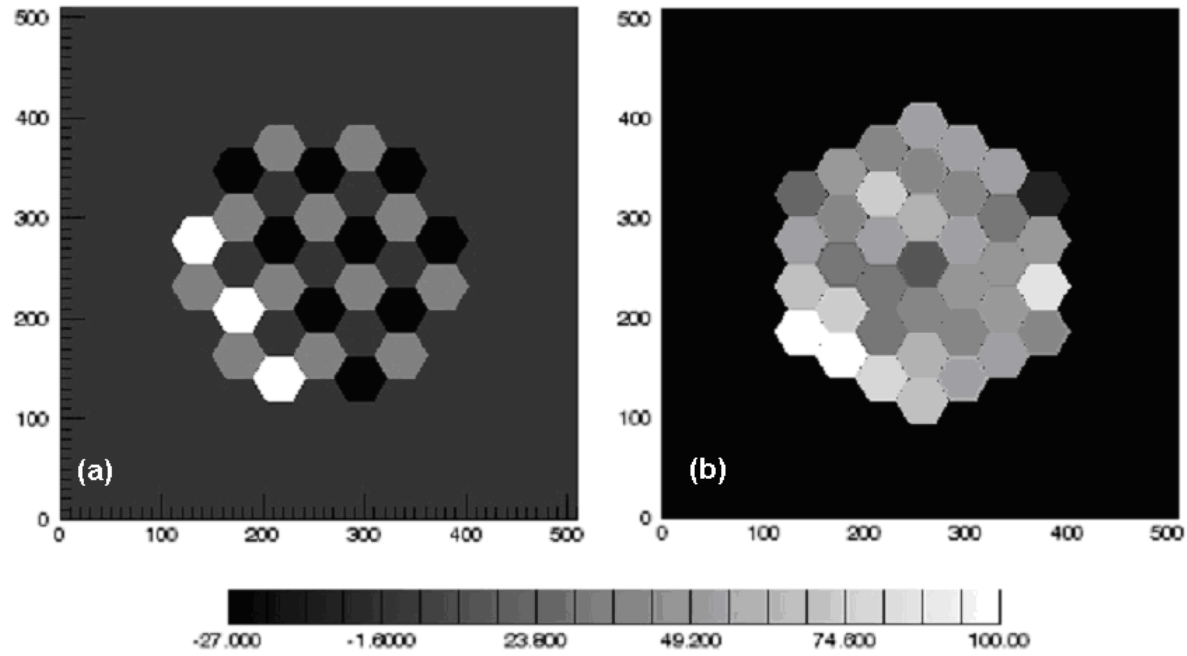

Figure 7-37. Piston steps distribution: Initial (a) and after 6th loop (b). The grey scale is in nm.

For a simulation of the closed-loop behaviour a segmented mirror has been generated with the same characteristics of the piston plate as the one used in the laboratory experiment (Figure 7-37 on the left hand side). Atmospheric turbulence has been simulated by using the phase screen corresponding to a seeing of 0.6", moving with a wind speed of 5m/s. The integration time for each measurement was 2 sec. Readout noise and the photon noise corresponding to a relatively bright star of magnitude 6 have also been included. Figure 7-37 shows on the right hand side the distribution of the phase errors after the 6th iteration. Figure 7-38 shows the convergence of the residual RMS error with the iterations using a gain of 0.5.

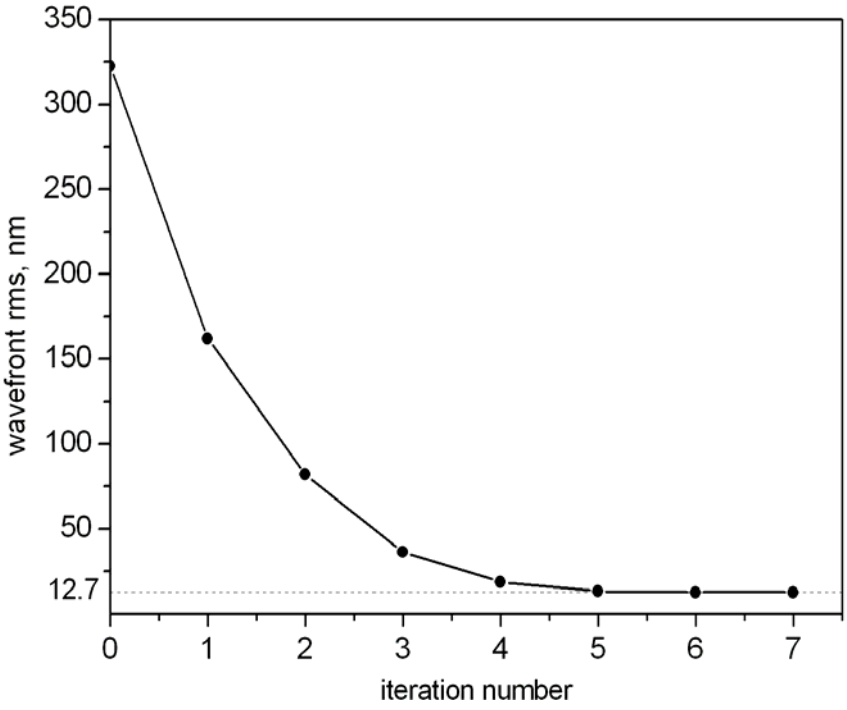

Figure 7-38. Closed loop simulations. Gain 0.5.
Initial wave front RMS = 322.5nm, final RMS = 12.7nm.

7.5.4.6 Phasing OWL

Owing to the obscuration by to the support structure of the M2 unit the primary mirror is, at least as seen by the phasing wavefront sensors, divided into six separate petals. Information about the piston steps between neighbouring segments can therefore only be supplied by the optical wavefront sensors for edges within a petal, and only individual petals can be phased with the matrix method desribed in the previous section. In a second stage the petals themselves have to be phased with respect to each other.

7.5.4.6.1 Phasing of one petal

The primary mirror of OWL has 2964 segments plus 54 segments obscured by the support of M2. In one petal alone one still needs to phase 494 segments having 1398 inter-segment borders. Therefore the matrix **A** mentioned above has 494x1398 = 690612 elements. Fortunately, this matrix is sparse to high degree. By using a specific indexation the matrix can be written in block-diagonal form. One can then apply matrix algebra techniques for sparse matrices and reduce the time for a SVD. This could be particularly useful if the matrix **A** changes during the operation because of a failure of edge sensors. Figure 7-40 shows the proposed indexation of segments and borders.

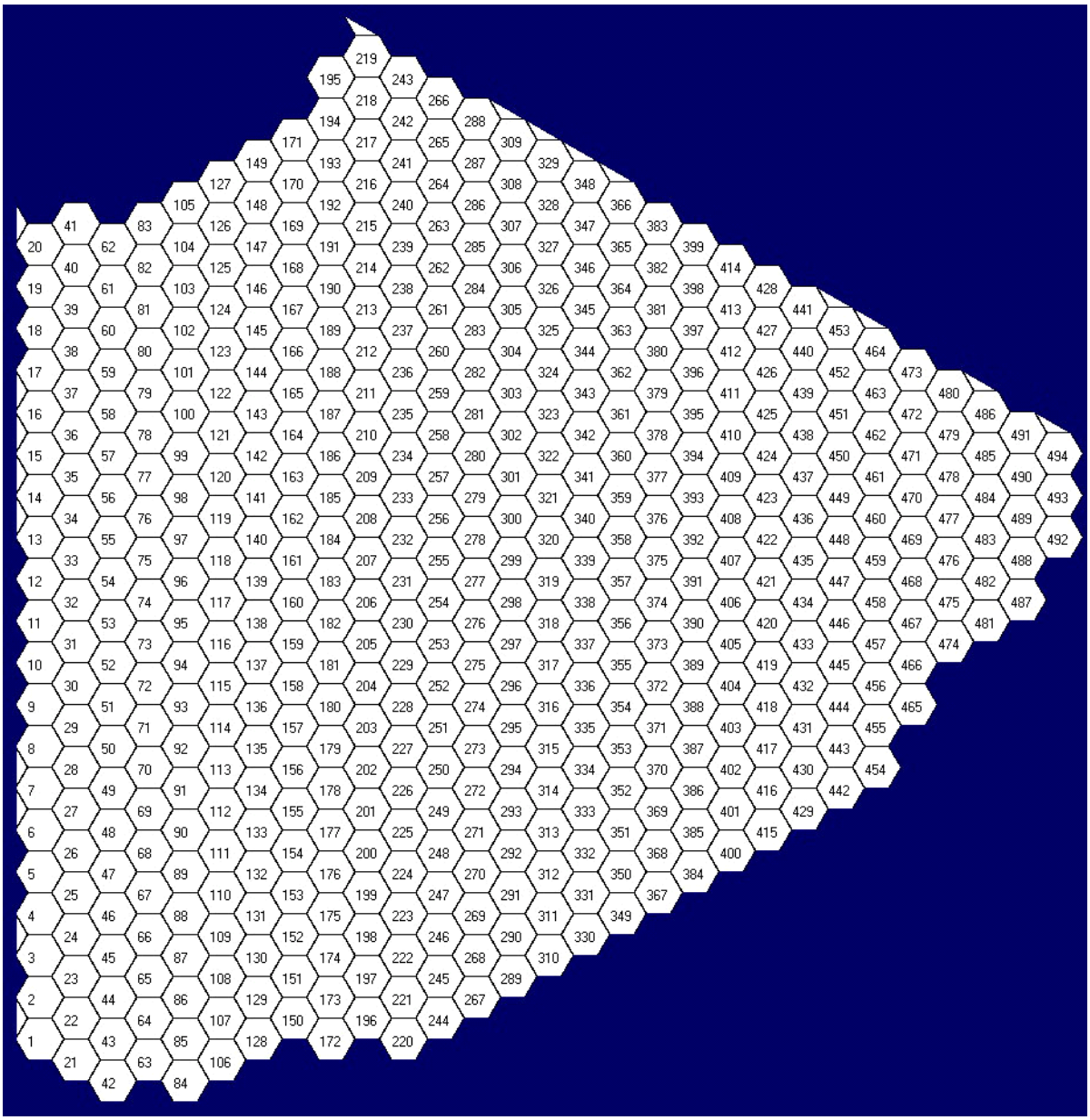

Figure 7-39 Indexation of the segments

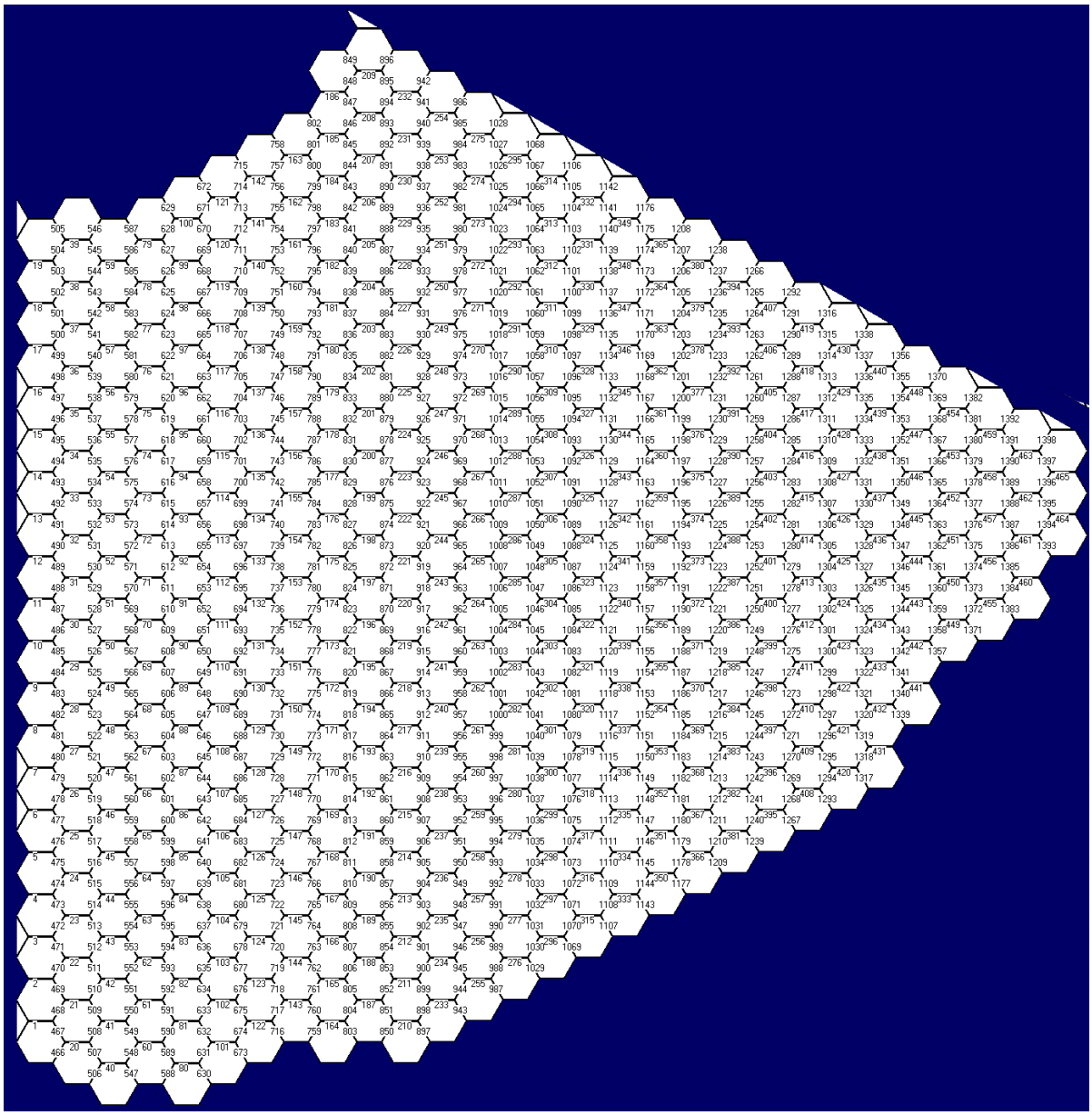

Figure 7-40. Indexation of the borders between the segments

This indexation allows writing the iteration matrix in a block form:

$$\boldsymbol{A} = \begin{bmatrix} \boldsymbol{Q} \\ \boldsymbol{P} \end{bmatrix}$$

where $\boldsymbol{Q}$ and $\boldsymbol{P}$ are also block matrices of dimension 29x29 (diagonal and quasi diagonal):

$$\boldsymbol{Q} = \begin{bmatrix} \boldsymbol{Q_{11}} & & \boldsymbol{0} \\ & \ddots & \\ & & \ddots \\ \boldsymbol{0} & & \boldsymbol{Q_{29\,29}} \end{bmatrix} \qquad \boldsymbol{P} = \begin{bmatrix} \boldsymbol{-P_{11}} & \boldsymbol{P_{12}} & & \boldsymbol{0} \\ & \ddots & \ddots & \\ & & & \\ \boldsymbol{0} & & \boldsymbol{-P_{28\,28}} & \boldsymbol{P_{28\,29}} \end{bmatrix}$$

The elements in the diagonal of the first matrix are 29 matrixes of the same type $\boldsymbol{B_n}$:

$$|Q_{11} \dots Q_{2929}|=$$

$$=[\ B_{20}\ B_{21}\ B_{21}\ B_{21}\ B_{22}\ B_{22}\ B_{22}\ B_{22}\ B_{24}\ B_{24}\ B_{24}\ B_{23}\ B_{22}\ B_{21}\ B_{20}\dots$$

$$\dots B_{19}\ B_{18}\ B_{17}\ B_{16}\ B_{15}\ B_{14}\ B_{13}\ B_{12}\ B_{11}\ B_{9}\ B_{7}\ B_{6}\ B_{5}\ B_{3}\ ]$$

The elements of the matrix P are quasi diagonal matrices of several types:

$$|P_{11} \dots P_{28\,28}|=$$

$$[C_{20}\ E_{21}\ D_{21}\ C_{21}\ D_{22}\ D_{22}\ D_{22}\ C_{22}\ D_{24}\ E_{24}\ F_{24}\ F_{23}\ F_{22}\ F_{21}\ \dots$$
$$\dots F_{20}\ F_{19}\ F_{18}\ F_{17}\ F_{16}\ F_{15}\ F_{14}\ F_{13}\ F_{12}\ F_{11}^{-}\ F_{9}^{-}\ F_{7}\ F_{6}\ F_{5}^{-}\ ]$$

$$|P_{12} \dots P_{28\,29}|=$$

$$[F_{21}\ D_{21}\ E_{21}\ F_{22}\ E_{22}\ E_{22}\ E_{22}\ F_{24}^{+}\ E_{24}\ D_{24}\ C_{23}\ C_{22}\ C_{21}\ C_{20}\ \dots$$
$$\dots C_{19}\ C_{18}\ C_{17}\ C_{16}\ C_{15}\ C_{14}\ C_{13}\ C_{12}\ C_{11}\ C_{9}\ C_{7}\ C_{6}\ C_{5}\ C_{3}\ ]$$

where B_n , C_n , D_n , E_n , F_n , F_n^+ F_n^- are block-matrixes consisting of values 1, -1 and 0 with corresponding dimensions [n-1, n], [2n, n], [2n-1, n], [2n-1, n], [2n-2, n], [2n-4, n], [2n-4, n]:

$$B_n = \begin{array}{c} \\ 1 \\ n-1 \end{array}\begin{array}{c} \begin{array}{ccccc} 1 & & & & n \end{array} \\ \begin{bmatrix} 1 & -1 & & & 0 \\ & 1 & -1 & & \\ & & \ddots & \ddots & \\ 0 & & & 1 & -1 \end{bmatrix} \end{array} \qquad C_n = \begin{array}{c} \\ 1 \\ 2n \end{array}\begin{array}{c} \begin{array}{ccccc} 1 & & & & n \end{array} \\ \begin{bmatrix} 1 & & & & 0 \\ 1 & & & & \\ & 1 & & & \\ & 1 & & & \\ & & \ddots & & \\ & & \ddots & & \\ & & & 1 & \\ 0 & & & 1 & \end{bmatrix} \end{array} \qquad D_n = \begin{array}{c} \\ 1 \\ 2n-1 \end{array}\begin{array}{c} \begin{array}{ccccc} 1 & & & & n \end{array} \\ \begin{bmatrix} 1 & & & & 0 \\ 0 & 1 & & & \\ & 1 & & & \\ & & \ddots & & \\ & & \ddots & & \\ & & & 1 & \\ 0 & & & 1 & \end{bmatrix} \end{array}$$

$$E_n = \begin{array}{c} \\ 1 \\ 2n-1 \end{array}\begin{array}{c} \begin{array}{ccccc} 1 & & & & n \end{array} \\ \begin{bmatrix} 1 & & & & 0 \\ 1 & & & & \\ & \ddots & & & \\ & \ddots & & & \\ & & 1 & & \\ & & 1 & 0 & \\ 0 & & & 1 & \end{bmatrix} \end{array} \qquad F_n = \begin{array}{c} \\ 1 \\ 2n-2 \end{array}\begin{array}{c} \begin{array}{ccccc} 1 & & & & n \end{array} \\ \begin{bmatrix} 1 & & & & \\ 0 & & & 0 & \\ & 1 & & & \\ & 1 & & & \\ & & \ddots & & \\ & & & 1 & \\ & 0 & & 1 & 0 \\ & & & & 1 \end{bmatrix} \end{array}$$

$$\boldsymbol{F}_n^+ = \begin{array}{c} \\ 1 \\ \\ \\ \\ \\ \\ 2n-4 \end{array} \begin{array}{c} \begin{array}{cccccc} 1 & & & & & n \end{array} \\ \begin{bmatrix} 1 & & & & & \\ & 1 & & 0 & & \\ & 1 & & & & \\ & & \ddots & & & \\ & & & 1 & & \\ 0 & & & 1 & & \\ & & & & 1 & 0 \end{bmatrix} \end{array} \quad \boldsymbol{F}_n^- = \begin{array}{c} \\ 1 \\ \\ \\ \\ \\ \\ 2n-4 \end{array} \begin{array}{c} \begin{array}{cccccc} 1 & & & & & n \end{array} \\ \begin{bmatrix} 0 & 1 & & & & \\ & & 1 & & 0 & \\ & & 1 & & & \\ & & & \ddots & & \\ & & & & & \\ & 0 & & & 1 & \\ & & & & 1 & \\ & & & & & 1 \end{bmatrix} \end{array}$$

7.5.4.6.2 Phasing of the petals

Six petals separated by secondary support obscuration may be considered as 6 large segments provided that all segments within each petal are aligned. For the phasing petals one could follow the same strategy as applied to the phasing of the segments. However, because of the small number of elements also other techniques may be implemented.

Two techniques are considered at the moment. The first one is based on the Shack-Hartmann method with two lenslets along each dividing line between two petals and centered on this line. The size of each of the 12 lenslets would correspond to a subaperture of approximately 12 m on M1. The principle of this measurement is the same as for the Shack-Hartmann sensor used for the phasing of segments described above.

The second method is a “dispersed - speckles” technique developed by A. Labeyrie for piston sensing in hypertelescopes with a densified exit-pupil. The method is based on an analysis of the image formed by multiple apertures and the extraction of the information about the piston errors from the structure of the speckle image [99].

7.5.4.6.3 Measurements under aberrations

Some types of sensors may be sensitive to other aberrations introduced by the telescope. These aberrations can be regarded as noise added to the piston sensing system, which reduces the resolution of the sensor. This may be a problem for the precision of the phasing if stars are chosen in the technical field which will be affected by field aberrations. The possible procedures for the alignment of the telescope based on measurements in the field have to take this feature into account.

7.5.4.6.4 Disentangling M1&M2

The precise determination of the positions of the mirrors in the image on the CCD is one of the critical points of the signal analysis. Besides, the signals from two segmented patterns (primary and secondary mirrors) overlap. As the two segmented pattern have different spatial scales, the signal can be disentangled using a Fourier filtering. To image the mirror gaps, a high pass filter is applied in the focal plane. It can be realized as the coronagraphic absorbing mask with a diameter of approximately 40-50 λ/D. In the next pupil plane the gaps appear as bright lines, corresponding to two segmentation grids (Figure 7-41). Then the Fourier filtering is applied with the spatial frequencies corresponding to the two patterns (Figure 7-41). The size of each spot is $2\lambda/D$. Fourier filtering can be implemented in the software or by optical devices. After the filtering one or the other of the two segmentation pattern will be revealed (Figure 7-41 c, d).

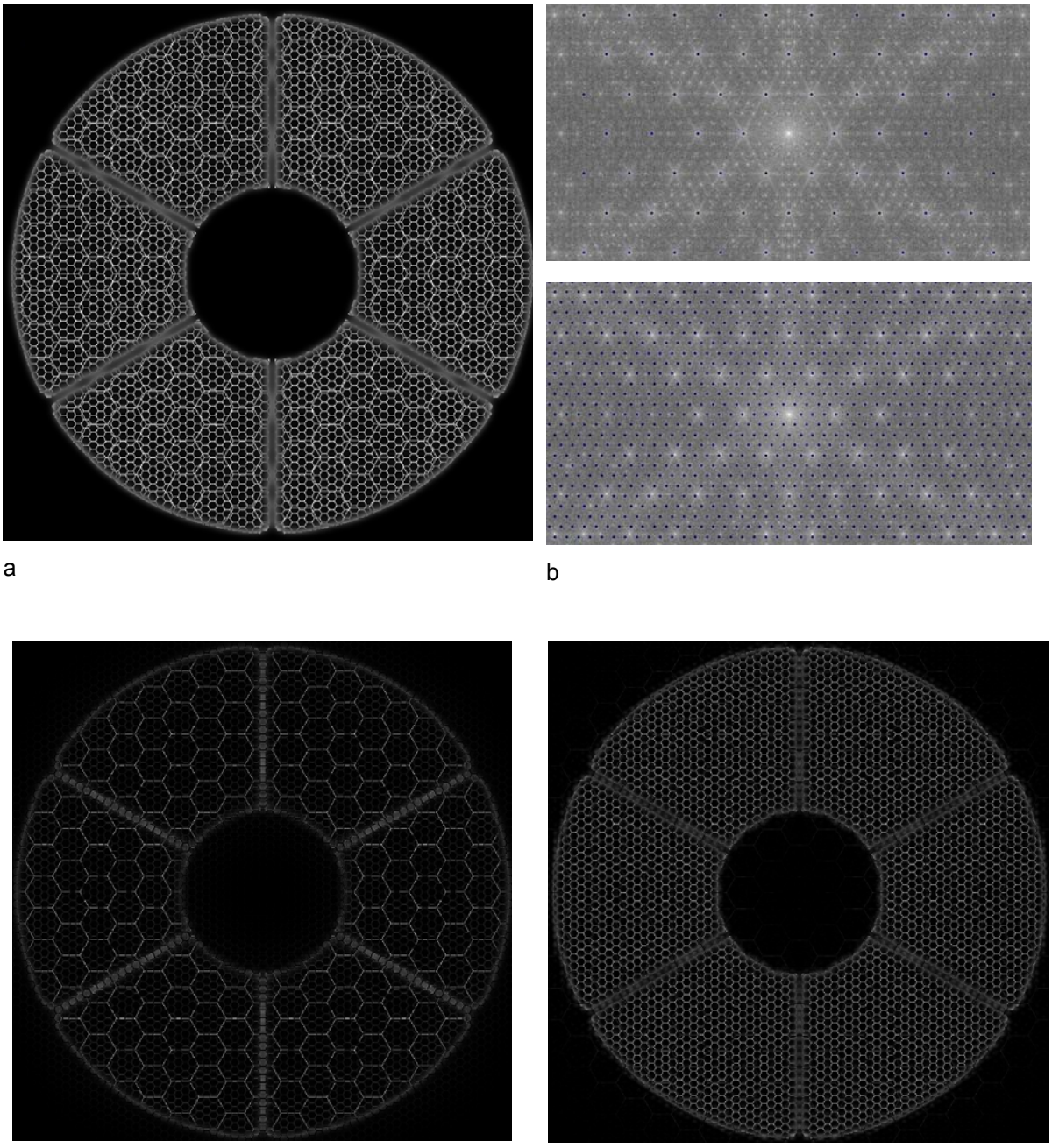

Figure 7-41. The signal from the gaps obtained by a high-pass filtering (a), two spatial Fourier filters (b), and the filtered patterns for the secondary (c) and primary (d) mirrors.

7.5.5 Control of segmented mirrors (M1 & M2)

To achieve the required optical performance, each segment should be positioned relative to adjacent segments with an accuracy of a few nanometers. In this section the segments are considered to be rigid bodies. Any wavefront aberrations due to segmentation are then introduced purely by deformations of the support structure of the segmented mirrors. At low temporal frequencies such deformations can be generated gravitationally by changes of the telescope altitude angle or by the effects of thermal variations. At higher temporal frequencies the major disturbance is the wind affecting the overall support structure and the individual segments.

A closed-loop control of the segment positions has to reduce these wavefront aberrations. The information about the discontinuities at the segment interfaces is obtained from two types of sensors: first, capacitive or inductive edge sensors and, second, optical wavefront sensors which generate the references for the first type of sensors. The corrections are done by position actuators, which can correct each segment position in three degrees of freedom. A control algorithm based on the measurements generates the command for the actuators.

The problem of segment control has extensively been studied by the Keck and CELT ([26], [27]) projects. The approach consists of two major steps. First, the required displacements for each actuator are estimated from the data obtained by the edge sensors with the help of a control matrix which has been obtained by inverting the influence matrix with singular value decomposition, and, second, an integral control law is used for the application of the corrections. The use of the integral control law is justified by the assumptions that the control is used only for correcting the slow perturbations generated by load and temperature variations, and that a low bandwidth control is sufficient. However, with faster perturbations due to wind buffetting, low bandwidth control system using proportional integral control would not necessarily deliver the required performance in the case of OWL. Hence, control laws with a higher bandwidth and better performance taking into account the dynamic behaviour of segments should be designed.

To develop a control strategy for the phasing of the segmented mirrors affected by wind perturbations a step by step approach has been adopted. First, the control of a single segment considering a stiff backstructure has been studied. The goal was to understand to what extent the local control system can 'freeze' the segments against the wind load perturbation. The outcomes of such a study are the requirements on the control bandwidth, position actuators and noise of the edge sensors. In the next step the effect of the back structure has been studied. The telescope structure has been represented by its equivalent inertia and stiffness.

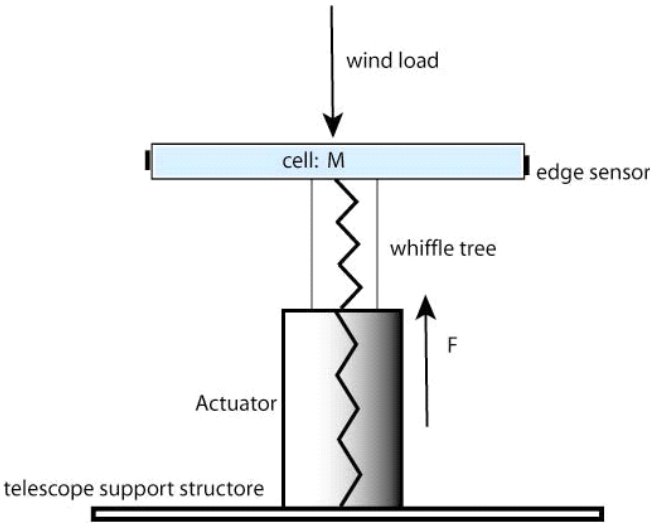

Figure 7-42 Scheme of segment system configuration

The wind load is characterized by a von Karman PSD, shown for a wind velocity of 10 m/s in Figure 7-43..

The control study for one segment has been extended to the case of a group of segments. First, the control of a ring of seven segments has been considered. The objective of the control has been to minimize the relative displacements between adjacent segments caused by wind perturbation. Two approaches for the control have been considered. In the first approach actuator movements are estimated via an inverted interaction matrix (the control matrix) from all edge sensor measurements. The correction is done in closed loop with a local controller. This approach is similar to the classical approach used in Keck, except for the design of the local controller. In the second approach the local controller for each segment uses only local information from the edge sensors around one segment. In this approach no inversion of an interaction matrix is needed. These issues will be discussed in more detail below.

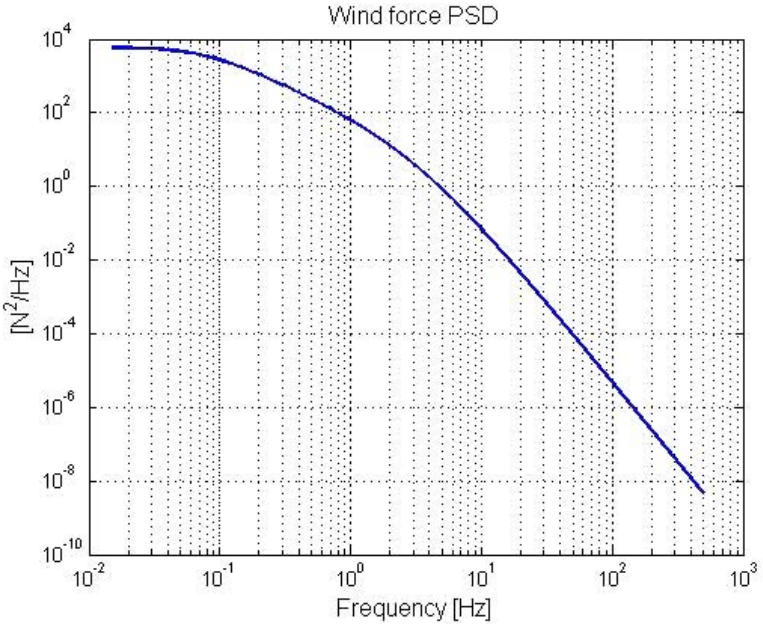

Figure 7-43 PSD of wind load on one segment

The study of the control of one segment is discussed in RD19. The mechanical description of the segment with a whiffle tree support system and three actuators is described in section 9.4.6. The dynamical model of the segment is given in RD20. The segment is modelled by a rigid body with three degrees of freedom and the whiffle tree system by a spring and a damper. The segment and the whiffle trees are connected to three actuators modelled by springs and the active forces that they can apply in response to the controller command. The complete system is subjected to an external wind load. A simplified scheme of a segment system is shown in Figure 7-42. Assuming a Zerodur mirror the weight of a segment is approximately 400 Kg. The frequency of the piston mode of the segment on its axial support system is expected to be at least 60 Hz and the structural damping on the whiffle tree system to be 1%.

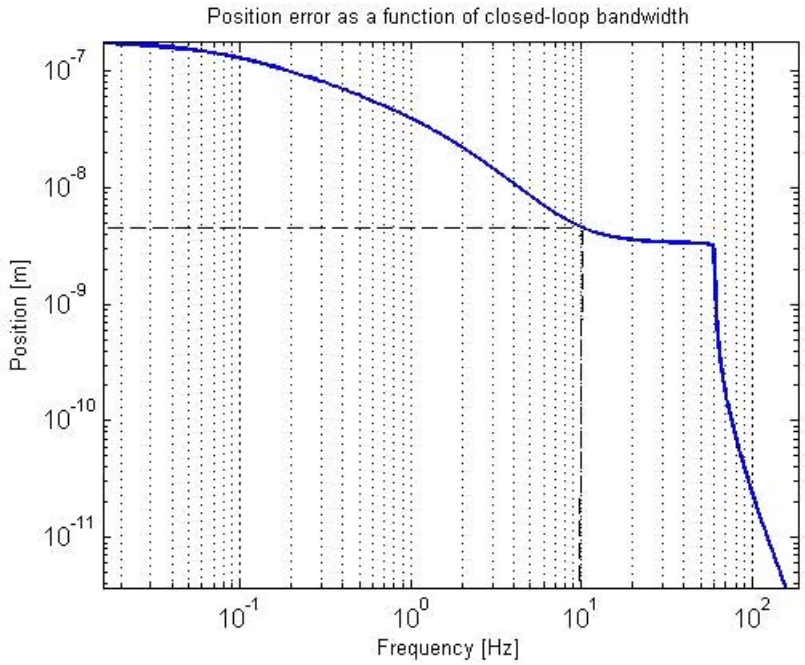

Figure 7-44 Position error RMS as a function of control bandwidth of each actuator

The objective of the segment control is to freeze the absolute position of a segment subjected to wind perturbations with an expected accuracy requirement in the range of 5 nm RMS. To obtain an initial crude estimate for the required control bandwidth for each actuator, the RMS of the position error has been calculated as a function of the closed-loop bandwidth with perfect control actions, shown in Figure 7-44.

The required accuracy can be obtained with a control bandwidth of at least 10Hz. A controller has now been designed taking into account the characteristics of the perturbation and the dynamics of the segment. The parameterisation and the design procedure, which is based on loop-shaping, are discussed in RD19. The control bandwidth for each actuator is set to 10Hz. Figure 7-45, comparing the PSDs of the position of the segment under closed-loop and open-loop control, shows that the controller considerably improves the performance of the system.

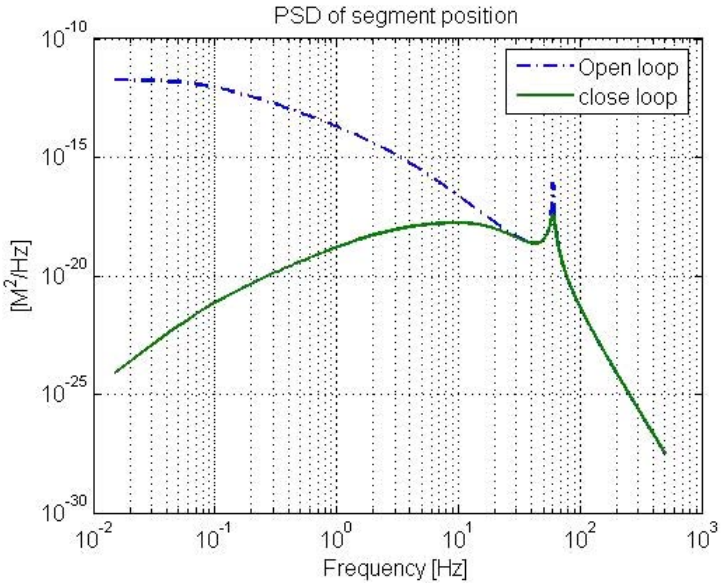

Figure 7-45 Closed-loop position error PSD compared to open loop PSD

The closed-loop performance has been verified by a simulation. The sensor noise was represented by a band-limited white noise with an amplitude of the spectral density of 0.7 nm/$\sqrt{Hz}$ [62] and has been introduced at the output, that is the absolute position of the segment. Sensor noise is usually amplified by the controller which consequently generates noisy input command to actuators. This can be avoided by installing a filter with a cut-off frequency higher than the control bandwidth after the output measurements. Figure 7-46 shows the results of the closed-loop simulation. The RMS error of segment position is 6.5 nm.

The rejection of the effects due to disturbances can be considerably improved if some prior information about the characteristics of the disturbances such as wind buffeting is available. This could be obtained by measuring the acceleration of segments which contains unfiltered information about the disturbing force at least for frequencies lower than the resonance frequency of the segment on its support. The control system will react faster to cancel out disturbances and the stringent requirement on the bandwidth of the position control can be relaxed. The results of a simulation of the position control of one segment with a control design including an acceleration feedback control (AFC), following the approach presented in [21], are shown in Figure 7-47.

The same position feedback controller has been used with the same parameters as in Figure 7-46.. Figure 7-47 shows that most of the correction the disturbance is done by the AFC part of the control, shown in red. This suggests that the desired performance can even be achieved using a position controller with a lower bandwidth. Figure 7-47 shows the simulation results

[62] Corresponding to 2 [nm] RMS sensor noise at 10Hz.

using the AFC and a position feedback control with a closed-loop bandwidth of 5 Hz for each actuator. The RMS error of the absolute position of a segment is now 4 nm as compared to 6.5 nm with the 10 Hz bandwidth without an AFC.

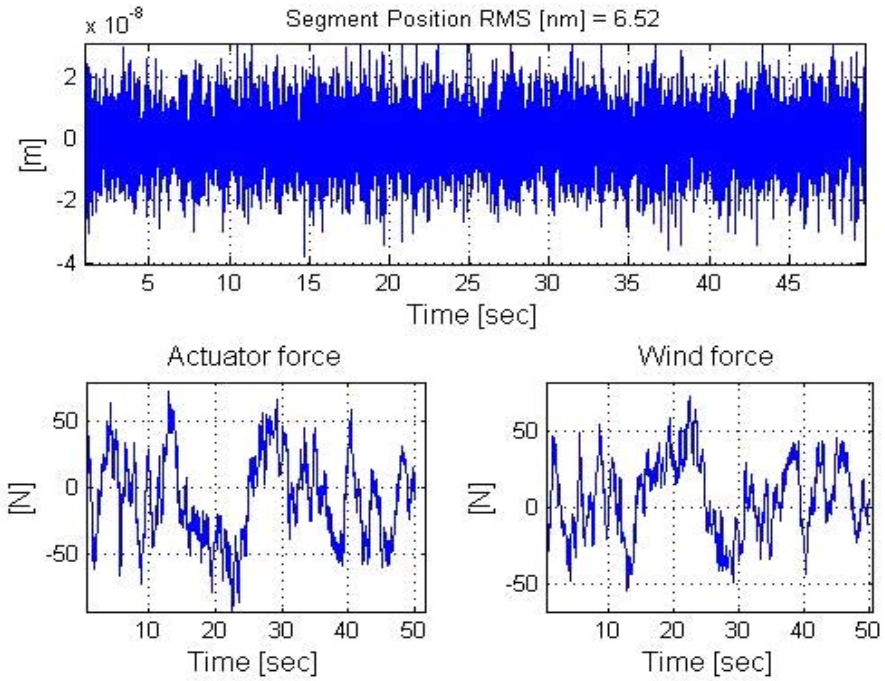

Figure 7-46 Closed-loop response of system--- closed-loop bandwidth: 10Hz

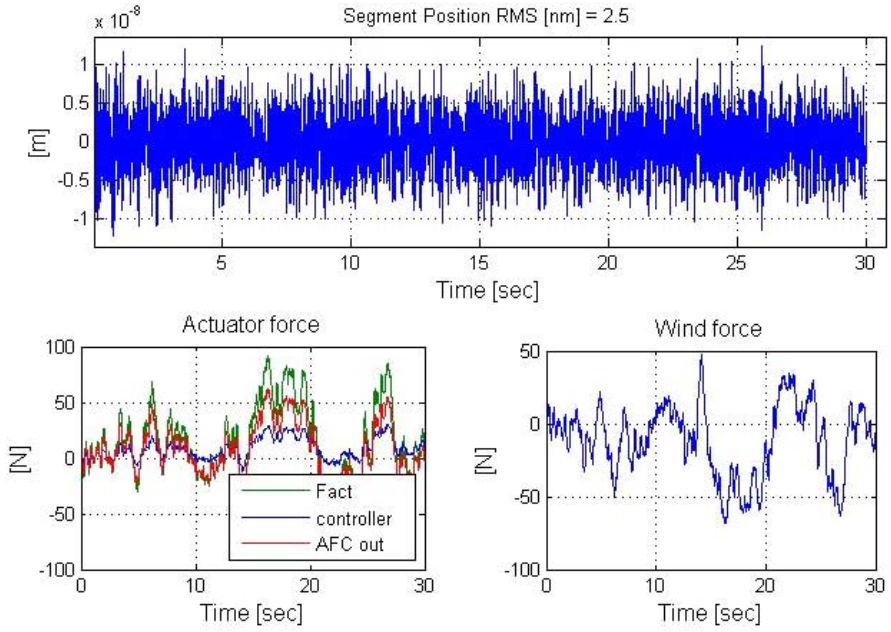

Figure 7-47 Closed-loop simulation ---- with AFC, closed-loop bandwidth 10Hz

Currently studies related to the control of a group of segments are under way. The coupling issues, i.e. coupling between the actuator commands on one segment, coupling between segments, and the effect of the control on the support structure will be studied in detail. The effect of wind on the segments, the control strategy and the performance of the actuators and edge sensors will be investigated in detail in the framework of the ELT Design Study (see RD506, RD504, RD502).

Some worry has been expressed that the control of segments at frequencies higher than the lowest frequencies of the telescope structure can generate resonances in the telescope structure. However, early studies have indicated that this is not the case for the control of the segments in segmented mirrors.

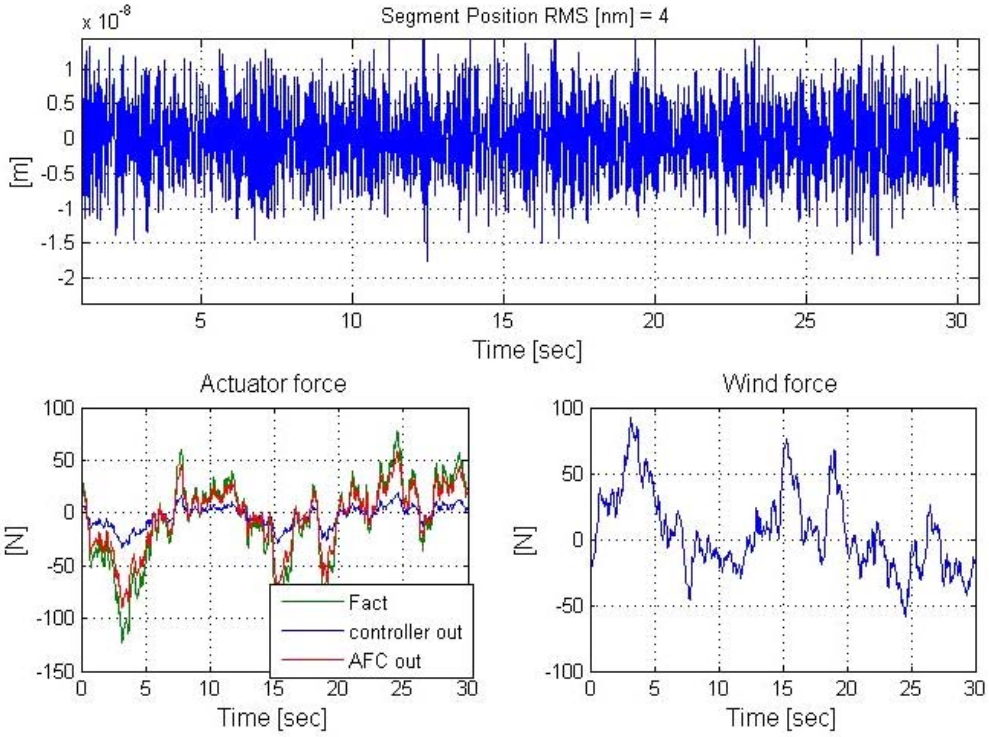

Figure 7-48 Closed-loop simulation ---- with AFC, closed-loop bandwidth 5Hz

The problem of controlling the segment can be decoupled from the dynamics of the support structure. The support structure will only be excited by wind perturbations and not by the actions of the control of the segments, regardless of the nature of the control and its bandwidth. The proof, which is given in RD19, is based on singular perturbation theory [24], [25]. The main idea behind the dynamic decoupling is the large separation between the time-scales related to the dynamics of the segments and the support structure. Since the natural frequency of 60 Hz of each segment unit is much larger than the lowest significant frequencies of 2.6 Hz of the telescope (see section 9.5.4.1), the system can dynamically be partitioned into to a fast subsystem, the segment control system, and slow subsystem, describing the dynamics of the support structure. The result of applying singular perturbation theory is that the only external force acting on the support structure is the perturbation due to the wind load.

The motion of the support structure caused by the wind will act as an external perturbation on the absolute position of a segment. This implies that a group of segments will move together with the back structure at low frequencies corresponding to the global modes of the structure.

To confirm the theoretical results, the telescope support structure has been modelled by an equivalent mass and a spring such that the lowest eigenfrequency of the telescope structure is 2.6 Hz. A simulation has been done for the closed-loop response of the segment system with a control bandwidth of 10Hz for each actuator. Figure 7-49 shows that the reaction force on the back structure is approximately equal to the wind force. The differences are comparatively small high frequency fluctuations around the time series of the wind load. The comparison between the PSDs of the wind and the reaction force, shown in Figure 7-50, also confirms that the wind load and the reaction force on the support structure have the same frequency content except at frequencies close to eigenfrequency of 60 Hz of the segment system.

Assuming a weak dynamical coupling between segments, the local controller for a single segment can also be used for the control of a group. The main difference between the control of a single and a group of segments is that the position errors are minimized relative to a reference for a single segment, but relative to each other for a group of segments. The relative errors between segments in piston, tip, and tilt are measured by the edge sensors. Two approaches can be distinguished: a) all edge sensor measurements used for calculation of the desired position of segments b) only local measurements are used to close the loop for each segment.

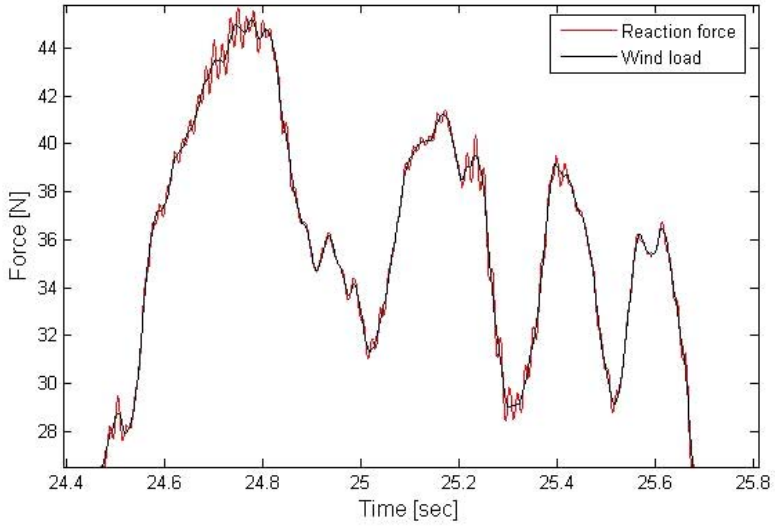

Figure 7-49 Reaction force on back structure and wind load on segment

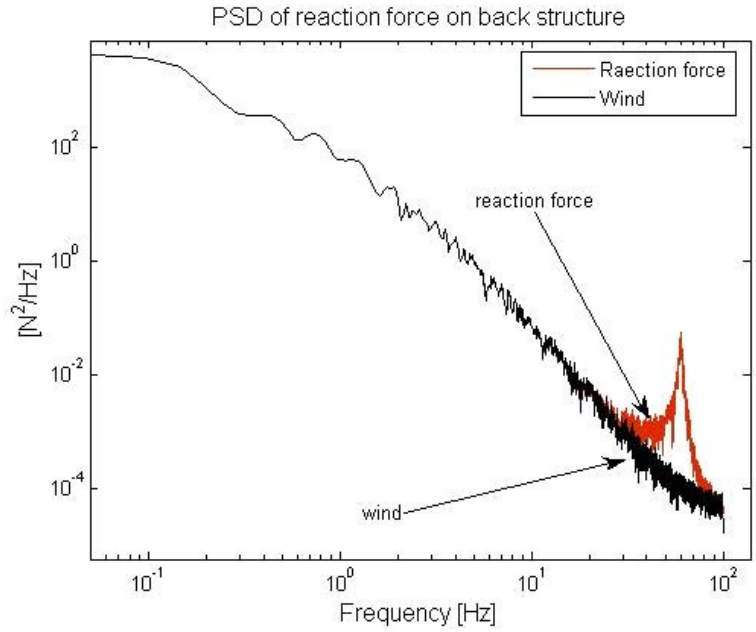

Figure 7-50 PSD of wind load and reaction force and back structure

a) Using the interaction matrix[63] these errors can be translated to relative displacements of the segment actuators. These error signals are then fed back to the corresponding segment controller. All sensor readings are used for the construction of the control matrix which is the

[63]A matrix defining the geometric relationship between the measurements of the edge sensor and the corresponding relative movements of the actuators.

pseudo-inverse of the interaction matrix. A large optical telescope such as OWL with thousands of sensors in the primary and secondary mirrors requires the manipulation of large matrices resulting in a high and unnecessary computational burden. In addition, when all sensor readings are used for the reconstruction, the noise in the sensors is propagated by the control matrix. The overall noise multiplier scales as the square root of the number of segments [89] and may produce problems as the number of segments increases.

b) To reduce the computational effort and the noise propagation several approaches relying on sparse-matrix operations have been proposed. Local control algorithms relying on measurements over restricted areas can be a good alternative solution. In [90] an approach combining local and global estimators in a hierarchical structure has been proposed. As an alternative approach, a local iterative algorithm using local sensor readings combined with prior state estimates has been proposed in the same paper.

Here a control approach where each segment uses the measurements from edge sensors on the segments has been studied (see RD19). Combinations of the readings from the sensors around one segment, as for example the average error, are directly fed back to the local controller.

The approach has been applied to a ring of seven segments. The dynamical model of the system is described in RD20. Figure 7-51 shows the locations and the numbering of the actuators and the sensors. The only coupling existing in the system is generated by the measurements of the edge sensors.

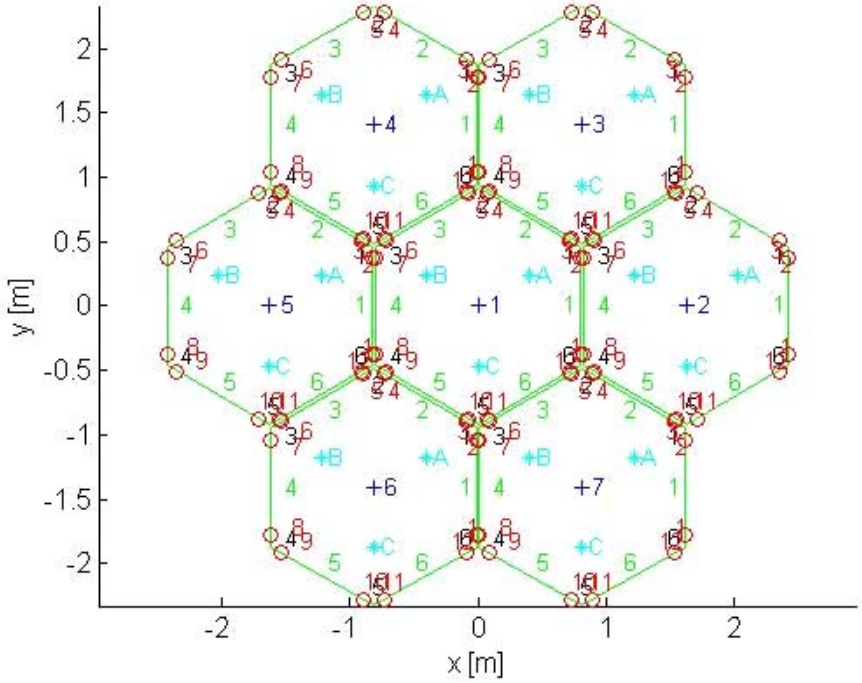

Figure 7-51 Seven segment configuration

Each segment has been subjected to wind perturbations (piston load only) with a mean velocity of 10 m/s. The wind is characterized by a von Karman-type PSD taking into account the correlations between the pressures on different segments. A typical time series of the wind force time is shown in Figure 7-52.

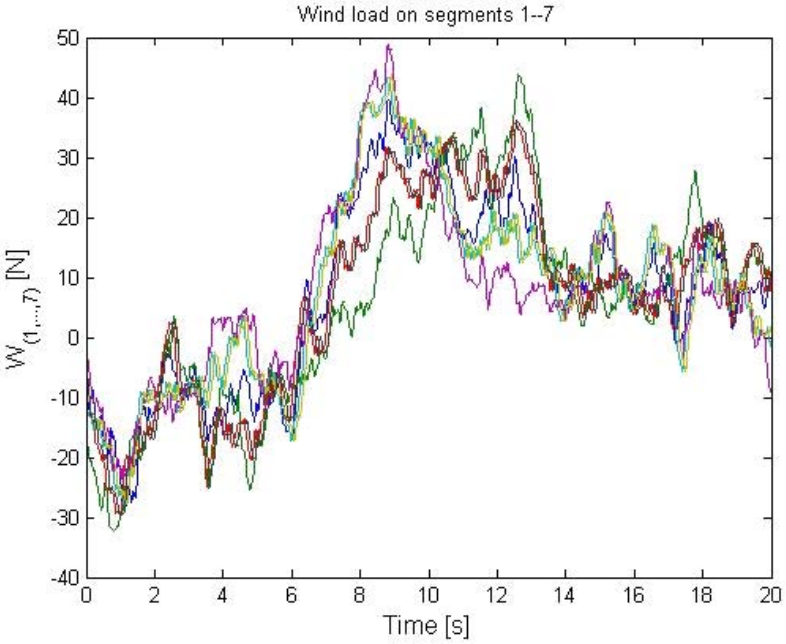

Figure 7-52 Wind load force on seven segments

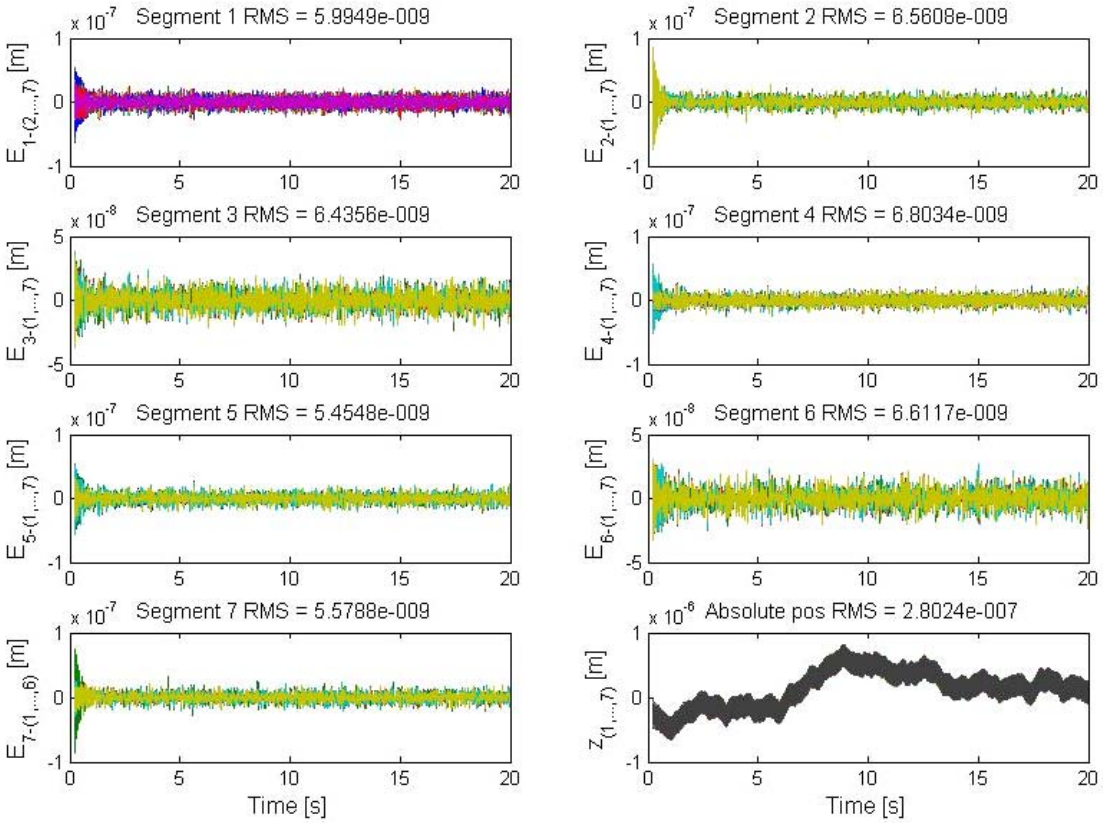

Figure 7-53 Seven segment closed-loop simulation: edge sensor readings and absolute position of the segments.

A band-limited white noise with an amplitude of the spectral density of 0.7 nm/$\sqrt{Hz}$ has been injected at the outputs of the edge sensors. The local controller is the one designed for a single segment piston control, i.e. with 10 Hz bandwidth for each actuator and no AFC control. The results of this simulation are shown in Figure 7-53. The RMS errors of all sensor readings are about 6 nm. All segments are moving together while the edge errors are minimized. As expected the absolute positions of the segments represented by the global piston mode are not controlled. It is well known from the modal analysis that four modes, three global rigid body motions and the change of curvature, are undetectable with edge sensors measuring piston steps only [89]. The system has also been simulated using the classical approach with the control matrix. For the few number of segments the results are quite similar and therefore do not allow for a comparison of the two approaches. However, it seems that for a large number of segments the local approach presented here will not suffer from the noise propagation and computational problems associated with the global approach. However, this should be verified later when a system with a larger number of segments will be simulated. This issue as well as the stability proofs related to the local approach are under investigation.

7.6 Active Phasing Experiment (APE)

The Active Phasing Experiment is part of the ELT Design Study and is briefly presented in appendix A-1.2. As explained in that section, the essential purpose of the APE experiment is to explore, integrate, and validate active, that is low temporal frequency, wavefront control schemes and technologies for an Extremely Large Optical Telescope. This includes the evaluation and comparison of the performance of different types of wavefront sensors in the laboratory and on the sky on the one hand and the integration of the control of a segmented aperture control into an already existing active system (including field stabilization and active optics) and driving both the active system and the control of the segments from the output of the full system on the other hand.

To accomplish those tasks APE will be designed as a technical prototype which will be installed and tested at a Nasmyth focus of a VLT Unit Telescope (UT). The telescope provides all active functions (field stabilization, focusing, centering, active deformable mirrors) and the APE instrument emulates the optical effects of segmentation. The latter is done within APE by reimaging the telescope pupil onto a small Active Segmented Mirror (ASM) whose shape is measured by an Internal Metrology (IM). The ASM is composed of 61 hexagonal segments and its inner aperture has a diameter of approximately 130 mm. Each segment is controlled in piston, tip and tilt by 3 piezoelectric actuators. The final wavefront is measured by three new types of Phasing Wave Front Sensors (PWFSs) and a Shack-HArtmann Phasing Sensor (SHAPS) combined in the Phasing Metrology Module. The new types of PWFSs are a phase filtering sensor called ZErnike Unit for Segment phasing (ZEUS), the DIffraction Image Phase Sensing Instrument (DIPSI) evolved from a curvature sensor, and a PYramid Phasing Sensor (PYPS). SHAPS is used for reference and comparison of the measurements of the phase errors at segment edges. SHAPS is also equipped with a lenslet array for the detection of the aberrations of the telescope to be corrected by active optics. The block diagram of this experiment is shown in appendix A-1.2.

7.6.1 Opto-mechanical design

The Active Phasing Experiment will be installed on a 3 m by 2 m optical table. This table will be placed at a height of 90 cm in the laboratory and at the height of the optical axis above the Nasmyth platform of the UT (2 m) as shown in Figure 7-54.

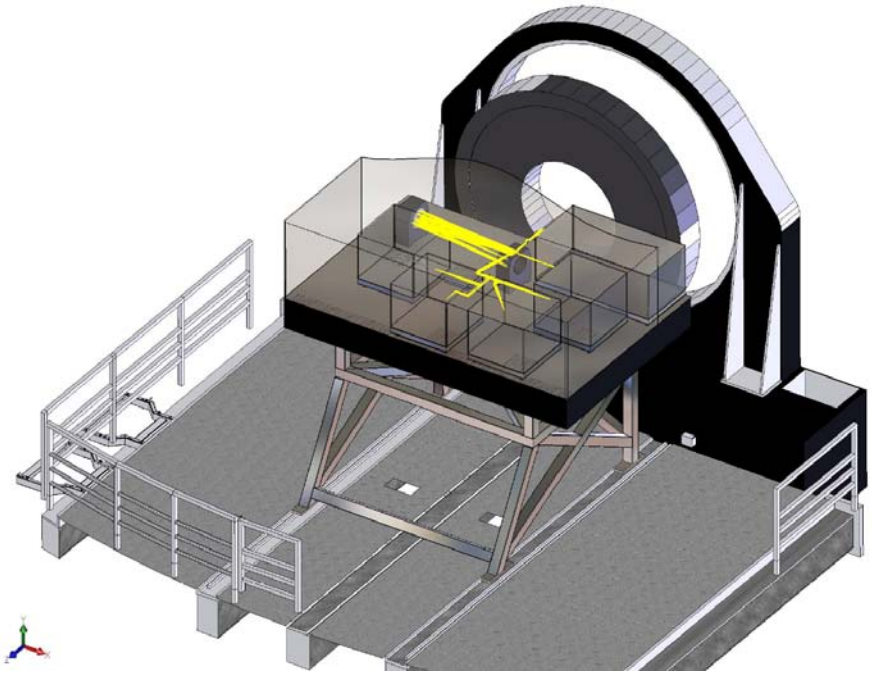

Figure 7-54: 3D view APE on the nasmyth platform

The plane defined by the optical axis on the APE experiment is 230 mm above the optical table. The major components of the optical design of APE are shown in appendix A-1.2. After a derotation of the beam from the telescope an off-axis parabola forms an image of the telescope pupil on the Active Segmented Mirror. The light selected by the field selector is then divided by a beam splitter. 20% of the light is sent to two cameras. One is a guiding camera for the control of the image position in the focal plane. The other one is an imaging camera which is used for the selection of a star for the wavefront sensors and for a direct measurement of the quality of the final images obtained after a correction of the telescope optics and the Active Segmented Mirror. The remaining 80% of the light is sent to the Phasing Wavefront Sensor module, where it is equally distributed among four different phasing wavefront sensors.

The Active Segmented Mirror is composed of 61 hexagonal segments. Its inner diameter is 130 mm, which exceeds the diameter of the image of the telescope pupil. Figure 7-55 shows a 3D view of the ASM. Each segment can be positioned by 3 piezoelectric actuators in piston, tip and tilt with a displacement range of 15 microns.

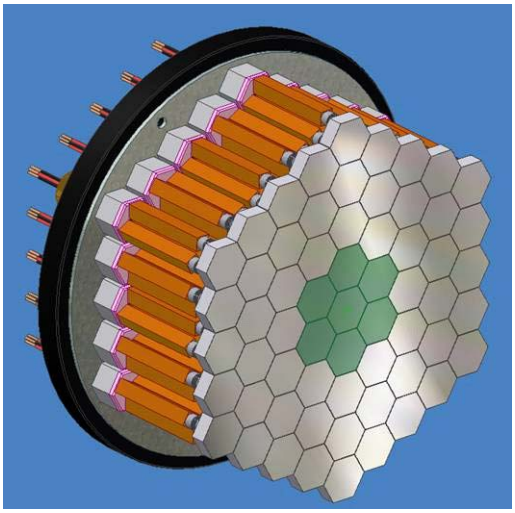

Figure 7-55: 3D view of the ASM

7.6.2 Internal Metrology

The ASM is controlled by an Internal Metrology system (IM). This device is based on a Twyman-Green interferometer. It uses a synthetic wavelength generated by 2 wavelengths to obtain a measurement range of more than 15 microns. Figure 7-56 shows the conceptual design of the Internal Metrology.

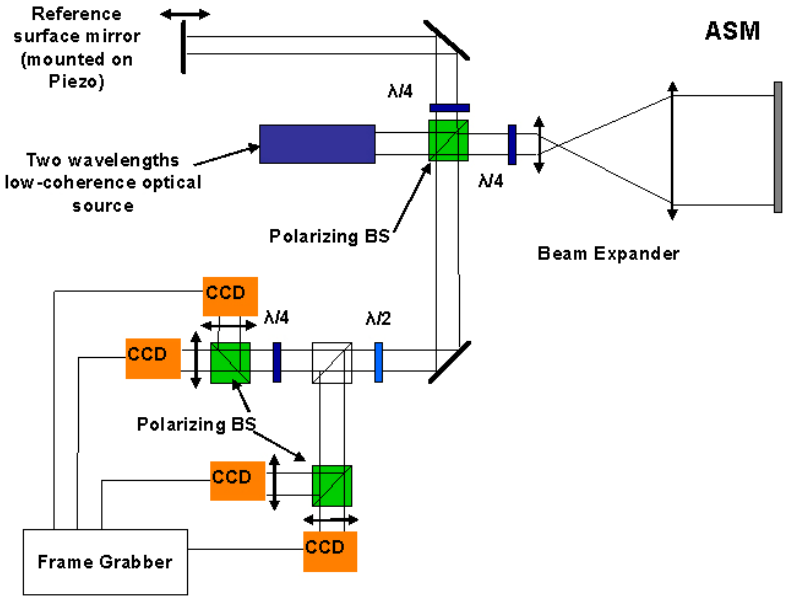

Figure 7-56: Conceptual design of the IM

The measurement frequency is 10 Hz. Apart from delivering the signals for the control of the Active Segmented Mirror it will also check the quality of the correction of the ASM based on the signals from the four phasing wavefront sensors.

7.6.3 The Phasing WaveFront Sensor Module

The PWFS module is composed of 4 different sensors which are based on four different technologies. They are: the Diffraction Image Phase Sensing Instrument (DIPSI) developed by the Instituto de Astrofisica de Canarias (IAC), the Zernike Unit for Segment phasing (ZEUS) developed by the Laboratoire d'Astrophysique de Marseille (LAM) in France, The Pyramid Phasing Sensor (PYPS) developed by INAF and the Shack-Hartmann Phasing Sensor (SHAPS) developed by ESO. DIPSI is based on curvature sensing explained in sect. 7.5.4.2.4 ZEUS on phase filtering explained in sect.. 7.5.4.2.2, PYPS on the pyramid sensing technique explained in sect.. 7.5.4.2.5, and finally SHAPS on the well known Shack Hartmann sensor explained in sect. 7.5.4.2.1.

The four sensors can be tested simultaneously under identical environmental conditions (temperature, humidity, wind speed and seeing) and with identical detectors. This offers the possibility to compare and quantify the capabilities of the four techniques applied to the measurement of phasing wavefront errors.

7.6.4 Schedule and observations

The design review of APE is planned for November 2005. The integration shall start during the second quarter of 2006 and the laboratory test will be performed during the last quarter of 2006. Two periods of one week each of test on the sky on one of the unit telescopes of the VLT on Paranal are planned for 2007.

8. Adaptive Optics

8.1 Introduction

Adaptive Optics is absolutely essential for OWL, to concentrate the light for spectroscopy and imaging and to reach the diffraction limit on-axis or over an extended FoV.

In this section we present a progressive implementation plan based on three generation of Adaptive Optics systems and, to the possible extent, the corresponding expected performance.

The 1st generation AO – Single Conjugate, Ground Layer, and distributed Multi-object AO – is essentially based on Natural Guide Stars (NGSs) and makes use of the M6 Adaptive Mirror included in the Telescope optical path.

The 2nd generation AO is also based on NGSs but includes a second deformable mirror (M5) conjugated at 7-8 km – Multi-Conjugate Adaptive Optics – or a post focus mirror conjugated to the telescope pupil with a much higher density of actuators -tweeter- in the case of EPICS.

The 3rd generation AO makes use of single or multiple Laser Guide Stars, preferably Sodium LGSs, and should provide higher sky coverage, better Strehl ratio and correction at shorter wavelengths.

More emphasis in the future will be given to the LGS assisted AO systems after having studied, simulated and demonstrated the feasibility of the proposed concepts.

The performance presented for the AO systems is based on advances from today's technology in areas where we feel confident that such advances will occur (e.g. the sizes of the deformable mirrors). Even better performance could be achieved if other technologies advance at the same rate as in the past (e.g. the density of actuators for deformable mirrors). While the level one requirements are not fully met with the technology assumptions made in this phase A study, assuming no show stoppers and/or favourable technology advances we have confidence that they eventually will.

8.2 First generation Adaptive Optics

The 1st generation Adaptive Optics for OWL relies on the availability of the M6 Adaptive Mirror unit (M6AM) in the telescope optical train, conjugated to the pupil. The M6AM unit, located in the corrector structure (Figure 8-1) provides both the Adaptive Optics and the Field Stabilization functions of OWL. The 1st generation AO is based on Natural Guide Star (NGSs) for wavefront sensing. As an option an additional post-focal corrector will be discussed in the following either to improve the correction on-axis by increasing the number of degrees of freedom of the

Deformable Mirror (DM) or to improve the correction in several specific positions in the 6 arc minute Field of View (FoV).

Three 1st generation AO facilities will be described: Single Conjugate AO (SCAO), Ground Layer AO (GLAO) and Multi-Object AO (MOAO).

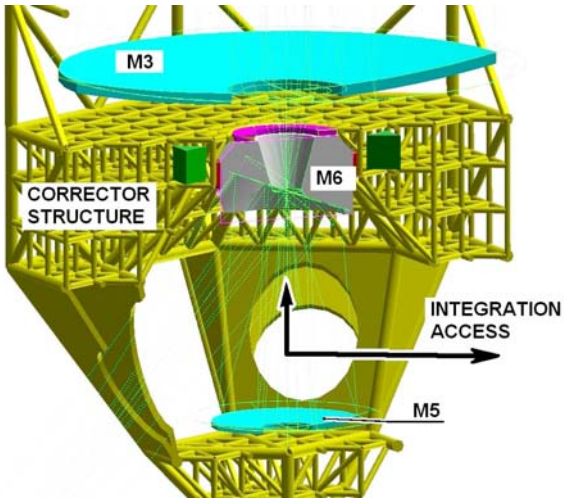

Figure 8-1: M6 Adaptive Mirror located in the corrector structure of the telescope.

8.2.1 Single Conjugate Adaptive Optics

The Single Conjugate Adaptive Optics (SCAO) facility – Figure 8-2 – is essentially an extension of the current AO systems for 8-10 m telescopes to OWL (NAOS, MACAO at the VLT for instance). The performance is usually defined by the Strehl ratio in K-band and ranges from 50 to 60% for bright reference star under average seeing conditions.

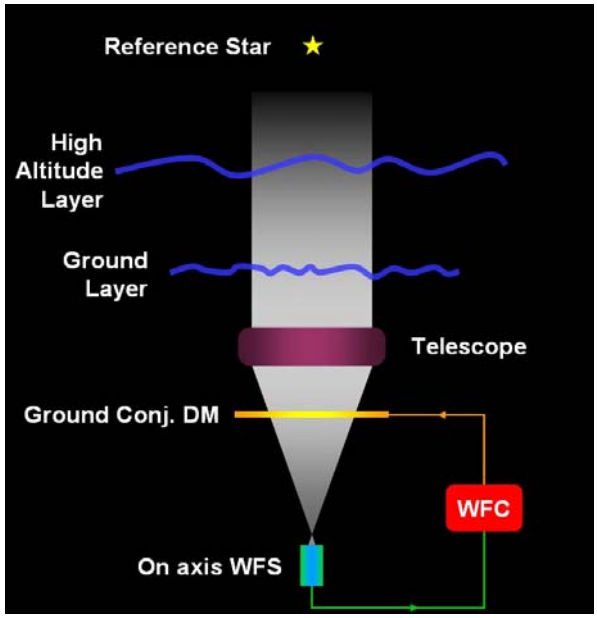

Figure 8-2: Single Conjugate Adaptive Optics concept

SCAO is the AO mode that will be used to commission the telescope at its diffraction limit capability in the Near Infrared.

8.2.1.1 Performance requirements

The SCAO performance requirements are as follows:

- SCAO aims at providing diffraction limited images at the Near Infrared wavelengths (J-K bands) using Natural Guide Stars (NGSs) for wavefront sensing
- SCAO should offer the possibility to observe at longer wavelengths up to 20 microns with a superb correction on-axis using a bright NGS in the visible, Mv<13, or in the IR, MH<12. A specific wavefront sensor close to the instrument is permitted in that case.
- The system should be optimized to obtain >50% Strehl ratio (in K) for bright NGSs and the best possible partial correction for faint NGSs.
- SCAO best correction will be offered on-axis; off-axis performance will essentially be limited by the anisoplanatism (Figure 8-3).
- SCAO should support both a visible and an IR wavefront sensor; the later being required to observe very embedded regions
- SCAO should be able to acquire the wavefront sensing NGS in the central 2' FoV (diameter).
- SCAO shall provide a partially corrected and unvignetted science FoV of 1' diameter.
- SCAO should support telescope nodding at 0.1 Hz by fast opening/closing the AO loop (0.1s)
- SCAO should support small amplitude -0.5"- low temporal frequency -0.1Hz- mosaicking in closed loop by offsetting the Wavefront Sensor (WFS). The accuracy of the WFS offset should be better than 1/2 of the spatial pixel size at the considered wavelength (~1mas in J-band)
- SCAO does not support chopping (chopping for TOWL will be performed in the instrument itself).
- SCAO should provide in closed loop Field Stabilization to the telescope with the maximum amplitude characteristics provided in Table 8-1. For wavefront sensor dynamic reasons, the telescope guider will support SCAO for closing the AO plus Field stabilization loop before the control of the field stabilization corrector is taken over by the SCAO in closed loop.
- SCAO should permit to observe without AO (but with Field Stabilization) without any transmission loss with respect to the telescope. In that case, the field stabilization corrector is not controlled by the AO system.
- SCAO should have the capability to correct for some of the telescope aberrations left by the active optics with an amplitude lower than 20% of the atmospheric wavefront at all spatial and temporal frequencies. Errors beyond these values are handled by the active optics.
- The transmission of SCAO should be maximized for the observing wavelength of the instrument for the visible WFS: T>95%. For the infrared wavefront sensor, the transmission toward the instrument depends on the best trade-off between object observed and the observing wavelength. This trade-off may require several beam splitter/dichroic elements.
- For the performance evaluation of SCAO seeing assumptions should be: 0.53" and 1" at 0.5 µm at zenith; with τ_0=3 and 2ms. For the performance evaluation the outer scale of turbulence should be L_0=25 m. For the determination of the AO design parameters the following atmospheric parameters should be assumed: turbulence outer scale L_0=100m, seeing=1.5", τ_0=2ms (Figure 8-4).
- SCAO shall be able to correct for differential atmospheric dispersion between the NGS and the Science object during an observation by applying offsets to the wavefront sensor. The calculation of the offset shall be done by the software based on the science beam effective wavelength provided by the instrument, the spectral type of the NGS provided by the

observer, the science and guide star coordinates provided by the observer, the relevant atmospheric data (Temperature, Pressure, and Humidity) provided by the observatory.

- SCAO will not correct for the atmospheric dispersion within the scientific band pass of the instrument.
- SCAO Strehl ratio versus magnitude, observing wavelengths and seeing characteristics are provided in Table 8-2 and Table 8-3. These are given at the telescope focus, without taking into account static aberrations created by the instrument.

Maximum tip-tilt signal amplitude (mirror tilt)	Frequency
± 75”	<0.1Hz
± 10”	0.1-1Hz
± 1”	1-10Hz
± 0.1”	>10Hz

Table 8-1: Spectral Envelope of maximum Tip-tilt signal (mirror tilt) to be corrected by M6AM. On-sky tip-tilt is ~ mirror tilt/20.

	Wave band	K-band		H-band		J-band	
	Guide star magnitude	V=12	V=16	V=12	V=16	V=12	V=16
seeing, r_0, L_0 @ 0.5µm	0.53”, 3ms, 25m	55	30	34	12	16	2
	1”, 2ms, 25m	25	10	8	1	1	0.08

Table 8-2: SCAO Strehl ratio (%) with the visible wavefront sensor

	Wave band	K-band		H-band		J-band	
	Guide star magnitude	K=9	K=12	K=9	K=12	K=9	K=12
seeing, r_0, L_0 @ 0.5µm	0.53”, 3ms, 25m	57	33	37	14	17	3
	1”, 2ms, 25m	27	14	10	3	1	0.2

Table 8-3: SCAO Strehl ratio (%) with the infrared wavefront sensor

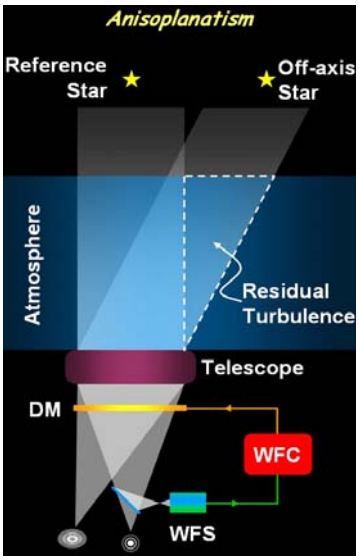

Figure 8-3: Limited corrected FoV due to anisoplanatism in the SCAO concept

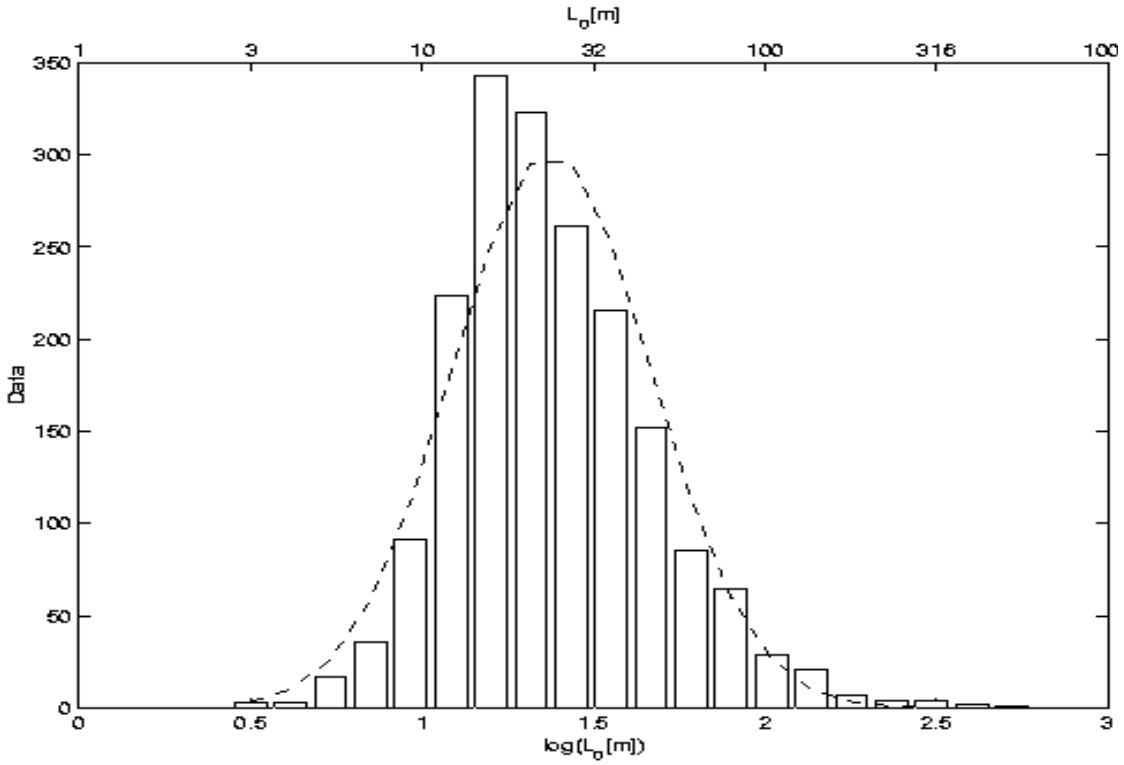

Figure 8-4: Statistical distribution of the outer scale

8.2.1.2 Implementation Concept

The SCAO concept is based on four key elements:

- The M6AM unit
- The Shack-Hartmann visible wavefront sensor
- The Pyramid Infrared wavefront sensor (option)
- The Real Time Computer

8.2.1.2.1 M6 Adaptive Mirror unit

The M6AM unit forms part of the telescope optical train and is tilted with respect to the ground. It is therefore conjugated conjugated to A= + 48.8 m (center), B= + 552 m, C= - 475 m, with A, B, C as shown in Figure 8-5, with positive values “above” the primary mirror, negative ones “below”.

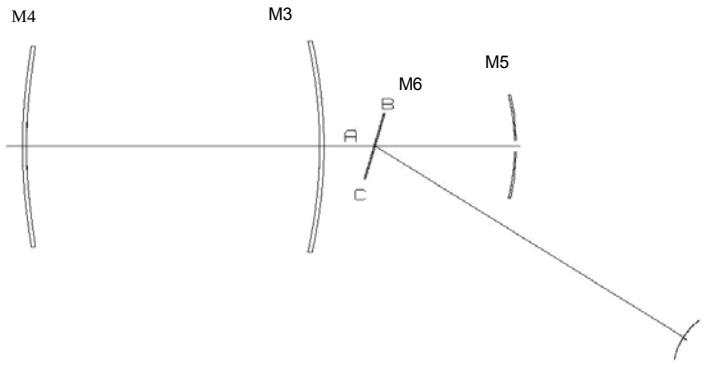

Figure 8-5: Conjugation altitudes of the M6AM unit

In addition to the Adaptive Optics correction, the M6AM unit will be capable of a tip-tilt motion about the mirror M6 vertex, in order to provide field stabilization with respect to the interface with instrumentation.

The mirror design and technology will preferably be based on a single, monolithic shell. A segmented geometry of the adaptive mirror, with six petals at 60^{o} and a maximum inter-petal gap of 15 mm may be considered as an alternative with a metrology for real-time phasing of the petals.

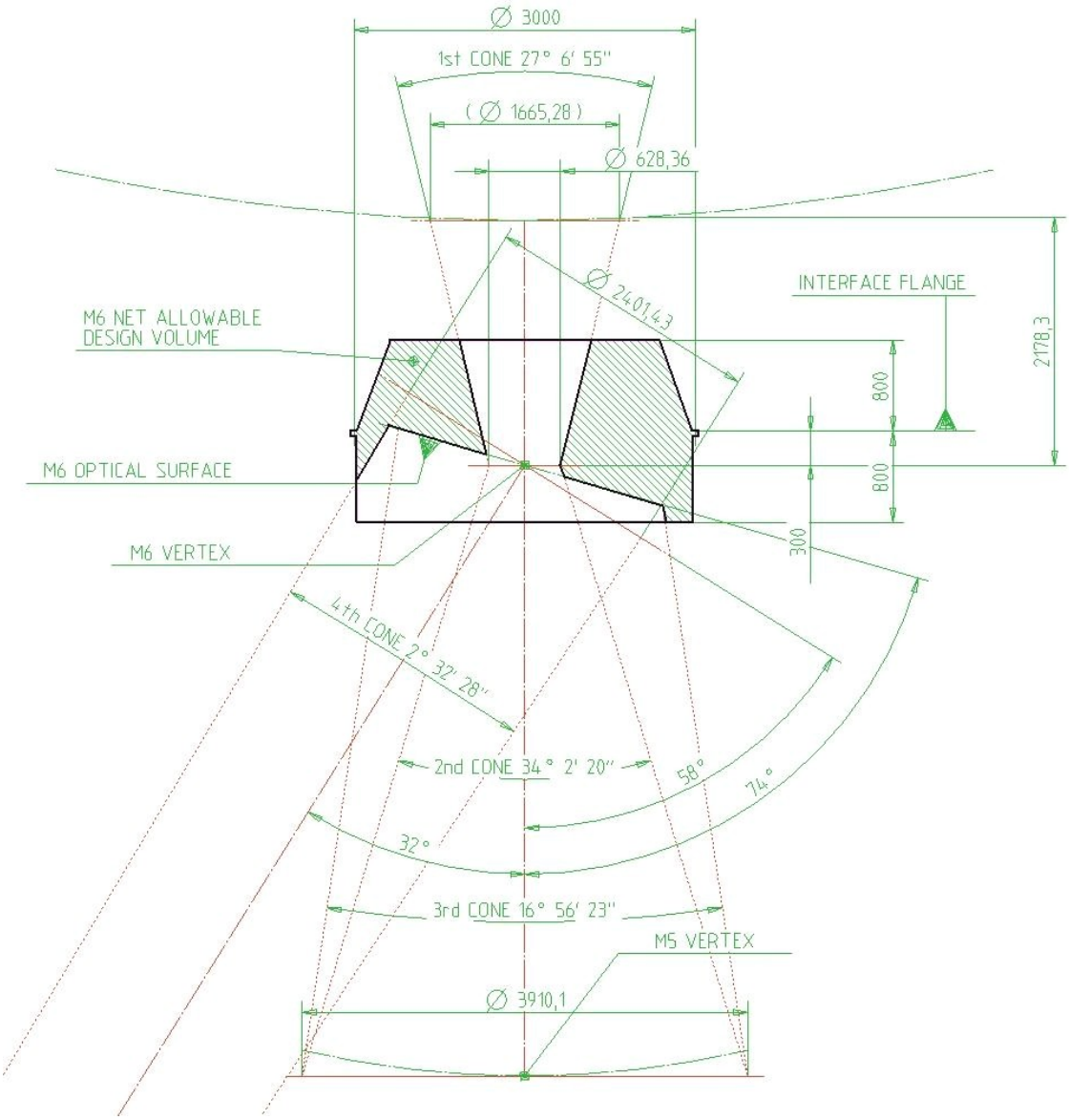

Figure 8-6: Geometrical characteristics of the M6 Adaptive Mirror

The detailed specifications of the M6AM unit are provided in RD23. The M6AM unit has a flat deformable mirror with an annular elliptical diameter of 2.6 x 2.4 m (tilted by 17º) and a linear central obscuration of 35%. The M6 actuator pitch is ~25 mm corresponding to ~1 m sub-aperture projected on the primary mirror of OWL leading to 6670 active actuators in the pupil - 98 actuators across the pupil-. This choice is a trade-off between the performance -from the experience acquired at ESO with NAOS and MACAO, the number of degrees of freedom and the technological steps to be achieved in the field of Large Deformable mirror (see section 8.2.1.4.3).

An important parameter of a deformable mirror is the total and inter-actuator mechanical stroke. For OWL this strongly depends on the outer scale of turbulence L_0 which reduces dramatically the amplitude of the disturbances and low spatial frequencies and therefore reduces significantly the mechanical stroke. For the specification of the mechanical stroke a pessimistic seeing of 1.5" (median value ~ 0.75" TBC) and L_0=100m (median value 25m) has been assumed at this stage: this is justified by the variability of these parameters during the nights and the rapid decrease of performance when the actuators are out of range. Nevertheless, these assumptions may be relaxed if it appears the M6AM requirements are too challenging. Assuming the von Karmann model is valid and adding 20% of stroke for the correction of the telescope residual aberrations, the total and inter-actuator mechanical stroke are respectively 90 µm and 6 µm excluding Field Stabilization.

The modal response time of the M6AM unit -for a stroke of ± 3µm- is specified to 1-2 ms at 90% respectively 95% of the command with a maximum overshoot of 10% of the command.

Figure 8-7 provides an overview of the control scheme of the M6AM unit and its interface to the external world in particular its interaction with the active optics. Actually, the Adaptive Optics will correct for all wavefront errors measured by the wavefront sensor. To avoid saturation of the AO WFS, it is necessary to off-load the large amplitude low temporal frequency to the active optics as shown Figure 8-7.

The M6AM unit will also be operated when AO is not required. In this mode the M6AM unit will provide either field stabilization or simply an optimum optical surface to the telescope. The flat vector of the M6AM is calibrated and can be applied to the unit in active mode. A local metrology loop makes sure the shape of the M6AM is maintained during operation.

Thanks to the outer scale effect the atmospheric tip and tilt is essentially inexistent and most of the Field stabilization specification comes from the telescope motion. The large amplitude requirements at low temporal frequency (<1Hz) is expected to be corrected with a tip-tilt stage while the high temporal frequencies might be corrected by the glass shell leading to a P-V stroke at the edge of 300µm. The dynamic aspect of the unit is currently under study.

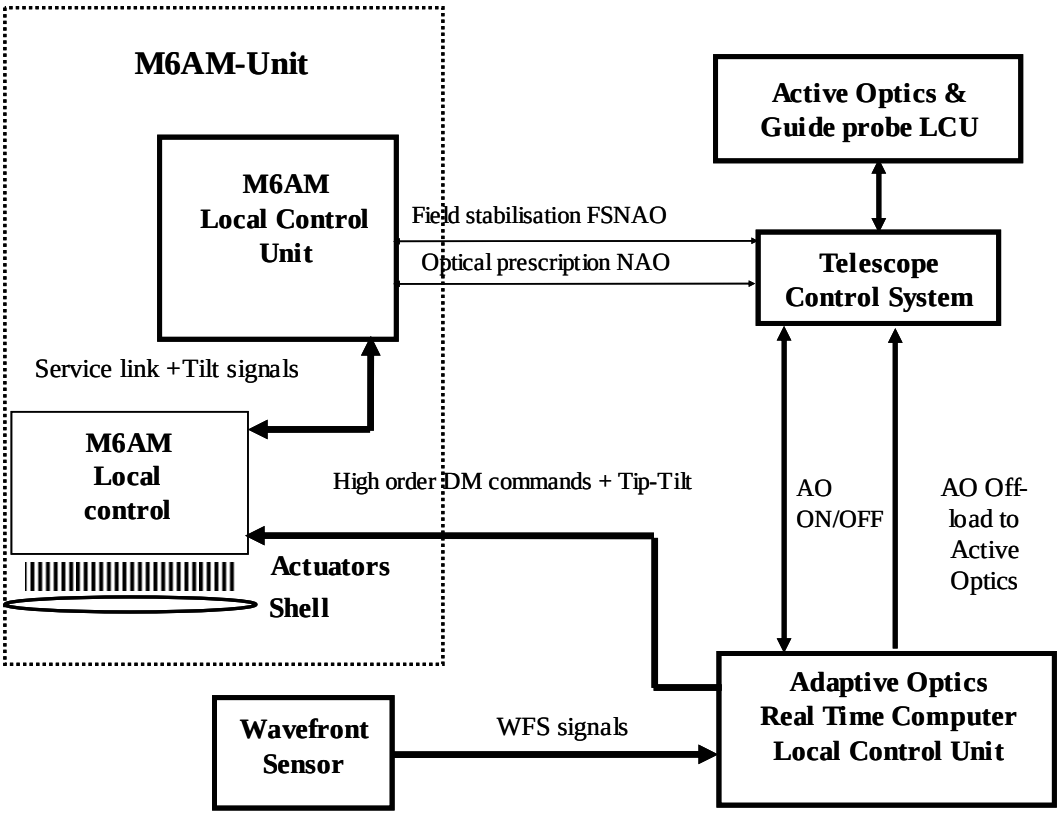

Figure 8-7: Control scheme of the M6AM unit and interface with the active optics.

8.2.1.2.2 Visible wavefront sensor unit

As a baseline, the wavefront sensor is a Shack-Hartmann with 97 x 97 sub-apertures and will be installed in the OWL adapter. A pick-up arm will allow acquiring the Natural Guide Star (NGS) within the central 2' FoV. The input optical beam is F/6.03 (2.920 mm/arcsec) and the pick-up arm will be located at 50-150 mm before the telescope focal plane. The pick-up arm will be equipped with a dichroic mirror reflecting the visible light toward the wavefront sensor and transmitting the infrared light for the instrument with a high efficiency (see Figure 8-8). The dichroic will be shaped in order to reduce the induced astigmatism when the convergent beam pass through it. The focus shift of the dichroic can be taken over by the science instrument or compensated by the WFS by changing the reference slopes. In general the non common path aberrations produced by the dichroic can be eliminated by applying static offset to M6AM measured with an independent method (for example phase diversity). This process has to be implemented for each science wavelength.

This pick-up arm will allow us to correct the differential atmospheric refraction between the observing wavelength and the effective wavelength of the wavefront sensor NGS. The tracking accuracy of the pick-up arm should be better than a fraction of the diffraction limit in J band: 2mas/5 = 0.4 mas corresponding to 1.2 µm.

Since the output focus of OWL is not telecentric, the pick-up arm displacement should have a concave trajectory such as the re-imaging of the M6 mirror always matches the lenslet array for all field positions. The amplitude of the angle along the trajectory (0-3 arcmin) is 0-2.1 degrees; the accuracy required on this trajectory is ±3" (corresponding to a pupil mismatch 1/50th of an actuator spacing).

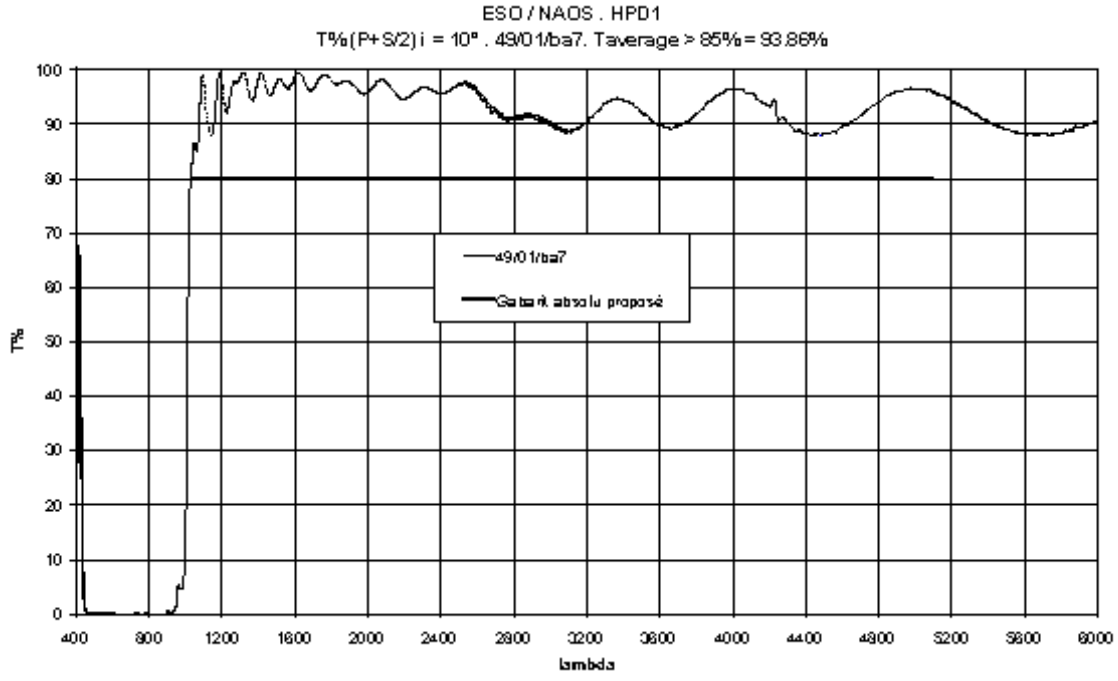

Figure 8-8: Transmission of the wavefront sensor pick-up dichroic

To correct for the convex field curvature of the OWL focal plane the wavefront sensor should be equipped with a focusing stage with a range provided in Figure 8-9.

To compensate for pupil rotation -M6 rotating with respect to the lenslet array- the wavefront sensor design will include an optical derotator. This optical derotator should have a rotation accuracy of ±0.02 degree (corresponding to a pupil mismatch of 1/50th of the actuator pitch). Wobble and run out of the optical derotator should be limited to another 1/50th of the actuator pitch. Pupil derotation by software is not envisaged at this stage because of the additional computing power required and complexity.

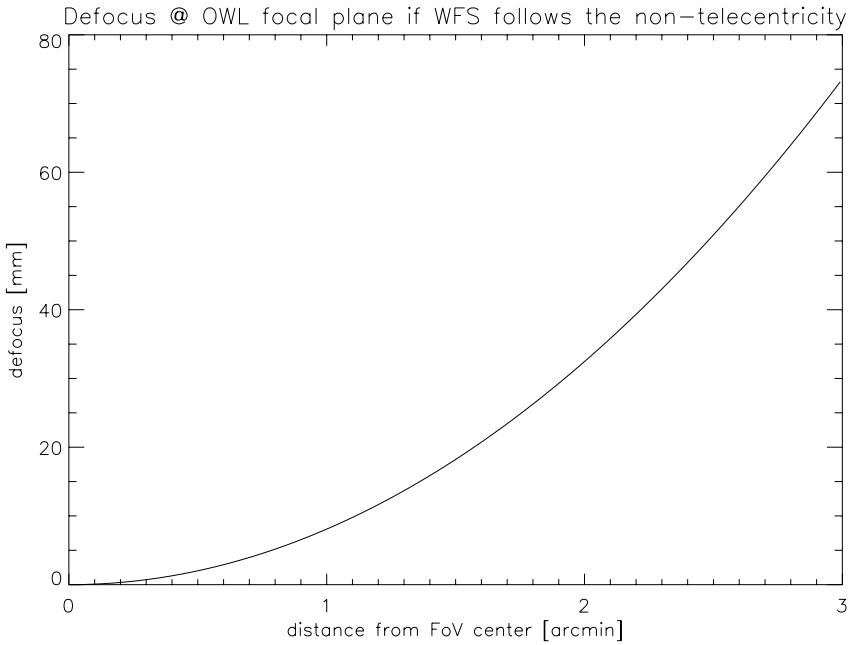

Figure 8-9: Defocus of the wavefront sensor versus field position

We expect that the mechanical flexures between the M6 Adaptive Mirror unit and the wavefront sensor pupil plane will contribute to another 2/50th of an actuator pitch maximum. The overall pupil mismatch will then be 1/10th of the actuator pitch leading to a Strehl reduction of 2% in K band.

The atmospheric dispersion within the band pass of the wavefront sensor - [450-900nm] - should be corrected with an Atmospheric Dispersion Compensator (ADC) for three reasons:

- spot elongation reduces the centroid accuracy in one direction
- spot elongation reduces the wavefront sensor linearity range
- tilt measurement will depend on star spectral type and will vary with zenith distance

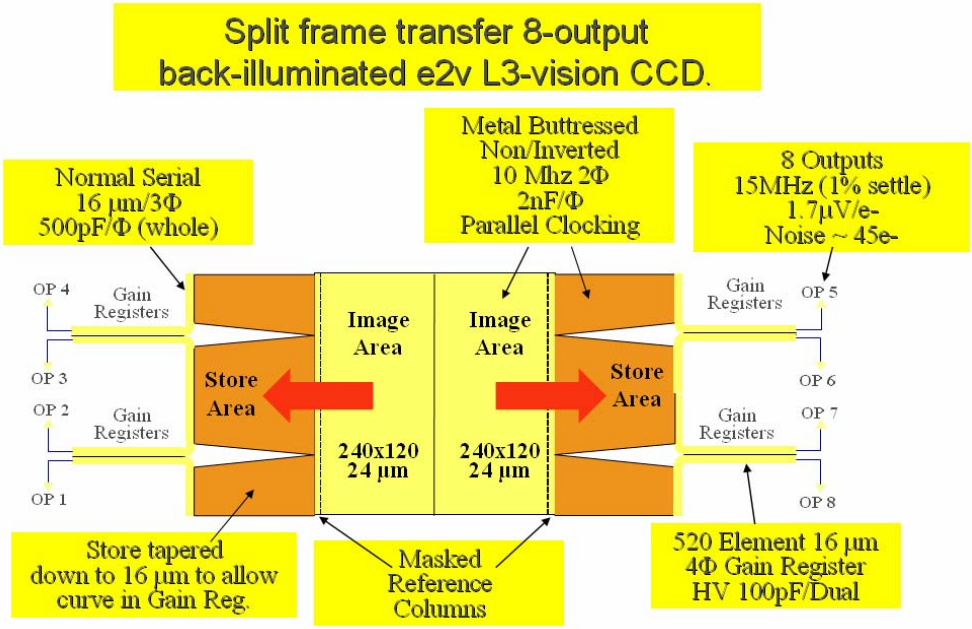

Figure 8-10: Technology concept of the WFS L3CCD detector

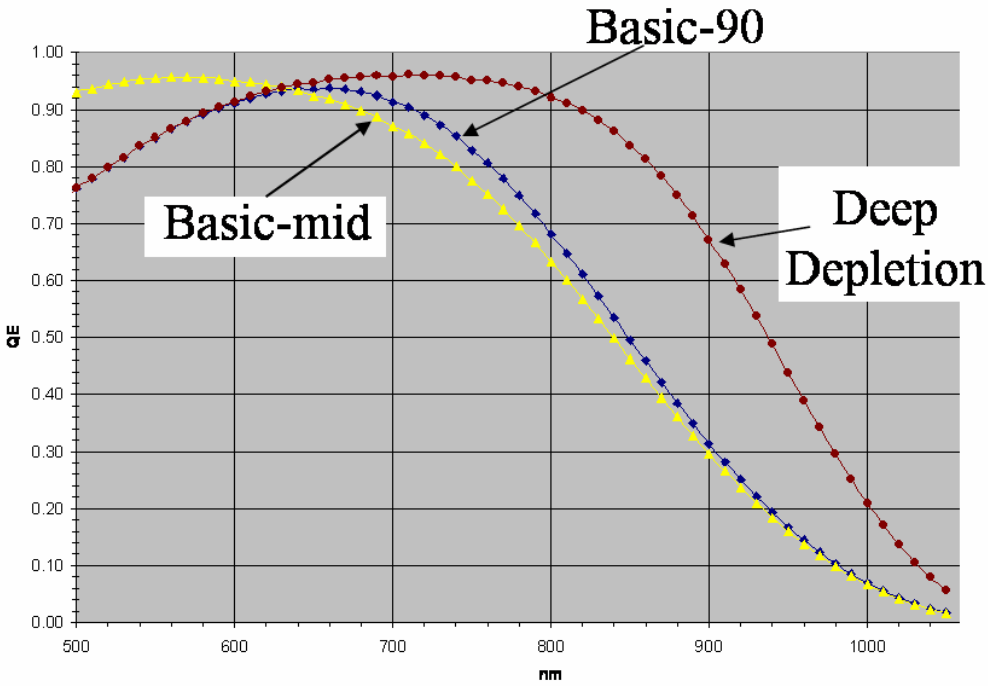

Figure 8-11: Quantum Efficiency with deep depletion enhancement in the red

To avoid pupil chromatism (and actuator-lenslet array mismatch), the ADC should be located very close to the pupil plane. For short integration time –few minutes- it may be acceptable to set the ADC to the zenith position at the start of the observation and not rotate the ADC during the observation.

For the wavefront sensor detector, one option is to make use of the CCD detector from E2V currently developed in the frame of the second generation Adaptive Optics system for the VLT - Figure 8-10. This detector (RD25) has 240 x 240 pixels and can be read up to 1.5 kframes/s using 8 outputs.

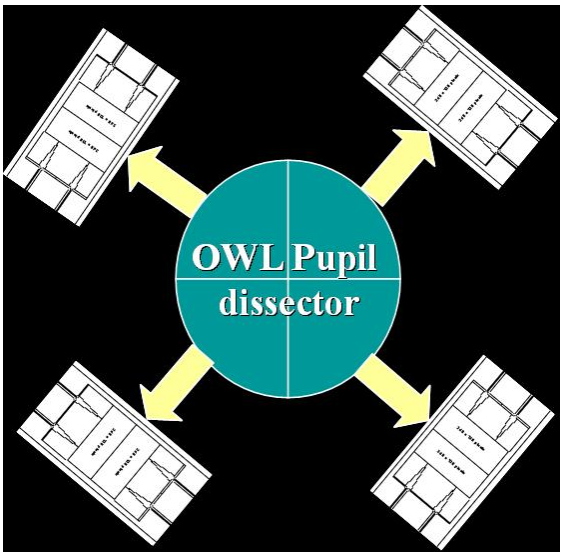

Figure 8-12: OWL pupil dissector for the Shack Hartmann wavefront sensor

It is based on the L3CCD technology using register amplification reducing the apparent Read-out Noise below $1e^-$. This detector technology has however amplification noise which is equivalent to a reduction in efficiency up to 2. A best effort contract is in place to complement

the excellent Read Out Noise (RON) performance with a deep depletion technology – see Figure 8-11- which will enhance the red response of such detector. Most of the Natural Guide Stars are very red and significant gain in limiting magnitude can be achieved with redder response.

However, the 240x240 pixels fast low noise CCD will not be large enough for the SCAO system of OWL. One way around is to implement on optical beam splitter which will send one quarter of the OWL pupil to each CCD detector equipped with its own lenslet array - Figure 8-12.

Alternatively, an extension of the present technology to 582x582 pixels - 6x6 pixels per sub aperture- possibly with a large pixel - 50µm - will need to be developed. For stability and compactness reasons, this option seems achievable and preferable at this stage.

The Shack-Hartmann will have 6x6 pixels per sub apertures with a pixel scale of about 0.4"/pixel (TBC) equivalent to a wavefront sensor FoV of 2.4" and to a magnification factor γ=0.03425. In this case the pupil size will be 29.1mm, sub aperture size 300 µm, the pupil re-imaging lens will have a focal length of 175 mm and the lenslet array focal length will be about $f_{\mu l}$=6mm (F/ratio=20).

Figure 8-13 shows an overview of the wavefront sensor design for SCAO.

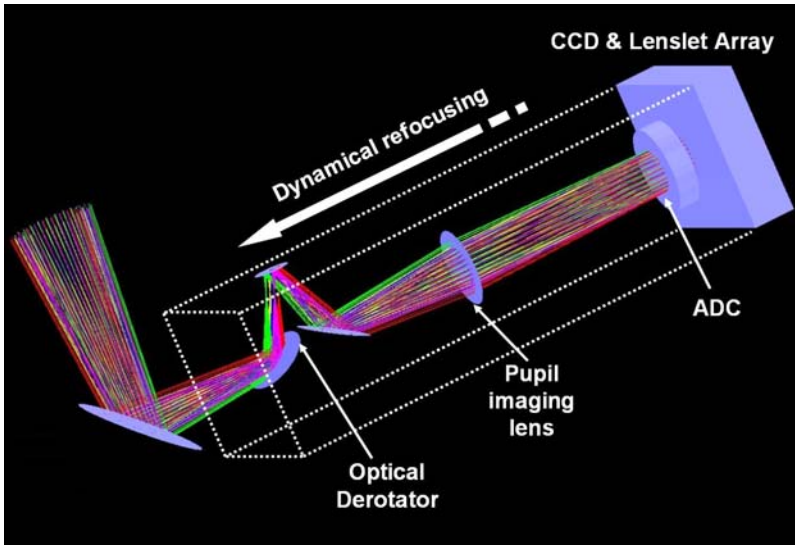

Figure 8-13: Shack Hartmann wavefront sensor concept

8.2.1.2.3 Infrared Pyramid WFS

The IR pyramid wavefront sensor is based on the concept of re-imaging the telescope pupil "filtered" by a refractive pyramid located at the OWL focal plane. In the near IR, the pyramid WFS benefits from the AO correction, and an (almost) diffraction limited spot is sent to the vertex of the pyramid, which makes the WFS process much more linear. This is not true in the visible, where non-linearities of the pyramid are much more severe (see RD26 for a more thorough analysis). As shown in 8.2.1.3, the performance if an (infrared) pyramid WFS is theoretically significantly better than that of a Shack-Hartmann, in terms of propagated aliasing. The depth of the aliasing "basin" is much larger, which is beneficial to some science cases (like high contrast imaging).A curvature sensing scheme was not considered because of the very high noise propagation coefficient for low order modes (f^{-4} on curvature, f^{-2} for SH).

The pyramid located at the focal plane acts as a 2-dimensional knife-edge spatial filter which produces four pupil images containing the information on the wavefront phase. The pupil sampling is 97 x 97 sub-apertures.

As in the Shack Hartmann wavefront sensor the infrared pyramid wavefront sensor is either installed on the OWL adapter or close to the instrument using reflection off the entrance window for instance. In case the infrared Pyramid wavefront sensor is installed in the adapter, a pick-up arm will acquire the NGS within the central 2 arcmin FoV. The input optical beam is F/6.03

(2.920 mm/arcsec) and the pick-up arm will be located at 50-150 mm before the telescope focal plane. The pick-up arm will be equipped with a dichroic mirror splitting the IR light (e.g. from 1.0 to 2.5 μm) between the wavefront sensor and the infrared instrument. The dichroic will be shaped in order to reduce the induced astigmatism when the convergent beam pass through it. The focus shift of the dichroic can be taken over by the science instrument or compensated by the WFS by changing the reference slopes. In general the non common path aberrations produced by the dichroic can be eliminated by applying static offset to M6AM measured with an independent method (for example phase diversity). This process has to be implemented for each science wavelength.

This pick-up arm will allow us to correct for the NGS field rotation and for the differential atmospheric refraction between the observing wavelength and the effective wavelength of the wavefront sensor NGS. The tracking accuracy of the pick-up arm should be better than a fraction of the diffraction limit in J band: 2mas/5 = 0.4 mas corresponding to 1.2 μm.

Since the output focus of OWL is not telecentric, the pick-up arm displacement should have a concave trajectory such as the re-imaging of the M6 mirror always matches the sub apertures or pixel of the pyramid wavefront sensor for all field positions. The amplitude of the angle along the trajectory (0-3arcmin) is 0-2.1 degrees; the accuracy required on this trajectory is ±3" (corresponding to a pupil mismatch $1/50^{th}$ of an actuator spacing).

To correct for the convex field curvature of the OWL focal plane the wavefront sensor should be equipped with a focusing stage with a range provided in Figure 8-9.

To compensate for pupil rotation -M6 rotating with respect to the IR detector- the wavefront sensor design will include an optical derotator. This optical derotator should have a rotation accuracy of ±0.003 degree (corresponding to a pupil mismatch of $1/50^{th}$ of the actuator pitch). Wobble and run out of the optical derotator should be limited to another $1/50^{th}$ of the actuator pitch. Pupil derotation by software is not envisaged at this stage because of the additional computing power required and complexity.

We expect that the mechanical flexures between the M6 Adaptive Mirror unit and the wavefront sensor pupil plane will contribute to another $2/50^{th}$ of an actuator pitch maximum. The overall pupil mismatch will then be $1/10^{th}$ of the actuator pitch leading to a Strehl reduction of 2% in K band.

As in the case of the Shack-Hartmann, and ADC is implemented to correct for atmospheric dispersion and be in a diffraction regime in closed loop in the Near Infrared (NIR) where the expected gain of the pyramid is expected.

As a baseline no pyramid modulation (i.e. fast shifting of the pyramid perpendicularly to the optical axis) is foreseen. Further theoretical and experimental studies are required to confirm this choice.

In order to keep low the thermal background given by refractive elements in the optical path of the WFS, the pyramid and the pupil re-imaging lens will be included in a cryostat with the IR detector.

The IR detector characteristics assumed for the performance estimate are those defined for the Calico-MUX development funded by Caltech and ESO (see Table 8-4). We expect that significant progresses can be achieved on this kind of component if resources can be invested in this development. With the current specifications four infrared detectors would be needed and a pupil dissection system should be implemented as in the case of the Shack Hartmann wavefront sensor - Figure 8-12. Alternatively a 240 x 240 format needs to be developed in order to locate all four pupil images on the same infrared detector.

The infrared pyramid wavefront sensor FoV is 2 arcsecs (5.8 mm) and a pupil re-imaging lens of 23.9 mm focal length is required for generating four pupils of 3.88 mm on the infrared detector – detector pixel assumed here is 40μm corresponding to one sub aperture-. The angle between the faces of the pyramid is 37 degrees in order to allow the four pupil images to be separated by ~40 pixels. The equivalent focal length of the pupil re-imaging lens is ~F/2, within the range of feasibility of normal lenses.

Figure 8-14 shown the implementation concept for the IR Pyramid WFS.

Parameter	Specification	Goal/Comment
Format	128 × 128	Design iterations to 512 × 512
Operating temperature	~ 80 °K	Goal cooling without liquid N2
Spectral range	0.80-2.3 μm	Actual spectral range of delivered FPAs will depend upon available assets but it will have NIR/SWIR cutoff wavelength
Pixel pitch	40 μm	-
Frame rate	800 Hz @ 128 × 128 1.5 kHz @ 2 × 2 window	8 outputs @ 3 MHz easily achieved
Read noise	< 1 e^- @ 250 fps < 5 e^- @ 500 fps < 7 e^- @ 800 fps	Prototype goals is < 5 e^- rms @ 800 fps
Well depth	TBD	Goal >> 10^4 e^-
Dynamic range	TBD	Goal > 5000
Quantum efficiency λ = 1.25 μm (J band) λ = 1.65 μm (H band) λ = 2.2 μm (K band)	 > 50% > 60% > 65%	Conservative numbers specified: with AR coating the quantum efficiency will be 10% higher than in non-AR coated devices
Uniformity	± 10%	-
Dark current	< 1 e^-/sec	< 0.1 e^-/sec
Operability	> 98%	> 99% goal
Cluster outages	-	Goal no cluster
Nonlinearity	-	Best effort goal: calibratable nonlinearity < 1%
Self emission dark count	Not to degrade the specified read noise by more than 10%	Expected to be <<1000 e^-/read
Power dissipation	< 100 mW	Goal < 40 mW

Table 8-4: Requirements for the Calico- Mux development funded by Caltech and ESO

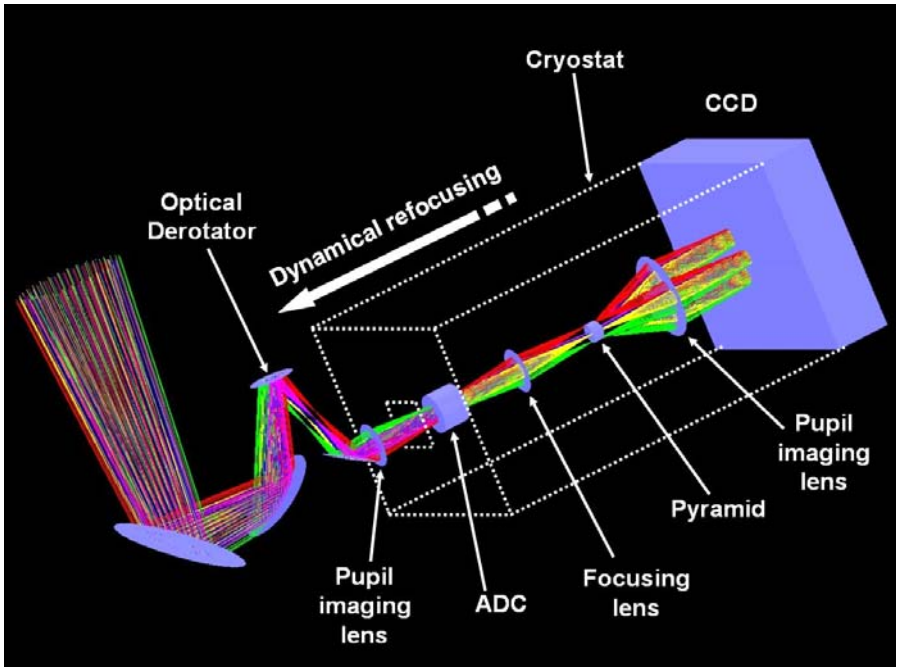

Figure 8-14: Pyramid wavefront sensor concept

8.2.1.2.4 Real Time Computer (RTC)

The proposed design for the Real Time Computer (RTC) is based on the SPARTA concept which is presented later in section 8.2.1.4.6. SPARTA is the platform that provides the RTC for all the AO instruments for OWL. In this paragraph we only present the relevant information for the SCAO system. More information can be found in [RD25].

SCAO is a single-sensor / single-mirror system with two architectural options: a Shack-Hartmann system and a Pyramid-based system. In both cases the deformable mirror will be the M6AM, which features a grid of 98x98 actuators. The detector technology is also common and it will be based on a 588x588 CCD, readable at 1.5 KHz. In both cases the loop frequency considered will be 500Hz and the maximum tolerable Real Time Computer delay will be of 10% of the loop frequency.

The architecture we will use is based on a hybrid structure where a chain of ***F**ield-**P**rogrammable **G**ate **A**rray* (FPGA) chips will create the hard real-time backbone that will compute the matrix-vector product, while on-board CPUs (Central Processing Unit) will monitor the system. The computational unit is based on a dual FPGA plus dual CPU system. The technology is available today: a board like this is already on the market, but it is not using the latest powerful chipset. We will assume that a new version of the same board uses the latest and most powerful chipset, commercially available but not yet integrated in off-the-shelf boards. Each CPU will feature a 10Gb/s optical input to receive the input stream. One FPGA in the board will be used to process the input stream, the second to process the matrix-vector computation, for one quarter of the input stream.

A fast internal bus (10Gb/s or more in the future) will let the FPGA chips exchange information. The last board will have an additional optical output to send the final results to the DM. The FPGA on this board will collect the results from all the other, compute the control signals and send the results to the DM.

The Real Time Computer delay of this architecture will be almost zero, i.e.: the computation can be completed before the next frame starts to be read-out. In this estimate we consider that FPGA-to-FPGA communication time is very fast: the amount of data that the chips need to exchange is rather low, consisting of partial controls.

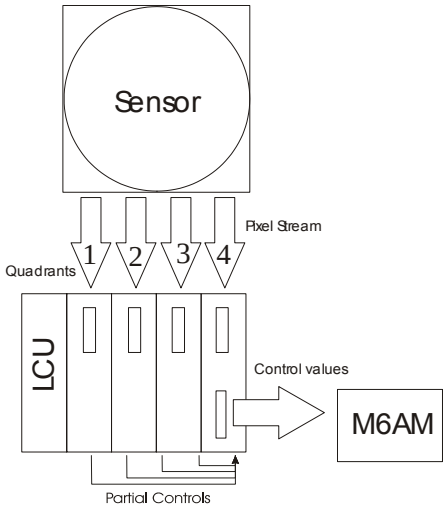

Figure 8-15: SCAO Shack Hartmann or Pyramid Real-time architecture

In the pyramid wave-front sensor case, the number of pixels to read out is smaller by a factor 4 to 9. Exploiting the faster read-out and using the same hardware, one can improve the RTC performance, i.e.: the computation can finish earlier by the amount of time saved in the read out. However, if one dimensions the Real Time Computer to complete in the same time as for the previous case (same performance) a significant saving can be achieved in the real time core, from 30% to 50% of the hardware cost, depending on the detector read-out architecture. While it is more difficult to assess what would be the effect on to the remaining functions a reasonable estimate is that hardware cost savings of a pyramid-based system will be around 15% to 20%.

Architecture of the Real-Time Control Computer is provided Figure 8-15.

8.2.1.3 Predicted performance

A detailed analysis of the SCAO performance based on end-to end simulations as well as the assumptions and AO parameters are provided in RD25. Note that the SCAO performances provided here do not include yet all error sources -calibration errors, optical quality of the telescope, wavefront sensor and instrument optical paths, mis-registration error, atmospheric chromatism etc…- but only the pure AO performance part. In the SCAO mode, the impact of all error sources on the final SCAO performance can become significant. It is planned to perform a full error budget of the SCAO system during phase B.

8.2.1.3.1 Visible Shack Hartmann wavefront sensor

In the following we provide the performance of the SCAO using a visible Shack Hartmann wavefront sensor for both the “good” and “bad” seeing conditions” respectively r_0~20cm and r_0~10cm -0.53” and 1” seeing at 0.5 µm.

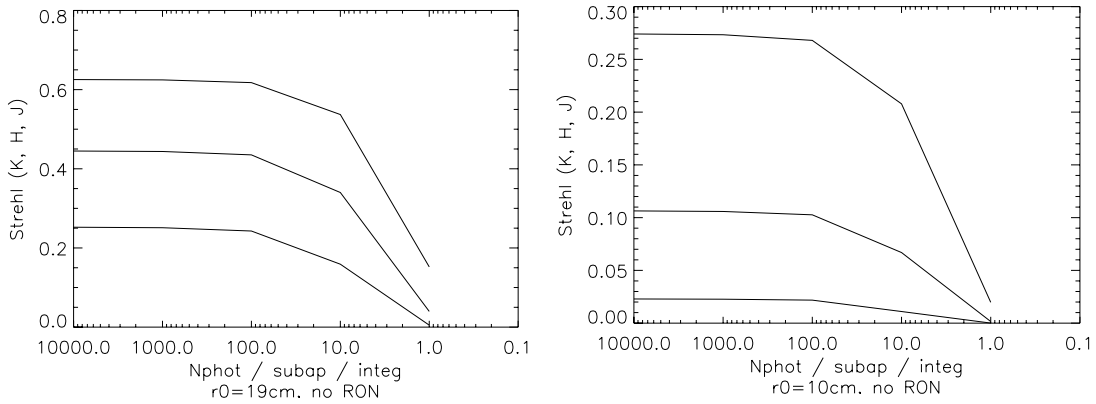

Figure 8-16: Strehl vs. Magnitude for the SH-WFS (without RON), in K, H, J bands (top to bottom), for the good seeing model (left) and bad seeing model (right). Results are on-axis

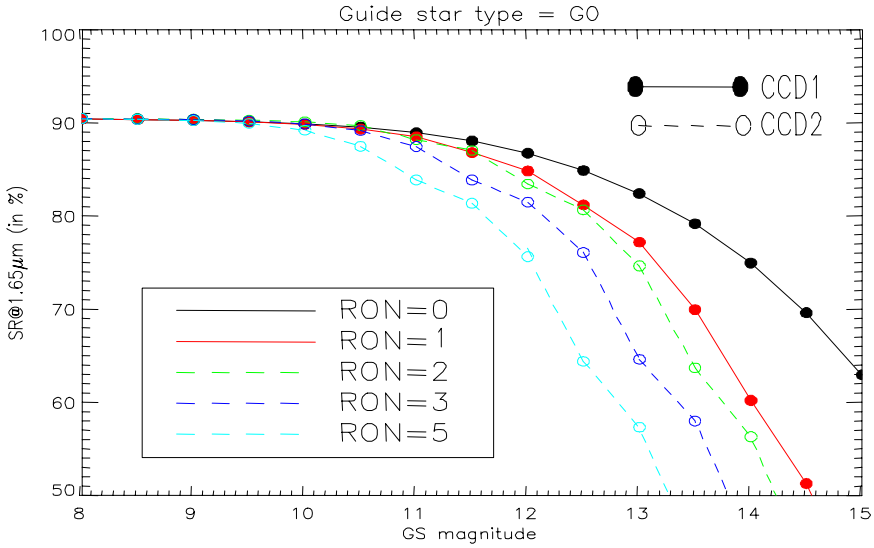

Figure 8-17: VLT Planet Finder performance for different Readout Noise

Figure 8-16 provides the Strehl versus the number of photons per sub aperture and integration time –frame rate is 500Hz- for different NIR wavelengths. 1 Photon/sub aperture/frame

corresponds Mv=17.5 for a G0 star. This limiting magnitude and the Sr(K)=15% are quite consistent with the performance obtained with the MACAO and NAOS systems under good seeing conditions. MACAO using Avalanche Photo Diode (APD) detectors without Readout Noise should in principle behave like SCAO with the L3CCD for low magnitude stars – note that the Quantum Efficiency band pass, especially the red response, and the peak response is higher for the L3CCD than for the APD but as mentioned earlier the excess noise due to the amplification gain limits this advantage. Extensive simulations performed in the frame of the VLT Planet Finder study show that no Readout Noise is always better than excess noise and not fully optimized red response.

Figure 8-18 provides the Ensquared Energy versus the pixel size for near infrared wavelengths in case a spectroscopic mode is intended to be used behind SCAO. From these curves, we see that 50% of the energy can be concentrated into a pixel of 10 mas under good seeing conditions.

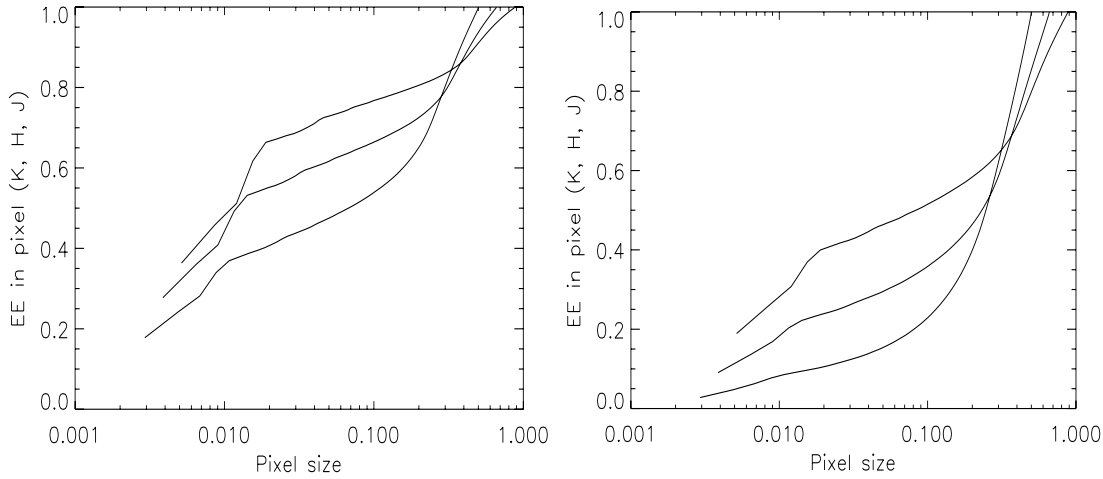

Figure 8-18: Ensquared Energy versus pixel size (K-H-J; top to bottom), for good seeing (left) and bad seeing models (right). Bright stars are considered.

The anisoplanatism effect for our two considered atmospheric models can be seen in the curves below. We can see that in good seeing, 50% of the Strehl is lost in the K band at a distance of ~30'' (radius). In bad seeing, this number drops to less than 20'' (radius).

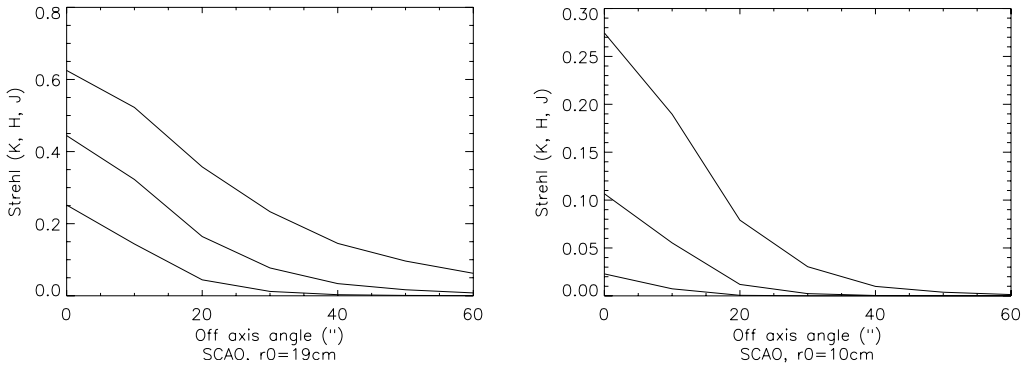

Figure 8-19: Affect of anisoplanatism on the performance of the SCAO system, in K, H and J bands (top to bottom), in good seeing model (left), and bad seeing (right).

8.2.1.3.2 Infrared Pyramid Wavefront sensor

In the following we provide the performance of the SCAO using an Infrared Pyramid wavefront sensor for both the "good" and "bad" seeing conditions" respectively r_0~20cm and r_0~10cm - 0.53" and 1" seeing at 0.5 µm: Figure 8-20. Two cases have been studied: infrared detector

without readout noise and with a more realistic 5e$^-$ readout noise. The performance curves show a dramatic drop of the Strehl for faint magnitude star due to the Readout noise. Note that the sky background in H band –mH~14.5- will be the limiting factor in the case of a noiseless near infrared detector. Some improvements is expected for faint stars in the case of the RON=5 if a larger pixel scale is used – this was used for NAOS to increase the limiting magnitude with the two set of lenslet array-. The Strehl ratio performance using the pyramid wavefront sensor is slightly higher than in the case of the Shack Hartmann wavefront sensor. Figure 8-21 shows the corrected Point Spread Function (PSF) image with the reduction of the aliasing in the area corresponding to the 1/actuator pitch. Figure 8-22 provides the Ensquared Energy after correction quite similar to the Shack Hartmann case.

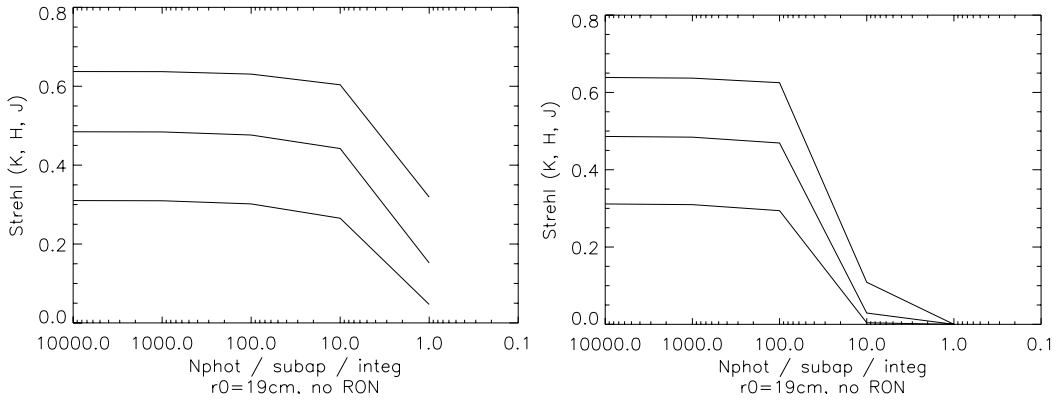

Figure 8-20: Strehl vs. Magnitude for the IR PYR (without RON on the left, 5e- ron rms on the right), in K, H, J bands (top to bottom), for the good seeing model. Results are on-axis.

Figure 8-23 shows the simulated deformable mirror shape during closed loop operation. The artifacts near the centre are probably due to diffraction effects in the area close to the telescope central obstruction. The exact explanation for this problem is not yet fully understood at this stage. We intend to continue the detailed simulations activities in the frame of the ELT design study as well as some complementary work on our High Order Test bench developed in the frame of OPTICON-JRA1.

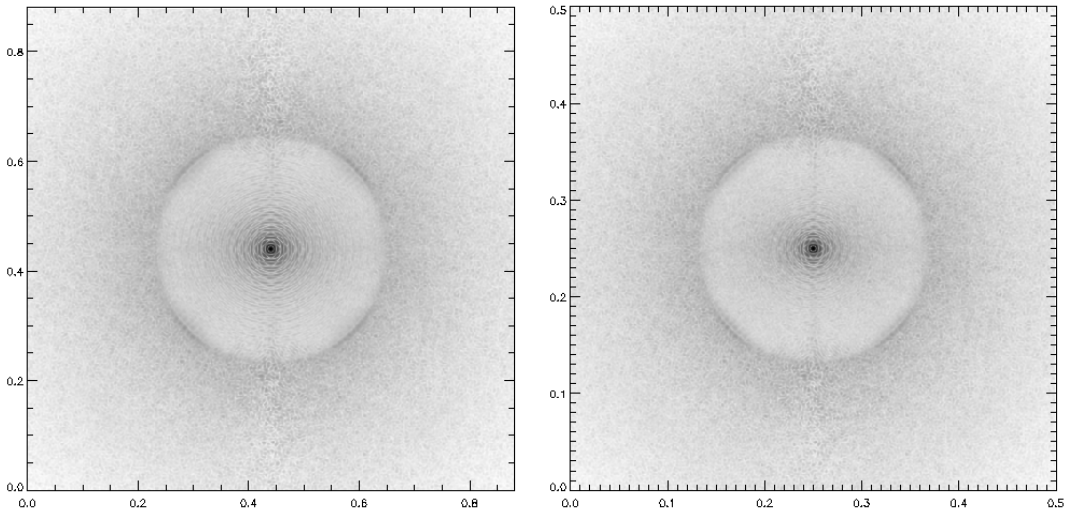

Figure 8-21: Long Exposure PSF with 10000 ph/subap/integ (bright NGS), for the K band (left) and J-band (right). Both pictures are on-axis. Stretch is logarithmic.

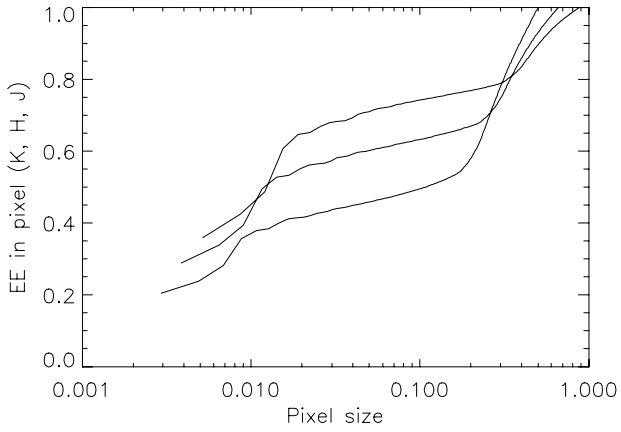

Figure 8-22: EE vs. pixel size, in the K, H and J bands, good seeing, and bright guide star.

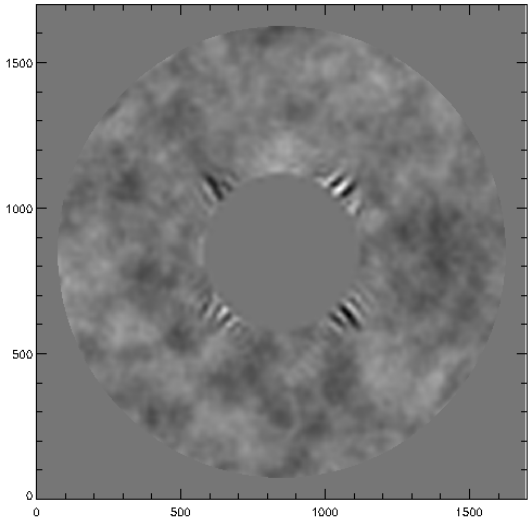

Figure 8-23: Shape for the DM during closed loop. The "spikes" near the telescope central obstruction, created by diffraction effects on the PYR WFS.

8.2.1.3.3 Performance at 10 microns and beyond

In the frame of the Mid-Infrared imager instrument (TOWL) presented in section 12.2.3.6, the performance of SCAO has been simulated.

Figure 8-24 provides the Strehl versus observing wavelength for good seeing conditions and a bright reference star. We see the Strehl ratio is essentially above 90 % longward of 5 micron. Figure 8-25 shows the Point Spread Function (PSF) at 2.2, 5 and 10 microns. Important point to note is the significant gain of contrast in the so-called “circle of correction” close to the PSF peak when the Strehl ratio is at 95%.

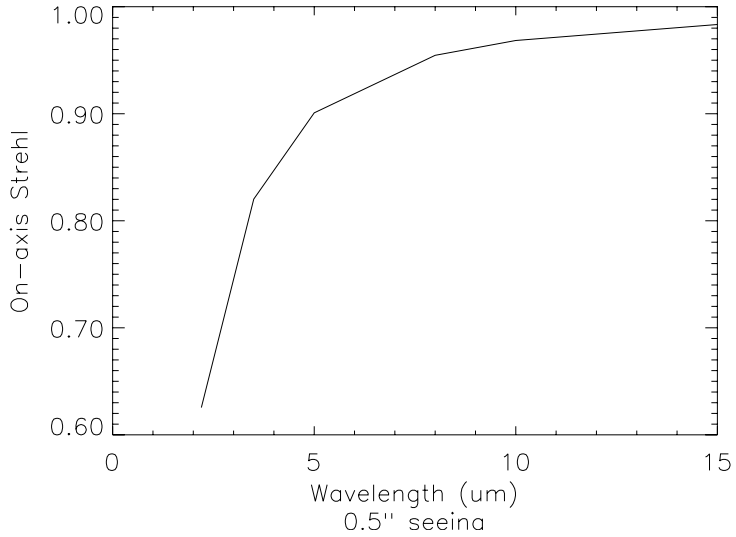

Figure 8-24: On-axis strehl versus wavelength for a bright reference star

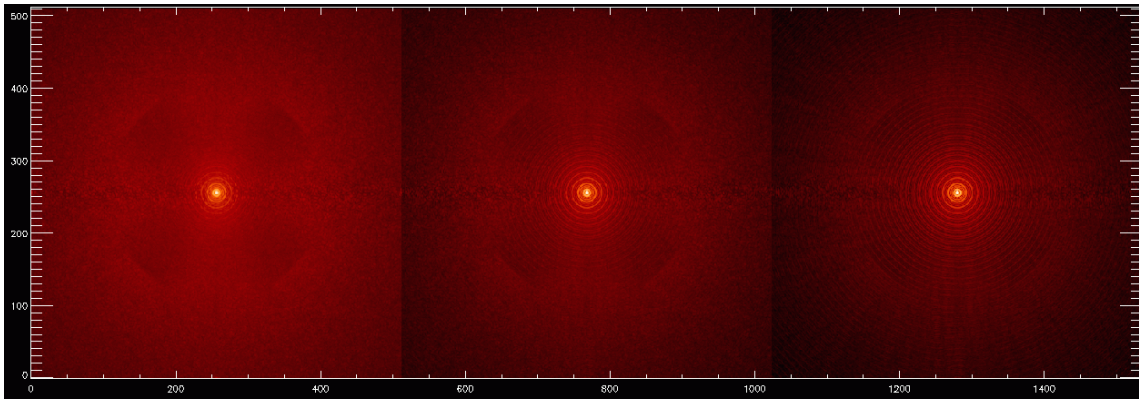

Figure 8-25: Point Spread Functions obtained with SCAO. From left to right 2.2, 5 and 10 µm. Good seeing conditions, bright on-axis star.

8.2.1.3.4 Effect of the outer scale of turbulence on performance

Apart from the seeing and atmospheric correlation time τ_0, the outer scale of the turbulence is an important parameter to be considered for the simulation and AO design parameters in the case of an ELT.

Assuming a von Karmann model the outer scale of the turbulence essentially reduces the amount of turbulence to be corrected at low spatial frequencies. The direct effect is to dramatically reduce the deformable mirror stroke requirements at high spatial scale as shown in Figure 8-26 in the case of very bad seeing conditions.

Figure 8-27 shows the SCAO performance depending on the Outer scale in the case of the SH WFS system.

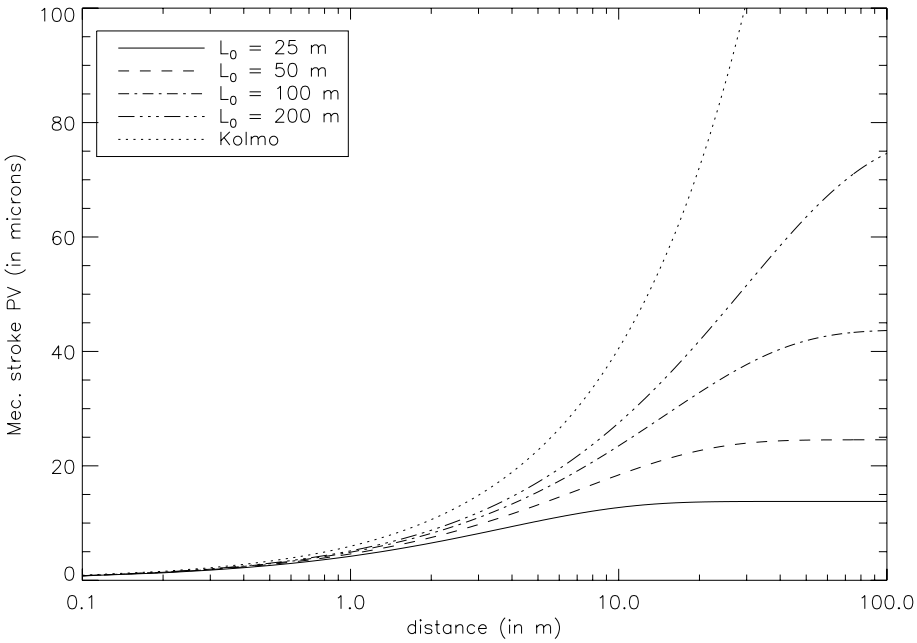

Figure 8-26: P-V DM mechanical stroke requirements versus spatial frequency for a seeing of 1.5" and different outer scales (Courtesy, T. Fusco-ONERA)

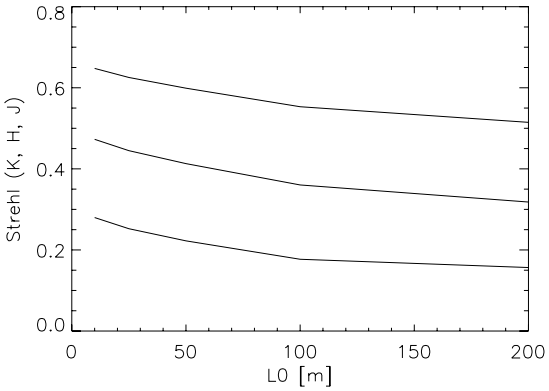

Figure 8-27: Strehl (on-axis) vs. L0, for the SH based SCAO system (good seeing), in K, H and J bands

8.2.1.4 Near-Term development plan

8.2.1.4.1 Modelling and Simulation

First order simulations have been performed to estimate the SCAO performances in near Infrared with a 98x98 actuator systems. Extensive parametric simulations remain to be done to tune the design parameters in particular:

- Optimization of the Shack Hartmann wavefront sensor geometry fitting the M6AM geometry (Circular, hexagonal, squared)
- Optimization of the Shack Hartmann wavefront sensor pixel scale and FoV
- Effect of wavefront sensor frame delays (depending on the wavefront sensor detector readout scheme) on performance for both wavefront sensors depending on the median τ0
- Study of the effect of the Deformable mirror- wavefront sensor lateral pupil matching for both the pyramid and Shack-Hartmann wavefront sensor
- Study of the diffraction effect on the Pyramid wavefront sensor

- Study of the pupil segmentation and cophasing error effects on the AO loop on performance
- Study of the variable M6AM conjugation altitude effect on the performance
- Optimization of the infrared wavefront sensor depending on the detector Readout noise and sky background
- Full error budget of the SCAO system
- Analysis of the differential atmospheric dispersion correction accuracy
- Analysis of the residual image motion after field stabilization in SCAO loop
- Effect of the atmospheric dispersion within the band pass of the wavefront sensor equipped with an ADC.

8.2.1.4.2 AO Concept and design

The detailed implementation of the SCAO wavefront sensors (visible Shack-Hartmann and Near Infrared Pyramid) into the OWL Adapter-rotator remains to be developed during phase B. Requirements and constraints for active and adaptive optics and for instruments need to be studied carefully and trade-offs analyzed in the context of the planned optical design iteration at the start of Phase B.

Accuracy of the wavefront sensor “Field Selector” functionality needs to be carefully analyzed. This is crucial in SCAO for the differential atmospheric dispersion compensation, for the Field stabilization and for the mosaicking capabilities.

The optimum wavelengths for the SCAO IR wavefront sensor s and the instruments will need to be reassessed in view of the selected instruments using SCAO: Commissioning instrument in Near Infrared, TOWL, first correction stage of EPICS, etc. This may require more than two SCAO wavefront sensors dichroic configurations in the adapter rotator. In some cases, like for the IR instrument TOWL, there might be some advantages to implement the wavefront sensors very close to or in the instrument itself to minimize the number of warm optical surfaces (for instance the dichroic as entrance window). The effect of the differential atmospheric refraction between the wavefront sensor NGS effective wavelength and the instrument observing wavelength may drive also these choices.

Compromises between the length of the wavefront sensor / instrument non-common optical path and the stability of the pupil matching should be studied. To correct for flexures, an internal metrology system may be required between the wavefront sensor and the instrument.

A feasibility and conceptual design for the M6AM is being developed based on the specifications provided in RD23 and will be available in the coming year. An extensive discussion of the currently available large deformable mirror technology is given in 8.2.1.4.3 based on the feasibility and conceptual design study performed for the VLT Adaptive secondary. The development of the VLT Adaptive secondary is an important element of our road-map securing and promoting this key technology in view of OWL.

The volume constraints due to the tilt of the M6AM unit may need special attention in particular for the positioning of the edge actuators. The large stroke and inter-actuator stroke requirements combined with the higher density of actuators will be carefully analyzed both in the frame of the feasibility study and the ELT design study. A trade-off between the glass shell thickness and material, the actuator force required and the power dissipated by the actuators will also be done. The field stabilization amplitude requirements – ±75” at f<0.1Hz – should be analyzed. Whether this should be produced by the shell itself or by a second stage tilt-tilt unit needs further investigation.

In case the required density of actuator appears not to be achievable in the time and budget allocated, a fall-back solution is envisaged, based on M6AM acting as a woofer plus a second stage post-focal deformable mirror (based e.g. on piezo technology with actuator spacing of ~ 4mm, extension of the VLT Planet Finder Deformable Mirror).

As in the case of the VLT Adaptive Secondary, a test facility will be designed for the extensive testing of the M6AM in the laboratory, first as a single unit then together with the rest of the

SCAO in closed loop. This test facility should also allow the testing of the other first generation AO modes like the GLAO and the MOAO modes (see section 8.2.2 and 8.2.3).

Simulations on both Shack Hartmann and pyramid wavefront sensors will need to be cross-checked experimentally on a dedicated test bench. The diffraction effect at the edge of the telescope central obstruction of OWL with the pyramid wavefront sensor will need to be studied experimentally. The segmentation and cophasing error effects on the final AO performance will also benefit from some experimental validation. The High Order Test bench developed in the frame of the VLT Planet Finder and OPTICON-JRA1 will be a good basis for these studies.

Accurate calibration of an Adaptive Optics system is crucial especially when using large deformable mirrors. In particular the measurement of the interaction matrix will require more investigations. Several solutions are being envisaged at this stage also in the frame of the VLT Adaptive secondary:

- Insert a calibration source at the focal plane close to M6 at the location of the central obstruction
- Perform synthetic interaction matrix using measured influence functions of the M6AM in the laboratory and calibration of the WFS optical path
- Perform on-sky interaction matrix measurements

Even if the synthetic interaction matrix is the most attractive solution (noiseless, simplicity, no calibration time required), it still has to be demonstrated that the accuracy of the models (DM and WFS) can be high enough to ensure the expected performance. In particular, the amplitude of the off axis static aberrations might be a problem.

Regarding the experimental estimation of the interaction matrix, novel techniques have to be investigated in order to deal with the new issues that we have to face:

- There is turbulent noise either because the calibration is performed on sky or because of the telescope internal turbulence. Indeed, the use of the calibration source at the focal plane may be limited by the internal turbulence of the telescope over long distances (M6AM unit-wavefront sensors) as already observed with MACAO at the VLT in which the calibration source is about 10 m from the wavefront sensor. Telescope flexures and optics drifts (temperature, gravity…) might also bias the measurement. Regarding the calibration of M5, it will have to be performed on sky since no artificial source will be available upstream.
- The calibration time may be long because of the large number of degrees of freedom.

Several methods are being investigated through simulations and laboratory tests as well as on sky tests when possible. The different schemes aim at minimizing the noise and bias on the measurement in order to optimize the quality of the reconstructor. Several modal bases (expansions) are under study to maximize the signal to noise ratio:

- Zonal: classical actuation of each Deformable Mirror electrode one after the other
- Hadamard: modal actuation of all electrodes at a given control voltage in order to maximize the signal in the Deformable Mirror space. This method is optimal for infinitely linear wavefront sensor. Another strong advantage is that the calibration time is independent of the system dimension for a given sub aperture size.
- System modes / mirror modes able to maximize the Signal to Noise within the dynamic range of the deformable mirror and of the wavefront sensor.
- Atmospheric modes: Zernikes, Karhunen Loeve
- Zonal-sparse basis using the sparseness of the influence function of the high order DM.

Using those modal bases, several techniques are foreseen and being compared:

- Open loop fast DM actuation, which allows freezing the disturbances between modal push and pull and thus avoid the turbulent noise as well as any low frequency effect as drifts, DM creep, etc…

- Open loop DM modulation and demodulation by homodyne or Fast Fourier Transform detection. The stimulus power is concentrated on a single frequency beyond the modal atmospheric bandwidth. Low frequency effects are canceled out and it allows for multiplexing. This way, several modes can be measured at the same time and time can be saved.
- Closed loop calibration. Dynamic bias is applied as offset on the wavefront sensor signal. The DM command is measured as a response to this bias and therefore the reconstruction matrix (or control matrix) is measured directly. This technique presents the strong advantage to calibrate the system around its operating point. Nevertheless, the turbulent noise instead of affecting the wavefront sensor measurements is translated to the DM closed loop command. To overcome this, we can couple the closed loop measurement to the modulation technique, the modulation being applied to the WFS offset. This calibration scheme is iterative and it has to be demonstrated that it converges well under nominal conditions of noise. To avoid an iterative process and keep the advantages of the closed loop scheme (wavefront sensor working in its linear regime), the bias could be applied at the DM level at a frequency well above the AO system bandwidth. The loop could also be closed on the Tip and Tilt modes only.

Furthermore, there is a key issue related to calibration. The pupil mis-centering may have a strong impact on the system performance and must be addressed properly. Indeed, for high order AO systems such as OWL, the tolerance in diameter ratio is very tight.

One must distinguish two different cases:

- A mismatch between the DM and the wavefront sensor, that is to say that the image of the DM in the lenslet array plane is shifted or rotated with respect to the lenslet geometrical pattern. This can affect the system performance if the misalignment was not calibrated in the Interaction Matrix (IM). A typical unacceptable shift is 10% of a sub aperture size.
- A misalignment between the telescope pupil and the whole adaptive optics system. This yields vignetting and therefore a non uniform illumination of the lenslet array inducing an error in the slope computation of the poorly illuminated sub apertures.

The impact of a pupil misalignment can be minimized in two different ways:

- Take it into account into the control matrix of the system by simulating it or by measuring its effect on the IM.
- Correct for it either statically (if it does not evolve with time during the observation) or dynamically by moving physically the pupil. Some solutions have already been investigated on the MACAO projects and the VLT Planet Finder design study.

8.2.1.4.3 AO key elements status and development

Introduction to the large deformable mirror technology

The concept of thin shell and force actuators is one of the most promising in the field of large deformable mirrors; the largest deformable mirror have been built/designed with this technology. A 642mm diameter convex secondary mirror with 336 actuators has been developed and is being used by the MMT (Multi-Mirrror Telescope, Mt Hopkins, Arizona), while the two 911mm diameter and 672 actuators concave secondary mirrors of the LBT (Large Binocular Telescope, Mt Graham, Arizona) are being integrated (at the time of this writing). A similar design is being studied for feasibility for one of the VLT Unit Telescope; the deformable secondary design is 1120mm in diameter and offers 1170 actuators for adaptive correction Figure 8-28, Figure 8-29 and Figure 8-30.

Figure 8-28: Conceptual design for the 1120mm diameter, 1170 actuators VLT deformable secondary mirror.

MMT-LBT-VLT large Deformable mirror concepts

These mirrors are composed of 3 basic elements: a back-plate, holding the voice-coil force actuators, a reference body and the thin shell. Each voice coil applies a force to a corresponding magnet glued onto the back face of the thin shell. A ring of conductive material (chrome, aluminium, gold…) is deposited around each magnet and is mirrored on the reference body. These two opposite coatings constitute a capacitance used as space sensor. The reference body being a calibrated optical surface, an equal spacing for all capacitive sensors insures a high optical quality on the shell.

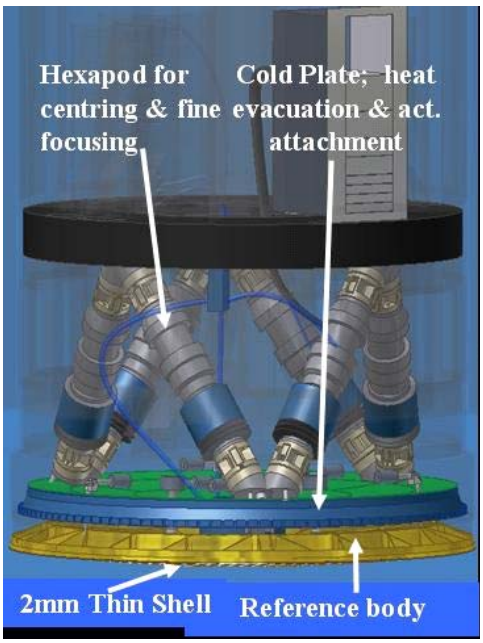

Figure 8-29: Force/thin shell mirror (VLT design) based on Cold plate, Reference body & thin shell. A Hexapod, attached to the cold plate, provides fine focusing & centering (Courtesy, Microgate/ADS, Italy)

A typical gap of ~50 μm is proposed for the VLT and provide air damping between the shell and the reference body. Increase of this gap to 200 μm is being studied in the frame of the ELT design study to meet the higher stroke requirements. An internal control loop at 80 kHz insures that the force applied maintains the capacitive sensor to a constant gap

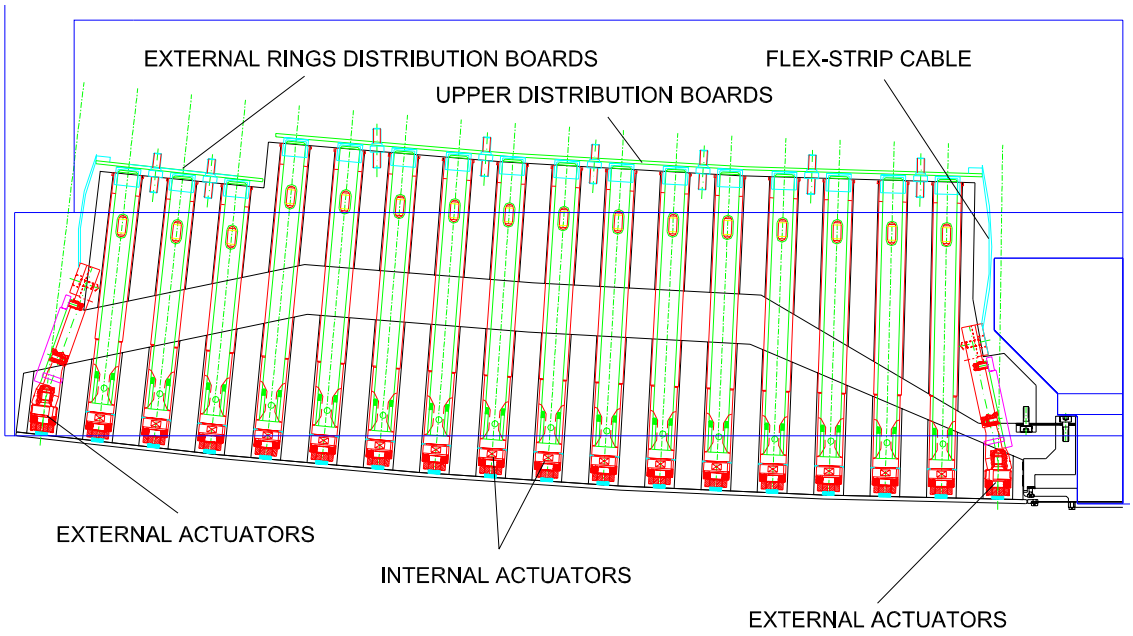

Figure 8-30: Closer view of the actuator distribution on one half of the DSM (Courtesy Microgate/ADS)

The back plate has two functions: holding the voice coil actuators and evacuating heat dissipated by the coils with the help of an integrated cooling fluid circuit. Therefore, the material used must combine rigidity and high thermal conductivity. It is made of aluminium for good heat conductivity and to reduce weight (compared to copper). Alternative materials like SiC are being studied in the frame of the ELT design study. The cooling circuit is divided in several sections in parallel providing cooling to an equivalent number of actuators; this insures more homogenous cooling & temperature across the cold plates & voice coil actuators. The back plate is usually cooled in series after the electronics crates (first components to be cooled) and before the Hexapod actuators (if present).

The reference body can be a conventional, thick, ULE or Zerodur optical component, with the exception of the numerous cylindrical openings allowing passage for the actuators. These are aligned toward the centre of curvature of the mirror (if it has optical power). More recent designs (VLT Deformable Secondary Mirror) explored with industrial partner a light-weighting scheme (50-60% light-weighted Zerodur or SiC) to reduce the weight of the complete assembly (realistic without being a huge cost driver). SiC offer the added advantage of being extremely rigid compared to ULE or Zerodur. Open-loop stability of the optical surface of the shell is directly linked to the reference body intrinsic rigidity, and a good optical quality of the reference body front surface insures an easy integration of the deformable mirror; constant gap on all capacitive sensors define a shell front surface perfectly matching the reference body figure. The light weighted option for the reference body is of prime interest for the M6AM unit in case the Field Stabilisation is performed with a second stage tip-tilt unit.

Note that the front surface of the reference body can be “rough”; the requirement is not strictly speaking the one of an optical surface. Image quality can be specified from the largest linear scale down to a fraction of the inter-actuator spacing. An increased surface roughness even improves the deposition of conductive coatings for the capacitive sensor.

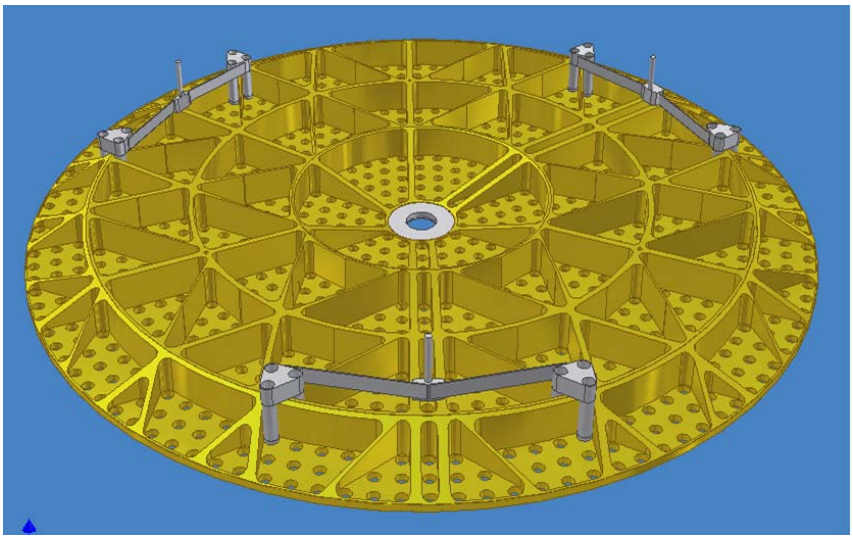

Figure 8-31: Light weighting scheme of the VLT design Reference Body; estimated weight (Zerodur) is 27kg while a monolithic design would lead to 130 kg (Courtesy Microgate/ADS, Italy)

Other materials can also be considered, e.g. SiC (Boostec, ECM CeSiC) providing high stiffness and proper optical quality polishing possibility. Price inquiries have been launched; trade-off areas for cost are the following:

- High surface roughness €↓
- No nickel plating for low roughness optical surface €↓
- Ease/low-risk of light weighting scheme compared to Zerodur €↓
- Lower large scale optical quality €↓
- Long polishing (hardness) €↑
- Costly fabrication €↑

To specify a lower optical quality on large scale would reduce price but at the expense of a more complicated integration; a proper test setup must be provided to insure an optical characterization of the mirror at the first integration and testing stage.

Thin glass shells for large DMs

This is a high-technology, costly, high risk venture. Up to now only the Steward Observatory Mirror Lab has been producing thin shells:

- MMT: Convex aspheric Rc=1795mm, k=-1.409, diameter=642 mm, 2mm thick, Zerodur 336 actuators
- LBT (2 units): Concave aspheric, k=-0.7328, diameter=911 mm, 1.6mm thick, Zerodur 672 actuators

A Call for Tender for the manufacturing of the Zerodur thin shell for the VLT DSM has been launched recently and results are expected in the coming months:

- VLT: Convex aspheric, Rc=4553mm, k=-1.66926, diameter=1120 mm, 1-1.8mm thick, Zerodur 1170 actuators

The production of an aspheric convex (VLT- Defromable Secondary Mirror) or concave (M5AM for OWL) thin shell adds substantial complexity to the manufacturing process. In that respect the flat M6AM unit for OWL is definitely “simpler”.

First estimate of the required glass thin shell thickness for the OWL M6AM is in the order of 1 mm. Several options are investigated in the framework of the ELT design study.

Other industrial partners have been involved in the fabrication of flat thin shell. There is a high synergy in the industry due to the high demand for thin glass plate for flat screen computer displays and digital TV's.

All the products listed below look promising but none has undergone detailed characterisation and it is unclear whether they fulfil the image quality criteria required. Most likely further optical polishing or ion beam polishing would be required. Furthermore, they do not have the advantage of low thermal expansion like Zerodur or ULE. This is not a show stopper for a deformable optics, but represents an added risk.

Corning EAGLE ^{2000} Display Grade substrates offer the following characteristics:

- 1100x1250 mm max. size
- 0.5-0.7 mm thickness
- <20□m thickness deviations

This line of product is available commercially. However, 0.7mm is thin for our applications and requiring a custom thickness would cancel the advantage of using this commercial line of production (at low cost).

SCHOTT also provide the following AF37 material also for LCD display applications:

- Alkaline-earth alumino silicate glass with high content of Al2O3
- 2160x2400 mm max. size
- 0.7mm thickness
- <50 □m thickness variations

This line of product is available commercially. Same comment as above on 0.7mm thickness.

SCHOTT BOROFLOAT® 33 is another line of products where thin shells are available:

- Material: B2O3 (13%), Na2O/K2O (4%), Al2O3 (2%), SiO (81%)
- 3000x2300mm max. size
- thicknesses in the range of 0.7mm to 25.4 mm
- ±70 µm thickness variations (for 0.7mm thick)

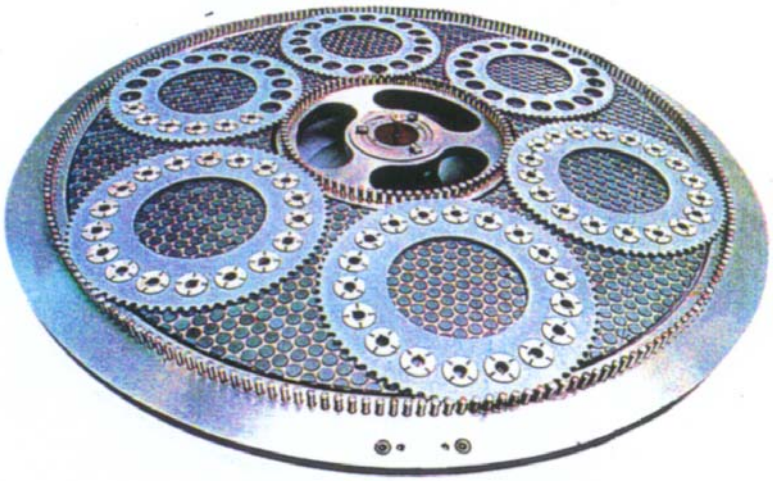

Figure 8-32: Double side polishing device for flat shell. Six shells, maximum diameter of 68mm each can be polished at once (Courtesy SESO, France)

SESO (Aix en Provence, France) have produced 680mm flat shell 3mm thick using a double side polishing apparatus (Figure 8-32). In the framework of the ELT design study they will investigated the possibility to manufacture a 1mm thick Zerodur thin shell of the same size.

- Different materials : glass, Zerodur, silica, ceramics, silicon, germanium
- Polishing of pieces with flatness of less than 3 μm up to 680 mm diameter
- Roughness as low as 1 Å RMS
- Parallelism of the 2 surfaces < 2" RMS

SAGEM is another company that is known to have contributed in the field of thin shell production. Especially space applications where lightweight mirrors are required (assembly of thin phase-sheet with reinforcing ribs).

Among the promising techniques to produce a thin shell with power (M5AM for OWL) are polishing under stress and slumping. The first technique is being investigated in the frame of OPTICON JRA1 and the second in the frame of the ELT design study.

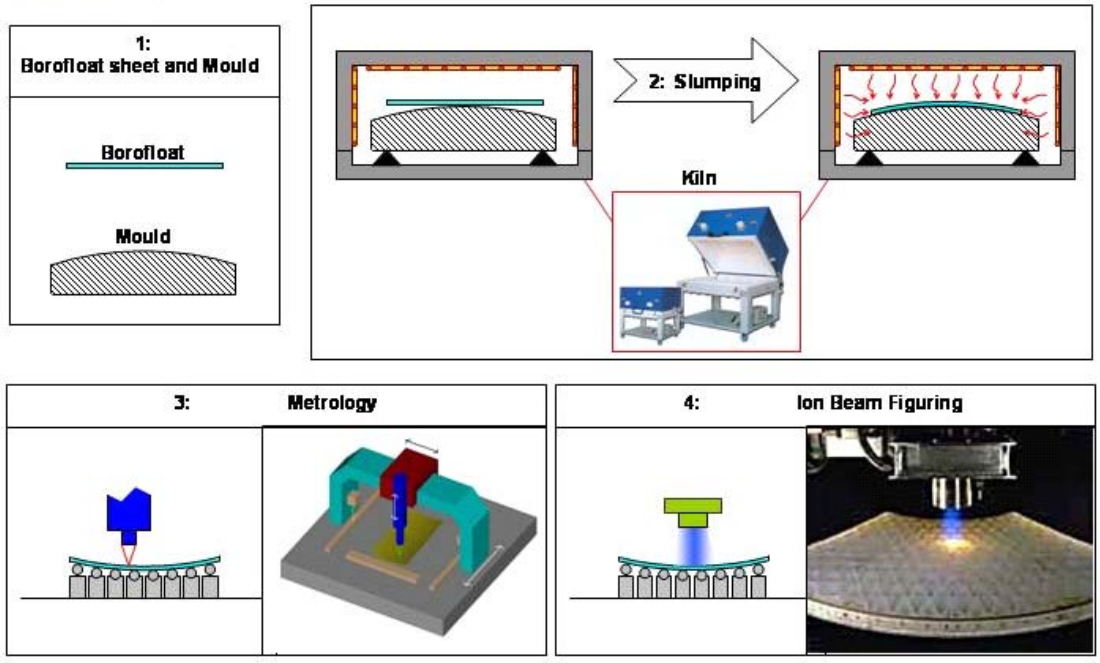

Figure 8-33: The successive steps of thin shell slumping (Courtesy INAF)

Stress polishing proceeds by grinding a thin meniscus being maintained in contact with a mandrel by air depression. The latest thinning steps are done by smoothing with finer tools. The process is completed after the proper optical quality is reached. If an aspherical shell needs to be produced the mandrel is aspheric and the polishing is spherical. Relaxation of the shell leaves it with the shape of the mandrel thus aspheric. This technique is still in development and has not produced a thin shell yet.

Slumping uses Borofloat glass and a high temperature oven to melt a flat thin shell onto a mould of the appropriate shape. Figure 8-33 shows the basic steps of this technique. The main disadvantage is the necessary use of non-Zerodur shell; due to thermal warming of the shell by the actuator local deformation at scale smaller than the inter-actuator spacing could be produced and could not be corrected for.

All the above possibilities are being investigated in the framework of OPTICON, ELT design study (Task 9300) and within the framework of the VLT Deformable Secondary Mirror (DSM) Feasibility study.

Control of large deformable mirrors

Contrary to piezo-stack DM's, this type of mirror implements a servo-loop between the capacitive sensor and the force actuator; this internal loop is sampled at a 80 kHz frequency for the VLT design and provides the capability to maintain the gap for each capacitive sensor at a predetermined value. A command vector sent to the DM defines a new position for each

capacitive sensor and the internal local loop sets the force corresponding to this new position for each sensor. Commands sent to perform a deformation are sent using a so-called “feed-forward” matrix which is a typical command matrix linking position to force (Figure 8-34)

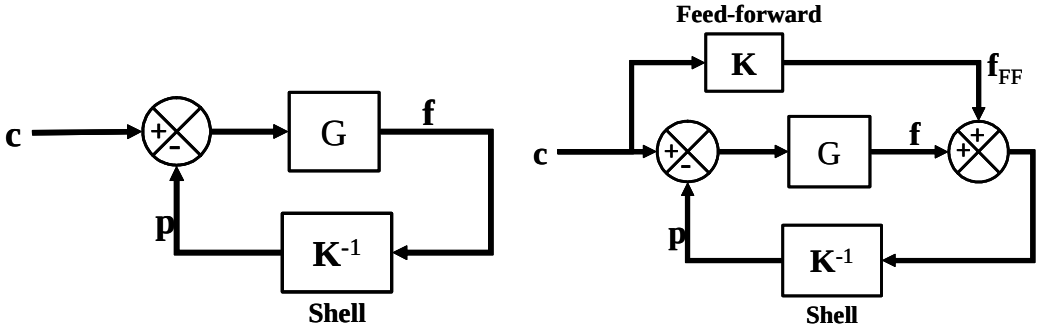

Figure 8-34: Scheme of internal control loop of actuator positions (left hand side). Feed-forward force added to the control schematic on the right hand side.

The derivative of the capacitive sensor positions provides a measure of the velocity of the shell displacement which in turn is used by the system to define an electronic damping matched to mode stiffness. This feature allows reaching high bandwidth for the system even if some control modes have low resonance frequency.

The electronics is organized in pair of racks that contain the DSP local processors; each individual rack contains up to 15 boards. In each rack two positions must be reserved for a communication board and a reference signal generation board. Each control board is populated with 2 DSP processors; one processor controls 8 channels (actuators) thus 16 channels per board. All boards are coupled with aluminium plates in contact with liquid cooled pipes for efficient vibration-less cooling.

The electronics receives commands from an external Real Time computer. Commands are transmitted via a 2.125 Gbit/sec bidirectional daisy chain connection. A service link (Gigabit Ethernet) insures diagnostic control of the DSM electronics.

Increased number of actuator does not preclude performance since a constant number of actuators are controlled per DSP.

Table 8-5 and Table 8-6 provide the overview of the typical control parameters.

Digital control loop frequency	80 kHz
Time latency between position update and command	41 µsec (transfer 10 µsec)
Local loop delay	4 µsec
Real time communication	100 Mbit/s (each crate)
Computational power	90 GMAC/s, float (6 crates)

Table 8-5: Local Loop Characteristics

Capa. Sensor bandwidth	-3dB @ 42kHz
Capa. Sensor noise	1.8 nm rms @ 50 µm gap
Capa. Sensor stability	1.5 nm/ºC
Capa. Sensor resolution	1.5 nm
Current driver bandwidth	-3dB @ 35 kHz
Actuator force resolution	140 µN
Maximum actuator force	±1.2 N

Table 8-6: Analog performance (Capacitive Sensor)

Large deformable mirror systems aspects

Mode stiffness

As for other AO system a base of modes can be defined for these mirrors. This base has the characteristic that low order modes are generally very "soft" while higher order modes are very "stiff". This can be understood easily; tilt or astigmatism have very low constraint and can be produced with weak forces. Conversely, high order modes imply very steep slope, and large local deformation of the glass; there forces required are important. Figure 8-35 illustrates this behaviour. One can see a substantial step at mode # 3; this corresponds to focus which is relatively stiff despite being a low order mode. This is due to the powered shell since it corresponds to trying to compress the shell in the radial direction.

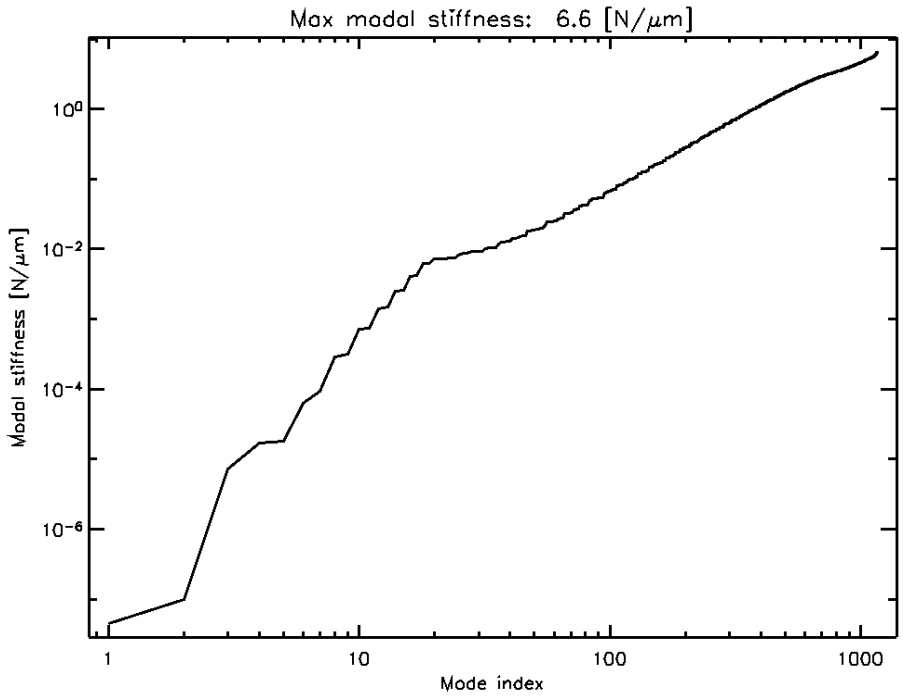

Figure 8-35: Mode stiffness versus mode number for the VLT DSM.

The implications of this is that the power required to control "n" high order modes is much larger (by order of magnitude) than the one to control "n" low order modes. The vertical axis spans 8 orders of magnitudes! Maximum force that can be applied by the actuator is ~1 N.

A consequence is that power consumption can greatly be reduced if one limits the number of modes corrected (by eliminating the stiffest modes).

Power dissipation is related to the force applied through the efficiency of the voice coil actuators. Present technology allows 0.52 N/√W. Knowing the mode stroke required (simulated wavefront time sequence) one can deduce the linear stroke requirement, link it to force through mode stiffness and obtain power requirement from the above efficiency. The total power consumption for the VLT Deformable Secondary Mirror is as follow:

- Median seeing conditions (ro=12.1cm @ 30deg), 1170 modes corrected, 62.5 nm rms WF fitting error, 1.48 kW dissipation
- Bad seeing conditions (ro=5.2cm), 738 modes corrected, 149 nm rms wavefront fitting error, 1.47 kW dissipation
- The following preliminary simulations have been run for a M6AM type mirror and lead to:
- 1.0mm shell (Zerodur); seeing 0.85" at 30º zenithal angle; Force 0.13 N rms, 0.6 N max.; 6.4 kW total power; 250 nm residual WF

- 1.0mm shell (Zerodur); seeing 1.5" ; Force 0.20 N rms, 0.9N max.; 6.8 kW total power; 400 nm residual WF
- 1.2mm shell (Zerodur); seeing 0.85" at 30º zenithal angle; Force 0.22 N rms, 1.0N max.; 6.9 kW total power; 250 nm residual WF
- 1.2mm shell (Zerodur); seeing 1.5"; Force 0.35 N rms, 1.5N max.; 7.9 kW total power; 400 nm residual WF

Note that in the last case the maximum force exceeds the 1 N maximum that can be produced by the currently available actuator; therefore the number of modes to be corrected should be limited and residual wavefront error correspondingly increased.

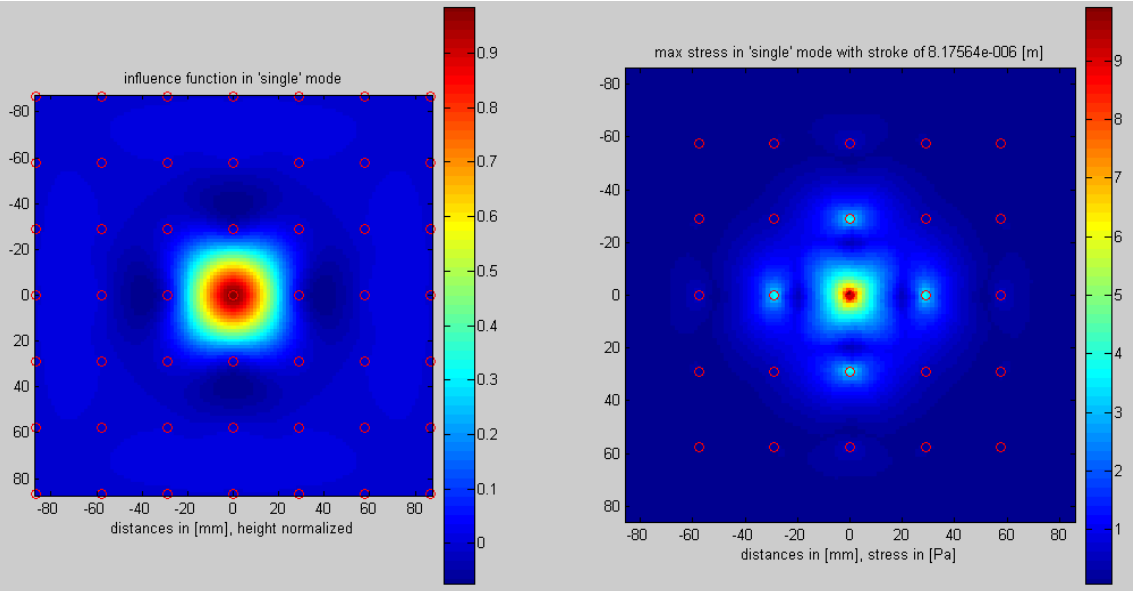

Figure 8-36: Theoretical Influence Function of a thin shell DM. Left: the IF (scale in mm), right: the associated stress in the glass (square grid of actuator at 29mm spacing, 2mm thick)

Influence functions

The typical influence function shape of this kind of DM is a damped sinc (*sin(x) / x)* function. Coupling as defined for other types of DM (piezo-stack) is irrelevant. When a displacement is commanded to a single actuator, neighbouring actuators get a command from the internal control loop to maintain their corresponding positions as defined by the capacitive position sensors. This explains the undershoot (below average surface) 1.5 actuator spacing from the deformation peak (see Figure 8-36).

The Figure 8-36 shows that the influence function of these mirrors is very close to a Sinus cardinal. The deformation is maximum at the position of the commanded actuator, crosses zero at the first next neighbours, goes through a minimum and again crosses zero at the 2nd next closer actuator and so on. The difference with a sinc function is that this function is slightly damped (the amplitude of the wave patterns decreases faster than a real sinc). This is a positive feature since a sinc function contains all spatial frequencies up to the Nyquist criteria for a given actuator spacing and its power is null for spatial frequencies above the inter-actuator spacing. Thus, such function appears ideal for wavefront correction since it provides full coverage of all useful spatial frequencies without introducing uncorrectable higher spatial frequencies. The damped sinus cardinal comes closest to this ideal influence function.

Note that with the increased performance of DSP based controllers, electronic damping is also used (proportional to the velocity of the shell at an actuator point; derivative of the capacitive sensor position is used). This damping allows limiting resonance of low order modes and increasing system bandwidth.

Large deformable mirror scaling laws and Trade-offs

Actuators and magnets

The magnets are made of a complex assembly of “pie shape” pieces providing an optimal force / magnet surface. A Zerodur “puck” is glued between the magnet and the shell back surface with no local deformation of the shell optical surface (Figure 8-37 and Figure 8-38).

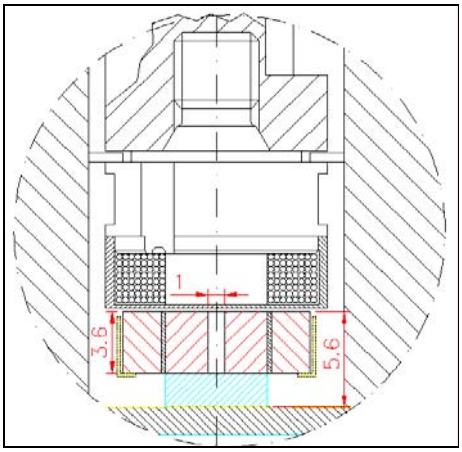

Figure 8-37. Permanent magnet mounted on the shell.

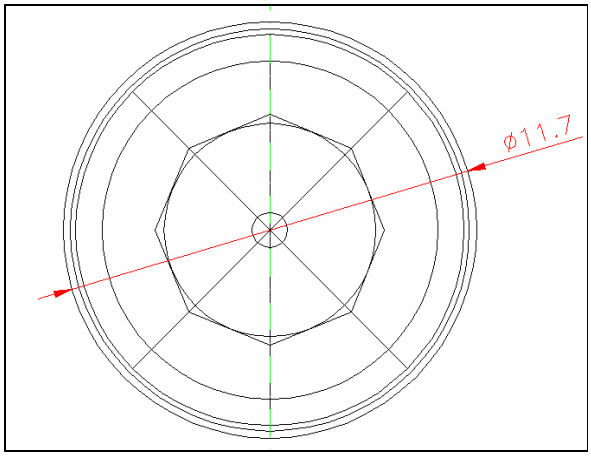

Figure 8-38. Permanent magnet sizing.

Actual technology imposes magnet sizes of the order of 12mm in diameter and this is what drives the minimum inter-actuator spacing. Reducing this size further brings also complications at the level of the voice coil, but would also reduce the actuator stroke (force).

Thin Shell

Let’s define the following parameters:

- t : shell thickness
- Y: shell material Young’s modulus
- ρ: shell material density
- a: actuator spacing
- r_o: force radius distribution (radius of the area on which the actuator force is applied)

Material	**Young’s Modulus N/m^2**	**Density Kg/m^3**	**Poisson Ratio (0.33=>adhoc)**
Zerodur	90.3 10^9	2.53 10^3	0.243
SiC	450 10^9	3.12 10^3	0.21
CVCSiC	466 10^9	3.20 10^3	0.33
Steel (17-4 PH)	200 10^9	7.80 10^3	0.29
Ester Graphite	101 10^9	1.8 10^3	0.33
Nickel	214 10^9	8.9 10^3	0.33
Borosilicate	63 10^9	2.23 10^3	0.22
ULE	67.6 10^9	2.205 10^3	0.25

Table 8-7: Characteristics of potential materials for thin shells.

The desired characteristics are a combination of trade offs. The list below summarizes the important characteristics:

- Weight: low density helps to reduce the total weight of the shell; less actuator power is used for compensating gravity. Compensation force is proportional to ρ.

- Quilting: this describes the sage of the shell between the actuators. High density makes it worse; high Young modulus helps prevent it. It is proportional to $a^2 / (Y\ t^2)$.
- Stroke: Low Young modulus helps, but mainly shell thickness. Proportional to $a^2\ \rho^2/(Y\ t3)$

Table 8-7 provides the characteristics of the investigated materials for the thin shell manufacturing.

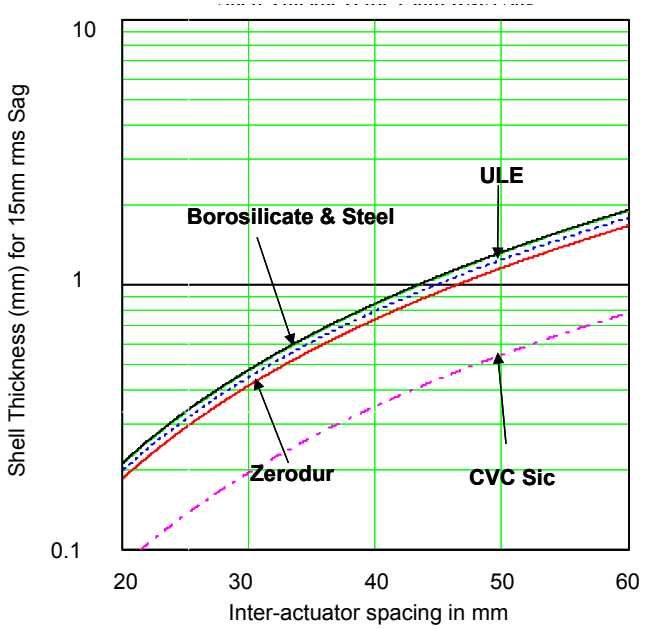

Figure 8-39: Shell thickness producing 15 nm rms gravitational sag (30nm rms wavefront error) vs. actuator pitch

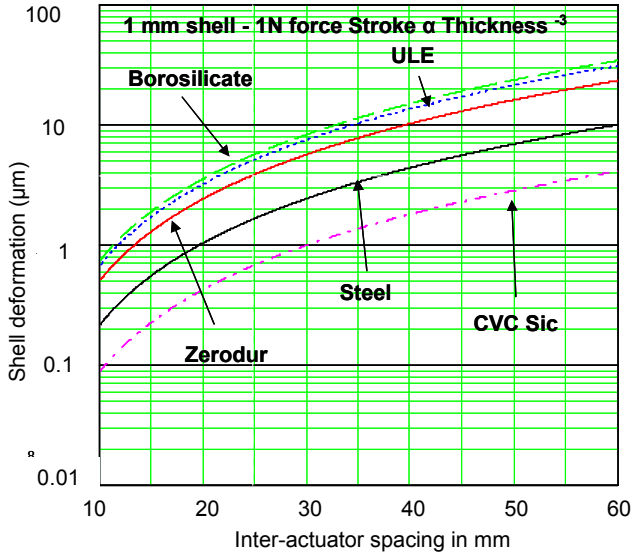

Figure 8-40: Shell gravitational sag (nm) vs. act. pitch for Zerodur, ULE, Borosilicate, Steel & CVCSiC.

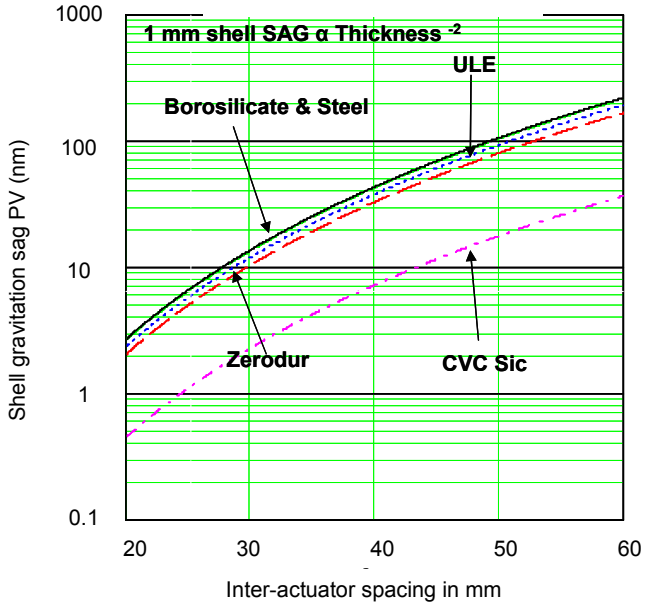

Figure 8-41: Shell deformation or stroke. Absolute analytical model accuracy: 50%; valid for relative material comparison

One may be tempted to study materials like steel since breakage is less likely than for glass. However, with Steel and ULE the ratio ρ/Y remains high which makes these materials worse from the point of view of quilting (see Figure 8-39). Note also that high conductivity material may trigger unwanted effects; besides sensitivity of the optical surface to ambient temperature variation, the actuators themselves dissipate and may induce local deformations. On the other hand the very low equivalent ratio for Silicon Carbide (SiC) does not represent a huge advantage because in order to benefit from it one would need to envision unrealistic and unpractical shell thicknesses (~200 μm).

As for stroke a CVCSiC shell would need to be nearly half the thickness of a Zerodur one in order to allow a similar stroke. Figure 8-41 shows a comparison of stroke between different materials considered. Note that this analytical model overestimate the stroke by ~50% with respect to Finite Element Analysis performed on the VLT Deformable Secondary Mirror shell.

From Figure 8-41 we see that a stroke of 4 μm can be achieved with a Zerodur thin shell of 1mm thick, an actuator spacing of 25 mm and a force of 1 N. The inter-actuator stroke requirement at the spatial scale of 1 m on OWL pupil is about 5 μm for a seeing of 1.5" and for an atmospheric outer scale of L_0=100m -Figure 8-26- which is the worse case.

We see that present technology is nearly able to meet the requirements for SCAO. Refining of the numbers should be done in the phase B. The production and the handling of 1mm glass thin shell of 2.4 m diameter remains challenging. However, the fact that M6 is flat relaxes significantly the difficulty of manufacturing this shell. Handling is a matter which has been partially addressed by industry for other applications (flat screen display). Fall back option would be to segment the M6AM unit in six flat petals following the OWL spider geometry

The conclusion of these considerations is that Zerodur although a conservative choice represents a safer approach to thin shell fabrication and can fulfil adequately the requirements.

Other exotic materials like Ester Graphite do not seem to present significant advantages. Note also that they are known to present sensitivity to humidity. Furthermore, homogeneity of the material depends on the number of anisotropic layer deposited and an adequate isotropy might require an excessive number of individual layers to represent a thin shell (few 100 μm per layer).

Power dissipation and control electronic

The actual VLT Deformable Secondary Mirror is expected to dissipate 1.47 kW. This power is distributed as such:

- 311 W in Coils, 1123 W in racks and 43 W in cables with a 2mm thick shell

For OWL M6 with a Zerodur shell of 1mm the estimated power dissipation is:

- Seeing 0.85":
  - Power at coil level: 0.25W/act (1.6kW total)
  - Power at crate level: 6.4kW total (non linear current drivers)
- Seeing 1.5":
  - Power at coil level: 0.39W/act (2.5kW total)
  - Power at crate level: 6.8kW total (non linear current drivers)

Other important properties are the size of the electronic racks. The VLT Deformable Secondary Mirror design is based on the following distribution of control per channels:

- 13 control boards per rack, 2 DSP per boards, 8 channels per DSP = 208 channels per racks (6 racks are required)

The actual design could implement a 16 channels control per DSP which would results in a gain by a factor of 2 leading to about 400 channels per rack. Table 8-8 provides the main characteristics of the OWL large deformable mirrors.

Mirror	Size (m)	# actuators	Act. pitch (mm)	Scale on sky (m)	# racks
M5	3.85	17241-6727	25-40	0.78-1.250	43-17
M6	2.44 x 2.66	6720	25	1.02	17

Table 8-8: Main characteristics of the OWL large DMs

Further improvement would require substantial new development. Electronic racks would be reduced drastically and most electronic miniaturized and deported in the actuator electronic. The actuator itself would contain its Deformable Secondary Mirror controller and switching power driver. Although the control requirements are reduced by a factor of 8-16 (1 CPU per channel) the driver would imply a substantial new development.

Hexapods are often used to produce fine motions on the back-plate; they are particularly well suited for this application allowing fine accurate repeatable motions and high rigidity. They can provide high accuracy movements and are extremely sturdy devices against gravitational flexures. Any motion applied to the back-plate is transmitted on the optical surface of the thin shell. It can be typically used for small focusing motion and centering correction. Table 8-9 lists a few basic characteristics of the VLT design.

Mass Budget		**Hexapod Actuators Req.**		**Achieved Performance**	
Mirror+magnets	9 kg	Stroke	16mm	Step response (10mm, 4000 N load; 23Hz sampling)	~2sec
Reference body	27 kg	Resolution	1 μm	Fixed position	10nm rms
Cold plate	89 kg	Op. Axial load	≤2000 N	Power Dissipation (3000N load)	Min: 6 W Max: 12 W
Actuators	54 kg	Survival axial load	≤14000 N		
Support levers	5 kg	Speed	≥0.5mm/sec		
Total weight	**184 kg**				

Table 8-9: Essential characteristics of the VLT adaptive secondary mirror.

8.2.1.4.4 Testing a large DM in closed loop

The testing of deformable mirrors of the size envisioned for OWL Telescope, or for 8m telescope class secondary mirrors for that matter, represents a new challenge for the integration phase of such systems. It is not only a question of size but also of shape; concave, convex or flat. A versatile and complete test facility to characterize and understand well these systems is necessary. An exhaustive integration and test phase with adequate equipment in Europe will insure a successful and shorter integration phase at the telescope.

It is with similar considerations in mind that the integration phase of the VLT Deformable Secondary Mirror was envisioned. Not only this facility shall allow testing of the Deformable Secondary Mirror itself, but it will provide also a turbulence generator and VLT standard opto-mechanical interfaces to the AO pre-stages SCAO and GLAO (GRAAL and GALACSI for the instruments HAWK-I and MUSE respectively).

The optical design shown in Figure 8-42 is composed of 2 mirrors plus the VLT Deformable Secondary Mirror. The latter is mounted on a vertical structure holding the M2 unit thus providing a support identical to the one of the VLT. Gravity vector is along the M2 optical axis. Two other optical components are required: a main 1.65 m diameter aspheric mirror and a smaller 140mm diameter aspheric mirror. The asphericity of the former can be handled by conventional polishing techniques while the fabrication of the second would require diamond turning. This setup would offer a 2 arcmin field of view and no pupil distortion. The image plane is located at the centre of curvature of the 3 mirrors system: 1.65 m concave aspheric, 1.1 m convex DSM, and strongly aspheric 140mm third mirror. 45º flat mirror and beam splitters are used to transport the source and image planes at convenient locations.

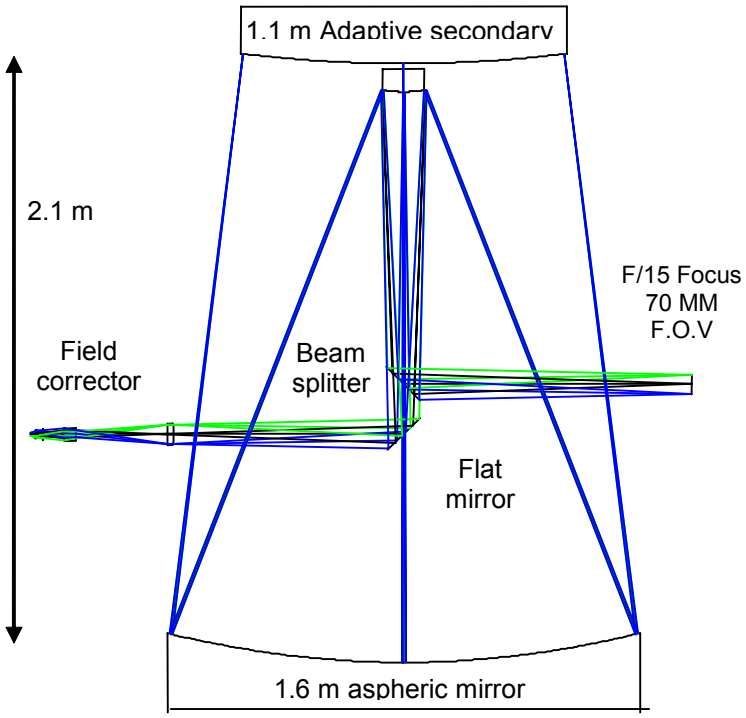

Figure 8-42: Optical diagram of the VLT Deformable Secondary Mirror test setup

Figure 8-43 illustrates the opto-mechanical implementation. The table on the right-hand side would support the turbulence generator and a 45º beam splitter re-directs the beam onto the 140mm mirror. After reflection onto the primary and DSM a 45º mirror will direct the beam toward the Nasmyth focus mechanical interface. There an f/15 beam is provided the SCAO and GLAO systems.

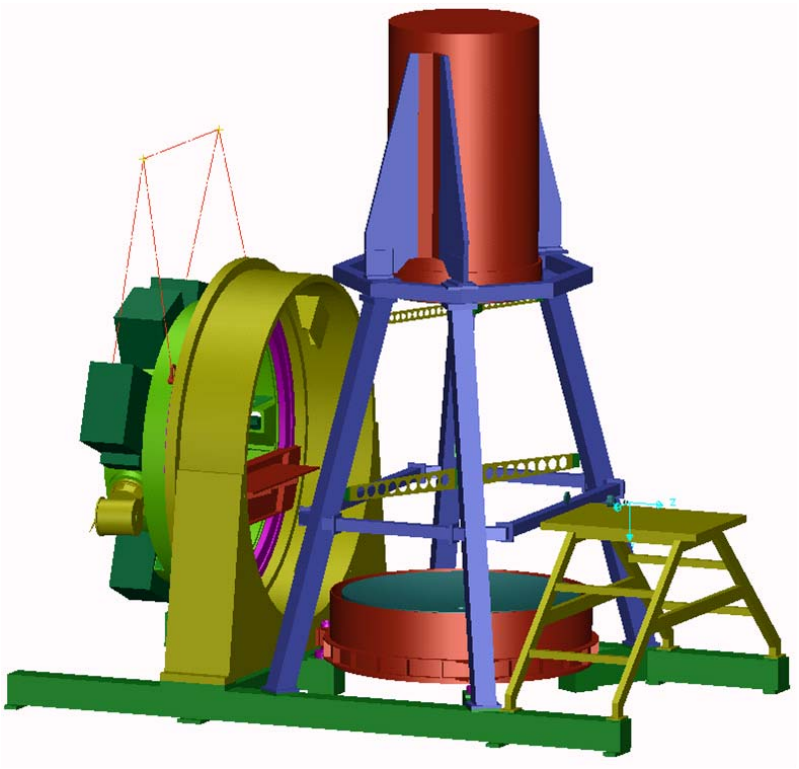

Figure 8-43: Mechanical setup of the VLT deformable secondary mirror Test facility.

As we have shown here, it is clear that a lot of experience will be gained on the VLT large deformable mirror to prepare for the next generation of even larger deformable mirror for OWL.

A similar strategy could be imagined for OWL M6 as shown in Figure 8-44. The optical set-up could consist either of a parabolic mirror or a spherical mirror with small focal ratio and a corrector. The orientation could be vertical to simulate conditions closer to the real ones.

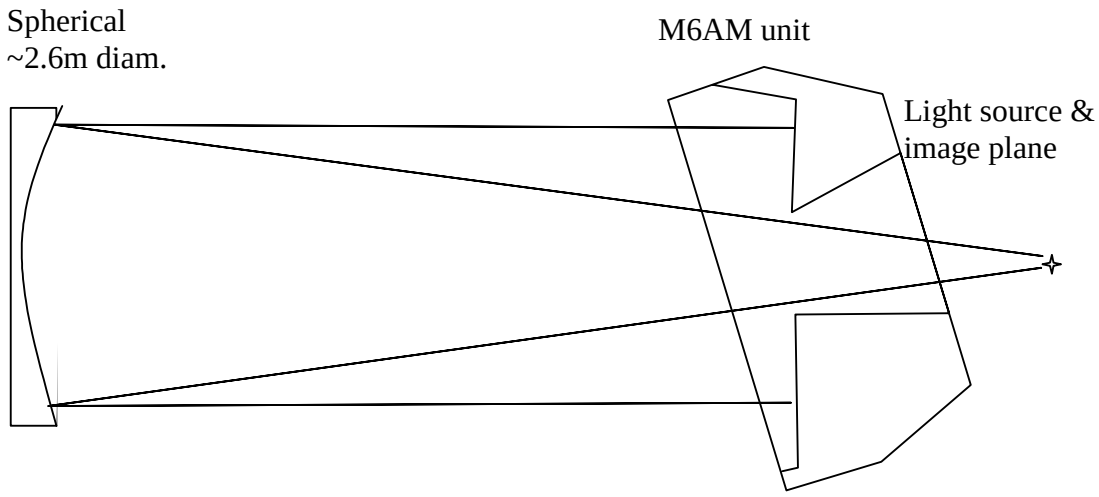

Figure 8-44: Possible test setup for the OWL M6. In the case of spherical mirror a corrector is needed for aberration compensation (not shown here)

The following items provide a non-exhaustive list of all tests and characterization that would be performed before any use at the telescope:

- optical characterization of the large DM

- optical measurement of the influence functions
- definition of the flat vector
- optical measurement of stroke, non-linearities, cross coupling
- Interaction matrices measurements (artificial source, with turbulence opened-loop and closed-loop)

- Closed loop operation with wavefront sensors of the instruments
- Characterisation of correction capability, image quality improvement
- Characterisation of different algorithm of correction (on-axis single source, GLAO multi-source, LGS correction etc.)

Finally it is undeniable that the experience gained while testing and operating the deformable mirror in Europe would be invaluable during integration and test at the telescope.

8.2.1.4.5 Detectors for wavefront sensors

An extension of the current Electron Multiplication CCD detector technology or equivalent for wavefront sensing will be launched early in Phase B in order to reach the required 600x600 pixels at a kilo frame per second. High depletion devices are very promising and should be pursued further. Larger pixel – up to 50 µm – combined with a low dark current at Peltier temperatures should also be investigated.

Alternative technology, like the Pn CCD detector developed by the semiconductor laboratory of the Max Planck Institut for Extraterrestrische Physik might become very attractive if the present RON – 2.4 e^- - can be further reduced. This type of detector has several advantages:

- Predicted high Quantum Efficiency down to the red - Figure 8-45-
- High parallelization for the output readout channels - up to 512 outputs for the existing 256x256 pixels detector
- On chip multiplexer to reduce the number of outputs -Figure 8-46-
- Large pixel –up to 50 µm-

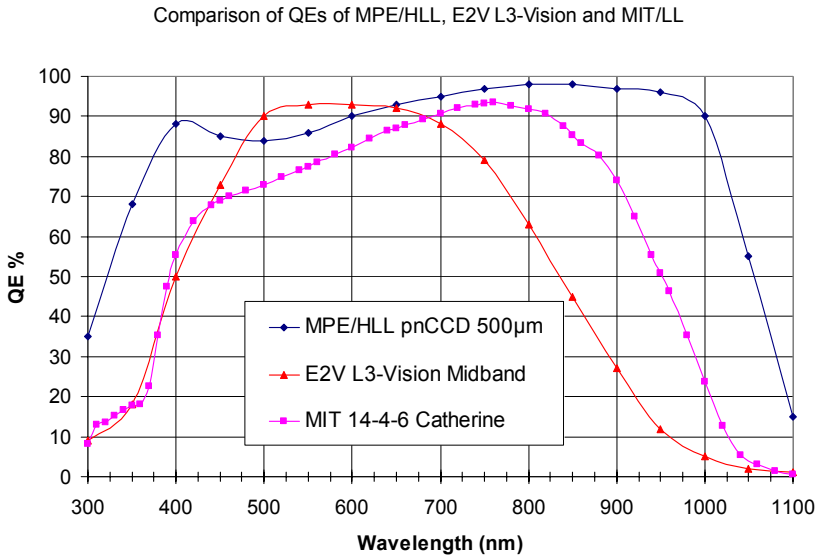

Figure 8-45: Quantum Efficiency curves of the L3 CCD and the PN-sensor

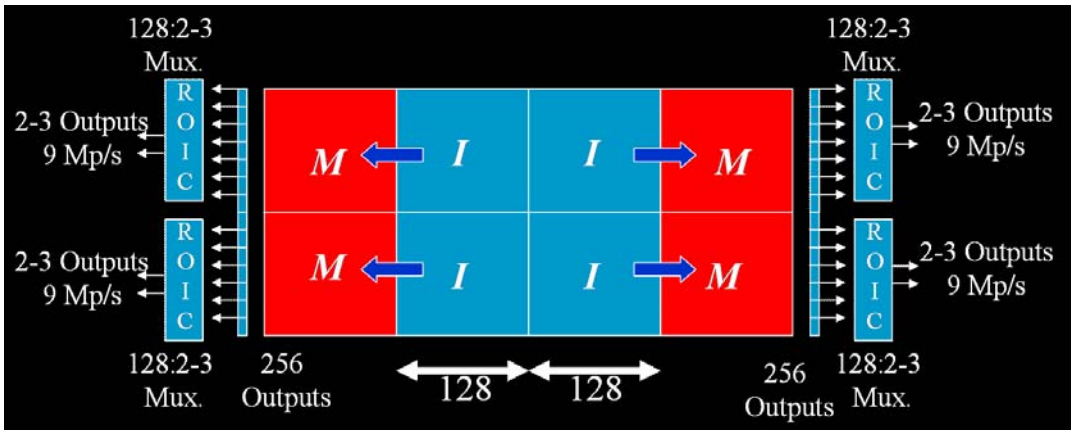

Figure 8-46: Pn-Sensor readout principle for the 256x256 detector.

The effort initiated by Caltech and ESO on low Readout noise high frame rate infrared detectors for wavefront sensing – for instance the Calico Mux from Rockwell – need to be further expanded to reach the level of few e^- Readout noise at 500-1000 frames/s. WFS volume constraints will benefit from cooling without Nitrogen and compact cooling system should be studied.

We plan also to investigate alternative approaches for IR detectors like the components developed by INTEVACS (US).

8.2.1.4.6 Real Time Computer

Real-Time Computers of past ESO-AO Projects

ESO has developed several AO systems:

- NAOS, a 14x14 Shack-Hartmann system with one 185-actuators mirror, driven at 480Hz. The RTC is a custom development made of an array of C40 chips tied together by custom designed boards
- MACAO for VLTI/SINFONI and CRIRES: a modular system installed in 6 different instances. It is a curvature system with 60 sub-apertures and a deformable mirror with 60 actuators, capable of running at 700Hz. The Real Time Computer is a dual-CPU system based on standard Power PC boards.

All these systems are routinely used at Paranal. The experience gained from the development, the commissioning and the operations of such instruments is being exploited for the new projects for the 2nd generation instrumentation.

Current Activities

The second generation instrumentation for the VLT includes several AO-assisted instruments – see Table 8-10. This new generation of AO systems require new development in several areas, including the Real Time Computer.

Currently no single-board computer is capable of processing the amount of real-time data required to run these AO systems. Extreme AO (XAO), Multi-conjugate AO (MCAO) or Multi-Target Ground Layer Correctors will require about one thousand actuators at a Kilohertz rate or more for the VLT and up to almost a million actuators and more than 2 Kilohertz frequency for OWL.

The new Adaptive Optics Real Time Computers will have to be based on multi-CPU multi-board computers in order to achieve the required computational power. The complexity of each of these systems and their number raise concerns about the complexity of their development, their reliability and their maintenance. Individual efforts aimed at developing different custom systems are not a solution, not only because of the duplication of the design and development effort to build similar products for different systems, but also for the amount of resources required to test, maintain and upgrade systems which are different in spite of being similar.

		MACAO	NAOS	MAD	Planet Finder	MUSE	HAWK-I	
Acquisition	Nb of detectors	1 Curvature	1+1 SH	3SH, 2Pyr	1 SH	4 SH	4 SH	1 SH
	Detector size (used size)	-	112x112	80x80 (64x64)	256x256 (240x240)	256x256 (192x192)	256x256	256x256 (240x240)
	Nb of subapertures	60	14x14	8x8	40x40	32x32	32x32	40x40
	Pixels per subaperture	-	8	8x8	6x6	6x6	8x8	6x6
	Tip/tilt sensor	-	-	-	-	quad-cell	yes	-
	Max. frame rate	420Hz	480Hz	400Hz	1.0/1.5kHz	1kHz	500Hz	1kHz
	Integration time	2381µs	2083 µs	2500 µs	1000/667 µs	1000 µs	2000µs	1000 µs
	Input bandwidth [per det/total]	0.1MB/s	11.48MB/s	9.38MB/s	110/165MB/s	70.31/281.25MB/s	62.5/250MB/s	110MB/s
	ACQ blocks	1		4				
DM	DM type	Bimorph	Piezo	2 Bimorph	Piezo	DSM	DSM	
	Nb of actuators	60	185	2x60	1370	1170	1170	
	Size of control vector	0.12kB	0.36kB	0.23kB	2.68kB	2.29kB	2.29kB	
	Output bandwidth	0.05MB/s	0.17MB/s	0.09MB/s	2.61/3.92MB/s	2.23MB/s	1.12MB/s	2.23MB/s
	Tip/tilt Mirror	TT mount	separate	TT mount	separate	no	no	
Control	Supported modes	SCAO	SCAO	SCAO, MCAO	SCAO	Wide/Narrow	SCAO,GLAO	SCAO
	Nb of used slopes	60	144	156	1096	800/3200	796	1096
	Control matrix size [elements]	60x60	288x185	312x120	2192x1370	1600x1170/ 6400x1170	1592x1170	2192x1170
	Control matrix size [Mbytes]	0.01MB	0.20MB	0.14MB	11.46MB	7.14MB/ 28.56MB	7.11MB	9.78MB
	Memory bandwidth for matrix access	4.2MB/s	96MB/s	56MB/s	11.46GB/s, 17.19GB/s	7.14GB/s, 28.56GB/s	3.56GB/s	9.78GB/s
	Controller type	integrator	integrator	integrator	integrator + Kalman(tip/tilt)	integrator	integrator	integrator

Table 8-10: AO systems commissioned or under development. SPARTA support starts with MAD

We believe that the solution is a common standard platform that can achieve all the goals of the AO systems. SPARTA is a standard platform that provides both a hardware and software common infrastructure in which all the previously mentioned applications can run.

The main goal of SPARTA is to provide a product for the 2nd generation AO facilities for the VLT and a concept for OWL. It is clear that the final RTC for OWL could be rather different from the one proposed from the SPARTA concept, since another goal of SPARTA is to be able to track the technology as it evolves.

The goal of the conceptual design of an RTC for OWL is to prove that it is feasible or to identify what has to be improved and to show that the “improvement factors” are within reach. To this end we will show that the SPARTA concept can be a possible solution.

The standard hardware platform will be scalable to accommodate different needs of the different projects. It will be easily maintainable, designed with deployment scenarios in mind and strongly based on Commercial Off-The-Shelf components. It will also be upgradable to follow the technological evolution, and will be reliable because it is based on a common software platform and it shares similar benefits as the VLT Common Software[64].

The main problem to face while designing such big AO controllers is not the total computational power, which can be easily reached by piling up a considerable number of CPUs, but, instead, the critical factor is the latency. It is in fact relatively simple to process gigabyte of data per

[64] Developed once, tested and run multiple times.

second, given a pipeline of CPUs which is long enough. What is difficult is ensure that the computation completes in the shortest possible time when the total available time is measured in hundreds of microseconds.

A standard CPU suffers from the instruction-fetch, load/store bottlenecks of the traditional von Neumann microprocessor architectures, shared also by most DSP chips. This prevents reaching the latency performance required in large parallel systems, where large means more than 4 chips. Instead FPGA-based systems achieve true parallel processing, executing DSP algorithms based on the inherent parallelism of the hardware. In addition, FPGAs are far more scalable into the higher throughput realms because they can dedicate specific logic for I/O functions. However FPGAs are harder to program and thus less flexible to use from a software point of view.

The choice for SPARTA falls into a hybrid architecture where the central computing element is a board with at least two last generation FPGA chips and two last generation multi-core CPUs. We can then create a double pipeline, one based on the FPGA talking to each other by using a very low latency bus, and another pipeline where the CPUs can talk using a standard fast fabric.

In fact SPARTA uses CPUs, DSPs and FPGAs in a equal ratio. Every FPGA is coupled with a last generation CPU that contains a DSP (AltiVec) so we are using all three worlds at the same time, with the goal of using each of them for the application it is best suited. In fact FPGAs will be used only for the very hard-time part, where every single microsecond counts and the intelligence is concentrated on the CPU that can use the companion DSP for mathematical computations.

SPARTA for the VLT has already reached some important milestones: a Conceptual Design is available together with the definition of the external interfaces, the CCD/IR controller and the deformable mirror controller. Important work on both the CPU pipeline and the FPGA pipeline has already been performed and several parts of the software architecture are under test on the ESO MCAO Demonstrator (MAD) project, which uses a scaled-down version of SPARTA.

Future Activities for SCAO

The AO system for SCAO is challenging but also will be operational in several years from now so that we can benefit from the technological advances that will take place during these years. It is therefore important to keep on the radar the most interesting technological developments that are surfacing now since they will take some time to become products we can actually buy. If the time interval is about 5 years, then only technology that is being talked about now could be usable in 5 years. A longer period could bring new developments that are not under consideration at the moment, so it is more difficult to predict what we could have.

There are two kinds of problems we will need to face in designing the RTC for OWL:

- The total computing power

While the control frequency remains more or less unchanged, the number of degrees of freedom needed to achieve a certain Strehl ratio increases with the square of the telescope diameter, so the number of DM actuators or sensor sub-apertures will be 100 fold if compared with the VLT. Since standard control algorithms use a matrix-vector multiply (MVM) as the core function in the control algorithm, then the required computing power is 10.000 bigger than an equivalent VLT system (the matrix dimensions are number of sub-apertures and number of actuators). This alone is not a big problem: as said above, one can create a massive CPU pipeline that is able to cope with the required throughput. This is a problem similar to the car industry where one can get one new car produced every hour, by lining up several workers in a production pipeline.

- The total latency

If throughput is about delivering one car per hour, latency is about the total time each car spends in the pipeline. It is relatively easy to build a computer able to implement a 100x100 Shack-Hartmann system at 1 KHz with a latency of one second. That means that this system can acquire sensor data at 1 KHz, but each frame takes one second to be fully processed by the system before any action based on those data is taken. In fact the system is processing 1000 frames at the same time, each frame in a different stage. This is of course would not work:

a closed-loop control system has not only to have the required throughput but also the latency in order to keep the complete computation associated with a certain frame short, ideally before the next frame arrives.

We considered several architectures and technologies to solve both the throughput and the latency problems. Those can be grouped into three main areas:

- General Purpose CPUs. These are the standard processors equipping PCs. They are characterised by a bus-based architecture: data normally reside in memory. Input devices store data through the bus into memory, where the CPU can fetch them, again through the bus to bring them into one of the caches for fast processing. Results are deposited into memory where output devices can take them for transmission. As it is clear from the description, the bottleneck is the bus since everything has to travel through it. However, CPUs feature very advanced technology, they have very fast cores and many includes a DSP unit inside.
- DSPs (Digital Signal Processors). These are specialised processors with special instruction to deal with standard signal-related operations. For the rest, they are similar to CPUs and share many advantages and drawbacks. We will not consider this option since modern CPUs come with integrated DSP units.
- FPGA (Field Programmable Gate Array). Those are specialised chips that include a large number of logical elements that can be logically wired together to create a circuit in which the flow of the current will “execute” the hardware program, in a similar way the core of a CPU is designed. In fact, to program these chips one needs to use a dedicated language which is the same used to design integrated circuits. All the gates of the FPGA chip can be active at the same time thus implementing a low-level massive parallelism. The chip can feature multiple busses to talk to memory and devices so that multiple areas of the chip can be active and process data at the same time with the advantage to be on the same chip.

General purpose CPUs are easier to program and better tools are available. DSP are slightly harder and FPGA are the most difficult ones, since one needs to deal directly with the hardware.

In terms of commercially available products, one can buy boards featuring any of the previous technologies and even a combination. DSPs are not very appealing for what said before if compared to CPUs. However custom designs that gather together a large array of DSPs (hundreds) can be made competitive with a standard board based on FPGAs. The first guideline for SPARTA is to maximise the usage of commercially available components, so here is another reason not to consider DSPs.

Technological evolution is an important factor in designing the RTC for OWL, since the deployment of the OWL-RTC will happen not before 5 years from now, so that we can benefit from the technological evolution. However different technologies will have a different rate of evolution. In RD25 we recall the so-called Moore’s Law “governing” the technological evolution of integrated circuits, but one can immediately observe the following:

- Current CPU architectures are approaching the limit. The major CPU manufacturers have focused in the past years on increasing the clock speed of the CPU as the best way to increase its computational power. In fact since the introduction of the Intel 80486, companies have been increasing the clock frequency of the CPU while leaving the bus speed unchanged or slowly increasing it. This is another factor why the peak computing performance of a general purpose CPU can never be achieved in AO because AO is not just computationally intensive, but it also needs to transfer a large amount of data to and from the CPU.

Moore’s Law predict the evolution of the transistor density, but computing power is more complex to predict since clock speed, bus speed, peripheral performance come into play. The 100 times increase that a plain application of the Moore’s Law would predict might not be applicable to CPUs.

- Instead, an FPGA is a huge array of logical elements. Making a more powerful FPGA is like adding more elements to the chip, which is much easier. Of course, real performance gain can be obtained by re-implementing the application to exploit the additional

parallelism. And of course clock speed increases for FPGAs too. So one can expect a bigger increase in performance for FPGAs than for CPUs.

The SPARTA architecture, which is based on a combination of CPUs and FPGA chips on the same computational unit, is then well positioned to benefit from the next generation of hardware and we are confident that it can deliver the performance required to implement the SCAO system for OWL and even more.

There are other developments that are required to run the RTC at the maximum speed, but that do not directly belong to the RTC and the SPARTA project.

The detector controller must provide multiple output interfaces, in order to split the pixel stream in multiple streams that can be computed in parallel by different sections of the SPARTA-RTC. To achieve this goal the detector controller (IR or CCD) must also offer switching capabilities, in order to route a certain pixel to a certain output interface, with a fixed routing map. This requirement is indepented from the number of detector amplifiers. The switching capability is of particular importance for the pyramid wavefront sensor where the equivalent concept of sub-aperture is distributed over the four pupils so to start the computation of the gradients one must first acquire a large portion of the detector if care has not been taken upfront by designing appropriate routing maps.

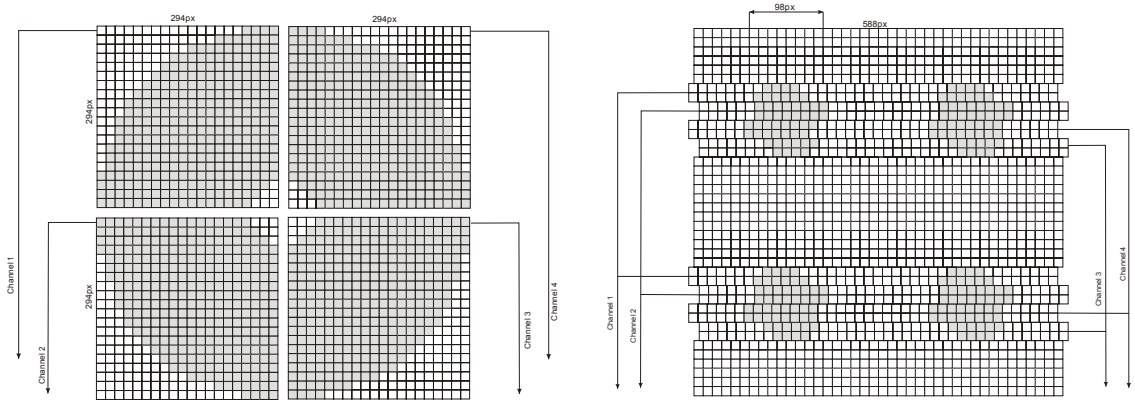

Figure 8-47: Left: Shack-Hartmann read-out; right: Pyramid read-out

Another required development is fast mirror drive electronics. At a very high loop frequency, a significant part of the processing time will be spent to send the control voltages to the deformable mirror electronics and have it distribute the commands to the actuators. A multi-channel parallel architecture would then be mandatory.

A critical issue that is common to all the RTC designs is to verify as soon as possible the degree of parallelism that can be achieved with this architecture. The estimate of the computing power of the FPGA chip here considered is quite reliable and rather easy to check since the Virtex4 is going to be integrated very soon into commercial products. What is more difficult and definitely more critical is to test a set of 2 or more boards based on this technology and verify that all communications (intra-board, board-to-board, I/O) are as expected.

Reference Architecture

The reference architecture is derived from the latest developments in the SPARTA Conceptual Design - Figure 8-48- and it is based on a hybrid architecture made of FPGAs running the hard real-time part and the CPUs running the remaining of the system. FPGAs do not show very good performance while dealing with floating point numbers thus one direction of research is the usage of integer arithmetic.

The advantage of using FPGA is the high degree of parallelism that can be achieved through a relatively slow device. Instead a CPU is much faster but requires serialisation while accessing resources as memory or input/output ports.

Several optimisations can be made by sharing the hard real-time part between the FPGA and the CPU and lower the final cost. But a very significant improvement can be made if FPGAs run

only in finite-precision (fixed point) arithmetic while the CPU can run the infinite-precision (floating point) arithmetic. By reducing as much as possible the infinite-precision arithmetic part, one could fully exploit the potential of this architecture and improve performance increasing the speed or reducing the cost.

This is, however, a long study which is inder way in the framework of the FP6 ELT Design Studies and results are expected by 2007.

A CPU-only based system can hardly be used because of the very high over-head required to transfer data to and from the CPU. This at the moment makes impossible to use even the most performing CPUs. Some optimism can be derived from the fact that technology is moving fast on bus technology and multi-core CPUs and in the near future it seems likely that proper exploitation of the floating point capability of the next generation CPUs will become possible.

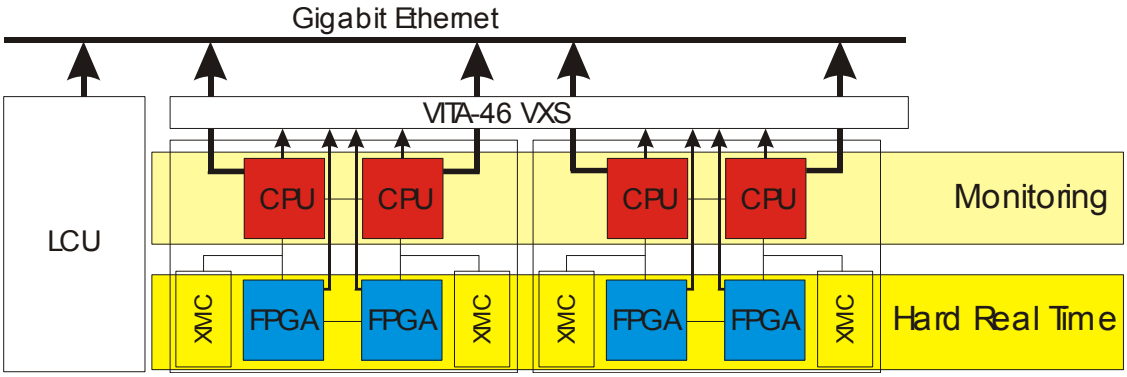

Figure 8-48: SPARTA Architecture

Required Developments

The hardware to build SPARTA for OWL does not need to be bought today and moreover a certain degree of hardware development still needs to be done. The dual-CPU plus dual-FPGA architecture implemented in a board with several banks of fast memory is sufficient to implement 4 of the 5 AO RTCs. A board similar to this one exists already on the market so the first steps in the design phase will be to acquire two of these boards and their interconnecting hardware and to measure their performance.

These two boards cannot be used for OWL RTC, but can be used as test bed and development system and could also be used for SPARTA for the VLT.

- It is also necessary to initiate a co-operation with the industry in order to ensure that the next generation of the same product based on the next generation FPGA chip (the Virtex4) is able to achieve the performance we require.

Given the SPARTA philosophy of maximising the usage of off the shelf products, we would not start a special development to meet the specifications, but instead we would like to work with the industry to see if there is a market opportunity for boards of such computing power in order for the industry to independently develop such boards and make them a real product.

Even if not critical for this first application, efforts shall be made to study new and efficient algorithms. More will be discussed about the more challenging systems, but efficient algorithms can help also at this level to reduce the hard real-time requirements of the RTC. In particular the impact of fixed point arithmetics or reduced precision computation shall be studied since significant improvements can be obtained with an FPGA-based hard real-time pipeline.

8.2.2 Ground Layer Adaptive Optics

Preliminary measurements of the turbulence profile (Cn2) made at Paranal with the SLODAR monitor have shown that 60% of the turbulence is located within the first two kilometers and that 40% of the turbulence is concentrated at 200m. We no have reasons to believe this type of turbulence profiles is specific to Paranal and at least similar properties can be assumed for the

site eventually selected for OWL. Even more favorable profiles have been observed in Antarctica: whether this is a reason sufficient to install OWL in Antarctica is of course debatable.

Based on this turbulence profile and assuming we intend to correct only for the ground layer, a simple geometrical approach shows that the well-known anisoplanatism angle limitation becomes very large and therefore permits to perform wavefront sensor tomography of the turbulence over a large FOV. The net result is an increase of the number of NGSs available for wavefront sensing and finally an increase of the sky coverage in which GLAO correction can be offered.

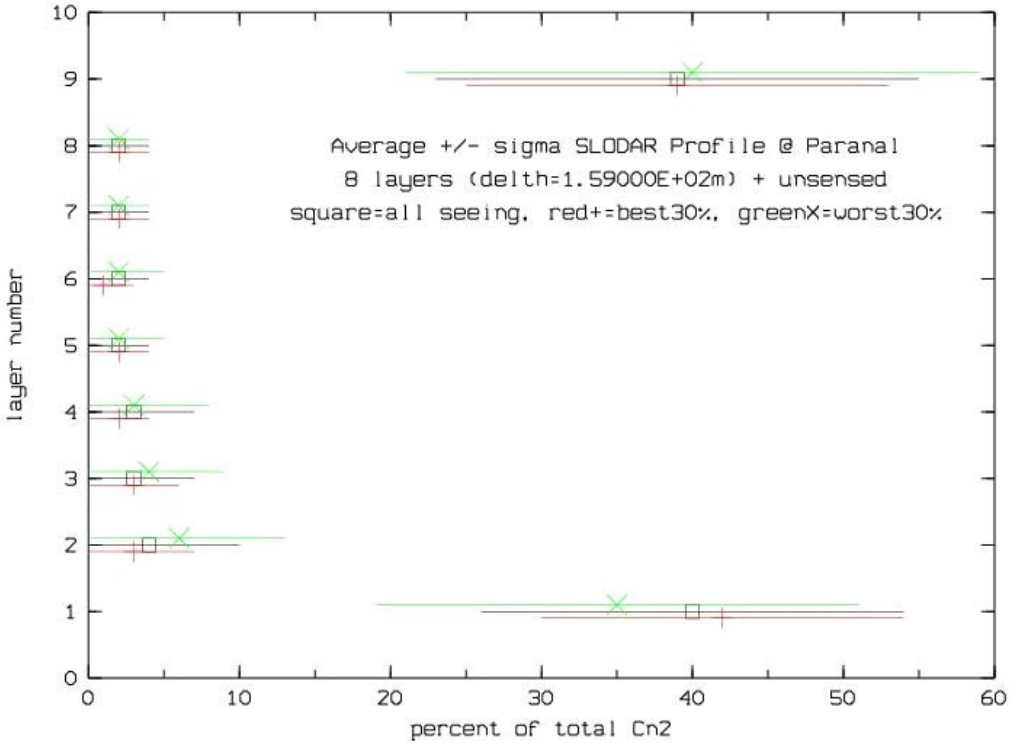

Figure 8-49: Preliminary statistics of the turbulence profile at Paranal

Correcting only the ground layer will in principle not be enough to achieve the diffraction limit of the telescope. However GLAO is a “seeing reducer” system which will provide a better sensitivity for a given integration time, a better ensquared energy and a reduction of confusion for very crowded fields. GLAO can also be considered as a “seeing stabilizer” providing at least median seeing values all the time and is therefore equivalent to install OWL on a better site.

Several scientific programs, especially those concerned with faint extended objects, do not require diffraction limited images because of the low surface when sampling the diffraction at Nyquist. For these programs, GLAO is probably an interesting option which in addition will be available over a much larger sky than SCAO.

The concept of Ground Layer Adaptive Optics is shown Figure 8-51.

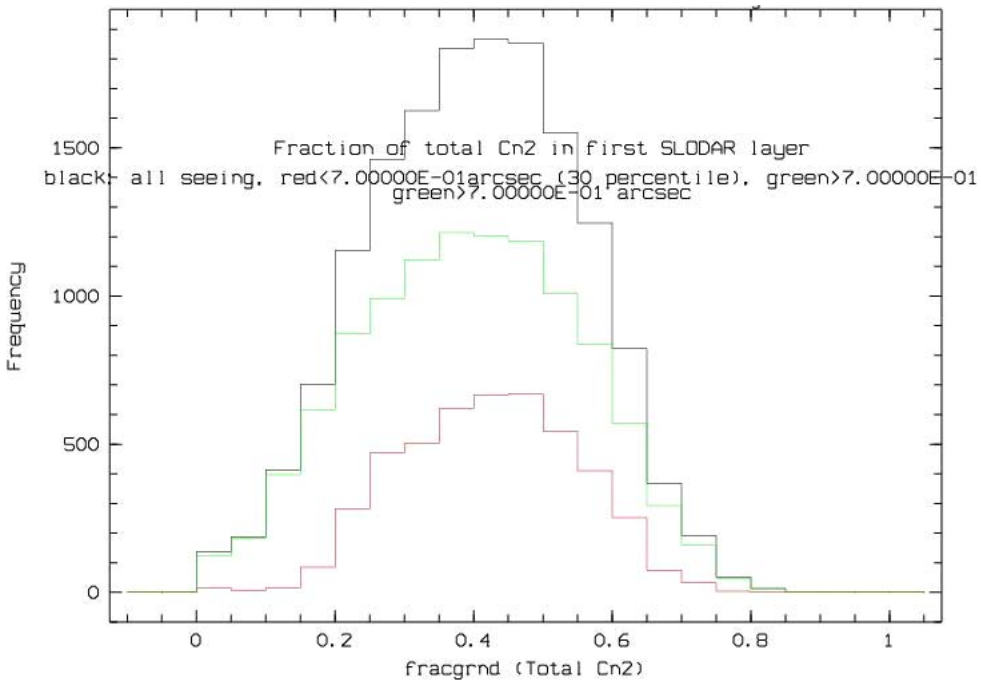

Figure 8-50: Fraction of turbulence located at 200 m as measured by the SLODAR at Paranal

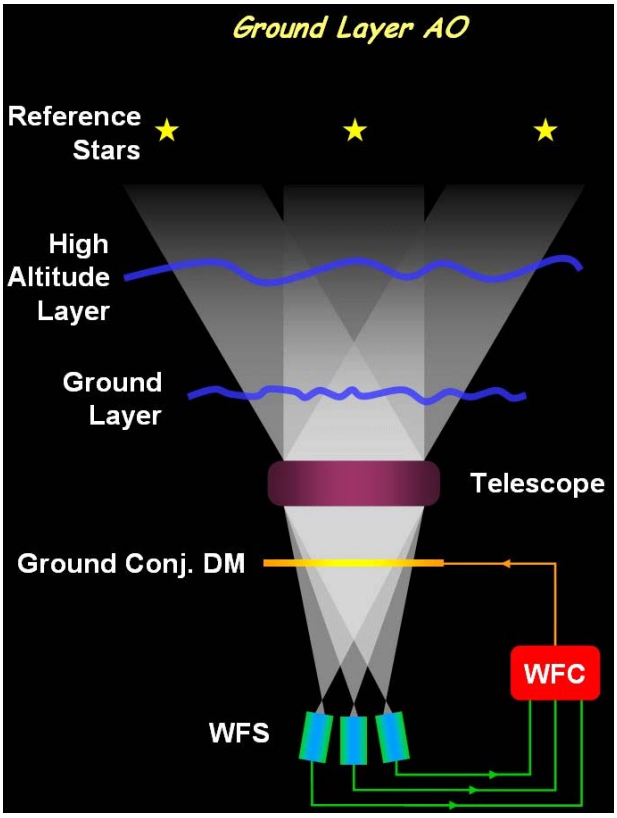

Figure 8-51: Ground Layer Adaptive Optics concept

8.2.2.1 Performance requirements

The GLAO performance requirements are as follows (FoVs specified herein are in diameter):

- GLAO aims at providing reduced seeing images at NIR wavelengths (J-K bands) using Natural Guide Stars (NGSs) for wavefront sensing.

- GLAO aims at providing improved Ensquared Energy (EE) within 50 mas pixel at NIR wavelengths (J-K) according to Table 8-11 and Table 8-12
- GLAO should provide the above correction over 3 goal 6' FOV.
- The maximum un-vignetted technical FOV usable by the GLAO system is 6'.
- GLAO should provide corrected PSF uniformity according to Table 8-13.
- GLAO should maximize the sky coverage over which the GLAO correction can be provided: 70-80 % at the North Galactic Pole and 100% at l=0° and b=50°
- GLAO should offer the possibility to optimize further the Ensquared Energy (EE) in a so-called "narrow field mode" (1-2') using the available NGSs over the technical 6'FoV. The expected gain is at least a factor 2 compared to the correction optimized over 6' FoV.
- GLAO should offer the possibility to optimize the correction on-axis ("very small narrow field mode") using the NGSs available over the 6' FoV. This can be seen as an extension of the SCAO at relatively low Strehl ratio but with a much larger Sky coverage.
- In this mode, GLAO should provide on-axis Ensquared Energy in 50mas pixel in K-Band of 20% and 6% under 0.53" and 1" seeing using a cluster of NGSs of 16th magnitude.
- GLAO should support telescope nodding at 0.1 Hz by fast opening/closing GLAO loop (0.1s).
- GLAO should support small amplitude -1"- mosaicking in closed loop by offsetting the WFSs synchronously. The accuracy of the offset should be better than 1/5 of the spatial pixel size -50mas-
- GLAO does not support chopping
- GLAO should provide in closed loop Field Stabilization to the telescope with the maximum amplitude characteristics provided in Table 8-1. For wavefront sensor dynamic reasons, the telescope guider will support GLAO for closing the AO plus Field stabilization loop before the control of the field stabilization corrector is taken over by the GLAO in closed loop.
- GLAO should permit to observe without AO (but with Field Stabilization) without any transmission loss with respect to the telescope. In that case, the field stabilization corrector is not controlled by the AO system.
- GLAO should have the capability to correct for some of the telescope aberrations left by the active optics with an amplitude lower than 20% of the atmospheric wavefront at all spatial and temporal frequencies. Errors beyond these values are handled by the active optics.
- The transmission of GLAO should be maximized for the instrument observing wavelength T>95%;
- Vignetting of the scientific FOV by the GLAO wavefront sensors should be minimized (TBC)
- For the performance evaluation of GLAO seeing assumptions should be: 0.53 and 1" at 0.5 μm at zenith; with τ_0=3 and 2ms. For the performance evaluation the outer scale of turbulence should be L0=25 m. For the determination of the AO design parameters the following atmospheric parameters should be assumed: turbulence outer scale L0=100m, seeing=1.5", τ_0=2ms – Figure 8-4.
- GLAO shall be able to correct for differential atmospheric dispersion between the NGS and the Science object during an observation by applying offsets to the wavefront sensors. The calculation of the offset shall be done by the software based on the science beam effective wavelength provided by the instrument, the spectral type of the NGS provided by the observer, the science and guide star coordinates provided by the observer, the relevant atmospheric data (Temperature, Pressure, and Humidity) provided by the observatory – with the required accuracy. GLAO will not correct for the atmospheric dispersion within the scientific band pass of the instrument.

	Wave band	K-band		H-band		J-band	
	Guide stars magnitude (per star)	V=15	V=17	V=15	V=17	V=15	V=17
seeing, τ_0, L_0 @ 0.5µm	0.53", 3ms, 25m	12	11	7	6	4	3.5
	1", 2ms, 25m	2.2	2	1.3	1.2	1	0.9

Table 8-11: GLAO Ensquared Energy (%) in 50mas pixel over 6' FOV

	Wave band	K-band		H-band		J-band	
	Guide stars magnitude (per star)	V=15	V=17	V=15	V=17	V=15	V=17
seeing, τ_0, L_0 @ 0.5µm	0.53", 3ms, 25m	4	3	2.8	2.3	2	1.7
	1", 2ms, 25m	2.9	2.6	1.9	1.7	1.5	1.4

Table 8-12: GLAO – Gain in Ensquared Energy in 50mas pixel over 6' FOV, corrected PSF vs. seeing.

	Wave band	K-band		H-band		J-band	
	Guide stars magnitude (per star)	V=15	V=17	V=15	V=17	V=15	V=17
seeing, τ_0, L_0 @ 0.5µm	0.53", 3ms, 25m	**±10%**	**±10%**	**±9%**	**±9%**	**±8%**	**±8%**
	1", 2ms, 25m	**±10%**	**±10%**	**±9%**	**±9%**	**±8%**	**±8%**

Table 8-13: GLAO Ensquared Energy variation in 50 mas pixel over FOV (PSF uniformity)

8.2.2.2 Implementation Concept

8.2.2.2.1 Corrector and wavefront sensors

The GLAO concept is conceived as an extension of the SCAO system equipped with 6 wavefront sensors. The corrective element is the M6AM unit described in section 8.2.1.2.1 and the wavefront sensor is essentially six units of the wavefront sensor described in section 8.2.1.2.2, which permits a high standardization in WFS design and allow the correction of high order modes, which is required by GLAO to pump energy from the PSF wings towards the core. The specific linearity requirement of the GLAO mode may require 6x6 pixels for the Shack Hartmann wavefront sensor already assumed for SCAO. The maximum closed loop update frequency is 500 Hz. Slower frames rates may be used, if the site shows a slow ground layer turbulence.

8.2.2.2.2 Control and Real Time Computer

The maximum closed loop update frequency is 500 Hz.

The slope computation is performed in the following way (2 options):

- The signal of each sub-aperture is obtained by co-adding numerically the signals of the same sub-aperture from all the wavefront sensors and then the related slope is computed;
- The slopes are computed for each wavefront sensor and averaged per sub-aperture.

Two types of reconstructions can be implemented in GLAO depending on the degree of uniformity across a specified FoV and the concentration of light required.

Control of Wide-field mode

The wide-field mode is designed to provide a uniform correction in the whole scientific FoV. A good estimate of the ground-layer phase perturbation is given by the average of the phases estimated from several wavefront sensors coupled to the NGSs located in the FoV.

The closed loop reconstructor is the average of the reconstructors computed individually for each wavefront sensor at a specified FoV location in order to take into account the field-dependent non common path aberrations and the possible difference in linearity of each WFS. The vector of reference slopes for each wavefront sensor is obtained by a look-up table previously calibrated.

Control of Narrow-field mode

The narrow-field mode is designed to boost the performance in a given direction (or smaller portion) of the scientific FoV. The improvement in correction at this specified direction is achieved at the expense of the uniformity of the correction in the whole FoV.

The wavefront reconstructor for the narrow-field GLAO mode is based on the minimum-variance (MV) reconstructor, R_{MV}, which can be expressed as the product of two matrices:

$$R_{MV} = P \times E \qquad \textit{Eq. 8-1}$$

The matrix E represents a full tomographic reconstruction of the turbulence volume (possible only when the vertical distribution of the atmospheric turbulence, obtained in real time from a vertical profilometer, is known), and the matrix P stands for an optimal projection from the reconstructed turbulent layers onto the deformable mirror taking into account the direction(s) where optimization is desired.

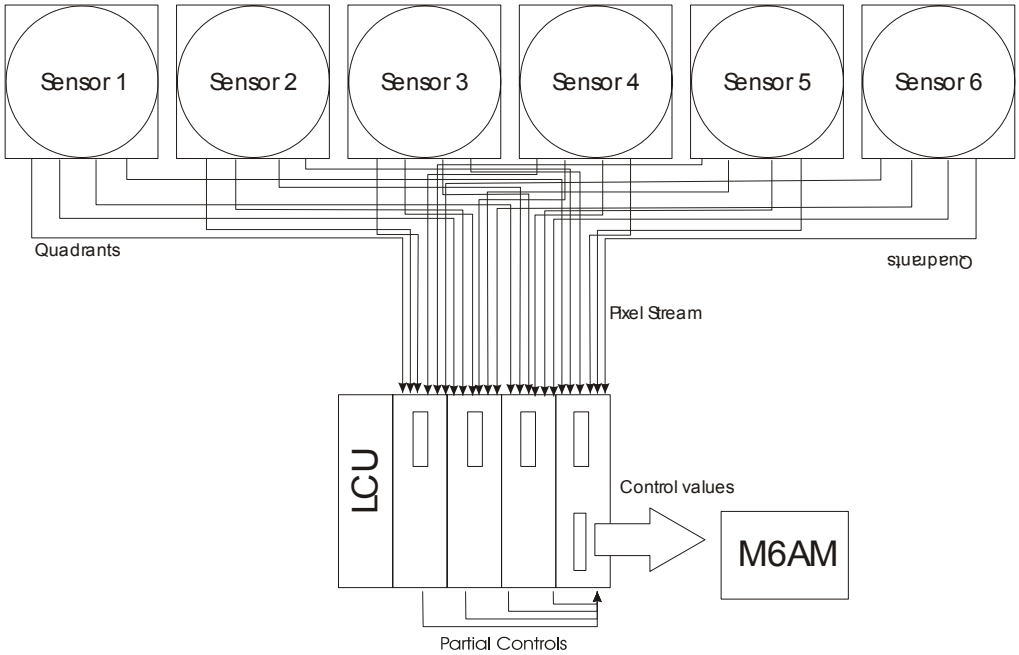

Figure 8-52: GLAO real-time hardware architecture

Real Time Computer

This mode is a multiple-sensors / single-mirror system. Only the option based on a Shack-Hartmann sensor will be considered here. Both the deformable mirror and the detector technology will be the same as for SCAO, although in this case we will have 6 sensors. Gradients computed on each sensor will be averaged before running the reconstructor. This operation approximates the ideal solution (reconstructing each sensor measurement individually and only later averaging them). In this way we average the gradients coming from each sensor and we multiply them with an average reconstructor: this is correct as long as the difference

between the various reconstructors is small. Therefore the complexity of such a system will be similar to the one previously analysed, where the additional complexity lies only in the acquisition. Control strategy, loop frequency and tolerable delay are also the same.

By using the same concept as in the previous case, we obtain that the only difference is the input architecture (Figure 8-52) where multiple streams coming from the 6 detectors have to be merged together. We assume the same architecture of the SCAO case, where the pixel data stream of each detector had been split in four channels, one for each quadrant. The corresponding quadrant of each detector will be routed to the same input processor for averaging. The rest of the system will be identical to the SCAO case.

8.2.2.3 Predicted performance

A detailed analysis of the GLAO performance based on end-to end simulations, as well as the assumptions and AO parameters, are provided in RD25. Note that the GLAO performances provided here does not include yet all error sources -calibration errors, optical quality of the telescope, wavefront sensor and instrument optical paths, mis-registration error, atmospheric chromatism etc…- but only the pure AO performance part. In the GLAO mode, we believe that the impact of the error budget on the final performance should have a little impact due to the partial correction provided by the GLAO system.

The evaluation of the GLAO performance should cover two main aspects:

- The Ensquared Energy within a given pixel size here assumed to be 50mas.
- The Sky Coverage over which the correction is available.

8.2.2.3.1 Sky coverage

The proposed GLAO system is based on Natural Guide Stars. In the following, we will present the sky coverage achievable with a GLAO system. More details about this are provided in RD27.

The Sky Coverage (SC) has been computed using the coordinates and the magnitudes of the star fields at different galactic latitudes. The star fields have been extracted from the USNO B1.0 catalogue.

In the following, we have limited the number of NGSs for wavefront sensing to 6, which is a reasonable trade-off between the complexity of the tomography and the sky coverage achieved. The determination of the optimum number of NGSs is a complex trade-off which involves a large number of parameters and simulations to be conducted during phase B:

- Layer Oriented (LO) vs. Star Oriented (SO) -see [124].-
- Optical or numerical co-addition of NGS flux over the whole FOV
- RON of the WFS detector versus feasibility of the optical co-addition
- Vignetting of the scientific FOV by the WFSs
- GLAO performance uniformity due to NGSs random distribution vs. number of GSs
- Faintest acceptable guide star for wavefront sensing
- Optimisation of NGSs magnitude difference for the LO

Figure 8-53 and Figure 8-54 provide the sky coverage achievable versus the NGS magnitude at the North Galactic Pole and at b=50. If the faintest guide star usable for wavefront sensing is around m_R =17 - RON=0e^- (which is typically the limiting magnitude of the ESO SINFONI-MACAO-NAOS systems -

Figure 8-55[65]- still providing a correction comparable with a “seeing reducer”) we see that the SC achievable is in 10% at the Galactic Pole and close to 50% for *l*=0° and *b*=|50°|.

[65] Note that Figure 8 55 has been produced with data taken on 1st August 2004 on UT4 with MACAO. The magnitude of the star is 15.7 and the other images have been obtained by using neutral density filters, so the sky background got

Extension to m_R =18 is not out of reach if detector with high QE in the red can be developed as explained in section 8.2.1.4.5. In that case the SC becomes ~25% at the Galactic Pole and ~85% at intermediate galactic latitudes. In this regime, the sky background $m_{V=}$[19 - 20.7] starts to contribute with a corresponding sky background flux received by the WFS of [145 - 30] e-/sub-aperture/s compared to the NGS flux = 375 e$^-$/sub-aperture/s.

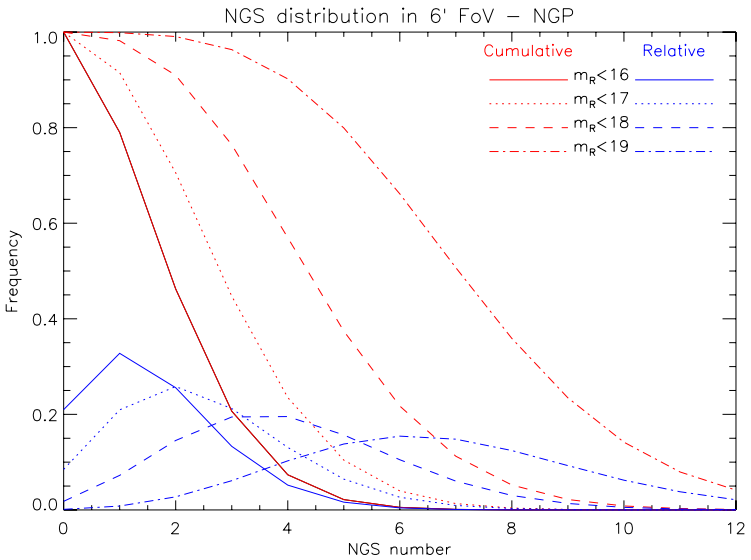

Figure 8-53: Frequency of circular 6 arcmin diameter fields as a function of the number of NGS included at the North Galactic Pole for different NGS limiting magnitudes

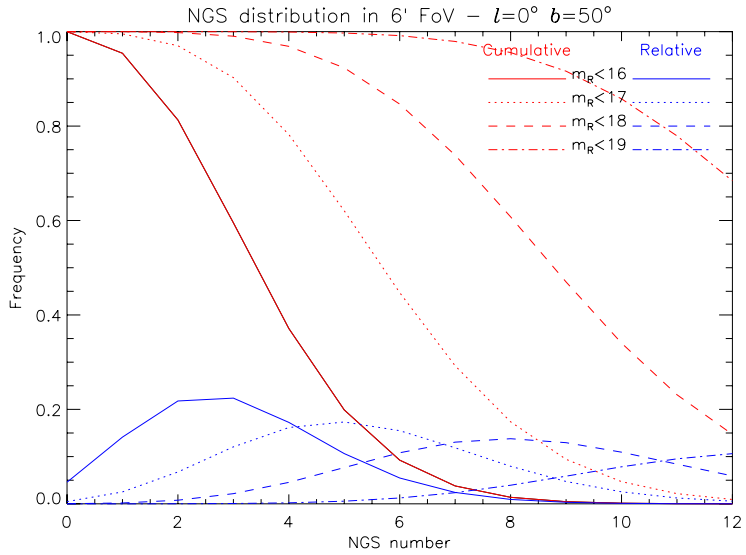

Figure 8-54: Frequency of circular 6 arcmin diameter fields as a function of the number of NGS included on them at at l=0° and b=|50°| for different NGS limiting magnitudes.

In the following we provide the performance of the GLAO using a visible SH WFS for both the "good" and "bad" seeing conditions" respectively r_0~20cm and r_0~10cm -0.53" and 1" seeing at 0.5 µm.

---

dimmed to. The label "dimmed" in the picture is there to emphasise this aspect. The images are exposures of 30 seconds, the seeing reported by DIMM was between 0.65" and 0.8" and tau0 was beween 1.9 and 3.3 ms.

Figure 8-56 provides the Ensquared Energy within a pixel of 50 mas at NIR wavelength. We see that for a NGS flux of 2e-/sub-aperture/s corresponding to m_R =17 the EE is about 12% in K band under good seeing conditions. This value drops to 2% for bad seeing conditions.

More detailed simulations can be found in RD25.

Higher Ensquared Energy values, or correction at shorter wavelengths, will require the implementation of multi- Laser Guide Stars as confirmed by the study made for the VLT GLAO system: GALACSI.

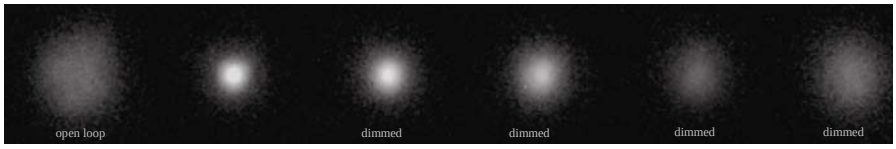

Magnitude:	**15.7**	**15.7**	**16.87**	**18.00**	**19.26**	**19.86**
CWFS raw flux:	**1.9e5 c/s**	**1.9e5 c/s**	**7e4 c/s**	**3e4 c/s**	**0.9e4 c/s**	**6e3 c/s**
FWHM:	**527 mas**	**89 mas**	**117 mas**	**143 mas**	**248 mas**	**401 mas**
Raw Strehl:	**2%**	**24%**	**15%**	**10%**	**5%**	**2.2%**

Figure 8-55: Performance of the VLT MACAO system on UT4

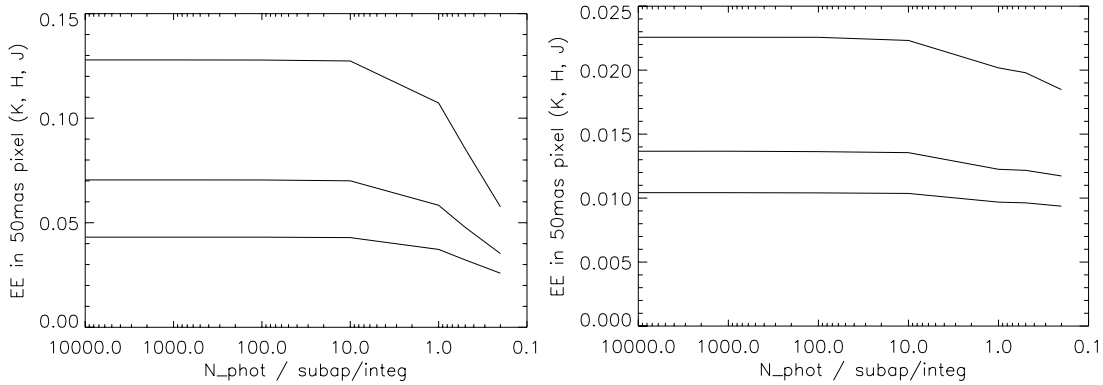

Figure 8-56: GLAO Ensquared Energy in 50mas for seeing of 0.53"(left) and 1" (right) at 0.5µm; 6 NGSs

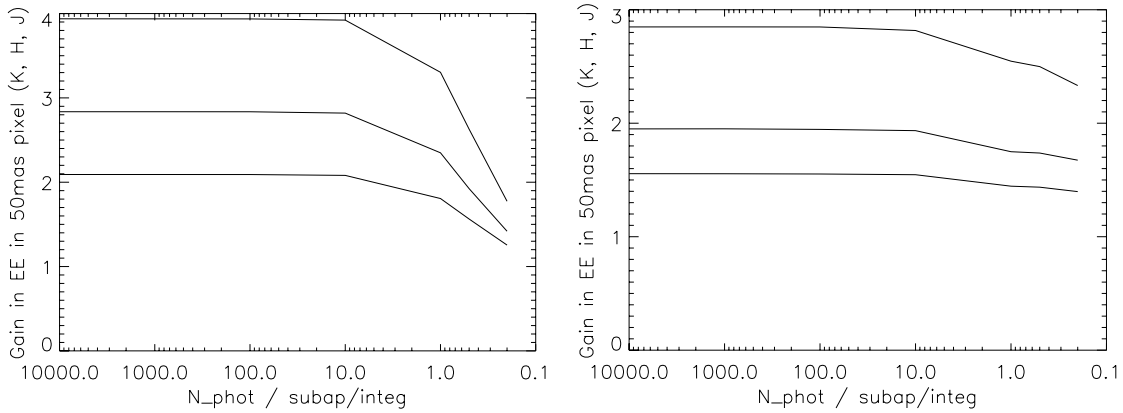

Figure 8-57: Gain of EE in 50mas brought by GLAO relative to seeing for seeing of 0.53"(left) and 1" (right) at 0.5µm; 6 NGSs

Figure 8-57 provides the gain of Ensquared Energy within a pixel of 50mas brought by the GLAO correction with respect to seeing. We see that this gain is between 3.5 and 2.5 in K-band for the good and bad seeing conditions for m_R =17.

Reducing the corrected FOV to 3' improves the EE from 12 to18%. However, if he technical FOV is also reduced to 3' this would affect the sky coverage.

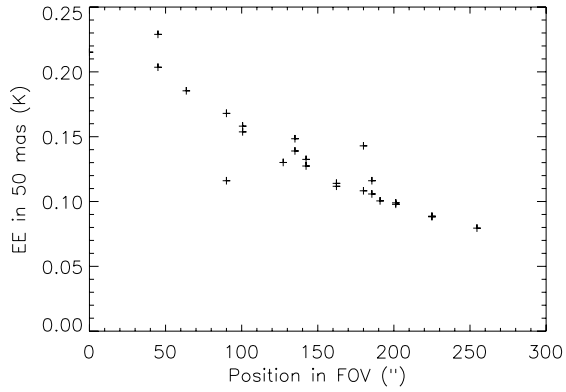

Figure 8-58: EE vs field of view position (K-band); 3NGS in 3' plus 3 NGSs [3-6']; faint star 1e-/sub-aperture/s, good seeing model

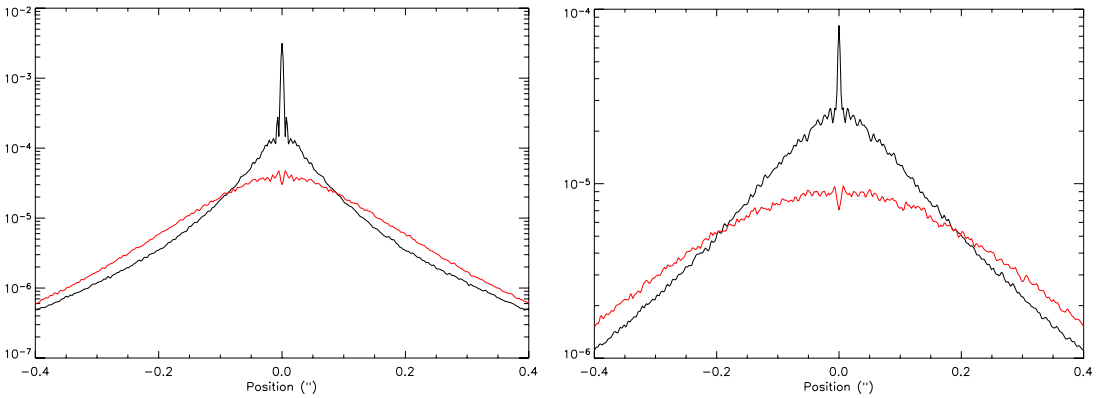

Figure 8-59: Corrected PSF with GLAO using 6 NGSs, 6', good seeing (left) and bad seeing (right), K band, on-axis, 10ph / subap / NGS top curve is GLAO, bottom curve is the uncorrected seeing.

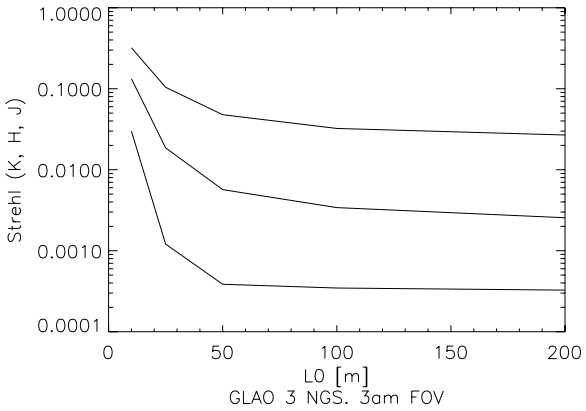

Figure 8-60: Effect of the outer scale of turbulence (L_0) on the Strehl obtained with GLAO with 3 NGSs within 3' FOV; good seeing; Top to bottom: K, H, J.

Another important performance parameter for GLAO is the corrected PSF uniformity over the FOV. Figure 8-58 provides the PSF uniformity assuming 3 NGSs within the central 3' FOV and 3 additional NGSs located in the annular FOV [3-6'].

Figure 8-59 provides the corrected PSF shapes with GLAO with 6 NGSs of magnitude of 15.1. Note the diffraction peak probably due to the effect of the turbulence outer scale L_0=25m also shown Figure 8-60.

8.2.2.4 Near-Term development plan

8.2.2.4.1 Modelling and Simulation

First order simulations have been performed to estimate the GLAO performance in near Infrared (NIR) with a 98x98 actuator systems. Sky coverage has been evaluated based on a maximum of 6 NGSs and wavefront sensors.

Statistics of turbulence profiles are now becoming available thanks to the special effort made to develop dedicated profiler tools like MASS (Multi-Aperture Scintillation Sensor) and the SLODAR (Slope Detection And Ranging). As measurements continue to be gathered, more information about the amount and the structure of the ground layer will be obtained. Based on these data, GLAO performance should be updated.

The number of NGSs to be used for wavefront sensing, the optimum technical FOV and the maximum magnitude difference between the NGSs should be tuned according to the science requirements: Ensquared Energy, corrected FoV, PSF uniformity, sky coverage.

Extensive parametric simulations remain to be done to tune the design parameters:

- Optimization of the Shack Hartmann wavefront sensor geometry fitting the M6AM geometry (Circular, hexagonal, squared)
- Optimization of the Shack Hartmann wavefront sensor pixel scale and FoV
- WFS linearity issues
- Effect of the turbulence produced by the telescope itself over the first 200-400m and variation of the turbulence along the telescope pupil
- Study of the variable M6AM conjugation altitude effect on the GLAO performance
- Full error budget of the GLAO system

8.2.2.4.2 AO concept and design

The detailed implementation of the GLAO wavefront sensors and their number into the OWL Adapter-rotator will be developed during phase B.

Although the present baseline is currently the Star Oriented concept with averaging of the wavefront measured from each wavefront sensor, concepts using the Layer Oriented approach with numerical or optical co-addition still needs to be studied.

The vignetting of the scientific FoV produced by the shadow of the wavefront sensors needs to be minimized. Potential use of a large dichroic may solve this issue but may require an evolution of the optical design towards longer backfocal distances. A reassessment of the optical design is planned at the beginning of the design phase.

Trade offs between the length of the wavefront sensor -instrument non-common optical path and the stability of the pupil matching should be studied. To correct for flexures, an internal metrology system may be required between the wavefront sensor and the instrument although this is less critical than in the case of SCAO.

In case the required density of actuators appears not to be achievable in the time and budget allocated, we have not identified at this stage any fall-back solution using a second stage post-focal deformable mirror mainly due to the large technical FOV to be propagated into the optical path up to the pupil plane where the second stage deformable mirror would have to be located.

We envisage developing the M6AM test facility such that the GLAO mode is fully tested before being installed at the telescope.

At ESO, several second-generation instruments are currently being designed for the VLT based on GLAO correction (GALACSI for MUSE, GRAAL for HAWK-I) combined with the development of the VLT Adaptive secondary and the new generation of the CCD WFSs. The purpose of GALACSI is to improve by a factor 2 the ensquared Energy within 0.2" in the visible over a FOV of 1', while GRAAL will increase the Ensquared Energy within a pixel of 0.1" in the IR over a FOV of 10' diagonal. Both GLAO systems make use of multiple LGSs providing higher sky coverage and the expected performance even under bad seeing conditions. Apart from their own scientific interest at the VLT, they are considered as an essential step toward the implementation of more performant GLAO systems at the OWL telescope.

Furthermore, preliminary studies on GLAO for ELTs are also in progress in the frame of OPTICON-JRA1 and the ELT design study in the AO WP. In this context, the MAD demonstrator can provide an early insight into important aspects of GLAO, such as wavefront reconstruction and control techniques.

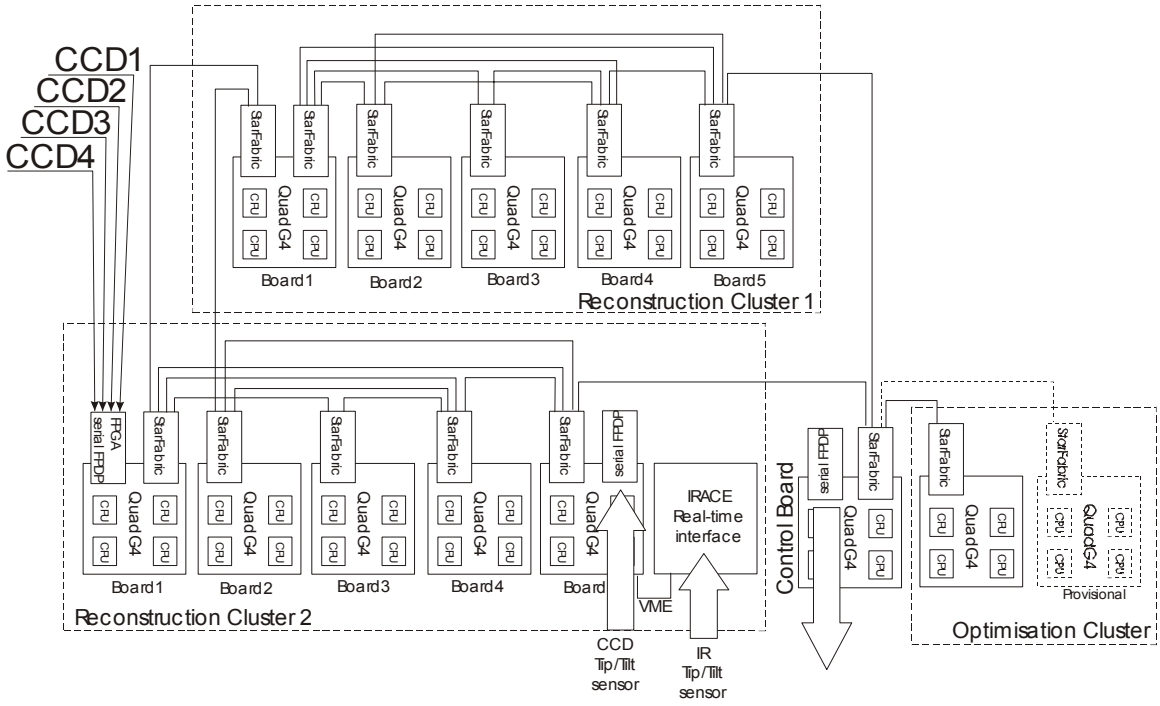

Figure 8-61: HAWK-I concept based in CPU-only SPARTA architecture. With the new FPGA architecture the number of computational units will be reduced.

The GLAO star-oriented configuration of MAD comprises three Shack-Hartmann WFSs and one bimorph DM conjugated to the telescope pupil. Also, the maximum scientific/technical FoV of MAD is 2 arcmin. With MAD we will be able to investigate different aspects of wavefront reconstruction for GLAO.

The calibration aspects regarding GLAO are also being studied on MAD. It essentially consists in minimizing the calibration error and the calibration time as described as described in the dedicated paragraph of SCAO and MCAO and in RD27..

8.2.2.4.3 AO key component status and development

The key components, corrector and wavefront sensors are essentially identical to the SCAO system. There is no additional component development required for the implementation of the GLAO system.

The RTC concept is based on the same modules used for the SCAO case, so no special development is needed apart from the development of a 6-channels input processor since the

current hardware developed under the OPTICON/JRA-1/SPARTA project supports only 4 input channels.

This concept is also used in MAD, with a prototype SPARTA architecture, and with higher performance in GALACSI and GRAAL.

8.2.3 Distributed Multi Object Adaptive Optics

A highlight science case is: First light- The First Galaxies and the Ionization State of the early Universe. It aims at peering into the Dark Ages of the Universe when the universe was re-ionized by the UV flux emitted by the first sources of light. Recent observations of the high redshift universe suggest that stars and galaxies started to form and to assemble early in the redshift range of 7-15. Understanding this key epoch is of paramount importance and requires the following exquisite instrument capabilities on OWL:

- Multi Integral Field Unit (IFU) observing mode
- Number of IFU targets: 30 or higher for a 6x6' FoV
- Image quality at 30% ensquared energy: 50 mas or better at selected area in the field (direction of the IFU targets)
- Spatial sampling: 10-30 mas
- Spectral resolution: 5000-8000
- Spectral coverage: Y (1.06 μm) to K (2.2 μm) bands
- IFU field of view 0.8''

The underlying Adaptive Optics concept – namely Multi-Object Adaptive Optics (MOAO) or Distributed Adaptive Optics - Figure 8-62- is therefore to correct atmospheric turbulence in selected directions of the sky where the IFU are pointing.

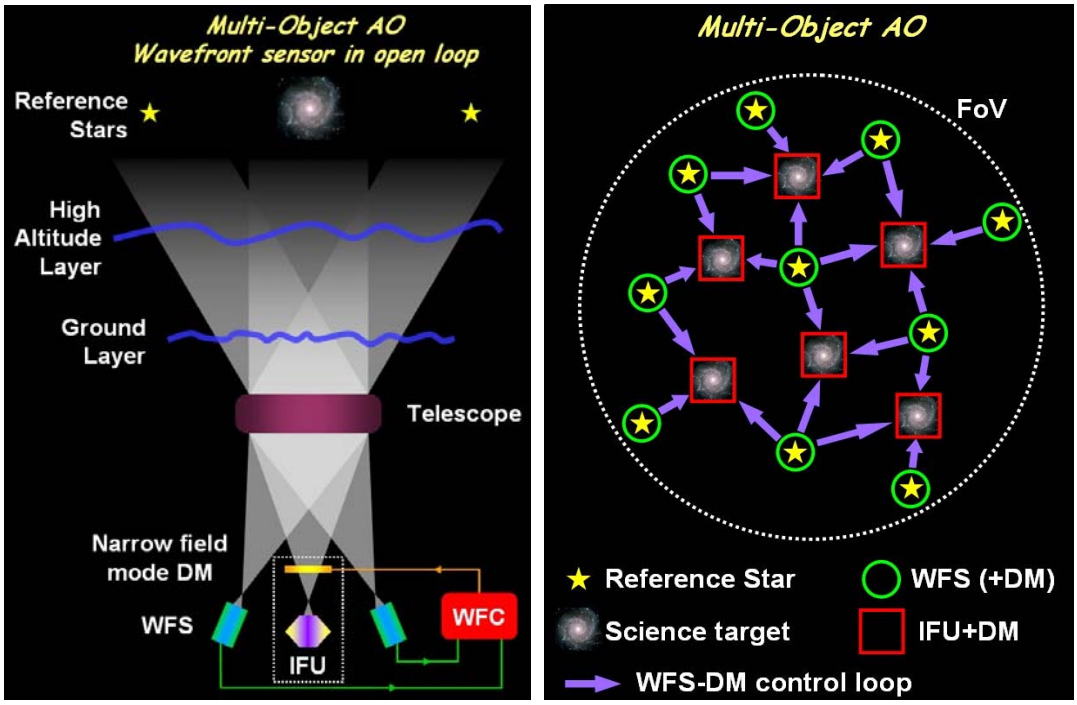

Figure 8-62: Concept of Multi-object Adaptive Optics or Distributed Adaptive Optics with wavefront sensors in open loop

This can be accomplished by paving the focal plane with WFSs units in the direction of the reference sources for a local determination of the turbulent wavefront and with Deformable

Mirrors (DMs) in each of the IFU channels. In this approach the Adaptive Optics system operate essentially in open loop as the wavefront sensors do not see the correction applied by the deformable mirror and therefore do not operate around the zero position. This concept requires wavefront sensors with a high dynamic and linearity and deformable mirror with high linearity and blind position accuracy. This extends the FALCON (Fiber-spectrograph with Adaptive optics on Large fields to Correct at Optical and Nar-infrared) concept described [102].

Alternative MOAO concepts are being considered to reduce the potential WFS dynamic and linearity issues by adding local deformable mirror to each wavefront sensor -Figure 8-63-. In this concept, the correction is optimized in each IFU and WFS directions. High linearity and blind position accuracy of the local deformable mirror are required. The drawback of this approach is the increase of complexity as more deformable mirrors need to be controlled.

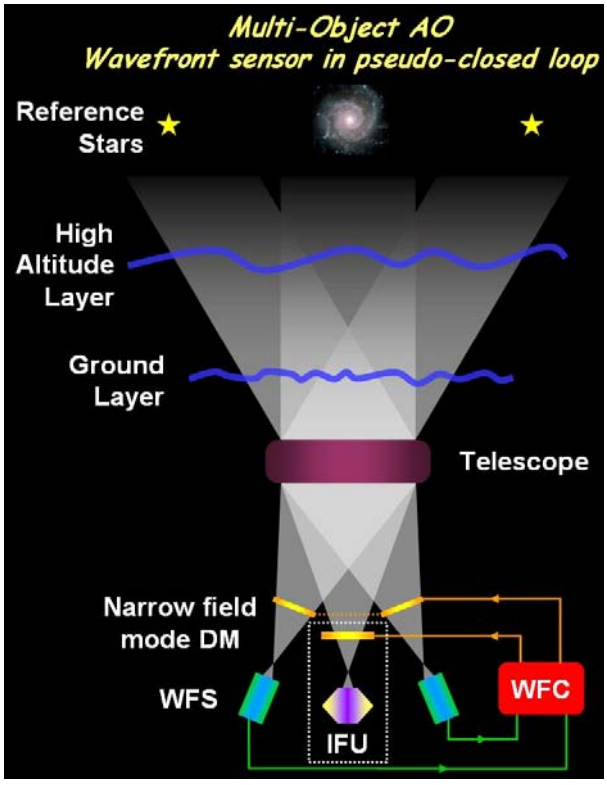

Figure 8-63: MOAO concept with the wavefront sensor in pseudo closed loop

In the following, we will assume that the MOAO system is combined with the GLAO system described in section 8.2.2. Several reasons motivate this approach:

- The availability of the M6AM unit
- The reduction of the local DM stroke requirements (expected to be critical)
- The complementarity of the two concepts

In this concept the wavefront of all available wavefront sensors in the FoV will be combined to control the M6AM unit in order to minimize the wavefront residual over the whole FoV while the local DM correction will be optimized in the direction of each IFU (and optionally each WFSs – Figure 8-64).

In the following section we will assume a GLAO + MOAO system with the WFSs in pseudo closed loop. This concept may evolve in phase B based on the studies and demonstration experiments planned. The possible AO implementation concept is derived from the MOMFIS (Multi-Object Multi Field Infrared Instrument) study described in 12.2.3.4 and a possible development plan towards the construction of such instrument.

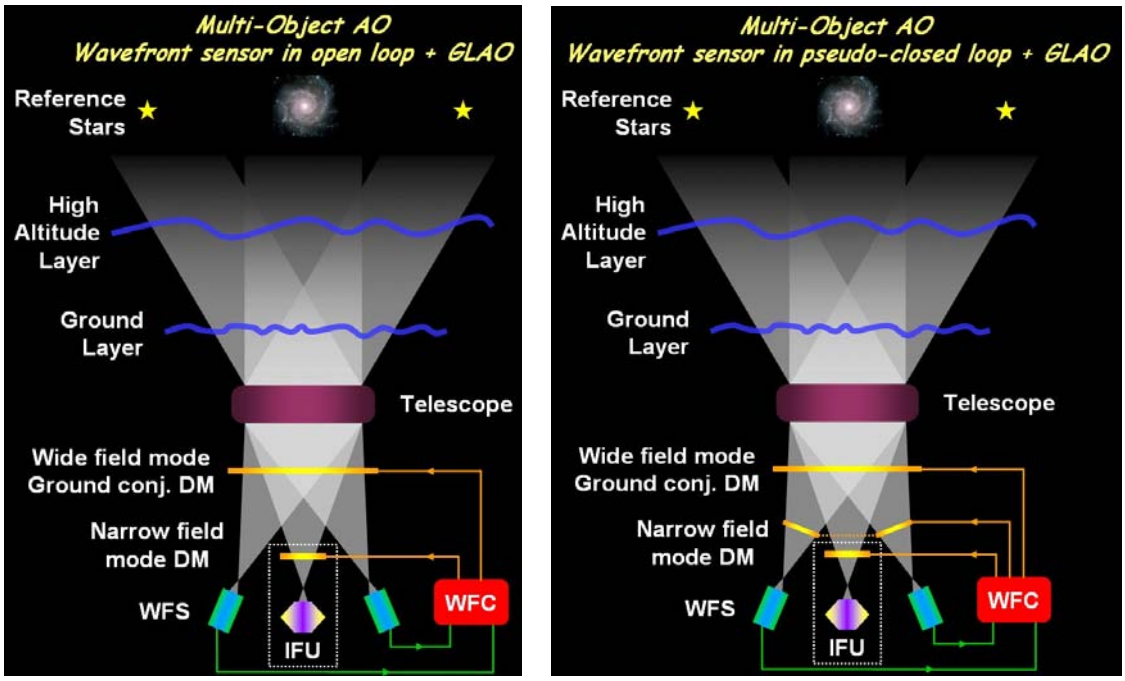

Figure 8-64: GLAO combined with MOAO concept with the wavefront sensor in open loop (right) and in pseudo closed loop (left)

MOAO should support telescope nodding at 0.1 Hz by fast opening/closing GLAO loop (0.1s).

MOAO should also be able to correct for differential atmospheric dispersion between the wavefront sensing NGS and the Science object during an observation by applying offsets to the wavefront sensor. The calculation of the offset shall be done by the software based on the science beam effective wavelength provided by the instrument, the spectral types of the NGSs provided by the observer, the science and guide star coordinates provided by the observer, the relevant atmospheric data (Temperature, Pressure, and Humidity) provided by the observatory –with the required accuracy. MOAO will not correct for the atmospheric dispersion within the scientific band pass of the instrument.

8.2.3.1 Implementation Concept

8.2.3.1.1 Overview

Figure 8-65 represents the high level functional diagram of the instrument. The Science channels are represented in blue and consist of:

- A target selection system: it direct a science beam from the telescope focal plane to the deformable mirror
- A deformable Mirror: it corrects the wavefront in the direction of the target
- An Integral Field Spectrograph (FoV 0.6-1”, sampling 20-30mas, spectral resolution 4000-8000).

The reference sources (assumed here to be NGSs but the concept can be applied to LGSs equally well assuming LGSs can be implemented) are represented in blue. The NGS beams are directed from the telescope focal plane up to the WFS with a selection system partly similar to the target selection system. These NGSs can be acquired over the full instrument FoV. In the implementation example 10 WFSs are foreseen, but this number can be freely adjusted.

Figure 8-66 provides the general implementation of the system. An important feature of MOMFIS is that it uses the same selection system (pickoff mirrors) to direct the light to the science and to WFSs channels, providing full configuration flexibility. NGS can be as close as 5” from the target FoV. Up to 10 or more reference sources can be selected.

8.2.3.1.2 Wavefront sensor

For linearity reasons important for the MOAO concept, the baseline for the WFS will be a Shack Hartmann with 100x100 sub-apertures and potentially with 6x6 pixels/sub-aperture. This is quite similar to the SCAO and GLAO WFSs. At this stage it is not clear whether the WFS buttons will also be equipped with a local deformable mirror reducing the linearity effect due to the pseudo-open loop or whether the number of pixels will be enough to ensure a good correction in this mode. Several control schemes will have to be studied during phase B.

To reduce the stroke requirements on the local deformable mirror, it is foreseen to use the wavefront measured by all wavefront sensors in the FOV to correct for the Ground layer using the M6AM unit. The wavefront to be corrected by the local deformable mirror in the direction of the targets or in the direction of the WFSs is essentially the remaining turbulent layers.

8.2.3.1.3 Micro deformable mirror

Preliminary studies performed in the frame of the VLT FALCON concept study have shown the importance of a linear response of the local deformable mirror. The micro-deformable mirrors based on the electrostatic concept seem well adapted for this application. Assuming a 250µm actuator pitch the size of the DM is 25mm. It remains to be determined whether the amount of residual turbulence to be corrected by the MDM is compatible with the stroke which can be delivered by this kind of technology.

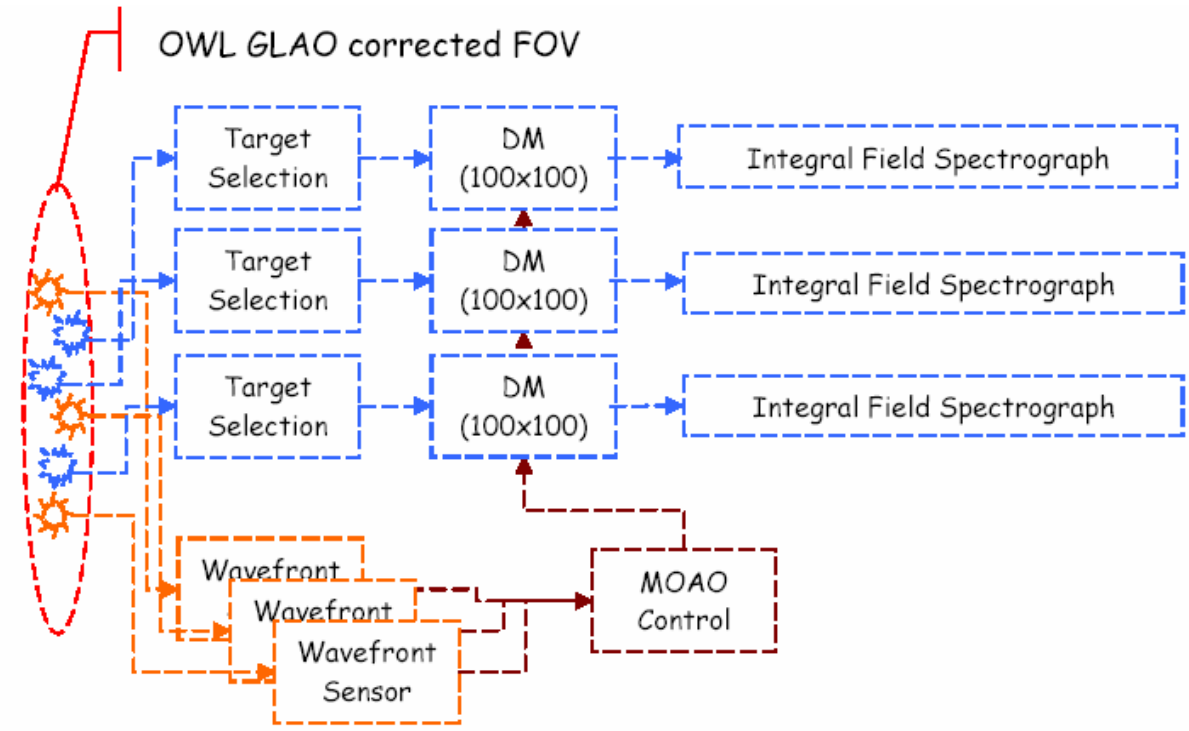

Figure 8-65: MOMFIS schematic functional diagram (Courtesy LAM, France)

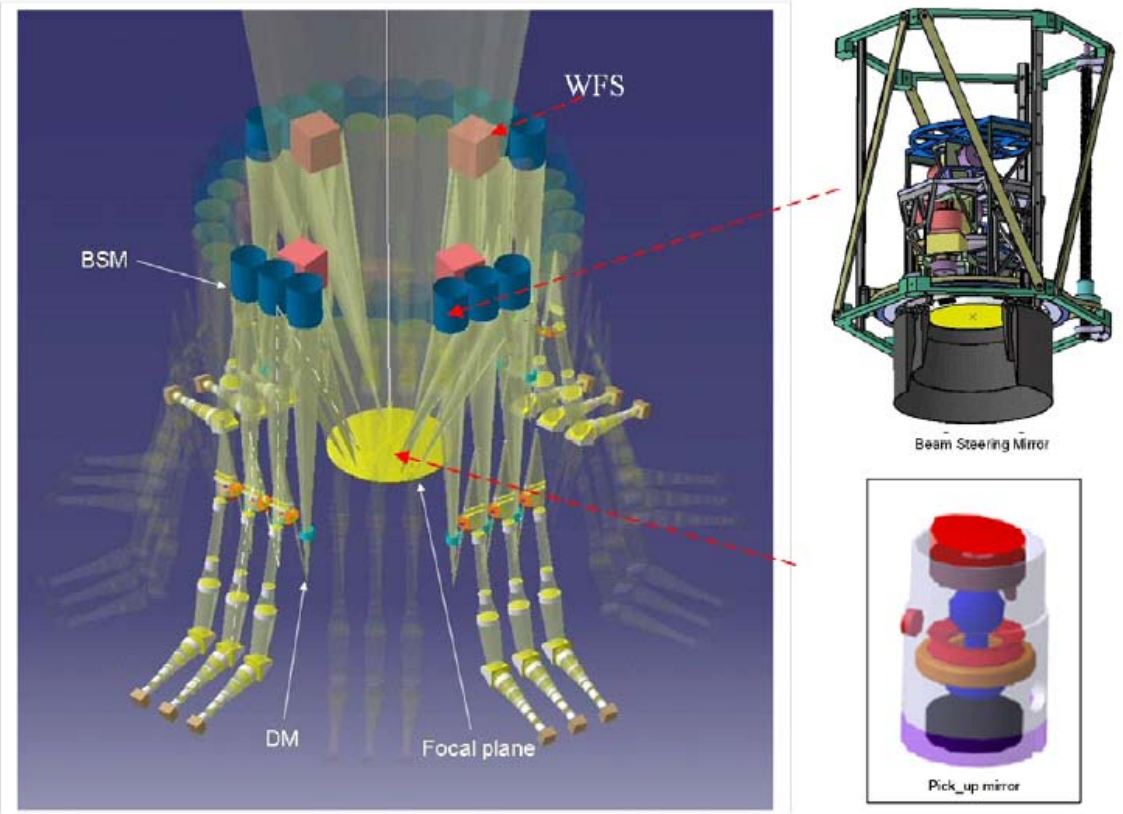

Figure 8-66: MOMFIS general view of the implementation: in the focal plane small pick-off mirrors are positioned with a robot, directing the target beams steering mirrors and the reference star beams to the WFS. The steering mirrors direct in turn the beam to the DM and IFU units (Courtesy LAM, France)

8.2.3.1.4 Control and Real Time computer

MOAO is a multi-sensors / multi-mirrors system. Sensors are actually complete AO systems and they incorporate a local mirror for local control (the local mirror is optional but it is the current baseline). Three sensor systems measurements can be combined to drive a mirror (the corrector, serving one IFU) placed to correct a different region of the sky, architecturally similar to the GLAO case, but without averaging the measures in order to optimize the correction in the direction indicated by the position of the correcting mirror. All the sensor measurements are also combined to control in common M6AM, used to correct for large common aberrations, including tip and tilt.

The sensor systems are distributed on the field over guide stars, while correctors (IFUs) are distributed on the field in correspondence to the scientific object(s) of interest. Guide stars are grouped in order to have 3 of them for each corrector. Groups are called “clusters” and there are as many clusters as correctors. A star can belong to multiple clusters.

Guide stars run a local control loop with the local DM.

Each cluster collects the measurement of each sensor of the cluster (and the DM position) to compute the correction on the cluster DM.

Figure 8-67 shows the control architecture of the MOAO system. The 10 sensor systems or buttons receive the light from different guide stars. The picture shows 3 of them. The control loop is a standard SCAO control for each sensor system (or button).

All the gradients of the 10 sensor systems are collected and averaged by another RTC that will drive M6AM with this input. This is fully equivalent to the GLAO control system.

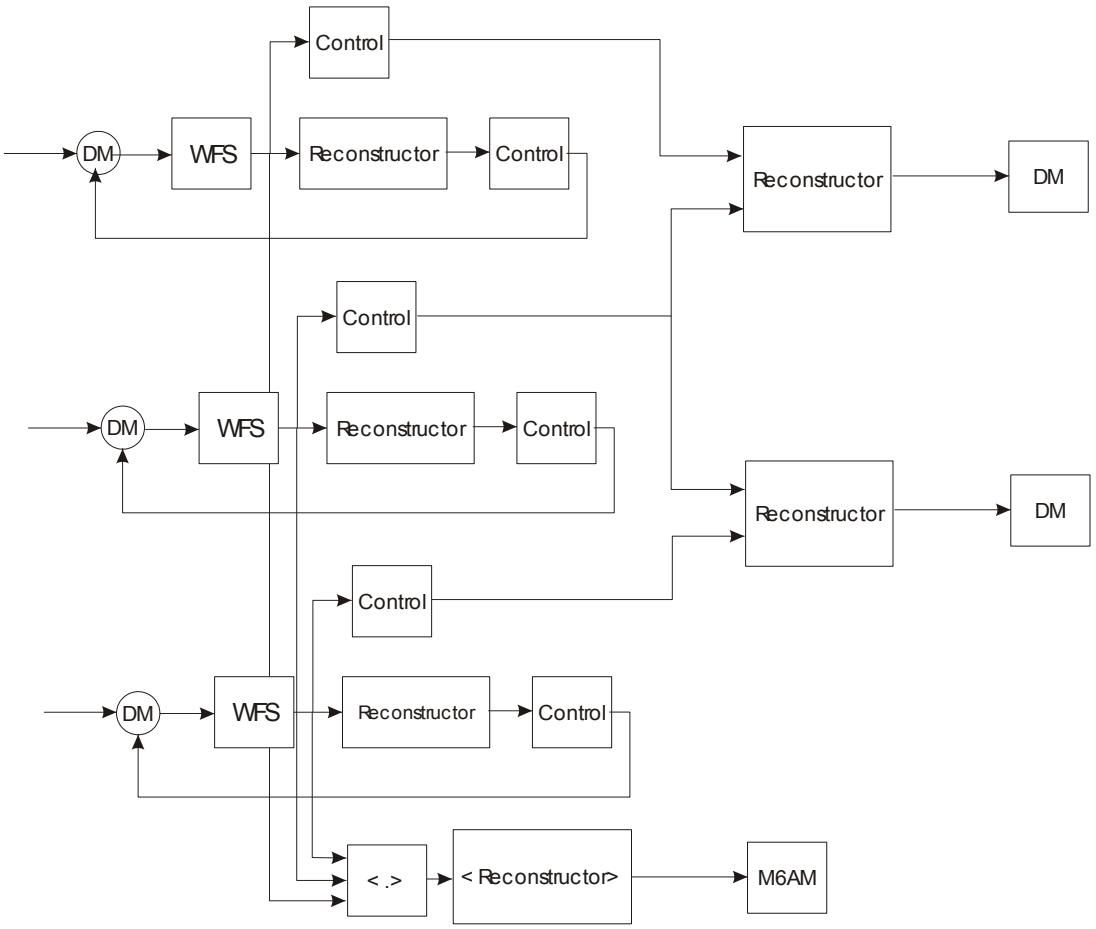

Figure 8-67: MOAO control loops

The goal of the MOAO system is to correct the field around 30 science spots. On the light path of each of them a deformable mirror corrects the light. To control the DM, each of the 30 science spots (or IFU) has its own RTC. This RTC is configured to receive the measurements of the atmosphere of the three closest buttons in order to reconstruct the turbulence in the direction it is actually looking. Of course, no button is looking exactly in the direction of any of the IFUs, so this reconstruction is done in open loop since the effect of the IFU DM is not observed by any sensor.

The IFU RTC needs to receive information about the atmosphere, not the residuals that the button sensor is looking at. This information is contained in the actual position of the mirror in each button. Unfortunately it would be inconvenient to wait for that information, since one full frame is required to produce it. In this case the IFU RTC would run with one additional frame delay, which is unacceptable. In the case of a simple integrator, the button control system will run with:

$$y[n]=y[n-1]-gAx[n] \qquad \textit{Eq. 8-2}$$

Where ‘y’ is the position of the mirror, ‘x’ is the gradient vector, ‘g’ the gain and ‘A’ the control matrix. If now we run the following system:

$$s[n]=s[n-1]-gx[n] \qquad \textit{Eq. 8-3}$$

$$y[n]=As[n] \qquad \textit{Eq. 8-4}$$

One can easily see that the output signal ‘y’ is identical to the previous case, but now we have a signal that is proportional to the DM position and that can be computed in a very short time. This

is the signal that will be sent to the IFU RTC without delay and that can be used to reconstruct the turbulence along the IFU direction.

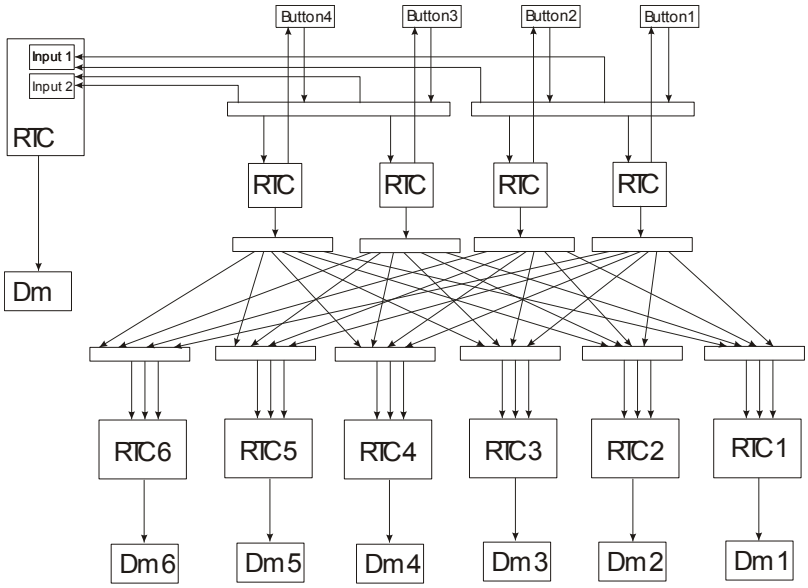

Figure 8-68: MOAO Real-Time Computer Concept. The diagram shows an example with only 4 wave-front sensors with local DM and 6 clusters each serving one IFU. The Dm on the right side is the M6AM.

Each wavefront sensor system is similar in concept to the SCAO system, so each of them will be a clone of such system. The correction of the global DM M6 is similar in concept to the GLAO system, with additional complexity due to the number of sensors. The real additional complexity is given by the cluster control since the measurements of the three sensors cannot be averaged together but a full reconstruction matrix has to be used.

The system is made by three classes of sub-systems, one which is identical to the SCAO case, one very similar to the GLAO case and a new concept to implement the cluster.

8.2.3.2 Predicted performance

The MOAO performance was estimated using real scientific targets, and the associated guide stars constellations (“fields”, see Table 8-14). The analytic simulation too, Cibola, was used for this performance estimation.

Field denomination	**Corresponding number in** Figure 8-68**,** Figure 8-70
UKIDSS-XMM-LSS (center)	Field 0
UDF (center)	Field 1
COSMOS (center)	Field 2
CFHTLS-d1 (center)	Field 3
AC114 (center)	Field 4
Abell 1689 (center)	Field 5

Table 8-14. Field references.

Using real astronomical fields allows us to show that even if sky coverage is limited, some interesting fields can still be observed. In Figure 8-69, we can see that Abell 1689 and AC114 can be observed with quite good performance (gain of a factor of ~20 in ensquared energy within a 50 mas pixel in H band, 1’’ seeing), whereas UKIDSS-XMM-LSS and UDF have rather small gains (factor ~2). We can also see there is a significant benefit in using 8 rather than 3

guide stars, and that it is better to take the brightest ones rather than those closer to the the observed fields. We have done the same analysis with 12 NGS instead of 8, and the gain was minimal, especially compared to the added system complexity. In Figure 8-69, the solid lines represent the 8 NGS case, the dashed lines the 3 NGS case. The top line is when the brightest 8 (or 3) stars are considered, the bottom line when the nearest (to the center) are used.

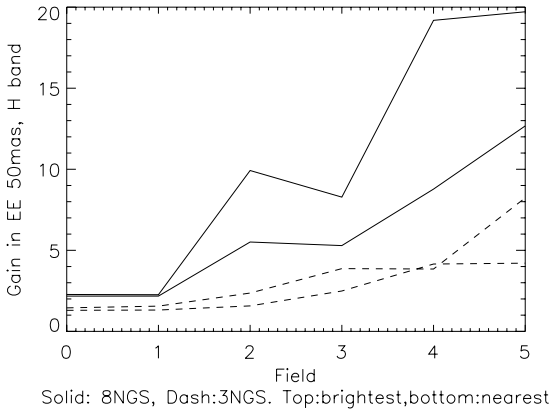

Figure 8-69: Gain in Ensquared Energy in a 50 mas pixel for each scientific target, H band, 1" seeing.

The distribution of the guide stars both spatially and in brightness can be seen in the following two plots (Figure 8-70). On these figures, the solid lines represent the 8 NGS case, the dashed lines the 3 NGS case. The top line is when the brightest 8 (or 3) stars are considered, the bottom line when the nearest (to the center) are used.

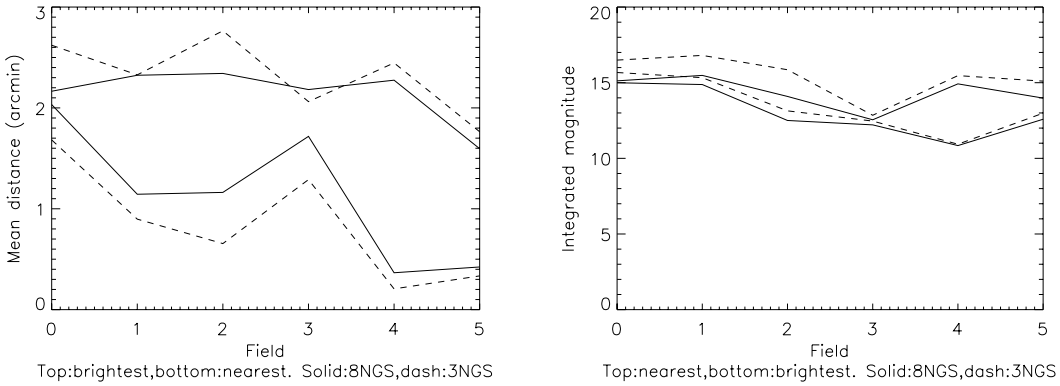

Figure 8-70. Left: mean distance to the center of the field (arcmin) for the considered constellations. Right: integrated magnitude of all the used NGSs

A more detailed analysis of the MOAO performance based on analytical simulations as well as the assumptions and AO parameters are provided in RD26.

8.2.3.3 Near-Term development plan

The following development plan aims at developing a MOAO instrument as a first generation OWL instrument. This assumes the availability of the GLAO correction capability at the telescope from the beginning.

It is worth noting that alternatives can be considered e.g. limiting the FoV of the instrument to the MCAO FoV and decresing the Multi-object capability. While such a solution would dramatically simplify the instrument, it is likely that it would also reduce its scientific value.

8.2.3.3.1 Modelling and Simulation

Simulations have been performed by ESO using CIBOLA software. Simulations efforts will be continued at ESO and at various institutes (LAM, GEPI, LESIA, ONERA) involved in MOMFIS & FALCON developments. A multi-simulations approach using different software environments is considered necessary to confront and compare the results. Simulations will be performed for a wide range of input parameters, such as seeing conditions, turbulent layer heights etc. Of crucial importance is the issue of Sky coverage which will be given special attention.

8.2.3.3.2 AO Concept and design

The following items are critical to an MOAO system and will need to be demonstrated / validated first with laboratory tests:

- Open loop wavefront measurements and operation, WFS linearity
- Control command algorithms
- DM performance: open loop, reliability, reproducibility, stability, linearity etc..
- Calibration issues

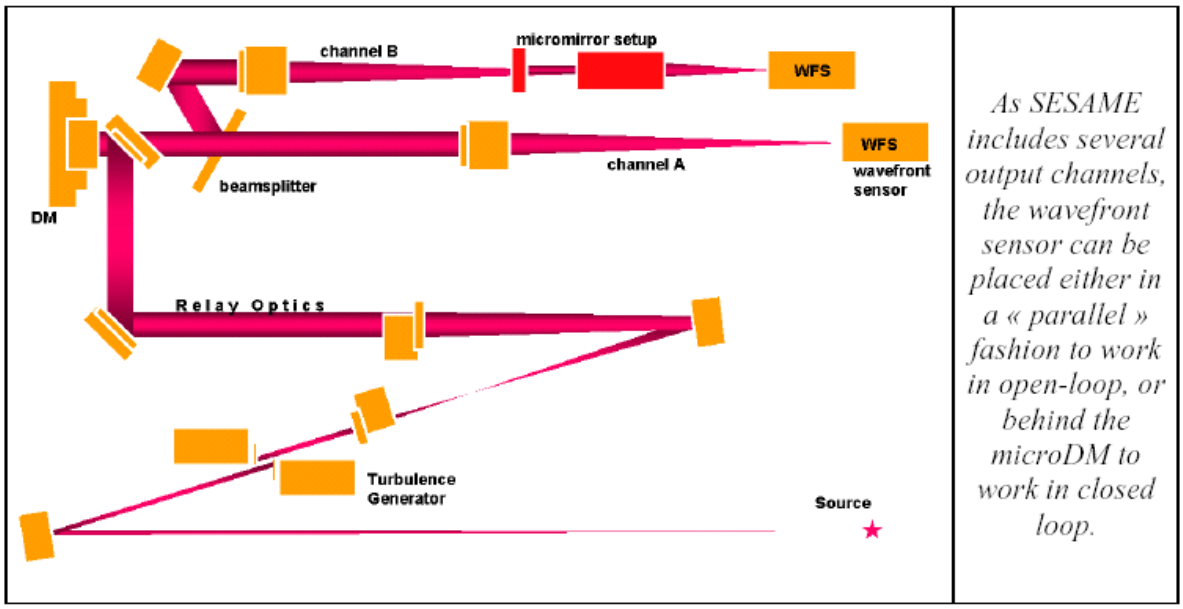

Figure 8-71: Optical setup of SESAME (Courtesy LESIA)

A test bench called SESAME is under construction at LESIA (France) and will be used for this purpose. It is shown in Figure 8-71. It allows carrying out tests either in closed loop or in open loop. It will be extensively used to characterize the MOAO approach both at component and at system level by the MOMFIS team:

- Mirror deformation, comparison to models, mirror calibration etc..
- Wavefront sensor test. The open loop WFS operation will be tested (in particular linearity and dynamic) by direct comparison of the reconstructed wavefront from two WFSs on two parallel channels. R&D is foreseen on reconstruction algorithms in the frame of OPTICON JRA1.
- Single direction, on-axis optimization. A wavefront sensor measures the turbulent wavefront on-axis and the MDM is controlled in open loop. The residual error is compared to the model. Calibration errors can be introduced and their impact measured.

- Single direction, off axis optimization. A tomographic reconstruction process is required and robustness of the tomographic reconstruction process with seeing and turbulence profile variation will be investigated.
- Simulation of the GLAO corrected turbulence by removing the ground layer phase screen
- Multi WFS operation. The core MOAO operation can be tested by placing several WFS in the FoV and controlling the DM(s).

After the results of the laboratory tests a demonstrator may be required to validate the MOAO concept on-sky- similarly to the MCAO demonstrator MAD.

8.2.3.3.3 AO key component status and development

MOMFIS will require the development of large stroke Micro-Deformable Mirror with 100x100 actuators with a high reliability, reproducibility and stability. The actuator pitch should be small -250µm- to be compatible with the volume requirement of the IFU and potentially WFS buttons.

The RTC concept is based on component and technologies already used in the previous systems with the exception of the switch that is used to dynamically route the buttons to the IFUs. Currently available products feature 8 ports with very low-latency figures. Products with 32 or more ports are also available but we have not tested them yet.

Some R&D is being pursued in the frame of the OPTICON JRA1 at LAOG (France) in this field: 2kx2k MDM with 6 µm goal 10 µm stroke and 1 µm goal 2 µm inter-actuator stroke. Although the inter-actuator may be on the short side, this is a first step toward large stroke MDM with a number of actuator close to what is required for the MOMFIS application.

8.3 Second generation Adaptive Optics

The second generation adaptive optics capability of OWL starts with the replacement of the passive, temporary M5 unit with an adaptive one. This should allow for a limited but not negligible increase of the corrected field of view, mirror M5 being conjugated to an altitude of ~7 km. The diameter of this mirror would be 3920 mm for 10 arc minutes unvignetted field of view but this diameter could be reduced to 3630 or 3420 mm if slight vignetting in the active, respectively adaptive control fields could be tolerated. The second generation Adaptive Optics includes:

- Multi Conjugate Adaptive Optics (MCAO)
- Extreme and high contrast Adaptive Optics for EPICS (Extra-Solar Planet Imaging Camera Spectrograph)

The MCAO makes use of the same wavefront sensors baseline described the for GLAO correction with optimization of the reconstructed wavefront on the portion of the field of view interested by the scientific instrumentation. The high altitude conjugated deformable mirror M5 has an actuator pitch of 25-40 mm depending on the error budget for the MCAO system. The single star footprint is 3.2 m and the meta-pupil (beam footprint) is 3.63m for 6'. For an actuator pitch of 25 mm the total number of actuator is 145×145 and 128×128 on a single footprint giving a pupil sampling of 0.78 m. The required stroke is lower than M6 due to the ground layer correction performed by M6. The Real-Time Computer technology for MCAO is essentially available today (albeit at a presumably high cost and with a non-optimal architecture).

EPICS will use M6 as a first corrector for large amplitude wave-front errors. A post focal XAO system with 1.710^5 degrees of freedom will provide the high Strehl and high contrast required for high dynamic range imaging. The current baseline for this system is to implement a two-stage correction, one based on a 500x500 micro-deformable mirror (20 cm actuator separation on pupil) to be controlled at about 1 KHz using a Shack-Harn sensor and a second stage with

150x150 actuators controlled at 3 KHz together with a Pyramid sensor. Significant technological devolpments are needed for the Real-Time-Computer.

8.3.1 Multi Conjugate Adaptive Optics

Multi-Conjugate Adaptive Optics (MCAO) aims to enlarge the FoV over which diffraction limit can be achieved. MCAO can be seen as a step forward on the GLAO concept where the correction is not applied only to the ground layer but also to other altitudes above the telescope aperture through additional deformable mirrors optically conjugated to them.

MCAO benefits from the simultaneous wavefront sensing of several NGS located in and/or around the FoV which is the target of the correction. The light of these NGS probes the atmospheric volume interested by the FoV and provides, up to a certain extent, the information on the vertical distribution of the atmospheric turbulence (see Figure 8-72).

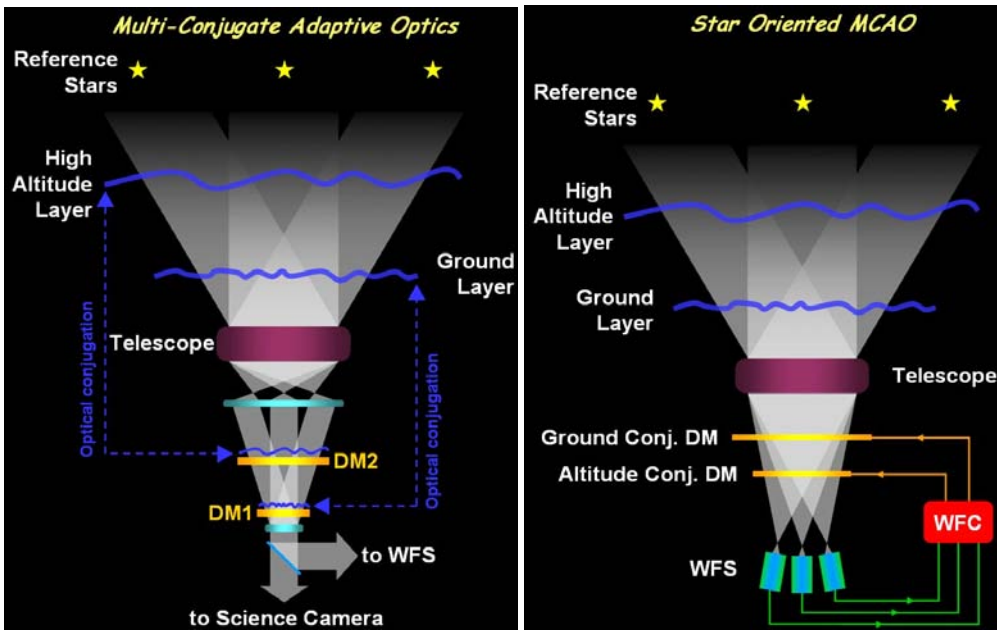

Figure 8-72: General MCAO concept (left). Star Oriented MCAO concept (right). Each NGS wavefront is measured with dedicated WFS and the signals are recombined to determine the correction to be applied to each DM conjugated at different altitudes.

MCAO suffers from limitations due to anisoplanatism, limited number of correction altitudes and availability of NGS (Sky Coverage). For these reasons the Strehl correction achieved with MCAO can be significantly lower than one obtained with SCAO and the correction uniformity across the field is not optimal.

The MCAO concept presented here for OWL is a Star Oriented facility and it is an extension of the GLAO facility: the WFS used are the same ones implemented for GLAO and the ground conjugated DM is M6. The high altitude conjugated DM is the adaptive version of M5 which is conjugated at ~7 Km above the telescope aperture. As the initial implementation of MCAO will probably be based on NGS the sky coverage is naturally limited, especially at the galactic poles, and the Strehl correction and uniformity are not as high as when Laser Guide Stars will be implemented.

- In the case of OWL one of the instruments which will benefit from MCAO correction is ONIRICA (Owl Near InfraRed Imaging Camera, see Figure 8-73). The central lens is for the narrow field imaging mode (diffraction limit) 1 arcmin FoV and the image is split into several channels to the IR detectors. The large array of microlenses is for the wide field imaging mode (non diffraction limited) which can benefit also from GLAO (see section 12.2.3.3 for more information about this instrument).

It is worth noting that if the instrument's requirements in terms of correction do not match the ones provided by the OWL MCAO facility, the instrument itself should be equipped with its own AO system which can in any case partially benefit from the OWL MCAO facility.

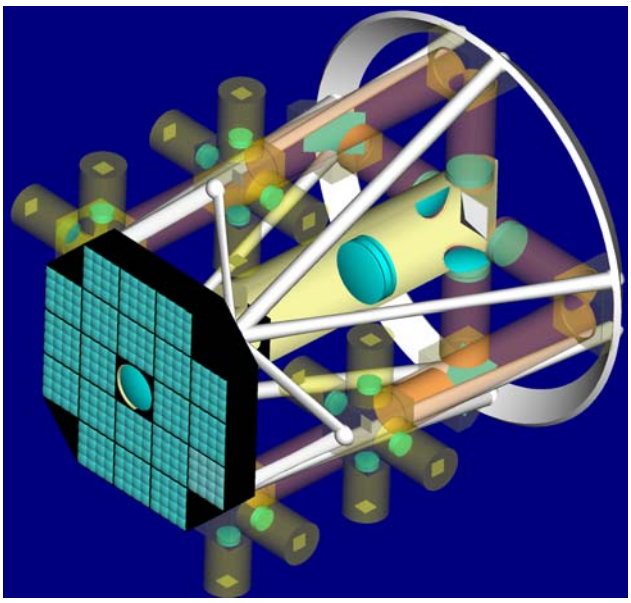

Figure 8-73: Opto-mechanical concept of ONIRICA (Courtesy INAF)

8.3.1.1 Performance requirements

The Multi-Conjugate performance requirements as applied to ONORICA are as follows (FoVs specified herein are in diameter):

- MCAO aims at providing diffraction limited images at NIR wavelengths (J-K bands) over a minimum 1' FOV using Natural Guide Stars (NGSs) for wavefront sensing.
- MCAO should provide the Strehl ratio performance according to Table 8-15 and Table 8-16 with a sky coverage of 5% at the North Galactic Pole and to sky coverage of 50% l=0° and b=50° (technical FOV of 6', NGS cluster of magnitude 16).
- The maximum un-vignetted technical FOV usable by the MCAO system is 6'.
- MCAO should support telescope nodding at 0.1 Hz by fast opening/closing GLAO loop (0.1s).
- MCAO should support small amplitude -1"- mosaicking in closed loop by offsetting the WFSs synchronously. The accuracy of the offset should be better than 1/2 of the spatial pixel size
- MCAO will not support chopping
- MCAO should provide in closed loop Field Stabilization to the telescope with the maximum amplitude characteristics provided in Table 8-1. For wavefront sensor dynamic reasons, the telescope guider will support MCAO for closing the AO plus Field stabilization loop before the control of the field stabilization corrector is taken over by the MCAO in closed loop.
- MCAO should permit to observe without AO (but with Field Stabilization) without any transmission loss with respect to the telescope. In that case, the field stabilization corrector is not controlled by the AO system.
- MCAO should make use of the two deformable mirrors (M5 and M6) conjugated at 0 and ~7 kms and implemented in the telescope optical train.
- MCAO should have the capability to correct for some of the telescope aberrations left by the active optics with an amplitude lower than 20% of the atmospheric wavefront at all

spatial and temporal frequencies. Errors beyond these values will be handled by the active optics.

- The transmission of MCAO should be maximized for the instrument observing wavelength T>95%;
- Vignetting of the scientific FOV by the MCAO wavefront sensors should be minimized (TBC)

- For the performance evaluation of MCAO seeing assumptions should be: 0.53 and 1" at 0.5 μm at zenith; with τ0=3 and 2ms. For the performance evaluation the outer scale of turbulence should be L0=25 m. For the determination of the AO design parameters the following atmospheric parameters should be assumed: turbulence outer scale L0=100m, seeing=1.5", τ0=2ms –Figure 8-4-
- MCAO shall be able to correct for differential atmospheric dispersion between the NGS and the Science object during an observation by applying offsets to the wavefront sensor. The calculation of the offset shall be done by the software based on the science beam effective wavelength provided by the instrument, the spectral type of the NGS provided by the observer, the science and guide star coordinates provided by the observer, the relevant atmospheric data (Temperature, Pressure, and Humidity) provided by the observatory – with the required accuracy. MCAO will not correct for the atmospheric dispersion within the scientific band pass of the instrument.

	Wave band	**K-band**		**H-band**		**J-band**	
	Guide stars magnitude	V=12	V=17	V=12	V=17	V=12	V=17
seeing, τ_0, L_0 @ 0.5μm	0.53", 3ms, 25m	32	24	13	8	3	1
	1", 2ms, 25m	7	4	1	0.3	0.04	0.008

Table 8-15: MCAO performance (Strehl Ratio, %) over 1' FOV vs. seeing and NGS magnitudes;

	Wave band	**K-band**		**H-band**		**J-band**	
	Guide stars magnitude	V=12	V=17	V=12	V=17	V=12	V=17
seeing, τ_0, L_0 @ 0.5μm	0.53", 3ms, 25m	2	0.1	0.8	0.1	0.2	0.03
	1", 2ms, 25m	0.3	0.07	0.06	0.03	0.006	0.001

Table 8-16: MCAO Strehl Ratio variation (in rms Sr) over the 1' FOV;

8.3.1.2 Implementation Concept

8.3.1.2.1 Corrective elements

The implementation of the MCAO system for OWL is conceived as an extension of the GLAO system with two deformable mirrors: M5 and M6. M6 is described in section 8.2.1.2.1.

M5 will be a 4-m class deformable mirror with an actuator pitch of 25-40 mm depending on the error budget for the MCAO system. It is conjugated to an altitude of ~7 Km, the single star footprint is 3.2 m and the meta-pupil is 3.63m for 6'. For an actuator pitch of 25 mm the total number of actuator is 145×145 (128×128 on a single footprint) giving a pupil sampling of 0.78 m. The required stroke is lower than M6 due to the ground layer correction by M6.

8.3.1.2.2 Wavefront sensors

As for the GLAO system six wavefront sensors patrolling the 6' FOV will be used for MCAO. The wavefront sensor design is similar to the one described in section 8.2.1.2.2.

As for the GLAO case, the vignetting due to the WFS buttons should be minimised within the central 2 arcmin FOV.

8.3.1.2.3 MCAO control

The MCAO loop control can be performed in different ways:

- Star Oriented Global Reconstruction;
- Optimization of Star Oriented Global Reconstruction for a given portion and direction in the FoV;

In all the cases the slopes retrieved by the WFSs are multiplied by the specific reconstructor to obtain the voltages to be applied to the two DMs. The vector of reference slopes for each WFS is obtained by a look-up table previously calibrated.

Star Oriented Global Reconstruction MCAO

In this approach the Interaction Matrix (IM) is obtained by stacking the WFS signals given by poking the single actuators (zonal control) or a set of actuators producing a selected base of modes (zonal control) of both DMs. Then the Reconstructor is obtained by inverting the IM in two possible ways:

- Least Square inversion via Single Value Decomposition (TSVD) with truncation of the zonal/modal eigenvalues with the lowest values;
- Pseudo open loop control [100] based on Minimum A-Posteriori variance reconstructor (MAP) which takes into account spatial a-priori knowledge on the turbulence and measurement noise. It gives a better performance in the whole FoV as it can properly handle the badly-seen modes that typically show up in MCAO systems.

Optimization of Star Oriented Global Reconstruction for a given portion and direction of the Field of View

This reconstruction approach boosts the performance in a given direction and smaller portion of the scientific FoV, as in the case of GLAO but giving a higher correction performance. The improvement in correction at this specified direction is achieved at the expense of the uniformity of the correction in the whole FoV.

The wavefront reconstructor is based on the minimum-variance (MV) reconstructor, R_{MV}, which can be expressed as the product of two matrices:

$$R_{MV} = P \times E \qquad \textit{Eq. 8-5}$$

The matrix E represents a full tomographic reconstruction of the turbulence volume (possible only when the vertical distribution of the atmospheric turbulence, obtained in real time from a vertical profilometer, is known), and the matrix P stands for an optimal projection from the reconstructed turbulent layers onto the two deformable mirrors taking into account the direction(s) where optimization is desired.

8.3.1.2.4 Real Time Computer

MCAO is a multi-sensor / multi-mirrors system. The proposed architecture is based on the Shack Hartmann Wavefront sensor.

The architecture of M6AM is the same as for the previous cases, as is that of the detector used. M5 will share the same technology for the actuators so given the additional size (3.5 m) the actuator grid will then be 145x145. In both cases the loop frequency considered will be 500Hz.

The architecture of the sensors is the same as for the GLAO system - Figure 8-74-. However measures cannot be averaged since all of them are required to reconstruct the turbulence at the desired altitudes. By reusing the same concepts described in the SCAO and GLAO cases, we

can allocate one computational unit for each quadrant of each detector, so we need 4*6=24 boards to implement the acquisition. Since sensor data are spread over 24 processing unit, it is convenient to keep this split and implement the reconstruction process in 24 different slices. Each slice will compute the matrix-vector product of 1/24th of the whole matrix by producing a partial command vector that needs to be summed to the other 23 to get to the final result that will then feed the PI controller.

The size of the system is rather big, but still achievable.

However the turbulence that has to be corrected by the upper DM M5 is expected to require much fewer actuators than the ones we actually have. This could lead to a reduction of these actuators on M5 or we can decrease the size of the control problem in the RTC by computing the reconstructor on a smaller basis and then interpolating the commands for the upper mirror in order to drive all the actuators.

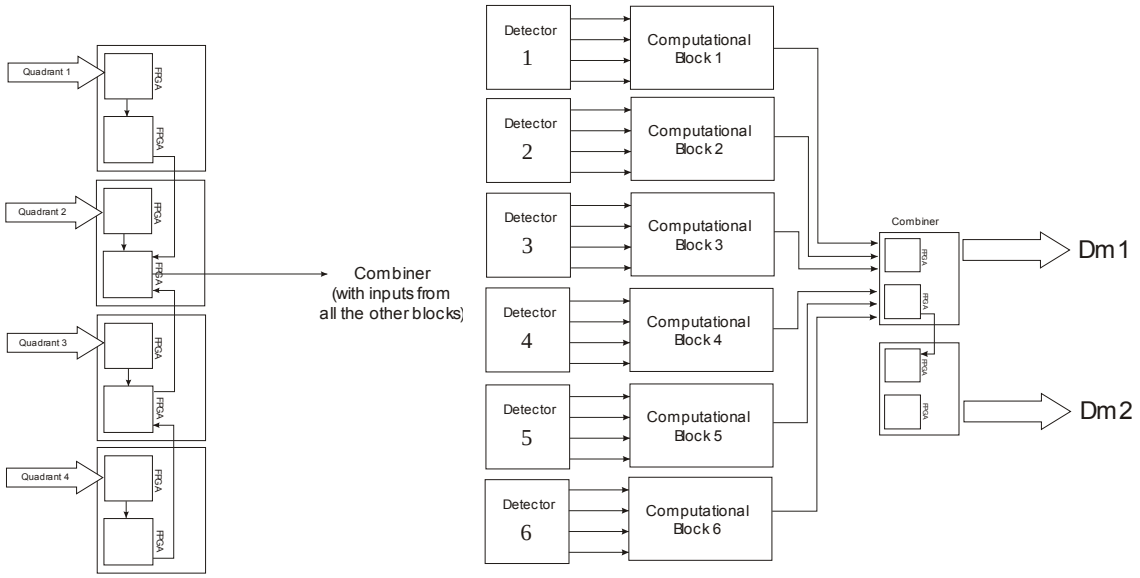

Figure 8-74: Architecture for a SH-based MCAO system with reduced number of reconstructed modes.

8.3.1.3 Predicted performance

A detailed analysis of the MCAO performance based on end-to end simulations as well as the assumptions and AO parameters are provided in RD25. Note that the MCAO performance provided here does not include yet all error sources -calibration errors, optical quality of the telescope, wavefront sensor and instrument optical paths, mis-registration error, atmospheric chromatism etc…- but only the pure AO performance part. In the MCAO mode, we believe that the accounting of the error budget on the final performance might have a significant impact for "high" Strehl and a small impact for the low Strehl.

The evaluation of the MCAO performance should cover two main aspects:

- The Sky Coverage for which the correction is available;
- The Strehl ratio performance in NIR

8.3.1.3.1 MCAO sky coverage

The proposed MCAO system is based on Natural Guide Stars. In the following, we will present the sky coverage achievable with the MCAO system proposed. More details about the SC are provided in RD27.

The Sky Coverage (SC) has been computed similarly to the GLAO case see 8.2.2.3.1.

The number of NGSs for wavefront sensing is limited to 6 which is a trade off between a minimum acceptable level of correction, Strehl uniformity and technological complexity of implementing multi WFS system in Star Oriented mode.

Figure 8-75 shows the frequency of 6 arcmin diameter fields as a function of the number of NGSs included in them. Several limiting magnitudes have been considered.

At the galactic poles (left) the sky coverage for fields with at least 3 stars of magnitude equal or brighter than 16 is ~20% and it drops dramatically when the minimum number of NGS moves to 6. In order to have acceptable sky coverage with at least 6 NGSs, it is mandatory to select stars down to 18, but at this flux levels a Star Oriented system may be severely photon starved unless high efficiency detectors become available.

At intermediate galactic latitudes (l=0° b=50°) the sky coverage for fields with at least 3 stars of magnitude equal or brighter than 16 rise up to 60% and also in the case the minimum number of NGSs is 6 the sky coverage increases up to 10%. Selecting 17 magnitude NGSs already provides sky coverage of ~50% at these galactic latitudes with the MCAO system working at flux regimes less critical than the one at the galactic poles.

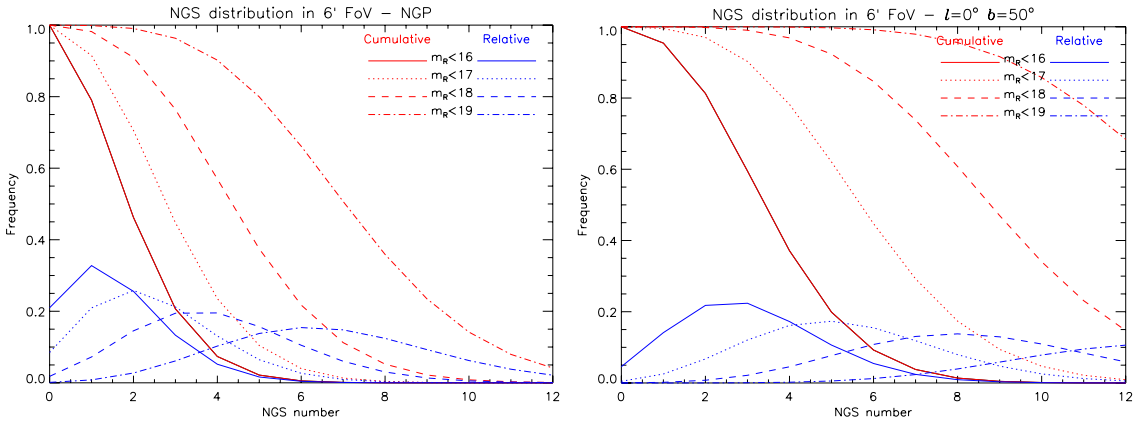

Figure 8-75: Frequency of circular 6 arcmin diameter fields as a function of the number of NGS included on them at the North Galactic Pole (left) and at an intermediate galactic latitude l=0° b=50° (right)

8.3.1.3.2 Simulation Results

In the following we analyze the Strehl correction performance in K Band for an asterism of different number NGS distributed in 6 arcmin FoV (see Figure 8-76). Figure 8-76 is based on an analytical model which is in reasonable agreement with our numerical model for bright stars but the analytical tool is more pessimistic for faint star (see Figure 8-77). Further investigations are being pursued to clarify this discrepancy.

In the plot of Figure 8-76, the analytical model (Cibola, written by B. Ellerbroek) was used to simulate the MCAO performance for 3, 6 and 8 NGSs, all of identical magnitudes. A good seeing model (0.5'') was adopted. The NGSs are placed in "reasonable" asterisms: in the 3 NGSs case, the three stars are in a triangle of 4' diameter. In the 6 NGS case, 3 stars are in a 3' (diameter) triangle) and 3 in a 6' triangle. In the 8 NGS case, 3 stars are in a 3' triangle, and 5 in a 6' (diameter) circle.The performance is shown on-axis (top curve) and 30'' off-axis (bottom curve). The solid line is for 5th magnitude NGSs, dash: 16th mag, dot-dash: 17th mag and dot-dot-dash for 18th magnitude (an A0 spectrum was assumed, which is about 1 magnitude less photons than a G0 star). We can see that for faint stars, even with 8 NGSs, Strehls below 10% (at K band) are obtained.Adding guide stars from 3 to 8 increases the performance by adding photons, but the performance remains fairly poor, in terms of Strehl ratio.

Figure 8-77shows the numerical simulation of a 3 NGS constellation, in 2' field, located at the edges of the field. 1 ph / sub-aperture / integration time (framerate is 500 Hz) corresponds roughly to 17th magnitude in the above plot. We can see that the bright end performance is in rough agreement, whereas for faint stars, the analytical code is more pessimistic.Top to bottom shows the performance in K, H and J bands. Same seeing as for the analytical model.

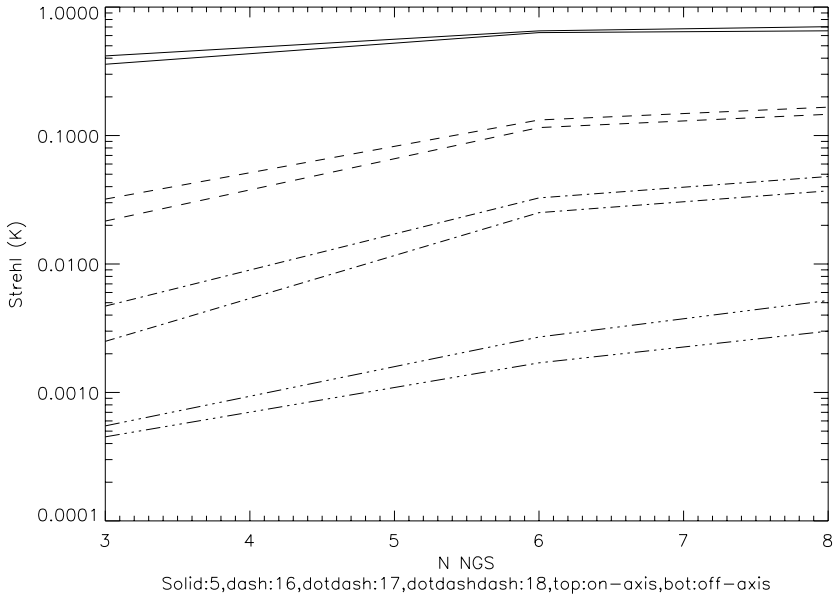

Figure 8-76: Strehl (K-band) as a function of the NGS number distributed on a 6 arcmin FoV optimized in the central 1 arcmin. Solid line: Mv=5, dashed line: Mv=16, dashed-dotted line: Mv=17, dashed-dotted-dotted line: Mv=18. For each magnitude: top line on-axis, bottom line: off-axis.

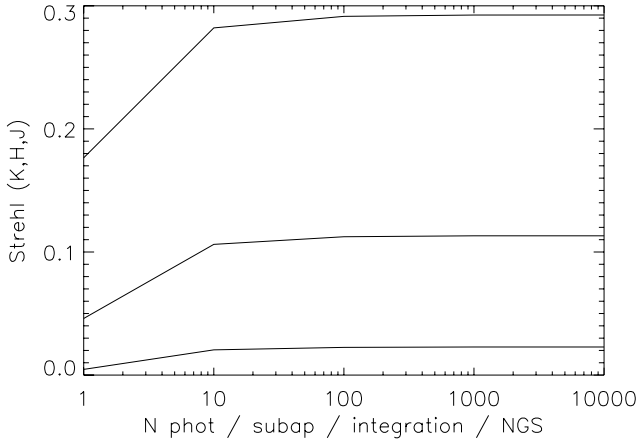

Figure 8-77: Strehl (on-axis) for the good seeing model, MCAO, 3 NGSs, 2' FOV, K, H, J (top to bottom), Mv=16 corresponds to 5 photons/subap/frame

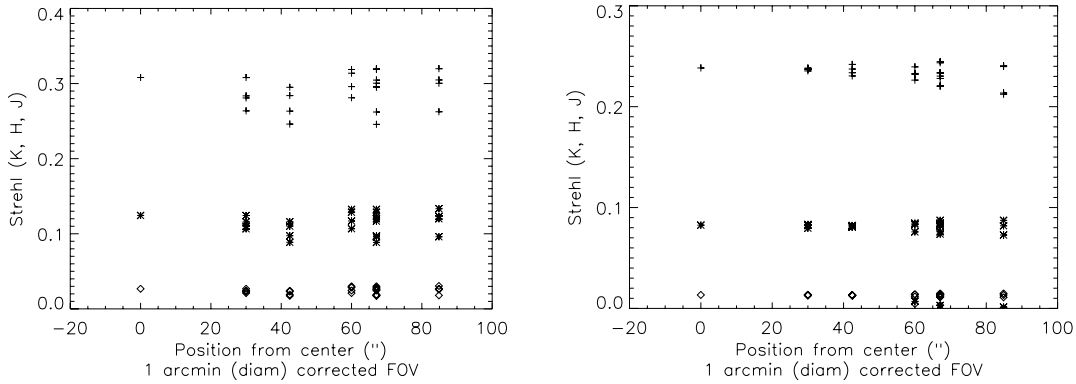

Figure 8-78: Numerical simulations of MCAO correction (Strehl ratio in K band, H and J bands (top to bottom)) on a 6 NGS asterism (Mv=5 (left plot) and Mv~16 (right plot)), the good seing model (~0.5'' was used). Correction is optimized for a 1' FoV (diameter).

The last plot shows the variability of the Strehl in the field of view (numerical model). The crosses show the Strehl at various locations. Some variation is seen, and the performance peaks towards the location of the guide stars. This is a well known effect, already observed in the MAD simulations. It may be possible to reduce it by adopting another control algorithm.

From Figure 8-76, we see also that the MCAO performance strongly depends on the angular separation of the NGS asterism. Ideally, one would select a compact NGS asterism to get better performance but of course this will limit immediately the sky coverage.

We see that the MCAO system needs to have a variable tomographic capability for both “small” and “large” FoVs to optimise the Sky coverage and the performance in the scientific FOV. Further numerical simulations remain to be done to confirm the NIR performance expected in MCAO.

From the above analysis, it is important to note that Strehl ratios in NIR using NGSs only for wavefront sensing will always be limited to a couple of tens of % in most cases because of the magnitude of the wavefront sensor NGSs. Extrapolation to higher Strehl ratios or to correction at shorter wavelengths will require the implementation of Multi- Laser Guide Stars. Moreover, the uniformity of the Strehl in the field of view is not maximal, because to gain sky coverage, large separation asterisms need to be used, creating “holes” in the Strehl ratio map where NGSs are not present

Combining the sky coverage plots and the results of the simulations for Strehl correction performance it is clear that in the NGS based MCAO the sky coverage is significantly low especially at high galactic latitudes. Moreover the correction achieved is already modest in K band and becomes very small at shorter wavelengths. The analysis presented here shows that at the Galactic poles the sky coverage is 25% with 5% Strehl and drop to 1% for a Strehl of 10%.

Laser Guide Stars can solve this problem because they can be available for any region of the sky and they can provide much higher fluxes increasing significantly also the MCAO correction performance extending it to shorter wavelengths. The number of Laser Guide star needed for OWL is still under investigation as well as the concept for they implementation (see sub-section on LGS in 3rd generation AO section).

On the other hand it is also possible to select specific targets which are surrounded by useful NGS to perform MCAO correction. The number of available fields with these characteristics will be low but for some astronomical applications where observing on a specific direction of the sky is not mandatory (i.e. Cosmology with deep fields) it may be sufficient.

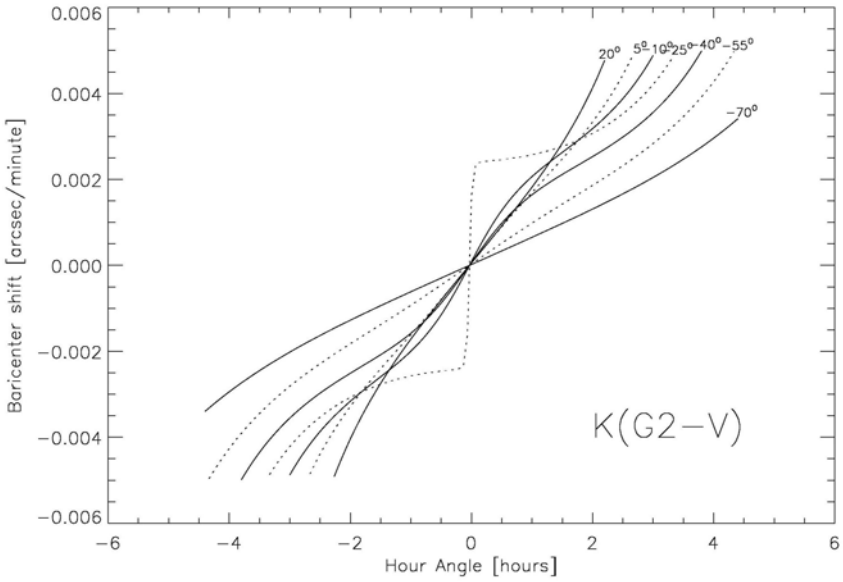

Figure 8-79: Barycentre speed of a G2-V star due to the differential atmospheric refraction between the WFS effective wavelength and the instrument observing in K band for different target declinations

Differential image motion - The differential image motion due to atmospheric dispersion between the WFS-NGS effective wavelengths and the science wavelength - Figure 8-79- should be taken into account. In the case of MCAO this effect is critical since the images are almost diffraction limited. The compensation can be implemented by applying offsets to the WFS which have to be updated continuously (~1 Hz).

There is a second order effect of the atmospheric dispersion within the FoV between stars of different spectral type observed through the band pass of the instrument filters.

Figure 8-80 shows the barycentre speed for a B5-V and a M5-V star with respect to a G0-V all observed in J band. The speed is computed at different declinations and hour angles for Paranal. In all cases the speed is always lower than 4×10^{-2} mas/minute, that is, 1/50 of the diffraction limit FWHM (Full width at half maximum) in J Band. This permits individual exposures of the order of 1 minute and even larger for H and K Band without smearing the diffraction limited PSF across the FoV –for different object spectral type. However, special care should be taken when co adding individual exposure for different Zenithal distances over long exposure times because of the "warping" of the FoV astrometry due to the different colours of the stars.

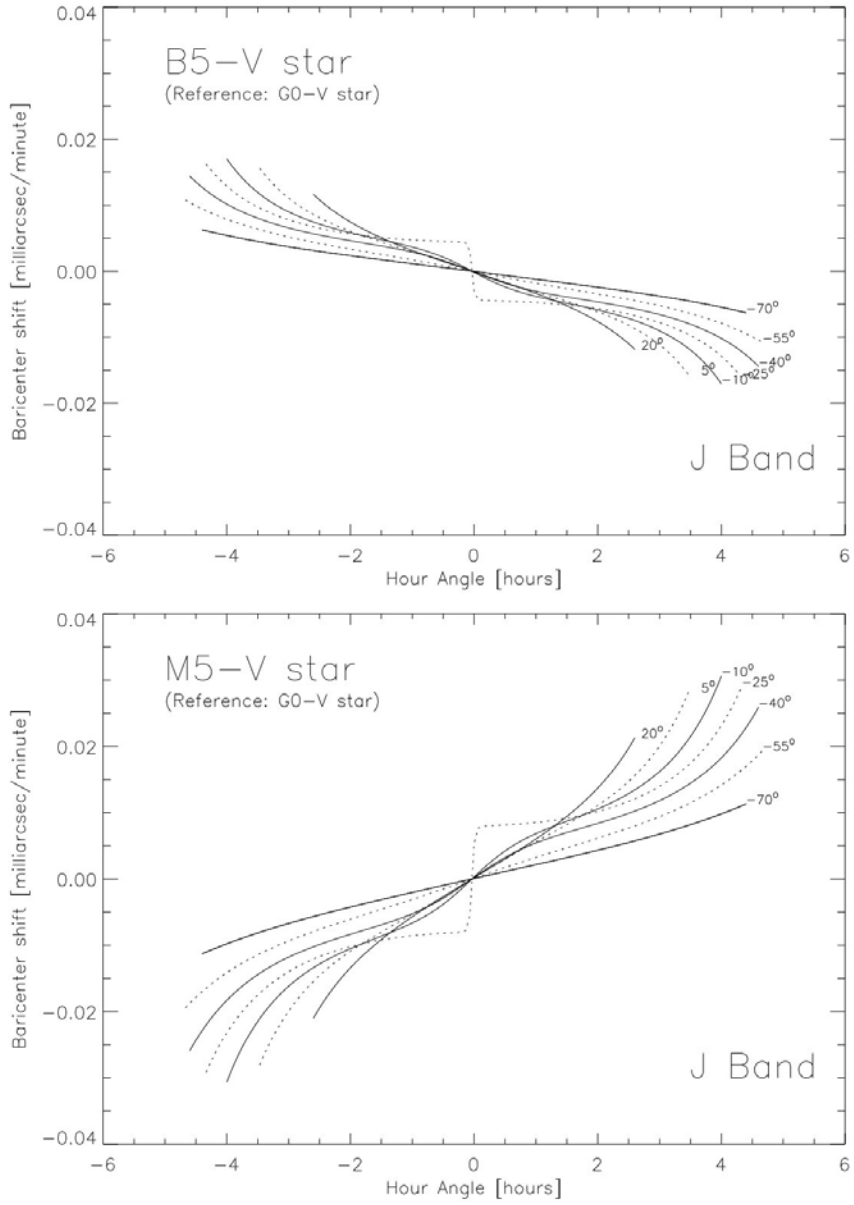

Figure 8-80: Barycentre speed of a B5-V star (top) and a M5-V (bottom) with respect to a G0-V star observed in J Band. The curves stop when the Zenithal distance is larger than 60°.

8.3.1.4 Mid-Term development plan

8.3.1.4.1 Modelling and Simulation

First order simulations have been performed to estimate the MCAO performances in NIR with a 98x98 M6 and a 145x145 M5 actuator system. Discrepancies between numerical and analytical simulations remain to be clarified and best Strehl ratio versus sky coverage needs to be tuned. Full numerical simulations of the MCAO system require a large amount of computing time on our cluster. Sky coverage has been evaluated based on a maximum of 6 NGSs and wavefront sensors but also this value will be subject to further investigation.

The number of DMs required both to increase the 2' FOV correction and the sky coverage needs to be investigated.

The corrected PSF uniformity needs to be assessed in detail as this parameter is scientifically important.

The actuator density for the M5 needs to be optimized in view of the error budget.

The effect of magnitude difference between the NGSs for wavefront sensing should be studied

Statistics of turbulence profiles are now becoming available thanks to the special effort made to develop dedicated profiler tools like MASS and the SLODAR. Measurements should be pursued to get more significant information about the amount and the structure of the layers and their variability. Based on these data, MCAO performance should be updated.

Extensive parametric simulations remain to be done to tune the design parameters in particular:

- Optimization of the SH WFS geometry fitting the M6AM geometry (Circular, hexagonal, squared)
- Optimization of the SH WFS pixel scale and FOV
- WFS linearity issues
- Effect of the turbulence produced by the telescope itself over the first 200-400m and variation of the turbulence along the telescope pupil
- Atmospheric refraction and differential atmospheric refraction needs to be studied
- Study of the variable M6AM conjugation altitude effect on the GLAO performance
- Full error budget of the MCAO system
- MCAO calibration issues beyond the experience acquired with MAD.

8.3.1.4.2 MCAO design

The detailed implementation of the MCAO wavefront sensors into the OWL Adapter-rotator will be developed during phase B.

As in the case of GLAO the present baseline is currently the Star Oriented concept with global reconstruction from each WFSs signal. Effort to define a Layer Oriented concept with numerical or optical co-addition will continue and the results compared with the SO approach.

The considerations made for GLAO (section 8.2.2.4.2) apply to MCAO as well. In addition:

Should a third deformable be required, the design of a post focal AO system with sufficient FOV –up to 6'- needs to be produced.

Activities on the M6AM unit are identical to the SCAO case.

The feasibility and conceptual design of the M5AM unit will be pursued in phase B.

As envisaged for the M6AM unit, a laboratory test facility of the M5 unit alone will be required. Ideally a thorough laboratory testing of M5 and M6 together in MCAO mode is highly desirable. The corresponding test facility needs to be studied for instance by replacing the spherical mirror proposed for the M6 unit by the M5 mirror and adding a corrector to correct for field aberrations.

This approach may not be compatible with the present schedule for OWL as the M6AM unit may be already in operation when the M5 will be tested. Options will be analyzed in Phase B.

In the domain of MCAO reconstruction and control, research should be pursued both in the frame of MAD and in collaboration with other world experts. In particular, the reconstruction and control methods optimizing the corrected field diameter require significant research and demonstration.

8.3.1.4.3 MCAO calibration issues

The calibration M5 and M6 with the 6 WFSs for different positions in the field is a complex subject which requires further work especially for the determination of the command matrices. This subject is partially being studied with MAD but the problem will be more complex with OWL because no internal source will be available to calibrate M5 and M6 for all field positions. In addition, internal telescope turbulence may limit the accuracy of the calibration. For these reasons, either synthetic values from field extrapolation of the interaction matrix or on-sky interaction matrix measurements should be looked at carefully already with MAD and its turbulence generator and on-sky and later with the VLT Adaptive secondary. The feasibility of a synthetically reconstructed AO system is under study. If it can be demonstrated that all hardware aspects can be simulated accurately enough to provide the required performance, this solution would obviously be the best. It is however possible that one need to combine simulated and measured interaction matrices. Several options to do so are being investigated.

Using a simulated IM to build the system control matrix is a possibility that is under investigation. The strategy is to stick as much as possible to the reality. Indeed, WFS and DM models must be accurate. Thus, when one can measure the influence functions of its DM, it is obviously more accurate to use this model instead of a simulated one. This is what has been chosen for MAD. As described in RD27 section 7, tests are being run on MAD with the turbulence generator MAPS in order to quantify the performance of a controller built by following such an approach. The measured DM influence functions and a diffractive model of the SH with a uniform subaperture plate scale are used to simulate the IM. The loop closes and provides a significant performance in terms of strehl ratio but worse than the one achieved with the measured IM. Indeed, the misregistration between DM actuators and SH subapertures still have to be measured and included in the simulations.

In RD27, the same approach is presented in the DSM case. The SH model is diffractive and the DM influence functions are the output of the FEM (because no influence function can be used when the mirror does not exist).

In the case of ALTAIR (the AO system currently in operations on GEMINI north), a synthetic IM has been used successfully since the start. The DM model consists in analytic influence functions that have been fitted on measured one. In this way, the computational time is reduced.

New calibration issues arise in the MCAO case. Indeed, the fact of dealing with several DMs and WFSs might increase the calibration time. If the calibration must be performed on sky, the night observing time will be reduced. Another potential problem may be the drift of the DMs (creep for example) while one of them is being calibrated. This will bias the interaction matrix and thus be detrimental to the system performance.

To overcome these issues, a possibility would be to consider all DMs as a single device and to define global modes (Hadamard or system) on this fictive meta DM. Then, both DMs will be actuated at the same time during the calibration. In this way, no DM will creep or drift during the calibration. In the case of the Hadamard modes, it is interesting to notice that the calibration time will be independent on the number of DMs for a given expected measurement signal to noise ratio.

Another idea would be to modulate both DM with different frequencies (multiplexing) and to disentangle their contribution in the Fourier space.

Global modes can also be defined in the WFS space considering all WFS as one device. Then, the calibration can be performed by applying a global bias to the WFS offsets. A modulation of the bias will certainly be necessary to overcome the turbulent residual on the WFS signal in MCAO. This scheme could be applied also to GLAO although in this case the closed loop residual would be higher.

The last issue to take into account in MCAO calibration is the mapping of the FoV. Indeed, the interaction matrix should rigorously be calibrated for each target asterism. The off axis aberration should be taken into account along each guide star direction. Since the altitude DM footprint position changes with the guide star angle, off axis calibration is fundamental in MCAO. The idea would be to define a grid sampling the FoV. An interaction matrix is measured for each position of this grid (in red on Figure 8-81). Then, when a real asterism of guide stars (in yellow on Figure 8-81) is observed, the interaction matrices for each WFS are built by interpolating the closest ones that were measured on the grid. In the framework of the PhD work of Johann Kolb (available end 2005), the required sampling of the FoV will be defined for MAD (with its bimorph DMs and SHWFS). The goal is to minimize the impact on the performance coming from the difference between the measured and the extrapolated interaction matrix. An acceptable threshold in terms of wave front error, strehl ratio and correction uniformity should be defined. The first results tend to show that a grid of about 50 recording points in the 2 arcmin FoV should be enough to extrapolate the IM to any GS position and bring a loss of SR smaller than 5% relative.

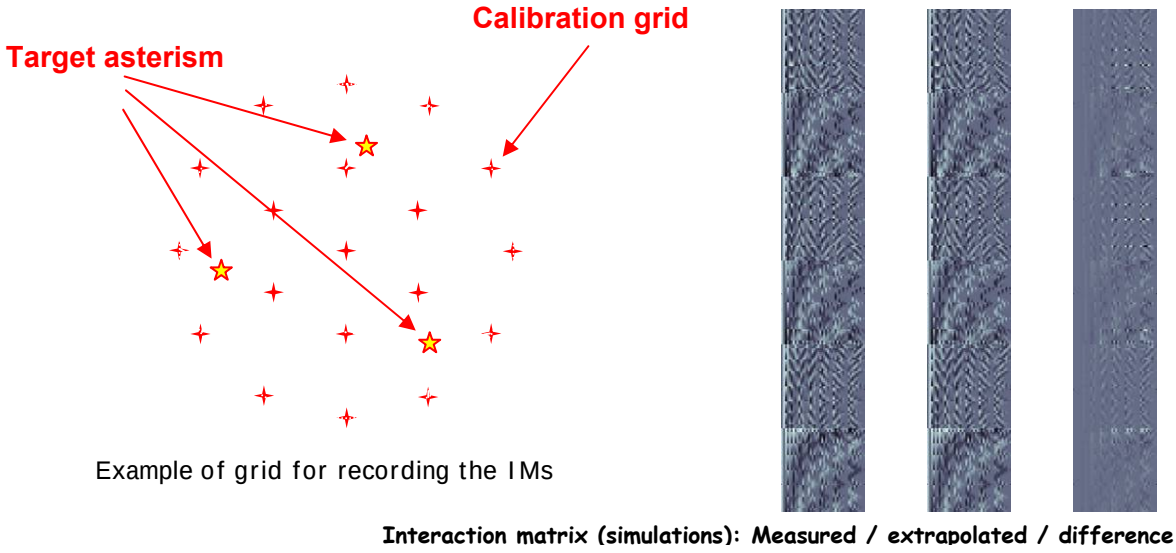

Figure 8-81: Mapping of the FoV for interaction matrix estimation in MCAO

8.3.1.4.4 AO key component status and development

Both the WFSs and the M6AM unit will be reused for MCAO.

The additional specific key component required for MCAO is the 4m-class deformable mirror with an actuator pitch of 25-40 mm. Detailed simulations may lead to larger actuator pitch. Apart from its diameter, the additional complexity of this deformable mirror is its concave shape. However, the actuator pitch and the high spatial frequency stroke – stiff modes requiring power to produce- are relaxed compared to the M6AM unit. These two effects will allow an increase of the thin glass shell thickness beyond 2mm, making the manufacturing easier. Main characteristics of the M6 and M5 deformable mirrors are provided in Table 8-8.

The RTC concept is based on technologies already considered previously. Worth of note is the presence of 10 port switches while we have tested so far only 8-ports, and the multi-layer RTC architecture: the latter case is significant and because board-to-board communication may play an important role. Therefore a prototype implementation (one small layer) is required.

MAD: An MCAO demonstrator

The European Southern Observatory has built and is testing a Multi-Conjugate Adaptive Optics Demonstrator (MAD) to perform wide field of view adaptive optics correction. The aim of MAD is

- To demonstrate on the sky the feasibility of the GLAO and MCAO techniques,

- To perform a first optimization of such techniques, and explore other innovative approaches through extensive in-lab testing
- To evaluate the critical aspects in building and running such instrument in the framework of OWL and of the 2nd generation VLT instrumentation.

MAD is seen as a crucial enabling milestone for OWL. It will be installed at a Nasmyth Visitor focus of the VLT to perform on-sky observations, planned in 2006. The MAD bench is shown in Figure 8-82.

MAD is a prototype GLAO and MCAO system performing wide Field of View (FoV) AO correction over 2 arcmin by using bright (m_v < 14) Natural Guide Stars (NGS) and it is built using existing technology and re-using as much as possible key components developed for existing ESO AO systems (Figure 8-82)..

MAD will be used to investigate two different approaches of GLAO and MCAO correction with two independent wavefront sensing techniques: the Star Oriented MCAO with a Shack-Hartmann Wavefront Sensors (SHWFS) sensing simultaneously 3 NGS with 3 sensors and the Layer Oriented MCAO with a Layer Oriented Wavefront Sensor (LOWFS), based on a Multi-Pyramid Wavefront Sensor sensing simultaneously 8 NGS. The Layer Oriented Wavefront Sensor is designed and built by an Italian consortium. The MAD Real-Time computer architecture is designed to support both reconstruction wavefront sensing approaches.

Adaptive correction with MAD relies on two deformable mirrors (DM, Figure 8-83). One is conjugated to the telescope pupil for ground layer turbulence correction, the other one to 8.5 Km above the telescope, thereby allowing for a larger corrected field than a single conjugate would permit. The MAD GLAO and MCAO correction are optimized for the K (2.2. μm) band for the median Paranal seeing conditions and the performance will be evaluated at this wavelength using a 1 arcmin IR camera (CAMCAO, supplied by a Portuguese consortium).

For the laboratory testing and tuning of the MAD system, a multi-layer turbulence generator MAPS (Multi Atmospheric Phase screens and Stars) is used to emulate atmospheric turbulence.

A detailed description of the system is provided in [8]

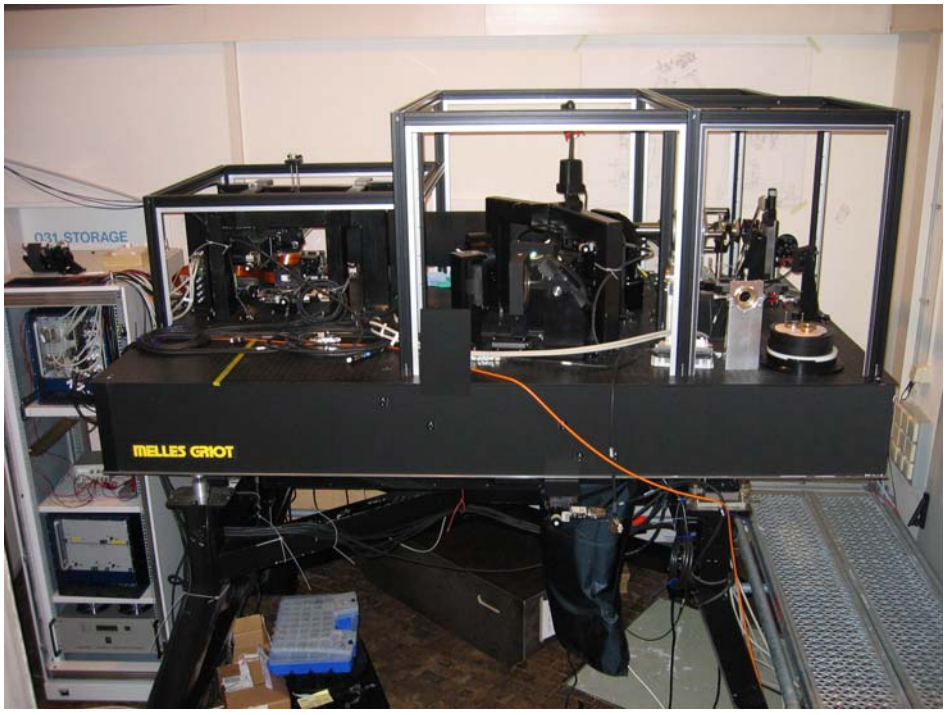

Figure 8-82: The MAD bench installed in the ESO optical laboratory during testing.

The multi-Wavefront Sensors unit (Figure 8-84) consists of 3 Shack-Hartmann sensors capable of scanning the whole 2 arcmin field of view. The lenslet array has 8 × 8 sub-apertures and a 2.4 arc seconds field of view.

The Layer-Oriented sensor (Figure 8-84) is based on a multi-pyramids Wavefront Sensor with eight pyramids allowing to observe simultaneously eight reference sources. Each pyramid is supported by a small cylinder with relay optics, the purpose of which is to enlarge the system focal ratio by a factor ~10 on the pyramids. The light modulated by the pyramid is split in two beams and the telescope pupil is re-imaged through two groups of lenses onto the detectors. The detectors are located at conjugates of the two deformable mirrors. The two sensor units (multi-sensors or layer-oriented) cannot be operated simultaneously.

The MAD detector system consists of 5 WFS cameras (3 for the SHWFS and 2 for the LOWFS) MAD has 5 CCD cameras (3 for the Shack-Hartmann sensors and 2 for the Layer-Oriented ones). The E2V CCD39 chips have FIERA controllers, which can drive the detectors simultaneously at identical (for the Shack-Hartmann CCDs) or different (for the Layer-Oriented CCDs) frame rates, up to 400 Hz.

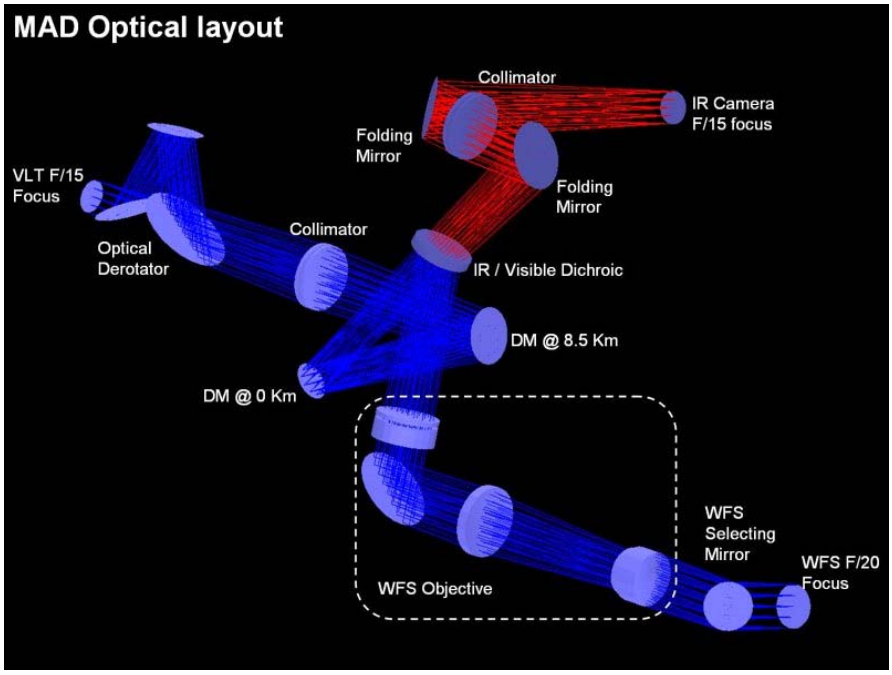

Figure 8-83: Optical layout of MAD.

The Deformable Mirrors (Figure 8-85) are copies of the ones developed for MACAO-VLTI and MACAO-SINFONI AO systems. The deformable mirrors are bimorph-type with a radial geometry of the actuators. The tip-tilt correction is provided by the MACAO-SINFONI Tip-Tilt supporting the MACAO-SINFONI DM.

The MAD Real-Time Control has been designed to support both the Star Oriented and the Layer Oriented wavefront sensing techniques and to implement both the Global and the Local Reconstruction.

The MAPS turbulence generator (Figure 8-85) emulates a time evolving three-dimensional atmosphere. The characteristics of the atmospheric turbulence will be similar to those of the Paranal observatory during median seeing conditions. The evolving atmosphere is reproduced by three rotating refractive plates (Phase Screens). The surface of the plate is chemically etched in order to generate spatially varying thickness.

Recently MAD passed two major milestones:

- 3rd March 2005: first light of Single Conjugated AO (SCAO) closed loop with one Shack-Hartmann sensor and the deformable mirror conjugated to ground;

- 3rd June 2005: first light of Ground Layer AO (GLAO) closed loop with three Shack-Hartmann sensors and the deformable mirror conjugated to ground.

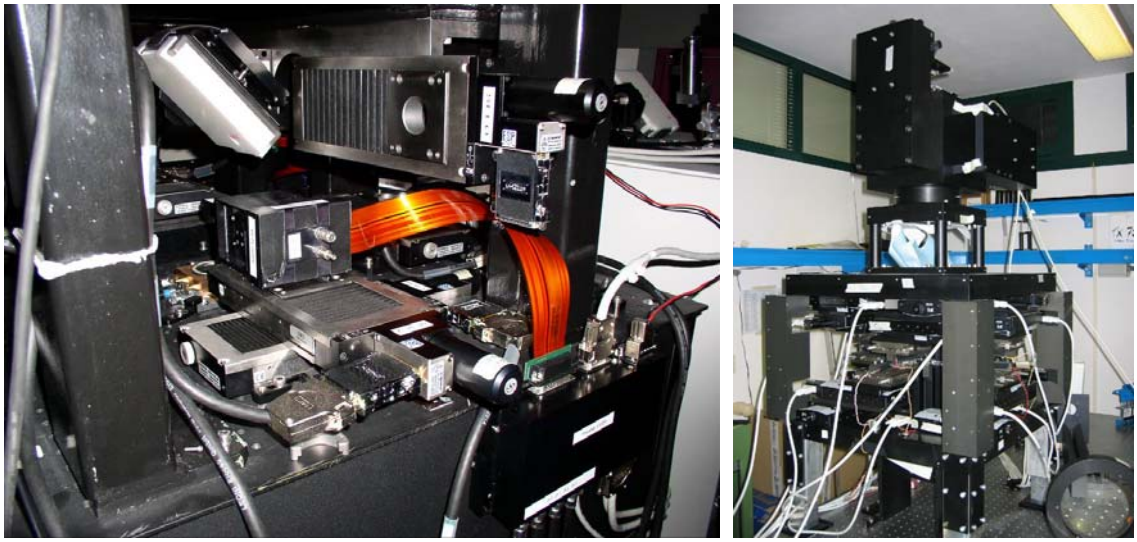

Figure 8-84: Left: the SH WFS area during integration. Right: the LOWFS during final testing.

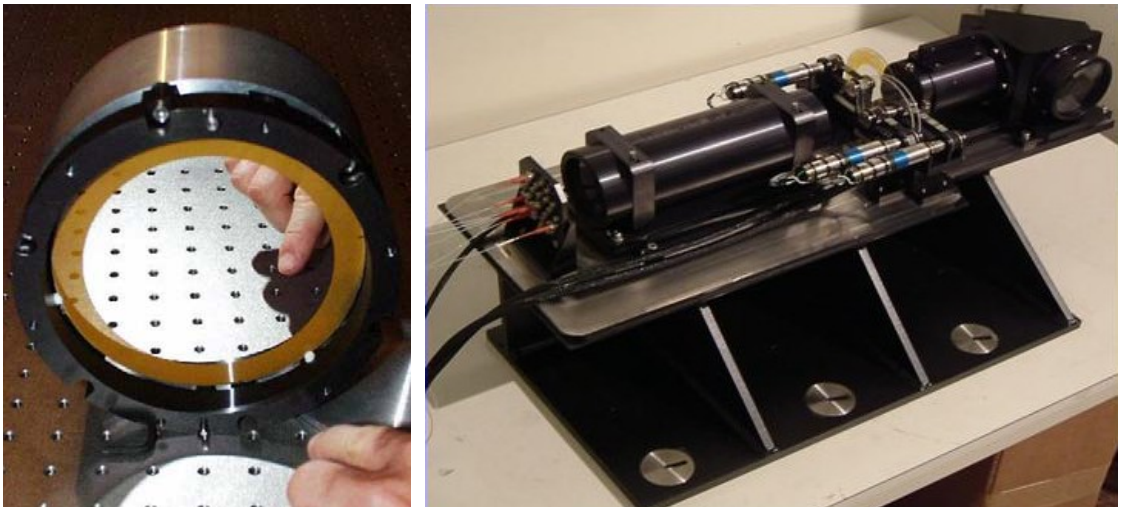

Figure 8-85: Left: MACAO bimorph DM used for conjugation at 8.5 Km. Right: the multi layer turbulence generator MAPS.

SCAO Closed Loop

The loop has been closed using one SH WFS and the ground conjugated DM. Only one rotating The loop has been closed using one Shack-Hartmann sensor and the deformable mirror conjugated to ground. Only one rotating phase screen with gentle atmosphere has been used in order to facilitate the first light operations. The seeing was 0.4" in V Band and the wind speed of 10 m/s. The loop was closed at a frequency of 115 Hz on m_v=6 star and a Strehl of 52% in K band has been obtained.

Figure 8-86 shows the open and closed loop images taken in K Band. The "cross- shaped" artefact in the closed loop image is due to a non perfect filtering of an unseen system mode.

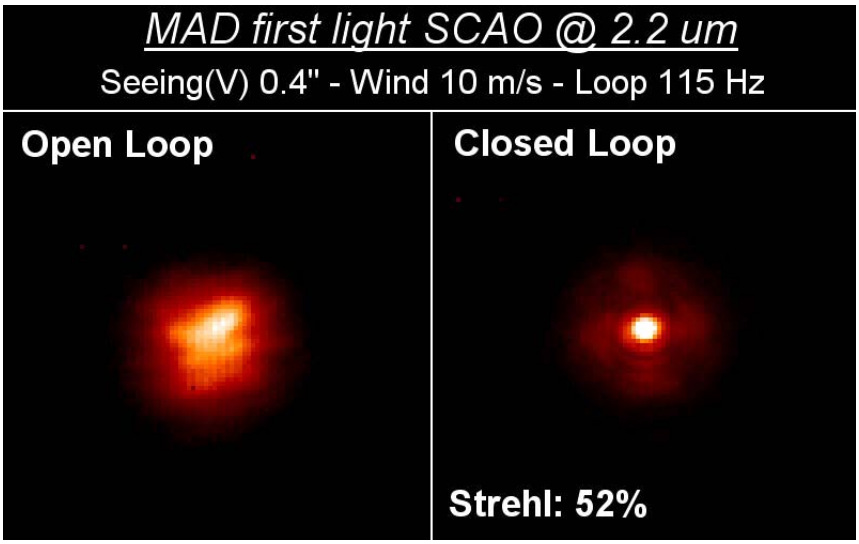

Figure 8-86: MAD first light SCAO closed loop

GLAO Closed Loop

The loop has been closed using three Shack-hartmann sensors located on a circle of 1.5 arc minutes diameter and at the vertex of an equilateral triangle. The correction was applied through the deformable mirror conjugated to ground. Only one rotating phase screen, located at 6 km altitude has been used to simulate a "gentle" anisoplanetism. The seeing was 0.45" in V Band and the wind speed 10 m/s. The loop was closed at a frequency of 115 Hz on m_v=6 star.

The FWHM in K band has been reduced by a factor ~2.5, thereby demonstrating experimentally that MAD is capable to perform GLAO correction (see Figure 8-87).

The gain in Encircled Energy is shown in Figure 8-88. Within the FWHM of the closed loop image, the gain of energy concentration is a factor ~2 in comparison with the uncorrected image.

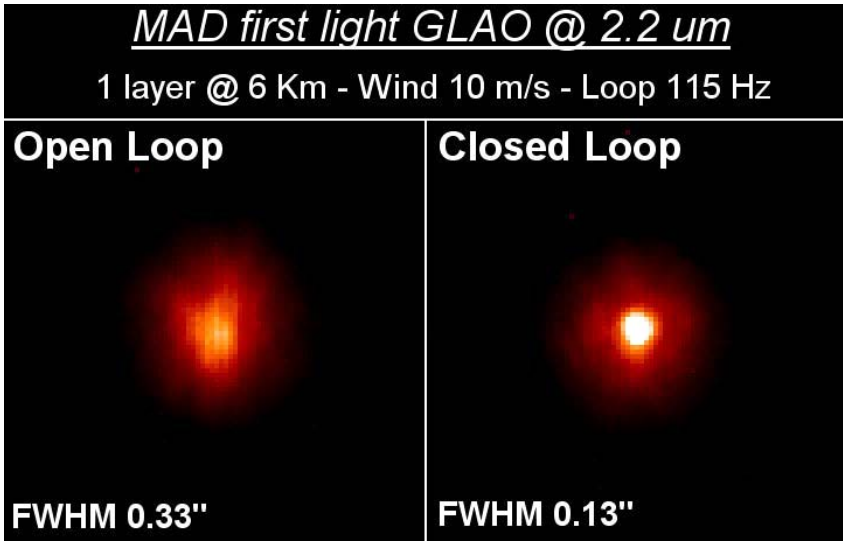

Figure 8-87: MAD first light GLAO closed loop. Only one phase screen at 6 Km altitude has been used and the guide stars were located on a circle of 1.5' diameter. The FWHM reduction factor is ~2.5.

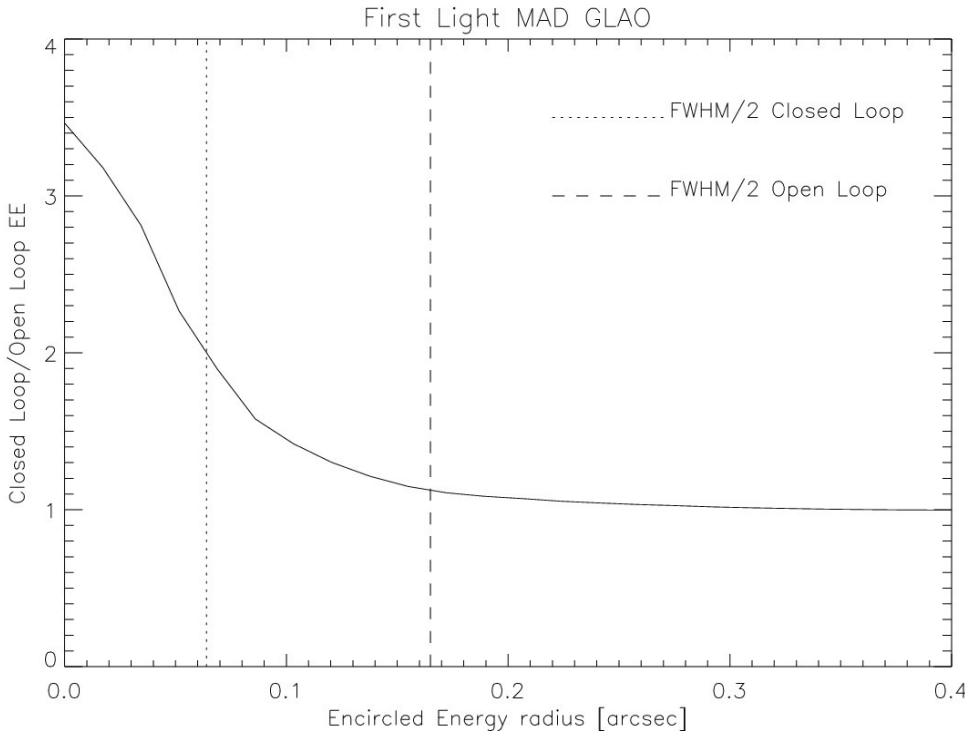

Figure 8-88: Encircled energy gain in the first light GLAO closed loop. At the FWHM radius of the corrected image the gain is ~2.

Optimal control algorithms for MCAO

The second generation AO will require more sophisticated control approaches, especially in the case of wide field AO as in MCAO.

In AO control, an AO system has to deal with a real time closed loop system with delays and linear models for the WFS measurements and for the DM correction. The optimal control problem actually breaks down into a stochastic estimation of the turbulent phase, followed by a deterministic control problem. The estimation problem is shown to be solved by Kalman filtering [101]. The specificities in MCAO are: a large number of degrees of freedom, the WFS measurements available only in particular directions corresponding to the Guide Stars in the star oriented point of view. Achieving a correction in a large Field Of View requires to interpolate the WFS measurements between the GSs. It implies a careful reconstruction process using prior information on the turbulent volume. This leads to a global optimization of the multi-variable servo-loop.

The Office National d'Etudes et de Recherches (ONERA, Paris, France) in the framework of OPTICON-JRA1 has developed an end-to-end MCAO simulation tool which includes the modellization of the spatial and dynamical behaviors of the different MCAO subsystems (spatial sampling, influence functions, temporal transfer functions) and the calibration errors and the capability to handle different control algorithms including Kalman filtering. The goal is to compare the different reconstruction-control algorithms in terms of correction performance and robustness with respect to different atmospheric conditions, guide star fluxes and calibration errors applied to MAD.

An experimental validation of the optimal control approach is also under progress at ONERA. This pioneering experimental work will validate the results obtained with the end-to-end simulation tool and help the specification and implementation of the future MAD optimal control. This validation is performed on the AO bench available at ONERA. The optimal control criterion consists in the optimization of the scientific off-axis performance using the on-axis WFS data. The first tests in static mode have been performed. The conventional on-axis correction has been compared to an off-axis Kalman-like regularized correction which uses the knowledge of the altitude and strength of the turbulent screen. A systematic gain brought by the off-axis optimization has been demonstrated ([126]).

The next step will be to define the optimal control algorithm (Kalman) to be implemented in the MAD star oriented configuration accordingly to the results obtained with the numerical simulations and the AO bench validations. ONERA and ESO in close collaboration will implement in the MAD system the optimal control algorithm and run MAD under the defined conditions.

8.3.2 Extreme Adaptive Optics and High Contrast Imaging: EPICS project

The Exo-Planet Imaging Camera Spectrograph for OWL (EPICS) feasibility study started significantly later than the other instrument conceptual studies, after the completion of the VLT Planet Finder phase A. The latter has demonstrated that it is necessary to combine XAO (eXtreme Adaptive Optics) with other methods (coronagraphy and differential detection methods) to reach the contrast permitting exoplanets detection. The interaction of error sources between the different sub-systems of EPICS calls for an absolute global system approach.

An overview of the whole EPICS instrument can be found in section 12.2.3.5 and the whole study in RD51. We present here an outline of the XAO system and of coronagraphy.

8.3.2.1 EPICS Top level performance requirements

A full system approach should be followed to meet the performance of EPICS. The top-level-requirements of the instrument are recalled in this paragraph.

- The instrument covers the wavelength range 0.6 – 1.7 micron
- The total field of view in all observing modes is at least 2″ in diameter at visible wavelengths and 4″ in diameter in the NIR.
- The inner working angle in all observing modes working at visible wavelengths is smaller than 30 mas (goal 15 mas).
- The spatial sampling will at least fulfill the Nyquist criterion at all working wavelengths. Over-sampling may be required to deal with interpolation issues in differential imaging.
- Earth-like planet up to 20 pc is detected in polarimetric and spectroscopic modes at SNR > 5 in one night of observation at a phase angle of 90°

Properties of Earth at 20 pc: Contrast 2e-10, m_V = 30.6, angular separation 50 mas.

- Jupiter up to 20 pc is detected in spectroscopic mode at SNR > 50 in less than 4 hours exposure time at a phase angle of 90°

Properties of Jupiter at 20 pc: Contrast 1e-9, m_V = 28.8, angular separation 250 mas.

- The AO control radius is larger than 0.4″ (goal 0.8”) at 800 nm

This control radius corresponds to about 1 AU at 2.5 pc, and ensures that – besides for the Alpha Centauri system – the prime targets are inside the control radius. Note that the control radius is given by the $\lambda/(2d)$, where λ is the observation wavelength and d is the actuator pitch of the deformable mirror. This Top Level Requirement corresponds to an actuator pitch of ~0.2 m (goal 0.1).

- AO limiting magnitude for achievement of Top Level Requirements: compatible with a sample larger than 100 stars for each spectral types G, K and M . This corresponds to the following limiting magnitudes for the three types of stars: Mv=7. for a G2 star at 25 pc, Mv=8.5 for M2 star at 20, Mv=9.5 for an M2 star at 15 pc.

8.3.2.2 EPICS Adaptive Optics concept

EPICS ultimate contrast requirement is 4-5 orders of magnitude higher than the VLT-Planet Finder science goal of about 10^{-5} – 10^{-6} contrast at 0.1 arcsec. When scaling from a 10-m to a

100-m class telescope, the contrast naturally improves by a factor of 100 for a given rms value of the wave-front error. This means that the XAO system for EPICS should provide a 2 or 3 orders of magnitude better starlight halo rejection than a simply scaled version of the VLT Planet Finder system. This matter of fact calls for system specifications that are tremendously more stringent.

- a significantly higher AO system frame rate (up to 3-4 KHz) to reach high rejection in the central part of the field-of-view (for separations less than 0.1 arcsec for the Earth-like planets detection goal).
- the systematic errors must be kept at a very low level on the low and mid spatial frequencies (f < 2.5 cycles/m in the entrance pupil frame). For VLT Planet finder, on these spatial frequency range, the static errors contributes by about 40-50 nm. A gain of at least an order of magnitude is needed (requirements: less than 5 nm rms).
- the wave-front sensing measurements error propagation on low and mid-spatial frequencies must be very low: the use of phase-type sensor instead of a slope sensor is needed at least for the correction of the halo at separations less than 0.1 arcsec.

The role of an XAO system for a planet finder is two-fold:

- Condition 1: to deliver a high Strehl Ratio (SR>90%) at the science wave-lengths in order to concentrate most of the candidate exoplanet's light in a diffraction core.
- Condition 2: to provide, in combination with a coronagraph, the level of rejection of scattered starlight, that permits planet detection and characterisation in a reasonable amount of time (intensity contrast better than 107 at 0.1 arcsec in J band.)
    - the part of the halo that averages out defines mainly the level of photon noise against which the planet needs to be detected. It directly impacts the total integration time needed.
    - the part of the halo that doesn't average out (mainly quasi-static speckles), is the most critical part and defines the ultimate level of contrast one can reach.

These guidelines are very important in the definition of the XAO post-focal system coupled to the coronagraph.

8.3.2.2.1 Common path system:

The common path AO system for EPICS is composed of M6 and a post-focal XAO system. The control of these two systems (M6 + XAO post-focal system) will be based on a Woofer - Tweeter scheme, where M6 is dedicated to the correction of the large PTV low spatial frequency aberrations whereas the post-focal system ensures the correction of the fast evolving aberrations and of the high spatial frequencies. To fulfil the requirements on the AO control radius, i.e. a 20 cm inter-actuator separation as projected on the 100-m pupil, the post focal corrector needs to be composed of at least 1.7×10^5 degrees of freedom. We use this number for the baseline system.

Wave-front sensing and computing time requirements trade-off:

The wave-front sensor in an XAO system is a very important component, and its noise propagation properties must be carefully taken into account. The ultimate science goal of EPICS calls for a very efficient scattered star light rejection very close to the center of the field-of-view. This translates, for an XAO system, to a very good sensitivity of the wave-front sensor to measure low and mid-spatial frequencies. This property is fulfilled by the so-called phase-type sensors. The noise propagation properties of the pyramid sensor are of phase-type nature: it has been shown that the gain in limiting magnitude can be quite important with respect to a Schack-Hartmann sensor for the correction of the scattered starlight halo at separations less than 0.1 arcsec [104].

Our first choice for the EPICS post-focal XAO system, was to couple a pyramid sensor with a single high density MEMS mirror with $1.7x10^5$ actuators and to control this system at 3 KHz. This is certainly a good choice in terms of noise propagation but revealed to be very risky in terms of required computing time and CCD read-out time requirements. Indeed, the signal provided by a pyramid sensor is a complex function of the entrance phase error, and is characterised by a very non-sparse interaction matrix (see RD51). As of today, the only way of deriving the correction commands from a pyramid sensor is to use a full rank matrix-vector multiplication. Some possibilities combining different approaches will be studied but are still in a very preliminary state.

Even taking into account a significant increase in computing power over the next 10-15 years, the control of a 1.7 10^5 degrees of freedom AO system at 3 KHz using a full rank matrix-vector multiplication seems extremely difficult, if not impossible, to achieve. For Shack-Hartmann-based systems the situation is different; at least two new methods for fast reconstruction exist : one using the sparseness of the zonal interaction matrices [106] and another one using Fourier methods permitting also a modal control [107], [108].

Two-stage post-focal XAO system.

The solution we propose is to split the wave-front sensing and the correction in two stages. This permits to alleviate a lot the requirements in terms of computing power as well as of WFSs CCDs read-out. Here is a brief description of this concept (see also Figure 8-89):

- the post focal corrector will be composed by two post-focal Deformable Mirrors:
  - post-focal DM_1 (with an equivalent d_1 = 0.2 m actuator pitch): $1.7x10^5$ actuators controlled at 1KHz or so, providing the required 0.4 arcsec control radius at 0.8µm. The cut-off spatial frequency of this system is $f_{c1} = 1/d_1 = 2.5$ cycles/m. This system alone already permits to get a high Strehl greater than 90% in J and H band (it fulfils condition 1), but is unable to provide an acceptable rejection in the central part of the field-of-view.
  - post-focal DM_2 (with an equivalent d_2 = 0.67 m actuator pitch): $1.5x10^4$ actuators controlled at 3 KHz. The cut-off spatial frequency of this system is $f_{c2} = (2d_2)^{-1} = 2.5$ cycles/m. This system will permit to increase by an order of magnitude the rejection of the scattered light for separations less than 0.1 arcsec (it fulfils condition 2).
- After reflection by the two DMs, the beam is split between two wave-front sensors with different pupil sampling. This solution, known as hierarchical wave-front sensing, has been proposed [109] as a way to increase the sensitivity of the Shack-Hartmann sensor. We use this concept with a different scope, i.e. to optimise the system in terms of correction bandwidths at the expense however of some moderate loss in terms of sensitivity. Moreover we propose to use two different types of wave-front sensors:
  - WFS_1 (Shack-Hartmann WFS): very High Order WFS (500x500 sub-apertures) to control the post-focal DM1 at a 1 KHz frame rate. A possible control algorithm for this stage is a Fourier reconstructor using optimized modal control in the Fourier domain [108] for spatial frequencies f such as fc2<f< fc1. The gain for spatial frequencies f < fc2 are essentially put to 0 (or to very low values) because the measurements of WFS1 for this range would be much more noisy than the one provided by WFS2.
  - WFS_2 (pyramid WFS): medium order WFS (150x150 sub-apertures) to control the post-focal DM2 at a 3 KHz frame rate. A full rank matrix-vector multiplication is used.

This way of control is also more flexible, depending on the goals of a given observation. For detection of both gas giants and rocky planets, the light splitting (50/50 for example) is ajusted to provide a level of the halo more or less balanced in the field-of view. For follow-up observations the light splitting and temporal control bandwidths can be ajusted in function of the location of the target. More light can be sent for example to WFS_1 to ensure a higher halo rejection in case of a follow-up observation of rocky planet near the center of the field of view.

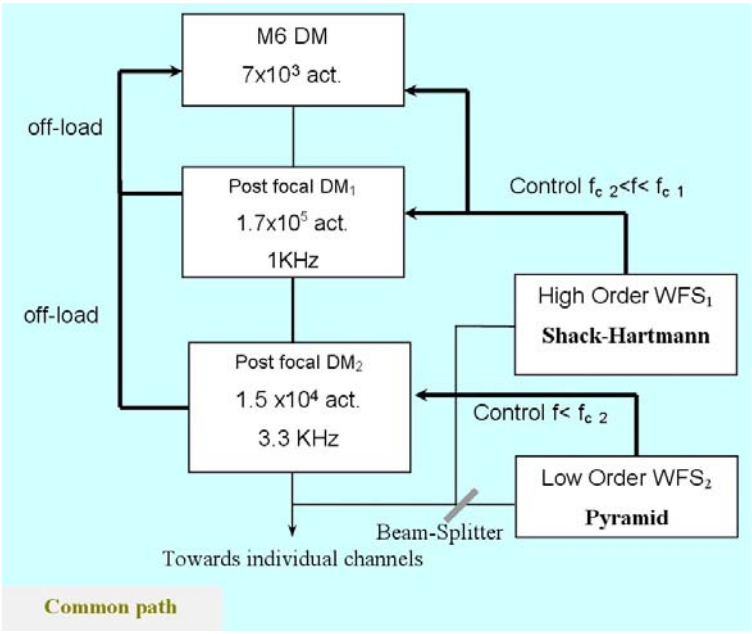

Figure 8-89: Common path XAO concept for EPICS.

8.3.2.2.2 Individual Channel paths

Each scientific channel will be equipped with an active mirror of about 10^4 actuators for the correction of the residual static error in the common path AO system before the coronagraph. A focal plane sensor (focal plane interferometer [111] and/or phase diversity) is used to measure and compensate the static errors using an artificial source for calibration and the starlight itself with a low temporal bandwidth (see Figure 8-90).

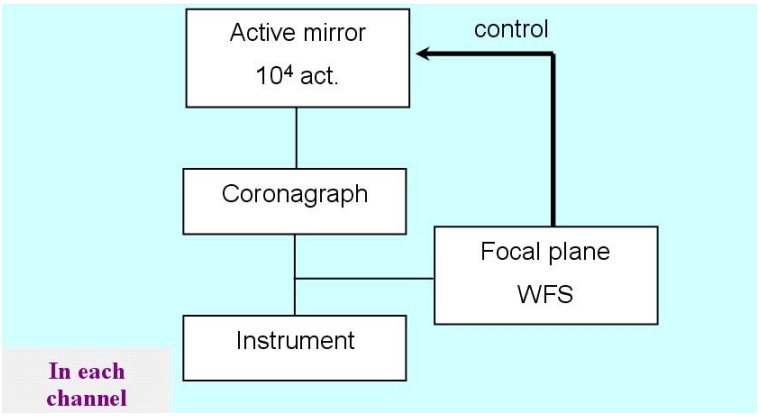

Figure 8-90: Individual scientific channel path.

8.3.2.3 Coronagraphy

The coronagraphs are very critical components of EPICS and their interaction with AO residuals needs to be carefully studied. Since the science instruments cover a very broad band of wavelengths, it has been chosen to equip each individual channel with its own coronagraph. This choice permits to optimise the coronagraph parameters with more flexibility. Whereas a sufficiently achromatic coronagraph dedicated for the visible range is probably the most challenging one, the ones for J and H band could eventually, if an acceptable concept is found, be combined in one single coronagraph. But no definite concept has now been chosen. Coronagraphy is a very fast evolving field with a lot of very new ideas that appeared recently (see RD22 for a review). For EPICS two concepts have been considered and some preliminary results have been obtained. The first concept, the double stage reticulated Lyot coronagraph is described in RD22 and permits to deal with diffraction residuals induced by gaps between the

segments. This concept is quite complex to simulate and has been studied only in the diffraction limited case for the moment. The second concept, a prolate apodized double stage Lyot coronagraph is less complex but doesn't reach a contrast as high as the reticulated double stage coronagraph.

An important issue about coronagraphy is the criterion to choose for its performance.

- The first obvious requirement is that the rejection of the coronagraph is such that the diffraction residuals are significantly lower than the AO residuals. This criterion ensures that the photon noise contribution to the halo induced by the coronagraph is negligible. If only this criterion were important, the requirements on the intrinsic performance of the coronagraph would be quite moderate.
- To be rigourous, one has to take into account the type of instrument behind the coronagraph. In case of differential imaging, one has to deal with the effect of the coronagraph on, for example, the differential chromatic aberrations in the case of wave-length splitting differential imager or an IFS. These have a direct impact on the ultimate contrast achievable and on the calibration procedures to be implemented.

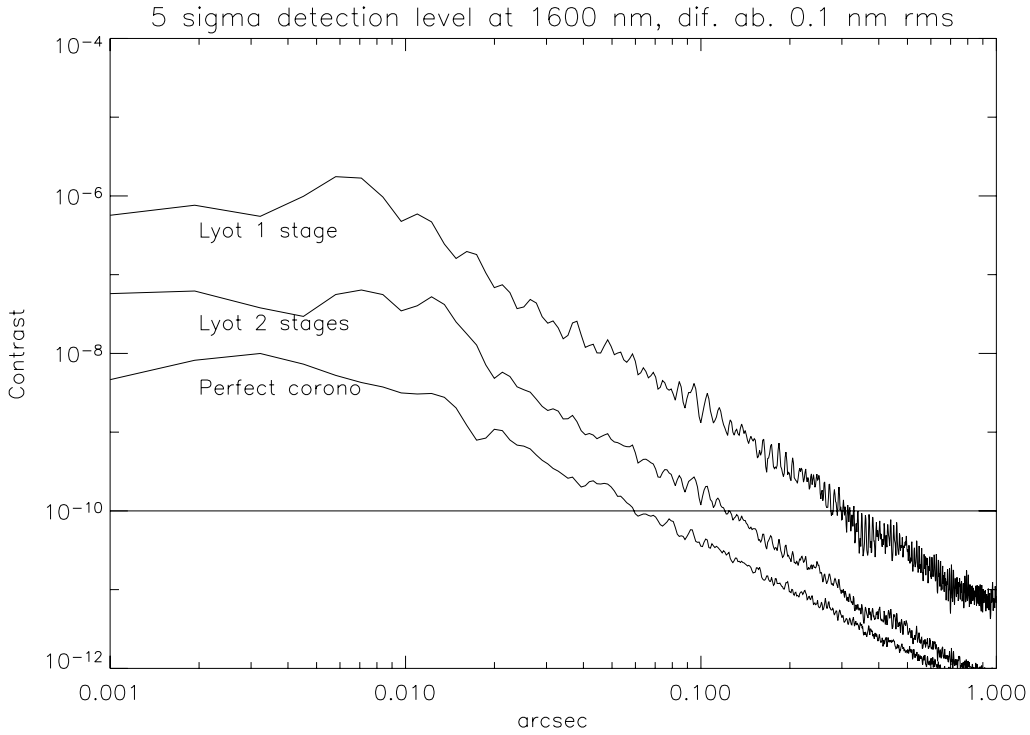

Figure 8-91: 5-sigma detection level after differential imaging for 0.1 nm rms differential chromatic error before the coronagraph (circular average). λ = 1600 nm.

In the example shown in Figure 8-91, we compared by numerical simulations a perfect coronagraph that is able to reject the whole diffraction residuals and the more realistic double stage Lyot coronagraph with prolate apodization (see RD22 for intrinsic preformance). The simulation considered monochromatic light and differential chromatic aberrations with 0.1 nm rms error occurring before the coronagraph.

One can see that with a perfect coronagraph the residuals are about 2×10^{-10} at 50 mas separation, compliant with the TLRs. The same differential error but as seen though the double stage Lyot coronagraph with prolate apodization translates in a 5 σ detection level of only 10^{-9}. Note that these curves have been obtained by circular averaging. A more complete study should take into account blind zones in the field of view like the diffraction by the spider. Figure 8-92 shows that the residuals for the perfect coronagraph are due to wave-front errors only, whereas the one for double stage prolate apodized Lyot coronagraph, the diffraction residuals are prominent and directly correspond to the so-called pinned speckles.

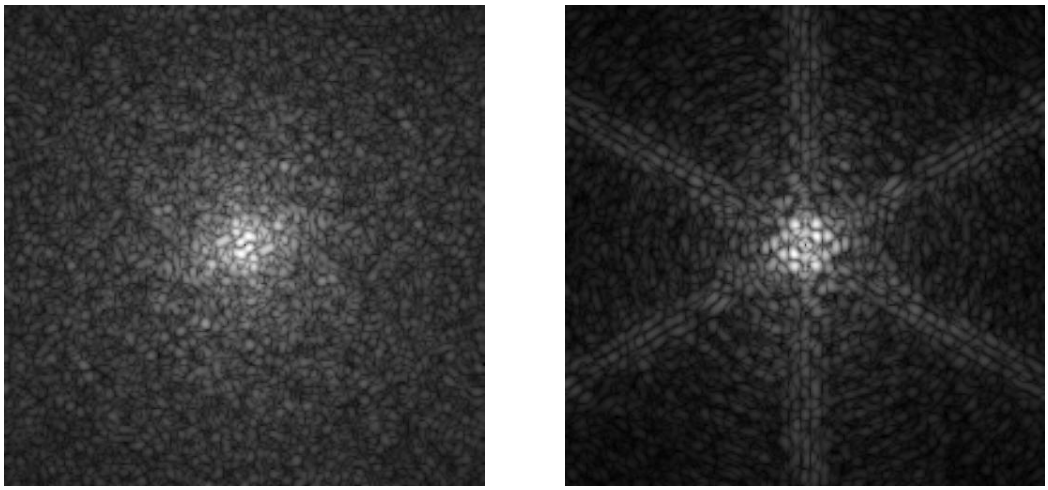

Figure 8-92: Residuals after dual imaging with a perfect coronagraph (left), and a double stage Lyot coronagraph with prolate apodization (right.)

This simulation shows that the intrinsic performance of the coronagraph has an important impact of the differential aberrations that can be tolerated in the system. The same simulation is foreseen for the double stage reticulated Lyot coronagraph but is more complex to compute since one needs to well sample the gaps between the segments.

8.3.2.4 Correction of co-phasing errors

Co-phasing residuals on an ELT is often presented as an important show-stopper for planet finding. Lardiere et al. [110] estimate that the co-phasing rms residuals should be at the level of 1 nm so that its contribution to the halo remains negligible with respect to the AO residuals. Their main argument is that piston errors cannot be corrected with usual continuous deformable mirrors, so that dedicated fast piston correctors should be implemented. We demonstrate that a continuous mirror can actually correct for piston errors, or more specifically it can correct for the Fourier components of the wave-front that affect the field-of-view of interest. For this we considered a typical co-phasing errors figure from M1 and M2 with 20 nm rms total error and fitted, using a Fourier method, a phase function whose spectral content is limited to spatial frequencies less than fc_2 the cut-off frequency corresponding to the second stage DM_2 inter-actuator separation (67 cm). The initial wave-front map and the DM_2 fitted correction wavefront are represented in Figure 8-93 and the residual wave-front (difference of the two) is represented in Figure 8-94.

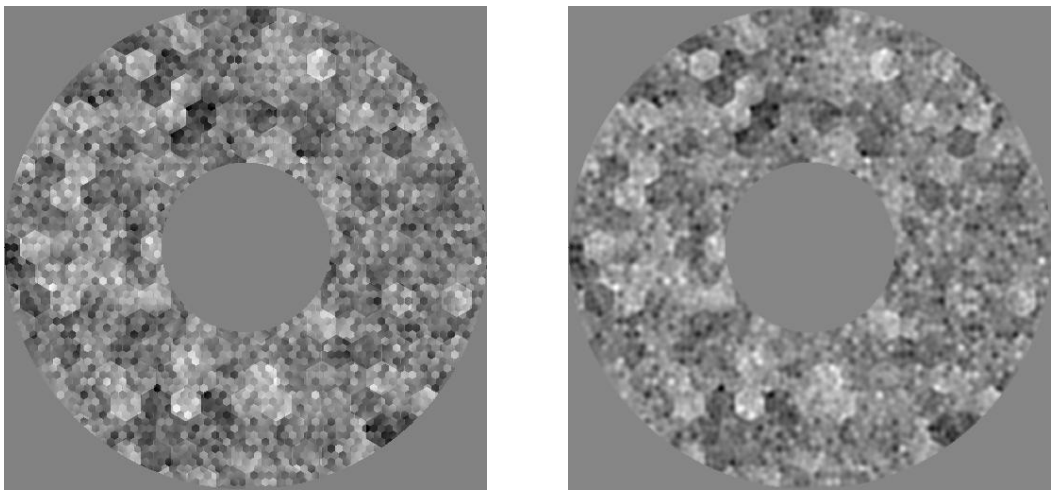

Figure 8-93: AO correction of co-phasing residuals. Left: initial co-phasing errors. Right: best fit with DM2 (0.67 actuator separation).

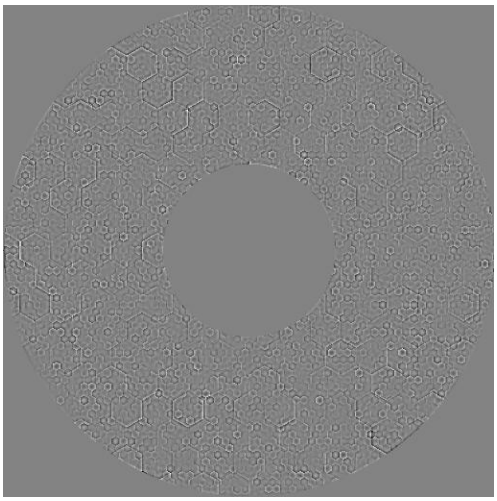

Figure 8-94: Residual left by best fit of DM_2.

The best fit obtained with DM_2 leaves a residual of 6 nm rms. A cut in the three wave-front maps is represented in Figure 8-95. One can verify that indeed, DM2 is unable to correct for the 'jumps' of the wave-front at the segment edges, and those appear still in the residuals. These jumps can even be as high as several tens of nanometers. However, what counts for imaging is the spatial content of the phase. Since we are interested to obtain a very high contrast in the centre of the field of view, the most important is to correct the low spatial Fourier components. It is exactly the case of the residual phase of Figure 8-94.

To convince ourself that such a residual error figure can be acceptable, we simulated the coronagraphic images corresponding to the wave-fronts with co-phasing residuals and co-phasing residuals plus correction by best fit of DM_2. The results are shown in Figure 8-95. One can see that indeed if the co-phasing residuals only are present, the halo is very bright and the raw contrast is larger than 10^{-6} at 50 mas. After correction by DM_2 the residual is only about 10^{-9} in the centre of the field of view, so negligible with respect to AO residuals.

It is important also to notice that the pyramid sensor is sensitive to piston errors [104] contrary to the Shack-Hartmann, so that it will be able to measure them. This is another reason of why a phase-type sensor should be used.

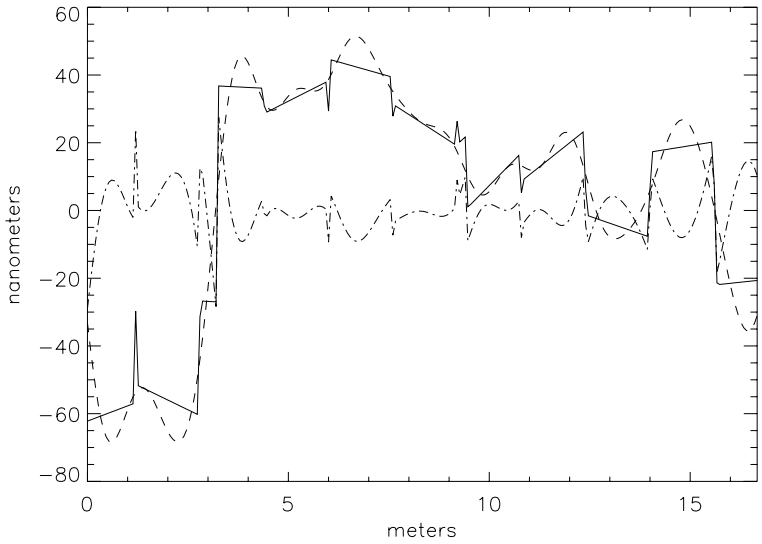

Figure 8-95: Cut in wave-front maps of Figure 8-102 and In Figure 8-94. Solid line: initial co-phasing errors (piston and tip-tilt, 20 nm rms). Dashed line: DM_2 fit. Dotted-dashed-line: residual error figure after correction by DM_2 (6 nm rms error residual of high spatial frequencies).

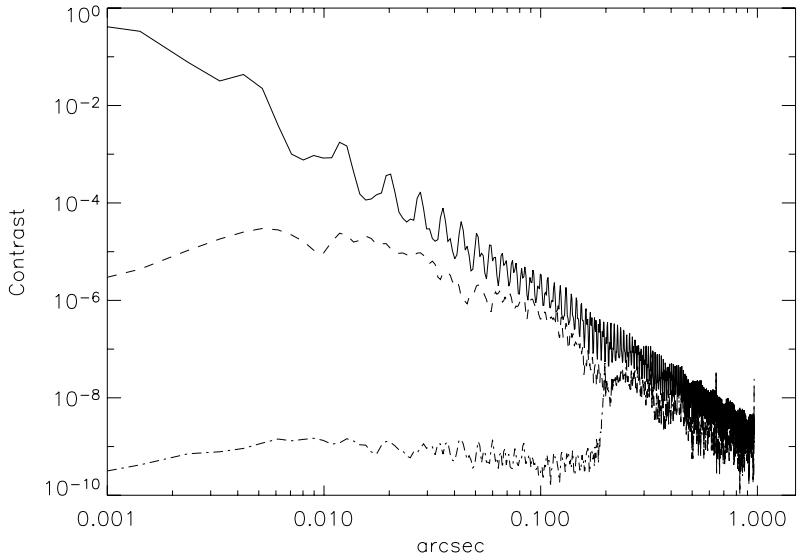

Figure 8-96: Effect of co-phasing on coronagraphic image at 1600 nm (Circular average of 2D image). Solid line: PSF without coronagraph. Dashed line: Coronagraphic image with initial co-phasing residuals of 20 nm rms. Dotted-dashed line: Coronagraphic image of residuals after AO correction (6 nm rms).

8.3.2.5 EPICS performance

The scientific spectral regions of EPICS are located in the R, J, and H bands and cover thus a wide range of wave-lengths. The choice has been made to use the I band [800-1000] for wave-front sensing since this region had a lesser scientific interest. Moreover, since the I band is located between the visible and Near IR scientific wave-lengths, the effects due to air chromaticity (anisoplanetism due to differential refraction, chromatic seeing) become acceptable. The high Strehl obtained in I band (nearly 80 %), is also an advantage for the pyramid sensor to work in a more linear though diffractive regime with best sensitivity. Typical Strehl Ratio values for medium seeing are given in Figure 8-97. In the near IR, the Strehl is larger than 90% and still attains 70 % in R band. The detailed error budget of EPICS AO system is described in RD51.

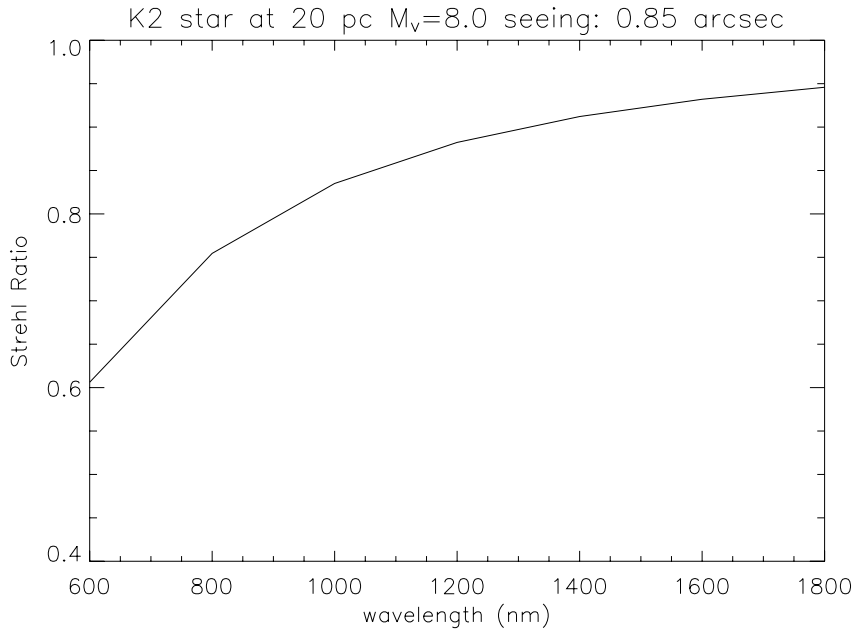

Figure 8-97: Strehl ratio versus wave-length.

More important than the Strehl ratio, the PSD of the phase error has a direct impact on the residual halo after coronagraphy thus on the final contrast. For this reason, the use of a phase-type sensor for correcting the central region of the PSF makes sense as it can be seen on Figure 8-98. The correction is however limited to about 30 mas, separation at which the air chromaticity becomes the main limitation.

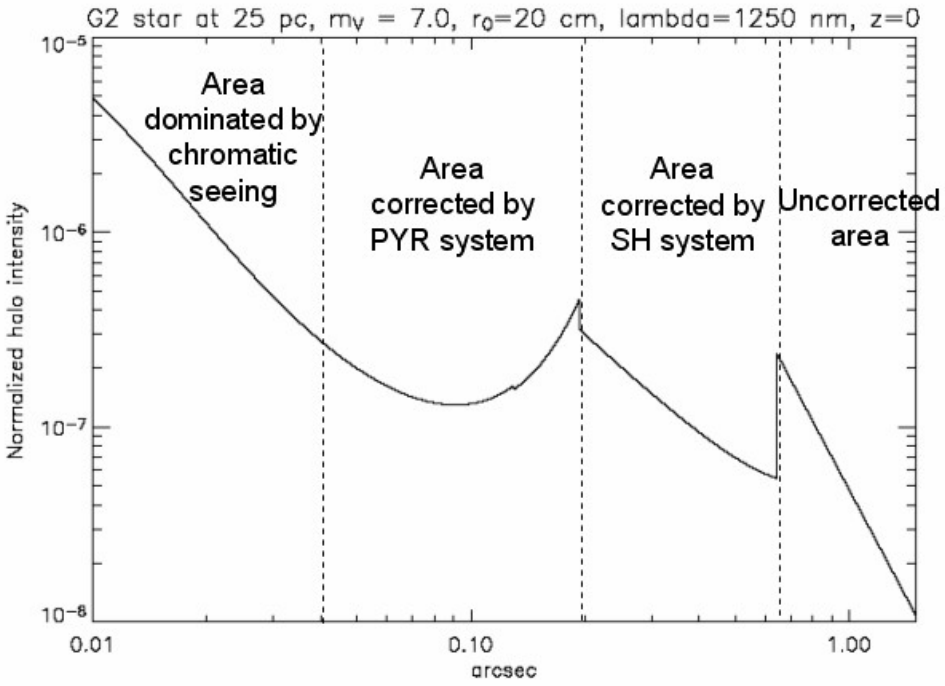

Figure 8-98: Theoretical point spread function after a perfect coronagraph.

An analytical model taking into account the main error sources has been developed to produce the kind of curves of Figure 8-98. The performance in terms of Signal-to-Noise ratio for the detection of exo-planets can be directly derived from these curves (see RD51).

8.3.2.6 Technological requirements for EPICS

EPICS requires significant technological developments of hardware:

- CCDs: 1KxK (goal 3Kx3K) detectors with fast read-out (3 KHz) and low noise (read-out noise less than one electron) are required. Developments of L3CCD are already part of the OPTICON Joint Reasearch Activity 1.
- Micro Deformable Mirrors): EPICS requires a micro deformable mirror with about 2.105 actuators. Actually only 1K micro DM2 with about 1 micron mechanical stroke are available (Boston Micro-Machine). A 2K micro DM with larger stroke will be developed in the frame of OPTICON.
- Real-Time-Computers
- Coronagraphic masks: high precision coronagraphic masks (in phase and in amplitude) are needed.
- Optical polishing and coating quality: a number of optical surfaces in the EPICS design need to be of extremely good quality (less than 1 nm rms error). The effect of coating on super-polished surface is an important aspect of this topic.

8.3.2.7 Future development plan

The EPICS feasibility study has shown the necessity of important Research and Developments in the field of high contrast imaging. This includes AO developments itself, new methods for wave-front sensing and instrument concepts and realisation of very high quality optics. High contrast imaging is an emerging and a very active research field: new limitations, new ideas and new instrumental concepts fundamentally different from the proposed approach here may appear in the coming years in the frame of high contrast instruments developed today –VLT or GEMINI PF- and demonstrators like ESO's High Order Test bench, HOT.

Laboratory experiments:

In particular we intend to study the following items theoretically and with laboratory experiments also beyond HOT in the frame of the FP6 ELT design study:

- optimation of pyramid wave-front sensor, by theoretical work with end-to-end simulations and with experiments
- Woofer-Tweeter control scheme theory and experiments
- Realisation and testing of "super-polished optics" and effect of coating on error figure.
- investigation of new concepts like the focal plane interferometer: this idea could permit ultimately to be unsensitive to static and differential aberrations, since the coherence of the speckles itself can be used to disentangle them from a planet image.
- Developments in coronagraphy
-

VLT Planet Finder studies:

The experience and results of the Planet finder development phase will be extremely valuable. Important feed-back is expected from extreme Adaptive optics developments as well as developments more related to the instruments: polarimetry, diffraction effects in an IFS, etc.

Real-Time Computers

Many developments are required to reach the goals of this ambitious system. To make it achievable we need to improve 4 technologies that are the foundations of the main design of all the other systems. Table 8-17 illustrates these four technologies and the improvement that is required in order to implement XAO in two specific cases 500x500 and 1kx1k sub-apertures.

Technology	500x500	1k x 1k
Input/output communications. Today it is based on a 2.5 Gb/s serial communication. The 10Gb/s is becoming available and it has been used as the baseline for the other designs. Here we need 50 Gb/s for the first case, 100Gb/s for the second	5	10
Faster processing elements, faster CPU-to-CPU busses, faster memory.	10	30
Integer arithmetic. FPGAs perform faster if integer arithmetic is used. By observing that input data (pixels) are integers and output data (control voltages) are as well, one could think of arranging the computation in integer arithmetics. Study is required here. However, performance gain is already known.	2	3
The sparseness of the interaction matrix of an XAO system is very high. However a control matrix (the inverse) is not. Smart algorithms will be able to take advantage of the sparseness of the IM and require less processing power.	5	10

Table 8-17. Four technologies to achieve the XAO requirements

Since this system is not supposed to be built before 2015, we can benefit from the technological advances that will happen in the next 10 year, and the corresponding efforts that can be spent

in studying better algorithms. Famous Moore's law predict an increase of computing power in 10 year by a factor 100, so the highest value we used, 30, is not so aggressive.

With the assumptions listed above, the 500x500 system would be made of 3 crates with 20 boards each, each carrying 2 high performance next-generation FPGA chips. Each crate will actually host 3 identical sub-systems, for a total of 9 identical sub-systems each processing one slice of the detector data. Final control values will be merged and exchanged with 6 back-end stages that will control the deformable mirror through multiple parallel lines.

The 1000x1000 system will have a similar complexity, but it requires more aggressive technological improvements and a higher parallelism.

In conclusion, the XAO system at 500x500 (more for the 1000x1000 case) is not achievable with today's available techonolgy. However, we identified 4 critical technologies to improve and the required factor of improvement is within reach for 2015.

Hardware Development

To get to the final performance of the last AO system, XAO, we need to strengthen the relationship with the industrial partner(s) even more than in the previous cases in order to aggregate in a super-performing board the latest technology in FPGAs, CPUs, busses and memory. This, of course, can only be done if the first level of co-operation had been successful. Unfortunately there not many similar applications around and industry could consider our as a small niche, so convincing them to develop the products we need might be difficult

Algorithms

The XAO system is too big to be implemented using plain matrix-vector multiply thus smart algorithms must be used. Fortunately there are several options.

Generic Algorithm Improvements

- The control matrix can be reduced in precision and compressed. Pixels are normally 16 bit values and mirror controls are 14 or 16-bit values. A loss-less compression, if possible, will allow us to reduce the storage size of the matrix, thus its loading time and the overall performance of the RTC.
- Fixed-point arithments. By observing that input data (pixels) are integers and output data (control voltages) are as well, one could think of arranging the computation in integer arithmetics.
- Multi-rate control: the RTC could send more than one command within a single frame time. Multiple commands can be generated by a sequence of approximated commands where the last is the final correct value. This technique is useful if the dynamic of the mirror is not particularly fast. In this way the mirror can be pushed toward the final value, even if approximated, very soon, and while it is reaching the position another refined value will be sent for the final adjustment.

Architecture Specific

- Local reconstruction algorithms can be used to maximise the parallelism of the reconstructor and the controller.
- Fourier domain techniques can be used to reduce the complexity of the reconstructor from n2 to nlog(n). However it has been developed so far only for Shack-Hartmann systems

System Specific

- SCAO and XAO systems are characterised by a large sparsity factor, i.e.: the interaction matrix is mainly made of zeros since the size of the influence functions is small. This characteristic can be exploited to design special algorithms that do not explicitly invert the interaction matrix.

8.4 Third generation Adaptive Optics

8.4.1 Introduction

The 3rd generation of Adaptive Optics relies essentially on the availability of the Laser Guide Stars for OWL. In the description of the 1st and 2nd generation AO systems, we have provided the performance of these systems and the corresponding limitations due to the number and magnitude of NGSs used for wavefront sensing. It should be noted that "3rdgeneration" is actually a misnomer: every effort will be made to have LGSs available as early as possible.

In the following:

- We will summarize the performance of the 1st and 2nd generation AO systems and identify where the LGS based AO systems should improve the situation
- We will provide preliminary performance expected for the GLAO and MCAO cases using LGSs in the ideal case
- We will summarize the main problems encountered with LGS systems on ELT in general and on OWL in particular and provide potential avenues to overcome these problems
- Finally we will introduce other LGS concepts which are being investigated in the frame of the European ELT design study.

8.4.2 Toward the 3rd generation AO systems with LGSs

Resorting to only natural guide stars for wavefront sensing allows one to have a simple AO system, since there is no need to produce a high quality reference in the atmosphere. However, this approach imposes some limitations for each AO system we have analyzed in this document.

Due to the limited time to prepare this document, the preliminary performance provided in this section does not include all specific ELT LGS issues listed later in 8.4.3.

8.4.2.1 From Single Conjugate to Laser Tomography AO

In the case of SCAO, the sky coverage is limited by the availability of bright (magnitudes 16-17) guide stars within the isoplanatic patch (~30''-1') from the object. The sky coverage is barely a few percent. This is well-known problem of this kind of AO system.

To improve this, one needs to resort to multiple laser guide stars. Indeed, using a single LGS is not sufficient, because of the cone effect (or focus anisoplanatism). The LGS being located at 90km and not infinity, the rays of light coming from the LGS do not follow the same path as those from the NGS. Therefore, an error is made when measuring the wavefront from an LGS to correct an object at infinity.

To overcome this issue, several LGSs have to be used, to probe the whole volume of turbulence above the telescope. This so-called LTAO (Laser Tomography AO) allows to use a single DM (M6 in our case) and to optimise the correction on-axis over a small FoV.

In the case of OWL, the LGSs should be located far enough off-axis to sense the whole volume of turbulence (geometrically the optimum distance is ~100" off-axis). If we want to limit the number of LGSs to 4-5, the optimum LGS off-axis angle should be compromised with the meta-pupil overlap at let say 8 km. For a given performance the corresponding optimum values remain to be determined by simulations. The expected performance of an LTAO system is expected to be slightly better than the MCAO with multi-LGS as the LTAO correction is optimised on-axis but lower than the SCAO system using bright NGSs because of the meta-pupil overlap and remaining cone effect. Detailed simulations are planned during phase B.

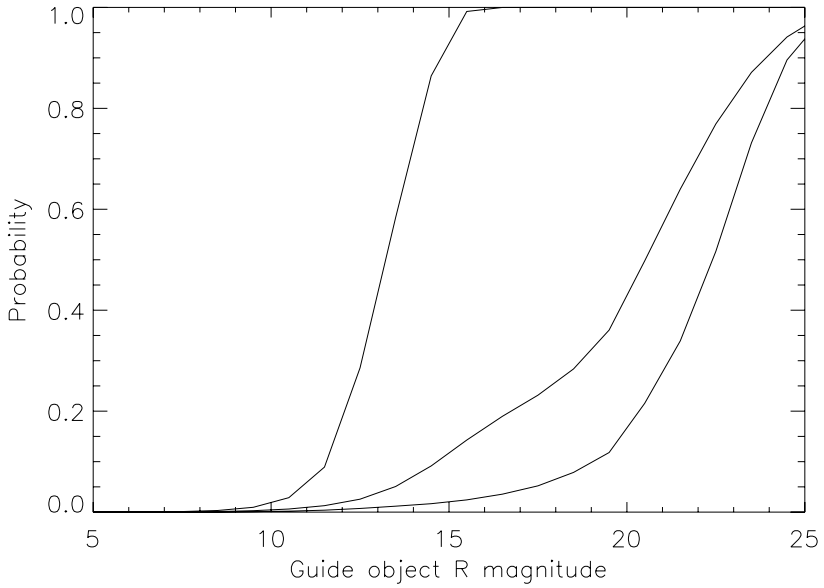

Figure 8-99: Probability to find a NGS/Galaxy versus magnitude over 2' FoV. Top to bottom: Galactic plane, 180-20°, Galactic Pole

It is known that LGS does not sense the atmospheric tilt. When using several LGSs, individual LGS tilts degenerate into unseen low order modes. To sense these modes a low order NGS WFS -3x3 Shack Hartmann for instance- either in the visible or in the IR is required. The limiting magnitude of this wavefront sensor scales with the telescope collecting area leading to an expected limiting magnitude of Mv=22-23 for a visible wavefront sensor.

In addition, the outer scale of turbulence reduces dramatically the phase variance of the unseen low order modes –see for instance Figure 8-26-. Based on this fact, we believe that an NGS located within a FoV of 2' around the object may be used to sense these modes with a marginal reduction of the on-axis performance due to the anisoplanatism. Alternatively three tip-tilt NGSs may limit the anisoplanatism effect. Figure 8-99 shows the probability to find such NGS or Galaxy within 2' FoV. We see that 60% Sky coverage can be achieved at the Galactic Pole with such concept.

The concept of LTAO (Laser Tomography AO) is planned to be demonstrated for the VLT second generation instrument, GALACSI, in narrow field mode. Multiple lasers are used in conjunction with a single deformable mirror to correct a small field of view. The multiple lasers are required to compensate for the cone effect. The advantage is that high sky coverage can be achieved through the use of LGSs and a high resolution (diffraction limited) can be achieved over a field limited by anisoplanatism.

8.4.2.2 Laser assisted Ground Layer Adaptive Optics

For GLAO, the lack of NGS also reduces the sky coverage, and can introduce non-uniformities of the PSF over the corrected FoV, because the brighter star will have better correction than the fainter ones.

One particularity of the GLAO is that only the low atmospheric layers are corrected. Those are well sensed by the sodium LGS. It is therefore conceivable that good performance can be achieved for GLAO with sodium LGSs, like it is the case for Rayleigh LGSs on 8m telescopes.

In has been recently suggested ([129]) to use a single LGS on an ELT, to provide ground layer correction at a low cost, with a large sky coverage. This is based on the approach proposed by SOAR telescope, to use an LGS to correct the ground layer, and "use" the cone effect to filter out the high altitude turbulence.

On a 4m class telescope, like SOAR, a Rayleigh LGS (at ~4km) is used.

We analyzed the performance (gain in EE in a 50 mas pixel) of such a system for OWL, as a function of the height of the LGS. The results can be seen in Figure 8-100.

In the K band, factors between 3 and 4 of gain can be obtained, over a field of view of ~2' (diameter), in good seeing. Even in J-band, a gain close to a factor of 2 can still be obtained. In this simulation, we have assumed that the spot elongation effect is perfectly corrected, and that a bright tip-tilt star is located on-axis.

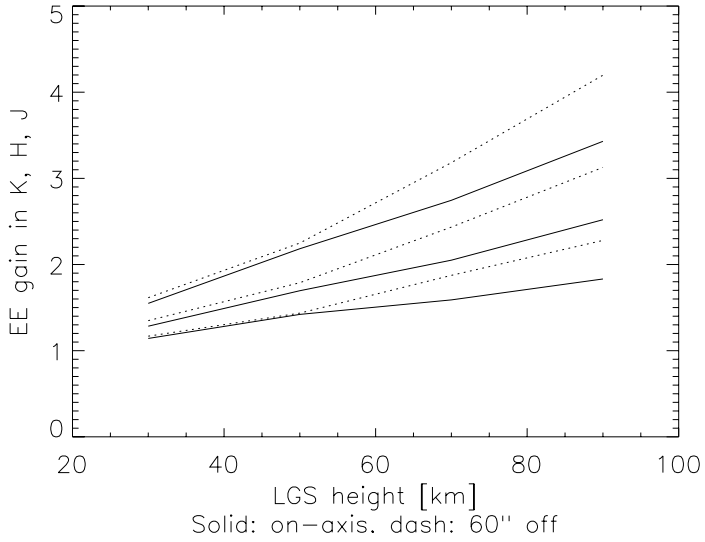

Figure 8-100: Performance (gain in EE compared to seeing) of a single on-axis LGS. Solid: on-axis, dash: off-axis. Top to bottom: K, H and J bands. The good seeing model was used (0.5'').

Since this idea was presented quite recently, we have not had time to thoroughly analyze the concept. It is not for the moment clear why the off-axis performance becomes better than the on-axis one when high altitudes LGSs are used. Intuitively, the opposite should happen. It might be due to the small number of iterations (500) for which the simulation was run.

The sky coverage for such a system should be close to 100%, since only the tilt needs to be corrected, and the diffraction limit is not the goal.

Further analysis is required, but this method shows some promise.

8.4.2.3 Laser Assisted Multi-Conjugate Adaptive Optics

The field of view of MCAO is significantly smaller than that of the GLAO. Therefore, the probability to find NGSs is even smaller. This introduces two effects:

- Low performance, because statistically, the NGS are far from the desired field
- High PSF variability, because the NGSs do not sample finely enough the atmosphere.

Using several LGSs helps solving the problem, by providing bright and nearby references to the WFSs.

Using multiple laser guide stars allows to obtain a large sky coverage in an MCAO system. We have modeled a system based on the M6 and M5 of OWL, correcting a field of view of 2' (diameter). The LGSs were placed in a configuration where 4 are at the corners of the field coordinates (± 1', ±1') and a central star. Sodium LGSs were assumed, providing enough flux so the WFS is not photon starved. The performance (Strehl in the K band) is analyzed in the 1' (radius) field of view. Good seeing conditions (0.5'') were used for these simulations - Figure 8-101-.

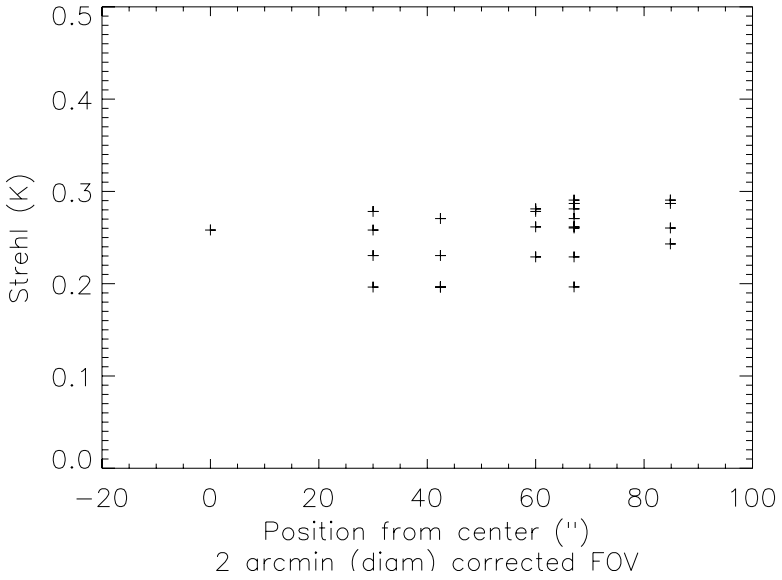

Figure 8-101: LGS MCAO performance (K-band). Tip - Tilt stars at LGS positions.

We can see that a Strehl ratio (K-band) between 20 and 30 % can be obtained over 2' (diameter) the field, in good seeing conditions.

It was assumed that each LGS provides a tip-tilt measurement. Of course, this is unrealistic, and the tilt problem of the LGSs must be solved with:

- Either a single NGS from which some low order modes are measured (presumably, a 3x3 SH sensor is sufficient). Due to the size of the telescope, this method should be quite sensitive.
- Multiple (at least 3) NGSs are used, from which only the tip and tilt are measured.

We have not yet investigated how to increase the performance of the system. In phase B, we will tackle this issue, and proceed to study the effect of increasing the number of sub-apertures, adding an extra DM, changing the number of LGSs.

However, we can see already here that 5 LGSs provide already acceptable performance.

8.4.2.4 Laser Assisted Multi-Object Adaptive Optics

The same sky coverage problems apply also to MOAO, and more particularly to the cosmological deep fields, which are the prime targets for MOAO. Although some fields are accessible with good performance (see Section 8.2.3.2), other fields are empty of bright stars, which have to be searched far away.

The use of Multi-LGSs for MOAO looks at this stage quite challenging as the number of LGSs may be increased to 10 or so. Further analysis and simulations remain to be performed to conclude on the performance and optimum number of LGSs.

8.4.3 ELTs and LGSs issues

The use of single or multiple Laser Guide Stars for ELTs has a series of difficulties described in this section. These issues depend on the telescope diameter and F/ratio. Table 8-18 provides a quantative evaluation of know LGS issues on ELTs versus telescope diameter.

These values have been computed according to the following formulae:

- Laser spot elongation for the subaperture at the edge of the telescope pupil :

$$\theta = \frac{\Delta H D}{2H_{Na}^{\ 2}} \qquad \textit{Eq. 8-6,}$$

where H_{Na} is the height of the sodium layer (90km), D the telescope diameter (100m) and ΔH the thickness of the sodium layer (10km).

- The seeing limited depth of field:

$$f = \frac{2H_{Na}^{\ 2} s}{D} \qquad \textit{Eq. 8-7,}$$

where, s seeing size disk and f is the depth of the field (taken from [113]). The stroke required in the WFS with dynamically steered sub-apertures is 23 μm (1m sub-apertures, 15 km refocusing):

$$x = \frac{d(D-d)r}{8H_{Na}^{\ 2} - 2r^2} \qquad \textit{Eq. 8-8,}$$

where x is the full mechanical stroke, d sub-aperture size, r is the range gate. If only 5km are used the stroke is 7.5 μm and if only 1 km is taken, then it reduces to 1.5 μm. The frequency requirement is above 1 kHz ([113])

Spot Elongation: The spot elongation is due to the thickness of the atmospheric sodium layer. The profile of sodium distribution varies in time, but a mean thickness of about 10 km is usually observed, with sometimes “spikes” of sodium density at given heights.

Observing the backscattered light from the extended sodium layer with an ELT is problematic, because from the side of the telescope (50 m in the case of OWL, if the LGS is launched from behind the central obstruction of the telescope), one doesn’t see a spot, but a stripe.

Spot aberrations: The spot aberrations are due to the design of any particular telescope, which are optimized to yield maximum optical performance for objects at infinity. Observing a LGSs at 90 km produces a severely aberrated image, on which wavefront sensing might be difficult. In addition, these aberrations change as a function of the distance to the sodium layer, which can vary from 90 km (observations at zenith) to ~180 km (observations at 60 degrees).

Number of LGSs: It has been argued that it may be necessary to add LGSs when the telescope diameter increases, as the cone effect gets bigger. On the other hand, simulations up to diameters of 30m have not shown large decreases of performance compared to 8 m telescope simulations ([127]). Therefore, the number of LGSs necessary on ELTs is still an open question, at least from the AO tomography point of view.

Fraticide Effect: The fratricide effect is due to the Rayleigh scattering cone of a LGS introducing noise into the measurements of a wavefront sensor from another LGS when using a continuous LGS. This effect also exists on 8 m telescopes and is being studied right now. On ELTs, it might be necessary to use more lasers to compensate for this effect or use pulsed laser which are more difficult to produce.

Laser defocus: When a sodium Laser Guide star is used the mean altitude of the sodium layer may vary with time. In addition, depending on the telescope zenith angle position the sodium layer is seen at 90 (zenith) or 160 km (at 50 degrees zenith angle) from the telescope. The wavefront sensor(s) sensing the laser scattered light should be defocused to follow the sodium layer. This defocus of the wavefront sensor becomes very important on ELT as it grows with the telescope diameter and is quadradic with the F-ratio. We believe that an optical design of a zoom up-front each wavefront sensor can be produced to compensate for that effect. However, one issue is the shadowing of the LGS wavefront sensor (s) in the scientific FoV due to the fact that the science focal plane is several meters before the average LGS focal plane – science beam foot-print-. The shadowing is independent of the F-ratio but linear with the telescope diameter. The easiest and may be the only way to overcome this problem is probably to

separate the LGSs and the science optical beams upfront the focal plane with a large sodium dichroic.

Depth of field: Finally, there is a depth of field issue due to the thickness of the sodium layer and the finite depth of focus of the telescope. The telescope might not deliver an image of the sodium layer where the whole layer is in focus. This will introduce a blur of the images of the LGS spot.

Finally, the depth of field issue is also due to the finite thickness of the sodium layer. When imaged through a telescope, the depth of focus might not be large enough compared to the thickness, which will introduce a blur of the images of the LGS spot.

Problem	OWL (100m, F/6)	60m F/15 F/6	30m F/15	8m F/15	Remarks
Spot elongation	13''	7.6''	3.8''	1''	Computed using Eq. 8-6
Spot aberrations	1.5''	0.33''	TBD	Diffraction limited	
LGS Number	7-12 ?	7-10 ?	5-9	5	For ~2' FOV
Fratricide effect	TBD	TBD	TBD	TBD	TBD
Laser defocus (90-160 km)	5.7-2.7 m	12.7-6 m 1.7-0.91 m	TBD	0.164m	
Depth of field of spot	390m	654m	1310m	4910m	Eq. 8-7

Table 8-18: Quantitative evaluation of the known LGS issues versus telescope diameter

8.4.4 Potential solutions to LGS issues

These, and other, possible solutions to LGS issues will be explored in the design phase.

8.4.4.1 Spot Elongation

One solution is the use of dynamic refocusing. In this scheme, a modulated membrane is used to follow the laser pulse as it propagates through the sodium layer. The beam is refocused (by changing the shape of the membrane) as the beam propagates, and therefore the circular shape of the spot is re-established. An experimental demonstration of this concept has already been made (see [112]). More recently, a variation on this scheme has been proposed, where the vibrating membrane and the microlens-array of a Shack-Hartmann WFS is replaced by a micro-mirror. The micro mirror is of piston-tilt type, and moving the mirror creates the sub-aperture and also follows the upgoing laser beam ([113]).

A completely different approach, which partly solves the problem of spot elongation is the design of a custom CCD for the WFS, which has elongated pixels and a radial geometry ([115]). This allows reducing the noise (since the CCD has the shape of the streak). Moreover, one could in principle follow the upward laser propagation by shifting the charges at the proper speed along the direction of the spot elongation, and hence reduce the effect.

8.4.4.2 Spot aberrations

To reduce the effect of the spot aberrations, one could design an optical corrector which acts like a deformable mirror in an AO system. The correction must be variable as a function of the sodium height. The stroke requirements for such a corrector must be investigated for the OWL case.

The concept of virtual wavefront sensor ([125]) permits to reduce, for some ELTs, the aberrations by putting the WFS before most of the optics. Options to implement this will be explored during the optical design iteration at the beginning of Phase B.

A “solution” is to investigate if one can tolerate these errors, i.e. to investigate if high order wavefront sensing is still possible from the aberrated beam and to correct the low order aberrations from a slow framerate natural guide star. In the case of OWL, the aberrations are concentrated in the lowest order modes, and vary at a moderate rate as the height to the sodium layer changes, so this could be a viable solution (see RD1).

8.4.4.3 Fratricide effect

To reduce the fratricide effect, one can increase the number of laser launch telescopes, and chose their location so as to minimize the impact on the WFSs

Pulsed lasers could be used, and different LGSs would be fired at different times. The WFS would then be synchronized so that it only sees the sodium return light and not the Rayleigh plume of any other WFS. In principle, this should work, provided a laser with the appropriate pulse format can be made.

8.4.5 New Laser Guide Star concepts

The subject of new Laser Guide Stars concepts is addressed in the ELT design study -WP 9400 “Novel Adaptive Optics concepts”-. In principle LGSs allow the achievement of full sky coverage, even at visible wavelengths, provided the laser power is sufficiently high to ensure a suitable spatial and temporal sampling of the turbulent layers. On the other hand it is well known that the use of LGSs presents several problems. Some of these are “intrinsic”, like the absolute tilt indetermination. Others, related to the finite distance of the artificial reference source are described in the previous section.

In this section we will introduce alternative wavefront sensing techniques, in order to overcome these problems. Four concepts are studied and are briefly described in the following. The study involves also an experimental validation. The participants of the task are: Durham University, ESO, Galway University, INAF, Lund University, MPIA Heidelberg, Tecnion.

8.4.5.1 Pseudo Infinite Guide Stars

The two main components of a “Pseudo Infinite Guide Stars (PIGS) wavefront sensor” are a mask with radial slits, placed in the focal plane of the telescope, and a reflective rod, placed on the image of the LGS (Figure 8-102). The focal plane mask selects specific angular directions, looking at the LGS rays as if they were coming from infinity (hence the name of the concept) and is sensitive to the radial wavefront aberrations. The reflective rod is optically conjugated to different portions of the LGS along its extension, thus allowing the use of the LGS light without temporal gating techniques; this device is sensitive to the azimuthal wavefront aberrations. The features of the two wavefront sensing devices make this concept well suited to an elongated artificial source at finite distance from the telescope, although the problem of the telescope aberrations has still to be investigated. PIGS is a pupil plane wavefront sensor and may be implemented in layer-oriented mode, using multiple LGSs.

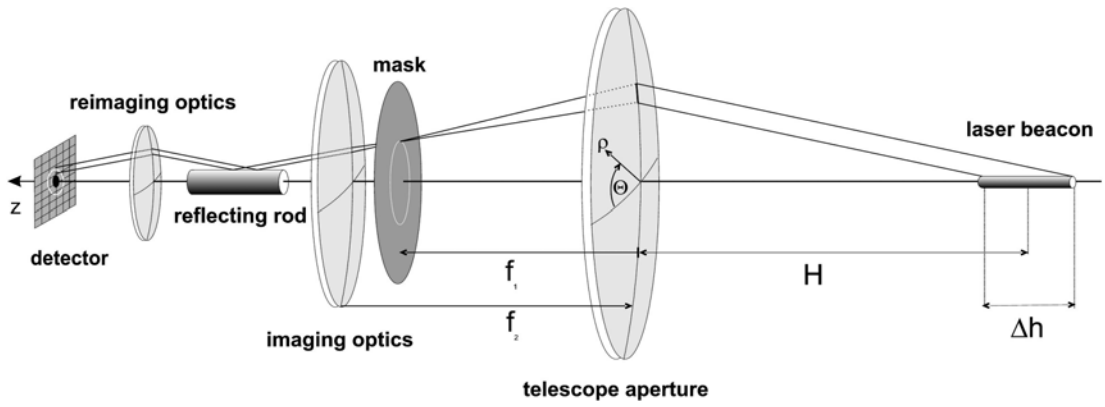

Figure 8-102: Pseudo Infinite Guide Star conceptual layout.

The concept, in particular the azimuthal part, has already been tested with positive results in the laboratory and on sky. Further experimental work is foreseen to test in deeper detail the radial wavefront sensing part and the multiple LGS mode.

8.4.5.2 Sky Projected Laser Array Shack-Hartmann

A Sky Projected Laser Array Shack-Hartmann (SPLASH) wavefront sensor is based on an array of focused laser beams, covering the whole telescope pupil and projected onto the Sodium layer (although the concept could also work with a Rayleigh laser); each beam is launched from an aperture of size comparable to r_0 and therefore the focal anisoplanatism is much reduced (Figure 8-103). This array of focused spots is imaged by the whole telescope and from the measurement of the instantaneous location of each spot it is possible to retrieve the local wavefront tilt, minus the global tilt over the full aperture. The applications of the concept to visible wavelengths seems to be limited by diffraction effects, although some solutions do exist, for instance the time-interleaving of the measurements, and others are under investigation.

The SPLASH concept is a way to measure the turbulence in the upward path. An interesting modifications, called Projected Pupil Plane Pattern, consists in projecting a collimated laser beam through the full telescope aperture and measuring the intensity fluctuations due to the wavefront curvature by taking snapshots at difference distances. In this approach the focal anisoplanatism is reduced thanks to the beam collimation.

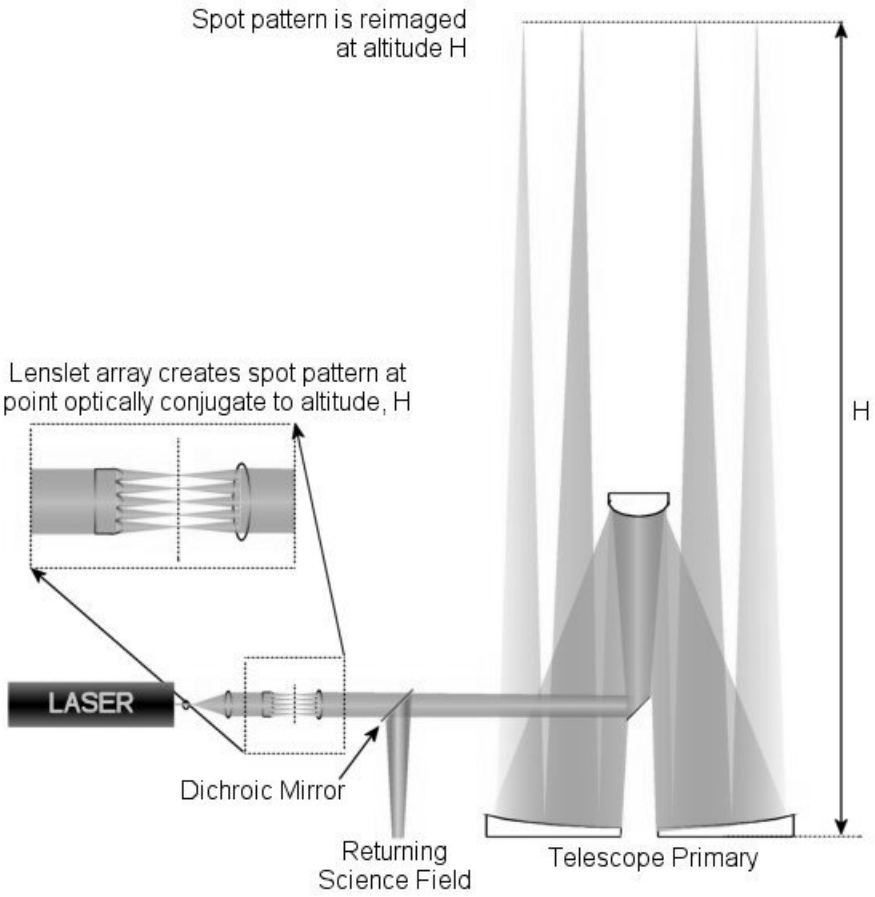

Figure 8-103: Sky-Projected Laser Array Shack-Hartmann conceptual layout.

8.4.5.3 Virtual Wavefront Sensor

The Virtual Wavefront Sensor concept (Figure 8-104) has been conceived in order to solve the LGS re-imaging problems typical of an ELT. It has been initially developed for EURO50 where

the only suitable LGS image is close to the Gregorian focus where the LGS WFS is also placed, responding to the atmosphere and to the shape of the adaptive secondary mirror. The wavefront measurement performed by this sensor (complemented by a NGS sensor to measure the low-order aberrations) does not allow to correct properly the image in the science focus, obtained by re-imaging the Gregorian focus. For this reason, a Test Source WFS is placed in the final image plane, looking at an artificial source placed in the Gregorian focus; this Test Source WFS controls a second deformable mirror placed in the optical train between the Gregorian and the final focus. The signals from the two WFSs (complemented by the NGS WFS mentioned above) are combined into what is properly called “Virtual WFS”, which works to null the virtual residual signal and thus controls both the adaptive secondary mirror and the deformable mirror placed in the post-Gregorian focus optical train.

A laboratory prototype has been set up to validate the concept.

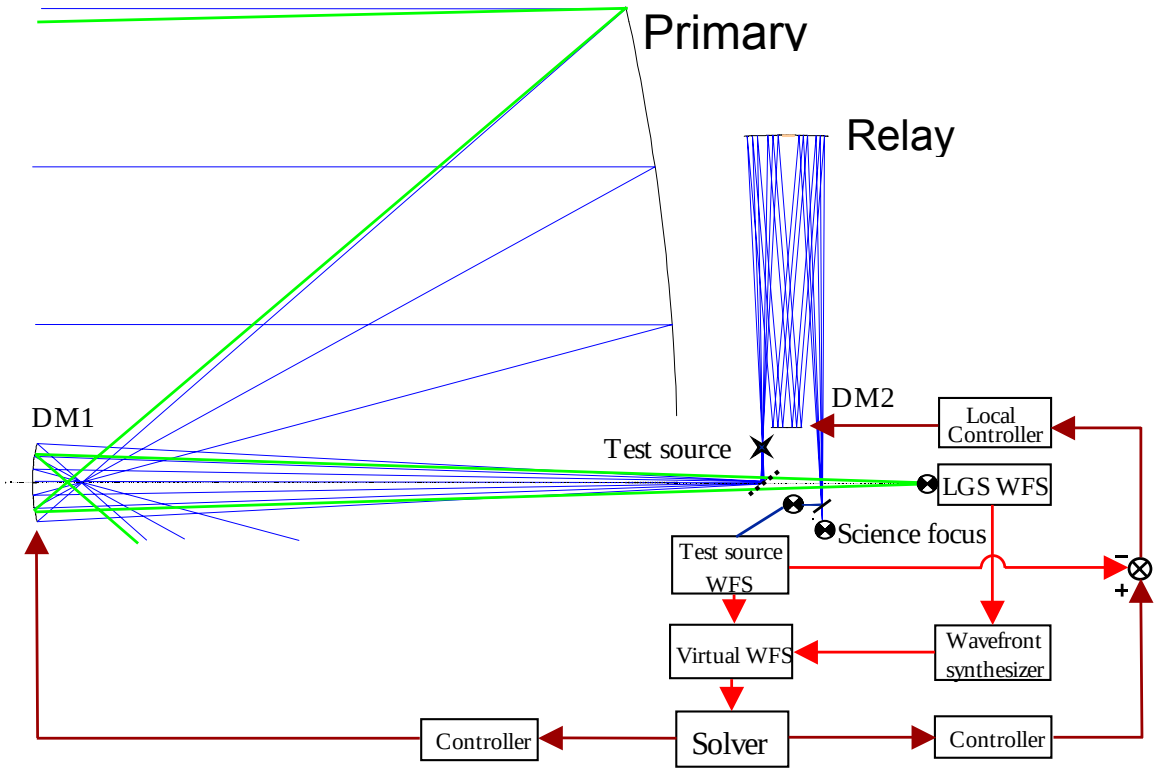

Figure 8-104: Virtual wavefront sensor conceptual layout.

8.4.5.4 Variable Wavefront Sensors

A Variable WFS may be realized by means of acousto-optics cells, devices which can modulate the intensity of a light beam by two orthogonal acoustic standing waves, creating a pattern similar to the one generated by a lenslet array; the lenslet pitch may be changed by simply changing the frequency of the acoustic wave -Figure 8-105-. Such a device may be placed in a pupil plane, realizing a variable Shack-Hartmann WFS. Several acousto-optics devices may be conjugated to the most relevant turbulent layers, realizing a multiple layer WFS (Figure 8-105). As opposed to a conventional Shack-Hartmann WFS, the idea proposed here is to image by each lenslet the whole field of view of interest; the image produced by the lenslet is shifted by the local wavefront tilt (over the lenslet aperture) and all the sources within the field (natural or artificial) contribute to the measurement of the local tilt. The most suited computational method for this kind of data is based on Fourier Transform, which is also less sensitive to spot elongation problems than simple centroid computation. The fact that each lenslet produces an

image of the whole field translates into the requirement of large detector formats and this, in turn, translates into large amount of data to process in real time. However windowing strategies may be implemented, reading only the relevant pixels, which are a small fraction of the total.

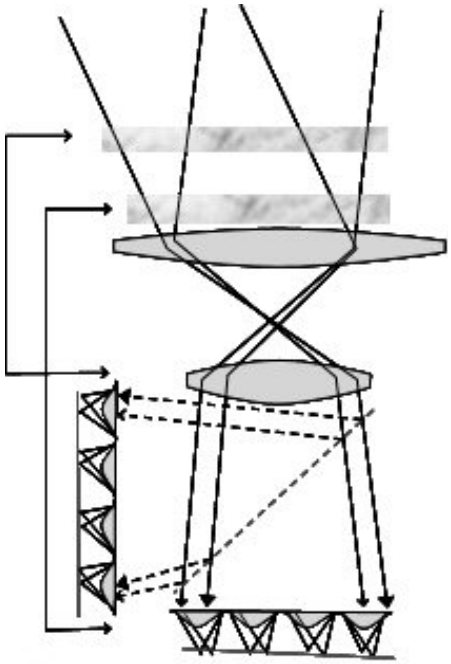

Figure 8-105: Variable wavefront sensor conceptual layout.

8.4.5.5 Laser Guided AO with on-sky phase shifting Interferometry

This method uses the coherent superposition of tilted laser wavefronts over the whole aperture of the telescope as indicated in Figure 8-106. Applying methods of laser phase shifting interferometry (LPSI) one can retrieve a local phase difference that can be used in the adaptive optics system like the gradients retrieved from a usual Hartmann sensor. The details of the proposed scheme are outlined in [103]. Here we summarize the principle and application to an extremely large telescope.

With a laser pulse split in two flat coherent laser wavefronts leaving the telescope- one tilted slightly with respect to the other- an interference pattern is created at any distance. When reaching a certain height in the atmosphere, both waves will have collected local phase changes. Due to the tilt in the wavefront, the path through the atmosphere to the point (x,y,H) of each wave is slightly different. This makes a phase difference occur which modulates the intensity of the interferogram that is written in the sky. With a wavefront camera that is gated at twice the time of flight to the point (x,y,H) the scattered light from this pattern can be imaged with the use of the full telescope aperture.

Using now several laser shots on timescales which are short compared to the coherence time of the atmosphere and applying known phaseshifts between the launched wavefronts, allows to retrieve the atmospheric induced distortions. It should be noted that the large wavefront distortions present in the atmosphere result only in gradients to be probed and choosing the distance *a* smaller than the coherence length r_0 of the atmosphere will avoid phase overlap.

With two beams overlaid, a tilt can be applied in one coordinate direction, though a phase difference -gradient- can be measured along this direction. To retrieve gradients in two coordinates several methods are possible, like overlapping more than two beams or polarization overlapping perpendicular measurements and disentangle the polarization planes at the detector as well.

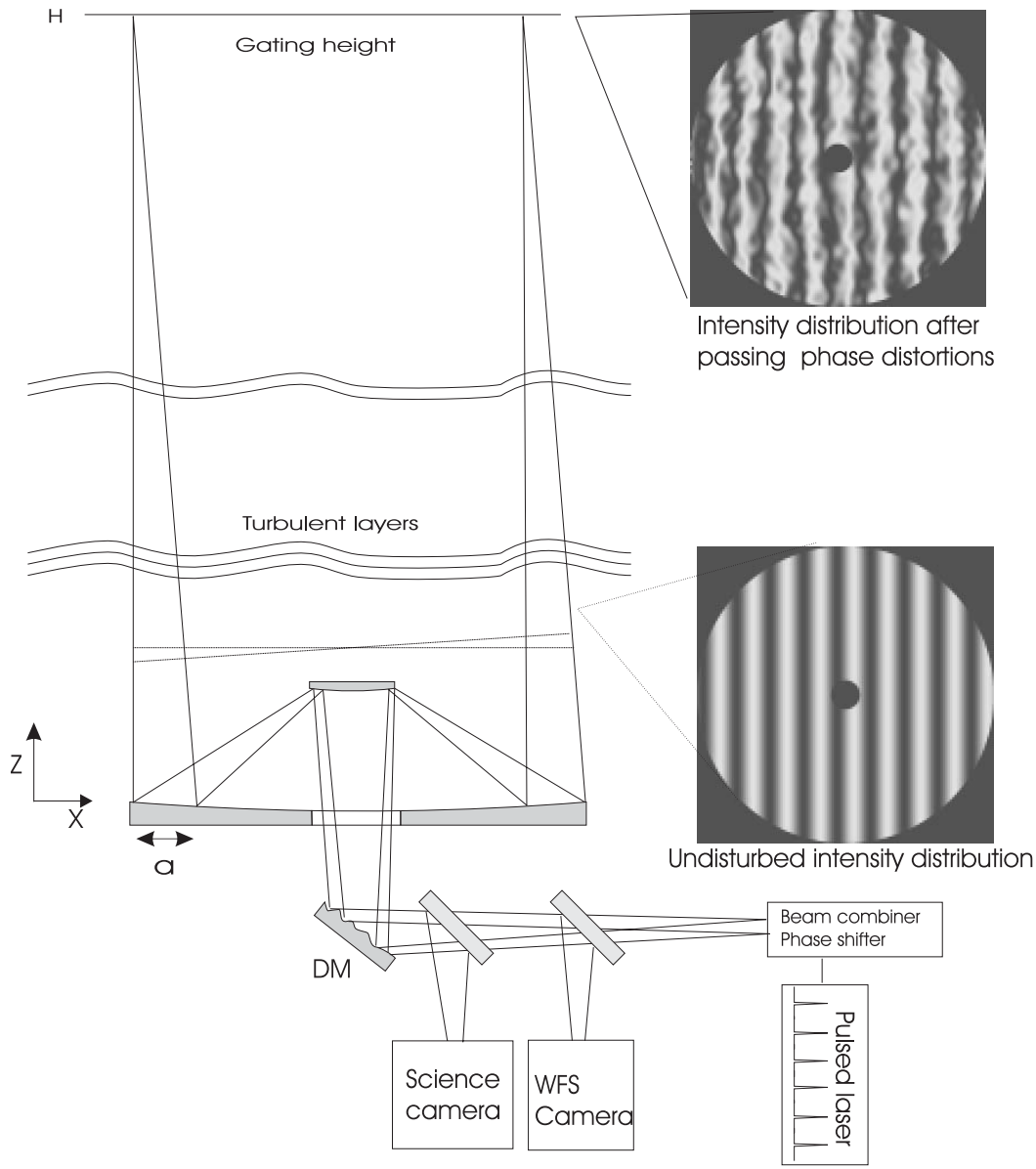

Figure 8-106: Basic principle of measuring atmospheric turbulence with phase shifting interferometry.

The resolution of the sensing can be chosen freely with the amount of tilt added to the beams to adapt to different conditions. Detecting the light scattered from low altitude will result in a ground layer correction. Extending the system to multiple detections at different heights or two beam systems with more deformable mirrors a complete sampling of the turbulent layers in the atmosphere is possible. Therefore high Strehl ratios are reachable and multiconjugate adaptive optics correction with an extended field of view is possible.

The extension of the proposed method to a multiconjugate correction is straightforward and illustrated in Figure 8-107. A first laser beam (consisting of the overlaid coherent wavefronts) is directed over the first deformable mirror to the telescope, expanded and launched over the full aperture as described before. This beam is detected at lower altitude and steers the first deformable mirror in a closed loop scheme. A second laser beam is then injected before that, hits the second DM and then joins the beam path of the first one at a beam splitter. To enable the splitting and separate properly both beams the two lasers could operate at different colors. The second laser is detected then at higher altitude, and DM number two is controlled, independent from loop number one, out of this signal. The type of backscatter which is used can be selected for the individual application. For the lower altitude scattering process Rayleigh scattering is probably a good choice. The upper altitude scatter could be Rayleigh-type as well, or resonance scattering in the earth sodium layer.

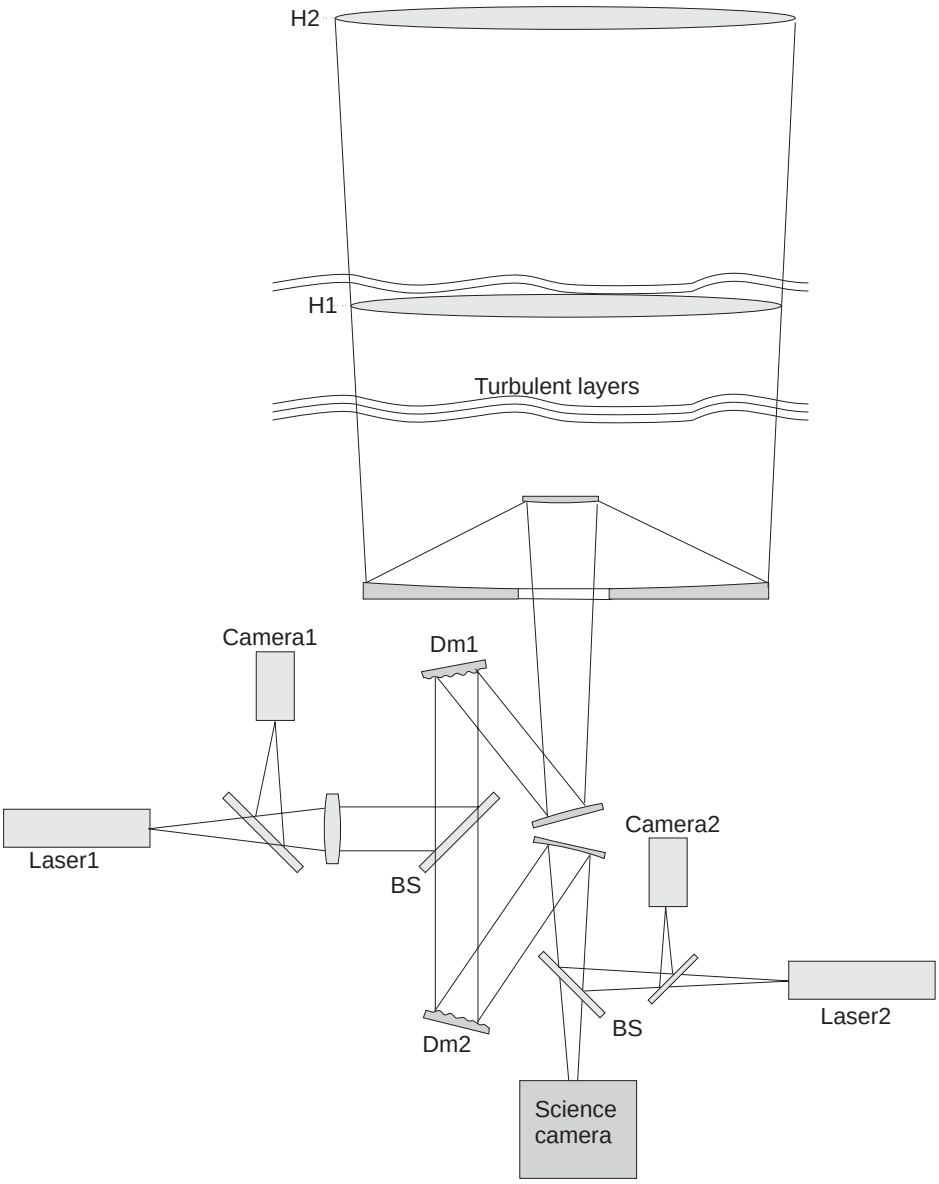

Figure 8-107 Schematic arrangement of a multiconjugate correction with lasers and LPSI.

The requirements for the laser have to be chosen accordingly. In general a pulsed system with 1-5kHz repetition rate and sufficient power to be detected at high signal-to-noise will be necessary. The power demands for the laser will decrease if a dynamical refocusing device is used, as proposed by [128]. Compared to usual guide star systems beam quality issues for the proposed scheme are totally relaxed, due to the full aperture launching of the laser. For Rayleigh scattering green lasers are available today that would fulfill all requirements.

The basic feasibility of the proposed method can be tested in laboratory experiments and on-sky with present day telescopes. The laser launching and detection system would not greatly change with telescope size.

Particular issues like field-of-view in the multiconjugate case, imaging capability of the main telescope for finite objects, stray light suppression onto the science camera or dynamical refocusing devices will be included in a feasibility study.

8.4.6 Strategies of the LGS program for OWL

8.4.6.1 Background

LGS-AO is in a maturing phase, with few systems starting to produce science and optimizing the operations or the subsystems.

ESO itself is placing the first LGS Facility on the UT4 telescope. Much experience has been already gained with the testing and integration in Garching, and will be increased further during integration and operation with AO in Paranal.

An increasing number of AO systems rely already or will rely on laser guide stars as reference sources for AO systems. LGS-AO is used for the visible range correction, at Palomar Observatory and in a number of air-force telescopes in New Mexico and Hawaii.

From the experience matured internationally so far, the following technological developments appear essential and are currently driving the ESO R&D strategy in this field:

- simplify, make possibly cheaper and ruggedize the laser sources at 589nm, to get 10W CW on air (15W CW in the lab), with a keys-on system.
- Propagate the laser beam up to the laser beam Launch Telescopes using single mode fibres, thus preserving the diffraction limited beam, avoiding mechanical vibrations to be transmitted to the beam, and avoiding stray lights in the telescope dome.
- Develop 3 kHz pulsed formats with macropulses of 2-3 microsec for the 589nm lasers
- Explore innovative propagation-sensing schemes, to avoid the focus anisoplanatism and the optical problems related to the imaging of the LGS with OWL.

8.4.6.2 Status and planned tasks

Fibre lasers (Figure 8-108) seem definitely the way to go for the second generation laser sources. Fibre lasers with powers of tens of watts are commercially available, but not at 589nm. We have followed the fibre Raman laser solution in-house at ESO, and collaborated with Lawrence Livermore Nat'l Labs for a sum-frequency fibre laser approach. The in-house activities have brought us to find together with industry a path to produce a fibre Raman laser at 1178nm, which is frequency doubled at 589nm using Periodically Poled non-linear crystals. We have chosen the name AFIRE (Advanced FIbre Raman Emitter).

Figure 8-108: Fiber laser

We are in the breadboarding phase, with ~2W CW at 589nm to be produced this summer, 5 W to be produced by December 2005, and a contract for a finally engineered fibre laser unit to be likely placed by March 2006. This laser will have the size of a 19 inch VME rack, servo-controlled in frequency, and deliver the beam via a single mode fibre right at the launch telescope focal plane.

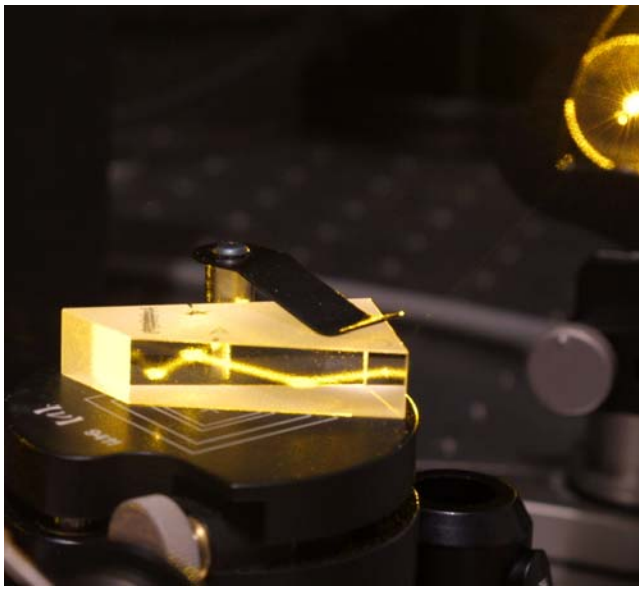

Figure 8-109: CW Raman laser

Since the laser delivers the beam via a single mode fibre, the problem of the laser beam relay disappears. In case of a solid state laser source, the beam has to be relayed. The fibre solution for future systems is Hollow Core Photonics Crystal Fibre Technology (HC-PCF). After the development of solid core PCF, we have started the development of HC-PCF. The throughput achieved with HC-PCF fibres is 1.2 dB/km, for the visible range it is possible to achieve 20 dB/km but the production technology has to be improved. We are placing at the time of this writing the contract with industry for this development, and have in place manpower and lab facilities for the two-year development.

The design of a pulsed format version of the ESO AFIRE laser will be developed via a contract with industry. A first assessment of the feasibility to obtain such a format from AFIRE is very promising.

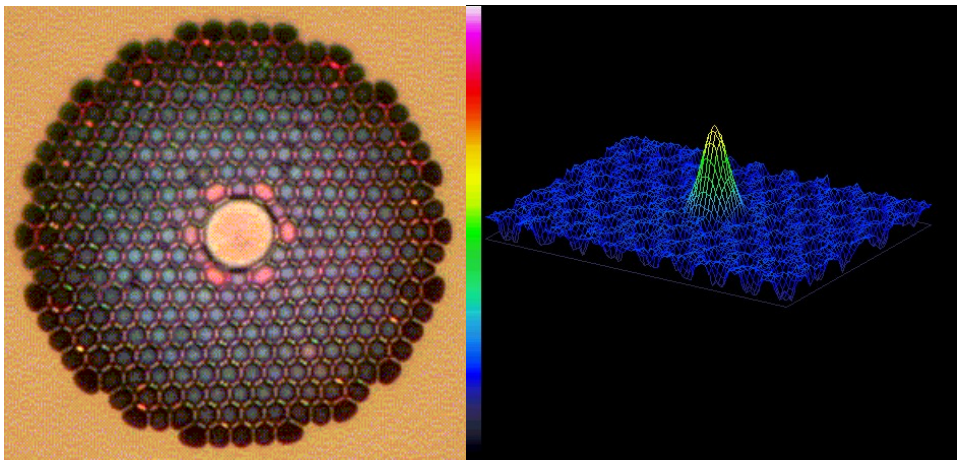

Figure 8-110: Hollow Core Photonic Crystal fibre.

9. Telescope structure and kinematics

The design, fabrication, integration operation and maintenance of the supporting structure of a 100-m class telescope is one of the major challenges of the OWL project. The structure must provide sufficient bandpass for the motion control system as well as the required tracking accuracy and dimensional stability under varying gravity, thermal and wind loads. The achievable limits of structural eigen-frequencies impose that image stabilisation be implemented downstream in the optical train.

The mechanical structure shall be seen as a "*skeleton*", which supports all the sub-systems of the telescope. The demonstration of its feasibility is therefore one of the major steps to be performed during the first phase of the project.

9.1 Design Principles

In order to have a coherent development of the telescope structure design, a set of design principles has been defined at a very early stage of the project.

Table 9-1 summarizes these design principles and it is a design tool, which helps to evaluate and control the most significant parameters involved on the project, to evaluate quickly new ideas and criticisms.

Domain	Problems	Guideline / remedy
Environment (Site)	Earthquakes. Wind. Solar radiation. Dust. Rain, Snow and Fog. Overall dimensions. Access roads.	Maximise the stiffness Minimise the wind-exposed area. Wind shield. Covers. Reduce solar absorption on exposed surfaces. Dust rejecting concept. Enclosure. Minimise the overall dimensions of the complete observatory.
Subsystems	Optical elements. Optical path. Re-centering system. Control. Passive Damping.	Integrated design, definition for each sub-system: Location. Volume. Mass.

Domain	Problems	Guideline / remedy
	Thermal Control. Drives. Auxiliary drives. Bearings. Cabling and Piping. Mirror covers. Cleaning units. Mirror handling. Instrument handling. Human access. Metrology system.	Supplies
Structural Parts Material	Dimensional instability Dynamic and static performances. Thermal expansion. Affordability.	Minimise the stresses (microyield strength) Run in. Differentiated parking positions. Specific modulus Mild Steel Composites
Large Optics Material	Suitability (polishable, etc) Dimensional stability. Homogeneity Thermal expansion. Dynamic and static performances due to the mass. Affordability.	Zerodur SiC
Control.	Friction disturbance. Wind load disturbance. Cross talk. Gravity. Thermal.	Minimise the friction Maximise the stiffness. Drives. Bearings. Wind screen. Passive damping.
Thermal Control	Solar Radiation Energy consumption. Thermal inertia.	Covers, Shields, Sliding or deployable enclosures,. Surface treatment. “Inner flow`” cooling system.
Fabrication	Affordability	Material choice Modular design. Mechanical tolerances. Commercial available parts. Maximise the number of potential Contractors. Minimise the gap between Design Phase and Fabrication Phase
Transportability	Oversized pieces. Access to the site Affordability	Modular design Max 2,4 m x 2,4m x 6 or 12m Max 20 Tons Fabrication on site
Assembly on site	Hoisting facilities Alignment. Safety.	Modular Design. Minimise the mass of each part. Self-machining structure. Self-supporting structure.
Operation	Sky coverage Change of modes. Energy consumption. Manpower resources. Safety.	± 60 degrees from zenith. Minimise the time between: Stand by mode. Operation mode Safety mode. Low mass.

Domain	Problems	Guideline / remedy
		High number of automatism.
Maintenance	Technical Down time. Manpower resources. Accessibility Large Optics handling Instrumentation. Cleaning. Safety.	Altitude rotation ± 90 degrees from zenith. Handling facilities. Cleaning facilities. Parking positions. Component standardisation.

Table 9-1: Design guidelines

9.2 Design Assumption

As per today the OWL site is not selected yet. Therefore the design has evolved based on the following design assumptions, which correspond to average environmental conditions typical of Astronomical Observatories around the world.

- Soil characteristic, value range:
  - Paranal 50000 MPa.
  - La Palma 5000 MPa.
- Existing infrastructures within reasonable distance.
  - Harbor.
  - Roads.
- Seismicity 0,2 g, intermediate value between:
  - Paranal 0,34 g
  - La Palma 0,06 g.
- Wind, observation mode.
  - 10 m/s.

9.3 Design Evolution

During the evolution of OWL optomechanical concept design, which started in 1997, some key parameters have been monitored. These values give an indication of the achieved design improvements. The total rotating mass (see Figure 9-2) of the telescope supplies an indirect estimation of the telescope costs and the locked rotor frequency (see Figure 9-1) gives a direct indication of how well the telescope will performe and how complex the various sub systems of the telescope have to be.

- Low rotating mass, implying low cost;
- High locked rotor frequency, implying good dynamic and static performance, lower complexity of sub-systems and eventually low costs;

From the early design phases the optical and mechanical design evolved in a synergetic manner. And the level of details modelled in the FE also evolved considerably. Because of

these reasons, the various design concepts cannot be compared exactly one to one. Nevertheless a clear trend can be deduced throughout all the designs.

- Decrease of the M1-M2 de-space.
- Decrease of the M2 size.
- Decrease of the stability tolerance of M2.
- Decrease of the total rotating mass.
- Increase of dynamic performance.
- Increase the level of details of the subsystems.
- Increase the level of details embedded into the concepts for manufacturing, transport, integration, operation, maintenance and safety.

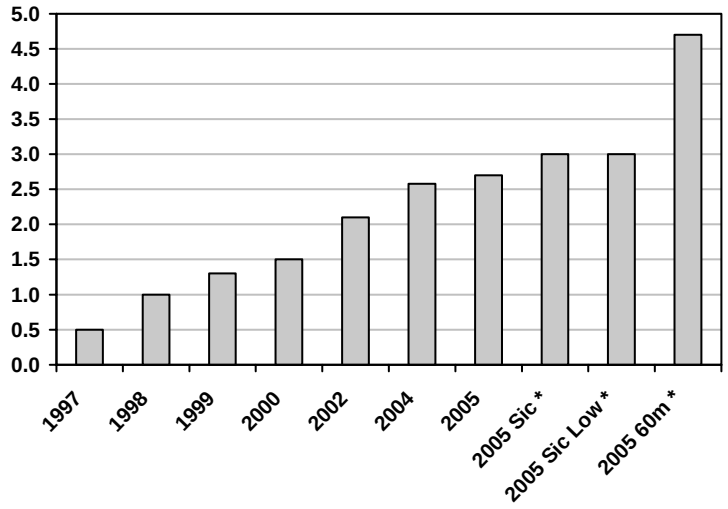

Figure 9-1: locked rotor mode evolution

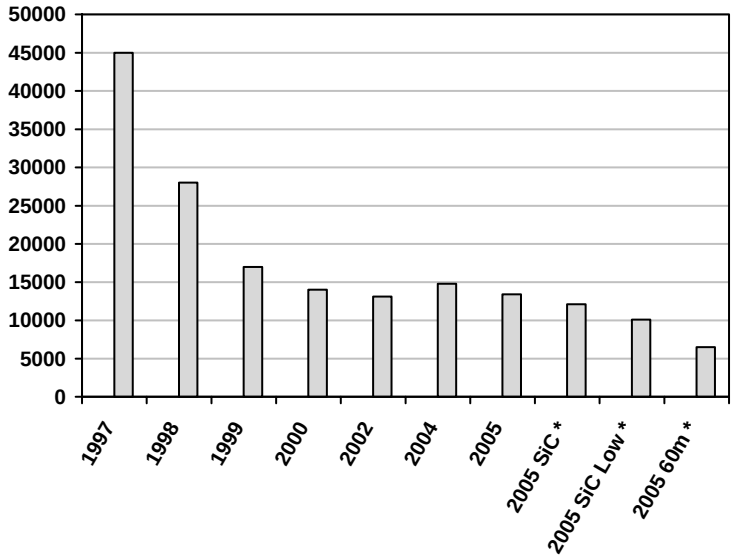

Figure 9-2: Rotating Mass evolution.

All the design concepts described in the following sections are based on:

- 6 mirrors optical design.
- Glass ceramic mirror substrate.
- Mild Steel for mechanical structural parts.

Figure 9-1 and Figure 9-2 summarize the design evolution. The 2005 designs are discussed in section 9.4.onwards.

9.3.1 1997 Design

Two optomechanical concepts (see Figure 9-3 and Figure 9-4) developed in 1997 and presented in [10].

Major Characterisitcs:

- The M1 – M2 de-space was 120 m
- The rotating mass 45000 tons.
- The Locked rotor frequency 0,5 Hz
- Only the altitude structure was modelled and analysed.

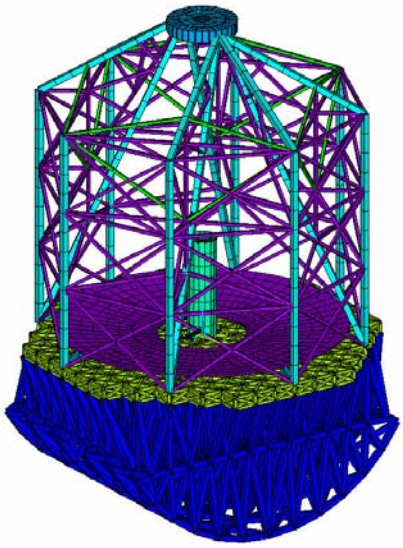

Figure 9-3: 1997 design, rocking chair design I.

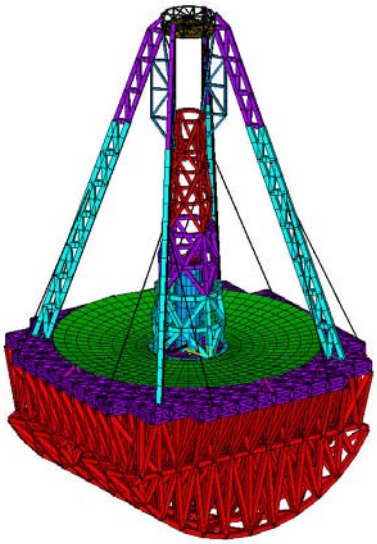

Figure 9-4: 1997 design, rocking chair design II.

9.3.2 1998 Design

The opto-mechanical concepts developed in 1998 (see Figure 9-5). Modular design was introduced, allowing to build up the complete telescope structure using the same basic modules. With subsequent designs this concept evolved towards a high level of standardization of parts. This was a major step forward in reducing the costs of the mechanics.

In the 1998 design, the aperture was divided in four sections, creating a larger primary mirror and leaving design volume for the mechanics around the four mirror petals.

Primary mirror cover and maintenance concepts integrated into the opto-mechanical design.

Major Characterisitcs:

- M1 – M2 de-space 150 m
- Primary mirror diameter 150 m
- Rotating mass 28000 tons.
- Locked rotor frequency 1 Hz
- Only the altitude structure was modelled and analysed.

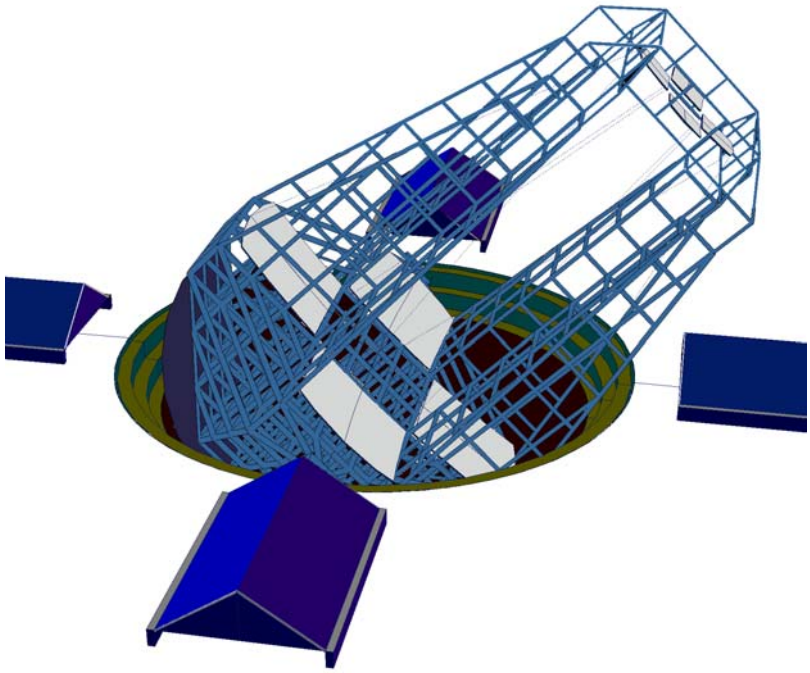

Figure 9-5: 1998 design. Four petals design.

9.3.3 1999 Design

Three optomechanical concepts developed in 1999 and were presented in [32]. These 3 concepts explored different configurations based on modular design principle set in 1998. A detailed Design guideline has been established in 1999, which provided a design strategy for the future evolution of the concept.

Concept 1: Attempt to decouple the secondary mirror from the rest of the optical elements (see Figure 9-6). The poor dynamic performance of the arch structure, indicated that this structural concept cannot deliver sufficient stability for adequate tracking accuracy.

Concept 2: Altitude structure rotating on 3 cradles (see Figure 9-7).

Concept 3: altitude structure rotating on one cradle and two altitude bearings (see Figure 9-8). The altitude cradle supplied the housing for the altitude drive. This concept delivered the best results in terms of rotating mass and dynamic performance. It also included design provisions for manufacturing, transport, integration, operation, and maintenance. Design aspects related to safety issues present during the whole life of the telescope were evaluated and provisions implemented into the concept.

Major Characterisitcs:

- M1 – M2 de-space 120 m
- Primary mirror diameter 100 m
- Rotating mass 16800 tons.
- Locked rotor frequency 1.35 Hz.
- Telescope altitude structure has a four fold symmetry along the altitude and drive axes.
- Only the altitude structure was modelled and analysed.

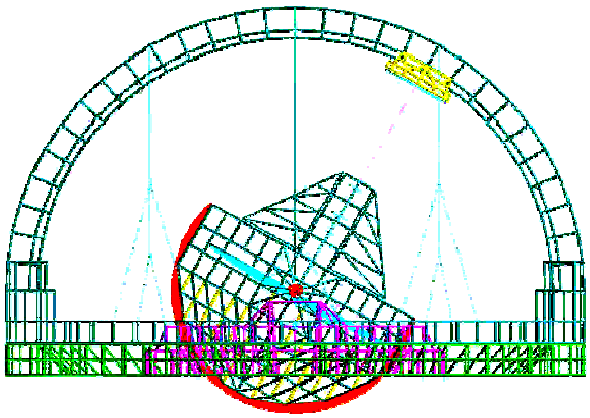

Figure 9-6: 1999 design I. Decoupled M2 unit.

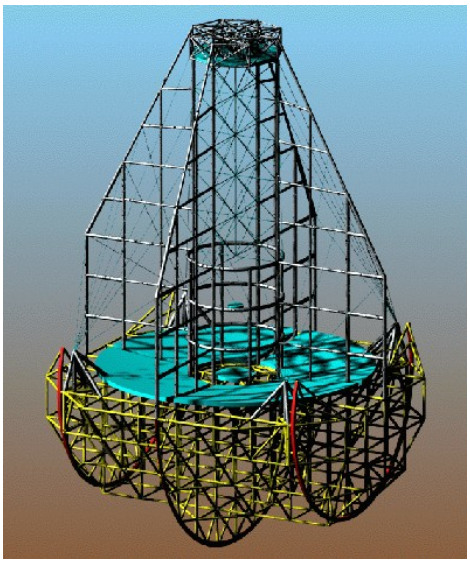

Figure 9-7: 1999 design II. Light rocking chair design.

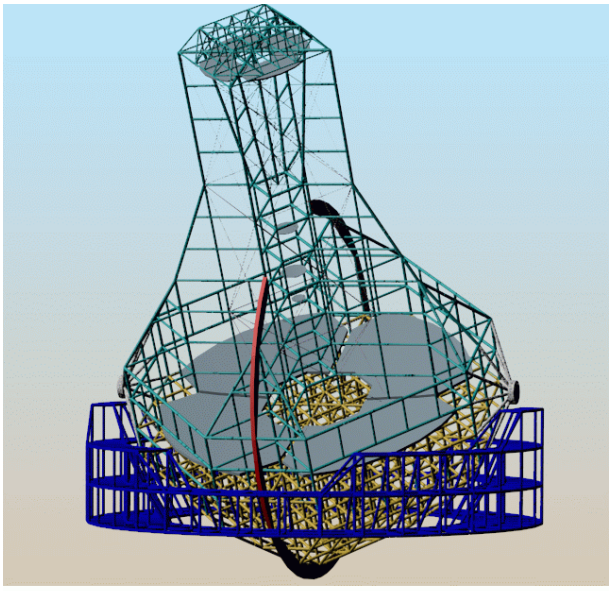

Figure 9-8: 1999 design III. Cradle and bearings design.

9.3.4 2000 Design

Optomechanical concepts developed in 2000 (see Figure 9-9) and were presented in [33]. A major optical design iteration reduced the M1-M2 de-space from 120m to 95 m. Major operation and maintenance operations have been analysed. Several design assumptions have been investigated and traded off: Iso static configuration, hyperstatic configuration, SiC substrate.

Major Characterisitcs:

- M1 – M2 de-space 95 m
- Primary mirror diameter 100 m
- The rotating mass 14500 tons.
- Locked rotor frequency 1.55 Hz
- Both altitude and azimuth structure were modelled and analysed.

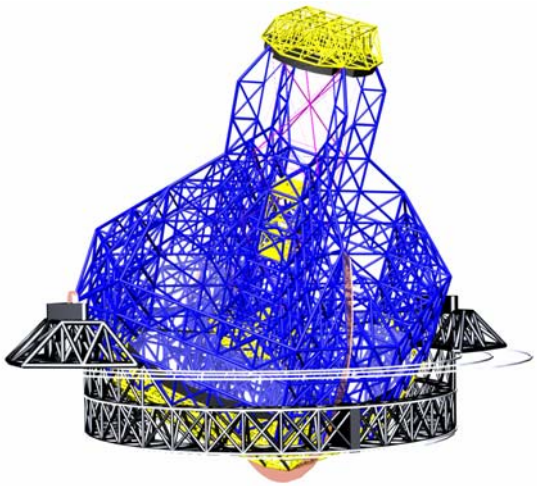

Figure 9-9: 2000 design. Cradle and bearings design evolution.

9.3.5 2002 Design

Optomechanical concepts developed in 2002 (see Figure 9-10) and were presented in [30], [31]. Further structure optimisation and performance improvement were achieved. Detail trade off of the main axes bearing and drive system with related cost analyses took place, as well as a first study on wind loading. Start feasibility and costs verification with industries, external engineering offices, and institutes.

Major Characterisitcs:

- M1 – M2 de-space 95 m
- Primary mirror diameter 100 m
- Rotating mass 13100 tons.
- Locked rotor frequency 2.1 Hz
- Drive and bearing systems trade-off.
- Friction drive and bogies base line.
- Foundation analyses

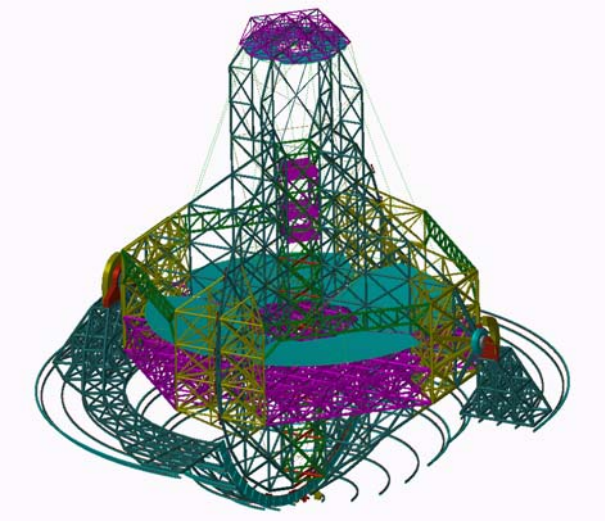

Figure 9-10: 2002 design. Cradle and bearings design evolution.

9.3.6 2004 Design

Opto-mechanical concepts developed in 2004 (see Figure 9-11) and were presented in [29]. Complete redesign of the mechanical structure based on “fractal” design derived from the mirror segment geometry.

Major Characterisitcs:

- M1 – M2 de-space 95 m
- Primary mirror diameter 100 m
- Secondary mirror diameter reduced to 25,6 m.
- Rotating mass 14800 tons.

  Increase of mass due to the higher altitude axis from the ground level and 500 tons for auxiliary equipments.
- Locked rotor frequency 2.6 Hz
- Friction drive and bogies were modelled and analysed.

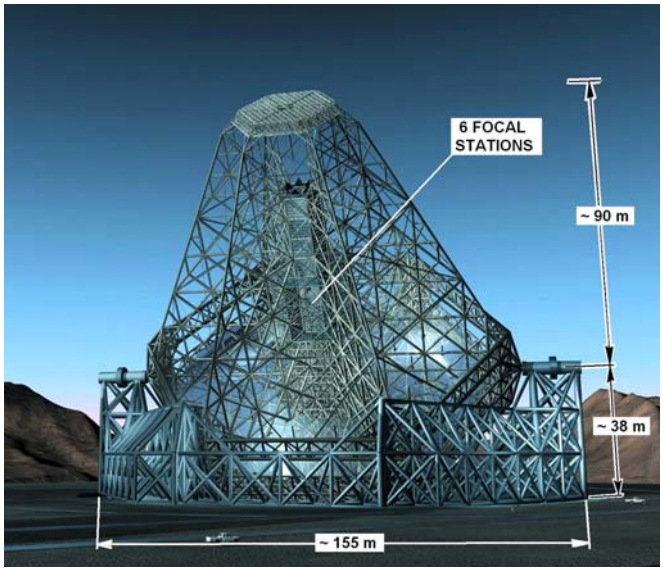

Figure 9-11: 2004 design. Fractal design.

9.3.7 2005 Design (current baseline).

The 2005 design is an improved version of the 2004 design. It differs only slightly from the 2004 version (see also section 9.6.1). Most significant changes are:

- Reduction of the rotating mass. Due to further optimization.
- Increase of Static and dynamic performance. Due to improved constrains of the altitude cradles. This is particular beneficial to the eigen-mode parallel to the altitude axis.
- Axial friction drives and bearings only for the azimuth axis. Dedicated analyses demonstrate that the radial friction drives and bearings do not contribute to the dynamic performance of the telescope. This design generates a substantial reduction of complexity and costs.

9.4 Conceptual Design.

Figure 9-12 and Figure 9-13 show the current design, and the overall dimensions of OWL alt-azimuth conceptual design.

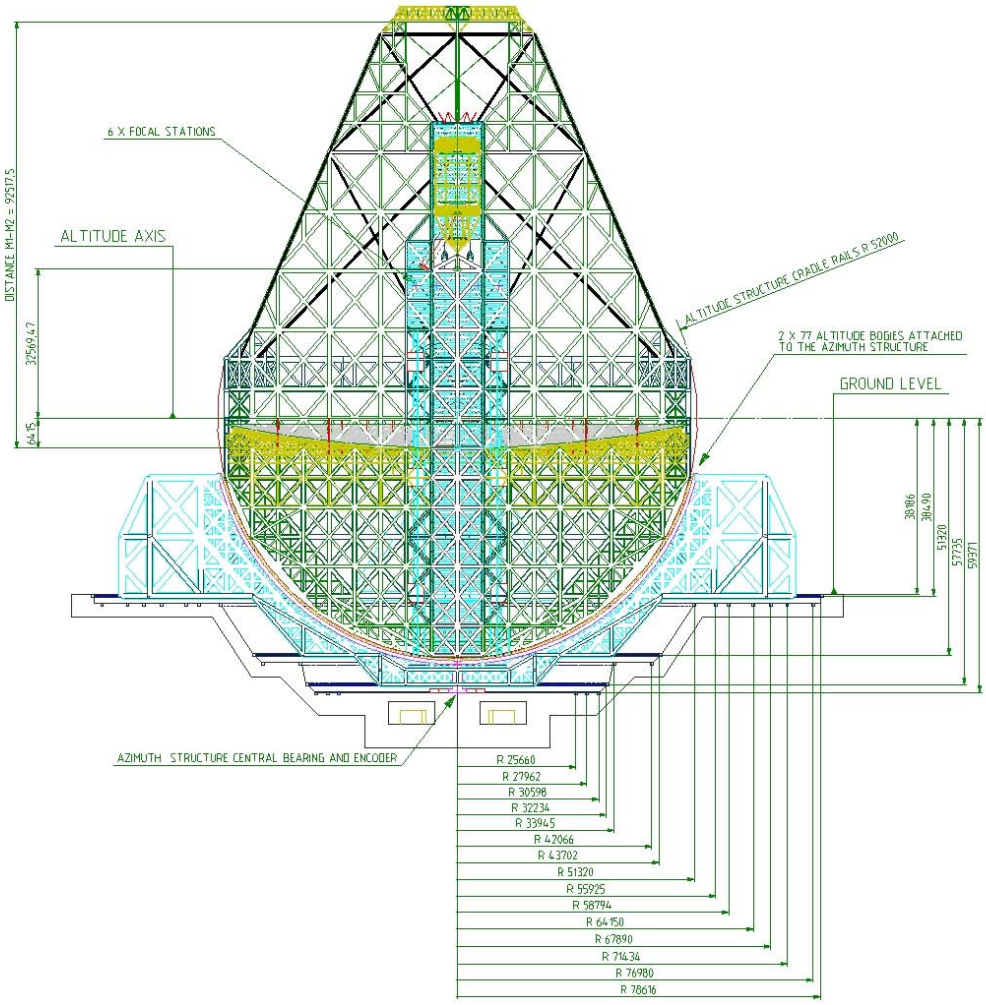

Figure 9-12: OWL telescope structure. Side view.

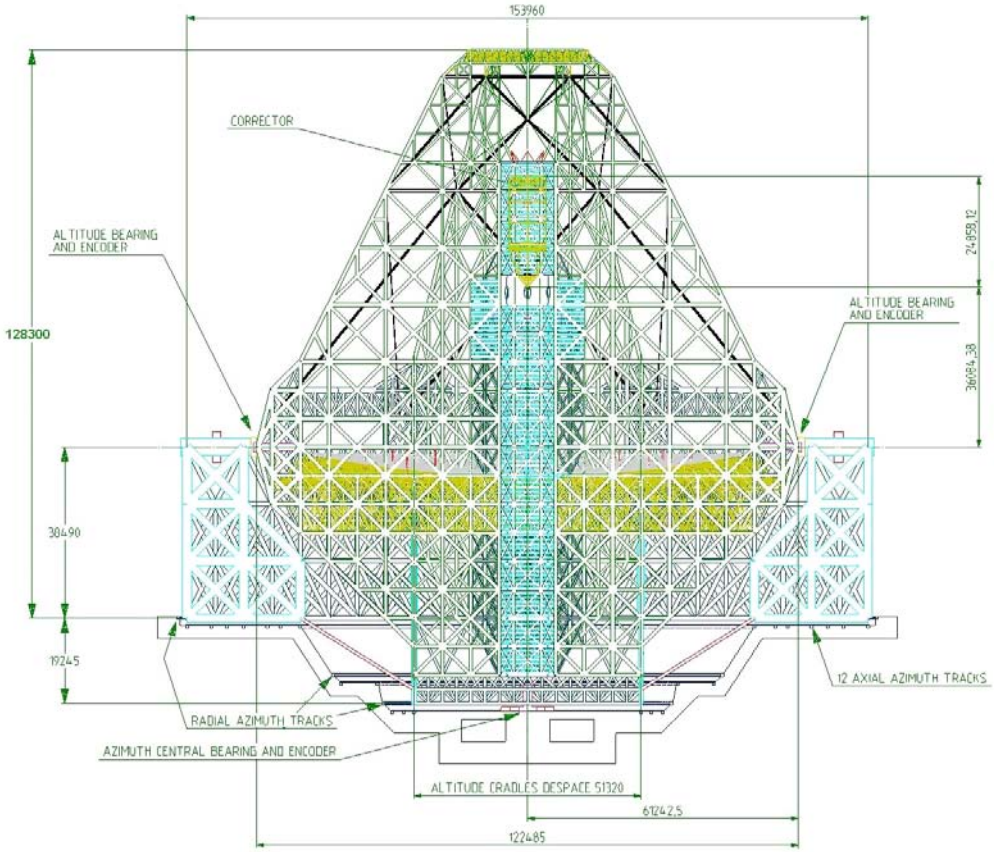

Figure 9-13: OWL telescope structure. Side view.

9.4.1 Structural design

9.4.1.1 Material selection

The following materials have been chosen for the structural part of the telescope:

- St 37 for the part with low-mid stresses.
- St 52 for part with higher stress (See RD29, RD30, RD31 and RD32)
- Kevlar 149 for ropes applications.

The choice of using mild steel for structural part fulfils the following criteria:

- Proven technology: Steel welding and machining technologies are well understood and do not represent risk areas.
- Availability of material: Material can be procured in large quantities at low cost. (See RD29)
- Availability of Contractors: Industries operating in steel construction are numerous and widespread. This will generate fair competition among potential suppliers, assuring low costs.
- Formability: Steel structure can be retrofitted or repaired at low cost. Thus assuring flexibility of adding or modifying sub systems during the telescope operational life.
- Analysis accuracy: Analyses of steel structures are well understood and highly predictable. Thus assuring a good optimization of the telescope structure and minimise risks associated to safety during construction and during the whole telescope operational life.
- Good specific strength / specific stiffness ratio: While the specific stiffness remains one of the most important parameter in the telescope structure design, the magnitude of stresses

is not anymore negligible and the specific strength becomes also a major design parameter (see Figure 9-14).

- Good cost / performance ratio:

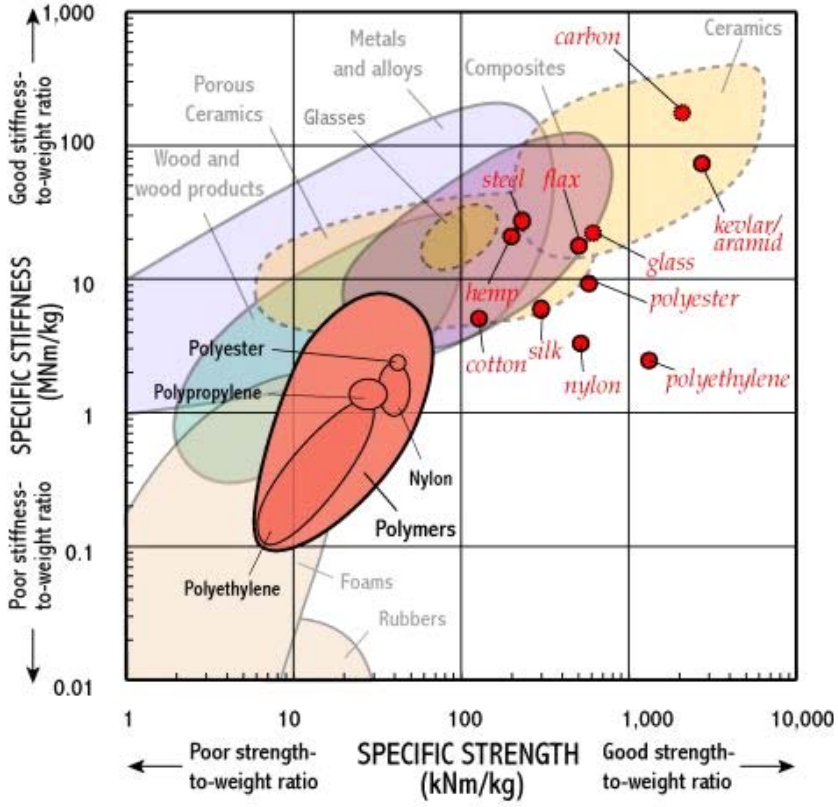

Figure 9-14: Structural materials stiffness and strength.

In the baseline design, composite material are only used for ropes applications (see section 9.4.4.2). Nevertheless designs options, which adopt partially composite material instead of steel, have been investigates and reported in section 9.5.

9.4.1.2 Structural element selection

The large majority of the mechanical structure elements are made from mild steel cylindrical pipes. The choice of using cylindrical pipes for structural part fulfils the following main criteria:

- Availability in large number of sizes and wall thickness. This makes an effective optimization of the structure.
- Formability, the pipes can be machined, welded and integrated in large structure at low cost. (See RD29)
- Cylindrical external surface offer less surfaces prone to dust deposition and make cleaning operation easier (see Figure 9-15).
- Smooth stress transition on the nodes.
- No sharp edges.
- Best wind drag coefficient
- Large external surface versus wall thickness. Low thermal inertia.
- Possibility of inner ventilation.

Figure 9-15: Typical welded node.

9.4.2 Fractal Design

From 2004 onward a so-called *Fractal Design* has been adopted for the telescope mechanical structure. This design is based on a six fold symmetry of the primary and secondary mirrors segments (see Figure 9-16). Each part of the telescope structure is a scaled down or scaled up replica of the mirror segment pattern. Similar to many “Natural fractals” like trees, clouds, ice crystal, rocks, etc. the OWL’s Fractal Design turned out to be very efficient and uses the structural material in the most economical manner. The main advantages of this design approach and fabrications are:

- Standardisation of parts.
- Homogeneous distribution of load in the structure.
- Even load transfer from the optical element to foundation.
- Low mass and high static and dynamic performance.
- Simplicity in manufacturing transport and site assembly.

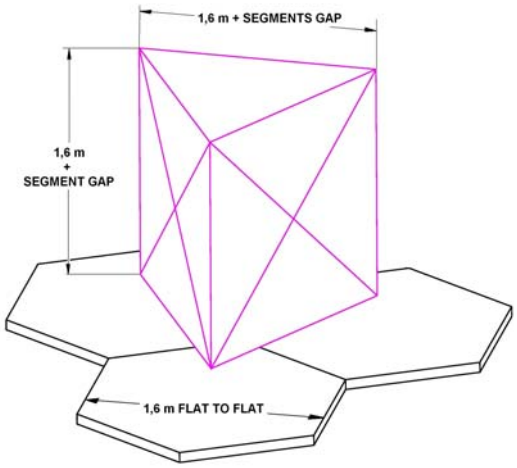

Figure 9-16: Base Fractal pattern.

9.4.2.1 Base module

From the segment hexagonal pattern, a base module has been derived (see Figure 9-17). It is made by cylindrical pipes which form a trusses structure. At the intersection of 2 or more pipes, standard nodes are realized using a minimum of different parts. Figure 9-18 shows the most complex node which is built up using only 3 different parts. Therefore the complete OWL mechanical structure can be assembled using the fairly simple base module geometry, or its integer equivalents.

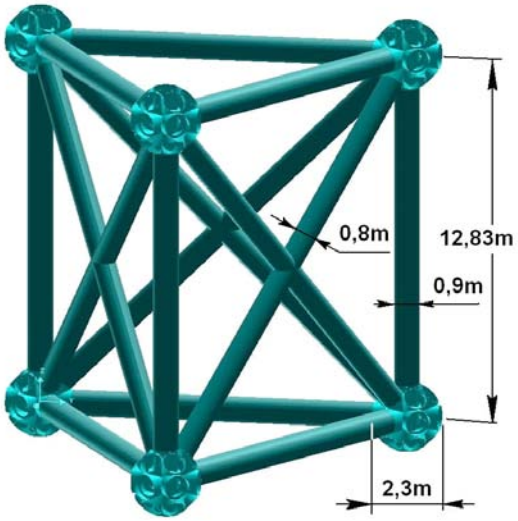

Figure 9-17: Base Module.

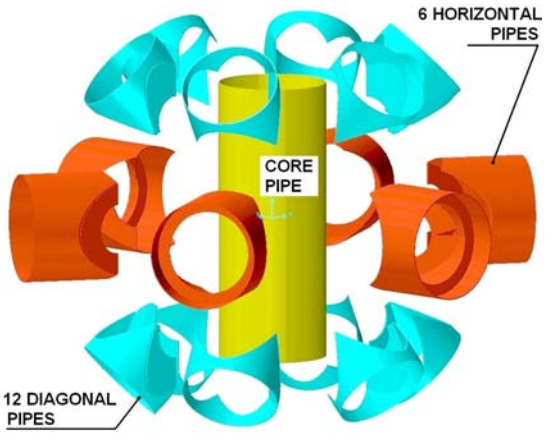

Figure 9-18: Node exploded view

9.4.3 Azimuth Structure.

The azimuth structure shown in Figure 9-19, is a steel trusses structure which copies the mirror segment hexagonal pattern. The trusses are made of cylindrical pipes.

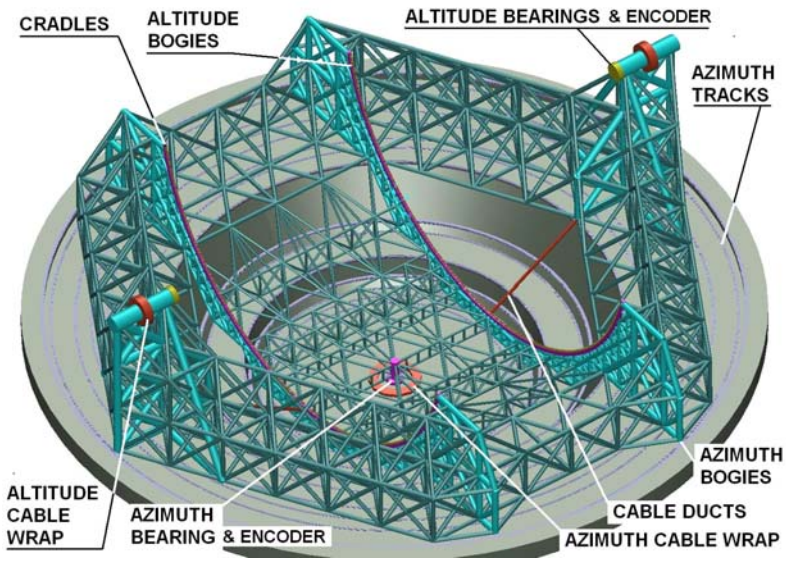

Figure 9-19: Azimuth Structure

Its major characteristics are:

- It is partially embedded in to the concrete foundation.
- One azimuth roller bearing, which constrains 3 translations DoF, defines the telescope azimuth axis and an absolute rotary encoder supply the position signal of the azimuth structure. The central bearing gives the absolute “X-Y-Z” reference to the azimuth structure
- The telescope altitude axis, at a height of about 38 m from the ground level, is defined by two roller bearing which constrain 3 translations DoF. Two absolute rotary encoders supply the position signal of the altitude structure.

- The azimuth rotation is realized by means of friction drives and bearings (azimuth bogies) which are attached to the azimuth structure and run on annular tracks embedded in the foundation.
- Two cradles supply the supporting structure for the altitude bogies.
- One azimuth cable wrap brings the fluid and electrical supplies and control signals from the technical rooms (shown in Figure 9-20) to the azimuth structure. Two altitude cable wraps further lead these supplies to the sub-systems located in the altitude structure.

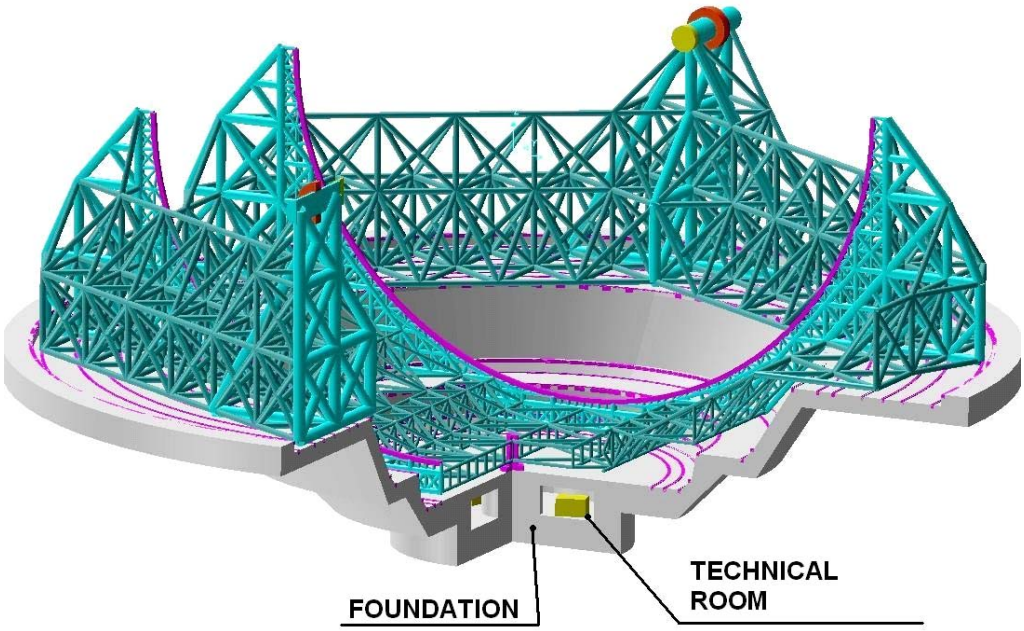

Figure 9-20: Azimuth structure and foundation interface

9.4.4 Altitude Structure.

The altitude structure shown in Figure 9-21, is a steel trusses structure with the same six-fold symmetry as the mirrors. The trusses are made of cylindrical pipes.

Its major characteristics are:

- It hosts all the optical elements.
- It has six focal stations.
- Supplies all the lift and access facilities to the optical elements.
- It supplies thermally insulated and clean environments for the optical elements and instrumentations.
- The altitude rotation is realized by altitude bogies, attached to the azimuth structure and running on the two altitude cradles.
- The telescope altitude axis is defined by two roller bearings which constrain 3 translations Degrees of Freedom (DoF). Two absolute rotary encoders supply the position signal of the altitude structure.

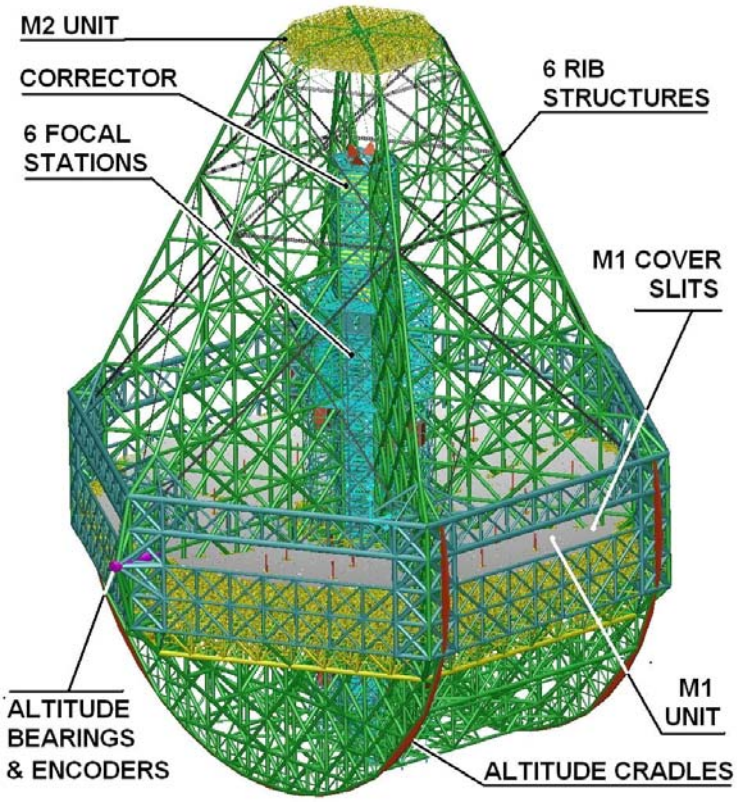

Figure 9-21: Altitude Structure

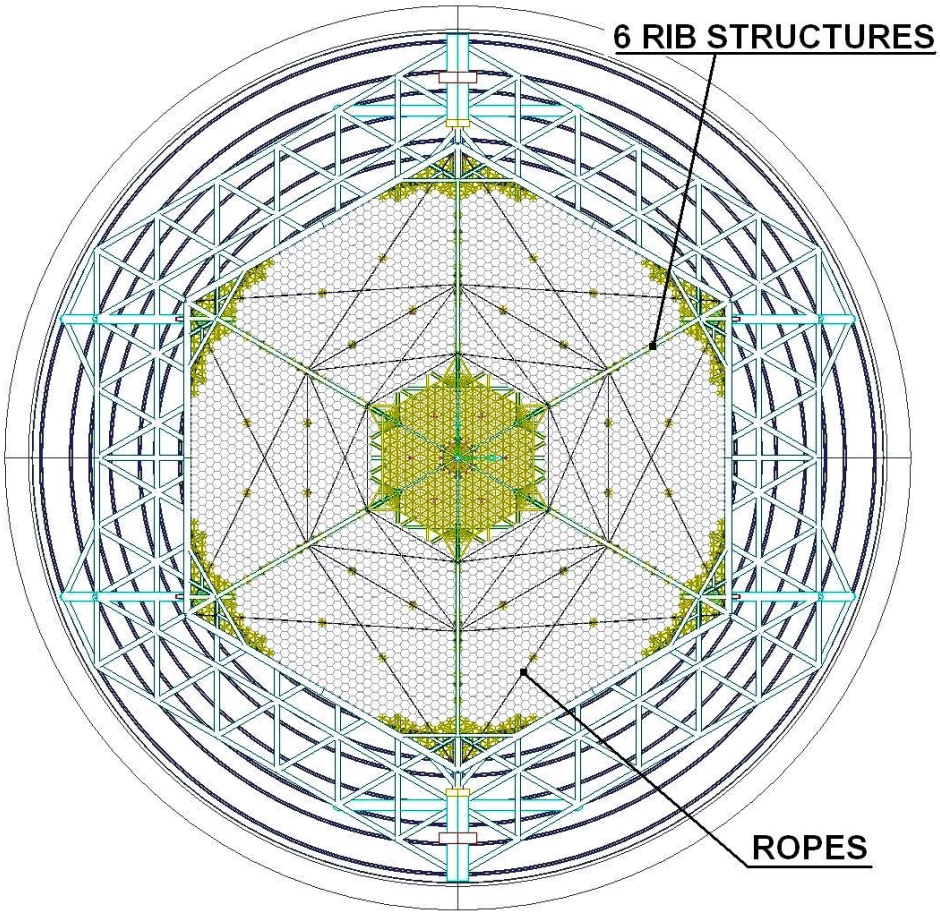

Figure 9-22: Top view

9.4.4.1 Primary mirror obscuration

The light from the sky is obscured (see Figure 9-22) by the following parts:

- 6 Ribs structures. These structures connect the secondary mirror unit to the lower parts of the altitude structure where the kinematics is located. The maximum section across the light beams is about 900 mm. The Primary mirror obscured area by the 6 ribs structure is about 410 m^2.
- Torsion ropes constrain the rotation DoF of the secondary mirror unit along its optical axis. The area obscured by the torsion ropes is about 70 m^2

9.4.4.2 Structural ropes

The altitude mechanical structure made of steel pipe elements can constrain 5 Degrees of Freedom (DoF) of the secondary mirror. The DoF around its optical axis θz is constrained by a set of ropes, which are placed in rows parallel to the incoming light beam from the sky (see Figure 9-23). Thus the optical obscuration is minimized (see also appendix A-1.4).

Major Functions:

- Stabilize the rotation DoF of the secondary mirror.
- Stabilize slender structural elements located in the upper part of the Altitude Structure.
- Increase global mode frequencies of the upper part of the Altitude Structure.

It shall be noted that, the structural ropes are not essential for static or quasi static survival load cases (with exception of Maximum Likley Earthquake (MLE). The telescope does not collapse if complete rope sets are missing (e.g. Up-grades or maintenance). However the telescope will not have sufficient stiffness to meet performance requirements.

The most important criterion is stiffness in tension. Because it is important that the telescope does not flex too greatly under strong winds or during the rotation of the altitude structure, the stiffness (Young's modulus) must be high. In addition, the weight of the ropes themselves is also important. For this reason a specific stiffness - specific strength chart (see Figure 9-14) is useful for identifying suitable materials - the chart shows a selection of materials available as fibres.

Until recently steel cables have been used for tensioning type applications. Steel wire can have a very high tensile strength, but it is quite heavy. Recently very high specific stiffness and strengths have been obtained with synthetic fibres. These are now used in suspension bridges and made by incorporating fibres into a matrix to form a composite bundle. This is then twisted with others to form a rope. Similar solutions could be adopted for OWL tensioning ropes.

Essential rope properties are listed below:

- Creep properties (the gradual extension over time under a tensile load). The dimensional stability of the ropes over time minimizes the need of resetting the tensioning forces.
- Internal damping properties shall absorb vibrations generated by wind disturbance or by the telescope drives.
- Fatigue resistance to cyclic tension due to wind disturbance and gravity changes during the altitude structure rotations.

The OWL rope system will be integrated in a mechanical structure made of mild steel. Therefore the following critical problems shall be solved by the rope system:

- Matching of differential thermal expansion.
- Tensioning forces calibration and control.

Therefore the structural rope system consists of:

1. Ropes.
2. Thermal compensation and tension control devices.

3. Mechanical interfaces (see Figure 9-24).

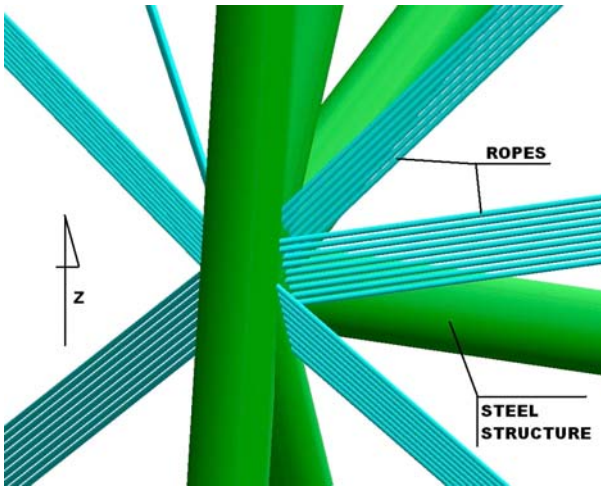

Figure 9-23: Sets of parallel rope

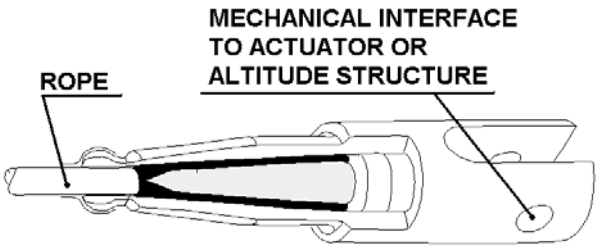

Figure 9-24: Rope mechanical interface

A dedicated study of rope implementation in ELTs including OWL is planned in the ELT Design Study. Further detail of the study "Structural ropes for ELT" can be found in the study Statement of Work (RD510).

9.4.4.2.1 Material selection

There are three grades of Kevlar available: Kevlar 29, Kevlar 49, and Kevlar 149. The table below shows the differences in material properties among the different grades. The Kevlar 149 has been selected.

Grade	Density g/cm^3	Tensile Modulus (GPa)	Tensile Strength (GPa)	Tensile Elongation (%)
29	1.44	83	3.6	4.0
49	1.44	131	3.6--4.1	2.8
149	1.47	186	3.4	2.0

Table 9-2: Kevlar available grades.

It is important not to expose Kevlar ropes to chemicals (e.g. soda of the recoating process) otherwise the Kevlar decomposes.

9.4.4.2.2 Wind on ropes

The ropes implemented in the altitude structure are vulnerable to wind induced vibrations and flutter. Due to constant section of the ropes vortex shedding can be generated (see Figure 9-25).

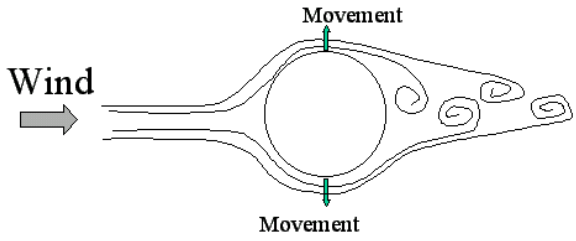

Figure 9-25: Wind vortex shedding.

The situation can be improved by increasing the damping in the system. Similar to the one reported in [34] for the cable stayed bridges (see Figure 9-26).

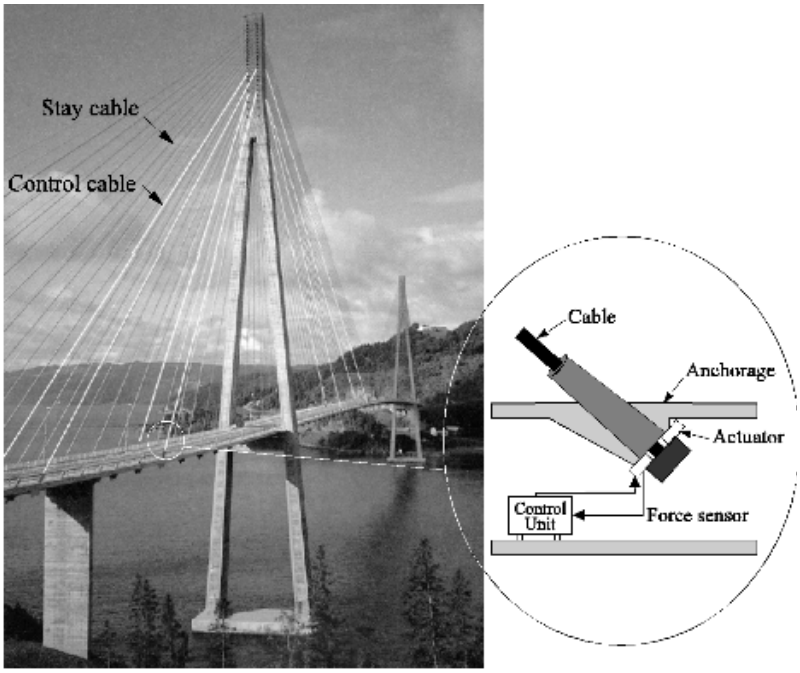

Figure 9-26: Cable damping system. (Courtesy of ULB).

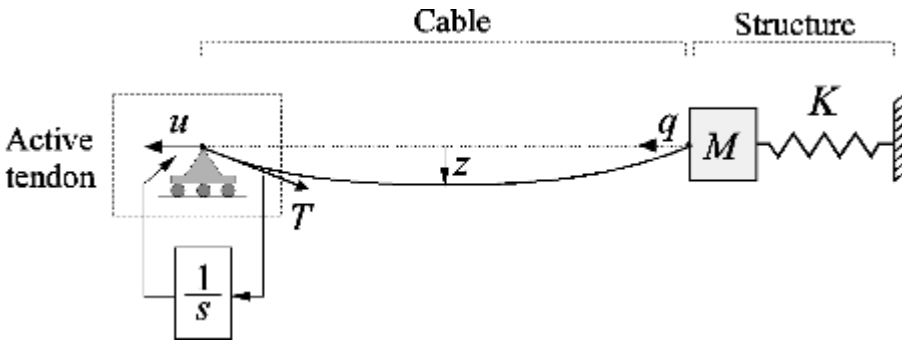

Figure 9-27: Active damping concept. (Courtesy of ULB).

Control strategy - The key feature of our control strategy is the use of a decentralized control system with collocated actuator/sensor pairs (displacement actuator and force sensor, see Figure 9-27). For this configuration, *Integral Force Feedback* (IFF) leads to guaranteed stability.

9.4.4.3 Focal Stations

At about mid-span between the primary and secondary mirrors 6 focal station are realised, placed symmetrically around the altitude structure optical axis. Figure 9-28, Figure 9-29 and Figure 9-30 show the layout dimension of the focal stations. The following allocations are foreseen:

- Focal station 1: Heavy scientific instrument (Attached to the structural element of the Focal Stations).
- Focal station 2: Light scientific instrument (Attached to the rotator).
- Focal station 3: Heavy scientific instrument (Attached to the structural element of the Focal Stations).
- Focal station 4: Light scientific instrument (Attached to the rotator).
- Focal station 5: Light scientific instrument (Attached to the rotator).
- Focal station 6: Technical instrument (Attached to the rotator).

Each Focal Station is equipped with a dedicated Adapter Rotator described in section 6. Accessibility to the focal station and instrument integration and maintenance are described in section 15.1.

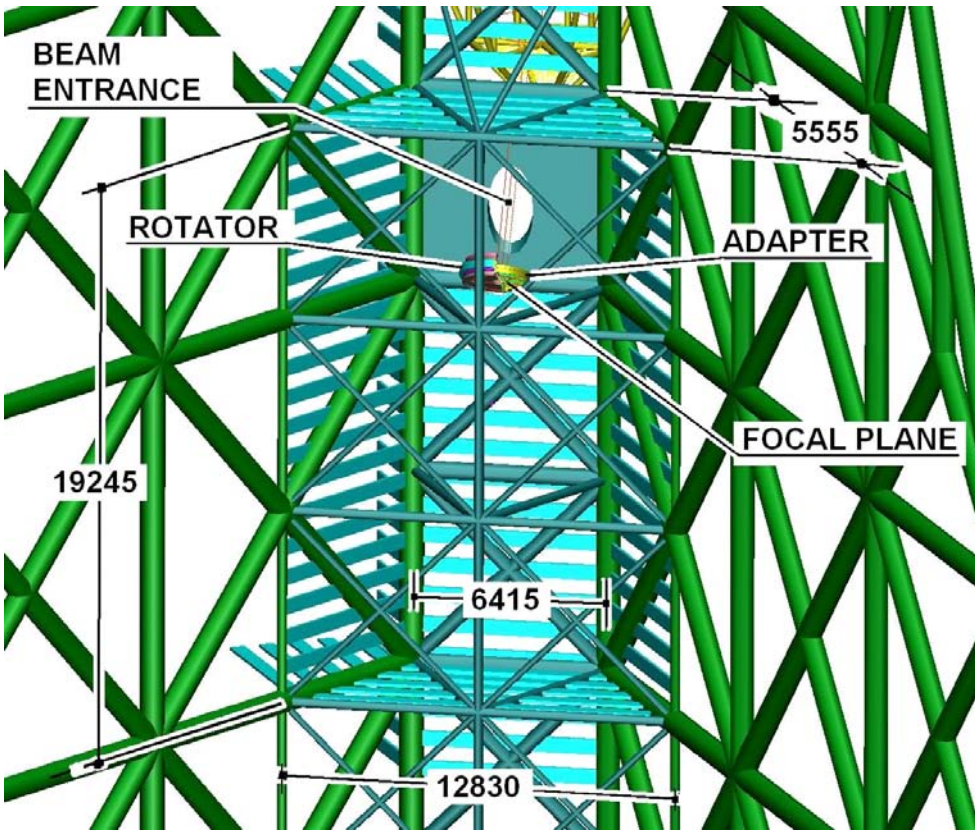

Figure 9-28: Focal station layout.

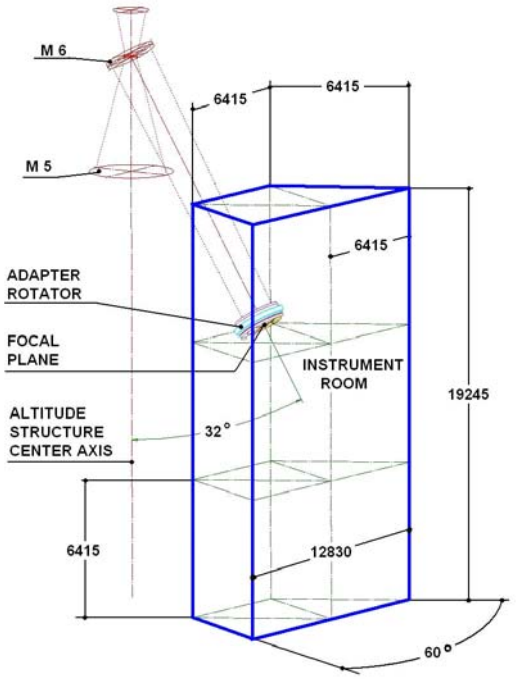

Figure 9-29: Focal station external dimensions.

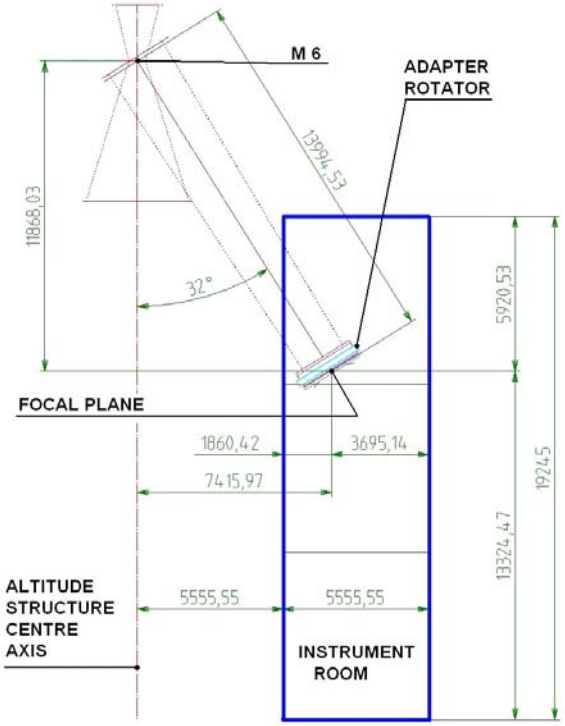

Figure 9-30: Focal station external dimensions. Side view.

9.4.4.3.1 Alternative focal station.

For instrument aiming at very high stability, presumably fed with optical fibers of about 300 m length, an instrumentation station can be implemented in the technical rooms. Possible dimensions are indicated in Figure 9-31. Foundations which are mechanically de-coupled from the telescope foundation can be realized. No loads need to be transferred from the roof of the technical room to the telescope foundation.

Nasmyth-type stations fed by suitable optomechanical relays remain to be assessed in the design phase.

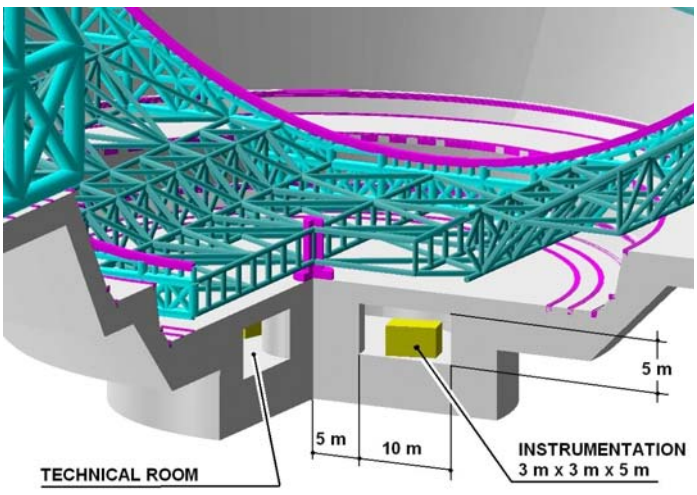

Figure 9-31: Fibre fed focal station.

9.4.5 Sub-Systems design.

9.4.5.1 Kinematics.

An essential function of the telescope altitude-azimuth mechanical structure is to provide a smooth, distributed and stiff transfer of loads to the site soil. The OWL telescope has its tracks embedded into the concrete foundation. The classical, traditional Fork / Tube concept standing on a pier has evolved into a Azimuth Structure / Altitude Structure concept embedded into a crater-like foundation. The smooth and even transfer of the loads from the optomechanical structures to the soil via the altitude structure, azimuth structure and concrete foundation can only be achieved using a large number of mechanical interfaces which shall also provide the kinematics of the telescope. The telescope is constrained in a hyper-static mode, which requires implementing accurate and reliable drive and bearing systems, thus avoiding concentration of stresses and deformation of the structural steel element and of the concrete foundation.

Different types of drives and bearings systems can be implemented between the azimuth structure and tracks, and between the azimuth-altititude structures. However a typical angular accuracy of few tenths of arcsec, must be well within the performance of the adopted solution, while interfaces and kinematics must ensure a homogeneous load transfer to the foundation.

9.4.5.1.1 Torque requirement.

The main axes drive systems are dimensioned to provide the following characteristics:

- Blind angle at zenith $\leq \pm$ 0,5 degree.
- Acceleration 0,1 degree s –2 (1,745 × 10-3 rad s-2).
- Maximum velocity 0,5 degree s –1 .
- Minimum tracking accuracy 1 arcsec.

9.4.5.1.2 Acceleration.

Altitude mass moment of inertia $1{,}121 \times 10^{10}$ kg m^2.

Altitude required torque 19,6 MNm.

Azimuth mass moment of inertia $3{,}366 \times 10^{10}$ kg m^2.

Azimuth Required torque 58,7 MNm.

9.4.5.1.3 Friction Drive & Bearing.

OWL performance and cost constraints require that different solutions be assessed. Several design iteration and trade off, indicate that merging drive and bearing functions into friction type mechanical devices ("bogies", shown in Figure 9-32, Figure 9-33 and Figure 9-34), reduces the complexity and cost of the design and allows to constrain the telescope in hyper-static mode, without jeopardizing the telescope operation.

The major design constrains in terms of feasibility and costs associated are listed below:

- Tracks alignment tolerances, cleanness and protection.
- Number of bearings.
- Cleanness and temperature control.
- Drive alignment tolerances, cleanliness and protection
- Inspection and maintenance operation.
- Stress concentration.

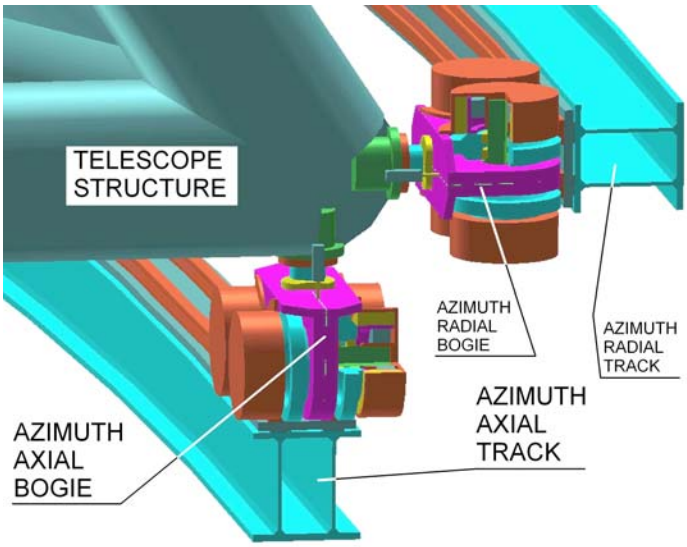

Figure 9-32: Axial and Radial Bogies.

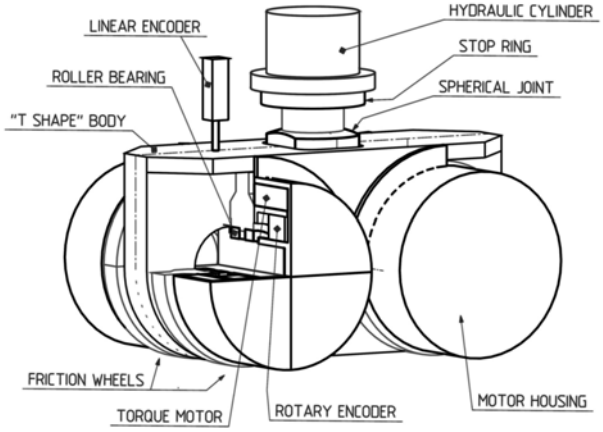

Figure 9-33: Bogie layout

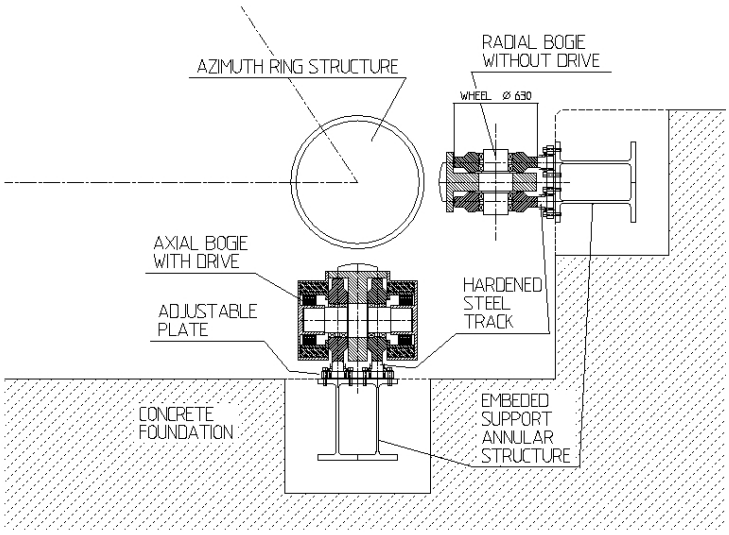

Figure 9-34: Axial And Radial Bogies cross section.

The large number of bogies, assures a smooth and homogeneous transfer of the loads to the site soil. Each bogie has 4 spherical or 4 cylindrical wheels, for the azimuth and altitude (cradle) flat tracks. Each wheel, with a diameter of 630 mm, is independently driven by a commercially available brushless ring torque motor, water cooled and equipped with an angular encoder. The required mean angular accuracy is 3 arcmin. at the wheel-motor axis. Each wheel has 2 self-aligning roller bearings.

430

In order to obtain homogeneous reaction forces on each bogie and consequently on the foundations, a "hydraulic whiffle tree" system is implemented, which consists of communicating hydraulic cylinders, their displacement being monitored by linear encoders. This whiffle tree system can be locked during observation to attain high dynamic performance.

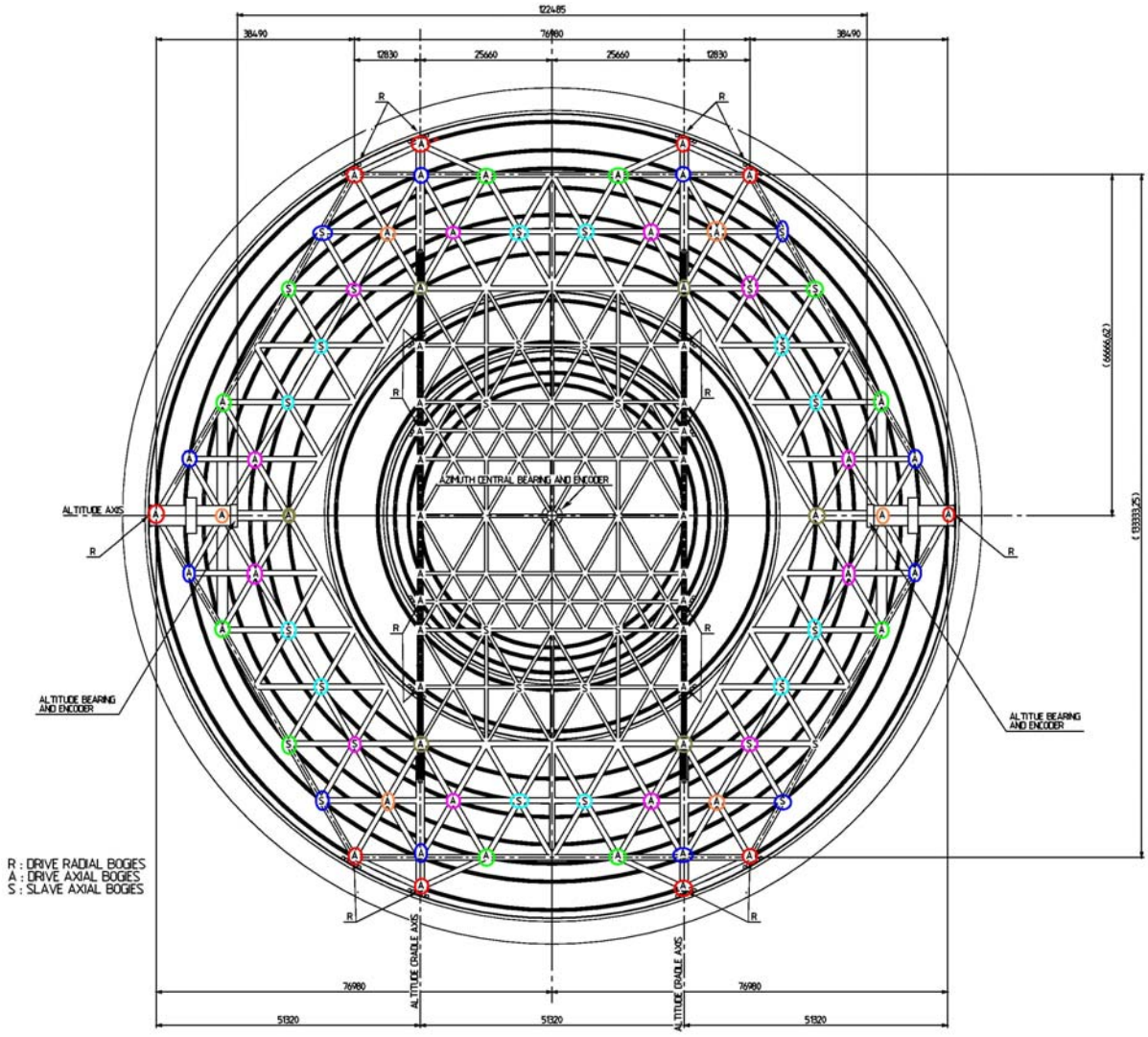

Figure 9-35: Azimuth bogies location.

Azimuth axis bogies system. - The azimuth structure integrates the azimuth bogies which are constrained by flexures (X and Y translation Degree of Freedom) and by Hydraulic jacks (Z translation DoF).

Technical solution implemented is shown in Figure 9-35 and consists of:

- Absolute “X-Y-Z” reference provided by the Azimuth central bearings
- 246 bogies attached to the azimuth structure.

- 192 axial bogies indicated with the letter “A” . The axial bogies support the entire mass of the telescope. This corresponds to about 80 tons per bogie.
- 54 radial bogies indicated with the letter “R”. Each radial bogie is pre-stressed with a nominal force of 785 KN (These 54 radial bogies could be eliminated in the 2005 design).
- There are 12 axial tracks and 3 radial tracks (the 3 radial tracks could be eliminated in the 2005 design), shown in Figure 9-35. The mean track radius is 57.647 m. The reduction ratio Friction wheel / mean track radius is 1/183.
- The slip friction generated at the azimuth axis is 26,43 MNm.
- 32 slave bogies are indicated with the letter “S”. These bogies do not have torque motor. Their function is to suppress local modes of the azimuth structure.
- In order to transmit the 1166 Nm peak torque of each drive motor the boogies shall be loaded with at least 20 tons.

Azimuth hydraulic wiffle tree - The main function of the hydraulic wiffle tree is to equalize the loads on the bogies. The key component hardware is described here below:

1. *Master bogies.*

   Six master axial bogies located at the 6 vertexes of the hexagonal shape of the azimuth structure.

   The stroke of the hydraulic cylinder of the master bogies, is controlled by the linear encoder (see Figure 9-33). An indicative hydraulic system diagram for double acting hydraulic cylinders is shown in Figure 9-36. However the bogies may also have single acting load return hydraulic cylinders, similar to ”Pancake Locknut Cylinders”. The final configuration will be defined after the breadboard test, see also Figure 9-38.

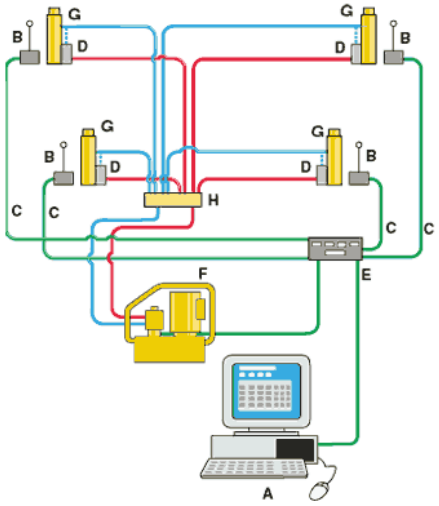

Figure 9-36: Computer controlled hydraulic cylinders of the master bogies

A: Controller.

B: Encoder.

C: Sensor Cable.

D: Valves (Needle, shut-off, check etc.) and pressure sensors.

E: Electro Box.

F: Power Source.

G: Hydraulic cylinder.

H: Control Valve Manifold Assembly.

2. *Needle valves.*

   In order to compensate the low spacial frequency flatness tolerance of the axial tracks and the cylindricity tolerance of the radial tracks, all the hydraulic cylinders are connected together. Needle valves minimise the exchange of oil among the cylinders. Thus the high frequency dynamic performance of the telescope is kept. The needle valves have a low pass filter function.

3. *On-board leveling system.*

   The global horizontal flatness of the telescope is measured using a system which allows real time continuous measurements, similar to the one shown in Figure 9-37 and based on communicating vessels principle.

Figure 9-37: Communicating vessels measurement

Altitude axis bogies system.- Technical solution implemented:

- 154 bogies attached to the two cradles of the azimuth structure.
- 60 radial bogie located in the central parts of the 2 cradles, support the entire mass of the altitude structure. This corresponds to about 80 tons per bogie.
- 94 radial bogies located at the extremities of the 2 cradles. Each radial bogie is pre-stressed with a nominal force of 785 KN (about 80 tons).
- 2 identical cradle tracks attached to the altitude structure. The cradle track radius is 52 m. The reduction ratio Friction wheel / mean track radius is 1/165.
- The slip friction generated at the altitude axis is 14,14 MNm.
- In order to transmit the 1166 Nm peak torque of each drive motor the boogies shall be loaded with at least 20 tons.

Altitude hydraulic wiffle tree - The altitude hydraulic wiffle tree is based on the same principle of the azimuth hydraulic wiffle tree. The main differences are listed below:

- Absolute “X-Y-Z” reference supplied by the 2 altitude bearings.
- Grouping the bogies symmetrically with respect to the azimuth axis. This configuration allows to control the loads and the forces applied to the bogies with function of their vertical coordinate.
- Alternatively it may also be possible to have different hydraulic cylinder effective area with function of their vertical coordinate.

Friction - The friction assumptions are quite conservative. Improved surface qualities and accurate alignment can reduce considerably the friction. Measurements on the friction drive systems of the VLT show that the final performance of a friction drive system can be much better than that calculated during the design phase. In order to determine the correct value of the friction, prototypes of the bogie, shown in Figure 9-38, will be manufactured and tested. A

dedicated Friction characterization measurement campaign, is planned in the ELT Design Study (see appendix A-1.4). Further detail of the “Characterization of friction drive and bearings” can be found in the Statement of Work RD513 and Technical Specification RD514.

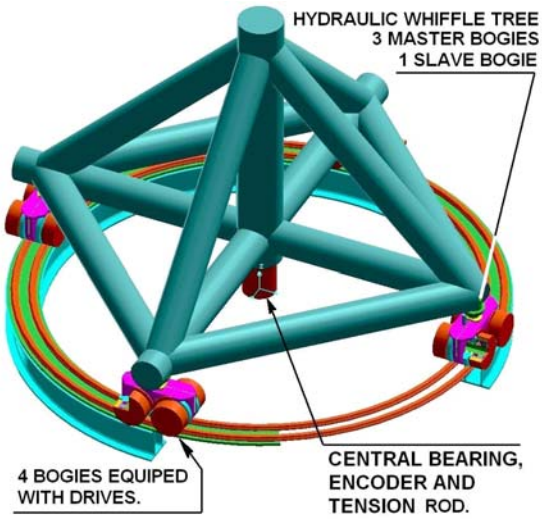

Figure 9-38: Bogies breadboard test setup

	Number of bogies.	Load per bogie [tons].	Number of wheels.	Load per wheel [tons].	Ratio wheel / track.	Number of mass loaded bogies.	Number of force loaded bogies.
Azimuth axis	246	76	984	19	1/183	192	54
Altitude axis	154	72	616	18	1/165	60	94

Table 9-3: Main axes friction drive and bearing topology.

	Nominal operational load per bogie [tons].	Minimum load per bogie [tons].	Minimum operational load per bogies [tons].	Maximum operational load per bogie [tons].	Survival load per bogie [tons].
Azimuth axis	80	15,09	20	150	240
Altitude axis	80	15,09	20	150	240

Table 9-4: Load cases.

	Total slip friction torque [MNm]	Yotal stick friction torque [MNm].	Roller bearings friction [MNm].	Total wind load torque [MNm].	Total acceleration torque [MNm].	Total required torque [MNm]
Azimuth axis	26.43	33.04	Negligible.	1.1	58.7	92.84
Altitude axis	14.14	17.7	0.15	7.1	19.6	44.55

Table 9-5: Main axes torque requirement.

	Torque motor type.	Continuous torque per motor [Nm]	Total continuous generated torque	Peak torque	Total peak torque

			[MNm].	[Nm]	[MNm].
Azimuth axis.	ETEL TMA 0530-050	859	**154.69**	1166	210
Altitude axis.	ETEL TMA 0530-050	859	**87.36**	1166	118.57

Table 9-6: Friction drive generated torque

The breadboard test will provide the following information:

- Stick and slip friction.
- Vertical and lateral stiffness.
- Pointing and tracking accuracy under wind disturbance.
- Performance of the hydraulic wiffle tree.
- Performance master and slave bogies concept.
- Performance of track misalignment compensation.
- Performance under load variations.
- Survival load case.
- Performance of the on-board hydrostatic leveling system.
- Test the control system.
- Test of alternative heavy-duty cycloidal drives.
- Induced vibration.
- Define maintenance criticality and concept.
- Identify suppliers.
- Costs evaluation.

9.4.5.1.4 Hydrostatic pads and direct drive.

During the 2002 Design iteration a detailed trade-off between Hydrostatic Pads and Direct Drive versus Friction Drive and Bearings has been performed.

	Direct drive & Hydrostatic bearing	**Friction Drive & Bearing (bogies)**
Azimuth tracks	87.3	12
Azimuth base plate	Not applicable	11
Azimuth understructure	15	12.8
Azimuth bearing	17.5	Not applicable
Azimuth drive	11.5	Not applicable
Azimuth bogies	Not applicable	21
Altitude cradle tracks	3.7	0.7
Altitude bearing	10	Not applicable
Altitude drive	4	Not applicable
Altitude bogies	Not applicable	4.5
Total	**149 MEuro**	**62 MEuro**

Table 9-7: Cost breakdown of OWL's drive and bearing systems

The following Table 9-7 compares the cost estimates associated to OWL's different drive and bearing systems. delivered ex works. Costs related to transport and integration on site are not shown.

Table 9-7 shows that the adopted solution of the telescope drive and bearing systems has a major impact on the total cost of the project. The difference in cost persists also for transport. integration on site and during the operational lifetime of the telescope in term of RAMS.

The main source of cost difference is the type of annular tracks. which have to be manufactured and aligned within the severe tolerance necessary to the hydrostatic bearings and direct drive systems. The values reported on the table are based on the 2002 design and extrapolation of the existing VLT systems

9.4.5.1.5 Magnetic Levitation.

Magnetic levitation (maglev) is a relatively new transportation technology in which non contacting vehicles travel safely at high speeds. while suspended. guided. and propelled above a guideway by magnetic fields. The guideway is the physical structure along which maglev vehicles are levitated. Figure 9-39. which show the Maglev system components applied to trains. depicts the three primary functions basic to maglev technology: levitation or suspension; propulsion; and guidance. In most current designs. magnetic forces are used to perform all three functions. although a nonmagnetic source of propulsion could be used.

These functions are also present in the drive and bearing systems of OWL. The similarity of functions can be better highlighted comparing Figure 9-39 and Figure 9-40 together.

The magnetic levitation bearings with integrated linear direct drives shall have the same functions as the friction drive and bearing systems tailored to OWL requirements. However some of the main critical requirements listed qualitatively in Table 9-8 differ from maglev transportation technology.

Radial and axial bearing forces.	Very High.
Tangential drive forces..	High.
Radial. axial and tangential stiffness.	Very High.
Accuracy	High.
Heat dissipation.	Low.
Energy consumption.	Low.
Induced vibrations.	Very Low.
System control.	Very High.
Electro Magnetic Compatibility	High
Reliability.	High.
Velocity.	Low.
Acceleration .	High.
Generated Friction.	Negligible.
Mechanical tolerances of the tracks.	Low.

Table 9-8: Maglev main requirements

To conclude this summary section. it can be stated that main major potential advantages of the maglev system applied to OWL. compared to other technology. are:

- Negligible friction.
- Low mechanical alignment tolerance of the tracks.
- Quasi perfect distribution of forces.
- High stiffness

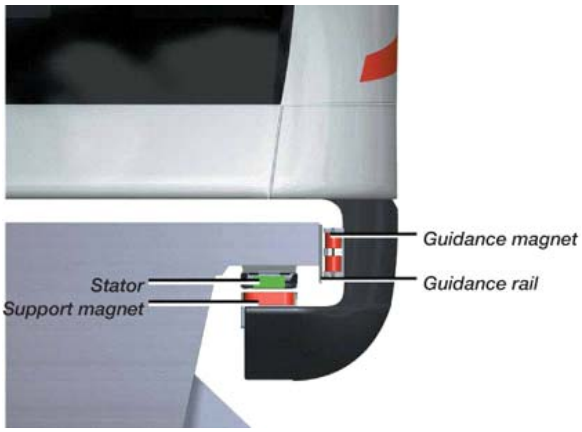

Figure 9-39. MagLev for trains

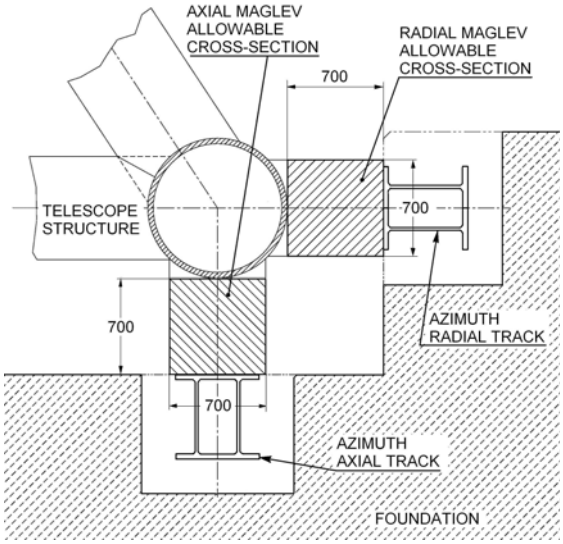

Figure 9-40. OWL MagLev available design location.

In the framework of the ELT Design Study. a dedicated study study will assess the feasibility and cost of the MagLev technology applied also to OWL main axes (see appendix A-1.4). Further detail of the study “Magnetically levitated systems and linear drives for ELT main axes” can be found in the study Statement of Work RD515.

This study will cover the following topics:

1. Conceptual design of the electro-mechanical system.
2. Generated forces vs. cost trade-off.
3. Stiffness vs. cost trade-off.
4. Gap vs. cost trade-off.
5. Conceptual design of the control system.
6. Define mechanical interfaces.
7. Analyses of performance.
8. Define maintenance criticality and concept.
9. Define suppliers.
10. Costs and schedule evaluation for a supply of ~ 300 meters of maglev system.
11. Final report.

Maglev generated forces - Each linear meter of the bearings and drives systems shall be able to generate as a minimum the forces reported in Table 9-9. during operation of OWL.

	Altitude Radial bearings & drives.	Azimuth axial bearings & drives	Azimuth Radial bearings & drives.
Linear Radial force [kN/m].	500	50	500
Linear Axial Force [kN/m].	50	500	50
Linear Drive Force [kN/m].	2	2	2

Table 9-9. Bearings & drives linear generate forces.

Maglev survival load case - During survival load case. the maglev system shall be able to generate forces which are 2 times the operational forces listed in Table 9-9.

Maglev minimum required stiffness - Each linear meter of the bearings and drives systems shall have as a minimum the stiffness reported in Table 9-10.

Characteristic	Altitude Radial bearings & drives.	Azimuth axial bearings & drives	Azimuth Radial bearings & drives.
Radial stiffness [N/mm/m].	20×10^6.	10×10^6.	20×10^6.
Axial stiffness [N/mm/m].	10×10^6.	20×10^6.	10×10^6.
Drive Stiffness [N/mm/m].	30×10^6.	30×10^6.	30×10^6.

Table 9-10. Minimum required stiffness.

9.4.5.2 Corrector.

The Corrector structure shown in Figure 9-41. is a steel trusses structure which copies the mirror segment hexagonal pattern. The trusses are made of cylindrical pipes.

It supports 2 Active mirrors (M3 and M4) and 2 Adaptive Mirrors (M5 and M6). It is equipped with a set of actuators which will supply alignment capabilities and can also compensate thermal and gravity deformation of the whole telescope structure in the x-y plane. The z axial bearing and actuator can re-focus the whole corrector.

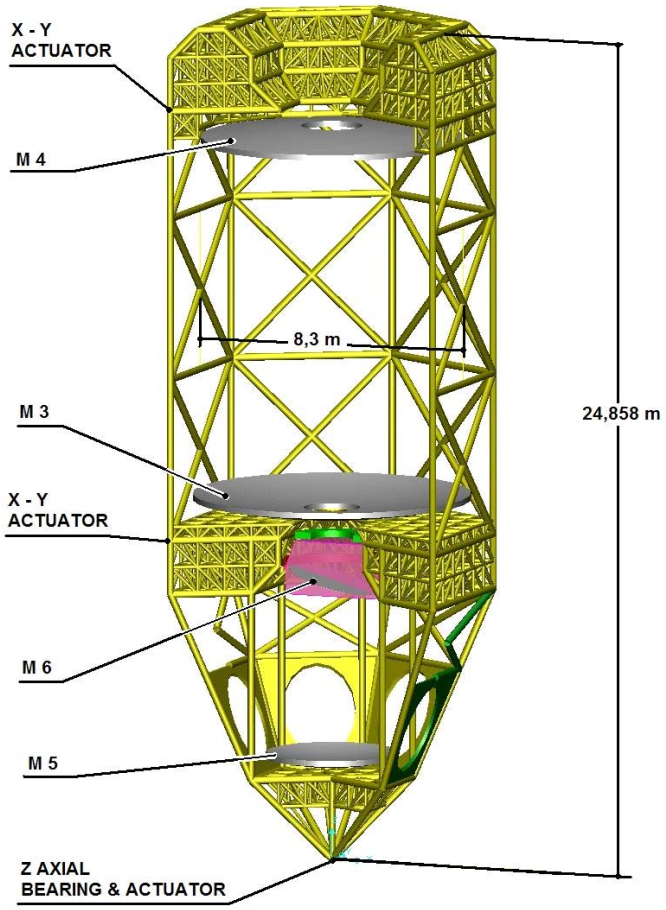

Figure 9-41: Corrector

9.4.5.3 M3 and M4 Unit

The M3 and M4 are 2 active mirror units with dimensions and mass similar to the VLT Primary mirror units. The baseline for the mirrors substrate is Glass Ceramic.

The corrector configuration allows:

- High stiffness of the 2 mirror cells.
- Comfortable design volumes around the mirrors.

9.4.5.4 M5 Unit

The M5 is an adaptive mirror unit with a 3.9-m adaptive shell. It provides active focusing. The baseline for the mirrors substrate is Glass Ceramic.

The corrector configuration allows:

- High stiffness of the mirror cell.
- Comfortable design volumes around the mirror.

9.4.5.5 M6 Unit

The M6 unit (see Figure 9-42 and Figure 9-43) is the most complex opto-mechanical unit in the corrector. It has a total mass of 4 tons. Its main functions are:

- Tip-tilt field stabilization. described in section 7.2.3. The field stabilization stage has a mass budget of 500kg.
- Adaptive optics. described in section 8.2.1.2.1.
- Directs the optical beam to the 6 focal station.

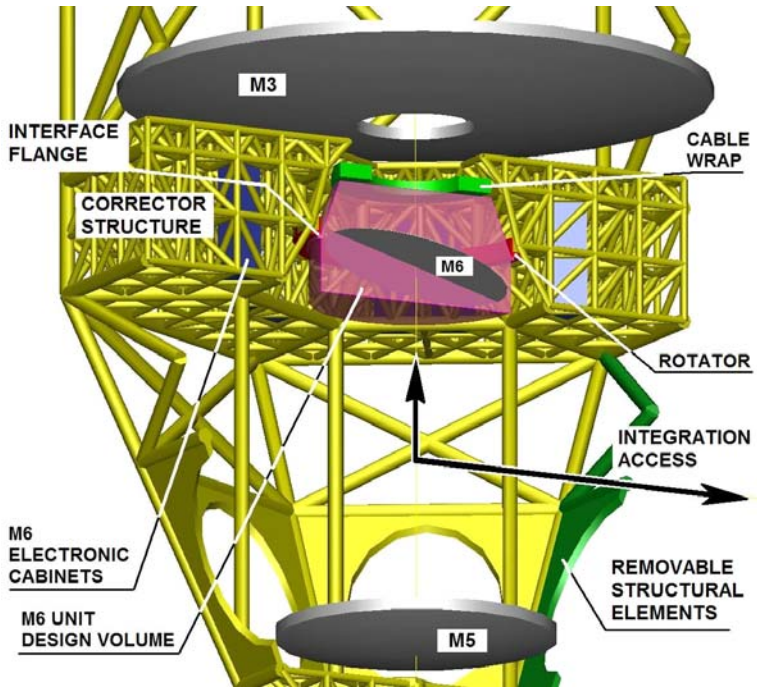

Figure 9-42: M6 lay out design and location

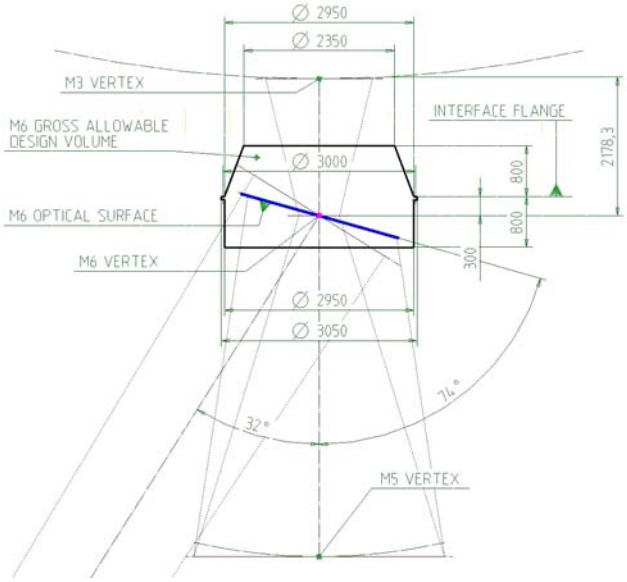

Figure 9-43: M6 unit overall dimensions.

9.4.5.5.1 Interface to the corrector.

The corrector is attached to a rotator bearing which is used to align the optical beam going out from the M6 to the 6 focal stations. The rotator bearing and its drive system are part of the corrector and provides the following interfaces:

- Mechanical
- Fluid and electrical supplies
- Signal
- Cable routing via a cable wrap.

9.4.5.5.2 M6 Unit design volume

Due to the intersection of several optical beams shown in Figure 9-44. the design volume shown in Figure 9-45 is restricted. This makes the inner design particularly challenging.

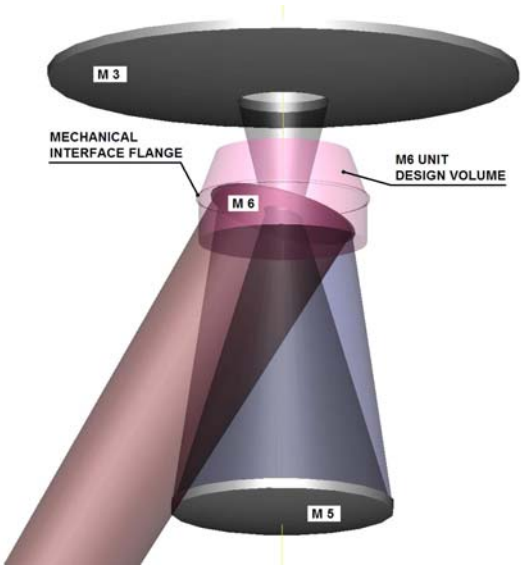

Figure 9-44: Optical bems intersection

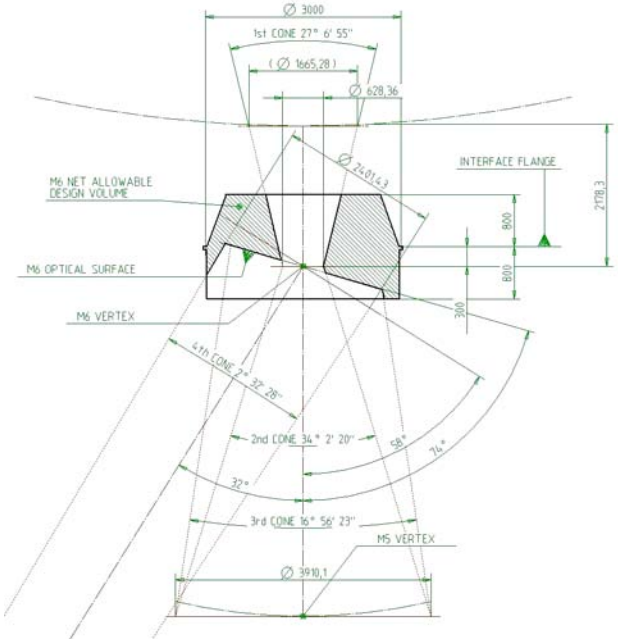

Figure 9-45: M6 available design volume.

9.4.6 Segments support system.

The surface of the OWL segmented mirrors must maintain the desired shape within an accuracy of a small fraction of the wavelength. This implies periodic re-adjustment of the piston and tip-tilt position of each segment at a frequency of a few Hz and within an accuracy of a few nanometers. The mirror shape is affected by external disturbances which can be classified in low and high temporal frequency:

- Low Gravity and thermal variation.
- High Wind buffeting.

The low temporal frequency disturbances imply a large stroke. typically several centimeters over time scale of several minutes or more. The high temporal frequency disturbances cause displacements of fractions of a millimeter. Therefore each segment is equipped with an active support (see Figure 9-46). including

- 1 Segment Support Structure
- 3 Position Actuators
  - Extractor
  - Coarse stage
  - Fine stage
- 18 axial support points whiffle tree system
- 1 Lateral support
  - Slave actuator
  - Membrane
- Hexagonal Segment
  - Edge sensors

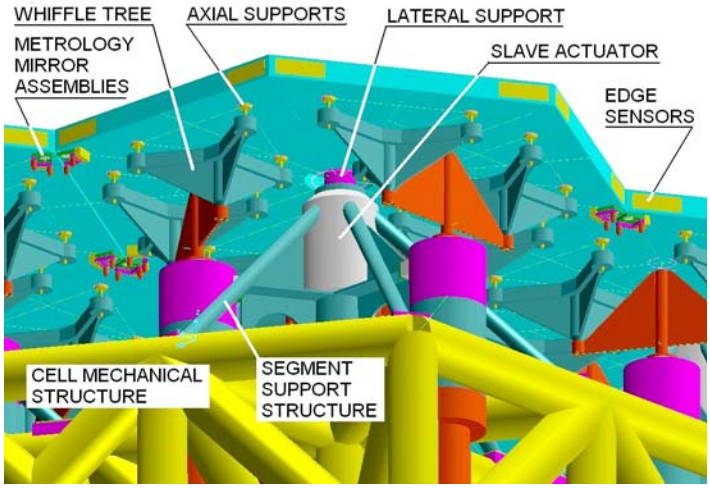

Figure 9-46: Segment support system.

9.4.6.1 Segment assembly.

The Position Actuators will be integrated into the mirror cell of the telescope mechanical structure and interface with the whiffle tree (see Figure 9-47). The whiffle tree distributes the axial loads of the hexagonal mirror segments. The Position Actuators may remain permanently mounted on the segment support structure.

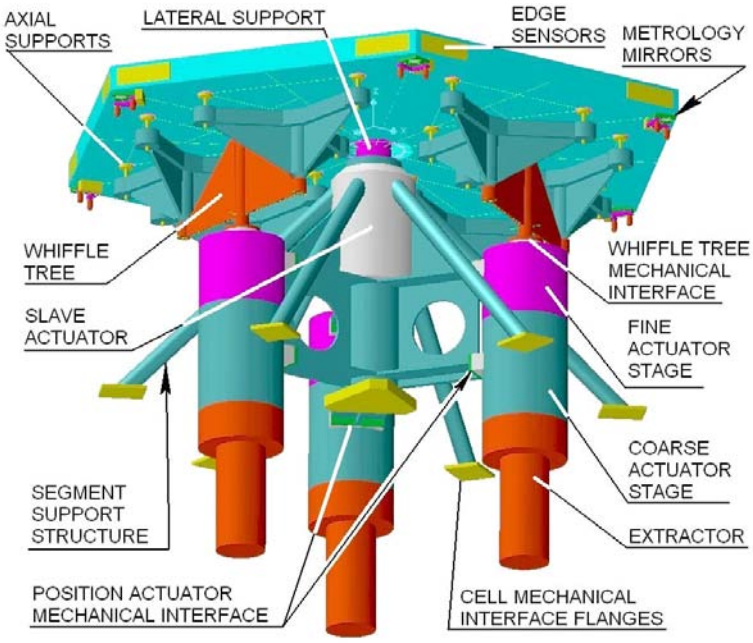

Figure 9-47: Hexagonal segment assembly

9.4.6.2 Extractors.

In order to simplify the handling of the hexagonal segments. each segment shall be extracted from the mirror (open configuration) using dedicated actuators called extractors. The extractor may also be integrated into the Position Actuator assembly. Once the segment is extracted from the mirror surface. a dedicated tool built in in the maintenance cover (see section 13.2.1.4 and 15.1.1.4) or in the M2 handling facilities (see section 15.1.1.6). will handle the segments to their way to the off-line maintenance facilities.

9.4.6.3 Position Actuators characteristics.

18 Position Actuator prototypes will be purchased in the frame of the ELT Design Study and tested on a Wind Evaluation Breadboard at the Observatory Roque de los Muchachos. La Palma (see section 9.4.7). Two types of actuators will have to be developed and manufactured:

- Position actuators for glass segments.
- Position actuators for lightweight Silicon Carbide segments.

The final Position Actuators performance specifications can be met using a two stages concept with coarse and fine stages or with a single stage concept. The required Position actuators performance are listed in the sections below.

9.4.6.3.1 Axial stiffness

The resonance frequency of a segment on its whiffle tree shall be at least 60 Hz. Therefore high axial stiffness is required for the Position Actuators.

The axial resonance frequency of a Position Actuator loaded with the masses indicated below shall be at least 120 Hz.

9.4.6.3.2 Load cases.

Compression Load

- Position Actuator for glass ceramic segments: 0 to 170 kg.
- Position Actuator for lightweight SiC segments: 0 to 60 kg.
- The continuous load changes are due to the rotation of the telescope altitude structure from horizon to zenith (around X axis).

Tension Load

- For the OWL secondary mirror. the Position Actuators are also compatible to tension loads equal to compression loads.

Wind load

- The wind buffeting on segments is a random process and it is defined by statistical parameters. An apprpriate description is the Power Spectral Density (PSD). Wind perturbation is characterized by the PSD of the wind speed. Based on which a theoretical model of the wind load perturbations can be obtained (Von Karman model). Assuming a mean wind speed of 10 m/s acting on the surface of each segment (1600 mm flat to flat) the RMS load is estimated to be 25 N (temporal values of wind load could reach values of 60 N).

9.4.6.3.3 Accuracy.

Two stages Position Actuator Concept

- Coarse stage ± 0.05 mm Goal ± 0.01 mm
- Fine stage ± 5 nm Goal ± 2 nm.
- Extractor 1 mm (open configuration)

One stage Position Actuator concept

- Accuracy ± 5 nm Goal ± 2 nm.

9.4.6.3.4 Stroke

The stroke of the Position Actuator shall compensate for the following sources of deformation:

- Gravity.

- Thermal.
- Track misalignment.
- Wind pressure on segments.
- Wind pressure on mechanics.

The strokes specified below consider the worst case assumption.

Two stages *Position Actuator* Concept

- Coarse stage 15 mm Goal 30 mm
- Fine Stage 0.5 mm Goal 1 mm
- Extractor 150 mm.

One stage PA concept

- Stroke 15 mm Goal 30 mm

9.4.6.3.5 Closed Loop Bandwidth.

These specifications shall be met assuming a 100 Hz bandwidth of the metrology signal and an infinitely rigid support system.

Two stages PA Concept

- Coarse stage 0.5 Hz.
- Fine stage 10 Hz Goal 20 Hz.
- Extractor (not applicable. only open and close configurations).

One stage PA concept

- Closed Loop Bandwidth 10 Hz Goal 20 Hz.

9.4.6.3.6 Maximum tracking rate

During observation of an astronomical object. OWL altitude structure can reach a maximum angular velocity of 15 degrees per hour. During this operation the PA shall compensate for the deformation of the altitude structure due to gravity acceleration (see coarse stage stroke goal 30 mm). This deformation follows cosine function during the altitude rotation. e.g. minimum at zenith maximum at horizon.

PA Maximum tracking rate: 0.0025 mm/s.

Accuracy ± 5 nm. Under wind disturbance as per section 9.4.6.3.3.

Accuracy goal ± 2 nm. Under wind disturbance as per section 9.4.6.3.3.

9.4.6.3.7 Maximum slewing rate

When OWL goes from one astronomical object to the next or during maintenance operations. the altitude structure of the telescope can reach a maximum velocity of 0.1 degree/s. During these operations the PA shall compensate for the deformation of the altitude structure due to gravity acceleration (see coarse stage stroke goal 30 mm). This deformation follows cosine function during the altitude rotation. e.g. minimum at zenith maximum at horizon. The PA shall maintain the mirror segment within the range of the edge sensors ± 0.5 mm. This deformation follows cosinus function during the altitude rotation. e.g. minimum at zenith maximum at horizon.

PA Maximum slewing rate: 0.06 mm/s.

Accuracy ± 0.1 mm.

9.4.6.3.8 Heat dissipation.

During operation. the external surface of the PA and of its electronic cabinets shall not exceed 1 ºC above ambient temperature at 0 m/s wind velocity.

Active cooling of the PA is regarded as an increase of complexity and shall be avoided.

Active cooling of the PA electronic cabinets is regarded as an increase of complexity and shall be avoided.

9.4.7 Wind Evaluation Breadboard

In order to define the objectives for the control of wind buffeting disturbance on OWL segmented mirrors. an electro-mechanical set-up called Wind Evaluation Breadboard will be realised in the frame of the FP6. which will simulate the real operational constrains applied to large segmented mirrors. Further detail of the “Wind Evaluation Breadboard” can be found in the Statement of Work RD507. and Technical Specifications RD503.

For the WEB the following critical sub-systems will be procured:

- 18 Position Actuator Prototypes. described in RD502 and RD503.
- 24 Edge Sensors. described in RD504 and RD505.

9.4.7.1 WEB layout.

The main WEB sub-systems and components shown in Figure 9-48. are listed below.

1. Seven hexagonal panel assemblies.
   1.1. Aluminium hexagonal panels.
      - 3 heavy type.
      - 3 lightweight type.
      - 1 master central panel
   1.2. Segment Support Structure.
   1.3. Metrology mirrors assemblies.
   1.4. Support and Phasing system.
      - 18 axial support points structure (Whiffle Tree).
      - 1 lateral central support point structure.
      - 1 slave actuator.
      - Torsion rods.
      - Fine actuators.
      - Coarse actuators.
      - Edge sensors.
      - Extractor.
2. Cell.
   2.1. Trusses structure.
   2.2. Hinges.
3. Base frame.
   3.1. Structure.
   3.2. Pads.
   3.3. Altitude Tilt actuator.
   3.4. Azimuth actuator.
4. Rear support structure.

5. Wind Skirt board.
6. Track.
7. Optical metrology set-up.
   7.1. Control Electronic.
   7.2. Hardware.
8. Software.
9. Civil engineering sub-systems
   9.1. Enclosure.
   9.2. Foundation.

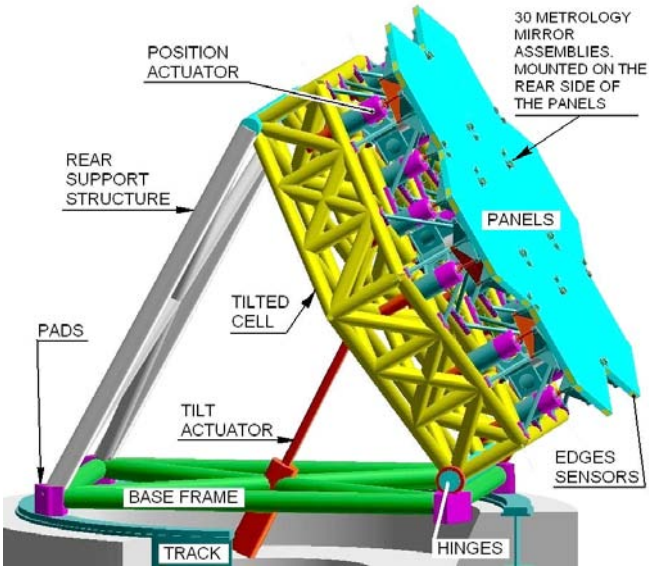

Figure 9-48: Layout of WEB.

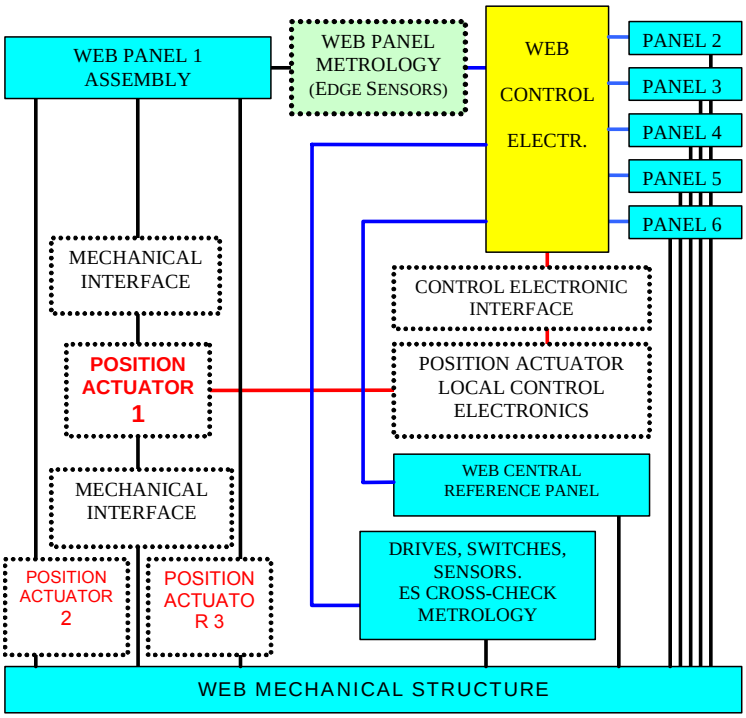

Figure 9-49: WEB Functional Layout.

Figure 9-49 show the functional layout of WEB and the interface between:

- WEB structure and kinematics
- Position actuators
- Position Sensors
- Metrology
- Control Electronics

9.4.8 Internal Metrology

Several internal metrology systems can be integrated in the telescope structure. These systems have the function of supplying absolute reference and measurements during stand-by and observation and maintenance modes. The main intended use of the internal metrology is to actively compensate the low frequency telescope deformation due to gravity and thermal disturbances.

The following telescope sub-systems are monitored by the internal metrology within a typical accuracy of 0.5 to 1 mm along the X-Y-Z axes. at low frequency rate (0.01 Hz) and over a maximum range of 160 m:

- Primary mirror.
- Secondary mirror.
- Corrector.
- Azimuth structure (horizontal level only).

Off-the shelf industrial products meet the requirements. Such products include

- Fibre optic based extensometer RD504.
- Laser tracker.
- Hydrostatic levelling system (see Figure 9-37).

9.4.9 Thermal control and design provision

9.4.9.1 Thermally controlled volumes

The following volumes shown in Figure 9-50. are thermally controlled during the day:

- Primary mirror: Total volume 102845 m3.Only for glass ceramic mirror substrate.
- Secondary mirror: Total volume 4115 m3.. Only for glass ceramic mirror substrate.
- Corrector: Total volume 4801 m3.
- Focal stations: Total volume 6172 m3.

These locations can be air conditioned via conduits which can be connected to the cooling facility located in the technical room. These connections can be realised in the vertical and horizontal parking positions.

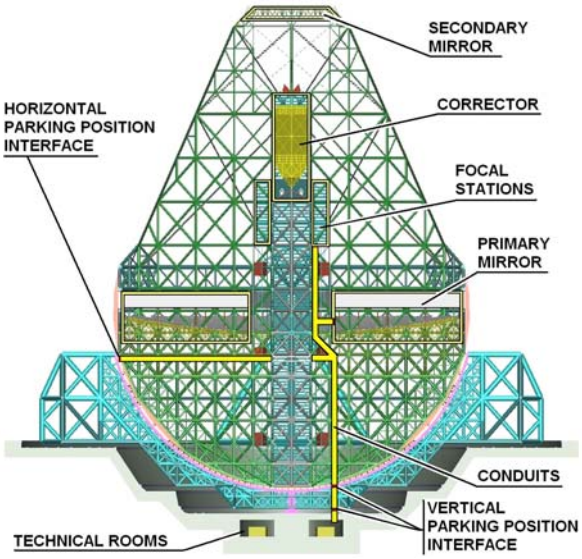

Figure 9-50: Air conditioning layout

9.4.9.2 Passive thermal control of the mechanical steel structure.

The mechanical steel structure of the telescope does not need to be thermally controlled. The large heat exchange area of the mechanical elements. along with their thin wall thickness. assures a very low thermal inertia. Experimental data (see section 5.4.1.3) and analysis show that the mechanical steel structure can enter in to temperature regime with the ambient air within few minutes after sunset.

If necessary the fractal design made of cylindrical pipes (see Figure 9-51) also allows an inner air flow. thus further reducing the thermal inertia of the telescope mechanical structure.

The inner air volume contained in the mechanical structural pipes is:

- Azimuth structure 20480 m3.
- Altitude Structure 18235 m3.
- Total volume 38715 m3.

The total volume of OWL structural pipes corresponds to about one VLT enclosure volume.

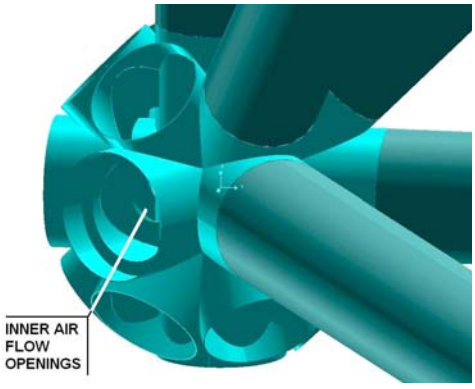

Figure 9-51: Inner ventilation.

9.4.10 Safety

The telescope structure concept has embedded safety provisions in the design. against hazards which can be generated during transport and integration (see section 13.2.2) as well as during maintenance and operation (see section 15.1.2). Particular attention has been paid to:

- Environmental hazards during integration.
- Human access to subsystems during maintenance and.operation.

9.4.11 Mass & Moment breakdown.

The mass and moment breakdowns are given in Table 9-11 and Table 9-12.

SUB-SYSTEMS.	Corrector [Tons]	Altitude structure [Tons].	Total Mass. [tons].
M1 - 3048 glass ceramic hexagonal segments.		1158.2	
M1 whiffle tree and actuators.		304.8	
M2 - 216 glass ceramic hexagonal segments.		82.08	
M2 whiffle tree and actuators.		21.6	
M3 and actuators.	31.5		
M4 and actuators.	30.5		
M5 and supports.	8.25		
M6. tip-tilt cell and actuators.	4		
Corrector steel pipes structure.	57		
Total corrector unit.	131.85	131.85	
Instrumentations (6 instruments).		90	
Altitude structure steel pipes and kevlar ropes.		7242	
Total altitude structure.		8918.63	8918.63
Total azimuth structure.			5415.9
Miscellaneous (electronics. cabling. piping. stairs. lifts. cat-walks. paint. welds etc.)			500
Total telescope rotating mass.			14834.53
Azimuth tracks.			~ 4500

Table 9-11: Telescope mass breakdown

AXES	MASS MOMENT OF INERTIA [KG M^2].
Altitude.	1.123×10^{10}
Azimuth	3.368×10^{10}

Table 9-12: Mass moment of inertia

9.5 Structural analysis

Structural analyses have been performed to assess the feasibility of the structural baseline design. The analyses are based on a set of global FE Models of the 2004 (see 9.3.6) OWL structure representing the altitude angle configurations 0º. 30º. 60º and 90º from zenith. Some analyses and analyses studies presented herein are based on the 2002 design (see 9.3.5) of OWL. Each configuration forms a different geometry with different number of interface bogies between altitude and azimuth structure. The FE Model in the zenith configuration is shown in Figure 9-52 and the side view of the 60º model including the boundary conditions is displayed in Figure 9-53.

The 2004 FE model comprises about 146000 elements and 40000 nodes representing 238000 degrees of freedom. The framework structure is modelled with pipe elements and the ropes with link elements. The latter transmit only longitudinal forces and no moments. The primary mirror segments as well as the mirrors M3 to M6 are represented as distributed mass elements which are connected to the cell structures by appropriate beam elements. The secondary mirror segments are modelled as shell elements connected to the M2 cell structure by appropriate beam elements. The mass of the M2 elements correspond to the real mass of the segments and their support system. The mirrors supporting structures are not modeled in detail. but their stiffness and mass is taken into account. The mirrors used in the baseline models are based on Zerodur material.

The altitude and the azimuth bogies are modelled as beam elements that represent the stiffness and mass assumptions described in RD33. RD13. The contact stiffness between the bogies' wheels and the rails has been taken into account. The connection of the altitude bogies in lateral x-direction is simulated only for the dynamic analyses. because in this case lateral forces are transmitted due to the friction of the bogies' wheels. In the static and stress analyses this degree of freedom connection is released. The hydraulic whiffle-tree system which provides a smooth reaction force distribution among the bogies is not simulated in the FE models presented herein. This is considered to be a conservative assumption in terms of stresses in the regions close to the bogies.

The mass budget of the FE Model corresponds basically to the mass breakdown listed in Table 9-13. A mass and mass moment of inertia summary extracted from the FE Model in zenith configuration is provided in Table 9-13. In order to take into account the "miscellaneous" additional mass allocation of 500 tons. the density of the steel has been adapted accordingly.

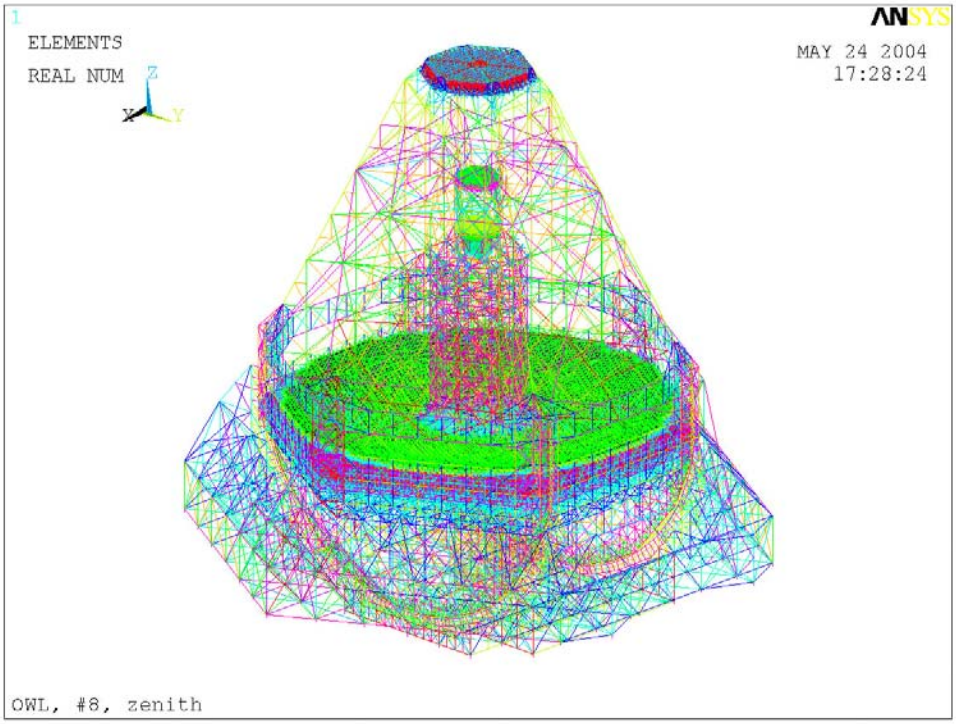

Figure 9-52: FE Model of OWL in zenith configuration.

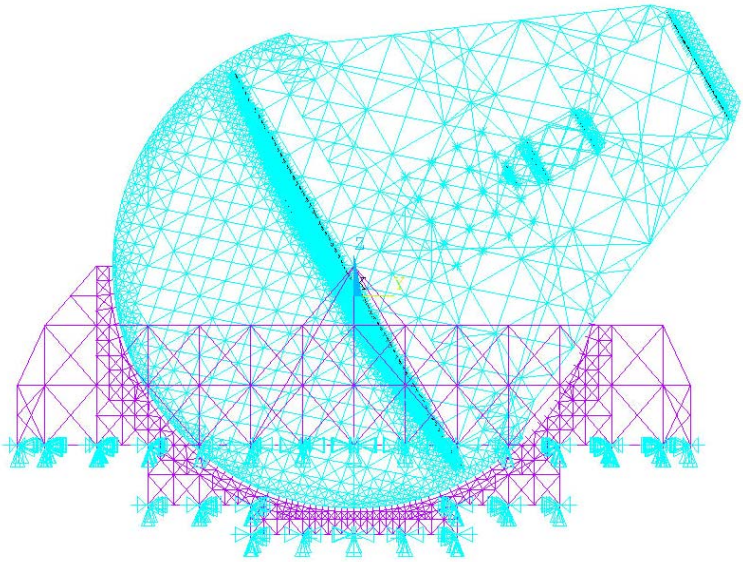

Figure 9-53: Side view of FE Model of OWL 60º from zenith.

Structure	Mass [ton]	Mass moment of inertia [$kgm^2 *10^{10}$]	CoG[66] [m]	Remarks
Altitude	8919	1.123	-0.370	Inertia of altitude structure about altitude axis
Azimuth	5416	3.368	-30.060	Inertia of complete structure about azimuth axis
Total	14287		-11.625	

Table 9-13: Mass and inertia budget of the FE model in zenith configuration.

The ground is assumed to be infinitely stiff and the model is fixed at the lower end of the azimuth bogies in the longitudinal directions. The influence of the foundation and soil stiffness to the telescope performance has been studied and is described in section 9.5.4.3.

The structural models used are adapted to the particular analyses for which they have been used and are accurate enough to provide a good representation of the structural behaviour in terms of displacements and frequencies. Local effects and stresses are usually simulated in the global models less accurately and will be evaluated with detailed local models if needed.

9.5.1 Analysis tree

The analysis tree shown in Figure 9-54 provides an overview of most of the analyses carried out during phase A. The flow chart describes the hierarchical order and the interconnections between requirements. design. analyses and results in a systematic way. Details of other disciplines and related interconnections like optics and control are not shown in this flow-chart.

[66] z coordinate with respect to altitude axis.

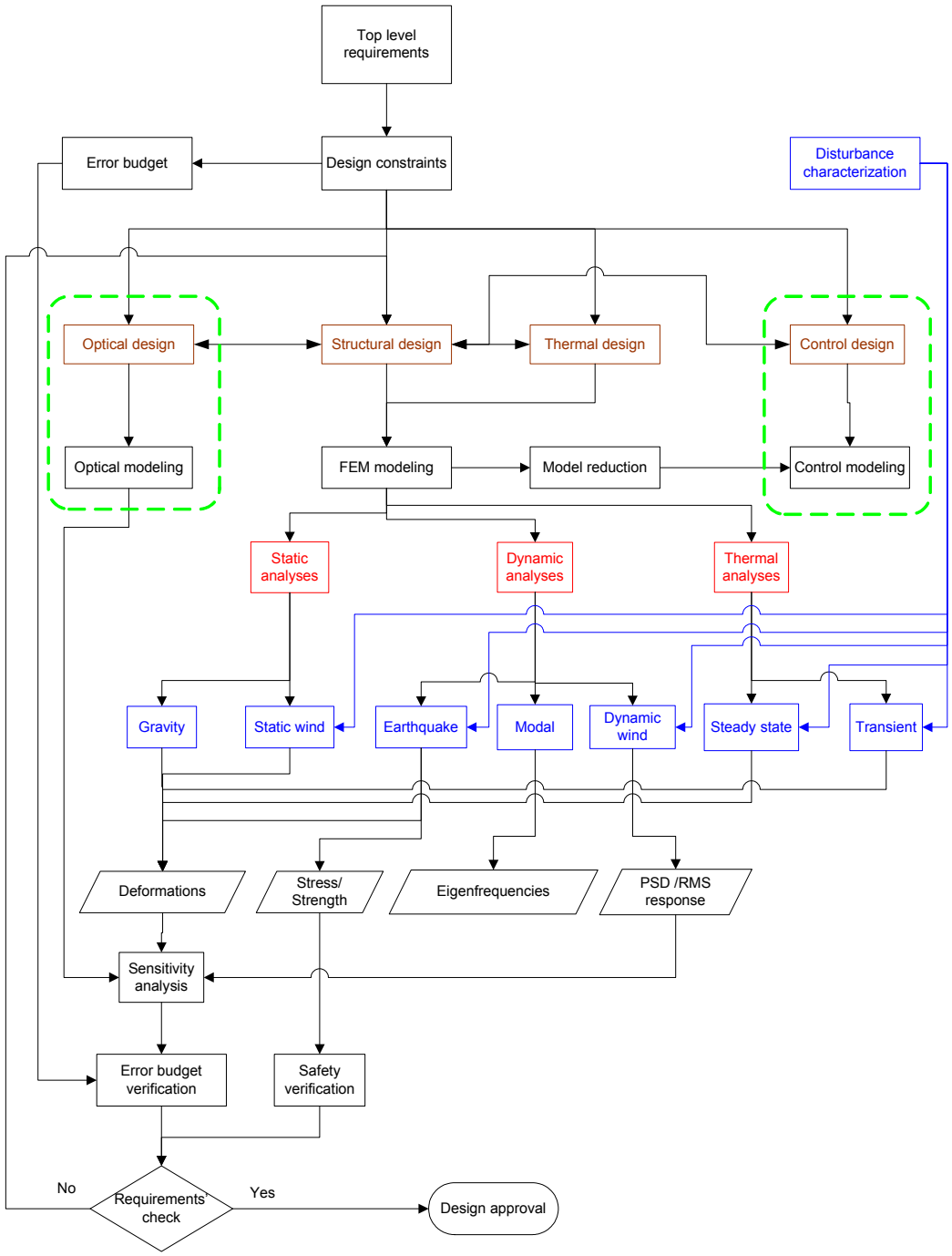

Figure 9-54. Analysis tree flow chart.

9.5.2 Static Analysis

The static analyses are based on the global FE models described above and aim at calculating the deformations and stresses under operational conditions like gravity and static wind load. The deformations of the optical components are used to define the required maximum range of the segment position and corrector actuators which are supposed to correct the static misalignments. In addition the rigid body (rb) displacements and rotations of the optical components are calculated based on a best-fit approach and multiplied with the optical sensitivity matrix to evaluate the individual influence of each mirror on the image motion error budget (see section 6.3.5). This will be very useful for further design improvements and optimisation studies in phase B.

9.5.2.1 Gravity

This section describes the analyses performed to evaluate the absolute and differential deformations due to gravity for the maximum operational altitude angle ranging from zenith to 60º. The gravity analyses include a certain initial vertical shift between the Altitude and Azimuth structures at the level of the main bearings. This shift of 15 mm has been preliminary optimised in a separate analysis run in such a way to transfer more load of the weight of the altitude structure through the main bearings and to reduce the maximum stress due to gravity.

The appropriate global 2004 models for zenith and 60º configuration have been analysed separately to calculate the differential displacements when the telescope is turning from zenith to 60º. Table 9-14 lists the differential global mean displacements of the optical elements in terms of piston. tilt and decenter. The differential piston and tilt between M2 and M1 is calculated to be 3.4 mm and 13.1 arcsec. respectively. These quasi-static errors will presumably be compensated for by the corrector actuators. As the secondary mirror is flat. its lateral decentre is irrelevant.

In order to define the required strokes of the segment position actuators. the local PTV displacements of the M1 and M2 segments have been evaluated and the worst case values are summarized in columns PTV of Table 9-14. Hence. the total required coarse segment actuator stroke results in 11 mm which includes 10.1 mm from the M1 piston and 0.9 mm contribution from the mirror segments tilt. i.e. 147 arcsec tilt corresponds to 0.9 mm actuator piston assuming an actuator distance of 1.2 m.

Mirror	**Piston [mm]**		**Tilt [arcsec]**		**Decenter [mm]**	
	rb	**PTV**	**rb**	**PTV**	**rb**	**PTV**
M1	7.8	10.1	0.3	147.1	13.2	8.8
M2	11.2	2.8	13.4	132.7	30.8	1.1
M3	12.0	2.1	-43.6	25.6	22.9	0.4
M4	13.0	1.7	-35.4	82.3	24.7	0.8
M5	11.1	1.7	-57.0	159.5	21.8	0.3
M6	12.1	0.6	-43.4	20.7	22.7	0.3
M2 - M1	3.4		13.1		17.6	

Table 9-14: Differential rigid body motions of the optical elements due to gravity.

The displacement distribution of the telescope under gravity load is displayed in Figure 9-55 and Figure 9-56 for the zenith and 60º configuration. respectively.

Fairly high stresses occur in the framework structure under gravity load. The maximum von Mises stresses in the order of 250 MPa occur in a region below the M1 segment supporting structure. In order to meet the stress safety requirements. several measures can be taken:

- Reinforce the framework structure in the critical areas by increasing the cross sectional areas of the beams
- Modify the topology of the framework structure in the critical regions (this has been already done in the 2005 model)
- Use higher strength steel in the critical areas. e.g. St52 instead of St37

The yield strength limits of the steel materials used are 240 MPa for St37 and 327 MPa for St52 and the ultimate tension strength limit of the steel cables is 1500 MPa.

It is foreseen to carry out an optimisation analyses campaign during phase B of the project. to evaluate the optimum beam cross-sections as well as optimum pretension of the ropes under various load scenarios.

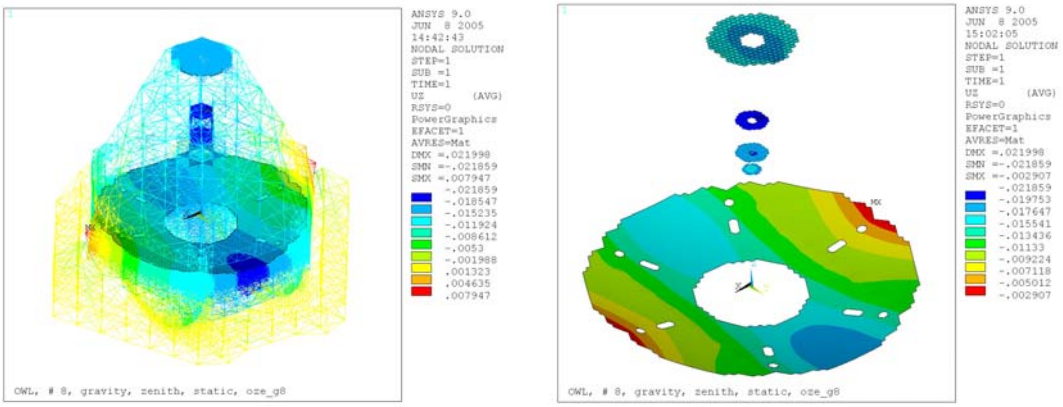

Figure 9-55: Vertical uz displacement distribution due to gravity for zenith configuration. Complete structure (left) and mirrors M1 to M6 (right).

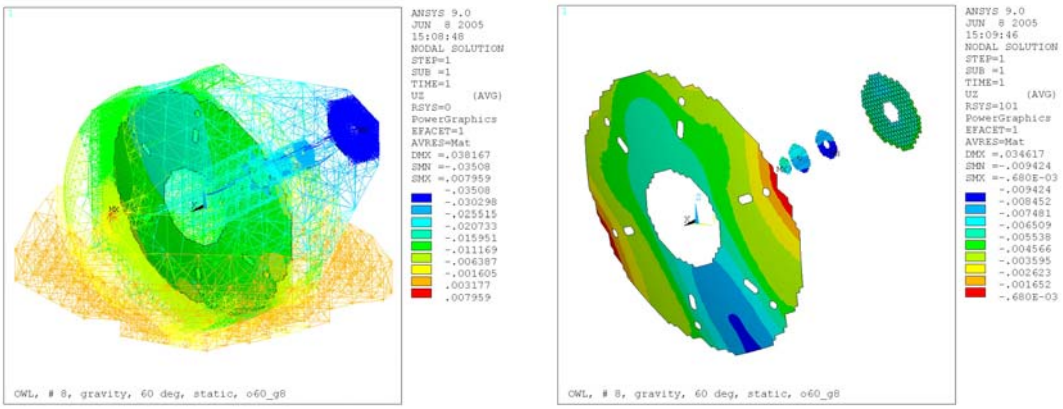

Figure 9-56: Displacement distribution due to gravity for 60º configuration. Complete structure in global vertical uz direction (left) and mirrors in normal displacements (right).

9.5.2.2 Steady State Wind

To estimate the influence of the steady state contribution of the wind loading. the deformation of the telescope has been calculated for a mean wind speed of 10 m/s. The corresponding pressure load distribution as described in section 5.4.1.1 is based on a wind speed profile and drag coefficients defined in standard norms. Three different altitude configurations (zenith. 30º and 60º) of the 2004 model have been investigated by applying pressure equivalent static forces. The rigid body displacements and rotations as well as the PTV errors of the optical elements were evaluated and the worst case values are listed in Table 9-15 for M1 and M2 in terms of piston. tilt and decenter. The maximum piston and tilt error occur for the 60º configuration and are -0.41 mm and 1.3 arcsec. respectively. These errors will presumably be compensated for by the fine segment position actuators. According to the PTV displacements of the M1 and M2 segments the required stroke of the fine segment position actuators is minimum 0.6 mm. Due to the small rigid body deformations of 0.4 mm a compensation of these errors with the fine segment position actuators will be investigated in the next phase.

Figure 9-57 shows the deformation of the optical elements for the 60º altitude configuration. The colours indicate the mirrors' normal displacements in meter.

Mirror	Piston [mm]		Tilt [arcsec]		Decenter [mm]	
	rb	PTV	rb	PTV	rb	PTV
M1	-0.29	0.60	1.30	4.57	-0.18	0.11
M2	-0.41	0.16	1.21	6.32	-0.80	0.03

Table 9-15: Worst case rigid body and PTV motions of M1 and M2 segments due to static wind.

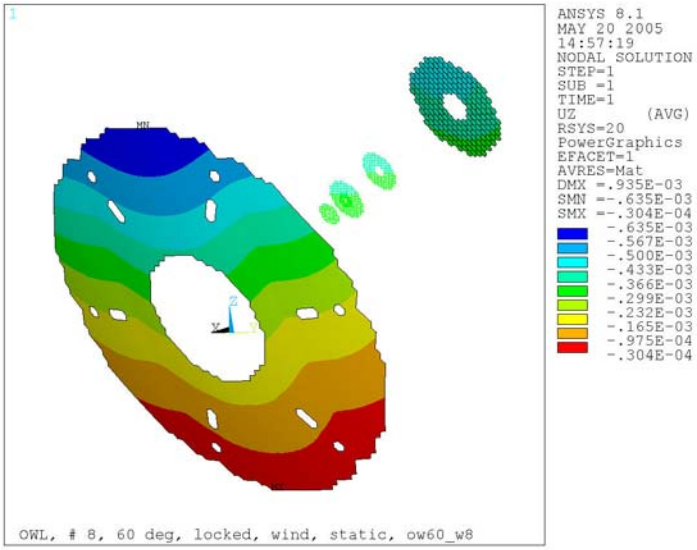

Figure 9-57. Normal displacement distribution of optical elements under static wind at60º.

9.5.3 Thermal analysis

The purpose of the thermal analyses described in this section is to predict temperature distributions of the OWL structure due to a set of nominal and accidental load case scenarios defined in section 5.4.1.3. The appropriate analysis results are used to assess the maximum segment position actuator ranges for maintaining the initial optical alignment requirement. The thermal analyses carried out are supposed to cover the following load conditions:

- The enclosure is closed and the telescope experiences a uniform temperature increase (nominal).
- The enclosure is closed and the telescope is exposed to a linear temperature gradient from bottom to top (nominal).
- The enclosure cannot be closed during the day and the telescope is exposed to direct sun radiation and outside air (accidental). This case covers also the thermal conditions during the installation process of the framework structure.

In the analysis models the thermal compensation system of the structural ropes. as well as the whiffle-tree systems of the altitude and azimuth bogies are not activated. Since this situation may occur in accidental cases like malfunctioning or failure of these systems. the effect on the thermal stresses are investigated and considered as worst case scenarios.

Based on the existing structural FE Model of OWL (2004 version) a simplified thermal FE model has been built which is able to calculate the steady state temperature distribution caused by sun radiation and natural convection with ambient air temperature. The convection coefficients and heat flux input load have been adapted to obtain the maximum temperature measured in the thermal experiments of a steel pipe on Paranal (see section 5.4.1.3). The thermal computations carried out until now are steady state analyses with conservative assumptions. but the thermal models allow performing transient analyses too. The accidental load cases comprise 17 different load configurations when the Enclosure is exposed to sun radiation during the day. Three different altitude angle configurations are combined with six different sun directions. After the calculation of the temperature distribution with the thermal FE model the appropriate displacements and stresses were computed with the structural FE model of OWL with the boundary conditions applied for the modal analysis.

Details about the thermal FE model. the analysis assumptions and results can be found in RD50.

The first nominal load case simulates a uniform temperature change of 10 °C (see 5.4.1.3. site 2) with respect to the reference (stress-free) temperature applied to the complete structure. This

load case represents a fairly conservative assumption. i.e. the temperature inside the enclosure follows directly the outside ambient air temperature. Due to this temperature change the M2 unit moves 17 mm in vertical z-direction (see Figure 9-58). This complies very well with a simple hand-calculation of a steel beam elongation with an equivalent length length of 147 m. The maximum radial displacement at the level of the primary mirror segments is calculated to be 7 mm at the outer edge. Hence. the maximum radial offset between two mirror segments is about 0.3 mm. This is well within the specified value of 4 mm.

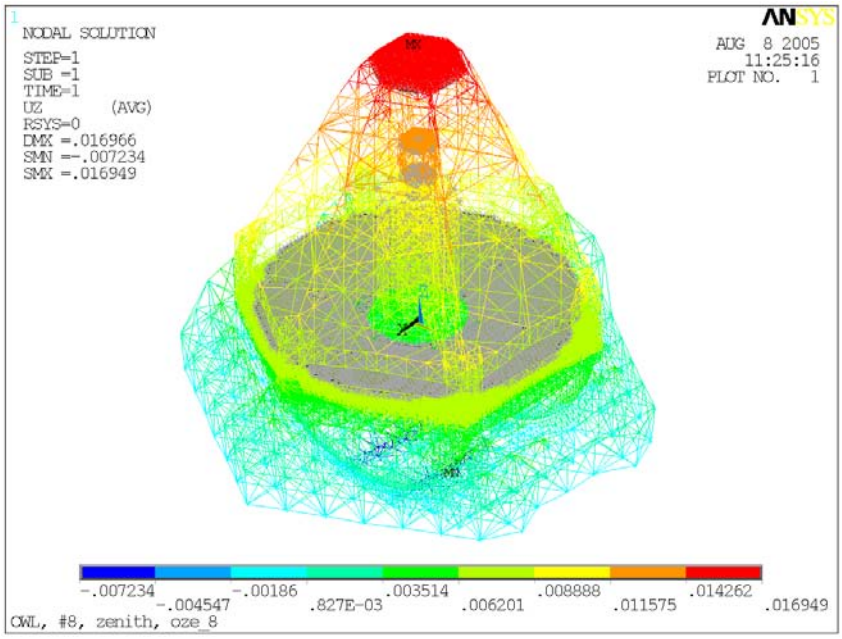

Figure 9-58: Vertical z-displacement distribution due to uniform temperature change of 10° C.

The corresponding von Mises stress distribution in the steel structure is displayed in Figure 9-59 with a maximum value of about 60 MPa occurring in the top region of the altitude bogies. The general stress level in the structure is fairly low. Stress peaks occur only in the overconstrained support and interface regions (bogies and structural ropes interfaces).

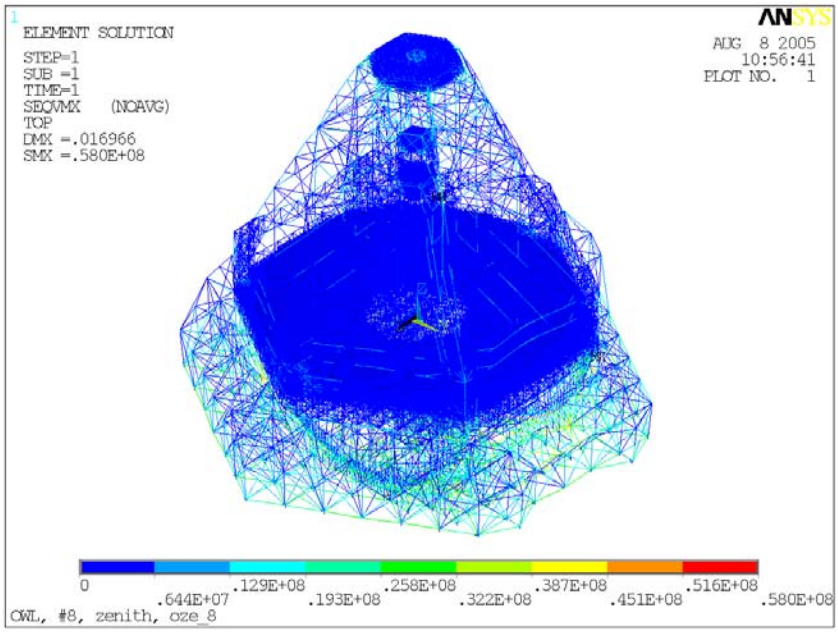

Figure 9-59: Equivalent stress distribution due to temperature change of 10° C.

The second nominal load case represents a linear temperature gradient of 10 °C from bottom to top. The appropriate displacement and stress results are much smaller than those of the first nominal load case.

Thermal accidental load conditions may happen if the enclosure cannot be closed during daytime. To simulate these cases the heat flux of the sun radiation has been applied in a simplified linear way by calibrating the external heat flux and the convection coefficient such to obtain in an equivalent pipe model the maximum measured temperature in the pipe experiment described in section 5.4.1.3.

Figure 9-60 shows a typical temperature distribution due the sun radiation direction at 60° altitude and 0° azimuth angle. The ambient temperature is 20 °C and the telescope is pointing to zenith. The maximum temperature is calculated to be 41 °C which complies with the highest average temperature measured in the pipe experiment on Paranal. The colder (blue) parts of the structure are located in the shadow of M1 and M2 which is taken into account in the analysis. As displayed in the deformation plot in Figure 9-61 this unsymmetric load scenario causes a global tilt of 45 arcsec of the secondary mirror unit with a maximum displacement of 27 mm in vertical direction. The differential displacement between M1 and M2 is 22 mm. which is confirmed by an equivalent hand-calculation assuming a temperature change of 20 °C in the structure between M1 and M2 (length 96 m).The resulting equivalent stresses in the framework structure are shown in Figure 9-62 with a maximum value of 163 MPa. Like in the other load cases the general stress level is fairly low and the peaks occur only in the overconstrained regions already mentioned before. The worst case tensile stress calculated for the structural ropes is 47 MPa due to thermal loading.

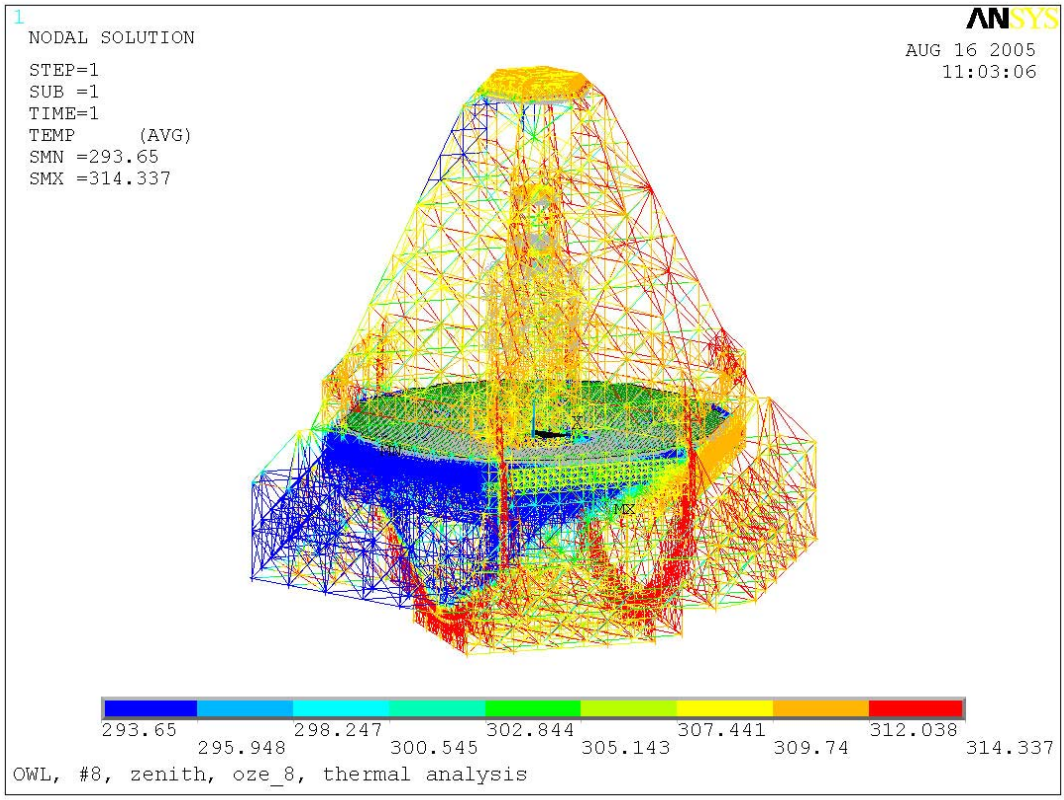

Figure 9-60: Temperature distribution due to sun radiation at 60° altitude angle.

For all load cases investigated until now a maximum stress of 182 MPa has been calculated. which is still below the allowable limit stress even under several conservative assumptions appearing simultaneously.

The overall maximum relative displacement between M1 and M2 is 25 mm for an altitude angle of 30° and a sun direction angle of 60°. This error occurs during the day and doesn't need to be compensated as long as the segment phasing is kept.

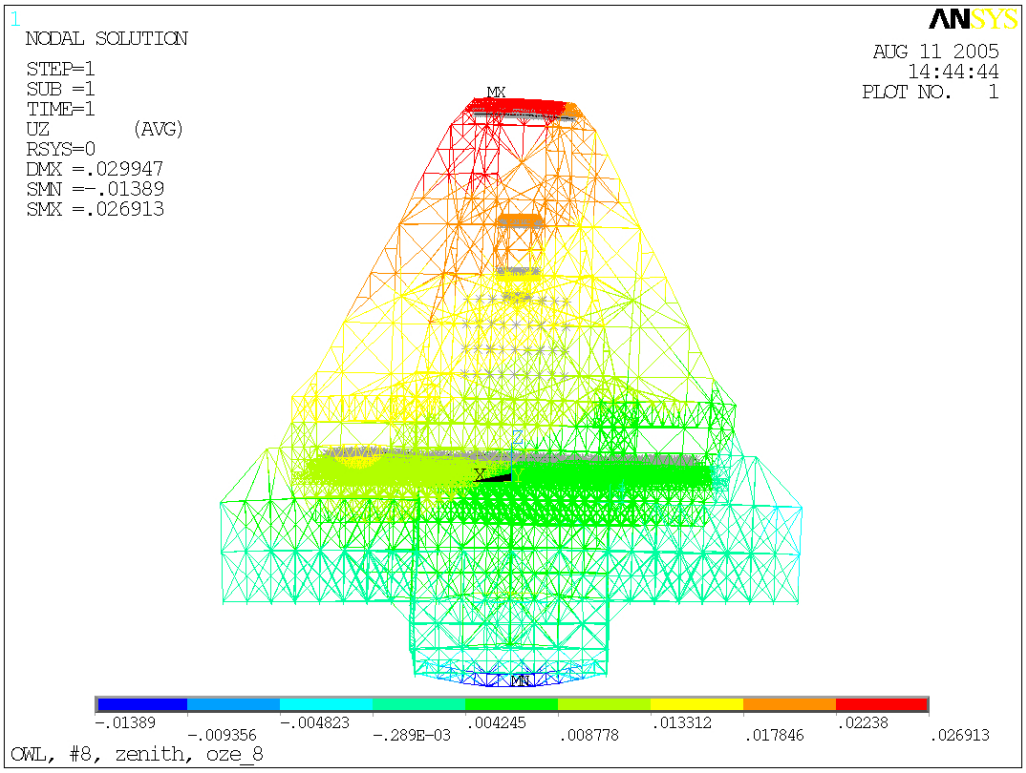

Figure 9-61: Vertical (uz) displacement distribution due to sun radiation at 60° altitude angle.

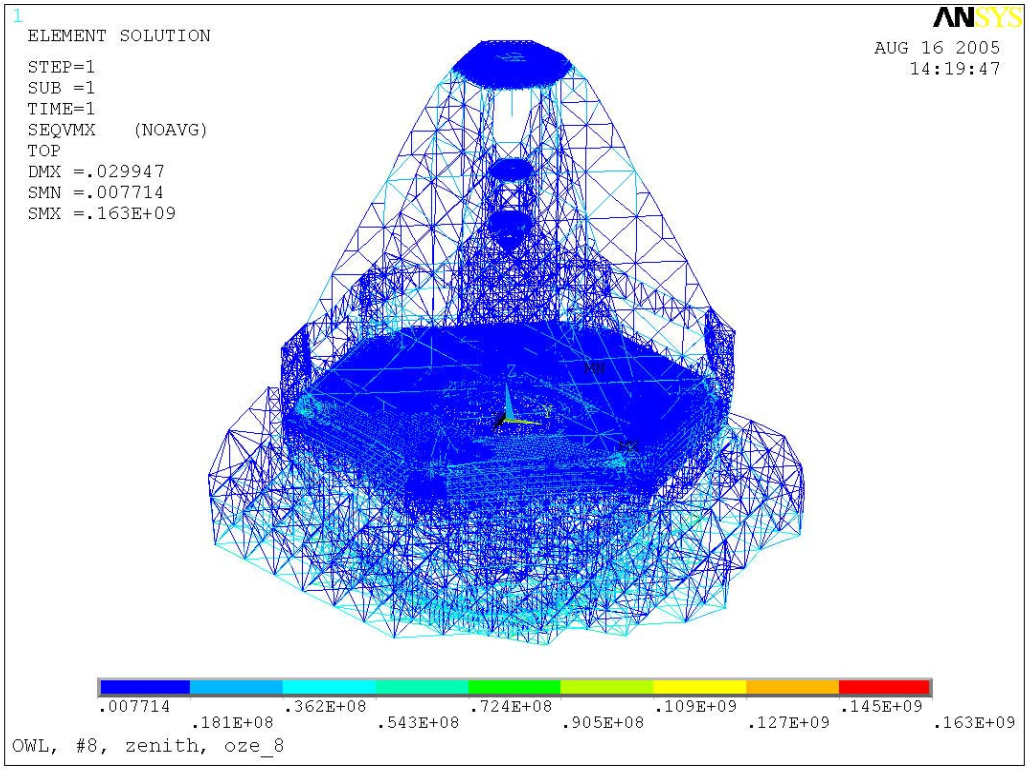

Figure 9-62: Equivalent stress distribution due to sun radiation at 60° altitude angle.

9.5.4 Dynamic Analysis

The basic scope of the dynamic analyses is to predict the dynamic behaviour of the telescope structure. The modal analysis aims at calculating the natural frequencies and mode shapes. The dynamic wind load analysis described in this section is able to evaluate the open loop response of the optical subsystems in terms of global RMS deformation due to the wind load spectrum defined in section 5.4.1.1

9.5.4.1 Modal

In order to assess the response to dynamic loading and the bandwidth limitations for the various control systems of OWL. it is important to calculate the eigenfrequencies. mode shapes and corresponding effective masses of the OWL structure. Therefore. modal analyses have been carried out with the global 2004 FE models for various altitude configurations. The lowest 2000 modes have been calculated for the zenith configuration to cover frequencies up to 16.8 Hz. Until now 700 modes (~11 Hz) have been computed for the other configurations. A summary of the predominant eigenfrequencies. effective masses and mode shapes is provided in Table 9-16.Table 9-17 and Table 9-18 for the 0º. 30º and 60º altitude configurations. respectively.

Mode	**Frequency**	**Effective mass / inertia in % of total**						**Mode shape**
		MX	MY	MZ	IXX	IYY	IZZ	
1	1.59	67	-	-	-	2	-	Cross elevation
2	**2.58**	**-**	**30**	**-**	**29**	**-**	**-**	**Altitude locked rotor**
3	**2.86**	-	-	-	-	-	**44**	**Azimuth locked rotor**
6	3.67	-	35	-	12	-	-	2nd alt. locked rotor (counter motion)
7	3.93	**-**	**-**	11	**-**	**-**	**-**	Piston M2
9	**4.03**	-	-	**46**	-	-	-	**Piston altitude structure**
260	**7.32**	-	-	**0.1**	-	-	-	**Piston M2 unit structure**

Table 9-16: Eigenfrequencies and effective masses of zenith configuration.

Mode	**Frequency**	**Effective mass / inertia in % of total**						**Mode shape**
		MX	MY	MZ	IXX	IYY	IZZ	
1	1.55	67	-	-	-	2	-	Cross elevation
2	**2.49**	**-**	**27**	**-**	**31**	**-**	**-**	**Altitude locked rotor**
3	**2.92**	**-**	**-**	**-**	**-**	**-**	**42**	**Azimuth locked rotor**
6	3.83	-	30	3	10	-	-	2nd alt. locked rotor (counter motion)
7	**3.92**	**-**	**-**	**47**	**-**	**-**	**-**	**Piston Altitude structure**

Table 9-17: Eigenfrequencies and effective masses of 30 º configuration.

Mode	**Frequency**	**Effective mass / inertia in % of total**						**Mode shape**
		MX	MY	MZ	IXX	IYY	IZZ	
1	1.56	67	-	-	-	2	-	Cross elevation
2	**2.06**	-	28	1	32	-	-	**Altitude locked rotor**
3	**2.83**	-	-	-	-	1	**39**	**Azimuth locked rotor**
6	**3.63**	**-**	**18**	**28**	**28**	**-**	**-**	**Piston and Altitude bending**
7	3.78	-	14	22	22	-	-	2nd piston and alt. rotor (counter m.)

Table 9-18: Eigenfrequencies and effective masses of 60 º configuration.

The lowest natural frequency for all configurations is the cross elevation mode at about 1.6 Hz. which is a lateral motion of the Altitude structure along the altitude axis. This mode is dominated by the stiffness around the altitude cradles and has been already increased significantly by changing the design topology in this region in the 2005 model. The most important modes in terms of main axis controllability are the locked rotor frequencies about the altitude and azimuth axis. respectively. While the Azimuth locked rotor frequency is above 2.8 Hz for all configurations. the Altitude locked rotor frequency decreases from 2.58 Hz at zenith down to 2.06 Hz at 60º from zenith. This performance reduction is caused by the reduced number of altitude bogies in contact. The lowest piston mode of the M2 structure is calculated to be 3.9 Hz for the zenith and 3.6 Hz for the 60º configuration. The piston mode of the M2 unit structure occurs at 7.3 Hz in the zenith configuration and will be excited by the wind load. The mode shapes of the predominant eigenfrequencies for zenith configuration are shown in Figure 9-63. Figure 9-64. Figure 9-65 and Figure 9-66. respectively. As already mentioned a significant improvement of the dynamic performance in terms of locked rotor eigenfrequencies has been obtained. i.e. more than 20 % frequency increase compared to the former design iteration (2002).

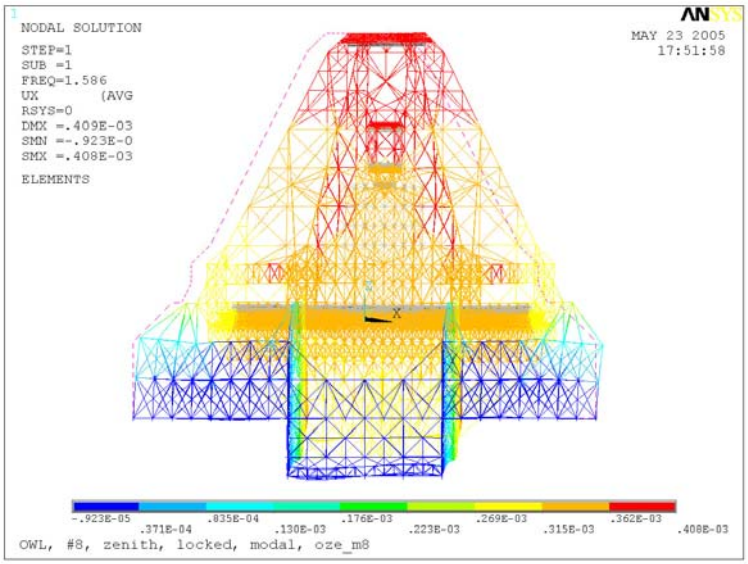

Figure 9-63: Mode shape of first eigenfrequency in zenith configuration at 1.59 Hz.

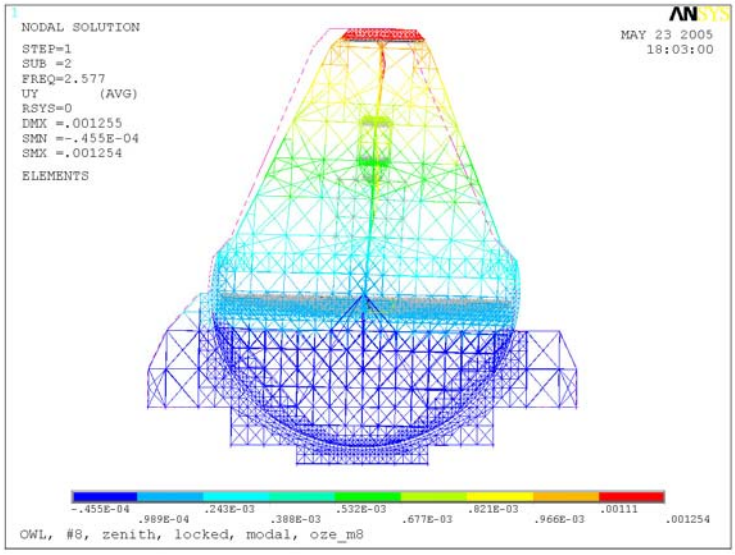

Figure 9-64: Altitude locked rotor mode shape in zenith configuration at 2.58 Hz.

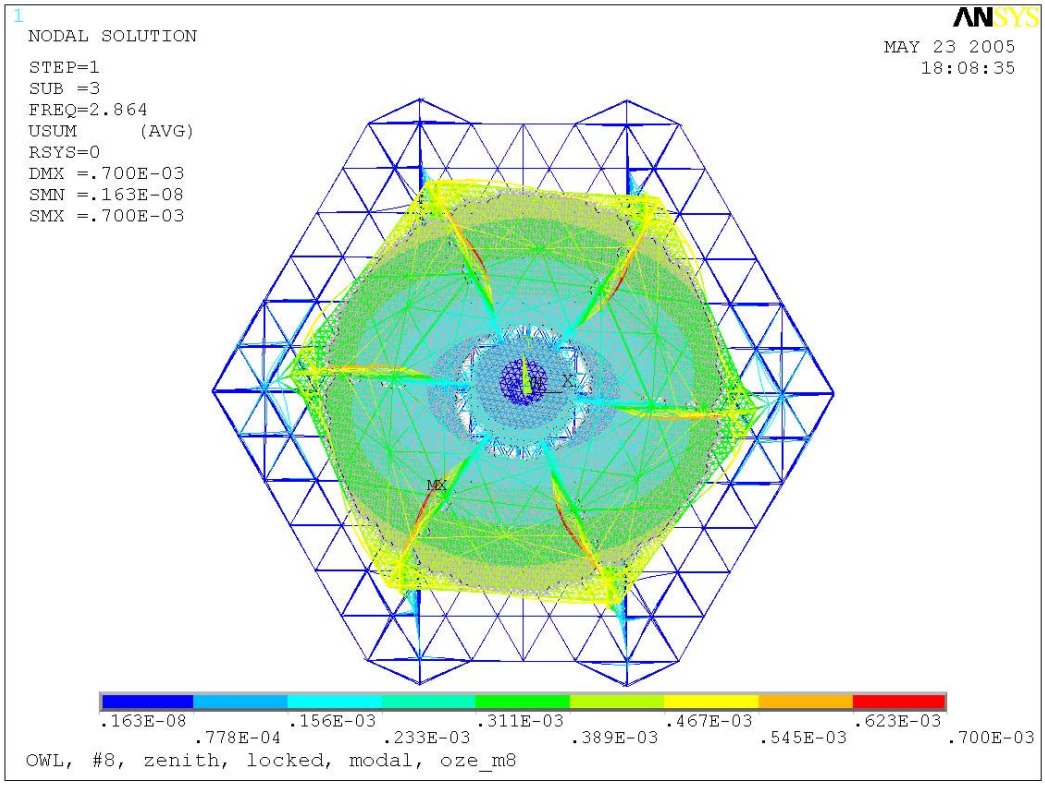

Figure 9-65: Azimuth locked rotor mode shape in zenith configuration at 2.86 Hz.

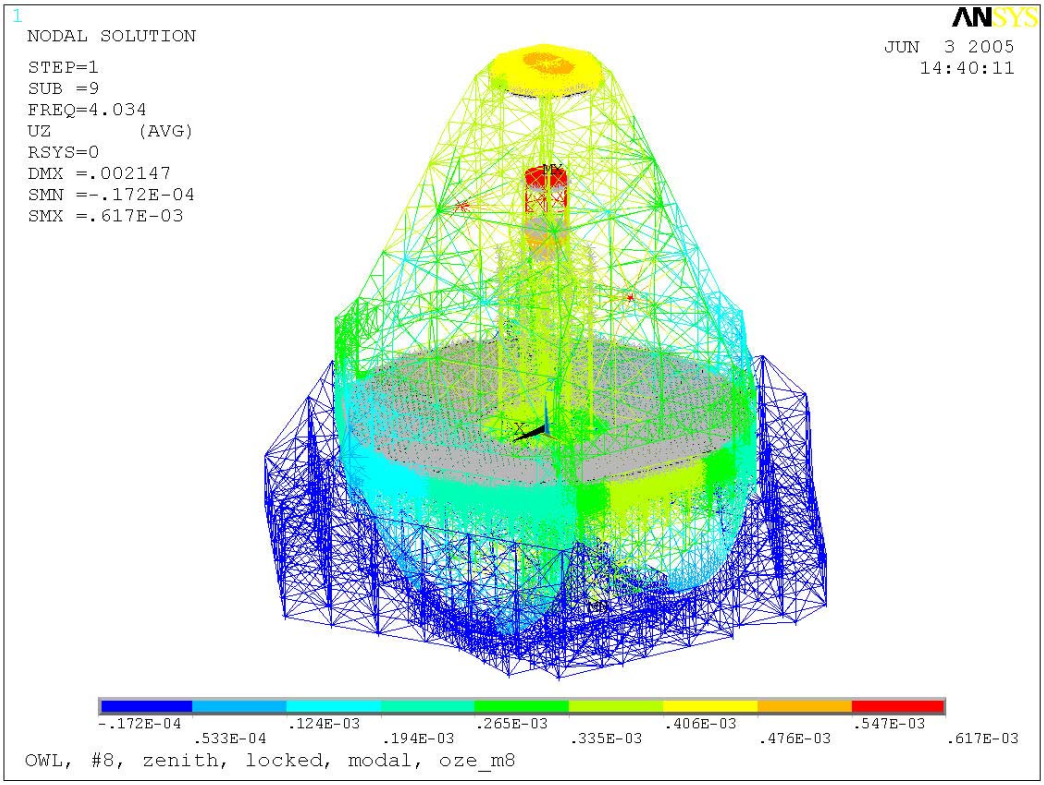

Figure 9-66: Piston mode of altitude and corrector structure at 4 Hz.

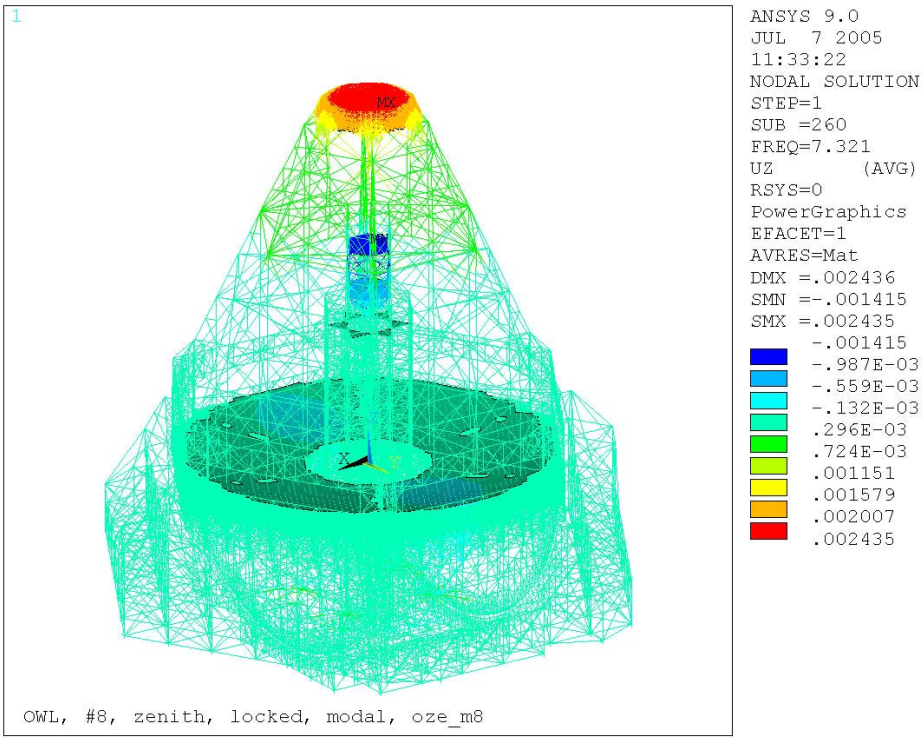

Figure 9-67: Piston mode of M2 unit structure at 7.3 Hz.

In order to evaluate the dynamic behaviour of the M1 and M2 cell structures. the corresponding parts of the global FE model have been extracted and modal analyses performed. The M1 cell structure has been fixed at the altitude bogies and the main bearings and the M2 cell structure at the interface to the upper interface part of the altitude framework structure. Both the models are shown in Figure 9-68.

Figure 9-69 displays the lowest piston mode of the M1 cell structure alone. It forms a kind of spherical shape and occurs at 5.1 Hz. This mode corresponds to the 4 Hz piston mode computed in the global model. The lowest piston mode of the secondary mirror cell structure alone occurs at 7.75 Hz forming a spherical shape. The corresponding mode of the global model occurs at 7.3 Hz

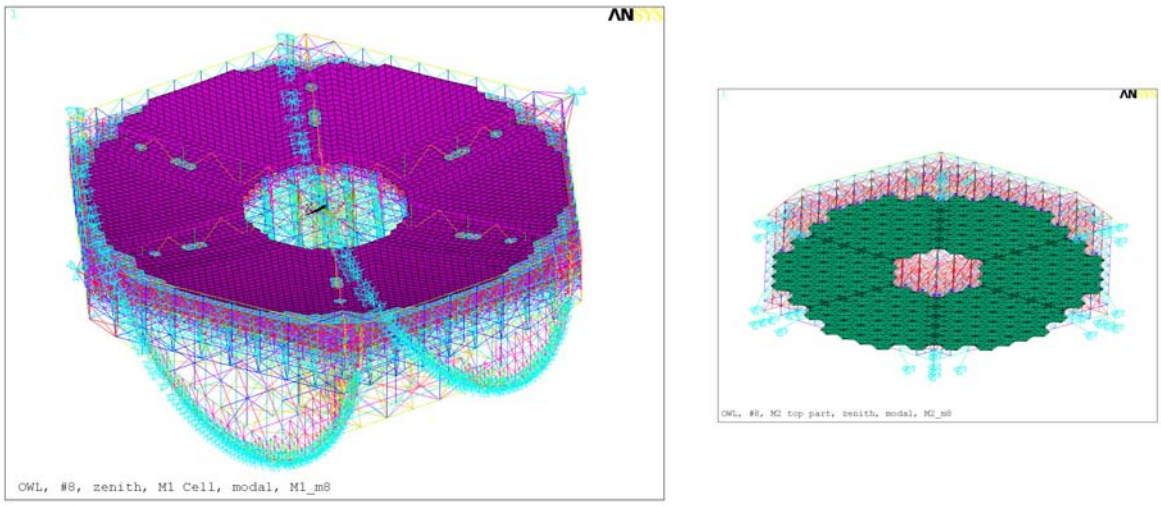

Figure 9-68: FE models of M1(left) and M2 cell (right) structures. respectively.

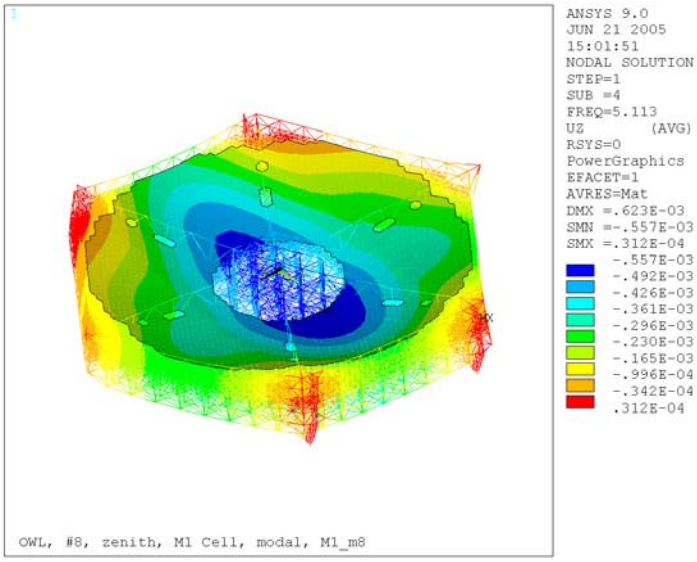

Figure 9-69: Piston mode of M1 Cell structure alone at 5.1 Hz.

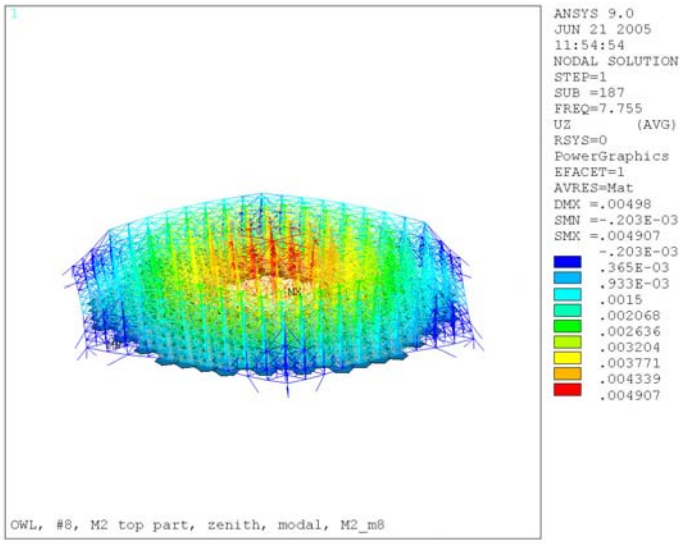

Figure 9-70: Piston mode of M2 cell structure alone at 7.8 Hz.

Figure 9-71 shows the natural frequencies versus the mode number for the zenith configuration. The 2000 frequencies are closely spaced and distributed in the range between 1.6 and 16.8 Hz. The first flat plateau represents about 200 modes at 6.3 Hz with very small effective mass contributions. The second plateau occurs at about 8 Hz and covers about 40 modes. All these modes are related to local rotational oscillations of the M2 mirror segments about the vertical axis and are caused by missing restraining devices in the model. These devices will be implemented in the next update of the FE model. Most of the modes above 14.6 Hz (mode 833) are local bending modes of the beams that represent in a simplified way the whiffle tree supporting structure of the M1 segments. Therefore. only a small frequency increase above 14.6 Hz is recognized. Since these (cantilever) beams are underestimating the lateral stiffness connection of the M1 segments. a more accurate modelling will be carried out in the next phase. Nevertheless. these modelling deficiencies have negligible influence on the FE analysis results presented herein.

The diagram in Figure 9-72 displays the three effective mass components associated with each frequency. It can be seen from this diagram and from the effective mass tables. that the first 10 modes (4.1 Hz) contain more than 50 % of the accumulated effective mass in all three

directions. The effective masses for frequencies up to 10 Hz (first 400 modes) accumulate in the three component directions to 78 %. 75 % and 63 %. respectively. The additional effective mass increase achieved for the modes between 400 and 2000 is only 8 % in all component directions.

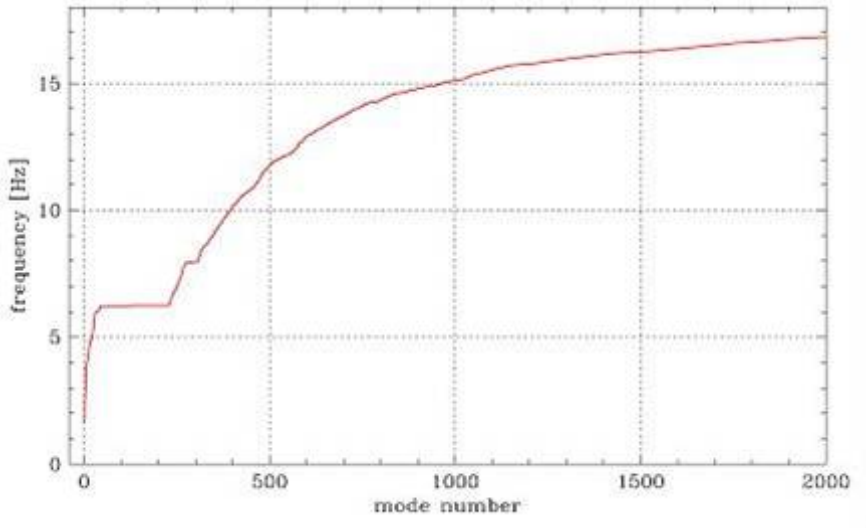

Figure 9-71: Natural frequencies versus mode number.

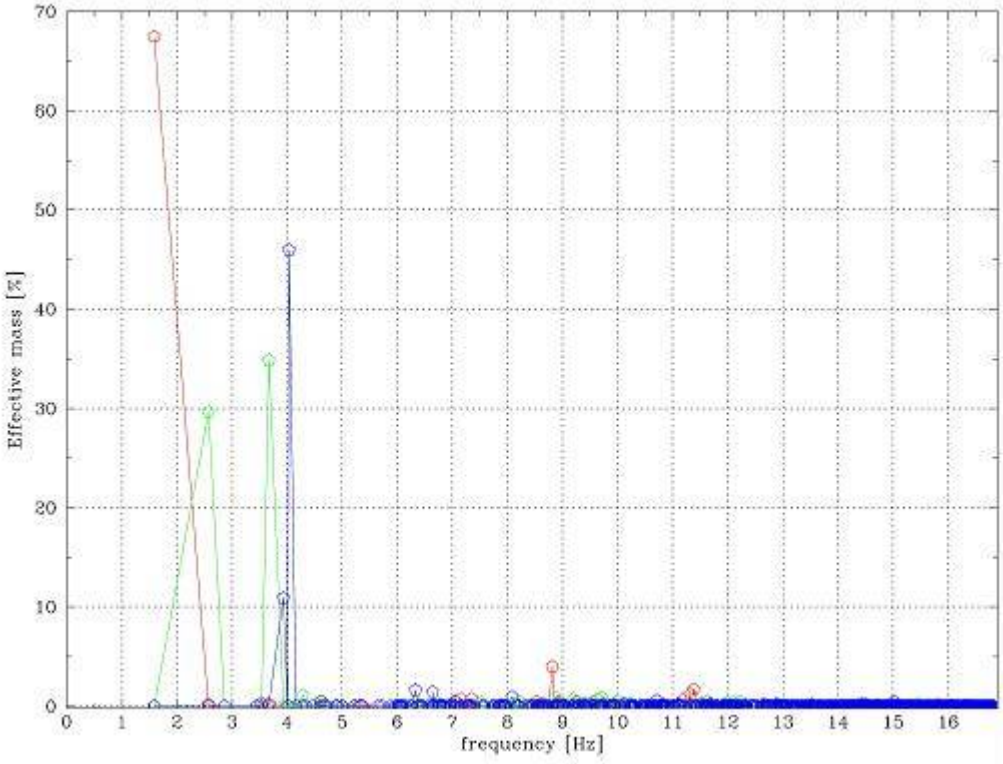

Figure 9-72: Effective masses versus frequency.

9.5.4.2 Dynamic Wind Load

The scope of the analysis study presented in this section is to investigate the global (macro scale) effect of the dynamic wind load contribution on the deformations of the segmented mirrors M1 and M2. respectively. The local (micro scale) dynamic behaviour between individual segments has been studied as well by applying the appropriate wind load to individual segments only by increasing the number of loaded segments stepwise. As the analyses account for frequencies up to 10 Hz. results represent the behaviour of the supporting M1 and M2 cell

structures. The much higher eigenfrequencies of the segment supports are not considered. The results have to be interpreted as open loop response to dynamic wind load excitation. They are indicative and form a conservative limit of the expected displacements which have to be corrected by the control loops. For the assessment of the effect of the wind disturbance on the closed loop phasing error it is referred to the appropriate simulations described in section 7.5.

The dynamic wind load characterization as defined in section 5.4.1.1 forms the load scenario for the Random Vibration analyses of the global FE model of OWL. This analysis method is used in place of time-history analysis to determine the response of a structure to random or time-dependent loading conditions such as wind loads. This technique allows evaluating statistics of the mirrors' deformation shapes and frequency dependant amplitudes. The Random Vibration analysis procedure is probabilistic in nature and is based on computing statistics of each modal response and then combining them. Using the theory of random vibrations. the response displacement PSD can be calculated from the input pressure PSD. With this response statistical output data like mean square response and 1σ values are derived.

9.5.4.2.1 Macro scale wind effect on segmented mirrors

Until now the zenith configuration of the 2004 FE model has been investigated by assuming the pressure load scenario of the 60° configuration which is considered to be the worst case wind load (see section 9.5.2.2). The wind load pressure has been applied only to the segmented mirror surfaces M1 and M2. The effect of the dynamically loaded framework structure will be studied in a later phase. The modal response is obtained from the modal analysis results for the lowest 400 modes that represent all frequencies up to 10 Hz. Based on the modal response and the input pressure PSDs the Random Vibration analysis has been performed by combining those modes which exceed a certain threshold value of their covariance ratio. i.e. the more the modes are separated the smaller are their contributions due to the interaction between them.

The following analysis assumptions have been used:

- For each mirror surface uniform input PSDs were applied to all nodes.
- The pressure PSDs applied to M1 and M2 are described in section 5.4.1.1. They take into account different wind velocities on M1 (10 m/s) and M2 (14 m/s) according to the wind profile and are fully correlated within each mirror.
- The pressure PSDs of M1 and M2 are uncorrelated to each other.
- For the calculation of the pressure PSD a conservative pressure (drag) coefficient of 1.0 was used.
- Constant damping ratio of 1 % to the full structure.

The distribution of the mirrors' surface deformation over the simulated frequency range has been evaluated in terms of the standard deviation 1σ. The contour plot in Figure 9-73 represents the 1σ deflection of M1. It is very similar to the mode shape of the main piston mode at 4 Hz and superimposed by a global tilt caused by the altitude locked rotor mode at 2.6 Hz. This behaviour is confirmed by the 1σ response PSD plot of the maximum and minimum displaced nodes of M1 as shown in Figure 9-75. The M1 deflections are clearly dominated by the main piston mode. whereas the highest peak in the M2 curve occurs at about 7.3 Hz which represents the piston mode of the M2 unit structure (see Figure 9-74). The locked rotor mode at 2.6 Hz is clearly visible on M1. but appears only marginally on the M2 curve (see Figure 9-76).

A comparison of the 1σ surface deflections of M1 and M2 for various frequency bands is summarised in Table 9-19. Due to the high wind energy content in the low frequency range the low band up to 1 Hz contains by far the highest contribution of 16.4 μm for M1 and 51 μm for M2. respectively. The open loop 1σ displacements for frequencies between 1 and 5 Hz become 304 nm for M1 and 1.4 μm for M2. It should be noted. that these deflections are of global nature and are supposed to be corrected mainly by the non-segmented mirrors.

Independent hand-calculations of the 1σ response PSDs agree quite well with the FE Analyses results for frequency bands up to 5 Hz. Higher frequencies are hardly comparable. because the hand calculation structure is based on a single spring-mass system with the locked rotor resonant frequency at 2.6 Hz for M1 and the main piston frequency at 3.9 Hz for M2.

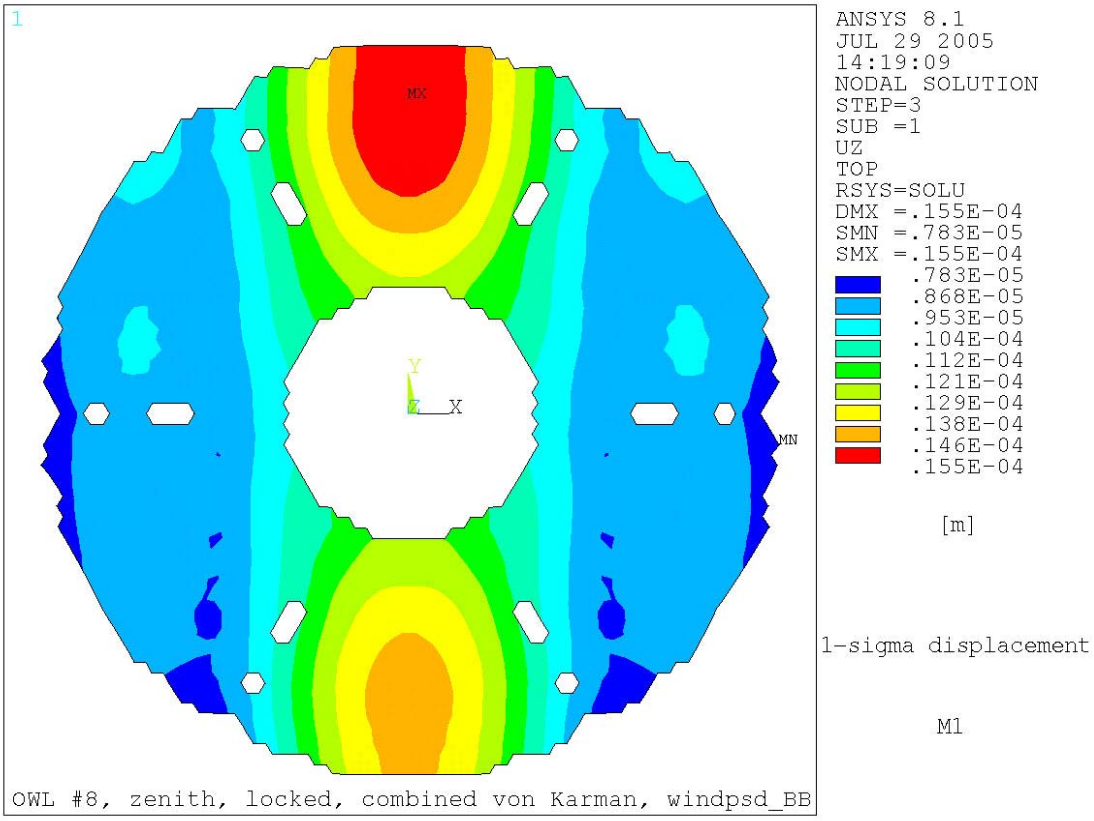

Figure 9-73: 1σ normal displacement distribution of M1.

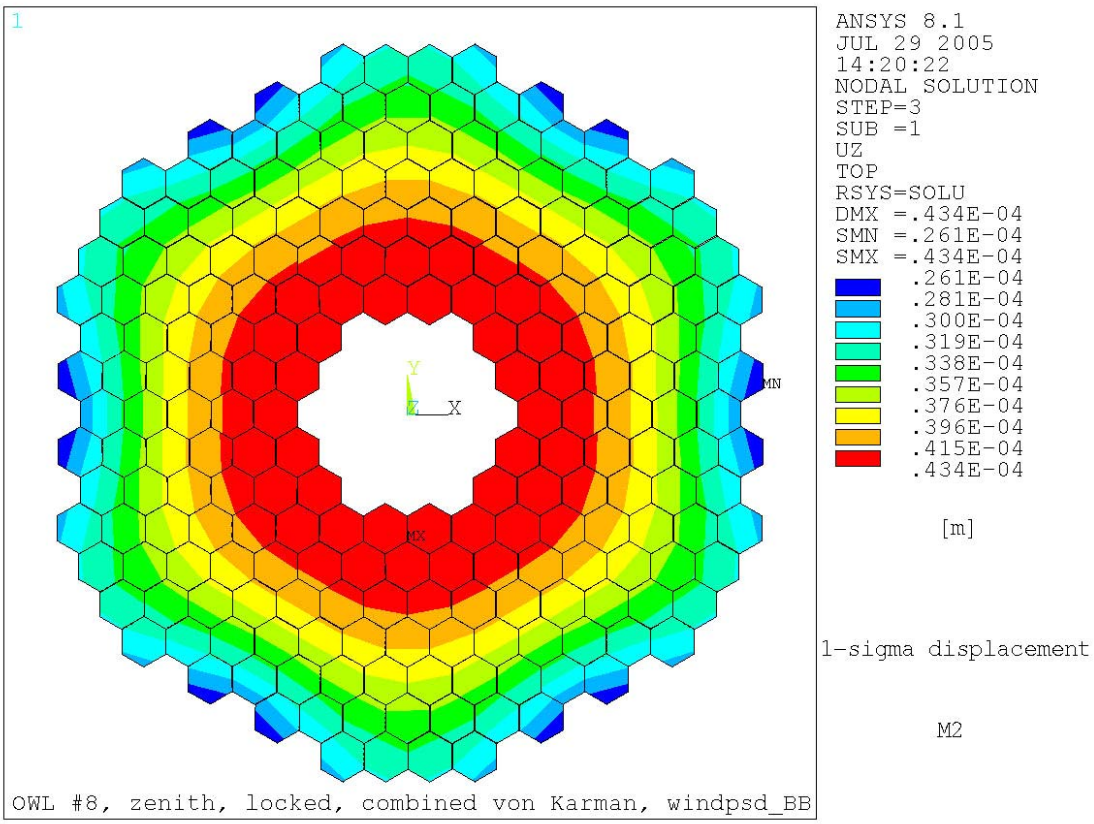

Figure 9-74: 1σ normal displacement distribution of M2.

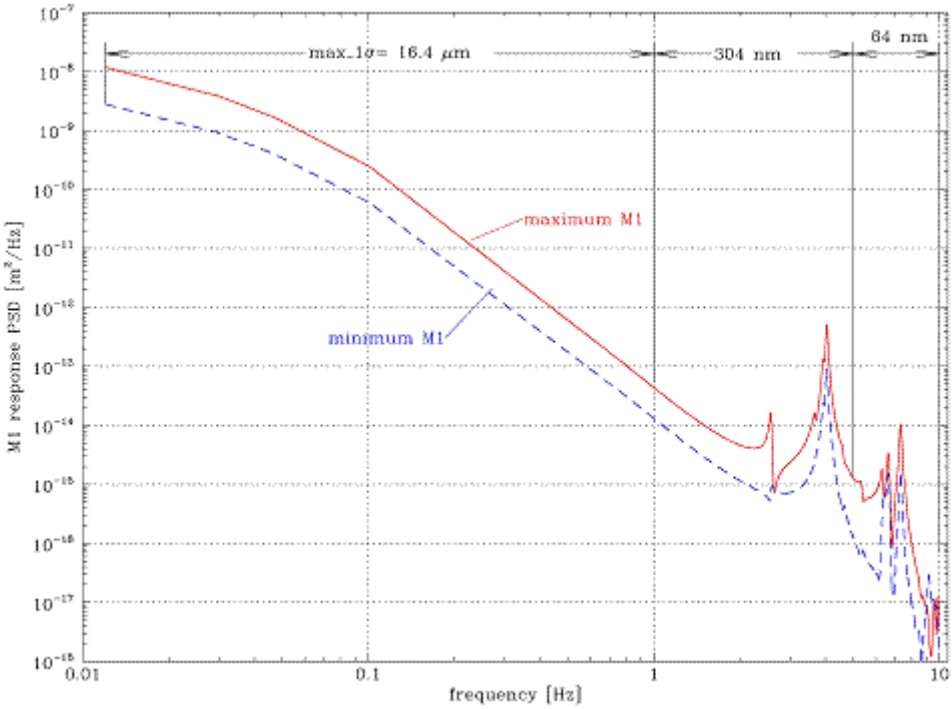

Figure 9-75: 1σ response PSD of piston displacement of M1

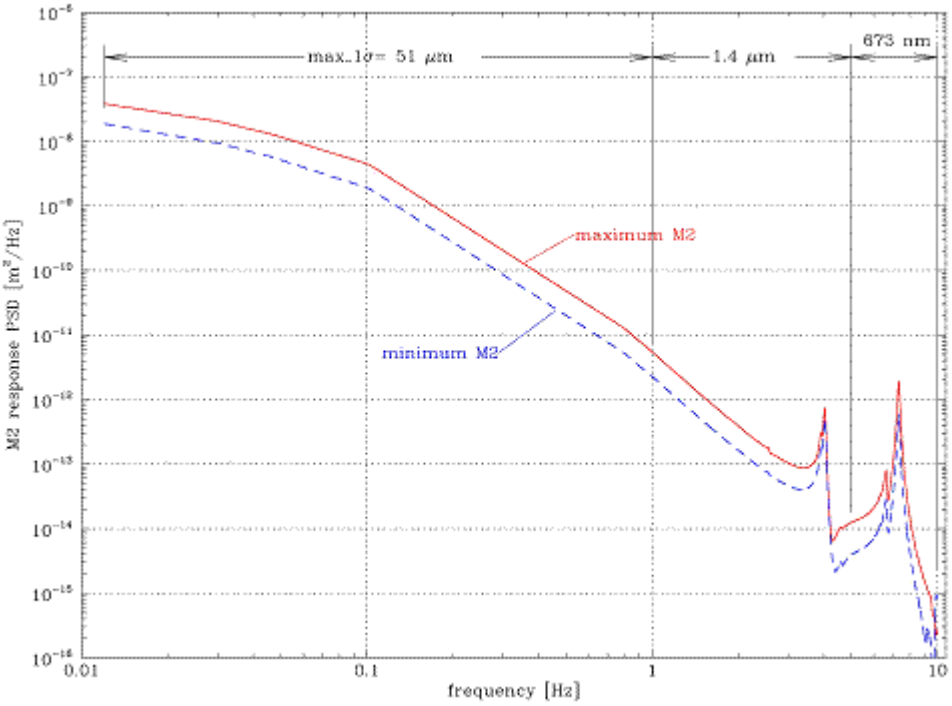

Figure 9-76: 1σ response PSD of piston displacement of M2.

Mirror	**1σ displacement in [μm]**			
Frequency range [Hz]:	0.012 to 1	1 to 5	5 to 10	full range
M1 (v_{mean}=10 m/s)	16.4	0.304	0.064	16.4
M2 (v_{mean}=14 m/s)	51.0	1.408	0.673	51.0

Table 9-19: 1σ maximum piston displacement of M1 and M2 due to von Karman wind load spectra applied to complete mirrors area.

9.5.4.2.2 Micro scale wind effect on phasing error

In order to assess the differential piston between two segments (phasing error measured by the segment edge sensors) under wind load. a series of PSD analysis has been carried out by loading only part of the M1 and M2 segments with the appropriate wind force spectra. Starting with the loading of only one segment the loaded area was stepwise increased until the full M1 and M2 area was loaded. For each analysis run the input PSD spectra were adapted to the loaded area in terms of the aerodynamic attenuation. The appropriate input PSD spectra applied for M1 and M2 are described in section 5.4.1.1.1.2. All the segments piston values have been compared with their neighbour segments to evaluate the maximum differential piston. Hence. this value can be interpreted as the maximum expected open loop 1σ phasing error. The resulting maximum differential 1σ piston displacements between two M1 and two M2 segments. respectively are summarised in Table 9-20 for various frequency bands. The associated absolute piston displacements are listed as well.

The absolute segment piston of M1 becomes 239 nm for frequencies between 1 and 5 Hz. whereas the differential piston becomes in the worst case only 16 nm for the same frequency band. For the frequency range between 5 and 10 Hz the differential piston is calculated to be only 3 nm. This is also an indication. that local modes of the M1 cell structure underneath the mirror segments are only slightly excited by frequencies below 10 Hz. To further illustrate these results the response PSD of the absolute and differential displacements for the worst case are shown in Figure 9-77. It represents a loaded area of 836 m^2. i.e. 75% of a 60° petal of M1. The response PSD demonstrates. that the energy content of the frequencies above 5 Hz is fairly small.

The resulting 1σ piston displacements of the M2 segments are much higher than those of the M1 segments. In the frequency range between 1 and 5 Hz the absolute piston becomes 1.46 µm and the differential piston about 210 nm in the worst case. For frequencies between 5 and 10 Hz the maximum differential piston is calculated to be 110 nm. This value is obtained when the full M2 area is loaded. It is obvious from the appropriate PSD response displayed in Figure 9-78. that the M2 unit piston mode at 7.3 Hz is significatnly excited and is the main contributor to this response.

Hence. the main reasons for the larger displacement response of M2 compared to M1 are the higher wind load (twice as high) and the lower stiffness of the M2 cell structure. To improve this situation. several design measures can be taken and will be investigated in the next phase:

- Improve the stiffness of the M2 cell structure to increase the M2 unit piston frequency.
- Use Silicon Carbide mirror segments.
- Include passive or active damping.

	1σ displacement in [µm]		
Frequency range [Hz]:	0.012 to 1	1 to 5	5 to 10
Absolute segment piston M1	13.8	0.239	0.037
Differential piston between segments M1	0.922	0.016	0.003
Absolute segment piston M2	37.3	1.463	0.659
Differential piston between segments M2	5.7	0.210	0.110

Table 9-20: 1σ maximum displacements of M1 and M2 segments (part of the mirror area loaded).

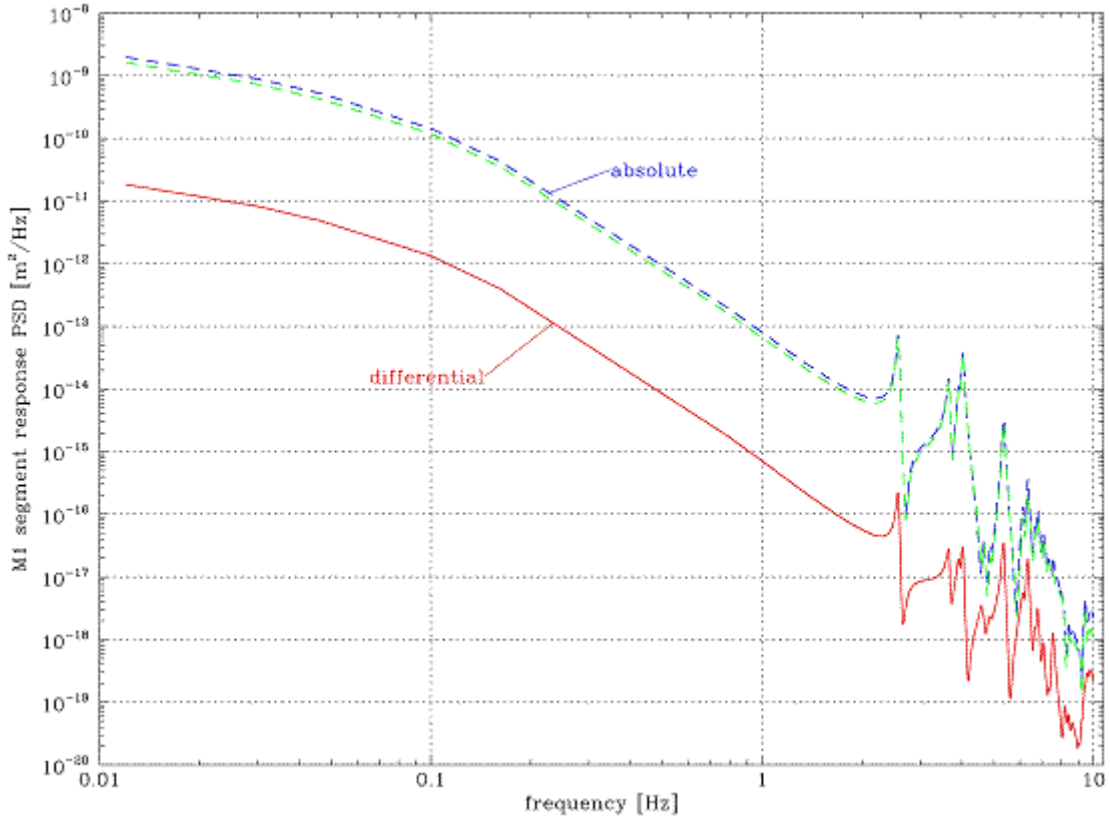

Figure 9-77: 1σ response PSD of segments piston displacement of M1.

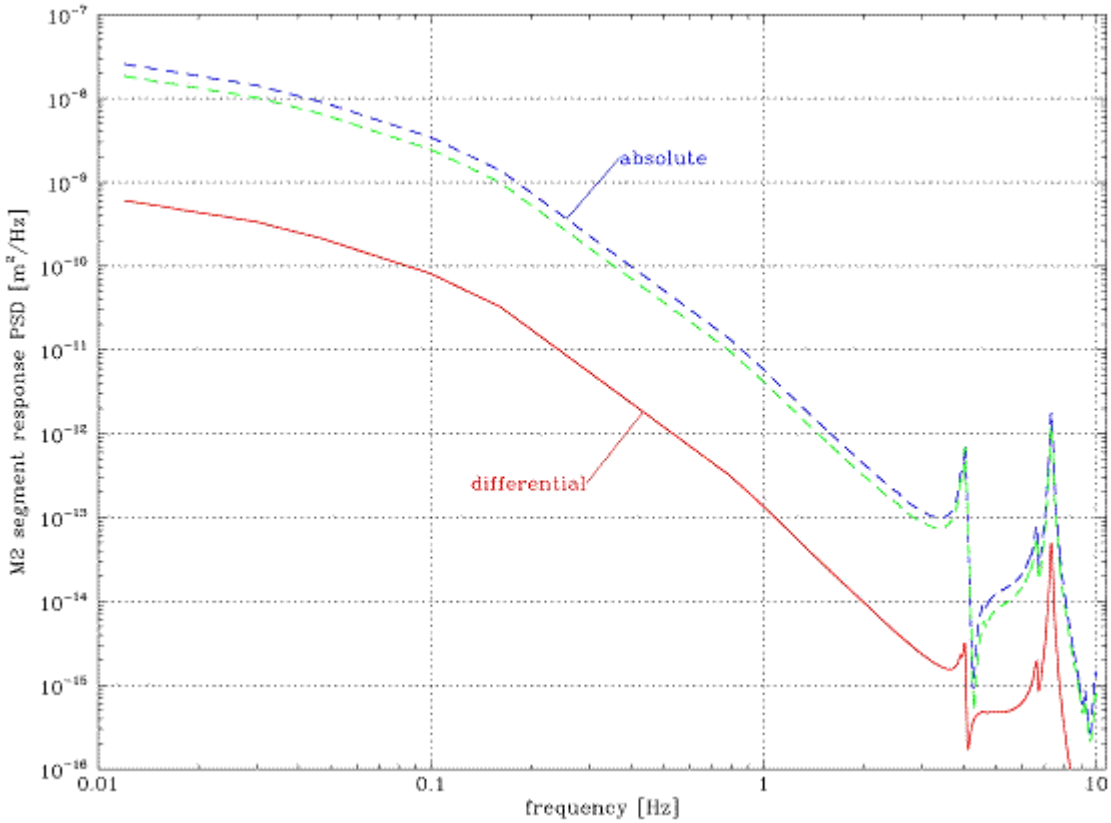

Figure 9-78: 1σ response PSD of segments piston displacement of M2.

An independent hand-calculation of the 1σ response PSDs of a single spring-mass system simulating the stiffness of a single M1 segment cell structure compares very well with the appropriate FE Analysis result.

In section 7.5.5 control loop simulations of individual mirror segments under dynamic wind loading are carried out to evaluate the closed loop phasing error assuming a single spring-mass system for the M1 cell structure (equivalent to the locked rotor frequency of 2.6 Hz). It is foreseen to simulate the phasing error by including the full dynamics of the telescope structure (e.g. M1 and M2 cell) in terms of the reduced state space model.

9.5.4.3 Effect of soil and foundation

In general the response of the soil influences the motion of the structure and the response of the structure influences the soil motion. The importance of this so-called soil-structure interaction depends on numerous parameters like soil material properties. structure mass and stiffness and foundation size. just to name some of them. The effect of the soil-structure interaction on the dynamic performance of OWL has been investigated depending on various soil properties and telescope foundation thicknesses. because the telescope site and its soil properties have not yet been chosen. For this purpose part of the soil and foundation structure has been modeled and attached to the 2002 OWL FE model. Focussing on changes in the modal properties of the telescope and changes in the influence of disturbances onto mirror positions. these dynamic effects are investigated applying the Finite Element Method in combination with a typical range of possible soil properties. Static strength considerations are out of the scope of these simulations. but must especially be considered for dimensioning the telescope foundation.

Soil shows in general a very non-linear and inhomogeneous behaviour. Assuming linear properties is a simplification. which is only valid for very small amplitudes of displacements and forces. The interaction between soil and telescope means firstly a finite stiffness for the foundation. but moreover energy transport by mechanical waves from the telescope to the ground and vice versa. Applying the FE method only a finite domain of soil can be included requiring appropriate transmitting boundary conditions at the artificial bounds. which means a matching of the local impedance properties at the boundaries. which do not exist in reality. To match this impedance. each boundary node is connected to a discrete damper with damping constants $d_{ni}=\rho c_P A_i$ and in the tangential plane with $d_{ti}=\rho c_S A_i$ (where A_i is the equivalent boundary area represented by node I. ρ is the density and c_P and c_S are the wave velocities for compression and shear waves. respectively).

Modelling the soil in sufficient resolution requires on one hand to use at least 6 FE-nodes per wavelength. On the other hand the transient boundary should be applied at least one wavelength distant from the source of radiation. in this case the telescope. This results in a modelled soil-cylinder of 150m height and 450m diameter. which corresponds to about three times the telescope dimensions (see Figure 9-79). Since most of the important modes are symmetric along the symmetry plane perpendicular to the altitude axis. only half of the structure has been modelled.

At present only the general effects are investigated assuming homogeneous soil properties covering the field from soft and light tuff stone (Young's modulus E=500 MPa) up to very stiff basalt or granite (E=80000 MPa). In addition to that. a quasi-rigid soil is modelled (E=1000000 MPa). which aims at representing the reference conditions used in the telescope global FE model (see section 9.1).

Since the telescope distributes its load onto a large area of ground. the effective stiffness of the soil is considerably higher than the one of the telescope. Under static wind load conditions and for soft tuff stone the deflection of M1 and M2 is increased by 3.3% and 1.8%. respectively. Therefore. these deflections are dominated by the flexibility of the telescope. (For massive basalt or granite rock the soil stiffness can be fully neglected.)

Adding the soil and foundation to the telescope model introduces –in addition to the telescope modes– pure ground modes (without any elastic deformations of the telescope) and mixed modes with deformations of both the telescope and the ground. The ground dominated eigenfrequencies depend on the structural soil properties. the size of the modelled soil volume and the boundary conditions. (Lower stiffness. higher density and larger volume of modelled soil

tend to decrease the eigenfrequencies.) For a sufficiently large modelled volume. the ground modes start already below the telescope eigenfrequencies.

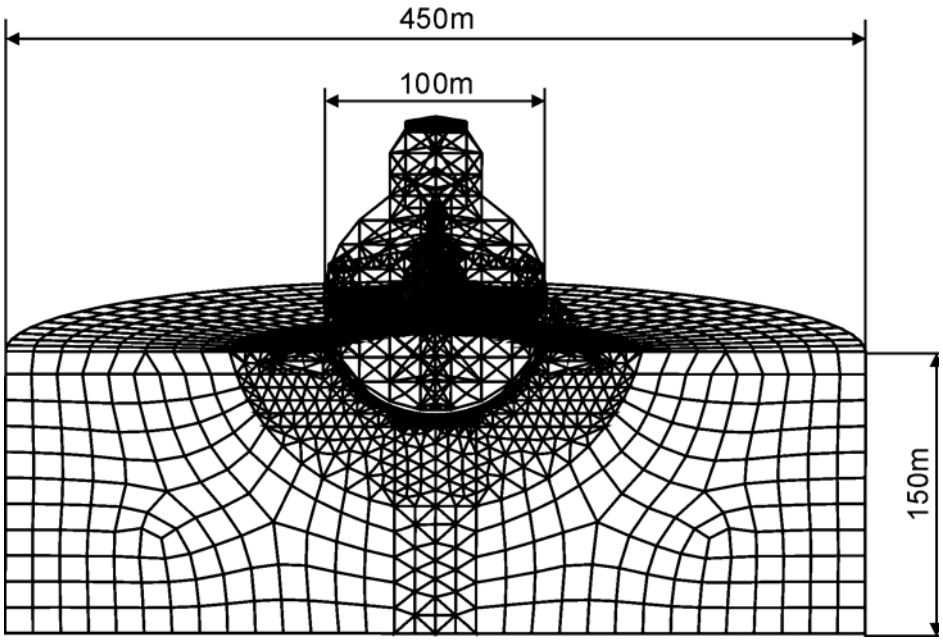

Figure 9-79: FE-model and major dimensions of the OWL with foundation and soil.

In order to better assess the influence of the soil under typical load conditions. the transfer functions due to wind load distribution have been calculated for different models. As can be seen in the transfer functions in Figure 9-80 the difference in terms of the horizontal displacement of the primary mirror between the extreme models is not significant. The models represent quasi-rigid soil and fixed boundaries (dash-dotted line) and very soft soil (tuff stone) and non-reflecting boundary conditions (solid line)**.** Both graphs are very similar and the maximum difference between the transfer functions is in the order of 1/10 of the peak amplitude. i.e. the transfer function is only slightly influenced by the soil. For stiffer soil properties. these effects are even smaller and diminish fully for massive rock like basalt or granite.

Based on the investigation of the soil-structure interaction of OWL it can be concluded that only a small dynamic effect of the ground can be expected within the range of the material parameters for the soil under research. It is expected that this conclusion is also valid for the actual baseline design of the 2004 OWL model. because its mass and modal properties are in the same order of magnitude as the previous model used for this study.

The influence of the foundation thickness variation in the range of the analysed values of 1.5. 3 and 6m is very small. The main reason is the relatively light telescope structure and the large area the telescope is supported on. which results in a mean ground pressure of 12 kN/m^2 only. Thus in relation to the telescope specific stiffness the foundation specific stiffness is high and the total deformations are dominated by the telescope flexibility. As the telescope mass is only 0.02%-0.04% of the soil volume modelled. telescope vibrations will involve ground vibrations of only very small amplitude. Though. this implies also nearly no radiation of energy out of the telescope structure into the foundation. which would cause an additional damping effect. The theoretical effect of the soil stiffness on the natural frequency of the system as illustrated in [35] complies well with the predictions of the FEA. e.g. a soil Young's modulus of 500 MPa corresponds to a frequency ratio[67] of 0.96 and a soil Young's modulus of 2000 MPa corresponds to a frequency ratio of 0.99.

More details of the study about the dynamic effects of ground and foundation can be found in RD36.

[67] Frequency ratio is the ratio between the natural frequency of the soil-structure system and the "fixed-base" system (rigid soil).

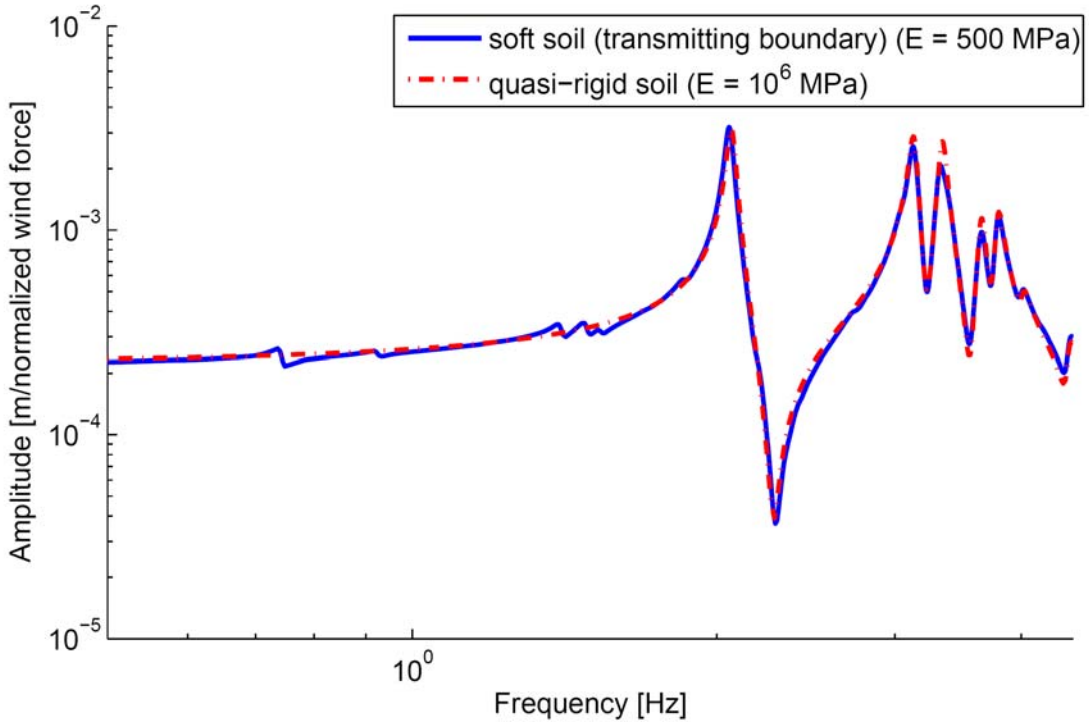

Figure 9-80: Transfer function from wind load to y-deflection of M1.

9.5.5 Safety Analysis

In order to assess the structural safety of OWL. several analysis studies have been carried out to evaluate the maximum stress and safety margins under various survival load conditions. As the permanent maximum stresses caused by gravity are relatively high. the individual survival load case results have to be superimposed to comply with realistic load combination requirements. This will be done in phase B of the project. Fortunately. the maximum stress regions of the gravity cases are in many cases different from those of the survival load cases (TBC). In these cases the maximum stress of the combined load cases will not increase.

9.5.5.1 Wind

The survival wind speed for the telescope is specified to be 30 m/s (TBC). To evaluate the maximum displacements and stresses. the results obtained with the static wind load analyses described in section 9.5.2.2 have been scaled with a factor of 9 (=$30^2/10^2$). The resulting maximum stress. displacement and safety margin values are summarised in Table 9-21.

Altitude angle	**Max. von Mises stress**	**Max. displacement**
	[MPa]	[mm]
Zenith	45	9
30	44	12
60	29	11

Table 9-21: Maximum stresses. safety margins and displacements or survival wind load cases.

The maximum stress of 45 MPa and the maximum displacements of 12 mm caused by pure survival wind load are not critical.

9.5.5.2 Earthquake

Depending on the site selected for the observatory. seismic aspects might be an important design driver for the telescope structure. In order to assess the expected level of displacements and stresses. three quasi-static load cases have been applied to each of the three 2002 OWL models (zenith. 60º and horizon orientation):

- 1g load in vertical z-direction
- 1g in vertical z- and horizontal x-direction
- 1g in vertical z- and horizontal y-direction

This load scenario represents approximately an earthquake with a maximum horizontal ground acceleration of 0.2 g which corresponds to a site with moderate seismic activities. For comparison. MLE on Paranal is 0.34 g and on La Palma 0.04 g.

The stress results of these analyses indicate that several structural beams of the 2002 model exceed the allowable stress limit by about 20 % and would have to be modified by using higher quality steel (St52) and/or by changing their cross-sections. The stress and safety factor verification for the 2002 model due to a 0.2 g level earthquake can be realised with moderate effort. However. under Paranal-like seismic conditions much more effort in terms of design modifications and design measures would be required. Some of the possible measures are listed here:

- Reinforcement of the beam structure around the altitude cradles.
- Considering the higher damping capacity of the bogies due to sliding friction.
- Implementation of local and/or global passive damping devices.

Significant design improvements in the region around the altitude cradles could be already achieved in the latest design version 2005. This results in a considerable increase of the cross elevation frequency and reduces the stresses and dynamic impact due to earthquake loads.

In phase B it is foreseen to use the Response Spectrum Analysis method to verify the structure under seismic loading. This method has been used for the VLT and is the standard technique. After conducting a geotechnical investigation and a hazard analysis of the observatory site. site specific parameters will be defined. Based on these parameters. two different seismic scenarios will be specified. the Operating Basis Earthquake (OBE) and the Maximum Likely Earthquake (MLE). The OBE is defined as an earthquake of moderate size with high probability of occurrence and the MLE is defined as an earthquake of large magnitude but with low probability of occurrence. More details about the Response Spectrum method and the determination of the spectrum for Paranal are provided in [36].

9.5.5.3 Buckling

The collapse of large structures due to buckling is an important safety aspect. Therefore. the OWL framework structure has to be designed such to withstand loadings that could cause buckling. Buckling failure might occur at loads smaller than that would be predicted from stress and strain calculations alone. Therefore. an extensive buckling analysis study based on the 2002 models has been performed (see RD30).

By using the linear buckling analysis the theoretical buckling strength of an ideal linear-elastic structure can be evaluated. The eigenvalues calculated by the linear buckling analysis represent buckling load factors. As imperfections and non-linearities prevent most of the real structure from achieving their theoretical elastic buckling strength. the linear buckling approach often yields insufficiently conservative results. Therefore. the nonlinear buckling analysis approach is more accurate and recommended for the verification evaluation. This technique employs a nonlinear static analysis with gradually increasing loads to find the critical load level.

Linear eigenvalue buckling and. wherever needed. non-linear buckling analyses have been carried out based on the earthquake loading scenario and the three 2002 models explained in section 9.5.5.2. The objective is to determine the critical load values at which the structure becomes unstable. The stability verification has been carried with all the framework beams of

the 2002 FE models by following the procedures defined in the standard norm DIN 18800. part 2.

1. Linear buckling and static analyses to calculate the lowest buckling mode shapes and the shapes for the static bending line.
2. Non-linear buckling analyses based on the pre-deformed buckling mode shapes. The maximum imperfections of these mode shapes were scaled according to the norm DIN 18800.
3. Evaluate global buckling stability and critical load factors for all beams.

The minimum critical load factor is calculated to be 1.7 and occurs for the horizontal altitude configuration when the unit gravity acts in vertical z- and horizontal y-direction simultaneously. As a result of the buckling analysis study it can be concluded that some moderate design modifications are needed for the 2002 design to meet the buckling failure requirements. It is expected that the increased stiffness inherent in the 2005 design will also be beneficial for the sensitivity to buckling failure.

9.5.5.4 Fatigue

In order to assess the risk of the structural failure of the telescope due to fatigue loading. an analysis study has been carried out (see RD32). Wind gust is considered to be the most critical load which could lead to fatigue problems of telescopes. as it is a dynamic load with a large number of amplitude cycles. Based on the 2002 FE model of OWL. simplified wind load distributions have been applied to the zenith configuration. The load distribution follows a wind speed profile over height with maximum 13 m/s at 100 m height above ground. Two load cases with wind directions in x- and y-direction respectively have been considered in separate analyses. The wind forces have been applied for each load case in two ways:

- Classification of the structure in framework groups according to DIN 1055 with consideration of the shadow effect.
- Uniform applied wind forces on all beams considering the wind speed profile. but without the shadow effect (worst case).

As the dead weight is a permanent load and contributes to the stress distribution significantly. it has been superimposed to the wind load distributions. By comparing the stresses due to pure dead weight with those of the combined load cases. the constant mean and variable amplitude portions can be evaluated. This is important for the assessment of the fatigue risk. Fortunately. the maximum stresses caused by wind are located in areas with low permanent stress levels. The maximum stress amplitude caused by the wind load applied results in 17 MPa for all load cases investigated. The mean stress at this position is only 8 MPa.

According to the Eurocode 3. part 1-1. a fatigue verification of a structure is only needed. if the maximum variable stress amplitude is above 19 MPa. This requirement is already fulfilled with the present wind load assumptions which are considered to be conservative. e.g. wind gust of 13 m/s corresponds to a static wind speed of about 40 m/s. the number of cycles under these conditions are far below the critical load cycle values and the locations of high stresses due to wind change vary often due to different telescope configurations and wind directions.

Nevertheless. Smith diagrams have been calculated to illustrate the mean and amplitude stress for each node in the structure with respect to the materials' endurance limit. permissible stress. alternating and pulsating strength.

Figure 9-81 displays a typical Smith diagram representing a uniform wind load case in x-direction with the component stress versus the mean stress. The red and blue dots are the lower and upper stress values. As can be seen. the majority of the stresses lie very close to the diagonal dashed line which represents the constant mean stress and are far away from the materials' limit strength curves (solid curves). The amplitudes are small. but due to the gravity load some static stress points are relatively high as already pointed out. They exceed the limit strength curve of the St37 material (red). but are still well inside the limit strength curve of the St52 material (dark purple).

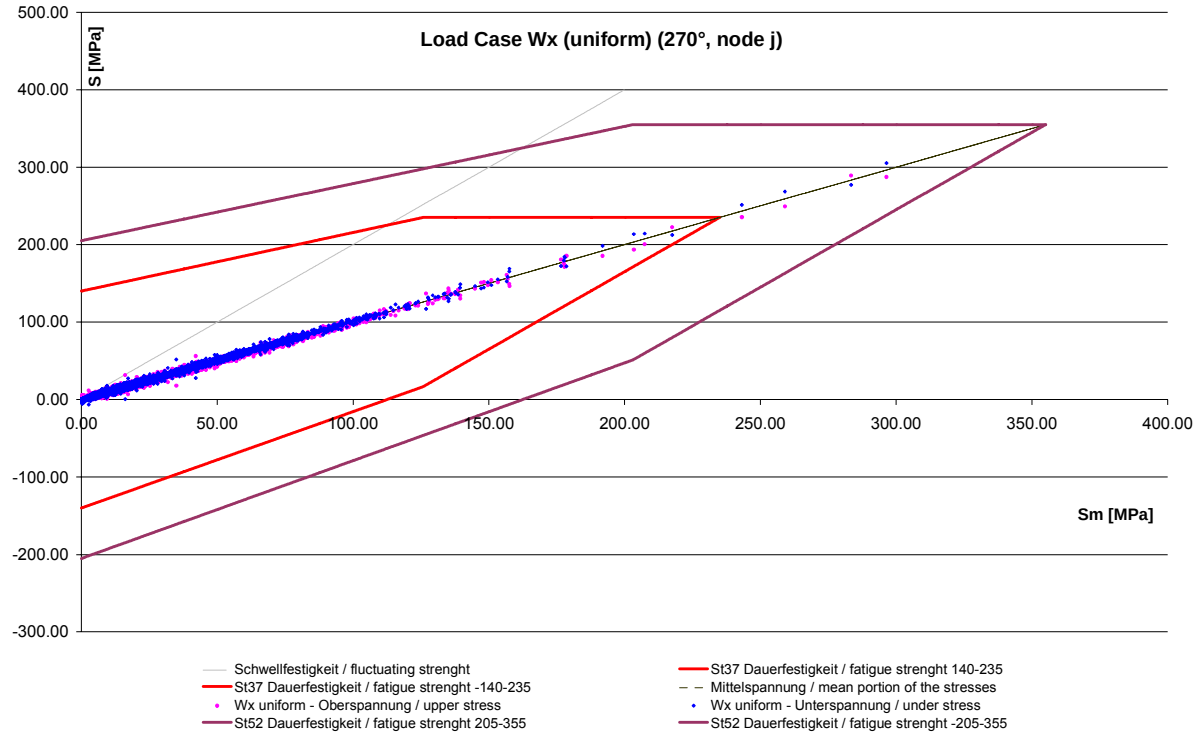

Figure 9-81: SMITH diagram

It has been demonstrated. that the 2002 model is insensitive to fatigue loading like wind and the risk of structural failure due to fatigue is very small. As the 2004 and 2005 OWL designs are much stiffer than the 2002 design. it is expected that fatigue remains a negligible issue.

9.5.5.5 Pretension of ropes

Since the purpose of the structural ropes is to provide sufficient tension stiffness in all altitude configurations (see 9.4.4.2). they have to be preloaded accordingly. This pretension process will change the existing stress distribution due to gravity. Therefore. an optimisation study has been performed with the 2002 FE model of OWL (see RD32). The objective was to evaluate an optimal pretension of all ropes by

- maintaining a certain minimum pretension of all cables for the two extreme altitude configurations under gravity.
- minimising the stresses and
- respecting the allowable strength limits of the framework structure and the cables.

Many optimisation analyses and iterations have been carried out to find a valid and preliminary optimal solution. because two different analytical models had to be optimised and ANSYS allows only a single-objective optimisation. The best solution of the optimisations results in a 5 % increase of the maximum stress caused by gravity without pretension. By changing the relevant parts in the structure into higher strength material (St52) the stress and safety factor requirements can be fulfilled. In phase B a multi-objective optimisation program will be used to find a better optimum for the pretension distribution.

Careful and extensive analyses will be required to simulate the pretension process. because the structural stresses react quite sensitive to variations of the cable pretension. As the 2005 model is considerably stiffer than the 2002 model. a significant stress level reduction is expected which is also beneficial for the pretension process.

9.6 Structure design Options

9.6.1 Base line High configuration (2005 design)

The Figure 9-82 shows the baseline configuration which has the altitude axis at 38.49 meters from the ground level. This height allows the primary mirror to remain above the ground level for a rotation of 50° from zenith. From 50° to 60° the primary mirror sinks partially bellow the ground level. However the small concerned portion of the primary mirror and the observation range close to the horizon. make this configuration acceptable in relation to the thermal turbulence disturbance. The various drawbacks. listed in the table below. which are generated by the increase in height. are justified by the fact that the thermal turbulence is minimized. Thermal turbulences are critical for a 100 m primary mirror where quasi “micro climates” can be generated. These aspects will be studied in more details during the next project phases.

Advantages	Disadvantages
Less thermal turbulence.	More structural steel is required.
Less excavation depth for the foundation.	Lower dynamic and static performance.
	More complex operation and maintenance.
	Larger enclosure.

Table 9-22: High configuration

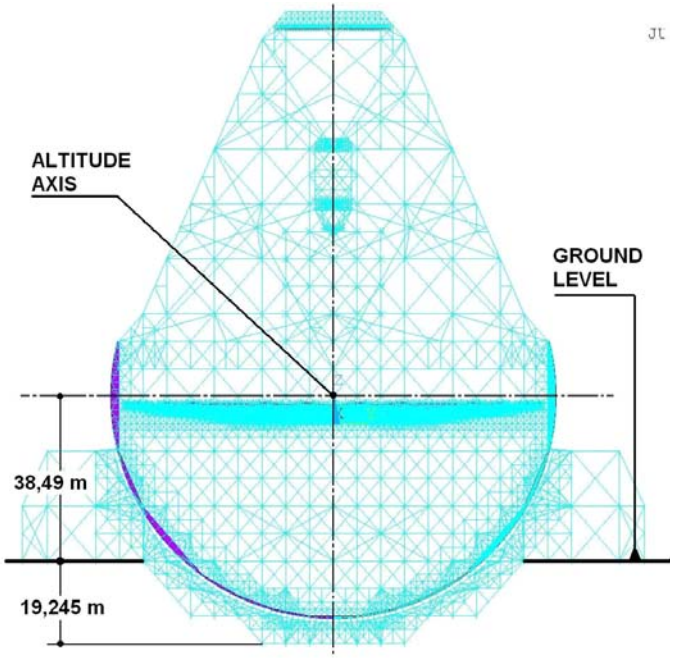

Figure 9-82: Base line. High configuration

9.6.2 Glass Ceramic low configuration

Figure 9-83 shows low configuration which has the altitude axis at 25.66 meters from the ground level. This height allows the primary mirror to remain above the ground level only for a rotation of 30° from zenith. From 30° to 60° the primary mirror sinks partially bellow the ground level. This may cause thermal turbulences on the primary mirror. The various advantages of this configuration (see table below). do not compensate for the time being the fact that dangerous

thermal turbulence on the primary mirror. may degrade the image quality. even after AO. Realization of opening in the foundation. to vent the primary mirror. are complex. expensive and counter productive in term of stiffness.

Advantages	Disadvantages
Less structural steel is required	High thermal turbulence
Higher dynamic and static performance	More excavation depth for the foundation
Easier operation and maintenance	
Smaller enclosure	

Table 9-23: Low configuration.

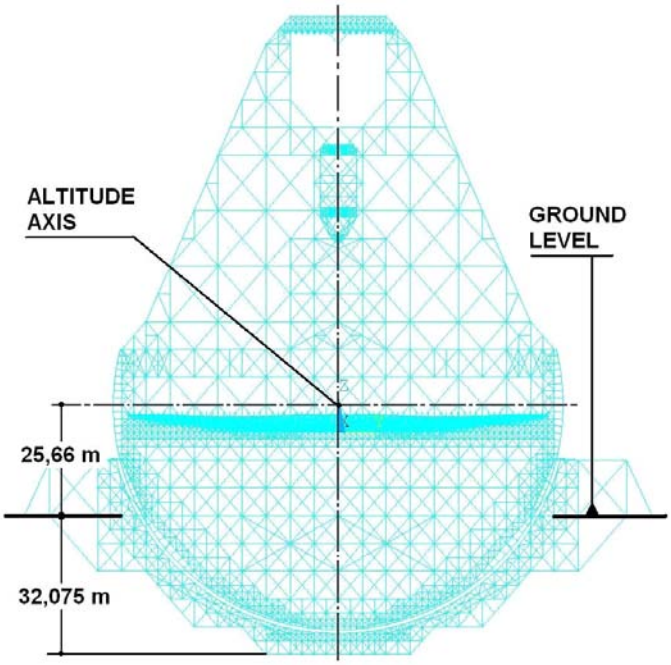

Figure 9-83: Low configuration

9.6.3 SiC high and low configurations

Options 2 (2005 SiC High) and 3 (2005 SiC Low) take into account SiC substrate and the implementation of Composite Materials of the upper part of the altitude structure.

Main Advantages of using SiC substrate and composite material are:

- Reduction of Rotating mass.
- Increase of static and dynamic performance.
- No air conditioning need for the primary and secondary mirrors.
- Higher safety factor for the primary and secondary mirrors.
- Decrease of cost on several other telescope subsystems
  - Mechanical Structure.
  - Drive and bearings.
  - Tracks and foundation.

- Maintenance and Operational costs.

Main disadvantages of using SiC substrate and composite material are:

- SiC substrate technology is not fully validated as per today.
- Composite material can limit eventual retrofitting of the telescope.

A dedicated study to Composite material structural elements applied to ELT including OWL is planned in the ELT Design Study (see appendix A-1.4). Further details about the study can be found in the study Statement of Work RD512.

9.6.4 Glass Ceramic 60 m configuration

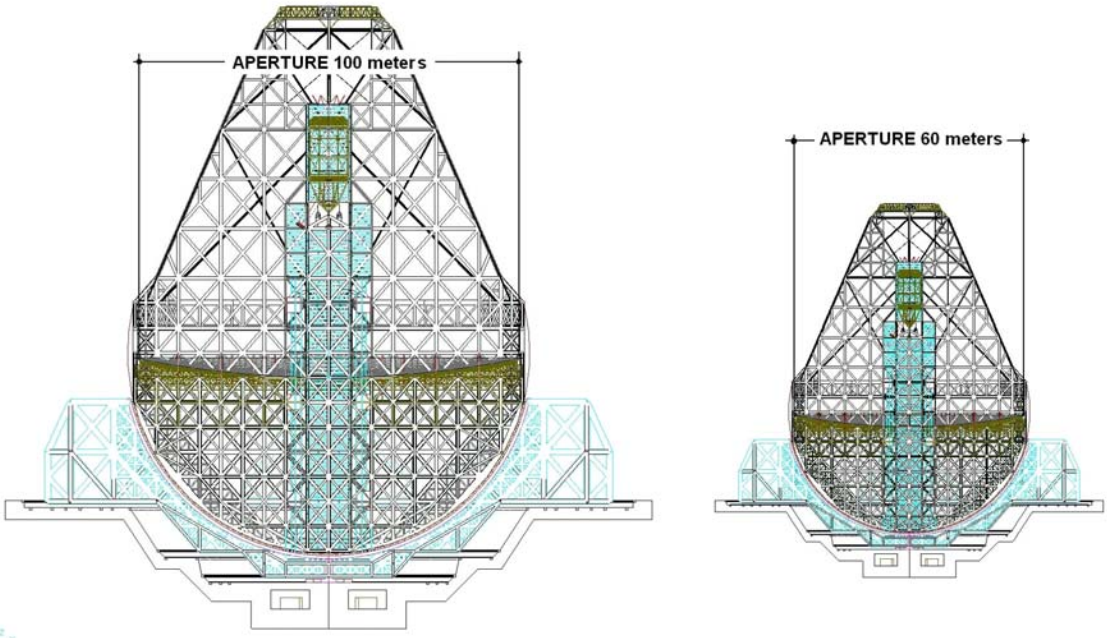

Figure 9-84: OWL scaled down 60 meters

Option 4 is a scaled down to 60m of the 2005 100m optomechanical design (see Figure 9-84). This design has been developed in order to get a first order values related to performance and costs. More accurate evaluation will require a design based on a dedicated optical design tailored to the 60 m aperture and taking into account the maximum size of the active mirrors which should be 8.3 m.

The obvious main advantages of this design are:

- Reduction of Rotating mass.
- Increase of static and dynamic performance.
- Higher safety factor for the primary and secondary mirrors.
- Decrease of cost on several other telescope subsystems
  - Mechanical Structure.
  - Drive and bearings.
  - Tracks and foundation.
  - Maintenance and Operational costs.

Main disadvantages of having an aperture of 60 m are science related. Therefore they are not discussed in this section.

#	Design Option.	Total Rotating Mass [tons]	Altitude Structure Mass [tons]	Dynamic Performance		
				Parallelogram mode (X axis direction) [Hz]	Locked Rotor Mode [Hz]	Torsion Mode [Hz]
1	100 m 2005 design Zerodur. Steel. Kevlar ropes. High configuration.	13347	7174	2.35	2.68	3.39
2	100 m SiC. Kevlar ropes. Composite M2 tower. High configuration.	12136	5963	2.6	3	3.5
3	100 m SiC. Kevlar ropes. Composite M2 tower. Low configuration	10095	5963	2.6	3	3.3
4	60 m Zerodur. Steel Kevlar ropes High configuration	6457	2753	4.3	4.7	6

Table 9-24. Design options. overall properties.

The Options 2. 3. and 4 have indicative values and need further refinement and optimization (performance should increase)

10. Adapter-Rotator

10.1 Requirements

The adapter-rotator is the interface between the telescope and an instrument. It has to fulfil the following requirements.

- Provide the sensors for the wavefront control. These are the sensors for tracking and field stabilization. for active optics and for adaptive optics. The design should allow for six sensors for active and adaptive optics each.
- Provide an attachment for the instrument (rotator interface flange).
- Provide the derotation of the field. This could be either a mechanical derotator at the outer edge of the adapter or an optical derotator.
- The back focal distance should be at least 100 mm. For "back focal distance " (BFD) at a telescope focus (see e.g. VLT) it is intended the distance between the Instrument Attachment Flange (Rotator interface flange Figure 10-1) and the focus on the optical axis measured outwards.
- The scientific field must have a diameter of at least 3 arcminutes.

Adapter-rotators requirements are highly provisional as feedback from instrument studies is. at the time of writing of this report. still being received. Extensive iterations shall take place in the design phase. The design may plausibly evolve towards specialized adapter-rotators tailored to specific functional modes (e.g. SCAO. MCAO).

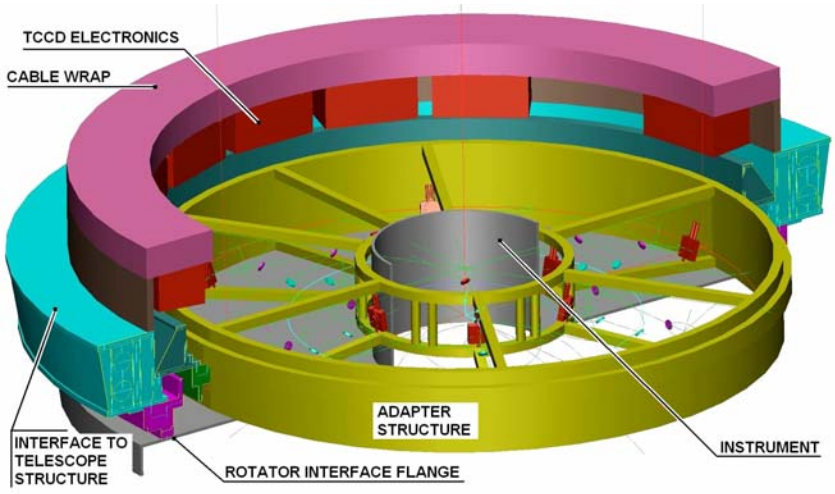

Figure 10-1: Adapter Rotator

Some of these requirements can also be supplied by the instrument itself. Therefore not all adapters have to be identical and have the full functionality. However. the type of adapter discussed in this section will fulfil all requirements mentioned above.

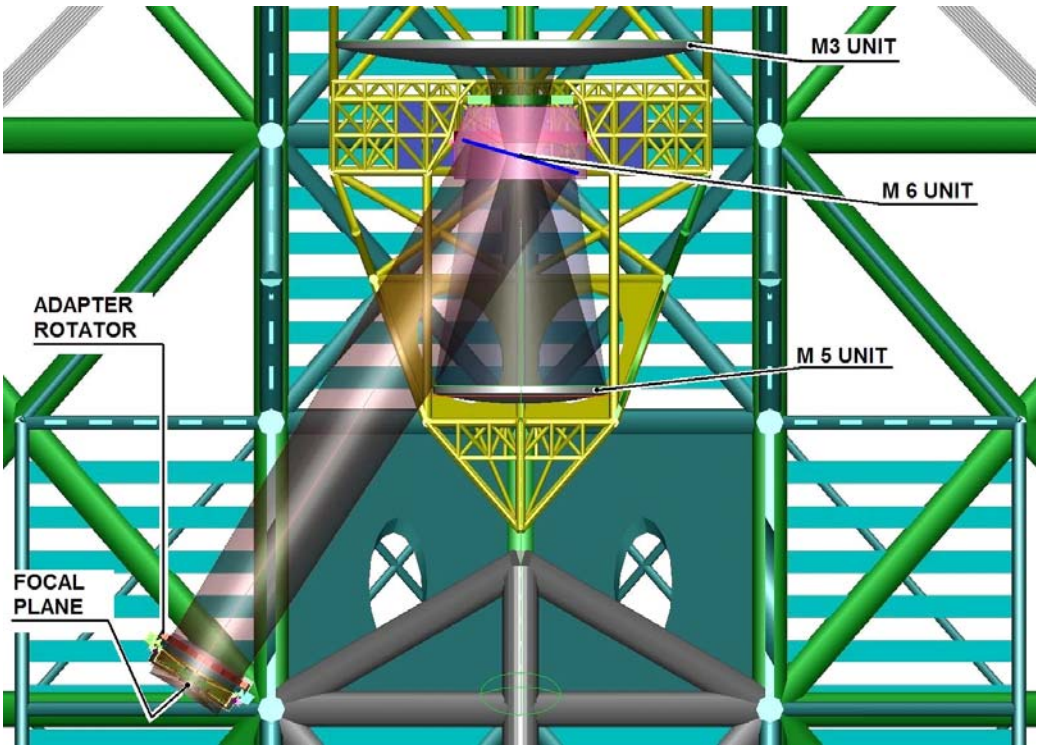

Figure 10-2: Adaptor Rotator location

10.2 Constraints

There are a few constraints for the design of the adapter:

- The diameter of approximately 2 meters is equivalent to a full field diameter of 10 arcminutes.
- The f-number is equal to 6.
- The maximum weight of an instrument to be attached to the Rotator is 4 tons(TBC).
- The focal surface is approximately a sphere with a radius of curvature of 2.210 metres.

The field of view will be divided into three areas.

- Instrument field: inner circle with a diameter of 3 arcminutes. This field is accessible to the instrument. Within this field the priority is given to the instrument. The field may be obscured by other devices of the adapter. but only if they are required by the instrument and do not interfere with the functionality of the instrument.
- Adaptive optics field: ring between 3 and 6 arcminutes diameter. In the field priority is given to the wavefront sensing for adaptive optics.
- Active optics field: ring between 6 and 10 arcminutes diameter. This field will be used for wavefront sensing for active optics.

10.3 Notional Design

A natural guide for the following notional design of the adapter is the symmetry of structure of the telescope.

- The wavefront sensor units are located on six radial bars with their axes of rotation on the center of the bars.
- Each unit consists of a rotating arm with the pick-up mirror on one side of the rotation axis and the detector on the other side.
- The distance of the pick-up mirror to the center of the unit is variable. The accessible area per unit is therefore an annular circle.
- The inclination of the pick-up mirrors follows the curvature of the focal surface.
- The planes of rotation of the units for active and adaptive optics are on different levels to avoid collisions between the units.
- To achieve sufficient instrument design volume of about 500 mm (measured from the focal plane vertex) the central instrument field (diameter of about 580 mm) will be unobstructed by mechanical devices. The instrument which will be attached to the adapter at a flange outside the 10 arcminutes field diameter will therefore have an additional design space at the center of the field with a diameter equivalent to the 3 arcminutes field diameter and a length of 500 mm.
- Located on an additional radial bar there will be one or more wavefront sensor units which can access the center of the field. These can be either close the focal surface for instruments which do not require a large back focal distance or at least at a distance of 500 mm from the focal surface for instruments which make use of the additional design space. In the latter case the pick-up mirror would have a size of at least 100 mm and could not be used to pick up a star close to the scientific target. If required the wavefront sensing for adaptive optics has to be provided by the instrument (for wavelength smaller than K and certain types of adaptive optics).
- Location of calibration units

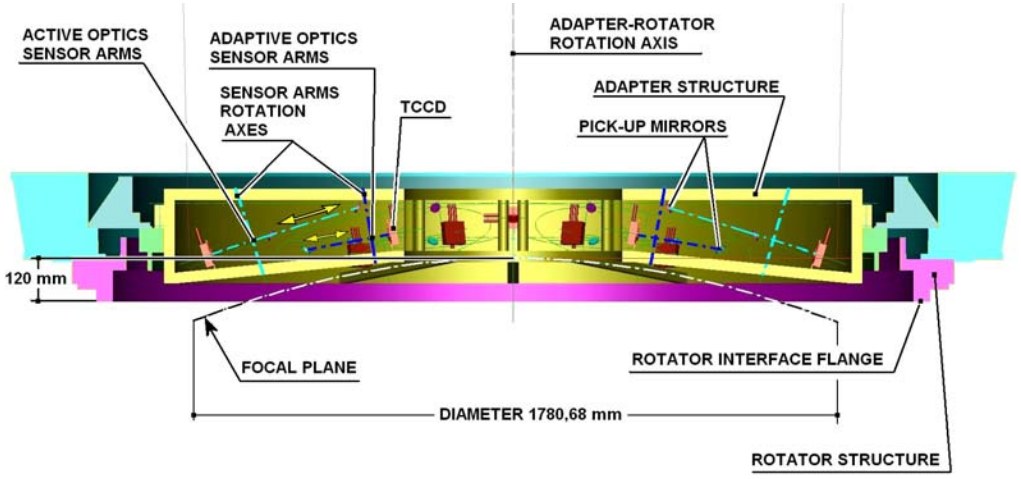

Figure 10-3: Adapter Rotator section

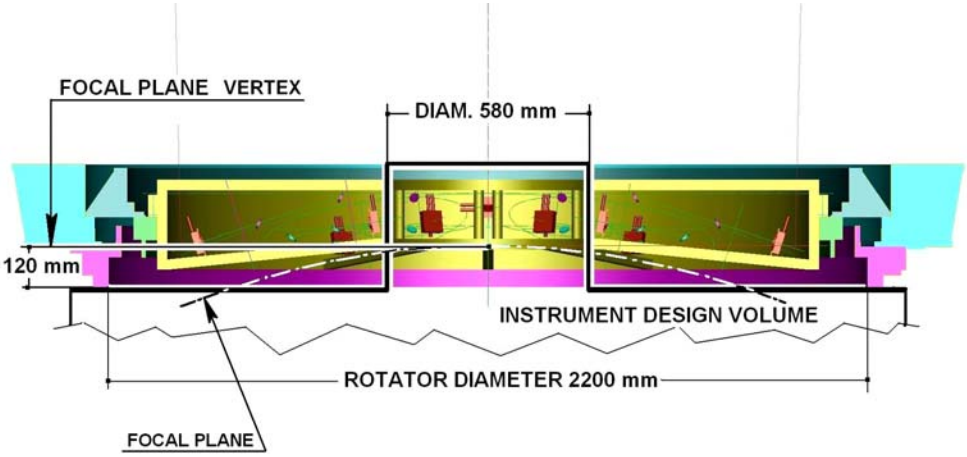

Figure 10-4: Adapter Rotator Instrument design volume

For heavy instruments which exceed the weight limit the focus could be transferred by an additional flat mirror to a platform perpendicular to the optical axis of the telescope.

Not all adapter have to be identical. On focal station may be reserved for technical instruments where the center of the field can be accessed without any restrictions imposed by scientific instruments

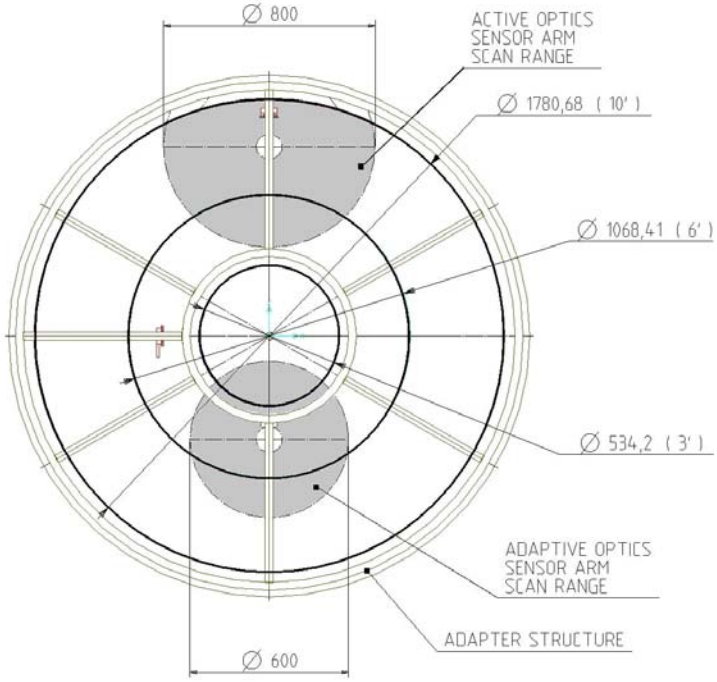

Figure 10-5: Pickup mirror scan range

10.3.1 Pick-up mirrors

The A/R design includes 13 pickup mirrors.

- 6 scanning pickup mirrors for Adaptive Opitcs
- 6 scanning pickup mirrors for Active Opitcs
- 1 pickup mirror for Active Opitcs which can be positioned on and off on axis.

The kinematics design and the scan ranges shown in Figure 10-5 are only tentative.

10.4 Adapter-Rotator configuration vs instruments and functions.

The Adapter Rotator configuration can be tailored to the different instrument and AO Systems requirement. Table 10-1. Table 10-2 and Table 10-3 indicate possible design requirements and options.

Instrument/ AO system	Wavelength Range of operation / Scientific FoV	Interface to telescope	AO type/ nr. WS pick up arms	ADC Requirements	Remarks
CODEX	400-700nm/ 4" (tbc)	Fed by fiber or optical train at a stable location	Low order AO (tbc)	Possibly . in the instrument	Target red light (via dichroic) to be used for WFS (m(l)=16-18)
T-OWL	2500-5000nm and 10-20μm/ ~ 17"x17"	Imager attached to adapter/possibly not requiring rotation.	AO not required in N.Q bands. SCAO for L.M (tbc)	tbd	Entrance window of instrument as dichroic to split the two spectral ranges. Spectrograph option not yet finalized.
QUANTEYE	400-700nm/ 120"	Attached to adapter. rotating	Low order AO (tbc)	Not required	Two apertures . one on the center field+ reference within 60 arcsec.
MOMFIS	800-2300 nm/ 360"	Present design cannot be attached to A/R. To heavy. to big.	MOAO/ WS to be distributed in field	In the instrument (1st order correction over the all field useful	Multi-LGS probably required. Need to have WF sensing close to actual targets
ONIRICA (central field)	30-60"	Attached. rotating. within 5 tons (tbc)	MCAO . high order correction	tbd	ONIRICA asks for more WFSs (up to 12. tbc)
ONIRICA (large field)	Annular 1'-6' (max)	Attached. rotating. within 5 tons (tbc)	MCAO. low order correction	tbd	
EPICS	R and J bands/ 4"x4" max	Detatched from adapter; possibly requiring gravity-invariant platform	XAO/Not in Adapter	External ADC could help .internal one needed in any case.	Postfocal AO with WFS
SCOWL	350.450 and 850 μm bands / 150 "	Attached to adapter. rotation not required. Weight at 5.6tons	No standard AO	Not required	Monitor of H2O at different position over aperture at 0.1-1 Hz resolution may be needed
Hyper-telescope Cam					No information available.

Table 10-1. Adapter-rotator requeirements for a set of representative instruments.

Instrument AO system	Scientific Field		AO Field					
	Scientific FoV [']	Allowable Obscuration	Scan FoV [']	Allowable Obscuration (adapter mechanics. % area)	AO pick up arms	AO pick-ip arm stability & tracking over 20' exposure time [µm]	WFS FoV ["]	Remarks
SCAO	1' (TBC)	Goal None Requ. TBD	1'	Goal None Requ. TBD	Not in Adapter	0.4 mas	2-3"	Optimized wavelength for the WFS and the overall stability requirements favors to have WFS close to the instrument (see also TOWL narrow field). IR Pyramid and visible SH WFS
GLAO	Goal 6' Requ. 3'	Goal None Requ. TBD	Requ. 2-6' Goal 1'-6'		6-8	3-5 mas	2-3"	Conflict between scientific and WFS FoV may require moving the WFSs in instrument with large dichroic (TBC)
TOWL narrow	~10" (TBC)		~10" (TBC)		Not in adapter	N.A	N.A.	Entrance window of instrument as dichroic
TOWL wide	TBD							TBD
MOAO MOMFIS	6'		6'	TBD	Not in adapter	N.A.	N.A.	Multi-LGS required
MCAO ONIRICA	1'	Requ. None	6'	TBD	6-12	0.4 mas	2-3"	ONIRICA asks for more WFSs (12) (TBC by study made by INAF)
EPICS/XAO	10"		10"		Not in Adapter	N.A.	N.A.	Postfocal AO with WFS

Table 10-2: Adapter-rotator requirements for a set of representative AO Systems.

Number of WFS	Scan Field	FoV	Tracking Accuracy	Remarks
6 Shack-Hartmann Type	From 6' to 10 '	2" - 3 "	0.1 " over 1' exposure time.	At least one piston step sensor. Baseline: Only on the technical focus for measurement at the beginning of the night. Focal: On every focus for closed loop control of th piston step by optical measurements.

Table 10-3 Adapter-rotator requirements for Active Optics.

11. Enclosure and infrastructures

This chapter deals with the telescope enclosure and the main infrastructures installations serving the observatory.

To a large extent infrastructures like power production plant. access roads. water supply. etc. are dependent on the site and sometime on the country where the observatory will be erected.

For the purpose of this document it has been decided to use the experience gained in constructing the Paranal Observatory in an undeveloped area close to reasonable industrial infrastructures (harbours. access roads in the vicinity). Extrapolation to more remote sites conditions have been done based on the study for the site characterization of Gamsberg in Namibia developed on 1993.

The enclosure is on the other hand defined largely by functional considerations which are less dependent on the site which will be chosen. The environmental and geotechnical characteristics of the site influence the actual structural design. and for this reason two typical astronomical sites with very different conditions have been compared to assess the impact on the feasibility and on the costs of the enclosure.

The assumptions taken in assessing requirements which are strongly site dependent. like water supply. power production. actual soil geomechanics. are simple and conservative and the final design/choice shall be made after detailed study when the site has been chosen.

11.1 Telescope enclosure

The aim is to design and build an enclosure for OWL. which can be built at reasonable cost and still provide the needed functions required to the sheltering structure of a telescope.

The cost impact on the project of such structure shall be limited to the minimum. not only as capital investment but also for maintenance and operations. For this reason it should be as small and as simple as possible. with the functions implemented as close as feasible to the ground level. and therefore easily reachable for maintenance. with the least number of mechanisms. It shall perform the functions of protecting the telescope from the sun exposure during the day. shelter the telescope from excessive wind load and from rain or snow. The need of protecting the telescope from wind load during operation will be assessed in the design phase. Only limited volumes enclosing those parts of the telescope with long thermal time constant are conditioned. The heat introduced by the solar radiation is removed passively using air volume exchange or natural convection close to the outside wall. Based on the above considerations the enclosure for OWL has been envisaged as a huge but simple hangar which. sliding on rails is moved away to allow observations. This type of sheltering structure is not new in astronomical application; see for example the first concept for the ESO VLT.

In designing the baseline concept the following requirements have been taken into consideration:

- Smallest possible enclosed volume and developed surface for economic reasons (the cost of such buildings can be considered proportional to the developed surface). yet allowing the telescope free rotation in all its allowable range.
- Protect the telescope from solar exposure during the day. from extreme environmental conditions like survival wind load. rain or snow / ice.
- Keep the inner air volume temperature at a convenient value. so that the telescope structure and optics are as close as economically attainable to thermal equilibrium with the external environment at the start of the observation. In this way the time that the telescope will need to go to thermal equilibrium with the outer air volume will be minimized and therefore the induced degradation of the seeing is minimized.
- Try to minimize the so-called "dome seeing". This function is obtained. in the modern enclosures. by letting the air flow inside the enclosed volume. so that the structural parts and the floor surrounding the telescope are brought in short time. and kept. at the thermal equilibrium with the external environment. In the case of OWL the enclosure is simply completely removed so that the “hot air” inside the telescope volume is swept away by the wind and the telescope platform is cooled by radiation and convection.

	Site 1	**Site 2**
Temperature		
Temperature Operational	0 to +15 ºC	-2 to +19 ºC
Temperature Survival:	-10 to +30 ºC	-10 to +35 ºC
Typical temperature gradient at night time	0.7 ºC/h	1.8 ºC/h
Average air temperature difference between day and night	4 ºC	10 ºC
Snow load		
Operational Max. snow height	65mm	200mm
Survival Max. snow height	65mm	2250mm
Ice load		
Operational Max. ice height	50mm	50mm
Survival Max. ice height	50mm	230mm
Wind speed		
Max. wind speed operational including gusts	27 m/s	27 m/s
Max. wind speed survival including gusts	51 m/s	67 m/s
Ground Peak acceleration (OBE)	0.24g	0.04g
Ground Peak acceleration (MLE)	0.34g	0.04g
Geotechnical characteristics		
Classification of soil according to EUROCODE 8	A	A
Density [t/m3]	2.7	2.6
Unconfined compressive strength [MPa]	98	20
Point load strength index (Is) [MPa]	9.8	2
Young modulus static [MPa]	10000	1100
Shear modulus static [Mpa]	3800	430
Young modulus dynamic [MPa]	45000	5400
Shear modulus dynamic [MPa]	17500	2100
Poisson ratio	0.27	0.29

Table 11-1. Main sites characteristics.

The protection of the telescope from wind action is left to yet to be abalyzed other means (e.g. wind screen). The reasons for this decision at this time are based on economical and structural reasons. Results of wind tunnel tests carried on within the VLT program in 1992 and 1994 where also used to assess the choice. In addition. CFD results suggested that a traditional enclosure would increase high frequency pressure turbulence.

In those tests (8.6.AR1 and 8.6.AR2) were measured the characteristics of the wind flow in the area of the primary mirror. The results have shown that to provide a good protection from turbulent wind in the whole frequency domain. and not only in low frequency. it is necessary to reduce the outside mean wind speed by a factor at least 70%. This means that in case of low open air wind speed it is necessary to vary the porosity of the wind screen to allow for mirror surface flushing.

In order to gain some feeling on the effect of environmental and geomechanical characteristics on the design. industrial studies have been carried out considering two typical observing sites with very different characteristics (RD38). The main ones are here summarized in Table 11-1 to facilitate the understanding of the following chapters.

11.1.1 Baseline design description

The concept for the OWL enclosure has been developed as a hanger which can be opened and moved away to allow the observation. This solution leaves the telescope in free air flow which will minimize the thermal effect which degrade the local seeing.

This design largely relies on already available technologies and is based on the design of the already existing Cargo-lifter building in Brandenburg (Figure 11-1).

This concept puts somehow unprecedented requirements on the site.

Figure 11-1: Cargolifter building

The site should provide

- A large flat summit or a summit with a shape that will not require large amount of blasting (in the order of 300x700 square meters for the operation of the enclosure plus the space needed for construction. and access for maintenance).

- It should exhibit a reasonable homogenous geomechanic situation. such that the operations of ground consolidation or over dimensioned foundations are not needed.

Compared to other preliminarily studied concepts. like the radome type. it will make use of less structural steel. and therefore will be less expensive. The costs due to the preparation of the site will be traded off at a later stage.

The design is based on already available technology and the mechanisms have been already widely proved in operation at the Cargolifter building.

Based on the experience gained by operating that building some simplifications have been implemented like the elimination of the large segmented door. The segmented door has proved to pose problems of design and construction because the precision needed in the structures is at the limit for these dimensions. For this reason. it has been decided to propose a symmetrical construction based on 4 arches hinged at the top. This brings better stability. less demanding requirements on the precision of the construction of the guides. and secures the hinge at a more stable point. which is safer from the earthquake pointy of view.

The enclosure is made of one fixed arch and three mobile arches which rotate about the central hinge held on the fixed arch. Boogies are mounted at the bottom of the three rotating arches to allow the opening of the doors. Each boogie has four motorised wheels with a diameter of 1 m. Boogies are also mounted at the bottom of the non-rotating central arch. When the three arches are opened and hosted by the central arch the enclosure is moved using a cable system. This allows to concentrate the drives power system in four points easily accessible for maintenance and servicing. is less expensive then a boogies system like the one used in the telescope drives. It allows to provide a cinematic cycle to meet the goal of sliding the enclosure between the two parking position in about 10 minutes. The three arches open in about 10 minutes. the telescope have full free view after a total of about 15 minutes. In case of closing the complete operation from start from night parking position to telescope completely protected would be about 29 minutes.

Cladding is made by insulated sandwich material. A Faraday cage is realised by the secondary structure on which the cladding panels are fixed. Inflatable seals are provided among the arches and at the bottom of structure to provide a water tight system.

The enclosure is designed to let the service platform with the primary mirror covers move close the telescope at the beginning of the night and at the end of the observing run to protect the mirror.

Figure 11-2 shows the enclosure at its day and night park position.

The central structural arch is the heavier and weighs about 15000 tons and is mounted on wheels. It will support the other three arches when they are opened.

The primary mirror is protected by 6 covers placed on a movable platform. The platform has to be moved close to the mirror to remove the segments at night start. In this concept the aperture through which the platform with the six covers for M1 will be brought in the position is provided by opening the middle arch segment of the enclosure.

The use of the four arches concept allows minimizing the wind cross-section while moving the opened enclosure.

A top view of the enclosure and foundations is shown in Figure 11-3.

In day parking position the foundations allow the transfer of the load under all possible survival conditions while in night parking position the foundations dimensioning take into consideration only the MLE conditions. The railing foundations take into account the possibility to have an MLE during the opening/closing operation. The foundations are presently calculated assuming a homogenous soil condition. that is no significant faults or difference in the geomechanics of the soil are present on the site. This has the consequence that the bearing capability of the soils is principally equal all over the site. and it allows to have almost independent foundations with no connections among them. This condition is expected to be found in many typical astronomical sites. especially on the Andes. in other areas a geomechanical study will be carried out to verify

this assumption. In the case that strong differences in bearing capability of the soil will be detected measures need to be taken which will impact more or less severely the costs.

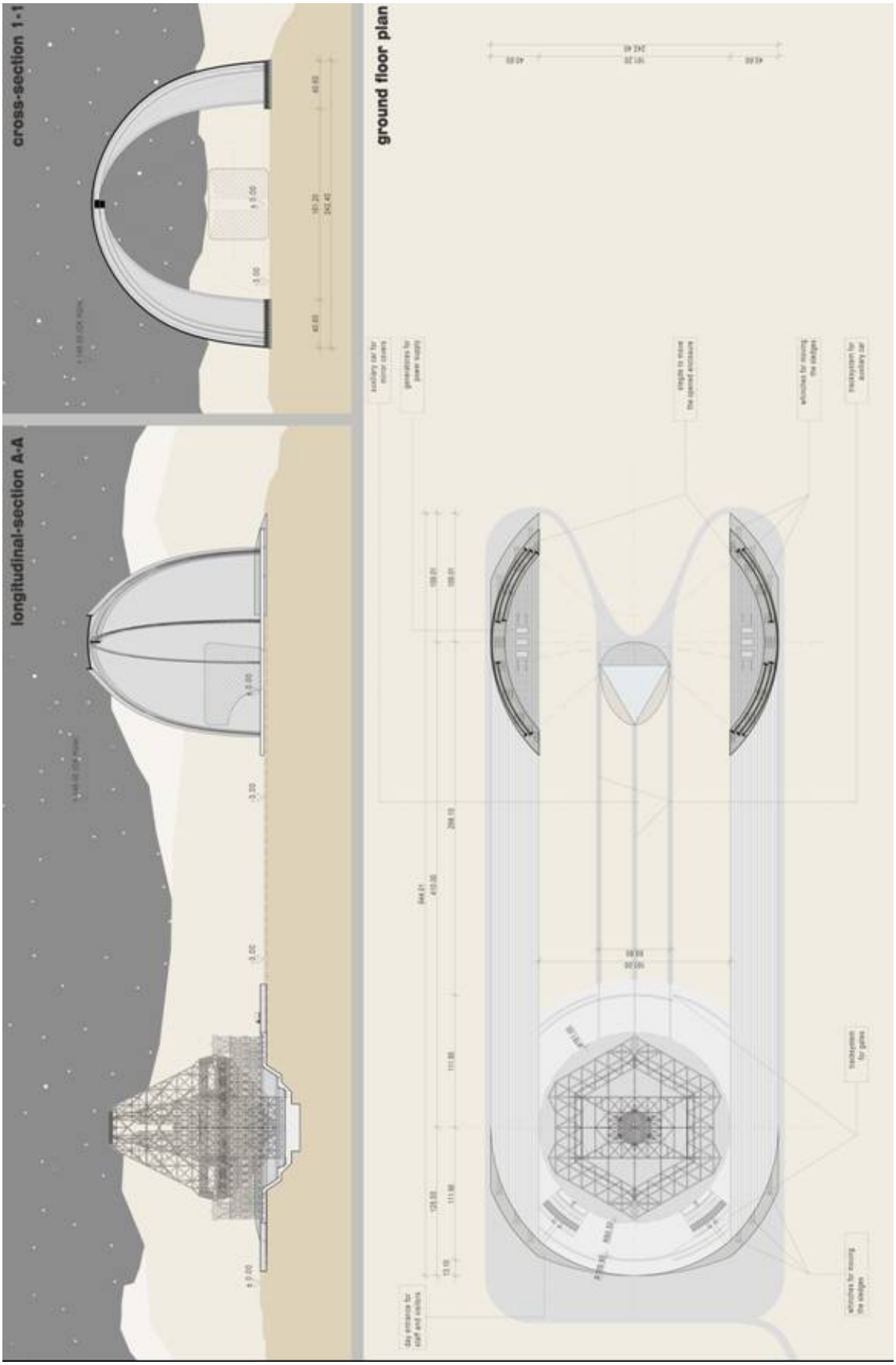

Figure 11-2: Baseline lay-out (courtesy CI-Map)

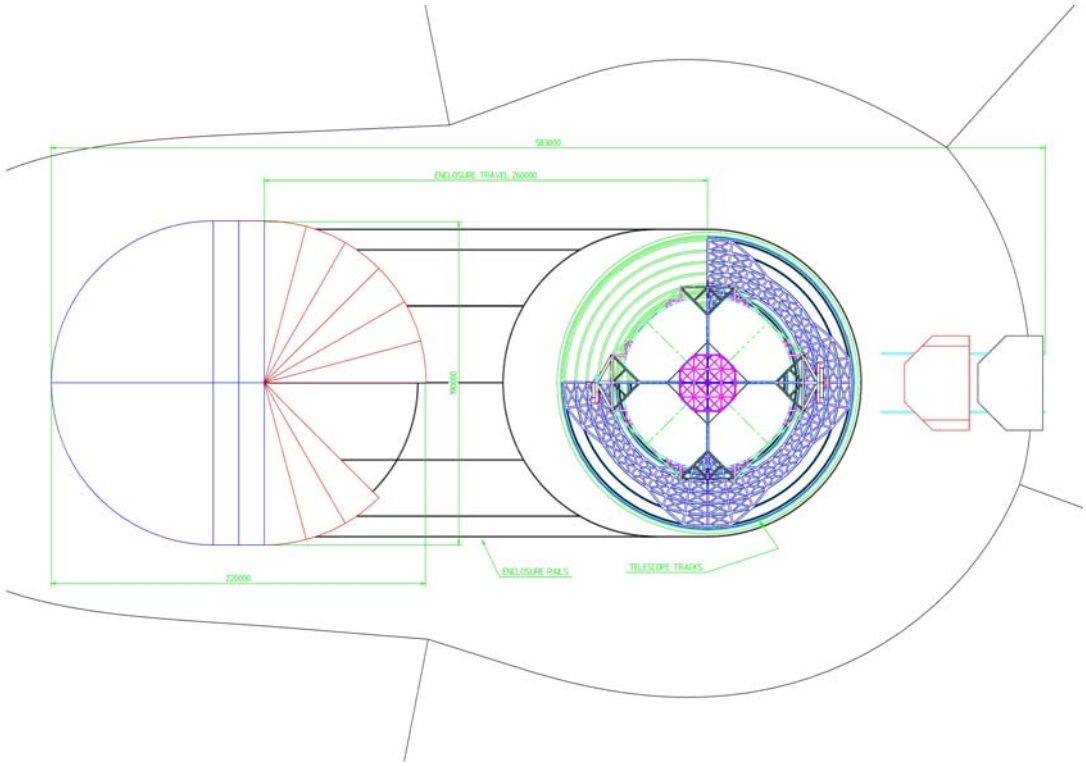

Figure 11-3. Top view of the enclosure and telescope foundations.

One of the requisite of classical enclosures is also to maintain during the day the same temperature inside which was measured the previous observing night. such that at the opening the telescope and its optics are already close to thermal equilibrium with the environment. avoiding local seeing degradation. This is normally obtained conditioning the overall enclosure volume. In the case of OWL the volume to condition would be in the order of 45000000 cubic meters (for comparison the complete conditioned volume at the VLT. four enclosures. is about 100000 cubic meters). This volume is unusual to be conditioned also in civil engineering because of its large demand of energy. Being an observatory erected in remote areas where energy must be normally locally produced. a more economic way to prepare the telescope for starting the observation must be found.

One of the typical characteristic of astronomical sites in desert areas at relatively high altitude (order of 2500 m) is that the temperature of the air during the day is not too far from the temperature of the air during night (typically the difference in average lies between 4 to 10 °C). Moreover the external surface of the building will be treated in such a way to reflect up to 90% the incoming solar radiation. The peak solar heat flow is estimated in 110 MW. therefore only about 10 MW will contribute to heat up the inner volume of the enclosure.

The baseline concept is to open windows placed at the top of the roof to allow the inner volume of air to be exchanged using natural convection. The natural convection is triggered by the difference of air density and the difference of height from the bottom and the top of the enclosure where appropriate openings have been built (see Figure 11-4 for a principle scheme).

The heat removing capability of such a stream can be estimated considering that the drag force or pressure difference (T) acting on a fluid volume with different density with respect to the outside and a difference in the geodetic terms is

$$T = \Delta P_{\text{bottom-top}} = g * \Delta\rho_{\text{bottom-top}} * \Delta z_{\text{bottom-top}} \text{ in } N/m^2$$

Where g is the gravity acceleration. ρ is the fluid density and z is height.

In our case Δρ bottom-top is in the order of .05 kg/m3 . assuming a difference in temperature of 10 ºC between inner and outer air. and Δz bottom-top is of the order of 200m. therefore the dragging pressure is in the order of T=98 N/m2 or 98 Pa.

Under these conditions and assuming that the losses in the generated flow are negligible (to be verified according to the type of filtering applied at the entering openings). and that the outgoing aperture is ~5 times smaller than the incoming section at the bottom. the outgoing flow speed is 5 times higher than the incoming flow speed. one can estimate the heat removing capacity of this induced flow.

The order of magnitude is:

$$V = (T*2/\rho_{fluid})^{1/2} = 12.9 \text{ m/s}$$

Where V= is the flow induced speed. ρ_{fluid} is the density of the internal fluid. equal to 1.17 kg/m3 (density of air at 25 ºC).

Assuming 80 m^2 as outgoing section. the flow is 1032 m^3/s. This flow has a heat removal capacity (H) of (assuming heat capacity equal to 1005 Ws/kg ºK)

$$H=1005[Ws/kg\ ºK]*1.17[kg/m^3]*1032[m/s]*10[ºK]=12.1 \text{ MW}$$

This is more than is expected to be introduced into the enclosure by solar radiation. More detailed estimation of the openings area shows that considering the actual pressure losses in the flow the openings' area will be about 600 m^2.

In such a case at the night opening the telescope would be warmer than the outside ambient air by 4 ºC or 10 ºC. depending on the site.

More specific though simple calculations. using the model shown in Figure 11-5. have shown that the inner air volume at opening will have in the average 6 to 12 °C (depending to the site). temperature difference with respect to the ambient air. The typical temperature evolution is shown in Figure 11-6.

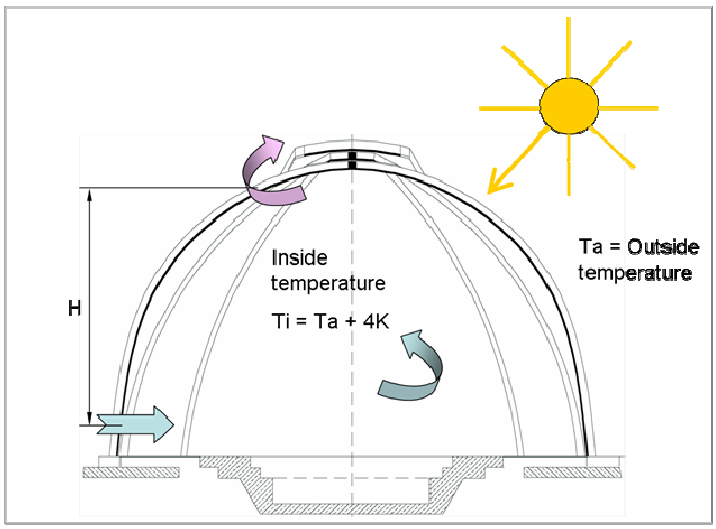

Figure 11-4: Principle scheme of natural cooling of the enclosure volume

Preliminary tests on a steel pipe (representative of an OWL sturtural beam) on Paranal have shown that the thermal equilibrium of the structural parts of the telescope should be reached shortly after opening the enclosure.

The operational cycle of the enclosure in a typical observation night will then be the following:

- 1 hour before the sunset the enclosure. open the central mobile arch to allow the platform holding the M1 covers to move close to M1 mirror to start the operation of uncovering the mirror (three minutes after the start of opening). and remove the mirror sectors 6 covers.
- 0.5 hour before sunset the enclosure opens the three arches and starts to move from day parking position (conditions must be operational; wind speed. ice and snow are operational; no OBE or MLE seismic event is taking place).

- The enclosure accelerates at a rate of 0.004 m/s^2 and after 125 m has reached the speed of 0.8 m/s. It will keep this speed for about 110 m and then will start to decelerate at a rate of -0.004 m/s^2 until the night parking position is reached. The complete operation will last 15 minutes.
- When the night parking position is reached the three segments will close. The operation will take 10 minutes.

The complete cycle of opening will last about 30 minute. In Figure 11-7 the opening cycle is shown in sequence.

As any other telescope shelter the enclosure needs to work reliably to avoid to leave the telescope exposed to precipitation or high wind speeds.

In the conceptual design it is envisaged to maximise the reliability providing redundancy in the drives sytem and it could be even envisaged to provide electrical traction on the enclosure itself as complete back up to power loss on the observatory (diesel generators on board of the enclosure structure. the economical impact is in the range of 10 M€).

In case of an emergency shut down. the time needed to protect completely the telescope. that is to bring the enclosure in day parking position and close the three arches. will take again 30 minutes.

This means that a meteorological forecast station needs to be put in place to monitor wind and precipitation conditions. The design of the enclosure allows to move it with up to 27 m/s wind speed and therefore it is needed to assure that the wind does not exceed this value within less than 30 minutes. from the start of the shut down cycle of the enclosure. In the conceptual design it has been assumed shut down operation will start when the wind speed reaches 16 m/s.

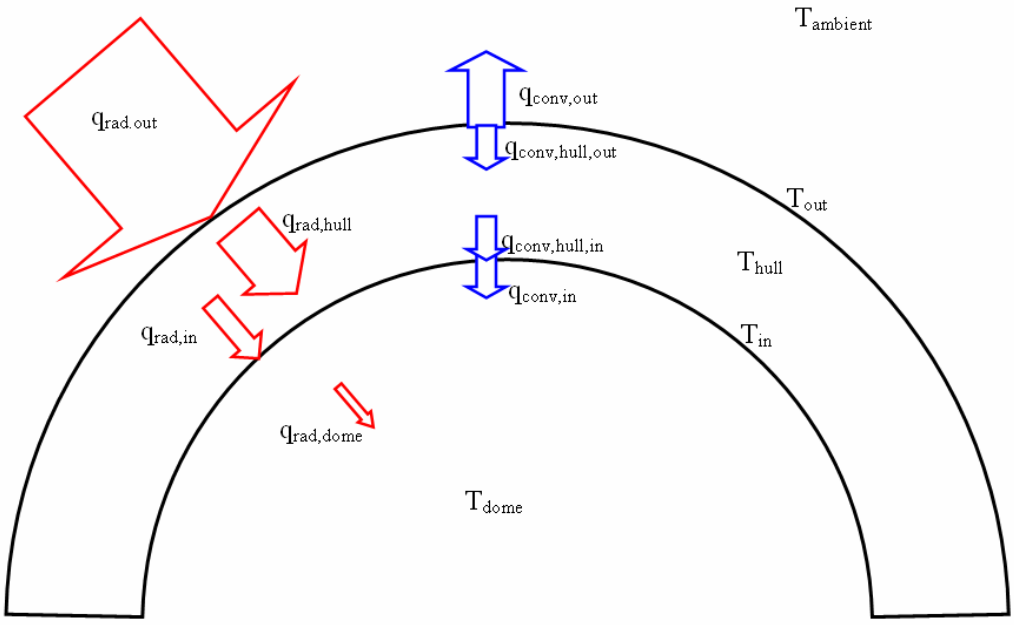

Figure 11-5 Simple thermal model of the enclosure

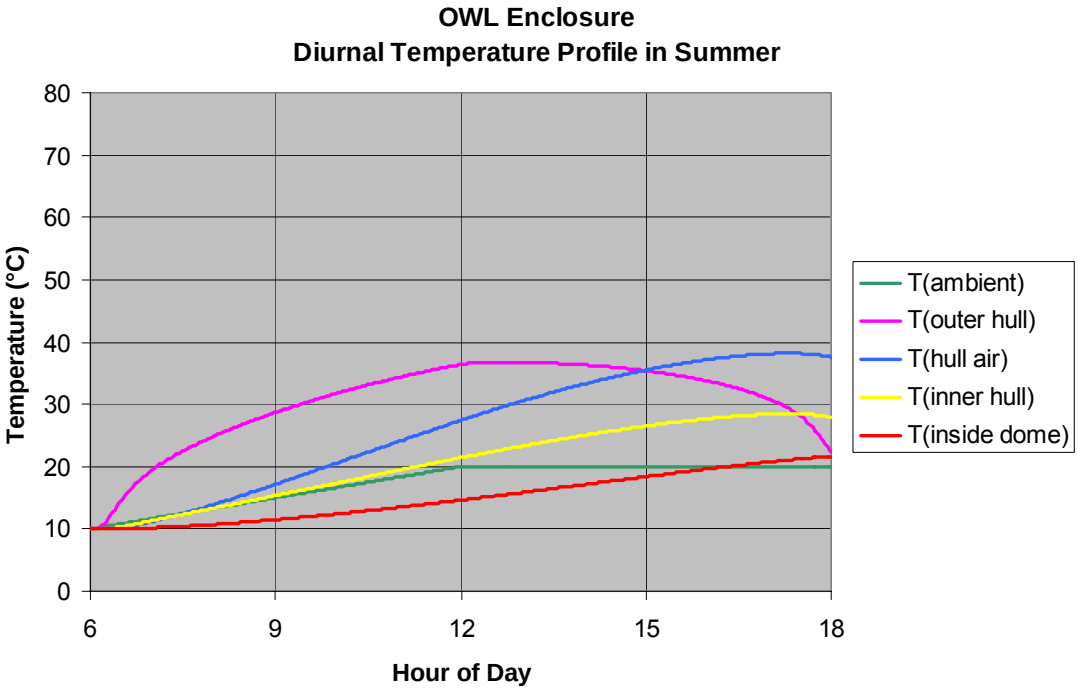

Figure 11-6 Typical temperature evolution of the enclosure assuming site 5 m/s wind speed

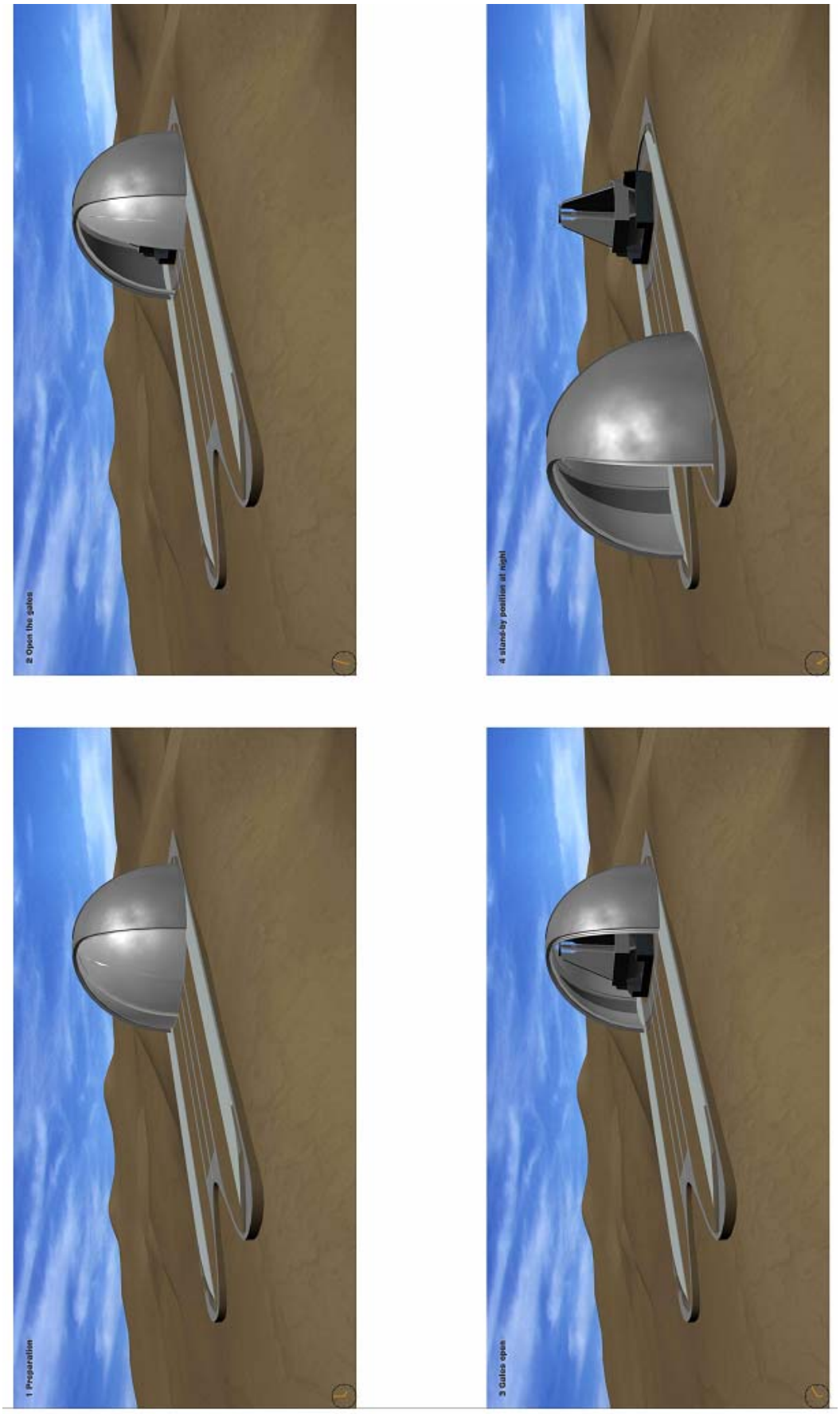

Figure 11-7 Enclosure opening cycle (courtesy CI-Map).

11.1.2 Concrete works

Under concrete works here are also included the auxiliary constructions like servicing roads and temporary construction/areas built during the construction phase.

The detailed conceptual design of the foundations is described in RD39.

The view of the foundations work is shown in Figure 11-8.

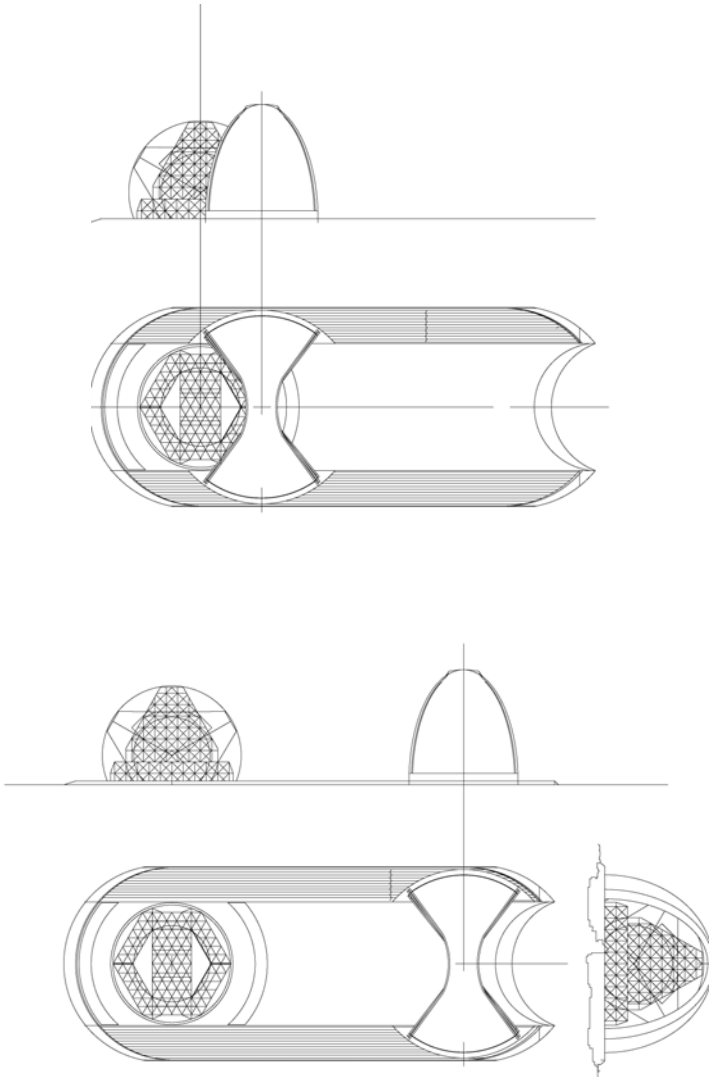

Figure 11-8: Enclosure foundations overview day park position (above). Night park position (bottom)

The main systems are:

- Day park position foundations
- The foundations of the guides on which the enclosure is sled
- Night park position foundations.

The loads which are to be considered while occupying the different positions are different. Namely. besides gravity:

- In day park position: survival wind. snow. ice loads and MLE earthquake loads are to be taken altogether.
- The foundation of the guides: operational wind. snow and ice loads plus MLE earthquake loads. and the loads deriving from the motion of the enclosure.

- Night park position: operational wind. snow and ice loads plus MLE earthquake loads.

The fact that the enclosure will be erected in night park position to allow parallel installation of the telescope requires that also the foundations at night park position are designed with the same load combinations than day parking position.

The foundations are built separately from the telescope foundations. such that in no case transfer of vibration will take place. In the foundations a number of auxiliary rooms are built to host utility rooms to store spare parts. working tools and equipment used for maintenance both for the enclosure and for the telescope.

Due to the large dimensions of the foundations and therefore the large quantities of concrete to be poured. special attention has to be given to removing the heat generated by the chemical reactions in the concrete curing process. Moreover an accurate management of the humidity content will be put in place in desert sites. to reduce cracking of the concrete.

The inert materials used to produce the concrete will be taken directly on site from the earth and rocks produced by the earth works to prepare the site.

The quantities of concrete and steel in the three main parts are summarised in Table 11-2.

	Concrete [m3]	Steel [t]
Day park position foundations	6500	506
Guides foundations	96000	7500
Night park position foundations	6500	506

Table 11-2: Concrete and steel quantities

Given the level of stresses calculated no special problems is present in the design of the foundations.

In Figure 11-9 the cross section of the doors guides and the typical reinforcement are shown.

During the erection of the enclosure and for operation and maintenance extra space and roads have been planned.

The area strictly needed for the enclosure is about 170000 m2. To preassemble the structural parts before erecting them an extra area of about 60000 m2 has to be flattened. This area is used to accommodate a road to access with heavy trucks all the points along the guides and the two parking position. The space in between the two parking position is used to preassembly the structural parts of the enclosure before erecting them. Four large cranes. which can lift higher than 300 m. will be used to erect the enclosure. They will be placed around the night park position.

In case of rain or melting snow. large quantity of water has to be evacuated. Therefore a special net of channels with flow breaking materials or gravel at the bottom to break the energy of the water is built in day park position.

The area around the day park position is paved only where traffic is planned for erection and maintenance. In these areas paving for heavy loads has been foreseen. Everywhere light colour paving is planned to reject 80% of the solar radiation as a minimum. Gravel will be used for levelling the site where possible. Infrared camera measurements made at Paranal have shown that gravel covered areas reach thermal equilibrium with ambient in a shorter time.

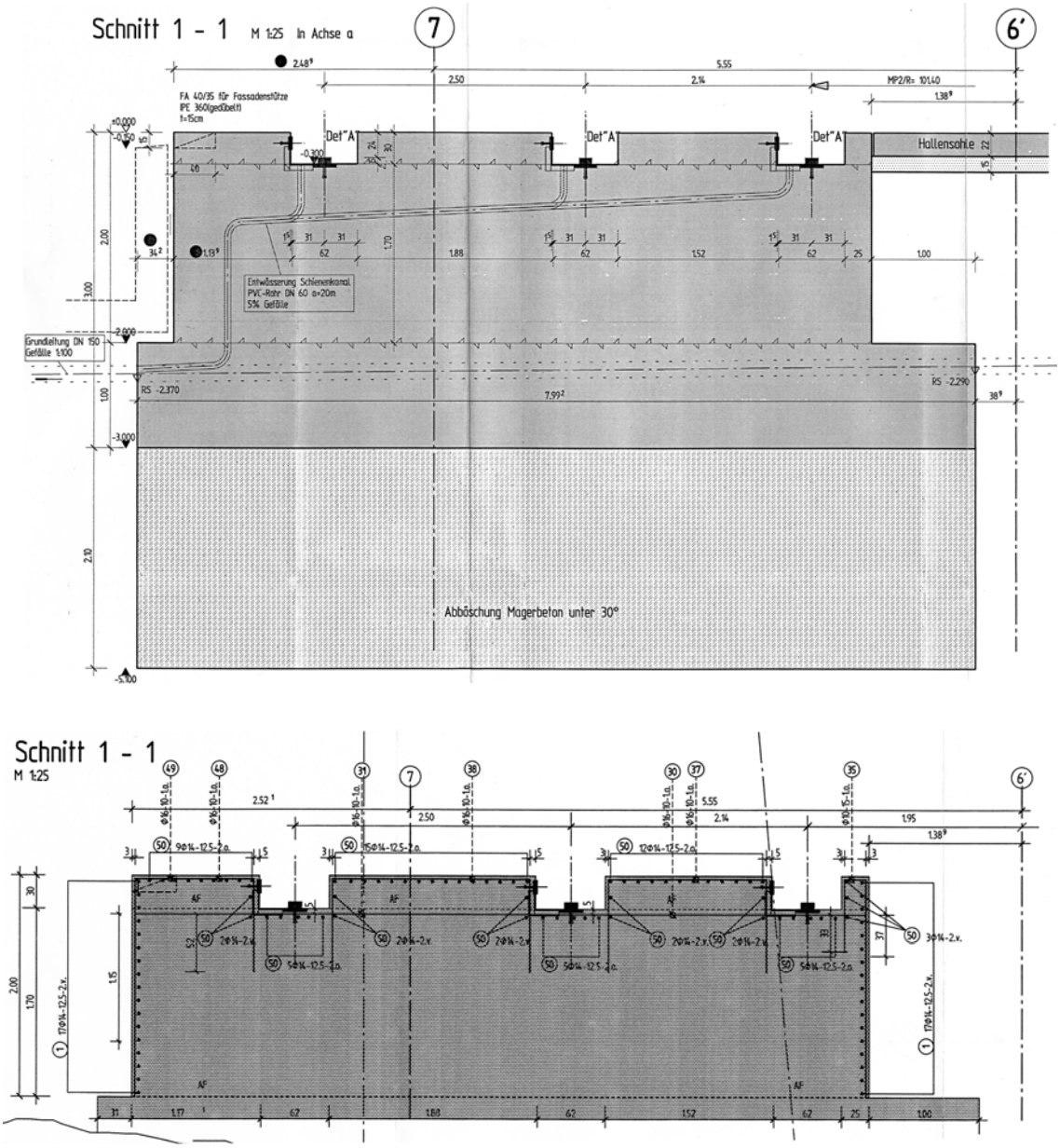

Figure 11-9: Typical reinforcement

11.1.3 Structure and mechanisms

The enclosure structure is made of one main arch and three rotating arches which rotate around a central hinge hold by the main arch.

Bogies are mounted at the bottom of the three rotating arches to allow the opening of the doors. Each bogie has four motorised wheels with diameter of 1m. Bogies are also mounted at the bottom of the non-rotating mainl arch. When the three arches are opened and supported by the main arch the enclosure is moved using a cable system. Cladding is made by insulating sandwich material Figure 11-10.

A Faraday cage is realised by the secondary structure on which the cladding panels are fixed.

The architecture of the central arch is shown in Figure 11-11. The hinge is designed based on the successful concept used for the Cargolifter. It is shown in Figure 11-12.

The masses are summarised here below:

- Main arch 15000 t

- Movable arch 4500 (*3)t
- Motorised boogie 2 t
- Passive boogie 5 t
- Cladding 5000 t

498

The bearings are subjected to loads which are in the order of 10MN while the doors are opening/closing with 27m/s wind speed.

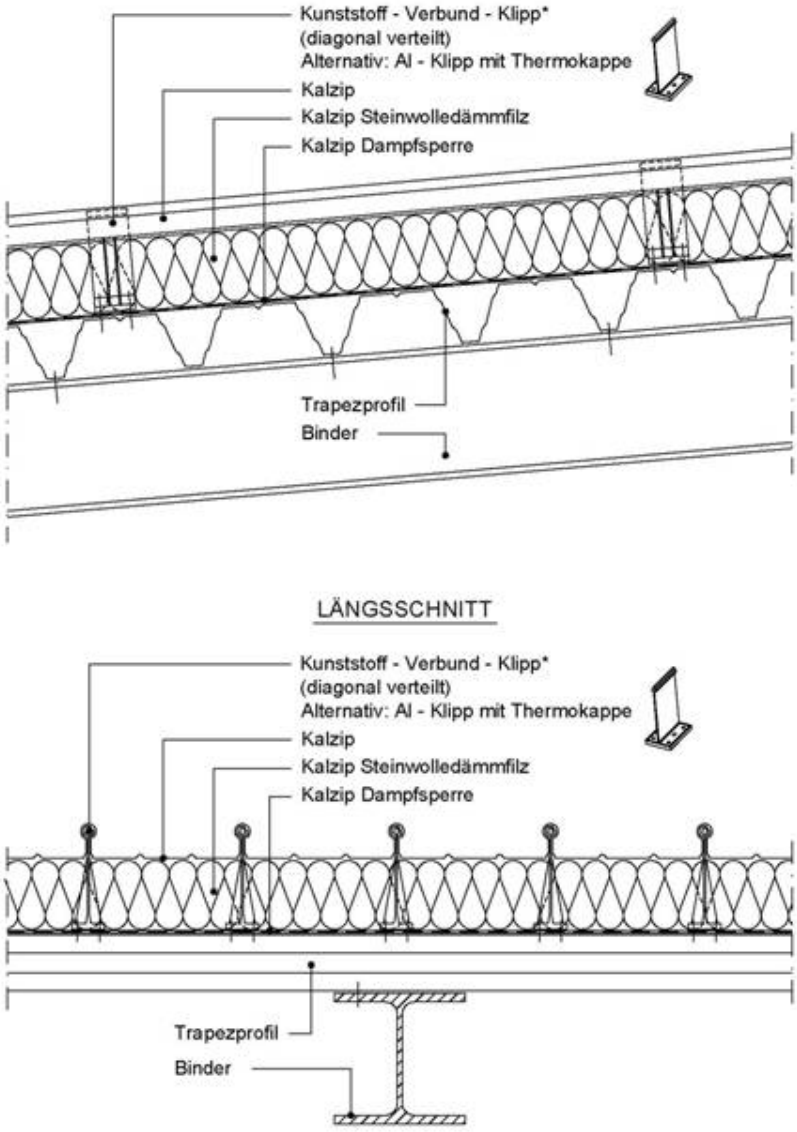

Figure 11-10 Typical cladding panel

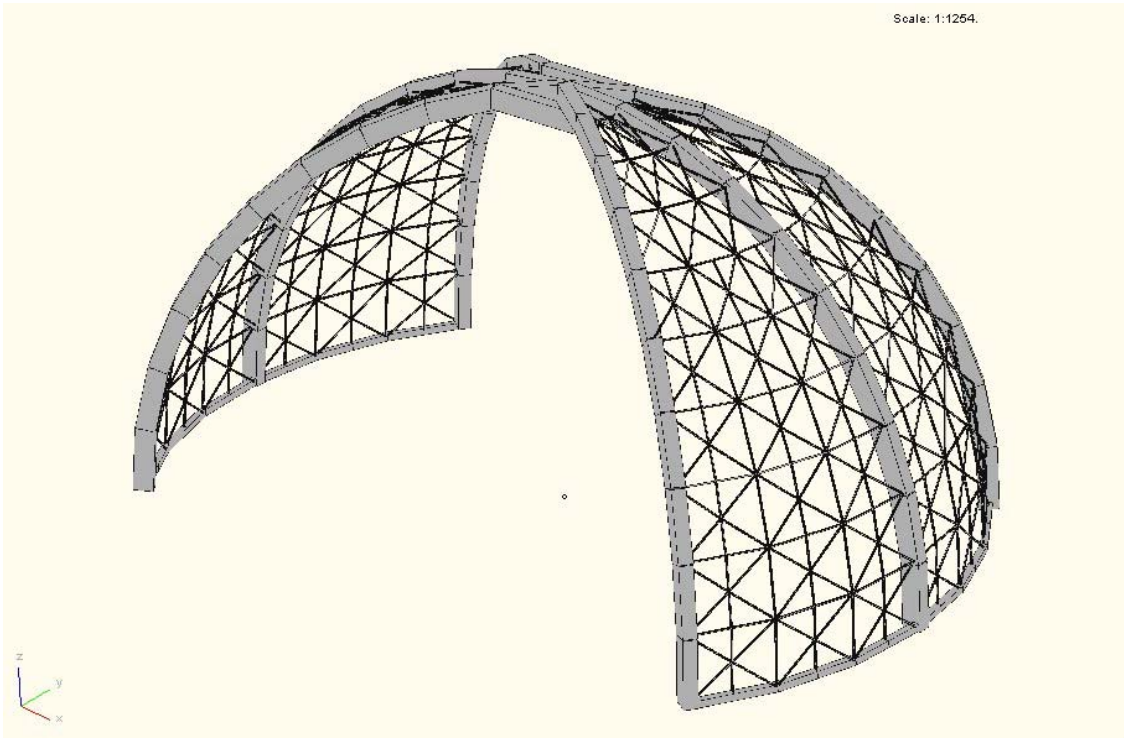

Figure 11-11: Main arch

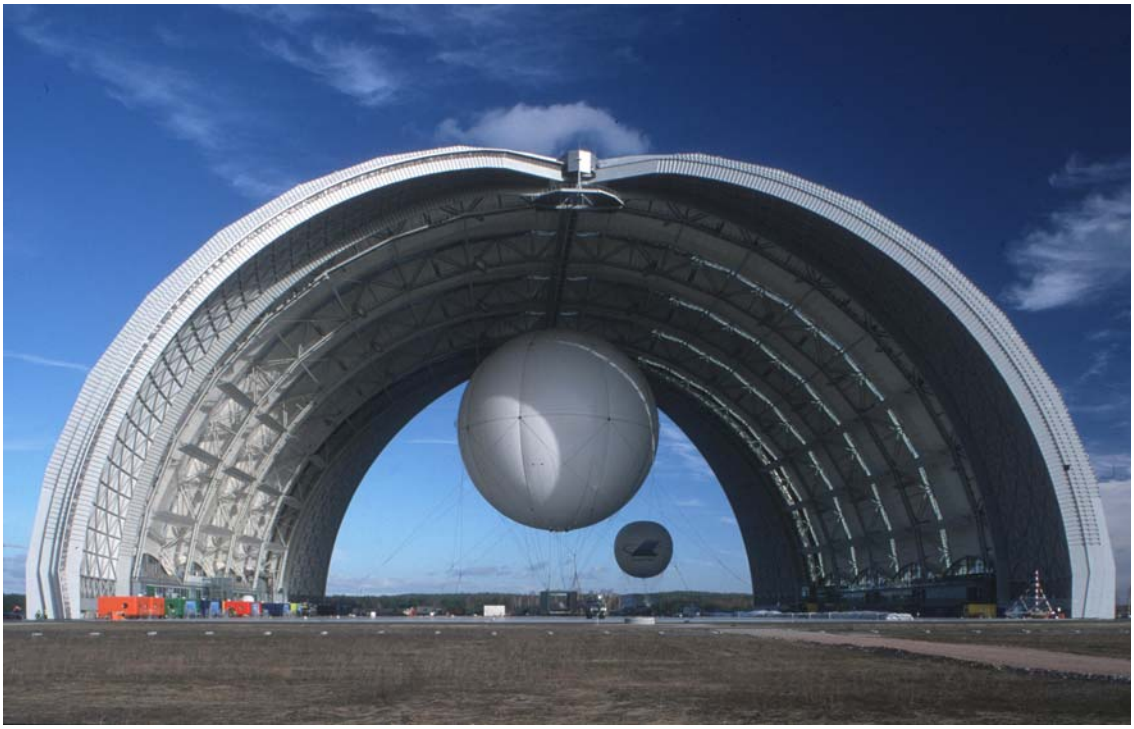

Figure 11-12: Hinge (courtesy cl-MAP)

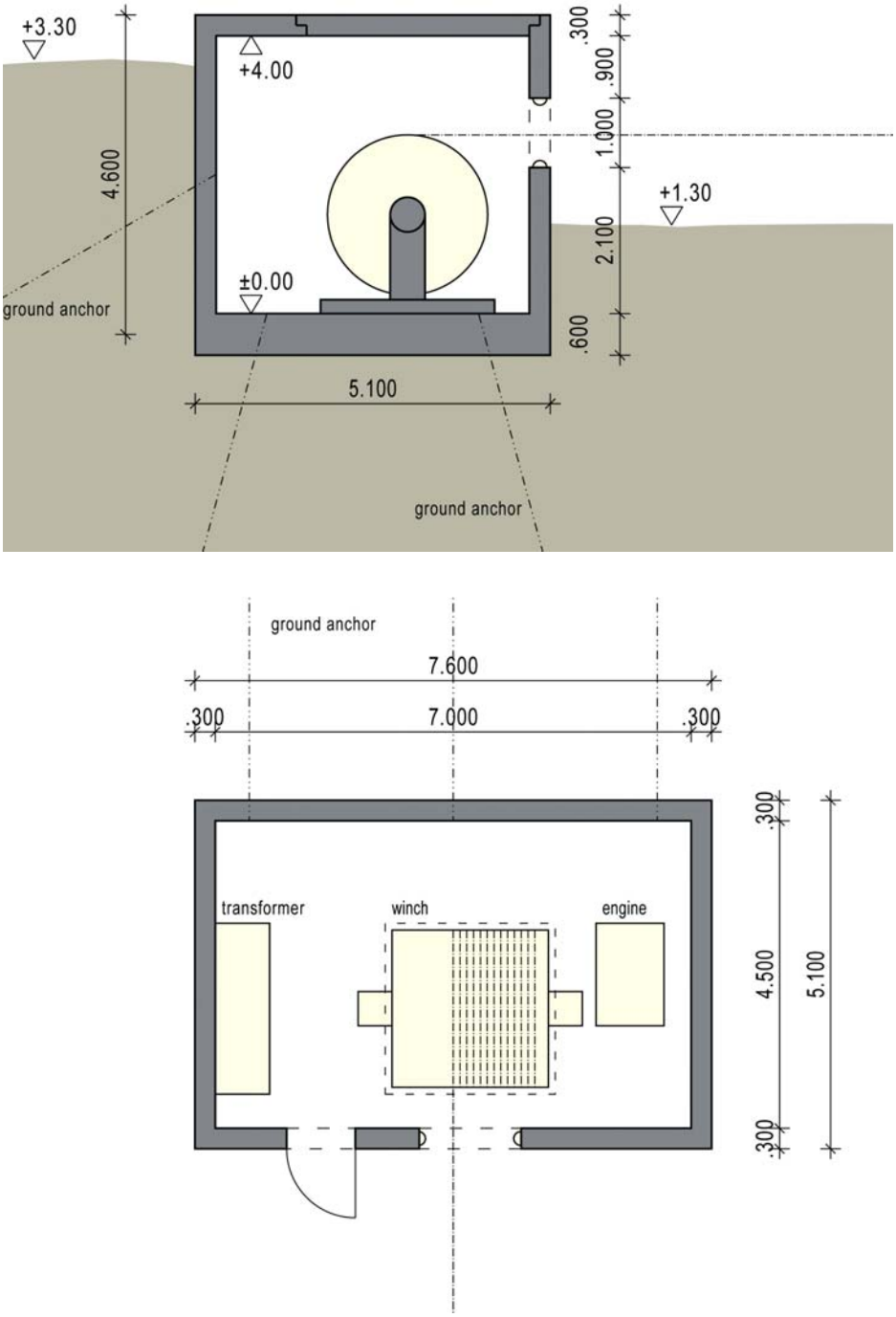

Figure 11-13: Conceptual design of the drive system

The dimensioning load cases have been the survival wind load .

Each segment has inflatable seals along the arch and at the base to realise water tight condition. In case during operation some water leak should happen. it will be easy to build a gutter system to collect it in a controlled way.

Smoke evacuation openings are built in at the top of the enclosure and are controlled and motorised. They are used also to perform the conditioning of the inner volume of air. The openings will be operated according to te wind blowing direction to assure their efficacity.

The drive system is realized with cables and winches.

The power needed to drive the enclosure in 10 minutes from day to night park position is composed of the power to drive the enclosure. the power needed to accelerate the enclosure and the power needed to win the wind resistance force in operational conditions.

Considering that the mass of the complete enclosure is about 34000 t. and assuming that the friction coefficient resisting to the motion if 0.005 the power required to drive the enclosure at a speed of 1 m/s against the 27 m/s wind opened as shown in Figure 11-8 is about 5.3 MW.

A schematic of the conceptual of the drive system is shown in Figure 11-13.

Ways to implement a purely mechanical safety closure system in case of catastrophic power loss when in emergency remains to be assessed in the design phase.

11.1.4 Alternatives

Alternative designed are still under consideration.

One alternative to the baseline is the same concept developed using an innovative approach to structural design. This design is described in RD40. The concept is still the sliding hangar. but the structure is supported by reinforced low pressure air cushions. This system allows to relieve the problem of buckling in the compressed trusses; therefore the quantity of steel used is much lower than in the classical structural design. Of course the design takes into account structural reserve to resist partially to compression so that in case of accidental loss of pressure in the auxiliary pneumatic structure the construction has reserve to take loads until repair.

The saving in material mass is considerable and brings to large cost savings. In Figure 11-14 the principle of this technology is illustrated in the typical case of building bridges. In Figure 11-15 the alternative developed design of the sliding hangar is shown.

The choice to build the main door in one segment is made possible by using this peculiar technology. The structure is very light. the structural steel. at this stage with no provision to resist to survival load in case of loss of pressure in the cushions. is as light as 5000 t. Taking into account the safety reserve to survive MLE event also in case of total loss of pressure. brings the total structural steel weight to about 10000 t.

The Membrane which covers the enclosure is plastic material cladded with sylicons.

Figure 11-14: Principle of the air supporting structure (courtesy Airlight)

Another concept investigated is the one referred to in SPIE paper year 2000.

The principle is shown in Figure 11-16

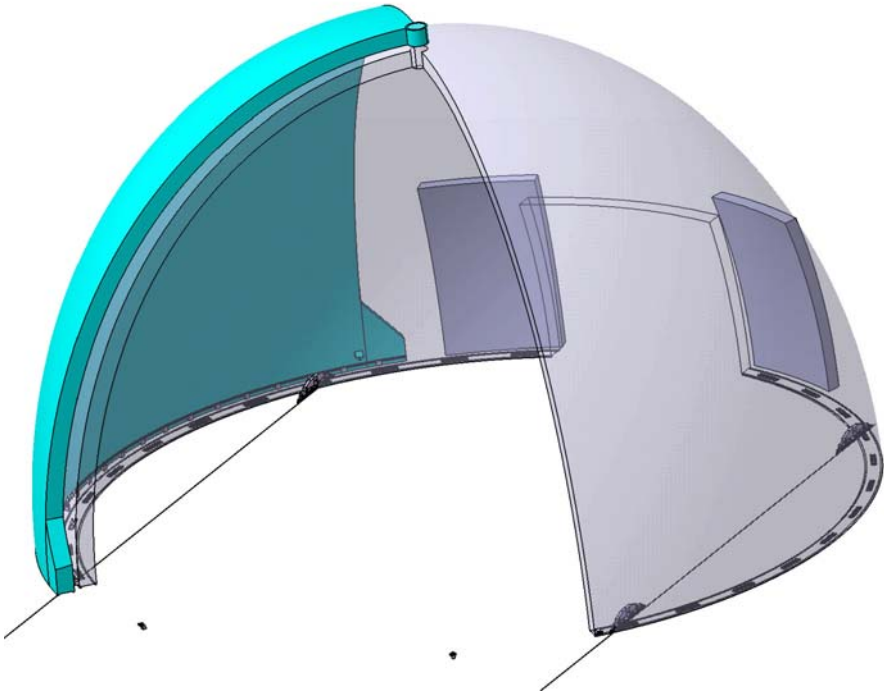

Figure 11-15: Lay out of the alternative design of the OWL enclosure

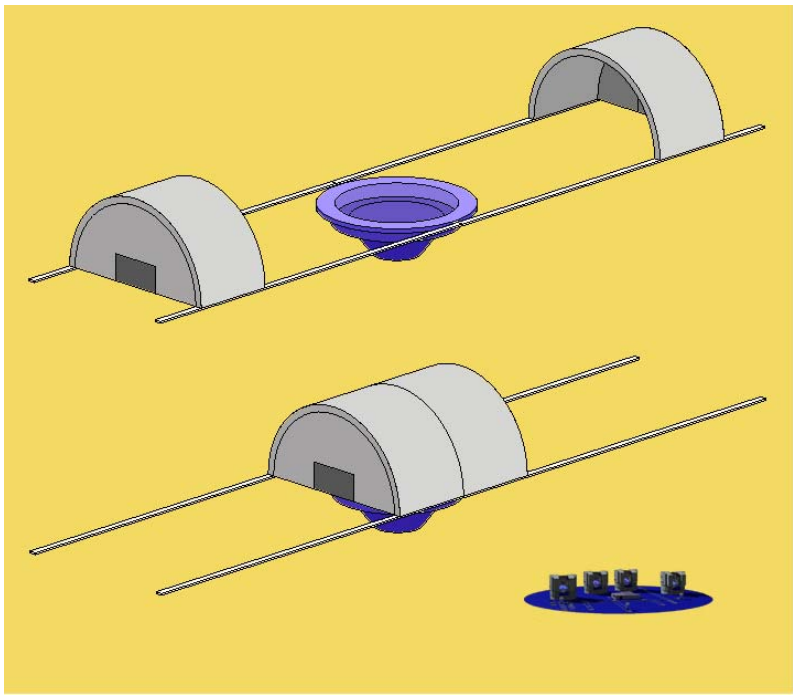

Figure 11-16. Two halves concept (right below teh VLT telescopes platform)

The main advantages of this concept are that no large arches are to be rotated. and this will facilitate the operation and the functionality of the enclosure. Moreover seals are needed only at the junction arch. which makes easier the water tightness management (in case of unforeseen leakage it is even easier to implement a conveyor system). The disadvantages are in the large space required to accommodate the concept.

Another concept only shortly investigated is the “radome” (cupola) concept shown in Figure 11-17

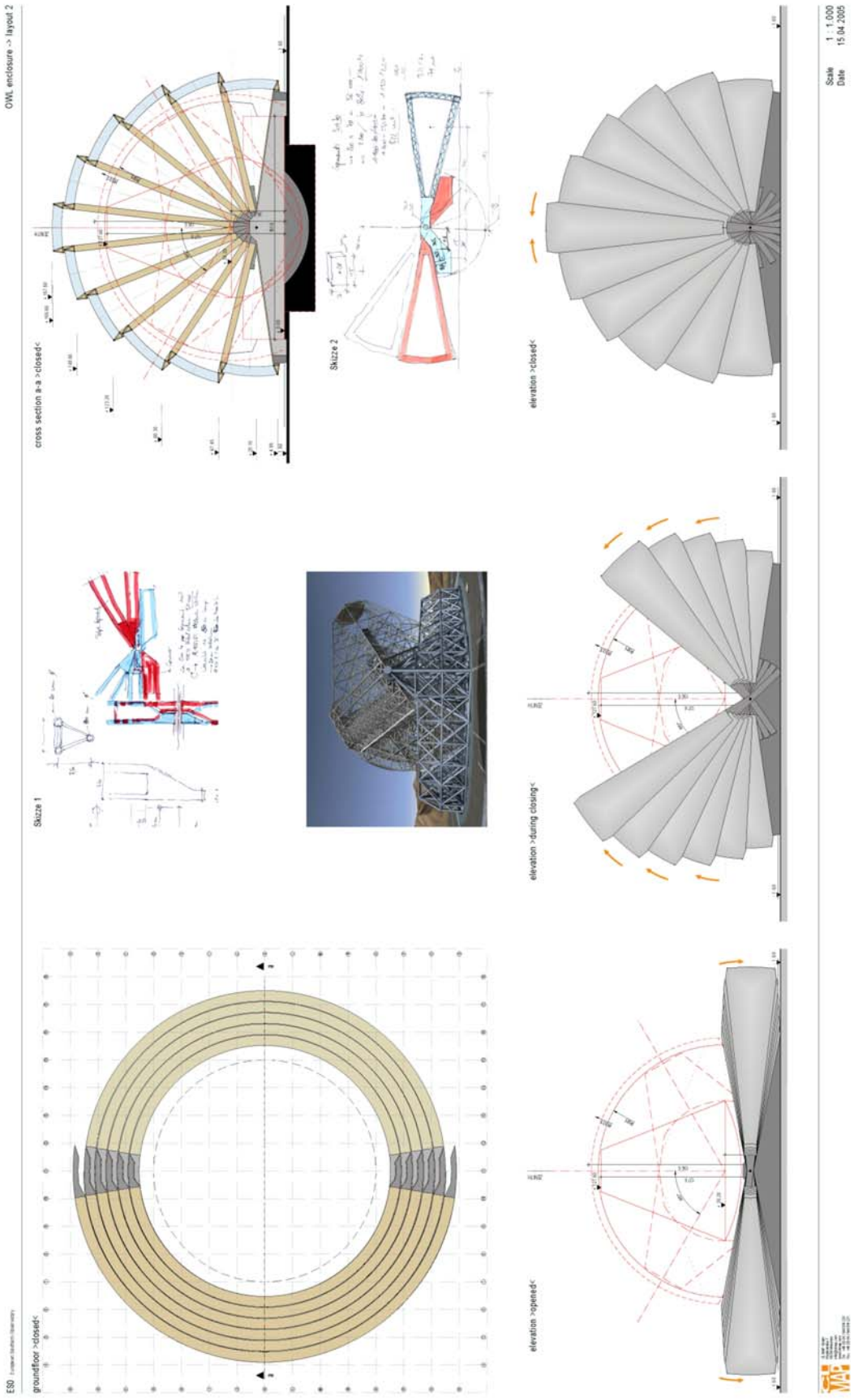

Figure 11-17: Radome concept (cupola) for OWL (courtesy cl-MAP)

This concept has significant advantages from the site dimension requirements point of view. On the other hand preliminary structural calculations have shown that a larger steel quantity is required to meet the technical specifications set for OWL enclosure than for the sliding hangar concept. and therefore the costs would have been much higher in this case. The biggest unknown in this concept is the two large hinges to which all arches are connected. So far no such a component with so high load bearing capability has ever been built.

Using the air cushion technology the same “radom” concept looks more viable. although prototyping will be needed to qualify it for the purpose. How this concept may look like is shown in Figure 11-18 The main feature which makes this technology interesting is the capability to close the dome using the same air pressure which stabilises the structural construction. The arches are hinged singularly on an arch-like structure and this way remove the problem of the previous design. see Figure 11-19.

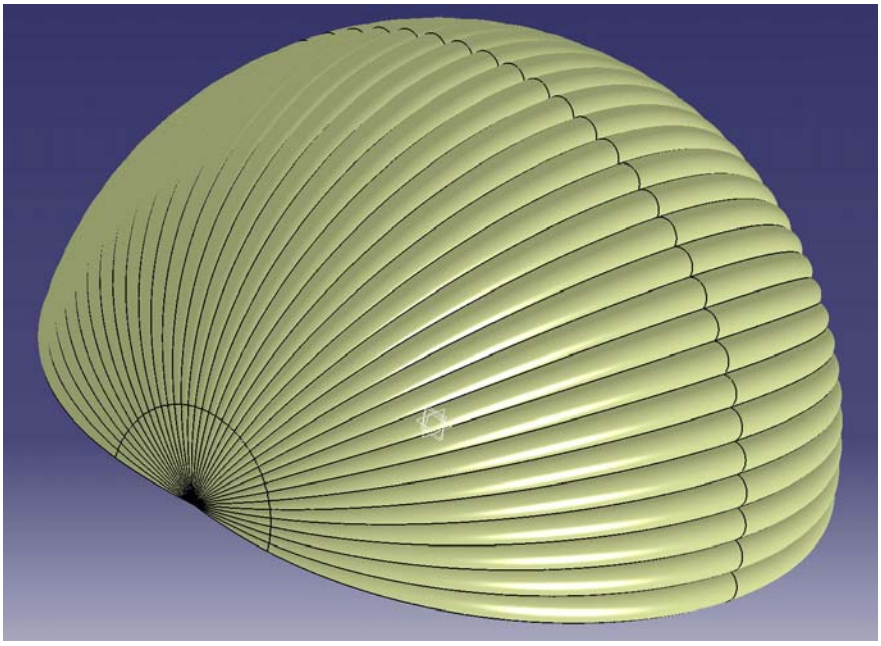

Figure 11-18: Radome concept using air cushion technology (courtesy AirLight)

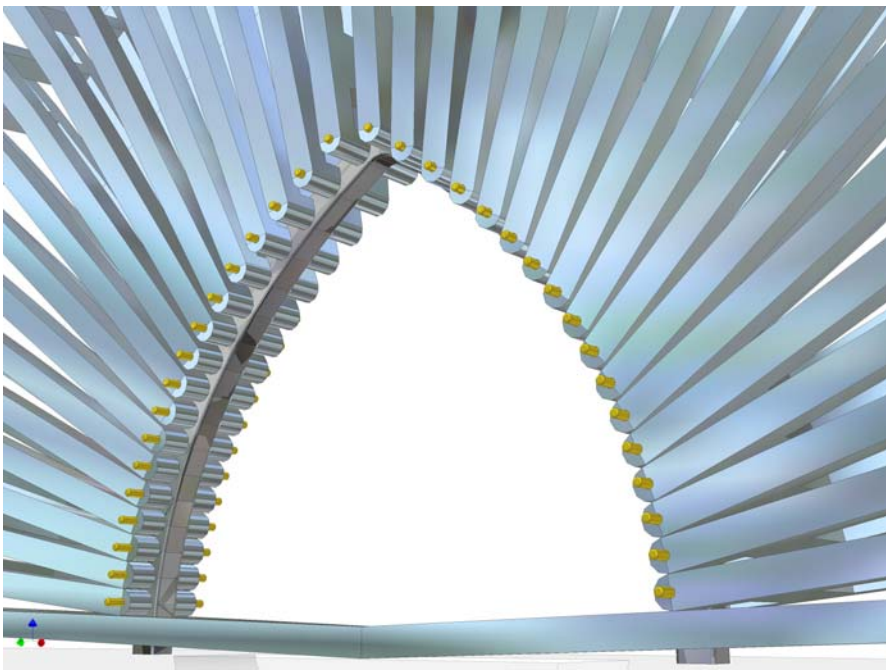

Figure 11-19 Arch-like structure fixing the arches holding the membranes

The airtensity technology allows to have arches with minimal structural cross section and therefore the cross section of the enclosure when open is reduced to minimum. about 9 m height.

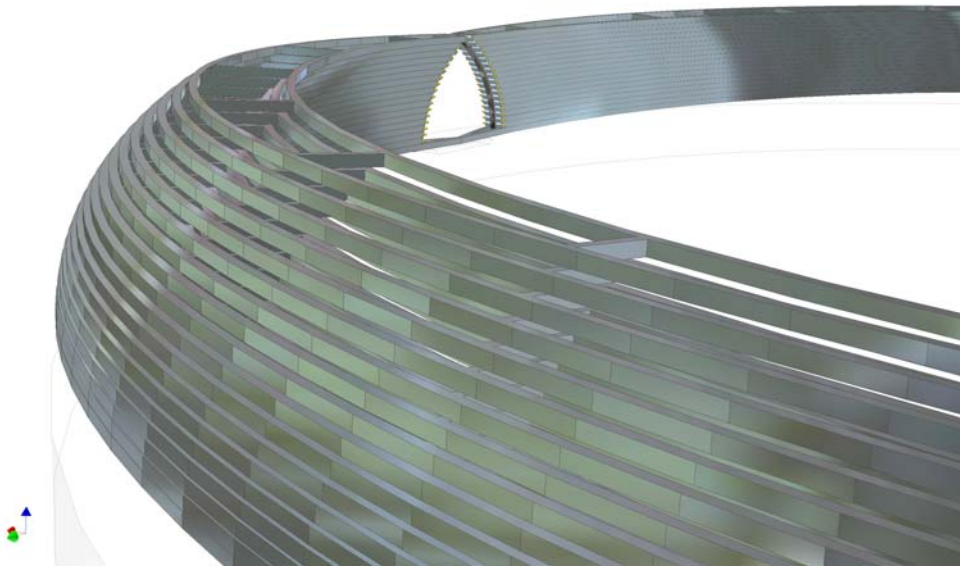

Figure 11-20 Airtensity concept radome enclosure open

In the future activities it is planned to look further in detail into the different alternatives to trade off the costs in all their aspects and therefore to identify the best solution. This may include building prototypes to validate promising construction technologies.

11.2 Infrastructures

As a starting assumption (and without prejudice to the global search for an OWL site) for the design the OWL infrastructure two typical observing sites have been considered. One is a new completely undeveloped site in northern Chile close to Paranal. at 2800 m altitude (Ventarrones). The required development of this site is very similar to the development carried out for Paranal. and allows a fairly accurate assessment of the costs involved.

The second site is Roque de los Muchachos at La Palma in The Canaris Islands. This site is developed. access roads are present. and power is delivered by the national net.

The two sites topography are shown in Figure 11-21 and Figure 11-22

Figure 11-21: Ventarrones (top right of the figure)

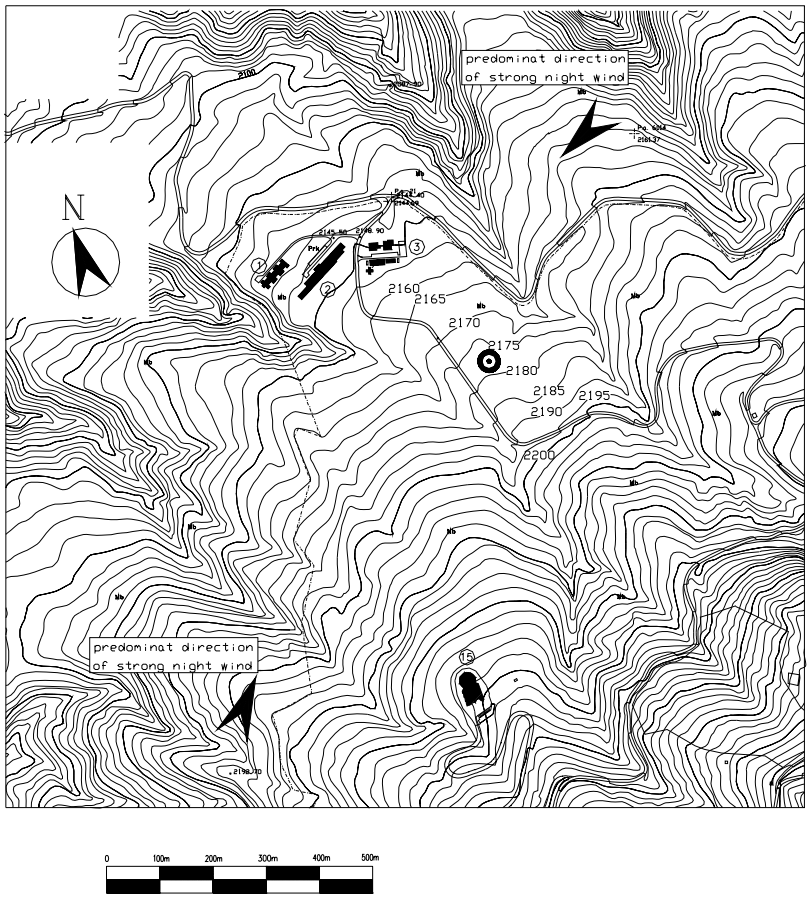

Figure 11-22: La Palma

The infrastructures here considered are the following:

- Mirrors maintenance building with mirror coating plant.
- Laboratories for mechanics. electronics. optics and instrumentation integration and testing.
- Offices and control room.
- Personnel accommodation building
- Power station
- Chilled water and conditioned air production plant
- Earth works and site preparation
- Access and services roads

The services will be supplied. as in the VLT. grouping them in Service Connection Points (SCP). Each SCP will be equipped with:

- Power supply: normal 230V and 400V. UPS 230V and 400V. current rated at 150 A. which allows to draw 104 kVA three-phase power and 34.5 kVA single-phase power.
- Cooling liquid inlet and outlet: flow at -8 ºC with respect to ambient temperature for economical reasons. The flow can remove 90 kW thermal power maximum (diameter of the pipe is 3". cooling liquid speed is 1.3 m/s and the temperature difference between inlet and outlet is 4 ºC). In case the difference between inlet and outlet is allowed to be 6 ºC the 130 kW thermal power can be removed.
- Compressed air.
- Optical fibres unit.
- Liquid nitrogen distribution: flow equal to 600 l/hours.

The needs for drinkable or sanitary water. fuel and services supply is not discussed here.

Two main buildings are considered in the conceptual design:

- The **service building**. this includes offices. laboratories. instruments assembly/test hall. mirror maintenance hall. utilities (air conditioning and chilled liquid production plants). electrical power distribution and storage area.
- The **hotel** which offers accommodation facilities for the personnel.

Moreover there is an area on which the construction which houses the electrical power production plant is built (if needed).

11.2.1 Mirrors maintenance

Depending on the ventual coating technology. OWL will require recoating of up to 5 segments every day. and every 2 years to recoat 4 mirrors with diameters varying from 2.3 m to 8.2 m.

For this operation we plan to use the same type of coating plant used in Paranal for the large mirrors with yearly need of recoating. and an in-line coating plant completely automatic for the everyday recoating of the segments.

A possible line horizontal coating plant is shown in Figure 11-23. A vertical in-line coating plant would also be possible (e.g. by Laybold Optics).

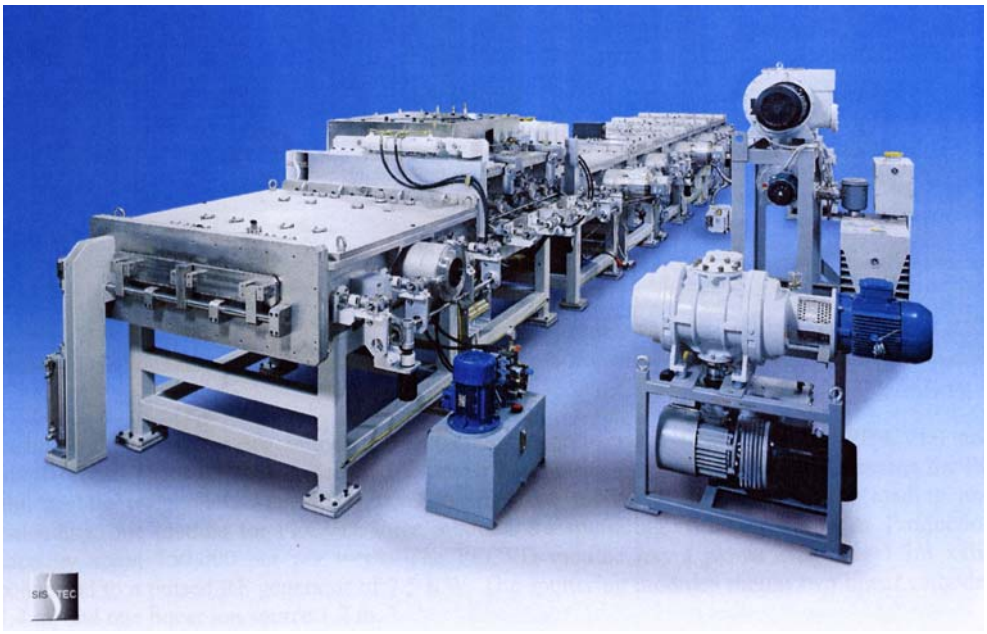

Figure 11-23: Horizontal in-line coating plant (courtesy SISTEC-It)

It might be possible to include in the in line plant a pre-cleaning treatment stage using linear ion source or plasma etching.

The plants are modular and can be designed to accept extensions or change in process like for example coating with Ag or Au.

The large number of spare segments allows to plan to build one in-line plant only. In case of failure during the repair period one can use the large coating plant to re-coat up to12 segments a day by changing the 8.2 m mirror support structure.

The use of one single coating vessel for the 4 large mirrors must be studied in detail. considering the different radii of curvature and inner holes diameters.

The mirrors maintenance building is located close to the storage building and to the laboratories.

The dimensions of the building are 50x30x10 m. In this space one finds:

- The handling area. in which the segments/mirrors are dismounted from the support.
- The Washing area. in which the surface is prepared for recoating housed in a clean room class 1000.
- The coating plant for large mirrors.
- The area in which the on line coating plant is installed.

A gantry crane with lift capacity of 30 t equips the building.

11.2.2 Laboratories

Under laboratories are included the areas where the mechanic. electronic and optics workshops will be housed and the instruments assembly and test hall will be provided.

The laboratory area in the building is subdivided as follows:

- Mechanical workshop 25m x 20m x 10m
- Electronic workshop 25m x 10m x 10m
- Optic workshop 25m x 10m x 10m

- Instruments assembly/test hall 25m x 20m x 7.5m. in this area a clean room class 10000 is located.

The height of the buildings is defined by the maximum height of the instruments. which is provisionally set at 5 m. and the space to operate the gantry crane.

The workshops are equipped as follows:

- Supplies are provided for water. cooling. compressed air. power. normal and UPS. 230V and 400V. signals.
- In the instrument assembly hall also a supply line for liquid nitrogen is provided.
- All the workshops are equipped with gantry cranes with following capacity:
  - Mechanical workshop: 20 t
  - Electronic workshop: 5 t
  - Optical workshop: 2 t
  - Instruments assembly hall: 20 t

The instrument assembly hall is dimensioned to allow the handling of a maximum of two instruments at a time.

An assembly hall where the correctore is separated into the different mirror units is provided before the mirror maintenance building. It has the dimensions of 40 m x40 m x15 m. It is equipped with agantry crane with the capacity of 50 t.

11.2.3 Control room and personnel offices

At the second floor of the service building an area of about 2100 m^2 3.5 m height is occupied by staff offices and by the telescope control room.

The control room is planned to occupy an area of about 200 m^2. The height of the room is 3.1 m and a false floor 40 cm deep is provided for cabling and services.

The offices space is planned to receive about 90 persons at up to 20 m^2 of space each.

11.2.4 Air conditioning and chilled water plants

For cost reason the design of OWL is such that only only limited volumes require air conditioning.

Those volumes are:

- M1 mirror: total volume enclosed 102845 m^3.
- M2 mirror: total volume enclosed 4115 m^3
- The corrector: total volume enclosed 4801 m^3
- The focal station: total volume enclosed 6172 m^3

The total volume to be conditioned is 117933 m^3. This volume is about the one conditioned in total in Paranal. The same installation type used in Paranal has been therefore foreseen. The total power needed is about 1 MW. The chilled liquid will be produced in the centralised plant placed in the utilities room. The global need is calculated as about 600000 l/h.

The cooling liquid will be delivered to the utilities by a pumping station installed in the utilities room.

11.2.5 Fluid distribution

Besides chilled water and compressed air. in the SCPs in the instrument room on the telescope and in the service building. it is planned to distribute liquid nitrogen and pure helium gas.

In the case of liquid nitrogen one has to provide a jacketed line under vacuum to have good thermal insulation. A total of about 500m line needs to be installed. Due to the length it is necessary to keep the vacuum using vacuum pumps about every 100 m.

In the utility room a tank will be installed to house the liquid nitrogen. No decision whether nitrogen should be delivered by a company or produced locally has been taken yet.

The nitrogen will be also made available in gaseous form for cleaning purposes. The supply and return line for clean helium gas Is under study. This will allow not mounting close cycle cooler on the telescope. avoiding source of vibration.

Dry and compressed air will be distributed at all Service and Connection Points (SCPs).

11.2.6 Power station

Unless electric power is derived from an interconnected system (*network*). a power station will have to be installed and operated. A medium-voltage power distribution system will be required to distribute the power to the main buildings and structures. each of which will be provided with its low-voltage (typically 400 V a.c.) power distribution system. The environmental impact of the choice shall be minimized.

The generators can be based on internal combustion engines (diesel engines. gas engines or gas turbines). according to the available fuels and their price. the use planned and while taking into account the maintenance services available in the country of the site.

By analogy with the solution adopted at the VLT Observatory at Cerro Paranal. four generating sets may be installed. To cover the maximum demand three gen sets will be required to operate in parallel while the fourth one in stand-by. The fourth gen set will be called upon duty when one of the others is out-of-order or in maintenance. A more reliable alternative would be a power station comprising five gen sets. three in operation to cover the maximum demand. one in hot stand-by and the fifth under preventive or corrective maintenance.

System/utility	Active power P [MW]	Apparent power S [MVA]	Power factor P/S (based on Paranal data)
Telescope	2	2.5	0.8
Enclosure	5.3	6.6	0.8
Chilling liquid plant	0.5	0.56	0.9
Air conditioning unit	1	1.25	0.8
Large mirrors coating plant	0.4	0.44	0.9
Line recoating plant	0.18	0.2	0.9
Small loads	0.1	0.13	0.8
Compressed air plant	0.2	0.22	0.9
SCPs instrumentation chamber	0.6	0.75	0.8
Total	10.28	12.65	0.81
Maximum demand during operation	8.58	10.58	0.81

Table 11-3: Power consumption estimation

If four gen sets are installed. each would be rated ~3.5 MW at 2800 m above sea level.

The maximum demand of the observatory is calculated based on the following assumptions about the time coincidence of the maximum demands of the individual structures and buildings.

- Enclosure is moved at maximum speed (1 m/s) and telescope is slewed at maximum speed with wind speed 16 m/s.
- The air conditioning of the telescope is off while telescope is moving.
- Chilled liquid production plant is on.
- Recoating process of the mirror segments is taking place.
- Recoating of the larger mirrors takes place when telescope and enclosure are in park position.
- The small power loads (lighting. socket-outlet circuits. etc.) are assumed to be like those in the VLT Observatory (the occupation of the site is similar).
- Only half of the Service Connection Points (SCP) are used at the maximum power.

The estimated power requirements are listed in Table 11-3.

Installing four generators rated 3.5 MW at 2800 m height. rated about 4.5 MW at 300 m height. and operating continuously one obtains a safety factor with respect to the maximum demand during operation of about 20%.

A choice of the power supply system shall be made only after a detailed specialized study. In this study the different possibilities shall be explored both technically and economically. An analysis of the power demand waveform shall also be performed to exclude the need to adopt flywheels to cope with fast switching mode. In this conceptual study this was excluded on the basis of ESO experience in operating the VLT.

11.2.7 Personnel accommodation building

The building to host the personnel and the visitors is located on the north side of Ventarrones to take advantage of the sun exposure during winter time.

In La Palma the hotel area is placed downhill of the telescope.

No concept desisgn has been developed. At this stage it is assumed that a solution similar to Paranal's would be adequate.

11.2.8 Site preparation

Site preparation activities are:

- Construction of the access roads
- Mountain blasting and levelling
- Telescope platform blasting/excavating for telescope. enclosure foundations and utilities
- Site blasting/excavating to create area for service building and hotel building.
- Preparation of first infrastructure like construction camp. sewage. drinkable water supply.
- Concrete foundations for buildings enclosure and telescope.

All these activities are strongly dependent on the nature of the site.

In order to cover the largest possible situations. the exercise to design and to estimate the effort involved has been carried out for two typical sites:

- Ventarrones in Northern Chile

and

- Roque de los Muchachos in La Palma. Canaris Islands.

The work performed in 1993 for the Max Planck Institute for Astronomy of Heidelberg to study the feasibility of infrastructure construction in Gamsberg in Namibia has been source of inspiration.

11.2.8.1 Camp and first infrastructures

Before starting the erection of the OWL observatory a camp will be established on the site.

The camp is made of standard containers. After a first phase during which occupancy is estimated in about 50 persons. to prepare the access roads to the telescope site. the occupancy will grow with the arrival of the contractors to prepare the site (Blasting).

It is expected that the camp will then grow in the first year up to a maximum occupancy of about 300 people during the integration of enclosure and telescope.

An unpaved road from the closest existing one to the site will be built (Old Panamericana in the case of Ventarrones and the closest observatory road for La Palma).

In Ventarrones also a service unpaved road will be built to connect the telescope platform to the service area.

11.2.8.2 Earth works for telescope platform

Due to the large dimensions of the installation the earthworks to flatten the telescope area. to prepare the trenches for the foundations of the enclosure and of the telescope and to prepare the areas to build the auxiliary buildings will be a non negligible cost in the project.

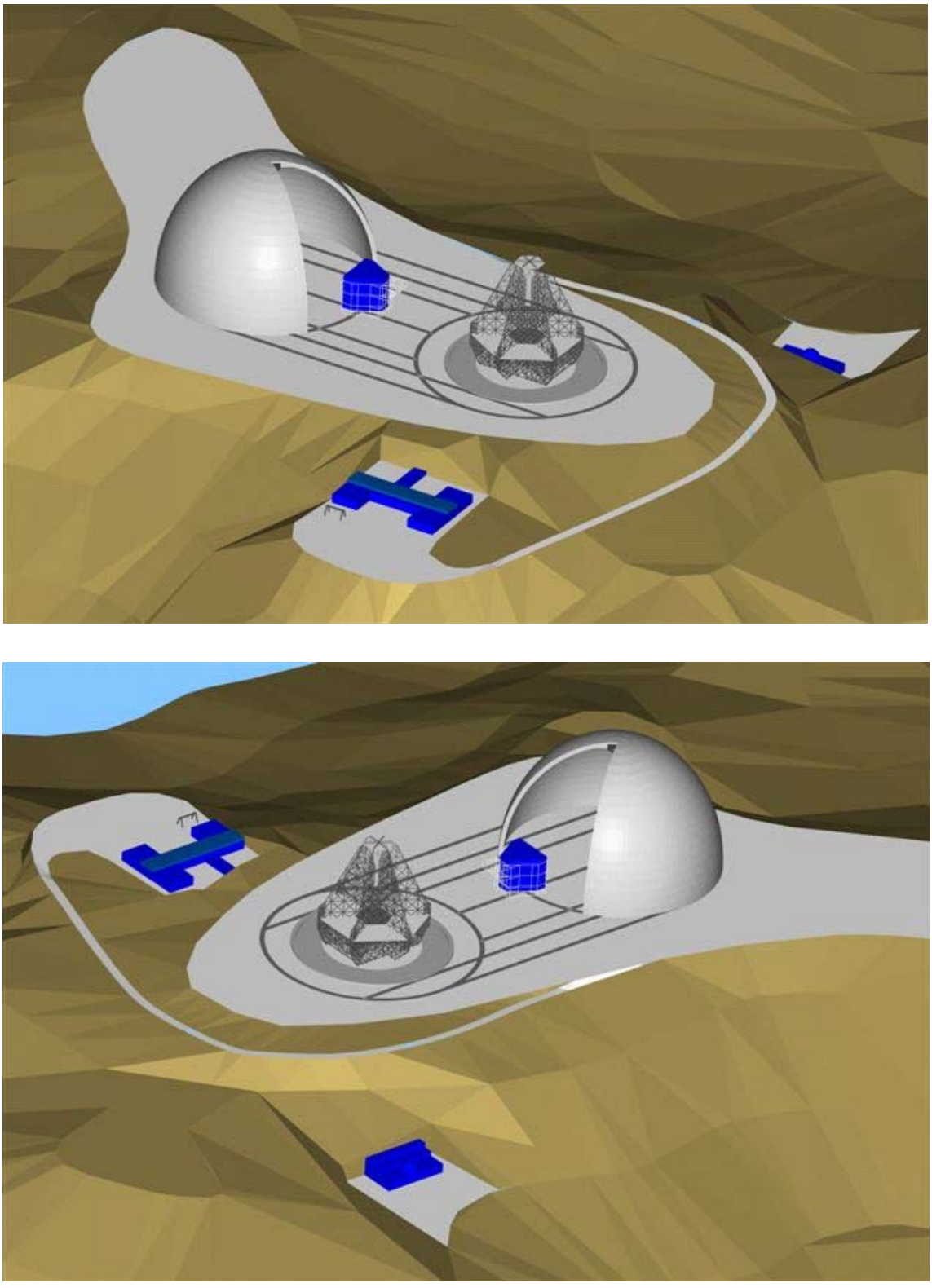

Figure 11-24: Ventarrones: Observatory lay out (auxiliary building side above; hotel side below)

Figure 11-24 and Figure 11-25 show a possible site excavation for the sites of Ventarrones and La Palma. respectively..

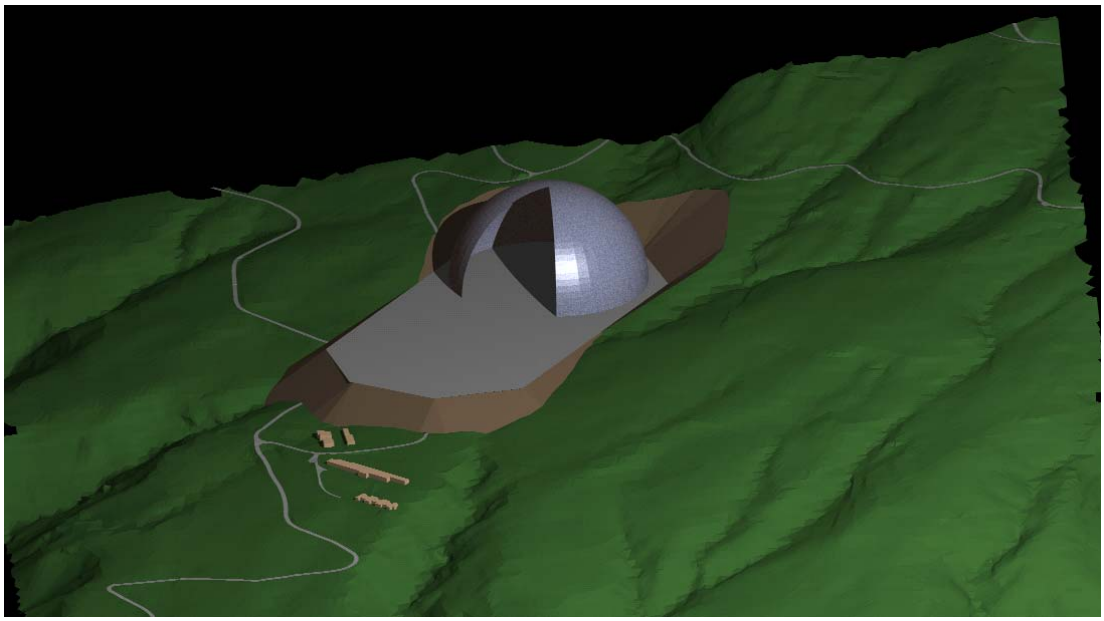

Figure 11-25 The enclosure installed in La Palma

The volume of rock to be blasted for the two sites is summarized in Table 11-4.

Due to the large quantity of material to be blasted and relocated in both sites. it will be most economic to bring up to the mountains the equipment which will be used also to crash the rocks in the right dimensions to prepare the aggregate for the concrete and for the compacted relocated material. In this case it is believed. and therefore assumed. that the cost to blast crash and relocate the material will be the same for the two sites.

item	**Ventarrones volumes [m^3]**	**La Palma volumes [m^3]**	**remarks**
Telescope platform	3000000	2375000	Here it is considered. conservatively that both enclosure's and telescope's foundations lies on solid rock and not on compacted soil. If one assumes that the enclosure's foundations can be built on compacted soil then the volumes decrease to about 2000000 for both sites.
Enclosure foundations	65000	65000	
Telescope foundations	170000	170000	
Service building	30000	21500	Includes the tunnel to telescope.
Hotel	9000	5000	

Table 11-4: Volume of earth to be removed to prepare the site.

11.2.8.3 Access roads to the Observatory

In a second phase the roads prepared will be paved. In the case of an undeveloped remote site this will require to build locally the plant to produce the tar.

The length of roads required for the two sites are of course very different.

In the case of Ventarrones the site is located at about 10 km from the Old Panamericana. a situation very similar to Paranal.

In the case of La Palma only the service roads are to be built.

The estimated total lengths of roads for the two sites are

- Ventarrones: 15 km
- La Palma: 3 km.

The roads have a maximum slope of 7%. and in Ventarrones are 15m wide.

11.2.8.4 Miscellaneous

During the construction of the observatory services will be needed. These services must be purchased. The following must be procured: drinkable water supply. catering services. transport services. transportation means and salty water supply to compact the roads before they are paved.

12. Instrumentation

12.1 Technical instrumentation

According to plan. one focal station (No 6) is reserved for permanently mounted technical instrumentation. Its purpose will be to provide extensive on-sky diagnostics. It will be OWL's first instrument but its operation will in principle not be limited to the integration phase of the system.

No conceptual design of the instrument(s) has been initiated yet. The following list provides a set of preliminary requirements:

1. It shall allow for simultaneous imaging of the pupil. of the seeing-limited Point Spread Function and of the adaptively corrected Point Spread Function (correction with M6 only or with M5 and M6).
2. It shall allow simultaneous imaging of the primary and secondary mirrors.
3. The wavelength range and field of view shall be defined in the design phase.
4. It shall allow simultaneous operation of
   - 4.1. At least 7 active optics wavefront sensors;
   - 4.2. At least 6 adaptive optics wavefront sensors;
   - 4.3. At least 3 phasing cameras;
   - 4.4. At least 3 guiding probes.
5. At least 1 active optics and 1 adaptive sensors and 1 phasing camera shall be able to simultaneously use an on-axis reference (with a magnitude v=8).
6. At least 3 active optics sensors shall be able to access field positions with a field radius of 3 to 5 arc minutes.
7. Filed de-rotation shall be provided by the adapter-rotator.
8. The adapter-rotator is not required to provide on-sky metrology.

It is expected that the instrument requirements and concept will be defined after laboratory and on-sky tests with the Active Phasing Experiment (APE. see appendix A-1.2).

12.2 Science instrumentation

12.2.1 Scope of the instrument concept studies

In the iterative process to establish OWL feasibility. it is essential to develop valid concepts for a set of instruments that addresses its main scientific drivers. ESO launched in 2004 8 instrument concept studies in collaboration with several European institutes (Table 12-1). In this phase of the OWL project. the studies had the following goals:

- to support the main OWL science cases with feasible and affordable instrument concepts
- to verify and optimize the interfaces and operation scheme of the telescope
- to evaluate the scientific impact of potential sites for the Observatory
- to identify the enabling technologies and the R&D required to develop them

In the selection of the initial instrument concepts. we have been guided by the science cases identified in the OPTICON study of the science case for a generic 50-100 m ELT and by preliminary studies on the OWL scientific goals. The selected instruments offer various imaging and spectroscopic modes of observing and address different wavelength bands from the blue to sub millimeters. They are well representative of the different possible modes of operation of OWL and probe the telescope ultimate capability. The sample is however by no mean exhaustive of all possible. potentially unique observations to be done with an ELT of the OWL class. High resolution spectroscopy in the near infrared. astrometry at the diffraction limit are examples of two interesting modes not explored in this phase.

Instrument	Wavelength range	Main Capability	Primary Science Goals	Institutes
CODEX	0.4-0.7 μm	High velocity accuracy. visual spectrograph	To measure the dynamics of the Universe	ESO. INAF-Ts. Geneve Obs. IoA Cambridge
QuantEYE	0.4-0.8 μm	Photometry at 10^{-3} - 10^{-9} second resolution	Astrophysical phenomena varying at sub-msecond time scale	Padova Univ. & Lund University
HyTNIC	1.1-1.6 μm	High-contrast diffraction-limited imaging	Imaging of massive planets. bright galactic and extra-gal. sources	LISE- Collège de France
EPICS	0.6- 1.9μm	Camera-Spectrograph at diffraction limit	Imaging and spectroscopy of earth-like planets	ESO + ext. experts
MOMFIS	0.8-2.5 μm	Near IR spectroscopy using many deployable IFUs	Masses of high z galaxies. regions of star formation. GC stars	CRAL. LAM. OPM
ONIRICA	0.8-2.5 μm	NIR Imaging Camera on a field up to 3 x 3 arcmin	Faint stellar and galaxy population	INAF Arcetri & Heidelberg MPIfA
T-OWL	2.5-20 μm	Thermal. Mid Infrared Imager and Spectrograph	Search. study of planets. high redshift Hα galaxies	MPIfA Heid.. Leiden. ASTRON. ESO
SCOWL	250-450-850 μm	Imaging at sub-millimeter wavelengths	Surveys of dusty regions. of extrag. fields for star-forming galaxies	ATC

Table 12-1. Instrument Concept Studies.

These studies were not started in vacuo. CODEX owes much to the results of QSO absorption spectra studies from high quality VLT-UVES observations and to the development of the

spectrograph dedicated to radial velocity studies of planets .HARPS. EPICS to the two competing feasibility studies for the VLT Planet Finder project. MOMFIS to the current development of KMOS at the VLT. Also. technological developments pertinent to e.g. EPICS & MOMFIS are currently pursued within the OPTICON FP6 program.

The scope and the content of various concept studies were defined in ad hoc Statements of Work. The study teams were asked to specify the science cases which were driving the instrument definition. to produce a first concept of the opto-mechanical layout of the instrument and to estimate its performance. They were also asked to identify whenever possible interface problems with the telescope or special requirements. to investigate the dependence on the telescope aperture and to compare the expected performance with those of the JWST and when applicable other planned space-born facilities. To support the work on the instruments ESO prepared a telescope interface document and made available on the web an Exposure Time Calculator.

The short time frame available for the completion of the OWL report (less than 1 year after the instrumentation activities were started) has constrained the choice of the groups to carry out the studies to the ones which had both the necessary expertise and the manpower to be assigned to this task in this time frame. Six of the instrument concept studies have been carried out under the responsibility of external P.I.. two were led by ESO.

The eight study reports are available as reference documents. In the next section the results of the various concept studies are presented in a synthetic form. Since the final version of the Concept Studies reports were delivered very close of after the closure of this version of the OWL study. it is possible that the information provided in the next section does not matched exactly the final content of the reports.

12.2.2 Instrument Concept Studies

12.2.3 CODEX: high resolution. ultra-stable VIS-R spectrograph

The concept study of **CODEX (COsmic Dynamics EXperiment)** summarized here was carried out jointly by scientists at ESO. the Institute of Astronomy in Cambridge. the Observatoire de Genève and the INAF-Osservatorio di Trieste. The Concept Study report is provided in RD52 and its content is summarized here.

The primary science objective- CODEX will provide the first direct dynamical measurement of the change of the global expansion rate of the Universe with time. This will allow to test whether the dark energy inferred from other (non-dynamical) cosmological measurements has the dynamical effect predicted by General Relativity.

Essential for this measurement is a significant improvement in the stability and wavelength calibration compared to current instruments and the collecting power of a 100m-class telescope. Capitalizing on the expertise of scientists and engineers at ESO and the other institutes with regard to high spectral resolution spectrographs and in particular to High Accuracy Radial velocity measurements for planetary searches (HARPS). we propose to build an array of ultra-stable high resolution spectrographs. capable of obtaining a radial velocity precision about two order of magnitudes more accurate than is achieved with the best current instruments.

.

CODEX will measure the time derivative of the redshift of objects at fixed cosmological (coordinate) distance using the Ly α forest. which is related in a simple manner to the evolution of the Hubble parameter.

$$\dot{z} = (1+z)H_0 - H(t_e)\,.$$

CODEX will thus measure the change of the global expansion rate with time and will be sensitive to the accelerating effect of the postulated dark energy. CODEX will use QSO absorption spectra taken at two different epochs separated by 10 years or more along many

lines of sight towards z ~1 to z ~ 4 quasars to measure the wavelength shift in the intervening Ly α forest and metallic lines due to the cosmic expansion as illustrated in Figure 12-1.

Measuring the time derivative of the redshift is challenging. Figure 12-2 shows the expected wavelength shift for a variety of cosmological parameters in cm/sec/yr. For the parameters of the concordance model the wavelength shift corresponds to ~6 cm/sec/10yrs at z = 4. It is thus necessary to achieve a velocity accuracy of around 1 cm/sec over a time span of 10 years or more. This is almost 2 orders of magnitudes better than achieved by the best current instruments. Our extensive simulations indicate that such an accuracy can be achieved for spectra with a sufficient S/N ratio. and that such S/N can be obtained with a reasonable amount of observing time on OWL. Figure 12-3 illustrates that the brightest QSO from existing catalogues will provide a sufficient number of photons to ensure the required 1 cm/sec accuracy.

Eq. 12-1

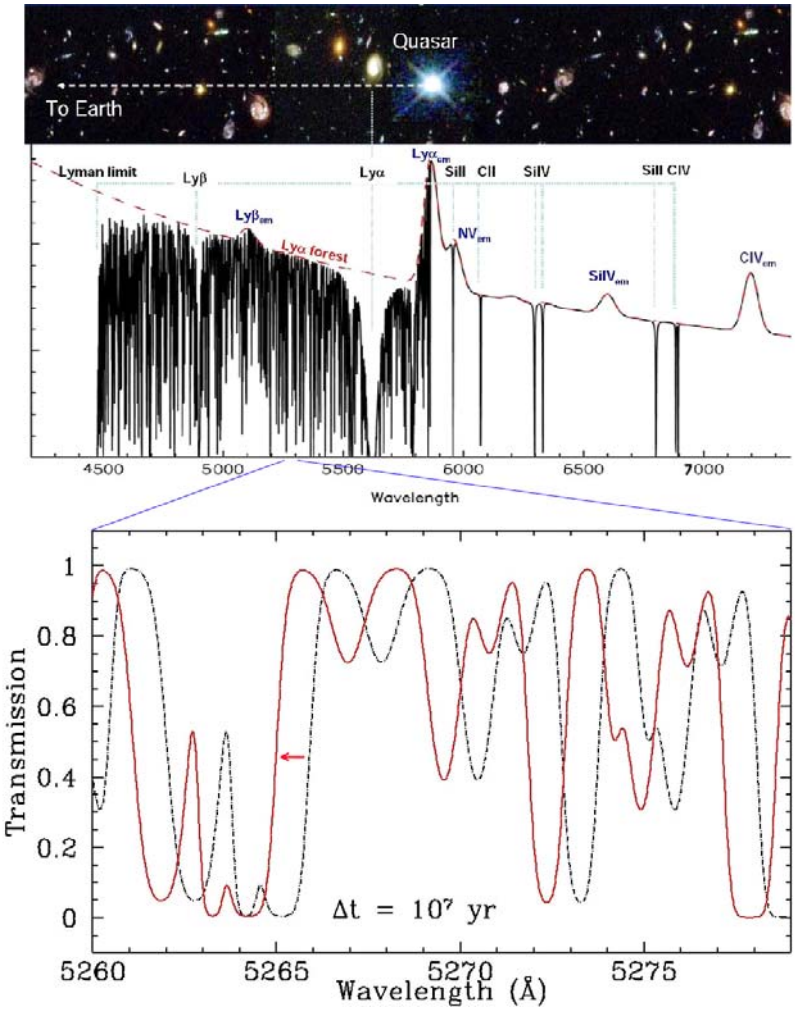

Figure 12-1. The CODEX concept. The simulation represents two observations of the Ly α forest of the same QSO taken at time T_0 (dotted line) and at time T_0+10^7 years (continuous). CODEX/OWL will measure this effect for a separation of the two epochs as short as 10 years by comparing a large sample of high S/N QSO absorption spectra obtained with OWL.

Large number of experiments are planned to further improve measurements of the cosmological parameters and in particular the contribution of the infamous dark energy to the total energy density (Ω_m. λ). These experiments are. however. predominatly geometrical in nature and assume that the Robertson-Walker-Friedman Universe based on General Relativity in 4 dimensions is the correct paradigm. CODEX does not aim (nor indeed will it initially be able) to compete with these measurements in terms of overall accuracy. CODEX will. however. be the

only experiment probing the evolution of the dark energy in the red shift range z =1.5-4. which corresponds to the epoch when the largest fraction of the star formation occurred.

More importantly. CODEX will be the only experiment aiming at directly measuring the dynamical evolution of the Universe. In this way CODEX will allow us to check if the dark energy actually has the dynamical effect predicted by General Relativity.

The CODEX measurement should be considered as a fundamental physics experiment which does not make any assumption regarding the dynamical evolution of the Universe. The measurement accuracy of an experiment like CODEX will improve linearly with time. The CODEX measurement will thus be an important legacy to future generations of astronomers who will be able to use the sample of extremely well calibrated high resolution spectra of bright QSOs obtained with CODEX/OWL as a 'first epoch' measurement .

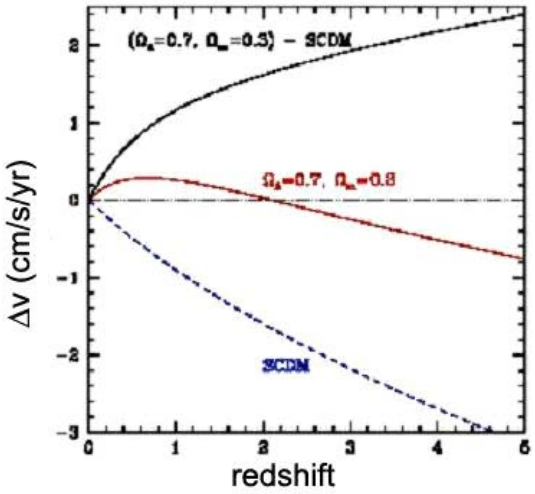

Figure 12-2. Expected wavelength shift for different cosmological models: Standard Cold Dark Matter (lower line. no cosmological constant) and Λ Cold Dark Matter (middle line) with cosmological constant = 0.7. The upper line gives the difference of the two. The signature of the non-zero cosmological constant is the change in sign of the wavelength shift.

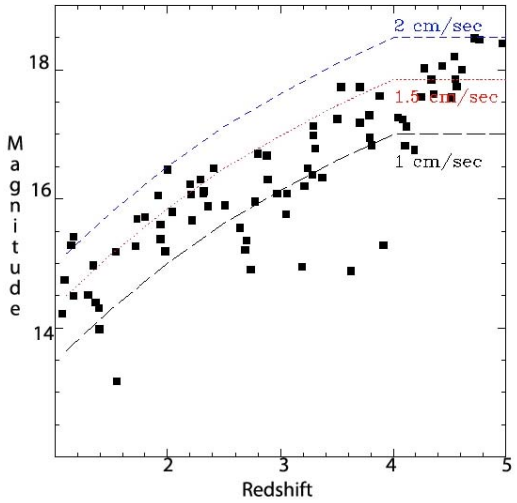

Figure 12-3. Magnitude distribution of known brightest QSO's vs. redshift. From photon statistics and simulations of measurements in the Ly α forest at different redshift one derives the "iso-accuracy" curves plotted in the diagram. The required 1 cm/s/ accuracy is obtained with all the QSO below the 'iso-accuracy' curve in 2000 hours integration (80m telescope. total efficiency 14%. S/N= 13600). In reality the required statistics will be obtained by observing with shorter integrations different QSOs (~40) distributed over the whole sky and at different redshifts.

Serendipity science and other science goals – A very high resolution spectrograph combining the large collecting power of OWL with the highest stability ever achieved by an astronomical spectrograph will have a tremendous impact on many astrophysical programs. many of which we cannot anticipate. The study report discusses three specific examples of great astrophysical relevance.

To achieve its main scientific goal. CODEX will produce a set of unprecedented high resolution (R~150000). high S/N (S/N~2000) QSO spectra. These data could be used in serendipity mode to determine the variations of the fine structure constant to a relative accuracy of 10^{-8}. comparable or better than what can be obtained in the OKLO natural reactor. at least 2 orders of magnitude more accurate than present astronomical measurements. CODEX will also be able to confirm. characterize and eventually discover earth masses planets in habitable zones around other stars. The radial velocity signal of terrestrial planets will have an amplitude of a few cm/sec/yr. but the most difficult (and time consuming) task will be to eliminate the stellar 'noise' mixed to it. CODEX will also be able to determine with exquisite accuracy the abundance of primordial elements (and their isotopes). providing the possibility of relating the physics of the first 20 minutes after Big Bang to that of ~$4x10^5$ years later: CODEX will produce Li^7 and Li^6 /Li^7 abundances for very metal poor stars in our Galaxy and our nearest companions.

The instrument concept and requirements on OWL - CODEX will be realized by building an array of super stable high resolution spectrographs (R=150000). fibre fed. and working in the 440-680 nm spectral range. The proposed concept uses five spectrographs to deliver a 0.65 arcsec entrance aperture for a 100m telescope (or a 1" aperture for a 60m telescope). The spectrographs are hosted in a stabilized laboratory outside the main telescope structure. The concept is modular and can be adapted to a variety of telescope diameters and sky apertures just by changing the number of spectrograph units (for example. a field of view of 1" on a 100m would need 11 spectrographs). In order to keep the grating size acceptable (160 x 20 cm) some novel approach (pupil slicing. anamorphic collimator and VPH) has been adopted. as shown in the optical scheme given in Figure 12-4 and detailed in the report.

CODEX requires seeing correcting active optics only. Its main requirement on the telescope is the need to be located in a thermally and gravity-stable laboratory. This most likely will have to be located outside the telescope structure. The instrument will have to be fed by fiber optics or. preferably. by a coude-type optical train which given the restricted spectral range can be very efficient.

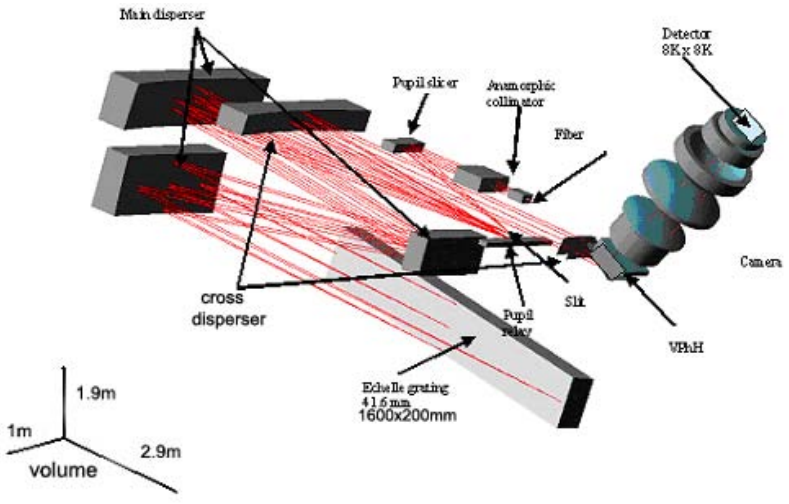

Figure 12-4. Optical Layout of one of the CODEX units. Each spectrograph is contained in a volume of ~3x2x1 meter. The 5 Units will be identical.

To achieve its outstanding long term accuracy CODEX proposes to develop a novel calibration scheme. based on laser frequency combs. which shall achieve the wavelength stability. reproducibility and accuracy typical of an atomic clock over the time scale of the experiment Some of the corrections (e.g. earth rotation. residual systematic trends) will be known only while

the experiment is running for some time. and re-processing of the whole data set could be performed several times with improved data extraction and correction techniques and increasing accuracy.

The concept study shows that CODEX although demanding. is technically feasible with present technology or low-risk developments. Research and development is required in several areas (fibre feeding. detectors. calibration system). and the project will require extensive prototyping and will benefit from targeted scientific programs. such as preparatory analysis of high resolution. high S/N ratio QSO spectra and surveys increasing the number of bright QSO known.

Cost and schedule - The estimated HW cost of the whole project is in 20-30 ME depending on the telescope size and spectyrograph numbers. in addition to ~100 FTEs; a development plan within 12 years is foreseen. which includes the development of a prototype and 3 years of its operations at the VLT.

12.2.3.1 QuantEYE

The QuantEYE study was carried out at the Department of Astronomy of the University of Padova and at the Lund Observatory. P.I. of the study report were C.Barbieri and D. Dravins. The Concept Study report is provided in RD52 and its content is summarized here.

QuantEYE is conceived to be the highest time-resolution instrument in optical astronomy. It is designed to explore astrophysical variability on microsecond and nanosecond scales. reaching down to the quantum-optical limit. Expected observable phenomena include instabilities of photon-gas bubbles in accretion flows. p-mode oscillations in neutron stars and quantum-optical photon bunching in time. The precise timescales of such phenomena are variable and unknown. and studies must be made of photon-stream statistics. e.g.. power spectra or autocorrelations. Such functions increase with the square of the intensity. implying an enormously increased sensitivity at the largest telescopes. QuantEYE covers the optical spectrum and its design utilises an array of photon-counting avalanche diode detectors. each viewing one segment of the OWL entrance pupil. QuantEYE can begin operation while the OWL pupil is only partially filled and it will not require [full] adaptive optics.

The concept study starts with a review of quantum optical phenomena in general and then focuses on those of potential interest in astrophysics. After examining the current state of high-speed astrophysics. it examines the instrumental requirements for extension to higher time resolution and then presents a conceptual design for an instrument that exploits the huge advantage offered by the OWL aperture.

High-Speed Astrophysics and Quantum Optics - Numerous discoveries have been made with resolutions of milliseconds and slower: optical and X-ray pulsars; planetary-ring occultations; rotation of cometary nuclei; cataclysmic variable stars; pulsating white dwarfs; flickering high-luminosity stars; X-ray binaries; gamma-ray burst afterglows. and many others. A limit to such optical studies has been that CCD-like detectors do not readily permit frame-rates faster than 1–10 ms. while photon-counting detectors either have low efficiency or else photon-count rates limited to no more than some hundreds of kHz. Such instrumental limitations have been compounded with the lack of adequate telescope light-collecting power. For reasonable sensitivity. the required photon flux must match the time resolution: microseconds require megahertz count rates.

QuantEYE on OWL is designed for sub-nanosecond resolutions with GHz photon count-rates to match. This will enable detailed searches for phenomena such as: millisecond pulsars; variability close to black holes; surface convection on white dwarfs; acoustic spectra of non-radial oscillations in neutron stars; fine structure across neutron-star surfaces; photon-gas bubbles in accretion flows; and possible free-electron lasers in the magnetic fields around magnetars. Nanosecond-resolution photon-correlation spectroscopy will enable spectral resolutions exceeding R = 100 million (as is probably required to resolve narrow laser-line emission around sources such as Eta Carinae); and QuantEYE will have the power to examine quantum statistics of photon arrival times (Figure 12-5)

QuantEYE Conceptual Design - With QuantEYE aiming at timescales down to nanoseconds. there is the corresponding need to count photons at sustained rates up to some GHz. The

requirement of a high quantum efficiency leads to single-photon counting avalanche diodes (SPAD) as the detectors of choice. although — at least at present — there appears not to exist any *single* detector that can handle such count rates. This leads us towards the concept of a multi-element — although not necessarily contiguous — detector array over which the light from the source is distributed. A further technical limit is set. at least at present. by the small physical size (of order 100 μm) of the detector elements which complicates the optical interface to large telescopes. Existing silicon-based SPAD cover the optical from 400–1000 nm. while for the near infrared (1–1.8 μm). SPAD based on germanium and similar materials are being developed in industry. Although such infrared SPAD already exist. their dark-count rates are still too high for our applications.

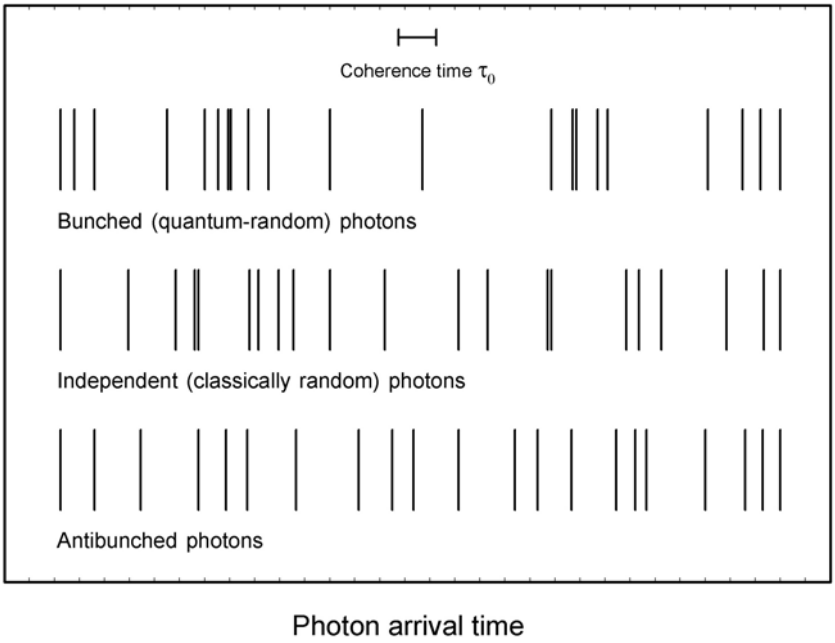

Figure 12-5. Statistics of photon arrival times in light beams with different entropies. Light may carry more information than that revealed by imaging and spectroscopy: Photons from given directions with given wavelengths give the same astronomical images and spectra. though the light may differ in statistics of photon arrival times. These can be "random". as in maximum-entropy black-body radiation (Bose-Einstein distribution with a certain "bunching" in time). or may be quite different if the radiation deviates from thermodynamic equilibrium. (Loudon: The Quantum Theory of Light. 2000).

For the first conceptual design. a "conservative" approach has been taken. shaping the system within existing detector technologies. Besides demonstrating the feasibility of concept. this means that a prototype instrument could be constructed along these lines and using commercially available components.

The optical design is for point source observations and uses pupil-slicing by optically subdividing the OWL 100m entrance pupil into one hundred 10m segments. Light from these 100 pupil segments is then focused onto an array of 100 fast (f/1) lenslets to feed an array of 100 SPAD through optical-fibers. Each detector can sustain photon-count rates of up to some 10 MHz. enabling a combined output of 1 GHz. Although. after photon detection. each detector has a deadtime of around 50 ns. the timing of each photon can be recorded with subnanosecond precision. as can the correlation between photon arrivals in different detectors. An exact differential timetag is assigned by a hydrogen maser clock (or future optical clock). and a GPS (or future *Galileo*) satellite receiver system provides an absolute time reference. thus enabling coordinated observations with other instruments on the ground or in space. A second detector unit. independently positionable over a 3 arcminute field of view. will allow calibration and reference measurements on a second source. Besides enabling GHz count rates. the segmented-pupil design has advantages in that (a) The detector redundancy enables the confirmation of possibly doubtful signals through their expected simultaneous occurrence in different channels; (b) Some events imply an illumination sweeping across the entrance pupil

(e.g. occultations by Kuiper-belt asteroids). which can be both spatially and temporally resolved; and (c) By suitable cross-correlations of the detected signal. a digital intensity interferometer of the Hanbury-Brown & Twiss type can be realized between a large number of different sub-apertures. Raw data rates of 100–1000 Mb/s will be highly compressed in real time by on-line digital signal processors outputting only the appropriate statistical functions. Thanks to the pupil-slicing concept. *QuantEYE* will be able to work already with a partially filled OWL pupil. and (assuming the source is kept within the 1 arcsec aperture) will function well also without [full] adaptive optics. The present optical solution is outlined in RD53 This present design has limitations. in particular only permitting observations of one point source per detector head at a time (field-of-view is one arcsecond). Developments in avalanche-diode array technology are in progress in industry and. when their performance reaches satisfactory levels. these should enable a fully *imaging* system with nanosecond resolution. For example. such an imaging device could observe a globular cluster containing an active X-ray source of unknown location. and then search for an optically rapidly variable object over a field of perhaps a megapixel.

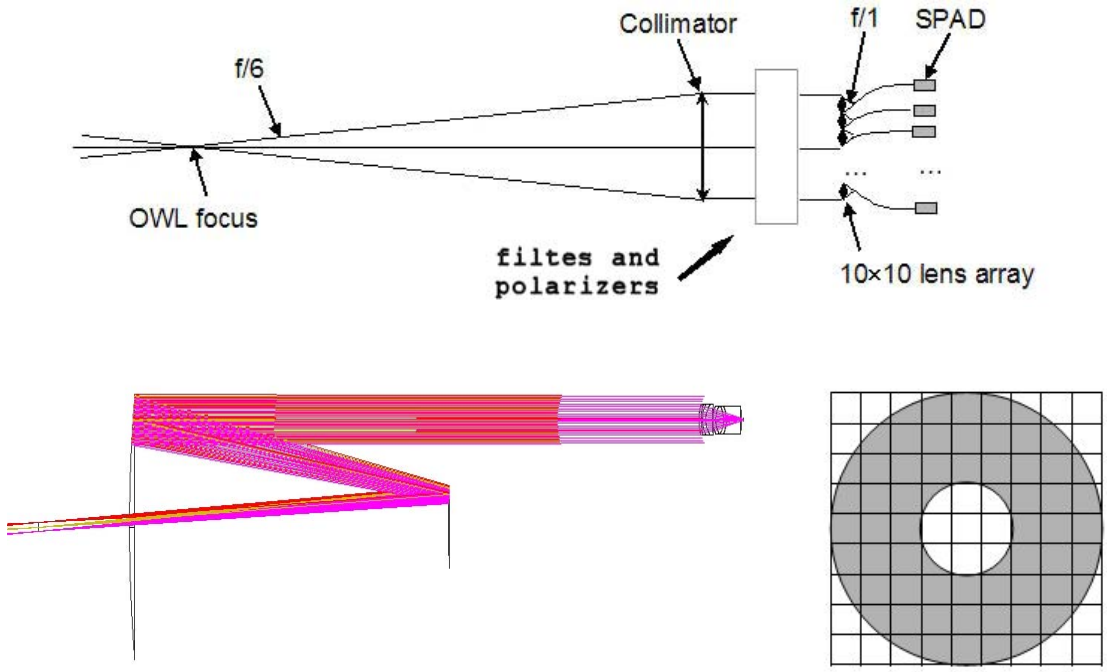

Figure 12-6 Current optical concept for a QuantEYE detector head: a distributed detector array and a segmented aperture. The collimator-lens system magnifies 1/60 times (collimator focal length = 600 mm. lens focal length = 10 mm). giving a nominal spot size of 50 µm for a 1arcsec source.

Telescope diameter	Intensity <I>	Second-order $<I^2>$	Fourth-order photon statistics $<I^4>$
3.6 m	1	1	1
8.2 m	5	27	720
4 x 8.2 m	21	430	185.000
50 m	193	37.000	1.385.000.000
100 m	770	595.000	355.000.000.000

Table 12-2. Gain in photon statistics with telescope size

The need for extremely large telescopes - The largest optical telescopes offer new opportunities for studying astrophysical variability on timescales of milli-. micro-. and nanoseconds. Since the astrophysical phenomena are normally not periodic. and their exact

timescales are both unknown and variable. studies must be of photon-stream statistics. e.g.. power spectra or autocorrelations.

Table 12-2.compares the observed signal (I). its square and fourth powers. for telescopes of different size. The signal for classical quantities increases with the intensity I; the signal in power-spectra as I^2; and that of four-photon correlations as I^4. This very steep dependence makes the largest telescopes enormously more sensitive for high-speed astrophysics and quantum optics.

12.2.3.2 Hyper-telescope NIR camera

This Section outlines the results of a 4-month study by O. Lardière. V. Borkowski & Antoine Labeyrie at LISE-Collège de France Laboratory at Observatoire de Haute-Provence. The study report is a reference document (RD58).

Giving the long lead time in the fabrication and installation of the M1 mirror segments. it is tempting to optimize the filling geometry of the 100-m aperture to achieve the best high resolution imaging capability during these first years of operation with reduced collecting area. A densified-pupil mode can improve OWL sensitivity during this phase. The report discusses initially various filling configurations and their intensification gain. It advocates the use of an adaptive fringe sensor unit to co-phase all segments in the case of a non-contiguous configuration. It finally mentions a speckle interferometry mode. suitable for observing faint objects in the absence of adaptive optics or of a suitable guide star. an adaptive imaging mode with a densified array. and a coronagraphic mode for imaging extra-solar planets .

A hypertelescope (Labeyrie et al. 1996. RD58) is a multi-element imaging interferometric array having a densified pupil. It allows direct imaging with high resolution. Indeed. densifying a pupil increases the ratio of the sub-aperture diameters to their spacing. It can be done by bringing closer optically the entrance sub-apertures or by increasing their diameter. It does not degrade the image properties if the geometrical pattern formed by the centre of each mirror is preserved. In an image given by a Fizeau interferometer. the light energy is spread across secondary peaks. unlike in an image given by a hypertelescope where almost all the energy is concentrated in the central peak surrounding by very few secondary dispersed peaks.

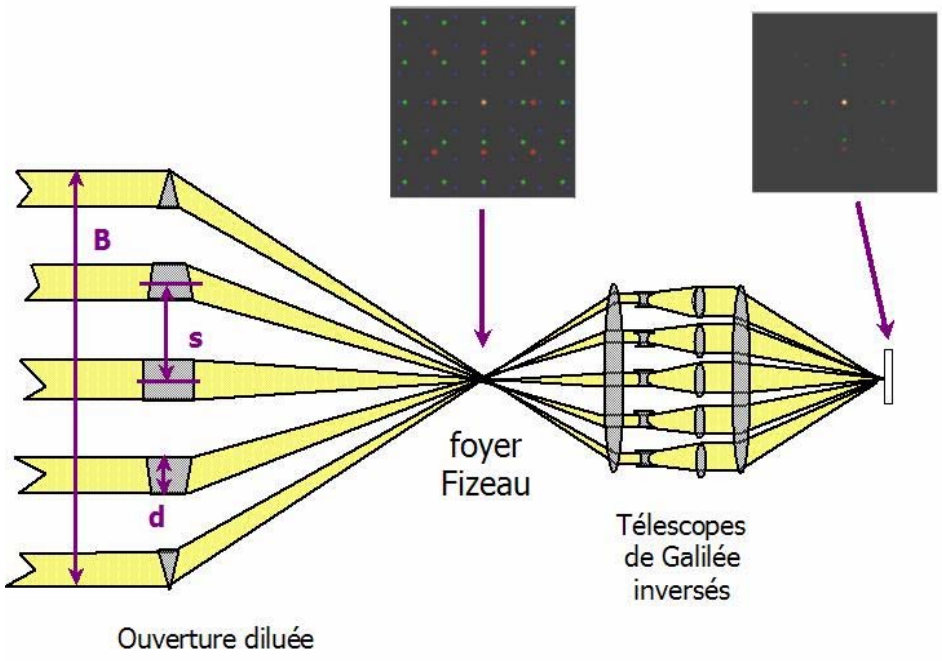

Figure 12-7 The concept of the Hypertelescope

12.2.3.3 ONIRICA: OWL NIR Imaging Camera

The study of ONIRICA was carried out by INAF Arcetri and MPIfA Heidelberg. P.I.of the study was R. Ragazzoni. The ONIRICA Concept Study report is provided in RD54 and its content is summarized here.

The large collecting area of a ground based ELT. together with its high resolving power. can provide unique observations of extremely faint objects. However. in order to reach this goal it is mandatory that the telescope be able to deliver nearly diffraction limit images. It is only under this condition that an ELT can gain significantly with respect to smaller aperture ground-based or space-born telescopes due to the increased contrast of sources with respect to the underlying background dominated by the sky emission.

This consideration led to a concept of a AO-aided NIR imaging camera that is working at (or very close to) the diffraction limit condition over a field where MCAO (Multi Coniugate Adaptive Optics) can achieve a competive concentration of light in the diffraction-limited central peak. This will be possible with AO with optimal seeing during 10 -30 percentile of the night time only. depending on the choice of the site. and with limitations on the sky coverage.

Science cases

Science cases based on deep imaging of faint point-like and extended objects with a 50-100 m telescope have been discussed extensively in the “Science Book”. Within the ONIRICA concept study. a few specific cases have been explored in more detail taking into account the proposed characteristics of the instrument and the results of simulations.

As an example. we recall here the study of the stellar population of massive elliptical galaxies performed through the analysis of color-magnitude diagrams (CMDs). These galaxies are noticeable absent in the Galaxy neibourhood but their old stellar population hold the key to understand galaxy formation in the early phases of the Universe. By the simple counting of stars of different ages in the CMD the rate at which stars where formed can be directly obtained. While the classical studies carried out so far were centered mainly in the B. V . I bands. more recent investigations are focussed on the NIR bands. where ONIRICA will operate. Theoretical isocrones from the Padova database for stars of solar metallicity are showm in the C-M diagram in Figure 12-8. The boxes superimposed on the CMD have been chosen so as to sample different age ranges. Specifically: the bright cyan box samples the youngest stars. in the core Helium burning phase; the blue box is populated with older core Helium burners; the orange box samples bright. intermediate age AGB (asymptotic giant branch) stars; and the red box targets the upper two magnitudes on the Red Giant Branch (RGB). populated with stars with ages from 2 Gyr up to the oldest ages. The detection limits for a star of m_K = 30 in Coma (m-M= 35.3). Fornax (m-M= 31.6) and Virgo (m-M= 30.9) are also marked

Using the stellar counts in the various regions one can sketch the average star formation (SF) history in a galaxy. or a portion of it. More sophisticated computations of synthetic CMDs can be used to test the SF modalities like bursting or costant SF rates. the initial mass function (IMF) slope and the effect of metallicity.

With the current instrumentation and telescopes these studies are feasible in galaxies up to a distance of 4-5 Mpc (distance modulus ~ 28). With a 100m class telescope it would make them feasible for objects up to 100 Mpc. thus allowing us to reach the members of the nearest rich clusters of galaxies and to derive the SF history of galaxies of all morphological types. including giant ellipticals. which are noticeably absent in the very nearby volume of the Universe.

At 100 Mpc. a field of view of 30” across corresponds to a diameter of ~15 kpc. comparable to a significant section of a massive galaxy. It would then be possible to derive the CMD of a substantial portion of one galaxy with two deep frames (one per photometric band) taken at time of best seeing.

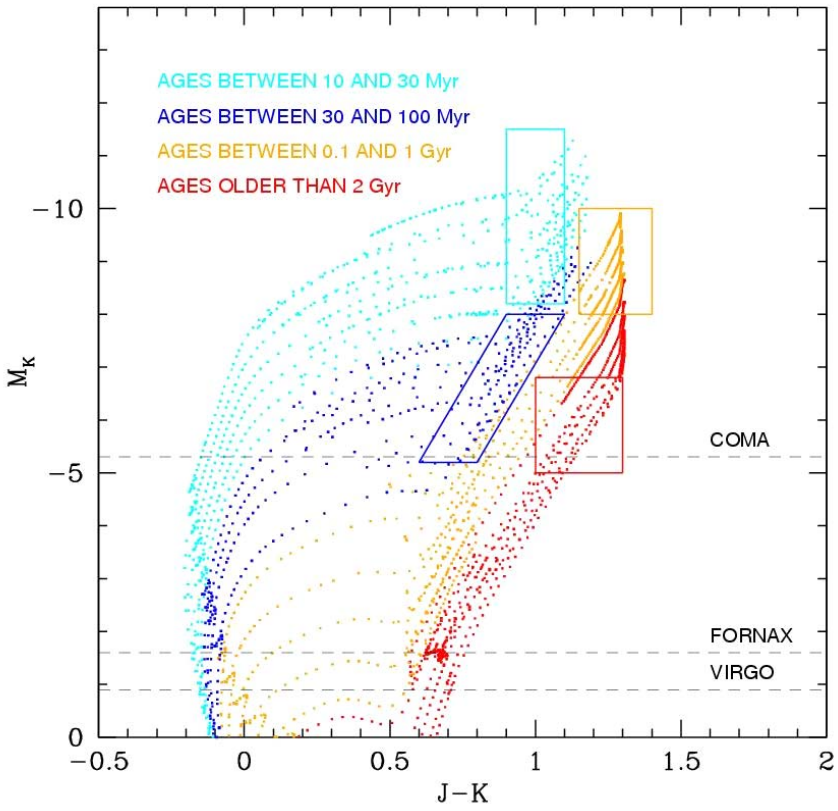

Figure 12-8: NIR C-M diagram from therotical isocrones by Girardi wt al. (2002. A&A 391.195)

Instrument Requirement and Limiting Magnitude

To surpass the performance of smaller ground-based or space-born telescopes. a camera is required which operates at diffraction limit over a relatively large (for AO–aided systems) field. The two cases of MCAO and GLAO are discussed at length in the report RD54 . The goal of the diffraction limited PSF over a field of 30" could be achieved with MCAO operating with two deformable mirrors and in conditions of optimal seeing. The predicted PSF is shown in Figure 12-9. Assuming this PSF and standard instrument properties the performance in limiting magnitude of ONIRICA has been studied for different telescope diameters (TMT = 30m. SMT = 60m and OWL = 100m) and compared also to JWST performance (Figure 12-10 and Figure 12-11. Table 12-3 and Table 12-4). There is a clear advantage with respect to JWST for imaging of point sources. These predictions have been supported by photometric measurements on simulated images based on a stellar population set at the distance of the Coma cluster with the predicted PSF of OWL.

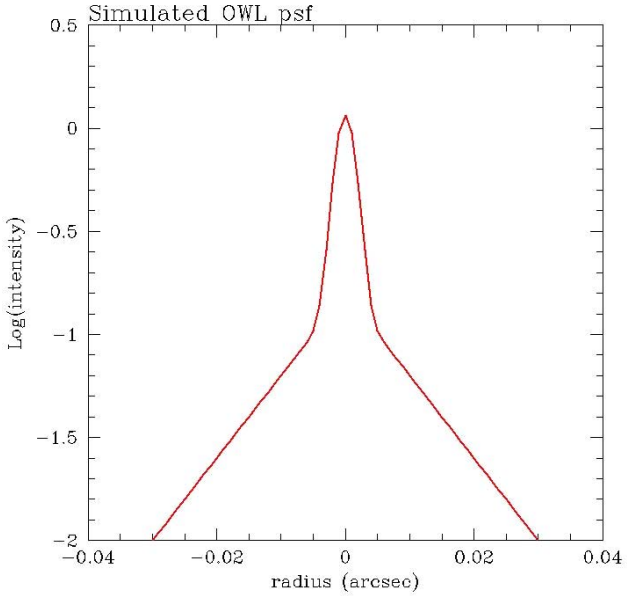

Figure 12-9 The PSF radial intensity distribution as derived from MCAO assessment for the central field of ONIRICA at OWL and used in the simulation of photometry in crowded stellar fields

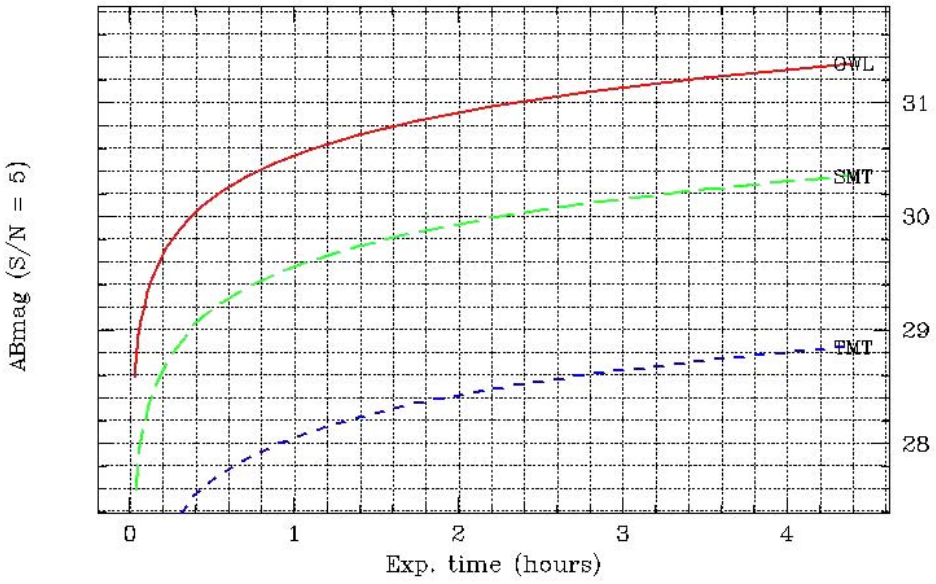

Figure 12-10 The limiting (S/N=5) magnitude $K_{(AB)}$ for point sources as a function of the exposure time

The same efficiencies are assumed for the three telescope diameters.

Telescope	**Diameter M1 (m)**	**Mag lim (1 hour. S/N=5)**
OWL	100	30.5
SMT	60	29.5
TMT	30	28.0

Table 12-3 Magnitude limits for point sources at 100m. 60m and 30m

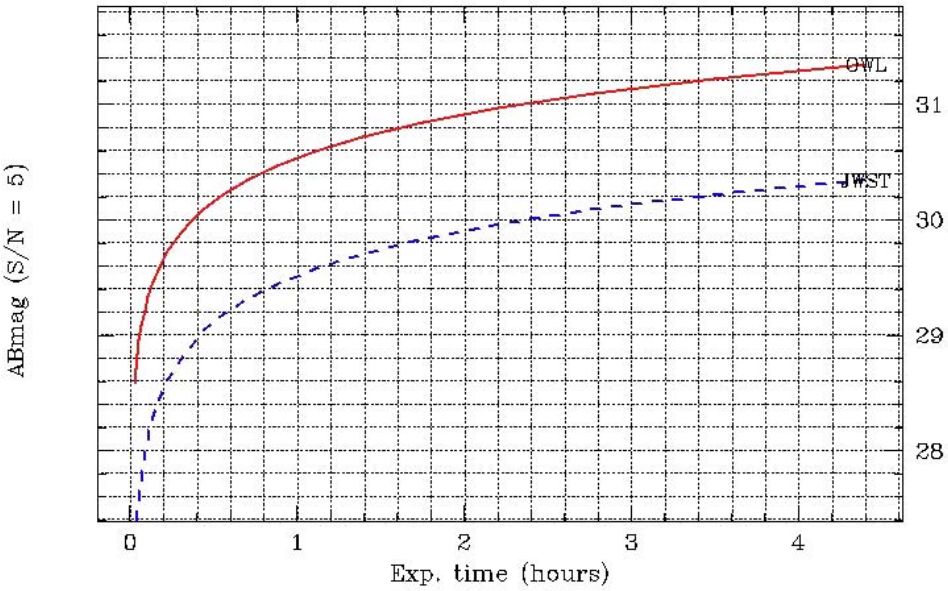

Figure 12-11 The limiting (S/N=5) magnitude K(AB) for point sources as a function of the exposure time for OWL and the JWST (assuming same instrument and detector performance)

Telescope	Diameter M1 (m)	Mag lim (1 hour. S/N=5)
OWL	100	30.5
JWST	6	29.5

Table 12-4 Magnitude limits (S/N=5) for 1 hour integration time for OWL and JWST

Optical design

The proposed ONIRICA optical concept. shown in Figure 12-12. couples a center field camera of 30”-60” diameter capable of delivering diffraction limited images with possibly a piggy-back one where preference is given to a larger field at a 10-20 times lower resolution. With this larger pixel scale in the sky the camera is less performing than the JWST. but it remains interesting e.g. for the observations of high z galaxies which have typical half intensity radii of 0.1 arcsec. with substructures at 1/10 this size.

Narrow field channel

The narrow field channel has a maximum 1 arcmin diameter centered on the optical axis This channel enlarges the diffraction limited images provided by a MCAO correcting system to obtain a correct sampling of the diffraction-limited PSF and splits the field over several subchannels in order to keep optics and detector array size small. Figure 12-13 shows the concept of two level splitting feeding 16 large IR detectors. The OWL focal plane (F/6) is doubled in size by an optical relay optimized for wavelengths between 1.0μm and 2.35μm and then split by a pyramidal mirror. The optical relay has an intermediate pupil image for placing a cold stop to reduce telescope emissivity. For each arm a second optical relay doubles (downsized copy of the previous one) again the FoV size and a second pyramidal mirror splits again the portions of the FoV which are then imaged on independent IR detectors with the proper sampling (at F/24 is 11.635mm/arcsec).

In the case of a 30” FoV and three level splitting (16 arms) each arm images 7.5 × 7.5 arcsec and requires a mosaic of 2 × 2 IR detectors of 4k×4k pixels of 18μm size for Nyquist sampling of the diffraction limited PSF in the J band.

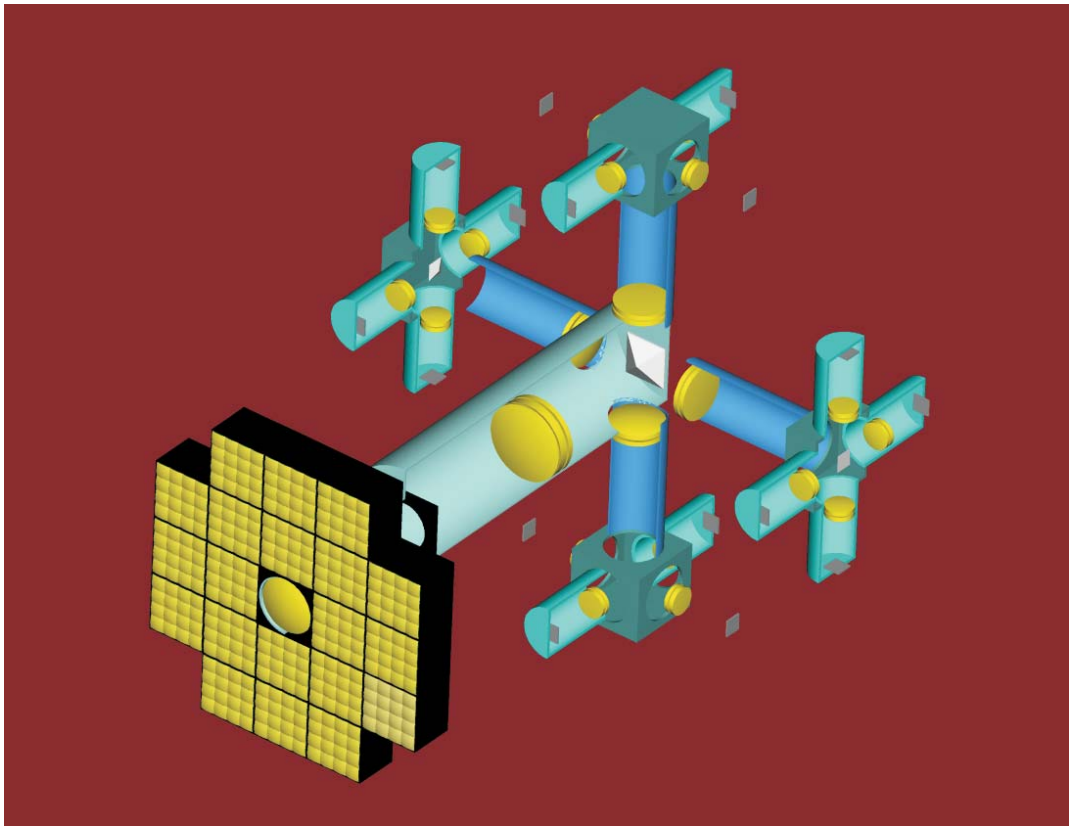

Figure 12-12 Optical layout of ONIRICA (central field)

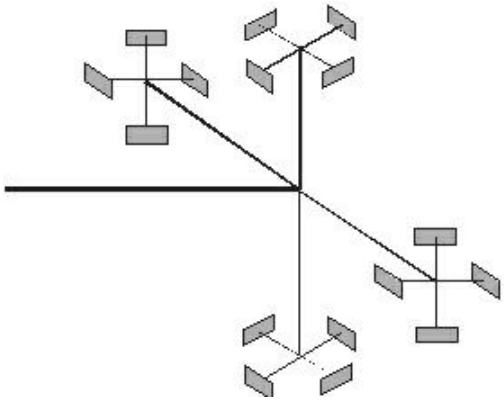

Figure 12-13: Concept of the channel splitting in ONIRICA. The FoV splitting is provided by a pyramidal mirror located at the intermediate focal planes.

Wide field channel

The wide field channel is surrounding the narrow field one and has a FoV of 3-6 arcmin (Figure 12-12).More extended simulations of the performance of this wide FoV channel with GLAO correction and of its scientific justification will be needed to fully define its scope and in particulat to optimize its pixel scale.

The channel refocuses partially GLAO corrected images with a coarser spatial sampling and it is based on a concept known as a Smart Fast Camera (SFC). It is essentially a focal reducer

with a relatively large plate scale. with the FoV split in smaller portions. each imaged by a lenslet array on a dedicated detector.

The array of lenslets of the dimension of about 15arcsec to 1 arcmin. In the pupil plane an array of aberration correctors is placed in order to correct the approximately constant aberrations in the FoV of each lenslet system. At the end an array of camera lenses produces an array of images detected by the scientific arrays. with the requested plate scale (Figure 12-14 and Figure 12-15). Different focal ratios can be considered depending on the sampling needed: for example a sampling of 15mas/pixel is obtained with F/2.5 lenslet and a FoV patch of 1×1 arcmin is covered by 1 IR detector of 4k×4k pixels of 18μm size.

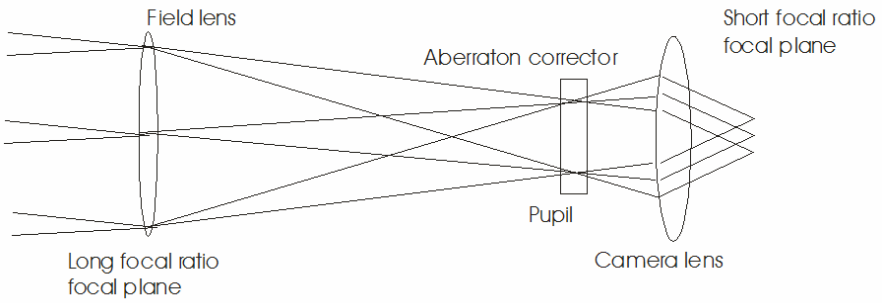

Figure 12-14: Sketch of a single unit of a Smart Fast Camera

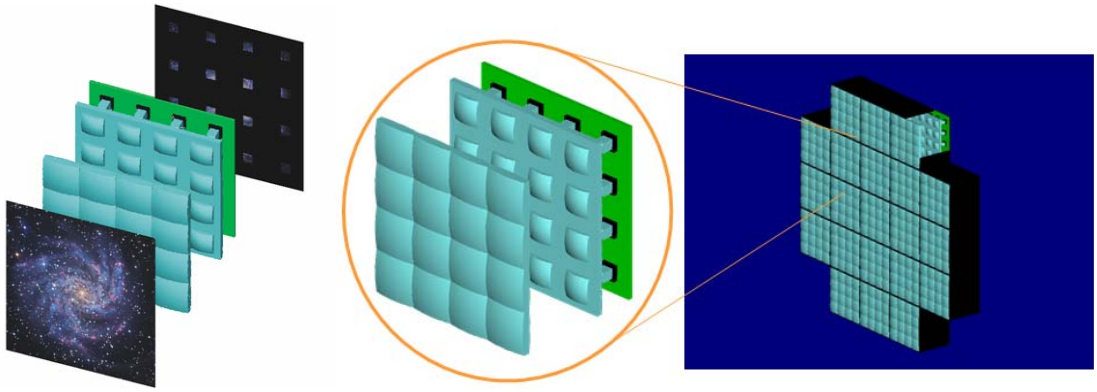

Figure 12-15: The picture on the left illustrates the SFC concept in which the light of a wide FoV is divided by a lenslet array.

Mechanical design

In Figure 12-16 is shown the opto-mechanical concept of ONIRICA. The whole instrument has a small size with respect to the typical size of other 100m class instruments. The SFC incorporates on its entrance side the flange for the rotator adapter. A system of tubular trusses is designed to give stiffness to the optical tubes. Figure 12-17 shows the accommodation of ONIRICA within the allowed volume for the OWL instrumentation.

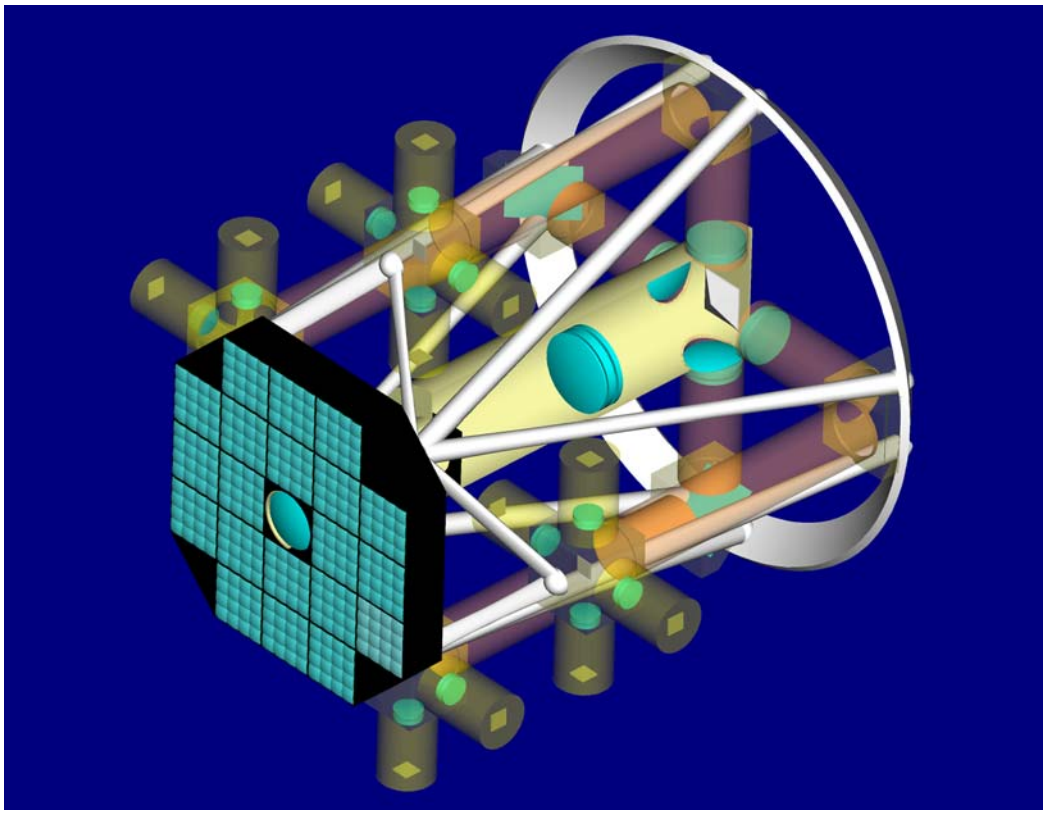

Figure 12-16: Opto-mechanical layout of ONIRICA including the two. wide and narrow. channels. The tubular trusses have the function to stiff the cryogenic tubes.

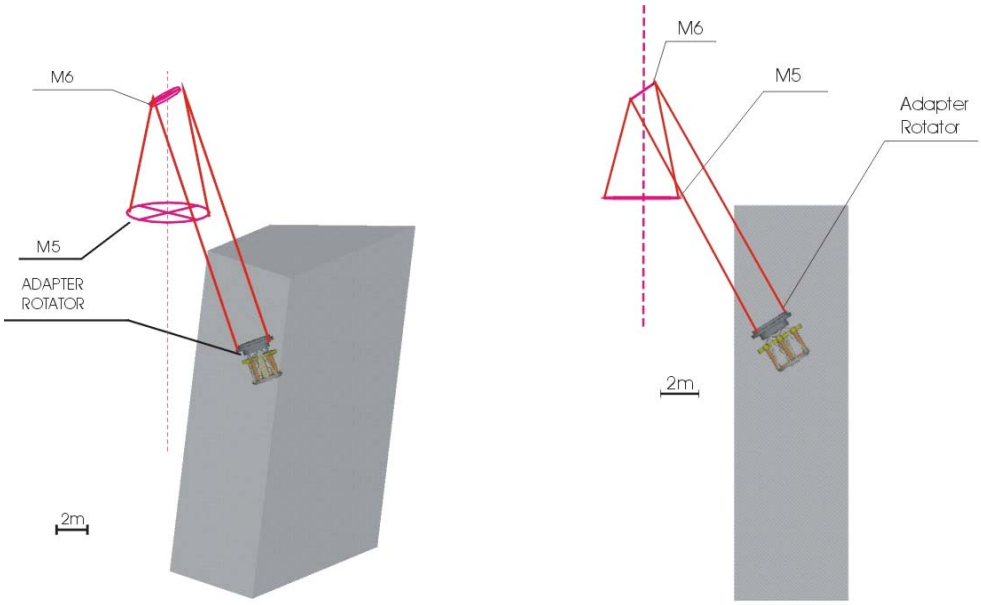

Figure 12-17 Two views of the instrument envelope in the instrument bay .

12.2.3.4 MOMFIS: Multi Object. Multi Field Near –IR Spectrograph

The study of MOMFIS was carried out by a consortium of LAM. CNRS/CRA Lyon. CNRS/GEPI . CNRS/LESIA and ONERA in France. J.G. Cuby was the P.I. The Concept Study report is provided in RD55 and its content is summarized here.

Scientific objective - A highlight science case of all the future large telescope projects is entitled: 'The End of the Dark Ages: First Light and Reionization'. After the recombination epoch. space was filled with dark matter. energy and neutral gas. As it continued to expand. regions of higher density stopped following the expansion. turned around and collapsed into the sites where the first objects formed. Primordial objects are thought to be primordial galaxies powered by young massive stars and early quasars accreting matter around growing black holes. As they lit up. they modified the gas between them. ionizing the hydrogen and making it transparent to ultraviolet light. In effect. the Universe underwent another phase transition. from a neutral to an ionized state. MOMFIS is designed for this highlight science case. it aims at pushing back as early as possible into the Dark Ages to observe and characterize these sources that once re-ionized the Universe.

Requirement specifications - The high-level science requirement specifications for MOMFIS on OWL were set as follows:

- Simultaneous observation of several targets over the OWL science field of view
- Spatially resolved spectroscopy of individual targets (integral field)
- Image quality: 50 milliarcseconds or better. This requires local adaptive optics correction
- A spectral resolution in the range 4000-8000 for OH suppression

The MOMFIS acronym is derived from these high level specifications: Multi-Object Multi-Field Infrared Spectrograph.

Sub-systems

MOMFIS provides for 30 independent channels. each channel consisting of the following sub-systems:

- A target selection system consisting of pick-off and beam steering mirrors which direct the science beams from the telescope focal plane to the deformable mirrors
- A deformable mirror correcting the atmospheric perturbations in the direction of the target
- An image slicer dividing individual fields of view into 40 slices 20 milliarcsecond wide
- A spectrograph providing one spectral band (Y. J. H or K) at once at a spectral resolution of ~ 4000.
- A 2k x 2k IR array.

In addition. the instrument is equipped with wavefront sensors which sample the atmosphere over the whole instrument field of view.

Conceptual design and performance - In total. the instrument features 30 fully identical beams and 10 cryostats with 3 spectrographs per cryostat. The instrument is modular. highly redundant. and designed for easy preventive or corrective maintenance. The principle of operation and overall design is shown in Figure 12-18. Figure 12-19. and Figure 12-20. As shown on the left side of Figure 12-18. pick-off mirrors are positioned and oriented in the telescope focal plane prior to the exposure to collect and rely the light of the distributed targets. They send the light to movable steering mirrors which in turn send the light to the fixed deformable mirrors and instrument (image slicers and spectrographs). On the right side of Figure 12-18 is the conceptual optical implementation showing the beam steering mirrors (BSM). the deformable mirrors (DM). the wavefront sensors (square boxes at top) and for each channel at the bottom the atmospheric dispersion compensators. the filter wheels. the slicer and spectrograph optics. The overall height of the instrument as shown is 3.5 m.

MOMFIS allows to observe 30 targets in integral field mode at once in the 5' (diameter) OWL scientific field of view down to IR AB magnitudes of ~ 28. This ideally meets the science high level specifications.

Interface with telescope - MOMFIS is big. As designed. it fits in the OWL instrument focal station. however exceeding the allowed mass budget within limits which are considered acceptable at this level of conceptual design. The main interface issue is with the telescope adapter / rotator which has a limited weight limit. To overcome this MOMFIS provides its own adapter / rotator replacing the telescope one. as well as wavefront sensors that can (and need to) be used by the telescope in place of the original ones.

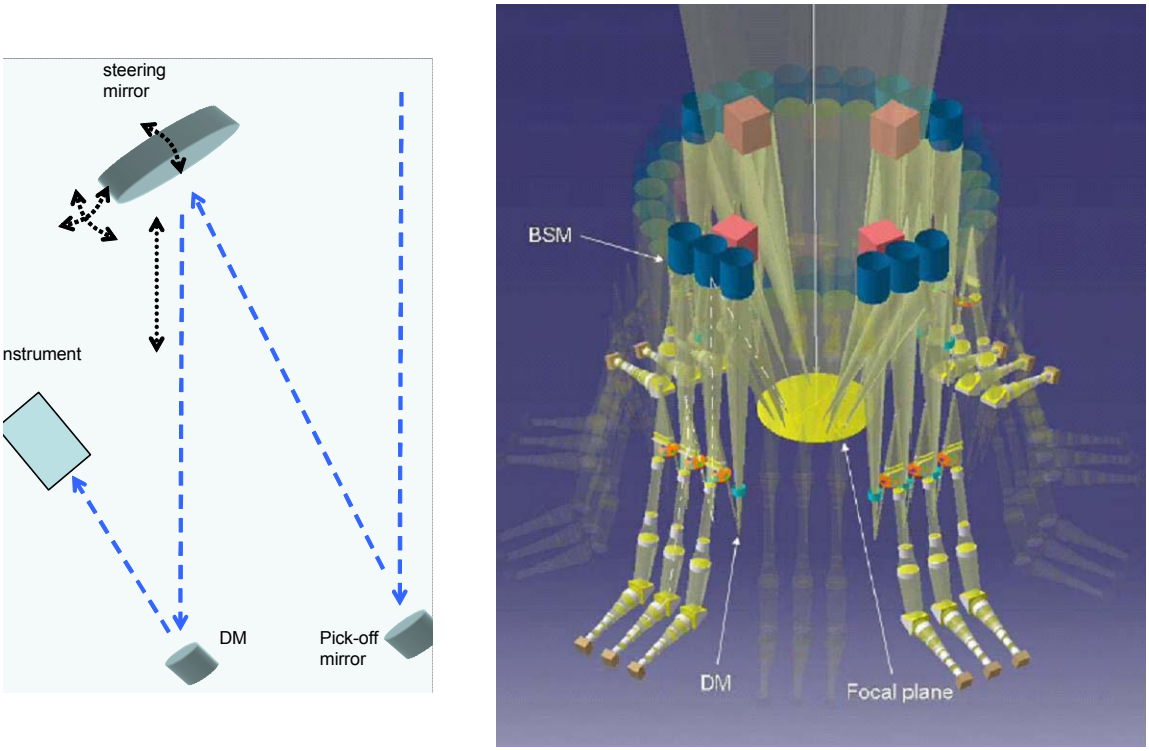

Figure 12-18 MOMFIS conceptual optical layout (see text).

Technological developments and roadmap - The entire instrument concept relies on existing and well demonstrated technologies. but for 2 items which will require specific developments and roadmaps:

- multi-object adaptive optics (MOAO). MOAO is at the core of the MOMFIS operation. it requires several wavefront sensors sampling the atmospheric wavefront over the telescope and one deformable mirror per channel (assuming telescope provides ground layer correction). The MOAO concept has never been implemented and needs further studies and laboratory and / or on-sky prototyping to be demonstrated and validated. Laser guide stars are a must for full sky coverage.
- Internal metrology. Internal metrology and control of the main optical elements is required in the instrument to compensate for flexures (the focal station is not gravity stable) that cannot all be absorbed by the stiffness of the structure. This internal metrology will also be used for alignment. calibration and operation purposes.

Options - At this stage. several options to the baseline instrument described above can be contemplated:

- 1st phase and / or fallback solution without adaptive optics. In a first implementation phase. MOMFIS could be deployed without the deformable mirrors which can be replaced by flat

mirrors. or low order deformable mirrors. Wavefront sensors would still be required for telescope control. Exquisite image quality could still be obtained in the central field of view (1 to 2 arcmin multi-conjugated adaptive optics field). gently degrading towards the outer edge of the OWL field of view (ground layer correction only). More than just a 1st light option. this option is actually also a fallback option in case MOAO developments fail or prove to be more difficult than expected to implement

- A second option is to resort to partial cryogenic cooling combined with moderate cooling (-40°C or so) of the whole instrument. This option allows to simplify the cryogenics and mechanics of the instrument. albeit at the expense of the performance in the K band.
- Other possible options are: smaller individual fields of view allowing to pack 2 target beams in one spectrograph. hence allowing to reduce by a factor 2 the number of spectographs and cryostats. An alternative option would be to use 1k x 1k detectors with twice as small (in area) individual fields of view and to combine with spectral dithering. A third to reduce the multiplex gain. All these options would give large savings in size. weight and cost at the expense of reduced scientific efficiency (but without affecting its limiting magnitude).

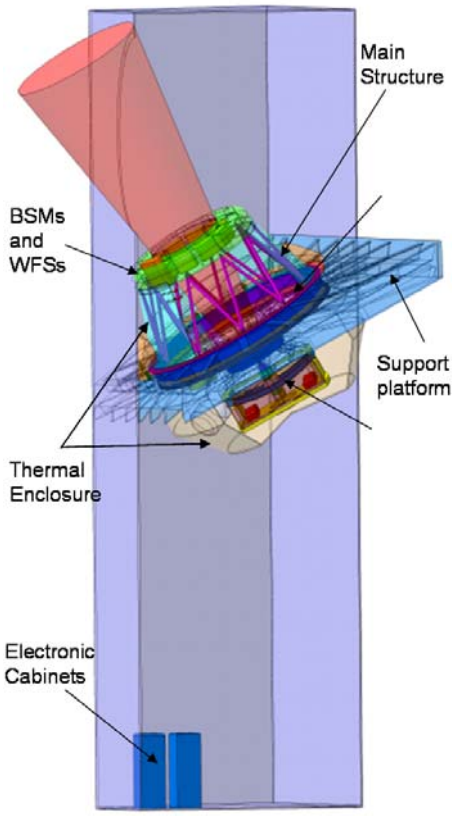

Figure 12-19. Overall MOMFIS implementation in the focal station.

Alternative designs - Alternative designs to MOMFIS have been considered. They could take the form of traditional multi-slit spectrographs (MOS). or fiber-fed spectrographs still requiring the pick-off and adaptive optics stages. Designs for these alternative designs are presented in the report. The MOS instrument could serve as an OWL first light instrument that could be used for commissioning and initial science.

Operation with a "growing" telescope - Both the MOMFIS baseline concept and the alternative multi-slit (MOS) concept could be used in the 'growing telescope' phase. under the condition that the telescope pupil is grown in an annular shape.

Development effort - MOMFIS is a complex instrument. Its development and integration will require a broad range of expertise and facilities across Europe. The hardware cost is estimated to be in the range 20-40 M€. depending on the selected options. and the required manpower (at

institutes) in the range 150-250 person-years. The instrument development requires 10 years. including a few years of continuing R&D activities.

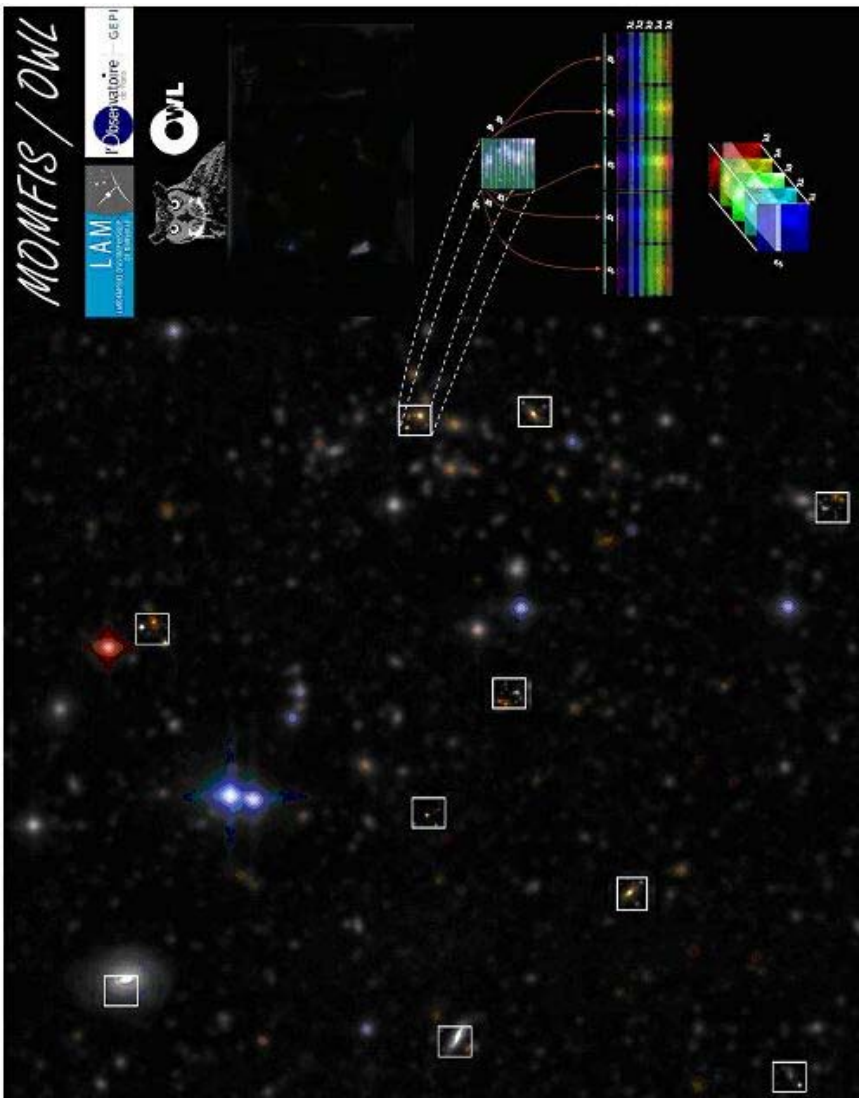

Figure 12-20. Illustration of the MOMFIS operation. Image Correction is performed locally along the line of sight of the target before image slicing and wavelength dispersion.

12.2.3.5 EPICS: Exo- Planet Imaging Camera Spectrograph

The study of **EPICS** was carried out at ESO with the support of scientists and engineers from different European Institutes. It was started significantly later than the other instrument conceptual studies. after the completion of the VLT Planet Finder phase A studies in late 2004. The EPICS concept has been naturally biased but also inspired by the VLT Planet Finder feasibility studies made by the two external European Consortia: the VLT PF led by LAOG and the CHEOPS instrument led by MPIA. Those studies have demonstrated that it is necessary to combine an “extreme” adaptive optics system (hereafter XAO) with other methods (coronagraphy and differential detection) to reach the contrast permitting exoplanets detection. The science case and the instrument are summarized here. the XAO in 8.3.2.2. The full Concept Study report is provided in RD51. XAO. the coronographs and the instrument modules are discussed together in the report. The need to understand the interaction and to control the error sources from the different sub-systems calls for a global system approach in the definition and in the evaluation of the performance of EPICS.

12.2.3.5.1 Science drivers

- Primary science goal: the detection of Earth-like planets

One of the most ambitious science objectives of OWL is the detection and characterization of extra-solar systems in an advanced evolutionary stage. for a statistically meaningful sample of stars. Rocky planets with possibly Earth-like features is the ultimate and most challenging goal of EPICS. The direct detection of exo-planets is made very difficult by the very high relative flux ratio from the star and planets orbiting it and their small angular separation. Figure 12-21 illustrates the requirements in contrast for different types of planets as a function of angular separation. Ultimately the primary science goal of EPICS requires the detection of faint point sources in proximity of a bright star with an object-star contrast down to about 2.10^{-10} at 0.05 arcsec from the star. Moreover. to observe a planet and to characterize its atmosphere. EPICS must be sensitive at the wavelengths of H_2O. CO_2 . CH_4 and O_2 molecular absorption lines.

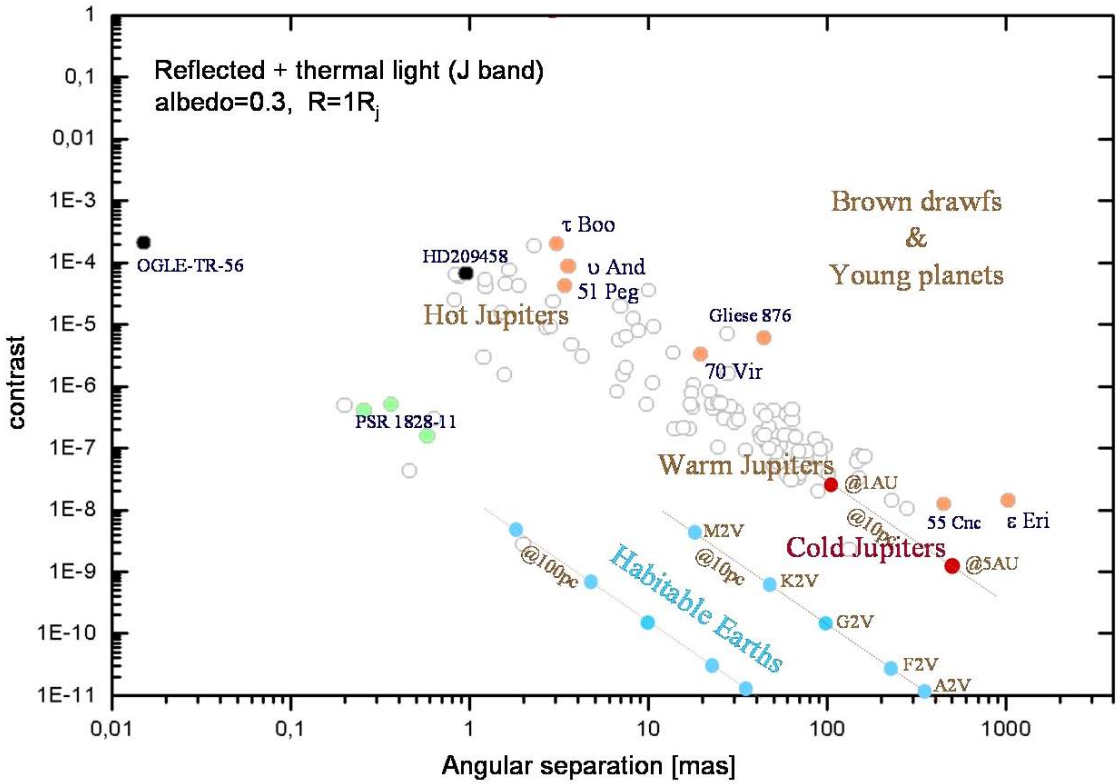

Figure 12-21. Contrast vs. angular separation for different types of planets. (Courtesy O. Lardiere).

- Gas giant planets in a late evolutionary stage

EPICS will also permit a significant breakthrough in the detection and characterisation of cold gas giant planets. The better contrast (the contrast of Jupiter at 5 AU is 10^{-9}) and larger separation. permits an easier detection. and opens the door to high resolution spectroscopy. In particular. radial velocity measurements and the analysis of atmospheric composition and dynamics of close-in giant planets will be possible. The contrast between a Jupiter mass planet at 0.5 AU and its star is around 10^{-7}. so roughly corresponding to the stellar AO residuals. For 10 pc distance from Earth. assuming a G2 star. its magnitude would be around 22.5 and the photon flux at resolution 50.000 would be about 0.5 photons per second and spectral bin (16% overall quantum efficiency). Therefore. a reasonably high SNR for the high resolution spectroscopy appears feasible in observing times of a couple of hours.

12.2.3.5.2 Targets

Performing the required XAO correction usually requires very bright NGSs (m_V <8-10). The number of possible targets has been investigated.

Figure 12-22 shows the number of stars as a function of distance from Earth listed in the NSTAR database (http://nstars.arc.nasa.gov) as visible from a low latitude site (e.g. Paranal) and the zenith angle is restricted to <30 degrees. In order to have access to about 100 stars of the spectral types G. K and M. one has to observe out to

- 25 pc for G-stars ($m_V \approx 7$)
- 20 pc for K-stars ($m_V \approx 8.5$)
- 15 pc for M-stars ($m_V \approx 9 – 16$ for M0 to M5). There are about 50 M-stars with $m_V < 10$ and 100 M-stars with $m_I < 10$ observable at low latitudes.

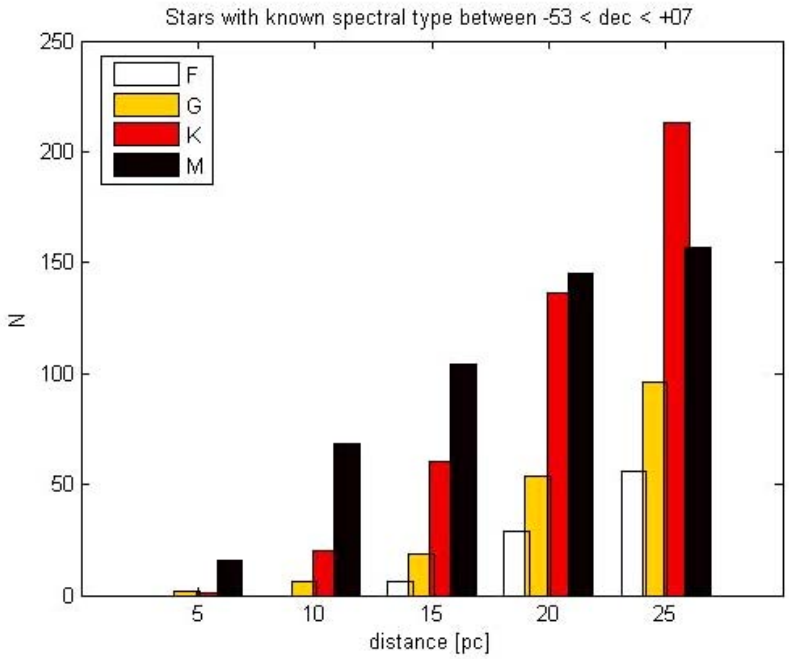

Figure 12-22: Number of stars versus distance from Earth for different spectral types

An acceptable sample of bright stars is available within a distance of 25pc for the purpose of a survey with OWL. This distance. and the resulting angular and magnitude scales. directly sets the instrument top-level requirements as described in paragraph 12.2.3.5.3.

12.2.3.5.3 Top level requirements

The top-level equirements to the instrument. the telescope+ AO and the site are summarized in the following sections.

12.2.3.5.3.1 Instrument. general

- The instrument shall cover the wavelength range 0.6 – 1.7 micron

  For the detection of terrestrial planets the wavelength range 600 nm – 800 nm (R band) is interesting because of the high degree of polarization of rocky planets at shorter wave-length. The very interesting O_2 band is also included in this wave-length range. In J- and H-band. one is sensitive to both Gas giants and Rocky planets. Gas giant planets spectra are dominated by the CH_4 features. and CO_2 and H_2O are part of the telluric planets' features detectable in J and H band.

- The total field of view in all observing modes shall be at least 2″ in diameter at visible wavelengths and 4″ in diameter in the NIR.

  A field of view of 2″ in diameter is large enough to cover terrestrial planets at 1AU. The bigger field in the NIR accounts for the larger separation at which giant planets are

searched. The 4″ field covers the solar system (apart from Neptune and Pluto) at distances larger than 10 pc.

- The inner working angle in all observing modes working at visible wavelengths shall be smaller than 30 mas (goal 15 mas).

  This inner working angle corresponds to 0.3 AU at 10 pc. small enough to cover the solar system at 10 pc or to resolve Earth-like planets out to 25 pc. The atmospheres of close-in and therefore bright giant planets could be studied at smaller angular separations down to 15 mas.

- The spatial sampling will at least fulfill the Nyquist criterion at all working wavelengths. Over-sampling may be required to deal with interpolation issues in differential imaging.

12.2.3.5.3.2 Instrument main observing modes and performance requirements

- There shall be a low resolution differential spectroscopic mode covering at least the following lines
  - O_2 at 760nm. R = 150. see Figure 12-23
  - CH_4 in J- and H-band. R > 15
  - H_2O between J- and H- bands. R > 15
  - CO_2 in H band. R> 15
- There will be a broad band (~200 nm. TDB) differential polarimetric mode
- The relative astrometric precision shall be better than ~100 μarcsec (goal 10 μarcsec)
- The photometric (absolute/relative) precision shall be better than 1% (tbc)
- Earth-like planet up to 20 pc shall be detectable in polarimetric and spectroscopic modes at SNR > 5 in one night of observation at a phase angle of 90°

Properties of Earth at 20 pc: Contrast 2e-10. m_V = 30.6. angular separation 50 mas.

- Jupiter up to 20 pc is detected in spectroscopic mode at SNR > 50 in less than 4 hours exposure time at a phase angle of 90°

Properties of Jupiter at 20 pc: Contrast 1e-9. m_V = 28.8. angular separation 250 mas.

- The AO control radius will be larger than 0.4″ at 800 nm

This control radius corresponds to about 1 AU at 2.5 pc. and ensures that – besides for the Alpha Centauri system – the prime targets are inside the control radius. Note that the control radius is given by the $\lambda/(2d)$. where λ is the observation wavelength and d is the actuator pitch of the deformable mirror. This Top Level Requirement corresponds to an actuator pitch of ~0.2 m.

- AO limiting magnitude for achievement of Top Level Requirements: compatible with a sample larger than 100 stars for each spectral types G. K and M (Figure 12-22).
- The operational efficiency of all modes. including acquisition and observation of the target and any required calibrations is better than 50%

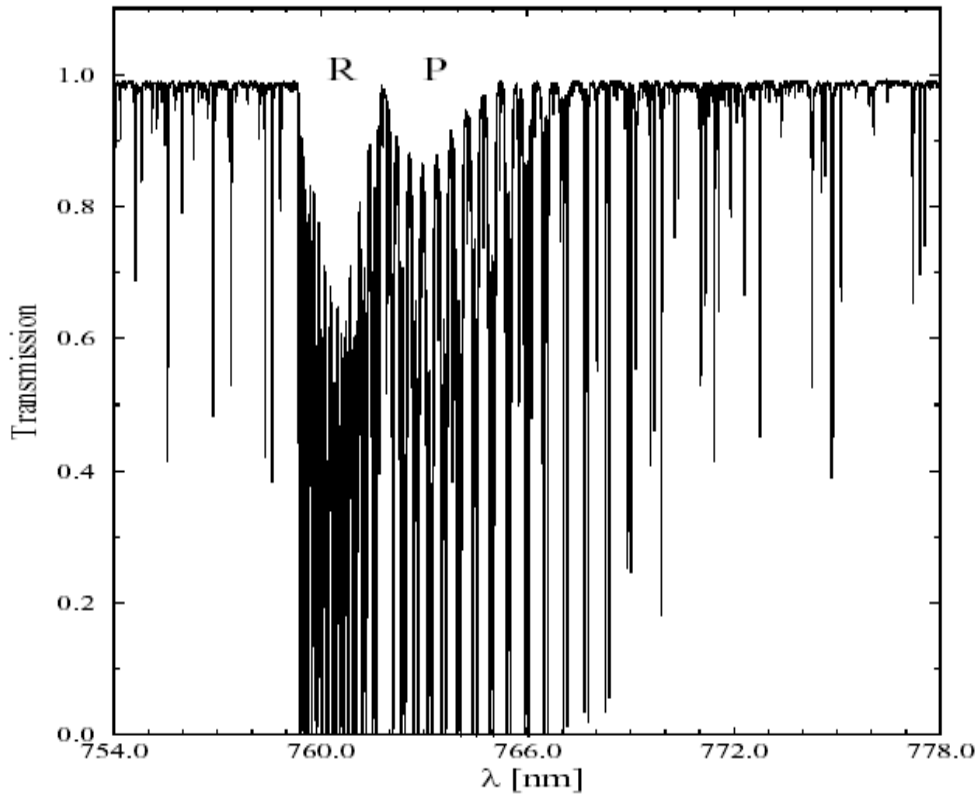

Figure 12-23: O_2 A-band at high spectral resolution.

12.2.3.5.3.3 *Requirements to the site . the telescope and observing time*

The properties of the site and the requirements to the telescope will be defined at a more advanced stage of the project.The following issues have been preliminarly identified:

- A dry site in terms of precipitable water vapor is required
- Sky accessibility: large enough to cover significant number of targets (~> ½ of sky)
- Polarimetric stability better than 1% over 4 hours
- Diffraction pattern. required SNR shall be reached for at least two/thirds of FoV. Coronagraphic performance should be close to ideal (variation < 20% (TBC)) for this fraction of the FoV
- A very significant fraction of telescope time will be required over several years. E.g. a survey of 300 objects. with 1 night for each target and follow-up observations would lead to 400-500 nights.

12.2.3.5.4 InstrumentConcept

The EPICS concept should be compatible with the detection of both gas giants and rocky planets. Due to different locations of the spectral and polarimetric features of these two groups of planets. different channels over the spectral domain are needed. Each scientific channel will be equipped with its own coronagraph.

The three main instruments will be:

- a wavelength splitting Differential Imager
- an Integral Field Spectrograph
- a Differential Polarimeter.

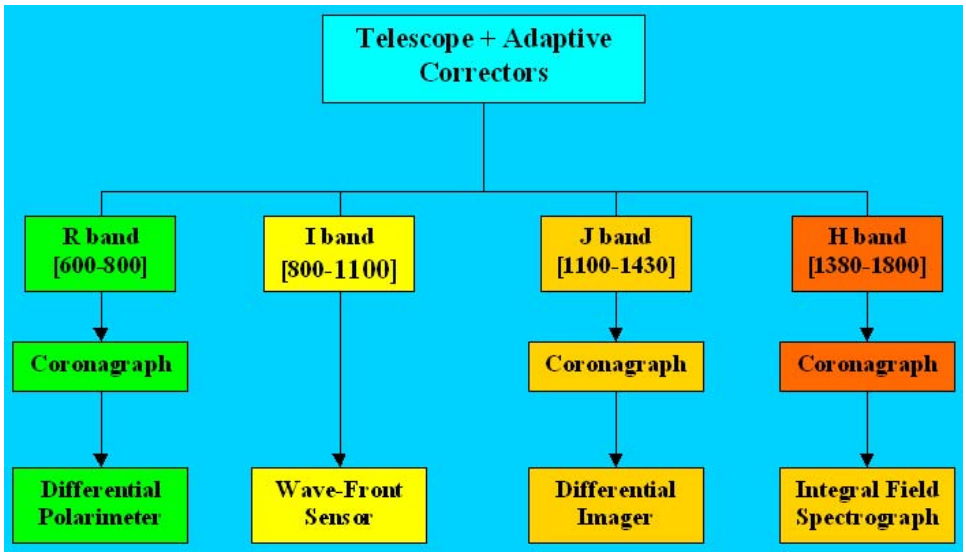

Figure 12-24: EPICS will be composed of three spectral channels for the scientific instruments and one for wave-front sensing.

- The **R band** is dedicated to the Polarimetric Differential Imager for detecting rocky planets and to the follow-up observations for the detection of O_2.
- The **J band** will be equipped with a differential imager using pairs of filters that will be sensitive to both CH_4 and H_2O absorption bands.
- The **H band** will be equipped with an Integral Field Spectrograph. The main features that can be detected in this band are CH_4 and CO_2.
- The **I band** is reserved for wave-front sensing. This band has been chosen because of the lesser scientific interest for planet detection. Moreover its location. spectrally speaking. between the visible and NIR instruments. is optimal with respect to important atmospheric chromatic limitations for XAO on ELTs.

The EPICS concept is summarised in Figure 12-24.

12.2.3.5.5 Adaptive optics

The EPICS ultimate contrast requirement is 4-5 orders of magnitude higher than the VLT-Planet Finder science goal of about 10^{-5} – 10^{-6} contrast at 0.1 arcsec. When scaling from a 10-m to a 100-m class telescope. the contrast naturally improves by a factor of 100 for a given rms value of the wave-front error. This means that the XAO system for EPICS should provide a 2 or 3 orders of magnitude better starlight halo rejection than a simply scaled version of the VLT Planet Finder system. This matter of fact calls for system specifications that are tremendously more stringent.

- a significantly higher AO system frame rate (up to 3-4 KHz) to reach high rejection in the central part of the field-of-view (for separations less than 0.1 arcsec for the Earth-like planets detection goal).
- the systematic errors must be kept at a very low level on the low and mid spatial frequencies (f < 2.5 cycles/m in the entrance pupil frame). For VLT Planet finder. on these spatial frequency range. the static errors contributes by about 40-50 nm. A gain of at least an order of magnitude is needed (requirements: less than 5 nm rms).
- the wave-front sensing measurements error propagation on low and mid-spatial frequencies must be very low: the use of phase-type sensor instead of a slope sensor is needed at least for the correction of the halo at separations less than 0.1 arcsec.

The likely characteristics of the XAO system coupled with the instrument are described in 8.3.2.2. The integrated EPICS concept is given in RD51.

12.2.3.5.6 Coronagraphy

The coronagraphs are very critical components of EPICS. Since the science instruments cover a very broad band of wave-lengths. it has been chosen to equip each individual channel with its own coronagraph. This choice permits to optimise the coronagraph parameters with more flexibility. Whereas a sufficiently achromatic coronagraph dedicated for the visible range is probably the most challenging one. the ones for J and H band could eventually. if an acceptable concept is found. be combined in one single coronagraph. But no definite concept has now been chosen. Coronagraphy is a very fast evolving field with a lot of very new ideas that appeared recently (see RD22 for a review). For EPICS two concepts have been considered and some preliminary results have been obtained. The first concept. the double stage reticulated Lyot coronagraph is described in section RD22 and permits to deal with diffraction residuals induced by gaps between the segments. This concept is quite complex to simulate and has been studied only in the diffraction limited case for the moment. The second concept. a prolate apodized double stage Lyot coronagraph is less complex but doesn't reach a contrast as high as the reticulated double stage coronagraph.

12.2.3.5.7 Instruments

12.2.3.5.7.1 Differential Imager

A differential Imager (IRDIS) based on filters has been studied for the VLT Planet Finder. The advantage of this kind of instrument is the less complexity but has the disadvantage of being less flexible and with a loss of 50 % of the light. For EPICS. we chose to study a dichroic based differential imager which main advantage is the high throughput and the possibility to implement more than two wave-lengths at the same time. A preliminary optical design has been studied (Figure 12-25). The most critical issue of this concept is the optical quality of the dichoics that should permit less than one nanometer differential aberration for the primary science goal requirements.

The proposed filter set presented in table Table 12-5 can be used either for CH_4 or for H_2O spectral differential imaging in J-band using multiple wavelengths.

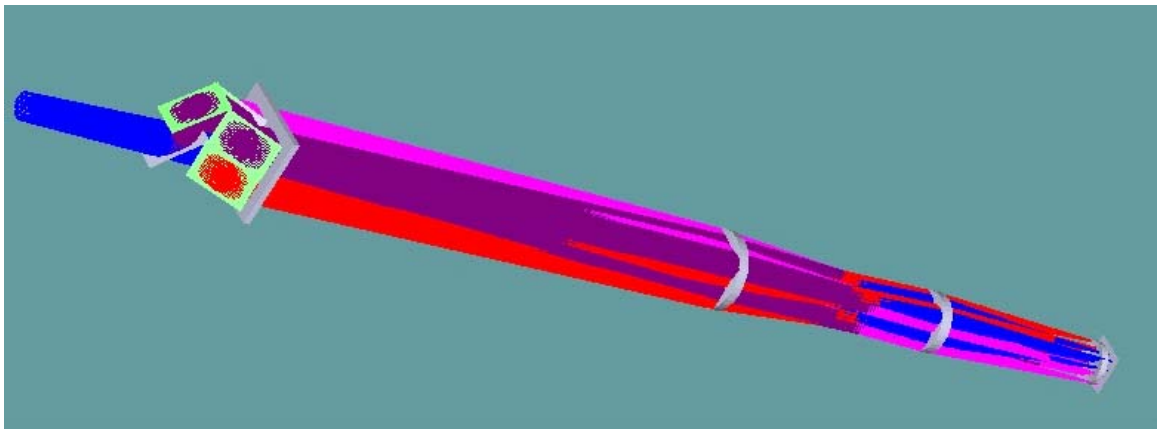

Figure 12-25: Differential Imager based on dichoics splitting the beam in 4 wavelengths.

Filter	Central wavelength	FWHM	λ/Δλ
1 ('on-line')	1140 nm	75 nm	~ 15
2	1220 nm	80 nm	~ 15
3	1300 nm	85 nm	~ 15
4 ('on-line')	1385 nm	90 nm	~ 15

Table 12-5 Proposed wave-lengths set for the differential imager

Filters 1 and 4 would be 'on-line'. i.e.. a planet with either CH_4 or H_20 would be significantly dimmed by them. while it would appear bright in the other filters 2 and 3. Three-wavelength imaging to further reduce chromatic speckle residuals would also be possible. The spectral resolution is kept nearly identical to avoid relative speckle elongation.

12.2.3.5.7.2 Integral Field Spectrograph

544

An Integral Field Spectrograph has been the proposed for the CHEOPS VLT planet finder project by the MPIA et al. consortium. In the frame of EPICS a Tiger-type IFS in the H band is being studied in collaboration between the two consortia. An IFS has an enormous advantage in terms of the multiplexing capability and allows to deal with unexpected spectral features. Another important adavantage is that. in principle. an IFS could be free of differential aberrations. However during the VLT Planet Finder Phase A study. the LAOG et al. consortium identified a serious problem regarding differential aberrations due to cross-coupling when using an IFS in the diffraction limited regime. In depth investigations of the problem are being pursued for the VLT Planet Finder and will naturally benefit to EPICS.

The EPICS IFS will operate in H band with a 2x2 arcsec field and with spectral resolutions per pixel from 15 to 30. Square and hexagonal shapes are studied in order to find a compromise between cross-coupling and size of the detector.

A Fourier Transform Spectrograph is also being studied. This concept could have a better performance in terms of differential aberrations but has some other complications due to time dependent effects. One important advantage is that the spectral resolution can be adjusted from low resolution to very high resolution. The FTS is a very good candidate for a follow-up instrument for the O_2 detection in R band.

12.2.3.5.7.3 Differential Polarimeter

The Differential Polarimeter for EPICS is directly based on the ZIMPOL concept proposed for the VLT Planet Finder. The main requirement is that the telescope polarisation remains low and relatively stable so that a suitable place can be found for the polarisation switch. Different possibilities are still under investigations. The implementation of the differential polarimeter in OWL and within EPICS is shown in Figure 12-26 .

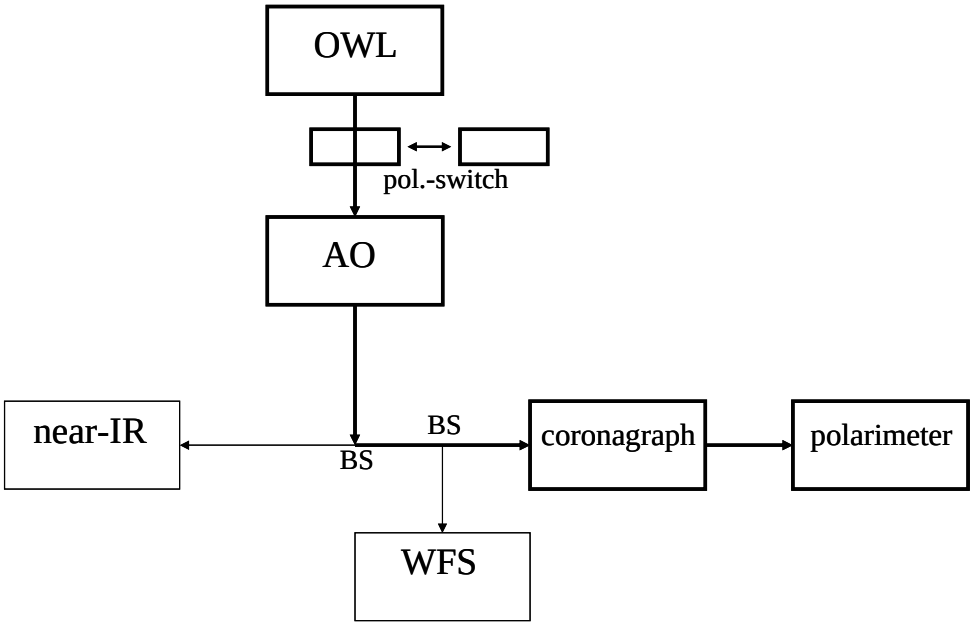

Figure 12-26: Block diagram for the EPICS polarimetric mode concept.

The concept of the polarimeter itself is described in Figure 12-27 .It is assumed that the beam comes from the coronagraphic focal plane and passes first through a collimating lens and a coronagraphic (Lyot) pupil mask before it enters the high precision polarimeter.

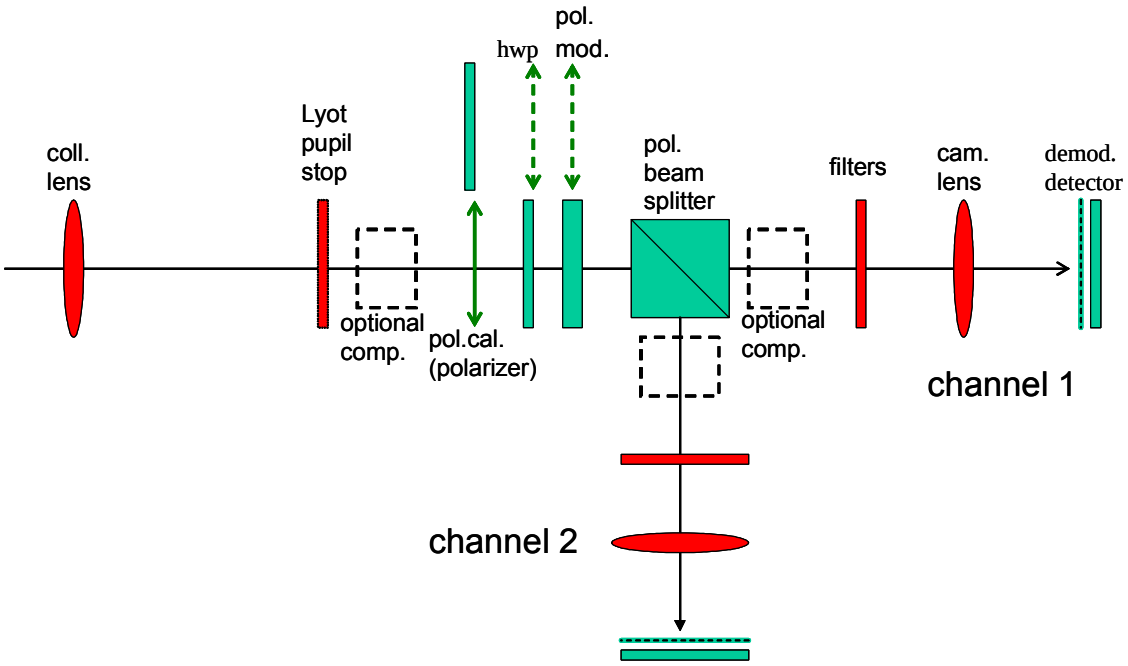

Figure 12-27: Optical scheme for the high precision polarimetric mode in EPICS

In the high precision polarimeter the beam passes first through a rotatable half wave plate which selects between a Stokes Q or U measurement. Then follows the polarization modulator package. including a modulator and a polarization beam splitter producing two beams (see Figure 12-27). Both beams will be recorded with their own detector systems in order to collect all light from the telescope. In both beams the same polarization signal is encoded as intensity modulation. Thus. double beam mode observations provide two full polarimetric observations which can be reduced and analysed independently of each other. The result from both beams can then be combined at the end in order to achieve maximum efficiency. This is the basic concept of all polarimeters based on fast polarization modulation.

12.2.3.5.8 Integration times for a 5 σ detection in case of background limited observation

Wavelength splitting differential detection (IFS and Differential Imager).

As a first step to compute the expected performance for planet detection with EPICS. an analytical model has been used to compute AO corrected PSFs after a perfect coronagraph. The detailed AO error budget taken onto account the most important error sources is described in the EPICS study report (RD51). An example of residual halo for a G2 star at 25 pc (V=7.0) is shown in Figure 12-28. One can notice the two AO control radii at 0.2 and 0.7 arcsec corresponding to the two stages of the currently envisaged XAO system.

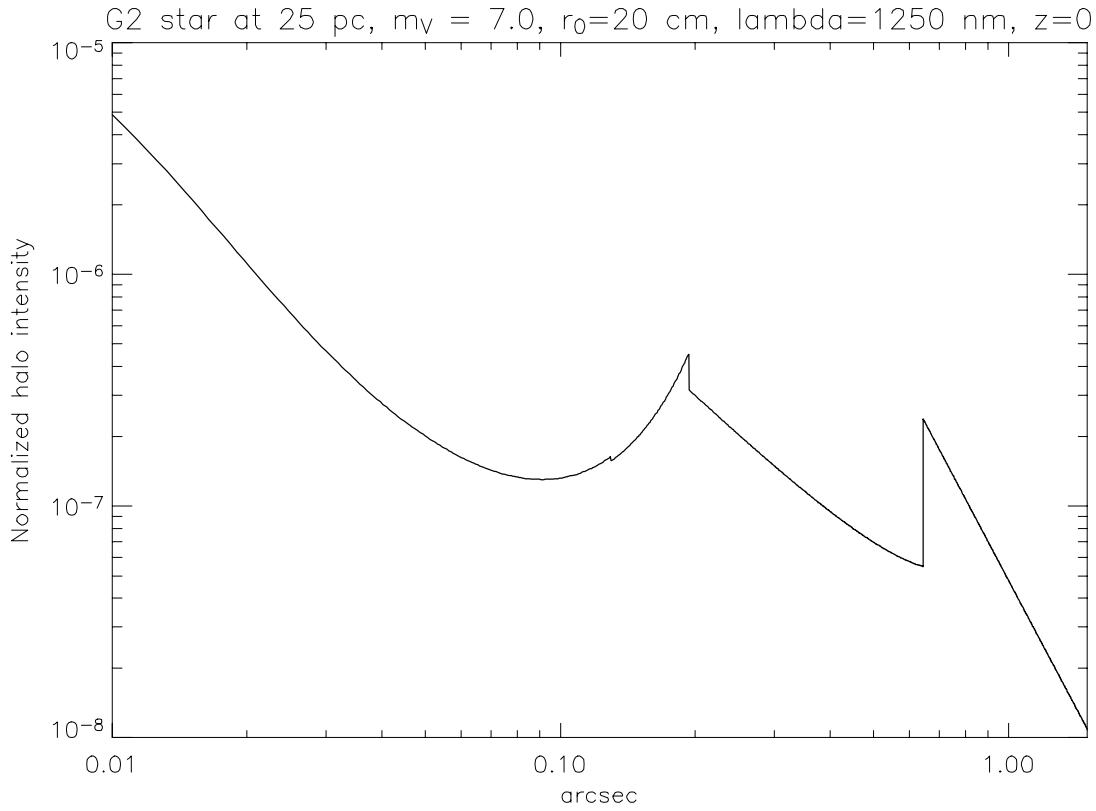

Figure 12-28: Example of halo intensity with perfect coronagraph after adaptive optics correction . Error sources: servo-lag. photon noise (30 % transmission + L3CCD noise excess in WFS). chromatic seeing. aliasing. fitting. static aberration (5 nm rms).

Different AO haloes have been computed considering the targets of EPICS. for three representative spectral types G2. K2 and M2 stars at distances ranging from 10 to 25 pc. Apparent star magnitudes range from V=5.0 for a G2 star at 10 pc to V=12 for a M2 star at 25 pc. For each spectral type. an Earth-like planet and a Jupiter-like planet are placed at separations depending on the star temperature so that the planets are in a thermodynamical equilibruium at similar temperature as in the solar system. For Earth-like planets. this ensures that the orbits are in the habitable zone. Contrast and angular separation for a 90 deg. Phase angle are then derived (see Table 12-6 and Table 12-7).

Spectral type	Star-planet distance (AU)	Star-planet contrast in NIR	Angular separation at 20 pc 90 deg phase
G2	1.00	2.21×10^{-10}	50 mas
K2	0.51	8.07×10^{-10}	25 mas
M2	0.16	8.30×10^{-9}	8 mas

Table 12-6: Characteristics of Earth-like planets used in the simulation.

Spectral type	Star-planet distance (AU)	Star-planet contrast in NIR	Angular separation at 20 pc 90 deg phase
G2	5.10	1.40×10^{-9}	250 mas
K2	1.67	5.32×10^{-9}	80 mas
M2	0.83	5.50×10^{-8}	40 mas

Table 12-7: Characteristics of Jupiter-like planets used in the simulation.

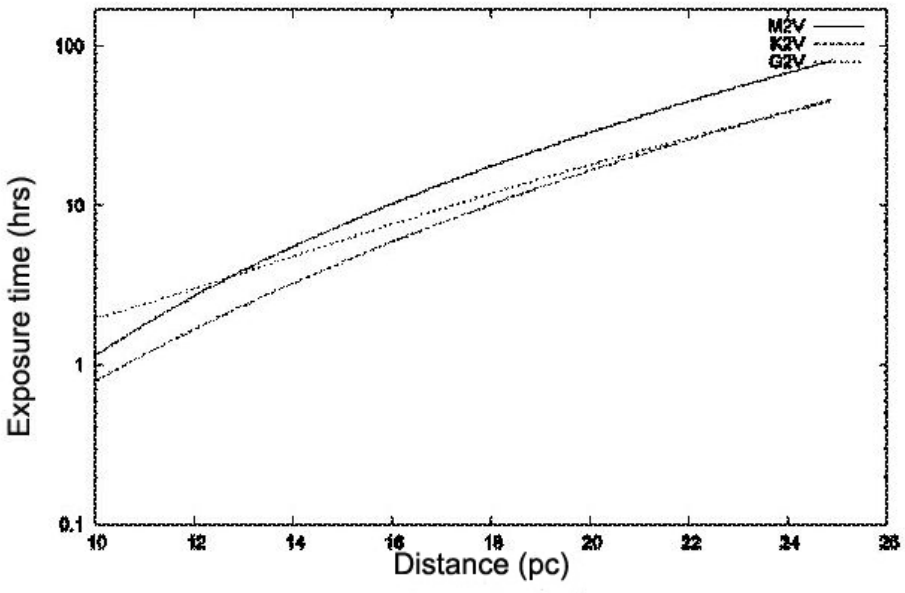

Figure 12-29: Minimum exposure time as a function of distance to detect at 5 σ an Earth-like planet in the H20 band (1.25μm. r_0=12.1cm. τ_0=10mn. Simple Differential Imaging. 0.08μm bandwidth. 0.44 atmospheric transmission)

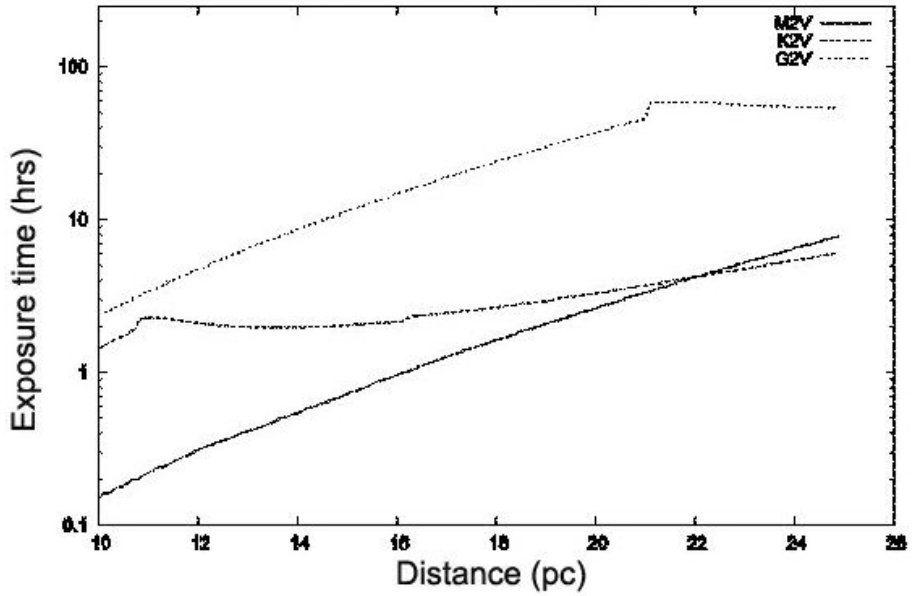

Figure 12-30: Minimum exposure time as a function of distance to detect at 50 σ a Jupiter-like planet in the CH4 band (1.60μ. r_0= 12.1cm. τ_0= 10ms. Simple Differential Imaging. 0.055μm bandwidth)

Exposure times have been computed for differential imaging (either with the Differential Imager or the IFS) to detect the planets around the 3 types of stars.

- The case of H_2O detection in J band for an Earth-like planet is shown in Figure 12-29. Planets around G2 and K2 stars are detected in one night up to 20 pc. and aound M2 stars up to about 15 pc. One can notice that from 10 pc to 20 pc the needed integration times

are roughly multiplied by 10 which comes from the less planet photons detected and the brighter halo in the direction of the centre. Transmission of our Earth atmosphere for a location at 4000-m has been taken into account. Note that this estimation doesn't take into account possible oceans and clouds cover which may decrease significantly the contrast of the features.

- Similar results can be obtained for detection of CO_2 in H band if abundant (see RD51).

- For O_2. the needed spectral bandwidth is of 5 nm (R=150) and is in the R band (760 nm). The combination of a low number of planet photons in the O_2 band and the significantly brighter halo in the visible. leads to integration times larger than 100 hrs for detection at 5 σ in an Earth at 10 pc (> 1000 hrs at 20 pc). For this reason. using the O2 line for detection will not be very efficient. Only follow-up observations for detection of O2 in near exo-Earths can be foreseen.
- Jupiter-like planets are very easily detected with very high SNR in the CH_4 absorption line in the H band (Figure 12-30).
- Performance with differential polarimetry: a preliminary estimation of the performance on detection of Earth-like planet with the Differential Polarimeter on the range [600n-800 nm] has been made. Assuming a 20% polarization. a 5 σdetection would require about 3hrs at 10 pc and 30hrs at 20 pc under medium turbulence conditions.

12.2.3.5.9 Need for 100m

The integration time to reach a given SNR scales as D^{-4} where D is the telescope diameter. in case of photon noise background limited observation as in our case. One can easily evaluate the performance that would be obtained with a 60-m telescope: the needed integration times presented in section 12.2.3.5.8 would be multiplied by about 8. To get the same performances the AO should deliver an 8 times better halo rejection. which would be basically impossible to obtain since the needed frame rate (~ 8-9 KHz) wouldn't leave much photons for the wave-front sensing. Moreoever all the requirements on systematic errors (static and differential) have also to be scaled down by about a factor 3 with the diameter since the contrast for a given error figure is proportional to D^{-2}.

Basically. for the primary science goal. only close Earth-like planets at distances less than 10 pc would be detectable with a 60-m telescope equipped with an instrument based on the current EPICS concept. The sample of targets stars would be rather limited. A more detailed discussion of the effect of the diameter is given in RD51. In particular new techniques favouring the use of broader bands. yielding thus more planet photons for the detection. may have a significant impact on the observation strategy and change the conclusions on the diameter dependence.

12.2.3.5.10 Systematic Errors

The study report (RD51) discusses how to correct two potential show-stoppers for planet findind at ELTs: cophasing errors and differential aberrations.

12.2.3.5.11 Technological requirements for EPICS

EPICS will require significant technological developments of hardware to achieve its goals:

- CCDs: 1KxK (goal 3Kx3K) detectors with fast read-out (3 KHz) and low noise (read-out noise less than one electron) are required. Developments of L3CCD are already part of the OPTICON Joint Reasearch Activity 1.
- Micro Deformable Mirrors): EPICS requires a micro deformable mirror with about 2.10^5 actuators. Actually only 1K micro DM2 with about 1 micron mechanical stroke are available (Boston Micro-Machine). A 2K micro DM with larger stroke will be developed in the frame of OPTICON.
- More powerful real-time-computers
- High precision coronagraphic masks (in phase and in amplitude) .

- High quality optical polishing for a number of optical surfaces (less than 1 nm rms error). The effect of coating on super-polished surface is an other important issue to be thoroughly investigated.

12.2.3.6 T-OWL: Mid-Infrared Imager

The study of T-OWL was carried out at the MPIfA. at Leiden University and at ASTRON. P.I. of the study was R. Lenzen with B. Brandl as Co P.I.. The Concept Study report is provided in RD56 and its content is summarized here.

Study Scope and Science Drivers - Scope of the study was first to review the science for an instrument to operate in the thermal infrared. that is the wavelength regime λ ≥ 3μm where the thermal emission of sky and telescope dominate all other noise contributions up to approximately λ = 24μm. where the atmospheric interferences become prohibitive for sensible astronomical research. Secondly. an instrument concept had to be developed with the capability to carry out the primary science cases.

In the study the science case and the instrument definition were developed in parallel. always keeping an eye on competing instrumentation on future air-borne and space-borne observatories to avoid costly duplication of observing facilities.

The study team could enlist a fair fraction of the scientific community interested in thermal IR astronomy in Europe. The science cases presented in the report cover most areas of present astronomical research from the inner Solar System to the nuclei of galaxies and on to observations of GRB in the early universe. They were used to set the initial set of requirements to the instrument. In this summary we point out as an example one of the most exciting science cases. the precise mass determinations of massive black holes. Figure 12-31 shows the rotation curve obtained close to the center of the Seyfert 2 galaxy NGC 7582 (M. Wold. 2005) with a spatial resolution of 0.4" (40pc). Various models for different black hole masses are compared with the observations. It can clearly be seen. that the increase of spatial resolution in long-slit spectroscopy by a factor of 12 to ~4pc linear scale (OWL vs. VLT) would be highly advantageous for a precise determination of the dust obscured central black hole.

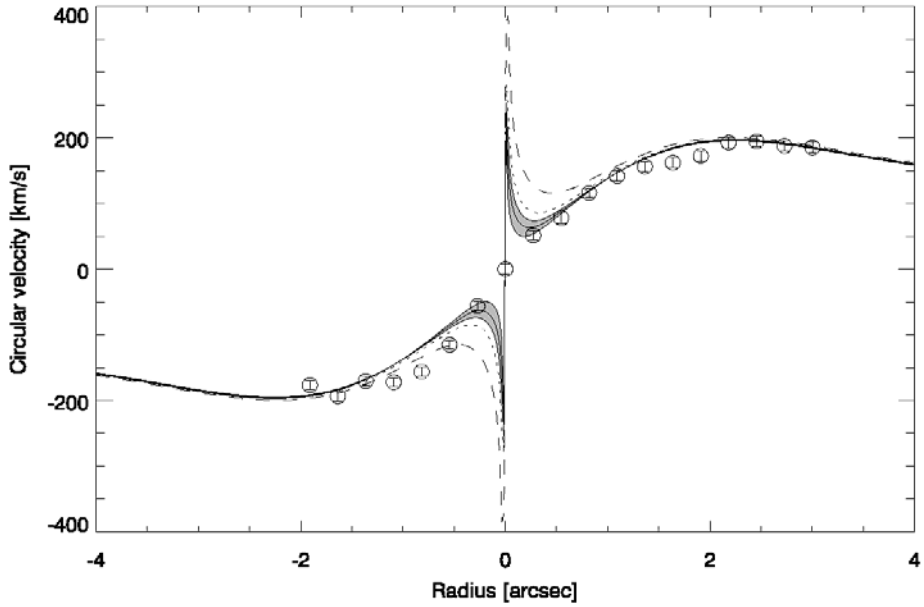

Figure 12-31. Rotation curve of the nucleus Seyfert 2 galaxy NGC 7582 (M. Wold. 2005). Circles: VLT-VISIR measurements using the [NeII] line at 12.8μm with a spatial resolution of 0.4" (40pc). Lines: models with different masses of the central blac hole..

In synthesis – keeping a balance in complexity and cost - the T-OWL requirements were set as follows:

- Wavelength range: 3μm - 20μm →LMNQ bands (goal : 3μm – 27μm) using two types of dedicated detectors (HgCdTe or InSb in the “blue” arm and As:Si in the “red” arm)
- Diffraction limited imaging using an all reflective system and typical pixel scales of 3.5mas for the “blue” and 7mas for the “red” part and a minimum field of view of the order of 50 arcsec^2 ; for the “blue” arm a tunable Atmospheric Dispersion Compensator (ADC) was found to be necessary and has been designed. albeit an experimental verification of the atmospheric dispersion formulae used is pending. As T-OWL works in the back-ground-noise limited regime. sensitivity will not be compromised by the too fine sampling in case the AO can not deliver diffraction limited images.

- spectroscopy should ideally encompass both low (R=300). medium (R=3000) and high resolution (up to $\lambda/\Delta\lambda \approx 50000$) and potentially an integral field- unit with ~10 arcsec^2

To select an optimum instrument configuration the design concepts of various 8m-class telescope IR instruments were compared: VLT-VISIR. VLT-ISAAC. VLT-NAOS-CONICA or Subaru COMICS. The mechanical and cryogenic designs adopted in these instruments provide for a repository of well-tested solutions. which can be re-cycled for T-OWL.

Figure 12-32 shows the T-OWL elementary instrument block in the imaging and low-resolution spectroscopic configuration: behind the cryostat entrance window (top left) a slit is positioned. A three mirror anastigmat (TMA). the building block of many ESO-VLT instruments. creates a collimated beam at the instrument pupil. To minimize the thermal background from the OWL central obscuration and the mechanical structure. a cold pupil stop is foreseen which can be combined with other enabling devices for high contrast imaging. such as apodizing masks. At this location filters and grisms for low resolution spectroscopy can be inserted. Behind this pupil stop a second TMA forms an image in the detector plane. “Blue” and “Red” ranges within the 3-24 μm would be selected by a detector exchange mechanism. The T-OWL imager in this relatively simple configuration could consist of 2-4 such elements. each covering e.g. 4 x 4 arcsec at the required pixel scale with a 2K x 2K array.

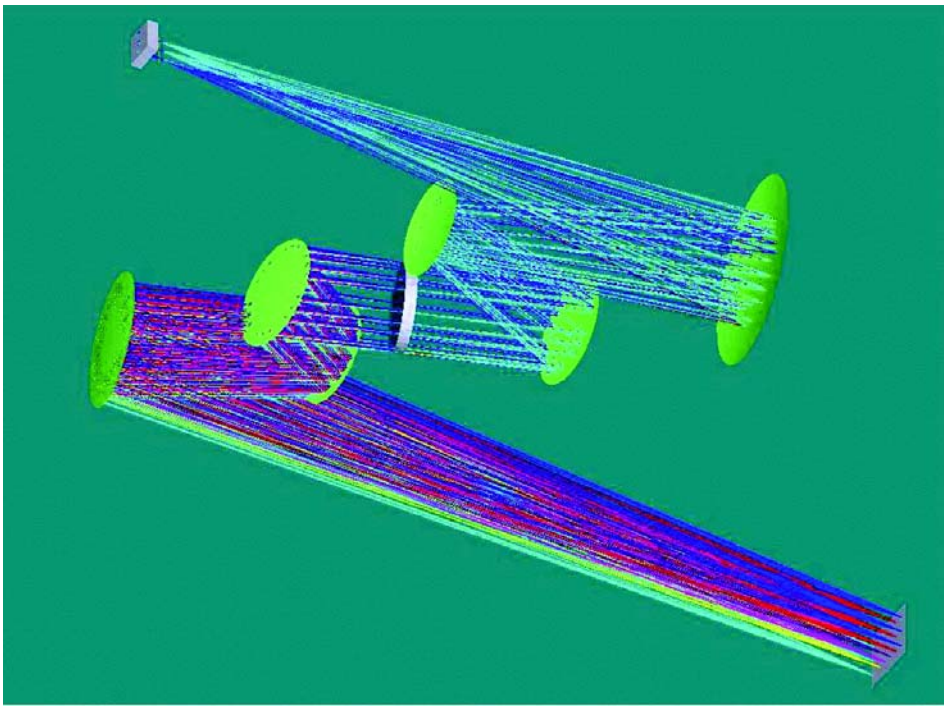

Figure 12-32: Optical concept of one of the imaging-low resolution spectroscopy of T-OWL.

Sensitivity and Context – The T-OWL imager will work in the background noise limited regime; this implies for diffraction limited performance of the telescope that the sensitivity scales with D^2. In that sense T-OWL would be a factor of 150 (or 5.5mag) more sensitive than the

present instruments on 8m class telescopes. A careful analysis of the emissivity of OWL has been done. under the assumption. that the central obscuration and the spiders can be masked by a adapted and motorized cold pupil stop. Detailed atmospheric transmission and emissivity calculations were done. as precise as possible without knowing the exact telescope site. The calculations were cross checked with values reported for ESO's VLT.

The T-OWL sensitivities have then been compared to the following contemporaries: JWST (6.5m diameter. MIRI and NIRCam instruments). SAFIR. a NASA FIR-space telescope (10m diameter) under study right now and to the Spitzer Space Telescope (0.85m diameter). The result is condensed in Figure 12-33. It should be noted. that in many cases the spatial resolution will be required to lift the confusion limit set by the brightness fluctuation of “empty” sky in the infrared.

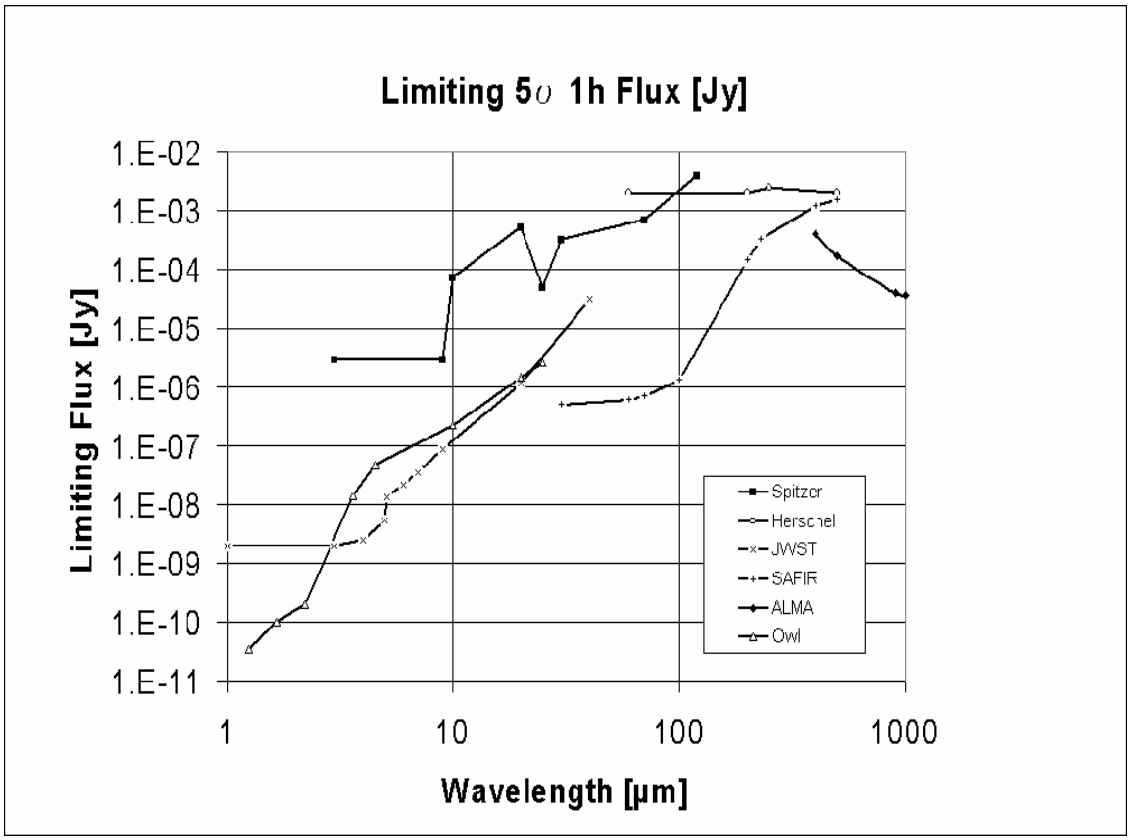

Figure 12-33. Sensitivity of T-OWL as compared to other thermal infrared facilities for imaging of stellar-like sources.

The concept study does also explore in a preliminary way the feasibility and performance of the R= 3000 and R = 50000 spectroscopic. with the following conclusions:

* The predicted line sensitivity in the N band provided by T-OWL at R=3000 is basically the same as for JWST/MIRI. The 15 times better spatial resolution makes its performance unique.

* The high resolution (R=50000) mode will provide unsurpassed sensitivity to measure unresolved lines and hence be a much more powerful tool to study very narrow spectral features than JWST+MIRI in the atmospheric windows.

T-OWL Interfaces and Compatibility with the Telescope

Optomechanical Interfaces - The T-OWL imaging module fits without problem into the design space provided for instruments at OWL. The situation for the spectrograph is more critical and needs further study. The problem of field de-rotation has been studied in great

detail. For f/6 an optical derotator can be excluded. A stationary instrument with derotation in software is possible. but leads to a variety of unpleasant constraints and a substantial amount of additional cryogenic mechanisms and much more demanding data handling. Thus the instrument should be interfaced to a VLT-type mechanical de-rotator. and the weight/torque limits might require to use a VLT-VIMOS-type support "leg" (or better a set of arms) supporting T-OWL with an additional rotational bearing from the instrument cabin structure.

Flexure in the instrument is not considered to be a problem as Piezo-driven active optics would be employed.

Adaptive Optics Interfaces - T-OWL spans a very wide wavelength range where the requirements for AO are quite diverse. The performance of any AO-system at λ>16μm can be considered just perfect. The most demanding requirements for T-OWL stem from 2 different roots: at λ~10μm T-OWL shall be used to do extremely high contrast imaging for the direct detection of extra solar planets. albeit in a small field and with rather bright reference stars right on-axis. while at 3-5 μm a moderately large field is necessary. generally no bright guide star will be in the field. and good control/understanding of the PSF over the field is necessary for further photometric processing of the data. For λ>8μm the isoplanatic patch is much larger than the OWL field of view. but even for the shorter wavelengths un-isoplanatism is not considered to be a major problem.

In all cases it can be assumed. that the best point for the wave-front reference star pick-off(s) is the entrance window to the T-OWL Dewar. the second best point would be a dichroic mirror at the cold pupil stop. In any case the AO wavefront sensor should work as far in the infrared as possible. e.g. at λ~2.2μm. just to keep all differential effects as small as possible.

The starting point for AO should be a natural-guide-star system using typically a 100x100 grid of sub-apertures and consequently approximately 10^4 actuators. A multi-conjugate plane AO system or a ground layer AO system might be of high interest for the "blue" region of T-OWL and further optimisation of the T-OWL AO-concept in this region on the basis of selected science cases is still needed.

Special Requirements - The operation of an instrument in the thermal infrared sets a strong requirement on the choice of the site for OWL. A very dry site is required to minimize the effect of the atmosphere and enhance the performance of the instrument.

The only non-standard requirement for T-OWL resulting from the study is the availability of liquid Nitrogen (500-1000 l tank) in the instrument compartments. Chopping by means of M6 as offered in the OWL documentation may be an asset to detect the faintest isolated point-like sources but generally new ways for modulation and noise filtering have to be found.

T-OWL Operations with a "Growing Telescope" - Various schemes of filling up the OWL M1 during the construction phase have been investigated at 10 μm (see Figure 12-34). A zero-order ranking of the possibilities would put a ring-like structure starting from the outer circumference of M1 at position #1. a cross shaped filling of the primary at position(#) and a filling up from the centre at #3. Both the outer-ring and the cross filling concept provide for the full spatial resolution from year 1. A detailed trade-off of the two strategies has to be based on the science cases.

Preliminary conclusions of the study - A T-OWL instrument would be highly desirable at OWL. While there is a solid broad general science case for such an instrument. there are at least the following truly unique opportunities:

- possibility for high contrast imaging for planet detection and characterisation involving coronagraphy and spectroscopy
- detection of signatures of planets in young circumstellar disks
- the study of massive black holes in galactic centers

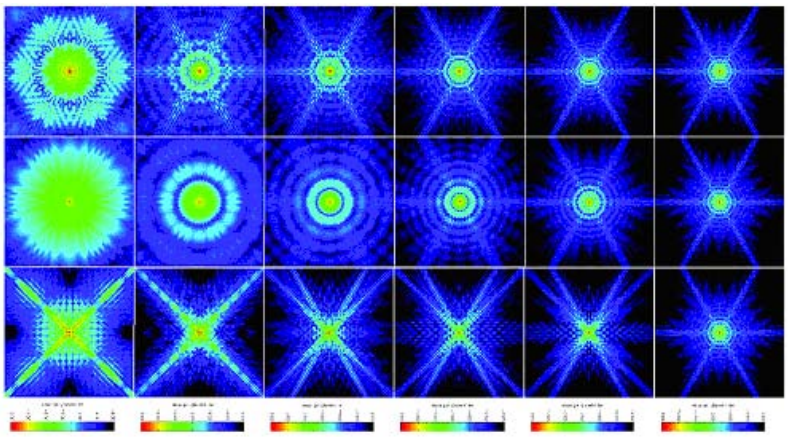

Figure 12-34. The effect of a "growing" telescope primary on the PSF . Each frame is a 2x2arcsec^2 field with the resulting PSF. The columns from left to right correspond to year after year until completion of the OWL-. The rows are for three filling strategies: the top row is by starting with a 100m x 100m cross. the middle row is a ring-like geometry starting from the outside and the lower row is a ring-like geometry starting from the inside.

At shorter wavelengths T-OWL has a meaningful sensitivity. exceeding or fully competitive with the next generation space telescope. the JWST; at longer wavelengths JWST is only in imaging moderately more sensitive. but lacks in any case at least an order of magnitude spatial resolution. An high resolution spectroscopic mode appears also potentially unique for the observations of narrow lines.

A T-OWL imager would be feasible with a modest extrapolation of state-of-the-art instrumentation at 8m-class telescopes. The hardware cost for a T-OWL would of course depend on the exact configuration. but a basic imager instrument could be built for 5M€ and <100 manyrs. A full implementation of high resolution spectroscopy. however. leads in the preliminary estimates to a very substantial growth of these numbers (hardware cost 18M€. manpower 240 person-years).

Important aspects which require future research –

- Properties of atmospheric dispersion beyond 5 μm. dependence on humidity
- Chopping needs for MIR observations with ELTs and possible solutions at 100m telescope
- Feasibility of high resolution mode in Q band
- Pixel size for detectors in the Q band (present 25 μm pitch makes the optical design of the camera very complicated)

12.2.3.7 SCOWL : Imager at Submillimeter Camera at OWL

The study of SCOWL was carried out at the Advanced Technology Center in Edinburgh with B. Dent as P.I.. The Concept Study report is provided in RD57 and its content is summarized here.

SCOWL is an initial concept for a large-format sub-millimetre camera to be used on the OWL Telescope. Such an imager would be unique. more sensitive than any other facility in the same spectral band. and be able to map large areas of sky a million times faster than ALMA. The results would impact a wide range of research. It could answer some of the most fundamental questions about the *origins* of dust. planets. stars and galaxies. and would significantly increase the scientific return from the OWL telescope. It requires a high altitude. dry site to operate efficiently.

Primary science objectives

Astrophysics at sub millimetre wavelengths (300μm to 1mm) is most sensitive to cold gas and dust. with for example the blackbody emission of a 10K source (or a 40K source at z=3) peaking at around 300μm. Such very cold material is associated with objects in formation. that is. the

mysterious earliest evolutionary stages of galaxies. stars and planets. To understand the origins of these most fundamental astronomical structures. the sub millimetre is the waveband of choice. An additional important feature of the sub millimetre is that the continuum emission from nearly all objects is optically thin. This means that observations probe right to the heart of the most crucial processes. and trace dust masses over a wide dynamic range. Some of the key science questions that would be addressed by SCOWL are illustrated here.

Why is the Solar System so free of dust: do we live in an unusual planetary system? Debris discs are the result of collisions and the grinding down of asteroids around main-sequence stars. Most images of them have been obtained in the submillimetre. but so far we have only been able to study the very dustiest examples. For the first time. *SCOWL will enable us to detect debris systems with dust masses similar to our Solar System*. This will not be possible with proposed far-infrared mission over the next ~20 years because of the large beams and subsequent confusion by the bright stellar photospheric emission. It will allow SCOWL to investigate the planetary systems with the least dust confusion. influencing the target selection for deep searches for thermal emission from Terrestrial Planets. The Planet Finder capability of other OWL instruments combined with SCOWL will allow us to investigate the complete range of objects around nearby stars. from giant planets down to dust grains.

How do the lowest and highest mass stars form? Existing surveys suggest that the stellar IMF may be controlled by the pre-stellar clump mass spectrum; however. even in the closest regions. they are incomplete below 0.1 Solar mass. The mass sensitivity limit of SCOWL can be translated to a 10σ detection of a 0.1 Jupiter mass clump in a 1 degree survey of Orion. It would therefore be able to study the formation of the lowest mass stars or even “free-floating” planets.

The early stages of *high*-mass star formation are also very poorly understood. partly because there are fewer high-mass stars. but also because the formation process is so fast and consequently rare. This is important to understand. because of the significant affect they have on the large-scale ISM. SCOWL would allow a full census of *all* high-mass star formation throughout the Galaxy. showing the rarest of phases. and allow us to understand what defines the highest-mass end of the stellar IMF.

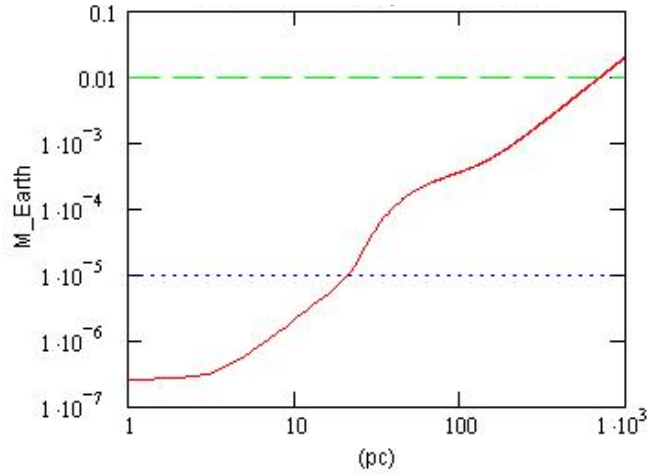

Figure 12-35: Dust mass detectable (10σ) by SCOWL at 450μm around nearby stars as a function of distance. The upper green line represents the mass of the dusty system ε Eri. and the lower line the dust mass of our own Solar System.

Where is the bulk of dust in Galaxies? Is there an additional “cold. dark” massive component? The only reliable way to trace the bulk of dust in galaxies is through submillimetre imaging. Dust in spirals is detected in extreme cold (<15K). low-surface brightness disks often extended far from the nucleus. Such cold dust radiates strongly in the submillimetre and is faint already in the far infrared. *This component dominates the total dust mass*. How far such dust extends beyond the disc is unclear: does it enter the intergalactic medium? Is it distributed in galaxy clusters or present in cooling flows? How much does it contribute to the rotation curve

and is there a relation to cold dark matter in Galaxies? High-sensitivity submillimetre mapping is the only way to answer these questions.

The origin of dust. It is unclear whether dust forms mostly in supernovae remnants or in evolved stars. Most SNR are too large and have too low surface brightness to be studied with current facilities. Other dust production factories may. Their episodic violent ejection produce rings of enhanced emission. High resolution imaging of arcmin large fields. as provided by SCOWL. is required to trace their inter-ring spacing. This will allow us to verify ejection time scales. production rates and also clumping.

What is the star formation history of the Universe? Detecting "normal" Galaxies to the edge of the Universe. The existence of submillimetre (or "SCUBA") galaxies has changed our view of Galaxy evolution. But currently we can only detect the very brightest "monsters" at high redshifts. with extreme star formation rates of ~10^3 Solar masses per year. 1000 times that of the Milky Way. SCOWL could map the field of view and detect objects ~1000x fainter at 850μm in ~50 hours. reaching well below the confusion limitations of the next decade of deep far-infrared or submillimetre surveys. Such a survey would resolve almost all the submillimetre background flux. The negative K-correction for dust emission in the submillimetre means that a galaxy like the Milky Way would have an 850μm flux of ~10μJy if observed at *any* redshift between 1 and 10. *SCOWL would therefore be able to detect normal Galaxies like the Milky Way throughout the Universe*.

Instrument capabilities

The basic design goal of SCOWL is to pave the full field of view with Nyquist-sampled pixels with sky-limited sensitivity at all three primary submillimetre wavebands. The huge OWL collecting area (effectively larger than ALMA) and high detector sensitivity means it will be possible to image objects at the 10μJy level at 850μm. more than two orders of magnitude better than existing instruments. The beam is sufficiently small that confusion from high-redshift galaxies and local galactic cirrus over most of the sky is at the level of a few μJy. At the shorter wavelengths. assuming a precipitable water vapour (pwv) content above the OWL site of 0.5-1 mm. a point-source sensitivity of 100-200μJy (10σ/1hr) at 450μm will be reached. This will deteriorate to ~1mJy (10σ/1hr) if the pwv is 2mm. and indicates that a high dry site such as Mauna Kea or Chajnantor would maximise the potential for short-wavelength observing. At 850μm the effect is significantly less pronounced.

As well as three-band imaging. SCOWL will also have a polarimetry capability. The basic specifications are given in Table 12-8

Parameter	Requirement	Notes
Wavelength	850μm. 450μm. 350μm (simultaneously)	Set by atmospheric transmission windows.
Sensitivity	50μJy at 850μm (100μJy at 450μm)	10σ. 1hr. per pixel
Resolution	1-2 arcsec	Diffraction limited
No of pixels	≥10000-20000 per wavelength	May be larger. depending on detector technology used
Field of view	2.5x2.5 arcmin	Set by telescope design
Mapping capability	2-10mJy per square degree per hour	10σ. 1hr. 1 square degree

Table 12-8 Main characteristics of SCOWL

SCOWL and ALMA complementarity

SCOWL and ALMA will both operate in the submillimetre. but their capabilities are clearly different. ALMA will be the facility of choice for the high resolution studies. But SCOWL is the only instrument capable of widefield mapping. For example. at 850μm SCOWL will map 1

square degree down to 1σ=40μJy within 10 observing nights. while ALMA even if it were possible would need 10Myr! Observing large sky areas in the submillimetre to high depth become feasible *only* with SCOWL. As such. SCOWL would also act as a pathfinder. searching for new objects for high-resolution followup with ALMA. However. even for sheer point-source sensitivity. on a similar site SCOWL beats ALMA by a factor of 20 at 450μm. and more at 350μm.

Instrument concept design

The baseline design of SCOWL uses the same basic system as SCUBA-2. currently the cutting edge of submillimetre continuum cameras. This is the lowest risk approach. and uses 48 of the existing TES detector arrays with a total of ~20000 pixels at each wavelength. The instrument layout is shown below. The cryostat volume is ~24m^3. with a total weight of 6t.

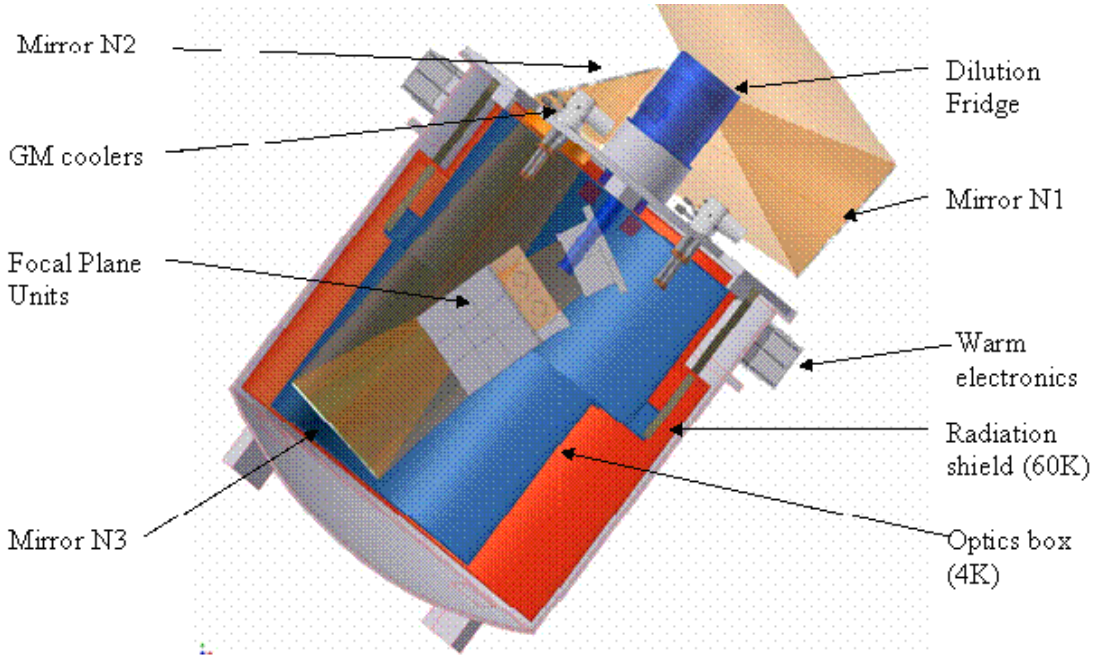

Figure 12-36: SCOWL cryostat cross section.

Advanced designs and risk items

The baseline design uses three wavebands (850. 450μm and 350μm). and partly paves the field of view with detectors. However. the goal is to fully cover the field of view.. The existing and projected TES detector technology is limited. both in the size of detector array. and in the cooling requirements it places on SCOWL. An alternative - Kinetic Induction Detectors - may prove in the next few years to be more capable. and significantly relax the cooling requirements as well as increasing the fraction of field of view covered by pixels. and reduce the cost. However. it will require a technology development programme. For the baseline design there are several areas where manufacturing capabilities must be developed. Cooling is a key risk area because the current generation of coolers required for the final stages of cooling at milliKelvin level are gravity dependent and therefore limit the operation of an instrument that moves with the telescope. In addition. manufacturing capabilities will need to be developed to allow filters. waveplates for polarimetry and the cryostat window to be produced as current sizes of these items are below what is required for SCOWL.

Cost and schedule

Based on SCUBA-2 technology alone the total cost is provisionally estimated to be of the order of €36M. with a construction time of ~5 years. These estimates are dependent upon the availability of the key components described above. Ideally development programmes would be

in place before a commitment to build SCOWL were made so that manufacturing techniques were established prior to the start of design activities.

12.2.4 Versatile Instruments and Dedicated Experiments or Surveys

The ESO Very Large Telescope (VLT) is by far the most important facility for optical and infrared astronomy completed in the last 20 yrs by the European (and probably worldwide) astronomical community. The VLT consists of four 8m telescope. each with the possibility to host permanently up to three instruments. The instrumentation plan for the VLT in its original conception before the telescopes were build and through the subsequent adjustments foresaw 11 instruments covering different wavelength ranges and. within a given range. different observing modes in imaging and spectroscopy. The science objectives and the actual programs being carried out with each instrument are much diversified. Most of the instruments have been actually used for discoveries ranging from nearby stars to the most distant universe. This versatility in the discovery space has been one of the main strength of the VLT observatory.

The OWL instrumentation Plan. and hence the selection of the first priority instruments. will take shape during the subsequent phase of the project. It is important to note however that it will not be possible to apply in full the VLT paradigm to OWL instrumentation. To reach the challenging goals of some of the OWL science. some of the instrument will have to be optimized to achieve an optimal performance in a specific mode of observations only. These OWL instruments could then be more conceived as experiments which will occupy a focal station at the telescope for the time required collecting a specific set of observations and then be dismantled leaving space for new dedicated projects. Other instruments like SCOWL are likely to express a large fraction of their scientific potential in an extended survey to be carried out at the beginning of their operational life. *The OWL Instrumentation Plan is likely to contain a balanced mixture of general capability instruments to be used for a large variety of science programs and experiment-type instruments mainly used by dedicated teams to pursue a specific scientific goal or to carry out a survey for the community*.

12.2.5 Telescope Interface and Deployment Considerations

As a cautionary note to this section. it is important to stress that the instrument concept studies have become available toward the end of the telescope study only and the OWL team had therefore very little time to incorporate the feedback from the studies in the design. This will happen at the beginning of the next phase of the project.

Telescope Properties

Non-optimal features for most of the instruments are the fast beam (F/6) and the short back focal distance (separation from the adapter flange and the focal plane. away from the telescope) and to a lesser degree the angle at which the beam from M6 enters the focal station room. A much slower beam would however not be free from technical drawbacks. One of these would be the very large physical dimension of the adapter-rotator. Ideally a F/8-F/10 beam would be a good compromise but it is not compatible with the present optical design of the telescope.

A scientific field of 3’ x 3’ is required by the distributed multi-object spectroscopy (MOMSI) and the wide field module of the ONIRICA imager. Both would operate with pixel size of ~10-30 mas.

Diffraction limited images at NIR and thermal infrared wavelengths are required over a field of at most 1 arcmin diameter.

Diffraction limit images at visual-red wavelengths are required by one observing mode of EPICS only and over a field < 5 arcsec.

Focal Stations

The present OWL design foresees 6 large focal stations which move with the telescope structure. Access is secured via lifts in the central body of the telescope structure. Working at these focal stations for integration and maintenance will be more cumbersome than at Nasmyth or Cassegrain foci of the VLT or other telescopes of the same class.

Of the instrument studied so far QuantEYE and the HyTNIC could be easily attached to the adapters. QuantEYE call for an atomic clock mounted in a stable environment in the telescope building.

CODEX requires a volume in excess of the present allocation and an ultra-stable environment. The instrument has been located in a laboratory outside of the telescope structure and could be fed by a long fiber. An optical feed via a coude train with a very small field would be however much preferable for reason of efficiency. It will be evaluated in the design phase.

EPICS call also for very high opto-mechanical stability. It will have to be mounted on a gravity-invariant optical bench in a protected enclosure. This solution has not been studied in any detail.

T-OWL would also require special arrangements within the focal stations if the spectroscopic module is fully implemented.

The very preliminary mechanical concept of ONIRICA appears in line with the available volume.

SCOWL would be attached to the adapter and does presently exceed the allocated volume by a small amount only.

MOMFIS will need to be mounted on a bench structure inclusive of a derotator. The present design exceeds the allocated volume by a relatively large amount. The design will have to be optimized or possibly partly descoped to fit in the focal station volume.

Most of the instruments include large cryostats. An overview of the cooling requirements has not been prepared yet. Effects of the changes in the orientation with respect to gravity for the large cryostats- cryo-tanks has also to be investigated.

Observatory Site

Both the thermal and sub-millimetre instruments (T-OWL and SCOWL) call for a site with a very low content of precipitable H_2O. For SCOWL a dry. high altitude site is a must to achieve a competitive performance.

Optimal results (in particular values close to the theoretical diffraction limit) with some of the foreseen AO systems will be achieved in nights of optimal seeing only. Atmospheric properties of the site must be carefully considered together with a likely instrument package to optimize the efficiency of the observatory.

Instrument / Requirement	CODEX	QuantEYE	HyTNIC	ONIRICA	EPICS	MOMFIS	T-OWL	SCOWL
Field diameter	Center (2")	Center (2") + pick-up arm over 3'	Center (1")	Diffr.limited ≤ 1'; 3' x 3' at ~10 times lower resol.	Center (2")	5'	≤ 30"	2.5' x 2.5
Wav. Range μm	0.4-0.7	0.4 – 0.8	1.1- 1.6	0.8- 2.5	0.6- 1.9	0.8- 2.5	2.5-20	250-450-850
AO system type	Not required*	Not required*	SCAO	MCAO. GLAO	XAO	MOAO	SCAO GLAO	Not req.+

Table 12-9 AO Requirements from Instruments

**: seeing-reduced image quality desirable*

+: high frequency monitoring of water content of atmosphere desirable

12.2.6 Adaptive Optics Requirement Overview

The development of AO system for OWL and the various configurations are described in detail in chapter 8 where references to the various instruments are also given. Table 12-9 gives an overview of the requirements from the instruments.

12.2.7 Detector Requirement Overview

The instruments for OWL which have been studied in this phase of the project do require special development of array detectors. The appear as possible extrapolation of current state of art but they will undoubtedly represent a major (in same cases dominant) fraction of the costs of the instruments. even taking into account the substantial cost/pixel reductions envisaged by potential suppliers.

Instrument	Wavelength-Range (μm)	Main Operating Modes	Pixel size (mas)	Instrument Detector needs
CODEX	0.4- 0.7	High velocity accuracy. visual spectrograph	n.a.	40-80 (4K x2K) CCDs or equivalent devices
QUANTEYE	0.4- 0.8	Photometry at 10^{-3} -10^{-9} second resolution	n.a.	2 (10 x 10) sparse SPAD arrays
HyTNIC	1.1- 1.6	High-contrast diffraction limited imaging	tbd	1 4K x 4K HgCdTe array (tbc)
EPICS	0.6- 1.9	Imaging and spectroscopy of earth-like planets (three observing modes)	1-2	2 (8K x 8K) HgCdTe mosaics; 8K x 4K frame transfer CCD; 8K x 8K HgCdTe mosaics
MOMFIS	0.9-2.5	Distributed multi IFU spectroscopy over 5 ‘ x 5’ field	20-30	~ 50 (2K x 2K) HgCdTe
ONIRICA	0.9-2.5	Imaging at diffraction limit over extended field	1-2(DL). 10-20 (wide field)	~ 60 (4K x 4K) HgCdTe arrays for 30” DL field.
T-OWL	2.5-27	Imaging. low. medium and high resolution spectroscopy	3.5- 7	2 (2K x 2K) InSb; 12 (1K x 1K) SiAs (tbc)
SCOWL	250-450-850	Imaging in three sub-mm bands	~1000	Mosaic of 16 (41 x 32) Transition Edge Sensors (SCUBA-2 detectors) or equivalent KIDs

Table 12-10 Detector Array Requirement

Table 12-10 presents an overview of the detector needs as derived from the possible focal plane configurations of the 8 instrument studied in this phase. It is obviously a very preliminary estimate.The suite of instruments which have been conceptually investigated in this phase of the OWL project does not represent the final complement of instruments to be built for the future European ELT. They can however be effectively used for a preliminary assessment of the likely needs in detector area and they give the following results:

- CODEX is the only instrument which requires a large number of CCDs or equivalent devices. The number of devices (~ 40 4K x 2K for the five spectrograph configuration) is of the same order of magnitude of what is used in wide field cameras of the last generation. Operating properties are also very close to those of existing devices. Given this. they should not represent a major procurement issue. The polarimetric mode of EPICS requires low noise. large size CCDs or equivalent devices to be read at relatively high speed. While

devices of that size and characteristics do not exist at present. they are conceivable as a development of current devices.

- OWL will deploy its unique diffraction-limited capability with the help of AO systems which for the first years of operation will be effective at IR wavelength only. Key OWL instruments like MOMFIS and ONIRICA operating at NIR wavelengths do require a very large number of NIR arrays to sample a field of reasonable size at or close to diffraction limit. At the current market value. the cost of these detectors will exceed the likely instrumentation budget for OWL by a factor ~10. NIR array manufacturers (specifically Rockwell Scientific. see RD528) have however signalled that substantial cost reduction could be achieved if the number of 4k x 4k arrays on order exceeds is significant (>100 units).

- Detectors for the thermal infrared (2 – 17 μm) do require a factor of ~4 increase in area with respect to today's arrays. Around 15 devices would be required by a T-OWL type instrument. This appears a manageable development.
- Instruments like QuantEYE and SCOWL do require very special detectors. which do represent significant upgrades of state-of-the art devices of the same type. Their development will have to be properly supported by dedicated funding.

In addition to the science arrays. it is necessary to account for the detectors needed for the telescope tracking. for the active controls of the mirror and for wavefront sensing. The preliminary concept of the adaptors (6 units) and its active optics sensing probes calls for ~ 30 (2K x 2K) visual-red CCDs to be read at ~1 Hz frequency. The requirement for the detectors for the wavefront sensing are more variate as they are strictly related to the type of AO system to be implemented and the wavelength region where the images have to be corrected. A preliminary view can be extracted from chapter 8.

13.Transport and integration

13.1 Transport

For cost and schedule reasons. the design of OWL takes in to account transport constraints and is based on the following principles:

- Avoid oversized special transport.
- Use of standard containers for critical parts.
- Redundancy in case of partial loss.

13.1.1 Design provisions

13.1.1.1 Mechanics

Most of the mechanical parts can be transported within standard dimensions. Critical parts such as Bogies. Tracks. Actuators Structural nodes (see Figure 13-1) can be transported in 20 or 40 feet containers. Other parts such structural truss elements can be transported without special precaution (see Figure 13-2).

Due to the high degree of design standardization. partial loss of a shipment does not represent a major draw back in the flow of the site integration activities. Lost or damaged parts can be immediately exchanged with others. while the repairing or re-manufacturing takes place.

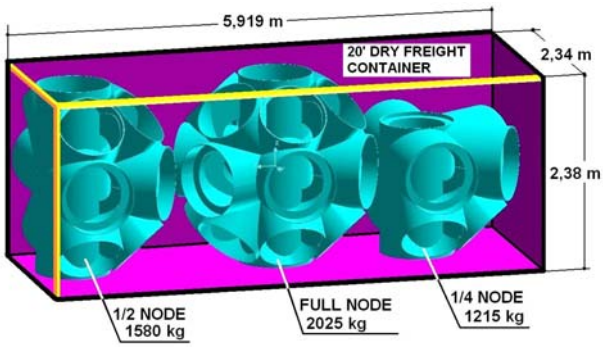

Figure 13-1: Structural nodes container

Figure 13-2: Pipe elements shipping

13.1.1.2 Optics

Optical units are the most critical parts to be transported. They can be classified according to the hazard involved:

- Mirror segments. The size of each segment allows transport in standard size containers. Inner fittings would have to be mounted for safety. The segments transport is not considered as critical..
- M3 and M4 Units. These mirror units. which are similar to the VLT primary mirror. are the most critical parts to be transported. Special transports have to be organised and no redundancy exists. thus the risk associated to this transport is most severe. Nevertheless VLT primary mirror transports and handlings have demonstrated that this can be achieved.
- M5 and M6 Units. Special transports have to be organised and no redundancy exists. Their reduced size makes the transport somehow less demanding then the M3 and M4 units.

13.2 Site integration

The design of OWL takes in to account integration requirement and constraints and it incorporates the following principles:

- Avoid oversize and heavy parts.
- Avoid tight assembling tolerances.
- Maximize standardization of parts.
- Redundancy of handling devices.
- Self standing structure.
- Avoid scaffolding structures.
- Avoid complex metrology and alignment systems.
- Avoid complex welding processes.
- Allow day and night shifts. with tasks tailored to the environmental condition.

13.2.1 Design provisions

13.2.1.1 Mechanics

13.2.1.2 Alignment metrology

By design the structural alignment tolerances of OWL are fairly generous and easy to achieve. The metrology used during the integration does not require high level of accuracy (see sections 13.2.1.3 to section 13.2.1.3.7). Real time measuring systems can be used to align time consuming sub-systems lsuch as:

- Annular azimuth tracks

  Figure 13-3 shows a hydrostatic levelling system which can be used for azimuth tracks alignment. This system assures a rapid convergence to the track flatness requirement. over a total developed length of about 5 km.

Figure 13-3: Azimuth tracks alignment metrology.

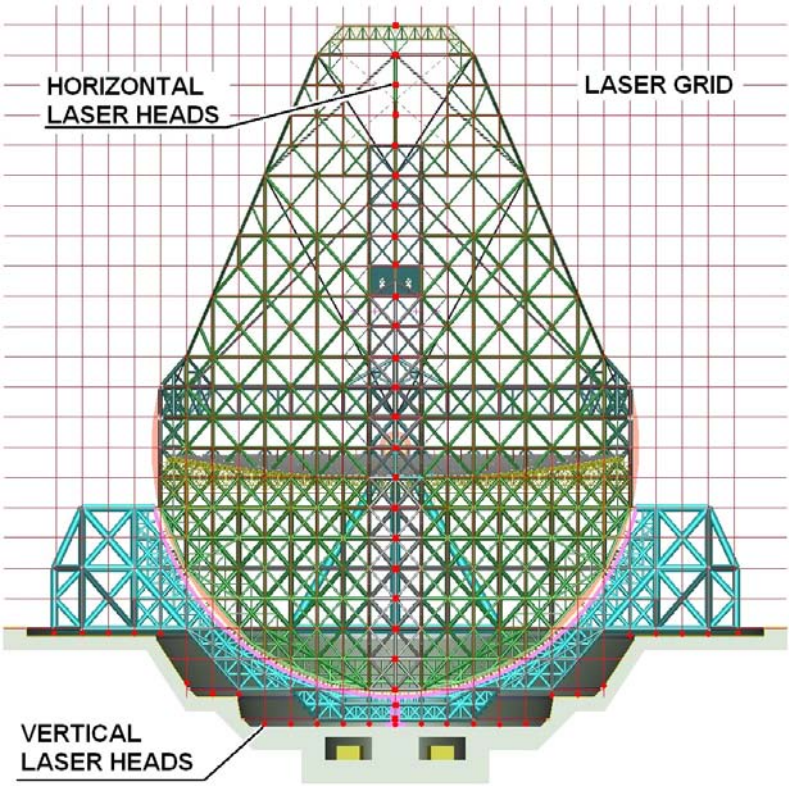

Figure 13-4: Structural elements alignment.

- Structural nodes

  Figure 13-4 shows a grid made by laser beams. This grid defines the X-Y-Z location of each node of the structure. Each node can be equipped with a reference target. Thus the alignment of the complete mechanical structure does not required complex calculations. but only simple visual checks of the target with the laser beams. Convergence time. risks and costs associated to complex metrology can thus be avoided.

13.2.1.3 Telescope truss structure integration

The following design provisions related to site integration. are embedded in OWL concept:

- The telescope structure and its sub-system can be integrated in parallel by several integration teams. using several light cranes with a maximum payload of 3 tons. thereby allowing for redundancy.
- The structural design allows self-supporting “floors” to be to built up progressively. Each floor serves as platform for the next one. Therefore scaffolding is limited and serves for access but not for supporting structural elements.
- Due to the large excursion of temperature during day time (see section 5.4.1.3) the following procedure will be adopted for all part which whose dimensions may be significantly altered under solar exposure:

  1. Day time — Transport to final location.
  2. Day time → — Rough alignment.
  3. Night time → — Fine alignment.
  4. Night time → — Spot welding or other preliminary joining techniques.
  5. Day time → — Final weld and local annealing
  6. Night time → — Final dimensional check.

The following section describes in more detail the various integration phases. The integration teams can cover different disciplines. such as Welding. Metrology. Electrical. Electronic and Control engineering. Each team can be specialized. Electronic and Control Engineering will be more intensive during the final phases.

The manpower required for the telescope integration. is a large part of the total 400 people planned on the site integration for a period of 10 years.

13.2.1.3.1 Phase 1

Integration steps - The first Phase is divided in the following integration and alignment steps:

- Azimuth central bearing. which defines the reference zero of the complete structure.
- Annular track pre-alignment
- Annular track joints (Welded or bolted joints)
- Annular tracks fine alignment Only the vertical DoF has to be aligned (Z axis).
  - Typical flatness accuracy per each track is 5 mm over the largest track diameter.
  - The vertical track to track distance ± 5 mm.
  - Cylindricity and concentricity tolerances 10 mm.

Manpower - Up to one integration team per track can work simultaneously.

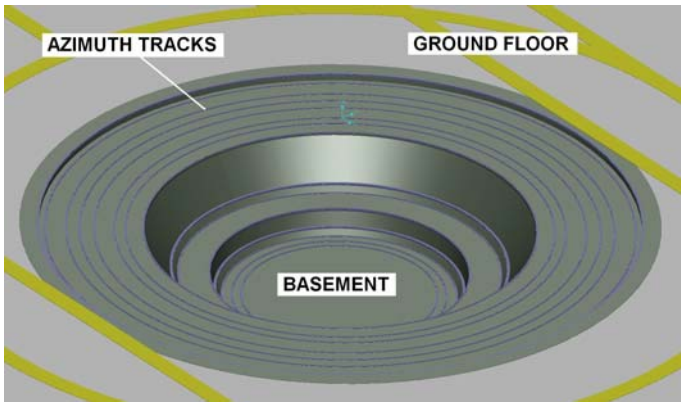

Figure 13-5: Azimuth tracks integration

13.2.1.3.2 Phase 2

Integration steps- The second phase is divided in the following integration and alignment steps:

- Define the location of the “master nodes” where the alignment laser beam can be installed and aligned. Tolerance ± 2 mm related to the azimuth central bearing.
- Place base blocks. To be exchange in phase 4 by azimuth bogies.
- Integrate the truss structure up to the ground level. Tolerance ± 5 mm related to the azimuth central bearing.
- Start of painting activities.
- Start of cabling activities.

Manpower - Up to 6 integration teams can work simultaneously.

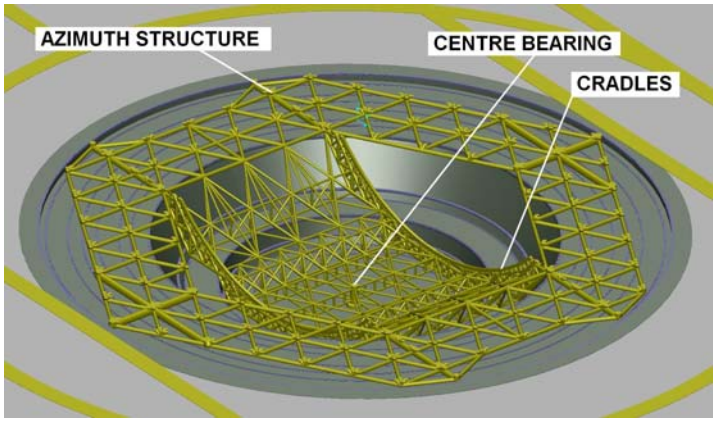

Figure 13-6: Azimuth Basement integration.

13.2.1.3.3 Phase 3

Integration steps - The third phase is divided in the following integration and alignment steps:

- Integrate the truss structure up to the first floor (12.8 m above ground level). Tolerance ± 5 mm related to the azimuth central bearing.
- Start of the altitude cradle integration

Manpower - Up to 6 integration teams can work simultaneously.

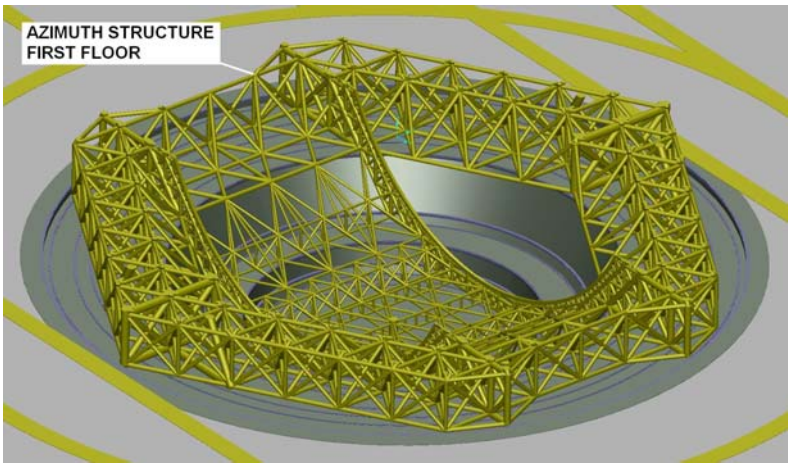

Figure 13-7: Azimuth first floor integration

13.2.1.3.4 Phase 4

Integration steps - The fourth phase is divided in the following integration and alignment steps:

- Complete integration of the truss structure up to the third floor (38.49 m above ground level). Tolerance ± 5 mm related to the azimuth central bearing.
- Complete the altitude cradle integration.
- Complete painting activities.
- Integration of azimuth cable wrap.
- Integration of altitude bearings.
- Complete cabling activities.
- Integration of azimuth bogies.
- Integration of azimuth control electronics.
- Functional test of the azimuth structure.
- Qualification of the azimuth axis.

Manpower - Up to 6 integration teams can work simultaneously.

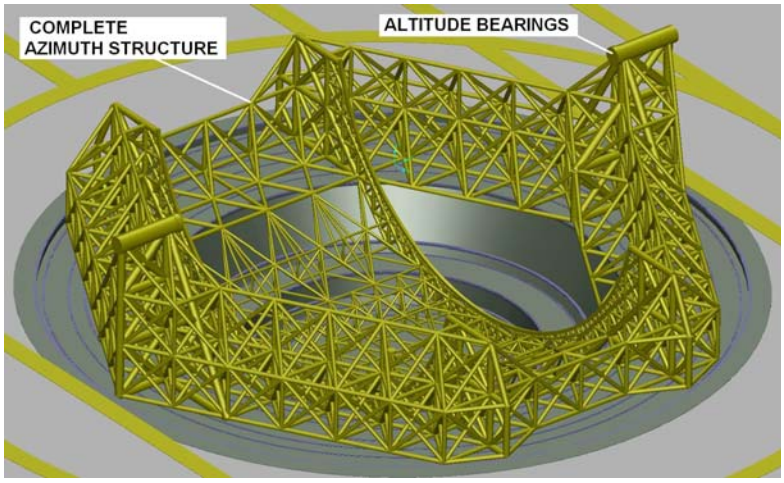

Figure 13-8: Azimuth structure complete integration

13.2.1.3.5 Phase 5

Integration steps - The fifth phase is divided in the following integration and alignment steps:

- Reposition the azimuth structure on base blocks
- Place base blocks on the altitude cradle. To be exchange in phase 7 by altitude bogies.
- Install a provisional supporting structure between the concrete foundation and the location where the altitude structure lower part ahs to be integrate.
- Integrate the truss structure up to the first floor (12.8 m above ground level). Tolerance ± 5 mm related to the azimuth central bearing.
- Start of painting activities.

Manpower - Up to 6 integration teams can work simultaneously.

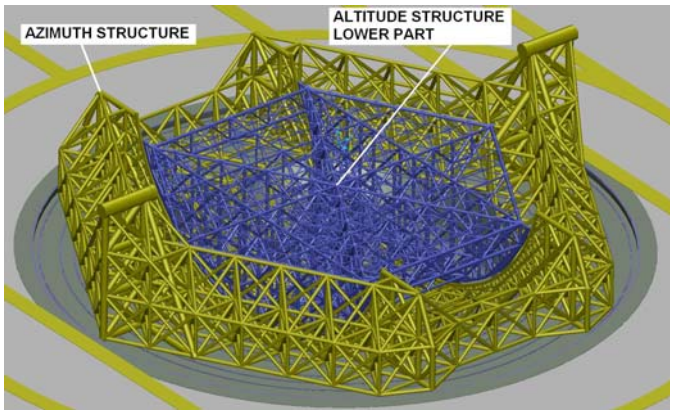

Figure 13-9: Altitude lower part integration.

13.2.1.3.6 Phase 6

Integration steps - The sixth phase is divided in the following integration and alignment steps:

- Integrate the truss structure up to the M1 cell (38.49 m above ground level).and the complete corrector and focal station central tower (102.64 m above ground level). Tolerance ± 5 mm related to the azimuth central bearing.
- Start altitude cradle track integration.
- Start of painting activities.

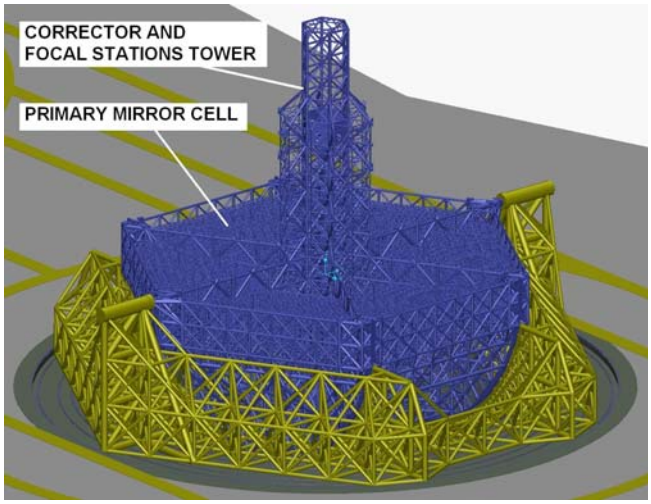

Figure 13-10: Altitude M1 cell and central tower integration.

Manpower - Up to 6 integration teams can work simultaneously. Only one integration team can work on the central tower

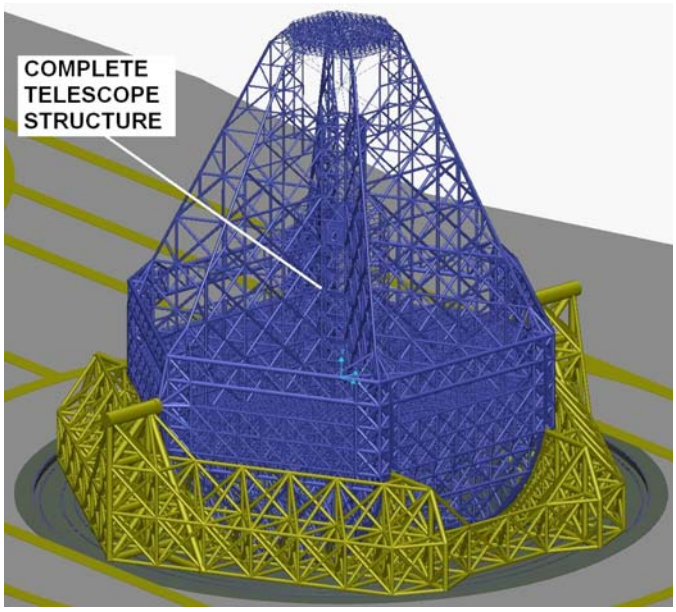

Figure 13-11: altitude structure complete integration.

13.2.1.3.7 Phase 7

Integration steps - The seventh phase is divided in the following integration and alignment steps:

- Complete integration of the altitude truss structure (128.3 m above ground level). Tolerance ± 5 mm related to the azimuth central bearing.
- Complete the altitude cradle track integration. Cylindricity and concentricity tolerance ± 2 mm related to the altitude central bearings
- Complete painting activities.
- Integration of altitude cable wraps.
- Complete integration of altitude bearings.
- Complete cabling activities.
- Integration of altitude bogies.
- Integration of optical unit dummies.
- Integration of altitude control electronics.
- Functional test of the altitude structure.
- Safety inspection. In particular dedicated to parts which may damage the telescope optics or personel.
- Qualification of both azimuth and altitude axes (Pointing and tracking)
- Functional tests of the mirror covers
- Qualification of the mirror covers
- Functional test of the segment handling facilites with segment dummies.
- Qualification of the segment handling facilities.
- Functional test of all the built-in access and lifting facilities.

Manpower - Up to 6 integration teams can work simultaneously.

13.2.1.4 Segment integration

After the kinematics test and verification. the integration of the segmented mirror can start.

Segment support structure

Each segment support structure (Figure 13-12) has to be aligned with its central axis converging toowards the M1 center of curvature. Then the 6 legs can be adjusted and interfaced to the mirror cell. The typical alignment tolerance is ± 2 mm (the reference being the nominal spherical shape of the primary mirror). This tolerance is rather generous because the segment position actuators (see 9.4.6.3) coarse range can compensate for large piston and tip-tilt misalignments.

Each segment support structure of the flat secondary mirror has to be aligned with its central axis parallel to the altitude structure main optical axis.

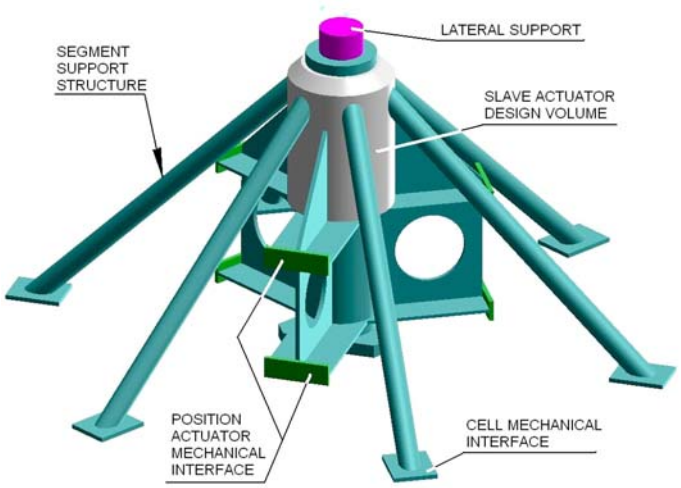

Figure 13-12: Segment Support Structure.

Hexagonal segments integration - To complete the segment integration (see Figure 13-13) the following preparatory steps will be performed:

- On the telescope primary and secondary mirror cell:
  - Integration of 3 Position Actuators per segment.
  - Integration of the slave actuator.
  - Integration of the central membrane attached to the slave section actuator.
- In the integration laboratory:
  - Integration of the Position sensors around the segment.
  - Integration of the waffle tree on the segment.

Primary mirror segments integration - The integration of the spherical segments on the primary mirror :

- Transport from the integration laboratory to the M1 maintenance cover (see section 15.1.1.4)
- Docking of the maintenance cover over one of the six primary mirror sectors.
- Automated handling of each segment to its segment support structure (see Figure 13-13 and Figure 13-16).

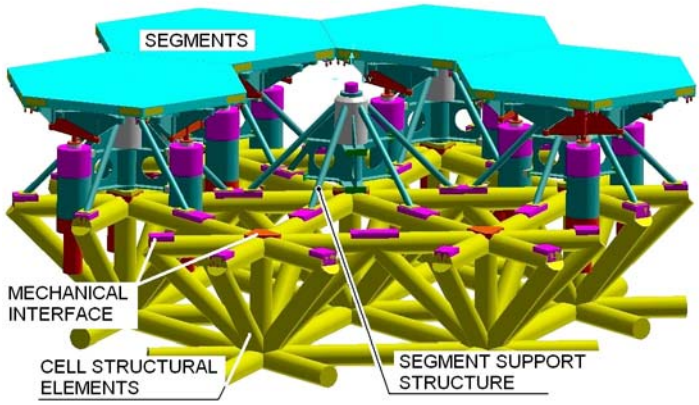

Figure 13-13: Segments integration.

Secondary mirror segments integration

The integration of the flat segments on the secondary mirror is made according to the following sequence:

- Transport from the integration laboratory to OWL horizontal parking configuration (see section 15.1.1.6).
- Docking of the maintenance facilities on the secondary mirror (see section 15.1.1.6).
- Automated handling of each segment to its segment support structure (see Figure 13-13 and Figure 13-16).

13.2.1.4.1 Segment handling tool

The integration of the segments into the primary and secondary mirrors will be realized with the help of a dedicated handling tool (Figure 13-14 and Figure 13-15) Its main characteristics are:

- 3 pairs of axial clamps. with clamp / unclamp kinematic function
- 3 radial constrains with on / off kinematic function
- 3 air bags for safety against handling tool failures.
- 6 sensors units. with 150 mm stroke and accuracy of ± 1mm.
- 36 sensors with stroke of 3 mm and accuraxy of ±1 µm

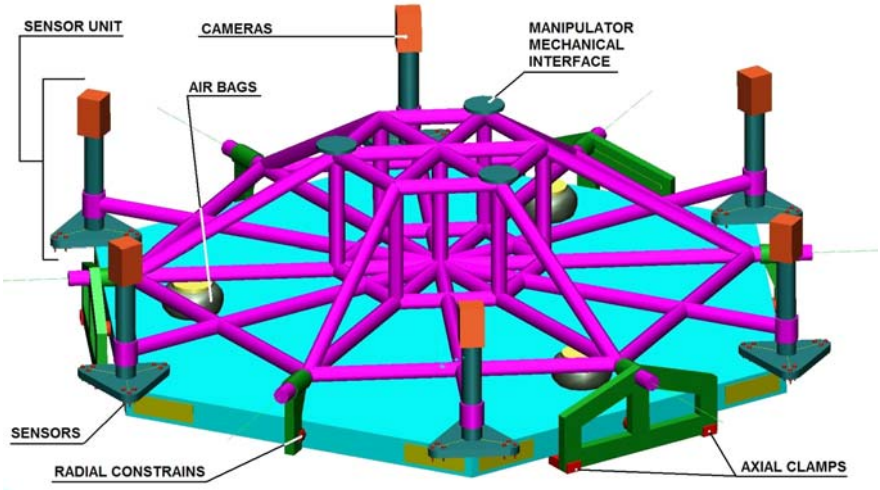

Figure 13-14: Segment handling tool. notional design.

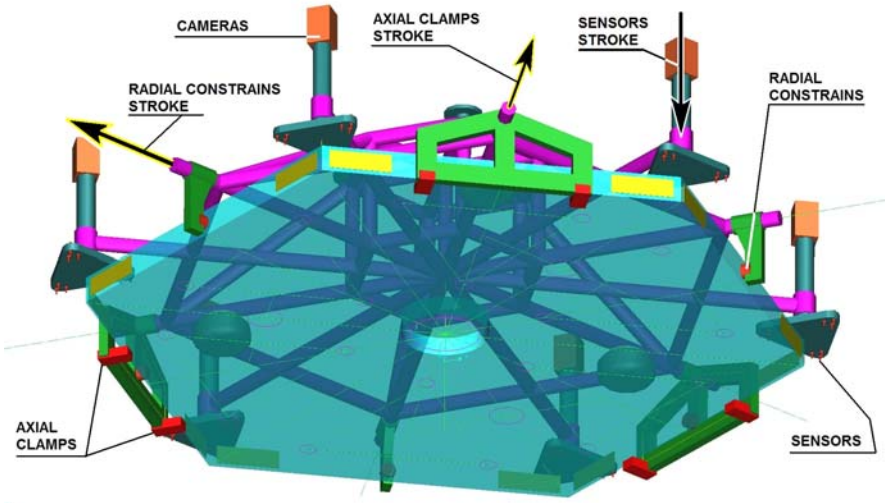

Figure 13-15: Segment handling tool. notional design

Segment docking operation.

An operator located in the M1 cover or in the secondary mirror handling facilities operates the handling tool which is attached to a manipulator integrated in the primary mirror cover (see section 15.1.1.4) or in the secondary mirror handling facilities (see section 15.1.1.6). The manipulator places the segment on the segment support assembly with the extractor in the open configuration. The segment optical surface is 150 mm above the mirror optical surface. The manipulator kinematic allows a fine translation of the segment in the 3 DoF and a fine rotation around the segment optical axis. The typical required position accuracy of the segment with respect to the segment support assembly is ± 0.5 mm. Cameras located on the sensors units help the operator to align the segment against fixed targets placed on the mirror cell.

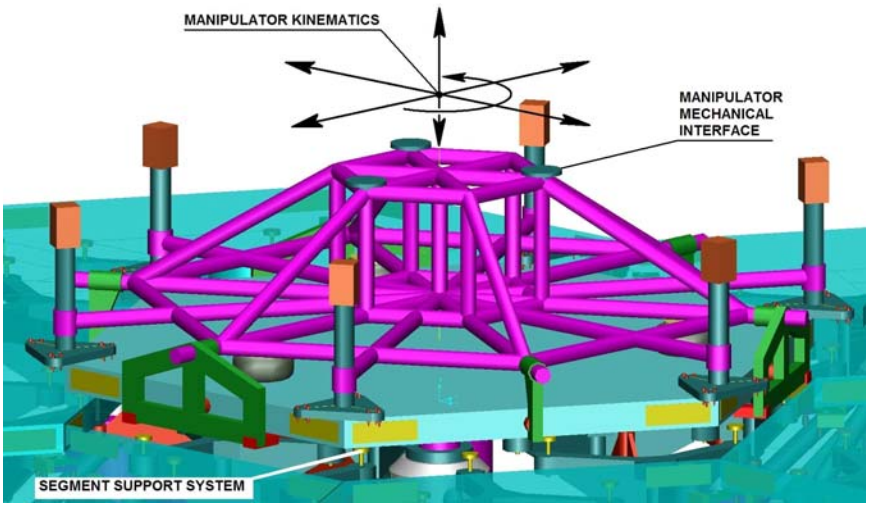

Figure 13-16: Handling of segment on the extractor.

Segment integration

An operator located in the mirror cell performs the following tasks

- Take the manual control of the handling tool.
- Connects the segment with the 3 position actuator units.
- Connects the segment to the lateral support and torsion bar.
- Connects the edge sensors.

- Sends the command to the handling tool for the unclamping operation (see also Figure 13-17 and Figure 13-18).
- Lowers the segment into the mirror using the extractor (stroke -150 mm).

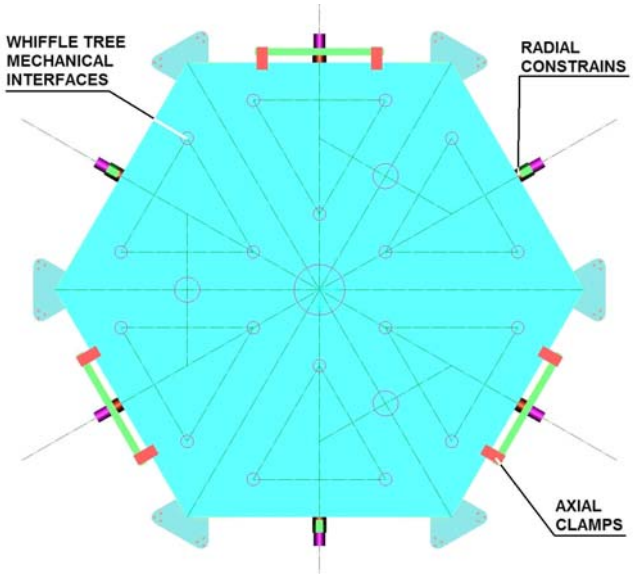

Figure 13-17: Clamped and constrained segment.

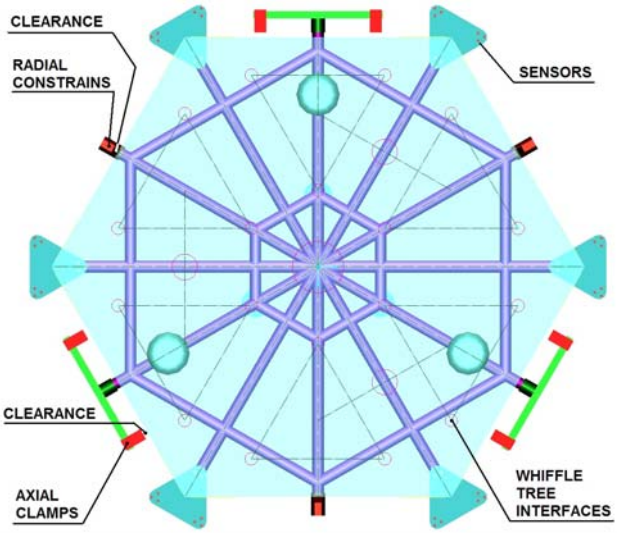

Figure 13-18: Un-clamped and un-constrained segment.

Segment pre phasing

Once the segment has reached its final location with a coarse accuracy of ± 1 mm. the following operation are performed:

- Lower the 6 sensor units until the sensors are in contact with the segment optical surface and the adjacent phased segments (see Figure 13-19)
- Fine pre-phasing of the segment within an accuracy of ± 0.01 mm (see Figure 13-20)
- Withdraw the sensor units.
- Return the handling tool control to the manipulator operator.
- Remove the handling tool using the manipulator.

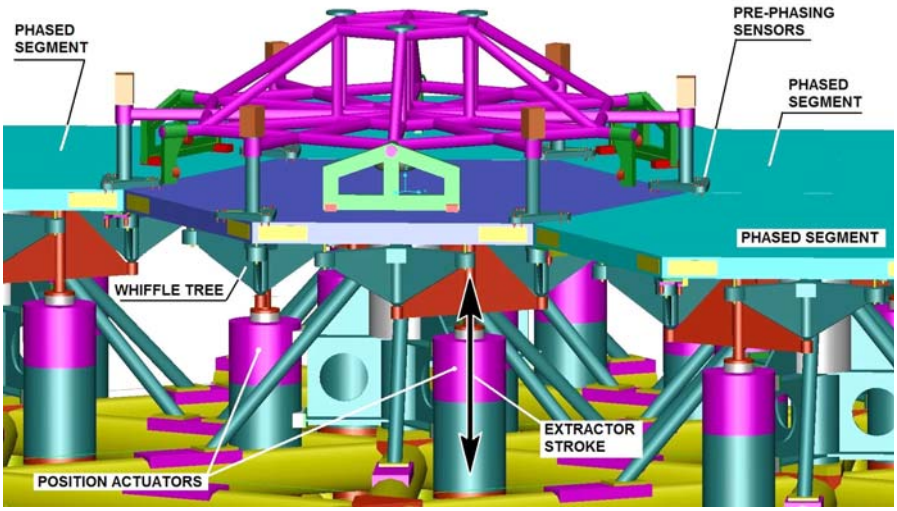

Figure 13-19: Segment coarse pre-phasing

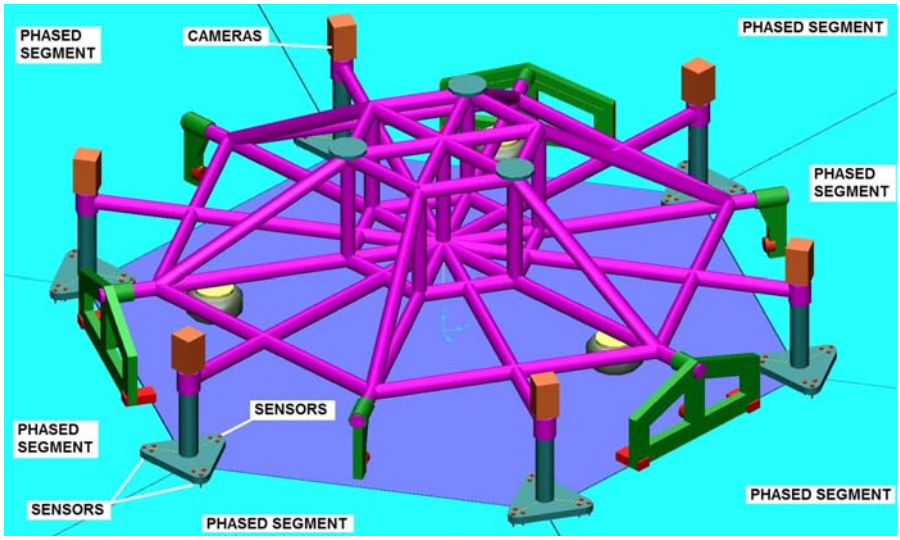

Figure 13-20: Segment fine pre-phasing

13.2.1.5 Optics

13.2.1.5.1 Initial alignment

This section describes the progressive integration of the segments and the corrector.

In a perfectly aligned telescope the optical axes of all mirrors are congruent with the mechanical axis of the adapter. Initially. at the end of the installation. the mirrors will be misaligned with respect to the axis of the adapter. the flexible meniscus mirrors will be deformed. and the segments will be misaligned both in piston and in tip/tilt. With the following steps the errors can be brought within the ranges of the control systems.

1. By autocollimation M6 would be aligned with the axis of the adapter. This would require an additional optical device at the center of M6.
2. The segmented mirrors would be aligned with the help of the edge sensors. These must be glued to the rims of the mirrors with an accuracy of approximately 200 micrometers with respect to the front surface of the segment. By moving individual segments and measuring when adjacent sensors go out of range. the differential displacements between the mirrors at the locations of each pair of sensors can be detected. From the data of all sensor pairs the optimum movement of all segments to minimize the rms of the differential

displacements can be calculated and applied. At the end of these procedure the rms. excluding the undetectable focus mode. should be of the order of 200 micrometers. The correction of defocus could be left to the stage of automatic corrections. In the case of the flat M2 it may also be feasible to measure it with a laser across the M2 surface.

3. The distance between the mirror surface and the support structures of M1 and M2 can then be measured by the fibre extensiometer.

4. All other mirrors could be aligned starting from M6 with the help of a fibre extensiometer. This requires fibre links between specified locations on all pairs of successive mirrors.
5. Finally. a second round of aligning the segments in tip-tilt could be done by stacking the images of individual segments or by using the Shack-Hartmann sensor.

At this stage one major error will be that low order aberrations in individual mirrors may compensate mutually but generate additional field aberrations. The other error will be caused by piston misalignments of the segmented mirrors.

From this point on the remaining errors can be calculated from simultaneous measurements by a few wavefront sensors distributed in the field and corrected by the actuators under all mirrors.

13.2.2 Safety

During the early erection. there are few difference with respect to erecting large scale structures. Once the telescope main axes are functional. more stringent safety rules shall be implemented. as done on Paranal:

1. Anybody entering a potentially dangerous area shall be directed to a specific corridor with safet station equipped with emergency push buttons and safety card reader at locking/emergency stations. That inhibits the telescope main axes rotation.
2. In addition the following surveillance and emergency devices are implemented:
   - Transceiver (GPS localizer).
   - Signal reflectors embedded in the clothes of the personnel. similar to those for avalanche rescue.
   - WEB camera. thermal cameras and infrared sensors.
   - Audio devices: Microphone. Loudspeakers.
   - Optical devices: Emergency and flash lights.

14.Site Characterisation

14.1 Introduction

Site characterisation is traditionally closely supervised by the institution in charge of the project with little or no input from the industry. Because each new astronomical development has particular site requirements. and because of the political and financial consequences of a site selection. inter-agency collaborations have been rather limited in the past. In the case of the ELTs however the picture has changed dramatically. mainly as a result of the apparition of new standards used in a decade of operational monitoring at the 8 meter class observatories. Site characterisation working groups have been setup to strengthen European (ELT-design study) as well as intercontinental (ESO-AURA) collaborations. Regular meeting take place (TMT workshops. IAU Site) which favour open-minded exchanges.

14.1.1 Instrumentation and methods

14.1.1.1 Cloudiness

Most institutions have developed all-sky cameras. in the visible or the infrared. with a 180 degree field of view which aim at visualising arriving clouds during telescope operation. Because of the poor optical quality of the fish-eye lens. there is currently no standard automated data processing which could be used for site characterisation. Both types of all-sky cameras (COBBER and ICECAM) were used by the Australian team in Antarctica Dome C and provided partial but valuable statistics before the first manned winter over was possible.

Statistics of photometric time on existing observatory still rely on the night reports written from visual inspections of the sky by the telescope operator. subject to post facto confirmation through analysis of calibration observations (photometric zero points). Most observatories follow a classical definition [44] of a photometric night. i.e. at least 6 night time hours in a row with sky clear down to 5 degree above horizon (night time is restricted to hours for which the sun has an attitude lower than 18 degrees below the horizon). On remote sites with some automated seeing monitoring. line of sight stellar photometry is used to estimate the amount of clear time.

On remote candidate sites without infrastructure. the analysis of satellite database described in 14.2.1.1. initially introduced by ESO [45] [46] [47]. is now used in a homogeneous way by most institutions [48] [49] [50]. The method is however limited by temporal under sampling (one image every 3 hour only) and variability of ground thermal footprints. Moreover. local perturbations like fog are not detected. Cross-calibration of the method with data from photometric surveys (2MASS) took place recently in the frame of the LSST site selection process [51]. It concluded that there is a maximum of 8% misses in Southern US. less than 2% in Northern Chile.

14.1.1.2 Precipitable Water Vapor

Specific PWV detectors have been developed in the 80's for the optical (IR sky monitor) and radio (Tipper) projects. The latter measures optical depth and conversion to PWV rely on an atmospheric model which limits the cross-calibration performance. Tippers are in use in Hawaii and South Pole and were a major tool in the selection of the ALMA site of Chajnantor.

Satellite measurements can be used to assess PWV and the method was successfully cross-calibrated [45] at Paranal with the IR sky monitor used during the VLT site survey. giving an rms error of 1mm H2O. On very dry sites like Chajnantor. the satellite method reaches critical limits. An attempt to compare to tipper data at Chajnantor [48] gave encouraging results but also raised questions which prompted a re-analysis of the tipper data. work is underway. On the other hand. satellite based PWV data produced regularly for La Silla are currently questioned by the Campanas team and a joint cross-calibration campaign is planned using spectroscopic observations as well as a newly developed IR sky monitor (IRMA) in operation at Cerro Pachon.

14.1.1.3 Aerosol Extinction

Normally measured from the ground using astronomical photometry (Geneva Observatory for La Silla. CAMC for La Palma). for instance the long term effects of major volcanic eruptions were accurately tracked from the ground. Large changes in atmospheric extinction can also be monitored from UV satellite observations. It was demonstrated for instance [52] that events of contamination of the Canarian and Moroccan sky by the Saharan dust could be extracted from the TOMS satellite records.

Other sources of sporadic extinction are the condensed trails (contrails) left by commercial jets along the main corridors over low populated areas normally chosen for their dark skies. Typically contrails can only form at temperatures below negative-76 degrees Fahrenheit and at humidity levels of 70 percent or more at high altitudes. Most contrails occur during the winter months and least during the summer [71]. Although nocturnal observations are not available. it appears that the contrails have a diurnal variation that peaks during mid morning over most areas. A significant correlation exists between mean contrail frequency and aircraft fuel usage above 7 km suggesting predictive potential. Projections for 2050 are available of the increase of the overall yearly traffic (see 14.2.1.3.2). but no distinction is made between day and night time. Such a distinction would be relevant for optical astronomy since in most common situations a jet contrail lasts no more than 30 minutes although it was observed that some of them linger for hours and actually become clouds.

14.1.1.4 Seeing

Most observatories are now equipped with the same kind of seeing monitor. based on the differential image motion method (DIMM) [61]. complemented by [62] and [63]. Because the method is rather robust. and provided no particular filtering of individual images was performed. the data obtained by thus monitors on various sites are comparable. The height above ground at which the measurements took place should be carefully analyzed because the depth of the ground thermal inversion layer is highly variable from site to site.

14.1.1.5 Turbulence Vertical Profiles

The complete profile of the turbulence along the optical path is only accessible by the SCIDAR technique which requires a telescope diameter larger than one meter is not applicable to remote sites. A portable version. the Single Star SCIDAR is currently under development at Nice University under FP6 ELT Design Study. Complete profiles are also obtained by balloon borne microthermal sensors. however drifting far away from the launching place in the course of their ascent. The balloon profiles present low statistical significance for site comparison but they are however extremely useful as input for the adaptive optics numerical modelling [68].

Turbulence in the surface layer (the first tens of meter above the ground) is best measured by microthermal sensors attached on a mast. following the technique mastered by Nice University [64] and in use everywhere. Attempts to use commercial and more robust sonic anemometers are underway.

Turbulence in the so-called ground layer (the first kilometre above the ground) is the most difficult to monitor accurately. Acoustic sounders (SODAR) used in various places did give interesting qualitative information but lack accuracy. More recently the SLODAR [58] [59] technique was introduced by Durham University and a currently unique portable version was developed for ESO Paranal monitoring (see 14.2.3.1) [60].

Turbulence above 1km is well monitored using the successful MASS instrument from Sternberg Institute Moscow [65]. the development of which was co-funded by ESO and CTIO. More than 10 such devices are now in operation around the world. one at ESO Paranal where the consistency of the MASS integral profile with DIMM records is excellent (see 14.2.3.2). The MASS was recently compared to SCIDAR during a few nights at Mauna Kea observatory [66] showing a good agreement in the higher layers but misplacement by MASS of the lower turbulence.

14.1.1.6 Turbulence Outer Scale

One single instrument is capable of measuring the outer scale of the turbulence. The GSM was developed by Nice University with ESO funding and the first data were obtained in 1997 at La Silla [67]. Since then. the GSM instrument has been visiting most large observatories and a consistent database is available.

14.1.1.7 Wave front coherence time

Only the balloons give an accurate value for the coherence time since they provide both wind and turbulence profiles [70]. however averaged during the 1 hour flight duration. There is no standard for permanent wave front temporal coherence monitoring but some methods are at reach. Computer intensive algorithms allow the SCIDAR to retrieve the velocity of the layers it has detected. The MASS is routinely estimating the global coherence time of the high altitude layers. The DIMM. associated to forecasts of wind velocity at the tropopause is providing a reasonable estimate of tau0 and theta0. the isoplanatic angle [69].

14.2 Parameters space

14.2.1 General astronomy

14.2.1.1 Cloudiness

Even nowadays. statistics of photometric nights at many observatories are compiled by trained telescope operators visually inspecting the sky anytime there is some doubt. Useful tools such as all-sky cameras are available but do not yet provide a reliable accounting of non-photometric events under the very demanding astronomical criteria.

The cloudiness is routinely monitored and forecasted at ESO La Silla and Paranal Observatory since 1999 using 3-hourly satellite imagery in the 10.7 and 6.7 micron. channels [46]. The general hit rate is considered as satisfactory; however there is each year several reports of misses when the clouds are either short lived or extremely thin.

It is of course tempting to derive photometric night statistics over any candidate site from satellite imagery using the same method as [49] in the frame of the TMT site survey. However caution is recommended when comparing sites in different climatic zones and with particular seasonal events (e.g. monsoon. Bolivian winter). Analysis of satellite data at 6.7µm and 10.7µm for Mt Hopkins has shown that the satellite-derived clear fraction for the site (56.6%) is similar to that determined for Kitt Peak (59.4%) in an earlier study using identical methodology [49]. As stated in a study for the LSST project [50]. the photometric fraction determined for Mt Hopkins by 2MASS (43.2%. adjusted) is significantly lower than the satellite clear fraction. Differences in methodology may account for about half of the observed difference. Using a time-based method

to determine the satellite clear fraction that is computationally similar to the method used to derive the 2MASS photometric fractions. the difference between the satellite and 2MASS clear/photometric fractions is reduced to about 8%.

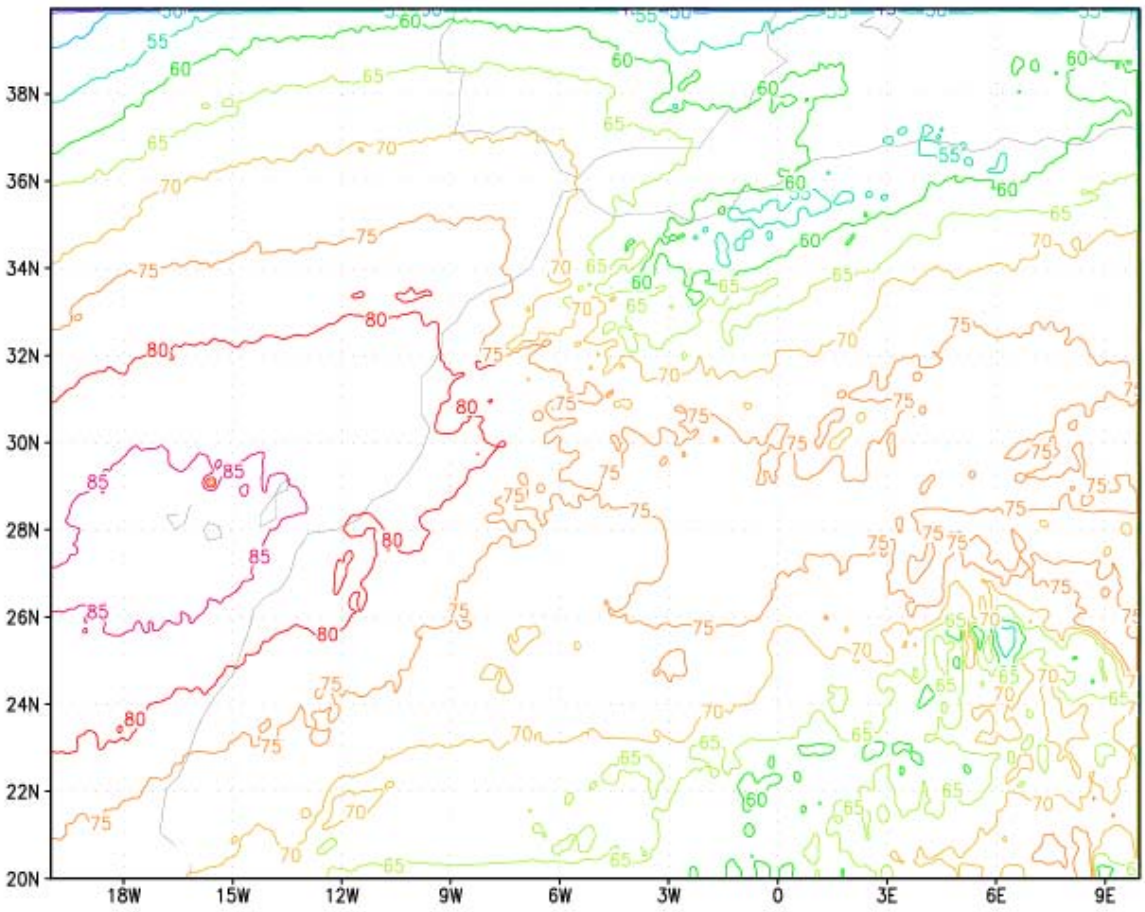

Figure 14-1: Fraction of time that skies are clear (%) at night for the years 1999 and 2000 over Canaries. NW Africa and Southern Spain (A. Erasmus. ESO Interim Report. Oct. 2004)

Nevertheless. the method can be used with confidence in relative terms. for optimizing the site selection within one area. In particular. the preliminary results of an ongoing 7-year survey have shown (Figure 14-1) the superiority of the Anti-Atlas summits over any others within the Moroccan territory. It is interesting to note on this diagram that. from the point of view of the general circulation. the Canary Islands appear as the best location over the whole studied area. Of course. the relatively low spatial resolution (10km) of the analysis does not allow taking into account local phenomena such as the Caldera effect.

14.2.1.2 Precipitable water vapour

Several studies [46]. [47] have shown that it was possible to accurately measure precipitable water vapour from satellite imagery in the 6.7 micron water vapour channel. A comparison of the results with ground based measurements at Paranal and Chajnantor (Table 14-1) have shown that the method could be accurate within 10% even in the driest sites. The PWV observing conditions are routinely monitored at Paranal since 1999 and forecasts are produced every three hours for the next 36h.

Site	Paranal		Chajnantor	
Sensor	Satellite	Site Monitor	Satellite	Site Monitor
Period	Day	Night	Day	24 hrs
10th percentile	1.83	1.70	0.30	0.26
1st Quartile	2.57	2.41	0.47	0.40
Median	4.05	3.66	0.72	0.77
3rd Quartile	7.27	5.21	1.26	2.16

Table 14-1: PWV (mm) statistics for Paranal (January - August 1998) and Chajnantor (January - September 1999) for satellite and ground based site monitor measurements of PWV.

The same method can be advantageously applied to site selection in areas which are not equipped with ground based monitoring. As an example a study by Erasmus [48] allowed to rank several candidate sites in NW Argentina. Northern Chile and Southern Bolivia (Figure 14-2).

No	Site	Latitude	Longitude	Size (kmxkm)	Altitude (m)	Max altitude
1	Chajnantor	-22.983	-67.629	10 x 10	5000	5639
2	Chalviri	-22.508	-67.716	10 x 7	5200	5780
3	Arg High	-25.065	-66.945	4 x 3	5100	5355
4	Arg Mid	-25.385	-66.746	8 x 5	4900	5163
5	Arg South	-26.540	-67. 887	10 x 6	4900	5308
6	Arg Low	-24.073	-67.434	> 10 x 10	4400	5665
7	Arg West	-25.171	-68.313	4 x 4	5200	5400

Table 14-2: Site locations and information

The 6.7µm (water vapor) and 10.7µm (IR window) satellite imagery used in this study are from the International Satellite Cloud Climatology Project (ISCCP) data set. Five years of satellite data covering the period July 1. 1993 to February 28. 1996 and June 1. 1997 to August 31. 1999 were purchased from the U.S. National Climatic Data Center (NCDC) by Cerro-Tololo Inter-American Observatory (CTIO) and University of Tokyo (UT). A data use agreement between these parties and ESO facilitates the use of these data for this study.

The results given in Figure 14-3 confirmed the superiority of Chajnantor. the ALMA site. over other candidates of similar altitude. Only one higher site in Southern Bolivia came out slightly better.

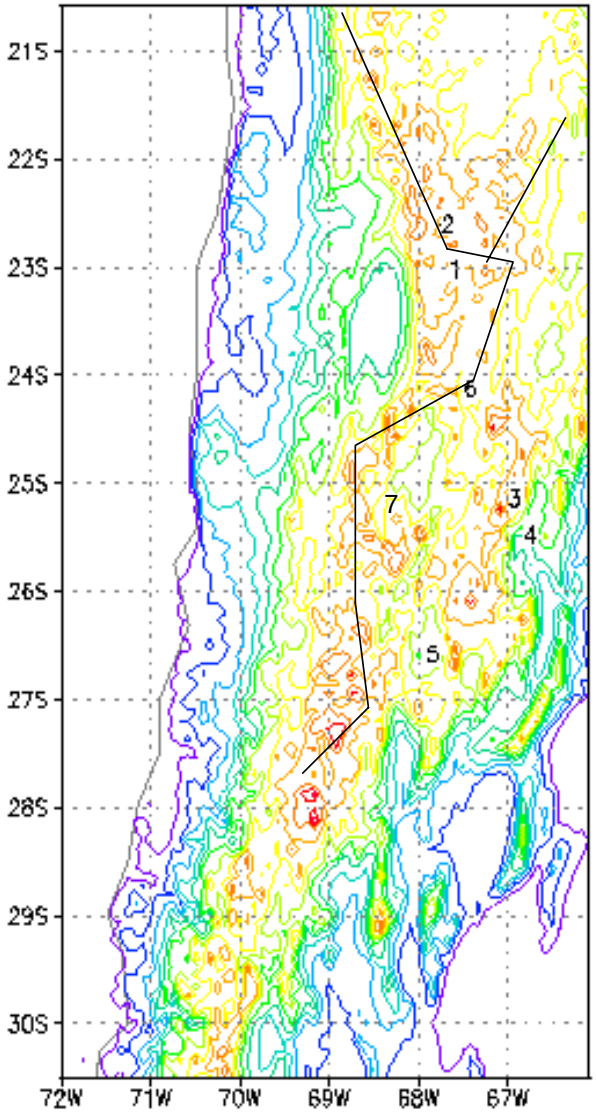

Figure 14-2: Locations of the sites in Chile. Bolivia and Argentina that were compared using satellite data. Contours show the topography at 500m intervals (see Table 14-2).

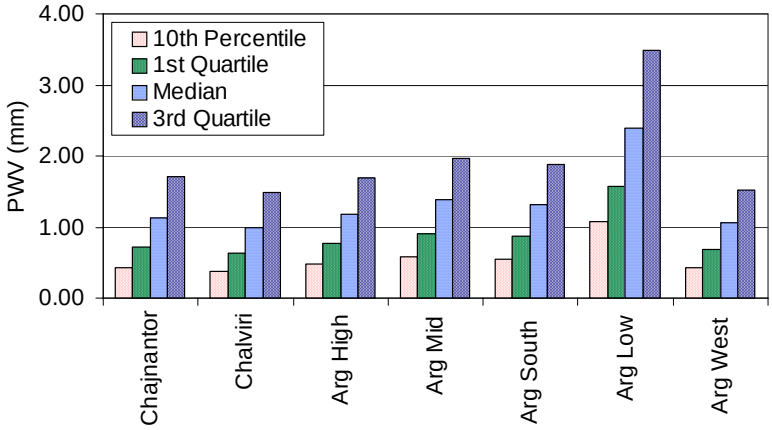

Figure 14-3: PWV percentile values at each site under clear conditions.

14.2.1.3 Aerosol Extinction

14.2.1.3.1 Saharan dust

Based on a comparison of extinction measurements made in the optical by CAMC at ORM Observatory (Figure 14-4). it has been demonstrated by Siher et al. that the events of contamination of the sky transparency by airborne aerosols could be detected from satellite observations in the UV.

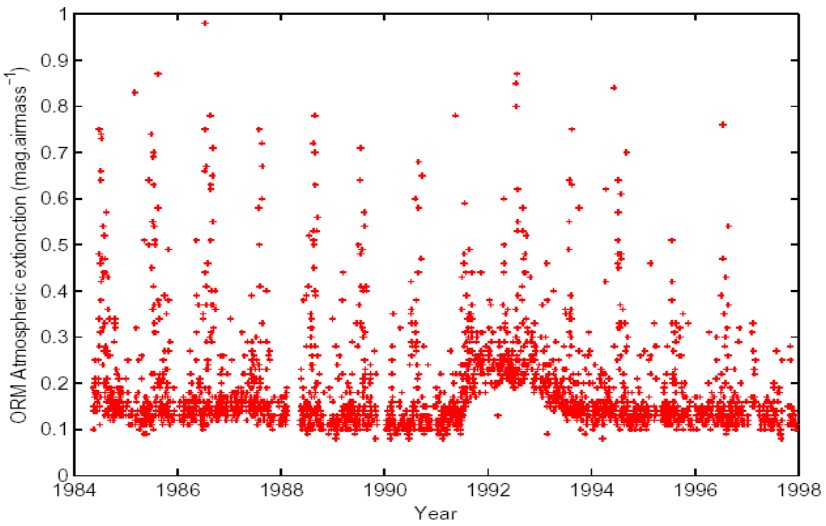

Figure 14-4: The Carlsberg Meridian Circle (CAMC) database at La Palma

As shown on Figure 14-5. the extinction coefficient at 680 nm divided by its sigma value presents a sharp slope change at K680=0.075 (K550~0.15). Siher et al. choose conservatively K550>0.2 for CAMC threshold of non photometric sky.

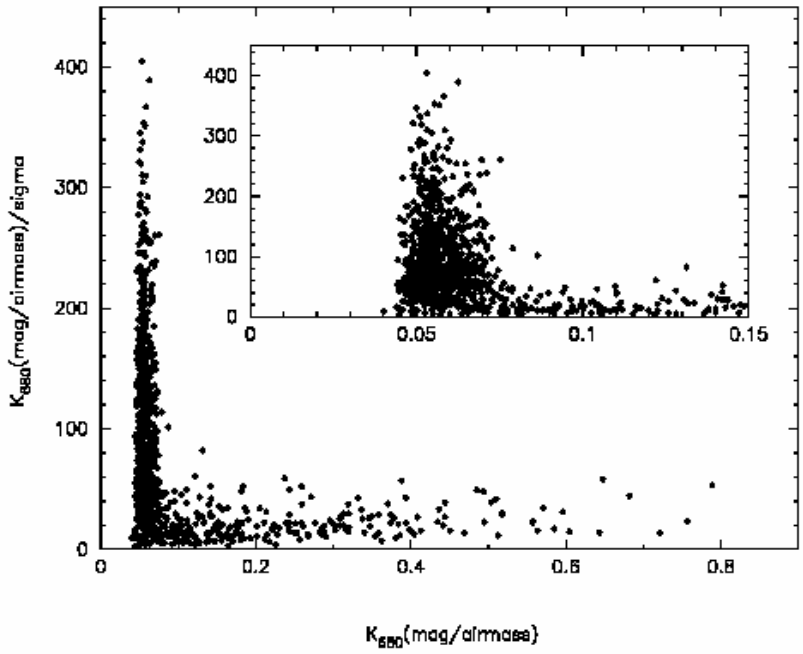

Figure 14-5: Diurnal Atmospheric Extinction over Teide Observatory (Tenerife. Canary Islands). Ref: A. Jimenez et al.. Fig.4

Using this threshold. it was shown that satellite data above a given optical depth were reasonably well correlated (Figure 14-6). Hence a UV satellite database was added to the FRIOWL site selection tool described in 14.3.3.2.

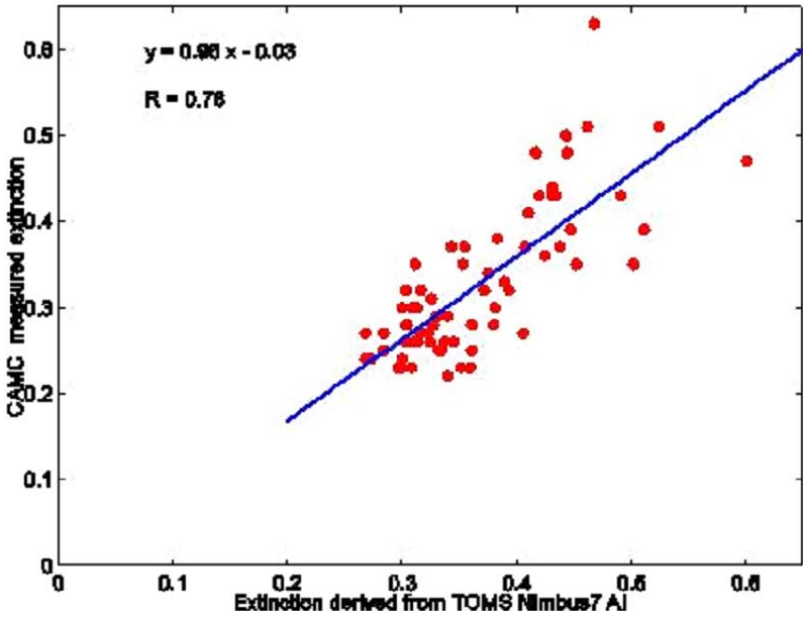

Figure 14-6: Correlation of satellite UV and ground based V monthly averaged measurements CAMC AE>0.20. NIMBUS7 AE>0.2. Pixel center < 55km from ORM

14.2.1.3.2 Contrails

The projections for OWL mid-life of the contrail coverage shown on Figure 14-7 are indeed very alarming for astronomy. mainly for daytime observations. Individual candidate sites should be examined carefully to assess the expected nocturnal contamination. Contrail formation from jet exhaust is much less probable at night and the traffic is mostly limited to inter-continental flights.

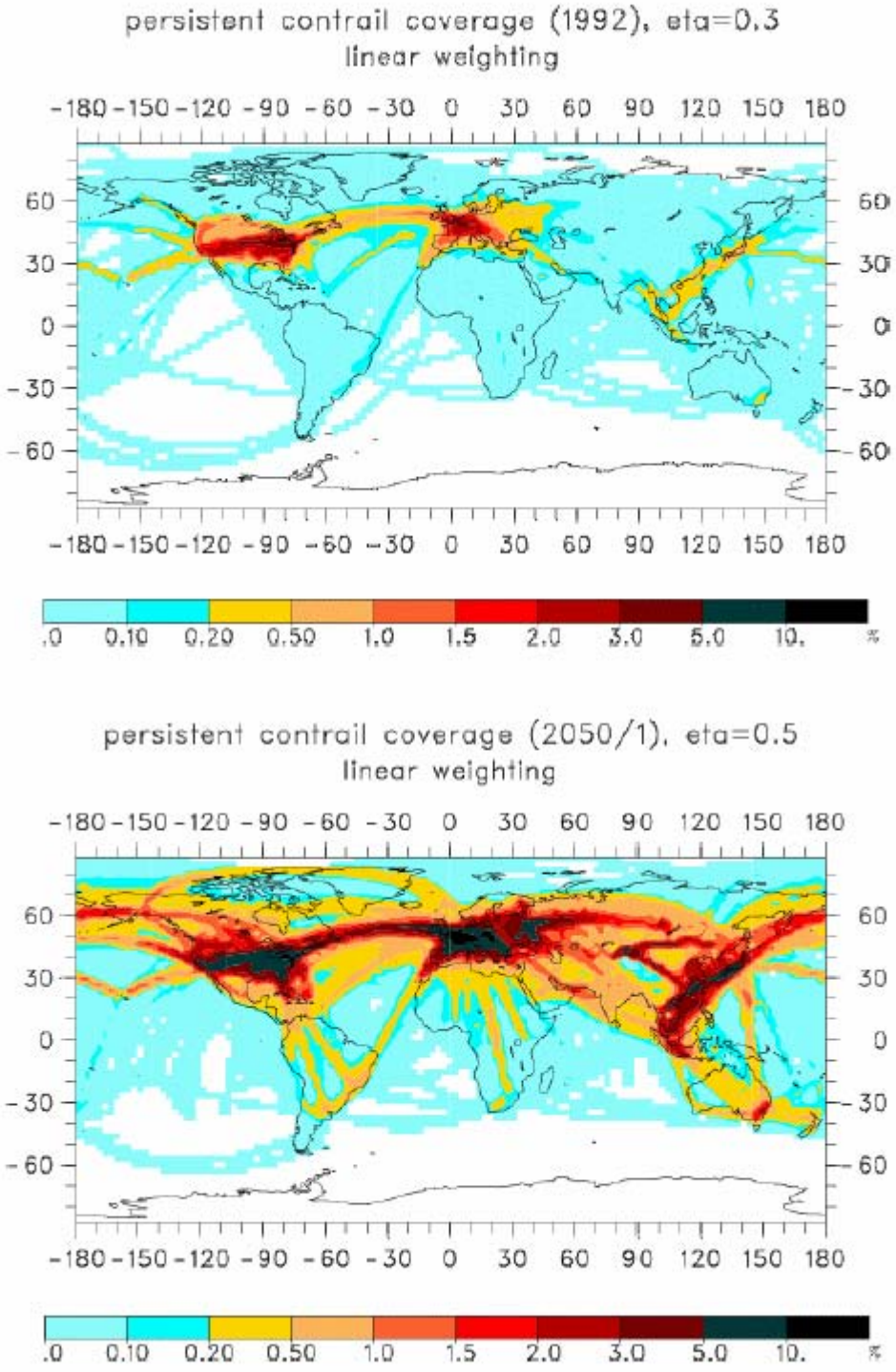

Figure 14-7: World map of jet aircraft contrails in 1992 (top). and predicted for 2050 (bottom). from [72]

14.2.1.4 Sky background

The sky background was not measured at Paranal during the VLT site survey. with the exception of the water lines used for the PWV monitoring. It was thus not part of the parameter space. with the assumption that no reason could be found that it would be worse than at La Silla. already considered as a very dark site. Accurate estimates of such a wavelength dependent parameter. which can only be obtained from analyzing science data. were made available one decade later. confirming the excellent quality of the site (Table 14-3 and Table 14-4).

Band	J	H	Ks	L	M-NB
Magnitude	16.5	14.4	13.0	3.9	1.2

Table 14-3: Typical IR Backgrounds at Paranal (mag/arcsec-2). from J. Cuby et al.. The Messenger 101. p.3. September 2000. Note that K. L and M values include telescope background.

Band	U	B	V	R	I
Magnitude	22.28	22.64	21.61	20.87	19.71

Table 14-4: Average background at Paranal (mag/arcsec-2). from >4000 FORS1 exposures during Apr.-Sep. 2001. by F. Patat. UBVRI Night Sky Brightness at ESO-Paranal during sunspot maximum. *The Messenger 115. March 2004.*

The light contamination of the visible sky background by public lighting is of course a concern for all major observatories sited at less than 100 km of urban areas. The efforts developed by ORM at La Palma as well as by CTIO in Chile have shown that it is possible. by proper legislation. to maintain the contamination at an acceptable level without impeding the economic development of the region. This has of course some limits (Palomar. Kitt-Peak) when mid-size cities turn into megalopolis. A clear projection of the expected economic development of each candidate over the expected lifetime of the observatory is thus required.

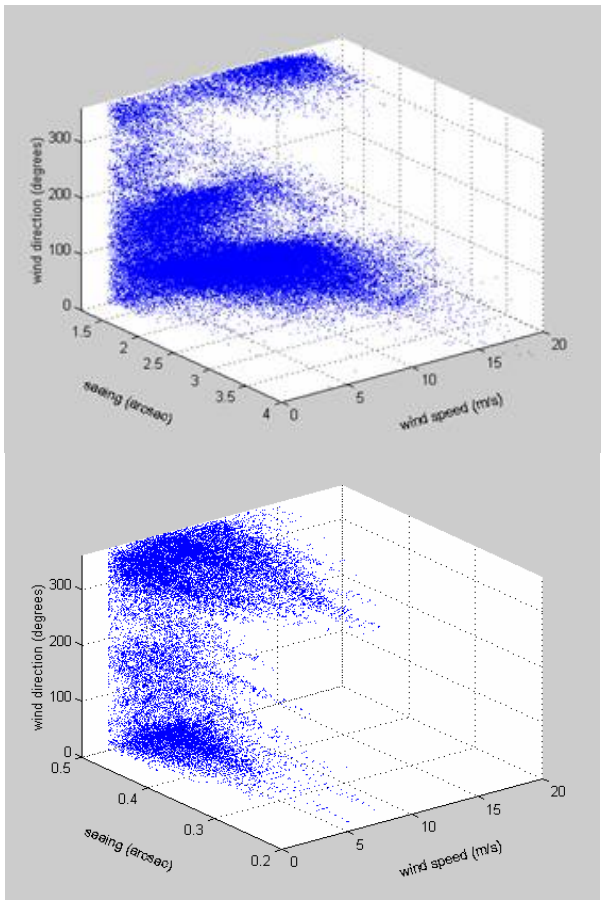

Figure 14-8: Seeing vs. local wind direction (0=North. 90=East etc.) and velocity at Paranal for best (right) and worst (left) observing conditions (2001-2004. over 778127 samples; J. Navarrete. ESO Observatory)

14.2.1.5 Seeing

The seeing is the result of the interaction of light with the numerous turbulence layers existing in the atmosphere above the site. Detailed vertical turbulence profiles described in 14.2.3 show that a large part of the turbulence is concentrated in the lower atmosphere. It is thus very useful.

as shown on Figure 14-8. to compare seeing records with local wind measurements to detect site related features which in turn shall be used to optimize telescope design and operation. It can be seen that the best seeing is obtained at Paranal for moderate wind (5m/s) coming from the North and North-West while the worst conditions are brought by strong winds (15m/s) from the North-East.

14.2.2 Telescope design & operation

14.2.2.1 Wind. temperature and humidity

Operation limits for an ELT are similar to those currently applied for the 8 to 10 meter class telescopes. However the emergency procedures are much slower to complete on extremely large structures. As an example. rolling the enclosure over the OWL telescope takes 30 minutes while a VLT Unit Telescope can be protected from rain or condensing clouds in a matter of a few minutes only. The consequence for OWL site survey is that the available clear time estimated for a given site cannot be a simple arithmetic addition of the periods when none of the meteorological parameters exceed the limits for observing conditions. The distribution in time of meteorological events shall be studied in detail and realistic strategy for emergency procedures shall be simulated.

14.2.2.2 Seismicity

Seismic hazard is basically the degree of earthquake shaking that one can expect in a given place during a given time. The map on Figure 14-9 is computed for solid rock and relatively fast shaking (0.2 second period). which strongly affects ordinary buildings.[68]

Different ground and different periods are important in determining the exact seismic *risk* for a particular structure. In the case of ELT's. and especially for the largest sizes. the structural design requires a substantial effort to cope with stresses caused by earthquakes. also because the order of magnitude of the eigen frequencies of the telescope structures falls into the region where the seismic response spectrum is the highest (2 to 6 Hz).

For this reason the seismic activity of a site. in terms of ground peak acceleration. is an important parameter which may decide whether an ELT can or cannot be built on that specific site. As shown in Table 14-4. these values make of Mauna Kea a site with a risk of seismic activity comparable to the one of Paranal. In particular a detailed study conducted for the Gemini project (Dames & Moore. 1994) concludes to a 10% exceedence probability in 50 years 20% higher at Mauna Kea than at Cerro Pachon. the Chilean site of Gemini South.

Site	Acceleration (g)
Mauna Kea	0.40
Paranal	0.34
La Silla	0.30
La Palma	0.06

Table 14-5: 50-years horizontal ground peak acceleration (g units) with 10% probability of exceedence.

[68] See also http://geology.about.com/library/weekly/aa010900a.htm.

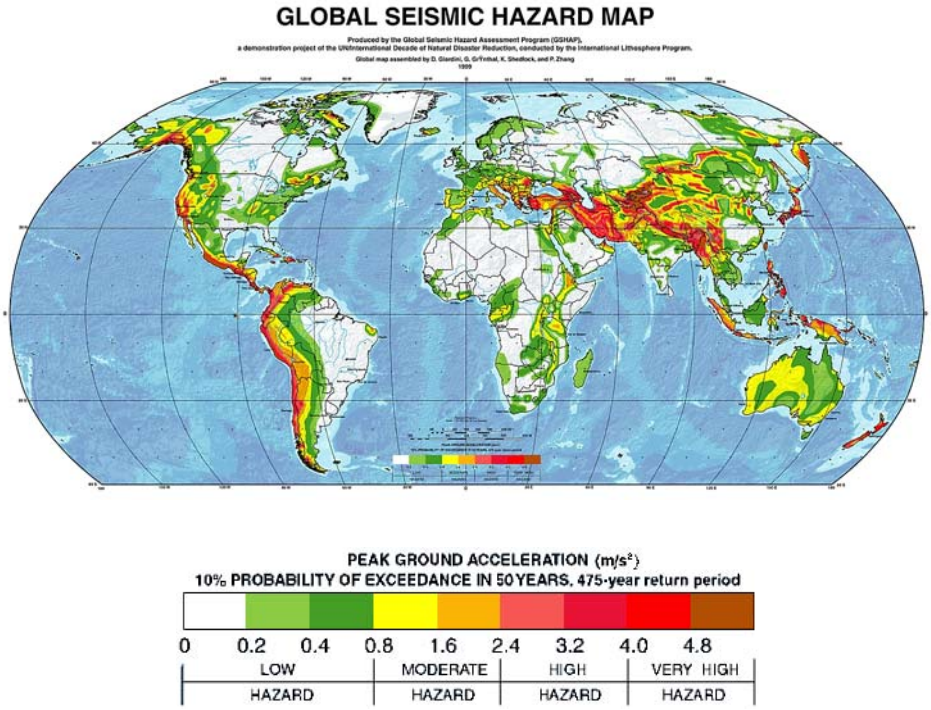

Figure 14-9: Peak ground acceleration (PGA) that a site can expect during the next 50 years with 10 percent probability GSHAP (Global Seismic Hazard Assessment Project)

14.2.2.3 Topology. soil characteristics

The extension of the site to accommodate the telescope platform of OWL is in the order of about .4 km^2 (about 34 football pitches). Foundations for the enclosure day and night parking positions and for the sliding system plus the foundations of the telescope will extend on a good part of the flattened area as shown in Figure 14-10.

The conceptual design has foundations which reach the maximum depth of about 30m from the level 0 of the flattened site. Moreover the design of the foundations has been carried out using site soil characteristics which assume compact ground and homogenous soil. therefore not including provisions for large consolidation works or large concrete works to build interconnected foundations. relying on the soil homogeneity.

The site survey shall start from the topology. Sites presenting large flat areas at the top of the mountain should be preferred for what concern civil work constraints. Quite extensive geotechnical tests shall be carried out on the site to gather the knowledge on its quality.

Following what was done for VLT the following tests should be performed:

- Density
- Unconfined compressive strength
- Point load strength
- Static elastic Young modulus
- Dynamic elastic Young modulus
- Shear modulus
- Poisson ratio
- Rock Quality Designation (RQD) via boreholes
- Status of soil fractures via sound propagation speed measurements.

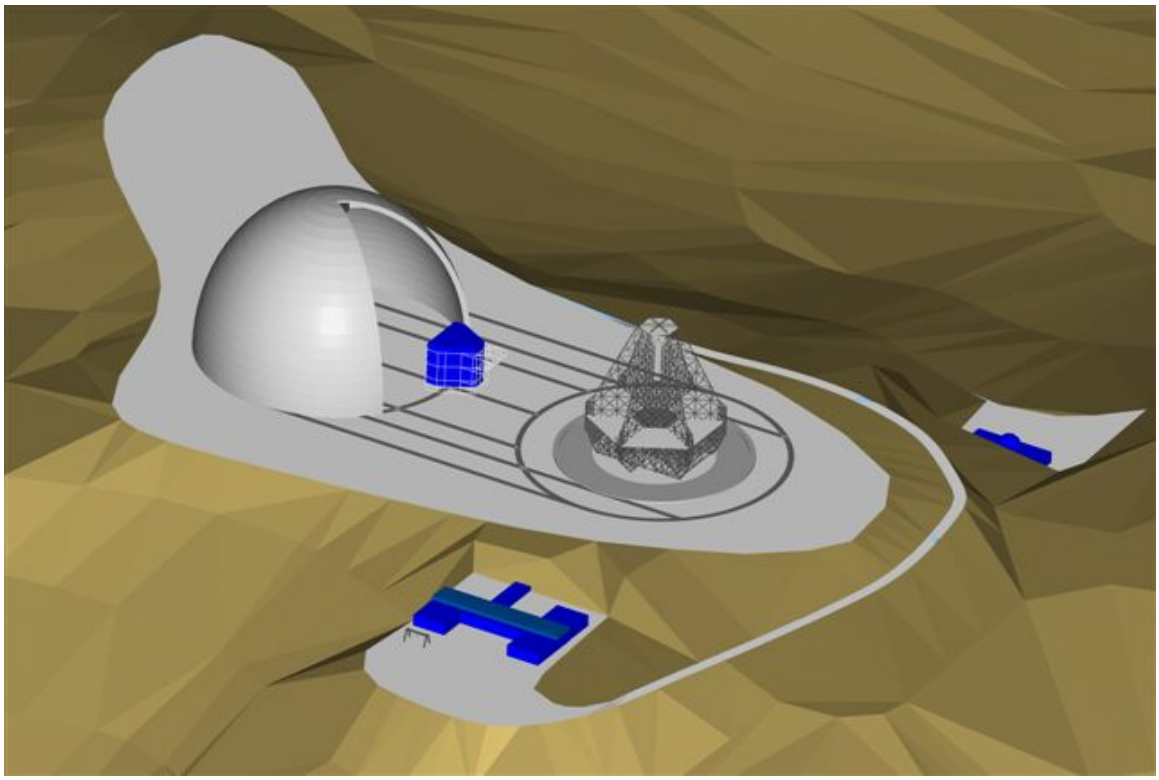

Figure 14-10: Site view

In Table 14-6 the characteristics measured for Paranal. also used to study the site of Paranal-North (Ventarones). and La Palma are summarised. Electrical resistivity of the soil should also be measured to assess the capability of a site to dissipate currents for equipment grounding purposes.

	Site I	**Site II**
Classification of soil according to EUROCODE 8 (defined by sound propagation speed (class A corresponds to waves speed propagation higher than 800 m/s)	A	A
Density [t/m^3]	2.7	2.6
Unconfined compressive strength [MPa]	98	20
Point load strength index (Is) [MPa]	9.8	2
Young modulus static [MPa]	10000	1100
Shear modulus static [MPa]	3800	430
Young modulus dynamic [MPa]	45000	5400
Shear modulus dynamic [MPa]	17500	2100
Poisson ratio	0.27	0.29

Table 14-6: Soil characteristics for Paranal area (Site 1) and La Palma (Site II)

14.2.2.4 Infrastructures

The dimension of the enclosure of OWL has some impact on the requirements that the site must have and on the equipment which must be installed to forecast meteorological events. The emergency shut down procedure takes 30 minutes until the telescope if fully protected. Moreover the enclosure can be moved with a wind speed as high as 27 m/s. These two characteristics imply the following:

- A meteorological station shall be in place which assures that the emergency shut down procedure starts at least half an hour before rain or other events start.
- Some modelling of the wind speed time gradient must implemented to start emergency shut down procedure at least half an hour before the wind exceeds 27 m/s.
- Possible need of further meteorological stations at different locations at several km from the site.

The other infrastructures of OWL do not present special demands on the site.

The distance from harbours qualified to handle large payloads. and to infrastructure like power network. drinkable water sources. industry for procuring supplies and services. should also come into the list of site requirements. although always subsidiary to astronomical parameters.

14.2.3 AO observations

14.2.3.1 Lower atmosphere turbulence and wind

A prototype portable seeing and turbulence monitor based on the SLODAR method was developed for ESO by R. Wilson from the AIG Durham[69]. The system comprises a Meade 40cm telescope equipped with an 8x8 element Shack-Hartmann WFS (5cm sub-apertures). The turbulence altitude profile is recovered from the time-averaged spatio-angular cross-correlation of the instantaneous wave front slopes. measured in the telescope pupil plane by using a Shack-Hartmann wave front sensor to observe a bright binary star. A vertical resolution of about 1.5km could be achieved for observations of narrow (5-7") binary stars (SLODAR-NB) and down to 150m when observing wide binaries (55-60"). Exposure times of the order 1-2 milliseconds are required in order to 'freeze' the seeing-induced motions of the WFS spots on 5cm apertures. placing strict requirements on the detector system. In order to achieve continuous monitoring. a limiting magnitude of V~7 for individual binary components is required to provide sufficient target stars. A detector with high QE. and read-out noise less than 1 electron rms is necessary. A camera based on the new E2V L3Vision CCD technology[70]. such as the Andor Technology iXon CCD cameras[71]. meet these requirements.

In Figure 14-11. the binary star projects 'copies' of the wave front aberration produced by the turbulent layer at altitude H onto the ground. with separation S. Hence there is a peak in the slope cross-correlation function for spatial offset S. H can be found by triangulation. given the binary star separation angle (theta). The strength of the layer is related to the amplitude of the cross-correlation signal (Figure 14-13). The full normalized profile is recovered from the cross-correlation via a de-convolution. where the autocorrelation of the wave front slopes for a single star of the binary is used as a measure of the (altitude-independent) impulse response of the system to a single turbulent layer. Although the cross-correlation is in two dimensions. we need only consider a cut through the function in the direction of the binary star separation. The total integrated turbulence. quantified by Fried's parameter r0. is found from the variances of the Zernike aberration terms for the centroid data (Figure 14-12).

[69] http://www.eso.org/astclim/paranal/asm/slodar/

[70] http://e2vtechnologies.com/introduction/prod_l3vision.htm

[71] http://www.andor-tech.com/

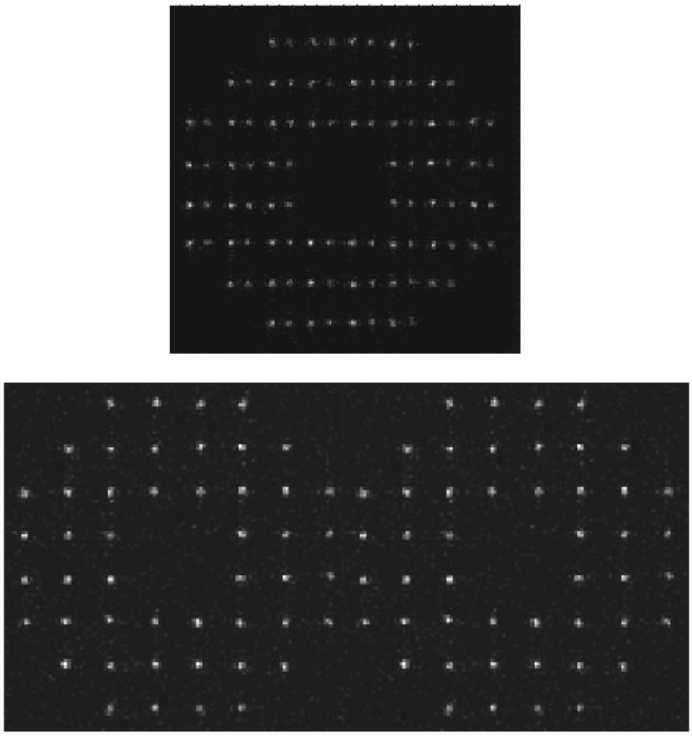

Figure 14-11: SLODAR Shack-Hartman pattern using narrow (left) and wide (right) binaries.

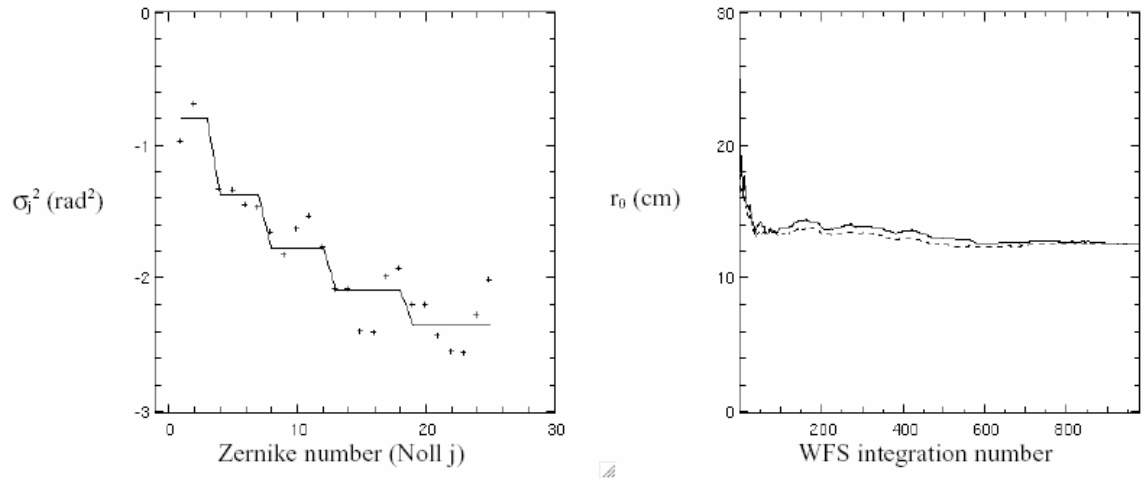

Figure 14-12: An example SLODAR determination of r0. Left: Measured Zernike coefficient variances. σj (crosses) and the theoretical (Noll) fit (solid line). Right: Calculated value of r0 versus WFS integration number (2ms CCD integrations at 190Hz)

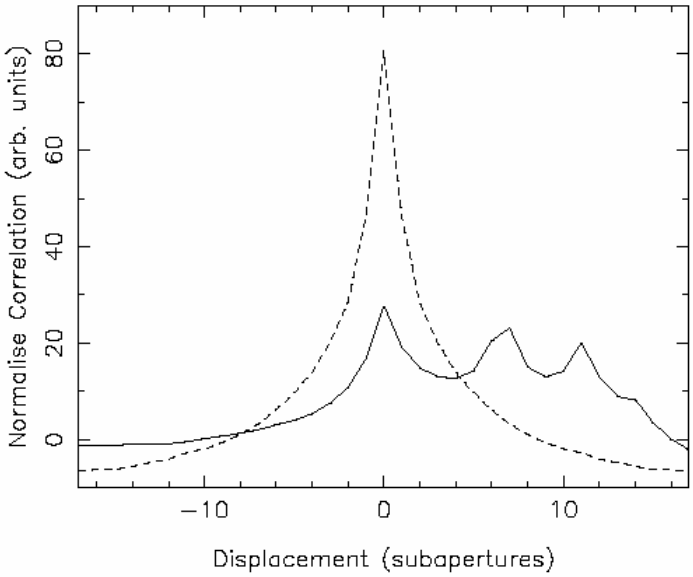

Figure 14-13 One-dimensional simulated cross-correlation (solid line) and autocorrelation (broken line) in the direction of the binary separation for a 24x24 sub-aperture.

Critical Data Analysis:

1. The altitude resolution of SLODAR depends on the separation of the selected binary and on the zenith angle. Thus for a given target. the altitudes of "layers" change with time. following the cos(z) law.
2. The SLODAR is at ground level. In case of very good seeing. the contribution of the first meters above ground is not negligible anymore compared to DIMM which is at 5m height. Note that the non-moving internal turbulence has been removed by temporal filtering.
3. The SLODAR has provisions to assess the wave front speed by temporal correlation of consecutive exposures. This function is however not yet implemented in the portable version.

14.2.3.2 Higher atmosphere turbulence and wind

MASS (Multi Aperture Scintillation Sensor) is a small instrument to measure vertical turbulence profile (http://www.ctio.noao.edu/~atokovin/profiler/). Unlike previous techniques. it is simple and inexpensive. destined to work continuously as a turbulence monitor at existing and new sites. MASS is based on a statistical analysis of stellar scintillations in four concentric ring apertures.

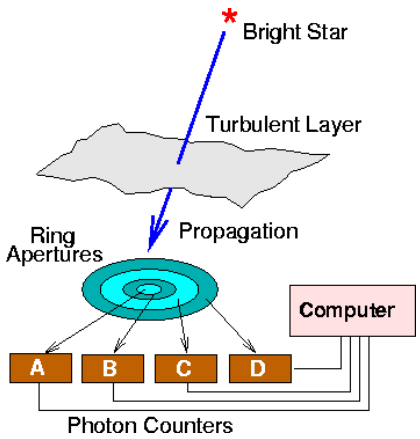

Figure 14-14: MASS principle. scintillation of a single star is measured through 4 concentric annular apertures.

This novel approach was proposed in 1998 and tested the same year at Mt. Maidanak in Uzbekistan (Kornilov. 2001). The first MASS instruments came into operation in 2002 at Cerro Tololo. It were built by a team at the Sternberg Astronomical institute (Moscow) led by Victor Kornilov under AURA and ESO contracts (Tokovinin. 2003). The control software provides on-line data reduction. so one can watch the turbulence evolution on a computer screen in real time.

The vertical resolution of MASS is low. only about 1/2 of altitude. The whole atmosphere is subdivided into 6 thick slabs (.5. 1. 2. and 4. 8 and 16 km) and the turbulence intensity in each layer is measured. Ground-layer turbulence does not produce any scintillation; it is not sensed by MASS. On the other hand. DIMM senses the whole atmosphere. Turbulence intensity in the ground layer can be found by combining MASS and DIMM data: the two instruments should always work together. For that purpose a combined MASS-DIMM pupil segmentator was developed where the same telescope feeds both instruments: two apertures are sent to the DIMM channel whereas four concentric apertures are cut to feed the MASS detectors.

Critical Data Analysis:

a) The integral characteristics of turbulence are measured by MASS quite reliably. However. the profile restoration is delicate; hence sometimes turbulence is attributed to wrong layers. The restoration errors are largest in the lowest (0.5km) layer. most important for GLAO.

b) MASS restoration is based on linear theory applicable to very weak scintillation. It was found that MASS systematically over-estimates the turbulence integral ("overshoots") when the scintillation index exceeds ~0.1. A first-order correction to overshoots. found by numerical simulations. is applied to the MASS data. However. in some cases (notably for fast turbulence) some residual over-shoots may remain. In this case the ground-layer turbulence estimated from DIMM minus MASS is under-estimated.

c) MASS is delivering estimates of the wave front coherence time based on the temporal spectrum of the scintillation. The comparison of MASS derived coherence time with estimates from combining DIMM seeing and 200 mb wind speed [69] show a very good agreement only during part of the time. A second regime exists when MASS and DIMM coherence time disagree. the nature of which is under investigation.

14.2.3.3 Full Atmospheric profiles

It is possible to combine contemporaneous SLODAR and MASS measurements to reconstruct the relative contribution of each of the layers sensed by the two instruments (Figure 14-15). Taking into account their respective thickness of integration. the complete atmospheric profile reduced to zenith can then be reconstructed (Figure 14-16) to be used as input for adaptive optics simulation purposes.

The deployment of MASS devices on all candidate sites is foreseen within the frame of the ELT-FP6 Design study (WP 12200). SLODAR. on the other hand exists as a unique transportable prototype.

An alternative system. also funded by the ELT-FP6 Design study is currently developed at Nice University: a Single Star SCIDAR (SSS) profiler which could make use of small size telescope down to 40cm. Compared to the classical SCIDAR which uses double stars and large (>1m) telescopes. the SSS would have the advantage of portability. at the cost of a lower altitude resolution. Moreover. the SSS would be able to monitor the velocity and direction of motion of all resolved turbulence layers.

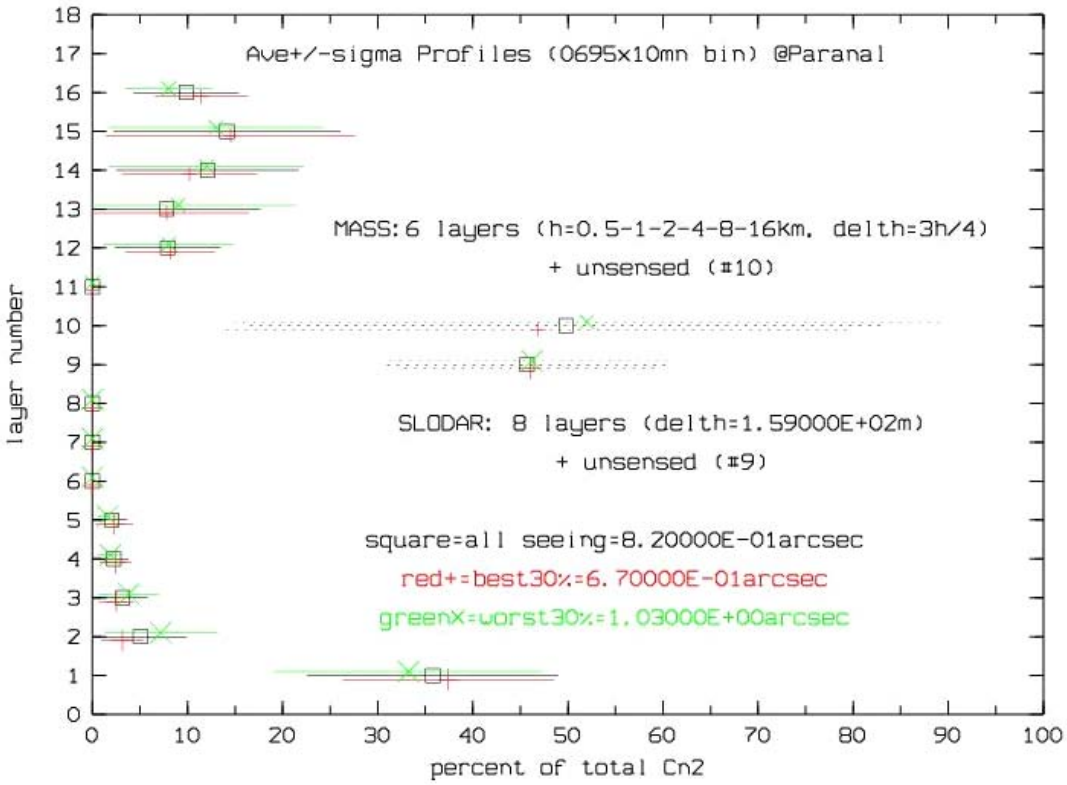

Figure 14-15: Relative contribution of the various atmospheric slabs to the integral of the turbulence obtained by combining SLODAR and MASS profiler data after reduction of the overlap area. The common database covers about 116 hours from February to August 2005.

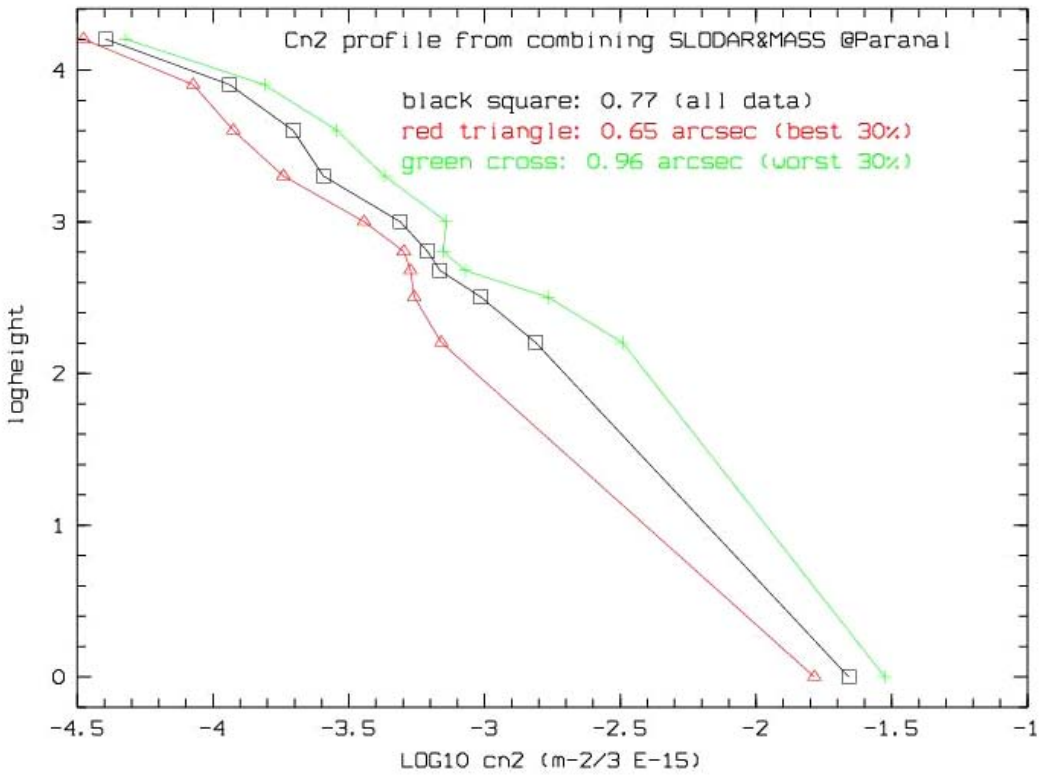

Figure 14-16: Complete atmospheric turbulence profile reconstructed from contemporaneous combined SLODAR and MASS measurements.

14.2.3.4 Sodium layer

The sodium layer considered here is situated in the mesosphere at 91.5±10 km and has a mean column density of $3x10^9 cm^{-2}$. This layer 'suffers' from seasonal. daily and short-term variations which are also strongly latitude dependent. The seasonal variations are 'sinusoidal' and affect the sodium column density. the average centroid position of the layer and its thickness. The sodium chemistry is known to be a sensitive function of temperature and the seasonal temperature variations appear to be largely responsible for the seasonal variations in the Na abundance which is maximal in winter (i.e. July-August in Chile). Measurements of sodium column density presently available for La Silla [114] show variations from 1 to $4.5x10^9$ cm^{-2}. Variations of the centroid position of the layer have a direct impact on the focus for laser guide star.

For Laser Guide Star Adaptive Optics. the short-term variations of the atmospheric sodium are the most worrisome. These variations can be classified in two types: the daily and 'hourly' ones.

Gravity waves are believed to be responsible for the daily modification of the Na layer. even though it is not yet clear how. These waves play an important role in the formation of sporadic Na layers (Nas). These are very thin (0.5 to 2 km thick) Na layers superposed to the mean mesospheric sodium layers. They are characterized by a rapid increase in sodium density over a narrow altitude range. They can last few seconds but in average few minutes up to few hours. The 'hourly' variations of the mesospheric sodium layer. mentioned above. are clearly dominated by these sporadic layers.

Sporadics have been detected more frequently at high and low latitude than mid-latitude sites. It has long been recognized that many Nas are associated with sporadic E layers. It has therefore been suggested that the apparition of these layers might be related to magnetic latitude more than to geographic latitude. Many groups have measured an enhancement of the sodium concentration during meteor showers. This can be understood since meteorite ablation is considered as the main source of mesospheric sodium.

Sporadics variations of the Na layers might be the most affecting effect for LGS AO. The coming LGS facilities at US and ESO observatories will clarify the relevancy of monitoring the sodium layer in the process of the site selection.

14.3 Site selection strategy

14.3.1 Identification of potential candidates

The site testing activity at ESO did not stop after choice of Paranal as the VLT site. In response to the tense situation about legal claims for land property. a one year site survey of an alternative site owned by the Max-Plank Institute was organized in Namibia in 1994-1995. The creation of Working Group on Alternative Sites was decided by Council during its April 19. 1995 meeting. with the task of proposing alternatives for the possible placement of one VLT telescope or the entire VLT/VLTI (ESO/Cou-549). It led to a detailed characterisation of Maidanak Observatory in Uzbekistan which ranks among the best for good seeing and low wind conditions [74]. This study was funded by the European INTAS program. The ESPAS (ESO Search for Potential Astronomical Sites) working group was revived after 2000. gathering specialists of climatology. turbulence modelling and atmospheric extinction. to prepare the site surveys for the next generation of optical telescopes. ESPAS gave a demonstration of what modern site characterization should be with a full assessment of Mauna Kea and a first climatological study of La Palma[72]. The emerging ELT projects in the U.S. also gave the opportunity of surveying the potential for the optical of Chajnantor [75]. where the ALMA project is currently being built. The TMT project currently conducts an ambitious site survey in Northern Chile. Mexico and Hawaii where automated stations have been deployed.

[72] http://www.eso.org/gen-fac/pubs/astclim/espas/espas_reports/

The long list of potential candidates for a European ELT was shortened in the frame of the ELT Design Study and the Site working group proposed to focus on the study of 4 sites shown on Figure 14-17 to Figure 14-20. keeping as a reference the recent results obtained at the newly operated Dome C Antarctic station.

Figure 14-17: Observatorio Roque de los Muchachos (ORM). La Palma. Canary Islands. Spain (http://www.otri.iac.es/sitesting/)

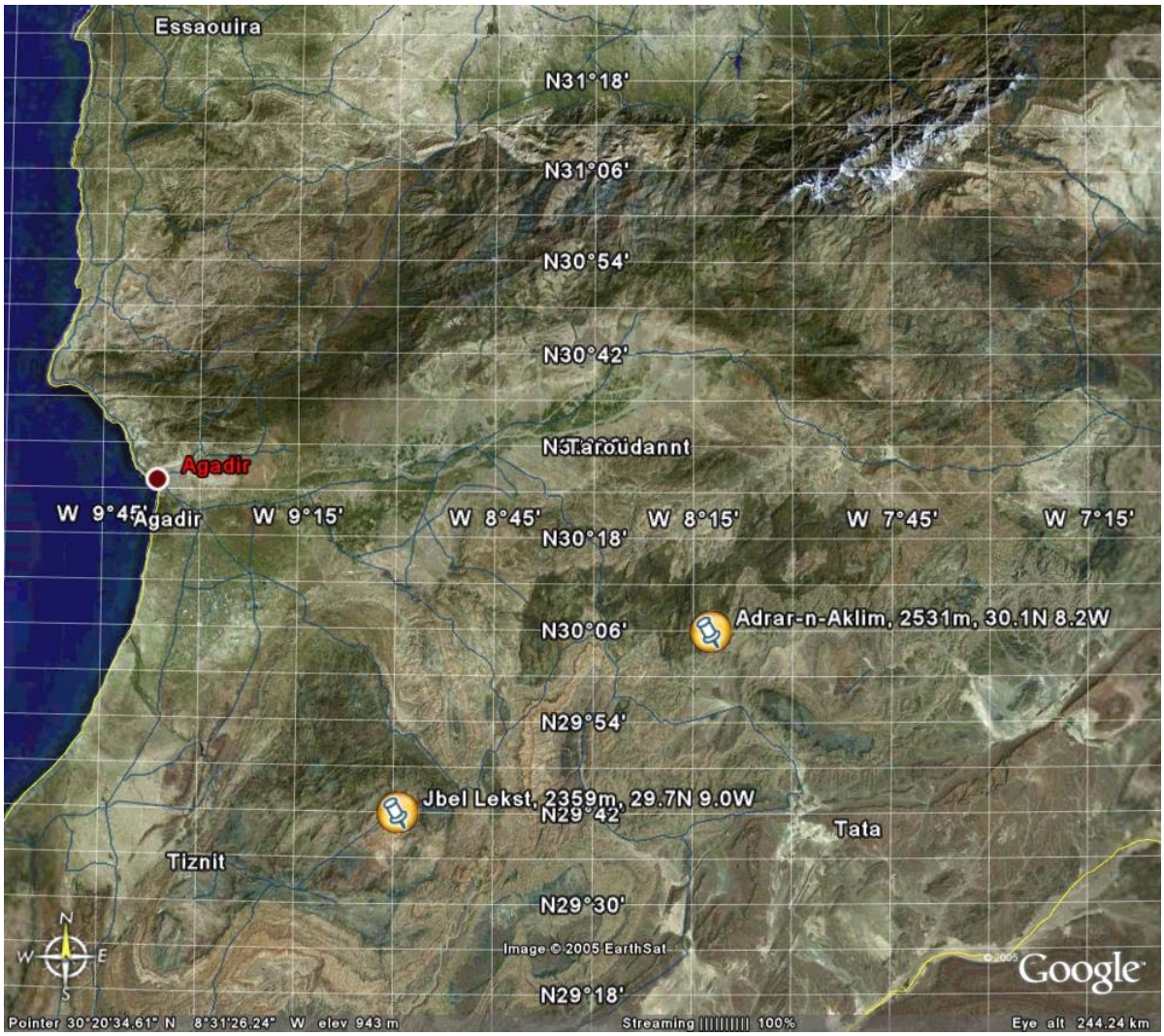

Figure 14-18: Morocco Anti-Atlas mountain area has the highest percentage of photometric nights along the North African continental west coast

Figure 14-19: Paranal North area proposes several candidate sites along what could become "the photon valley" of the 21st century

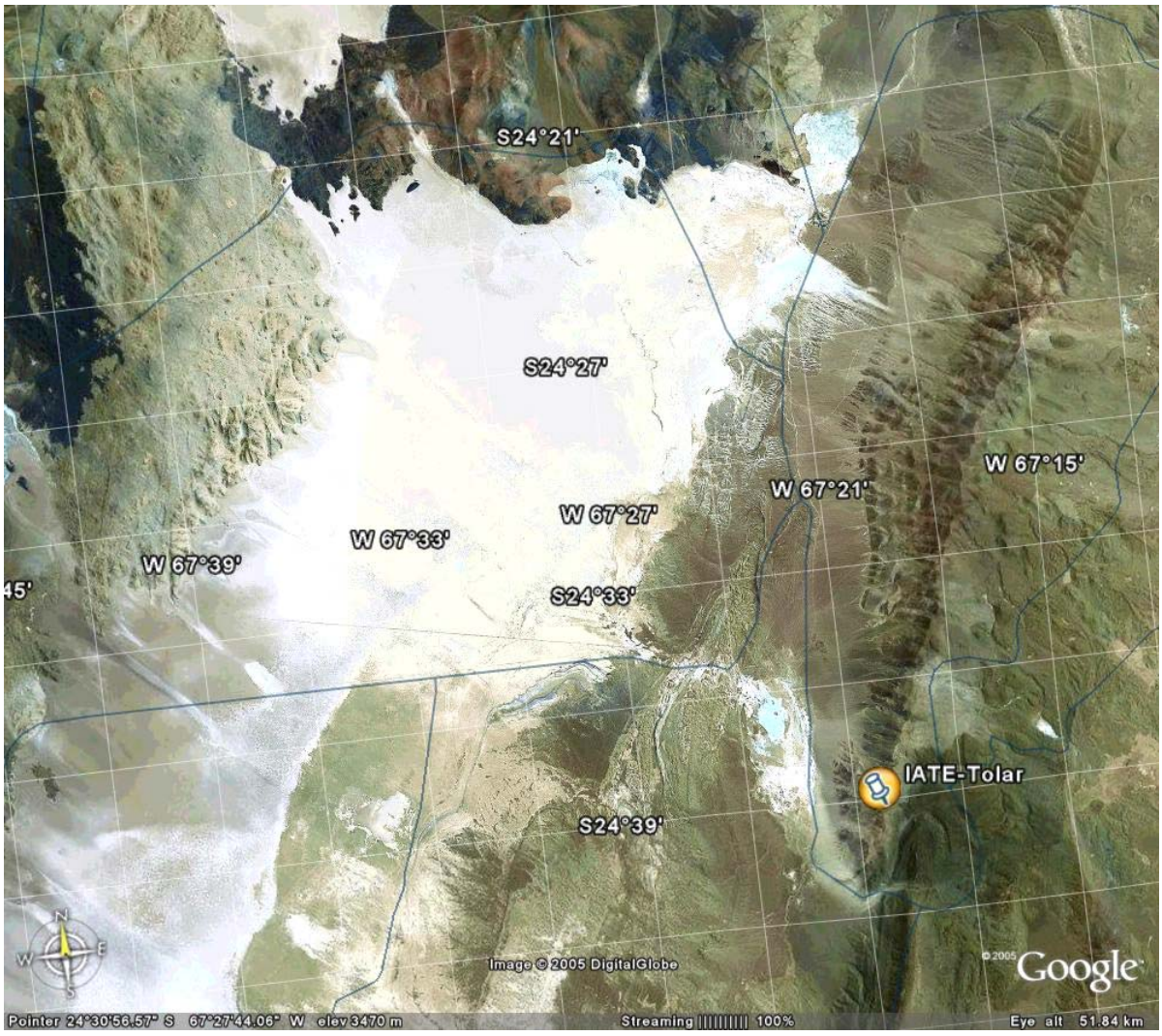

Figure 14-20: the Macon range. to the East of the huge Arizaro salt flat in NW Argentina allies high altitude (>4500m) and lower seismic activity (http://www.iate.oac.uncor.edu/tolar/)

14.3.2 Characterization of the parameter space

The OWL site characterization and the definition of figures of merit. as specified in section 2.9. should encompass. as a minimum. the following criteria (the ordering of the list below is not meant to reflect priorities):

1. Cloudiness;
2. Humidity. Precipitable Water Vapour;
3. Atmospheric Extinction;
4. Seeing or atmospheric coherence length;
5. Ground temperature. air temperature gradient and microthermal turbulence over the first 100 m;
6. Structure of the atmospheric turbulence. with a resolution not worse than +- 500 m in altitude up to ca. 20km;
7. Isoplanatic angle;
8. Turbulence coherence time;
9. Outer scale of the atmospheric turbulence;

10. Sodium layer density;
11. Wind speed and direction;
12. Precipitations (snow. rain. ice. fog);
13. Airborne aerosols. including dust chemical composition. particle size distribution and abrasive characteristics;
14. Site topology;
15. Soil properties. including typical stiffness.
16. Seismicity;
17. Survival loads (earthquakes. wind. precipitations);
18. Present and future potential light pollution; contrails;
19. Access to pre-existing infrastructures (roads. harbour. etc.); development costs;
20. To the foreseeable extent. long-term exposure to climate change;
21. To the foreseeable extent. potential long-term political stability.
22. Site-dependent operational costs.

14.3.3 Analysis of climate stability

14.3.3.1 The experience of ESO Observatory

It is not possible anymore. like it had been implicitly done during the VLT site survey. to consider any area of the world as climatically stable. The past climate. for sure was known to have been different [Grenon. 1990]. but on paleoclimatological scales much longer than a telescope lifetime. Indeed in the last decade. reports in the media. some of them very alarming. have shown that the equilibrium on which rests our current climate was very fragile. and also contained imbedded oscillations of various nature. Which of these oscillating meteorological parameters are relevant for the quality of astronomical observations? This is the object of an ongoing study using 20 years of cloudiness and seeing records at ESO Observatory (Figure 14-22 and Figure 14-23). aiming at finding links with well documented. although not yet predictable. events like such as El Nino Southern Oscillation Index (SOI) or the longer term Pacific Decadal Oscillation (PDO. Figure 14-21).

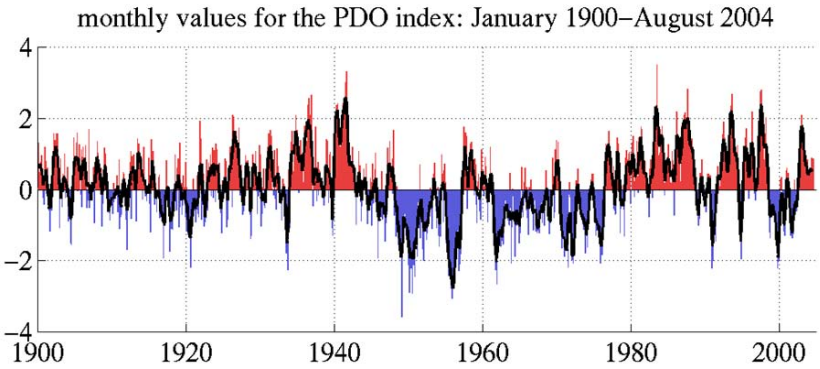

Figure 14-21: 20th century PDO "events" persisted for 20-to-30 years. while typical ENSO events persisted for 6 to 18 months

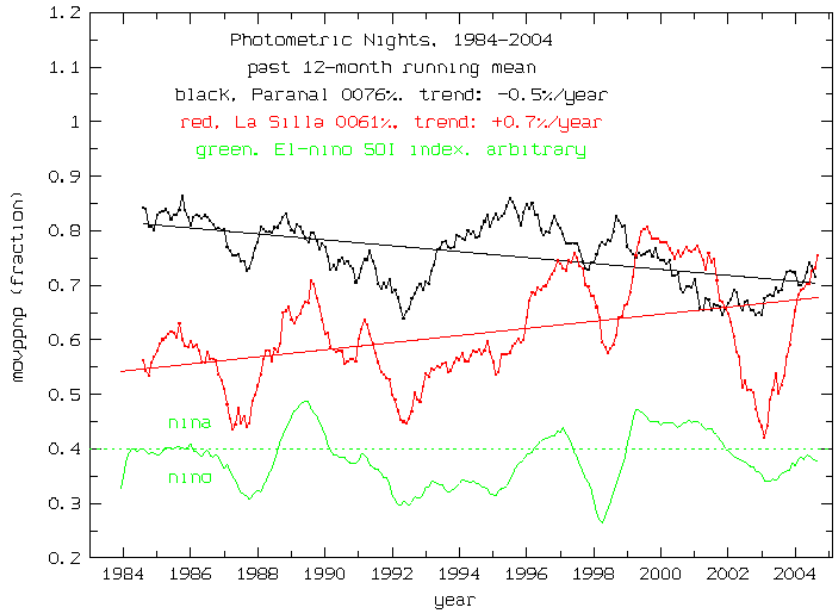

Figure 14-22: Monthly statistics of photometric nights at Paranal and La Silla and their relation to El-Nino Southern Oscillation Index

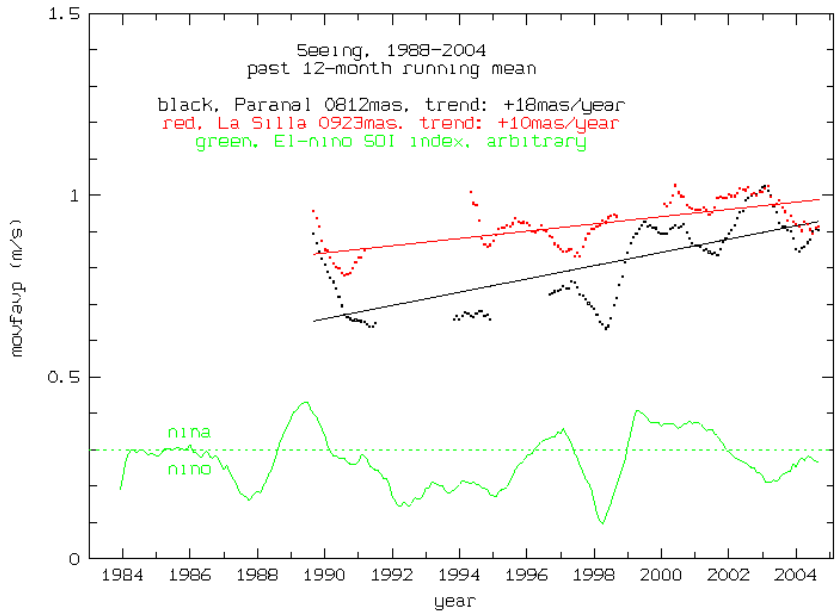

Figure 14-23: Monthly statistics of seeing at Paranal and La Silla and their relation to El-Nino Southern Oscillation Index

14.3.3.2 FRIOWL

For the most rigorous and best possible site selection process. a lengthy and detailed climatic database is needed. Added to this is the fact that global climate is changing and it will continue to do throughout the 21st century. An ideal site in today's climate may not prove ideal within 30 to 50 years. Therefore. future climate information (taken from the output of General Circulation Models) is also of great interest in the site selection process.

A composite database has been designed and built for the site selection task at the Department of Geosciences. University of Fribourg. The climatological database is mainly composed of ECMWF and NCEP-NCAR Reanalysis data at a global resolution of between 1° and 2.5°. Using

a Java computer language based interface. programmed in GIS fashion. all of this relevant information can be interrogated in order to find the best possible sites for the new telescope.

The historic climatological database is composed mainly of “Reanalysis” datasets from the European Centre for Medium Range Weather Forecasting (ECMWF) and the National Center for Environmental Protection / National Center for Atmospheric Research (NCEP-NCAR). A Reanalysis is a look backwards in time. re-creating the weather charts again for each time step in the past. but using the same climate model to do so.

600

Typically. both the ECMWF and NCEP-NCAR Reanalysis data have a global resolution of between 1° and 2.5° latitude / longitude. Although a resolution of 1° latitude still represents a distance of more than 100km on the ground. this is the best possible resolution available in current reanalysis projects. This resolution will probably increase with more advanced reanalysis projects in the future. Currently. the NCEP-NCAR Reanalysis project spans the period from 1948 to present (see http://www.cdc.noaa.gov/cdc/reanalysis/reanalysis.shtml for more information). The ECMWF Reanalysis project (ERA-15) spans a shorter period from 1979 to 1993 (http://www.ecmwf.int/research/era/ERA-15/index.html). although a new ERA-40 Reanalysis product is in the process of being made available from ECMWF. spanning the period from 1957 to 2001 (see http://www.ecmwf.int/research/era/). At a later stage of the OWL project. it is hoped to include the new improved ERA-40 dataset.

The full listing of meteorological and climatological parameters used in this study is given in Table 14-7 to Table 14-9. Of primary importance are variables such as cloud cover. atmospheric humidity. airflow direction and strength. aerosol content. and air temperature. Seismicity and topographic layers will be added to the database at a later time. Other secondary or computed variables (e.g. severe weather indices) may also be added.

File specification	Resolution	Period	File description
air2m.mon.mean.nc	T62 Gaussian grid (192 x 94 pts ~1.865°)	1948 – present	*Statistic:* air 2-metre temperature monthly mean. *Level:* 2m *Unit:* K
olr.mon.mean.nc	2.5°	1948 - present. but gap (1978)	*Statistic:* outgoing long wave radiation monthly mean. *Level:* other. *Unit:* not specified. probably W/m^2
pr_wtr.mon.mean.nc	2.5°	1948 - present	*Statistic:* monthly means of precipitable water vapour *Level:* integrated all levels as one. *Unit:* kg/m^2

Table 14-7: NCEP / NCAR Reanalysis datasets used

File specification	Resolution	Period	File description
Tcc	2.5° (144 by 73 grid points)	1979-1993	*Statistic*. total cloud cover [as a fraction between 0 and 1]. Fields of quantities accumulated over 24h periods centred on 12 UTC.
Surface	2.5° (144 by 73 grid points)	1979-1993	*Statistic:* U & V components of wind [m/s] at 10 metre level. Fields of quantities centred on 12 UTC.
850mb	2.5° (144 by 73 grid points)	1979-1993	*Statistic:* U & V components of wind [m/s] at 850mb level. Fields of quantities centred on 12 UTC.
200mb	2.5° (144 by 73 grid points)	1979-1993	*Statistic:* U & V components of Wind [m/s] at 200mb level. Fields of quantities centred on 12 UTC.

Table 14-8: ECMWF Reanalysis datasets used (ERA-15)

Air temperature (air2m) is provided by NCEP-NCAR as monthly means of 2-m air temperature from 1948 to present. Astronomical optics and engineering are sensitive to extremes of temperatures. so it may be necessary to include higher frequency air temperature datasets at a later stage of this project.

Outgoing Long wave Radiation (olr) is an indirect way of measuring cirrus clouds. which can be detrimental to astronomical viewing. Cirrus clouds strongly trap infra-red radiation. so negative anomalies of outgoing long wave radiation indicate a higher than normal presence of cirrus clouds. Large positive and negative anomalies of outgoing long wave radiation in the tropics are related to El Nino / La Nina weather patterns. which have been shown to affect astronomical viewing quality (*2*)

File name	Resolution	Period	File description
gmMMYY.n7a gmMMYY.epa	1.25° by 1.0° (288 by 180 grid points)	1978-1993 (Nimbus 7) 1996-1999 (Earth Probe)	Statistic: TOMS aerosol index as calculated from Nimbus-7 satellite (n7a) and Earth Probe (epa).

Table 14-9:TOMS Aerosol datasets used

Precipitable water vapour (pr_wtr) is provided as a monthly mean of integrated total column precipitable water vapour in kg/m^2 (which is equivalent to millimetres). It is the mean total amount of water that could be precipitated from the atmosphere. Values typically range from a few mm in cold regions to over 50mm in the tropics. An excellent site for OWL would be areas with a mean precipitable water content of less than 3mm throughout the year. In practice. such areas are only found in high altitude deserts or in the Antarctic.

Total cloud cover (tcc) information is provided by the ERA-15 dataset at a global resolution of 2.5° latitude / longitude. The data is calculated as the mean fraction of cloud cover (all levels) between 0 and 1. Cloud cover has obvious detrimental effects on astronomical viewing. blocking the incoming visible radiation. Preferential sites should have a cloud fraction of 0.1 or less.

Turbulence is a complex phenomenon. acting on many different scales. We will initially. however. investigate turbulence only at broad scales. such as that related to the jet stream winds. Therefore. daily wind direction and strength data has been obtained for the 200mb level from the ERA-15 period (1979-1993) at a grid resolution of 2.5°. Surface and 850mb level winds will also be included in the database in order to look at lower atmospheric effects.

Atmospheric aerosols also deteriorate astronomical viewing. as they can both absorb and scatter lights of different wavelengths. Therefore. Total Ozone Mapping Spectrometer (TOMS) aerosol data is been used in the OWL project database. The data is available from NASA[73] at a grid resolution of 1.25° by 1.0°. Due to the position of the TOMS satellite. however. data is only available for latitudes between 60° N and 60° S. It has been shown that TOMS aerosol index is related to aerosol optical depth and to atmospheric extinction.

A user-friendly web-based interface shown Figure 14-24 was designed at the University of Fribourg (Switzerland). It combines the ease-of-use of a GIS application. together with the climatological and geomorphologic database described above. There are several different operations that can be undertaken on the data and the maps displayed. Firstly. using the plus and minus buttons. the user can zoom into areas of interest on the chosen map. Secondly. he/she can choose different colour maps or palettes to display the maps. These colour maps are based on those provided by the software IDRISI Release 3.2 (*7*). Thirdly. he/she can choose an operation. These are simple mathematical operations performed on the selection of maps in your user-window. As of January 2004. the following operations are currently enabled on FRIOWL:

a) AVERAGE: the arithmetic average of all chosen user-maps is displayed

[73] see http://toms.gsfs.nasa.gov/aerosols/aerosols.html.

b) SUM: the arithmetic sum of all chosen user-maps is displayed

c) MAX: the maximum pixel value of all pixels of all chosen user-maps is displayed

d) MIN: the minimum pixel value of all pixels of all chosen user-maps is displayed

e) ANOMALY: this is a special feature; which displays the average of all certain selected maps. minus the average of all certain non-selected maps. In other words. it displays the mean of a set of maps. subtracted from the mean of another set of maps (i.e. the anomaly). You need to have a range of maps selected in the “Selected Files” window in order for this option to work.

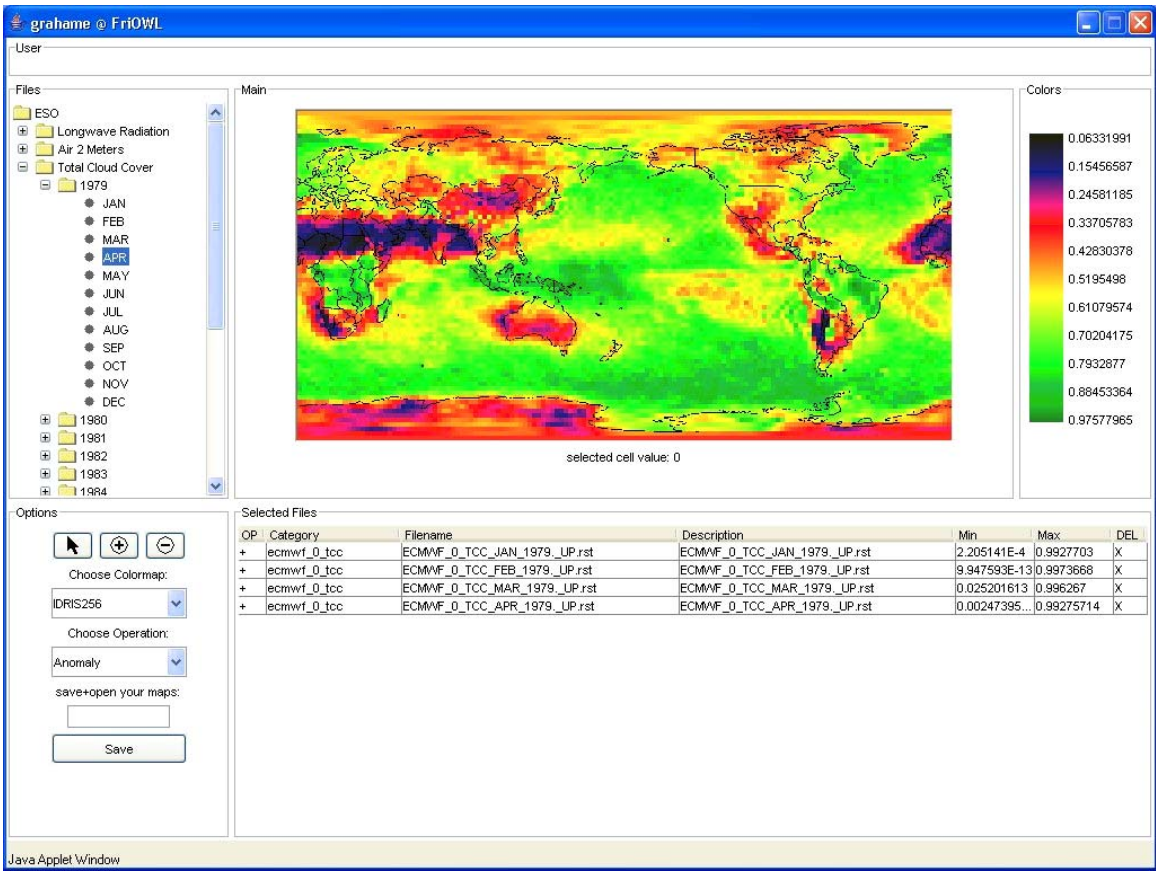

Figure 14-24: The FRIOWL user interface

14.4 Site preservation and monitoring

14.4.1 Local Seeing control

The measures taken at the VLT seem adequate for preserving the observing conditions inside and outside the enclosures. However an accurate estimate of the local contributions to the total image quality is very difficult to obtain. as discussed in the next section. In the case of OWL. the local thermal environment of the telescope shall receive a particular attention because the primary mirror lower edge can be close or even below ground when observing away from zenith. Obviously the local seeing conditions between the lower and the upper edge of M1 cannot be made equal but the differential seeing should be reduced as much as possible by a proper control of the ground temperature in the vicinity of the telescope.

It is important to develop a new generation of compact. cheap and easy to use seeing monitoring devices so as to adequately map the telescope 'observing volume' during operation (see next section). Maybe it will be considered interesting in this respect to attach a few such self-pointing devices on key locations like the rim of M1. or/and in the shadow of M2.

14.4.2 Astronomical Site Monitoring Station

Monitoring the astronomical observing conditions during the operation of the observatory has proven useful for increasing the observing efficiency in real time as well as for tracking long term changes. A typical monitoring station includes a meteorological station. seismic recorder. all sky monitor and seeing monitor. To these can be added if required single or double stars turbulence profilers.

It is important however to verify that the monitoring device. which has to be small and automated. is indeed picturing the actual environment of the ELT. A particular example is given by the seeing measurements using the DIMM (Differential Image Motion Monitor) at the VLT observatory. The seeing measured by the DIMM at 6 meter height above ground located at the northern edge of the VLT telescope area is used to characterise the expected image quality at the focus of the 8m unit telescopes as well as of the 1.8m auxiliary telescopes. A comparison with measurements obtained from the image quality at the focus of the active optics Shack-Hartmann lenslet array with 40cm diameter subapertures shows (Figure 14-25) that the distribution of both data sets is clearly different on the high range limit. The UTs. at seen from the active optics wave front sensor after correction for atmospheric dispersion. seem less sensitive to bad seeing than the DIMM would let believe. The comparison of two UTs on Figure 14-26 using a limited data set shows a good agreement in this respect although with a dispersion of 0.2 arcsec standard deviation. Thus one can deduce an improvement of the median seeing of the site. as seen by 10m class telescopes and larger. of about 0.15 arcsec in the visible. The reasons for the observed discrepancies are currently under study. One very satisfactory result is that UTs and DIMM agree very well in good seeing conditions. thus confirming that local conditions on the 8m mirror and inside the dome are very well controlled.

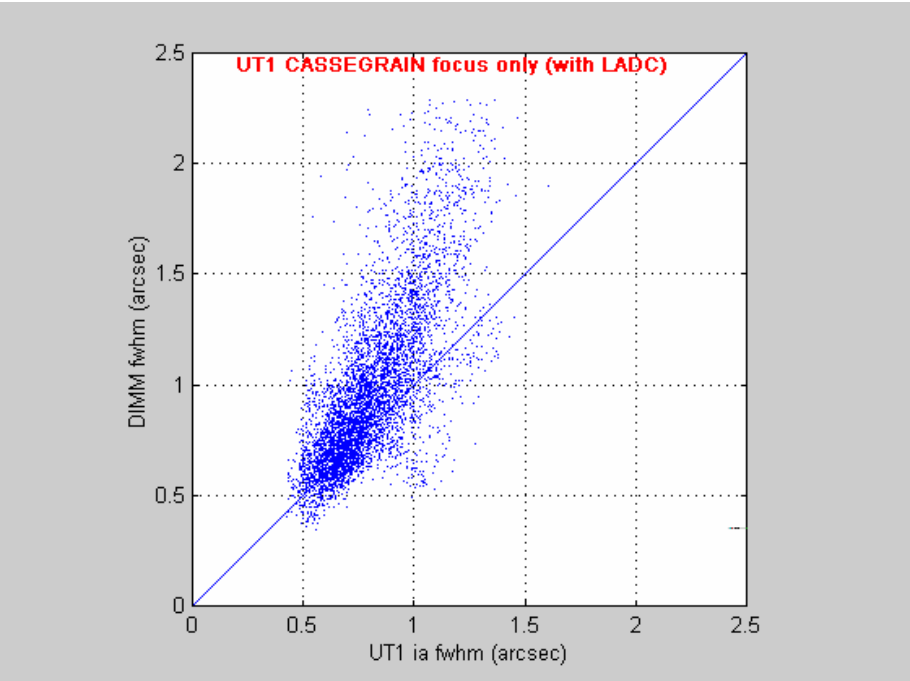

Figure 14-25: DIMM seeing (1mn average) versus contemporaneous UT1 Cassegrain Active Optics Image Quality (atmospheric dispersion corrected) estimates for January-August 2005 (compilation. J. Navarrete. Paranal).

The UT intrinsic focal plane seeing. as well as the final science image quality. is even more difficult to estimate from DIMM data. particularly in the infrared. because they have to be corrected from the finite nature of the outer scale of the turbulence. This correction improves the predicted large telescope image quality in a very chromatic manner [63]. This is well illustrated in Figure 14-27 which shows that fitting a 10m outer scale von-Karman correction to DIMM data is hardly sufficient to picture ISAAC IQ in bad seeing conditions. Moreover it would require a 0.3" local image degradation to explain the saturation during good seeing of the ISAAC IQ. Such local image degradation is not confirmed by active optics wave front sensor measurements of Figure 14-25. Discussion on the best outer scale modelling is still going on and a dedicated experiment is foreseen at Paranal in the frame of the ELT Design Study to actually measure the characteristics of wave fronts up to 50m in width

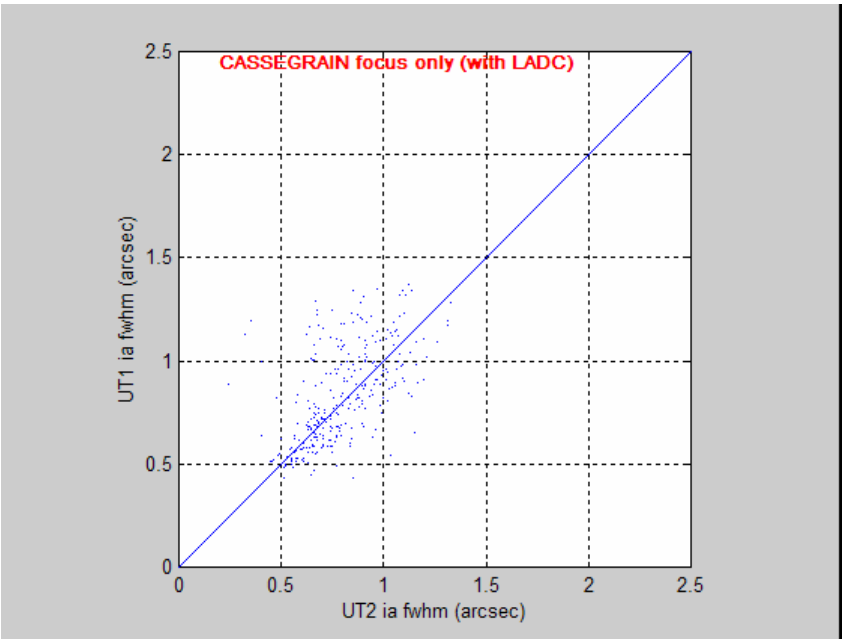

Figure 14-26: UT1-UT2 comparison of contemporaneous Cassegrain Active Optics Image Quality (atmospheric dispersion corrected) estimates for January-August 2005 (compilation. J. Navarrete. Paranal).

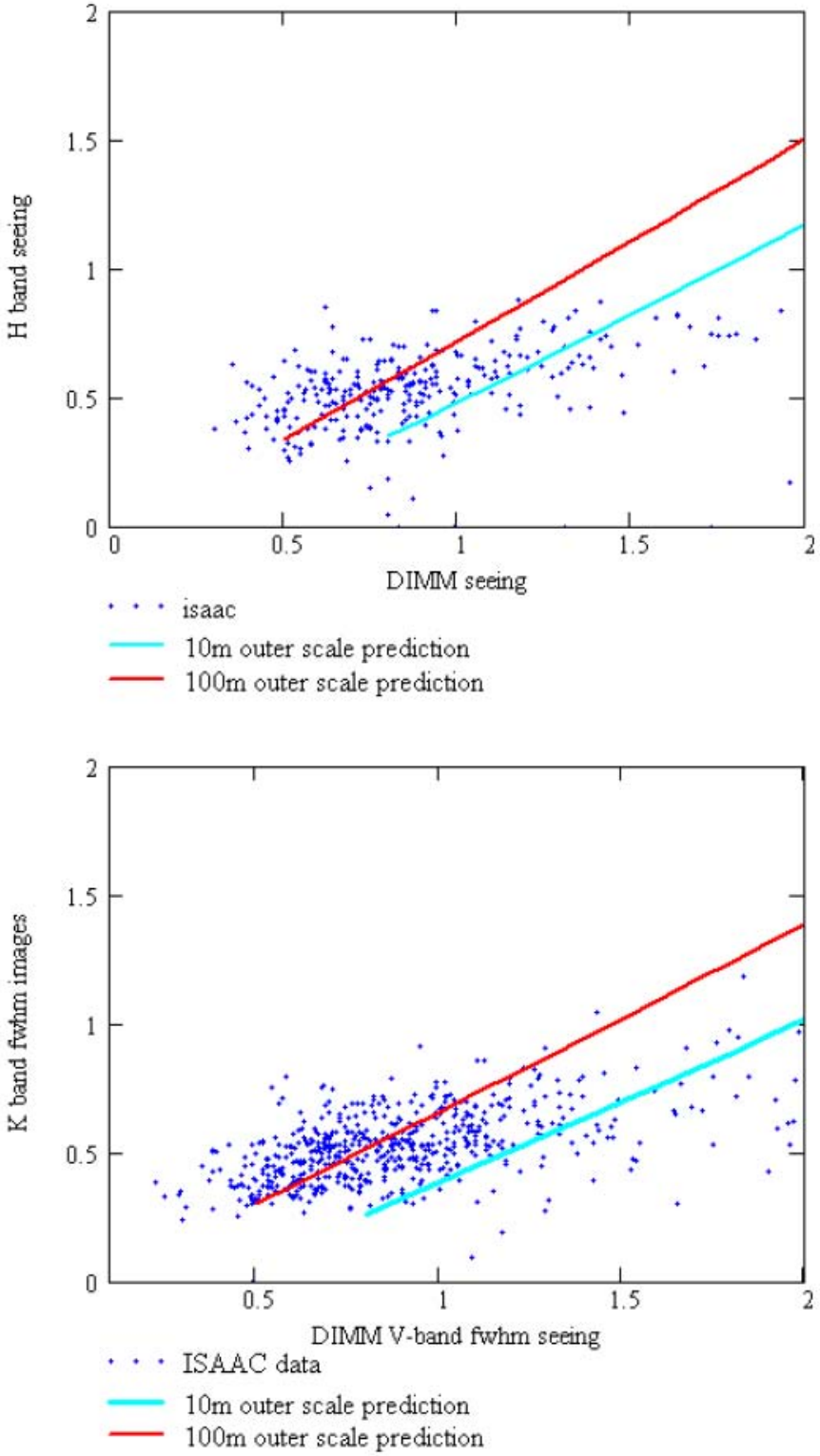

Figure 14-27: ISAAC. K (lower graph) and H (upper graph) band zenith image quality as measured (dots) and as exprected from DIMM after outer scale correction following [63]; M. Casali. I.R. image quality at the VLT. ESO Internal Report. 02 June 2005.

15. Maintenance and operations

15.1 Maintenance

15.1.1 Design provisions

The design of OWL takes in to account maintenance requirements and constraints. It incorporates the following principles:

- Easy. fast and safe human access to all subsystems.
- Provision for the integration of lifts. stairs. catwalks. platforms etc.
- Dedicated handling equipment for major subsystems.
- Disassembly and reassembly of major sub-systems.

15.1.1.1 Human access and handling

15.1.1.1.1 Human access

Two types of activities requiring human access: Normal and Extraordinary Maintenance:

- During normal maintenance activities. human access is allowed by several built-in lifts. platforms. catwalks (see Figure 15-1):
  - M1 segments assemblies.
  - Instruments.
  - Corrector.
  - M2 segments assemblies.
  - Periodic cleaning of the structure.
  - Etc.
- During extraordinary maintenance activities. human access may be allowed with mobile lifting and hoisting devices (to be defined) purchased or rented according to the particular need:
  - Repainting.
  - Cleaning.
  - Repair after seismic events.
  - Retrofitting activities.

- Installation of new subsystems or new telescope functions.
- Etc.

Table 15-1 indicates the allowable access to the various telescope sub-systems.

	During Azimuth rotation.	During Altitude rotation.	Vertical parking configuration. Figure 15-1	Horizontal parking configuration. Figure 15-9	During observation.
Technical rooms	Yes	Yes	Yes	Yes	Yes
Basement.	No	No	Yes	Yes	No
Azimuth structure.	Yes	No	Yes	Yes	Yes
Altitude Structure.	No	No	Yes	Yes	No
M1 Unit.	No	No	Yes	No	No
Focal stations.	No	No	Yes	Yes	No
Corrector.	No	No	Yes	Yes	No
M2 Unit.	No	No	No	Yes	No
Paved area around the telescope; radius 90m (Figure 15-9)	No	No	Yes	Yes	No

Table 15-1: Human access.

15.1.1.1.2 Handling Facilities

Two major handling facilities are built-in in the telescope structure (see Figure 15-1):

- Heavy pay load core lift:
  - Payload 150 tons
  - Volume: central hexagonal section which allows transport of the corrector
  - Operation not limited to the vertical parking position (see Figure 15-2)
- One Light pay load side lift per focal station:
  - Payload 6 tons
  - Volume 2.0 m width x 3.5m depth x 3.5 m height
  - Operation in vertical parking position.

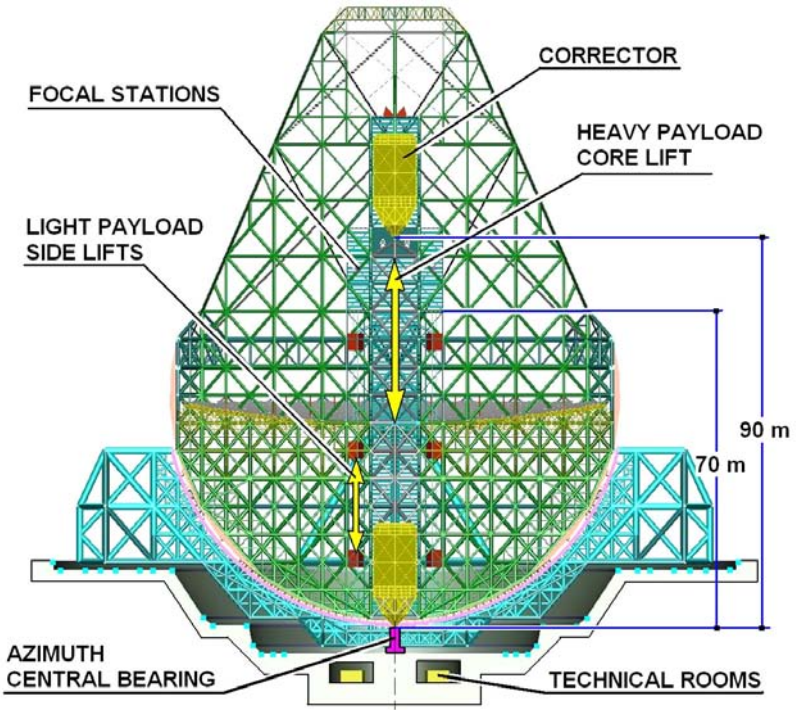

Figure 15-1: Accessibility

15.1.1.2 Corrector Handling

The corrector is the most bulky and massive opto-mechanical sub-system to be handled in one single part (see 9.4.5.2). A dedicated transporter will be designed and procured to transport the corrector from the integration laboratory to the telescope. In the integration laboratory. the corrector can be separated into several parts and each single mirror can be extracted for maintenance and re-aluminization. These operations are similar to the VLT primary mirror maintenance operations.

The integration of the corrector in to the altitude structure will be performed with the altitude structure inclined (see Figure 15-2). The core lift transports the corrector from the transporter to its final location. The altitude of the altitude structure will depend on the final design of the telescope. A low configuration (see 9.6.1) implies less demanding overall sizes of the transporter.

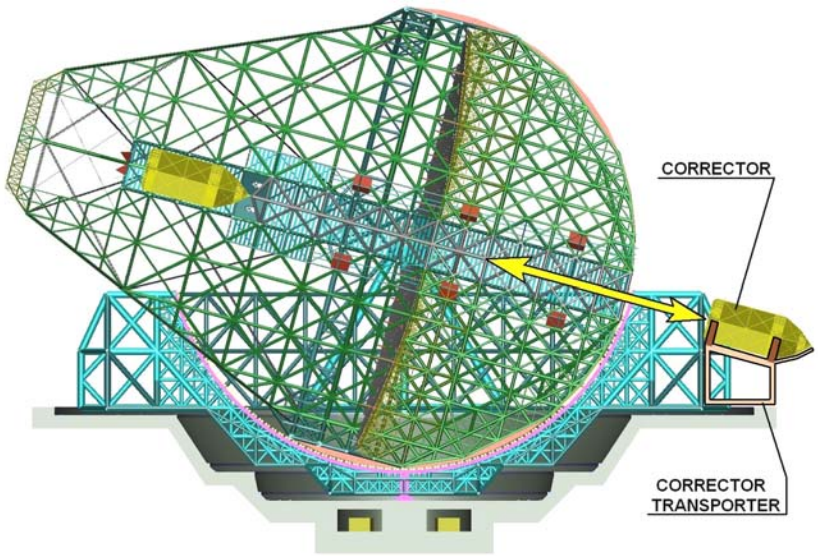

Figure 15-2: Corrector integration route

15.1.1.3 M6 Unit Handling

M6 Unit shall be assembled in the corrector when the corrector is already placed in its operational location. Frequent maintenance or upgrade activities are to be expected for M6 unit. Therefore the M6 unit maintenance routing has been studied in detail:

610

- The side lifts are dimensioned to be able to transport the M6 Unit and its handling device. (about 6 tons payload).
- Sufficient access inside the corrector (see Figure 15-4 and Figure 15-5).
- Provisions for handling operations inside the corrector are integrated in the design.
- Provisions against damaging the M5 Unit are integrated in the design.

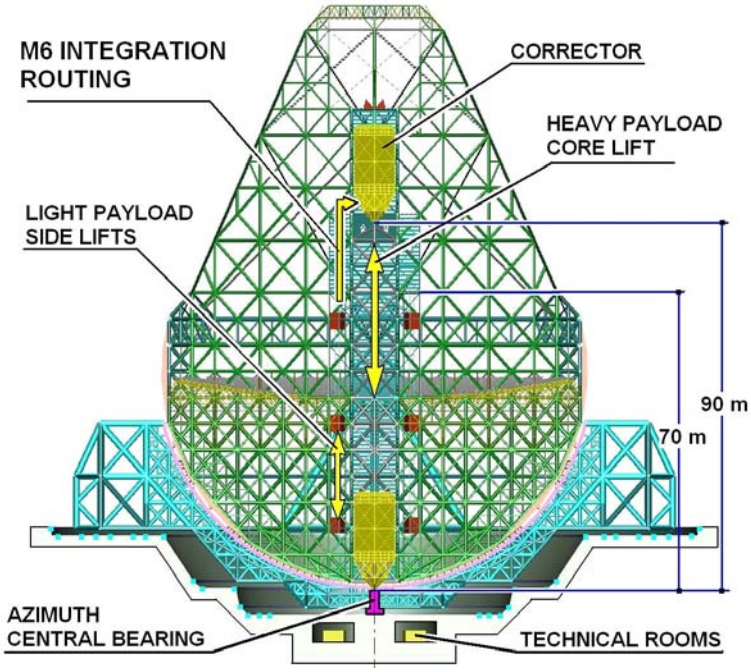

Figure 15-3: M6 unit integration route.

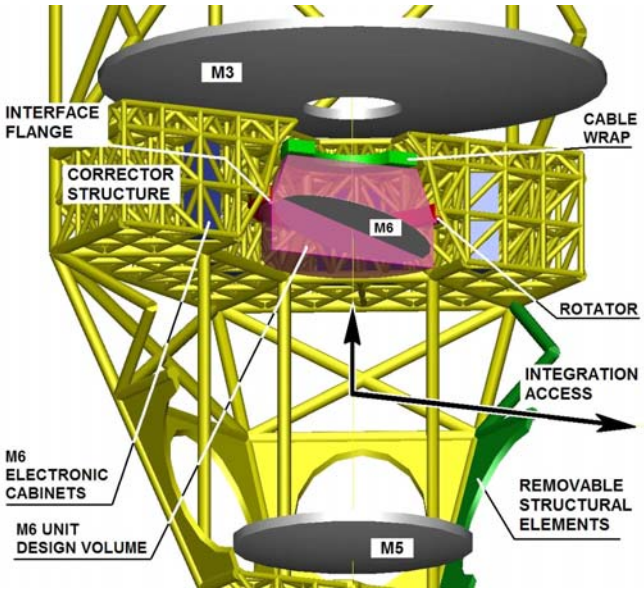

Figure 15-4: M6 unit integration route inside the corrector

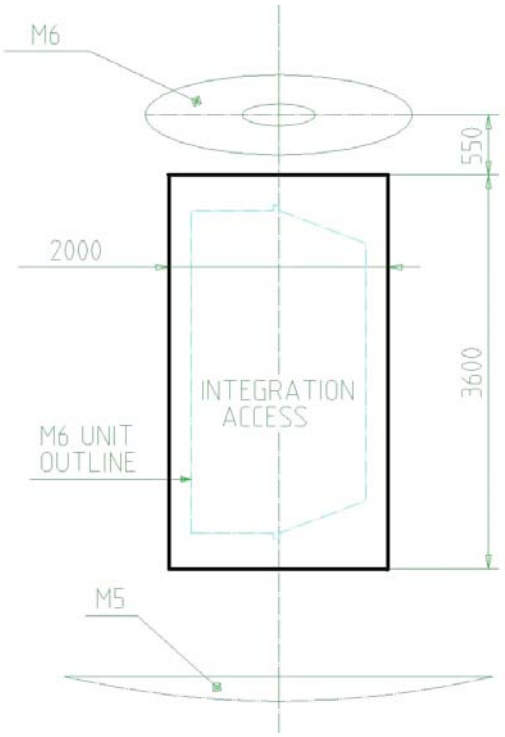

Figure 15-5: M6 unit integration access

15.1.1.4 Primary mirror covers handling

Due to the six fold symmetry of the altitude structure (see 9.4.2). the primary mirror is divided in 6 sectors. Each sector is protected during day time by a cover (see Figure 15-7). The main function of the cover are:

- To protect the mirror segments from dust. water and mechanical shocks
- To provide thermal insulation (not necessary with a SiC mirror substrate. see 9.6.3 and 9.4.9.1).
- After docking. to allow altitude structure rotation. without the need of counter ballast loads. Centres of gravity of the sectors are nearly aligned with the centre of the altitude rotation. Once at their docking location. these sectors do not hinder the altitude rotation. The imbalance is small and can be compensated by the altitude bogies.
- Segment handling and in-situ cleaning units. integrated in the maintenance cover (see Figure 15-7).
- The maintenance cover has a segments storage rack. where about 20 newly coated segments can be stored and exchanged.
- Each cover can be located over any of the six primary mirror sectors.

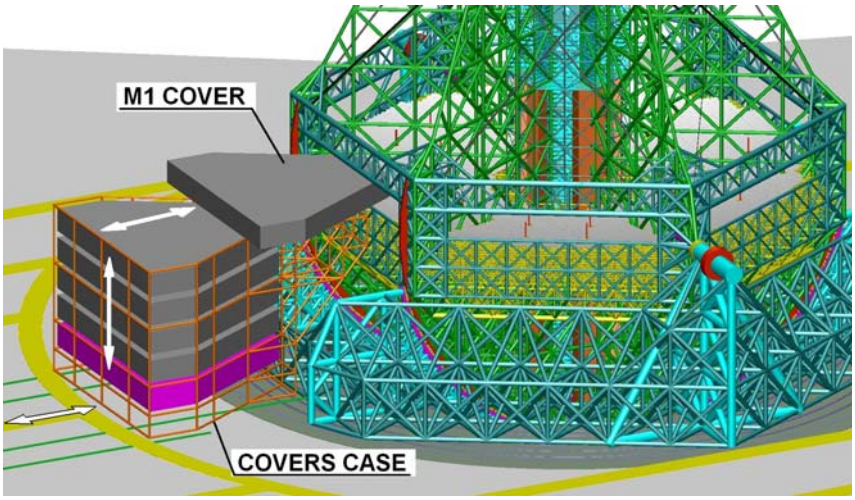

Figure 15-6: Primary mirror cover docking operation.

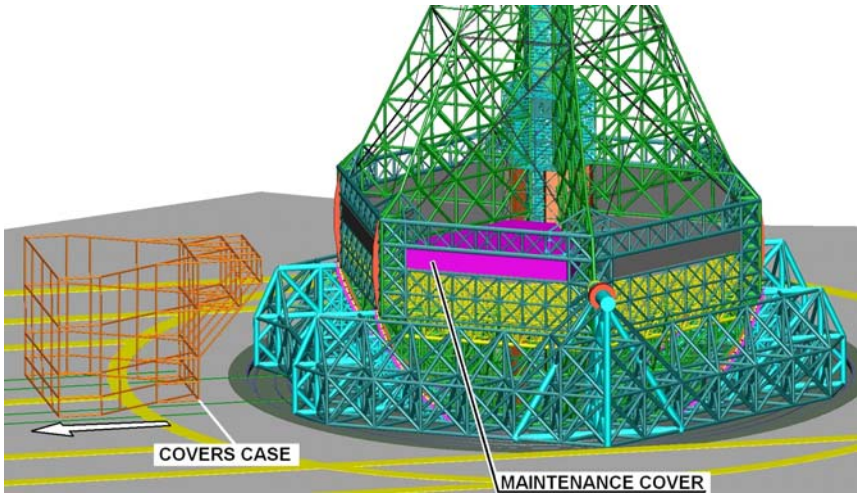

Figure 15-7: Covers on Primary mirror.

15.1.1.4.1 Covers Docking and undocking operations.

The covers docking operation steps (see Figure 15-6) are described below:

1. Store newly coated segments in the maintenance cover. which is located close to the ground level.
2. Move the cover case from its parking position to the telescope in vertical parking configuration.
3. Insert the first cover (presumably at dawn)
4. Withdraw the covers case (by about 25 m).
5. Rotate the azimuth axis by 60°.
6. Move forward the cover case by about 25 m.
7. Repeat steps 3 to 6 for the remaining covers.
8. Withdraw the empty cover case to its parking position -about 1 hour after sunrise.
9. Start maintenance operations inside the maintenance cover.

The covers un-docking operation steps (see Figure 15-6) are described below:

1. Move the empty cover case from its parking position to the telescope in vertical parking configuration. about 1.5 hours before sunset.

2. Withdraw the first the maintenance cover.
3. Withdraw the covers case by about 25 m.
4. Rotate the azimuth axis by 60°.
5. Move forward the cover case by about 25 m
6. Repeat steps 2 to 5 for the remaining covers
7. Withdraw the cover case to its parking position. about 0.5 hour before sunset.
8. Send segments to the aluminization plant if applicable.

15.1.1.5 Sliding Enclosure

The sliding enclosure is designed for minimum maintenance requirements. All active components are mounted at ground level. except the motors of the louvers allowing ventilation (passive thermal control).

The components which need maintenance are summarized in Table 15-1.

Component	Maintenance interval	personnel	Comments
Carriages	6 months	2 persons 1 day	
Bogies	6 months	2 persons 1 day	
Motors	6 months	2 persons 1 day	
Compressed air unit	In case of damge or 3 months	2 persons 1 day	Used to inflate seals
Pneumatic seals	In case of damage or 3 months	2 persons 1 day for 4 days	
Lighting	In case of damage		
Air louvers	12 months	2 persons 1 day for 1 week	
Winches and cables	6 months	2 persons 1 day for four days	
Cladding	In case of damage or 5 years	3 persons 4 weeks	From outside using permanent lift platform
Steel construction	In case of damage or 5 years	3 persons 4 weeks	
Rails	Daily	2 persons 1 hour	Verify cleanliness

Table 15-2 Sliding enclosure maintenance requirements

All components mounted above ground level can be accessed using ladders. Local platforms are installed to allow inspection and dismounting of the components if needed. The components mounted at the top of the enclosure (e.g. motors of the top louvers) will have to be lowered down to ground level. if needed. using jacks and intermediate platforms.

In case of repair of the cladding the same procedure (using locally mounted lifting devices) will be used to remove panels and to lower them down to the ground level.

Such platforms also routinely used for assembling and inspection are shown Figure 15-8

In case major maintenance / repair is required at the level of the hinge at the top of the arches. the same cranes as used for the construction may be needed. according to the level of damage. This operation would require a long time. therefore the top hinge has been over-dimensioned for resistance against potential damage.

Detailed maintenance procedures will be developed during the next phase of the project.

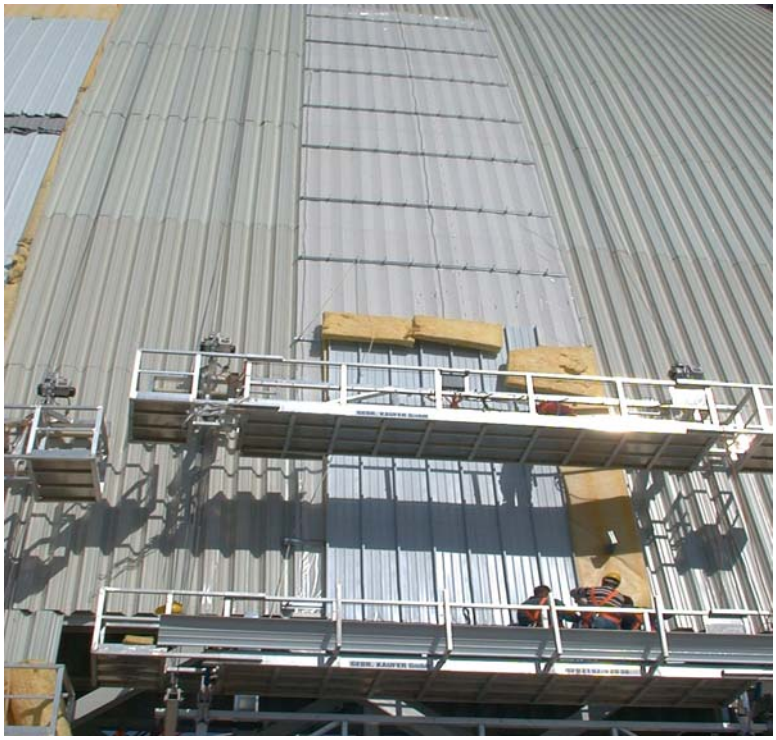

Figure 15-8 lifting platform for inspection and maintenance of cladding

15.1.1.6 Secondary mirror handling

The secondary mirror unit is not reacheable when the telescope is in a vertical parking configuration. Therefore maintenance operations are only possible in a horizontal configuration (see Figure 15-9). M2 unit handling facilities can be integrated in the sliding enclosure structure (see Figure 15-10). or they can be located in a platform standing on the ground level. As for the corrector transporter. a low configuration (see 9.6.1) requires less demanding overall sizes of the handling facilities.

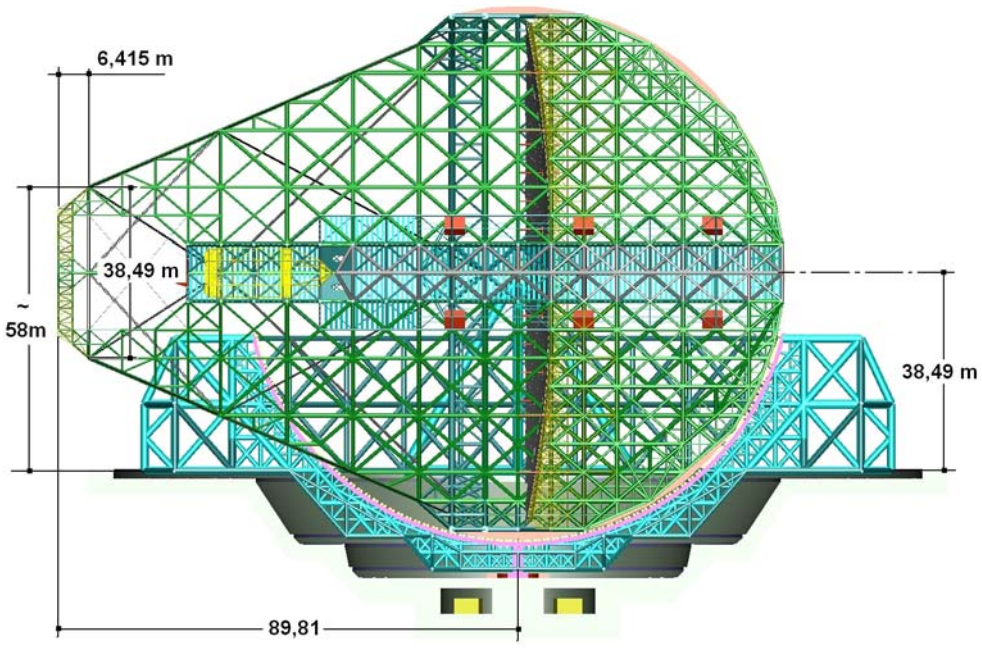

Figure 15-9: OWL horizontal parking configuration.

The major function. of the secondary mirror handling facilities are:

- Handling the complete secondary mirror unit.
- Handling of each individual flat segment.
- Maintenance of the mirror cover.

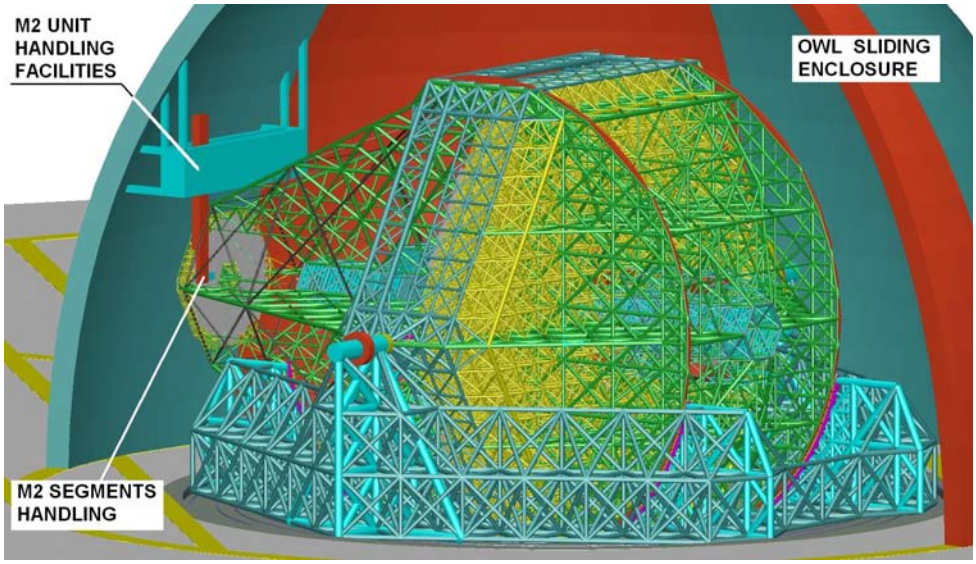

Figure 15-10: Secondary mirror handling facilities.

15.1.2 Safety

The safety precautions during operation and maintenance are partialy described and covered in section 13.2.2. However during the operational life of the telescope. which may extend over several decades. it is essential to establish maintenance procedures which also include traceability of all the eventual modifications. retrofitting and up-grades of the telescope. Special attention has to be dedicated to the implementation of the following methods:

- Continuous training and smooth transition of know-how from different generations of telescope operators and maintenance crews.
- Rigourous traceability of maintenance tools and parts which are transported to and from the telescope under the responsibility of the maintenance warehouse inventory.

15.2 Observatory operations

The operation of OWL as an observatory is expected to present demands significantly different from those of currently existing optical observatories hosting 8m-class telescopes. In many respects a closer comparison is provided by the operation of observatories hosting a facility that enhances the capabilities of pre-existing ones by orders of magnitude. or those hosting a unique experiment for which no similar precedent exists. By the time that the operations model of OWL becomes fully developed ESO will have gathered unparalleled experience in setting up operations in observatories with both of those characteristics. namely ALMA in the first case. and VLTI in the second.

Furthermore. depending on the chosen location of OWL its regular operations will benefit from the ESO VLT/VLTI experience in setting up an observatory designed to host a specific facility.

as opposed to classical observatories in which new telescopes are added to a previously existing infrastructure. Given the strong environmental constraints placed by the optimal scientific exploitation of a telescope with its characteristics. it is doubtful that the latter approach is at all an option for OWL.

Many fundamental principles of the operation and maintenance of the OWL as a facility derive from the observatory design as described in detail in chapters 6 to 13. Here we focus on additional demands not strictly related to the observatory design. but rather to the management of operations to the extent that they can be foreseen at the current stage.

The OWL observatory will include the telescope. its instrumentation. and the on-site infrastructure and technical and scientific operations groups. as well as a distributed network of remotely located sites hosting a number of activities related to development and operations. This network includes the locations where activity takes place in areas such as:

- Instrument building and upgrading.
- Hardware maintenance and repair.
- Telescope and instrument control software development.
- Scheduling.
- Development and maintenance of software for data reduction and scientific analysis.
- Data archiving. distribution. and publication in the Virtual Observatory
- User support.

As the VLT has proven it is fundamental to design OWL operations so that these activities are regarded as an integral part of the observatory. Special attention will be paid to defining clear interfaces among the groups in charge of all such tasks. The VLT/VLTI provides a framework for such a model. as well as a considerable amount of lessons learned after six years of regular operations at the time of writing this.

OWL will undergo an extended phase of partial completion (see section 2.7) in which science operations will be possible while the telescope is being completed. Such early operations stage has the twofold role of enabling an early scientific exploitation of the capabilities of the facility that are already unique even in the partial completion phase. and the progressive scientific verification and tuning of such a complex facility as it develops. The observatory operations plan will take into account such phase in which construction and telescope commissioning coexist with the scientific exploitation of the facility. A clear parallel with ALMA exists in this regard. where aspects such as staff recruitment and training. development of operations management tools and procedures. and the implementation of the end-to-end data flow system are designed to take place during the early operations phase. Furthermore. even once completed OWL will be in a continuous maintenance mode that will directly affect operations. Again. the experience to be acquired with ALMA. and in particular with the management of line-replaceable units (LRU) will play an important role in streamlining routine maintenance operations so that the impact on science operations is minimized.

The actual location of OWL may preclude the presence on-site of a volume of staff and auxiliary services beyond what is critical to ensure the safety and the most essential troubleshooting of the telescope. Most of the facility services will be located in that case in a remote facility with human-friendly environmental conditions and within a reasonable driving time of the site. The ALMA model. where such services are located in an operations support facility (OSF) located in San Pedro de Atacama. provides the baseline reference for observatory operations in this situation.

The ultimate scientific legacy of OWL will reside in the quality of its data products. At the VLT/VLTI the standardization of procedures across instruments. implementation of calibration plans. quality control and instrument trending procedures has led to the build-up of a data archive that follows in many ways the model of the HST science archive. leading to well-characterized data products whose further processing will form one of the main contributions of ESO to the Virtual Observatory. We elaborate on some of these aspects in Section 15.3. but

what is relevant in the planning of observatory operations is that the hardware infrastructure (computing power. storage. communications bandwidth) and specialized support staff must not represent a bottleneck given the foreseeable demands placed by data rates and rapid data transfer needs. This is an area where the final design will heavily depend on the state-of-the-art technology by the time when OWL becomes operational. and can hardly be predicted now. Moreover. it is also important to keep in mind that technologies not yet developed. or in their early development stages at the present time. may drive fundamental operations design aspects. such as instrument capabilities. data rates. or the way in which users interact with the facility.[74] Superconducting Tunnel Junction (STJ) detectors or GRID computing are possible examples of technologies that may become mature early in the life of OWL.

15.3 Science operations

The 8m-telescope era has brought innovative science operations models that optimize the scientific exploitation of such facilities and converge in several ways with the operation of space-borne facilities. Science operations at OWL will ultimately depend on the combination of its science cases with design constraints on the telescope and the capabilities of its instrumentation. but in any case they may be expected to represent a further evolution over the most advanced models currently existing and a further departure with classical operations schemes. in which the astronomer directly interacts with the telescope and instrument using relatively simple interfaces and with limited assistance from observatory staff.

It may be questioned whether the types and scope of observing programs currently executed at facilities like the VLT. dominated by short-duration projects with limited science goals. will retain their validity in the OWL era. or rather emphasis will be given to the conduction of long-term experiments with specifically-designed instrumentation as some science cases suggest. In either case. the science operations scenario of OWL will implement rigorous calibration and quality assessment procedures based on data reduction pipelines to ensure the full characterization of the data. the proper instrument modelling. and to facilitate their reusability (see below). It is also to be expected that regardless of the actual breakdown of the programs. the principles and advantages underlying queue scheduling will continue to be valid for OWL and that the observatory staff will be the main or even the sole responsible for the execution of the observations. Staffing. policies. and procedures will be structured around an operations model in which queue scheduling will be the main or single mode of operation of the telescope.

The extensive use of metrology that is planned in the wavefront control of OWL will make possible a close link between the image characterization at the focal plane and the active and adaptive optics settings. Given the complexity of the PSF delivered by OWL. an attractive possibility is the customization of the PSF to the scientific goals of the observations. so as to enhance those features that are of greatest interest for the purpose of the observations (e.g. enhancement of the PSF core at the expense of having bright wings when high resolution is needed. versus reduction of wings at the expense of a broader PSF core when requiring high contrast imaging).

The OWL design will unavoidably lead to compromises that may disfavour scientific areas having particularly stringent requirements on the telescope. such as the possibility to preset to a given position and close the loop within a very short time. The science operations plan will identify such design compromises early. so that mitigating strategies can be devised and whenever possible factored in the telescope design.

[74] A look back into VLT prehistory is illustrative in this respect: the generalized access to the world-wide-web was unsuspected only ten years before the VLT entered operations, and the applications of CCDs to astronomy were beginning to be considered only two decades before that date, at a time when the concepts of 8m-class telescopes were already well advanced.

The design of front-end tools for the operation of the telescope and instruments will strongly depend on state-of-the-art IT at the time when their technical specifications are defined. It is unlikely that. given the complexity of the OWL instruments. common users will be asked to interact with them to the same level of depth as is currently done at the VLT. in which instrument setups and exposure characteristics are normally defined by the user by means of templates. both for service and visitor mode observations. An alternative scenario seems more plausible. in which users will define the requirements of the observations at a higher level and the observatory staff will carry out their translation to instrument configurations. This would imply that the front-end tools are mainly designed for use by staff astronomers rather than by the common user. Besides this difference. it is to be expected that the baseline functionality of front-end tools will be similar to that of the existing VLT data flow system. which in turn have numerous aspects in common with the ALMA data flow system tools currently under development[75].

Dedicated software to process the output of the instruments must be regarded as an integral part of the instrument already in the VLT and an important part of science operations. and this will be even truer at the scale of complexity of OWL instruments. in which such dedicated software is likely to become mandatory to allow the scientific exploitation of the data. Instruments will have to be provided to the facility together with pipelines to be used at the observatory for quality control. trending and health check purposes. They will also be provided with interactive data reduction software packages allowing the full processing of data up to the point where they can be used for scientific analysis. The data reduction software will meet the appropriate requirements for its integration in data reduction facilities that may be expected to have become widely adopted standards when OWL enters operations. The output science-ready data produced by these data reduction packages will be compliant with Virtual Observatory protocols so that they can be directly published in the Virtual Observatory.

Data distribution in the OWL era may or may not involve the delivery of data packages to users in physical media. Distributed computing through the GRID may allow scientists to remotely process data and download only scientifically significant results. The decision on the distribution of data packages will be taken in due time based on a cost analysis of the possibilities offered by technology at the moment.

[75] It is worth noting that most key front-end tools used for the preparation and execution of VLTI observations are essentially identical to those used in VLT operations, despite the great differences between observing techniques.

Design parameters – Summary

Overall characteristics		
Entrance pupil diameter	100-m	
Entrance pupil location	Primary mirror	
Exit pupil location	On M6	
Focal ratio	6.03	
Plate scale	2.924 mm / arc second	(on-axis)
Total field of view	10 arc minutes	(unvignetted)
Linear field size	13994.53 mm	
Diffraction-limited field of view (Strehl Ratio ≥ 0.80)		As-designed
λ=0.5 μm (on curved field with R=2209.8 mm)	142 arc seconds (diameter)	Field concave in the direction of light propagation
λ=2.2 μm (on curved field with R=2215.4 mm)	245 arc seconds (diameter)	
λ=5.0 μm (on curved field with R=2243.1 mm)	360 arc seconds (diameter)	
Image quality at edge of field (10 arc mins)		
Wavefront RMS	1.476 μm	
RMS spot size	0.052 arc seconds	
Field curvature	2209.8 mm	Oncave in the direction of light propagation
Central obscuration	35%	(linear)
Distortion at edge of 10 arc minutes field of view	1.31%	
Emissivity (with pupil mask)	20.3%	Incl. intersegments gaps, tensioning ropes
Telescope mount	Alt-az	Elevation axis above primary mirror

Overall characteristics				
Focal stations			6	Incl. 1 reserved for engineering instrumentation
Optical design characteristics				
Primary mirror	Shape		Spherical	
	Focal ratio		f/1.25	
Secondary mirror	Shape		Flat	
	Diameter		25.8-m	
M1-M2 separation			92517.5 mm	
M1 segments	Number		3048	Plus min. 98 spares
	Mass		387 Kg each	(if solid Zerodur)
	Cut		Hexagonal	
	Optical shape		Spherical	
	Radius of curvature		230-m	
	Dimension (flat-to-flat)		1.6-m	Incl. bevels
	Thickness		70 mm	For solid glass-ceramic substrate
	Substrate		Zerodur, ULE or Astrosital	Silicon Carbide or lightweight Zerodur as alternatives
	Axial support		18 points whiffle-tree	TBC; actively positioned (3 actuators per segment)
	Lateral support		Central	
M2 segments	Number		216	Plus min. 7 spares
	Mass		387 Kg each	(if solid Zerodur)
	Cut		Hexagonal	
	Optical shape		Flat	
	Dimension (flat-to-flat)		1.6-m	Incl. bevels
	Thickness		70 mm	For solid glass-ceramic substrate
	Substrate		Zerodur, ULE or Astrosital	Silicon Carbide or lightweight Zerodur as alternatives
	Axial support		18 points whiffle-tree	TBC; actively positioned (3 actuators per segment)
	Lateral support		Central	
Corrector			Four-elements	
M3	Type		Thin active meniscus	
	Shape		Aspheric, concave	
	Diameter (useful area)	Inner	1674.0 mm	No vignetting, natural guide stars
		Outer	8241.8 mm	
	Radius of curvature		18690 mm	
	Mirror substrate		TBD	Low-expansion glass or glass-ceramic
M4	Type		Thin active meniscus	

Overall characteristics				
	Shape		Aspheric, concave	
	Diameter (useful area)	Inner	1352.0 mm	No vignetting, natural guide stars
		Outer	7762.8 mm	
	Radius of curvature		19970 mm	
	Mirror substrate		TBD	Low-expansion glass or glass-ceramic
M5	Type		Thin adaptive shell	
	Shape		Aspheric, concave	
	Diameter (useful area)	Inner	420.0 mm	No vignetting, natural guide stars
		Outer	3916.4 mm	
	Radius of curvature		8504 mm	
	Mirror substrate		TBD	Provisional unit may be aluminium.
M6	Type		Thin adaptive shell	On tip-tilt mount for field stabilization
	Shape		Flat	
	Tilt angle		16^{o}	
	Diameter (useful area)	Inner		Elliptical; no vignetting, natural guide stars
		Outer	2440 x 2660 mm^2	
	Radius of curvature		Infinite	
	Mirror substrate		TBD	Provisional unit may be aluminium
Distance M2 – vertex of M4			28235 mm	
M3-M4 separation			11280 mm	
Distance vertex M4 to vertex M6			2150 mm	
Distance vertex M6 to vertex M5			5260.54 mm	
Backfocal distance (vertex M6 to vertex image surface)			13994.53 mm	
Adaptive Optics design characteristics				
SCAO				
Deformable mirror			M6	
Number of guide stars			1	
Number of sensing elements across pupil			97	Total active sub-apertures: 6354
Wavefront sensor type			Shack Hartman or IR Pyramid	
CCD pixels on Wavefront sensor			388x388 (SH), 194x194 (Pyr)	
Number of actuators across pupil			98	Total active actuators: 6820
Control bandwith			500 Hz	
Corrected field of view (diameter)			~1 arc minute	Limited by anisoplanatism
Wavelength range (science)			1.25µm - 20 µm	

Overall characteristics		
GLAO		
Deformable mirror	M6	
Number of guide stars	Up to 6	
Number of sensing elements across pupil	97	Total active sub-apertures: 6354 per WFS
Wavefront sensor type	Shack Hartman	
CCD pixels on Wavefront sensor	388x388	
Number of actuators across pupil	98	Total active actuators: 6820
Control bandwith	500 Hz	
Corrected field of view (diameter)	Up to 6 arc minutes	
Wavelength range (science)	1.25µm - 2.5 µm	
MCAO		
Deformable mirror	M6+M5	
Number of guide stars	Up to 6	
Number of sensing elements across pupil	97	Total active sub-apertures: 6354 per WFS
Wavefront sensor type	Shack Hartman	
CCD pixels on Wavefront sensor	388x388	
Number of actuators across pupil (M6)	98	Total active actuators: 6820
Number of actuators across the meta-pupil (M5, 6 arcmin)	145	Total active actuators: 16512
Control bandwith	500 Hz	
Corrected field of view (diameter)	1’	
Wavelength range (science)	1.25µm - 2.5 µm	
XAO		
Deformable mirror	M6 + 2 post focal	
Number of guide stars	1	
Number of sensing elements across pupil	150 and 500	
Wavefront sensor type	Pyramid and Shack Hartman	
CCD pixels on Wavefront sensor	300x300 and 1000x1000	
Number of actuators across pupil	~150 and ~500	
Control bandwith	3000 Hz and 1000Hz	
Corrected field of view (diameter)	~4’’	
Wavelength range (science)	0.6µm-0.8 µm and 1.0µm -1.7µm	
MOAO		
Deformable mirror	M6 (stroke) + up to 30 MEMs	MEMs DM button for each IFU (30 simultaneously)
Number of guide stars	Up to 10	

Overall characteristics			
Number of sensing elements across pupil		97	Total active sub-apertures per WFS button 6354
Wavefront sensor type		Shack Hartman	
CCD pixels on Wavefront sensor		388x388	
Number of actuators across pupil		98	Total active actuators per IFU: 6820
Control bandwith		500 Hz	
Corrected field of view (diameter)		0	Correction on each object individually
Wavelength range (science)		1.25µm - 2.5 µm	
Mechanical design characteristics			
Overall Dimensions	Diameter	155 m	
	Height	130 m	From ground level
Rotating Mass		14834.5 tons	(2004 design iteration)
Focal Stations	Number	6	1 focal station reserved for engineering instrument
	Max. instrument mass	15 tons each	including Adaptor Rotator
Main structural material		Mild steel	
Altitude Mass Moment of Inertia		1.123×10^{10} kg m^2	(2004 design iteration)
Azimuth Mass Moment of Inertia		3.368×10^{10} kg m^2	(2004 design iteration)
Main axes Drive and Bearing Systems		Friction Drive and Bearing	Bogies
Azimuth Rotation		360 degrees	
Altitude Rotation		$\pm$ 90 degrees	maximum maintenance range
Altitude require torque		19.6 MNm	2004 Version
Azimuth require torque		58.7 MNm	2004 Version
Sky coverage (altitude)		0.5 to 70 degree (ZD)	From 60 to 70 vignetting due to foundation
Blind angle at zenith		$\leq \pm$ 0,5 degree	Paranal location
Maximum Altitude and Azimuth Acceleration		0.1 degree s^{-2}	
Maximum Altitude axis velocity		0.1 degree s^{-1}	
Maximum Azimuth axis velocity		0.5 degree s^{-1}	
Locked rotor frequency		2.58 Hz	2004 version
Gravity M1-M2 differential rigid body displacements			
Piston		3.4 mm	
Tilt		13.1 arcsec	
Decenter		17.6 mm	
Altitude axis control bandwith		1.8 Hz	Tailored to high wind disturbance rejection
Azimuth axis control bandwith		0.6 Hz	Tailored to low wind disturbance on azimuth axis
Tracking accuracy (Altitude and Azimuth axes)		0.3 arcsec rms	With 10m/s wind speed

Overall characteristics			
Field stabilization range (M6 surface tip-tilt)		Min. ± 31 arcsec PTV	Equivalent to ±1.44 arc seconds on-sky
Field Stabilization bandwith		2 Hz	Performed at Mirror 6
Fiel Stabilization accuracy (M6 surface tip-tilt)		0.01 arcsec rms	Equivalent to 0.00046 arc seconds on-sky
Segment Position actuators			
	Maximum load	1700 N	Compression (M1) or tension (M2)
	Accuracy	± 5 nm	Goal ± 2 nm
	Stroke	15 mm	Goal 30 mm
	Control bandwitdh	10 Hz	Over fine stroke at nm level
Sliding enclosure			
Overall dimensions	height	147 m	
	Length	242 m	
	Width	242 m	
Enclosed volume		4100000 m^3	
Surface area		102000 m^2	
Mass		37000 t	30000 t structural steel, 7000 t cladding
Material			
	Structure	Mild steel	
	Cladding	Aluminium sandwich panels	
	Pneumatic seal	Polyester canvas	Coating: polychloroprene
Maximum deflection under gravity load		150 mm	Vertical
Maximum deflection under operational wind load		200 mm	
Maximumdeflection under OBE		300 mm	
Maximum delection under survival wind load		450 mm	
Maximum deflectin under MLE		550 mm	
First eigenfrequency		0.4 Hz	
Maximum displacement speed		0.8 m/s	Time to move from day to night position 15 minutes
Minimum time for opening arches		TBD	
Distance between day and night parking position		410 m	Axis to axis
Arches drive system		bogies	
Enclosure drive system		Winches and cables	
Site Integration design characteristics			
Handling and hoisting facilieties		3 tons	Most of the telescope structure parts can be integrated using small payload facilities.
Metrology		Low tolerances	Most of the telescope structure parts can be integrated using

Overall characteristics		
		low accuracy measurement devices.
Maintenance design characteristics		
Redundancy		The redundancy of parts and sub-systems embedded in to the design, assures the avalability of the telescope.
Segments recoatings	5.1 per day (peak)	Assuming unprotected Al coating, 2-years lifetime
Corrector mirrors recoating (duration)	2 weeks	Expected maximum frequency once every 2 years.

References

Project documents

RD1 6-mirror solution, f/1.42 primary mirror - Optical design and properties, OWL-CSR-ESO-00000-0003 Issue 2

RD2 6-mirror solution, f/1.25 primary mirror - Optical design and properties, OWL-CSR-ESO-00000-0175 Issue 1

RD3 Effect of CTE inhomogeneities and of thermal gradients in the primary and secondary mirror segments, OWL-CSR-ESO-00000-0007 Issue 1

RD4 Atmospheric dispersion effects, OWL-CSR-ESO-00000-0008 Issue 1

RD5 Preliminary requirements for OWL segments integration and maintenance, OWL-TRE-ESO-00000-0140 Issue 1

RD6 Final Report (SCHOTT) - Feasibility Study for Glass-ceramic Primary & Secondary Mirror Segment Blanks; OWL-CSR-ESO-00000-0074 Issue 1.

RD7 Final Report (ZEISS) - Feasibility Study for Glass-ceramic (AstroSitall) Primary & Secondary Mirror Segment Blanks; OWL-CSR-ESO-00000-0022 Issue 2.

RD8 Final Report (CORNING) - Feasibility Study for Glass-ceramic (ULE) Primary & Secondary Mirror Segment Blanks; OWL-CSR-ESO-00000-0076 Issue 1.

RD9 Feasibility of SiC segment blanks - final report (BOOSTEC); OWL-CSR-ESO-00000-0045 Issue 1.

RD10 Final Report - Feasibility Study for Cesic Mirror Blanks for the OWL telescope (ECM); OWL-CSR-ESO-00000-0143 Issue 1.

RD11 Final Report - OWL Mirror Feasibility Study (SAGEM) ; OWL-CSR-ESO-00000-0144 Issue 1.

RD12 Study Report - Figuring and Polishing of OWL Primary and Secondary Mirrors Glass/Glass Ceramics Segments (SESO); OWL-CSR-ESO-00000-0141 Issue 1.

RD13 Contact Stiffness and Stress of OWL Bogies. Doc number: OWL-CSR-ESO-00000-0116.

RD14 Modelling of friction drive bogie for Main axes Control of OWL. Doc.: OWL-CSR-EPFL-00000-0134. Date: 18-12-2003. Author: Laboratoire d'Automatique, École Polytechnique Fédéral de Lausanne.

RD15 Control and Coordination of friction drive bogies for the Main axes Control of OWL. Doc.: OWL-CSR-EPFL-00000-0135. Date: 27-5-2004. Author: Laboratoire d'Automatique, École Polytechnique Fédéral de Lausanne.

RD16 Main axes Control of OWL. Complete system study. . Doc.: OWL-CSR-EPFL-00000-0137. Date: 1-7-2004. Author: Laboratoire d'Automatique, École Polytechnique Fédéral de Lausanne.

RD17 Main axes Control of OWL. Study linear case. Doc.: OWL-CSR-EPFL-00000-0133. Date: 1-07-2004. Author: Laboratoire d'Automatique, École Polytechnique Fédéral de Lausanne.

RD18 Friction drive bogies: characterization tests and identification of friction paramaters. Doc.: OWL-CSR-EPFL-00000-0136. Date: 27-3-2004. Author: Laboratoire d'Automatique, École Polytechnique Fédéral de Lausanne.

RD19 Control Study of OWL Segmented Mirrors, Requirements and Limitations, Doc: OWL-CSR-ESO-00000-0158. Issue 3.

RD20 Structural models for OWL segments control study, Doc: OWL-CSR-ESO-00000-0157. Issue 1.

RD21 Coping with phasing failures, OWL-CSR-ESO-00000-0043 Issue 1.

RD22 High Contrast Imaging, OWL-CSR-ESO-00000-0184 Issue 1 DRAFT.

RD23 Technical Specifications for the Conceptual Design of OWL M6 Adaptive Mirror M6; OWL-SPE-ESO-083800-0171 Issue 1

RD24 Adaptive Optics WFS detectors; VLT-SPE-ESO-14690-3320 issue 3

RD25 SPARTA for OWL: Straw-man Design, Doc. OWL-CSR-ESO-00000-0178 Issue 1

RD26 OWL Adaptive Optics Analysis Report OWL-TRE-ESO-00000-0169 Issue 1

RD27 Calibration strategies overview for large DM AO systems, VLT-TRE-ESO-11250-3761

RD28 Sky coverage for OWL Adaptive Optics GLAO and MCAO cases, Doc. OWL-CSR-ESO-00000-0177 Issue 1

RD29 Feasibility Study of OWL Framework Structure. Date 30 September 2002. CCI AG Winterthur CH (Former SULZER THERMTECH LTD).
RD30 Buckling Analysis of OWL Framework Structure. 18.08.2002: IHF Ingenieurbüro Huß &Feickert
RD31 Analysis study of OWL Framework nodes. IHF Ingenieurbüro Huß &Feickert
RD32 Pretension and Fatigue Analysis of OWL Framework Structure. 2-6-2003
RD33 OWL 6 mirrors design. Telescope mechanical structure. Friction Drive and Bearing Systems. OWL-CSR-ESO-60000-114. Isssue: 01. Date: 06 October 2003.
RD34 OWL Steel Structure Thermal model tests. Doc number: OWL-TRE-ESO-00000-0172 26-7-2005.
RD35 Owl test tube temperature measurements, Michael Cantzler 23-1-2005.
RD36 Effect of the foundation onto the dynamic performance of OWL. Doc. OWL-CSR-ESO-00000-0150. Issue 1
RD37 OWL Product Structure Codes, OWL-TRE-ESO-00000-0148 Issue 1.
RD38 Owl Enclosure conceptual design: Statement of Work and Technical Specifications, OWL-CSR-ESO-00000-0132 Issue 1
RD39 Final Report: Conceptual Design of the enclosure fro the ESO 100m Telescope. Issue 1 26.08.2005, CL-MAP
RD40 OWL Enclosure Phase 2, Report nr. 113128100-002. Issue 1, 04.10.2005. Airlight, Helbling, Passera Pedretti & Partners.
RD41 Level 1 requirements, OWL-CSR-ESO-00000-0001
RD42 Feasibility study for glass/glass-ceramic primary and secondary mirror segments blanks; Technical Specifications and Statement of Work; OWL-CSR-ESO-00000-0004 Issue 2.
RD43 Feasibility study for CESIC primary and secondary mirror segments blanks - Technical Specifications and Statement of Work; OWL-CSR-ESO-00000-0117 Issue 1.
RD44 Figuring and polishing of OWL primary and secondary mirrors glass/glass-ceramics segments, Technical Specifications; OWL-CSR-ESO-00000-0014 issue 2.
RD45 Figuring and polishing of OWL primary and secondary mirrors Silicon Carbide segments, Technical Specifications; OWL-CSR-ESO-00000-0015 Issue 2.
RD46 Primary mirror inter-segment gaps variations, OWL-CSR-ESO-0000-0012 Issue 1.
RD47 OWL-Axial Support of Zerodur Solid Segments (FEM report), OWL-TRE-ESO-0000-0115 Issue 2.
RD48 OWL Alternative Optical Designs, OWL-CSR-ESO-00000-0181 Issue 1.
RD49 Instructions to perform Earthquake Analysis for OWL Subsystems, OWL-SOW-ESO-00000-0168, Issue 1.
RD50 OWL preliminary thermal analysis report, OWL-CSR-ESO-00000-0182.
RD51 EPICS: Earth-like Planet Imaging Camera and Spectrograph; OWL–CSR-ESO-00000-0166
RD52 CODEX: COsmic Dynamics EXperiment; OWL–CSR-ESO-00000-0160
RD53 QuantEYE, OWL–CSR-ESO-00000-0162
RD54 ONIRICA,OWL NIR Imaging Camera, OWL–CSR-ESO-00000-0165.
RD55 MOMFIS: Multi Object Multi Field Infrared Spectrograph; OWL–CSR-ESO-00000-0164.
RD56 T-OWL: Thermal Infrared Imager and Spectrograph for OWL; OWL–CSR-ESO-00000-0161.
RD57 SCOWL: Submillimeter Common User Bolometer Array for OWL; OWL–CSR-ESO-00000-0163.
RD58 HyTNIC : Hypertelescope NIR Camera ; OWL–CSR-ESO-00000-0167

External documents

RD501 Computation of the long-exposure PSF and of the Central Intensity Ratio CIR, VLT-TRE-ESO-10000-0407 Issue 2.
RD502 Position Actuators - Technical specifications. ELT-SPE-ESO-04300-0002 Issue 1.0
RD503 Position Actuators – Statement of Work. ELT-SPE-ESO-04300-0001 Issue 1.0
RD504 Metrology – position sensors and internal alignment system, Statement of Work ELT-SOW-ESO-042000-0001
RD505 Position Sensors. Technical Specification ELT-ESO-SPE-04200-0002
RD506 Wind Experiment Breadboard - Technical specifications. ELT-SPE-ESO-04800-0002 Issue 1.0.
RD507 Wind Experiment Breadboard – Statement of Work. ELT-SPE-ESO-04800-0001 Issue 1.0.
RD508 APE Instrument Requirements Specification – ELT-SPE-ESO-04600-0001 Issue 1.0
RD509 Contract for a DESIGN STUDY implemented as SPECIFIC SUPPORT ACTION, Annex I - “Description of Work”; Proposal/Contract No: 011863
RD510 Polishing and testing of 1-m SiC segments prototypes - Statement of Work, ELT-SOW-ESO-05100-0001 Issue 1.

RD511 Structural Ropes for ELT. Statement of Work. ELT-SOW-ESO-06100-0001 Issue 1.
RD512 Composite material structural elements applied to ELT. Statement of Work. ELT-SOW-ESO-06200-0001 Issue 1.
RD513 Characterization of Friction Drives and Bearings. Statement of Work. ELT-ESO-SOW-06400-0001 Issue 1.
RD514 Characterization of Friction Drives and Bearings. Technical specifications. ELT-ESO-SPE-06400-0002 Issue 1.
RD515 Magnetically levitated systems and linear drives for ELT main axes. Statement of work. ELT-SOW-ESO-06300-0001
RD516 Statement of Work for the Enclosure Concepts Design; ELT-SOW-GRA-08100-0001 Issue 1.
RD517 Statement of Work for the Wind studies; ELT-SOW-ESO-8300-0001 Issue 1.
RD518 1st Generation AO & MCAO design for ELT - Statement of Work. ELT-SOW-ESO-09200-0001 Issue 1.
RD519 Large deformable mirrors – Statement of Work. ELT-SOW-ESO-09300-0001.
RD520 Statement of Work: ELT Instrument Impact Studies: Small Studies. ELT-SOW-UKA-11200-0001 Issue 1.
RD521 Statement of Work: ELT Instrument Impact Studies - Point Design Studies. ELT-SOW-UKA-11100-0001 Issue 1.
RD522 Site Characterization. Instrumentation, measurements and modelling - Statement of Work. ELT-SOW-UNI-12200-0001 Issue 1.
RD523 Wind studies for the VLT enclosure-Paranal, Chile - DMI 92051 dated 12.08.92
RD524 Model test for the flow behaviour behind the wind screen of the VLT enclosure at the position of the telescope – Report R 485/0894 dated 02.08.94
RD525 Integrated Modelling - Development of Tools. ELT-SOW-LUN-13100-0001 issue 1.
RD526 The science case for the European Extremely Large telescope", 2005, Isobel Hook (Ed), published by Opticon ("Science Book").
RD527 OWL Control study preparation, Final Report, issue 2, Technische Universität München.
RD528 Infrared Focal Plane Arrays for the OWL Telescope- J. Beletic – Rockwell Scientific Company

Bibliographic references

[1] R. Geyl, private communication
[2] 16. P. Dierickx, Optical Quality and Stability of 1.8-m Aluminum Mirrors, in Metal Mirrors, University College London, 1992..
[3] Keck Observatory Report No. 163. Segment Figure Correction Using Leaf Springs on Whiffletrees. Vassilis Panoskaltsis, Katerina Papoulia, T. S. Mast, and J. E. Nelson (April 1987).
[4] R. Geyl, M. Cayrel, M. Tarreau, Gran Telescopio Canarias optics manufacture: Progress Report No 2, 2004, SPIE 5252, 63-68.
[5] R. Gilmozzi, B. Delabre, P. Dierickx, N. Hubin , F. Koch, G. Monnet, M. Quattri, F. Rigaut, R.N. Wilson*, The Future of Filled Aperture Telescopes: is a 100m Feasible?*; 1998, Advanced Technology Optical/IR Telescopes VI, SPIE 3352, 778
[6] G. A. Chanan, M. Troy, C. Ohara, Phasing the primary mirror segments of the Keck telescopes: a comparison of different techniques; 2000, SPIE 4003.
[7] P. Dierickx, 1992, J. Mod. Optics, vol. 39, No. 3, 569-588.
[8] E. Marchetti, R. Brast, B. Delabre, R. Donaldson, E. Fedrigo, C. Frank, N. Hubin, J. Kolb, M. Le Louarn, J.-L. Lizon, S. Oberti, R. Reiss, J. Santos, S. Tordo, R. ragazzoni, C. Arcidiacono, A. Baruffolo, E. Diolaiti, J. Farinato, E. Vernet-Viard, *MAD status report*, SPIE 5490, 236-245, 2004.
[9] P. Dierickx, B. Delabre, L. Noethe, OWL *optical design, active optics and error budget*, 2000, SPIE Proc. 4003.
[10] R. Gilmozzi, B. Delabre, P. Dierickx, N. Hubin , F. Koch, G. Monnet, M. Quattri, F. Rigaut, R.N. Wilson*, The Future of Filled Aperture Telescopes: is a 100m Feasible?*; 1998, Advanced Technology Optical/IR Telescopes VI, SPIE 3352, 778.
[11] Conclusions of the Workshop on Coronographic Methods for the Detection of Terrestrial Planets, A. Quirrenbach Ed., 2005 European Space Agency.
[12] J. Nelson, T. Mast, S. Faber, The Design of the Keck Observatory and Telescope, Keck Observatory Report No 90, 1985, p. 5-60.
[13] E. Sein, Y. Toulemont, J. Breysse, P. Deny, Pierre, D. de Chambure, T. Nakagawa, M. Hirabayashi,*A new generation of large SIC telescopes for space applications*, 2004, SPIE Proc. 5528.
[14] K. J. Aström, B. Wittenmark. ," Computer controlled systems – Theory and Design", Printice Hall, Englewood Cliffs, NJ, USA, 1984.
[15] I. D. Landau, R. Lozano, and M. M'Saad, " Adaptive Control", Springer-Verlag, London, 1997.

[16] K. Zhou, J.C. Doyle., “Essentials of Robust Control’’, Printice Hall, Upper Saddle River, New Jersey, 1998.
[17] B. Armstrong-Hélouvry, P. Dupont, C. Canudas de Wit, “ A survey of models, analysis tools and compensation methods for the control of machines with friction”, Automatica, Vol 30, No. 7, pp 1083-1138, 1994.
[18] D. Karnopp, “ Computer simulation of stick-slip friction in mechanical dynamic systems”, Trans ASME: Journal of dynamical systems, measurement and control, Vol. 107, pp 100-103, 1985
[19] C. Canudas de Wit , H. Olsson, K. J. Aström, P. Lischinsky, “A new model for control of systems with friction”, IEEE Trans. Automatic Control, Vol 40, pp 419-425, 1995.
[20] A. Preumont, “Vibration Conrtrol of active structures, an introduction”, 2nd Edition, Kluwer academic publishers, 2002
[21] A. Babinski, T. C. Tsao, “Acceleration feedback design for voise coil actuated direct drive”, Proceedings of the American Control Conference, pp 3713-3717, 1999.
[22] M. Jamshidi, “Large-scale systems: Modelling and Control”, Elsevier science Ltd, 1983.
[23] M.S. Mahmoud, M.F Hassan, M.G. Darwish, “Large-scale control systems”, Marcel Dekker, 1985.
[24] H. K. Khalil, “Nonlinear Systems”, Printice Hall, Third edition, 2002.
[25] P. V. Kokotovic, H. K. Khalil, “Singular Perturbations in Systems and Control”, IEEE Press, New York, 1986.
[26] T. Mast, J. Nelson, “Segment Control Control system Hardware for CELT”, Proc. SPIE, vol. 4003, 2000.
[27] R.C. Jared, “The W. M. Keck telescope Segmented Primary Mirror Active Control System ”, SPIE 1236 Advanced technology Optical Telescope IV. pp. 996-1008, 1990.
[28] S. Stanghellini, E. Manil, “ Design and Preliminary Test of the VLT Secondary Mirror Unit”, SPIE Vol. 2871, pp 105-116, 1996
[29] E. Brunetto, M. Dimmler, F. Koch, M. Quattri, M. Mueller, B. Sedghi, *OWL opto-mechanics, phase A*; 2004, Proc. SPIE 5489, in press.
[30] M. Quattri, F. Koch, L. Noethe, A. Correal Bonnet, S. Nölting; OWL *wind loading characterization: a preliminary study*; 2002, SPIE Proc. 4840.
[31] E. Brunetto, F. Koch, F. Biancat Marchet, M. Dimmler; Friction drive and bogies for owl's main axes, technological step backwards or cost effective alternative ?; 2002, Proc. SPIE 4840.
[32] E. Brunetto, F. Koch, M. Quattri, OWL: first steps towards designing the mechanical structure; 2000, Bäckaskog Workshop on Extremely Large Telescopes (Eds T. Andersen, A. Ardeberg, R. Gilmozzi), p 109.
[33] E. Brunetto, F. Koch, M. Quattri, OWL: further steps in designing the telescope mechanical structure and in assessing its performance; 2000, SPIE Proc. 4004.
[34] F. Bossens, Amortissement actif des structures câblées: de la théorie à l'implémentation, PhD thesis, Oct 2001
[35] Steven L. Kramer, Geotechnical Earthquake Engineering, University of Washington, 1996 Prentice-Hall, Inc., ISBN 0-13-374943-6
[36] Franz Koch, Analysis concepts for Large Telescope Structure under Earthquake Load, SPIE 2871-14, 1996.
[37] Chanan, G., MacMartin, D.G., Nelson,, J., and Mast, T., Control and alignment of segmented-mirror telescopes : matrices, modes, and error propagation, 2004, Appl. Optics, 43, 1223
[38] Noethe, L., Analytical expressions for optimum alignment modes of highly segmented mirrors, 2005, J. Mod.. Optics, 52(4), 603-632
[39] Tessieres, R., Analysis for alignment of optical systems, MSc. Thesis, Department of Optical Sciences, University of Arizona, 2003
[40] Tessieres, R., Burge, J.H., Alignment strategy for the LSST, LSST Observatory, June 2004
[41] Noethe, L., Active optics in modern large optical telescopes, 2002, Progress in Optics, Vol. 43, 1-69
[42] Ragazzoni, R., Marchetti, E., and Rigaut, F., 1999, Modal tomography for adaptive optics, Astron. Astrophys. 342, L53-L56
[43] Fusco, T., Partial correction and anisoplanetism in adaptive optocs : a posteriori processing and multi-conjugate adaptive optics, Thesis, ONERA PUB 2000-2, FR ISSN 0078-3780
[44] VLT Site Selection Working Group final report, VLT Report 62, November 14, 1990; Ed. M. Sarazin
[45] Erasmus, D.A. and D.S. Maartens, 1999: Operational Forecasts Of Cirrus Cloud Cover And Water Vapour Above Paranal And La Silla Observatories. European Southern Observatories Report under contract number 52538/VPS/97/9480/HWE.
[46] Erasmus, D.A. and M. Sarazin, 2000: Forecasting Precipitable Water Vapor and Cirrus Cloud Cover For Astronomical Observatories: Satellite image processing guided by synoptic model dissemination data. SPIE Conference on Image and Signal Processing for Remote Sensing IV. Paper SPIE-4168, Barcelona. 25-29 September, 2000.
[47] Erasmus, D.A. and D.S. Maartens, 2001: Maintenance, Upgrade and Verification of Operational Forecasts of Cloud Cover and Water Vapour above Paranal and La Silla Observatories. European Southern Observatories Report under contract number 58311/ODG/99/8362/GWI/LET.
[48] Erasmus, D.A., 2002: An Analysis of Cloud Cover and Water Vapour for the ALMA Project: A Comparison Between Chajnantor (Chile), Chalviri (Bolivia) and Five Sites in Argentina using

Satellite Data and Verification of Satellite PWV measurements. The ALMA Project, European Southern Observatory, Final Report. 66814/ODG/02/6419/GWI/LET. (Available from: http://www.eso.org/gen-fac/pubs/ astclim/espas/radioseeing/)

[49] Erasmus, D.A., and C.A. van Staden, 2003: A Comparison of Satellite-Observed Cloud Cover and Water Vapor at Mauna Kea and Selected Sites in Northern Chile, the Southwestern U.S.A. and Northern Mexico. Final Report. 31 August, 2003. New Initiatives Office, Aura Inc. 75pp.

[50] Erasmus, D.A., 2004: An Analysis and Comparison Of Satellite-Observed Cloud Cover and Water Vapor At Hanle, India and Yanbajing, Tibet. Experimental Particle Physics and High Energy Astrophysics Group. The Max-Planck-Institute for Nuclear Physics Heidelberg. Final Report. 31 January, 2004.

[51] Erasmus, D.A., 2004: An Analysis Of Satellite-observed Cloud Cover at Mt Hopkins Observatory and a Comparison with Ground-based Observations. The LSST Project Group, interim report, October 2004.

[52] E. Siher, S. Ortolani, M. Sarazin, Z. Benkhaldoun; *Correlation between TOMS aerosol index and astronomical extinction*; SPIE Conf. on astronomical Telescope and Instrumentation, Glasgow, Scotland, UK; SPIE 5489, 138-145 (2004).

[53] A. Jimenez et al. A&A Sup. Ser. 129, 413-423, 1998.

[54] E. Graham, M. Sarazin, M. Beniston, C. Collet, M. Hayoz, M. Neun, P. Casals; Climate-based site selection for a Very Large Telescope using GIS techniques; Meteorol. Appl. 12,

[55] M. Grenon, The Northern Chile Climate and its Evolution: a pluridisciplinary approach to the VLT site selection; *ESO Messenger* **61**, 11-16 (1990)

[56] Kornilov V.G., Tokovinin A.A. Measurement of the turbulence in the free atmosphere above Mt. Maidanak. Astron. Zhurn., 2001, V. 45, P. 459-473 (Astron. Rep., V. 45, P. 395-408). [in English: PDF, 470K]

[57] Tokovinin A., Kornilov V., Shatsky N., Voziakova O. Restoration of turbulence profile from scintillation indices. MNRAS, 2003, V. **343**, p. 891-899 [PDF, 419K]

[58] Wilson R.W., "SLODAR: Measuring optical turbulence altitude with a Shack--Hartmann wave-front sensor", MNRAS **337**, 103, 2002

[59] Wilson, R.W & Saunter, C.D., "Turbulence profiler and seeing monitor for laser guide star adaptive optics", proc. SPIE **4839**, 446, 2003

[60] R.W. Wilson, J. Bate, J. Guerra, N. Hubin, M. Sarazin, S. Sounter; Development of a portable SLODAR turbulence profiler; SPIE Conf. on astronomical Telescope and Instrumentation, Glasgow, Scotland, UK; SPIE 5490, (2004)

[61] M. Sarazin, F. Roddier The E.S.O Differential Image Motion Monitor; Astron. Astrophys. 227, 294-300 (1990)

[62] J. Vernin, C. Munoz-Tunon; Measuring astronomical seeing: The DA/IAC DIMM; vol. 107, no. 709, p. 265-272, 03-1995

[63] Tokovinin A. From differential image motion to seeing. PASP, 2002, V. 114, p. 1156-1166

[64] F. Martin, R. Conan, A. Tokovinin, A. Ziad, H. Trinquet, J. Borgnino, A. Agabi and M. Sarazin; Optical parameter relevant for high angular resolution at Paranal from GSM instrument and surface layer contribution; Astron. Astrophys. Supplement, v.144, p.39-44; June 2000

[65] Kornilov, V., Tokovinin A., Vozyakova O., Zaitsev A., Shatsky N., Potanin S., Sarazin M.; MASS: a monitor of the vertical turbulence distribution.; SPIE Conf. on astronomical Telescope and Instrumentation, Waikoloa, Hawaii, USA, Aug. 2002, paper SPIE-4839-102.

[66] Tokovinin, A.; Vernin, J.; Ziad, A.; Chun, M.; Optical Turbulence Profiles at Mauna Kea Measured by MASS and SCIDAR, PASP Volume 117, Issue 830, pp. 395-400, 04-2005

[67] A. Tokovinine, A. Ziad, F. Martin, R. Avila, J. Borgnino, R. Conan, M. Sarazin; Wavefront Outer Scale Monitoring at La Silla ; SPIE Vol. 3353, Adaptive Optical System Technologies, Kona, Hawaii (USA), 20-28 March 1998

[68] N. Hubin, M. Le Louarn M. Sarazin, A. Tokovinine; *New challenges for adaptive optics: the OWL 100m telescope* ; SPIE 4007, 27-31 March 2000, Munich, Germany

[69] M. Sarazin and A. Tokovinin; The statistics of isoplanatic angle and adaptive optics time constant derived from DIMM data Beyond Conventional Adaptive Optics, Venezia, 7-10 May 2001, ESO Conference Proceedings.

[70] Azouit, M.; Vernin, J.; Optical Turbulence Profiling with Balloons Relevant to Astronomy and Atmospheric Physics; PASP Volume 117, Issue 831, pp. 536-543, 05-2005.

[71] Patrick Minnis, J. Kirk Ayers and Steven P. Weaver, Surface-Based Observations of Contrail Occurrence Frequency over the U.S., April 1993--April 1994, NASA RP-1404, December 1997.

[72] Sausen, R., K. Gierens, M. Ponater, and U. Schumann, 1998. ADiagnostic study of the global distribution of contrails. Part I: Present day climate. Theoretical and Applied Climatology 61:127-141.

[73] Dames & Moore Inc., 1994, Seismic Hazard Analysis at two telescope sites, Mauna Kea, Hawaii and Cerro Pachon, Chile, Final Report for Gemini 8m Telescope Project.

[74] Sh.A. Ehgamberdiev, A.K. Baijumanov, S.P. Ilyasov, M. Sarazin, Y.A. Tillayev, A.A. Tokovinin, A. Ziad; The Astroclimate of Maidanak Observatory in Uzbekistan; Astron. Astrophys. Supplement v.145 p.293-304; August 2000

[75] Giovanelli, Riccardo; Darling, Jeremy; Sarazin, Marc; Yu, Jennifer; Harvey, Paul; Henderson, Charles; Hoffman, William; Keller, Luke; Barry, Don; Cordes, James; Eikenberry, Stephen; Gull, George; Harrington, Joseph; Smith, J. D.; Stacey, Gordon; Swain, Mark; The Optical/Infrared Astronomical Quality of High Atacama Sites. I. Preliminary Results of Optical Seeing; The Publications of the Astronomical Society of the Pacific, Volume 113, Issue 785, pp. 789-802, 07/2001.
[76] M. Jamshidi, “Large-scale systems: Modelling and Control”, Elsevier science Ltd, 1983.
[77] W. B. Rouse, “Engineering Complex Systems: Implications for Research in System Engineering”, IEEE Trans. on Systems, Man, and Cybernetics, Vol. 33, No.2, pp 154-156, 2003.
[78] M.S. Mahmoud, M.F Hassan, M.G. Darwish, “Large-scale control systems”, Marcel Dekker, 1985
[79] Y. Bar-Yam: “When Systems Engineering Fails --- Toward Complex Systems Engineering”, International Conference on Systems, Man & Cybernetics, Vol. 2, pp 2021- 2028, IEEE Press, 2003.
[80] S. P. Sethi, Q. Zhang, “Hierarchical Decision Making in Stochatic manufacturing System”, Birkhaeuser, 1994.
[81] T. Andersen, A. Ardeberg, M. Owner-Petersen, Editors,“ Euro 50-Design Study of a 50m Adaptive Optics Telescope”, Lund Observatory, 2003.
[82] G. Z. Angeli, J. Dunn, S. Roberts, D. MacMynowski, A. Segurson, K. Vogiatzis, J. Fitzimmons, “Modelling tools to estimate the performance of the Thirty Meter Telescope: an integrated approach”,SPIE, pp 5497-24, 2004.
[83] N. Yaitskova, K. Dohlen, P. Dierickx, “Diffraction in OWL: effects of the segmentations and segments edges misfigures”, SPIE 4840 p171-182
[84] N. Yaitskova, K. Dohlen, P. Dierick, “Analytical study of diffraction effects in extremely large segmented mirror” J. Opt. Soc. Am. A. p 1563-1575 2003
[85] M. Troy, G. Chanan Diffraction Effects from Giant segmented mirror telescopes spie 4840, p81-92)
[86] G. Chanan et al. Phasing the mirror segments of the Keck telescopes: the broadband phasing algorithm, Appl. Opt. V.37, No.1 p140-155
[87] N. Yaitskova, Performance analysis of Mach-Zehnder interferometer for detection of wavefront discontinuities, SPIE 5169, pp 62-71 (2003)
[88] N. Yaitskova et al.: Mach-Zehnder interferometer for piston tip tilt sensing in segmented telescopes: theory and analytical treatment, J. Opt. Soc. Am. A. Vol 22, No6, 2005
[89] G. Chanan, D. G. MacMartin, J. Nelson, T. Mast, “Control and aligment of segmented-mirror telescopes: matrices, modes, and error propagation”, Applied Optics, Vol. 43, No. 6, pp 1223-1232, 2004.
[90] D. G. MacMartin, “Local, hierarchic, and iterarive reconstructors for adaptive optics”, J. Opt. Soc. Am. A, Vol. 20, No 6, pp 1084-1093, 2003.
[91] G. Chanan, D. G. MacMartin, J. Nelson, T. Mast, “Control and aligment of segmented-mirror telescopes: matrices, modes, and error propagation”, Applied Optics, Vol. 43, No. 6, pp 1223-1232, 2004.
[92] D. G. MacMartin, “Local, hierarchic, and iterarive reconstructors for adaptive optics”, J. Opt. Soc. Am. A, Vol. 20, No 6, pp 1084-1093, 2003.
[93] F. Roddier Curvature sensing and compensation: a new concept in adaptive optics; Appl Opt, 27, 1223-1225, 1988
[94] R. Gonzales and J. Fuensalida Diffractional treatment of curvature sensing in segmented mirror telescope, proc spie 4837 726-736, 2003
[95] Schumacher, N. Devaney, DIPSS: cophasing segmented mirrors with minimal hardware requirements.
[96] G. Chanan, M. Troy, E. Sirko, Phase discontinuity sensing: a method for phasing segmented mirrors in the infrared, Applied Optics, 38,4, 704-713, 1999
[97] S. Esposito et al.: Cophasing of segmented mirrors using the pyramid sensor, SPIE, Volume 5169, pp. 72-78, 2003
[98] M. Loefdahl and H.Eriksson, “An algorithm for resolving 2p ambiguities in interferometric measurements by use of multiple wavelength”, *Optical Engineering*, **40**(6), pp. 984-990, 2001.
[99] V. Borkowski, A. Labeyrie, F. Martinache, D. Peterson, “Sensitivity of a “dispersed-speckles” piston sensor for multi-aperture interferometers and hypertelescopes”, A&A 429, 747-753 (2005)
[100] B. Ellerbroek and C. Vogel, Simulation of closed-loop wavefront reconstruction for multi-conjugated adaptive optics on giant telescopes,SPIE 5169, 206-217, 2003.
[101] C. Petit, F. Quiros-Pacheco, J.-M. Conan, C. Kulcsár, H.-F. Raynaud, T. Fusco, G. Rousset, *Kalman filter based control loop for adaptive optics*, SPIE 5490, 1460-1471, 2004
[102] F. Hammer, M. Puech, F. Assemat, E. Gendron, F. sayede, P. Laporte, M. Marteaud, A. Liotard, F. Zamkotsian, *FALCON: a concept to extend Adaptive Optics corrections to cosmological fields*, SPIE 5382, 220- ,2003
[103] S. Rabien, 2005 in preparation
[104] C. Verinaud, Optics Communications, Volume 233, Issue 1-3, p. 27-38 (2004).
[105] O. Guyon, The Astrophysical Journal, Volume 629, Issue 1, pp. 592-614 (2005).
[106] B. Ellerbroek, Journal of the Optical Society of America A: Optics, Image Science, and Vision, vol. 19, iss. no. 9, p. 1803-1816 (2002)

[107] L. Poyneer, Gavel D.T., Brase J.M., Journal of the Optical Society of America A, vol. 19, Issue 10, pp.2100-2111 (2002)
[108] L. Poyneer, J.P Veran, accepted in Journal of the Optical Society of America A, (2005).
[109] Le Roux, B.; Coyne, J., Ragazzoni, R., Applied Optics IP, vol. 44, Issue 2, pp.171-177 (2005).
[110] Lardiere, O., Carbillet, M, Riccardi, A., Salinari, P. Proceedings of the SPIE, Volume 5490, pp. 516-526 (2004).
[111] Codona, J.L., Angel, R., The Astrophysical Journal, Volume 604, Issue 2, pp. L117-L120 (2004).
[112] Stalcup, Thomas E., Jr.; Georges, James A., III; Snyder, Miguel; Baranec, Christoph; Putnam, Nicole; Milton, N. Mark; Angel, James Roger P.; Lloyd-Hart, Michael , Field tests of wavefront sensing with multiple Rayleigh laser guide stars and dynamic refocus, proc. SPIE, 5490, 2004
[113] Baranec, Christoph J.; Bauman, Brian J.; Lloyd-Hart, Michael, Concept for a laser guide beacon Shack-Hartmann wave-front sensor with dynamically steered subapertures, Optics Letters, Volume 30, Issue 7, pp. 693-695 (2005).
[114] Ageorges N., Els, S., 2004, Proc. SPIE Vol. 5490.
[115] Beletic, J, Follow the yellow-orange rabbit: a CCD optimized for wavefront sensing a pulsed sodium laser guide star. Proc. SPIE, 5499, 2004.
[116] Beletic, J, Follow the yellow-orange rabbit: a CCD optimized for wavefront sensing a pulsed sodium laser guide star. Proc. SPIE, 5499, 2004.
[117] Gilmozzi, R, 2000, "Science with 100m telescopes", Proc. SPIE Vol. 4005, p. 2-8, Discoveries and Research Prospects from 8- to 10-Meter-Class Telescopes, Jacqueline Bergeron (Ed)
[118] Hawarden, T, 2000, ISAS Report SP 14, 249
[119] Aparicio, A and Gallart, C, 2004, Astron J 128, 1465
[120] Adapted from a Table by I. Hook derived from the Science Book [RD526] (personal communication).
[121] Martin et al.,"Optical parameters relevant for high angular resolution at Paranal from GSM instrument and surface layer contribution", A&A 144, pp 39-44, 2000
[122] Conan et al., "Results of AO simulations at ESO", SPIE 4840, pp393-403, 2003
[123] Tokovinin, Le Louarn, Sarazin, "Isoplanatism in a multiconjugate adaptive optics system", JOSA A, 17, pp 1819-1827, 2000.
[124] Nicolle et al., "Ground layer adaptive Optics: analysis of the wavefront sensing issues", Proc. SPIE 5490, pp 858-869, 2004
[125] Gontcharov et al, 2005
[126] Petit et al, "Off-axis adaptive optics with optimal control: experimental and numerical validation. Proc SPIE 5903, pp 188-196, 2005
[127] Ellerbroek, CfAO retreat presentation, 2004
[128] Angel 2000
[129] Britton, M., "SLGLAO: an all-sky, wide field adaptive optics concept for TMT", Ringberg, 2005

Acknowledgements

Special thanks to

Adriano	Fontana	*INAF*
Alan	Moorwood	*ESO*
Almudena	Prieto	*MPIA / IAC*
Anders	Wallander	*ESO*
Andreas	Glindemann	*ESO*
Andreas	Kaufer	*ESO*
Andy	Longmore	*ATC*
Anthony	Boccaletti	*LESIA*
Antonio	Manescau	*ESO*
Arno	van Kesteren	*ESO*
Bernard	Delabre	*ESO*
Bertrand	Koehler	*ESO*
Brice	Le Roux	*INAF*
Bruno	Leibundgut	*ESO*
Christian	Thalmann	*Swiss Federal Institute of Technology*
Constanza	Araujo	*ESO*
Daphne	Stam	*Astronomical instiute of Amsterdam*
David	Mouillet	*LAOMP*
Etienne	Le Coarer	*LAOG*
Fabio	Biancat Marchet	*ESO*
Florian	Kerber	*ESO/ST-ECF*
Franck	Selsis	*ENS Lyon*
Françoise	Delplancke	*ESO*
Gero	Rupprecht	*ESO*
Gerry	Gilmore	*Cambridge University*
Gianpaolo	Bertelli	*INAF*
Hans Martin	Schmid	*ETH Zurich*
Hans Walter	Rix	*MPIA*
Harald	Kuntschner	*ESO*
Hneri	Bonnet	*ESO*
Jaap	Tinbergen	*Astronomical instiute of Amsterdam*
Jacopo	Antichi	*INAF*
Jean Gabriel	Cuby	*LAM*

Jean-Luc	Beuzit	*LAOG*
Jutta	Quentin	*ESO*
Kjetil	Dohlen	*OAMP*
Krister	Wirenstrand	*ESO*
Laura	Greggio	*INAF*
Massimo	Castellano	*INAF*
Markus	Feldt	*MPIA*
Martin	Cullum	*ESO*
Massimo	Della Valle	*INAF*
Massimo	Turatto	*INAF*
Matteo	Lombini	*INAF*
Maximilian	Kraus	*ESO*
Michael	Cantzler	*ESO*
Philippe	Gitton	*ESO*
Pierre	Baudoz	*LESIA*
Roberto	Ragazzoni	*INAF*
Rainer	Lenzen	*MPIA*
Ralf	Conzelmann	*ESO*
Regina	Esteves	*ESO*
Reinhold	Dorn	*ESO*
Remi	Soummer	*STSCI*
Silvano	Desidera	*INAF*
Stefano	Stanghellini	*ESO*
Timoty	Butterley	*Durham University*
Tom	Herbst	*MPIA*
Uli	Kauefl	*ESO*
Wolfgang	Gässler	*MPIA*

Airlight	(Switzerland)
AMOS	(Belgium)
Arup Gmbh	(Germany)
ASTRIUM	(France)
ASTRON	(The Netherlands)
Astronomical Technology Centre - ATC	(UK)
BOOSTEC	(France)
Centre de Recherches Astronomiques de Lyon	(France)
CGI AG Winterthur	(Switzerland)
CL-MAP Gmbh	(Germany)
CORNING	(USA)
Donges Stahlbau	(Germany)
ECM	(Germany)
Ecole Polytechnique Fédérale de Lausanne	(Switzerland)
FOGALE	(France)
GRANTECAN	(Spain)
Helbling	(Switzerland)
IHF Ingenieurbüro Huss & Feickert	(Germany)
Innauen-Schaetti AG	(Switzerland)
Innaune-Schaetti	(Switzerland)
Instituto de Astrofisica de Canarias	(Spain)
Jodrell Bank Observatory	(UK)
Laboratoire d'Aéronomie de Marseille	(France)
Leiden University	(The Netherlands)
LISE, College de France	(France)

LZOS	(Russia)
Max Planck Institut für Astrophysics	(Italy)
MenloSystems GmbH	(Germany)
Micromega	(Belgium)
Observatoire de Genève	(Switzerland)
Observatoire de Paris	(France)
ONERA	(France)
Osservatorio di Arcetri	(Italy)
Osservatorio di Padova	(Italy)
Osservatorio di Trieste	(Italy)
Passera Pedretti & Partners	(Switzerland)
PSP-Technologien im Bauwesen GmbH	(Germany)
SAGEM	(France)
SCHOTT	(Germany)
SESO	(France)
SNECMA	(France)
Université Libre de Bruxelles	(Belgium)
University of Cambridge	(UK)
University of Lund	(Sweden)
ZEISS	(Germany)

We wish to express our heartful thanks to all Astronomers who contributed to the *Science Book*[76] for their innovative ideas and stimulating discussions.

[76] The science case for the European Extremely Large telescope", 2005, Isobel Hook (Ed), published by Opticon ("Science Book").

Contributors

Aglae	Kellerer	*ESO*
Andre	Erasmus	*SAA Observatory*
Andrei	Tokovinin	*CTI Observatory*
Armando	Riccardi	*INAF*
Babak	Sedghi	*ESO*
Bernhard	Brandl	*Leiden University*
Bill	Dent	*UKATC*
Brice-Olivier	Demory	*Geneva Observatory*
Carlos	Correia da Silva	*ESO*
Catherine	Césarsky	*ESO*
Cesare	Barbieri	*Padova University*
Chris	Saunter	*Durham*
Christophe	Vérinaud	*ESO*
Dainis	Dravins	*Lund University*
Deli	Geng	*Durham*
Domenico	Bonaccini	*ESO*
Edward	Graham	*Fribourg University*
Emiliano	Diolaiti	*INAF*
Enrico	Fedrigo	*ESO*
Enrico	Marchetti	*ESO*
Enzo	Brunetto	*ESO*
Farid	Rahoui	*ESO*
Fernando	Quiros-Pacheco	*ESO*
Franz	Koch	*ESO*
Frédéric	Derie	*ESO*
Frédéric	Gonté	*ESO*
Gerard	Rousset	*ONERA*
Guy	Monnet	*ESO*
Hans-Ulrich	Kaeufl	*ESO*
Isabelle	Surdej	*ESO*
Isobel	Hook	*Oxford University*
Jason	Spyromilio	*ESO*
Jean Marc	Conan	*ONERA*
Jerome	Paufique	*ESO*
Johann	Kolb	*ESO*
Julio	Navarrete	*ESO*
Lothar	Noethe	*ESO*
Marc	Sarazin	*ESO*
Marco	Quattri	*ESO*
Mark	Casali	*ESO*

Mark	Robinson	*ESO*
Markus	Kasper	*ESO*
Martin	Dimmler	*ESO*
Michael	Müller	*ESO*
Miska	le Louarn	*ESO*
Nancy	Ageorges	*ESO*
Natalia	Yaitskova	*ESO*
Norbert	Hubin	*ESO*
Peter	Quinn	*ESO*
Philippe	Dierickx	*ESO*
Pierre	Sansgasset	*ESO*
Rafaele	Gratton	*INAF*
Ralf	Siebenmorgen	*ESO*
Richard	Wilson	*Durham University*
Roberto	Gilmozzi	*ESO*
Roberto	Tamai	*ESO*
Robin	Arsenault	*ESO*
Sandro	d'Odorico	*ESO*
Sebastien	Rabien	*MPE*
Sergio	Ortolani	*Padova Observatory*
Simone	Esposito	*INAF*
Stephen	Goodsell	*Durham*
Sylvain	Oberti	*ESO*
Tatyana	Sadibekova	*ESO*
Thierry	Fusco	*ONERA*
Wolfram	Freudling	*ESO/ST-ECF*

Appendix 1.The ELT Design Study

This appendix provides a brief descriptive of the Work Packages of the ELT Design Study. Work Packages are outlined in section A-1.1 and a more detailed description is provided in A-1.2 to A-1.10. The list of participants is provided in Appendix 2

A-1.1 Work Packages

WBS No	Descriptive Title	Leading participant	Short description and specific objectives of the task
01000	*Project Coordination & Management*	**ESO**	Overall coordination of the project, reporting to the EC. Operation of the Project Office. Project management and top level system engineering incl. management of interfaces. Verification and consolidation of technical and managerial data.
02000	Science requirements	**INAF**	Consolidation and prioritization of top level requirements applicable to 50- to 100-m visible and near-infrared telescope.
04000	Wavefront Control	**ESO**	Technical and managerial coordination of tasks No 04100 to 04800; reporting to Project Management.
04200	Metrology	**ESO**	Objectives: • Feasibility and performance of a metrology system for coarse alignment of the optics of an Extremely Large Telescope; • Feasibility and performance of low-cost position sensors for the phasing of segments. Tasks: development, design, supply and testing of cost-effective metrology systems, in particular alignment systems and position sensors for the phasing of segments. Fabrication of 24 position sensors for WEB. Feasibility study for serial production and integration of up to 20,000 position sensors.

04300	Position actuators	**ESO**	Objective: feasibility of nm-accuracy, cost-effective segments position actuators. Tasks: development, design, supply and testing of actuators for the positioning of segments; supply of 18 position actuators for the Wind Evaluation Breadboard (04800); feasibility study for cost-effective serial production and integration of up to 10,000 units.
04400	Characterization of image properties	**ESO**	Objectives: quantify crucial system requirements in relation to science objectives. Tasks: Parameterization of image properties in relation to scientific requirements, error sources, design and fabrication constraints; determination and specification of most suitable parameters for the characterization of science image contrast.
04500	High contrast imaging	**ESO**	Objectives: identify and quantify extreme contrast imaging techniques (mainly for Exoplanets imaging and spectroscopy). Tasks: review, development of high contrast imaging methods. Identification of most promising techniques, performance evaluation (by way of simulations); implications on system / subsystems specifications.
04600	APE (Active Phasing Experiment)	**ESO**	Objectives: representative testing of control strategies and techniques. Tasks: Design, construction, laboratory and on-sky testing of a technical instrument emulating active wavefront control functions of an Extremely Large Telescope, including three distinct on-sky phasing techniques.
04800	WEB (Wind Evaluation Breadboard)	**ESO**	Objectives: quantify ability to cope with high frequency wind disturbances. Tasks: Design, construction, verification and on-site testing of a bench emulating 7 segments, including electromechanical support systems and support structures. The bench will eventually be exposed to wind flow on a representative observatory site (la Palma, Canary Islands, Spain), in order to ascertain the performance of the segments supports and control systems in relation to wind excitation, with a view to verifying that high spatial and temporal frequency wind disturbances can be controlled to acceptable accuracy.
05000	Optical Fabrication	**ESO**	Technical and managerial coordination of tasks 05100 and 05200; reporting to Project Management.
05100	Silicon carbide prototypes	**ESO**	Objectives: validate Silicon Carbide as a suitable substrate for segmented apertures, improve figuring techniques in relation to segment edge misfigure (eliminate the need for wasters). Tasks: fabrication and testing of 1-m class Silicon Carbide segments (up to 8 pcs): segments design and fabrication process optimization; evaluation of polishable overcoatings and alternatives to diamond slurries; control of high spatial frequency misfigure.
05200	Optical finishing and edge control	**UCL**	Development of optical finishing processes for fast, cost-efficient removal of high spatial frequency misfigure on classical substrates and Silicon Carbide, with particular emphasis on the control of segment edge misfigure.
06000	Mechanics	**ESO**	Technical and managerial coordination of tasks 06100 to 06400; reporting to Project Management.

06100	Structural ropes	**ESO**	Objective: improve stiffness of telescope structures (qualify alternative to steel ropes). Tasks: • Define alternative material to steel ropes. • Define fittings and mechanical interfaces. • Define thermal compensation and tension control devices. • Define maintenance criticality and concept. • Define suppliers and costs.
06200	Composite structural elements	**ESO**	Objectives: reduce structure mass at critical locations; improve structural performance (stiffness, safety). Tasks: • Define alternative material to steel cylindrical pipes. • Define fittings and mechanical interfaces. • Define manufacturing and installation methods. • Define maintenance criticality and concept. • Define suppliers and costs.
06300	Magnetically levitated systems and linear drives	**ESO**	Objectives: evaluate an alternative to friction drives, with a view to relaxing dimensional tolerances of an ELT kinematics, improving performance, reliability and simplicity of the kinematics control system. Tasks: • Define an integrated solution of Magnetic Levitation, guidance and linear drives applied to ELT requirements. • Define different kinds of geometry. • Define Specifications for an eventual construction of a prototype. • Define maintenance criticality and concept. • Define suppliers and costs.
06400	Characterization of the friction drive and bearing	**ESO**	Objective: characterize the performance of a friction drive solution (telescope kinematics). Tasks: design, fabrication and testing of a breadboard friction drive; provide cost estimate and potential suppliers for the production of several hundreds units.
08000	Enclosure & infrastructure	**Grantecan**	Technical and managerial co-ordination of 08100 and 08300; reporting to Project Management.
08100	Enclosure concepts	**Grantecan**	Objectives: conceptual design and characterization of enclosure concepts. Tasks: Specification, statement of work and follow-up of the conceptual design of 3 enclosure concepts. The design will include studies on cost and feasibility; analysis of structures, materials and mechanisms, in relation to size.
08300	Wind studies	**ESO**	Objectives: characterize and quantify wind buffeting on structures and optics. Tasks: Specification, statement of work and follow-up of wind studies. Computational fluid dynamics and wind tunnel test will be carried out. The influence of the enclosure type on the telescope performance will be studied from the mechanical point of view (wind buffeting on the primary mirror) and from the thermal point of view (air renovation in the telescope chamber).
09000	Adaptive optics	**INAF**	Technical and managerial co-ordination of 09200 to 09600; reporting to Project Management.

09200	1st generation AO & MCAO design for ELTs	**ESO**	Objectives: Develop a roadmap for the implementation of Adaptive Optics on a European ELT, incl. 2 conceptual designs, Single Conjugate (SCAO), Ground Layer (GLAO), and 1 straw man design of a dual-conjugate AO system for ELT. Tasks: Analysis of the Scientific top level requirements, and input interfaces, development of 2 conceptual and 1 strawman designs, review of the system trade-off, development of the two AO conceptual designs (SCAO, GLAO), organize 2 conceptual design reviews.
09300	Large format, high density DMs R&D	**ESO**	Objectives: development of large (2-4m) adaptive mirror solutions. Tasks: Specification and analysis of three possible large deformable mirrors with 100-50mm (DM-TEC 0), 25 (DM-TEC 1) and 10 mm (DM-TEC 2) actuator inter-spacing. Trade-off studies for the selection of the best type of actuators for DM-TEC 0 and DM TEC 2. Design and development of prototypes for DM-TEC 0 (actuator only), DM-TEC 1 and DM-TEC 2. Manufacturing of a 650 mm flat thin shell using double face large dimension polishing machine. Manufacturing of curved thin glass membrane mirrors involving slumping technique.
09400	Novel AO concepts	**INAF**	Objectives: develop AO concepts for high sky coverage down to visible wavelengths. Tasks: studies, at conceptual level, of novel concepts in Adaptive Optics, with particular focus on 1) wavefront sensing assisted by artificial Laser Guide Stars and 2) resolution of cone anisoplanetism in telescopes with apertures in the 50 to 100m range.
09500	AO & MCAO simulations	**ESO**	Objectives: Develop analytic and numerical simulation tools to support the design activities defined in WP 09300. Provide performance estimates of the SCAO, GLAO, dual conjugate AO for given input parameters provided by WP 09300 Tasks: Analysis of the Scientific Top Level Requirements and input parameters. Develop the analytical and numerical simulation tools for the SCAO, GLAO, Dual conjugate AO systems for an ELT diameter of 60-100 m. Provides first order performance estimates for the strawman design review. Provide accurate performance estimates for each AO system at their respective conceptual/straw man design review.
09600	Algorithms for reconstruction & control	**INSU**	Objectives: optimize Adaptive Optics reconstruction algorithms and control; relax computing power requirements; provide Real Time Computer (RTC) conceptual designs for WP 09300 Tasks: Define and analyse the AO system parameters (SCAO, GLAO, Dual Conjugate AO), define control and reconstruction algorithms, define Real Time Architecture estimate the RTC computing time, dimensioning using classical (full matrix) methods and identification of critical issues, development and analysis of new methods. Evaluate performance of algorithms, control and platform.
10000	Observatory & science operations	**ESO**	Analysis of technical and scientific operational scenarii for an ELT.
11000	Instrumentation	**UKATC**	Technical and managerial coordination of tasks 11100 to 11300; reporting to Project management

11100	Point designs	**UKATC**	Objectives: produce advanced point designs of up to three instruments. Tasks: utilizing results from DS38 pursue 3 conceptual designs in sufficient detail to establish their full scientific potential and their implications and requirements for the Telescope design. Candidate designs are: • WFSPEC (Wide-Field seeing-limited or Boundary-layer-corrected Optical/NIR Spectrometer) • MOMSI (Multi-Object and Multi-field Spectrometer and Imager for operation with MCAO in the NIR/optical) • MIDIR (Mid-IR spectrometer and imager).
11200	Other design prospection	**UKATC**	Objectives: produce instruments conceptual designs. Tasks: pursue Phase A studies of 8 instrument concepts to confirm the 3 selected in activity #11100, maximize understanding of telescope design impacts and scientific relevance, and provide broader perspective on ELT instrumentation requirements. Concepts include: WFSPEC, MOMSI and MIDIR, plus Planet Finder (XAO-coronagraphic instrument seeking terrestrial-sized planets, HiTRI (High time-resolution Instrument), HISPEC (very high spectral-resolution optical/NIR spectrometer), GRB-catcher (Imager-spectrometer for rapid response to transient phenomena) and SCUBA-3 (large-format submm imager). A survey for innovative new concepts will also be carried out.
11300	Atmospheric Dispersion Compensation	**UKATC**	Initial study of Atmospheric Dispersion and its compensation will be carried out to inform the other Phase A studies.
12000	Site Characterization	**Université de Nice**	Objectives: define the 5 top astronomical sites suitable to install an ELT under best conditions, and characterize them. Review, discuss and synthesize the site observations.
12100	Review of site parameters space	**Université de Nice**	Objectives: define standard site parameters for an ELT. Tasks: review the relevant parameters to fulfill the goals of an ELT, including but not limited to Adaptive Optics and Multi-conjugate AO.
12200	Instrumentation, measurements and modelling	**Université de Nice**	Objectives: design, build and operate standard site measurement equipment. Tasks: construct and set up an instrumentation adapted to fulfill 12100 requirements. Homogeneous, standardized measurements of these parameters at all the sites.
12300	Large scale atmospheric properties	**Université de Nice**	Investigate wave front properties over large baselines (100-200m).
13000	System layout, analysis & integrated modelling	**Lund University**	Technical and managerial coordination of interfaces to other work packages, reporting to Project Management.

13100	Integrated modelling – development of tools	**Lund University**	Objective: Establish integrated simulation tools to predict system performance under influence of disturbances from atmospheric turbulence, wind, gravity and temperature... Tasks: For a cluster computer, formulate algorithms, set up framework, code, and validate building blocks for integrated simulation of an Extremely Large Telescope including subsystems such as structure, control systems, telescope optics, adaptive optics, wavefront sensors, and deformable mirrors. Establish and validate models of atmospheric seeing and wind disturbances. Crosscheck models using control theory wherever possible. Establish ordinary differential equation solvers for large, stiff systems on cluster computers.

660

Table A- 1. ELT Design Study - overview of the Work Packages.

A-1.2 Wavefront control

This Work Package covers the development of essential, non-adaptive wavefront control technologies, the assessment of diffractive properties, and the development and evaluation of high contrast imaging techniques. All tasks in this Work Package are directly relevant to OWL and were indeed initially conceived as integral part of its development. They have been transferred into the ELT Design Study framework because of their relevance to any ELT design.

Internal Metrology – Any ELT will have to rely on internal metrology systems to guarantee coarse alignment of the optical surfaces and phasing of the segmented ones.

Analysis of the OWL design shows that controlling relative distances of the optical surfaces within 10 ppm (goal 1 ppm) provides significant advantages (performance, overheads) for subsequent closing of the active optics loop –including fine alignment. FOGALE[77] is developing a fibre extensometer, which itself is an evolution of the subsystem delivered to SALT and used to track the prime focus payload alignment. A proof-of-concept experiment is foreseen, and if successful a prototype fibre extensometer will be tested on the VLT.

A second task of FOGALE is the development of position sensors for controlling local piston between adjacent segments. Bandwidth, accuracy and low cost[78] are essential requirements. The current baseline is and inductive sensor technology, capacitive sensors being a backup. After prototyping and laboratory testing, a set of 24 sensors will be delivered for subsequent integration into the WEB experiment (see below). The sensors main specifications are listed in Table A- 2, and the design volume and implementation in Figure A- 9 and Figure A- 2.

Characteristic	**Specification**	**Remark**
Short term noise:	< 0.2nm/sqrt(Hz)	over the bandwidth [1;100] Hz
Long term noise:	< 5 nm/sqrt(Hz) (TBC)	over the bandwidth [5.8.e-6;1] Hz.
(includes the low frequency drift of the sensor over a period of 2 days)		
Maximum operation range	+/-0.5mm	
Absolute accuracy	≤ 0.1% of measuring range	
Bandwidth	≥ 100 Hz at -3dB	The position shall be delivered in digital format at a rate of up to 1kHz.

Table A- 2. Position sensors main specifications.

[77] A French SME specialized in metrology systems.

[78] Target cost ≤ € 1,000.- per unit sensor, taking into account a total production of up to 20,000 units.

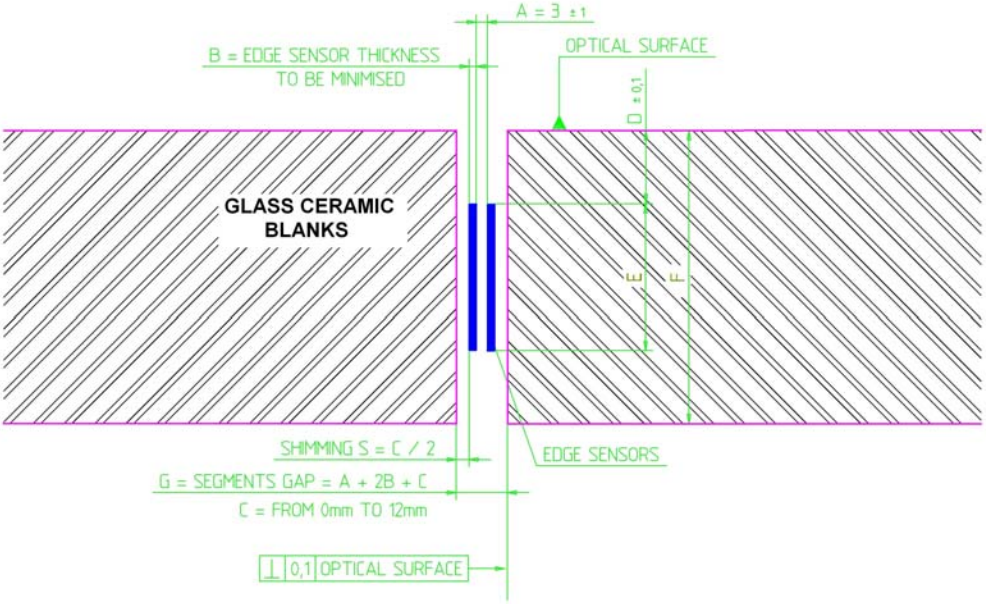

Figure A- 1. Allocated volume for the Position sensors (Glass ceramic blanks).

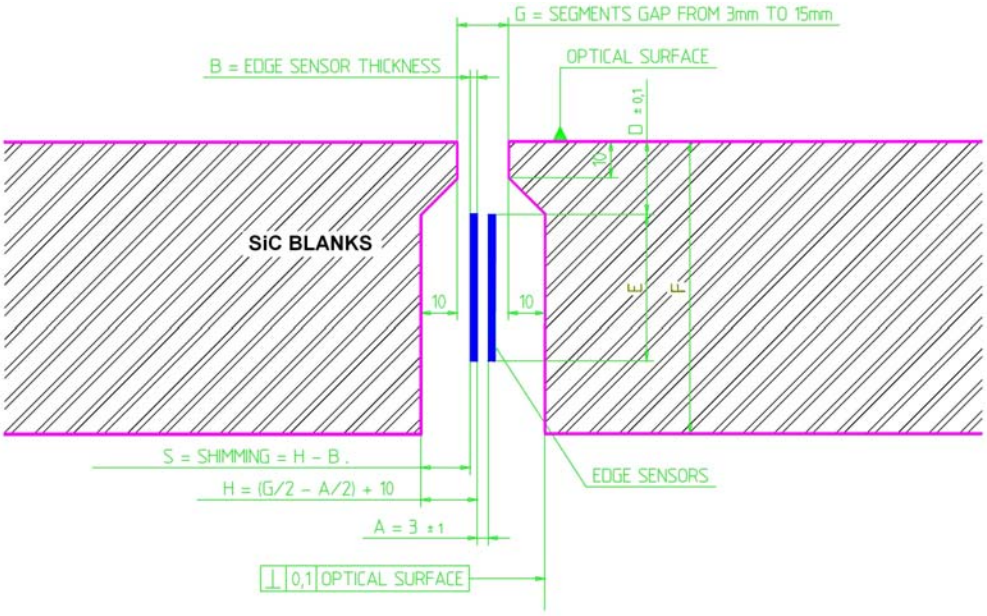

Figure A- 2. Allocated volume for the Position sensors (Silicon Carbide blanks).

Position actuators – This task covers the development and testing, under ESO contract, of actuators for the active positioning of the segments. Technical specifications are provided in reference document RD502. In the following we assume 2-stages actuators, with a coarse stage for low frequency, large amplitude correction and a fine stage for high frequency, fine adjustment.

Two types of actuators are under development, one for solid, glass or glass-ceramic segments, one for lightweight, presumably Silicon Carbide segments. Table A- 3 gives the essential characteristics of the position actuators, and their implementation is shown in Figure A- 3. A total of 18 actuators, 9 of each type, will be delivered for integration and testing in WEB.

Characteristic		Requirement	Goal
Max. axial load[79]	Glass ceramic segments	1,700 N	N/A
	SiC segments	600 N	N/A
Minimum axial resonance frequency		120 Hz	N/A
Accuracy	Coarse stage	± 0.05 mm	± 0.01 mm
	Fine stage	± 5 nm	± 2 nm
Stroke	Coarse stage	15 mm	30 mm
	Fine stage	0.5 mm	1.0 mm
Closed Loop Bandwidth	Coarse stage	0.5 Hz	N/A
	Fine stage	10 Hz	20 Hz
Maximum unit cost[80]	Glass ceramic segments	€ 4,000.-	€ 3,000.-
	SiC segments	€ 3,500.-	€ 2,000.-

Table A- 3. Position actuators, essential characteristics.

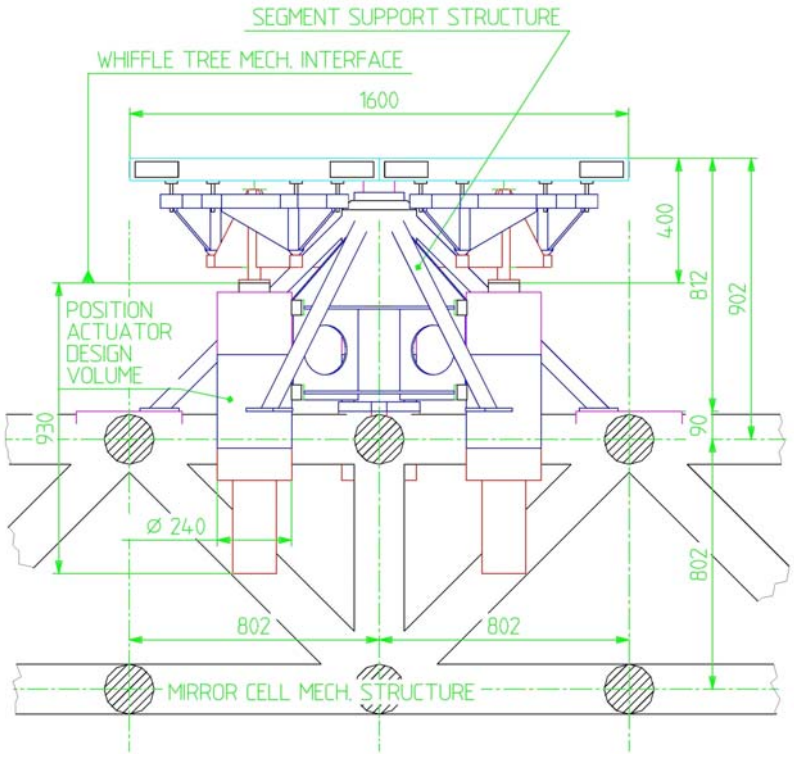

Figure A- 3. Position actuators. Implementation and design volume.

Wind Evaluation Bench – WEB is a crucial experiment for the assessment of performance under wind excitation. Being high temporal hence spatial frequencies the most hazardous ones (and the most difficult to model), experimentation does not require building a large subset of an ELT primary mirror. Currently in the design phase (see Figure A- 4 and Figure A- 5), WEB will incorporate 7 aluminium panels emulating either solid or lightweight segments, and be exposed to open air at a representative site (ORM on La Palma). One panel is rigidly fixed on a structure emulating the primary mirror support substructure, the other 6 mounted on position actuators

[79] In compression and tension.

[80] assuming a production of up to 10,000 units.

and fitted with edge sensors. The edge sensors signal will be regularly cross-checked by means of laser metrology or equivalent. The bench can be rotated azimuthally and inclined to vary its orientation with respect to wind. A skirt can be mounted around the outer edge to avoid that measurements be contaminated by turbulence at the edge of the assembly. WEB will, therefore, allow direct measurement of phasing performance under representative conditions. Detailed specifications are available in RD503.

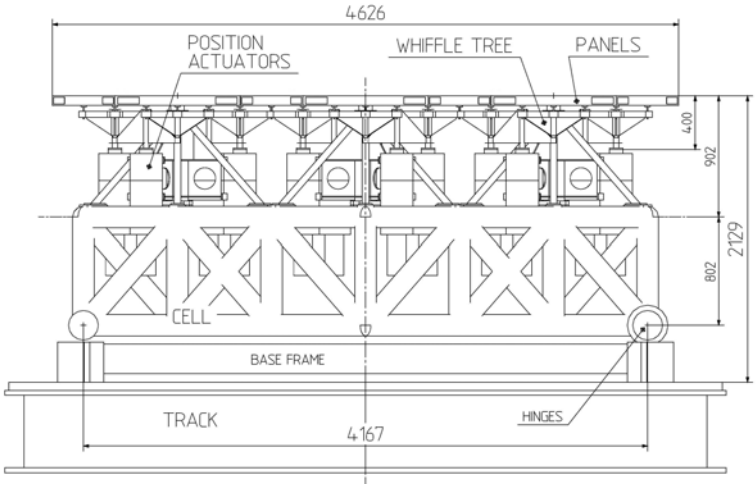

Figure A- 4. WEB 0º layout (zenith), side view.

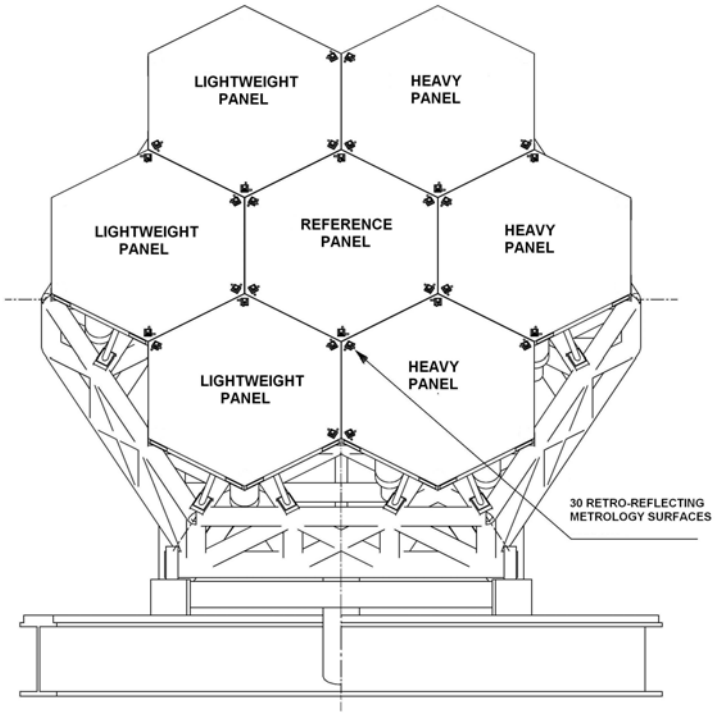

Figure A- 5. WEB 60º layout, front view.

The WEB experiment shall be completed by end of 2007, in-time for a final decision as to open air operation and for the final specifications of the actuators (taking into account the fact that the segments substrate technology will be selected by 2008, see also section A-1.3). ESO has overall responsibility for the experiment; other main contributors include IAC, MEDIA, and JUPASA.

Active Phasing Experiment **–** The essential purpose of the APE experiment is to explore, integrate and validate non-adaptive wavefront control schemes and technologies for an ELT. This includes:

- Evaluating and comparing the performance of phasing wavefront sensors, in the laboratory and on-sky;
- Integrating segmented aperture control into an active system (including field stabilization and active optics), and driving both the active system and the segments control system from the output of the system.

To this end, APE is conceived as a technical instrument to be installed and tested on-sky at a Nasmyth focus of a VLT unit telescope and shall have two options:

- The telescope shall provide all active functions (field stabilization, focusing, centering, active deformable mirrors) and the APE instrument shall emulate the optical effect of segmentation only.
- Or the telescope shall provide only the active deformable mirrors functions and the APE instrument shall emulate the optical effect of segmentation and shall command the other active functions (field stabilization, focusing, centering).

In practice, this is to be realized by re-imaging the telescope pupil onto a small segmented mirror (ASM), and by directing the output beam(s) of the instrument towards a metrology module (see Figure A- 6 for a block-diagram of the instrument and Figure A- 7 for the layout of the optical design).

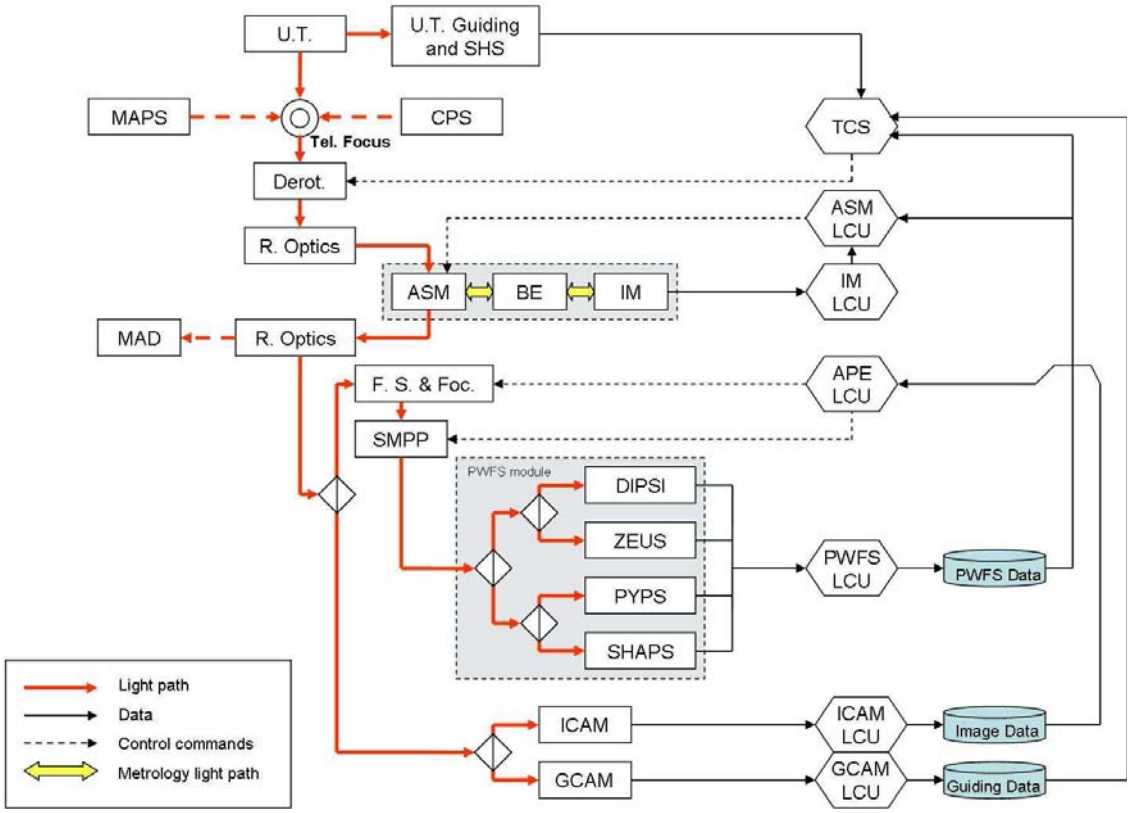

Figure A- 6. Block-Diagram of APE.

The segmented mirror will be controlled in piston and tip-tilt of the segments, being it implied that each segment would be mounted on 3 position actuators. The phasing wavefront sensor module will include four phasing wavefront sensors PWFS, each based on a different technology (curvature sensor, phase filtering, pyramid sensor, Shack-Hartmann sensor).

Tests will be performed stepwise as specified in Reference Document RD508, and include:

- Open- or deferred closed-loop laboratory measurements of the performance of the phasing WFS on a point-like polychromatic source;
- Open- or deferred closed-loop laboratory measurements of the performance of the phasing WFS on a point-like polychromatic source, in the presence of atmospheric turbulence (the latter being emulated by suitable turbulence generator). Wavefront offsets may be introduced in the input beam to emulate field aberrations.
- Open- or deferred closed-loop laboratory measurements of the performance of the phasing WFS and of the guiding & active optics WFS, in real conditions at the focus of a VLT unit telescope.

These tests will be performed with a single segmented mirror, and then repeated after introducing a piston plate simulating a secondary segmented mirror in the light path, with a view to emulating multiple segmentation with mismatched patterns. In a possible follow-up to the above, APE may be interfaced to MAD for laboratory testing of the combined two systems.

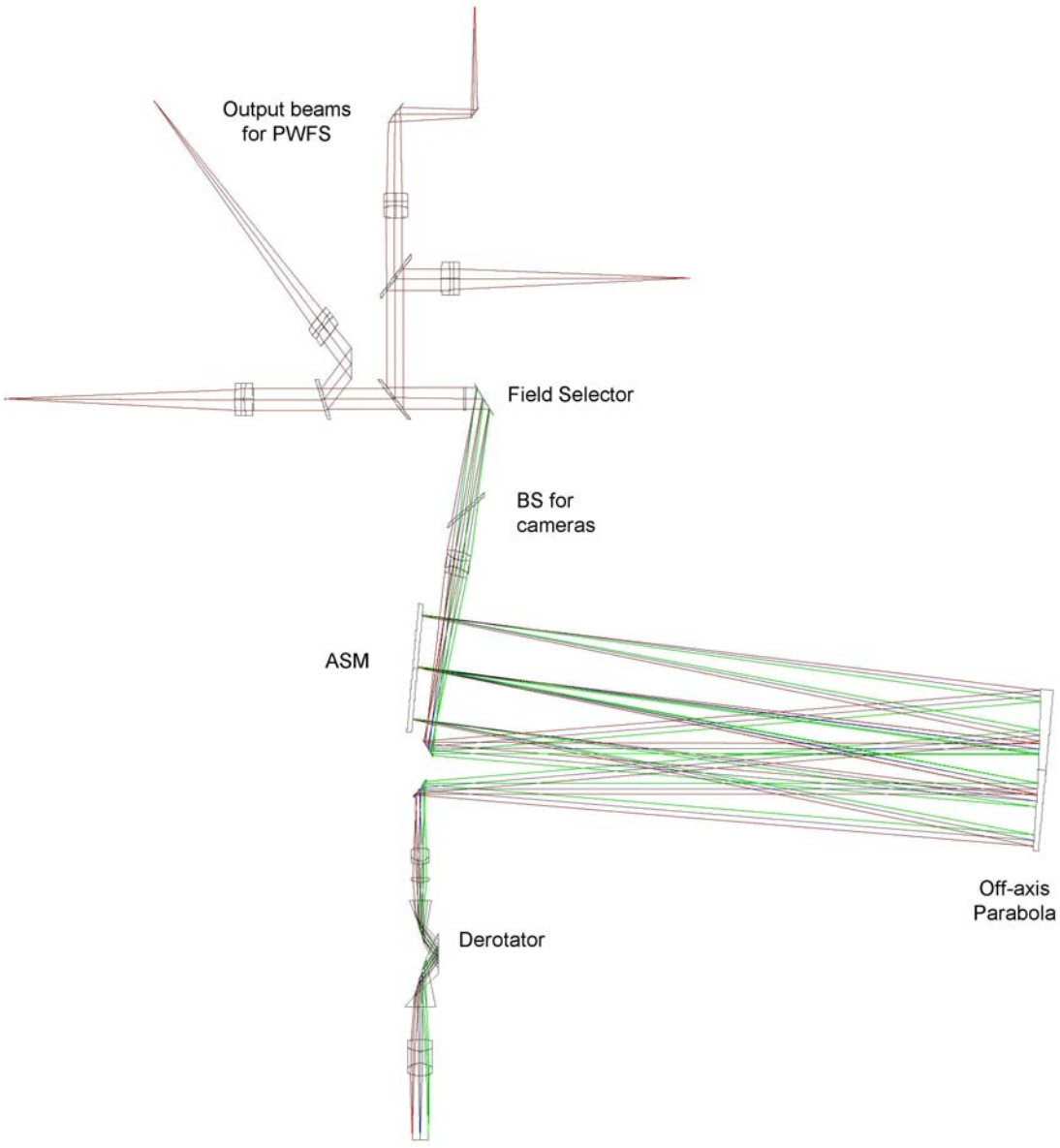

Figure A- 7. APE optical design; the telescope focus is at the bottom of the figure. PWFS: Pyramid WaveFront Sensor; BS: Beam Splitter; ASM: Active Segmented Mirror.

To a large extent extrapolation of current telescope technologies to extreme sizes relies on proven fabrication technologies. Indeed there is little doubt that the major components of a giant telescope could readily be produced. At system level, however, successful integration and performance will rely on complex, interacting control systems. APE is conceived as a crucial test and learning tool i.e. as a major step towards alleviating system risks.

Currently in the design phase, APE shall deliver laboratory and on-sky results by 2007, in-time for the final design of OWL active and phasing control systems. ESO has overall responsibility for the instrument; other main contributors include the FOGALE, IAC, INAF and INSU (Laboratoire d'Astrophysique de Marseille).

Characterization of image properties – Not strictly speaking a subset of wavefront control, characterization of image properties forms part of a global approach towards specifying performance. A similar undertaking with the VLT led to a consistent formalism[81] towards specifying performance and establishing error budgets [7]. The essential objectives of this task are

- To translate science requirements into performance criteria which can be subsequently used for error budgeting and specifications.
- To establish a consistent description of image properties, with a view to allowing scientists to perform simulations and assess performance in relation to their science objectives.

In view of the fact that most science objectives require at least some degree of adaptive correction, the role of diffraction is primordial and this task is considerably more complex than it was with the VLT.

The main contributor is ESO.

High contrast imaging – Very high contrast imaging techniques are required, most notably for exoplanets. Several techniques are described in RD22 and are explored in the framework of the ELT Design Study. Diffraction by the segmented aperture is an evident –and unavoidable- source of concern. There are indications, however, that this effect could be alleviated to some extent, by using suitably designed –albeit rather complex- apodization masks. It should be noted that coronagraphic techniques become more efficient with extremely large telescope diameter, because a given angular size of the mask corresponds to a correspondingly larger area in terms of λ/D.

The main contributors are INSU and ESO.

A-1.3 Optical fabrication

The optical fabrication Work Package focuses on the validation of Silicon Carbide as an alternative to conventional glass-ceramics material. According to industrial studies (see RD9 and RD10), moderately lightweight silicon carbide blanks[82] could be an alternative to conventional glass or glass-ceramic. Optical figuring is substantially more expensive see RD11 and RD12) but substantial simplification of the telescope structural design and higher bandwidth of the segments phasing control system would potentially compensate for such drawback. Silicon carbide blanks, however, are not directly polishable to acceptable micro-roughness and a polishable overcoating is generally required.

The main tasks of this Work Package are:

- To determine optimal characteristics (technology, process, thickness) of polishable overcoatings;

[81] See also RD501.

[82] With an aerial mass of 45 to 70 kg/m²

- To verify whether or not such overcoatings introduce non-repeatable bimetallic effects;
- To determine a suitable (i.e. compatible with cost-effective serial production) process for the production and finishing of the segments, and in particular for the control of edge misfigure.

To this end, a total of up to eight 1-m class SiC segments will be produced and tested (see RD510 for a complete definition of tasks). Four blanks were already supplied to ESO by BOOSTEC (Figure A- 8) and have been shipped to the optical manufacturers. Up to four more will be purchased from a different blank supplier. The segments will be polished and tested by SAGEM and SESO with support by the Laboratoire d'Astrophysique de Marseille. By end 2007 all segments will be polished and tested, allowing for a final decision on OWL primary mirror technology by 2008.

As for Wavefront Control, this Work Package is directly relevant to OWL. The Boostec blanks were ordered on OWL budget before the inception of the ELT Design Study.

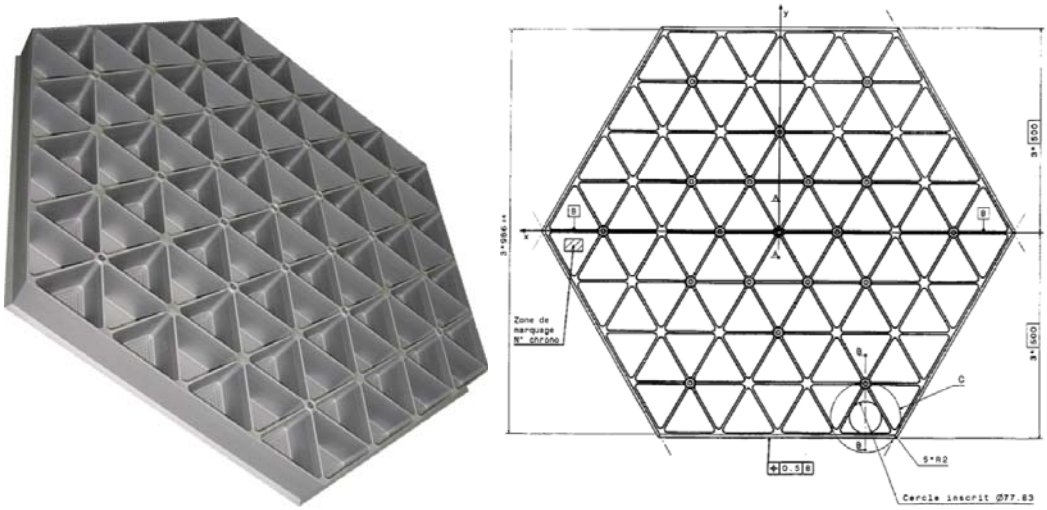

Figure A- 8. 1-m silicon carbide BOOSTEC blank prototype.

A-1.4 Mechanics

The mechanics Work Package concentrates on

- The use of advanced materials in targeted applications: structural ropes, composite structural elements;
- The testing of friction drives;
- The evaluation of magnetic levitation as an alternative to friction drives.

Structural ropes, composite elements – A detailed definition of the tasks is given in reference documents RD510 and RD512.

In order to minimize obscuration, all ELT concepts apply tensioning ropes to stabilize slender structural elements located in the upper part of the altitude structure, and to increase global mode frequencies (see also 9.4.4.2). Steel cables provide adequate tensile strength, but are quite heavy. Synthetic fibres with very high specific stiffness and strength are now commonly used in suspension bridges; they are made by incorporating fibres into a matrix to form a composite bundle. This is then twisted with others to form a rope. Similar solutions could be adopted for OWL tensioning ropes. A study is under way with MEDIA, with particular emphasis on ropes dimensioning, interface couplings and thermal aspects (see RD510).

For evident reasons, upper structural parts of the telescope must have highest possible stiffness and lowest possible mass. High static and dynamic performance, superior safety characteristics, low wind cross-section and low weight are essential requirements. OWL design and analysis shows that these requirements could be made with all-steel structures, but also indicate that significant advantages could be obtained by targeted use of composite materials. A detailed study by MEDIA is under way, with a view to comparing the relative performance and cost of a typical secondary mirror steel truss substructure with a composite one (see RD512 for a complete definition of the tasks).

These studies will be undertaken in 2006 and completed by mid-2007. The main contributor is MEDIA.

Magnetic levitation **–** Magnetic levitation is a potential alternative to friction drives, with major advantages in terms of dimensional tolerances (tracks) over large distances, and in terms of stiffness, which is essentially provided by the control system. Safety is likely to be very high as well, the technology having to meet highest safety standards for transportation.

Preliminary discussions with experts at University of Lausanne indicated that the technology might be applicable to OWL kinematics. A theoretical study will be contracted by ESO and is due for completion by mid-2007.

Friction drive breadboard **–** Classical hydraulic pads and tracks being ruled out for reason of unrealistic dimensional tolerances over very large scales, extremely large telescopes will have to rely on friction drives (or magnetic levitation, see above) for their kinematics. A control analysis (see RD14 and RD15) performed with OWL friction drive shows that effective friction compensation can be incorporated into the control system. The friction drive breadboard is essentially the experimental verification of such analysis. The conceptual design of the breadboard, which is currently in the design phase and will be tested by AMOS, is shown in Figure A- 9. The definition of tasks and the technical specifications are provided in reference documents RD513 and RD514, respectively.

The main contributors are AMOS and ESO.

All activities in the Mechanics Work Package are directly relevant to OWL design and construction.

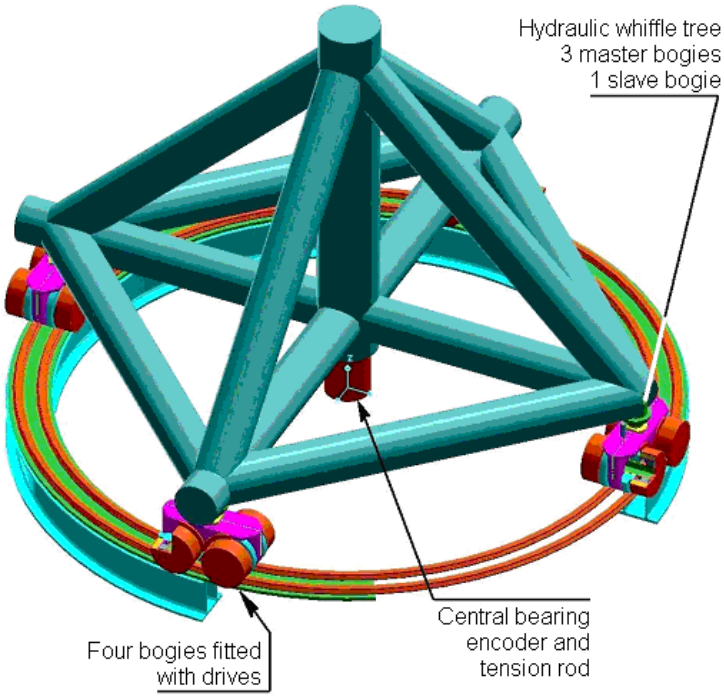

Figure A- 9. Friction drive breadboard

A-1.5 Enclosure & wind studies

This Work Package covers the conceptual design of low-cost enclosure concepts for Extremely Large Telescopes with a diameter of 50 to 100-m (see RD516 for a detailed definition of tasks), and the performance of wind simulations and wind tunnel tests, with a view to assessing, most notably, the effectiveness of wind screens (see RD517). GRANTECAN is supervising the enclosure concept studies and ESO the wind studies.

The enclosure concepts elaborate on the sliding and co-rotating enclosure concepts, with a view to evaluating the merits and cost of both. An open call has been issued for the development of a third alternative.

The wind studies will provide quantitative information on the wind loads and on the turbulent pressure structure function on the telescope main optics, inside an enclosure and behind a wind screen. The aerodynamic turbulent load will be characterised in a wide frequency range, up to about 10 Hz full scale, in wind tunnels qualified to provide reliable information up to this frequency limit. To characterise the air volume renovation and the thermal behaviour in the telescope chamber Computational Fluid Dynamic simulations will be performed being this method better suited than wind tunnel tests to analyse thermally driven phenomena.

The contributors are GRANTECAN, IAC, ESO, CIMNE, Galway University, and ITER.

The activities under the Enclosure & Wind Studies Work Package are seen as complementary to the OWL development, which will pursue design-specific aspects of said activities.

A-1.6 Adaptive Optics

The adaptive optics Work Package covers concepts development, point designs, thin shell development and prototyping, as well as simulations and control algorithms. All activities in this Work Package are directly relevant to OWL, with the sole exception of the development of an adaptive mirror technology with low actuator density (DM-TEC-0, see below).

First generation AO and MCAO designs – This includes the conceptual design and analysis of single conjugate, ground layer and multi-conjugate AO subsystems (Natural Guide Stars). The essential objectives are to acquire experience in the design of first generation subsystems, evaluate their potential performance, identify critical issues and derive realistic specifications. This task is under ESO responsibility, with contribution by INAF. A detailed definition is given in RD518.

High actuator density, large deformable mirrors – Three technologies are explored:

1. DM-TEC-0: Low order, large amplitude correctors;
2. DM-TEC-1: IR correctors for 50- to 100-m class apertures, the corrector being part of the telescope optical train;
3. DM-TEC-2: High order correctors, either as part of the telescope optical train or as post-focal correctors.

Typical actuator interspacing is 80-100-mm for the first technology, 25 mm for the second, and 10-mm for the third. The assumed corrector size is in the range of 2-m upwards for the first two, and up to ~2-m for the third.

The technology development includes:

1. DM-TEC-0
    1.1. Feasibility study of Large, up to 2-m class Deformable Mirror with 100-mm actuator spacing (DM-TEC 0) including the development of a high efficiency electromagnetic

actuator, distributed lateral support of the thin shell, back structure with suitable stiffness-weigth ratio. Development and testing of an actuator prototype.

1.2. Demonstration of slumping of concave/convex thin glass shells based on hot slumping of borosilicate type glass on a polished mould. The technology for 0.5 m size mirror samples will be developed and tested in the 1-10 mm thickness range.

2. DM-TEC-1

   2.1. Feasibility study of Large, up to 2-m class Deformable Mirror with 25-mm actuator spacing (DM-TEC 1) including the study of distributed lateral support of the thin shell, the study of the back structure with suitable stiffness-weigth ratio, the study of the actuator to shell interface in terms of optical mirror quality.

   2.2. Development of a scaled down prototype to validate the design and technology solution.

3. DM-TEC-2

   3.1. Feasibility and conceptual design study of a 2-m class deformable mirror unit with 10-15 mm actuator spacing (DM-TEC2), including design, development, fabrication and testing of a demonstration prototype.

   3.2. Manufacturing of a flat ~600 mm thin glass shell for Large deformable mirror with thickness of 1.5 mm goal 1mm

Novel AO concepts - Another essential task is the prospective development of novel AO concepts, with emphasis on alternative routes to using Laser Guide Stars: Pseudo-Infinite Guide Stars (PIGS, see section 8.4.5.1), Sky Projected Laser Array Shack-Hartmann (SPLASH, see 8.4.5.2), Virtual Wavefront Sensors (8.4.5.3) or Variable Wavefront Sensors (8.4.5.4).

A detailed definition of the tasks is provided in RD519. The main contributors are ESO, INAF, Laboratoire d'Atrophysique de Marseille and SESO.

AO & MCAO simulations – In cooperation between ESO, INAF and LUND University, simulation tools are being developped, with a view to predict performance and eventually integrate adaptive optics into an Integrated Modelling Tool.

Algorithms for reconstruction & control – This task covers the development of algorithms for wavefront reconstruction and control, with a view to minimizing computational requirements and making best effective use of the data collected by the metrology systems. The main contributors are ESO, IAC, INAF, and University of Padova.

A-1.7 Operations

The tasks and objectives of this Work Package are outlined in section 2.8. The main contributor is ESO. The underlying activities were initially conceived as part of OWL development, and transferred into the framework of the ELT Design Studies for its relevance to (virtually) any ELT design.

A-1.8 Instrumentation

The instrumentation Work Package covers exploratory designs of possible instruments, complemented by design and analysis of atmospheric dispersion compensators. This activity is complementary to specific instrument conceptual designs undertaken for OWL under ESO

contracts with European prominent Institutes. The timeframe for the conceptual design of OWL instruments (completion by fall 2005) allows for ideal feedback to the corresponding effort in the ELT Design Study (start in fall 2005).

The exploratory designs are addressed in two phases. The first phase includes brief conceptual designs and analysis of a relatively wide variety of possible instruments. The Representative Instruments currently envisaged are:

- GRB (Gamma-Ray Burst) Catcher
- High-resolution Spectrometer (HISPEC)
- High Time-Resolution Instrument (HiTRI)
- Mid-IR Instrument (MIDIR)
- Multi-Object Multi-field Spectrometer-Imager (MOMSI)
- PlanetFinder
- Submillimetre Common-User Bolometer Array -3 (SCUBA3)
- Wide-Field Spectrometer (WFSPEC)
- Innovative Instrument Concepts

In the second phase, up to three conceptual designs will be pursued in more details. The instruments which will be included in the second phase will be selected on the basis of the science case and of the results of the first phase.

The detailed definition of tasks is provided in reference documents RD520 and RD521. The contributors are UKATC, ESO, ASTRON, DURHAM University, Galway University, INSU, Leiden Observatory, MPIA and Oxford University.

A-1.9 Site characterization

This Work Package covers all activities required to undertake a standardized site characterization campaign. The first step is to compile a comprehensive list of relevant parameters and define corresponding metrics, with a view to establishing a template figure of merit. The parameters space is extended to all characteristics which may affect performance, cost, schedule, and design of an ELT. Under ESO contract, a software tool (FRIOWL) is under development. This tool allows dynamic screening of databases (ground meteorological stations and satellite databases) according to selected criteria and to assess the variability of such criteria over decades. Where necessary, dedicated instrumentation is being designed and built, and will be installed on candidate sites. The detailed definition of tasks is given in reference document RD522.

Two sites, ORM and Paranal, will be taken as test cases and their statistics fed into the model. This does not imply that these sites have de facto been pre-selected; further measurements in Argentina and the Moroccan Atlas, as a minimum, are planned. This activity should be viewed in the global framework of site searching for Extremely Large Telescopes, with continued feedback between project groups worldwide, consolidation and sharing of databases, and a general convergence towards measurements standards.

In addition, this Work Package includes the direct measurement of turbulence properties over large scales. The few measurements of outer scale of turbulence conducted so far by Université de Nice at various sites are generally in the 20-30m range, occasionally decreasing to values as small as 8 m. There is indeed anecdotic evidence that the VLT regularly provides a Point Spread Function sharper than the seeing inferred by Paranal seeing monitors, which rely on Kolmogorov model. Measuring turbulence amplitude over large scale is necessary to derive

specifications for the maximum amplitude of adaptive correction, which has potentially strong impact on deformable mirror technology.

These activities will be completed about one year ahead of the time at which a decision about OWL site is required. Main contributors are Université de Nice, IAC, and ESO. The site characterization Work Package is evidently relevant to OWL and allows for a more extended effort than could be undertaken by a single organization.

A-1.10 Integrated modelling

This task covers the design and coding of a toolkit for integrated simulation of optical, structural, and controls performance of Extremely Large Telescopes with a segmented primary mirror and adaptive optics. It includes, in particular:

- Definition of a suitable architecture for the software
- Subsystem models
    - Submodel for simulation of telescope structures, suitable methods for model reduction;
    - Rigid body dynamics for a segmented primary mirror
    - Submodel of a typical control system for a segmented mirror using edge sensors, singular value decomposition.
    - Secondary, tertiary, quaternary, quinternary and hexary mirror position control.
    - Deformable mirrors and their controllers.
- Ray tracing through conic mirror systems; sensitivity matrices
- Simulation model of a generic typical wavefront sensor
- Building block for simulation of an adaptive optics controller.
- Model for estimation of atmospheric aberrations from suitable atmospheric models
- Submodels describing typical wind disturbance scenarios using either standard spectra, wind tunnel data, or results from computational fluid dynamics runs.
- A separate module will establish a graphical user interface to allow the user to input data and to do a first “sanity verification” of the input data.
- Computation of PSF and other key data
- Visualization and presentation of results

The main contributor to this task is Lund University. A detailed definition of the tasks is provided in RD525. It is expected that most tools developed in the framework of this Work Package will eventually be integrated by ESO into an OWL end-to-end model.

Appendix 2.ELT Design Study Participants

Participant No	Organization	Short name	Short description (i.e. fields of excellence) and specific roles in the consortium
1.	European Southern Observatory *International Organization; Garching bei München, Germany*	ESO	Lead organization for the ELT Design Study. Main European astronomical infrastructures provider, with 40 years experience in design, integration and operation of modern facilities. ESO has currently 11 Member States (Belgium, Denmark, Finland, France, Germany, Italy, Netherlands, Portugal, Sweden, Switzerland, United Kingdom). It has built and runs 2 optical/infrared observatories in Chile, where it is also constructing a third one on the Chilean Altiplano (ALMA project, in cooperation with the US).
2.	Advanced Mechanical and Optical Systems (AMOS) *Liège, Belgium*	AMO	AMOS was founded in 1983, employs 65 people specialized in design and manufacturing of high accuracy mechanical and optical systems, mainly realized for space industry and astronomical observatories. Within the framework of the ELT Design Study, AMOS will be in charge of the design, construction and testing of a representative friction drive breadboard.
3.	ASTRON *Dwingeloo, The Netherlands.*	AST	ASTRON (formerly NFRA) is a scientific governmental organization with the goal to promote the orderly and successful development of astronomy in the Netherlands. Its programme to implement this strategy has two principal elements: • the operation of front line observing facilities, incl. especially the Westerbork Radio Observatory. • a strong technology development program, encompassing both innovative instrumentation for existing telescopes and the new technologies needed for future facilities.
4.	The Australian National University, Mt Stromlo Observatory *Weston, Australia.*	ANU	The Australian National University contributes with its expertise in design, and construction of advanced optical systems of exacting tolerances, numerical simulation, modelling and optimization, and thermal analysis.

5.	CIMNE - Centre Internacional de Mètodes Numèrics en Enginyeria *Barcelona, Spain.*	CIM	Research centre in the development and application of numerical methods to a wide range of engineering problems. CIMNE takes an active part in R&D, in co-operation with universities, research organizations and industry world-wide. In the last 15 years, CIMNE has taken part in more than 470 R+D projects with the financial support of the European Community, the Spanish Ministry of Industry, CIDEM, CIRIT and CICYT, among others, as well as some 200 Spanish and international enterprises.
6.	Durham University *Durham, United Kingdom*	DUR	The Astronomical Instrumentation Group in Durham has specific expertise in the design, construction, and commissioning of astronomical adaptive optics systems and spectrographs. It is one of the largest groups of its kind in the UK consisting of 30 academics, research scientists, engineers, technicians, and graduate students.
7.	Fogale *Nimes, France.*	FOG	SME with strong expertise in metrology, including but not limited to metrology for the integration and operation of modern astronomical telescopes. Major supplier for the 11-m South African Large Telescope project, currently under construction.
8.	Galway University *Galway, Ireland.*	GAL	University groups in Physics and I.T. Departments with particular expertise in astronomical instrument design and construction (e.g. high time resolution instrumentation), adaptive optics and atmospheric modelling, and applications of high performance computing to engineering modelling and simulations.
9.	Grantecan *La Laguna, Spain.*	GRA	Spanish public company, in charge of the design, development, installation and commissioning of the 10 meter telescope GTC, under construction at the Roque de los Muchachos Observatory (ORM) in the Canary Islands. Strong experience in segmented telescopes and infrastructures design and construction.
10.	Instituto de Astrofisíca de Canarias *La Laguna, Spain.*	IAC	Major Spanish public research and technology organization (RTO) in the field of astrophysics; in charge of the European Northern Observatory (ENO) at the Canary Islands, hosting a significant battery of telescopes that are owned and operated by more than 60 research institutions from 19 countries. Large experience in Site Characterization and instrumentation design and manufacturing.
11.	Instituto Nazionale di Astrofisica *Florence, Italy.*	INA	National government organization for research in astronomy, astrophysics and related technologies. It embraces the former 12 astronomical Italian Observatories. INAF operates a 3.5m telescope in Canary Island and shares the Large Binocular Telescope in Arizona. Within INAF, the Observatory of Arcetri is leading technological research on Adaptive Optics.
12.	CNRS-INSU	INS	INSU laboratories include:
	CRAL, *Saint Genis Laval, France*		CRAL has a well known track record in instrumentation of major observatories, particularly in the field of 3D spectroscopy. It has developed instruments for major ground- and space-based telescopes. CRAL also has strong expertise in high resolution imaging techniques, adaptive optics, laser guide stars, MCAO, image deconvolution, etc.
	LAM, *Marseille, France.*		The Laboratoire d'Astrophysique de Marseille (LAM) is part of the Observatoire Astronomique de Marseille-Provence (OAMP). LAM has a well known track record in telescope optics (design, aspherics, polishing, etc.) and in ground and space instrumentation.

	Observatoire Paris-Meudon *Meudon (Paris), France.*		Observatoire de Paris is the largest astronomical center in France with about 1000 employees, out of which 750 are permanent. It consists of 7 laboratories. It has a well known track record in various ground and space instrumentation projects.
13.	ITER - Instituto Tecnológico y de Energías Renovables *San Isidro, Spain.*	ITE	The main objective of ITER is the development of research projects related to Renewable Energies and realization of tests in the Wind Tunnel. The Wind Energy Department staff has a 15-years experience in the development of wind studies as well as in carrying out projects of calculation of wind loads and pressure distribution in the wind tunnel.
14.	JUPASA Transformados Metálicos *Yuncos, Spain.*	JUP	SME specialized in the field of precision mechanics of large items, ranging from space application to renewable energy technology.
15.	Leiden Observatory *Leiden, The Netherlands.*	LEI	University group with substantial experience in astronomical techniques, instrument definition, and instrument design. Specific expertise in instrument control and real-time software. The group also has relevant experience in adaptive optics.
16.	Lund University *Lund, Sweden.*	LUN	University group with wide experience in design of optical and radio telescopes for astronomy. The group has carried out a design study of a 50 m ELT (the Euro50), and led a collaboration for this purpose. It has expertise within systems design, science case, adaptive optics and integrated modelling for astronomical telescopes.
17.	Media C. I. *Las Rozas (Madrid), Spain.*	MED	SME with expertise in precision mechanics and structures for large telescopes and ground-based instrumentation. Other fields of expertise are aeronautics, aerospace, railroad transportation and automobile. MEDIA provides engineering support for complete product development: design, simulation, production, project management, product assurance and system engineering.
18.	Max-Planck Institut für Astronomie *Heidelberg, Germany.*	MPIA	Max-Planck-Institute with expertise in cryogenic astronomical instrumentation for large ground-based telescopes. Special experience in precision cryo-mechanics and cryo-physics, IR-detector read out electronics and detector test procedures and facilities. In addition, there is detailed expertise in development and application of astronomical AO systems.
19.	Oxford University *Oxford, United Kingdom.*	OXF	A university department with a strong research group and experience with design and construction of instrumentation for large telescopes, including VLT and Subaru. The department also hosts the UK Gemini support group, providing experience with observatory operations and strategic planning.
20.	SAGEM (REOSC) *Paris, France.*	SAG	The REOSC High Performance Optics unit of SAGEM is world leader in large optics manufacturing with key references like the ESO VLT primary (8-m) and secondary mirrors, Coudé Train and delay line mirrors, Gemini primary (8-m) mirrors and instrumentation optics. It also has unique Know How in large optics mass production, with the 42 1.8-m Zerodur segments of the Gran Telescopio Canarias presently under production and several hundreds 80 cm diffraction-limited amplifier slabs supplied to the French Megajoule Laser project.

21.	SESO *Aix-en-Provence, France.*	SES	The Société Européenne de Systèmes Optiques (SESO), located in Aix-en-Provence (FRANCE), is involved in optical manufacturing of components according to customer specifications as well a complete design, manufacturing and testing of any kind of optomechanical systems. Moreover, SESO is one of the world leaders in polishing of large mirrors (by traditional means and/or computer controller machine) with flat, spherical, aspherical, on-axis and off-axis shapes, etc.
22.	Technion – Israel Institute of Technology *Haifa, Israel.*	TEC	The physics department has been doing adaptive optics for nearly thirty years. Among its achievements are the invention of the bimorph mirror, new wave front sensors, multi-conjugate adaptive optics, laser and plasma guide stars, stellar interferometers, and more.
23.	UK Astronomical Technology Centre *Edinburgh, United Kingdom.*	UKA	Part of the UK Particle Physics and Astronomy Research Council (PPARC), the UK Astronomy Technology Centre (UK ATC) is the national centre for the design and production of world leading astronomical telescopes, instruments and systems. Current major projects include the delivery of systems to the high altitude mountain sites of the Gemini Telescopes Project (8m telescopes in Hawaii and Chile), the Isaac Newton Group of Telescopes (La Palma), the UK Infrared Telescope (Hawaii), the James Clerk Maxwell Telescope (Hawaii), the Herschel Space Observatory (HSO), Mid InfraRed Imager (MIRI) for the James Webb Space Telescope (JWST) and the design and build of VISTA - a 4m wide field telescope in Chile.
24.	Universidad Politecnica Catalunia *Barcelona, Spain.*	UPC	The Electromagnetic and Photonics Engineering Group of the Universidad Politecnica Catalunia is a well known expert in LIDAR Remote Sensing and Boundary Layer Profiling. In charge of key experiments within the Site Characterization to determine large scale atmospheric properties.
25.	Université de Nice *Nice, France.*	UNI	The atmospheric optics group of the Laboratoire Universitaire Astrophysique de Nice has a unique expertise in atmospheric optics for astronomy, both from theoretical and experimental points of view. Most of the major observatories have been characterized by this group: La Silla, Paranal, Cerro Tololo, Cerro Pachon, Roque de los Muchachos, Mauna Kea, South Pole and now Dome C in Antarctica. It developed a whole set of instruments for site testing.
26.	University of New South Wales *Sydney, Australia.*	UNW	University group with experience in instrument development and modelling of adaptive optics performance for both temperate sites and Antarctic locations. UNSW operates a wide-field patrol telescope at Siding Spring Observatory and has developed many novel instrument techniques.
27.	Universita di Padova *Padova, italy.*	UPD	The System and Control theory research group of the University of Padova consists of 12 faculty members and about 20 Ph.D. and post-graduate students. It operates in the Department of Information Engineering of the Faculty of Engineering, which has about 100 faculty members and 150 graduate students and research fellows. The areas of expertise of the group comprise analysis, modelling and control of multidimensional systems; modelling, control, estimation and identification of stochastic systems; algorithms for linear and nonlinear filtering, using Kalman filter-based techniques; computational vision with application to control of autonomous vehicles; robotics.

Appendix 3. System status at construction readiness review

Code	Item	R&D	Specifications / Plans	Conceptual design	Preliminary design	Final design	Completion	Remarks
30000	**Project Engineering**							
32000	System engineering IT tools						x	
32000	Wind tunnel testing	Completed						
33000	AIV		x					
34000	Commissioning		x					
35000	R&D, major breadboards and experiments							
35100	Adaptive optics concepts & technologies							
35100	LGS Wavefront sensing development & experiments	Ongoing						
35100	LGSF Technology development	Ongoing						
35100	Wavefront sensor 512x512 CCD development	Ongoing						
35100	Wavefront sensor IR detector development	Completed						
35100	Wavefront sensor IR detector development	Ongoing						
35100	WFS detector controller development	Completed						
35100	Real Time Computer development & algorithms	Completed						
35100	Micro-Deformable Mirror (MDM) prototype (10kact)	Ongoing						
35100	MDM drive electronics development (10kact)	Ongoing						

Code	Item	R&D	Specifications / Plans	Conceptual design	Preliminary design	Final design	Completion	Remarks
35200	Physical optics R&D	Completed						
35300	Non-adaptive wavefront sensing							
35300	Phasing cameras - experiments (on GTC)	Completed						
35300	Phasing cameras - preliminary designs	Completed	x	x	x			
35400	Optical materials & processes							
35400	Silicon Carbide	Completed						
35400	Instrumentation - filters / glasses	Completed						
35500	Advanced structural materials	Completed						
35600	Advanced enclosure concepts & technologies	Completed						
35700	Telescope drives							
35700	Breadboard friction drive	Completed						
35700	Magnetic levitation	Completed						
40000	**Site infrastructure**							
41000	Integration infrastructures							
41100	Enclosure integration infrastructures				x	Ongoing		
41200	Telescope structure & kinematics integration infrastructures				x	Ongoing		
41300	Optomechanical subsystems integration infrastructures							
41310	M1 & M2 units integration tools & equipments		x	x				
41320	Corrector unit integration tools & equipment		x	x				
41330	Focal Stations integration tools & equipment		x	x				
41340	Telescope pre-alignment unit integration tools & equipment		x	x				
41400	Other temporary integration facilities		x	x				
42000	Operation infrastructures							
42100	Maintenance infrastructures[1]		x	x				
42200	Science operation infrastructures		x	x				
42300	Other infrastructures[2]		x	x				
42400	Power plant / supply		x	x	x	x	First stage	
42500	Services		x					
42600	Technical buildings		x					
43000	Site preparation		x	x	x	x	Ongoing	
43000	Site preparation							
49000	Site infrastructure maintenance facility		x					
50000	**Enclosure**		x	x	x	Ongoing		

Code	Item	R&D	Specifications / Plans	Conceptual design	Preliminary design	Final design	Completion	Remarks
51000	Enclosure foundations		x	x	x	Ongoing		
52000	Kinematics		x	x	x	Ongoing		
53000	Enclosure structures		x	x	x	Ongoing		
59000	Enclosure Maintenance Units		x	x	x	Ongoing		
70000	**Telescope structure & kinematics**							
71000	Azimuth structures		x	x	x	Ongoing		
71100	Azimuth tracks		x	x	x	Ongoing		
71200	Azimuth drives		x	x	x	Ongoing		
71300	Azimuth structural mechanics		x	x	x	Ongoing		
71400	Central azimuth bearing and encoder assembly		x	x	x	Ongoing		
71500	Azimuth Cable wrap		x	x	x	Ongoing		
71600	Azimuth cooling system		x	x	x	Ongoing		
71700	Auxiliary equipments[3]		x	x	x	Ongoing		
72000	Altitude structures		x	x	x	Ongoing		
72100	Altitude cradle		x	x	x	Ongoing		
72200	Altitude drives		x	x	x	Ongoing		
72300	Altitude structural mechanics		x	x	x	Ongoing		
72400	Altitude bearings and encoders assemblies		x	x	x	Ongoing		
72400	Kevlar ropes		x	x	x	Ongoing		
72400	Ropes tension devices		x	x	x	Ongoing		
72500	Altitude Cable wraps		x	x	x	Ongoing		
72600	Altitude cooling system (corrector, instrumentation).		x	x	x	Ongoing		
72700	Auxiliary equipments[4]		x	x	x	Ongoing		
73000	Wind screens		x	x	x	Ongoing		
74000	Mirror covers		x	x	x	Ongoing		
75000	Telescope foundations		x	x	x	Ongoing		
76000	Telescope diagnostic systems.		x	x	x	Ongoing		
79000	Telescope structure & kinematics maintenance units		x	x	x	Ongoing		
80000	**Optomechanical subsystems**							
80000	Segments actuators		x	x	x			
80000	Local metrology - (position sensors)		x	x	x			
81000	Primary mirror unit							
81110	Segment assembly		x	x	x	x		Incl. prototypes
81120	Whiffle trees		x	x	x	x		Incl. prototypes
81130	Active supports		x	x	x	x		Incl. prototypes

Code	Item	R&D	Specifications / Plans	Conceptual design	Preliminary design	Final design	Completion	Remarks
81140	Local metrology assembly		x	x	x	x		Incl. prototypes
81150	Subcells		x	x				
82000	Secondary mirror unit							
82110	Segment assembly		x	x	x	x		Incl. prototypes (same as M1)
82120	Whiffle trees		x	x	x	x		Incl. prototypes (same as M1)
82130	Active supports		x	x	x	x		Incl. prototypes (same as M1)
82140	Local metrology assembly		x	x	x	x		Incl. prototypes (same as M1)
82150	Subcells		x	x				
83000	Corrector unit							
83100	Corrector structure & kinematics		x	x				
83200	Instruments racks		x	x				
83300	M3 subunit							
83310	M3 mirror assembly		x	x				
83320	M3 cell		x	x				
83400	M4 subunit							
83410	M4 mirror assembly		x	x				
83420	M4 cell		x	x				
83500	M5 subunit							
83510	M5 provisional assembly		x	x	x			
83520	M5 adaptive assembly		x	x	x			
83600	M6 subunit							
83510	M6 provisional assembly		x	x	x			
83520	M6 adaptive assembly		x	x	x			Incl. prototypes
84000	Focal stations							
84100	Electromechanical subunits		x	x				
84200	Active optics metrology		x	x				
84300	Phasing metrology		x	x	x			
84400	Guiding and field stabilization metrologies		x	x				
84500	Adaptive optics metrology & real-time computers		x	x				
85000	Telescope pre-alignment unit		x	x				
89100	M1 & M2 offline maintenance facility							
89110	Segments clean room		x	x				
89120	Segments washing & coating tanks		x	x				
89130	Segments carts and transporters		x	x				
89140	Segments support stands (emergency support)		x	x				

Code	Item	R&D	Specifications / Plans	Conceptual design	Preliminary design	Final design	Completion	Remarks
89150	Segments racks		x	x				
89160	Segments storage room		x	x				
89200	M1 & M2 in-situ maintenance devices							
89210	M1 in-situ cleaning robot		x	x				
89220	M1 segment assembly in-situ handling robot		x	x				
89230	M1 cover in-situ cart holder		x	x				
89240	M2 in-situ cleaning device		x	x				
89250	M2 segment assembly in-situ handling tool		x	x				
89300	Corrector maintenance facility							
89310	Corrector maintenance hall		x	x				
89320	Corrector transporter		x	x				
89330	M3 & M4 subunits extractor		x	x				
89340	M3 & M4 subunits transporter		x	x				
89350	M5 subunit extractor		x	x				
89360	M5 subunit transporter		x	x				
89370	M6 subunit extractor		x	x				
89380	M6 subunit transporter		x	x				
89400	M3 & M4 assemblies maintenance facility							
89410	M3 & M4 assemblies maintenance hall		x	x				
89420	M3 & M4 clean room		x	x				
89430	M3 & M4 assemblies lifting device		x	x				
89440	8-m class washing & coating tanks		x	x				
89450	M3 mirror assembly washing & coating cart		x	x				
89460	M4 mirror assembly washing & coating cart		x	x				
89470	M3 mirror assembly support stand (emergency support)		x	x				
89480	M4 mirror assembly support stand (emergency support)		x	x				
89500	M5 & M6 assemblies maintenance facility							
89510	M5 & M6 assemblies maintenance hall		x	x				
89520	M5 & M6 clean room		x	x				
89530	M5 mirror assembly lifting device		x	x				
89540	M6 mirror assembly lifting device		x	x				
89550	M5 assembly washing & coating cart		x	x				
89560	M6 assembly washing & coating cart		x	x				

Code	Item	R&D	Specifications / Plans	Conceptual design	Preliminary design	Final design	Completion	Remarks
89570	4-m class washing & coating tanks		x	x				
89580	M5 mirror assembly support stand (emergency support)		x	x				
89590	M6 mirror assembly support stand (emergency support)		x	x				
89600	Corrector in-situ cleaning devices		x	x				
89700	Focal Stations maintenance facility		x	x				
90000	**Instrumentation**							
91000	Technical instrumentation		x	x	x			
92000	Science instrumentation		x	x	x			At least 2 instruments
93000	Post-focal AO units		Draft	x				
99000	Instruments maintenance facility		x	x				
100000	**Laser Guide Stars Subsystem**							
101000	Laser units		Draft					
102000	Beam Propagation units		x	x				
103000	Control & Metrology units		x	x				
109000	LGS maintenance facility		x	x				
110000	**Central Control Systems**							
111000	Central Control environment		x	x				
115000	IT Systems		x	x				
119000	Central Control maintenance facility		x	x				
120000	**Site characterization**							
121000	Weather stations		x	x				
122000	Turbulence monitoring units		x	x				
123000	Sky Monitoring Units		x	x				
129000	Site characterization maintenance facility		x	x				

Appendix 4. Phase B Schedule estimate

ID	Prod. Code	Task Name	Duration	Start
17		**OWL PHASE B**	**1519 days**	**01/01/06**
18		**Major milestones**	**1080 days**	**01/01/06**
19		Kick-off Phase B	0 days	01/01/06
20		Optical design iteration-1 complete	0 days	11/08/06
21		Telescope structure - concept design iteration complete	0 days	09/05/07
22		Process flow studies complete	0 days	20/07/07
23		Subsystems requirements critical review	0 days	17/08/07
24		Optical design frozen	0 days	12/10/07
25		M1 & M2 substrate technology selected	0 days	15/02/08
26		Interim review	0 days	04/04/08
27		Site selection	0 days	16/05/08
28		Groundbreaking (site preparation)	0 days	03/10/08
29		First gen. instruments PDR (4 instr.)	0 days	10/04/09
30		M6 subunit PDR	0 days	05/06/09
31		Enclosure PDR	0 days	28/08/09
32		Telescope structure PDR	0 days	09/10/09
33		PHASE C/D READINESS REVIEW	0 days	19/02/10
34	**010000**	**Project Management**	**1100 days**	**02/01/06**
35		Project control & reporting	1070 days	02/01/06
36		Contingency management	1070 days	02/01/06
37		**Project reviews**	**752 days**	**12/05/06**
42		Phase B Project Plan (update)	15 days	02/01/06
43		Phase B Management Plan (update)	20 days	23/01/06
44		Phase B Product Assurance Plan	20 days	20/02/06
45		Phase B Documentation Plan	5 days	20/03/06
46		**Phase C/D draft plans**	**50 days**	**23/01/06**
53		**Phase C/D plans**	**50 days**	**19/05/08**
60		Site development plan (draft)	10 days	23/01/06
61		Site development plan	60 days	02/06/08
62		PA Procedures	15 days	02/01/06
63		Documents Templates	75 days	02/01/06
64	**012000**	**Supply, integration, commissioning and operation process**	**215 days**	**25/09/06**
72	**012000**	**Costing**	**600 days**	**23/07/07**
73		Interim end-to-end cost evaluation	15 days	23/07/07
74		**External study - project costs**	**202 days**	**13/08/07**
81		Final end-to-end cost evaluation	20 days	12/10/09
82		**Interim review**	**45 days**	**18/02/08**
86		**Phase C/D readiness review**	**95 days**	**09/11/09**
91	**020000**	**Science Objectives**	**950 days**	**02/01/06**
92		**Top level Requirements - Iteration-1**	**95 days**	**02/01/06**
98		**Top level Requirements - Iteration-2**	**95 days**	**04/06/07**
104		**Top level Requirements - Final**	**95 days**	**13/04/09**

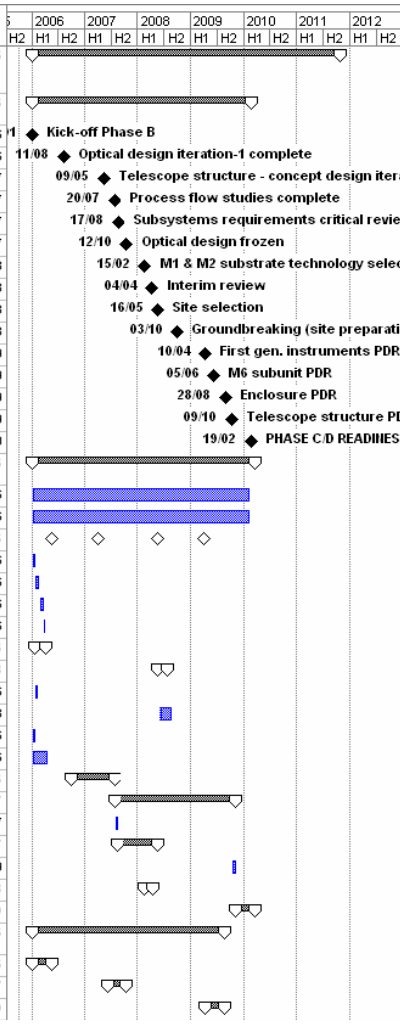

ID	Prod. Code	Task Name	Duration	Start
111	**030000**	**Project Engineering**	**1140 days**	**02/01/06**
112	**031000**	**Overall project engineering**	**720 days**	**02/01/06**
113		**Optical design - Iteration**	**90 days**	**10/04/06**
117		**Optical Design finalization**	**95 days**	**04/06/07**
121		**Site selection**	**720 days**	**02/01/06**
122		Site characterization	530 days	02/01/06
123		Site modelling	530 days	02/01/06
124		Site prospecting	530 days	02/01/06
125		Shortlist	0 days	11/01/08
126		Compilation & review preparation	60 days	14/01/08
127		Review	20 days	21/04/08
128		Site negotiations	100 days	19/05/08
129	**032000**	**System engineering**	**1140 days**	**02/01/06**
130		**Configuration control**	**1025 days**	**17/03/06**
137		Level-1 requirements (update-1)	15 days	15/05/06
138		Level-1 requirements (update-2)	10 days	15/10/07
139		Level-1 requirements (update-3)	10 days	24/08/09
140		Product tree - update	10 days	05/06/06
141		Interface definitions	30 days	19/06/06
142		**Error budgets - iteration-1**	**70 days**	**19/06/06**
146		**Error budgets - iteration-2 (after SCAO End-to-End mod**	**65 days**	**01/06/09**
150		**Error budgets - iteration-3 (after MCAO End-to-End mod**	**70 days**	**02/11/09**
154		**Error budgets - iteration-4 (after XAO End-to-End model**	**30 days**	**05/04/10**
158		Emissivity budget	10 days	10/05/07
159		Reliability budget	30 days	02/08/07
160		**Integrated modelling**	**817 days**	**15/02/07**
169		**Analysis**	**185 days**	**10/05/07**
178		**Wind**	**980 days**	**02/01/06**
179		**Wind experiments on GTC**	**285 days**	**02/01/06**
185		**Wind tunnel testing**	**225 days**	**15/02/07**
193		**Modelling**	**430 days**	**11/02/08**
196		**Subsystems requirements (Level-2)**	**245 days**	**25/09/06**
197		Site infrastructure	15 days	25/09/06
198		Enclosure	23 days	25/09/06
199		Telescope structure & kinematics	23 days	25/09/06
200		**Optomechanical subsystems**	**210 days**	**25/09/06**
213		**Instrumentation**	**45 days**	**25/09/06**
218		Laser Guide Stars unit	45 days	25/09/06
219		Central Control	45 days	25/09/06
220		**Site characterization**	**40 days**	**25/09/06**
226		**Subsystems requirements critical review**	**35 days**	**16/07/07**
229	**033000**	**AIV**	**485 days**	**03/09/07**
233	**034000**	**Commissioning**	**45 days**	**15/10/07**
235	**035000**	**R&D, major breadboards and experiments**	**1000 days**	**02/01/06**
236	**035100**	**Adaptive optics concepts & technologies**	**1000 days**	**02/01/06**
237		LGS Wavefront Sensing R&D	1000 days	02/01/06
238		General laser development	780 days	02/01/06
239		Wavefront sensor 512x512 CCD Development	750 days	02/01/06
240		Wavefront sensor IR detector development	750 days	02/01/06
241		WFS controller development	750 days	02/01/06
242		Real Time Computer development	750 days	02/01/06
243	**035200**	**Physical optics R&D**	**725 days**	**02/01/06**
244		**High contrast imaging R&D**	**725 days**	**02/01/06**
249		**Optical characterization R&D**	**725 days**	**02/01/06**
254	**035300**	**Non-adaptive wavefront sensing**	**130 days**	**03/12/07**
255		Phasing cameras - experiments on GTC	130 days	03/12/07
256	035400	Instrumentation - large components development	650 days	23/04/07
257	035500	Advanced structural materials - development	330 days	02/01/06
258	035700	Telescope drives - MagLev development	330 days	02/01/06
259	**040000**	**Site infrastructure**	**460 days**	**28/09/09**
260	**041000**	**Integration infrastructures**	**160 days**	**28/09/09**
261	**041300**	**Optomechanical subsystems integration infrastructure**	**160 days**	**28/09/09**
262	**041310**	**M1 & M2 units integration tools & equipments**	**160 days**	**28/09/09**
266	**041320**	**Corrector unit integration tools & equipment**	**130 days**	**28/09/09**
270	**041330**	**Focal Stations integration tools & equipment**	**130 days**	**28/09/09**
274	**041340**	**Telescope pre-alignment unit integration tools & e**	**35 days**	**28/09/09**
278	**041400**	**Other temporary integration facilities**	**60 days**	**28/09/09**
282	**042000**	**Operation infrastructures**	**410 days**	**28/09/09**
283	**042100**	**Maintenance infrastructures**	**150 days**	**28/09/09**
287	**042200**	**Science operation infrastructures**	**100 days**	**16/11/09**
291	**042300**	**Other infrastructures**	**125 days**	**16/11/09**
295	**042400**	**Power plant / supply**	**410 days**	**28/09/09**
296		Specifications & Statement of Work	25 days	28/09/09
297		CfT	75 days	02/11/09
298		Review of offers	25 days	15/02/10
299		Contract award	0 days	19/03/10
300		Design	125 days	22/03/10
301		CDR	0 days	10/09/10
302		Supply & integration - Stage-1	160 days	13/09/10

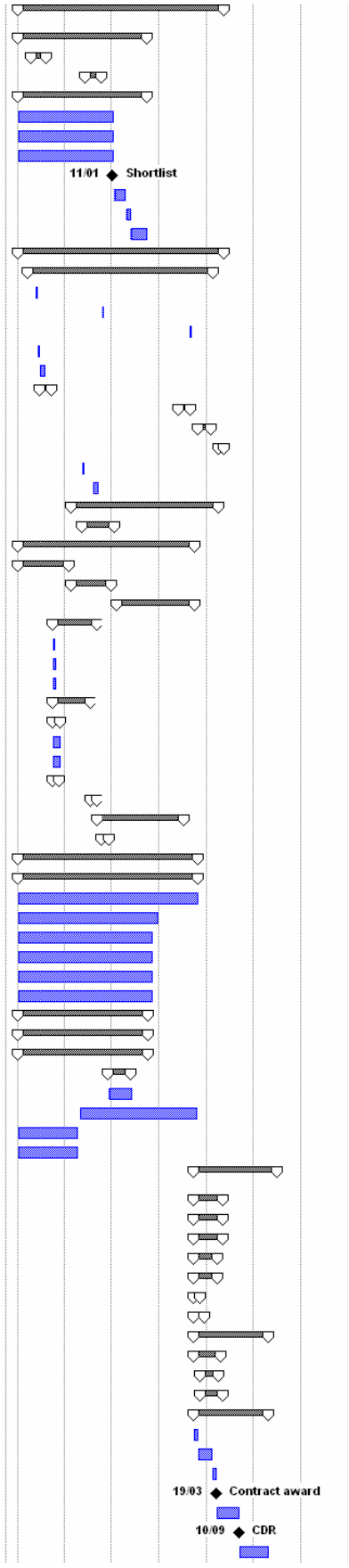

ID	Prod. Code	Task Name	Duration	Start
318	050000	**Enclosure**	615 days	19/05/08
319		Specifications & statement of work	30 days	19/05/08
320		CfT for preliminary design	100 days	30/06/08
321		Review of offers	45 days	17/11/08
322		Contracts award	0 days	16/01/09
323		Contract-1 - preliminary design	160 days	19/01/09
324		PDR-1	0 days	28/08/09
325		Contract-2 - preliminary design	160 days	19/01/09
326		PDR-2	0 days	28/08/09
327		Preliminary design selection	20 days	31/08/09
328		Final design	260 days	28/09/09
329	070000	**Telescope structure & kinematics (**	1162 days	22/06/06
330		Conceptual design iteration	230 days	22/06/06
331		Specifications & Statement of Work	45 days	19/05/08
332		CfT for preliminary design incl. covers, foundations, diagnostics, ma	75 days	21/07/08
333		Review of offers	35 days	03/11/08
334		Contracts award	0 days	19/12/08
335		Contract-1 - preliminary design	210 days	22/12/08
336		PDR-1	0 days	09/10/09
337		Contract-2 - preliminary design	210 days	22/12/08
338		PDR-2	0 days	09/10/09
339		Preliminary design selection	40 days	12/10/09
340		Structure preliminary design selected	0 days	04/12/09
341		Final design	260 days	07/12/09
342	080000	**Optomechanical subsystems**	1519 days	02/01/06
343		**Primary and secondary mirror segments subunits**	1180 days	02/01/06
344		**Active supports**	520 days	14/07/08
345		Specifications & Statement of Work	45 days	14/07/08
346		CfT for preliminary design	75 days	15/09/08
347		Review of offers	35 days	29/12/08
348		Contracts award	0 days	13/02/09
349		Contract-1 - preliminary design	190 days	16/02/09
350		PDR-1	0 days	06/11/09
351		Prototype-1 fabrication & testing (2x3 units)	130 days	09/11/09
352		Contract-2 - preliminary design	190 days	16/02/09
353		PDR-2	0 days	06/11/09
354		Prototype-2 fabrication & testing (2x3 units)	130 days	09/11/09
355		Preliminary design selection	45 days	10/05/10
356		Actuator preliminary design selected	0 days	09/07/10
357		**Local metrology assembly**	400 days	14/07/08
358		Specifications & Statement of Work	30 days	14/07/08
359		CfT for preliminary design	50 days	25/08/08
360		Review of offers	35 days	03/11/08
361		Contracts award	0 days	19/12/08
362		Contract-1 - preliminary design	130 days	22/12/08
363		PDR-1	0 days	19/06/09
364		Prototype-1 fabrication & testing (6 units)	130 days	22/06/09
365		Contract-2 - preliminary design	130 days	22/12/08
366		PDR-2	0 days	19/06/09
367		Prototype-2 fabrication & testing (6 units)	130 days	22/06/09
368		Preliminary design selection	25 days	21/12/09
369		**Glass/ceramic segments**	420 days	02/01/06
370		**Whiffle trees**	345 days	02/01/06
371		Conceptual design	50 days	02/01/06
372		Specifications & Statement of Work	20 days	13/03/06
373		CfT for preliminary design	50 days	10/04/06
374		Review of offers	25 days	19/06/06
375		Contracts award	0 days	21/07/06
376		Contract - preliminary design	110 days	24/07/06
377		PDR	0 days	22/12/06
378		Fabrication of 1 prototype	90 days	25/12/06
379		**Primary and secondary mirrors subcells**	130 days	02/01/06
380		Conceptual design	40 days	02/01/06
381		Specifications & Statement of Work	20 days	27/02/06
382		Price inquiry	50 days	27/03/06
383		Specifications & Statement of Work - Update	20 days	05/06/06
384		**Segment prototype (1 unit)**	380 days	02/01/06
385		Substrate - Specification & Statement of Work	15 days	02/01/06
386		CfT	75 days	23/01/06
387		Supply (blank)	160 days	08/05/06
388		Polishing - Specifications & Statement of Work	15 days	08/05/06
389		CfT	75 days	29/05/06
390		Supply (polishing & I/F)	130 days	18/12/06
391		**Test frame**	235 days	02/01/06
392		Design	75 days	02/01/06
393		Fabrication	130 days	17/04/06
394		Integration	30 days	16/10/06
395		Segment prototype integration	15 days	18/06/07
396		Testing	20 days	09/07/07
397		De-integration & readying for SiC segments	5 days	06/08/07

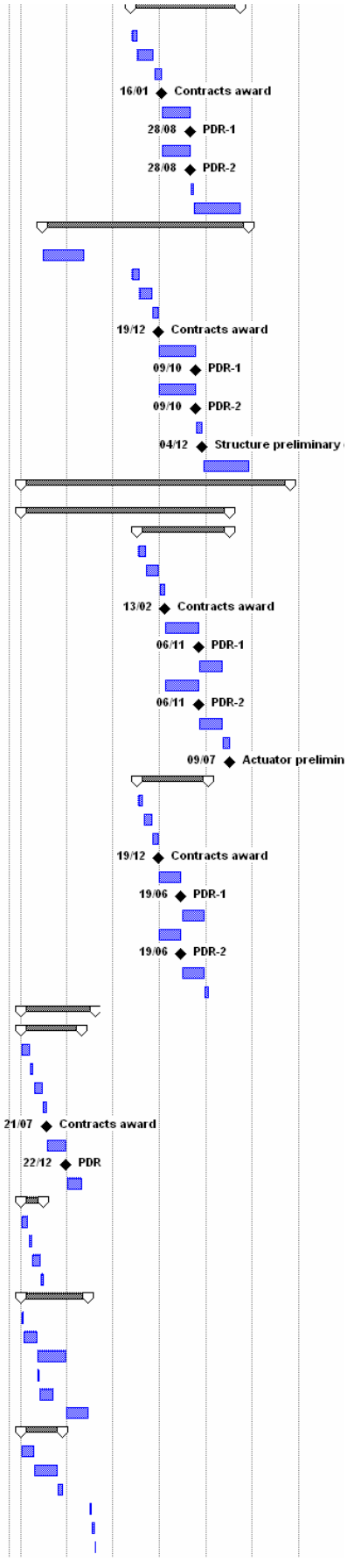

ID	Prod. Code	Task Name	Duration	Start
398		**Silicon Carbide segments**	**505 days**	**02/01/06**
399		**Whiffle trees**	**355 days**	**02/01/06**
400		Conceptual design	60 days	02/01/06
401		Specifications & Statement of Work	20 days	27/03/06
402		CfT for preliminary design	50 days	24/04/06
403		Review of offers	25 days	03/07/06
404		Contracts award	0 days	04/08/06
405		Contract - preliminary design	110 days	07/08/06
406		PDR	0 days	05/01/07
407		Fabrication of 1 prototype	90 days	08/01/07
408		**Primary and secondary mirrors subcells**	**130 days**	**02/01/06**
409		Conceptual design	40 days	02/01/06
410		Specifications & Statement of Work	20 days	27/02/06
411		Price inquiry	50 days	27/03/06
412		Specifications & Statement of Work - Update	20 days	05/06/06
413		**Segments prototypes (3 units)**	**480 days**	**02/01/06**
414		Substrates - Specification & Statement of Work	20 days	02/01/06
415		CfT	50 days	30/01/06
416		**Supply (blanks)**	**310 days**	**10/04/06**
420		Polishing - Specifications & Statement of Work	25 days	10/04/06
421		CfT	50 days	15/05/06
422		**Supply (polishing & I/F)**	**220 days**	**01/01/07**
426		**Testing**	**85 days**	**13/08/07**
435		Wrap-up primary& secondary mirror substrate	50 days	10/12/07
436		Primary mirror segments substrates - Specifications & Stateme	25 days	18/02/08
437		Secondary mirror segments substrates - Specifications & State	25 days	18/02/08
438		Primary mirror segments polishing - Specifications & Statement	25 days	18/02/08
439		Secondary mirror segments polishing - Specifications & Statem	25 days	18/02/08
440		**Segments transport & storage containers**	**90 days**	**18/02/08**
441		Conceptual design	75 days	18/02/08
442		Specifications & Statement of Work	15 days	02/06/08
443	**083000**	**Corrector unit**	**1130 days**	**23/10/06**
444	**083100**	**Corrector structure & kinematics**	**835 days**	**23/10/06**
449	**083200**	**Instruments racks**	**210 days**	**04/06/07**
454		**M3 & M4 subunits**	**615 days**	**23/10/06**
455		**Mirror assemblies**	**405 days**	**23/10/06**
456		Support systems design & analysis (distribution & cha	160 days	23/10/06
457		Blanks - preliminary Specifications & Statement of Wo	25 days	04/06/07
458		Price inquiry	75 days	09/07/07
459		Blanks - Specifications & Statement of Work - Update	15 days	22/10/07
460		Polishing - preliminary Specifications & Statement of V	45 days	22/10/07
461		Price inquiry	75 days	24/12/07
462		Polishing - Specifications & Statement of Work - Upda	25 days	07/04/08
463		**M3 & M4 mirror cells**	**210 days**	**12/05/08**
464		Conceptual design	75 days	12/05/08
465		Specifications & Statement of Work	40 days	25/08/08
466		Price inquiry	75 days	20/10/08
467		Specifications & Statement of Work - Update	20 days	02/02/09
468	**083500**	**M5 subunit**	**445 days**	**08/06/09**
469		**M5 provisional & adaptive assemblies**	**445 days**	**08/06/09**
470		Specifications & Statement of Work	75 days	08/06/09
471		CfT for Preliminary Design	75 days	21/09/09
472		Review of offers	35 days	04/01/10
473		Contract award	0 days	19/02/10
474		Preliminary design	260 days	22/02/10
475		PDR	0 days	18/02/11
476	**083600**	**M6 subunit**	**790 days**	**15/10/07**
477		**M6 provisional & adaptive assemblies**	**740 days**	**15/10/07**
478		Specifications & Statement of Work	75 days	15/10/07
479		CfT for Preliminary Design	75 days	28/01/08
480		Review of offers	50 days	12/05/08
481		Contract award	0 days	18/07/08
482		Preliminary design - 1	230 days	21/07/08
483		PDR - 1	0 days	05/06/09
484		Prototype - 1	310 days	08/06/09
485		Preliminary design - 2	230 days	21/07/08
486		PDR - 2	0 days	05/06/09
487		Prototype -2	310 days	08/06/09
488		Wrap-up & preliminary design selection	50 days	16/08/10
489	**084000**	**Focal Stations**	**535 days**	**02/07/07**
490	**084100**	**Electromechanical subunits**	**240 days**	**02/07/07**
495	**084200**	**Active optics metrology**	**275 days**	**02/07/07**
500	**084300**	**Phasing metrology**	**475 days**	**02/07/07**
501		Conceptual designs (min. 2)	130 days	02/07/07
502		**Phasing cameras - preliminary designs (2 competit**	**235 days**	**02/06/08**
511	**084400**	**Guiding & field stabilization metrologies**	**170 days**	**02/07/07**
516	**084500**	**Adaptive Optics metrology & Real-Time computers**	**535 days**	**02/07/07**
521	**085000**	**Telescope pre-alignment unit**	**865 days**	**09/10/06**
522		Conceptual design	90 days	09/10/06
523		Specifications & Statement of Work	20 days	12/10/09
524		Price inquiry	50 days	09/11/09
525		Specifications & Statement of Work - Update	10 days	18/01/10

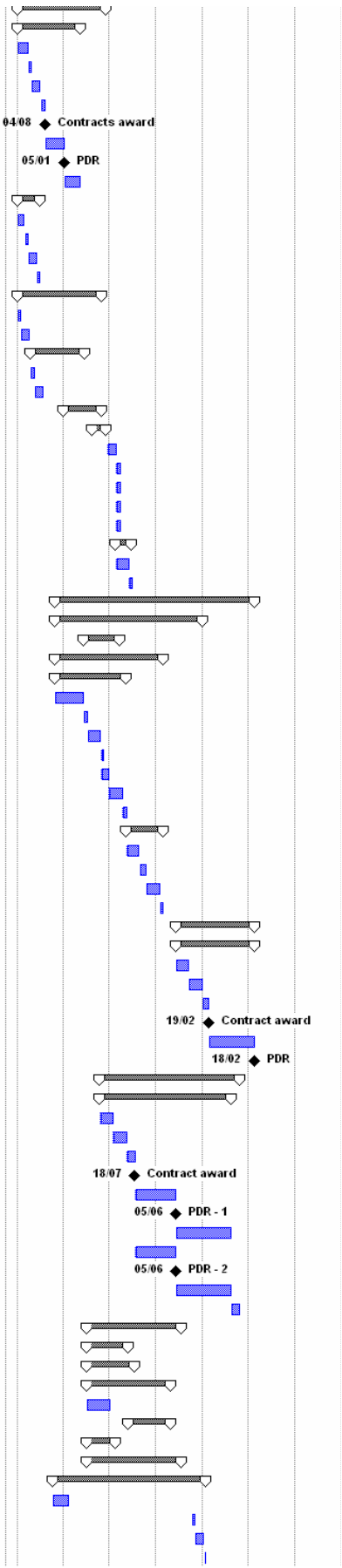

ID	Prod. Code	Task Name	Duration	Start
526	089000	**Optomechanical subsystems maintenance facilities**	**474 days**	**04/01/10**
527	089100	**M1 & M2 offline maintenance facility**	**260 days**	**12/07/10**
528	089110	**Segments clean room**	**110 days**	**07/02/11**
533	089120	**Segments washing & coating tanks**	**110 days**	**12/07/10**
538	089130	**Segments carts and transporters**	**150 days**	**12/07/10**
543	089140	**Segments support stands (emergency support)**	**75 days**	**12/07/10**
546	089150	**Segments racks**	**145 days**	**12/07/10**
551	089160	**Segments storage facility**	**85 days**	**12/07/10**
556	089200	**M1 & M2 in-situ maintenance devices**	**170 days**	**12/07/10**
557	089210	**M1 in-situ cleaning robot**	**130 days**	**12/07/10**
562	089220	**M1 segment assembly in-situ handling robot**	**170 days**	**12/07/10**
567	089230	**M1 cover in-situ cart holder**	**100 days**	**12/07/10**
572	089240	**M2 in-situ cleaning device**	**160 days**	**12/07/10**
577	089250	**M2 segment assembly in-situ handling tool**	**170 days**	**12/07/10**
582	089300	**Corrector maintenance facility**	**100 days**	**04/01/10**
583	089310	**Corrector maintenance hall**	**60 days**	**04/01/10**
586	089320	**Corrector transporters**	**65 days**	**04/01/10**
589	089330	**M3 & M4 subunits extractor**	**100 days**	**04/01/10**
592	089340	**M3 & M4 subunits transporters**	**100 days**	**04/01/10**
595	089350	**M5 subunit extractor**	**100 days**	**04/01/10**
598	089360	**M5 subunit transporters**	**100 days**	**04/01/10**
601	089370	**M6 subunit extractor**	**100 days**	**04/01/10**
604	089380	**M6 subunit transporters**	**75 days**	**04/01/10**
607	089400	**M3 & M4 assemblies maintenance facility**	**175 days**	**24/05/10**
608	089410	**M3 & M4 assemblies maintenance hall**	**75 days**	**24/05/10**
611	089420	**M3 & M4 clean room**	**40 days**	**24/05/10**
614	089430	**M3 & M4 assemblies lifting device**	**100 days**	**24/05/10**
617	089440	**8-m class washing & coating tanks**	**75 days**	**24/05/10**
620		**M3 & M4 mirror assemblies washing & coating cart**	**100 days**	**06/09/10**
623		**M3 & M4 mirror assemblies support stands (emer**	**40 days**	**24/05/10**
626	089500	**M5 & M6 assemblies maintenance facility**	**179 days**	**21/02/11**
627	089510	**M5 & M6 assemblies maintenance hall**	**35 days**	**04/07/11**
630	089520	**M5 & M6 clean room**	**45 days**	**04/07/11**
633	089530	**M5 mirror assembly lifting device**	**95 days**	**21/02/11**
636	089540	**M6 mirror assembly lifting device**	**95 days**	**21/02/11**
639	089550	**M5 assembly washing & coating cart**	**95 days**	**17/06/11**
642	089560	**M6 assembly washing & coating cart**	**95 days**	**17/06/11**
645	089570	**4-m class washing & coating tanks**	**84 days**	**21/02/11**
648	089580	**M5 mirror assembly support stand (emergency su**	**25 days**	**21/02/11**
651	089590	**M6 mirror assembly support stand (emergency su**	**25 days**	**21/02/11**
654	089600	**Corrector in-situ cleaning devices**	**60 days**	**21/02/11**
657	089700	**Focal Stations maintenance facility**	**125 days**	**21/02/11**
660	090000	**Instrumentation**	**1045 days**	**14/08/06**
661	091000	**Technical instrumentation**	**740 days**	**15/10/07**
662		Specifications	30 days	15/10/07
663		Conceptual design	190 days	26/11/07
664		Conceptual design review	0 days	15/08/08
665		Update of specifications	15 days	20/07/09
666		Preliminary design	265 days	10/08/09
667		PDR	0 days	13/08/10
668	092000	**Science instrumentation**	**745 days**	**14/08/06**
669		Call for proposals	60 days	14/08/06
670		**Conceptual designs (8 candidates)**	**120 days**	**06/11/06**
671		Conceptual design Instrument 1	120 days	06/11/06
672		Conceptual design Instrument 2	120 days	06/11/06
673		Conceptual design Instrument 3	120 days	06/11/06
674		Conceptual design Instrument 4	120 days	06/11/06
675		Conceptual design Instrument 5	120 days	06/11/06
676		Conceptual design Instrument 6	120 days	06/11/06
677		Conceptual design Instrument 7	120 days	06/11/06
678		Conceptual design Instrument 8	120 days	06/11/06
679		Conceptual design review (Instruments 1-8)	0 days	20/04/07
680		Feedback analysis (telescope design)	30 days	23/04/07
681		**Instruments preliminary designs (4 instruments)**	**390 days**	**15/10/07**
686		Selection of first 2 instruments	50 days	13/04/09
687	093000	**Post-focal AO units**	**255 days**	**15/10/07**
688		Draft specifications	75 days	15/10/07
689		Conceptual design - 1	130 days	28/01/08
690		Conceptual design - 2	130 days	28/01/08
691		Conceptual design - 3	130 days	28/01/08
692		Conceptual design review	0 days	25/07/08
693		Specifications & Statement of Work	50 days	28/07/08
694	099000	**Instruments maintenance facility**	**125 days**	**13/04/09**
697	100000	**Laser Guide Stars Subsystem**	**345 days**	**02/11/09**
698	101000	**Laser units**	**125 days**	**02/11/09**
701	102000	**Beam propagation units**	**240 days**	**02/11/09**
707	103000	**Control & metrology units**	**270 days**	**02/11/09**
713	109000	**LGS maintenance facility**	**75 days**	**15/11/10**

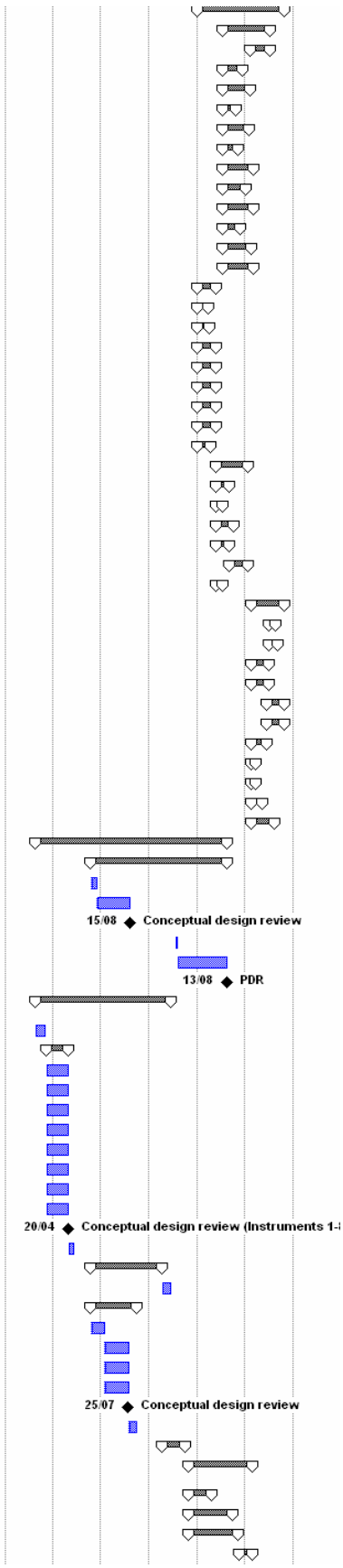

ID	Prod. Code	Task Name	Duration	Start
715	**110000**	**Central Control**	**150 days**	**21/02/11**
716	**111000**	**Central Control environment**	**100 days**	**21/02/11**
719	**112000**	**IT Systems**	**140 days**	**21/02/11**
724	119000	Central control maintenance facility - definition	10 days	05/09/11
725	**120000**	**Site characterization**	**665 days**	**19/05/08**
726	**121000**	**Weather stations**	**110 days**	**19/05/08**
730	**122000**	**Turbulence monitoring units**	**135 days**	**19/05/08**
734	**123000**	**Sky monitoring units**	**135 days**	**19/05/08**
738	124000	Operational forecast units (R&D)	530 days	24/11/08
739	**129000**	**Site characterization maintenance facility**	**10 days**	**24/11/08**

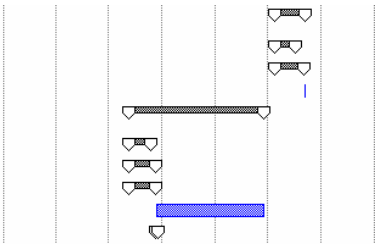

Appendix 5. Phase C/D schedule estimate

ID	Prod. Code	Task Name	Duration	Start
741		**OWL PHASE C/D**	**2815 days?**	**19/02/10**
742		**Major milestones**	**2815 days**	**19/02/10**
743		Kick-Off	0 days	19/02/10
744		M3 & M4 blanks contract award	0 days	13/08/10
745		Enclosure FDR	0 days	24/09/10
746		M1 & M2 Critical Design Review	0 days	08/10/10
747		Telescope structure FDR	0 days	03/12/10
748		M5 subunit PDR	0 days	18/02/11
749		M3 & M4 polishing contract award	0 days	04/02/11
750		M1 segments blanks contract award	0 days	25/03/11
751		M2 segments blanks contract award	0 days	25/03/11
752		Technical instrument FDR	0 days	19/08/11
753		M1 segments polishing contract award	0 days	12/08/11
754		M2 segments polishing contract award	0 days	12/08/11
755		First two science instruments FDR	0 days	17/02/12
756		M3 & M4 cells PDR	0 days	13/04/12
757		Start of M3 polishing	0 days	18/01/13
758		Azimuth functional tests completed	0 days	18/01/13
759		M3 & M4 cells FDR	0 days	19/04/13
760		Enclosure Technical Acceptance (TAC)	0 days	25/10/13
761		First batch of M1 segments on-site	0 days	18/10/13
762		First batch of M2 segments on-site	0 days	18/10/13
763		Start of M4 polishing	0 days	17/01/14
764		Post-focal AO (XAO) units PDR	0 days	21/03/14
765		M3 & M4 cells on-site	0 days	09/01/15
766		Telescope structure TAC	0 days	05/12/14
767		Start of M1 segments integration	0 days	12/12/14
768		Start of M2 segments integration	0 days	12/12/14
769		Post-focal AO (XAO) units FDR	0 days	23/10/15
770		Dummy corrector integrated	0 days	09/12/15
771		M3 & M4 assemblies on-site	0 days	04/03/16
772		Corrector integrated (provisional units)	0 days	18/05/16
773		***FIRST LIGHT [Seeing-limited, Equiv. dia. 57-m]***	***0 days***	***15/06/16***
774		***SCAO First light [Equiv. dia. 67-m]***	***0 days***	***20/12/16***
775		***Start of science [SCAO & GLAO, 2 instr., Equiv. dia. 75-m]***	***0 days***	***31/05/17***
776		M2 complete	0 days	08/09/17
777		XAO (post focal AO) first light	0 days	28/09/18
778		***MCAO first light [Equiv. dia. 89-m]***	***0 days***	***18/12/18***
779		***Laser Guide Star first light***	***0 days***	***05/04/19***
780		M1 complete	0 days	25/09/20
781		End of construction review	0 days	04/12/20

Phase C/D schedule estimate

ID	Prod. Code	Task Name	Duration	Start
782	010000	**Project Management**	2815 days	19/02/10
783		Project planning, control & reporting	2815 days	19/02/10
786		Contingency management	2815 days	19/02/10
789		Project reviews	2348 days	01/04/10
800	013000	Overheads	2815 days	19/02/10
803	020000	**Science Objectives**	2610 days	19/02/10
804		Top Level Requirements Configuration Management	2610 days	19/02/10
807		Commissioning plan	75 days	22/02/10
808	034000	Commissioning	1605 days	01/07/13
821		Science verification plan	130 days	20/02/12
822		Science verification	712 days	01/06/17
828	030000	**Project Engineering**	2815 days?	19/02/10
829	031000	Overall project engineering	2815 days	19/02/10
832	032000	System engineering	2815 days	19/02/10
835	033000	AIV	2275 days?	09/01/12
836		Site infrastructure (acceptance)	35 days	13/05/13
839		Enclosure (acceptance)	75 days	23/09/13
843		Telescope structure & kinematics (acceptance)	100 days	29/09/14
847		Optomechanical subsystems	2275 days	09/01/12
848		M1 & M2 Support preparation	1645 days	26/03/12
849		Whiffle trees unpacking, verification & preparat	1590 days	26/03/12
856		Actuators unpacking, verification & preparatior	1590 days	04/06/12
863		Assembling actuators / functional test	1590 days	11/06/12
870		Supports storage prior to integration	565 days	15/06/12
873		Primary mirror unit	2155 days	25/06/12
874		Subcells storage prior to integration	640 days	25/06/12
877		Subcells integration into telescope	1060 days	08/12/14
882		Segments storage prior to preparation	195 days	14/10/13
885		Segments preparation	1617 days	14/07/14
886		Unpacking & cleaning	1590 days	14/07/14
893		Mounting position sensors / cross-check (	1590 days	21/07/14
900		Washing & coating	1590 days	04/08/14
907		Mounting on whiffle trees & actuators	1590 days	18/08/14
914		Functional test	1590 days	20/08/14
921		Segments storage prior to integration	78 days	26/08/14
924		Segments integration	1510 days	12/12/14
925		Blind-1	258 days	12/12/14
928		Blind-2	78 days	27/01/16
931		Blind-3	20 days	18/05/16
934		Phased on-sky -1	97 days	15/06/16
937		Phased on-sky -2	126 days	06/12/16

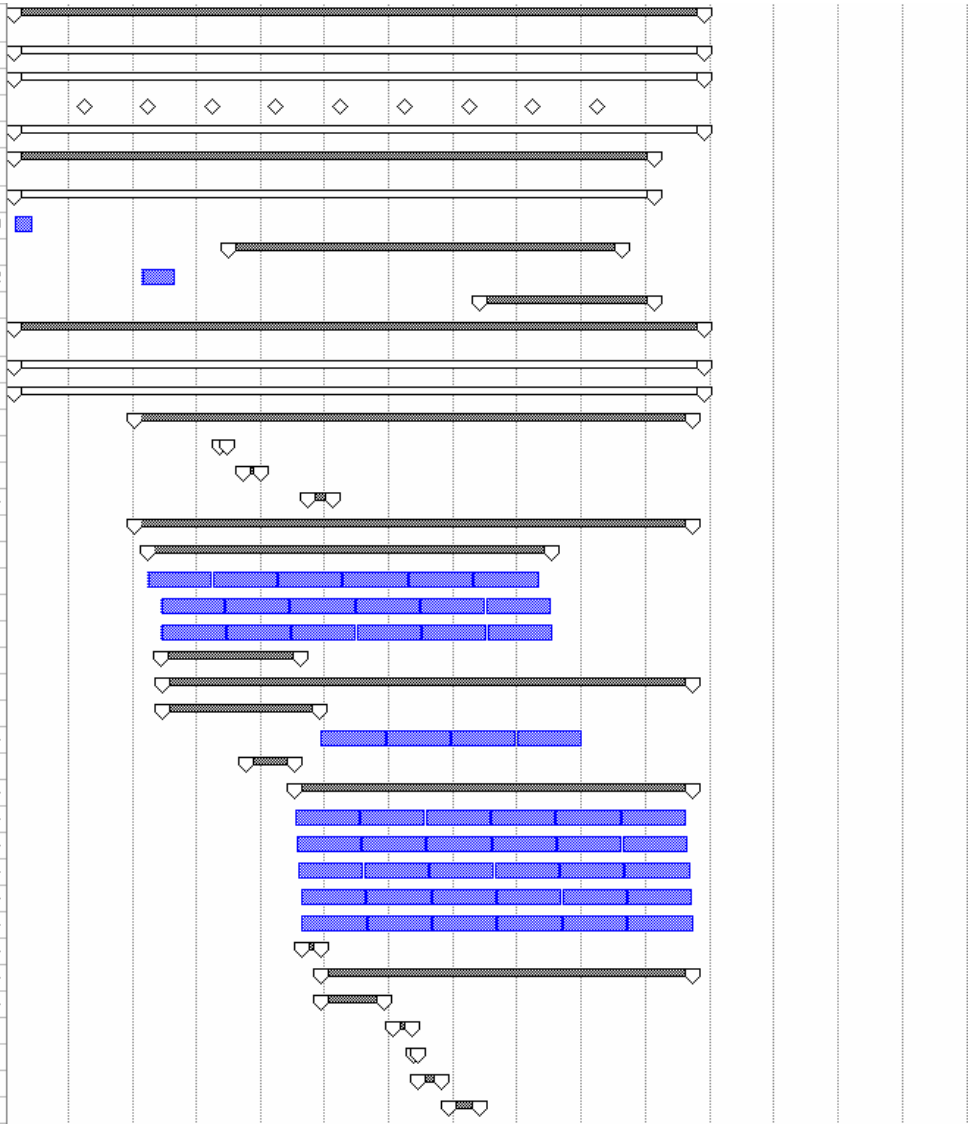

ID	Prod. Code	Task Name	Duration	Start
940		**Phased on-sky -2 (continued)**	**367 days**	**31/05/17**
943		**Phased on-sky -2 (continued)**	**473 days**	**04/12/18**
946		**Secondary mirror unit**	**1480 days**	**09/01/12**
947		**Subcells storage prior to integration**	**760 days**	**09/01/12**
950		**Subcells integration into telescope**	**530 days**	**08/12/14**
953		**Segments storage prior to preparation**	**195 days**	**14/10/13**
956		**Segments preparation**	**822 days**	**14/07/14**
957		**Unpacking & cleaning**	**795 days**	**14/07/14**
961		**Mounting position sensors / cross-check**	**795 days**	**21/07/14**
965		**Washing & coating**	**795 days**	**04/08/14**
969		**Mounting on whiffle trees & actuators**	**795 days**	**18/08/14**
973		**Functional test**	**795 days**	**20/08/14**
977		**Segments storage prior to integration**	**78 days**	**26/08/14**
980		**Segments integration**	**715 days**	**12/12/14**
981		**Blind-1**	**263 days**	**12/12/14**
984		**Blind-2**	**78 days**	**27/01/16**
987		**Blind-3**	**20 days**	**18/05/16**
990		**Phased on-sky -1**	**97 days**	**15/06/16**
993		**Phased on-sky -2**	**126 days**	**06/12/16**
996		**Phased on-sky -2 (continued)**	**72 days**	**31/05/17**
999		**Corrector unit**	**1442 days**	**10/06/13**
1000		**Corrector structure & kinematics**	**100 days**	**20/01/14**
1003		**Instrument racks**	**750 days**	**10/06/13**
1004		**Standard racks**	**500 days**	**10/06/13**
1011		**Gravity-stable racks**	**250 days**	**11/05/15**
1018		**M3 & M4 subunits**	**471 days**	**26/05/14**
1019		**M3 & M4 mirror assemblies**	**471 days**	**26/05/14**
1024		**M3 & M4 mirror cells**	**172 days**	**12/01/15**
1035		**M5 subunit**	**1128 days**	**02/07/14**
1036		**M5 provisional assembly**	**195 days**	**02/07/14**
1041		**M5 adaptive assembly**	**125 days**	**07/05/18**
1048		**M6 subunit**	**542 days**	**26/05/14**
1049		**M6 provisional assembly**	**200 days**	**26/05/14**
1054		**M6 adaptive assembly**	**102 days**	**01/02/16**
1062		**Corrector w. dummy mirrors preparation**	**198 days**	**09/03/15**
1075		Integration of dummy corrector into telescope	5 days	10/12/15
1076		Testing (incl. gravity and open-air)	25 days	17/12/15
1077		De-integration of dummy corrector from telescope	5 days	21/01/16
1078		Corrector structure & kinematics TAC	0 days	27/01/16
1079		**Corrector preparation for first light**	**45 days**	**15/03/16**
1112		Corrector integration into telescope	2 days	17/05/16
1113		Alignment & First light preparation checks	15 days	19/05/16
1114		De-integration of corrector from telescope	3 days	31/10/16

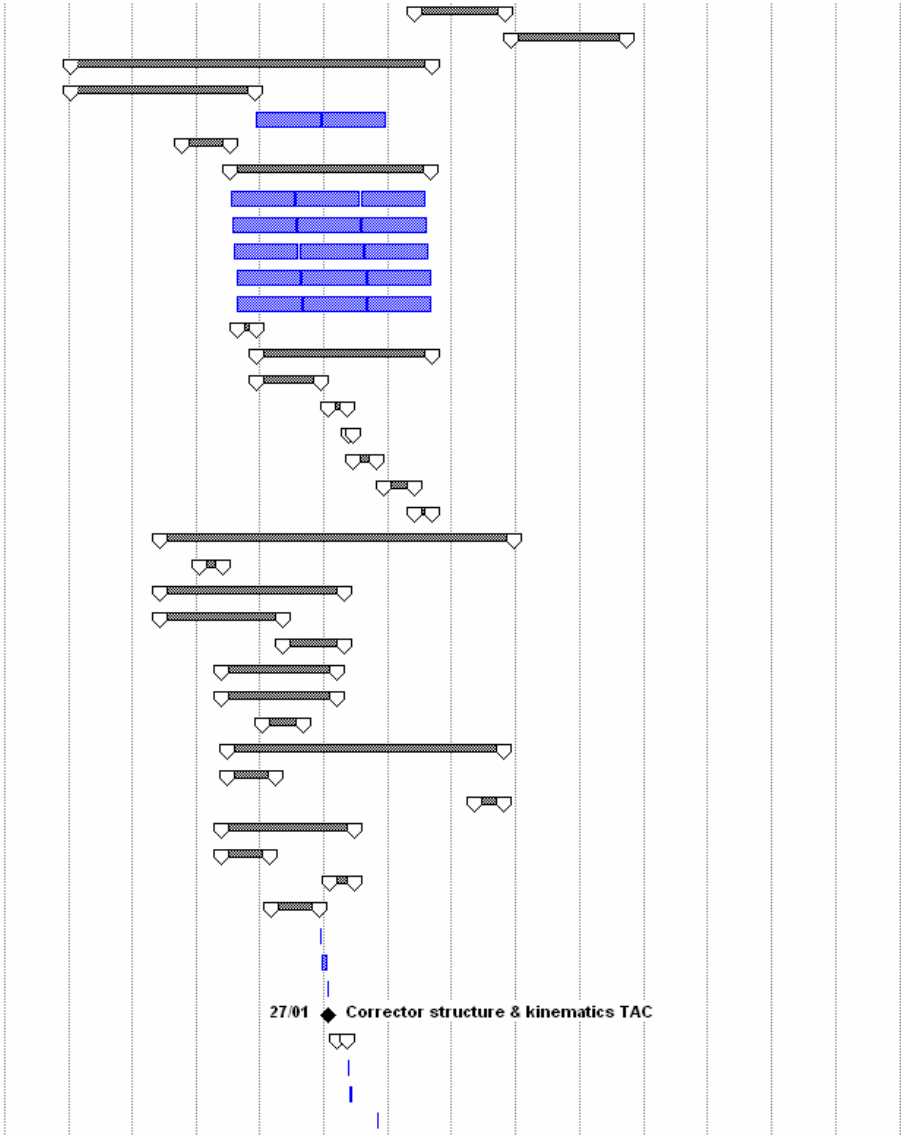

Phase C/D schedule estimate

ID	Prod. Code	Task Name	Duration	Start
1115		**Corrector preparation for SCAO first light**	**22 days**	**03/11/16**
1139		Re-integration of corrector into telescope	2 days	05/12/16
1140		Alignment & preparation	10 days	07/12/16
1141		De-integration of corrector from telescope	3 days	29/10/18
1142		**Corrector preparation for MCAO first light**	**22 days**	**01/11/18**
1166		Re-integration of corrector into telescope	2 days	03/12/18
1167		Alignment & preparation	10 days	05/12/18
1168		**Focal stations**	**825 days**	**18/05/15**
1169		**Focal station - 1**	**115 days**	**13/06/16**
1175		**Focal station - 2**	**115 days**	**13/06/16**
1181		**Focal station - 3**	**140 days**	**24/04/17**
1187		**Focal station - 4**	**130 days**	**15/01/18**
1193		**Focal station - 5**	**130 days**	**15/01/18**
1199		**Focal station - 6**	**110 days**	**18/05/15**
1206		**Telescope pre-alignment unit**	**448 days**	**29/09/14**
1215		**Opto-mechanical subsystems maintenance facilitie**	**983 days**	**23/07/12**
1216		**Clean rooms**	**275 days**	**06/05/13**
1220		**M1 & M2 offline maintenance facility**	**515 days**	**23/07/12**
1221		**Segments washing & coating tanks**	**100 days**	**24/02/14**
1226		**Segments carts and transporters**	**40 days**	**27/01/14**
1230		Segments support stands (emergency support)	15 days	23/07/12
1231		**Segments racks**	**30 days**	**04/11/13**
1235		Segments storage facility - verification	5 days	05/11/12
1236		**M1 & M2 in-situ maintenance devices**	**125 days**	**19/05/14**
1237		**M1 in-situ cleaning robot**	**45 days**	**08/09/14**
1242		**M1 segment assembly in-situ handling rob**	**45 days**	**16/06/14**
1247		**M1 cover in-situ cart holder**	**75 days**	**19/05/14**
1252		**M2 in-situ cleaning device**	**40 days**	**08/09/14**
1257		**M2 segment assembly in-situ handling too**	**40 days**	**16/06/14**
1262		**Corrector maintenance facility**	**538 days**	**02/09/13**
1263		**Corrector maintenance hall**	**15 days**	**02/09/13**
1266		**Corrector transporters**	**45 days**	**18/11/13**
1270		**M3 & M4 subunits extractor**	**60 days**	**07/04/14**
1274		**M3 & M4 subunits transporters**	**383 days**	**07/04/14**
1282		**M5 subunit extractor**	**65 days**	**02/09/13**
1288		**M5 unit transporters**	**417 days**	**02/09/13**
1293		**M6 subunit extractor**	**55 days**	**02/09/13**
1299		**M6 subunit transporters**	**395 days**	**02/09/13**
1304		**M3 & M4 assemblies maintenance facility**	**112 days**	**30/03/15**
1305		**M3 & M4 assemblies maintenance hall**	**10 days**	**30/03/15**
1308		**M3 & M4 assemblies lifting device**	**96 days**	**13/04/15**
1315		**8-m class washing & coating tanks**	**102 days**	**13/04/15**
1324		**M3 & M4 mirror assemblies washing & coa**	**100 days**	**13/04/15**

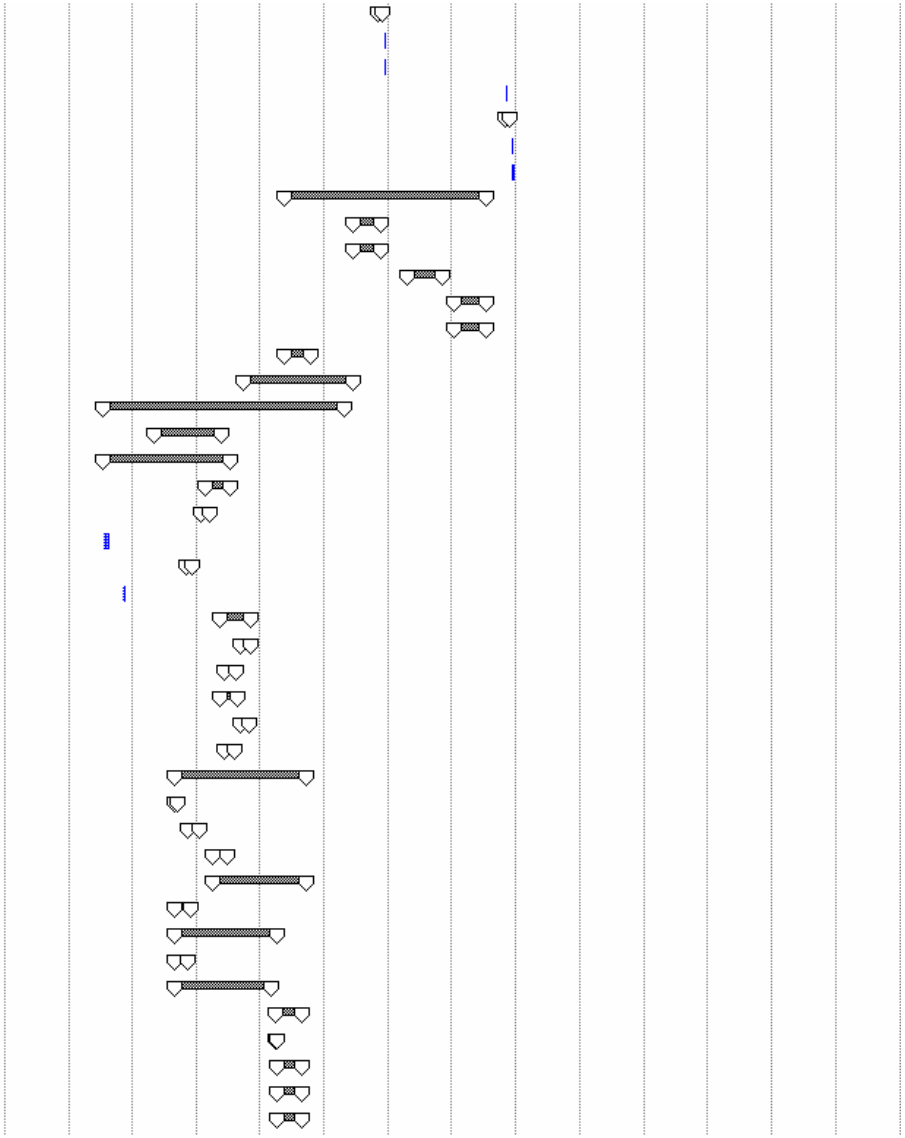

Phase C/D schedule estimate

ID	Prod. Code	Task Name	Duration	Start
1330		**M3 & M4 mirror assemblies support stand**	**98 days**	**13/04/15**
1335		**M5 & M6 assemblies maintenance facility**	**524 days**	**16/11/12**
1336		**M5 & M6 assemblies maintenance hall**	**10 days**	**18/10/13**
1339		**M5 mirror assembly lifting device**	**58 days**	**15/08/14**
1345		**M6 mirror assembly lifting device**	**58 days**	**15/08/14**
1351		**M5 assembly washing & coating cart**	**155 days**	**11/04/14**
1357		**M6 assembly washing & coating cart**	**155 days**	**11/04/14**
1362		**4-m class washing & coating tanks**	**104 days**	**27/06/14**
1371		**M5 mirror assembly support stand (emerg**	**515 days**	**16/11/12**
1375		**M6 mirror assembly support stand (emerg**	**515 days**	**16/11/12**
1379		**Corrector in-situ cleaning devices**	**428 days**	**08/09/14**
1385		**Focal stations maintenance facility**	**20 days**	**12/10/12**
1388		**Instrumentation**	**1235 days**	**06/01/14**
1389		**Technical instrumentation**	**100 days**	**18/05/15**
1393		**Science instrumentation**	**495 days**	**16/03/15**
1394		**Instrument -1**	**495 days**	**16/03/15**
1400		**Instrument -2**	**495 days**	**16/03/15**
1406		**Post-focal AO units**	**120 days**	**16/04/18**
1412		**Instruments maintenance facility**	**30 days**	**06/01/14**
1415		**Laser Guide Stars Subsystem**	**540 days?**	**13/03/17**
1416		**Laser units**	**185 days**	**16/04/18**
1422		**Beam Propagation units**	**185 days**	**23/07/18**
1429		**Control & Metrology units**	**135 days?**	**20/08/18**
1435		**LGS maintenance facility**	**50 days**	**13/03/17**
1438		**Central Control Systems**	**535 days**	**16/03/15**
1439		**Central Control Environment**	**335 days**	**21/12/15**
1443		**IT Systems**	**310 days**	**16/03/15**
1447		**Central Control maintenance facility**	**15 days**	**21/12/15**
1450		**Site characterization**	**605 days**	**07/01/13**
1451		**Weather stations**	**30 days**	**28/01/13**
1454		**Turbulence monitoring units**	**75 days**	**28/07/14**
1458		**Sky monitoring units**	**75 days**	**07/04/14**
1462		**Operational Forecasts units**	**125 days**	**10/11/14**
1464		**Site characterization maintenance facility**	**15 days**	**07/01/13**
1467	**035000**	**R&D, major breadboards and experiments**	**1200 days**	**22/02/10**
1468	**035100**	**Adaptive optics concepts & technologies**	**800 days**	**22/02/10**
1469		LGS Laser technology development & prototyping	800 days	22/02/10
1470		High order DM technology development & prototyping	800 days	22/02/10
1471		Detectors development	800 days	22/02/10
1472	**035200**	**Physical optics R&D**	**1200 days**	**22/02/10**
1473		Data reduction R&D	1200 days	22/02/10
1474		High contrast imaging R&D	1200 days	22/02/10
1475	035300	Non-adaptive wavefront sensing / control R&D	1200 days	22/02/10

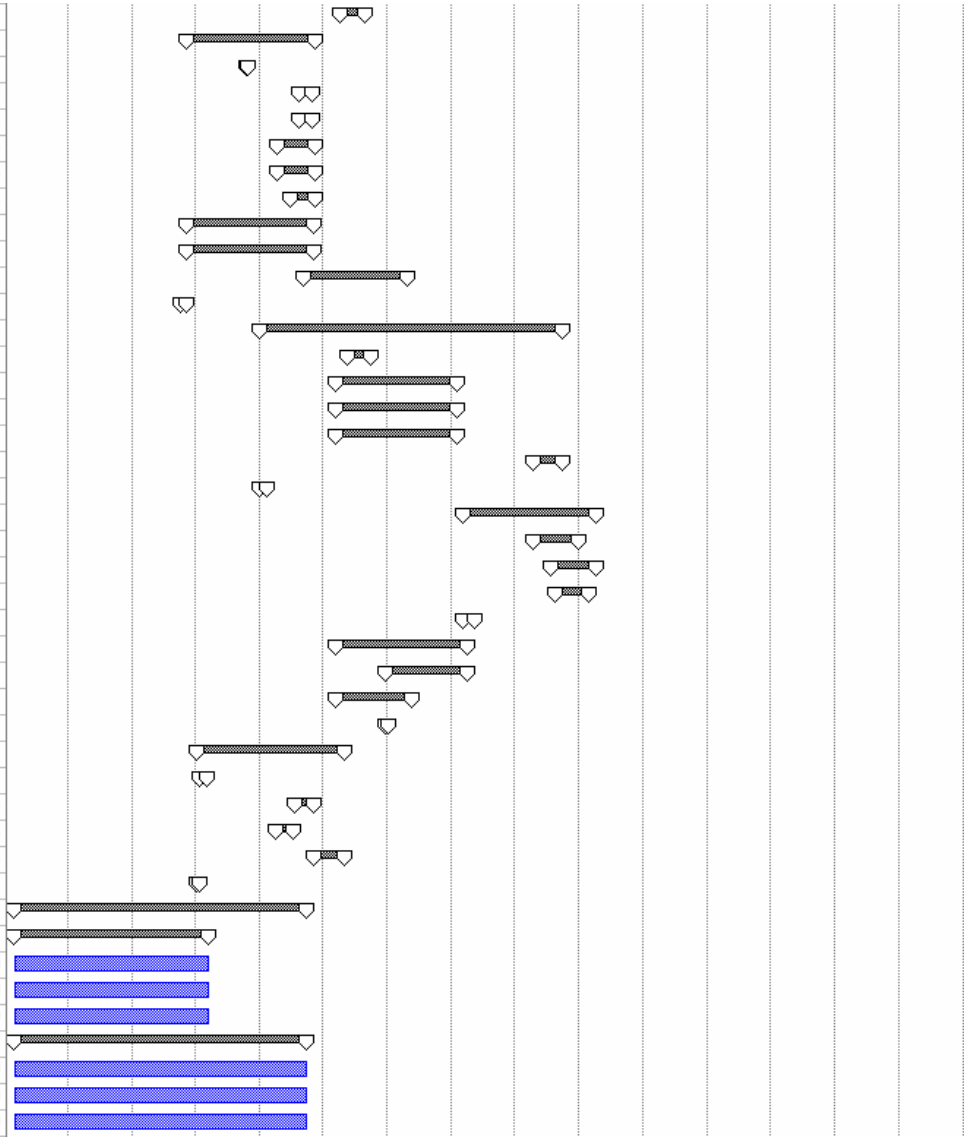

Phase C/D schedule estimate

ID	Prod. Code	Task Name	Duration	Start
1476		**Final design / supply / constructior**	**2540 days**	**22/02/10**
1477	**040000**	**Site infrastructure**	**840 days**	**22/02/10**
1478	**041000**	**Integration infrastructures**	**530 days**	**22/02/10**
1479	041100	Enclosure integration infrastructures - Installation / verifica	75 days	10/05/10
1480	041200	Telescope structure & kinematics integration infrastructure	75 days	23/08/10
1481	**041300**	**Optomechanical subsystems integration infrastruc**	**490 days**	**22/02/10**
1482	**041310**	**M1 & M2 units integration tools & equipments**	**435 days**	**10/05/10**
1488	**041320**	**Corrector unit integration tools & equipment**	**425 days**	**29/03/10**
1494	**041330**	**Focal stations integration tools & equipment**	**465 days**	**29/03/10**
1500	**041340**	**Telescope pre-alignment unit integration tools**	**295 days**	**22/02/10**
1506	**041400**	**Other temporary integration facilities**	**530 days**	**22/02/10**
1513	**042000**	**Operation infrastructures**	**840 days**	**22/02/10**
1514	**042100**	**Maintenance infrastructures**	**620 days**	**26/04/10**
1520	**042200**	**Science operation infrastructures**	**810 days**	**05/04/10**
1526	**042300**	**Other infrastructures**	**650 days**	**10/05/10**
1532	042400	Power plant / supply - Stage-2	150 days	25/04/11
1533		Power plant / supply - Stage-3	150 days	21/11/11
1534	**042500**	**Services**	**750 days**	**22/02/10**
1540	**042600**	**Technical buildings**	**750 days**	**22/02/10**
1546	049000	Site infrastructure maintenance facility	130 days	04/07/11
1547	**050000**	**Enclosure**	**780 days**	**27/09/10**
1548	051000	Enclosure foundations	130 days	27/09/10
1549	052000	Kinematics	130 days	28/03/11
1550	053000	Enclosure structures	520 days	26/09/11
1551	059000	Enclosure Maintenance Units	130 days	10/09/12
1552	**070000**	**Telescope structure & kinematics (supply / erection / verifi**	**995 days**	**06/12/10**
1553	**071000**	**Azimuth structures**	**555 days**	**06/12/10**
1554	**071100**	**Azimuth tracks**	**290 days**	**06/12/10**
1557	**071200**	**Azimuth drives**	**480 days**	**06/12/10**
1561	**071300**	**Azimuth structural mechanics**	**330 days**	**06/12/10**
1564	071400	Central azimuth bearing and encoder assembly	90 days	16/01/12
1565	071500	Azimuth Cable wrap	90 days	21/05/12
1566	071600	Azimuth cooling system	60 days	24/09/12
1567	071700	Auxiliary equipments	130 days	06/12/10
1568		Azimuth functional tests	25 days	17/12/12
1569	**072000**	**Altitude structures**	**995 days**	**06/12/10**
1570	**072100**	**Altitude cradle**	**630 days**	**06/12/10**
1573	**072200**	**Altitude drives**	**995 days**	**06/12/10**
1577	**072300**	**Altitude structural mechanics**	**865 days**	**06/12/10**
1580	072400	Altitude bearings and encoders assemblies	50 days	21/01/13
1581	072500	Altitude Cable wraps	75 days	01/04/13
1582	072600	Altitude cooling system (corrector, instrumentation).	75 days	15/07/13

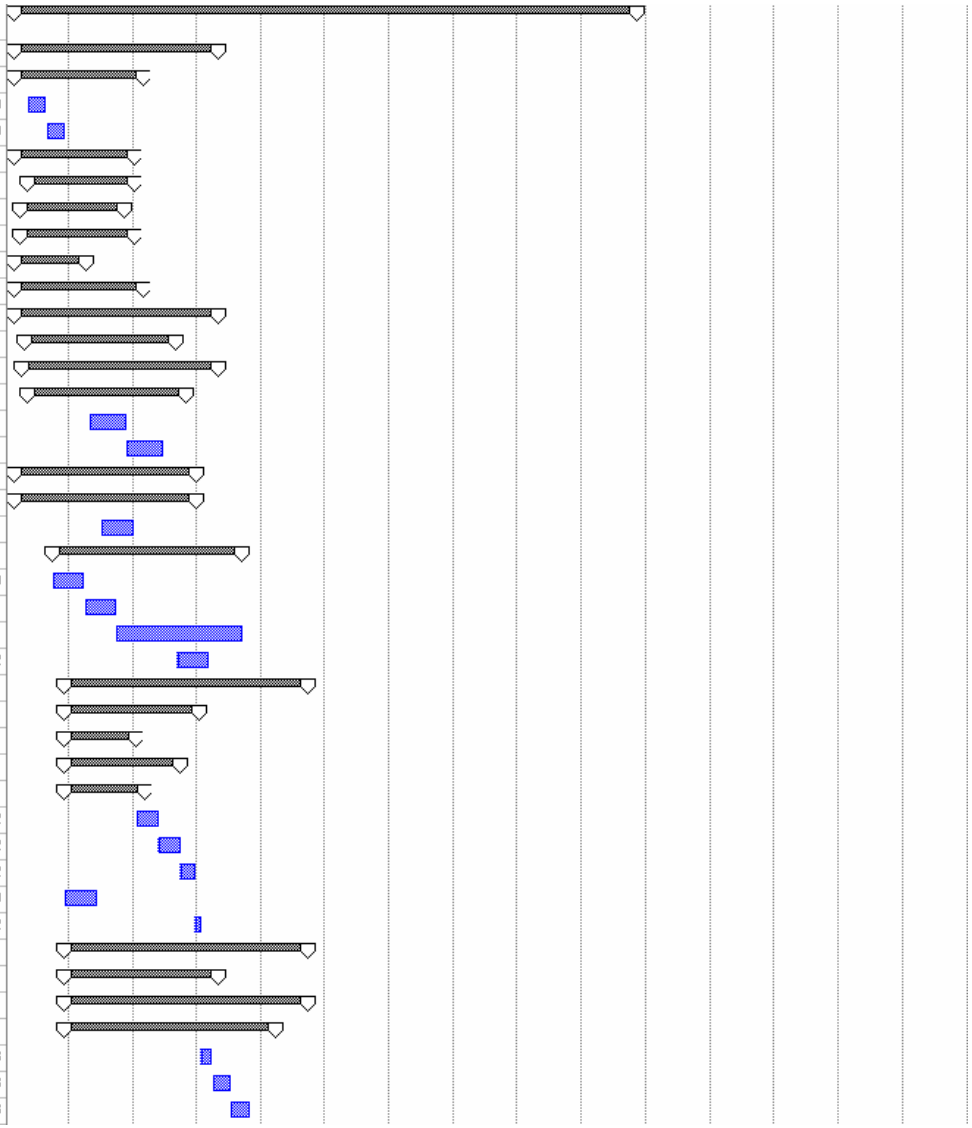

ID	Prod. Code	Task Name	Duration	Start
1583	072700	Auxiliary equipments	130 days	06/12/10
1584		Azimuth & Altitude functional tests	25 days	31/03/14
1585	**073000**	**Wind screens**	**220 days**	**06/12/10**
1586		Supply & transport to site	190 days	06/12/10
1587		Integration	130 days	11/04/11
1588	**074000**	**Mirror covers**	**905 days**	**06/12/10**
1589	**074100**	**M1 cover**	**900 days**	**06/12/10**
1593	**074200**	**M2 cover**	**905 days**	**06/12/10**
1597	075000	Telescope foundations	160 days	06/12/10
1598	076000	Telescope diagnostic systems.	75 days	06/12/10
1599	079000	Telescope structure & kinematics maintenance units	130 days	10/09/12
1600	**080000**	**Optomechanical subsystems**	**2540 days**	**22/02/10**
1601		**M1 & M2 segments design review**	**85 days**	**12/07/10**
1605		**Whiffle trees (incl. lateral support)**	**1840 days**	**28/03/11**
1606		Final design	190 days	28/03/11
1607		Production tests	60 days	19/12/11
1608		**Production & transport to site**	**1590 days**	**12/03/12**
1615		**Active supports**	**1890 days**	**28/03/11**
1616		Final design	210 days	28/03/11
1617		Production tests	90 days	16/01/12
1618		**Production & transport to site**	**1590 days**	**21/05/12**
1625		**Local metrology assembly**	**1890 days**	**28/03/11**
1626		Final design	210 days	28/03/11
1627		Production tests	90 days	16/01/12
1628		**Production & transport to site**	**1590 days**	**21/05/12**
1635		**Segments transport & storage containers**	**520 days**	**28/03/11**
1642	**081000**	**Primary mirror unit**	**2355 days**	**08/11/10**
1643	**081100**	**Segment subunit**	**2355 days**	**08/11/10**
1644	**081110**	**Segment assembly**	**2355 days**	**08/11/10**
1645		CfT segments blanks	100 days	08/11/10
1646		Award of contract	0 days	25/03/11
1647		Facilitization	520 days	28/03/11
1648		Pre-production	120 days	08/10/12
1649		**Segments blanks production**	**1590 days**	**25/03/13**
1656		CfT polishing	100 days	28/03/11
1657		Award of contract	0 days	12/08/11
1658		Facilitization	520 days	15/08/11
1659		Pre-production	120 days	25/02/13
1660		**Segments polishing & I/F**	**1590 days**	**12/08/13**
1667		**Packing & Transport to site**	**1590 days**	**14/10/13**
1674	**081150**	**Segments subcells**	**1915 days**	**28/03/11**
1675		CfT	75 days	28/03/11

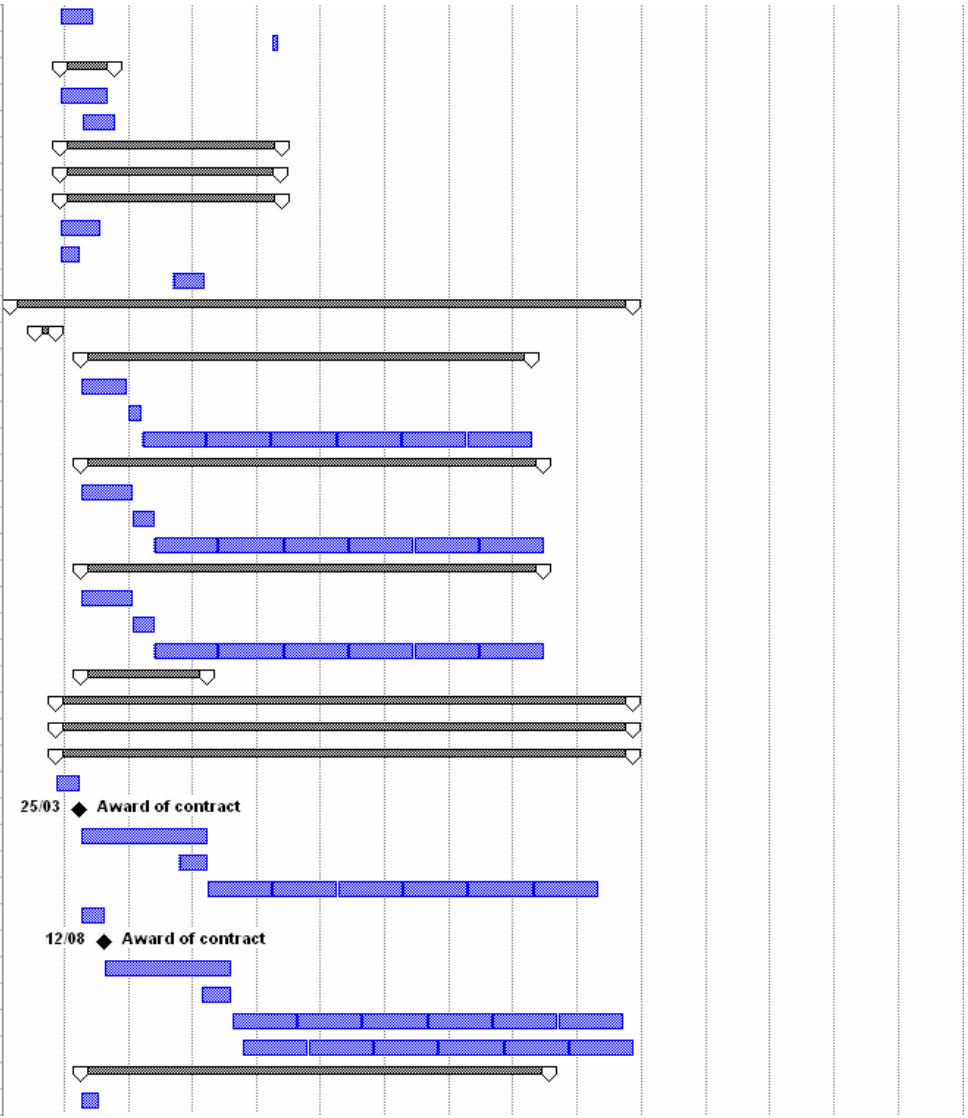

ID	Prod. Code	Task Name	Duration	Start
1676		Award of contract	0 days	08/07/11
1677		Design	125 days	11/07/11
1678		CDR	0 days	30/12/11
1679		Tooling & preparation	125 days	02/01/12
1680		Pre-production	50 days	16/04/12
1681		**Production & transport to site**	**1590 days**	**25/06/12**
1688	**082000**	**Secondary mirror unit**	**1745 days**	**22/02/10**
1689	**082100**	**Segment subunit**	**1745 days**	**22/02/10**
1690	**082110**	**Segment assembly**	**1560 days**	**08/11/10**
1691		CfT segments blanks	100 days	08/11/10
1692		Award of contract	0 days	25/03/11
1693		Facilitization	520 days	28/03/11
1694		Pre-production	120 days	08/10/12
1695		**Segments blanks production**	**795 days**	**25/03/13**
1699		CfT polishing	100 days	28/03/11
1700		Award of contract	0 days	12/08/11
1701		Facilitization	520 days	15/08/11
1702		Pre-production	120 days	25/02/13
1703		**Segments polishing & I/F**	**795 days**	**12/08/13**
1707		**Packing & Transport to site**	**795 days**	**14/10/13**
1711	**082150**	**Segments subcells**	**1095 days**	**22/02/10**
1722	**083000**	**Corrector unit**	**2140 days**	**22/02/10**
1723	**083100**	**Corrector structure & kinematics**	**905 days**	**22/02/10**
1732	**083200**	**Instruments racks**	**990 days**	**22/02/10**
1742		**M3 & M4 subunits**	**1575 days**	**22/02/10**
1743		**M3 & M4 mirror assemblies**	**1575 days**	**22/02/10**
1744		**Mirror blanks**	**975 days**	**22/02/10**
1756		**Optical figuring**	**1405 days**	**16/08/10**
1795		M3 & M4 assemblies - transport to site	45 days	04/01/16
1796		**M3 & M4 mirror cells**	**1150 days**	**16/08/10**
1812	**083500**	**M5 subunit**	**1880 days**	**21/02/11**
1813		Final design	420 days	21/02/11
1814		FDR	0 days	28/09/12
1815	**083510**	**M5 Provisional assembly**	**962 days**	**21/02/11**
1816		Electromechanical assembly fabrication & preass	360 days	01/10/12
1817		Functional tests (with dummy mirror)	50 days	17/02/14
1818		Dummy de-integration	2 days	28/04/14
1819		Dummy packing & shipment to site	45 days	30/04/14
1820		**M5 provisional mirror**	**735 days**	**21/02/11**
1823		Provisional M5 mirror integration	25 days	30/04/14
1824		Provisional Acceptance Tests	35 days	04/06/14
1825		De-integration & packing	25 days	23/07/14
1826		Shipment to site	45 days	27/08/14

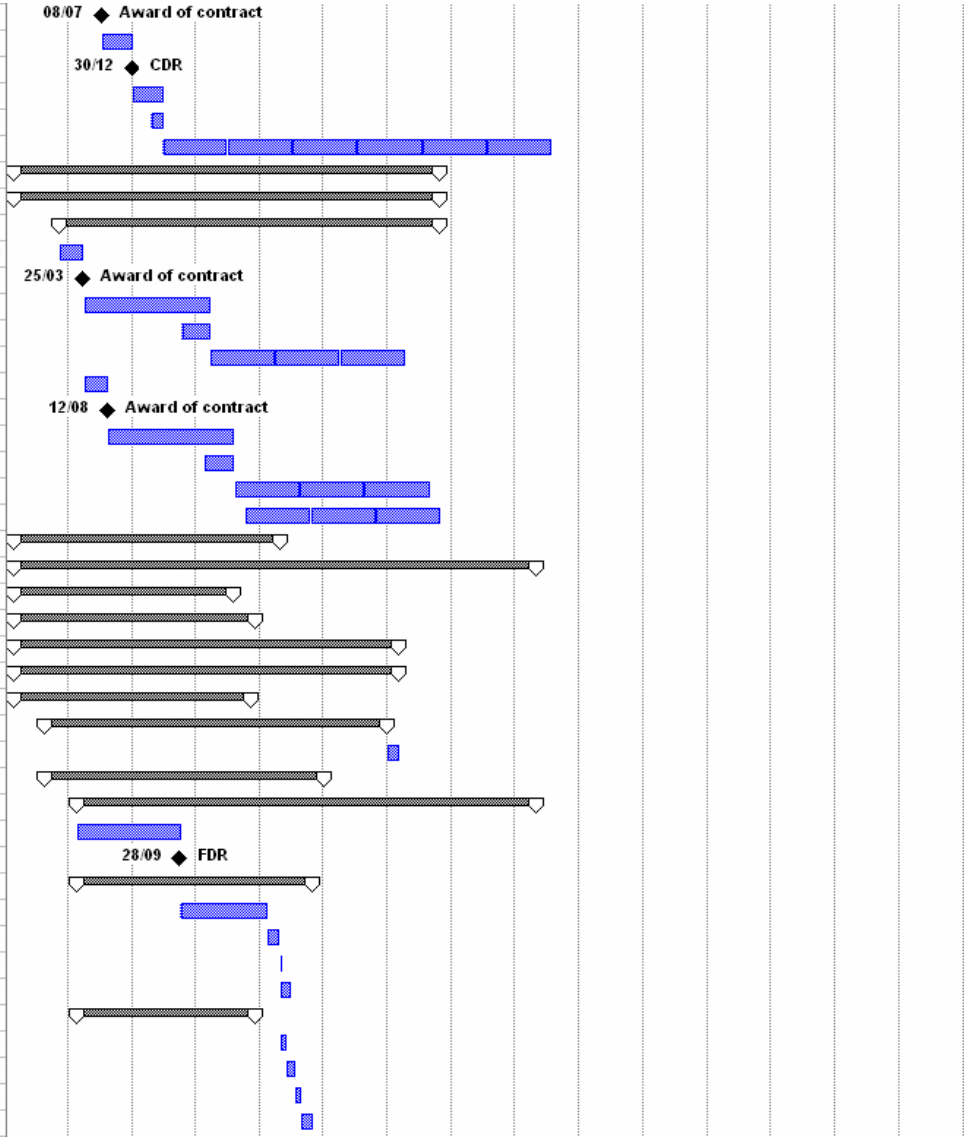

Phase C/D schedule estimate

ID	Prod. Code	Task Name	Duration	Start
1827	**083520**	**M5 adaptive assembly**	**1460 days**	**01/10/12**
1828		Electromechanical assembly fabrication & preass	520 days	01/10/12
1829		Functional tests (with dummy mirror)	75 days	29/09/14
1830		**M5 adaptive shell**	**1245 days**	**01/10/12**
1842		M5 shell integration	25 days	10/07/17
1843		Provisional Acceptance Tests	35 days	14/08/17
1844		Additional test / characterization runs	75 days	02/10/17
1845		De-integration & packing	35 days	15/01/18
1846		Shipment to site	45 days	05/03/18
1847	083530	M5 test facility (design & construction)	520 days	01/10/12
1848	**083600**	**M6 subunit**	**1375 days**	**25/10/10**
1849		Final design	365 days	25/10/10
1850		FDR	0 days	16/03/12
1851	**083610**	**M6 provisional assembly**	**660 days**	**19/03/12**
1852		Electromechanical assembly fabrication & preass	360 days	19/03/12
1853		Functional tests (with dummy mirror)	50 days	05/08/13
1854		Dummy de-integration	2 days	14/10/13
1855		Dummy packing & shipment to site	45 days	16/10/13
1856		**M6 provisional mirror**	**530 days**	**19/03/12**
1859		Provisional M6 mirror integration	25 days	31/03/14
1860		Provisional Acceptance Tests	35 days	05/05/14
1861		De-integration & packing	25 days	23/06/14
1862		Shipment to site	45 days	28/07/14
1863	**083620**	**M6 adaptive assembly**	**1010 days**	**19/03/12**
1864		Electromechanical assembly fabrication & preass	440 days	19/03/12
1865		Functional tests (with dummy mirror)	50 days	25/11/13
1866		**M6 adaptive shell**	**825 days**	**19/03/12**
1878		M6 shell integration	20 days	18/05/15
1879		Provisional Acceptance Tests	35 days	15/06/15
1880		Additional test / characterization runs	50 days	03/08/15
1881		De-integration & packing	35 days	12/10/15
1882		Shipment to site	45 days	30/11/15
1883	083630	M6 test facility	400 days	19/03/12
1884	**084000**	**Focal stations**	**2060 days**	**22/02/10**
1885		Focal station - 1 shipment to site	45 days	11/04/16
1886		Focal station - 2 shipment to site	45 days	11/04/16
1887		Focal station - 3 shipment to site	45 days	20/02/17
1888		Focal station - 4 shipment to site	45 days	13/11/17
1889		Focal station - 5 shipment to site	45 days	13/11/17
1890		Focal station - 6 shipment to site (incl. technical instrument	45 days	16/03/15
1891	**084100**	**Electromechanical subunits**	**2015 days**	**22/02/10**
1892		CfT	100 days	22/02/10
1893		Review of offers	50 days	12/07/10

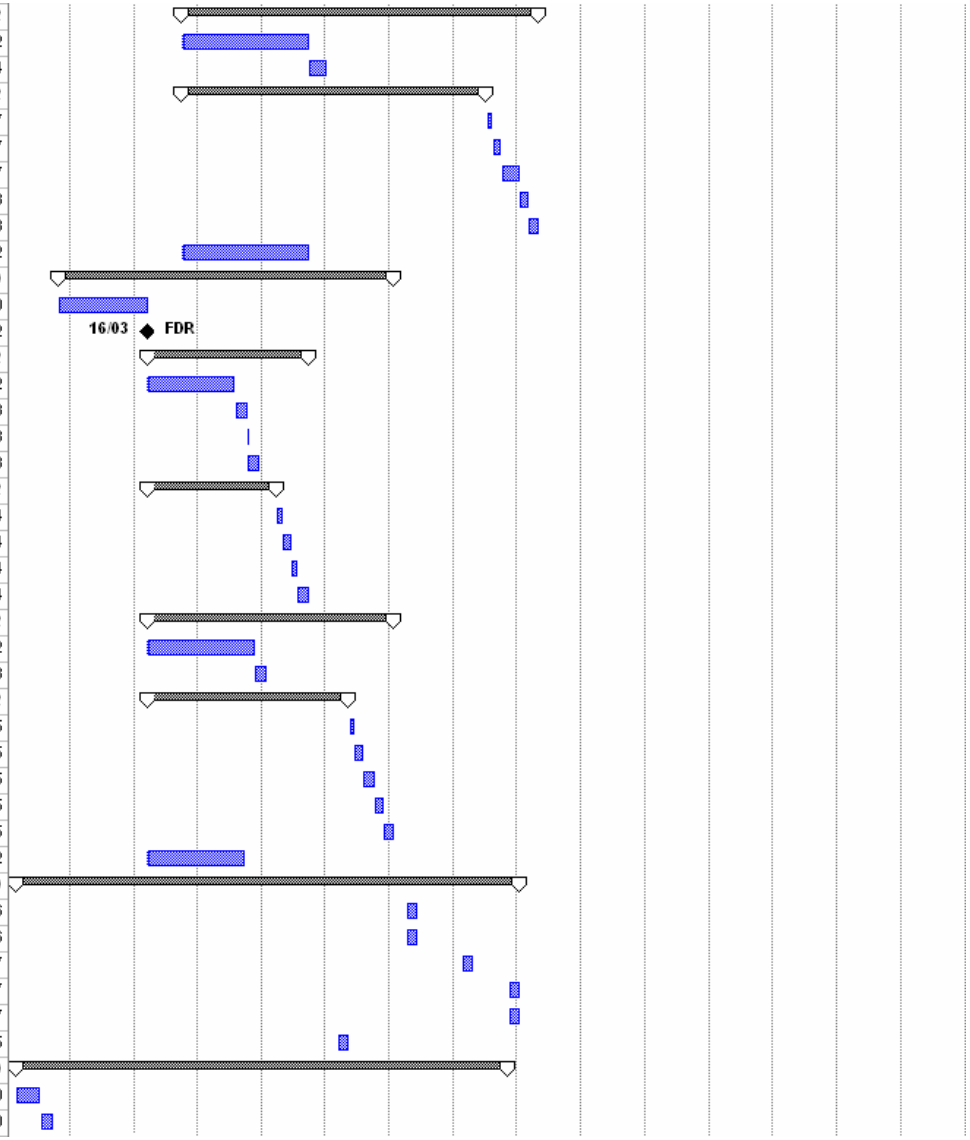

Phase C/D schedule estimate

ID	Prod. Code	Task Name	Duration	Start
1894		Contract award	0 days	17/09/10
1895		Preliminary design	210 days	20/09/10
1896		PDR	0 days	08/07/11
1897		Final design	265 days	11/07/11
1898		FDR	0 days	13/07/12
1899		**Focal station - 1**	**435 days**	**11/08/14**
1908		**Focal station - 2**	**435 days**	**11/08/14**
1917		**Focal station - 3**	**530 days**	**09/02/15**
1926		**Focal station - 4**	**720 days**	**09/02/15**
1935		**Focal station - 5**	**720 days**	**09/02/15**
1944		**Focal station - 6**	**695 days**	**16/07/12**
1953	**084200**	**Active Optics metrology**	**800 days**	**22/02/10**
1965	**084300**	**Phasing metrology**	**915 days**	**22/02/10**
1966		CfT	75 days	22/02/10
1967		Review of offers	25 days	07/06/10
1968		Contract award	0 days	09/07/10
1969		Final design	190 days	12/07/10
1970		Critical Design Review	0 days	01/04/11
1971		**Production / testing / shipment to electromech**	**625 days**	**04/04/11**
1977	**084400**	**Guiding and field stabilization metrologies**	**530 days**	**22/02/10**
1978		CfT	75 days	22/02/10
1979		Review of offers	25 days	07/06/10
1980		Contract award	0 days	09/07/10
1981		Design	130 days	12/07/10
1982		Critical Design Review	0 days	07/01/11
1983		**Production / testing / shipment to electromech**	**300 days**	**10/01/11**
1989	**084500**	**Adaptive Optics metrology & Real-Time Computers**	**1570 days**	**22/02/10**
1990		CfT	100 days	22/02/10
1991		Preliminary design	190 days	12/07/10
1992		PDR	0 days	01/04/11
1993		Final design	330 days	04/04/11
1994		Prototype Wavefront sensor- fabrication	190 days	04/04/11
1995		Prototype wavefront sensor - characterization	50 days	26/12/11
1996		FDR	0 days	06/07/12
1997	**084510**	**Focal Station – 1 (SCAO station)**	**180 days**	**09/02/15**
2000	**084520**	**Focal Station – 2 (GLAO station)**	**180 days**	**09/02/15**
2003	**084530**	**Focal Station – 3 (MCAO station)**	**275 days**	**09/02/15**
2006	**084540**	**Focal Station – 4**	**275 days**	**09/02/15**
2009	**084550**	**Focal Station – 5**	**275 days**	**09/02/15**
2012	**084560**	**Focal Station – 6**	**275 days**	**09/07/12**
2015	**085000**	**Telescope pre-alignment unit**	**760 days**	**22/02/10**
2025	**089000**	**Optomechanical subsystems maintenance facilities**	**925 days**	**12/09/11**

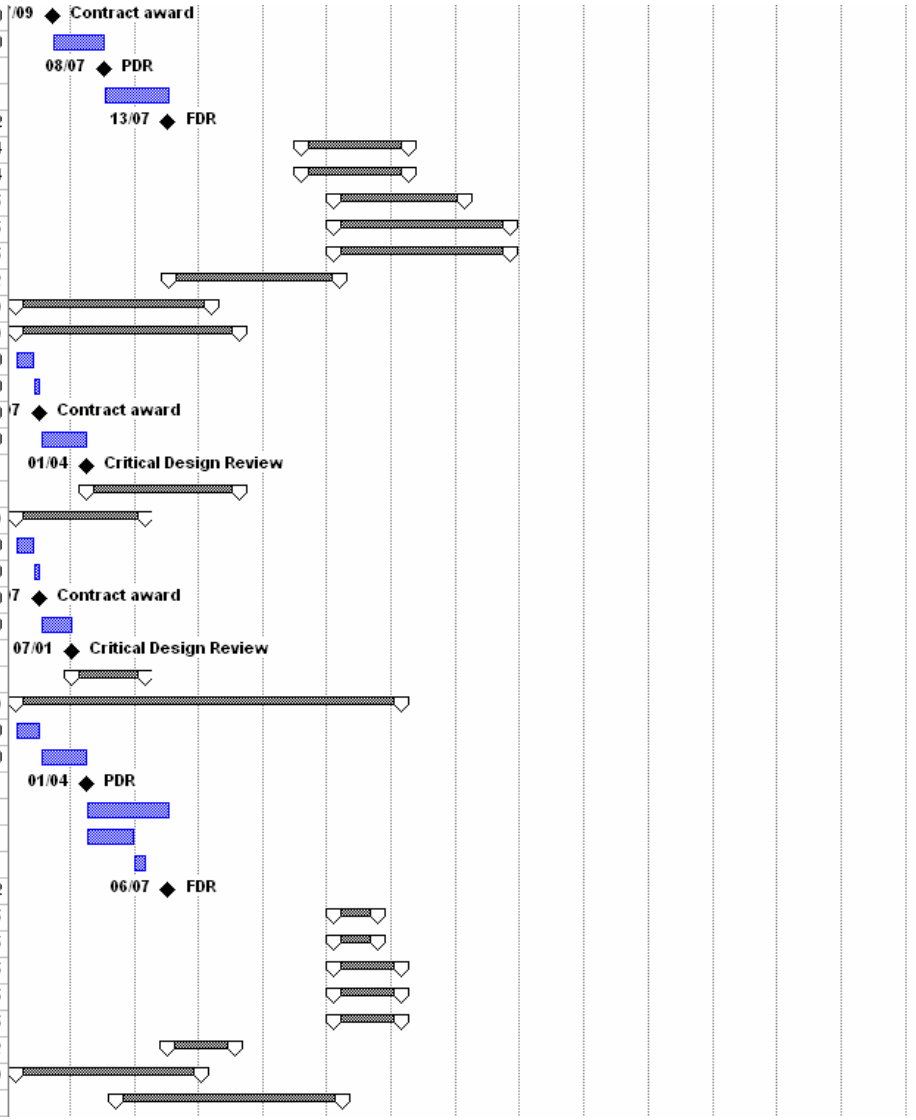

Phase C/D schedule estimate

ID	Prod. Code	Task Name	Duration	Start
2026		**Clean rooms**	**565 days**	**12/09/11**
2033	**089100**	**M1 & M2 offline maintenance facility**	**640 days**	**12/09/11**
2034	**089120**	**Segments washing & coating tanks**	**640 days**	**12/09/11**
2045	**089130**	**Segments carts and transporters**	**620 days**	**12/09/11**
2056	**089140**	**Segments support stands (emergency suppor**	**225 days**	**12/09/11**
2060	**089150**	**Segments racks**	**560 days**	**12/09/11**
2071	**089160**	**Segments storage facility**	**300 days**	**12/09/11**
2078	**089200**	**M1 & M2 in-situ maintenance devices**	**780 days**	**12/09/11**
2079	**089210**	**M1 in-situ cleaning robot**	**780 days**	**12/09/11**
2089	**089220**	**M1 segment assembly in-situ handling robot**	**720 days**	**12/09/11**
2099	**089230**	**M1 cover in-situ cart holder**	**600 days**	**12/09/11**
2109	**089240**	**M2 in-situ cleaning device**	**780 days**	**12/09/11**
2119	**089250**	**M2 segment assembly in-situ handling tool**	**720 days**	**12/09/11**
2129	**089300**	**Corrector maintenance facility**	**670 days**	**12/09/11**
2130	**089310**	**Corrector maintenance hall**	**515 days**	**12/09/11**
2137	**089320**	**Corrector transporters**	**570 days**	**12/09/11**
2145	**089330**	**M3 & M4 subunits extractor**	**515 days**	**16/04/12**
2153	**089340**	**M3 & M4 subunits transporters**	**515 days**	**16/04/12**
2161	**089350**	**M5 subunit extractor**	**515 days**	**12/09/11**
2169	**089360**	**M5 subunit transporters**	**515 days**	**12/09/11**
2177	**089370**	**M6 subunit extractor**	**515 days**	**12/09/11**
2185	**089380**	**M6 subunit transporters**	**515 days**	**12/09/11**
2193	**089400**	**M3 & M4 assemblies maintenance facility**	**770 days**	**16/04/12**
2194	**089410**	**M3 & M4 assemblies maintenance hall**	**515 days**	**16/04/12**
2201	**089430**	**M3 & M4 assemblies lifting device**	**710 days**	**16/04/12**
2211	**089440**	**8-m class washing & coating tanks**	**770 days**	**16/04/12**
2222		**M3 & M4 mirror assemblies washing & coating**	**695 days**	**16/04/12**
2232		**M3 & M4 mirror assemblies support stands (e**	**275 days**	**16/04/12**
2236	**089500**	**M5 & M6 assemblies maintenance facility**	**730 days**	**28/10/11**
2237	**089510**	**M5 & M6 assemblies maintenance hall**	**515 days**	**28/10/11**
2244	**089530**	**M5 mirror assembly lifting device**	**730 days**	**28/10/11**
2254	**089540**	**M6 mirror assembly lifting device**	**730 days**	**28/10/11**
2264	**089550**	**M5 assembly washing & coating cart**	**640 days**	**28/10/11**
2274	**089560**	**M6 assembly washing & coating cart**	**640 days**	**28/10/11**
2284	**089570**	**4-m class washing & coating tanks**	**695 days**	**28/10/11**
2295	**089580**	**M5 mirror assembly support stand (emergenc**	**275 days**	**28/10/11**
2299	**089590**	**M6 mirror assembly support stand (emergenc**	**275 days**	**28/10/11**
2303	**089600**	**Corrector in-situ cleaning devices**	**780 days**	**12/09/11**
2313	**089700**	**Focal stations maintenance facility**	**285 days**	**12/09/11**
2316	**090000**	**Instrumentation**	**2125 days**	**22/02/10**
2317	**091000**	**Technical instrumentation**	**840 days**	**16/08/10**
2318		Final design	265 days	16/08/10

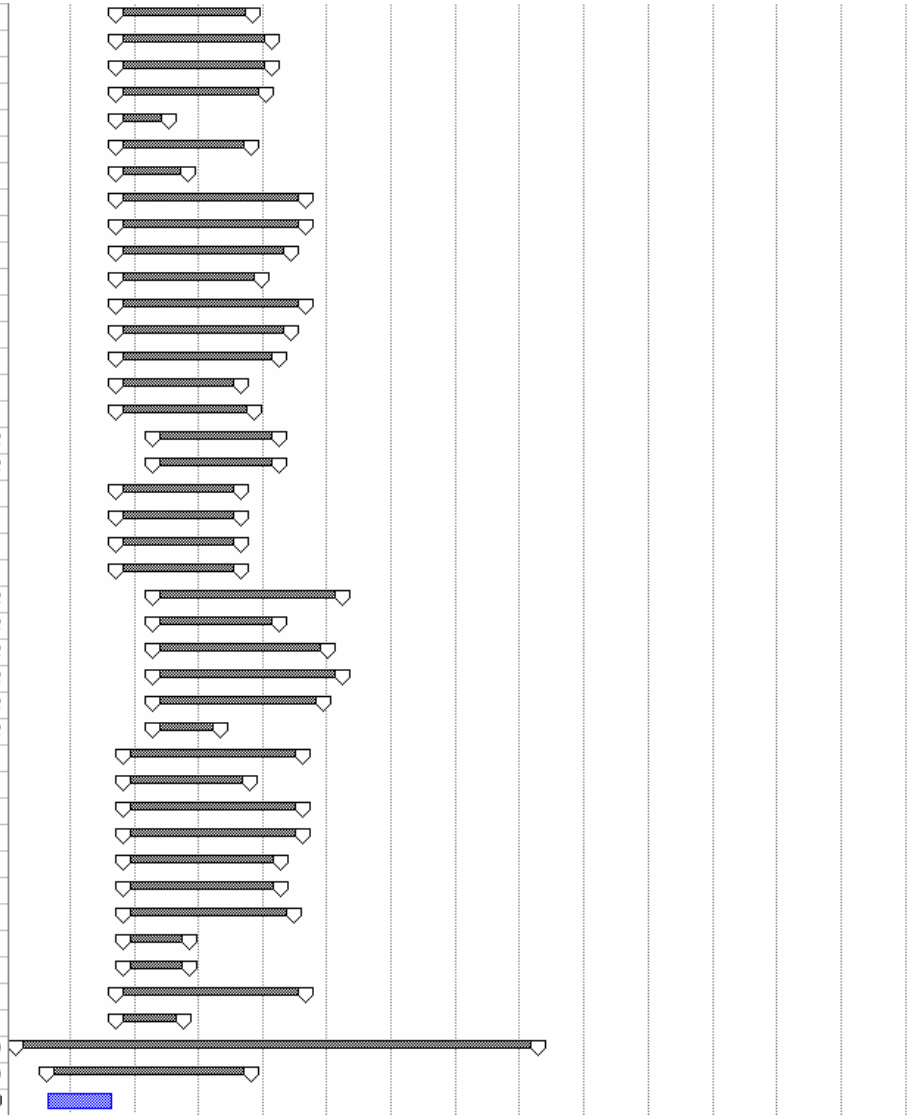

Phase C/D schedule estimate

ID	Prod. Code	Task Name	Duration	Start
2319		FDR	0 days	19/08/11
2320		Construction & testing	530 days	22/08/11
2321		Packing	25 days	02/09/13
2322		Shipment to focal plane electromechanical assemblies con	20 days	07/10/13
2323	**092000**	**Science instrumentation**	**1320 days**	**22/02/10**
2324		**Instrument - 1**	**1320 days**	**22/02/10**
2325		Procurement of critical parts	400 days	22/02/10
2326		Final design	520 days	22/02/10
2327		FDR	0 days	17/02/12
2328		Fabrication	520 days	20/02/12
2329		Integration & testing	190 days	17/02/14
2330		Packing	45 days	10/11/14
2331		Shipment to site	45 days	12/01/15
2332		**Instrument - 2**	**1320 days**	**22/02/10**
2333		Procurement of critical parts	400 days	22/02/10
2334		Final design	520 days	22/02/10
2335		FDR	0 days	17/02/12
2336		Fabrication	520 days	20/02/12
2337		Integration & testing	190 days	17/02/14
2338		Packing	45 days	10/11/14
2339		Shipment to site	45 days	12/01/15
2340	**093000**	**Post-focal AO units**	**1325 days**	**18/03/13**
2341		Preliminary design	265 days	18/03/13
2342		PDR	0 days	21/03/14
2343		CfT for final design, fabrication & testing	100 days	24/03/14
2344		Review of offers	50 days	11/08/14
2345		Award of contract	0 days	17/10/14
2346		Procurement of critical parts	400 days	20/10/14
2347		Final design	265 days	20/10/14
2348		FDR	0 days	23/10/15
2349		Fabrication	400 days	26/10/15
2350		Integration & testing	150 days	08/05/17
2351		Packing	50 days	04/12/17
2352		Shipment to site	45 days	12/02/18
2353	**099000**	**Instruments maintenance facility**	**395 days**	**02/07/12**
2356	**100000**	**Laser Guide Stars Subsystem**	**1415 days**	**18/03/13**
2357	**101000**	**Laser units**	**1325 days**	**18/03/13**
2370	**102000**	**Beam Propagation units**	**1130 days**	**24/03/14**
2383	**103000**	**Control & Metrology units**	**1150 days**	**24/03/14**
2394	**109000**	**LGS maintenance facility**	**775 days**	**24/03/14**
2403	**110000**	**Central Control Systems**	**1420 days**	**11/07/11**
2404	**111000**	**Central Control Environment**	**1420 days**	**11/07/11**

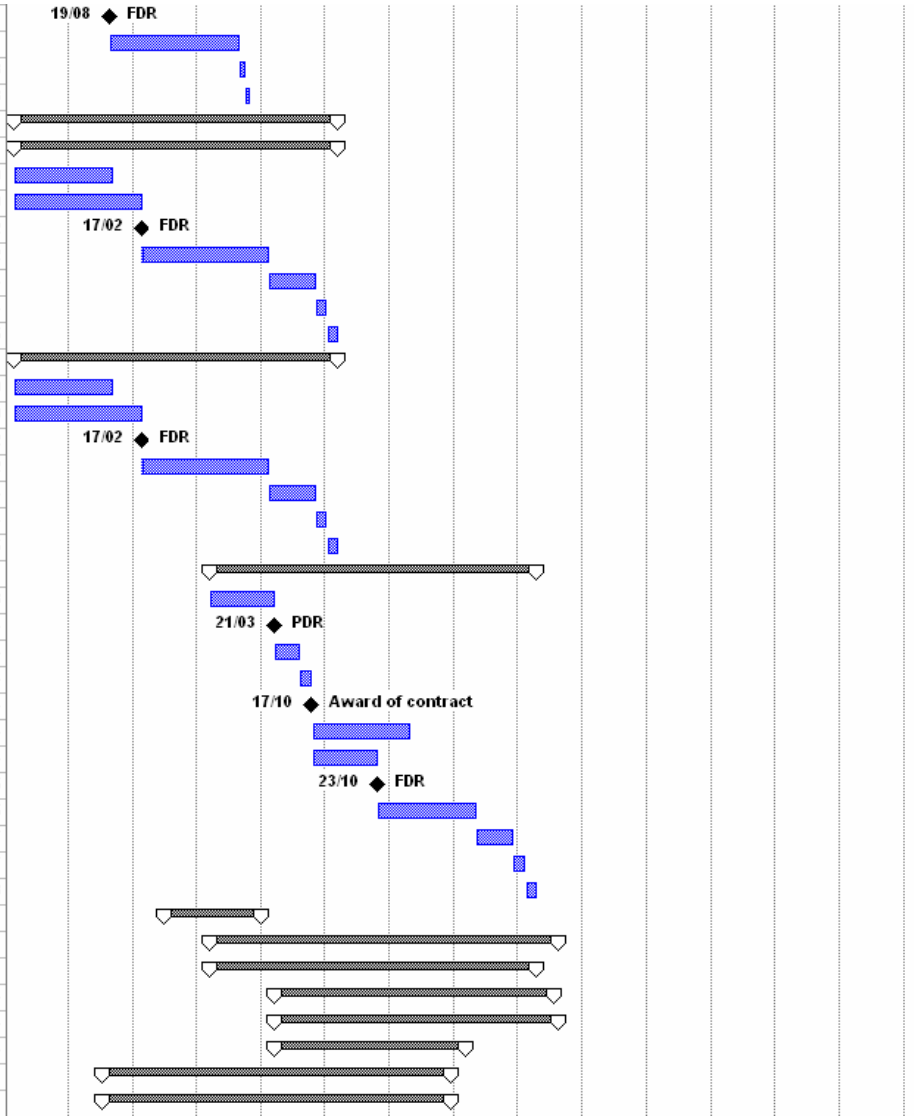

Phase C/D schedule estimate

ID	Prod. Code	Task Name	Duration	Start
2410	**112000**	**IT Systems**	**1180 days**	**05/09/11**
2416	**119000**	**Central Control maintenance facility**	**395 days**	**02/09/13**
2419	**120000**	**Site characterization**	**950 days**	**06/12/10**
2420	**121000**	**Weather stations**	**520 days**	**06/12/10**
2426	**122000**	**Turbulence monitoring units**	**950 days**	**06/12/10**
2435	**123000**	**Sky monitoring units**	**870 days**	**06/12/10**
2444	**124000**	**Operational Forecasts units**	**520 days**	**06/12/10**
2446	**129000**	**Site characterization maintenance facility**	**395 days**	**06/12/10**

Appendix 7. Software tools

	Disciplines	Project domains	Application specialities
ANSYS	Mechanics Civil Eng. Electrical Eng.	System Design System Integration Commissioning Maintenance	FEM Analyses Static, Modal, Thermal, Non Linear Analyses (Buckling, etc.), PSD, Fatique, Transient wind load.
SOLIDWORKS	Mechanics Opto- Mechanics Civil Eng. Electrical Eng.	System Design System Integration Commissioning Maintenance	CAD-CAM Mechanical design Opto-mechanical design Building and foundation design Cable routing. Kinematics simulations Design communication Rendering Drawings Limited FEM Analyses
PDM WORKS	Mechanics Opto- Mechanics	System Design System Integration Maintenance	Product Data Management of CAD Models, Drawings and Documents management
CFX	Mechanics	System Design System Integration	Fluid Dynamics simulations
MATLAB	Mechanics Control AO Active Optics Meteorology	System Design System Integration	Control Simulations Analytical AO simulations Site Characterization
SMI	Control	System Design	Structural Modelling Interface Between ANSYS and MATLAB
SIMULINK	Mechanics Control	System Design System Integration	Control Simulations
MathCad	All.disciplines	System Design System Integration Commissioning Maintenance	Mathematical models and solver.
modeFrontier	Mechanics Opto- Mechanics	System Design	Opto-Mechanical Design Optimisation

	Disciplines	Project domains	Application specialities
	System Eng.		
TBD	Electronics	System Design System Integration Commissioning Maintenance	
TBD	Electrical Eng.	System Design System Integration Commissioning Maintenance	
TBD	Software Eng.	System Design System Integration Commissioning Maintenance	
CODE V	Optics	System Design	Telescope and instrument Optical Design and analyses
ZEMAX	Optics	System Design	Telescope and instrument Optical Design and Analyses
BEAM WARRIOR	System Engineering Optics	System Design	Opto-mechanical analyses
DOORS	System Engineering	System Design System Integration Commissioning Operation Maintenance	System Requirements Managment
Hardware Configuration Control	System Engineering	Integration Commissioning Operation Maintenance	Maintenance, Treceability of parts, and components.
Interactive Data Language	AO Meteorology and Geodesy	System Design System Integration Commissioning	Plotting and EPICS simulations (coronography), Sky Coverage, atmospheric dispersion, simulations. Site Characterization. Meteorological and geothechnical investigation data analysis and visualisation.
C code ESO written	AO Optics Active Optics	System Design System Integration Commissioning	Segmentation error analysis, Difraction analysis. Operation of Active Optics
Fortran code ESO written	Active Optics	System Design	Elastic deformation of meniscus mirrors
PASCAL code ESO written	Optics	System Design System Integration Commissioning	Difraction analysis
MIDAS	Meteorology and Geodesy	System Design System Integration Commissioning	Site Characterization Meteorological and geothechnical investigation data analysis and visualisation.

	Disciplines	Project domains	Application specialities
GEO JAVA based SW	Meteorology and Geodesy	System Design System Integration Commissioning	Site Characterization Meteorological and geothechnical investigation data analysis and visualisation.
Microsoft Project	Project management & Control	System Design System Integration Commissioning	Planning, Schedule and Resource Management; Budget and Cost tracking
NAVISION	Project management & Control	System Design System Integration Commissioning	Project Management; Resource control and planning; Budget Management

Appendix 8.Optical design – criteria and merit function

	Requirement / characteristic	Weight (1-5)	Remarks
	Diffraction-limited FOV	5	Min. 1 arc minute in the visible.
	Total field of view	5	Min. 8 arc minutes.
	Optical quality at edge of field of view	3	Must be seeing-limited.
	Field curvature	3	Convex in the direction of light propagation preferred.
	Focal ratio	3	Optimal range f/6-f/7.
	Maximum monolithic mirror diameter	5	Maximum allowable is 8.3-m.
	Emissivity (number of surfaces)	5	May be alleviated by high performance coatings.
	Sensitivity to M1-M2 decenters	5	Includes image motion and decentering aberrations.
	Sensitivity to M1-M2 axial despace	5	
	Sensitivity to decenters of M3, M4, …	3	Lower weight than for M1-M2 decenters because of (presumed) higher local stiffness.
	Sensitivity to axial despace of M3, M4, …	3	Idem.
	Central obscuration	3	
	Vignetting in the science field	5	
	Vignetting outside the science field	2	Relevant for wavefront sensing; generous tolerances if several references & wavefront sensors available.
	M1-M2 separation	5	Ideally ≤ aperture diameter
	Structure aspect ratio	4	Ideal structure is (presumably) a cone with 60 degrees angle.
	Built-in IR adaptive optics (SCAO & GLAO)	5	
	Built-in IR MCAO	5	
	Separation of active and adaptive functions in different units (correctors)	5	Large amplitude, low temporal frequency (Active Optics) would over-constrain the adaptive mirror technology.
	SCAO / GLAO mirror dimensions	5	Assumed optimum ~2-3m.
	MCAO mirror(s) dimensions	5	Assumed optimum ~2-3m.
	Intermediate focus for AO calibration	2	On-sky calibration is an alternative, albeit an undesirable one.
	Number of segmented mirrors	4	
	Feasibility of secondary mirror	5	Includes test set-up feasibility.
	Difficulty of fabricating most aspheric mirror(s)	4	
	Compatibility with serial production & maintenance of segments	5	
	Segments optical testing	4	Ideally against one unique reference.
	Compatibility with lightweight segments	3	
	Baffling options	2	
	Allowable design volume for active/adaptive units	2	
	Allowable design volume for instruments	3	

	Requirement / characteristic	Weight (1-5)	Remarks
	Access to gravity-stable platform(s)	3	For critical instrumentation.
	Rapid switch between permanently mounted instruments possible	2	For minimum overheads and maximum operational flexibility.

Table A- 4. Function of merit, criteria and relative weights.

	Objective / guideline
1.	Diffraction-limited (Strehl Ratio ≥ 0.80, λ=0.5μm) over at least 1 arc minute FOV.
2.	Field aberrations over the science field (3 arc minutes diameter) shall be axisymmetrical or negligible.
3.	The field of view (diameter) available for adaptive optics wavefront sensing shall be 6 arc minutes.
4.	The design shall provide suitable surfaces for active optics, including deformable mirror(s), active centring, focusing, and field stabilization
5.	Monolithic mirrors shall be less than 8.3m in diameter (useful area).
6.	Field stabilization shall be done in a pupil image
7.	The design shall provide a suitably located surface for single-conjugate IR SCAO and GLAO.

Table A- 5. Mandatory requirements.

	Requirement / characteristic	Ratings
1	Diffraction-limited FOV	0: fails to meet requirements 1: 60 arc seconds diameter 2: 90 arc seconds diameter 3: 120 arc seconds diameter 4: 150 arc seconds diameter 5: 180 arc seconds diameter or more.
2	Total field of view (0.1 arc seconds RMS image quality or unacceptable vignetting, whichever comes first)	0: Less than 6 arc minutes 1: Up to 7 arc minutes 2: Up to 8 arc minutes 3: Up to 9 arc minutes 4: Up to 10 arc minutes 5: Up to 11 arc minutes or more.
3	Optical quality at edge of field of view	0: Larger than 0.2 arc second RMS diameter 1: Up to 0.15 arc second RMS diameter 2: Up to 0.10 arc second RMS diameter 3: Up to 0.08 arc second RMS diameter 4: Up to 0.06 arc second RMS diameter 5: Up to 0.04 arc second RMS diameter
4	Field curvature	0: Up to 1.5-m 1: Up to 2-m 2: Up to 3-m 3: Up to 4-m 4: Up to 6-m 5: 10-m or more NB: subtract one point if concave in the direction of light propagation.
5	Focal ratio	0: Less than f/3 or more than f/10 1: Less than f/4 or more than f/9 2: Less than f/5 or more than f/8 3: Less than f/5.5 or more than f/7.5 4: Less than f/6 or more than f/7 5: Between f/6 and f/7
6	Maximum monolithic mirror diameter	0: Larger than 8.3-m 1: Up to 8.3-m 2: Up to 7.0-m 3: Up to 6.0-m 4: Up to 5.0-m 5: Up to 4.0-m
7	Emissivity (number of surfaces)	0: 9 surfaces or more 1: 8 surfaces

	Requirement / characteristic	Ratings
		2: 7 surfaces 3: 6 surfaces 4: 5 surfaces 5: 4 surfaces
8	Sensitivity to M1-M2 decenters	Qualitative; representative of image motion and decentering aberration induced by gravity load z=0 to z=60 degrees
9	Sensitivity to M1-M2 axial despace	Qualitative; representative of defocus induced by gravity load z=0 to z=60 degrees.
10	Sensitivity to decenters of M3, M4, …	Qualitative; representative of the effect of gravity load from z=0 to z=60 degrees, taking into account combined motion of mirrors.
11	Sensitivity to axial despace of M3, M4, …	Qualitative; representative of defocus induced by gravity load z=0 to z=60 degrees.
12	Central obscuration	0: More than 50% (linear) 1: 40% or more 2: 30% or more 3: 20% or more 4: 10% or more 5: Less than 10%
13	Vignetting in the science field	0: More than 10% (linear) 1: More than 8% 2: More than 6% 3: More than 4% 4: More than 2% 5: Less than 2%
14	Vignetting outside the science field	0: 50% of more 1: More than 40% 2: More than 30% 3: More than 20% 4: More than 10% 5: Up to 10% Add one score point if 3 wavefront sensors, 2 points if 5 or more.
15	M1-M2 separation	0: More than 1.4 x D 1: Up to 1.3 x D 2: Up to 1.2 x D 3: Up to 1.1 x D 4: Up to 1.0 x D 5: Up to 0.9 x D
16	Structure aspect ratio	Qualitative; ideal structure is (presumably) a cone with 60 degrees angle.
17	Built-in IR adaptive optics (SCAO & GLAO)	0 : none or SCAO only (inappropriate conjugate for GLAO) 3: SCAO & some (non-optimal) GLAO capability 5: SCAO & GLAO
18	Built-in IR MCAO	0: No MCAO 3: Two-layers with optimal (~7-9 km) 2nd conjugate 5: Three-layers with optimal conjugates
19	Separation of active and adaptive functions in different units (correctors)	0: No separation 3: Active and adaptive functions with different subsystems 5: Field stabilization, active and adaptive functions with different subsystems.
20	SCAO / GLAO mirror dimensions	0: Less than 1-m or more than 4-m 1: Less than 1.2-m or more than 3.8-m 2: Less than 1.4-m or more than 3.6-m 3: Less than 1.6-m or more than 3.4-m 4: Less than 1.8-m or more than 3.2-m 5: Between 2 and 3-m
21	MCAO mirrors dimensions	0: Less than 1-m or more than 4-m 1: Less than 1.2-m or more than 3.8-m 2: Less than 1.4-m or more than 3.6-m 3: Less than 1.6-m or more than 3.4-m 4: Less than 1.8-m or more than 3.2-m 5: Between 2 and 3-m
22	Intermediate focus for AO calibration	0: None 3: Yes, requires aberrations compensation 5: Yes, does not require aberration compensation
23	Number of segmented mirrors	0: More than two

	Requirement / characteristic	Ratings
		3: Two 5: One
24	Feasibility of secondary mirror	Qualitative; includes test set-up feasibility.
25	Difficulty of fabricating most aspheric mirror(s)	Qualitative; includes test set-up feasibility.
26	Compatibility with serial production & maintenance of segments	Qualitative.
27	Segments optical testing	Qualitative.
28	Compatibility with lightweight segments	0: No; 5: Yes.
29	Baffling options	From 0 (none) to 5 (excellent baffling options)
30	Allowable design volume for active/adaptive units	Qualitative
31	Allowable design volume for instruments	Qualitative
32	Access to gravity-stable platform(s)	5: Coude focus 4: Nasmyth-type focus (foci) 0: None of the above.
33	Rapid switch between permanently mounted instruments possible (without additional relay optics).	5: Yes, 6 instruments or more. 4: Yes, 5 instruments 3: Yes, 4 instruments 2: Yes, 3 instruments 1: Yes, 2 instruments 0: No, only one instrument permanently mounted.

Table A- 6. Merit function; guidelines for ratings.

Appendix 9. Optional corrector

The optical prescription is given in Table A- 7. The primary and secondary mirrors have the same prescription as in the baseline design.

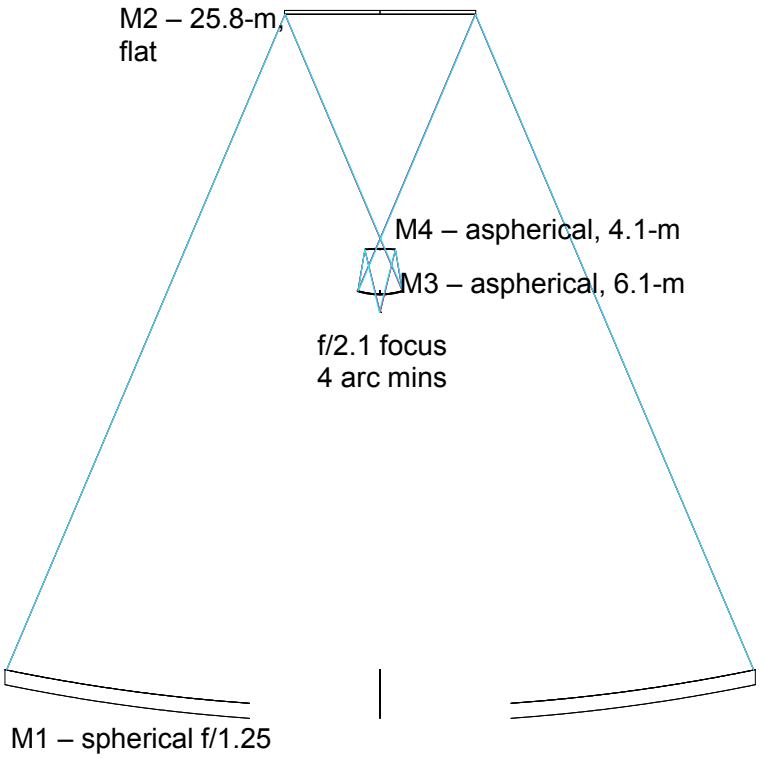

Figure A- 10. Optional two-mirror corrector (f/2.1 focus, 4 arc minutes total field of view).

Surface M4 can be used for tip-tilt correction albeit at a reduced frequency in view of its size. Fast (≥ 1 Hz) correction of image motion would have to be provided in the instrument and in the wavefront sensors.

Image quality at the f/2.1 focus is seeing-limited (0.15 arc seconds RMS) at the edge of the 4 arc minutes field. In principle, only the central one arc minute would be used for science, the field outside one arc minute being essentially for adaptive and active optics sensing. Figure A- 11 gives the Strehl Ratio at different wavelengths rom 2.2 to 10 μm, and Figure A- 12 provides the optical quality over the entire field of view.

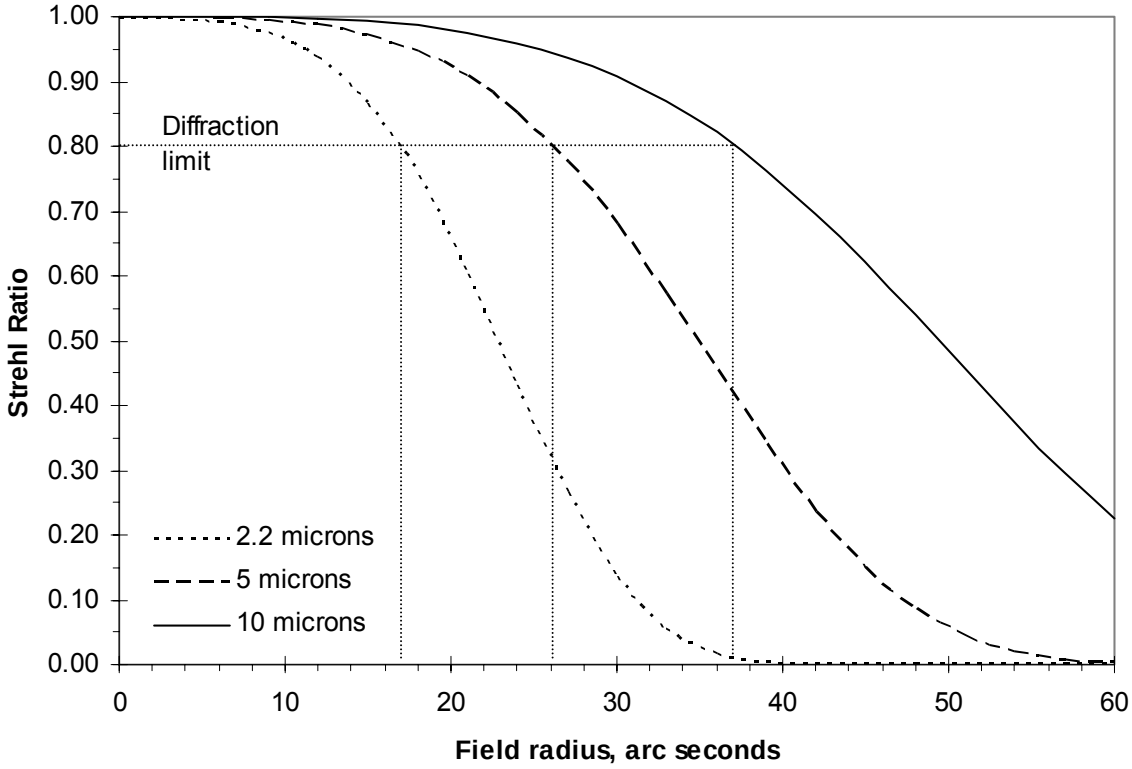

Figure A- 11. Optional corrector; Strehl Ratio vs field radius.

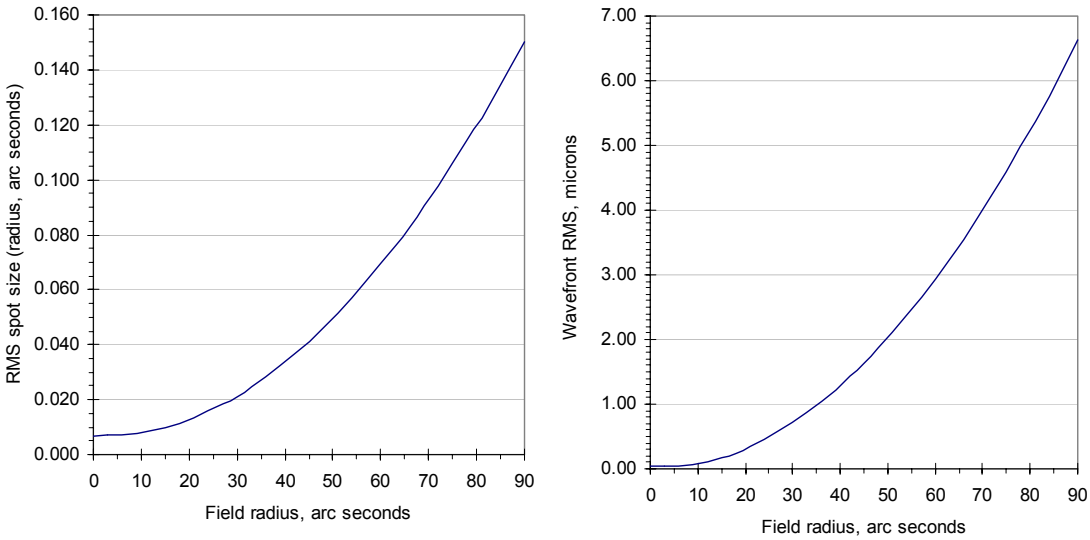

Figure A- 12. Optional corrector; RMS spot size, RMS wavefront error vs. field radius.

System/Prescription Data

```
File : OWL-1250-92518-100m-OPTIONAL_CORRECTOR_2.ZMX
Surfaces                :               8
Stop                    :               2
System Aperture         : Entrance Pupil Diameter = 100000
Effective Focal Length  :       -208928.6 (in image space)
Back Focal Length       :        236757.9
Total Track             :         92517.5
Working F/#             :        2.093617
Stop Radius             :           50000
Entrance Pupil Diameter :          100000
Entrance Pupil Position :         92517.5
Exit Pupil Diameter     :        4451.553
Exit Pupil Position     :       -9301.553
Field Type              : Angle in degrees
Maximum Radial Field    :         0.03333
Primary Wavelength      :               5 µm
Lens Units              :   Millimeters
```

SURFACE DATA SUMMARY:

Surf	Type	Radius	Thickness	Glass	Diameter	Conic
OBJ	STANDARD	Infinity	Infinity		0	0
1	STANDARD	Infinity	92517.5		100101.8	0
STO	STANDARD	-250000	-92517.5	MIRROR	100000	0
3	STANDARD	Infinity	31312	MIRROR	25599.08	0
4	STANDARD	Infinity	5995.9		1362.146	0
5	EVENASPH	-10004	-5995.9	MIRROR	6090.72	0.9151138
6	EVENASPH	15900	5995.9	MIRROR	4101.446	-1.239024
7	STANDARD	Infinity	2424.224		1364.185	0
IMA	STANDARD	6050.087			244.9009	0

SURFACE DATA DETAIL:

```
Surface OBJ     : STANDARD
Surface   1     : STANDARD M2 OBSCURATION
 Aperture       : Circular Aperture
 Minimum Radius :         15000
 Maximum Radius :         51000
Surface STO     : STANDARD M1
 Aperture       : Circular Aperture
 Minimum Radius :         17500
 Maximum Radius :         50200
Surface   3     : STANDARD M2
Surface   4     : STANDARD HOLE M4
Surface   5     : EVENASPH M3
 Coeff on r  2  :                0
 Coeff on r  4  :   6.7373593e-013
 Coeff on r  6  :  -8.5515616e-020
 Coeff on r  8  :   1.1646497e-026
 Coeff on r 10  :  -1.0944848e-033
 Coeff on r 12  :   6.5980757e-041
 Coeff on r 14  :  -2.2477154e-048
 Coeff on r 16  :   3.2455245e-056
Surface   6     : EVENASPH M4
 Coeff on r  2  :                0
 Coeff on r  4  :  -2.6703784e-012
 Coeff on r  6  :   4.2436167e-021
 Coeff on r  8  :   2.7130365e-026
 Coeff on r 10  :  -2.0785384e-032
 Coeff on r 12  :   6.4138293e-039
 Coeff on r 14  :  -9.3103508e-046
 Coeff on r 16  :   5.2806034e-053
Surface   7     : STANDARD HOLE M3
Surface IMA     : STANDARD IMAGE
```

Table A- 7. Optional corrector, optical prescription.